SP-475

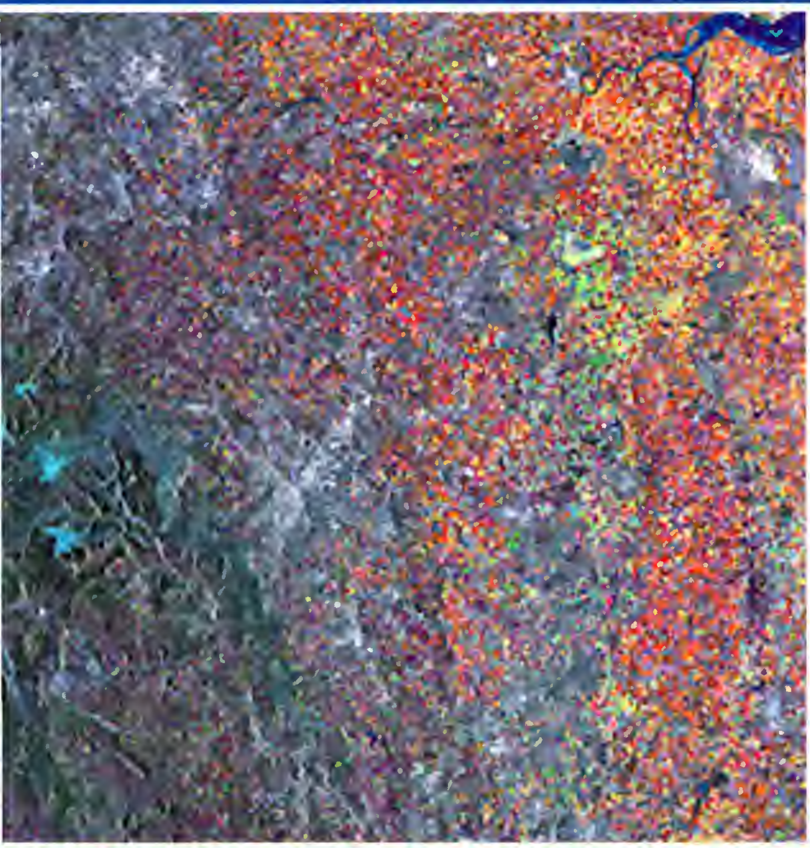

Proceedings
Third International Symposium

Retrieval of Bio- and Geophysical Parameters from SAR Data for Land Applications

11-14 September 2001
Sheffield, UK

European Space Agency
Agence spatiale européenne

SP-475
January 2002

Proceedings of the

Third International Symposium on

Retrieval of Bio- and Geophysical Parameters from SAR Data for Land Applications

11-14 September 2001
Sheffield Centre for Earth Observation Science
University of Sheffield, UK

European Space Agency
Agence spatiale européenne

Publication	Proceedings of the 3rd International Symposium on 'Retrieval of Bio- and Geophysical Parameters from SAR Data for Land Applications' SCEOS, University of Sheffield, UK (ESA SP-475, January 2002)
Edited by	A. Wilson ESA Publications Division
Scientific Coordination by	S. Quegan SCEOS, University of Sheffield
Published and distributed by	ESA Publications Division ESTEC, Noordwijk, The Netherlands
Printed in	The Netherlands
Price	130 Dutch Guilders / EUR 60
ISBN	92-9092-741-0
ISSN	0379-6566

CONTENTS

Foreword xi

S. Quegan

Forests

Chairmen: J. Askne

Keynote
On the Relationships between Radar Measurements and Forest Structure and Biomass 3
T. Le Toan et al.

Forest Stem Volume Retrieval with VHF-Band SAR 13
G. Smith et al.

Biophysical Forest Type Characterisation in the Colombian Amazon by Airborne Polarimetric SAR 19
D.H. Hoekman & M.J. Quiñones

Biomass Mapping using Biophysical Forest Type Characterisation of SAR Polarimetric Images 25
M.J. Quiñones & D.H. Hoekman

JERS Repeat Pass Coherence for Observation of Siberian Forest 33
L. Eriksson, A. Wiesmann & C. Schmullius

Large Area Boreal Forest Investigations using ERS InSAR 39
J. Askne et al.

Agriculture and Land Cover

Chairmen: H. Skriver

Keynote
SAR for Agriculture: Advances, Problems and Prospects 47
P. Ferrazzoli

High Resolution Measurements of Scattering in Wheat Canopies – Implications for Crop Canopy Retrieval 57
S.C.M. Brown et al.

Assessment of Crop Discrimination using Multi-site Databases 63
M.C. Gonzalez-Sampedro et al.

ERS SAR Tandem Data for Crop Discrimination and Irrigation Monitoring in Southeast Spain 69
T. Pearson et al.

Comparison of Hymap/E-SAR Data with Models for Optical Reflectance and Microwave Scattering from Vegetation Canopies 75
P. Saich et al.

Merging Unmixed Landsat TM Data in a Semi-Empirical SAR Model for the Assessment of Herbaceous Vegetation Biomass in a Heterogeneous Environment 81
T. Svoray & M. Shoshany

Operational Control with Remote Sensing of Area-based Subsidies in the Framework of the Common Agricultural Policy: What Role for the SAR Sensors? 87
X. Blaes et al.

The Potential of SAR in Crop Classification using Multi-Configuration Data 93
F. DelFrate et al.

Systematic Investigation on the Effect of Dew and Interception on Multifrequency and Multipolarimetric Radar Backscatter Signals 99
T. Riedel et al.

Land-Cover Map Information from Polarimetric SAR using Knowledge-based Techniques 105
H. Skriver

Detecting Anthropogenic and Natural Disturbances in Wetland Ecosystems with Multitemporal ERS 2 Data 111
J.M. Martinez et al.

ESA Co-ordination for the Scientific Exploitation of ERS and Envisat Data 117
S. Rémondière et al.

Hazards and DTM

Chairman: G. Wadge

Keynote
Seismic Faults Analysis in California by Means of the Permanent Scatterers Technique 125
C. Colesanti et al.

Hazard Mapping with Multi-temporal SAR and InSAR 133
A. Wiesmann et al.

On the Use of RADARSAT-1 for Monitoring Malaria Risk in Kenya 139
S.G. Ross et al.

JERS-SAR Interferometry for Land Subsidence Monitoring 145
T. Strozzi et al.

Extraction of Surface Topography from SAR Stereo Pairs using an Airborne X-band Sensor: Preliminary Results 151
A. Schubert et al.

Soils and Hydrology

Chairman: M. Davidson

Surface Parameter Estimation using Fully Polarimetric L- and P-band Radar Data 159
I. Hajnsek et al.

Remote Measurement of the Evaporation of Groundwater from Arid Playas 165
G. Wadge & D.J. Archer

The Pyla Dune Experiment: Sub-surface Moisture Detection by Combining GPR and Airborne SAR 171
Ph. Paillou et al.

The Influence of *a priori* Information on Soil Moisture Retrieval from SAR Data 177
G. Satalino et al.

Snow and Ice

Chairman: H. Rott

Keynote
Progress and Challenges in Radar Remote Sensing of Snow 185
M. Hallikainen et al.

Process Modelling

Chairman: A. Rosenqvist

Keynote
Remote Sensing Data Assimilation in Land Surface Process Modelling 195
H. Bach & W. Mauser

What Can Radar Remote Sensing do for Improving our Knowledge of the Global Carbon Cycle? 205
W. Wagner

Systematic Data Acquisitions – A Pre-requisite for Meaningful Biophysical Parameter Retrieval? 211
A. Rosenquvist

Embedding Remote Sensing Data in Models for Forest Carbon Dynamics 215
S. Quegan & T. Le Toan

Posters: Agriculture, Land Cover and Hazards

Assessing Land Features in Semi-Arid Regions from Multi-Temporal SAR Data 223
M. Bianchini et al.

Potential Contribution of ENVISAT ASAR Alternating Polarisation and Wide-Swath Modes Images for Crop Discrimination at the Regional Scale 227
X. Blaes et al.

Farm Crop and Agri-Environment End-User Requirements for Remote Sensing 233
P.M.R. Dampney et al.

Monitoring Crop Cycles by SAR using a Neural Network Trained by a Model 239
F. Del Frate et al.

Multitemporal INSAR in Land-Cover Classification 245
M.E. Engdahl & J. Hyyppä

Upscaling Water Cycle Parameters using Geomorphometric Terrain Parameters and Topographic Indices Derived from Interferometric DEM 251
N. Etzrodt, R. Zimmermann & O. Conrad

Change Detection in Multisensor Remote-Sensing Data for Desertification Monitoring 255
D. Fernández Prieto

Using Very High Resolution Data to Assess the Limitations of Polarimetric Interferometry for Height Measurement 261
J. Gomez Dans et al.

Acquisition and Evaluation of Field Measurements from the Alling-SAR 2000 Campaigns 267
M. Herold et al.

A Priori Accuracy Assessment of the DEM Derived by InSAR 273
C. Lucau et al.

Radar and Ground Measurements on Wheat Fields over the Matera Site: An Experimental Study 279
F. Mattia et al.

Influence of Diurnal Variations of Surface Wetness on Classification of Agricultural Crops using Multi-Parametric E-SAR Data with Respect to Future TerraSar Applications 285
C. Pathe et al.

A Backscatter Model for Wheat Canopies. Comparison with C-band Multiparameter Scatterometer Measurements 291
G. Picard et al.

Scene Understanding for Settlements from Metric Resolution Data 297
M. Quartulli & M. Datcu

Multi-baseline Airborne Pol-InSAR Measurements for the Analysis and Inversion of Scattering Processes within Vegetation Media 301
O. Stebler, E. Meier & D. Nuesch

Potential Roles for Space-borne SAR in Disaster Management and Humanitarian Relief 307
U. Wegmüller et al.

Posters: Forestry, Soils and Snow & Ice

Retrieving Surface Roughness and Soil Moisture from SAR Data using Neural Networks 315
N. Baghdadi, S. Gaultier & Ch. King

Forest Stand Structure from Airborne Polarimetric InSAR 321
H. Balzter et al.

Monitoring of Soil Moisture and Rain Precipitation's with In-situ Measurements and ERS C-band Radar Backscattering Data 327
M. Borgeaud et al.

The Glen Affric Project: Forrest Mapping using Dual Baseline Polarimetric Radar Interferometry 333
S.R. Cloude et al.

Extraction of Surface Parameters from SAR Data using Polarimetric Descriptors 339
L. Ferro-Famil, S. Allain & E. Pottier

A Comparison between Laser, Needle-like and Meshboard Techniques for Soil Roughness Measurements 345
A.M. Gatti et al.

Subsurface Imaging with Low Frequency SAR: Field Validation in Egypt using a Ground-penetrating Radar 351
G. Grandjean et al.

Derivation of Land Cover and Soil Moisture from Airborne Polarimetric SAR-Data 355
V. Hochschild, C. Thiel & S. Grünler

LAI-Estimation of Boreal Forests using C-Band VV and HH Polarization Radar Images 359
T. Manninen et al.

On the Information Content of L-band Polarimetric SAR Data over Forested Areas 365
P. Melon et al.

The Applicability of C-band SAR and Optical Data for Snow Monitoring in Boreal Forest 371
S. Metsamaki et al.

Feasibility of DINSAR for Mapping Complex Motion Fields of Alpine Ice- and Rock-Glaciers 377
T. Nagler, C. Mayer & H. Rott

Assessment of InSAR Tree Mapping Accuracy in Tropical Rain Forests 383
K. Prakoso

Remote Sensing of Boreal Forest with Polarimetric L- and C-band SAR 389
J. Praks & M. Hallikainen

Empirical Assessment and Modeling of Topographic Induced Variations in the Radar Backscattering from Different Vegetation Formations in Mediterranean Environment 395
M. Shoshany & T. Svoray

SAR Monitoring for Tropical Forest in Indonesia 399
R.A. Sugardiman

Estimating Soil Moisture in Rainfed Paddy Fields using ERS-2 C-band SAR Data 403
D. Ugsang et al.

Conclusions 409
S. Quegan

List of Participants 415

Foreword

FOREWORD

S. Quegan – Symposium Chairman

Sheffield Centre for Earth Observation Science, University of Sheffield, Hicks Building, Hounsfield Rd, Sheffield S3 7RH, UK.
Tel: +44 114 222 3778 Fax: +44 114 222 3809 Email: S.Quegan@sheffield.ac.uk

The Third International Symposium on "Retrieval of Bio- and Geophysical Parameters from SAR Data for Land Applications" began on September 11, 2001. This was not the best of days. Towards the end of the afternoon, news from New York begin to filter into the meeting, bringing with it questions of reality and importance. And throughout the week, always close to the surface, was an awareness of events unfolding in a bleakened world. The mood of the meeting was, however, that when intimidation brings normal life to a halt, intimidation wins. That is not acceptable.

In recent years, interest in SAR data for land applications has experienced tremendous growth, for a range of reasons:

- the ready availability of SAR data acquired by spaceborne sensors (ERS-1/2, SIR-C/X-SAR, RADARSAT-1, JERS);
- the imminence of new space sensors (Envisat, ALOS-PALSAR);
- new data from airborne sensors (e.g., the DLR E-SAR, the TUD EMISAR, CARABAS);
- significant advances in scattering theory;
- the increasing maturity of existing techniques (e.g., SAR interferometry);
- the emergence of new techniques (e.g., polarimetric interferometry).

In addition, important progress has been made over the three years since the last Symposium in this series, held in ESTEC, in understanding how to assimilate SAR data into process modelling. The main purposes of the Symposium were therefore to provide an overview of these developments, to crystallise the state-of-the-art in retrieving biophysical and geophysical parameters using SAR data, and to show how this enhances our understanding of land surface processes.

In total, 80 papers were presented in the oral and poster sessions. The make-up of these presentations tells us a lot about the main thrusts of recent work: 31% were concerned with agriculture and land cover, 23% were on forestry, 20% dealt with soils and hydrology, 13% were about hazards and DEMs (lumped together because of the importance of interferometry in many of the papers for both applications), 7% were on snow and ice and 5% explicitly considered the use of SAR in process models. This is probably fairly representative of the distribution of effort world-wide, despite western European researchers having the largest presence at the Symposium (although there were attendees from the US, Canada, Argentina, Australia, Russia, Japan, Israel and Thailand). An obvious exception is the lack of papers on geology and geomorphology, where SAR certainly has an impact.

By design, the Symposium did not contain papers on instruments, methodology or satellite programmes, except where these were seen as central to developing applications. Nonetheless, the types of sensor and technique encountered during the Workshop were very diverse (interferometry, multitemporal analysis, polarimetry and polarimetric interferometry, multi-frequency, VHF, combination of sensors, backscatter modelling, interfacing SAR data with other data sources and process modelling).

Overall, the Symposium provided a snapshot of where we currently stand in exploiting SAR data to understand geophysical and biophysical processes. It identified important areas for future research, in terms of specific problems and general trends. Getting so many active workers together in a focussed but informal atmosphere allowed easy exchange of ideas and productive discussion. However, perhaps the most lasting contribution will be the papers in these Proceedings. Like those from the ESTEC meeting in 1998 and the Toulouse meeting in 1995, they provide an invaluable statement of our current understanding. They also form a baseline from which to measure our progress when we meet at the next Symposium in Innsbruck in 2004.

Forests

Chairman: J. Askne

ON THE RELATIONSHIPS BETWEEN RADAR MEASUREMENTS AND FOREST STRUCTURE AND BIOMASS

Thuy Le Toan, Ghislain Picard, Jean-Michel Martinez , Pierre Melon and Malcolm Davidson

Centre d'Etudes Spatiales de la Biosphère
CNES, CNRS, Université Paul Sabatier
18 Avenue Edouard Belin, Toulouse cedex 4, 31401 France
tel: +33 561 556671/ fax: ++33 561 558500/ email: Thuy.Letoan@cesbio.cnes.fr

ABSTRACT

This paper examines the information content of SAR data with respect to the retrieval of two categories of forest information of interest, for which radar data play a major role compared to ground measurements and other remote sensing methods. Those are forest vertical structure and forest biomass.

The physical background will be discussed in terms of the relationships between the forest parameters and the SAR measurements at different polarisations , incidence angles and frequencies (X, C, L, P and VHF bands). This will include results from experiments carried out to investigate these relations, and the development of modelling approaches to interpret and extend the observations.

Illustrations with spaceborne SAR data (ERS, ERS tandem InSAR, JERS, RADARSAT), and airborne data (AIRSAR, ESAR, CARABAS, HUTSCAT) will be presented.

INTRODUCTION

The need for systematic assessment of forest areal extent, forest structure and forest biomass has become important at global and regional scales, since the forest ecosystem status as a net sink or source of carbon needs to be assessed, e.g. for the purposes of implementing the Kyoto protocol requirements. For systematic observations at different scales, remote sensing is considered as a component of forest monitoring programmes. The focus to date, however, has mainly been on the use of optical data. Meanwhile, research results indicate that Synthetic Aperture Radars (SARs) has a significant role to play in forest observations.

Satellite SAR data have been continuously available since 1991, provided by ERS-1 and ERS-2, JERS and RADARSAT. Planned future systems such as ENVISAT ASAR (2002), RADARSAT II (2003) and ALOS-PALSAR (2004) will ensure operational data provision well into the next decade. Advanced airborne systems have also been developed to explore new possibilities for surface parameter retrieval. Before the operational use of radar data in forest monitoring programmes, the real extent to which SAR observations can contribute to the requirements of environmental science and forest management needs to be assessed.

FOREST INFORMATION REQUIREMENTS

The interest in using radar remote sensing for monitoring forest cover raises from the two following assets of radar data. The first is that radars can provide information related to the canopy volume, which cannot be collected by other means. These have been identified as: above ground biomass , annual increment of stand biomass, and vertical distribution of biomass. The other advantage of radars is the possibility to acquire data over areas with frequent cloud or haze coverage, and the possibility to acquire data during and rapidly after events such as fires or storms.

The forest information covers a large range of requirements in terms of information accuracy and spatial resolution. Very high resolution and accurate forest vertical structure are needed in ecophysiology, biodiversity or forestry practices. At the other end, global mapping of coarse classes of biomass is required in estimates of the carbon budget at a global scale.

This paper will focus on the assessment of the capability of SAR data to provide information on the canopy volume. A non exhaustive summary of the relationships between forest parameters and radar measurements will be presented. First, the physical background gained from modelling work is summarised. Secondly, the relations between radar measurements and forest vertical structure and forest above ground biomass are discussed in the light of the physical background. The paper will not discuss polarimetric and polarimetric interferometry, due to the lack of fully validated physical models.

MODELLING APPROACH

Radar backscatter models of forests are important to understand the various influences of forest properties and environment conditions on the radar backscatter, to interpret the imagery, to determine basis for robust methods of mapping of forest covers and retrieving of forest parameters, and also to investigate the performance and the use of new sensors and to define optimum future sensors.

Numerous models have been published in the literature. The models differ basically in two respects : the characterisation of forest and the calculation of its scattering properties.

Proc. 3rd International Symposium, 'Retrieval of Bio- and Geophysical Parameters from SAR Data for Land Applications', Sheffield, UK, 11-14 September 2001 (ESA SP-475, January 2002)

Characterisation of the forest :
The question to be addressed in the description of the forest is how the radar systems see the forest. In the frequency range from P band to X band, the wavelengths are of the same order of magnitude as the dimensions of the forest elements which interact with the wave.

Frequency band	X	C	L	P	VHF
Main scatterers	Leaves, Twigs	Leaves Small branches	Branches	Branches & Trunk	Trunk

Table 1: Tree elements which are the main scatterers at different frequency bands

In a first approach, the tree elements that play a major role in the scattering and attenuation at different frequency bands are summarised in table 1. However, the relative contribution of different components may change with the tree species and their development state. Likewise, at a given frequency, the scattering and attenuation sources can change with the polarisation and incidence angle.
Since the forest is a very complex medium, in most models, the characterisation of the forest was simplified according to the frequency, polarisation and incidence angle to be addressed and according to the related assumptions on the importance of the forest elements in the scattering.
One of the earliest models was the water cloud model, developed by Attema and Ulaby (1978). In this model, the vegetation canopy was treated as a cloud of spherical droplets, characterised by the total water content, and the ratio of the droplets' backscattering cross sections to their attenuation cross section. At high frequencies it may be appropriate to treat a forest as a cloud. At lower frequencies, where larger scatterers which are the trunks and branches become important, it is necessary to consider their shapes, size and orientation distributions.
In scattering models, the forest has been described by a homogeneous horizontal layer over a reflecting surface (Attema and Ulaby 1978), by multi-layers (Ulaby et al. 1990, Karam et al. 1992), multilayers with gaps (Mc Donald and Ulaby, 1993) and by a set of geometric shapes representing the tree crowns (Sun and Ranson 1995).
The parameters which are inputs to the scattering models have been characterised in different ways.
The first category of forest description models is based upon allometric equations to characterise geometric properties. These equations could be found in literature as well as through direct measurement of the trees in the study area. Sun and Ranson (1995) and Wang et *al.* (1993) have used allometric equations to derive geometric properties of scatterers but also tree crown structures described through a simplified geometrical shapes, such as spherical, ellipsoidal or conical, depending on tree species. However, it is difficult to acquire a realistic and accurate forest description, e.g. for coherent models where scatterer relative positions are needed. For this purpose, new ways of tree characterisation such as vectorisation or computation approaches have been recently used.
The vectorisation method is a fine 3D-tree architecture reconstruction. based on similarity principles that are used to rebuild whole branches from the sample portions. However, the methodology, often derived for a single tree, needs to be repeated at each growth stage, which is limiting and sample dependent. Another recent approach is the use of mathematical models. These models are used in computer graphics domain, where algorithms based on: fractals, L-systems or combinatorial tree already exist. For example, Lin and Sarabandi (1996) apply L-systems to the development of the red maple tree with branching structure in order to feed a coherent model. However, because of the difficulty to modify the topology of the tree, they lack botanical meaning and flexibility. A new approach was developed that exploited existing tree growth models to derive input parameters for the scattering models. using the architectural plant model, which relies on both qualitative and quantitative architectural plant growth description and leads to realistic 3D computing plants.

Figure1 : Examples of Austrian pine simulations at 16,24,32,36,45 years old by AMAP (Castel et al., 2000)

The method developed through the AMAP model (Atelier de Modélisation de l'Architecture des Plantes, CIRAD, Montpellier, France) is based on architectural analysis and growth and branching processes modelling. Architectural analysis consists in morphological observation and description of individuals of different ages and growing stages in various environmental conditions. This is achieved by characterising the strategy used by the plant to build the different elements of its structure – belonging to the trunk, branches, twigs, etc. – including the description of some specific morphological expressions of shoot growth and branching processes. All these characters allow defining the architectural unit of the species. Then, comparisons of the architecture of the trees at different ages enable to distinguish main stages of development; each stage is related to an important event of plant structural edification. The succession of the different stages represents the architectural sequence of the species. Figure 1 shows examples of Austrian pine trees at a range of ages, simulated by the AMAP tree growth model. Compared to previous methods , the tree growth models appear a good method of forest characterisation, in view of simulations of radar measurements at a large range of frequency, polarisation and incidence, for intensity but also for polarimetric and interferometric data (Castel et al. 2000). However, the tree growth models and their interface to backscatter modelling, available for few tree species and validated at few forests, need to be extended to a large range of species and forests .

Scattering models :
Various approaches to the backscatter modelling have been used, relying on the same physical basis, but differing in the assumptions they include and in their validity domain.
Exact methods of calculation (Method of Moments and FDTD) are in most cases not appropriate to calculate the scattering from forest, except when the description of the forest can be simplified, for example at VHF frequencies, where the trunks and large branches may be considered as the main scatterers.
The use of approximate models is imperative for such complex media. Two approaches were considered : radiative transfer and the distorted Born approximation.
The radiative transfer (RT) theory is based on arguments requiring that the number of scatterers is large, and that they are sparsely and randomly distributed in space so that the fields add incoherently. The method is popular in remote sensing of forest, optical and radar, being simple and not time consuming. Its drawback is that the theory ignores the phase of the wave, so the models cannot be used to simulate interferometric data for example. Also, to simplify the calculations, only first order iteration is considered in most models. This can result in underestimation of the cross polarised signal.
The Water Cloud model is the simplified RT model with a single category of scatterers. MIMICS (Ulaby et al. 1990) is a RT model describing the forest as a superimposition of layers (crown layer, trunk layer) containing cylinders (trunk, branches, needles) and ellipsoids (leaves) scatterers. The MIT/CESBIO model (Hsu et al. 1994) includes in addition certain structural effects through the branching model (Yueh et al., 1992). MIMICS2 considers a discontinuous canopy, and the Santa Barbara model (Sun and Ranson 1995) various simple shapes of the crowns. The model due to Karam and Fung (1992) includes second order scattering.

The RT model at CESBIO , as described by Picard et al. (2001) was improved by a) adding the second order, b) applying to a *n* horizontal layers, c) including the horizontal inhomogeneity within each layer. Such an improvement is only possible because of the accurate description of the layer vertical and horizontal inhomogeneity, e.g. using the tree growth model.
The Distorted Born approximation (DBA) is a analytical wave theory, in that it includes information on both the amplitude and the phase of the scattered waves, thus can be used to simulate interferometric data, or low frequency data. The Born approximation calculates the total scattering by adding the complex scattered fields from all the elements. In addition, the DBA takes into account attenuation and refraction by replacing the free space containing the elements by an effective medium. The model provides identical results to first order radiative transfer theory for volume scattering with randomly positioned scatterers. But when the elements are not randomly distributed , e.g. tree elements in a forest structure, the DBA, being sensitive to the positions of the scatterers, can take benefit of a precise description of the forest. Also, when surface-volume scattering is included, the coherent nature of this mechanism can be taken into account (Saatchi and McDonald, 1997). DBA simulations have been compared to laboratory measurements of the backscatter of a tree (Lang et al. 1995).
In summary, the last few years have seen improvements in the existing scattering models, together with the improvements of the forest description. The improvements were required to interpret SAR data at various frequencies, polarisations and incidence angles.

FOREST VERTICAL STRUCTURE

Vertical distribution of forest foliar biomass is an important structural characteristic for quantifying energy and mass exchange inside forest canopies. A better characterisation of the foliar biomass distribution would allow a better modelling of the light transmittance inside tree canopies, which is an important regulator of canopy carbon gain. Several studies have shown that foliar vertical distribution plays a major role in photosynthetic activity. It has interest for process-based forest growth models in which canopy characteristics are often required. Vegetation distribution is also an indication of the growth competition between trees and of the impact of the sylvicultural practices.
The approach to measure the vertical structure of the tree consists in using a airborne ranging scatterometer. In the following, the results obtained using the helicopter-borne FM-CW scatterometer developed by the Laboratory of Space Technology at the Helsinki University of Technology (HUT) are presented (Martinez et al. 2000).
The example is also used as illustration of how improved modelling and observations can provide more insight into the interaction mechanisms. In the experiment performed over the Lozère forest in France, the forest backscattering profiles were calculated along each measurement transect, with a 0.68 meter vertical resolution. Profiles were obtained for different tree ages.

Fig. 2 presents a backscatter profile of HUTSCAT at X band, 23° of incidence acquired over stand of corsican pine of 40 years. The measured profiles suggest that a significant proportion of the backscatter comes from lower parts of the crown (several metres from the top), contrarily to the common knowledge for which the penetration depth at X band is of the order of a metre. In the first modelling simulations using the RT model, the canopy was considered as horizontally infinite homogeneous layers. The simulation predicted that the principal backscattering sources are localised in the first top layers of the trees.

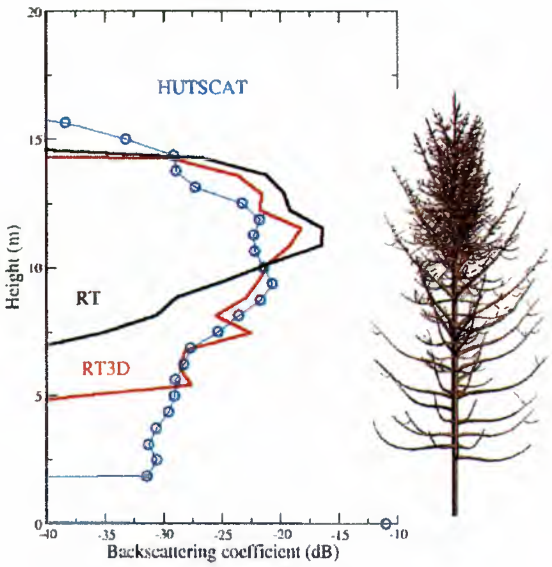

Figure 2: Comparison between HUTSCAT backscatter profile at X band, HH, 23° and RT modelling results applied on a) infinite homogeneous layers, b) layers from 3D description of the forest.

The disagreement can be interpreted as follows : at low incidence angle, the external part of the largest branches at the lower part of the crown can be seen without attenuation by the upper layers. But when the crown is considered as infinite homogeneous horizontal layers, the contribution of the lower part is attenuated by the uppermost and therefore is reduced.

A 3-D Vector Radiative Transfer model (VRT3D) was developed to take into account the horizontal and vertical structure. The model presented here is a full polarimetric RT model coupled with the ray tracing method (Picard et al. 2001). At the tree level, the position, orientation and size of scatterers, and the shape of the tree are described using the AMAP model. At the stand level, the tree position are derived from ground data or simulated using measurements of tree density and spacing. With respect to the azimuthal symmetry of the trees, layers are cylinders of diameter equal to diameter of the crown (Fig. 3).

The model is in better agreement with the data, indicating that the penetration depth within a canopy is of several meters, even at X band. The results show that a precise description of the vertical and horizontal structure of forest and measurements provided by a ranging scatterometer can contribute to refine our understanding of the interaction mechanisms.

Similarity between the vertical distributions of the backscatter and the foliar biomass suggested the possibility to retrieve the foliar biomass distribution from the radar backscatter profiles.

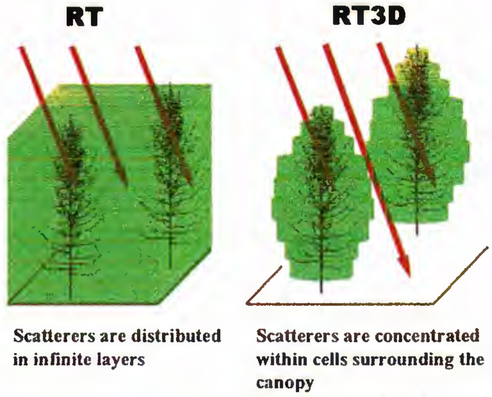

Fig.3. Scattering geometry in RT and RT 3D modelling

Fig. 4 presents the comparison between measured and radar-derived LAI vertical profiles, for the 40- year old stands (Martinez et al. 2001)

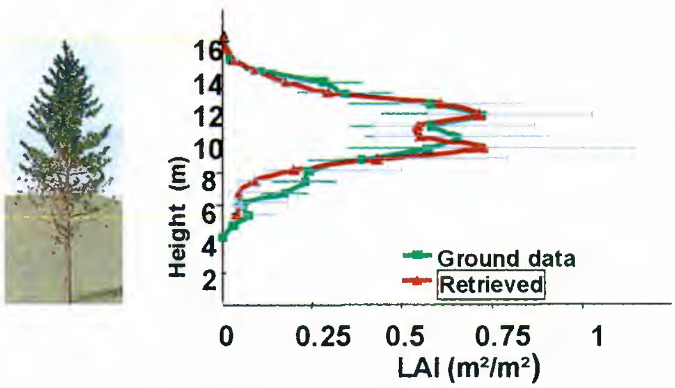

Fig 4: Measured and radar derived LAI profiles

Such a method of measurement of the vertical structure of forest can be made operational using an airborne scatterometer. The performance and cost need to be assessed and compared to that of other new techniques, e.g. using airborne lidars.

FOREST BIOMASS

Forests cover 28% of the land surface but contain 46% of the terrestrial carbon, stored as biomass and soil organic carbon. In global environment and climate studies, forest biomass is a key variable in annual and long term changes in the terrestrial carbon cycle, and needed in modelling carbon uptake and redistribution within the ecosystems. The amount and distribution of biomass over the earth's surface is one of the major uncertainties that hampers our progress to understand the global carbon cycle.

Various definitions exist for biomass. Biomass can be described as the plant material being produced by or resulting from photosynthesis. In forestry, biomass has by far less intensively studied as stem volume which can be estimated by ground measurements. Biomass cannot be assessed directly but is derived by models. One approach is to transfer stem volume of individual trees into biomass by tree species specific conversion factors. A tree is made up of several biomass components: foliage, stem, stump, root, bark and branches. The proportion of these components varies with tree species and with tree age. While young trees have a rather high biomass proportions of leaves/ needles and roots, old trees have a high proportion of stem biomass. Conversion factors, or allometric equations, do not provide information on biomass components with accuracy, unless they are validated for the species, age and site under consideration.

Physical background:

Several studies have demonstrated that approaches using optical remote sensing data do not work for most terrestrial biomass densities. With their longer wavelength, microwaves are expected to penetrate into the canopy, to interact with different components of the tree and to provide biomass estimates.

The conditions for the radar backscatter to provide biomass information can be summarised as follows: a) the wave should penetrate into the canopy, and interact with certain vegetation components (e.g. branches or leaves etc..), b) the backscatter should be sensitive to variation of biomass within the penetration layer, c) the backscatter should be related to the biomass of the vegetation components involved, and d) the biomass of the components involved should be related to the biomass estimates of interest, such as above-ground biomass.

As regard the wave penetration, the previous section indicates significant penetration depth in the canopy, even at X band.

The relationship between the backscatter and the biomass of the vegetation components involved in the interaction can be discussed as follows.

The sensitivity of the backscatter to vegetation characteristics is explained by the scattering of the vegetation elements and /or through attenuation of the ground return by the vegetation. Basically, the scattering and the attenuation increase with the increasing volume of free water contained in tree components involved in the interaction mechanisms. When the vegetation scattering is dominant (small ground contribution), the backscatter intensity increases. The increasing function depends on the structural properties of the main scatterers. When the ground scattering is dominant, the backscatter intensity decreases. The decreasing function, caused by attenuation, depends less on the structural properties of the scatterers. The backscattering coefficient, being normalised by the surface, is a function of the volume of water contained in the involving scatterers per unit surface. Since there is high correlations between the water volume and the fresh biomass of the living vegetation components, the backscattering coefficient increases (or decreases if the ground is dominant) with the fresh biomass of these components (leaf or branch or trunk), expressed e.g. in kg/m2 or tons/ha. For a given tree species, biomasses of different components, leaf, branch, trunk, root, and above ground biomass are correlated. The above ground biomass is the biomass estimate usually related to the backscattering coefficient because a) it is meaningful in the vegetation process and b) it can be derived from the measured stem volume. In summary, it should be understood that the relationship between radar measurements and above ground biomass is very indirect.

The main conditions to be required for inversion of such relationships are: a)a good dynamic range of the radar measurements with respect to the measurement uncertainties, b) reduced noise due to external effect such as ground conditions or topography.

High dynamic range means large difference between the backscatter at high and low biomass. Backscatter at low biomass depends first on the relative ground/ vegetation contribution. When the vegetation scattering is dominant, as for HV polarisation, or HH and VV at high incidence angles, the backscatter depends on the volume of the main scatterers. Since the size of the main scatterers are wavelength dependent, there are smaller volume of scatterers at low frequency than at high frequency. This results in lower backscatter at low biomass for P band compared to L and C band. When the ground scatter is important, as at low incidence angles for HH or VV, the backscatter at low biomass is higher than in the case of dominant vegetation scattering , lowering the overall dynamic range. The backscatter at high biomass varies as a function of the dielectric and structural properties of the main scatterers. In a first approximation, the following assumptions can be formulated: the forest medium can be considered as a homogeneous medium containing a large number of scatterers of a single category, and attenuation is sufficiently important to make the ground scattering negligible. In this case attenuation and scattering compensate each other and the increase of volume of scatterers (increase in number for a given size or increase in size for a given number) will not change the backscatter value. The "saturated" backscatter value depends mainly on the orientation, size, dielectric constant distributions of the backscattering and forward scattering functions of the individual scatterer.

It depends on the wavelength through the scatterer type, and through the wave number. Observations show that for most forest, at a given polarisation/ incidence, the saturated backscatter value is found within a few dB

range, typically -8 to -11 dB at HH or VV, and -11 to -15 at HV, except extreme conditions such as freezing.
The dynamic range is thus primarily determined by the backscatter at low biomass. It increases with decreasing frequency, and it is higher at HV polarisation than HH and VV polarisations.
The noise effect caused by the ground variability is minimised with cross polarisation or with high incidence angles at HH and VV. Other sources of uncertainties are caused by the characteristics of the forests such as species or density. The relationship between the radar backscatter and above ground biomass is less noisy if a) a single species is involved b) a single category of scattering elements is involved.
The other important characteristic of the relationships between the radar return and biomass is the biomass level at the signal saturation. The above-ground biomass saturation level depends on multiple factors such as the radar frequency, polarisation and incidence, which determine the category of dominant scatterers. It depends on the tree species which determine the relation with above ground biomass through allometric relationships, it depends also on the ground conditions (flood, topography) which may change the category of scatterers involved, and the weather conditions. However, the most important factor is the SAR wavelength. Since the size of the dominant scatterers increases with the wavelength, biomass saturation level is expected to increase from X to C, L, P and VHF band. The general saturation level cannot be determined with accuracy, since it depends on the forest type and the uncertainties of the biomass estimates. We use experimental observations over different forests to determine the range of biomass saturation level. Experimental studies with AIRSAR and E-SAR over different types of forests (temperate, boreal and tropical) (Le Toan et al. 1992, Dobson et al. 1992, Beaudoin et al. 1994, Hsu et al. 1994, Rignot et al. 1995, Mougin et al. Mougin et al. 1999, Hoekman et Quinones 2000) indicate that the backscatter intensity saturates at 30, 50 and 150-200 tons/ha at C, L and P bands respectively. Note that these saturation values are indicative of a range and depend also on the radar incidence angle and polarisation

Biomass range	*SAR frequency*
Up to 50 tons/ha	**L-band SAR, C-band InSAR**
Up to 150 tons/ha	**P-band SAR**
Up to 500 tons/ha	**VHF SAR**

Table 2: Ranges of biomass sensitivity of SAR data

C-band data:

At C band HH or VV, the backscatter from the ground can be higher or lower than the vegetation saturation level, depending on ground conditions and the incidence angle. Several observations indicate higher return from the ground in temperate forest plantations , and lower return in boreal forests. Fig. 5 illustrates backscatter over the Landes forest in France.

The observations show that a) for the 3 incidence angles, the backscatter saturates at around 10-12 years (above ground biomass of about 30 tons/ha), b) the sensitivity to increasing biomass until saturation decreases with the incidence angle, from 4dB (26°) to 2 dB (46°) . The low and variable sensitivity of the backscatter to biomass has prevented development of biomass retrieval algorithms using ERS and Radarsat intensity data. On the other hand, the temporal stability of forest versus non forest and low biomass forest has been used for mapping of forest extent (Quegan et al. 2000).

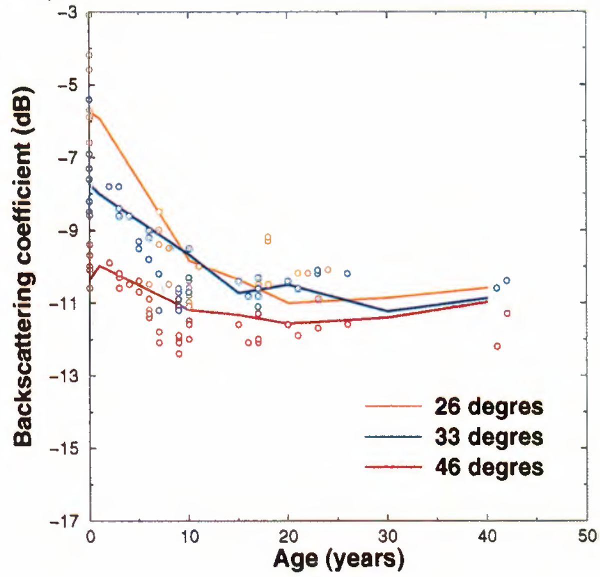

Fig. 5. Radarsat backscattering coefficients as a function of stand age at 26°, 33° and 46° at the Landes forest.

At cross polarisation (C-HV), an increasing trend due to vegetation scattering should be observed at all incidence angles. The dynamic range is, as expected, small at this frequency (~2 or 3 dB). However, the relationship is less noisy, and should make inversion of ENVISAT HV into very low biomass class (<30 tons/ha) possible.
C band interferometric coherence acquired at short time intervals, as in the Tandem ERS missions, shows a particular use of C-Band SARs. The coherence shows a decline with increasing biomass, caused by an increased contribution of the temporally unstable scatterers in the vegetation canopy as biomass increases.
The decorrelation results from the movements of the scatterers between two acquisitions. The scatterers at C-band being needles or leaves, twigs and small branches, are highly sensitive to wind effects. For different forest stands, the coherence decreases with an increase in the number of the leaves, needles, small branches etc.. in the stands. These means that, indirectly, the *coherence decreases as a function of the biomass or stem volume*. As the biomass increases, the coherence drops and can reach the noise level. The decreasing function as a function of biomass can be affected by the backscatter of the ground surface, which is variable e.g. as a function of rain induced soil moisture. However, the

relationship is site and time dependent. The variability can be attributed to differences in interferometric baselines, meteorological conditions and ground conditions (fig.6). The site variability needs to be taken into account in a general inversion algorithms. In the frame of the SIBERIA project, a consortium of European institutes have developed methods applied to the middle part of the Siberian forest using ERS tandem coherence and JERS data. acquired over a region of about 1000 km x1000 km to map forest biomass up to 80 m^3/ha (or 50 tons/ha) in central Siberia (Schmullius et al. 2001). The algorithm was applied to all the available frames to form a mosaic of biomass map of a large region (113 frames of 100x100 km) into 6 classes.

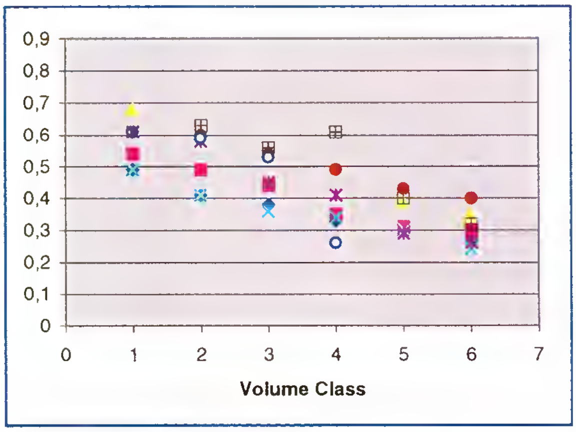

Figure 6 : ERS tandem interferometric coherence as a function of volume class at various test sites in central Siberia. Theclasses 1 to 6 correspond to volume ranges of 0-20, 20-50, 50-80, 80-130, 130-200 and >200 m^3/ha..

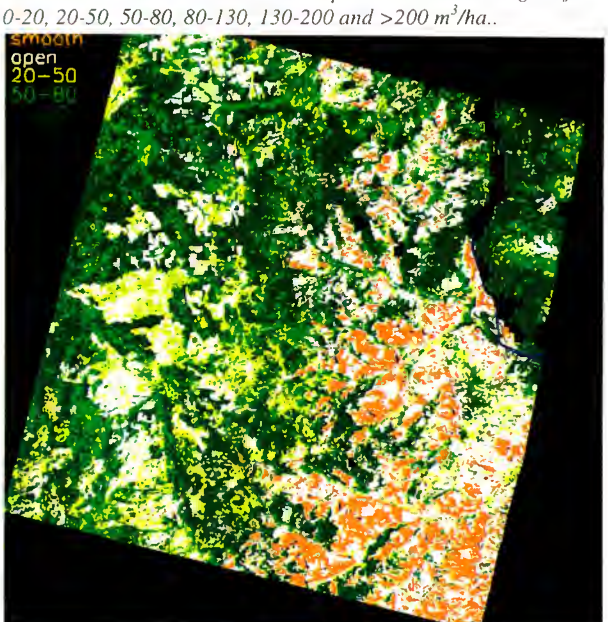

Figure 7 : 100x100 km map of land use and forest classes using JERS and ERS interferometric coherence , forest site in Siberia. From light to dark green: volume classes 0-20, 20-50, 50-80, >80 m3/ha, blue; water, orange: smooth fields.

Fig. 7 presents one of the 100 km map sheet. Such a consistent map can be used to replace the global biomass map used in global vegetation dynamic modelling, and used at regional scale to update existing forest maps for the effect of fire or clearcutting.
The ERS tandem coherence is thus a valuable measurements to provide biomass information. Unfortunately, this source of data does not exist anymore in the foreseen future.

L-band data

At L band, the backscatter results from a more complex interaction , where the main scatterers are the primary or secondary branches.
At low incidence angle, HH or VV return from the ground can be of the order of the vegetation saturation level, giving raise to non monotonic relationships between the radar backscatter and biomass. Figure 10 illustrates the relative importance of the ground compared to vegetation scattering at 26° HH. The vegetation scattering increases until a certain age, then decreases. Physically, at L band, if we calculate the backscatter of a semi-infinite layer of cydrindric scatterers of diameters increasing from 0.2 to 2 cm (branch diameter increasing with age), the backscatter increases then decreases after a certain size is reached (Floury 1999).
Meanwhile, the ground return predicted by the RT3D, being not negligible as the tree density decreases, shows a reverse trend. The saturation observed in the total backscatter is a particular compensation in this case (Fig 8).

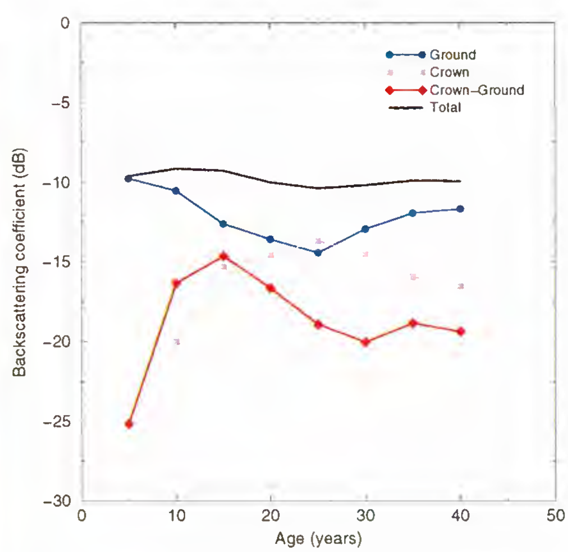

Figure 8 : Scattering mechanisms at L-HH-26°as predicted by RT3D model

At high incidence angles, since the bare surface backscatter at L band is often lower than that of the canopy backscatter, the signal increases with increasing biomass until saturation The increasing trend has been observed in a majority of cases with JERS-1 (L band, HH polarisation and 35° of incidence) until saturation at approximately 50 tons/ha. However, the sensitivity to biomass is small, of the order of 2-3 dB for the biomass range up to 50 tons/ha and depends in addition on the ground conditions. During the lifetime of JERS (1992-1998), several works have been published on the use of JERS data for forest mapping, and not many for the provision of biomass maps.

HV, being governed by the vegetation scattering, increases with increasing biomass, at low and high incidence angles (fig 9). The main scatterers were found to be the secondary branches at low incidence angles, with increasing contribution of secondary angles at high incidences (fig.10).

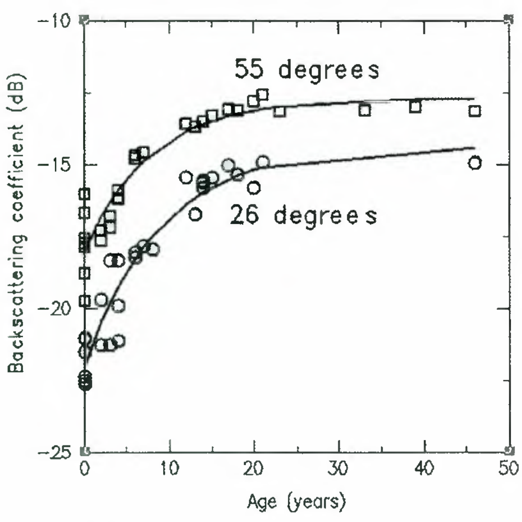

Fig.9 : L-HV as a function of stand age in the Landes forest. Data from SIR-C.

To assess the generality of such relationships, e.g. for the use of ALOS-PALSAR, data at different test sites are compared. Fig. 11 shows L-HV acquired by ESAR versus stem volume over Ruokolahti, a natural boreal forest in Finland, as compared to data acquired by the airborne Ramses system in the plantation Landes forest in France. Despite the possible differences in calibration of the two airborne systems, and the large incidence angle range (35°-45°), the general trend is similar: increase of

The backscatter with biomass until 50 t/ha, dynamic range of the order of 7, 8 dB. The Ruokolahti curve appears more noisy than the Landes curve, due to mixture of species, topography, and horizontal homogeneity.

L-HV as provided by ALOS PALSAR data can be used to update biomass maps similar to maps provided in the SIBERIA project.

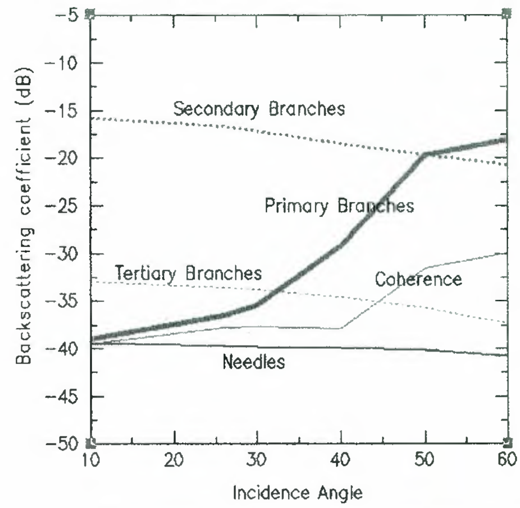

Fig.10. Contribution of tree elements in the backscattering at different incidence angles for stands of 40 years, L-HV-26°

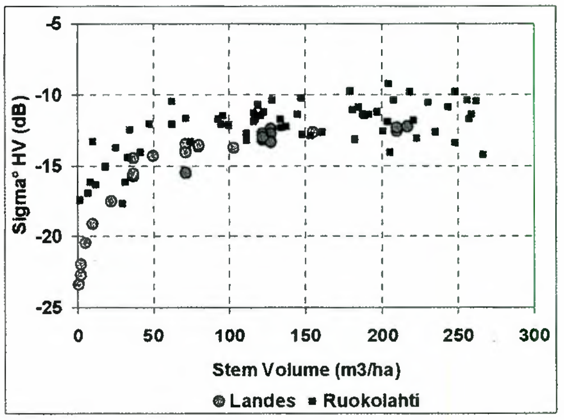

Figure 11. L-HV versus stem volume with ESAR data over a boreal forest, and Ramses data over Landes forest. Incidence angle range: 35-45°

P-band SAR data

At P band, previous experimental and modelling works (Le Toan et al. 1992, Hsu et al. 1994) using AIRSAR at the Landes forest have indicated that in the range of incidence of 45-50°, the main scatterers at HV and VV are the primary branches, and the main scattering mechanisms at HH is the trunk-ground interaction. Simulation studies showed that only HH was strongly dependent on the topography, whereas VV and HV are much less. The backscatter was found increasing up to 150 tons/ha (the maximum biomass value in the Landes) and the dynamic range is of the order of 12-15 dB. During the last ten years, several experiments have been conducted in temperate, boreal and tropical forests over a diversity of forest types and conditions. In general, there are an agreement about a) the high dynamic range of P band compared to L band, b) HV is more sensitive to biomass than HH and VV. Concerning the biomass saturation, it is more difficult to have quantitative statement about the exact biomass saturation values. An example is shown in figs. 12, from Hoekman et al., 2000, where it is clear that L-HV saturates earlier than P-HV, at possibly 30 t/ha for L band and 150 t/ha for P band. However, the lack of data in the range of 30-150 t/ha makes it difficult to define the biomass saturation value. This lack of data is rather common in reported datasets when the experiments were conducted in natural forests, often not covering a good range of biomass, unlike the regularly exploited plantation forest. The large dynamic range of P band is particularly adapted to robust algorithms inverting the backscatter signal into biomass classes e.g. of 10-15 tons/ha interval. There is a need to assess the generality of inversion methods for both the operational use of airborne and the definition of spaceborne system. Until now, P-band spaceborne SARs could not be envisaged mainly because no frequency band is allocated for remote sensing at P band. At present, the official request for frequency allocation appears to have a good chance of success in the next World Radio Conference. With this condition, it is probable that P band SAR payload will be defined in the future.

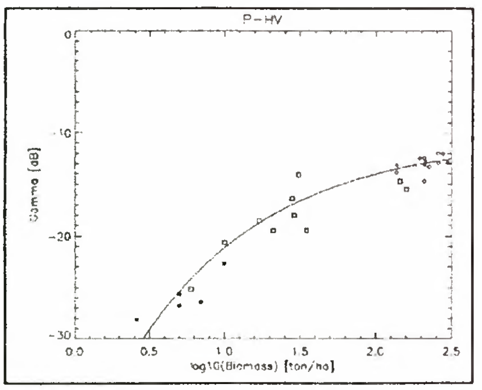

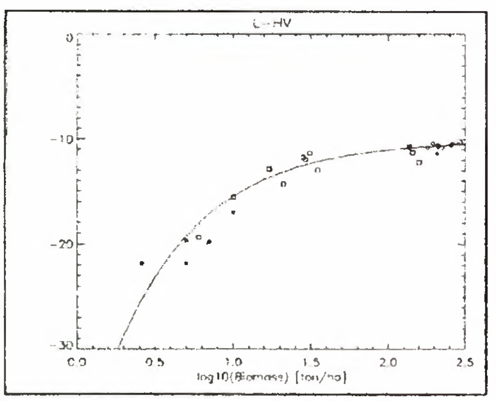

Fig. 12: P-HV and L-HV as function of biomass in the Colombian forest. The backscatter is expressed in Gamma (Sigma 0/cos(incidenc angle)). From Hoekman and Quinones, 2000.

VHF SAR data

In recent works, even longer wavelengths have been studied. The CARABAS-II system developed by the FOI (Swedish Defence Research Establishment) is an airborne ultra-wideband and widebeam SAR operating in the lower VHF band (20-90 MHz). Fig. 13 shows the backscattering coefficient as a function of biomass at two forest sites, Landes and Lozere in France. The measurements indicate that the VHF SAR backscatter is sensitive to biomass up to very high values (Melon et al. 2001). The figure indicates no visible saturation until 700-900 m3/ha, and also a species and site effect. The observations are confirmed by simulations using the Distorted Born Approximation. The result shows that the trunk-ground is the main mechanism, but when the branch dimension becomes non negligible compared to the trunk, as in deciduous species, the branch contribution, and thus the species effect, can be significant (fig. 14). The effect of topography is also found important and needed to be accounted for.

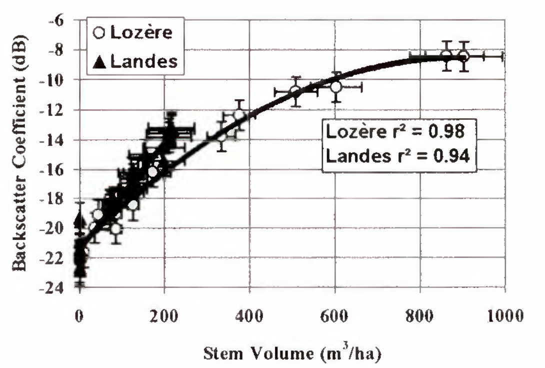

Fig 13. Backscattering coefficients measured by VHF SAR Caraba at HH polarisation, vs stem volume at two forest sites, Lozere (pinus nigra) and Landes (pinus pinaster)

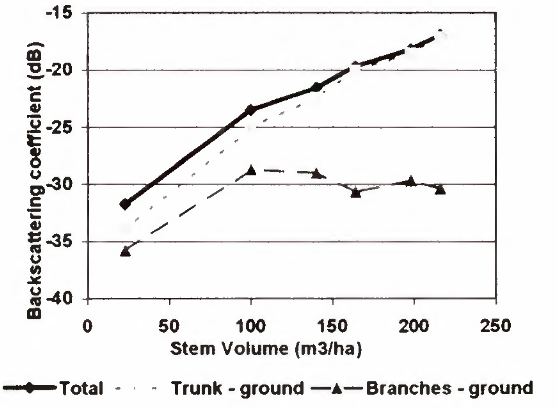

Fig. 14. Scattering mechanisms depicted by a model using Distorted Born Approximation.

Mapping of forest biomass , especially at the higher range of biomass (> 150 t/ha) can be done with VHF SAR. Because of important ionospheric effects at these frequencies, the operations should be conducted using airborne systems.

REFERENCES

Attema E P W and F.T. Ulaby; Vegetation modelled as a water cloud. Radio Science, 13 (2):357-364, 1978

Beaudoin A., T. Le Toan, S. Goze, E. Nezry, A. Lopes, E. Mougin, C. C. Hsu, H. C. Han, J. A. Kong, and R. T. Shin, "Retrieval of forest biomass from SAR data," *International Journal of Remote Sensing*, vol. 15, pp. 2777-2796, 1994.

Castel T., A. Beaudoin, N. Floury, T. Le Toan, Barczi J.F., and Caraglio Y., "Deriving Forest Parameters for Backscatter Models Using the AMAP Architectural Plant Model", IEEE Transactions on Geoscience and Remote Sensing, March 2000.

P. de Reffye, F. Houllier, F. Blaise, D.Barthelemy, J. Dauzat, and D.Auclair, "A model simulating above- and below-ground tree architecture with agroforestry applications", Agroforestry systems;vol. 30, pp.175-197, 1995.

Dobson M. C., F. T. Ulaby, T. Le Toan, A. Beaudoin, E. Kasischke and N. L. Christensen, 'Dependence of radar backscatter on coniferous forest biomass', *IEEE Trans. Geosci. Remote Sensing*, 30, no. 2, pp. 412-415, 1992.

Floury N., 'Modélisation Radar des Couverts Forestiers. Applications à la Télédétection', PhD Thesis, Université Paris 7, March 1999.

Hoekman, D.H. and Quinones, M.J., 'Land cover type and biomass classification using AirSAR data for evaluation of monitoring scenarios in the Colombian Amazon', *IEEE Trans. Geosci. Remote Sensing*, 38, no. 2, 685-696, 2000.

Hsu, C. C.,C. Han, R. T. Shin, J. A. Kong, A. Beaudoin and T. Le Toan, 'Radiative Transfer theory for polarimetric remote sensing of pine forest at P band', *Int. J. Remote Sensing*, 15, 2943-2954, 1994.

Karam M. A., A. K. Fung, R. H. Lang, and N. S. Chauhan, "A microwave scattering model for layered vegetation," *I.E.E.E. Transactions on Geoscience and Remote Sensing*, vol. 30, pp. 767-784, 1992.

Lang R. H., R. Landry, Ö. Kavakhoglu, and J. C. Deguise, "Simulation of microwave backscatter from a red pine stand," *SPIE*, vol. 2314, pp. 538-548, 1995.

Le Toan T., A. Beaudoin, J. Riom and D. Guyon, 'Relating forest biomass to SAR data', *IEEE Trans. Geosci. Remote Sensing*, 30, 403-411, 1992.

Lin Y.-C. and K. Sarabandi, "A coherent scattering model for forest canopies based on Monte Carlo simulation of fractal generated trees," *in Proceedings of IGARSS'96 Symposium*, Lincoln Nebraska, USA, 1996.

Mc Donald K.C. and F.T. Ulaby. Radiative transfer modelling of discontinuous tree canopies at microwaves frequencies. Int Journal of Remote Sensing, 14(11):2097-2128, 1993.

Martinez J.M., N. Floury, T. Le Toan, A. Beaudoin, M.T. Hallikainen, and M. Makynen." Measurements and modelling of vertical backscatter distribution in forest canopy", IEEE Transactions on Geoscience and Remote Sensing, vol. 38, no 2, 710-719, March 2000.

Martinez, J.M.,T. Le Toan, E. Mushinzimana; M. Deshayes, "Retrieving vertical foliage distribution using high resolution airborne scatterometer data", in press, Tree Physiology, 2001

Melon P., J.M. Martinez, T. Le Toan,L.M.H. Ulander and A. Beaudoin, 'On The retrieving of Forest Stem Volume from VHF SAR data: Observation and Modelling', *IEEE Trans. Geosci. Remote Sensing*, Nov 2001.

Mougin E, Proisy C. et al., 1998, 'Radar Remote Sensing of a mixed deciduous forest during EMAC 94', Proc. EMAC final meeting, ESTEC, pp 105-109, April 1997, ESTEC.

Mougin, E., Proisy, C., Marty, G., Fromard, F., Puig, H., Bétoulle, J. L., Rudant, J.P., "Multifrequency and multipolarization radar backscattering from mangrove forests", IEEE Transactions on Geoscience and Remote Sensing, 1999, 37(1): 94-102.

Quegan S., T. Le Toan, J.J. Yu, F. Ribbes, N. Floury. "Estimating temporate forest area with multitemporal SAR data", IEEE Transactions on Geoscience and Remote Sensing, vol. 38, no 2, 741-753, March 2000.

Picard G., T. Le Toan, M. Davidson and P. Melon " A three-dimensional radiative transfer backscatter model applied to forest.", submitted to *IEEE Trans. Geosci. and Remote Sensing*, 2001.

Rignot, E.J.M., Zimmermann, R. and van Zyl, J.J., 'Spaceborne applications of P band imaging radars for measuring forest biomass', *IEEE Trans. Geosci. Remote Sensing*, **33**, pp. 1162-1169. 1995.

Saatchi and K. McDonald, "Coherent effect in microwave backscattering modelling for forest canopies" IEEE Trans. Geosci.Remote Sensing, vol. 35, pp585-598, May 1997.

Schmullius, C. et al., 'SIBERIA – SAR Imaging for Boreal Ecology and Radar Interferometry Applications', European Commission 4th Framework Project ENV4-CT98-0743 (DG12-EHKN), Final Report, September 2001.

Sun G. and K. J. Ranson, "A three-dimensional radar backscatter model for forest canopies," *I.E.E.E. Transactions on Geoscience and Remote Sensing*, vol. 33, pp. 372-382, 1995.

Ulaby F. T., K. Sarabandi, K. Mc Donald, M. Whitt, and M. G. Dobson, "Michigan microwave canopy scatterring model," *International Journal of Remote Sensing*, vol. 11, pp. 1223-1253, 1990.

Wang Y., J. Day, and G. Sun, "Santa Barbara microwave backscattering model for woodlands," *International Journal of Remote Sensing*, vol. 14, pp. 1477-1493, 1993.

Yueh, S.H., J.A. Kong, J.A. Jao, R.T. shin, and T. Le Toan, "Branching model for vegetation" IEEE Trans. On Geosci. And Remote Sensing, 30:390-402, 1992.

FOREST STEM VOLUME RETRIEVAL WITH VHF-BAND SAR

G. Smith[1], L. M. H. Ulander[2], J. E. S. Fransson[3], F. Walter[4] and A. Gustavsson[2]

[1]Chalmers University of Technology
Department of Radio and Space Science
SE-412 96 Gothenburg, Sweden
tel: +46-31-772-1844 / fax: +46-31-772-1884
email: smith@rss.chalmers.se

[2]Swedish Defence Research Agency (FOI)
Division of Sensor Technology, P. O. Box 1165
SE-581 11 Linköping, Sweden

[3]Swedish University of Agricultural Sciences
Department of Forest Resource Management and Geomatics
SE-901 83 Umeå, Sweden

[4]Dianthus
Sommarstigen 13
SE-961 32 Boden, Sweden

ABSTRACT

Forest stem volume is an important parameter to retrieve using remote sensing; for global biomass studies as well as local forestry planning. In this paper, we use a polarimetric scattering model to discuss the possibilities of using low frequency SAR to retrieve stem volume. The benefits of using low frequencies (low attenuation, Rayleigh scattering and low sensitivity to terrain slopes) are presented, and we discuss some of the problems restricting the accuracy of stem volume retrieval, related to attenuation by the forest canopy, and the dependence of the backscatter on the ground properties due to the dominance of the dihedral trunk-ground scattering. For the essentially HH-polarised backscatter measured by the CARABAS airborne SAR system, terrain slopes are a major disturbing factor on the accuracy of stem volume retrieval, and we present results of using images from different flight directions to compensate for this effect.

INTRODUCTION

The potential of remote sensing to aid in forest management and planning has long been recognised, due to the ability to obtain information over large areas that are often sparsely populated. While great progress has been made in mapping the extent of forest cover, species and structure, attempts to automate mapping of one of the most important properties of forests, namely biomass, have been of limited success. This is an area where there is a definite need for remote sensing, on scales ranging from global to small-scale mapping. In the former case, total biomass is of interest for global climate studies, and monitoring of changes within international agreements, for example the Kyoto Protocol to the UN Framework Convention on Climate Change. On the smaller scale, commercial forestry operations require information on tree species, number density and, above all, wood volume, to aid sustainable management of resources, as well as in planning of logging operations. For the latter, the most important information is the size of the trunk. In Scandinavia, this is usually measured in terms of *stem volume,* i.e. average volume of tree trunks within a specified area (m^3/ha). Trunk dimensions are also important for mapping of biomass because for most species the trunk contains a significant fraction of the total biomass.

Many attempts have been made to measure stem volume using different types of remote sensing data. In most cases the electromagnetic waves used are scattered from the tree crowns (leaves, needles, branches), and do not penetrate to the trunks, hence they provide only an indirect approach to stem volume retrieval. Often the measurements have shown good correlation with stem volume in the early stages of growth, but reached a saturation level at relatively low stem volumes.

An exception to this is the use of low frequency SAR, where the long wavelengths allow penetration of the forest canopy and the scattering from the trunks allows the stem volume to be estimated directly. CARABAS is an airborne SAR system [1], using frequencies in the lower VHF-band (20-90 MHz). The wide bandwidth gives a high range resolution (~2.5 m), and to achieve similar resolution in azimuth, a wide aperture angle is required, with 90° being typical. The transmit and receive polarisation is essentially horizontal, and the image formation and calibration procedure is described in detail in [2], and is estimated to give an absolute calibration accuracy of ±1 dB, over the range of incidence angles normally used (~45°-70°).

In previous investigations, low frequency scattering from forests has been studied using scattering models and measurements [3-7]. The modelling suggests that on flat terrain the backscatter is directly related to stem volume through the trunk-ground dihedral scattering. On sloping terrain this scattering is reduced, however, in [7] it was shown that the dihedral scattering is still the most important mechanism for forests on moderate slopes (up to ~20°), and hence the measurements may be used for stem volume retrieval.

In this paper we review the reasons for the good results obtained using lower VHF-band SAR for forest stem volume retrieval. Based on experience with the second generation CARABAS SAR (CARABAS-II), and a

Proc. 3rd International Symposium, 'Retrieval of Bio- and Geophysical Parameters from SAR Data for Land Applications', Sheffield, UK, 11-14 September 2001 (ESA SP-475, January 2002)

simple backscattering model, we discuss the advantages of using SAR in this band, as well as some of the difficulties encountered, and possible strategies for overcoming those problems, with the aim of developing a cost-effective, automatic procedure for mapping of stem volume [8].

BACKSCATTER MODELLING

Modelling has been used to aid understanding of the backscatter measurements' dependence on forest and ground properties. A detailed description of a numerical scattering model for CARABAS measurements of coniferous forests is given in [7]. In this paper we will use a more generalised version of the model, to illustrate the most fundamental aspects of the scattering from forests at low frequencies. In this approach, the trunks and branches are treated as dielectric cylinders located above a tilted dielectric ground plane. The total backscatter is calculated as a coherent addition of the scattering from these cylinders using the distorted Born approximation. At the low frequencies used by CARABAS, the ground surface acts as a (lossy) mirror, and comparison with numerical models using the finite-difference, time-domain (FDTD) method has shown that to a first approximation the scattering may be calculated using image theory [3], where the most important contributions to the total backscatter are a) direct backscatter b) trunk-ground and ground-trunk dihedral scattering and c) ground-trunk-ground scattering. These different scattering mechanisms add coherently to give the total backscatter from each scattering element. Thus, if the scattered electric field, $\mathbf{E}^s$, is related to the incident electric field, $\mathbf{E}^i$, by

$$\mathbf{E}^s = \frac{e^{-ikr}}{r}\mathbf{S}\mathbf{E}^i \tag{1}$$

where k is the wavenumber, and the harmonic variation of the field in time has been suppressed, the total scattering matrix can be written as the sum of the four different scattering mechanisms, i.e.

$$\mathbf{S} = \mathbf{S}_t + \mathbf{S}_{gt} + \mathbf{S}_{tg} + \mathbf{S}_{gtg} \tag{2}$$

with $\mathbf{S}_t = \mathbf{S}^0\left(\hat{\mathbf{k}}_s, \hat{\mathbf{k}}_i\right)$

$$\mathbf{S}_{gt} = e^{i\tau_s}\mathbf{\Gamma}\left(\hat{\mathbf{k}}_s, \hat{\mathbf{k}}_{sg}\right)\cdot \mathbf{S}^0\left(\hat{\mathbf{k}}_{sg}, \hat{\mathbf{k}}_i\right)$$

$$\mathbf{S}_{tg} = e^{i\tau_i}\mathbf{S}^0\left(\hat{\mathbf{k}}_s, \hat{\mathbf{k}}_{gi}\right)\cdot \mathbf{\Gamma}\left(\hat{\mathbf{k}}_{gi}, \hat{\mathbf{k}}_i\right)$$

$$\mathbf{S}_{gtg} = e^{i(\tau_i+\tau_s)}\mathbf{\Gamma}\left(\hat{\mathbf{k}}_s, \hat{\mathbf{k}}_{sg}\right)\cdot \mathbf{S}^0\left(\hat{\mathbf{k}}_{sg}, \hat{\mathbf{k}}_{gi}\right)\cdot \mathbf{\Gamma}\left(\hat{\mathbf{k}}_{gi}, \hat{\mathbf{k}}_i\right) \tag{3}$$

The directions of the incident and scattered fields are denoted by $\hat{\mathbf{k}}_i$ and $\hat{\mathbf{k}}_s$, while

$$\hat{\mathbf{k}}_{gi} = \hat{\mathbf{k}}_i - 2\hat{\mathbf{n}}_g\left(\hat{\mathbf{n}}_g \cdot \hat{\mathbf{k}}_i\right) \tag{4}$$

is the direction of the incident wave after reflection from the ground, and similarly $\hat{\mathbf{k}}_{sg}$ is the direction of the wave scattered from the cylinder to the ground ($\hat{\mathbf{n}}_g$ is a unit vector perpendicular to the ground surface). $\mathbf{S}^0$ is the scattering matrix for an isolated scattering element, and $\mathbf{\Gamma}$ is the reflection matrix for the ground surface. For backscattering, reciprocity requires that $\mathbf{S}_{gt} = \mathbf{S}_{tg}$, and we will refer to the sum of these two terms as dihedral scattering.

For most scattering elements in forests, the generalised Rayleigh-Gans theory can be applied to calculate the scattering matrix $\mathbf{S}^0$, since the branches, and even the trunks in boreal forests, satisfy the criteria that $k \cdot a \ll 1$, and $\frac{h}{a} > 20\sqrt{\varepsilon_r}$, where h and a represent the length and radius of a dielectric cylinder with relative permittivity, ε_r. In the limit of long thin cylinders (a/h→0), the scattering from a cylinder with axis defined by $\hat{\mathbf{z}}_c$, with incident and scattered polarisations (using the cylinder axis to define vertical) of $\hat{\mathbf{q}}$ and $\hat{\mathbf{p}}$ respectively, can be expressed [9] as

$$S^0_{pq}\left(\hat{\mathbf{k}}_s, \hat{\mathbf{k}}_i\right) = V\frac{\varepsilon_r - 1}{\varepsilon_r + 1}\frac{k^2}{4\pi} \left[2\left(\hat{\mathbf{p}}\cdot\hat{\mathbf{q}}\right) + \left(\varepsilon_r - 1\right)\left(\hat{\mathbf{p}}\cdot\hat{\mathbf{z}}_c\right)\left(\hat{\mathbf{z}}_c\cdot\hat{\mathbf{q}}\right)\right]\mu\left(\hat{\mathbf{k}}_s, \hat{\mathbf{k}}_i\right) \tag{5}$$

where V is the cylinder volume, and the modifying function, μ, is

$$\mu\left(\hat{\mathbf{k}}_s, \hat{\mathbf{k}}_i\right) = \operatorname{sinc}\left(\frac{kh}{2}\left(\hat{\mathbf{k}}_s - \hat{\mathbf{k}}_i\right)\cdot\hat{\mathbf{z}}_c\right), \tag{6}$$

with $\operatorname{sinc}(x) = \frac{\sin(x)}{x}$.

Equation (5) shows that the strength of scattering from a given cylinder depends strongly on the volume of the cylinder. In typical boreal coniferous forests, this means that most of the scattering comes from the tree trunks.

The modifying function, μ, in (5) results in the strongest scattering being in the specular direction, while the width of the scattering lobe depends on the length of the cylinder compared to the wavelength. In reality, the trunks and branches of trees are not perfect cylinders, but taper towards the tips, in a form closer to that of a cone than a cylinder. This results in a widening of the main scattering lobe, equivalent to scattering from an "effective" scattering cylinder approximately 2/3 of the length of the trunk, as well as smoothing the strong variations with scattering angle (nulls between sidelobes), which are due to resonance effects [7].

The ground reflectivity matrix, $\mathbf{\Gamma}$, is diagonal on flat ground, with the reflectivity for horizontal and vertically polarised waves determined by the Fresnel reflection coefficients Γ_H and Γ_V respectively. On sloping terrain, however, the change in scattering geometry may result in significant off diagonal terms, indicating a change in the wave polarisation on reflection.

Finally, to include the effects of wave propagation through the forest canopy, the optical path lengths τ_s and τ_i in (3) must be included. These are of the form $\tau_s = 2k' z_c \cos\theta_s$, where z_c is the height of the trunk's phase scattering centre above the ground plane, and k' is a propagation constant for the mean field in the forest canopy, which can be calculated using the effective field approximation (EFA). For an azimuthally isotropic medium, the characteristic waves correspond to vertical and horizontal polarisations, and their associated propagation constants, k'_p, for the direction, $\hat{\mathbf{k}}$,

$$k'_p = k + \frac{2\pi}{k}\left\langle \rho\, S^0_{pp}\left(\hat{\mathbf{k}},\hat{\mathbf{k}}\right)\right\rangle_{st} \qquad (7)$$

where ρ is the volume number density of scatterers, and $\langle\ \rangle_{st}$ represents ensemble averaging over the scatterer properties (permittivity, size, orientation and number density). For more details, see [10].

POLARIMETRIC SCATTERING FROM TREE TRUNKS ON FLAT TERRAIN

As a starting point for the discussion of scattering from forests in the lower VHF-band, we will first consider the scattering from a vertical trunk ($\hat{\mathbf{z}}_c = \hat{\mathbf{z}}$), which for the coniferous forests studied with CARABAS is a reasonable approximation. In this section we also limit the discussion to the case of flat ground ($\hat{\mathbf{n}}_g = \hat{\mathbf{z}}$). For young trees, where the "effective" tree height is of the order of the wavelength, the modifying function results in a wide mainlobe, and all four of the scattering mechanisms in (3) contribute to the total scattering. However, as the tree height increases, the scattering from the trunk becomes more concentrated in the specular direction, and dihedral scattering tends to dominate. An important point to consider is that in a wideband system, such as CARABAS, the scattering lobe (and hence the importance of the different scattering mechanisms) varies considerably with frequency. Since the scattering amplitude scales with the square of the frequency, the higher frequencies tend to dominate the total response. Another factor which determines the relative strengths of the different scattering mechanisms, is the polarisation. For HH scattering (and HV and VH), the second term in the square brackets in (5) vanishes, and the dihedral scattering mechanism can be written

$$S_{dihedral,HH} = -V\frac{\varepsilon_r - 1}{\varepsilon_r + 1}\frac{k^2}{\pi}\Gamma_H \qquad (8)$$

Thus the dihedral scattering depends on incidence angle only through the ground reflectivity. Also, since $\varepsilon_r \gg 1$ the backscatter is only weakly dependent on the trunk permittivity.

For VV backscatter, the situation is complicated by the presence of the second term in the square brackets of (5). Since the dielectric constant of the trunk is relatively high (ε_r~20), this term can play an important role in determining the backscatter, except for steep (small) angles of incidence. For the relatively shallow incidence angles used by CARABAS, the vertically polarised scattering from the trunk is large. However, in the case of the dihedral scattering, the strong scattering from the trunk is offset by the low ground reflectivity (resulting from ground reflection close to the Brewster angle). Hence the total backscatter depends on both the direct backscatter, and the dihedral scattering, which add coherently with a phase relationship determined by the scattering phase centre of the trunk.

The effect of propagation through the forest canopy is also different for the two polarisations. CARABAS measurements indicate very low attenuation for horizontally polarised waves (~2 dB even in dense forests) [11]. Through modelling based on the EFA, it has been shown that the attenuation is due in roughly equal parts to the tree crowns and trunks, and (for coniferous forests) is relatively independent of stem volume, as the scattering loss from the trunks is so small. However, for vertical polarisations the attenuation is much greater (~10 dB), due principally to the strong scattering from the trunks at large angles of incidence. In this case, the attenuation varies significantly with stem volume, and tends to negate the increased backscattering, thus weakening the relationship between measured backscatter and stem volume.

Considering the complexity of the polarimetric scattering from a vertical trunk on flat terrain, it appears that HH-polarisation has significant advantages for stem volume retrieval. The low attenuation, which appears to vary only slowly with increasing stem volume, does not disturb the measurement of the trunk scattering. The scattering itself is also less sensitive to changes in incidence angle using HH-pol., which allows the use of a wider imaging swath. If vertical polarisation is desired, the model suggests that steeper incidence angles are more useful, to reduce incidence angle by reduction of interference between direct backscatter and the dihedral scattering, as well as avoiding the rapid changes of ground reflectivity expected close to the Brewster angle. Steep incidence also reduces the attenuation.

STEM VOLUME RETRIEVAL WITH CARABAS ON FLAT TERRAIN

Since CARABAS uses essentially HH-polarisation, we will consider the relationship between backscatter and stem volume (for reasonably large trees), as determined by (8). It can be shown that this gives a radar cross-section for a single tree proportional to the square of the tree's volume. In a forest, consisting of many trees, the total backscatter is an addition of the scattering from the individual trees. For older forests, the spacing between trees is often larger than the spatial resolution of CARABAS, which opens the possibility of measuring the radar cross-section (and hence volume) of each tree. In this case it was suggested in [5] that by averaging the backscatter amplitude s^o (rather than intensity, σ^o), a measure which is linearly related to stem volume, v, could be obtained, i.e. $s^o \propto v$. This would be preferable to using backscattered intensity, which due to the non-linear dependence on stem volume is expected to depend on the number density of the trees, n, i.e. $\sigma^o \propto \frac{v^2}{n}$. When the tree spacing is less than the resolution, coherent interference between the scattered fields occurs. In most (semi-)natural forests the random distribution of trunks means that the backscattered power adds incoherently so that the average intensity should be used as an unbiased measure of the backscatter, rather than average amplitude.

In practice we have seen little difference between using the average backscattered amplitude or the square root of the average intensity as a measure of stem volume [12]. This is believed to be due to the fact that stem volume and tree density are generally correlated, and hence it is difficult to separate the effects of stem volume from number density. In addition, modelling predicts that, for the range of stem volumes within the forests studied in Scandinavia, the variation of number density will cause only small differences which can be obscured by other effects.

Another factor which can reduce the correlation of CARABAS measurements with forest stem volume is the dependence of the scattering on the ground reflectivity. The reflectivity can vary independently of the forest stem volume, depending on a) soil dielectric properties (moisture, grain size), b) incidence angle and c) surface slope. Of these, the effects of soil moisture and incidence angle are expected to be minor compared to the effect of the slope, and to-date, only weak evidence of their influence has been observed in CARABAS images [12], since in many cases they are obscured by variations caused by sloping terrain.

INFLUENCE OF SLOPING TERRAIN

The effect of sloping terrain on CARABAS measurements of forests is principally a result of changes in the dihedral scattering from the trunk. This is because of the change in scattering geometry, which changes both $\mathbf{\Gamma}$ and $\mathbf{S}^0$ in (3). Firstly, $\mathbf{\Gamma}$ is changed by the reduction of the diagonal terms (co-polarised reflectivity) and the introduction of significant off-diagonal terms (cross-pol.). However, modelling indicates that for moderate slopes (up to ~20°), at the incidence angles used by CARABAS, this is a minor change [7]. More important is the change in the trunk scattering matrix $\mathbf{S}^0$, caused by shift of the dihedral backscattering from the specular direction (i.e. the changes in $\hat{\mathbf{k}}_{gi}$ and $\hat{\mathbf{k}}_{sg}$). This means that the backscattering is determined mainly by the modifying function μ, so that the backscattering may be written as

$$\sigma^o_{slope} \approx \sigma^o_{flat} f\left(k, h_{eff}, \hat{\mathbf{n}}_g, \hat{\mathbf{k}}_s\right) + \sigma^o_{background} \qquad (9)$$

where σ^o_{flat} is the backscatter coefficient expected on flat terrain, and

$$f = \frac{\left\langle k^4 \mathrm{sinc}^2\left(\frac{kh_{eff}}{2}\left(\cos\theta_{sg} - \cos\theta_i\right)\right)\cos^2(\phi_{sg} - \phi_i)\right\rangle}{\left\langle k^4 \right\rangle}$$

The angles θ and ϕ are the Euler angles for the directions, $\hat{\mathbf{k}}_i$ and $\hat{\mathbf{k}}_{sg}$, and h_{eff} is an effective tree height, approximately 2/3 of the true tree height. $\sigma^o_{background}$ represents a background noise level due to

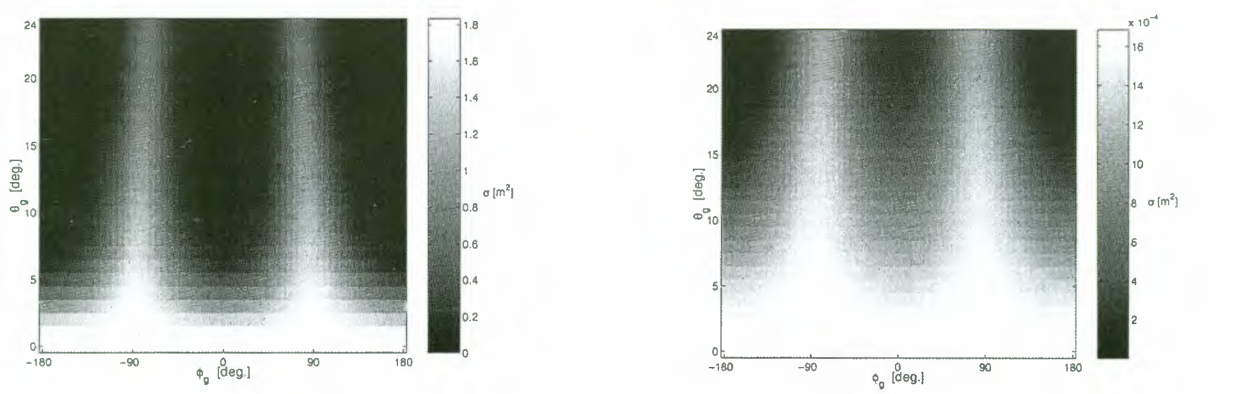

Fig. 1. Model of variation of radar cross-section for a dielectric cylinder on a sloping plane, for trees with height=30 m, dbh=35 cm (left), and height=10 m, dbh=10 cm (right). θ_g denotes the slope, and ϕ_g the aspect angle relative to the look direction. The calculations are performed at 60° incidence.

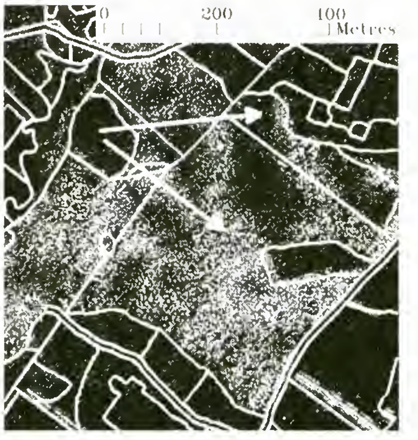

Fig. 2. CARABAS image examples for a dense forest area (high backscatter), with forest stand boundaries superimposed. A comparison of the two images shows that apparent within-stand variations of high and low backscatter are reversed when imaged from a different direction.

image noise and (weak) scattering which does not show the same dependency on slope as the dihedral response (i.e. direct backscatter from the trunk, scattering from branches, ground scattering, etc.). Since the effect of the slope depends strongly on the system frequency and the look-direction, the triangular brackets indicate averaging over the different frequencies, and azimuth angles used in the image formation process.

To illustrate the effects of sloping terrain on backscatter, Fig. 1 shows simulations for two different sized tree trunks, (adapted from [7]). It can be seen that the backscatter for a given slope varies significantly with aspect angle, with the maximum backscatter at angles of $\pm 90^{\circ}$ where the slope has no range component. An example of the variations with look direction can be seen in Fig. 2, where an area of dense forest has been imaged from 2 different directions. In this case, the variations in backscatter (note particularly the areas marked with arrows), are reversed from one image to another. This is due to the effects of topography, and the direction of slope relative to the look direction.

STEM VOLUME RETRIEVAL OVER SLOPING TERRAIN

The variations in backscatter described above represent a problem for retrieving stem volume from a single CARABAS image. Particular problems occur where the slope is in the range direction, and the dihedral backscattering may be reduced below the background scattering. In this situation, the backscatter measurement is no longer a directly related to stem volume. To illustrate one technique to avoid this difficulty, we have used a combination of images acquired from four flight tracks over the Tönnersjöheden test-site described in [4,7]. Fig. 3 shows a comparison of the results obtained by inverting the CARABAS measurements to retrieve stem volume. The crosses mark an inversion performed using an empirically derived relationship between backscatter amplitude measured in one image and stem volume. The circles, on the other hand, are from a retrieval performed by selecting data from the four images to minimise the effects of topography. As expected, the main difference between the two techniques is for stands with tall trees (high stem volume) standing on steep slopes. With a single image there is significant underestimation of these stands, whereas the combination of 4 images results in much better stem volume estimation.

DISCUSSION

This paper reviews the basic physical mechanisms determining the backscatter from forests, and the correlation between VHF-band SAR measurements of backscatter and stem volume. We have shown that the use of wavelengths which are long compared to the diameter of the trees has the advantages that a) the scattering is dominated by the trunk, and b) the scattering is essentially Rayleigh, and thus proportional to scatterer volume. The main problem with using low frequencies is that, since the dihedral scattering dominates the response, the scattering is also dependent on the properties of the ground. In particular, terrain slopes can cause large changes in measured backscatter, which must be compensated. We have presented one possible method to achieve this, using images from multiple look directions. Another possibility is to use the model described in [7] to correct for topography. However, in this case the dependence on tree height complicates the retrieval of stem volume. In this respect, the use of complementary measurements, such as lidar or dual frequency InSAR to retrieve tree height and surface topography may be of interest.

The polarimetric model described in this paper, suggests that HH-polarisation has advantages for stem volume retrieval, as it is less sensitive to changes in incidence angle than VV. This is particularly important when combining images from different flight directions, where the incidence angle will vary from one image to another. Related to this is the need for good calibration of the images.

Another possible method for slope estimation and correction is that suggested in [13], where the shift in the polarimetric response is used to estimate the azimuth tilt of the surface. This method is under investigation for low frequencies, where the strong variation of scattering with surface slope may be an advantage.

Finally, it is important to note the effect that tree species may have on the stem volume retrieval. For trees with significant biomass in large branches, the attenuation of the forest canopy, and backscatter from the branches will increase. This will tend to obscure the scattering from the trunk, particularly on sloping terrain where the trunk dihedral scattering is reduced. This effect is strongly frequency dependent, since higher frequencies result in stronger attenuation of the trunk scattering by the canopy, a greater sensitivity to surface slopes, and a generally higher "background" noise due to increased scattering from branches. In this situation, the total backscattering may still be correlated with stem volume, but as a result of the measurement of branch biomass, not direct measurement of the trunk.

ACKNOWLEDGEMENTS

The work reported here was funded by the Swedish National Space Board. The authors thank everyone involved in the CARABAS project for making this study possible.

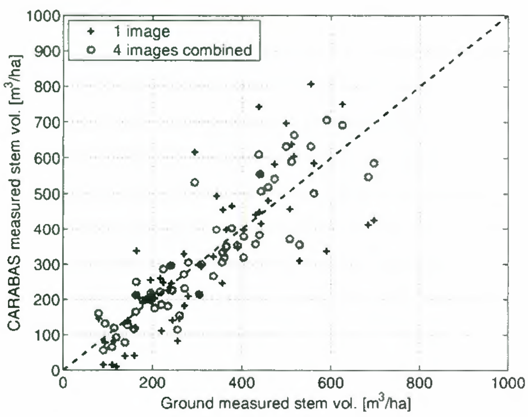

Fig. 3. Illustrating the improvement in standwise stem volume retrieval when 4 images are used in combination, compared to a single image. With a single image the coefficient of determination, R^2=0.63, and the rms error is 120 m^3/ha. The use of 4 images improves these values to 0.80 and 80 m^3/ha respectively.

REFERENCES

[1] H. Hellsten, L.M.H. Ulander, A. Gustavsson, and B. Larsson, "Development of VHF CARABAS II SAR," *Proc. Radar Sensor Technology*, SPIE, vol. 2747, Orlando, FL, 8-9 April 1996, pp. 48-60.

[2] L.M.H. Ulander, P.-O. Frölind, and T. Martin, "Processing and calibration of ultra-wideband SAR data from CARABAS-II," *Proc. CEOS SAR Workshop*, 26-29 October 1999, Toulouse, France.

[3] H. Israelsson, L.M.H., Ulander, T., Martin, and J. Askne, "A Coherent Scattering Model to Determine Forest Backscattering in the VHF-Band", *IEEE Trans. Geosci. Rem.Sens.,* vol. 38, no. 1, pp. 238-248, 2000.

[4] J.E.S. Fransson, F. Walter, and L.M.H. Ulander, "Estimation of forest parameters using CARABAS-II VHF SAR data," *IEEE Trans. Geosci. Rem. Sens.*, vol.38, no.2, pp.720-727, 2000

[5] G. Smith and L.M.H. Ulander, "A model relating VHF-band backscatter to stem volume of coniferous boreal forest," *IEEE Trans. Geosci. Rem. Sens.* vol. 38, no. 2, pp. 728-740, 2000.

[6] P. Melon, J.-M. Martinez, T. Le Toan, L.M.H. Ulander, and A. Beaudoin, "On the retrieving of forest stem volume from VHF SAR data: Observation and modelling," submitted to *IEEE Trans. Geosci. Rem. Sens.*

[7] G. Smith, L.M.H. Ulander, and X. Luo, "Low frequency scattering of coniferous forests on sloping terrain," submitted to *IEEE Trans. Geosci. Rem. Sens.*

[8] A. Gustavsson, F. Walter, L.M.H. Ulander, J.E.S. Fransson, P.O. Frölind, T. Jonsson, B. Larsson, G. Smith, and G. Stenström, "A pilot experiment for stem volume retrieval based on VHF SAR data", presented at IGARSS'01, Sydney, 9-13 July 2001.

[9] M.A. Karam, A.K. Fung, and Y.M.M. Antar, "Electromagnetic wave scattering from some vegetation samples," *IEEE Trans. Geosci. Rem. Sens.*, vol. 26, no. 6, pp. 799-808, 1988.

[10] Y.-C. Lin and K. Sarabandi, "A Monte Carlo Coherent Scattering Model for Forest Canopies Using Fractal Generated Trees," *IEEE Trans. Geosci. Rem. Sens.*, vol.37, no.1, pp.440-451,1999.

[11] G. Smith, L.M.H. Ulander, T. Martin and X. Luo, "VHF SAR Models and Measurements of Targets Under Coniferous Forest Canopies", *Proc. IGARSS 2000, Honolulu, Hawaii*, vol. 3, pp.990-992.

[12] L .M. H. Ulander, J. Askne, J. E. S. Fransson, A. Gustavsson, T. Le Toan, T. Manninen, J.-M. Martinez, P. Melon, G. Smith, and F. Walter, "Retrieval of Stem Volume in Coniferous Forest from Low VHF SAR," *Proc. IGARSS 2000, Honolulu, Hawaii,* vol. 1, pp. 441-443.

[13] J.-S. Lee, D.L. Schuler, and T.L. Ainsworth, "Polarimetric SAR Data Compensation for Terrain Azimuth Slope Variation," *IEEE Trans. Geosci. Rem. Sens.* vol. 38, no. 5, pp. 2153-2163, 2000.

BIOPHYSICAL FOREST TYPE CHARACTERISATION IN THE COLOMBIAN AMAZON BY AIRBORNE POLARIMETRIC SAR

Dirk H. Hoekman and Marcela J. Quiñones

Wageningen University, Dept. of Environmental Sciences, Nieuwe Kanaal 11, 6709 PA Wageningen, The Netherlands
tel:+31-317-482894, fax:+31-317-484885, email:dirk.hoekman@users.whh.wau.nl

ABSTRACT

Fully polarimetric C-, L- and P- band data were collected by NASA's AirSAR system at the *Araracuara* test site, a well-surveyed forest reserve in the centre of the Colombian Amazon. The area is characterised by a high diversity of forest types, soil types and flooding conditions. A polarimetric classification technique is used to assess AirSAR's potential for forest structural type mapping and, indirectly, forest biophysical characterisation. Field observations were made at 23 0.1 ha plots to obtain additional quantitative descriptions on forest structure and ground surface conditions, but also to assess the suitability of existing map legends for SAR mapping. It could be shown that a new type of legend leads to physically better interpretable results. A method based on iterated conditional modes is introduced and is shown to yield radar-derived maps with a high level of agreement with existing maps, as well as with the ground observations. The following results may indicate the high level of accuracy obtained: 15 classes can be differentiated, the average radar map agreement ranges from 68-94% (depending on the type of map and approach) and for only a few classes the agreement is less than 70%. The relation between physical forest structure and polarimetric signal properties is studied explicitly using polarimetric decomposition. A new method is introduced based on the decomposition of polarimetric coherence, instead of power. It is based on simple physical descriptions of the wave-object interaction. The accuracy of the complex coherence estimation derived from the complex Wishart distribution. Thus several interesting physical relations between polarimetric signal and forest structure can be revealed. The physical limitations of this technique and its relation with sample size are indicated.

I. INTRODUCTION

The utility of multi-band polarimetric airborne SAR for tropical forest inventory is evaluated by analysing experimental data collected by NASA's AirSAR system. Such a system may fulfil information needs related to the mapping of forest types and the assessment of biophysical characteristics at a scale of 1:50,000 or larger. At the well-surveyed *Araracuara* test site, a forest reserve in the Colombian Amazon, it collected fully polarimetric C-, L- and P- band data in May 1993. The study was facilitated by detailed inventory and extensive field observations resulting in a very detailed landscape ecological unit map [1].

II. FIELDWORK AND LEGEND

The radar images show a lot of variation, however this variation is not always reflected well in the variation shown on the landscape ecological map. Partly this is a consequence of the aggregation level of the map. For example, small units (mostly units of rare types) are not shown and complexes of different forest types are shown as separate aggregated classes. Within a single mapping unit, differentiation in the radar image can occur because of flooding (at the time of image acquisition) or soil type. The latter, for example, related to the depth of peat layers. On the other hand, mapping units which are clearly distinct, floristically or geologically, but are not distinct in terms of biophysical characterisation, are not discernible on the radar images. The fieldwork was designed to capture the variation found in the landscape ecological map as well as in the radar data. Eventually a new legend could be developed which appeared to be suitable for radar image classification and which can be linked to the existing mapping units. In the legend proposed here (Table 1) the flooding state is the most dominant level (Map 1), followed by drainage type (Map 2), soil type (Map 3) and structural type (Map 6) (vegetation type). Also the forest type map (8 classes) (Map 7) can be aggregated from Map 6. A biophysical characterisation of forest types is given in Table 2.

III. CLASSIFICATION, VALIDATION AND MAPPING

The creation of a classified image as well as the evaluation of the classification results, in general, are not very straightforward tasks. This may be particularly true for the complex structure of the tropical rain forest. Some points of consideration are the occurrence of many rare types of forests, absence of well-defined boundaries and presence of gradients between forest types, complexes of forest types and *chagras*, small areas of shifting cultivation along the river. It could be shown that 15 classes can be defined on the basis of carefully selected training areas.

Proc. 3rd International Symposium, 'Retrieval of Bio- and Geophysical Parameters from SAR Data for Land Applications', Sheffield, UK, 11-14 September 2001 (ESA SP-475, January 2002)

Table 1. Biophysical and structural characteristics of vegetation types. H = high forest; L = low forest; P = palm forest. Biomass includes only individuals with a *dbh* ≥10 cm (source: [Duivenvoorden and Lips, 1991]).

	height (m) upper canopy	biomass (tons/ha)	basal area (m^2/ha)	Density (no. / 0.1 ha) treelets	trees	palms	species
high forests							
(H1)	26	340	36	640	71	4	39
(H2)	22	240	26	570	44	3	26
(H3)	20	190	25	650	71	7	32
low forests							
(L1)	14	130	27	680	117	7	14
(L3)	8	20	7	1700	40	3	10
palm swamp forests							
(P1)	20	250	34	620	92	9	17
(P2)	21	200	29	490	89	27	26
(P4)	6	50	8	1420	12	9	4

Table 2. Proposed legend for Maps 1, 2, 3, 6 and 7 for classification of AirSAR polarimetric data in the study area, the number of training areas (*N*) for each of the classes of Map 6, and the class Code number.

Flooding	Drainage	**Soil**	***Cover type***	**Structural type**	***Landscape unit***	**Forest type**		
Map 1 2 classes	***Map 2 3 classes***	*Map 3 8 classes*		*Map 6 15 classes*		*Map 7 8 classes*	*N*	*Code*
Flooded	Permanently flooded or wet	Peat	Palm forest (peat)	P2 (peat)	Ec, (Eb1	P2	36	11
				P4 (peat)	Tb3, (Eb3)	P4	22	12
			Low forest (peat)	L3 (peat)	Tb2, (Eb2)	L3	89	13
		Thin organic deposit	Palm forest	P2	Cb1	P2	36	14
		Thin organic deposit and peat	Palm forest	P2	Tb1	P2	36	7
		Thick H horizon	Low forest	L3	Hp2, Hp3	L3	18	15
		Hydrous and thin organic deposits	Palm forest (flooded)	P1 (flooded)	Ac	P1	10	6
		Hydrous organic deposits	Palm forest (flooded)	P4 (flooded)	Eb3	P4	18	8
			Low forest (flooded)	L3 (flooded)	Eb2	L3	9	9
				L2 (flooded)	Cm2	L2	18	10
	Sporadically flooded	Thin H horizon	High forest (flooded)	H3 (flooded)	Ce		10	17
				H2 (flooded)	Ac, Ec		-	
				H1, H3 (flooded)	Cc		20	16
Non-flooded	Never flooded	Thin and thick H horizon	Primary high forest	H2, (or H1, H3)	Ac, Ec	H2, (H1, H3)	114	1
				H3	Ce	H3	11	2
				H1, (or H3)	Hp1, Tp, Dp, Sv	H1, (H3)	431	3

The method of Iterated Conditional Modes (ICM) [2] appeared very useful. It was shown that a new approach, combining ICM with several types of *prior* information, can yield very good classification results. Fig. 1 shows how results develop from cycle to cycle for each individual class. The starting value is the ML-solution (denoted as cycle 0), with an overall accuracy of 50.5%, the final value is ICM(30), with an overall accuracy of 88.8% (Table 3). For most classes the results improve significantly during the first 10-15 cycles. The table also shows values for other maps, aggregated from Map 6. These other maps have less classes and, consequently, higher accuracy.

Table 3. Overall classification results for training areas and validation areas for Map 6, and for the other maps after aggregation from Map 6, after application of the extended ICM method.

	Map 1	**Map 2**	**Map 3**	**Map 6**	**Map 7***
training areas	93.6%	93.2%	88.8%	**88.8%**	89.0%
validation areas	94.1%	92.6%	76.3%	**68.9%**	73.7%

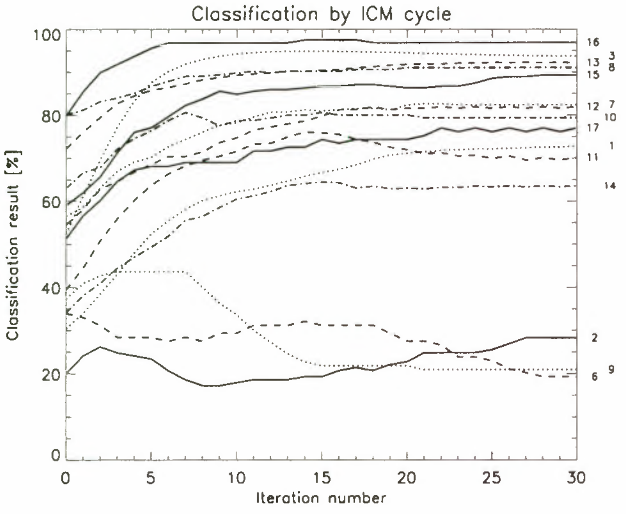

Fig. 1. Evolution of the % well-classified pixels of the training areas for all 30 cycles of the extended ICM approach. The starting value is the ML-solution (denoted as cycle 0).

IV. POLARIMETRIC MODELLING

The frequency dependence of the complex coherence shows some characteristic features which may be related to forest structure and which may be described well with existing physical backscatter models. Fig. 2 gives some examples. For non-flooded high forests, with increasing wavelength, the coherence decreases and the polarisation phase difference (PPD) increases from low values to values typically around 45°. For flooded high forests the coherence increases again when moving to P-band and the phase increases to values around 120°. Other forest types sometimes show a different behaviour. Such behaviour is not well described in literature.

In many backscatter models, notably radiative transfer models, the backscatter is thought of as composed of three incoherent contributions [3, 4]. These are (1) the direct backscattering from the vegetation layer, (2) the direct backscattering from the ground attenuated by the vegetation cover and (3) the backscattering originating from the ground-trunk interaction attenuated by the vegetation cover. These are sometimes referred to as the diffuse term, the single-bounce term and the double-bounce term, respectively [5].

Suppose the received electric field can be thought of as composed of these three incoherent terms. Then, for H-polarisation:

$$E_{h,tot} = E_h = E_{h,1} + E_{h,2} + E_{h,3} \tag{1}$$

and, for example, the estimation of the HV cross-product follows as:

$$\begin{aligned}\left\langle E_h E_v^* \right\rangle &= \left\langle \left(E_{h,1} + E_{h,2} + E_{h,3}\right)\left(E_{v,1}^* + E_{v,2}^* + E_{v,3}^*\right)\right\rangle \\ &= \left\langle E_{h,1} E_{v,1}^* \right\rangle + \left\langle E_{h,2} E_{v,2}^* \right\rangle + \left\langle E_{h,3} E_{v,3}^* \right\rangle \end{aligned} \tag{2}$$

This leads to the following expression for complex coherence:

$$\rho_{hhvv} = \rho_{hhvv,1} + \rho_{hhvv,2} + \rho_{hhvv,3}\,, \tag{3}$$

which is the sum of contributions from the three above-mentioned scatter mechanisms. The first component can be written as

$$\rho_{hhvv,1} = f_1\, r_1 \exp(i\phi_1) \tag{4a}$$

where

f_1 = the relative strength of the vegetation layer. Note that $f_1 = \sqrt{\dfrac{\sigma^0_{hh,1}}{\sigma^0_{hh}} \dfrac{\sigma^0_{vv,1}}{\sigma^0_{vv}}}$.

r_1 = the HHVV coherence magnitude of the vegetation layer

ϕ_1 = the HHVV coherence phase of the vegetation layer

Similarly

$$\rho_{hhvv,2} = \alpha\, f_2\, r_2 \exp(i\phi_2) \tag{4b}$$

and

$$\rho_{hhvv,3} = \alpha\, f_3\, r_3 \exp(i\phi_3)\,, \tag{4c}$$

with $\alpha = |\alpha| \exp(i\phi_\alpha)$,

where $|\alpha|$ = the (effective two-way H x V) attenuation through the vegetation layer

ϕ_α = the (effective two-way H x V) phase shift caused by propagation through the vegetation layer

f_2 = the relative strength of the ground surface.

r_2 = the HHVV coherence magnitude of the ground surface

ϕ_2 = the phase of the HHVV coherence of the ground surface

f_3 = the relative strength of the trunk-ground interaction component.

r_3 = the HHVV coherence magnitude of the trunk-ground interaction component

ϕ_3 = the phase of the HHVV coherence of the trunk-ground interaction component.

It is noted that

$$f_1 + |\alpha|(f_2 + f_3) \leq 1 \tag{5}$$

and, therefore, the complex coherence can be regarded as a addition of three vectors in the complex plane for which the sum of the three vector magnitudes is ≤ 1. Fig. 3 gives a decomposition example.

Without going into additional elaboration it may be stated that this model gives insight into the physical scattering mechanisms of the plots under consideration, or any other homogeneous area of the scene. The accuracy of such an interpretation depends on the accuracy of the coherence estimation, which in turn depends on the number of independent looks in the sample. Fig. 4 shows the 50% and 90% confidence interval for the plot 5 sample shown in Fig. 3. It may be obvious that a large number of looks is required to enable a useful interpretation and that working on a pixel-basis may have too many limitations. Figure 5 illustrates this effect.

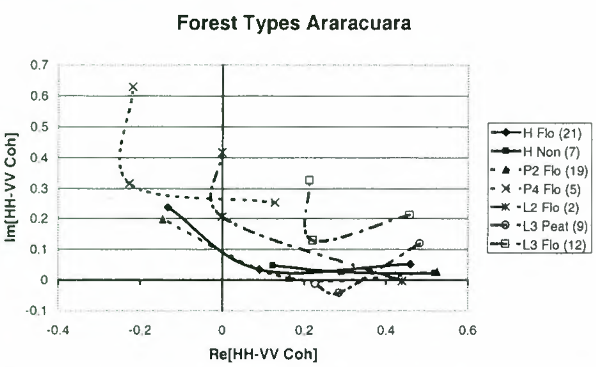

Fig. 2. Multi-frequency complex coherence curves for high forests, (b) flooded palm forest and low forests. The curves connect the C-band coherence (in these examples always the right-most point), with the L-band and the P-band value (at the other end of the curve).

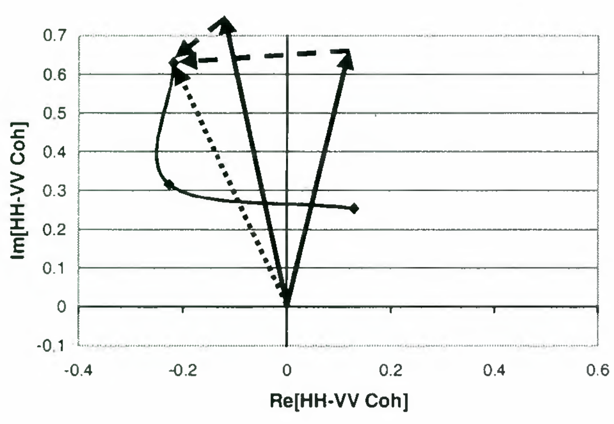

Fig. 3. Two examples of solutions for the decomposition of the P-band complex coherence of plot 5. Vegetation components (solid lines) and double-bounce components (dashed lines) add to the total (dotted line). The single-bounce component is ignored.

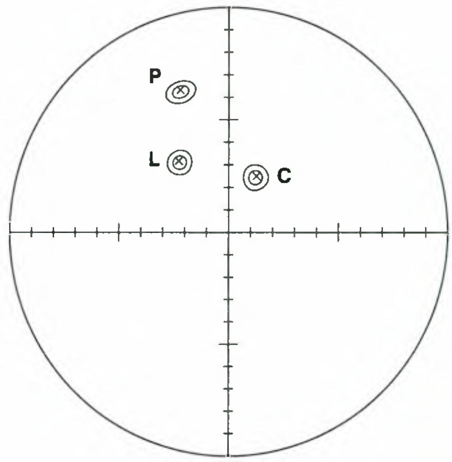

Fig. 4. Confidence intervals at 50% and 90% for the three points of plot 5 shown in Fig. 3. The sample contains 706 independent looks in C- and L-band and 403 independent looks in P-band.

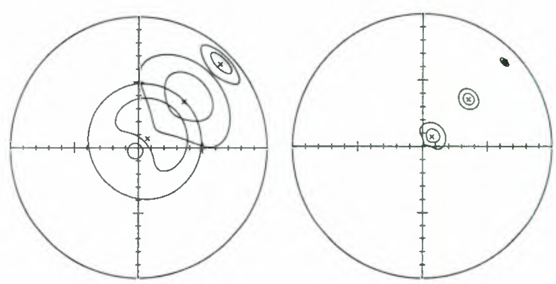

Fig. 5. Confidence intervals for the complex coherence at 50% and 90% for (left) 14-look and (right) 280-look samples, for a phase difference of 45°, and $|\rho_i|$ values of 0.1, 0.5 and 0.9.

V. CONCLUSIONS

A mapping approach for tropical rain forests consisting of three conceptual steps has been presented. These three steps are: (1) legend development, including hierarchical aggregation, (2) mapping, including spatial aggregation and (3) physical interpretation of units mapped.

It was found that the legend of the existing landscape ecological map of the Araracuara region, though very detailed, not seems to describe well the class distinction radar can make. Partly this is due to the use of geologically and floristically related parameters, and partly because of the aggregation of fine-structured forest complexes into separate legend units. The proposed radar legend is solely based on biophysical parameters and has a hierarchical structure based on flooding conditions, drainage, soil type and vegetation structure type, respectively. This hierarchy can be explained in terms of existing physical backscatter models. It should be noted however that there is no unique one-to-one correspondence between the existing legend and the new radar legend. These findings may be true in general, i.e. for different forests in the world different and non-compatible legends have been developed. Physically based 'radar' legends may prove to have a more general applicability.

At the lowest hierarchical level all 15 classes can be distinguished well on the basis of their full polarimetric information content and for homogeneous samples of a sufficient number of independent looks. Such results cannot be related easily to image classification results because of the presence of texture, relief and speckle. Commonly used image processing techniques to mitigate or to capitalise on these effects appear to be of limited use for several reasons. A technique based on iterated conditional modes appeared to be useful, especially when extended to incorporate prior knowledge on texture, relief and class occurrence. The final overall result is 88.4% agreement between classified image and existing forest map. It is hard to give a good judgement on the actual accuracy of the mapping. For a proper validation the number of 23 fieldwork plots may be insufficient. Moreover, the existing map is not free of error. Nevertheless, the general agreement between landscape ecological map, the radar-derived map and the validation set is very high. This may be especially true when considering the fact that some classes, which show substantial confusion, actually may not differ very much in biophysical characterisation.

Being able to classify the forest in many structural hierarchically grouped classes which can be linked to well-described units enables making a relation with parameters such as forest height classes or biomass level classes. A more direct approach would be beneficial in case mapping of less well-known areas is pursued. Any supervised or unsupervised classification, or, when feasible, segmentation, can yield accurate and unbiased estimations of the complex polarimetric coherence. In this paper a new approach is proposed to interpret multi-frequency complex coherence numbers, how to link it with concepts of scattering mechanisms, physical backscatter models and number of independent samples. In principle the larger the samples (or homogeneous segments) obtained, the larger the possibilities for physical interpretation. More research remains to be done to be able to fully exploit this new physical polarimetric decomposition approach. However, first results clearly show that different sets of multi-frequency complex coherence numbers can be recognised and linked to different structural types. In some cases, based on physical assumptions made, decomposition into vegetation and trunk-ground double bounce terms may be done well, which may open the way to, for example, improvement of biomass inversion algorithms.

Future campaigns would benefit from using an interferometric mode (such as the TopSAR mode presently available). A higher resolution would also be very beneficial enabling forest structure characterisation by texture or tree-mapping. A new campaign has been conducted over Indonesian tropical rain forests in the framework of NASA's PacRim-2 deployment enabling furthering of mapping approaches along these lines.

ACKNOWLEDGMENT

NASA is acknowledged for provision of AirSAR 1993 S. American Deployment data. Logistic support was provided by the Tropenbos foundation through Tropenbos – Colombia and the *Instituto Amazonico de Investigaciones Cientificas* (SINCHI). Martin Vissers of VDM is acknowledged for support in data processing and data management.

REFERENCES

[1] Duivenvoorden, J. and H. Lips, 1991, *Mapa de la ecologia del paisaje del medio Caquetá*, Tropenbos - Colombia, Bogotá, Colombia.

[2] Besag, J., 1986, On the statistical analysis of dirty pictures, *Journal Royal Statistical Society B*, Vol.48, No.3, pp.259-302.

[3] Ulaby, F.T., R.K. Moore, and A.K. Fung, 1986, *Microwave Remote Sensing, Volume III: From Theory to Applications*, Artech House.

[4] Fung, A.K., 1994, *Microwave Scattering and Emission Models and Their applications*, Artech House.

[5] Van Zyl, J.J., 1989, Unsupervised classification of scattering behaviour using radar polarimetry data, *IEEE Transactions on Geoscience and Remote Sensing*, vol.GE-27, no.1, pp.36-45.

BIOMASS MAPPING USING BIOPHYSICAL FOREST TYPE CHARACTERISATION OF SAR POLARIMETRIC IMAGES

Marcela J. Quiñones and Dirk H. Hoekman

Wageningen University Dept. of Environmental Sciences, Nieuwe Kanaal 11, 6709 PA Wageningen, The Netherlands tel:+31-317-484827, fax:+31-317-484885, email: Marcela.Quinones@users.whh.wau.nl

ABSTRACT

Studies on the relationship between biomass and radar backscatter have relied on field data to construct empirical relationships with radar backscatter that can be used for biomass estimations and mapping. In general, inversion of radar data for biomass estimations is limited by the variations on backscatter produced by structural parameters and soil moisture and limited to a certain maximum biomass level dependent on the structural class.

In this work we created biomass maps of two study sites at the Colombian Amazon (Guaviare and Araracuara) by using results from polarimetric classification algorithm that combines power, phase and correlation of C, L and P band of AirSAR data. Two different approaches were used. For the Guaviare site, (dry and flat) the biomass classes selected are related to Land Cover types and an empirical relationship between biomass and the average backscatter ((LHV+PRR)/2) is used to create the biomass map. High consistency with the cover map is found. For the Araracuara site (hilly and flooded) a biomass map is created by reclassifying a biophysical forest structural map with biomass values obtained from field available data.

Field data is used to validate maps and to study the behavior of radar polarimetric signatures according to different forest structures. A new approach of analysis is based on the description of the polarimetric coherence according to a physical explanation of the wave-object interactions. The same type of analysis is used to study systematically the influence of different forest structural parameters and soil moisture conditions on the polarimetric signatures. Simulated radar data from the UTARTCAN backscatter model is used.

I. INTRODUCTION

In the last decade scientists and modellers of different disciplines like ecologist, hydrologist and bio-geo-chemist are requiring data on the amount and distribution of biomass over the earth surface. The study of carbon cycle and its influence in important processes related to climate change require accurate biomass quantification. The processes related to changes in biomass levels are very dynamic i.e. deforestation, therefore the development of straightforward (simple) algorithms for biomass mapping is required. Remote sensing data have proved to be useful for that purpose but important limitations have been found for both optical and microwave systems. Radar remote sensing is one of the more promising tools for biomass mapping due to its sensitivity to the amount of scatterers (branches, leaves and trunks) directly related to the standing biomass. So far the use of radar for biomass mapping and estimations have yield two main conclusions: 1) the biomass dependency on radar backscatter varies with radar wavelength and polarisation. 2) The sensitivity of radar return values to biomass changes saturates at certain biomass levels. In general it can be said that saturation point increases with wavelength and that HV polarisation is more sensitive to biomass changes [8,9,10]. In addition studies have revealed that forest structure affects radar backscatter giving constraints for direct biomass estimations. [1].

In this paper we present an approach of four steps of analysis to study the relation between biomass and radar return values. The first two steps present two different methodologies of biomass mapping depending on the biophysical conditions of the terrain. The last two step searches deeper into the effect of forest structure on the radar return values and its effect on biomass estimations. Radar data from field measured plots and simulated radar values from hypothetical forest stands are used.

II. BRIEF DESCRIPTION OF TEST SITES

Both study areas are located at the Colombian Amazon. Then first is located in the district of Guaviare (2.5°N, 72.5°W), and is a colonisation area characterised by a flat and non-flooded terrain. Biomass values vary according to the vegetation cover type. The second area is a pristine natural forest located in the vicinity of Araracuara (0°40'S, 72°

Proc. 3rd International Symposium, 'Retrieval of Bio- and Geophysical Parameters from SAR Data for Land Applications', Sheffield, UK, 11-14 September 2001 (ESA SP-475, January 2002)

15'W) with complex geomorphology and diverse flooding conditions. The biophysical description of the forest types occurring in the area is well reported in the Landscape ecological map available[2]. Variations on biomass are related to forest type. (Table1, Hoekman and Quiñones, this proceedings)[3].

III. DATA BASE

In May 1993, the AirSAR (POLSAR mode) collected fully polarimetric C-, L- and P- band data [4] in both study areas. The AirSAR images [5] are in 16-look Stokes matrix format with a pixel spacing of 6.66 m in range and around 8.20 m in azimuth. The incidence angle (θ_i) varies from about 20° to 60°. For the identification and polarimetric description of the land cover and forest types polygons were digitised over the images, in areas corresponding to the areas corresponding to fieldwork plots and field observations. For the Guaviare site detailed forest structural data were made for 13 plots of primary forest, 10 plots of secondary and 5 plots of pasture. For the Araracuara site measurements were made over 23 plots, additional information was acquired on flooding conditions. For the estimation of (total aboveground wet) biomass, for the plots measured at both study sites, an allometric equation was applied, using trunk diameter and height to the first living branch.[7].

In addition with the help of the land cover map of Guaviare and the landscape ecological map of Araracuara a set of independent polygons were delineated for the defined classes [6,2]. The training set samples, consisted of 778 delineated areas for the Guaviare site and 759 for the Araracuara site. Polygons were at least of 50 pixels in a 25°-60° range of incidence angles. The field averaged Stokes scattering element data of the database is used to calculate field averaged values for backscatter, phase differences and correlation. Since each field has at least 50 pixels, or N=800 independent looks, for homogeneous fields these averages closely approach the underlying values and can be regarded free of the effect of speckle

IV. APPROACH

a) For the Guaviare site an empirical relationship between the biomass and the radar values is used for the classification of the image. Saturation occur at low levels of biomass (100 tons/ha). Definition of biomass classes can be linked with the biomass levels of vegetation cover types. The accuracy of the map was asses by analysing the percentages of the training polygons labelled with cover type classes into the expected biomass range values.

b) For the Araracuara site biomass mapping is done by classifying structural vegetation types (15 classes) stratified by flooding conditions and forest structure (Hoekman and Quiñones. this proceedings) [3]. Biomass values are assigned to each structural type according to field available data therefore no saturation point exist Accuracy of the biomass map was calculated by using confusion values from the confusion matrix of the forest structural map (Map 6, [3]). Structural types were rearranged by biomass level. The number of biomass classes for the biomass map depends on the number of structural types with different biomass. Percentages of correct classified training areas were calculated for each defined biomass level.

c) Radar data corresponding to the field measurement areas was extracted from C, L and P bands, linear polarisation and multi-frecuency complex coherence signatures are analysed for forest stands of different structure at the same biomass levels. The analysis of the signatures give insights into the relation between structural parameters, soil moisture and radar values. The analysis of signatures is based on the model presented by Hoekman and Quiñones, this proceedings) [3] This data can be used to generate knowledge for future biomass retrieving algorithms.

d) A polarimetric scattering model for layered vegetation (UTARTCAN) was used to generate simulated radar scattering data of hypothetical forest stands with controlled structural characteristics. The systematic change in a structural variable elucidates its effect over the radar signatures. The UTARTCAN model is based on an iterative solution of the radiative transfer equation up to the second order for multiple scattering within the canopy and between the canopy and the ground. It is applicable to C, L and P band data of the AirSAR system. The model computes de polarimetric backscatter coefficients. The vegetation is described as a layered random medium of discrete scatterers.

Trunks and branches are modelled as cylinders and leaves as circular discs. Each layer contains a number of scatters types and for each type a density, a dielectric constant, dimensions, orientations and distributions are specified. The soil is described as a random rough surface and the backscatter properties are modelled using the Integrate Equation Method. For the translation of the field data into input files for the UTARTCAN model, the Life Form interface model was developed. The model reads the field data and creates four three types of outputs. 1) The input file for UTARTCAN model, 2) Forest profiles drawings and 3) biomass and surface structural data for each plot. Simulations of the measured data serve to evaluate the performing of the Model.

e)

V. RESULTS

a) Guaviare site: Land cover type classification and biomass mapping

The potential for biomass class mapping was studied by evaluating the backscatter for 5 fields of pasture, 10 fields of secondary forest re-growth and 13 fields of primary forest for which biomass was estimated. For these fields the above ground fresh biomass was found to vary over the range of 2.9-10 ton per hectare (1 ton = 1,000 kg; 1 ha = 10,000 m^2) for pastures, 6-159 ton/ha for secondary forest and 137-297 ton/ha for primary forest. Since biomass varies over several orders of magnitude γ_i values (in dB) were fitted to the logarithm of biomass (x) using a log-log functional relationship of the form γ_i [dB]= $a\exp(bx) + c$. The main results are summarised in table 1. For the C-band the correlation is not very high. The maximum value for r^2 is 0.66 and was found for the VV-polarisation. For L-band with HV-polarisation and for P-band high values are found . However there are some differences: L-band with HV-polarisation has a high correlation but the signal tends to saturate at high biomass levels. For P-band the saturation appears at higher biomass levels, however the *SEE* (Standard Error of Estimate) is higher. The combination of these bands can be used to improve overall results for the whole biomass range under study. Averaging backscatter of P-band with RR-polarisation and L-band with HV-polarisation, for example, results in a slightly higher correlation (r^2 is 0.94) and a considerably lower *SEE*. The ratio of the total range of backscatter and the *SEE* for this particular combination is high, namely 13.2. This number may be interpreted as 6.7 times 1.96 standard deviations or, in other words, at least 6 classes of biomass may be distinguished at the 95% confidence level. (This should be interpreted as the confidence level for the real class being not more than one class away from the estimated class). Also, since biomass values of the savannah, beyond the lower end of the range shown here, and biomass values of higher biomass primary forest (at other test sites) beyond the higher end of the range shown here, seem to obey this functional relationship well, it is believed that up to 8 biomass classes may be discerned using this particular combination.

Table 1. Relationship between backscatter, expressed as γ_i [dB], and biomass expressed as log10 of the above ground fresh biomass in ton/ha, for several frequency and polarisation combinations. The correlation coefficient r^2, the standard error of estimate (*SEE*), the total range of γ_i of the experimental data and the ratio of range and *SEE* are shown

	r^2	*SEE* [dB]	range [dB]	Range/ *SEE* [dB]
C-HH	0.32	0.41	3.2	8.0
C-HV	0.62	0.33	3.2	9.6
C-VV	0.66	0.51	4.8	9.5
L-HH	0.81	1.07	9.3	8.7
L-HV	0.93	1.05	11.6	11.0
L-VV	0.78	0.83	7.7	9.3
P-HH	0.90	1.39	11.1	8.0
P-HV	0.94	1.70	16.1	9.5
P-VV	0.91	0.82	9.6	11.6
P-RR	0.93	1.23	13.2	10.7
L-HV+P-RR	0.94	0.93	12.3	13.2

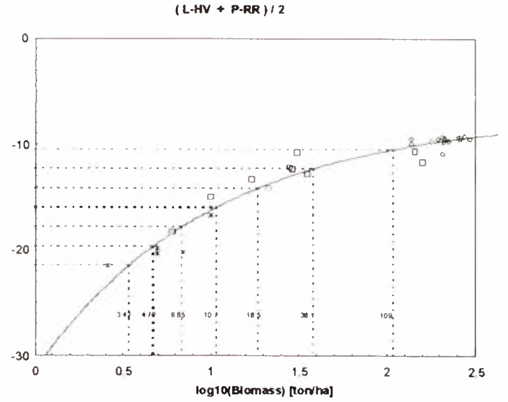

Fig. 1. (PRR+L HV/2)-polarisation average as function of biomass. The biomass is the fresh weight above ground biomass (in tons/ha) at the logarithmic scale (i.e. 1.0 is 10 ton/ha, 1.5 is 31.6 ton/ha, etc.). Experimental data for primary forest (◊), secondary forest (□) and pasture (*) are fitted to a curve of the

form γ[dB]= a + b(1-exp(-cx)), where x is the logarithm of the biomass.

Using the functional relationships between biomass and the average backscatter of the Lhv and Prr bands a map of biomass classes can be created. This was done for eight arbitrarily chosen biomass classes, namely: (1) ≤3.42, (2) 3.42-4.72, (3) 4.72-6.85, (4) 6.85-10.7, (5) 10.7-18.5, (6) 18.5-38.1, (7) 38.1-109 and (8) > 109 (in ton/ha). Classes 2 until 7 correspond to equidistant values of backscatter separated at 1.96 standard deviation intervals as indicated in Fig. 1.

Since the relationship does not hold for the class of recently cut areas, these areas have been excluded from the biomass classification. It is difficult to validate the accuracy of these results since acquiring a sufficient number of additional biomass values is a huge task. The consistency between biomass classification and land cover type classification can be checked, however. Table 2 shows for each land cover class (excluding recently cut areas) the distribution of biomass classes as a percentage of the total area.

Table 2. Percentages of areas corresponding to the classification of the four main land cover types and the eight biomass classes. The land cover types are encoded as: (1) Primary forest, (2) Secondary forest, (3) recently cut areas, and (4) Pastures.

Biomass classes (ton/ha)	1	2	3	4
Masked	0	0	100	0
0-3.42	0	0	0	16
3.42-4.72	0	0	0	18
4.72-6.85	0	1	0	23
6.85-10.7	0	3	0	20
10.7-18.5	1	12	0	12
18.5-38.1	2	28	0	6
38.1-109.	12	40	0	3
>109.	84	14	0	1

The agreement with expected biomass ranges is high for all three land cover types.

b) Araracuara site: Structural Forest type classification and Biomass mapping

For The Araracuara site, the relationship between biomass and the linear polarisation of the C, L and P band were studied. The relation with gamma co-polarised data on the three frequencies presented a lot of deviations for the different forest types and the flooding conditions. With the L and P band cross-polarised data the deviations were not significant but as expected the saturation point is reached at very low biomass level .[31.6 tons /ha]. Because of the variations on backscatter due to structural differences and flooding conditions for the same biomass level, the same methodology used for the Guaviare site could not be applied Therefore for biomass mapping at this site the biophysical structural differences between forest types should be included in the classification. For this purpose the biophysical forest type characterisation of the study area was used. The map of structural types (15 classes) (table 3 of Hoekman and Quiñones, this proceedings) was reclassified using the biomass field data corresponding to the forest type of that particular structural class. In total 8 biomass classes can be mapped (Table 3). The confusion matrix of the structural map (Map 6) after the application of the ICM method, (95 looks), was used to assess the accuracy of the biomass estimations for the training areas. Structural types under the same biomass level were grouped and the number of right and wrong classified polygons were added. In that way the percentages of accuracy between the classes could be calculated as shown (Figure 3). The calculated

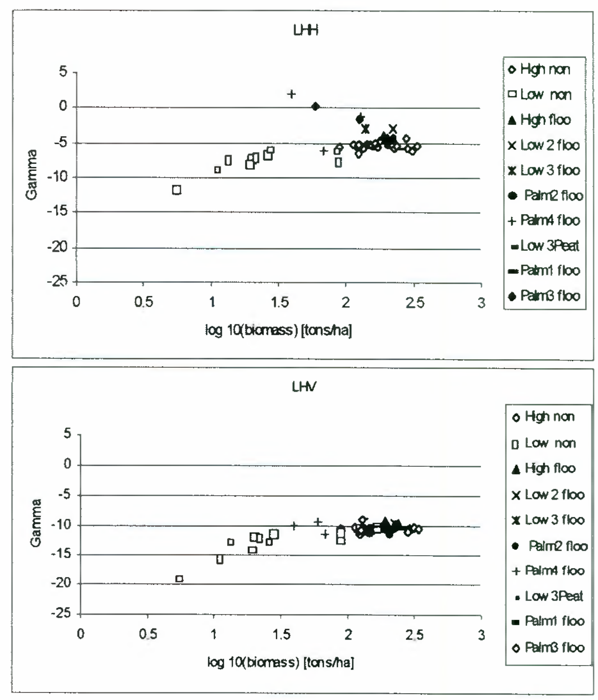

Figure 2: Scatter plots between the estimated biomass and the radar return values for LHH (upper) and LHV (lower) radar backscatter. The biomass is the fresh weight above ground biomass (in tons/ha) at the logarithmic scale (i.e. 1.0 is 10 ton/ha, 1.5 is 31.6 ton/ha, etc.). The experimental data for different forest structural types i.e. High non= High forest-non

overall classification accuracy for the biomass map was 92%. One advantage of the previous method is that there is not a saturation effect because the classification has been based on structural characteristics, using field biomass available data. .

Table 3: Defined biomass classes in Tons/ ha for the area of Araracuara. The Map 6 (code) and Forest Type corresponds to the codes presented in Table 1 & 2 in Hoekman and Quiñones, this proceedings.).

Biomass class [Tons/ha]	Map 6 (code)	Forest Type
0- 20	13, 9, 15	L3
20-50	12, 8	P4
50-140	10	L2
140-190	17	H2 flooded
190-200	11, 14, 7	P2
200-240	1	H2 non flooded
240-250	6	P1
250-340	16, 3	H1-H3

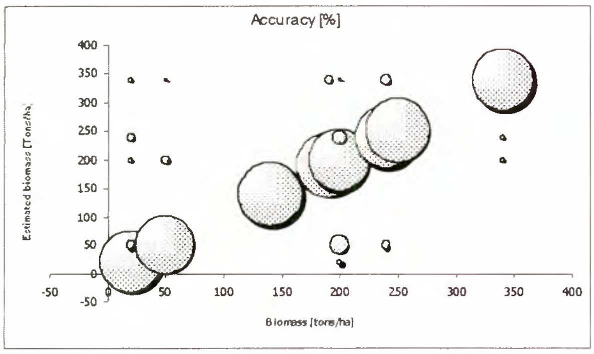

Figure 3: Accuracy of estimated biomass expressed in percentages of right and wrong classified training areas within the same biomass class.

c) Field data analysis

The analysis of the gamma multi-frequency linear polarisation signature and the complex coherence signature was made using radar data from field plots of different structural characteristics in the same biomass level using a physical model (introduced by Hoekman and Quiñones this proceeding).

Signatures for three different forest structures on high biomass level (230 tons/ha) (Figure 4.) are presented The first forest type is high forest in non-flooded terrain with close canopy and with trees of high DBH (>30cm). The second type is palm forest with high palm density (DBH>30 cm) and open canopy over flooded terrain. The third is a low forest with high density of small trees (DBH < 10 cm.) over flooded terrain. The gamma linear polarisation signatures produced by these forest types are different for the three bands. For the C band the gamma backscatter values are higher for the Palm forest on the three polarisations. For the L and P band the co-polarised data is higher for the flooded forest types (2dB- L band and 4dB –P band)and the cross-polarized data does not change with the forest type. The multi-frequency complex coherence of the high forest shows an increase in the phase angle and a decrease in the correlation with the wavelength. This can be interpreted as an increase of the volume scattering due to the penetration capabilities of longer wavelengths and the presence of big scatterers in this forest type.

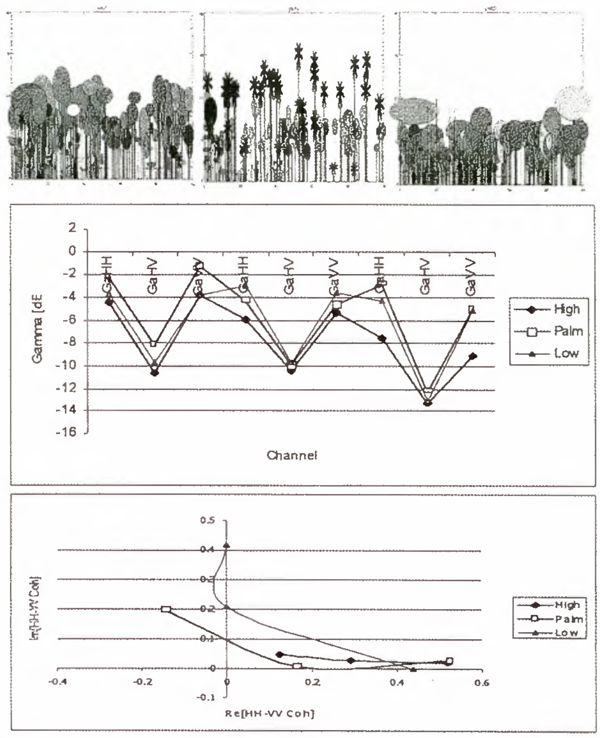

Figure 4: Field forest structure profiles and corresponding multi-frequency, linear polarisations and complex coherence signatures. Three different forest structures from left to right: high forest, palm forest and low forest. Biomass level 230 tons/ha

The attenuation produced by the thick dense canopy decreases the possibilities of double bounce scattering For the Palm Forest there is a decrease in the correlation from C to L band but no significant change on the phase angles. From L to P band there is an increase on the phase angle and the correlation That can be interpreted as an increase on the volume scattering from C to L band due to the presence of big leaves and thick palms (< 30 cm DBH). The dense low canopy attenuates the L band and little double bounce occurs. P band on the other hand penetrates the canopy of medium size scatterers and larger contribution from the trunk-ground interactions occurs (i.e. double bounce between the trunks of the palms and the inundated forest floor). For the Low forest the phase increases from C to L and P bands and the correlation is high for the three bands. In this case there is high single scattering from the C band meanwhile volume scattering dominates in L band decreasing in the P band. The absence of big scatterers (thick trunks and big leaves) can be responsible for the decrease in the volume scattering on the P band. For this same reason the penetration of the waves into the forest floor can be high and an influence from the flooding condition can be affecting the phase.

f) UTARTCAN Simulation

For each of the hypothetical forest stands the gamma multi-frequency linear polarisations and complex coherence values were calculated. This part of the analysis is still under development and one example is presented in this paper.

In this example the effect of layering is evaluated by analysing the signature of a controlled forest stand compared to the signature produced by forests with same biomass and density (i.e. same number of scatters) but different distribution of the vertical components. In the control plot all the trees have the same DBH, total height and canopy height; in the emergent plot trees have the same structural characteristics as the control plot but 20% of the trees are located above the canopy simulating an emergent layer. The sub-canopy plot has the same characteristics but 20 % of the trees are creating a new layer under the canopy. The signature of the linear polarisations was almost the same for the tree plots a difference of 1 dB was observed for the cross-polarised data of L and P band. The difference on the complex coherence signature was more evident. In this case the phase and correlation of the C band is the same for the three plots, indicating that for single bounce scattering mechanisms is dominating. For the L band there are changes on the phase and the correlation especially for the emergent plot in which the phase increases and the correlation decreases, indicating that more volume scattering is occurring in this plot. For the P band there is a slight increase on the phase and the correlation. That can be interpreted as a decrease in the single and increase in the volume scattering.

VI. CONCUSIONS AND RECOMMENDATIONS

Two algorithms for biomass mapping have been presented in this paper. The first is a maximum likelihood classification using and empirical relationship between biomass and the combination of channels that gave the best correlation between the variables and the highest sensitivity. In this case only

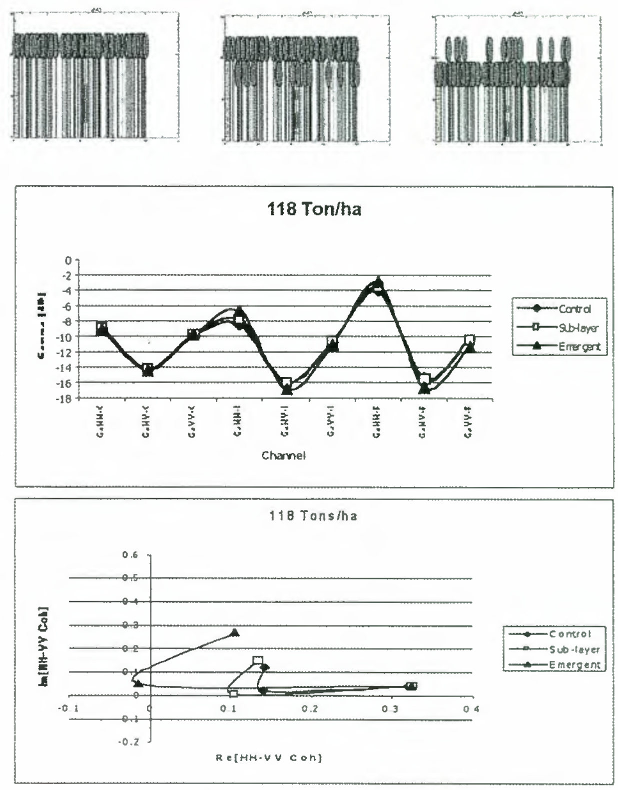

Figure 5: Multi-frequency, linear polarizations and complex coherence signatures for simulated forest stands. Forest profiles from left to right: control, sub canopy layer and emergent layer.

two (PRR and LHV) radar polarizations were used. The use of empirical relationships is constrained by the effect of radar saturation at a certain biomass level, affecting the number of biomass mapping classes, in this case 8 biomass classes could be mapped. Biomass classes were related to the land cover classes mapped in the area and the agreement between this two could be used to asses the biomass map accuracy The resultant biomass map showed high consistency with the land cover map created for the area.

The second algorithm includes the prior biophysical forest type classification by using multi-frequency polarimetric data. Biomass data was then associated to each structural class overcoming the saturation effect and allowing the definition of classes beyond the saturation level.

It should be noted that both biomass maps show broad biomass classes over several orders of magnitude and, thus, is useful for assessment of spatial patterns associated with land and forest degradation and secondary re-growth processes. It does not show accurate biomass value estimations and, thus, is of limited value for, say, foresters who want to assess parameters such as timber volume.

At this stage of the research field forest structural data and biomass field data are needed for both biophysical characterisation and biomass mapping. Deeper analysis of field data as presented on the steps 3 and 4 of the analysis will allow to define some specific effects of structure and biomass levels over the radar signatures. Ongoing research includes the analysis of the signatures in relation to specific structural characteristics (DBH distribution, layering, life form composition, height and density) and to conditions of the terrain (soil moisture and soil roughens). In the future it is expected that biophysical forest characteristics and soil conditions can be extracted from the polarimetric analysis of the images without prior field knowledge.

The biomass mapping will benefit from additional information given by interferometric systems. Topographic mapping and possible forest height estimations will increase accuracy in biophysical characterisations.

By the study of the polarimetric signatures of different structural types in other study sites (forest types) around the word a knowledge based classification system could be designed in order to generate vegetation structural maps without field information. Extension of the actual data base of tropical forest including areas in, South-east Asia, Africa or Australia will be of great help in understanding the variations of radar values with structure and biomass.

ACKNOWLEDGEMENTS

NASA is acknowledged for provision of AirSAR data and execution of the AirSAR South American Deployment. Logistic support was provided by the Tropenbos foundation through Tropenbos - Colombia, Martin Vissers of VDM is acknowledged for support in data processing and data management.

REFERENCES

[1] Imhoff, M. L., 1995, A Theoretical Analysis of the effect of Forest Structure on Synthetic Aperture Radar backscatter and The Remote Sensing of Biomass. *IEEE Transactions on Geoscience and Remote Sensing*, Vol. 33, No. 2, pp. 341-353.

[2] Duivenvoorden, J. and H. Lips, 1991, *Mapa de la ecologia del paisaje del medio Caquetá*, Tropenbos - Colombia, Bogotá, Colombia.

[3] Hoekman D.H. and M.J. Quiñones. Biophysical Forest type Characterisation in the Colombian Amazon by Airborne Polarimetric SAR. Proceedings 3rd International Symposium on Retrieval of Bio-Geophysical Parameters from SAR Data for Land Applications. 11th-14th September 2001. SCEOS, University of Sheffield, UK.

[4] NASA, 1993, AirSAR South American Deployment, Operation Plan 4.0.

[5] Van Zyl, J.J., R. Carande, Y. Lou, T. Miller and K. Wheeler, 1992. 'The NASA/JPL three-frequency polarimetric AirSAR system'. In: *Proceedings of IGARSS'92; International Space Year: Space Remote Sensing*. Houston, May 26-29 1992, Volume I, pp.649-651.

[6] Andrade, A and A. Etter, 1987, Levantamiento ecologico del área de colonización de San José del Guaviare, Corporación de Araracuara, *Proyecto IDAINCO-CASAM*, Bogotá.

[7]. Brown, S. A.J.R. Guillespie and A. Lugo, 1989. Biomass Methods for Tropical Forest with applications to Forest inventory Data. Forest Science. Vol. 35, No 4, pp881-902.

[8] Kasischke, E.S., N.L. Christensen, Jr. And L.L Bourgeau-Chavez, 1995, Correlating radar backscatter with components of biomass in loblolly pine forest, *IEEE Transactions on Geoscience and Remote Sensing*, Vol 33, pp.643-659.

[9] Ranson, K.J. and G. Sun, 1994, Mapping biomass of a northern forest using multifrequency SAR data, *IEEE Transactions on Geoscience and Remote Sensing*, Vol 32, pp.338-395.

[10] Rignot, E.J, R. Zimmermann, J.J. van Zyl, 1995, Spaceborne applications of P band imaging radar for measuring forest biomass, *IEEE Transactions on Geoscience and Remote Sensing*, Vol 33, pp.1162-1169.

JERS REPEAT PASS COHERENCE FOR OBSERVATION OF SIBERIAN FOREST

Leif Eriksson[1], Andreas Wiesmann[2], and Christiane Schmullius[1]

[1]Institute for Geography – Geoinformatics
Friedrich Schiller University
Address: Löbdergraben 32, D-07743 Jena, Germany
Phone: +49-3641-948878; Fax: +49-3641-948852; E-mail: leif.eriksson@geogr.uni-jena.de

[2]Gamma Remote Sensing AG
Address: Thunstrasse 130, CH-3074 Muri b. Bern, Switzerland
Phone: +41 31 951 70 05; Fax: +41 31 951 70 08; E-mail: wiesmann@gamma-rs.ch

ABSTRACT

This paper presents the first results from a study of JERS repeat pass coherence. The goal of the study is to find out if JERS repeat pass coherence can be used for observation of Siberian forests and to compare it with results for ERS tandem coherence. Two forest territories in Siberia are used as test sites. These two territories, Bolshe-Murtinsky and Chunsky, are chosen for their good availability of satellite and ground data. The test sites were also studied in the EC-financed SIBERIA project (SAR Imaging for Boreal Ecology and Radar Interferometry Applications), but a detailed study of the JERS coherence has previously not been done for these regions. The data analysis show that JERS coherence in combination with JERS backscatter intensity can be used for forest/non-forest monitoring.

INTRODUCTION

The ERS coherence has already proved to provide valuable information for forest studies (Askne et al. 1997, Fransson et al. 2001, Santoro et al. 2000, Wagner et al. 2000), but after the loss of ERS-1 it is not likely that C-band coherence with only 1-day acquisition difference will be available in the near future. This makes it important to study the possibilities for L-band repeat pass coherence, in preparation for the upcoming Japanese satellite ALOS and its L-band SAR, PALSAR.

The interferometric coherence is affected by several factors. One of the most important for forests is the temporal decorrelation, caused by changes in the scattering between the two image acquisitions. These changes are caused by natural motion of the scatterers, but also by changed conditions like snow melting and soil moisture differences, or bigger changes like forest fire, clear cutting or thinning of the forest. The 44-day repeat cycle for JERS allows more changes to happen than the 1-day repeat cycle for the ERS tandem mission. Some of the effects can be reduced by selecting image pairs from the winter season when conditions are more stable, but in our case JERS coherence was only available for the summer. Motion of the scatterers also affects coherence from JERS and ERS differently. Due to its higher operating frequency, ERS is more sensitive to motions of smaller structures like twigs and small branches that are less stable over time. Conclusively, the temporal decorrelation from motion of scatterers is smaller for JERS coherence, but due to longer temporal baselines it is more affected by meteorological and antropogenic effects.

FIELD DATA

The two selected test territories, Bolshe-Murtinsky and Chunsky, are located near the rivers Yenisey and Angara in Krasnoyarsk Kray in central Siberia. These are two of the 13 test territories that were used in the SIBERIA project (Figure 1). In each test territory there is a certain number of smaller test areas for which an extensive GIS based forest database is available. The Bolshe-Murtinsky territory include 4 test areas, and Chunsky 5. In addition, information about temperatures and precipitation was available from WMO weather stations in the vicinity of the test areas.

Figure 1. The 13 test regions that were used in the SIBERIA project.

Proc. 3rd International Symposium, 'Retrieval of Bio- and Geophysical Parameters from SAR Data for Land Applications', Sheffield, UK, 11-14 September 2001 (ESA SP-475, January 2002)

SAR DATA

In this study, JERS data recorded by the mobile receiving station of DLR during the summer 1998 have been used. Table 1 shows the tracks which cover the Bolshe-Murtinsky and Chunsky test territories. For the comparison with ERS coherence the tandem pairs listed in Table 2 have been used.

Table 1. JERS tracks covering the Bolshe-Murtinsky and Chunsky test territories.

RSP-number	Date 1	Date 2
141	Missing	980725
142	980612	980726
144	980614	980728
146	980616	980730
148	980618	980801
149	Missing	980802
151	980621	980804
152	980622	980805

Table 2. ERS tandem pairs covering the Bolshe-Murtinsky and Chunsky test territories.

Track	Frame	Orbit	Date
348	2457	32400	970925
		12727	970926
305	2439+2457	32357	970922
		12684	970923
33	2439	32586	971008
		12913	971009
491	2439	32543	971005
		12870	971006
448	2439	32500	971002
		12827	971003

PROCESSING

The JERS data were synchronized by DLR and the orbit information was added by NASDA. The resulting level 0 data were processed track by track by Gamma Remote Sensing within the SIBERIA project (Wiesmann et al. 2000).

Figure 2 shows the JERS data processing chain. For many tracks repeat pass data were available with a temporal baseline of 44 days and a spatial baseline of less than 2 km. These tracks were all processed interferometrically.

The processing was carried out on the JERS-1 raw data using the Gamma SAR interferometry processing system which includes a calibrated range/Doppler processor. Data were filtered for radio frequency interference (RFI). The radiometric calibration accounts for JERS sensitivity gain control (STC), and automatic gain control (AGC). In addition it corrects for the JERS range antenna pattern.

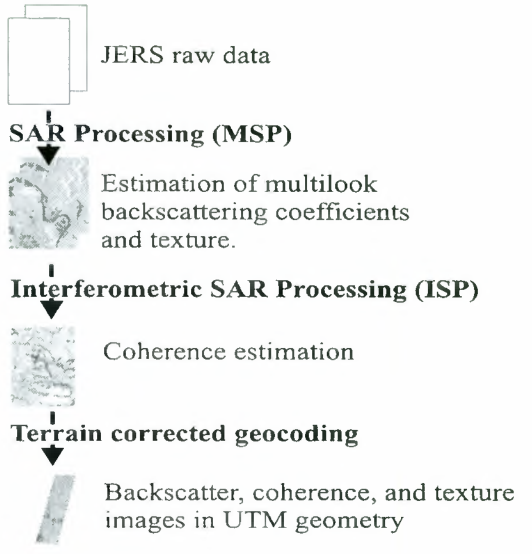

Figure 2: JERS data processing chain.

The corresponding SLC data are registered to common slant range geometry. The quality of the coherence estimate depends on the coregistration accuracy. Therefore emphasis is given on this task. An automated approach based on the coregistration of many image chips is used (Wegmüller et al., 2001). The standard deviation of the SLC registration in range and azimuth is of the order of 1/20 pixel depending on image content. Common band filtering is applied.

As a compromise between accurate estimation and high spatial resolution the coherence estimation is done with adaptive window size. The size of the estimation window is determined by the coherence values from a rough first estimation with fixed window size (Wegmüller and Werner, 1996). The used window sizes vary between 3x3 and 9x9 pixels.

Geocoding is used for the registration of the JERS with the ERS images and the available in-situ data. The global DEM "gtopo30" was used as geometric reference. Quadratic spline interpolation algorithms were used for the data interpolation necessary in the single resampling step. The pixel spacing is 50 m in northing and easting. The effective number of looks, determined with the method of moments, is about 25. An error of 200m in height in the "gtopo30" DEM results in an error of 220m (far range) to 270m (near range) in localization. An additional fine registration with the ERS image is done to improve the data for analysis. The processing and geocoding of the ERS data was done by DLR-DFD (Roth 1998, 1999).

COMPARISON OF ERS AND JERS COHERENCE

Already from a simple visual comparison between the JERS repeat pass coherence and the ERS tandem coherence it is possible to see that many of the features that can be seen in the ERS images are also visible in the JERS images. An example from test area 2 in the

Bolshe-Murtinsky test territory is showed in Figure 3. However, it is also obvious that clear-cuts and other open areas do not reach the same high coherence values as in the ERS images. This is clearly illustrated by the missing second peak in the histogram for the JERS image. For this reason boarders between open areas and low density forest is not as marked as for ERS. This indicates that it will be difficult to use only JERS coherence for forest/non forest mapping.

Another outstanding difference between the two images is the clearly marked network of rivers and streams in the JERS coherence that are hardly visible in the ERS coherence. This is an effect of the long temporal baseline between the JERS acquisitions, and is probably caused by big differences in the water levels and moisture in the river beds between the two dates (June 22 and Aug. 5). This indicates that L-band repeat pass coherence could be an interesting tool for mapping of river catchments, and since the composition of the forest often is dependent on the vicinity to water, this can also tell something about the distribution of tree species. It is likely that this change in vegetation is causing the brighter bands that can be seen along the rivers in the ERS coherence image.

In the SIBERIA project, the ERS coherence and the JERS backscatter intensity were found to be the best information sources for the growing stock volume classification that was performed (Wagner et al., 2000). Two-dimensional histograms plotting the ERS coherence against the JERS intensity clearly show how water, forest and open areas are separated into clusters when these two data sources are combined. Examples of these histograms are displayed for two ERS frames in Figure 4 a) and c). Areas with low backscatter and low coherence are classified as water, low backscatter and high coherence as smooth open areas, and high backscatter and low to medium coherence as forest. In general low coherence correspond to dense forest, medium coherence to sparse or young forest, and high coherence to rough open surfaces with little vegetation. The properties of JERS were not analysed in the SIBERIA project, since it was not foreseen that this type of data would be available.

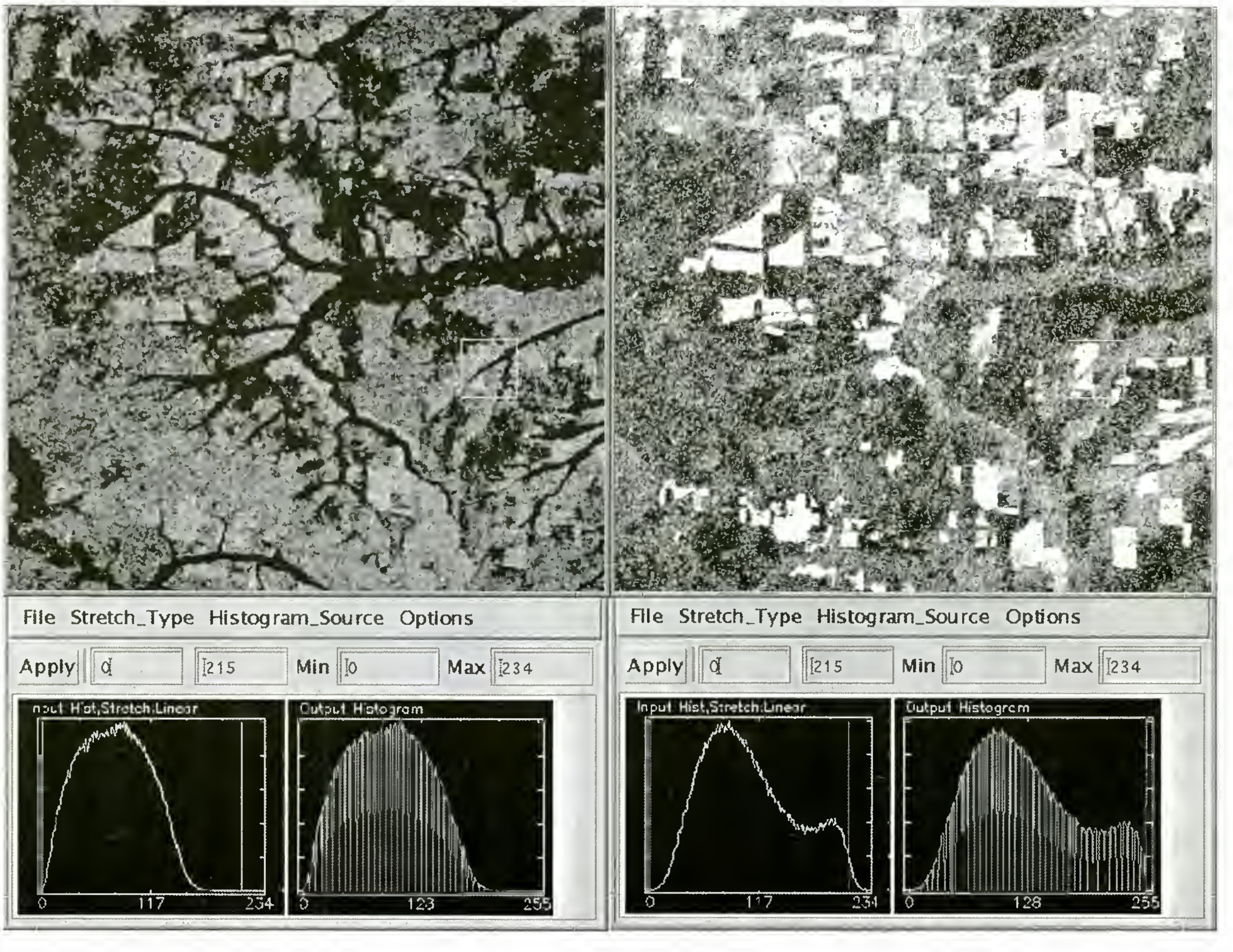

Figure 3. Comparison of coherence images from JERS (left) and ERS (right) for test area 2 in the Bolshe-Murtinsky test territory. The images are scaled between the same coherence values to make them visually comparable. Values on the x-axes of the input histograms should be divided with 255 to give the correct coherence values.

In Figure 4 b) and d), the same type of two-dimensional histograms as for the ERS coherence are showed for JERS coherence. The area for which the histogram in b) is created is the same as in a), and in the same way d) correspond to the same area as in c). Comparing the histograms for the ERS and JERS coherence, a number of remarks can be done:

- Apart from a shift of about 0.1 towards lower coherence in the JERS histogram, the water cluster seems to remain almost unchanged.
- The forest clusters loose some of their dynamic range for the JERS coherence. This indicates that the decorrelating effects over 44 day during summer are bigger for very sparse or young forest than for dense forest. It is also interesting to observe that for b) the peak of the forest cluster remains at the same place, while in d) it is shifted from 0.4 to 0.1.
- The most dramatic changes occur for smooth open areas. Here the decorrelating effects are so big that the whole cluster moves down from coherence values around 0.8 for ERS to 0.3 for JERS. However, by including the JERS backscatter intensity in the analysis it is still possible to differentiate open areas from forest.
- For JERS coherence, values exist all the way down to 0, while for ERS only very few values are below 0.1.

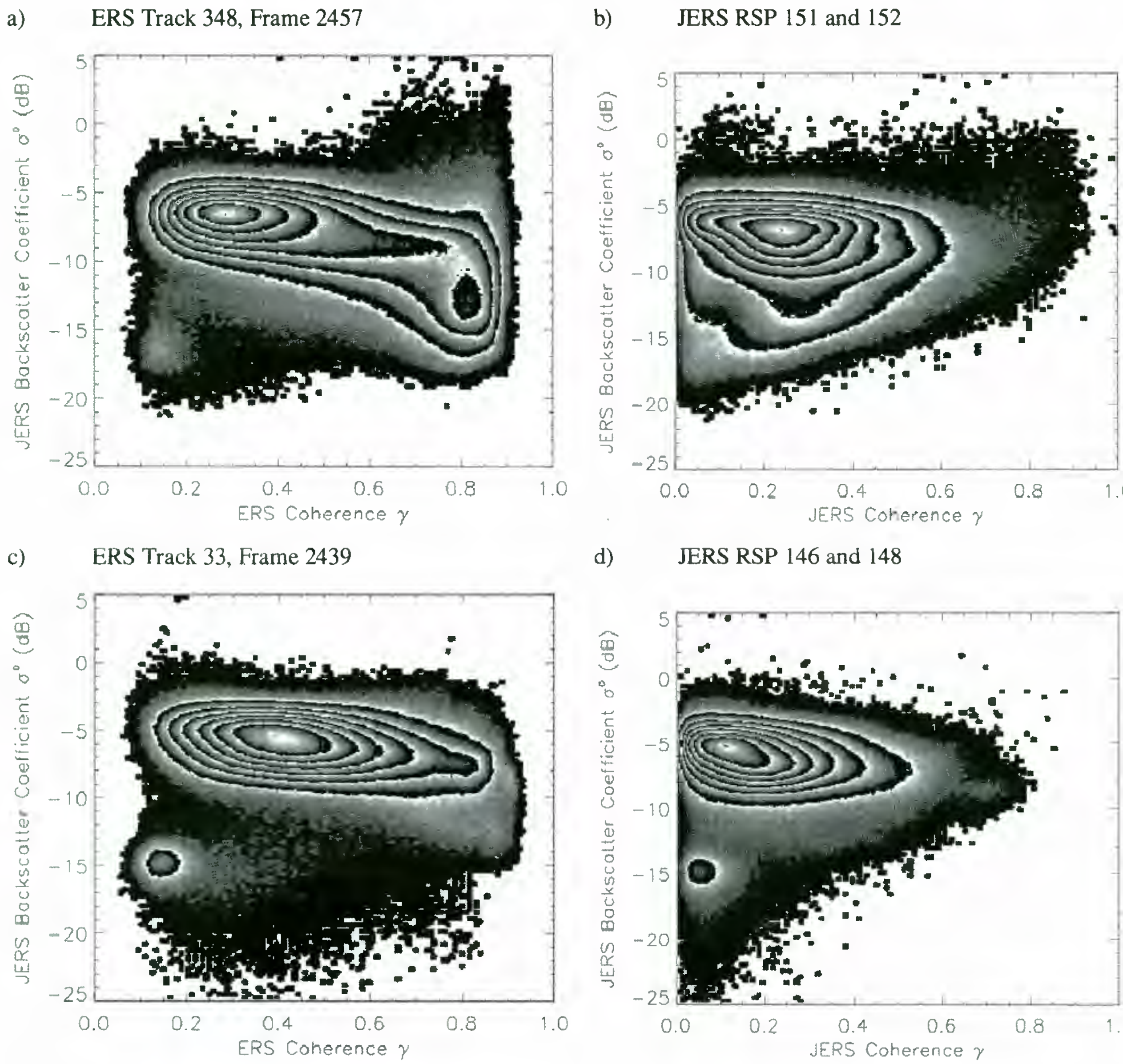

Figure 4. Two-dimensional histograms showing the distributions of the coherence values for ERS and JERS together with the JERS backscatter coefficient for two frames. The JERS tracks in b) are coregistered to the ERS data, mosaicked together, and cut to cover the same area as the ERS scene giving the histogram in a). In the same way the histogram in d) correspond to the same area as the histogram in c).

DATABASE ANALYSIS

In the SIBERIA project, methods and programs were developed to coregister the field data with the satellite data, to create database files for each test area, and to plot the interesting parameters against each other. To find a way to determine the growing stock volumes was one of the main goals, and the ERS coherence showed to be the best satellite parameter for this purpose. In Figure 5 a) and c) database plots showing the relationship between the ERS coherence and the growing stock volume are displayed for two test areas. Due to time constraints database plots for the JERS coherence were only created for a few test areas, including one in the Bolshe-Murtinsky and Chunsky test territories, and no analysis of the results were performed. In this study this work has been continued, and Figure 4 b) and d) show new database plots for the JERS coherence from the same test areas as in a) and c).

These database plots show the same general trends for the coherence as have been pointed out in Figure 4. Open areas (growing stock volume = 0) are moved down from coherence values between 0.6 and 0.8 for ERS to between 0.3 and 0.5 for JERS. Forest with growing stock volumes below 50 m^3/ha also show a relatively large shift towards lower coherence, while the shift for growing stock volumes above 50 m^3/ha is much more moderate.

One thing that is more clearly visible in these database plots than in the two-dimensional histograms is that for a certain growing stock volume the standard deviations are larger for the JERS coherence than for the ERS coherence. This makes it more difficult to use JERS repeat pass coherence for estimations of the growing stock volume in the same way as was done with the ERS tandem coherence.

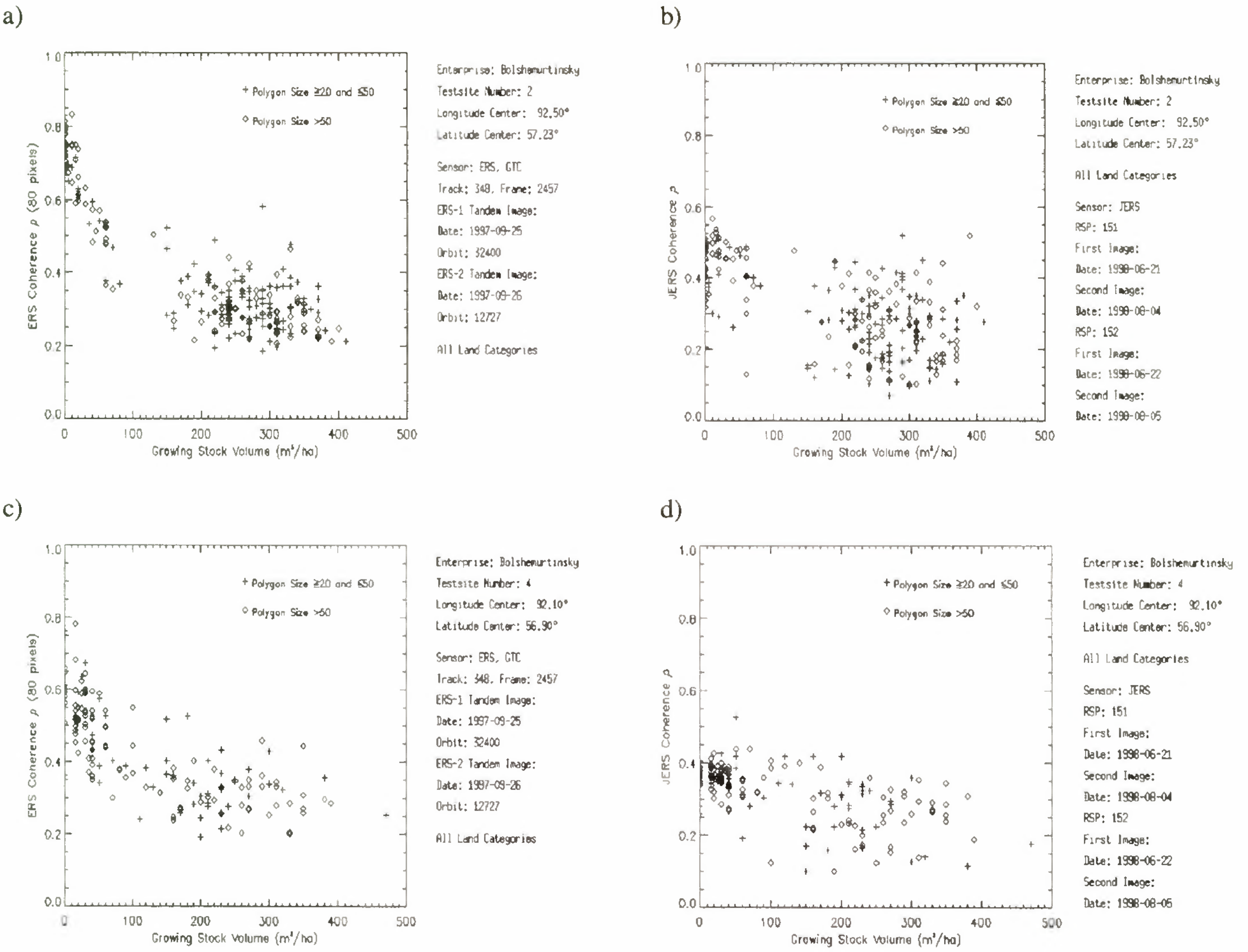

Figure 5. Plots of ERS and JERS coherence against growing stock volume. Plot a) and b) shows the results for test area 2 in Bolshe-Murtinsky, while c) and d) originate from test area 4 in the same territory.

CONCLUSIONS

Due to the long repeat cycle of the JERS satellite, agricultural fields, clear cuts, and other types of non-forested areas often get as low coherence as forest during summer when harvest and other changes occur between the image acquisitions. This makes it difficult to use JERS repeat pass coherence for forest/non-forest classification, but the ambiguity can be resolved by adding the JERS backscatter intensity to the analysis. When this is done, JERS gives results comparable to those for ERS coherence. The first analysis of the JERS coherence together with forest data from the database also show that the lower dynamic range and higher standard deviations of the coherence values reduce the possibilities to use JERS repeat pass coherence for estimations of growing stock volume. Further studies will show if it is possible to increase the accuracy when the JERS backscatter intensity is added to the analysis.

ACKNOWLEDGEMENTS

This work was funded by the German Ministry for Education and Research (BMBF) through the project FKZ 50 EE 9725 SIBERIA. SAR processing and preparation of ground database was done within the EU project SIBERIA (Contract No. ENV4-CT97-0743-SIBERIA), which was financed through the 4th Framework Programme of the European Commission. Satellite data were made available through ESA's 3rd ERS Announcement of Opportunity (Project Number AO3.120 SIBERIA) and NASDA's JERS initiative "Global Boreal Forest Mapping". The satellite data were received by a mobile receiving station of the German Aerospace Center (DLR). Meteorological data was supplied by the German Weather Service (DWD).

REFERENCES

Askne J. I. H., P. B. G. Dammert, L. M. H. Ulander, G. Smith, "C-band Repeat-Pass Interferometric SAR Observations of the Forest", IEEE Trans. on Geoscience and Remote Sensing, vol. 35, no.1, pp. 25-35, 1997.

Fransson J. E. S., G. Smith, J. Askne and H. Olsson, "Stem Volume Estimation in Boreal Forests using ERS-1/2 Coherence and SPOT XS Optical Data", International Journal of Remote Sensing, 2001

Roth A., W. Knöpfle, M. Hubig and N. Adam, "Operational Interferometric SAR Products", in Proc. IGARSS'98, vol. I, pp.324-326, 1998.

Roth A., W. Knöpfle, B.Rabus, S. Gebhardt and D. Scales, "GeMoS – A System for the Geocoding and Mosaicking of Interferometric Digital Elevation Models", in Proc. IGARSS'99, vol. 1, pp. 631-633, 1999.

Santoro M., J. Askne, G. Smith, P.B.G. Dammert, and J.E.S. Fransson, "Boreal Forest Monitoring with ERS Coherence", in Proc. ERS-Envisat Symposium, Gothenburg, Sweden, 16-20 October 2000.

Wagner W., J. Vietmeier, C. Schmullius, M. Davidson, T.Le Toan, S. Quegan, J. J. Yu, A. Luckman, K. Tansey, H. Balzter and D. Gaveau, "The Use of Coherence Information from ERS Tandem Pairs for Determining Forest Stock Volume in SIBERIA", in Proc. IGARSS 2000, Honolulu, 24-28 July 2000.

Wegmüller U. and C. L. Werner, "Land applications using ERS-1/2 Tandem data", in Proc. ESA - Fringe'96, July 1996, Zürich, CH, http://www.geo.unizh.ch/rsl/fringe96/papers/wegmuller-werner/, 1996.

Wegmüller U., C. Werner, T. Strozzi, and A. Wiesmann, "Automated and Precise Image Registration Procedures", in Proc. First International Workshop on the Analysis of Multitemporal Remote Sensing Images, 13-14 September 2001, University of Trento, Trento, Italy, 2001.

Wiesmann A., U. Wegmüller, and T. Strozzi, "JERS SAR processing for the boreal forest mapping project SIBERIA", Proceedings of CEOS SAR Workshop, 26-29 October 1999, Toulouse, France, ESA SP-450, pp. 19-23, March 2000.

For more information about the SIBERIA project: http://pipeline.swan.ac.uk/siberia/

LARGE AREA BOREAL FOREST INVESTIGATIONS USING ERS INSAR

Jan Askne*, Maurizio Santoro*, Gary Smith*, Johan E. S. Fransson**

*Dept of Radio and Space Science, Chalmers University of Technology
** Dept of Forest Resource Management and Geomatics, Swedish University of Agricultural Sciences
e-mail: Jan.Askne@rss.chalmers.se etc, Johan.Fransson@resgeom.slu.se

ABSTRACT

Multi-temporal InSAR data from a boreal forest area in Sweden is analyzed in order to estimate stem volume using coherence and backscatter. A model-based regression is performed using 21 forest stands and tested on another 21 forest stands, 2 to 14 ha in size, from an area with accurate in situ stem volume data varying from 8 to 335 m^3/ha. The model approach is discussed and compared with other approaches found in the literature. Results from the different pairs are combined to give a best stem volume estimate. The accuracy in terms of RMSE for standwise estimated stem volume corrected for sampling errors is 10 m^3/ha. Evaluation at plot level (20m diameter - 216 plots) showed an RMSE of 55 m^3/ha. The best pairs are characterized by below zero temperature and snow on the ground. For the large area (4325 km^2) 166 Swedish National Forest Inventory (NFI), plots were used as reference resulting in an RMSE of 71 m^3/ha i.e. 30% worse than the reference area located up to 50 km away. The plot based accuracy estimates illustrate effects of the limited resolution of the coherence estimate and the variability of the forest and stresses the need for evaluations over forest stands. By averaging over larger areas we obtain an accuracy of ≤ 30 m^3/ha for areas ≥ 150 km^2. We conclude that InSAR can for areas above 2 ha provide forest stem volume estimates of similar order of accuracy as ground data.

INTRODUCTION

There is a need for forest information related to environmental aspects (e.g. the Kyoto protocol) as well as related to forest managing aspects. In the latter case high resolution and high accuracy is normally needed and costs effectiveness is a less limiting factor compared to the first case when large areas far away from society have to be covered. In this case satellite observations can be particularly useful since an internationally acceptable method is needed.

This study reports investigations of boreal forest using interferometric synthetic aperture radar (InSAR). Accurate field observations in a 5.5 km^2 area have been used for training and testing a model and then the results have been used to extend the retrieval to a 4325 km^2 large area for which the Swedish National Forest Inventory has a number of reference plots. The data will first be described, the model for the model-based estimation will be summarized, and finally the results and conclusions presented.

AREA STUDIED AND DATA SETS USED

Areas studied and in situ data

The reference areas used for this investigation are located near Kättböle (5.5 km^2, 60°N 17°E) together with a large area (4325 km^2), including the Kättböle site, in the regions of Sala and Uppsala, northwest of Stockholm, Sweden. The areas are dominated by typical boreal coniferous species, Scots pine *(Pinus sylvestris)* and Norway spruce *(Picea abies)*, but some broad-leaf trees are also present, the commonest being birch *(Betula pendula)*. The topography is relatively flat varying between 75 and 110 m above sea level for Kättböle and 30 and 154 above sea level for the large area. The mean stem volume for the large area is 164 m^3/ha and the standard deviation is 124 m^3/ha.

In 1995 an inventory was made in Kättböle and accurate estimates of forest stem volume (18%), type of trees, etc were made (Fransson et al., 2001). 42 stands with stem volumes varying between 8 and 335 m^3/ha and 2 to 14 ha in size are used in this paper. For the large area the Swedish National Forest Inventory, NFI, information has been used for comparison with the InSAR data. The NFI is conducted as an annual systematic field sample of circular plots with plot radius of 10 or 7 m for permanent and temporary plots, clustered in squares of 0.3 and 1.8 km side respectively. By averaging the values from the plots good estimates of the mean forest properties are obtained for areas of the order of counties (5000 km^2). The NFI plots are too small to be used for training or verification since the resolution of the measurements is approximately 1 ha. For this reason NFI plots located at forest boundaries were excluded, and for the area studied by InSAR we had 166 remaining NFI plots.

ERS-1/2 SAR scenes

We have used nine ERS-1/2 tandem pairs from 1995 and 1996, which means all the tandem pairs available over the studied area. The scenes cover approximately a

Proc. 3rd International Symposium, 'Retrieval of Bio- and Geophysical Parameters from SAR Data for Land Applications', Sheffield, UK, 11-14 September 2001 (ESA SP-475, January 2002)

full year, and include two pairs from March and April 1996. Radar backscatter and coherence values for the 42 forest stands in the reference area are illustrated in Figure 1 for the acquisition in March 12 and 13, 1996. The backscatter observations are not well correlated with stem volume and there are clear changes between the two days. (The rms. difference between the backscatter values from 12 and 13 March is 0.6 dB with a higher mean on 12 March than 13 March.) In spite of this difference the coherence for this SAR pair is well correlated with stem volume. Although this is the best pair to illustrate that coherence is much better than backscatter to characterize stem volume, the conclusion is true for all the pairs.

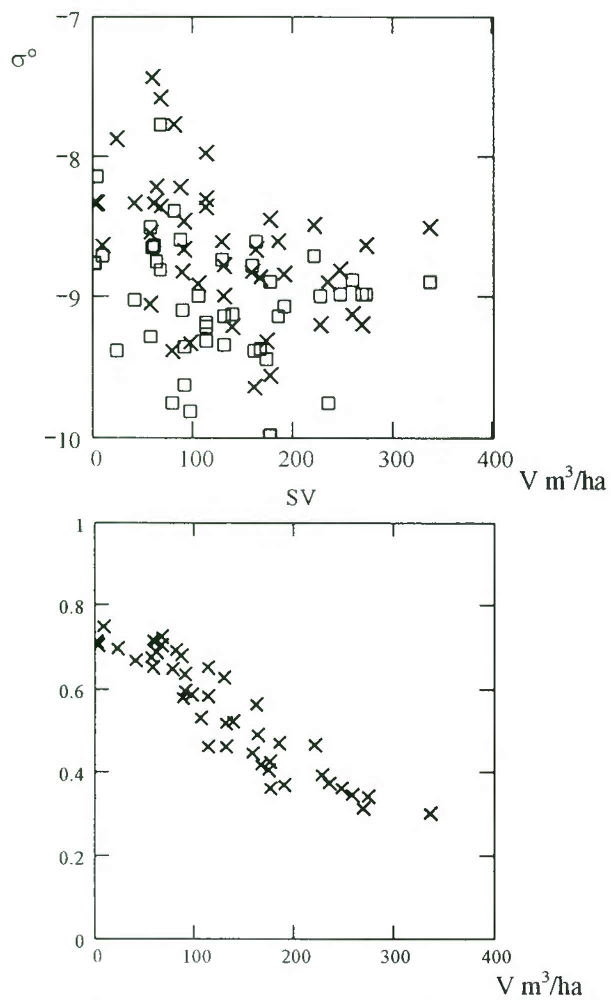

Figure 1. Observations from ERS-1 and ERS-2 on 12 and 13 March 1996 of 42 forest stands in Kättböle, a) backscatter (crosses for 12 March and boxes for 13 March), and b) coherence as function of stem volume.

Meteorological data

Meteorological data in the form of temperature, wind speed, and precipitation are obtained from nine meteorological stations scattered over the large area. From the meteorological data we may divide the ERS-1/2 scenes in two groups: stable weather conditions - both March 96 pairs, August 95, 2nd pair of April 96, and changing weather conditions - June, July, September 95 (all affected by rain), October 95 and 1st pair of April 96 (affected by temperatures oscillating around 0°C).

DATA ANALYSIS

The coherence is estimated by

$$\hat{\gamma} = \left|\sum_{1}^{N} g_{1,i} g_{2,i} e^{-j\varphi_i}\right| / \sqrt{\sum_{1}^{N} |g_{1,i}|^2 \sum_{1}^{N} |g_{2,i}|^2} \tag{1}$$

where $g_{1,i}$ and $g_{2,i}$ are the pixel values representing the amplitude of the scattering backscatter in the two images, and φ_i is the phase difference between image 1 and 2. The window size was set to 5×25 pixels in range and azimuth of the original SLC scenes, or approximately 1 ha. For further details on the InSAR processing, see (Santoro et al., 2000).

The complex coherence can be divided in a number of different contributions of which some can either be neglected or corrected for (Askne et al., 1997). One of these effects is the baseline decorrelation. It is important to identify the parts related to the vegetation in order to characterise the forest influence and to compare different observations. The effect of volume decorrelation and temporal decorrelation is defined by (Askne et al., 1997)

$$\gamma_{volume}\gamma_{temporal} = \int_{0}^{h} \sigma^0_{ve}(z') e^{-jKz'} dz' / \int_{0}^{h} \sigma^0_{v}(z') dz' \tag{2}$$

where $K = 4\pi B_n/(\lambda R \tan\theta)$ and σ^0_v denotes the volumetric backscattering coefficient for the two passes (assumed to be equal). σ^0_{ve} is the volumetric backscattering coefficient from stable scatterers from the two passes. We could express σ^0_{ve} as $\gamma_v(z')\sigma^0_v(z')$ where $\gamma_v(z')$ represents the percentage of stable scatterers. In the following we will simply denote expression (2) by γ_{for}.

A model-based regression has the advantage over methods not based on models that the model parameters can yield information on details in the scattering process. For radar backscatter from a vegetation layer a simple model in line with the Water Cloud Model (Attema and Ulaby, 1978) is given by (Pulliainen et al., 1994) based on helicopter borne scatterometer measurements

$$\sigma^0_{for} = \sigma^0_{gr} e^{-\beta V} + \sigma^0_{veg}(1 - e^{-\beta V}) \tag{3}$$

The contribution from ground, σ_{gr}, and the contribution from the vegetation layer, σ_{veg}, could be separated and a transmissivity coefficient, βV, was identified proportional to the stem volume, V, of the boreal forest. This ground transmissivity is interpreted in (Askne et al., 1995; Askne et al., 1997) as caused not only by radiation going back and forth through a canopy layer, but also from radiation going through gaps of the canopy. The "area fill", η, was introduced, describing to what extent the canopy fills the resolution cell, and 1-η, to what extent the resolution cell is described by gaps in the canopy. The two-way attenuation through the canopy layer (height h) is determined by exp(-αh). As an alternative to Eq. (3) we can then describe σ_{for} by means of

$$\sigma^0_{for} = \eta\left[\sigma^0_{gr} e^{-\alpha h} + \sigma^0_{veg}(1-e^{-\alpha h})\right] + (1-\eta)\sigma^0_{gr} \qquad (4)$$

as long as

$$1 - e^{-\beta V} = \eta(1 - e^{-\alpha h}) \qquad (5)$$

The forest transmissivity, exp(-βV), is then understood as caused by two contributions, the gaps and the canopy transmissivity, i.e. we have introduced one parameter for the horizontal and one for the vertical variations of the forest. In the case of C-band observations we believe that the canopy transmissivity is small and that the main scattering is coming from the tree tops, and we have used α = 2 dB/m. This means that β is mainly determined by the gaps in the vegetation. This was illustrated by photographic observations of canopy gaps, see (Santoro et al., accepted).

The factor exp(-jKz') complicates Eq. (2), and we will first neglect this factor, assuming zero height of the forest or zero baseline. As we have two (independent) types of scatterers associated with the ground surface within the resolution cell, the coherence would then be determined by the normalized value for the stable parts of each scatterer weighted by its radar backscatter, i.e. (assuming equal backscatter at the two acquisitions)

$$\gamma_{for} = \frac{\gamma_{gr}\sigma^0_{gr} e^{-\beta V} + \gamma_{veg}\sigma^0_{veg}(1-e^{-\beta V})}{\sigma^0_{for}} \qquad (6)$$

where γ_{gr} and γ_{veg} represent the temporal coherence for ground and vegetation (or percentage of stable scatterers).

However, some of the scattering from the forest is coming from the different height levels of the canopy and associated with a phase shift as first neglected. Assuming that the stability is constant with height and the variation of the scattering is determined by a single parameter, the penetration depth, i.e. $\sigma_v(z) \propto e^{-\alpha(h-z)}$, we obtain

$$\gamma_{volume}(B_n, h, \alpha) = \frac{\alpha}{\alpha - jK}\,\frac{e^{-jKh} - e^{-\alpha h}}{1 - e^{\alpha h}} \approx e^{-jK(h-\frac{1}{\alpha})} \qquad (7)$$

where the last part is approximately correct if α is large. γ_{volume} is dependent on the actual scattering and then dependent on α and not β. These assumptions are of course simplifications compared to the true variation of the scattering, as measured e.g. in (Castel et al., 2001) and an assumed varying stability with height. However, in (Floury et al., 1996) it was indicated that the interferometric effective height seemed to be determined by the actual height corrected by the penetration depth, i.e. as given in (7). Of course, γ_{volume} tends to 1 if either B_n or h, tends to zero. The expression for the coherence in the case we have scattering canopy layers above the ground reference level is then given by

$$\gamma_{for} = \frac{\gamma_{gr}\sigma^0_{gr} e^{-\beta V} + \gamma_{veg}\sigma^0_{veg}(1-e^{-\beta V})\gamma_{volume}}{\sigma^0_{for}} \qquad (8)$$

where the volume decorrelation term is related to the vegetation part. This expression was in principle derived in (Askne et al., 1995; Askne et al., 1997), where special height variations of the scattering and the stability were assumed. Any model to be used for inversion is a compromise between a small number of parameters describing the most essential phenomena and a large number of parameters describing the phenomena more in detail. This means that some parameters are "effective" parameters representing complex phenomena. We will also use an empirical relation between height and stem volume for the boreal forest, which has been found to apply for all our investigated boreal forest areas

$$h = h(V) = (2.44 \cdot V)^{0.46} \qquad (9)$$

Besides Eq. (8) some other expressions for γ_{for} have been used in the literature. If we neglect the volume decorrelation effect we would obtain the expression (6), which was recently proposed in (Koskinen et al., 2001) by means of regression technique. If σ_{for} also had been constant with stem volume we would obtain an exponential variation of the coherence as function of V. Such an expression was recently proposed in (Wagner et al., 2000). None of these forms give the possibility to correct for baseline effects or for the effect of the forest height. As regression expressions any of these two expressions may be equally good due to the typical noisiness of the data, but γ_{veg} is then to be considered as a regression coefficient with no physical meaning. As an example to be studied below we will see that the case illustrated in Figure 1 with B_n=218 m will result in non-physical negative values of the vegetation decorrelation if we neglect the volume decorrelation term. The so called Interferometric Water Cloud Model, Eq. (8), was introduced in order to use a minimum number of parameters for inversion purpose, but still base the expression on physical models and system properties. Further developments of interferometric model aspects can be developed starting from tree growth models in combination with scattering theories, see e.g. (Floury et al, 1999, Castel et al, 2001, Luo et al, 2000)

RESULTS FOR MODEL PARAMETERS

The model parameters for each interferometric pair are determined by minimizing the quadratic difference between the expressions for σ^0_{for}, Eq. (3), and γ_{for}, Eq. (8), and the observed values using all the 42 Kättböle forest stands. The nine pairs cover almost a full year, but are too few to draw conclusions regarding seasonal variations. The temperature interval is -4.5 °C to 19.5 °C, the wind speed interval is 0 m/s to 4 m/s. We find significant correlation only between γ_{gr} and γ_{veg}, γ_{gr} and β, γ_{veg} and wind, and σ^0_{veg} and temperature. The correlation between σ_{veg} and temperature was found to be 0.86, see Figure 2. This may be related to an increased respiration and water content of the main scatterers at higher temperatures. To explain the correlation between γ_{veg} and wind we assume that $\gamma_{veg} = e^{-(2k\delta_{rms})^2/2}$ with $k=2\pi/\lambda$ and δ_{rms} is the rms. variability of the scatterers (Askne et al., 1997). We find a correlation of 0.71 between δ_{rms} and the maximum wind speed at the two acquisitions of the tandem pair, see Figure 2. This is in line with the assumption that wind is causing the decorrelation of the vegetation layer, and the results would indicate complete decorrelation of the vegetation layer at approximately 4 m/s.

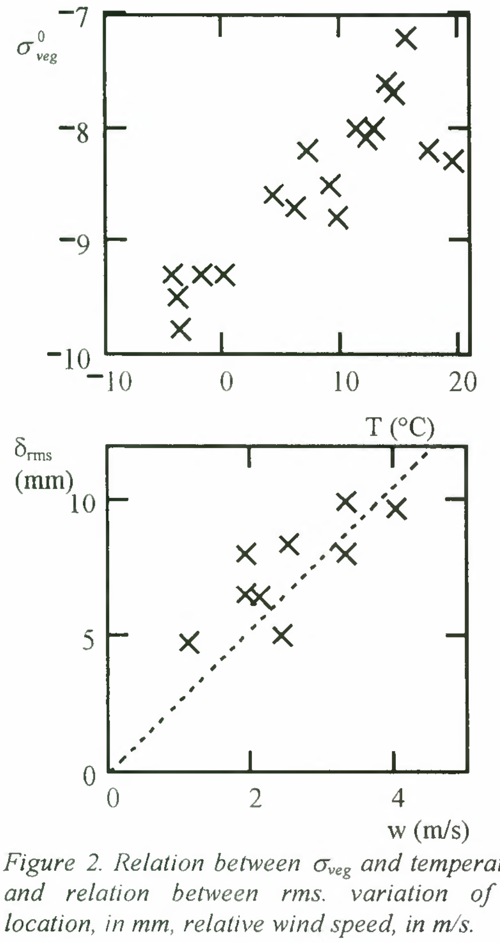

Figure 2. Relation between σ_{veg} and temperature (top), and relation between rms. variation of scatterer location, in mm, relative wind speed, in m/s.

RETRIEVAL OF FOREST STEM VOLUME

To describe the results of retrievals the root mean square error, RMSE, corrected for the sampling errors due to the field inventory design, is used. This statistical measure was also used for a multi-temporal combination of all the image pairs, where each pair was weighted by the RMSE, after eliminating outliers in the different pairs. For details in the retrieval, see (Santoro et al., 1999; Santoro et al., 2000; Santoro et al, accepted).

Kättböle area

The forest stands in the Kättböle area are divided in two groups, one data set for training and one for testing. The results from the test dataset are presented in Figure 3. In practice only the four best image pairs contribute to the multi-temporal result. In this case the RMSE, corrected for sampling errors is 10 m^3/ha. Note that the retrieval is based on training using 21 stands and evaluation of 21 other forest stands, all with sizes varying between 2 and 14 ha. If we instead would use the individual 216 forest plots in the testing dataset we would obtain an RMSE of 55 m^3/ha. This illustrates the importance of averaging over forest stands due to the resolution of the coherence estimates and the variability of the forest.

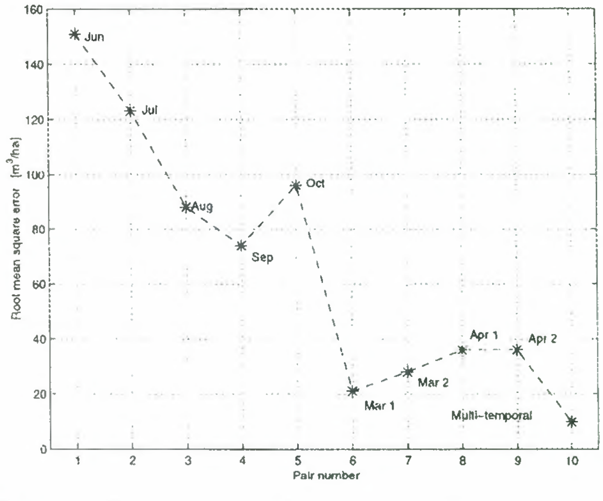

Figure 3. Stem volume retrieval accuracy from each one of the nine InSAR pairs and from the multi-temporal retrieval.

NFI plots within large area

All the forest stands in the Kättböle area are used to determine the model parameters. To verify the accuracy of the retrieval in the large area we need accurate in situ observations of forest stands within the area. Unfortunately, such observations for forest stands are not available and expensive to collect, and instead we have used NFI data, which are the standard procedure to estimate large area (county level) forest stem volume.

To obtain as accurate model parameters as possible we used all the 42 stands in Kättböle, which is located more or less in the middle of the large area. Since our model parameters are depending on meteorological parameters we would expect that the parameters might be less representative with increasing distance from the training area. One test of the data sets we can perform is to check the consistency of stem volume values derived from different pairs. Inconsistencies can then be attributed to variations of coherence due to changing meteorological properties and only those pairs showing consistent values should be used. Examples are illustrated in Figure 4. Of the four best pairs as illustrated in Figure 3, the first pair acquired in March and the second in April were selected to be used for the large area. We find an RMSE error of 71 m^3/ha on plot basis as compared to 55 m^3/ha for Kättböle. The degradation is believed to be caused by variable conditions over the 4325 km^2 large area.

Areas of varying size were randomly distributed within the large area and averages of the InSAR multi-temporal coherence based stem volume estimate were compared to the mean value of the NFI plots available within the same area. In the multi-temporal retrieval coherence outliers in each pair were first eliminated. Results are illustrated in Figure 5, and we see that the RMSE error decreases with window size reaching a value of 30 m^3/ha for areas larger than 150 km^2. (Only plots with stem volumes $\leq$ 350 m^3/ha were used, as this was the maximum for the training set.)

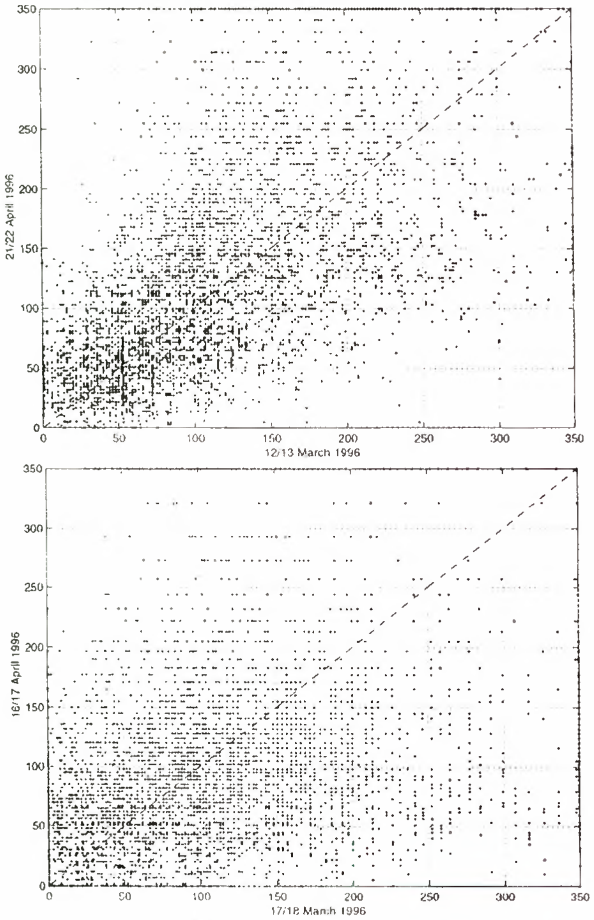

Figure 4. Illustrating that the consistency between stem volume values derived 12/13 March and 21/21 April is acceptable but not that for 17/18 March and 16/17 April.

CONCLUSIONS AND DISCUSSIONS

We have evaluated InSAR forest inventory for an area from which we have a highly accurate field

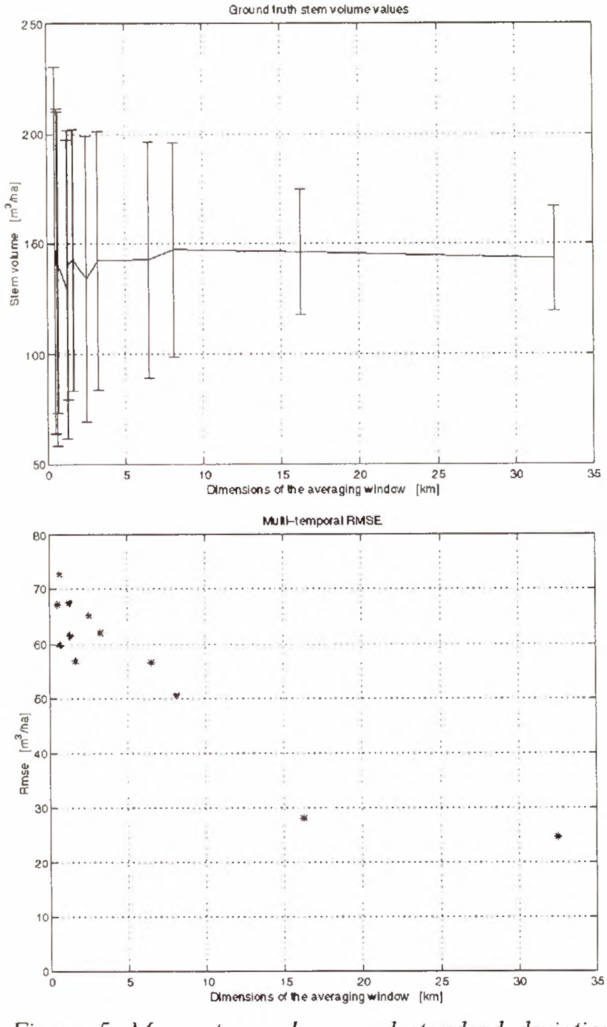

Figure 5. Mean stem volume and standard deviation within each window according to NFI plots within window (top), RMSE between NFI and InSAR values(bottom). A window size of 1000 corresponds to 25 km.

measurements. We think this is one crucial aspect for verification of InSAR data, which is not very often available due to the cost of such inventory.

The area studied is typical for forest areas in the central part of Sweden and the results probably apply also for northern areas. We believe that the forest structure is important for the results and that the gaps in the forest play an essential role. For this reason the results cannot easily be extended to non-boreal forests.

The results depend on meteorological conditions and the best results are obtained for stable conditions with the ground covered by non-melting snow. We have earlier investigated another similar area in Tuusula, Finland, (Santoro et al., 1999), and obtained worse results since the winter scenes were obtained when the snow was partly melting. Earlier we have also studied an area further north in Sweden using 3-day repeat-pass orbit data (Askne and Smith, 1996). The forest stands are only eleven but the results seem to be with similar accuracy as in Kättböle. Due to the limited number of forest stands this should be verified using cross-validation technique.

We find that InSAR in the studied case can be as accurate as in situ data collected for forest stands larger than 2 ha. The accuracy for a multi-temporal retrieval can be of the order of 10 m^3/ha.

Comparison with NFI data shows an RMSE of ≤ 30 m^3/ha and a relative RMSE of $\leq 20\%$ for areas larger than 150 km^2.

Optical remote sensing is used for regional mapping. SPOT (Fransson et al., 2001), and Landsat (Fazakas et al., 1999) have been analyzed for the Kättböle area. The analysis is based on training and testing data sets. In both cases the reported accuracy is somewhat less than the one reported here.

Finally, it can be concluded that in order to use satellite data for forest inventory it may be considered to change the present NFI method to include forest stands for training data sets.

ACKNOWLEDGEMENT

Images were provided by ESA through AOT-S104. DIAPASON, and ISAR have been used for the interferometric analysis. Funding was provided by the Swedish National Space Board.

REFERENCES

Askne, J., et al., 1995, Retrieval of forest parameters using intensity and repeat-pass interferometric SAR information. *Retrieval of Bio- and Geophysical Parameters from SAR Data for Land Applications, Symposium held in Toulouse, 10-13 October, 1995,* (ACTES), pp 119-129

Askne, J., et al., 1997: C-band repeat-pass interferometric SAR observations of forest, *TIEEE GRS* 35(1): 25-35.

Askne, J. and G. Smith, 1996, Forest INSAR Decorrelation and Classification Propeties. *Fringe 96, Symposium held in Zurich, CH,* SP-406 (ESA), pp 95-103

Attema, E. P. W. and F. T. Ulaby, 1978: Vegetation modelled as a water cloud, *Radio Science* 13(2): 357-364.

Castel, T., et al., 2001: Deriving forest canopy properties for backscatter models using the AMAP architectural plant model, *TIEEE GRS* 39(3): 571-583.

Fazakas, Z., M. Nilsson and H. Olsson, 1999: Regional forest biomass and wood volume estimation using satellite data and ancillary data, *Agricultural and Forest Meteorology* 98-99: 417-425.

Floury, N., 1999: Modelisation radar des couverts forestiers. Applications a la teledetection. Universite Paris 7, Denis Diderot, Paris. 217 pages.

Floury, N., et al., 1996, Interferometry for forest studies. *Fringe 96, Symposium held in Zürich,* SP-406 (ESA), pp 57-70

Fransson, J. E. S., et al., 2001: Stem volume estimation in boreal forests using ERS-1/2 coherence and SPOT XS optical data, *International Journal of Remote Sensing* 21(14): 2777-2791.

Koskinen, J. T., et al., 2001: The seasonal behavior of interferometric coherence in boreal forest, *TIEEE GRS* 39(4): 820-829.

Pulliainen, J. T., et al., 1994: Backscattering properties of boreal forests at the C-and X-band, *TIEEE GRS* 32(5): 1041-1050.

Santoro, M., et al., 1999, Retrieval of biomass in boreal forest from multi-temporal ERS-1/2 Interferometry. *Fringe 99: Second International Workshop on ERS SAR Interferometry, Symposium held in Liège,* SP-478 CD-ROM (ESA Publications Division)

Santoro, M., et al., 2000, Boreal forest monitoring with ERS coherence. *ERS-Envisat Symposium "Looking down to Earth in the New Millenium", Symposium held in Gothenburg, on 2000,* SP-461 CD-ROM (ESA Publications Division).

Santoro, M., et al., accepted: Stem volume retrieval in boreal forests from ERS-1/2 interferometry, *Remote Sensing of Environment.*

Wagner, W., et al., 2000, The use of coherence information from ERS tandem pairs for determining forest stock volume in Siberia. *IGARSS 2000, Symposium held in Honolulu, Hawaii,* (IEEE)

Agriculture and Land Cover

Chairmen: H. Skriver

SAR FOR AGRICULTURE: ADVANCES, PROBLEMS AND PROSPECTS

P. Ferrazzoli

Università Tor Vergata, Ingegneria, DISP, Via di Tor Vergata 110, I-00133 Rome, Italy
Tel. +39 06 72597420, Fax +39 06 72597460, E-mail ferrazzoli@disp.uniroma2.it

ABSTRACT

The aim of this paper is to illustrate the state of the art in SAR data use for agricultural applications, discuss the main problems and give suggestions for future work.

The paper is introduced with some short historical notes about the evolution of ground based, airborne and spaceborne radar observations, as well as about the advances in scattering modeling.

Then, the paper considers three aspects of the retrieval problem, corresponding to three fundamental steps: i) identification of a convenient radar configuration; ii) development of reliable relationships between backscatter coefficient and agricultural variables (direct problem); iii) retrieval in the strict sense (inverse problem). For each of the three topics, the important recent advances are summarized and the author's point of view about the state of the art is given.

1. INTRODUCTION

The objective of this paper is to illustrate and discuss the state of the art in SAR data use for agricultural applications. This topic has been the object of many investigations, in the last decades.

A first extensive experimental data base was provided by several ground-based measurements carried out in the 70's and early 80's, mainly in the US, using calibrated scatterometers. Single fields of various crop types, e.g corn, soybeans, alfalfa, wheat, grass, etc., were monitored during their growth cycle. Observations over vegetated fields were mainly carried out in a frequency range between 4 and 18 GHz and in a linear copolar configuration (i.e. at VV and HH polarizations). Extensive results were published in several papers, e.g. Ulaby (1980), and summarized in important books (Ulaby et al., 1986; Ulaby & Dobson, 1989). In general, experimental results indicated that the radar backscatter coefficient σ° is sensitive to vegetation parameters. Over some specific fields, a very nice correlation versus important vegetation variables was observed, e.g. in Figure 21.53 of Ulaby et al. (1986) This first activity gave a fundamental stimulus to microwave remote sensing for agricultural applications.

In the late 80's, some airborne campaigns made radar signatures available to a wide community of users (Hoekman, 1992; Churchill & Attema, 1992). The instruments, in this case, observed large agricultural areas including several fields. In order to monitor fields developments, the areas were observed 3-4 times during the Summer season. However, the temporal extension of the observations was more limited than in the case of ground based observations. The correlation between σ° and ground parameters was investigated considering several fields observed simultaneously during limited time intervals. In general, correlations versus vegetation variables were not as good as with multitemporal single-field ground based observations. Soil properties and plant structure were different among the various fields. Therefore, σ° was not simply correlated to a single variable, but was influenced by complex interactions among soil scattering, vegetation attenuation and vegetation scattering, as well as differences in geometry and permittivity of vegetation components (stem, leaf, petiole, ear, etc.). Moreover, the calibration problems were not yet completely solved, especially for airborne observations.

In the late 80's and in the 90's important advances were achieved, opening prospects of a full future utilization of SAR data for agricultural applications. First of all, significant improvements in calibration techniques were obtained using corner reflectors, extended targets and active calibrators (Van Zyl, 1990; Zebker & Lou, 1990; Freeman et al., 1990). Moreover, fully polarimetric instruments were realized. A lot of sites worldwide were overflown by AIRSAR (Held et al., 1988) and SIR-C (Stofan et al., 1995), thus allowing several scientists to get an insight into the problem of interaction between waves and natural media. Important activities were also carried out by means of EMISAR (Christensen et al., 1998). The launches of ERS-1, ERS-2, JERS-1 and RADARSAT made spaceborne multitemporal signatures available to many users for the first time. Finally, in par-

Proc. 3rd International Symposium, 'Retrieval of Bio- and Geophysical Parameters from SAR Data for Land Applications', Sheffield, UK, 11-14 September 2001 (ESA SP-475, January 2002)

allel with the quantitative and qualitative improvements of experimental data bases, very important progresses were achieved in modeling, leading to a significant expansion of our capabilities in interpreting radar signatures. A simple "cloud" model gave a first key to understand σ° dependence on main soil and vegetation variables (Ulaby & Attema, 1978). Important studies led to simulate σ° using a discrete Radiative Transfer (RT) model, with vegetation elements represented as discs and cylinders (Eom & Fung, 1984), (Karam & Fung, 1988). Further studies, aimed at refining the models in order to include leaf curvature and/or coherent effects, are in progress.

To summarize, tremendous efforts have been carried out, leading both to a significant expansion of experimental data bases available to us and to an important improvement of our capability to interpret the data. From the application point of view, the main objective is the retrieval of important agricultural variables such as Water Content (WC, kg/m^2) and Leaf Area Index (LAI, m^2/m^2). The work aimed at solving this problem may be subdived into three main steps. The first step consists in identifying a convenient radar configuration, i.e. one or more combinations of frequency, incidence angle and polarization for which σ° is sensitive to the variable to be retrieved. As a second step, a relationship between σ° and all soil and vegetation variables by which it is influenced has to be established. The relationship must be reliable, in the sense that must be valid in different sites and under different operational conditions. Finding this relationship, which is constituted by a model, solves the direct problem. Finally, the inverse problem has to be solved, i.e. retrieving the variables of interest using data collected in a convenient radar configuration and with the aid of a reliable direct model.

The three steps will be the objects of Sections 2, 3 and 4, respectively. For each of them, some important recent advances will be summarized and the author's point of view about the state of the art and the main present problems will be illustrated. Suggestions about future research directions will be given.

2. STUDIES ON RADAR SENSITIVITY

In order to retrieve a variable, the remote sensing system must be sensitive to the variable itself. In case of agricultural crops, since we are generally interested on variables associated to crop growing and crop senescence (i.e. WC and LAI), we need to identify combinations of frequency, incidence angle and polarization for which the σ° value is significantly influenced by the crop cycle. This is ensured by a high σ° dynamic range between full growth and early stage and a gradual transition between the extreme values. Since the various crop types show different geometries, the convenient radar configuration is not the same for all crops, but must be considered for any specific type, as it will be evident in Section 2.2.

2.1. Recent advances

As stated in the Introduction, the problem of radar sensitivity to vegetation variables has been investigated since the 70's using experimental data and models of various complexity. Some important papers, published during the last three years, are shortly summarized below.

Skriver et al. (1999) have illustrated polarimetric multitemporal signatures collected by EMISAR at L and C band over several crop types in Denmark. Main features have been discussed in comparison with previous works.

Saich & Borgeaud (2000) have analyzed ERS SAR signatures collected at Flevoland (NL) site in 93, 94, 95 and 96 over potato, sugarbeet, wheat, barley and grass fields. Crop typical temporal patterns and year-to-year variabilities have been analyzed, also using a second order RT model.

Macelloni et al. (2001) have investigated the different relationships between σ° and biomass of narrow and broad leaf crops. Critical comparisons with previous works have been shown. Radar signatures collected by various airborne and spaceborne instruments, as well as a first order RT model, have been used.

De Roo et al. (2001) have investigated the radar sensitivity to soil moisture and vegetation water content of soybeans fields. L and C band signatures and a semiempirical model have been used.

Important advances have been achieved in studies on rice cycle monitoring. Ribbes & Le Toan (1999) have investigated the performance of RADARSAT SAR, also in comparison with ERS SAR. Rosenquist (1999) has studied the temporal and spatial characteristics of JERS-1 SAR signatures.

2.2. Survey

Considerations about convenient radar configurations, based on studies carried out till now, are shown in this Section. For sake of concreteness, a set of 7 crop types, i.e. potato, corn, sugarbeet, rape, wheat, barley and rice, has been selected. This set is limited, but statistically significant, in that covers a high fraction of world crop area. For each of the seven crop types, diagrams or references to the literature are used to identify convenient radar configurations, on the basis of multitemporal trends or comparisons vs. σ°'s of bare soils and other crops. Most of the diagrams are plotted using σ° data made available in the framework of the ERA-ORA Project, founded by ECC. Results are interpreted by means of electromagnetic considerations.

2.2.1. Potato crop

At L band, HV polarization, higher angles, σ°'s of developed potato fields are clearly higher than σ°'s of other crops and bare soils. This configuration appears to be convenient since produces a high dynamic range. Figure 1 shows results, obtained by AIRSAR over Flevoland site in 1991, made available by University of Wageningen. Signatures collected in other experiments, shown by Ferrazzoli et al. (1998) and by Skriver et al. (1999), are in agreement with data of Figure 1. Stem density of potato is low (10-15 m^{-2}). Crop structure is ramified with large twigs (diameter > 4 mm). The feature of Fig. 1 may be explained by the crosspolar scattering of twigs.

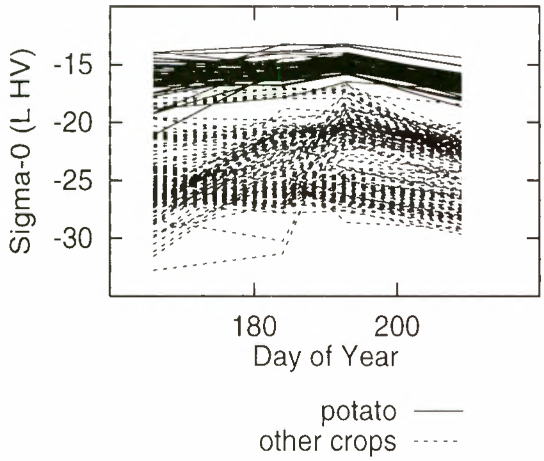

Figure 1. Multitemporal signatures collected at Flevoland in 1991. L band, HV polarization. Comparison between potato and other crops

2.2.2. Corn crop

At L (S) band, HV polarization, high angles, an appreciable σ° increase is observed in corn fields during the time interval of plant growth. This property is observed in Figure 2, showing again L band AIRSAR data collected at Flevoland in 1991. Results shown by Ferrazzoli et al. (1997) and Macelloni et al. (2001) confirm this increasing trend. Experimental data collected by the RASAM multifrequency scatterometer at the Central Plain site in Switzerland (Wegmüller, 1993) show a similar trend also at S band. Stem density of corn is low (7-10 m^{-2}). The crop shows broad leaves with large ribs and petioles. The feature of Fig. 2 may be explained by the crosspolar scattering of ribs and petioles.

2.2.3. Sugarbeet crop

For sugarbeet, a clearly convenient configuration is not easy to be identified. A good contrast with respect to bare soil is generally achieved at HV polarization, high angles. Moreover, σ° increase vs. frequency is more evident than in other crops or in bare

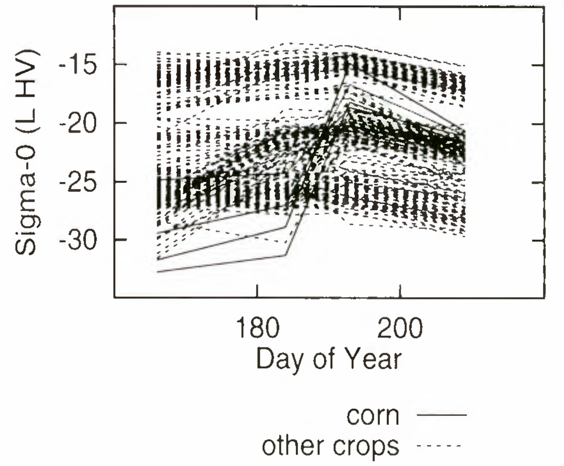

Figure 2. Multitemporal signatures collected at Flevoland in 1991. L band, HV polarization. Comparison between corn and other crops

soils. These properties may be observed in Figure 3, showing crop averaged σ°'s measured by RASAM and made available by GAMMA. Stems are sparse (7-10 m^{-2}) and low. Scattering is dominated by the wide and thick leaves, particularly at the higher frequencies.

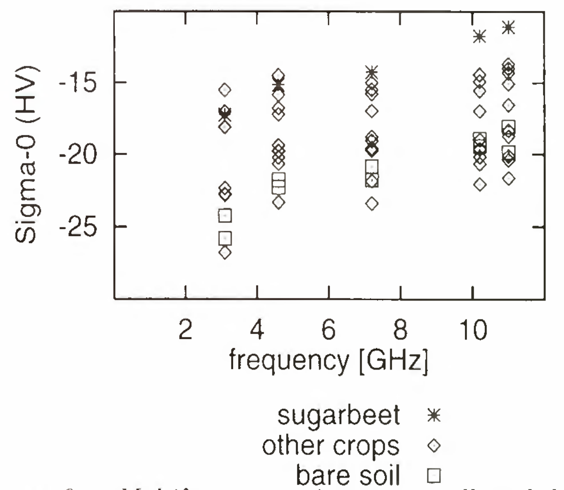

Figure 3. Multifrequency signatures collected by RASAM at Central Plain. HV polarization. Comparison between sugarbeet, bare soil and other crops

2.2.4. Rape crop

At C band, HV polarization, high angles, σ°'s of developed rape crops are clearly higher than σ°'s of other crops and bare soils. Therefore, this radar configuration is convenient for rape. Figure 4 compares C band HV signatures collected by AIRSAR at Flevoland. The high rape backscatter before harvest is evident. Signatures collected in Italy (Ferrazzoli et al., 1997) and in Denmark (Skriver et al., 1999) agree with these statements. Stem density of rape is typically 70-80 m^{-2}. Plants are ramified, with several small twigs (< 2 mm diameter) and pods. The feature of Fig. 4 finds explanation in the crosspolar scattering of twigs and pods.

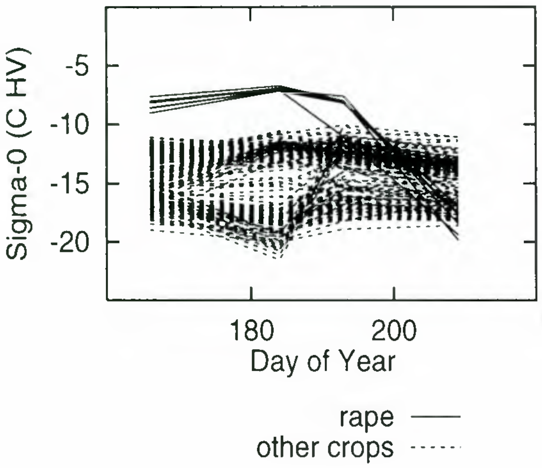

Figure 4. Multitemporal signatures collected at Flevoland in 1991. C band, HV polarization. Comparison between rape and other crops

2.2.5. Wheat crop

At C, VV polarization, low angles (20°-30°) wheat σ°'s show and evident lowering during crop growth. This is clearly observed in Figure 5, where multitemporal ERS SAR σ°'s of wheat fields are compared against the ones of potato, corn and sugarbeet fields. Data were collected at the Flevoland site in a 4-years period, from 93 to 96, and have been made available by ESA/ESTEC. This wheat behavior is observed and discussed also by Saich & Borgeaud (2000), Cookmartin et al. (2000) and Macelloni et al. (2001). The ERS SAR configuration appears to be convenient for cycle monitoring. According with the results published by Del Frate et al. (2001), VV polarization contains useful information also at S and X band. Wheat stems are thin and dense (500-1000 m^{-2}) with narrow leaves. Ears are present on top in the mature stage. The feature of Fig. 5 finds explanation in the increasing attenuation suffered by VV soil backscattering due to growth of vertical stems and ears.

At HV polarization, wheat σ° is mostly related to ear bending; therefore, this polarization does not appear to be reliable for crop monitoring. As far as L band is concerned, useful information could be added by its availability, in that the sensitivity to crop density is improved. However, L band signatures are heavily influence by azimuth orientation, as demonstrated by Stiles et al. (2000).

2.2.6. Barley crop

The general behavior of barley signatures is similar to the one observed for wheat. This may be ex-

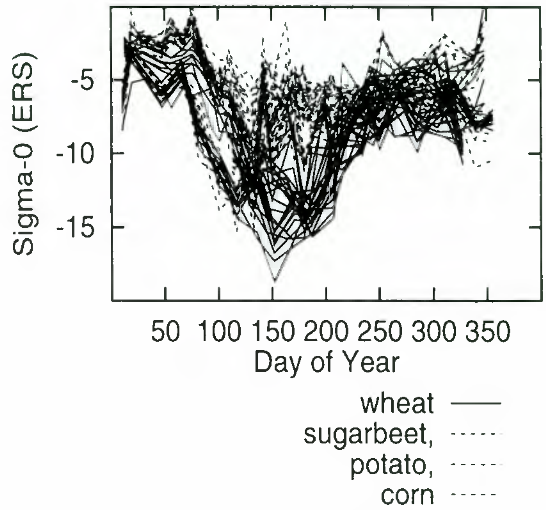

Figure 5. Multitemporal ERS signatures collected at Flevoland. Comparison between wheat and other crops

plained by the general similarity between the two crop structures. Figure 6 compares multitemporal ERS signatures of barley with the ones measured over potato and sugarbeet. Considerations similar to the ones of Fig. 5 may be applied. In the mature stage, barley ear bending is more enhanced than wheat ear bending. Therefore, the use of HV polarization for growth monitoring is not appropriate, and may be even misleading.

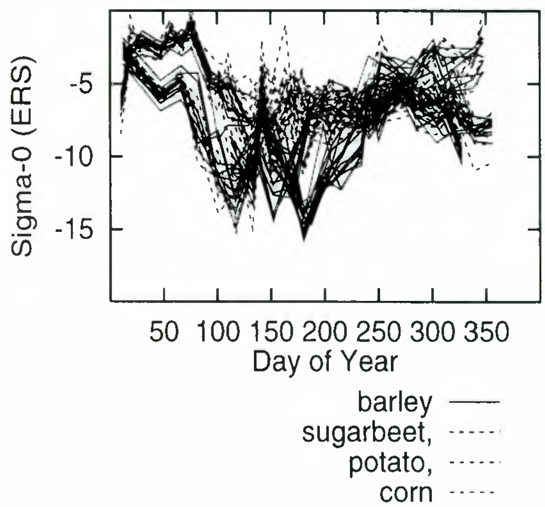

Figure 6. Multitemporal ERS signatures collected at Flevoland. Comparison between barley and other crops

2.2.7. Rice crop

Rice crop backscatter has been the object of several experimental and modeling studies, in the recent years. Measurements carried out over various sites indicate ERS SAR configuration to be convenient. An evident σ° increase is observed during crop growth, with limited variability. Model simulations give a theoretical basis to this result (Le Toan et al., 1997). Rice stem density is relatively high (~ 200 m^{-2}). Stems are grouped in bounches. The soil is flooded during the growing phase. At early stage σ° is low, since the flooded soil is smooth. Crop growth is associated with a soil/stem double bounce effect, producing a gradual σ° increase. The direct vegetation backscatter dominates in full growth.

Also RADARSAT and JERS-1 rice signatures have been analyzed. The σ° contrast between full growth and early stage is lower in RADARSAT than in ERS signatures. This is explained by the lower interaction of stem with HH polarization, with respect to VV polarization (Ribbes & Le Toan, 1999). Investigations carried out by Rosenquist (1999) indicate that, for manual planting, also L band signatures (JERS-1 configuration) are well correlated with crop growth. The situation is more complex in case of mechanical planting, since a significant dependence on azimuth angle is observed, due to coherent interactions.

Studies about rice are at an advanced stage. Some applications, such as classification and crop monitoring, are preoperational (Ribbes & Le Toan, 1999). Unfortunately, few data in HV polarization are available.

2.3. Considerations about coherence

The considerations of Section 2.2 are relevant to σ° amplitude. In the recent years, the application potential of interferometric coherence data collected by using SAR tandem overpasses has been investigated. This research has been stimulated by the availability of tandem images obtained by ERS-1 and ERS-2 with 1 day time delay. Some works indicate that the coherence contains useful information about vegetation type and vegetation status (Wegmüller & Werber, 1997). In order to get an insight into this problem, some coherence data made available by GAMMA have been analyzed. Figure 7 shows some multitemporal trends, obtained over the Flevoland site in 1995, relevant to wheat, potato and sugarbeet fields. For most of potato and sugarbeet fields, coherence is low in full growth and increases during drying. However, there are some anomalous samples of difficult interpretation. Coherence of wheat fields is high: this property could be due to a more advanced drying, with respect to other crops, or to the differences in geometrical characteristics. According to the data of Fig. 7, coherence confirms to have a good potential for agricultural applications, but its dependence on canopy and soil properties needs further investigations.

2.4. Summarizing considerations

The analysis of section 2.2 indicates that general conclusions, valid for all crop types, cannot be drawn, since the radar sensitivity is affected by single crop properties. However, two observations of general validity may be done.

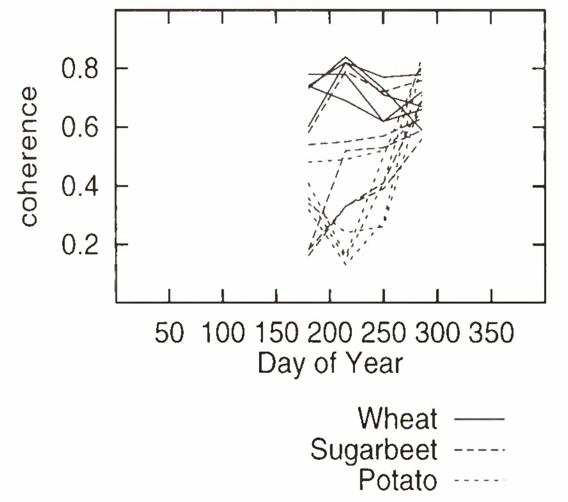

Figure 7. Multitemporal coherence data collected at Flevoland by ERS tandem overpasses. Comparison between potato, sugarbeet and wheat

- An increase in stem density, generally associated to a decrease in stem diameter, leads to an increase of the convenient frequency. For wheat, barley, rice, rape (higher stem density, lower stem diameter) a high interaction with C (X) band waves is observed, making high frequencies interesting for monitoring. For corn and potato (higher stem diameter, lower stem density) lower frequencies (L and S band) appear to be more convenient.
- HV polarization is particularly useful when crops are well ramified, i.e. the relative weight of twigs, pods, petioles and leaf ribs becomes important. It is the case of potato, corn and rape. For crops dominated by vertical structures, such as wheat and barley, the most significant information is contained in the attenuation and/or double bounce effects produced at VV polarization.

It must be remembered that L band, HV polarization, has proved to be a convenient configuration also for sunflower (Ferrazzoli et al., 1997) and soybeans (De Roo et al., 2001).

The above considerations are valid when scattering is dominated by cylindrical elements. Their applicability to sugarbeet, characterized by large leaves and very low stems, is not straightforward.

From a system point of view, the forthcoming considerations apply.

- The configurations of present spaceborne SAR's, particularly ERS SAR, are interesting for some crops, such as rice, wheat and barley.

- ENVISAT ASAR signatures, provided ground resolution will be sufficient, will produce a significant improvement in monitoring, in that may contain HV polarization.
- A general good potential in monitoring of the main crops could be achieved in the future by simultaneous availability of L and C band observations.

The analysis has been limited to linear polarizations. However, previous studies indicate that the availability of fully polarimetric data is very useful for classification (Ferrazzoli et al., 1998; Skriver et al., 1999) and, to a lesser extent, for crop monitoring (Ferrazzoli et al., 1997; Skriver et al., 1999).

3. MODELING

It is well recognized that σ° of crops depends on several soil and vegetation variables. The latter may show simultaneous variations. As an example, crop growth and soil drying processes, both influencing σ°, generally occur simultaneously in springtime and early summertime. In order to correctly describe the scattering process, it is necessary to single out vegetation effects from soil effects and to distinguish among the influences of the various vegetation variables. To this aim, a model is required. A model is a relationship linking σ° to the observation parameters (i.e. frequency, incidence angle, polarization) and to N surface variables:

$$\sigma^\circ = F(f, \theta, \psi_r, \chi_r, \psi_t, \chi_t; a_1, a_2, ...a_N)$$

where f is the frequency, θ is the incidence angle ψ_r and χ_r are the rotation and ellipticity angles in reception, ψ_t and χ_t are the rotation and ellipticity angles in transmission (Ulaby & Elachi, 1990). The N variables $(a_1, a_2, ...a_N)$ include the objectives of the observation, useful for applications, as well as other variables less useful for applications but influencing σ° anyhow. The complexity of the model ranges from a simple empirical relationship, linking σ° with few general vegetation and soil variables, to complex physical models taking the canopy geometry and the complex interactions among scatterers into account.

3.1. Recent advances

A fully phase-coherent model has been proposed, including coherent interactions among single plant elements and among different plants (Stiles & Sarabandi, 2000; Stiles et al., 2000). Leaf and stem curvature effects have been also considered. The model has been tested over scatterometer data collected over a wheat canopy. It has been found that L band signatures are severely affected by coherent effects, depending on azimuth direction and radar resolution. At C band, single scatterer geometry is important. Soil direct backscatter is low.

Chauhan & Lang (1999) have modeled alfalfa canopies as conical clumps of stems that are clustered with leaflets. Coherent effects are considered within each clump. The model is able to explain some high σ° values measured over alfalfa canopies at L band.

Chiu & Sarabandi (2000) have developed a coherent model and tested it against experimental soybeans signatures, collected at L and C band. Coherent effects result to be appreciable at L band.

Cookmartin et al. (2000) have tested a second order RT model against multitemporal ERS signatures collected over wheat fields. The agreement is good in the growing season, but crop attenuation is overestimated in the drying season. Laboratory studies are in progress to investigate the problem (Brown et al., 2001)

3.2. The state of the art

A lot of models have been proposed till now to represent σ°'s of agricultural fields. Models may be classified in increasing order of complexity, as indicated below.

- The simples approach may consist in an empirical formula relating σ° to soil moisture and crop WC (or LAI) with 2 regression coefficients. The latter may be computed by fitting over a statistically significant amount of experimental data at a given frequency, angle and polarization.
- The "Water Cloud" approach (Ulaby & Attema, 1978) is physically based, in that considers soil scattering, vegetation attenuation and vegetation scattering. For each frequency, angle and polarization σ° is related to WC (or LAI) and soil moisture by 4 coefficients to be computed by statistical fitting over experimental data.
- A significant progress in physical representation is achieved using discrete RT models, representing soil as a homogeneous half-space with rough interfaces, and vegetation elements, i.e. stem, leaf, twig, ear, etc. as lossy dielectric scatterers. In general, stems, twigs, ears, etc. are represented as cylinders, while leaves are represented as circular or elliptic discs (Eom & Fung, 1984; Karam & Fung, 1988). The various scattering contributions may be combined by a simple single scattering model or by a more complex multiple scattering model. The number of variables is higher than in the case of empirical and semiempirical models. As a minimum, the following inputs are requested: soil permittivity; soil hstd. and correlation length; permittivity of stem, ear and leaf; height and diameter of stem and ear; length, width and thickness of

leaf; distribution of Eulerian angles describing leaf orientation.

- Refinements of RT models include near field interactions among scatterers (Fung et al., 1987) and/or leaf curvature (Stiles & Sarabandi, 2000). New input variables are required: the average distance among scatterers in the first case, curvature parameters (typically 3) in the second case.
- The models indicated above are based on an incoherent approach, i.e. the contributions of the different scattering sources are summed incoherently within each pixel. Of course, this is an approximation. As pointed out in Section 3.1, several works are in progress, aimed at considering coherent interactions. In coherent models the number of variables is even larger, since geometrical locations of several kinds of scatterers must be correctly characterized.

In order to be useful for remote sensing applications, models must be reliable, i.e. must save their validity under different operational and environmental contexts. From this point of view, empirical models suffer the disadvantage of depending on coefficients fitted over limited data sets. Physical models have an intrinsic more general validity. Moreover, they allow us to understand scattering processes more deeply and compute scattering effects more accurately. However, while increasing model complexity, the input variables characterization becomes more and more critical. In fact, the influence on σ° played by some variables (e.g. scatterer orientation and/or location) is smoothed by something like an averaging process in simple models, while is explicitly considered in physical models. Therefore, the latter lead to a real accuracy improvement only if the input variables characterization is accurate as well.

Model reliability is ensured by comparisons with calibrated experimental data. This leads to: "fitting" for (semi)empirical models, "validation" for physical models. In the reality, some parameters are sometimes defined as "equivalent" and "fitted" also in physical models.

In spite of the important progresses recently achieved, some discrepancies with experimental data are observed and recognized in some papers, see e.g. (Cookmartin et al., 2000; Del Frate et al., 2001). Discrepancies may be due to various reasons, as indicated below.

- Interactions among scatterers are not correctly considered by incoherent models. Coherent models may be more accurate with this respect, provided vegetation elements locations are described with high precision.
- The vegetation canopy is often subdivided into various layers. Some unavoidable arbitrary decisions are taken in this process.
- The single scatterer characterization is not yet a solved problem. Leaves are neither plane nor regularly bent. Stems are hollow cylinders. Ears are not homogeneous cylinders, but have a complex internal geometry and are partially empty. Moreover, presently used permittivity models have not received so many new validations, in the recent years.

Studies aimed at solving the above mentioned problems are recommended. Moreover, if the physical model has to be used to train a retrieval algorithm (see next Section) it could be appropriate to define some variables as equivalent and fit their values over experimental data, provided the model represents well the basic physics of the scattering process and fitting is carried out over mutifrequency and multitemporal data sets, and over various fields of the same crop type.

4. RETRIEVAL

As observed in Section 3, modeling studies are still in progress and refinements are under way. Nevertheless, what has been learned till now by experimental and modeling investigations may be used to develop preliminary retrieval algorithms. Future refinements in the direct problem will produce parallel refinements in the retrieval techniques as well.

4.1. Recent advances

Wigneron et al. (1999) have retrieved crop biomass of a soybeans field using a multitemporal set of σ° data, collected by a C band scatterometer, using a simple "cloud" model calibrated by a discrete RT model.

Prévot et al. (2001) have retrieved the temporal evolution of wheat variables using the STICS crop model in addition to RT models. An assimilation technique has been adopted. Results obtained using only optical data have been compared with the ones obtained by using both optical and SAR data.

Bouman et al. (1999) have tested a composite model including crop growth (SUCROS), water balance (SAHEL) and radar backscatter (CLOUD). ERS signatures collected at Flevoland site over potato, sugarbeet and wheat fields have been used. The paper contains information useful to develop retrieval algorithms.

4.2. State of the art

Among the several variables influencing σ°, WC and LAI are considered particularly important for applications, and studies are mainly aimed at retrieving them. A list of possible approaches to the problem is given below.

- Direct inversion of simple empirical models. This is a straightforward method. However, empirical relationships are validated over restricted data sets and do not prove to be accurate when used in different operational or environmental contexts.

- Inverting simple models after calibration by physical models. This approach shows a more general validity with respect to the previous one. However, also this procedure has been tested over limited data sets, till now. Therefore, further checks are required.

- Multi-variable inversion of physical models. As stated in Section 3, physical models represent a scattering process in which σ° is dependent on several soil and vegetation variables. From a purely mathematical point of view, the inverse problem may be solved, provided the site is observed in several radar configurations, in such a way as to achieve a number of σ° data at least equal to the number of unknowns. The mathematical complexity of the problem could be overcome, due to the tremendous advances recently achieved in computational systems and in retrieval techniques (e. g. neural networks). However, even limited inaccuracies of the direct model may produce severe effects.

- Using multitemporal radar data, eventually associated with optical data, and assimilation of a-priori information provided by crop models. This technique appears to be promising, although requires further work.

In the author's opinion, due to the high number of variables influencing σ°, a feasible and reliable algorithm should take the maximum benefit from: i) multitemporal observations, ii) available a-priori information. The vegetation variables are not independent from each other, but evolve following some rules, for a given crop type and crop variety. Moreover, the temporal evolution is different from field to field, but shows some common aspects which may be assumed as a-priori known.

In order to clarify these concepts, the temporal evolutions of WC measured at different sites have been compared. Ground measurements were carried out over wheat fields at Avignon (F) in 93 and 96 and at Central Plain (CH) in 88 and 89. Central Plain data have been provided by GAMMA in the framework of ERA-ORA Project, while Avignon data have been made available by INRA. The various trends are shown in Figure 8.

All trends show a typical "bell" shape, but there are large differences in maximum WC value (full growth value) as well as in temporal location and temporal

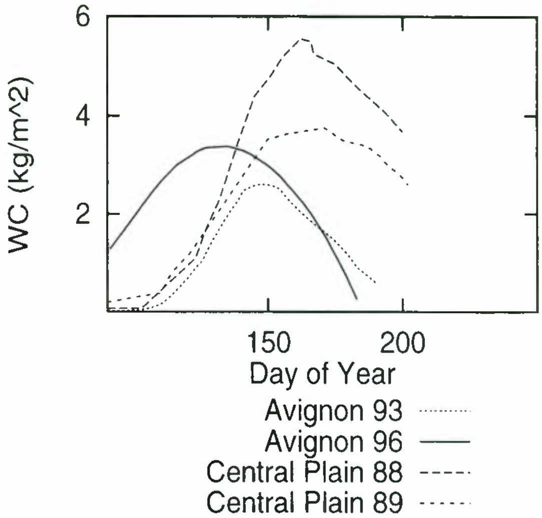

Figure 8. Examples of multitemporal WC trends of wheat fields

duration of the cycles. By applying a simple normalization as:

$$WCn(t) = K \cdot WC(at + b)$$

(where t is the time) and optimizing the a, b and K parameters for each cycle, the trends of Figure 9 are obtained. The latter appear to be well close to each other.

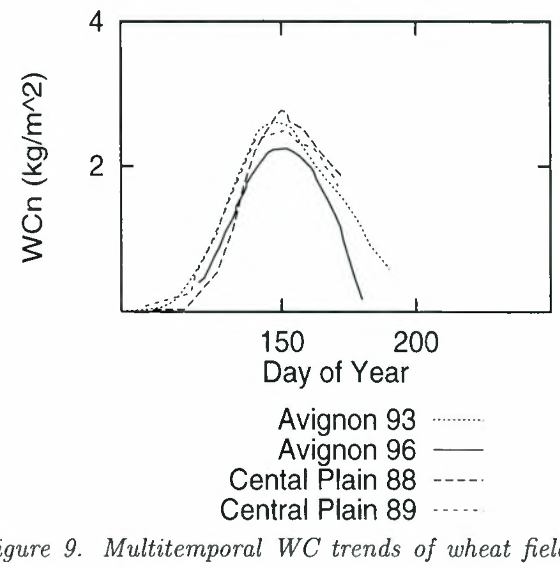

Figure 9. Multitemporal WC trends of wheat fields after normalization

Therefore, a possible retrieval technique could assume a reference "bell" function as a priori known and use remote sensing data to find the a, b and K parameters, which are specific of the observed field. This could be done using: i) a crop model and a simple model relating σ° to WC with coefficients fitted over data collected in previous experiments, possibly over fields of the same variety and in the same environment; ii) multitemporal ground truth previously collected over fields of the same crop type and a physical model. An attempt to retrieve the cycle of a wheat field using the second approach is shown by Del Frate et al. (2001). The inaccuracy of the results is mainly due to the direct model, while the algorithm works well. Figure 2 of the same paper indicates that, for 3 fields of the same site, geometrical variables are different from field to field, but evolve following similar trends.

5. CONCLUSIONS

In the work aimed at retrieving crop variables, three main phases have been considered: i) identification of a convenient radar configuration, ii) modeling and iii) solution of the inverse problem. According with the results obtained till now, a future satellite radar system, operating at L and C band, at linear co- and cross-polarization and at an intermediate θ range (30° - 40°), should acquire most of the potential information for crop monitoring. Advances in modeling have been important, but further refinements are needed to correctly describe single scatterers and understand the importance of coherent interactions. Retrieval techniques based on multitemporal data and assimilation of crop models appear to be promising.

ACKNOWLEDGMENTS

The data collected at Flevoland and Central Plain sites have been made available in the framework of the ERA-ORA Concerted Action, founded by ECC (Contract No. ENV4-CT97-0465).

The author wishes to thank all the colleagues who gave a tremendous help in several ways: direct cooperation, data exchange, suggestions, severe criticism. In particular: D. Solimini, G. Schiavon, L. Guerriero, F. Del Frate, P. Pampaloni, S. Paloscia, J.-P. Wigneron, A. Chanzy, T. Strozzi, U. Wegmüller, D. Hoekman, M. Vissers, M. Borgeaud, S. Quegan.

REFERENCES

Bouman B.A.M., van Kraalingen D.W.G., Stol W., van Leeuwen H.J.C., 1999, "An acroecological modeling approach to explain ERS SAR radar backscatter of agricultural crops", Remote Sens. Environ., vol. 67, 137-146

Brown S.C.M., Quegan S., Bennett J.C., 2001, "High resolution measurements of scattering in wheat canopies - Implications for crop canopy retrieval", This issue

Chauhan N.S., Lang R.H., 1999, "Radar backscattering from alfalfa canopy: a clump modelling approach", Int. J. Remote Sensing, vol. 20, 2203-2220

Chiu T., Sarabandi K., 2000, "Electromagnetic scattering from short branching vegetation", IEEE Trans. Geosci. Remote Sensing, vol. 38, 911-925

Christensen E.L., Skou N., Dall J., et al., 1998, "EMISAR: an absolutely calibrated polarimetric L- and C-band SAR", IEEE Trans. Geosci. Remote Sensing, vol. 36, 1852-1865

Churchill P.N., Attema E.P.W., 1992,"The MAESTRO-1 European airborne polarimetric Synthetic Aperture Radar campaign", MAESTRO-1/AGRISCATT Final Workshop Proceedings, ESA wpp-31, 1-11

Cookmartin G., Saich P., Quegan S., et al., 2000, "Modeling microwave interactions with crops and comparison with ERS-2 SAR observations", IEEE Trans. Geosci. Remote Sensing, 658-670.

Del Frate F., Ferrazzoli F, Guerriero L., et al., 2001, "Monitoring crop cycles by SAR using a neural network trained by a model", This issue

De Roo R.D., Du Y., Ulaby F.T., et al., 2001, "A semiempirical backscattering model at L-band and C-band for a soybean canopy with soil moisture inversion", IEEE Trans. Geosci. Remote Sensing, vol. 39, 864-872

Eom H.J., Fung A.K., 1984, "A scatter model for vegetation up to Ku-band", Remote Sens. Environ., vol. 19, 139-149

Ferrazzoli P., Schiavon G., Solimini D., et al., 1997, "The potential of multifrequency polarimetric SAR in assessing agricultural and arboreous biomass", IEEE Trans. Geosci. Remote Sensing, vol. 35, pp. 5-17

Ferrazzoli P., Guerriero L., Schiavon G., 1998, "Experimental and model investigation on RADAR classification capability", IEEE Trans. Geosci. Remote Sensing, vol. 37, pp. 960-968

Freeman A., Shen Y., Werner C.L., 1990, "Polarimetric SAR calibration experiment using active radar calibrators", IEEE Trans. Geosci. Remote Sensing, vol. 28, 224-240

Fung A.K., Chen M.F., Lee K.K., 1984, "Fresnel field interaction applied to scattering from a vegetation layer", Remote Sens. Environ, vol. 23, 35-50

Held D.H., Brown W.E., Freeman A., et al., 1988, "The NASA/JPL multifrequency multipolarization airborne SAR system", IGARSS'88 Proceedings, 345-349

Hoekman D. H., 1992,"Introduction to the Agriscatt'87 and '88 campaigns", MAESTRO-1/AGRISCATT Final Workshop Proceedings, ESA wpp-31, 13-21

Karam M.A., Fung A.K., 1988, "Electromagnetic scattering from a layer of finite length, randomly oriented, dielectric, circular cylinders over a rough interface with application to vegetation", Int. J. Remote Sens., vol. 9, 1109-1134

Le Toan T., Ribbes F., Wang L.-F., et al, 1997, "Rice crop mapping and monitoring using ERS-1 data based on experiment and modeling results", IEEE Trans. Geosci. Remote Sensing, vol. 35, 41-56.

Macelloni G., Paloscia S., Pampaloni P., et al., 2001, "The relationship between the backscattering coefficient and the biomass of narrow and broad leaf crops", IEEE Trans. Geosci. Remote Sensing, vol. 39, 873-884

Prévot L., Chauki H., Troufleau D., et al, 2001, "Assimilating optical and radar data into the STICS crop model for wheat", 8th ISPRS Proceedings, 753-758.

Ribbes F., Le Toan T., 1999, "Rice field mapping and monitoring with RADARSAT data", Int. J. Remote Sensing, vol. 20, 745-765

Rosenquist A., 1999, "Temporal and spatial characteristics of irrigated rice in JERS-1 L-band SAR data", Int. J. Remote sensing, vol. 20, 1567-1587

Saich P., Borgeaud M., 2000, "Interpreting ERS SAR signatures of agricultural crops in Flevoland, 1993-1996", IEEE Trans. Geosci. Remote Sensing, vol. 38, 651-657

Skriver H., Svendsen M.T., Thomsen A.G., 1999, "Multitemporal C- and L-band polarimetric signatures of crops", IEEE Trans. Geosci. Remote Sensing, vol. 37, 2413-2429

Stiles J.M., Sarabandi K., 2000, "Electromagnetic scattering from grassland - part I: a fully phase-coherent scattering model", IEEE Trans. Geosci. Remote Sensing, vol. 38, 339-348

Stiles J.M., Sarabandi K., Ulaby F.T., 2000, "Electromagnetic scattering from grassland - part II: measurement and modeling results", IEEE Trans. Geosci. Remote Sensing, vol. 38, 349-356

Stofan E.R., Evans D.L., Schmullius C., et al., 1995, "Overview of results of spaceborne imaging radar-C, X-band Synthetic Aperture Radar (SIR-c/X-SAR)", IEEE Trans. Geosci. Remote Sensing, vol. 33, 817-828

Ulaby F.T., Attema E.P.W., 1978, "Vegetation modeled as a water cloud", Radio Science, vol. 13, 357-364

Ulaby F.T., 1980, "Vegetation clutter model", IEEE Trans. Antennas Propagat., vol. 28, 538-545

Ulaby F.T., Moore R.K., Fung A.K., 1986, Microwave Remote Sensing. Active and Passive. Vol III, Artech House

Ulaby F.T., Dobson M.C., 1989, Handbook of Radar Scattering Statistics from Terrain, Artech House

Ulaby F.T., Elachi C., eds., 1990, Radar Polarimetry for Geoscience Applications, Artech House

van Zyl J.J., 1990, "Calibration of polarimetric radar images using only image parameters and trihedral corner reflectors responses", IEEE Trans. Geosci. Remote Sensing, vol. 28, 337-347

Wegmüller U., 1993, "Signature research for crop classification by active and passive microwaves", Int. J. Remote Sensing, vol. 14, 871-883.

Wegmüller U., Werner C., 1997, "Retrieval of vegetation parameters with SAR interferometry", IEEE Trans. Geosci. Remote Sensing, vol. 35, 18-24

Wigneron J.-P., Ferrazzoli P., Olioso A., et al., 1999, "A simple approach to monitor crop biomass from C-band radar data", Remote Sensing Environ., vol. 69, 179-188.

Zebker H., Lou Y., 1990, "Phase calibration of imaging radar polarimeter Stokes matrices", IEEE Trans. Geosci. Remote Sensing, vol. 28, 246-252

HIGH RESOLUTION MEASUREMENTS OF SCATTERING IN WHEAT CANOPIES – IMPLICATIONS FOR CROP PARAMETER RETRIEVAL

Sarah C.M. Brown*, Shaun Quegan, Keith Morrison**, John C. Bennett and Geoff Cookmartin

Sheffield Centre for Earth Observation Science, University of Sheffield,
Hicks Building, Hounsfield Rd, Sheffield S3 7RH, UK.
Tel: +44 114 222 3778 Fax: +44 114 222 3809 Email: S.Quegan@sheffield.ac.uk

ABSTRACT

Polarimetric X and C band measurements by the University of Sheffield GB-SAR indoor system provide three-dimensional images of the scattering processes in wheat canopies, at resolutions of around a wavelength (3-6 cm). The scattering shows a pronounced layered structure, with strong returns from the soil and the flag leaves, and in some cases a second leaf layer. Differential attenuation at H and V polarisation, due to the predominantly vertical structure of the wheat stems and flag leaves, gives rise to marked effects. Direct return from the canopy exceeds the soil return at larger incidence angles at VV and for both frequencies, but is comparable to or less than the soil return in all other cases. At HV, the apparent ground return is probably due to a double bounce mechanism, and volume scattering is never the dominant term. Direct sensing of the crop canopy is most effective at X band, VV and large incidence angles, under which conditions the return is dominated by the flag leaf layer. Field measurements with the outdoor GB-SAR system suggest however, that for sensitivity to biomass and reduced susceptibility to disturbances by rainfall, a two channel C band system operating at a medium range of incidence angles is preferred.

I. INTRODUCTION

Many experimental studies, using scatterometers (Le Toan et al., 1984; Ulaby and Bush, 1976; Bouman, 1991; Bouman and van Kasteren., 1990; Toure et al., 1994), airborne (Bouman and Hoekman, 1993; Ferrazzoli et al., 1997, 1999) and spaceborne (Cookmartin et al., 2000; Saich and Borgeaud, 2000) radars have demonstrated that the backscatter from wheat (and other agricultural crops) is significantly affected by the state of the crop canopy. Here we report on the use of multi-parameter radar to recover two particularly important agronomical wheat parameters, biomass and Green Area Index (GAI), that are hard to measure by other means. The study is based on two multi-temporal measurement campaigns carried out during 1999 and 2000.

The main contribution of the 1999 indoor campaign was to provide, for the first time, three-dimensional measurements with sufficient resolution to localise the scattering processes within a wheat canopy. In the past, radar measurements have typically used much coarser resolutions than the scattering elements in the crop. Hence their interpretation has relied on progressively more sophisticated models (Toure et al., 1994; Cookmartin et al., 2000; Attema and Ulaby, 1978; Bracaglia et al., 1995). However, these employ very simplified representations of how the radar wave interacts with a canopy. Since wheat canopies contain a complex mixture of components (stems, leaves, ears) with strong vertical structure in the stems and ears, it is not clear that the models adequately capture the overall behaviour of scattering and attenuation involved in the radar response. The 1999 indoor campaign was specifically designed to test the assumptions and calculations involved in radiative transfer models.

While the indoor campaign aimed at **understanding** the radar response from a canopy, the 2000 outdoor campaign was more concerned with elucidating the relation between the radar return and biomass (and GAI). To this end, multi-temporal measurements of wheat canopies under a range of field conditions were gathered across the growing season.

II. INDOOR EXPERIMENTS

The GB-SAR indoor microwave facility (Morrison et al., 2001) is housed in a 6m x 4m x 3m chamber internally covered with radar absorbing material. It contains a roof-mounted rectangular planar scanning frame holding four closely spaced horn antennas, with one transmit and one receive antenna for both vertical (V) and horizontal (H) polarisations. A vector network analyser provides swept frequency signals at each

* Now at BAE Systems Advanced Technology Centres, West Hanningfield Rd, Great Baddow, Chelmsford, Essex CM2 8HN, UK
Tel:01245 242611 Fax: 01245 242103 Email: sarah.brown@baesystems.com
** Now at Qinetiq, St Andrews Road Great Malvern Worcs. WR14 3PS Tel: 01684 897107 Fax: 01684 894 185 Email: kmorrison@qinetiq.com

position during two-dimensional scans of the antenna cluster. The stored returns are used to reconstruct three-dimensional, polarimetric imagery of targets imported into the chamber on a computer controlled trolley. The imaging geometry is shown in Fig. 1. The imaging algorithm (Bennett and Morrison, 1996) allows very high resolutions to be achieved: the images described below have resolutions of around a wavelength in each dimension.

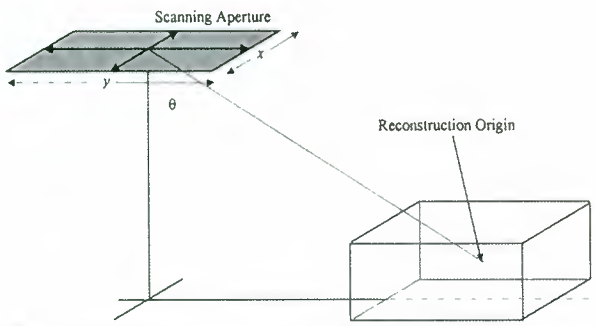

Fig. 1. Geometry of the indoor measurements.

Calibration to radar cross-section (RCS) is based on measurements of a sphere and a depolarising target, as described in Sarabandi et al. (1990). Note that RCS is the most appropriate measure at the very high resolution of the data. The system has a minimum detectable RCS better than –75 dBm^{-2} at C band.

Wheat samples (spring wheat, variety Chablis) were hand-sown in plastic containers measuring 58 x 39 x 25cm in March 1999, and were then exposed to normal outdoor growing conditions in the UK. The soil in the boxes was Kettering loam, composed of 41% sand, 37% silt and 22% clay. At regular intervals throughout the growing season, batches of containers were delivered to the University of Sheffield. After removing the rims from the containers, they were packed tightly together on the trolley to form a wheat canopy 1.53m by 1.69m in size. Spaces around and between the containers were filled with spare soil to ensure there were no visible gaps or large irregularities in the soil surface. The trolley was then moved into the anechoic chamber in order to make microwave measurements.

Agronomic and architectural parameters were collected from the wheat and soil for each canopy. The agronomic data comprised measurements of green area index (using a Licor plant canopy analyser) and shoot number. The architectural data consisted of information about the dimensions, orientations and moisture contents of the individual canopy components, such as ears and leaves, as well as soil roughness and moisture. These data were sufficiently detailed to drive a radiative transfer model, but the modelling results are not discussed here.

Although the pulse synthesis technique allows great flexibility in choice of frequency, the radar measurements presented here are restricted to C and X bands, at VV, HH and VH polarisations, and cover incidence angles from 20° to 50°.

Fig. 2 displays images generated from measurements made on 18th June, just after ear emergence. The canopy was green, 58 cm tall, and with canopy moisture

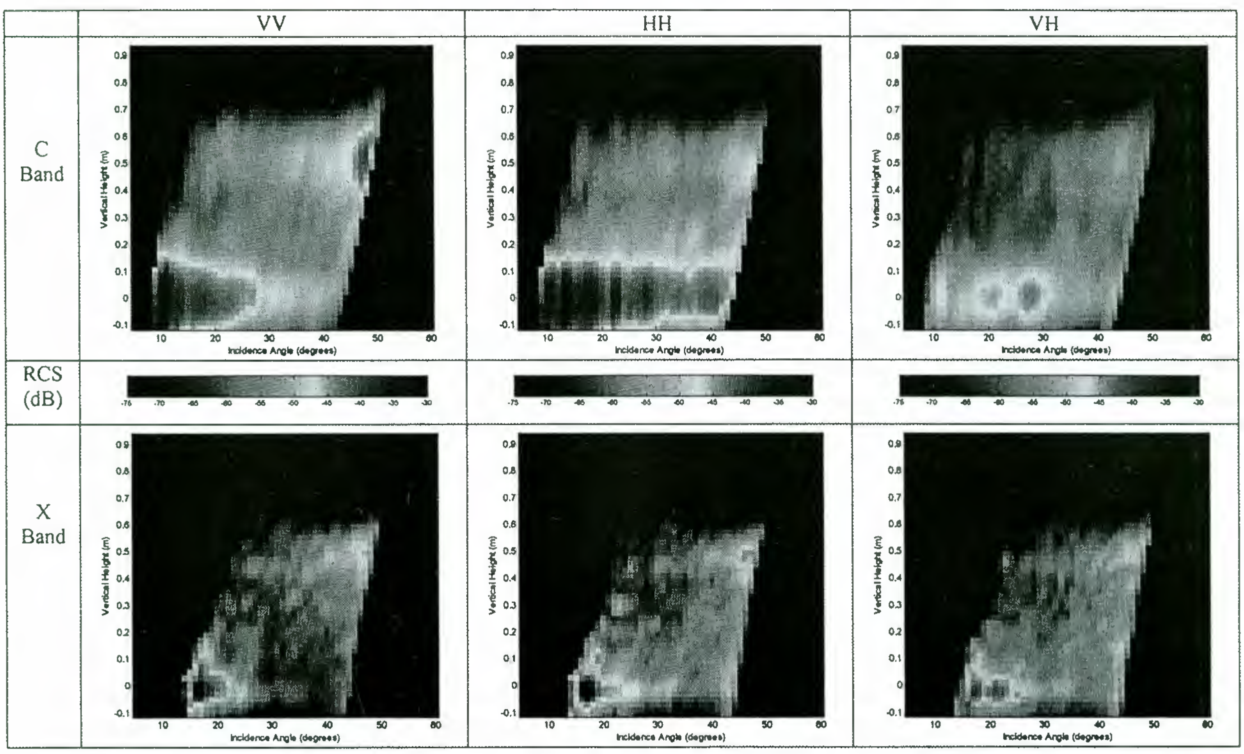

Fig. 2. Images of wheat canopy RCS, averaged in azimuth at constant height and incidence angle, for C and X bands at VV, HH and VH polarisations.

varying between 71% and 80%. It had a shoot density of 441 shoots m^{-2} and a GAI of 2.88. The soil had an rms height of 1 cm, and soil moisture values were less than 10% during the measurements.

Incidence angle and height above the soil are shown on the horizontal and vertical axes, respectively, and the grey scale indicates RCS (in dB). Because the array is close to the canopy, incidence angle varies with height, so that the imaged region does not appear rectangular. Note that these images are not individual slices through the three-dimensional data set, but have been averaged in azimuth, at a given height and incidence angle, to bring out the overall scattering pattern more clearly.

Obvious in Fig. 2 (and much more obvious in a colour display) is the layered structure of the data. The lower layer corresponds to the attenuated soil return. (Note that soil returns on the extreme left have not passed through a complete canopy, since the scanning array is above and to the left of the canopy in each image.) The marked scattering layer at a height of ~40 cm corresponds to the location of the flag leaf ligules. Data gathered in July (not shown) exhibit a second weaker layer at ~20 cm, corresponding to a lower layer of leaves.

In the C band images, the soil return dominates the backscatter at HH polarisation for all incidence angles, but at VV is dominant only for angles less than 35°. This difference is explained by strong attenuation of the vertically polarised wave by the vertically oriented wheat stems on both the forward and return propagation paths (Lopes and Le Toan, 1985). Soil returns are also dominant at VH polarisation for all but the largest angles. Since the direct cross-polarised backscatter from the soil is expected to be small, this probably indicates stem-soil double scattering. The important point for parameter recovery is that the cross-polarised return is not dominated by volume scattering in the vegetation but is strongly affected by the soil.

At all polarisations, the soil return decreases with increasing incidence angle, as a result of the incidence angle dependence of surface scattering and increasing attenuation as the path through the canopy gets longer. In contrast, direct canopy backscatter increases with increasing incidence angle. This is especially noticeable at VV polarisation for angles greater than 40°, where the backscatter is generated by the flag leaves and/or ears.

The higher resolution in the X band images of Fig. 2 allows more detailed visualisation of the scattering, but the behaviour is broadly similar to that at C band. One quantitative difference arises from the higher attenuation at X band. This limits penetration into the canopy, causing the ground return to dominate the backscatter only for angles less than 35° at all polarisations. As at C band, ground scatter dominates out to higher incidence angles at HH than at VV. The VH return shows strong ground returns out to 35°, after which scattering appears to be distributed through the canopy, with the strongest returns from the flag leaf/ear layer. Direct canopy backscatter increases with increasing incidence angle.

A useful way to synthesise the overall behaviour in Fig. 2 is by evaluating the integrated power from different parts of the canopy. This aids comparison both with calculations by scattering models, most of which adopt a layered medium approach, and with data from airborne and spaceborne sensors. Three layers are considered: an upper layer (for heights greater than 35cm) containing mostly flag leaves and ears, a lower layer containing the stems and remaining leaves with heights up to 35cm, and a soil layer. The powers from these layers for the data of Fig. 2 are shown in Fig. 3.

At C band, soil scatter is the dominant term for HH and VH for all incidence angles. For VV, the upper canopy dominates for angles exceeding 37°. The power from the soil declines steadily with incidence angle at VV, falling by about 10 dB across the swath. At HH, after an

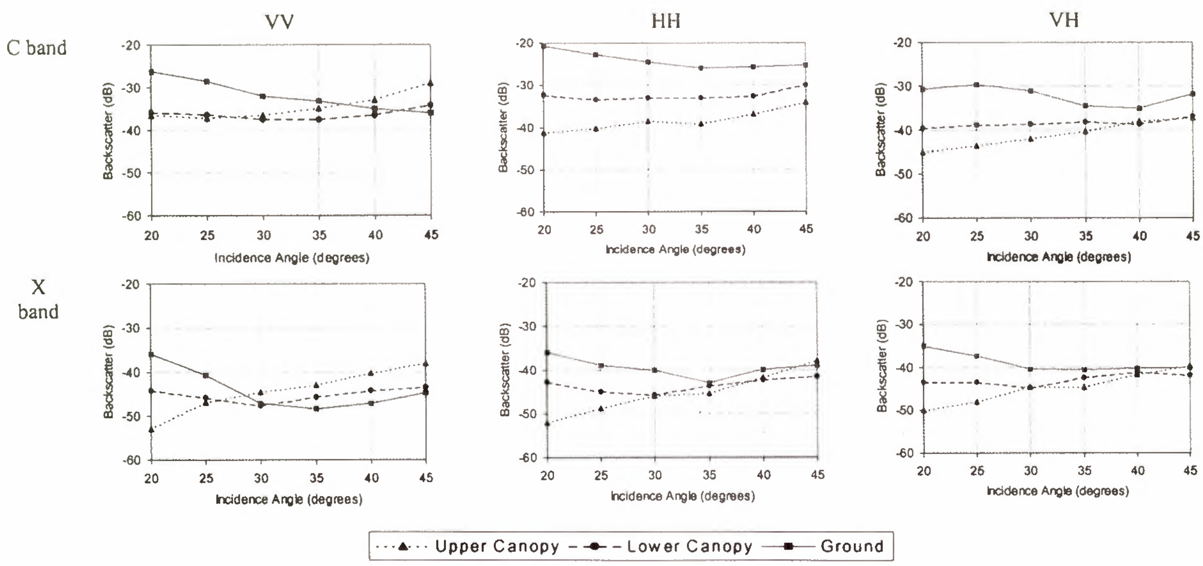

Fig. 3 Mean C and X band measured backscatter from different layers in the canopy imaged in Fig. 2.

initial decline of about 4 dB, the ground return remains fairly constant. The X band measurements show the upper canopy becoming dominant at VV for angles greater than 28°. For HH and VH, soil dominates out to 35°, after which the contributions from all three layers become comparable. Surprisingly, the soil return does not show monotonic behaviour, but declines then increases for both HH and VV. The sharper decline at VV is the principal reason why the upper canopy becomes dominant at this polarisation. The increase in the soil return is almost certainly due to a canopy-soil interaction, which cannot be separated from the direct ground return in these images.

Summarising the results from the indoor measurements, we find that:

1. The radar sees the wheat crop essentially as a 2 or 3 layer medium.
2. The soil return decreases relative to the canopy as incidence angle increases.
3. For VV polarisation, the canopy dominates the soil at significantly smaller incidence angles than for HH.
4. The canopy is dominant over a greater range of incidence angles for X band than for C band.
5. The HV return is not dominated by volume scattering, but contains a very significant soil return.

Hence, for direct sensing of the vegetation, we should use X band (or higher frequencies), VV polarisation and large incidence angles. However, as we show below, these conclusions may not apply if our concern is the recovery of crop information.

Before leaving the indoor measurements, we note some important results from an experiment performed on 18th June, when 21 litres of water (equivalent to 8mm of rain) were sprayed over the canopy, using a watering can fitted with a rose to simulate the effect of rain. Fig. 4 compares the integrated C band backscatter from the wet and dry canopies. Wetting caues increases of 3-5 dB for all polarisations and incidence angles, except for reduced differences in VV at the higher incidence angles. Detailed analysis reveals that most of the wet-dry variation occurs in the lower canopy and soil regions. The VV signal at large incidence angles is less sensitive to wetting because here the scattering comes mainly from the upper canopy (see Figs. 2 and 3).

III. OUTDOOR MEASUREMENTS

The GB-SAR facility includes a portable outdoor radar system mounted on a trailer-borne hydraulic lift. This operates on the same principles as the indoor system, but with only a 4 m linear scanner, so it cannot perform 3-D imaging. This sensor can provide fully polarimetric measurements covering the frequency range from K to L band, over an area of typically 1,000 m^2.

During the 2000 growing season, trial plots of winter wheat (variety Claire) were provided by ADAS Consulting Ltd on an experimental farm near Cambridge, UK. By managing the plots in different ways, a wide range of shoot number, biomass and GAI conditions were generated. The different management regimes included use of two drilling dates, two seed rates and three different levels of applied nitrogen fertiliser. Identical levels of fungicides and herbicides, consistent with a normal commercial crop, were applied to each of the plots.

Accompanying the radar measurements were agronomic data (shoot number, fresh biomass, GAI and growth stage) and architectural data, consisting of detailed information on the dimensions, orientations and moisture contents of all the components within the wheat canopy, i.e. leaves, stems and ears. Soil roughness and moisture were also measured, along with crop height. These architectural data were sufficient to drive a radiative transfer model, but these calculations are not described here.

The most complete dataset was at C band, for which nine sets of measurements were collected on three trial plots on different dates. Issues connected with the antenna patterns meant that comparable coverage for all nine datasets was only possible at around 40° incidence angle. Fig. 5a shows the mean radar backscatter derived from these data against fresh biomass, for VV, HH and VH polarisations. Backscatter decreases with increasing biomass for both VV and VH polarisations, but HH polarisation exhibits little variation, except for one bare

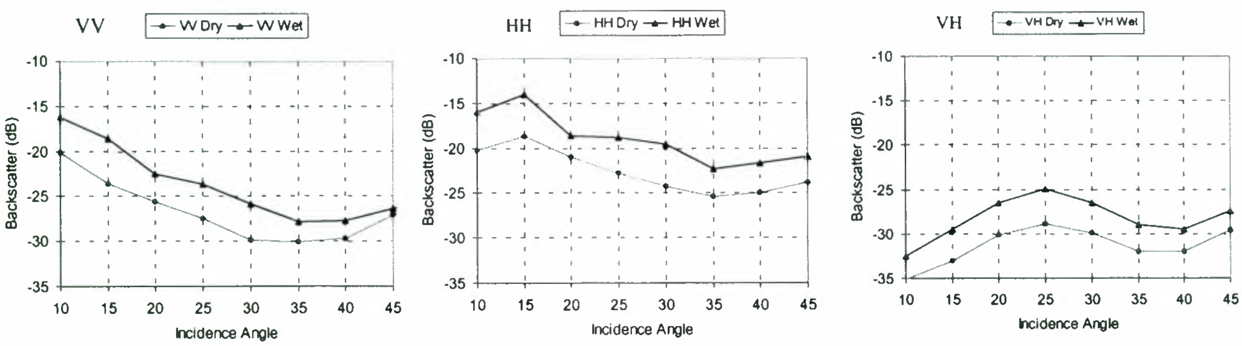

Fig. 4 Total C band backscatter from a canopy imaged on 18 June, 1999, before and after wetting.

soil value early in the season. Similar trends were observed in comparisons between backscatter and GAI.

Based on the indoor measurements discussed in section II, but bearing in mind the wetter soils in the outdoor measurements, it is likely that the measured backscatter consists largely of an attenuated soil contribution. Consequently, biomass is being expressed through its effect on extinction, rather than by its contribution to direct canopy backscatter. Since soil attenuation is a measure through the whole canopy, it in a sense integrates the overall canopy biomass. The VV and VH returns are much more strongly affected by attenuation than HH, hence their greater sensitivity to biomass.

A problem in using single channel backscatter as a biomass indicator is implicit in Fig. 4: rainfall causes large changes in the radar return, rendering the inversion unreliable. However, Fig. 4 also shows that the different channels exhibit very similar responses to wetting. This suggests that the difference particularly between the VV and HH backscatter might be a useful indicator of biomass. This relation is shown in Fig. 5b. Not surprisingly, given the results shown in Fig. 5a, the HH-VV difference increases sharply with biomass.

IV. CONCLUSIONS

The argument in Section III identifies differential attenuation of the soil return by the HH and VV channels as the key biomass indicator. Inter-channel differences are preferred because they are less prone to disturbances from rainfall than single channels. The HH-VH difference could also be used, but suffers from greater sensitivity to noise (in the cross-polarised channel) and possible bad behaviour under conditions of bare soil (or low biomass) due to very low values in the VH return. This argument, if its general validity can be demonstrated, has strong implications for the design of a system to be used for measuring biomass. The central requirement is that both the HH and VV returns are dominated by attenuated scattering from the soil. This requirement is more easily met at C band than at X band. Also, the difference between the HH and VV soil returns increases with incidence angle, because the path through the canopy gets longer, implying use of larger incidence angles. However, at some point the VV return will switch over to being dominated by the upper canopy (see Figs. 3 and 4), at which point the relationship between biomass and the HH-VV

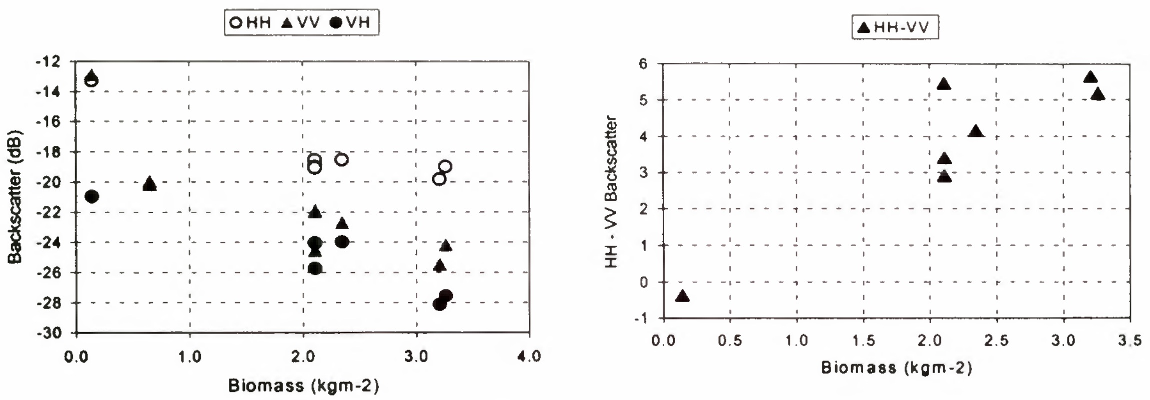

Fig. 5 Mean C band backscatter and HH-VV difference at 40° incidence angle vs biomass.

An unfortunate feature of Fig. 5 is the large gap in biomass values between 0.75 and 2 kg m^{-2}, caused by poor weather conditions in April. This is the period of most rapid growth and increasing biomass. Also, the measurements stop in early June, due to a combination of bad weather and staffing difficulties after this time. Hence all the measurements occur during the declining phase of the wheat growth curve, i.e., the plot of the wheat backscattering coefficient against time, and they do not continue into the increasing phase which normally follows (Le Toan et al., 1984; Saich and Borgeaud, 2000). This means that neither the overall shape of the plot of biomass against the HH-VV difference nor the limits of its sensitivity can be inferred from this dataset.

difference will break down. The results in this paper suggest a transition point around incidence angles of 35° to 40°, dependent on soil moisture conditions.

It can be seen that these conclusions are not the same as those in Sect. II, where the indoor measurements seemed to suggest X band, VV and larger incidence angles as the preferred sensor characteristics for wheat sensing. However, this configuration principally measures a specific aspect of the canopy, namely the flag leaf layer, which may be only weakly related to more interesting agronomic properties. In contrast, the argument in Sect. III suggests that a two channel C band sensor operating at moderate incidence angles is most fitted to the task of biomass measurement. Hence Envisat is likely to be a better sensor for this purpose than, for example, the X band sensor mooted for TerraSAR.

The inferences above must be treated with some care, as there are significant weaknesses in the dataset on which they are based:

1. Only a small number of canopies were measured;
2. There were no measurements during the period of most rapid growth;
3. Insufficient X band data were gathered to allow comparison with C band;
4. Only a single wheat variety was considered in each of the campaigns.

Scatterometer measurements indicate the importance of point (4). For example, in Le Toan et al. (1984), significant differences were found between two different varieties of wheat. In particular, although both showed an approximately linear relationship between LAI and backscattering coefficient, the slope of this relation was quite different for the two varieties.

It is clear that more measurements are needed to address these defects in the data, but the work reported here provides a better insight into which are the key questions. It should be added that attempts to reproduce the observed results using a sophisticated radiative transfer model (which is described in Cookmartin et al., 2000) were not very successful, indicating that an improved theoretical treatment is needed, in parallel with the experimental programme.

ACKNOWLEDGEMENTS

The authors gratefully acknowledge experimental assistance from Mr A. Race, Mr. D. Cox and Dr A.J. McDonald. They would also like to thank Mr P. Dampney and Mr A. Gay of ADAS Consulting Ltd, UK, for providing the wheat canopies, and Craig Anderson and Ralph Cordey of BAE Systems for help in field measurements and advice on backscatter modelling. Financial support for this work came from the UK's BNSC/LINK programme (Project R4/025) and the Natural Environmental Research Council (reference DST/26/61).

REFERENCES

E. P. W. Attema and F. T. Ulaby, "Vegetation modelled as a water cloud", *Radio Sci,* vol. 13, no. 2, pp. 357-364, 1978.

J. C. Bennett and K. Morrison, "Development of a Ground-Based, Polarimetric Synthetic Aperture Radar," *IEEE Aerospace Applications Conference*, Los Alamitos, CA, USA, 1996.

B. A. M. Bouman, "Crop parameter estimation from ground-based X-band (3 cm wave) radar backscattering data", *Remote Sens. Environ.*, vol. 37, pp. 193-205, 1991.

B. A. M. Bouman and H. W. J. van Kasteren, "Ground-based X-band (3 cm wave) radar backscattering of agricultural crops. II. Wheat, barley and oats; the impact of canopy structure", *Remote Sens. Environ.*, vol. 34, pp. 107-119, 1990.

B. A. M. Bouman and D. H. Hoekman, "Multitemporal, multi-frequency radar measurements of agricultural crops during the Agriscatt-88 campaign in the Netherlands", *Int. J. Remote Sensing*, vol. 14, No. 8, pp. 1595-1614, 1993.

M. Bracaglia, P. Ferrazzoli and L. Guerriero, "A fully polarimetric multiple scattering model for crops", *Remote Sens. Environ.*, vol. 54, pp. 170-179, 1995.

G. Cookmartin, P. Saich, S. Quegan, R. Cordey, P. Burgess-Allen and A. Sowter, "Modelling microwave interactions with crops and comparison with ERS-2 SAR observations", *IEEE Trans. Geosci. Remote Sensing*, vol. 38, no. 2, pp. 658-670, 2000.

P. Ferrazzoli, L. Guerriero and G. Schiavon, "The potential of multifrequency polarimetric SAR in assessing agricultural and arboreous biomass", *IEEE Trans. Geosci. Remote Sensing*, vol. 35, no. 1, pp. 5-17, 1997.

P. Ferrazzoli, L. Guerriero and G. Schiavon, "Experimental and model investigation on radar classification capability", *IEEE Trans. Geosci. Remote Sensing*, vol. 37, no. 2, pp. 960-968, 1999.

T. Le Toan, A. Lopes and M. Huet, "On the relationships between radar backscattering coefficient and vegetation canopy characteristics", in *Proc. IGARSS'84*, ESA SP-215, pp. 155-160, 1984.

A. Lopes and T. Le Toan, "Effet de la polarisation d'une onde electromagnetique dans l'attenuation de l'onde dans un couvert vegetal", *Proc. 3rd Int. Coll. on Spectral Signatures in Remote Sensing, Les Arcs*, ESA SP-247, pp. 117 - 122, 1985.

K. Morrison, J. C. Bennett, G. Cookmartin, A J. McDonald, A. Race and S. Quegan, "Three-dimensional X-band SAR imaging of a small conifer tree", *Int. J. Remote Sensing*, Vol. 22 , no. 4, pp. 705-710, 2001.

P. Saich and M. Borgeaud, "Interpreting ERS SAR signatures of agricultural crops in Flevoland, 1993-1996", *IEEE Trans. Geosci. Remote Sensing*, vol. 38, no. 2, pp. 651-657, 2000.

K. Sarabandi, F. T. Ulaby and M. A. Tassoudji, "Calibration of polarimetric radar systems with good polarization isolation", *IEEE Trans. Geosci. Remote Sensing*, Vol. 28, no. 1, pp. 70-75, 1990.

A. Toure, K. P. B. Thomson, G. Edwards, R. J. Brown and R. G. Brisco, "Adaptation of the MIMICS backscattering model to the agricultural context - wheat and canola at L and C bands", *IEEE Trans. Geosci. Remote Sensing*, vol. 32, no. 1, pp. 47-61, 1994.

F. T. Ulaby and T. F. Bush, "Monitoring wheat growth with radar", *Photogrammetric Eng. and Remote Sensing*, vol. 42, no. 4, pp. 557-568, 1976.

ASSESSMENT OF CROP DISCRIMINATION USING MULTI-SITE DATABASES

M.C. Gonzalez-Sampedro (1), T. Le Toan (2), M.W.J. Davidson (2) and J. Moreno (1)

(1) Universitat de València
Facultad de Física, Departamento de Termodinámica
Dr. Moliner 50, Burjassot (Valencia), 46100, Spain
tel: + 34963983112 / fax: + 34963983385
e-mail: mcgonzal@uv.es / moreno@uv.es

(2) CESBIO (Centre d'Etudes Spatiales de la Biosphère)
18 Avenue Edouard. Belin
31401 Toulouse Cedex 4, France
Tel: + 33561556671/ Fax: + 33561558500
e-mail: Thuy.Letoan@cesbio.cnes.fr / Malcolm.Davidson@esa.int

ABSTRACT

Within the framework of the ERA-ORA (European Radar-Optical Research Assemblage) project funded by the EC, an extensive database including both remote sensing data and coincident ground data, collected by several institutes in Europe, has been assembled and organized. The remote sensing data consists of radar data acquired mainly by ERS and airborne SARs at different sites across Europe.

Overall, this compilation of data from different sites represents an opportunity to examine the generality and robustness of remote sensing methods and algorithms. In the past much of the literature published on retrieval algorithms has been based on observations over a single site. The extension of these results to larger areas and different sites thus represents and important step in the development and validation of generalized retrieval algorithms applicable to a variety of situations.

INTRODUCTION

In this paper, we will analyze and interpret part of the database collected at different European agricultural sites to address several questions related to crop classification, keeping in mind that the launch of ENVISAT in the next few months will open new perspectives for radar satellite applications. In particular, this work addresses the following questions related to the classification of crops:

a) Can multitemporal ERS data be used to discriminate crop types based on their temporal backscatter signal?
b) With the known limitations of current systems, can ENVISAT/ASAR with its different polarisations and incidence angles be used to discriminate crop types at a given time with fewer temporal acquisitions.
c) What are the relative contributions of polarimetry at C, L and P bands to the overall crop classification results?
d) What is the role of synergy between optical and radar sensors (e.g. ASAR and MERIS) for large agriculture fields?

MULTI-SITE DATABASE

Study Areas

This work has been focused on the following study areas (Fig. 1):

Flevoland (The Netherlands):

This area is located in Zuid Flevoland (centered at 52.4° North and 5.4° East) in the Netherlands, approximately 30 Kilometers east of Amsterdam. The Zuid Flevoland polder was reclaimed from lake Ijsselmeer in 1966 and its topography is almost perfectly flat, the general altitude of the area being three meters below the mean sea level. The reclaimed polder is used mainly for agriculture and forestry, the main cultivated crops are sugar beet, potato and winter wheat [1].

Barrax (Spain):

This area is located in Castilla-La Mancha, Spain (with coordinates 39° 3' North and 2° 6' West) and it has been used for several previous experiments: EFEDA (Field Experiment in Desertification-threatened Areas), STAAARTE (Scientific Training and Access to Aircraft for Atmospheric Research Throughout Europe), MAC (Multisensor Aircraft Campaign), DAISEX (Digital Airborne Imaging Experiment) among others. Its flat topography is of great advantage for remotely sensed data corrections and its interpretation. In Barrax, there are large uniform crop fields both irrigated and non

Proc. 3rd International Symposium, 'Retrieval of Bio- and Geophysical Parameters from SAR Data for Land Applications', Sheffield, UK. 11-14 September 2001 (ESA SP-475, January 2002)

irrigated mostly consisting of barley, corn, sugar beet, wheat, as well as bare soils areas.

Figure 1.- Location of the study areas

ERS-SAR time series

ERS-SAR temporal series from Flevoland over the period 1993 to 1996 have been used to assess crop separability and annual variations in crop radar signatures.

Polarimetric data

We have used JPL-AIRSAR data (C, L and P band) from the Flevoland site that were acquired in two different experiments, MAESTRO-89 and MAC-Europe 1991. The data collection was conducted from August 16, 1989 to July 28, 1991 (there are a total of five acquisition dates: 89-08-16, 91-06-15, 91-07-03, 91-07-12, 91-07-28). The crop signatures were averaged in every field. The incidence angle for both years falls in the 26 to 65 degrees range.

Optical-radar synergy

In addition, we have used hyperspectral optical data to investigate the radar-optical synergy from the ESA/DAISEX-1999 EFEDA campaigns that took place at Barrax. The airborne hyperspectral scanner HyMap [2] has 128 channels covering the 0.4-2.5 µm spectral range. HyMap images from the DAISEX-1999 campaign were compared with the ERS-SAR images. The JPL-AVIRIS [3] airborne sensor images (224 bands along the 0.4-2.5 µm range) acquired during the EFEDA campaign were used in combination with AIRSAR data.

Ground measurements:

Detailed crop maps for each year were available for the Flevoland and for the Barrax area as well. For some of the fields, several agronomic parameters such as biomass, crop height, canopy water content and soil moisture status were measured.

RESULTS

Temporal series:

We have selected two complete ERS-SAR annual series data from the Flevoland area, corresponding to the years 1993 and 1995. Figure 2 shows those temporal series for four crops (barley, wheat, sugarbeet and potato). The curves were obtained by averaging all the crops of the same kind. Standard deviation is shown as error bars.

For one particular year it is possible to distinguish between two main groups (cereals and broad leaves crops) in the period that follows the maximum cereals development: for 1995 near day 180 (beginning of July) and for 1993 near day 150 (end of May). It is important to notice that even for the same site there are shifts of one month in crops phenology. Bigger shifts are expected when comparing temporal curves from different sites.

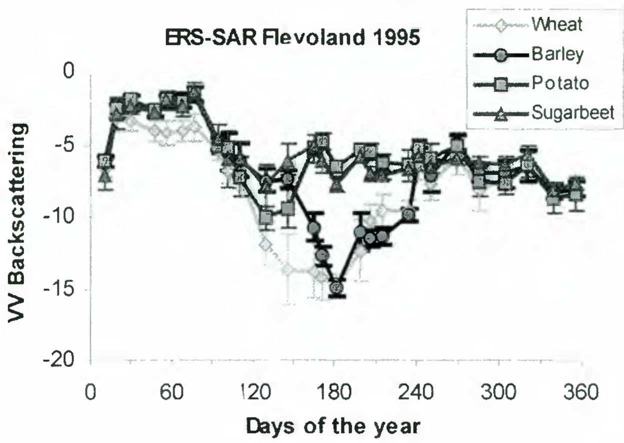

a)

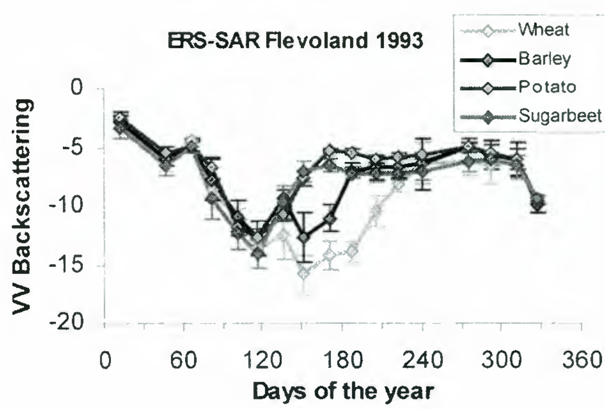

b)

Figure 2.- Radar signatures of the dominant crops in the region of Flevoland a) Year 1995, b) Year 1993.

AIRSAR data:

Using more than one polarisation channel, higher levels of separation between crops can be achieved, even if the information comes from only one frequency. Among the available Flevoland AIRSAR data we have selected field averaged C band signatures with incident angle between 45 and 55 degrees. The reason to choose this angular interval was that it included the biggest amount of fields. A total number of 450 signatures were available (88 of sugarbeet, 134 of wheat, 129 of potato, 51 of barley and 48 of grass) corresponding to 4 dates from the same year. Table 1 contains these details.

Date	Sugar-beet	Wheat	Potato	Barley	Grass
91/06/15	15	30	28	16	10
91/07/03	19	32	26	12	17
91/07/12	25	35	34	13	11
91/07/28	29	37	41	10	10

Table 1.- Number of crops per date used for the analysis

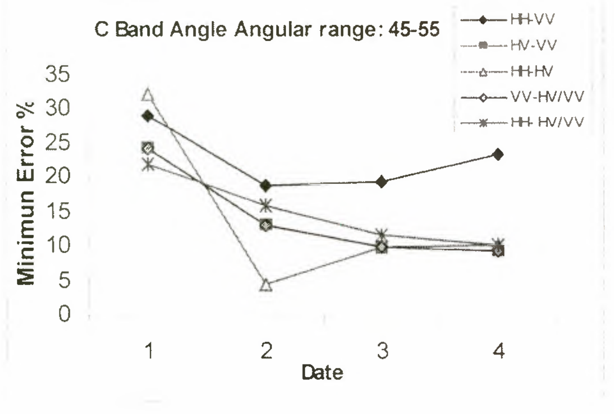

a)

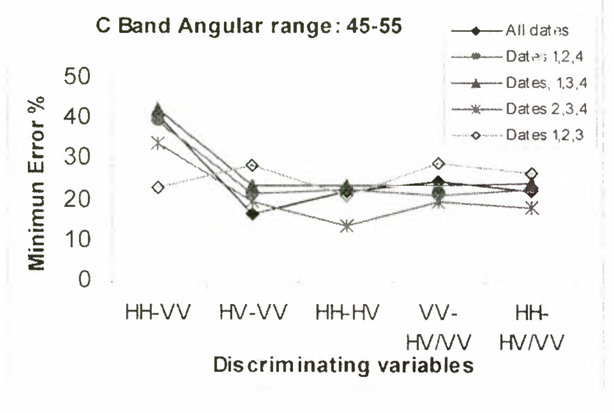

b)

Figure 3.- Minimum error achieved in the classification of 5 crop types using the maximum likehood algorithm.

Figure 3 shows the minimum error in the classification of five types of crops (sugar beet, potato, barley, wheat and grass) using the algorithm of maximum likelihood [4]. A case has been considered in which only one day and two discriminating variables were utilized (Figure 3.a) as well as the case in which all the dates or combinations of the three dates are utilized (Figure 3.b). For all the combinations of different polarisations (HH-VV, HV-VV, HH-HV, VV-HV/VV, HH-HV/VV) we have found that date 1, which corresponds to June 15 has the largest errors. Date 2, corresponding to July 3, is the optimum date due to the separation between crops which is maximum utilising HH and HV polarisations.
We have seen that including more than one date in the analysis does not improve the error of the classification but worsens it as it is seen in Figure 3.

Optical-radar synergy:

The error of the separability among the 5 classes in our dataset was never lower than 10% even when using polarisation information. For some combinations of dates, errors were higher than 40%. In these cases, other sources of information, such as optical data, may help to overcome the limitations of radar data.

For exploring the optical-radar synergy we have done a pixel by pixel comparison of two pairs of images from the Barrax site:

a) ERS-SAR (2nd of June, 1999) / HyMap (3rd of June, 1999)
b) AIRSAR (19th of June, 1991)/ AVIRIS (29th of June, 1991)

In order to make possible a pixel by pixel comparison of the images we need first to superpose them. After geo-rectification of the optical images and slant-to-ground range correction of the radar images, these have been registered over optical images by means of ground control points. The final resolution is that of the optical images (5 meters for HyMap and 20 meters for AVIRIS). HyMap image was geometrically and atmospherically corrected at DLR [5]. Due to the flat topography of the Barrax site the topographic effects are not critical.

In Figure 4, we have compared a near infrared band, where the vegetation response is very high, with radar backscattering. The grey scale represents the density of points. If the same information were contained in both optical and radar data, a high correlation between the two quantities would be found. However, Figure 4 shows a very low correlation. Points are grouped into two clouds, corresponding to the optical signal of soils (low reflectance) and to green vegetation (high reflectance). Radar signal was not able to distinguish these two classes. For each surface type, the variability in radar images was due to roughness and moisture changes. Higher levels of noise were present in the ERS-SAR image as opposed to the HyMap image.

Figure 6 shows very clearly the complementarity of optical and radar data. The CHV/LHV ratio obtained from the AIRSAR (radar) image has been represented against two indexes derived from the AVIRIS (optical) image. These two indexes are: a chlorophyll index (Fig 6a) and a plant water index (Fig 6b). In Fig 6a there is an imaginary line parallel to the x-axis illustrating how bare soils (very low index) and vegetation (higher index) have the same radar backscatter value. However, in the region of bare soils all the sensitivity comes from the radar signal. Although a low level of correlation between both kinds of data is justified by the fact that radar signal is insensitive to chlorophyll, the comparison between the water in the plant (Fig 6b) shows how information coming from the two different sources (optical and radar) is not redundant.

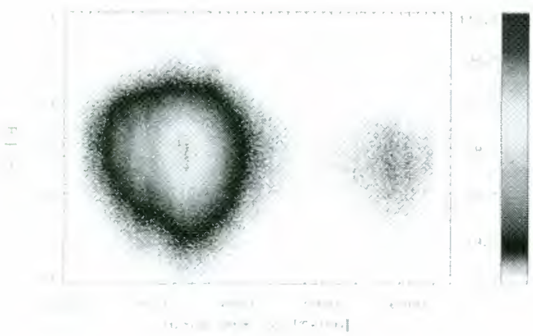

Figure 4.- ERS (radar) CVV backscattering versus HyMap (optical) 868 nm band reflectance in %*100

DRAWBACKS

In the classification of crops with radar data two main drawbacks are present:

a) Angular Variability
b) Temporal Variability

Airborne radar systems have a wide range of incident angles. In Figure 5, the angular variability (in some cases it can be of more than 6 dB for the same crop type) is higher than the variation from one crop to another, thus there is confusion among classes.
To obtain better results in the classification it is necessary to restrict the incident angle range.

Classification results are strongly dependent on the time sequence because of the differences in the phenological state of the crops. Development of crops occurs very quickly in a short period of time, which is different for every crop and changes from one site to another. So depending on the overlapping of the phenological cycles of every kind of crop, there will be an optimal date or an optimal combination of dates that ensure the highest crop separability. With the current satellite systems with time resolutions of 35 days (ERS case) it is not possible to guarantee an image acquisition in those optimal dates for an particular area.

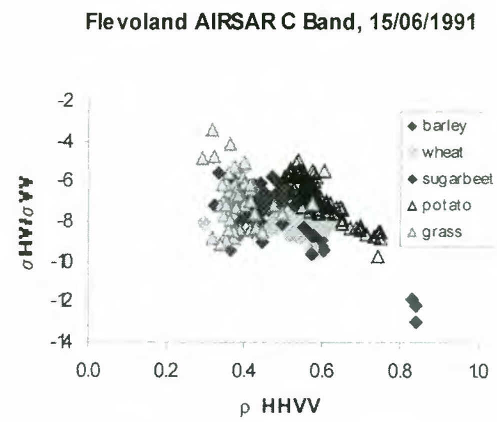

a)

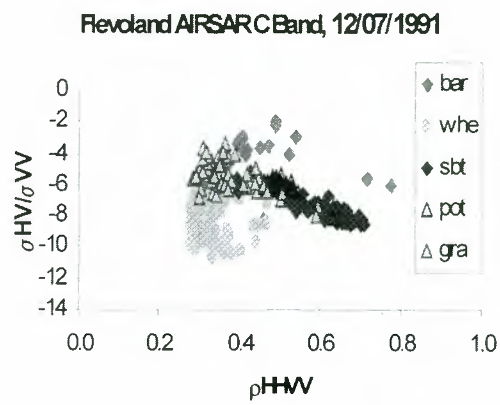

b)

Figure 5.- C band HV/VV ratio versus HH-VV correlation for two different dates at Flevoland

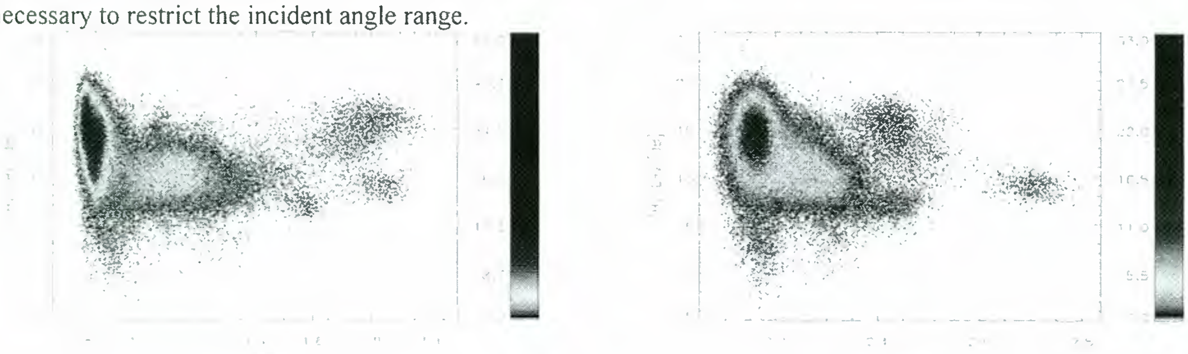

a) b)

Figure 6.- CHV/LHV ratio from the AIRSAR (radar) image versus to two indexes from AVIRIS (optical) image. a) chlorophyll index and b) plant water index.

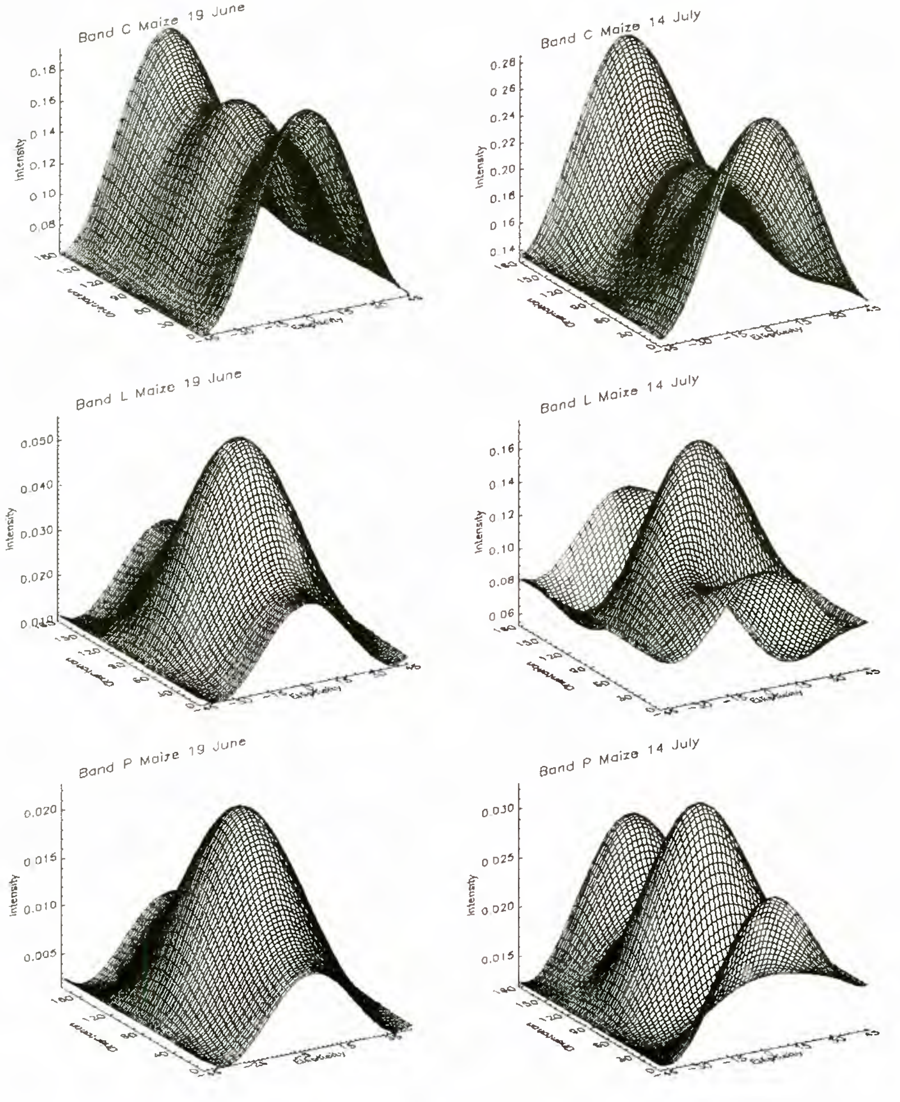

a)

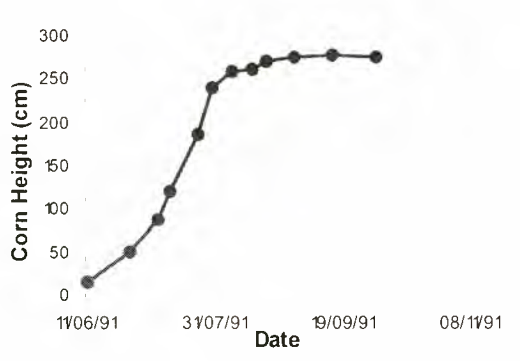

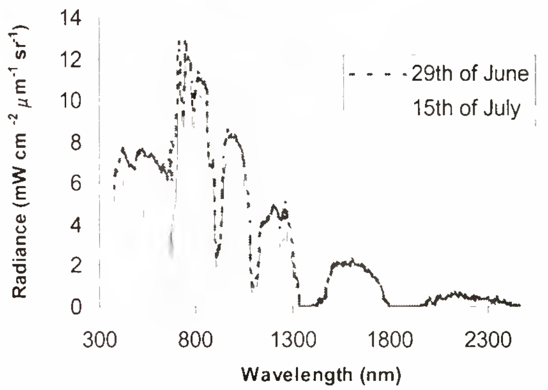

b) c)

Figure 7.- Ideal case for the optical-microwave synergistic study.
a) In these figures the averaged radar backscattering intensity for a corn pivot in the area of Barrax has been plotted for all the possible polarisation states of the transmission and received co-polarised waves. We can observe that for longer wavelengths the response is more sensitive to the surface structure. b) This figure shows a considerable increase in the height and biomass of corn from June 19th through July 14th. c) AVIRIS hypespectral signatures of the same corn pivot.

FUTURE PERSPECTIVES

In the frame of the points we deal with in this paper ENVISAT satellite opens two new perspectives:

a) Use of polarimetric information

ASAR sensor on board ENVISAT operating in C band, is technologically more advanced than ERS and will acquire images in VV (as ERS), HH and cross polarisations allowing for the first time the use of polarimetric information from satellite.
Although homogeneous surface have a characteristic polarisation signatures (see Fig. 7), at satellite resolutions polarimetric information may be difficult to interpret for non homogeneous surfaces.

b) Radar/optical synergy

Radar/optical synergy is not a well explored field of study, partly due to the sparse availability of radar/optical data for the same study area. This lack of data comes from two different causes: 1) For the time being, there are no satellites equipped with both kinds of sensors. Referring to airborne remote sensing, there have been few campaigns in which radar data together with optical data were acquired. 2) In regions where the probability of having clouds is high, available optical data are not always useful.

The launch of ENVISAT will allow for the first time to have radar and optical images systematically acquired for the same study area by means of the ASAR and MERIS sensors. The MERIS optical sensor will provide high spectral resolution images (bandwidth in nm) that will allow new applications, not possible with broad band sensors (LANDSAT, SPOT). Although its spatial resolution (300x300 m) is much coarser than the spatial resolution of SPOT (20x20 m), radar/optical synergy for areas with extensive crops, such as Barrax, would still be possible (see Figure 8).

Figure 8.- RGB composition in a Barrax HyMap image showing MERIS pixel size. One of the channels has been degradated to 300x300m resolution.

CONCLUSIONS

• Temporal evolution is confirmed as the dominant effect in crop discrimination for single band (CVV) imagery.
• The potential of polarimetric information in crop discrimination cannot be demonstrated by means of airborne polarimetric systems with a wide range of incidence angles. Spaceborne polarimetric systems can be more effective with a limited range of incidence angles for the same area coverage.
• ENVISAT/ASAR opens new perspectives, but radar-optical synergy is still necessary to discriminate between soil and vegetation scattering with C band.

ACKNOWLEDGEMENT

This work has been supported by the European Union under contract ENV4-CT95-0465 for the ERA-ORA project (European Radar-Optical Research Assemblage) and by ESA under the contract no. 13390/98/NL/GD for the ESA/DAISEX-1999 campaign.

REFERENCES

[1] M. Engdahl and M. Bourgeaud, "ERS-1/2 Tandem Interferometric Coherence and Agricultural Crop Height", Proc. 2nd International Workshop on Retrieval of Bio-&Geo-physical Parameters from SAR Data for Land Applications, ESA SP-441, December 1998, ISBN 92-9092-764-X.
[2] T. Cocks, R. Jenssen, A. Stewart, I. Wilson, and T. Shields, 1998, "The HyMap Airborne Hyperspectral Sensor: The System, Calibration and Performance", Proc. 1st EARSeL Workshop on Imaging Spectroscopy, October 1998, Zurich, EARSeL, Paris, p. 37-42.
[3] G. Vane, R. O. Green, T. G. Chrien, H. T. Enmark, E. G. Hansen and W. M. Porter, 1993, "The Airborne Visible/Infrared Imaging Spectrometer (AVIRIS)", Remote Sensing of Environment, 44:127-143.
[4] J. A. Richards, "Remote Sensing Digital Image Analysis" An Introdution. Springer-Verlag, ISBN 3-540-58219-3
[5] R. Richter, "Atmospheric correction methodology for imaging spectrometer data", Proc. of the Final Results Workshop on DAISEX (Digital Airborne Imaging Spectrometer Experiment), ESA SP-499, July 2001, ISBN 92-9092-809-3.

ERS SAR TANDEM DATA FOR CROP DISCRIMINATION AND IRRIGATION MONITORING IN SOUTHEAST SPAIN

T Pearson[1], M Wooding[1], M-C Gonzalez[2], J Moreno[2] and P Wursteisen[3]

[1]Remote Sensing Applications Consultants Ltd.
2 Prospect Place, Mill Lane, Alton, Hants, GU34 2SX, UK
Telephone: +44 1420 88777 Fax: +44 1420 87111 Email: consultants@rsacl.co.uk

[2]Remote Sensing Unit, Department of Thermodynamics, Faculty of Physics, University of València
c/ Dr Moliner 50, E-46100 Burjasot (València), Spain
Telephone: +34 96 398 3112 Fax: +34 96 398 3385 Email: jose.moreno@uv.es

[3]ESA Scientific Campaign Unit, ESTEC
Keplerlaan 1, 2200 AG Noordwijk, The Netherlands
Telephone: +31 71 565 4818 Fax: +31 71 565 5675 Email: patrick.wursteisen@esa.int

ABSTRACT

Presented below are a number of observations that came out of a study performed within the framework of the DAISEX project (Digital Airborne Spectrometer Experiment). The study assesses the potential of spaceborne SAR to compliment hyperspectral data in the measurement of surface characteristics, providing important indicators of geophysical variables related to biogenic processes.

For an agricultural test site located at Barrax in Southeast Spain, a series of six ERS SLCI SAR images covering the growing season of 1999 have been acquired. Amongst them is a tandem pair that coincides with the airborne campaign and synchronous ground survey constituting the core of the DAISEX dataset, thus enabling direct comparison and synergistic assessment. Evaluation is based on the ability to identify crop types, to isolate variations in SAR data that are not apparent in other imagery and to attribute these to geophysical variations. The standard ERS Interferometric Land Use product (ILU) proved to be the most useful SAR derivative for analysis.

Whilst resolution and clarity compare unfavourably with airborne optical data, spaceborne radar demonstrates advantages of texture and moisture sensitivity sufficient to distinguish crops and identify within-field variation. The multi-temporal capacity of ERS, particularly during the tandem mission, is its greatest asset, enabling observation of dynamic change, particularly related to irrigation practices.

INTRODUCTION

For three consecutive years, the European Space Agency has conducted scientific campaigns to investigate the feasibility of quantitatively retrieving geo- and biophysical variables as the requisite inputs for process models of the biosphere and geosphere. As such, the Digital AIrborne Spectrometer EXperiments (DAISEX-98, -99, -00) utilised a variety of airborne sensors, including DAIS 7915, HyMap, ROSIS, POLDER and LEANDRE. Investigators from Universities in Spain, France, Germany, Switzerland and Italy were involved in the project, working at three European test sites.

The main scientific objective of DAISEX-99 was "to demonstrate the retrieval of geophysical variables from imaging spectrometer data." Target variables included surface temperature, canopy parameters related to biomass, structure (including LAI) and water content and soil properties such as moisture. Their quantification will allow greater understanding of biogenic processes such as productivity, evapotranspiration and nutrient cycles. Airborne measurements acquired from two simultaneously operated hyperspectral instruments focused on key surface characteristics including albedo, fPAR and temperature, which relate to such geophysical variables. These and other indicators were also measured directly on the ground to enable a full programme of intercomparison (ESA Scientific Campaign Unit, 1999).

This paper is concerned with the potential of spaceborne synthetic aperture radar (SAR) to compliment hyperspectral data in the analysis of some of these indicators. The nature of radar makes it sensitive to surface texture, moisture and the structure of volume scatterers, and thus well suited to this application.

Proc. 3rd International Symposium, 'Retrieval of Bio- and Geophysical Parameters from SAR Data for Land Applications', Sheffield, UK, 11-14 September 2001 (ESA SP-475, January 2002)

INTERFEROMETRIC LAND USE PRODUCT

ILU is a standard ERS product processed from a tandem pair of single-look complex data (SLCI). It exploits the capability of interferometric coherence for bio- and geophysical parameter retrieval in the context of land applications (Walker et al., 1998). In its most familiar form, the product is a false colour composite comprising the following channels:

Red =	interferometric coherence
Green =	average backscatter intensity
Blue =	intensity difference
or	magnitude of intensity change

The resultant display (stretched to fill the 24-bit colour cube) discriminates heavily vegetated surfaces, bare land, cropped agricultural fields and urban centres.

DATA AND TEST SITE

This study is focused on one of the DAISEX test sites, located near Barrax in Southeast Spain (inset, figure 1). The area is very flat and characterised by pivot-irrigated agriculture. An intensive campaign of measurement took place during the first week of June 1999, including ground survey and airborne observation using the HyMap and DAIS sensors. An ERS Tandem overpass on 2 and 3 June 1999 coincided perfectly with these acquisitions.

In total, six ERS SAR SLCI images of the test site during the growing season of 1999 were available for processing, including a second tandem pair acquired in September. These are summarised in table 1. Note that most scenes were acquired on ascending orbits that pass over the test site at approximately 2225hrs. Whilst the period of the first tandem pair brackets the airborne mission (which took place at 1400hrs on 3 June), it is important to consider that individual acquisitions do not coincide exactly. Also, some geophysical measurements taken during the daytime would vary significantly after dark.

Date	Satellite	Orbit	
June 2	ERS1	ascending	(track 144; frame 765-783)
June 3	ERS2	ascending	perpendicular baseline = 72m
June 29	ERS2	descending	(track 8; frame 2817)
July 8	ERS2	ascending	
Sept 15	ERS1	ascending	
Sept 16	ERS2	ascending	perpendicular baseline = 233m

Table 1: ERS SAR data set for the Barrax test site.

Calibrated intensity images (backscatter coefficient, σ^0 in dB) and coherence products were generated using the ERS SAR Toolbox and subsequently converted to ground range and georeferenced to the Spanish digital cadastre.

DISCRIMINATING LAND COVER

Comparison of the ILU product generated from data acquired on the 2 and 3 June (figure 1) with hyperspectral imagery from the HYMAP airborne sensor, flown on 3 June, (figure 2) at once demonstrates their complimentarity. The textural and spectral variations across the scenes expose quite different patterns; the remainder of this paper investigates whether the patterns in the ILU are of any significance.

Given an understanding of radar and interferometric principles, a logical interpretation of the ILU product can be made based on the additive colour system. For example, bare soil would be expected to have high coherence over 24 hours (red gun), a moderate backscatter coefficient (dependent on roughness) (green gun) and little backscatter change (blue gun), giving an orange signature. Lush vegetation would have low coherence and moderate to high backscatter with random change, giving a blue-green signature.

The crops growing in individual fields were recorded at the time of the ground survey. Preliminary qualitative assessment of dominant ILU signatures over entire fields reveals that there is overall consistency within crop types, particularly barley, wheat and alfalfa, as seen in figure 1. This is encouraging, since areas of the same crop are assumed to be *texturally* uniform. It provides a backdrop against which within-field variation can be analysed.

Figure 3 shows the location in feature space of selected crops. Green, leafy crops (alfalfa and beet) are separated from thin-stemmed cereals and bare soil along the coherence axis. This is a reflection of the density of vegetation cover and the proportion of radar energy allowed to penetrate to the soil surface. The cereal crops merge on both axes because of their similar physical appearance.

The ILU product exposes a number of interesting within-field features that are not apparent in the hyperspectral data but which may be a result of geophysical variations. In particular, the corn fields exhibit variation between bluey-pink and yellow-orange hues (see figure 1). Although the variation is marked in the image (particularly in field SV3, emboldened in figure 1), it is disappointing that no trend was found in any of the ground data (plant weight/moisture/dry matter, LAI, soil weight/moisture or chlorophyll levels) to account for it.

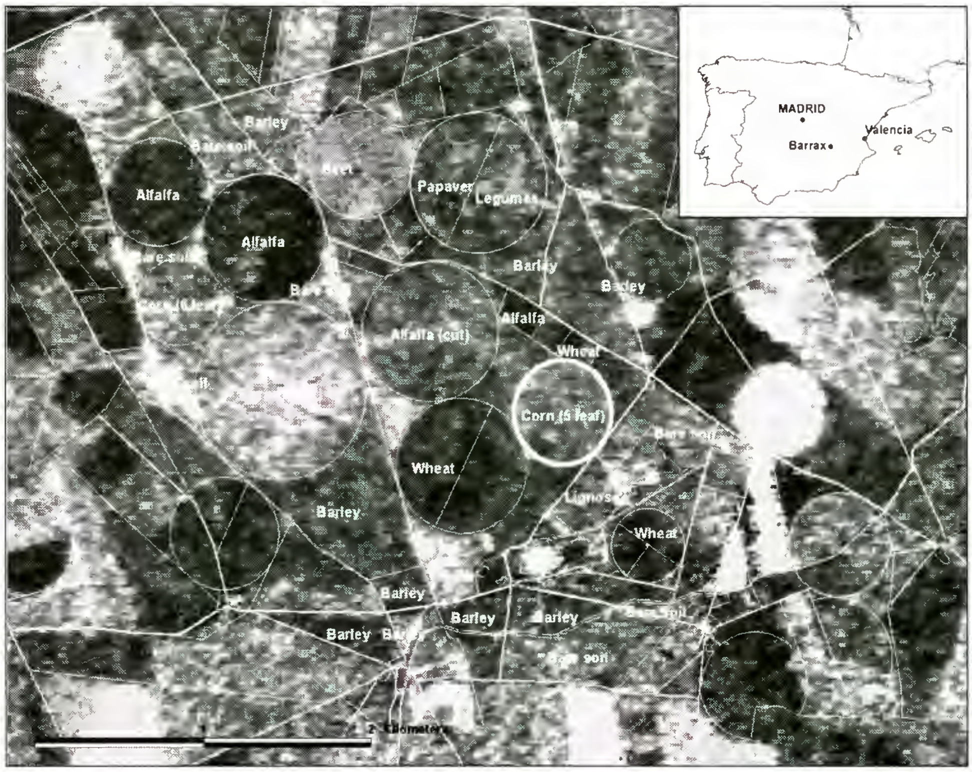

Figure 1: ILU product of the Barrax test site on 2-3 June 1999 overlaid with digital cadastre and crop type information. There is considerable colour variation indicating high information content. Despite the speckle, some individual fields are clearly discernable by virtue of their dominant tones and distinct edges. Note that fields of barley (2 distinct groups), wheat and alfalfa have unique but consistent hues.

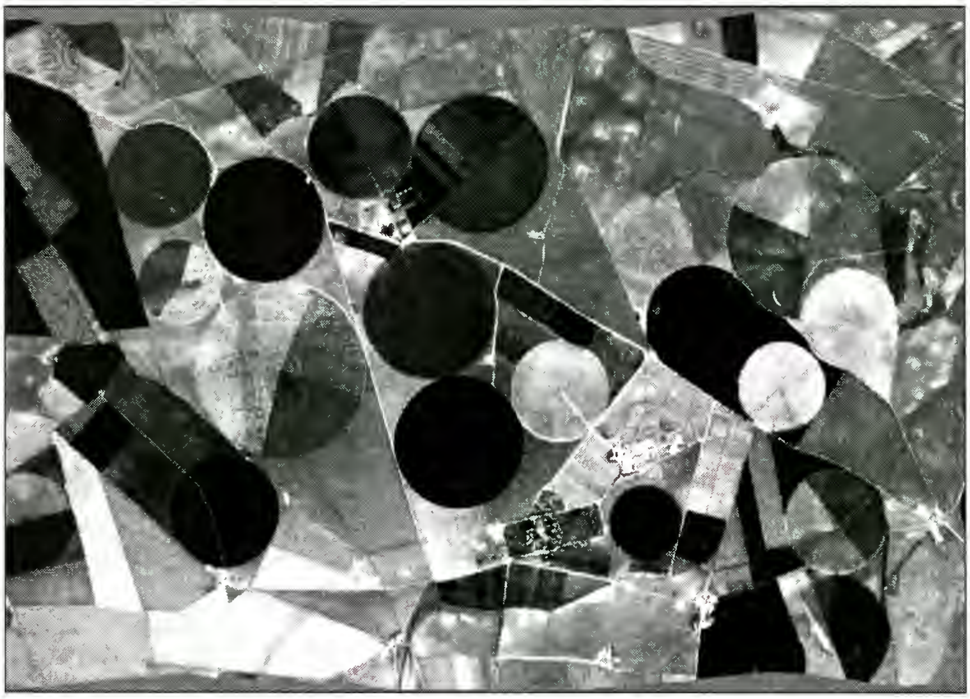

Figure 2: Colour composite of HYMAP data (bands 3, 9 and 19 in RGB) for comparison with figure 1. There is a significant improvement in resolution (inevitable in a comparison of air- and spaceborne data). However, it is immediately clear that variation between and within fields that is not seen in this image can be observed in the ILU and vice versa.

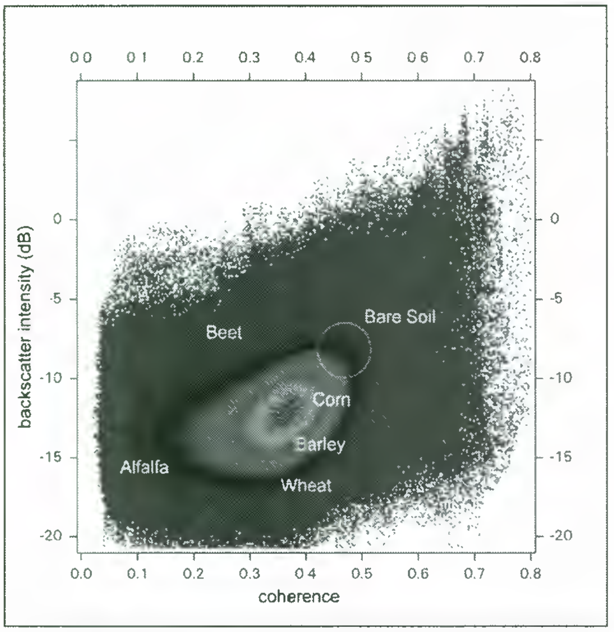

Figure 3: Feature space plot of interferometric coherence between 2 and 3 June against calibrated backscatter intensity on 3 June for the Barrax test site. Hue denotes point density; ellipses indicate typical crop signature means. The data is well spread throughout feature space in this plane, but note that coherence does not exceed 0.809 anywhere in the scene, probably due to thermal and spatial losses.

OBSERVING DYNAMIC CHANGE

So far, only the coherence and backscatter elements of the ILU (red and green channels) have been considered. The blue channel is coded with backscatter difference, calculated between the same two images used to compute coherence. There are two ways to derive this indicator:

$$\sigma^o_{diff} = \sigma^o_{latter} - \sigma^o_{former}$$

$$\sigma^o_{change} = \left|\sigma^o_{latter} - \sigma^o_{former}\right|$$

The first (backscatter *difference*, dB) shows stable areas ($\sigma^o_{diff} = 0$) as mid greys with positive and negative changes between the dates as bright and dark tones respectively. The second (backscatter *change*, dB) returns the magnitude of change such that stable areas ($\sigma^o_{change} = 0$) are dark and the greatest changes, positive or negative, appear bright. Selection depends on the objectives of the study.

Closer inspection of the individual components of the June ILU reveal that within-field variation noted earlier is exclusively present in the blue channel. This implies some sort of physical change in surface characteristics between the night of 2 June and the night of 3 June,

Figure 4: ILU product of 15-16 September 1999 overlaid with digital cadastre and crop type information (June 1999). There is much less variation between fields because many crops have reached a similar state of dryness or been harvested to leave bare soil. It is only possible to identify corn (no within-field variation now) and alfalfa as growing crops.

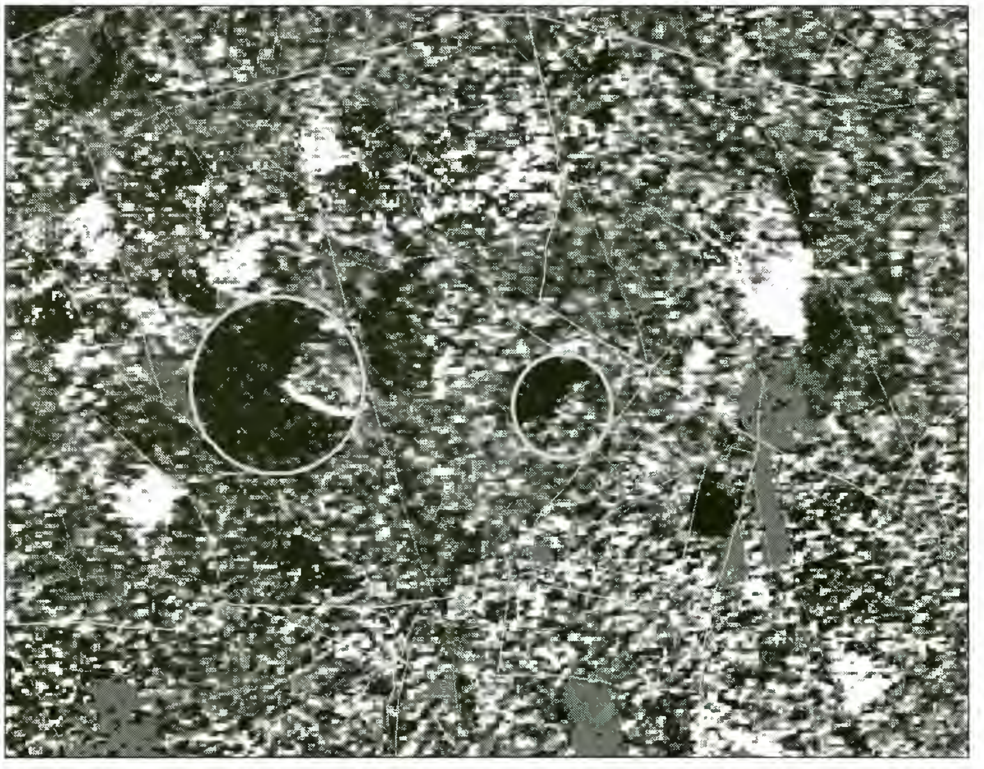

Figure 5: Backscatter difference between 2 and 3 June. The highlighted fields (both containing corn, cf. figure 1) exhibit dark features that indicate a reduction in backscatter. Homogeneous grey regions represent areas that are saturated in both images and therefore exhibit no change (0dB).

which could be man-induced or caused by a meteorological effect.

It is most probable that such a change is related to the dielectric constant, which varies with soil moisture in the soil and plant cover. Because of the Mediterranean climate, irrigation takes place mainly at night for greater efficiency. An area that is wet from recent irrigation will have higher backscatter than surrounding dry areas with the same cover and, therefore, appear brighter in a radar image. Assuming the land has dried by the following night and no more irrigation takes place, a reduction in backscatter would be observed. Similarly, an area irrigated on the second night would have increased backscatter. Both features highlighted in Figure 5 have a radial pattern focused on the field centre. This would be consistent with the operation of a pivot irrigation system. Furthermore, in the larger field, a bright spoke may represent the irrigation boom itself on the 3 June.

Consultation of irrigation records kept for the duration of the growing season confirms that the smaller corn field was indeed irrigated on 2 June, as were several other fields where reduced backscatter is observed. Over the rest of the scene, outside the area for which records are available, many other fields contain dark or light toned areas that are likely to correspond to similar irrigation activity shortly before 2225hrs on one of the nights in question.

CONCLUSIONS

Whilst resolution and clarity compare unfavourably with airborne optical data, spaceborne radar demonstrates advantages of texture and moisture sensitivity sufficient to highlight within-field variation. The standard ILU product generated from ERS SAR data emphasises vegetation properties to discriminate certain crop types, primarily on the basis of crop structure, but in this case there is insufficient correlation between satellite-derived data and ground-based measurements to suggest links with specific geophysical variables.

The multi-temporal capacity of ERS, particularly during the tandem mission, is its greatest asset, enabling observation of dynamic change within the scene over the period of the acquisition. In an area characterised by pivot irrigation, changes in backscatter are most likely to reflect the artificially fluctuating soil moisture in this otherwise semi-arid environment.

ERS SAR provides a worthwhile addition to the DAISEX-99 dataset, complementing the information content of hyperspectral imagery and broadening the range of remotely retrieved indicators. In addition, these observations demonstrate the potential of frequent-repeat SAR imagery for wider irrigation monitoring.

ACKNOWLEDGEMENT

The authors wish to thank the Universtiy of Castilla La Mancha for the provision of Spanish digital cadastre data.

REFERENCES

ESA Scientific Campaign Unit (1999) *DAISEX-99 Experimenters Handbook*, ESTEC

Walker, N, Mica, S and Laur, H (1998) The ERS Interferometric Quick Look Processor: a powerful system to assess and exploit the ERS Tandem archive for land use information retrieval, *Proc. 2nd International Workshop on Retrieval of Bio- and Geo-physical Parameters from SAR Data for Land Applications*, 21-23 October, ESA SP-441, pp 579-583

COMPARISON OF HYMAP / E-SAR DATA WITH MODELS FOR OPTICAL REFLECTANCE AND MICROWAVE SCATTERING FROM VEGETATION CANOPIES

P. Saich[1], P. Lewis[1], M. Disney[2] and G. Thackrah[1]
[1]*Department of Geography, University College London, 26 Bedford Way, London WC1H 0AP, UK, tel +44-20-7679-4282, fax: +44-20-7679-4293,*
[2]*Department of Geography, Birkbeck College, London*
email: psaich@geog.ucl.ac.uk / plewis@geog.ucl.ac.uk

ABSTRACT

We present the results of combined modelling of optical and radar signatures of cereal canopies. An optical model based on Monte Carlo ray tracing simulations of scattering behaviour in the vegetation canopy is used to simulate spectral reflectance, and a coherent microwave scattering model is used to simulate multi-frequency polarimetric microwave signatures. These use similar descriptions of the vegetation structure, and therefore provide a link between the two regimes. During the "SAR-Hyperspectral Airborne Campaign" (SHAC), conducted in the UK during summer 2000, datasets were acquired using the E-SAR and Hymap. Coincident with the E-SAR overflights, a ground measurement campaign was conducted, to characterise the moisture status of the vegetation, soil and the leaf area index (LAI), as well as more detailed measurements of the vegetation properties. We discuss the comparison between model simulations and the observed signatures, and highlight aspects of the link provided by the structural vegetation canopy model.

INTRODUCTION

Recent attempts at retrieving vegetation canopy characteristics from remote sensing data have focussed on the development of physically-based algorithms. Historically, however, the optical and microwave communities have tackled these problems separately. In this paper, we describe our first attempts at the parallel simulation of optical reflectance and microwave backscattering signatures of cereal canopies. The optical model is based on Monte Carlo simulations of ray-tracing in the vegetation canopy. The microwave model is based on a coherent summation of scattering from the vegetation elements (leaves and stems) in a simulation cell. Whilst these models are independent, they are both intended to make use of the same description of the vegetation architecture. We are therefore able to show how changes in the state of the vegetation canopy impact on both optical and microwave measurements, and how to combine such measurements more effectively.

In the following sections we discuss the various datasets and present preliminary analysis of optical and microwave scattering behaviour of the canopy. We describe a model for the three-dimensional structure of wheat, and then present the microwave and optical modelling techniques. The microwave model uses a degraded representation of the wheat canopy, and we highlight the importance of improving this description by comparing model simulations with the experimental data. We then show the comparisons of modelled optical reflectance and the observed data.

DATASETS

Airborne remote sensing data were acquired during summer 2000 at Barton Bendish, UK, as part of the "SAR-Hyperspectral Airborne Campaign" (SHAC). Barton Bendish is an agricultural site that is currently being used as a core validation site for EOS MODIS. During SHAC, the DLR E-SAR imaged the site on 2 June, acquiring data in X- (HH and VV), C- (VV and VH) and L- (HH, VV and HV) bands with a range of polarisation combinations. The 4-look products have a spatial resolution of approximately 4m x 2.5m (range x azimuth) and the site is imaged at a range of incident angles between ~40°-60°. For the analysis shown here, field-averaged backscattering coefficients are used. An example of the image data is shown in Figure 1.

On 17th June, images were also acquired with the Hymap. An example is shown in Figure 2. The measured reflectance data comprise 126 bands (437-2486 nm) of spectral reflectance derived as field averages of 4m resolution data. Five Hymap images were used, flown as slightly overlapping flightlines in a North-South direction. As each image has a cross-track view zenith angle variation of +/- 30°, some fields at the site are sampled at multple view angles. The Solar angles at the time of the overflights were around 60° elevation, 171° azimuth, varying slightly for each flightline. Geometric correction of the data was carried out using flightpath information provided with the data to a high degree of accuracy. Atmospheric correction was performed using ATREM. Masks were generated for each of the 50 field samples in the data and viewing angle and reflectance data statistics extracted.

Coincident with the E-SAR overflights, a ground measurement campaign was conducted, to characterise

Proc. 3rd International Symposium, 'Retrieval of Bio- and Geophysical Parameters from SAR Data for Land Applications', Sheffield, UK, 11-14 September 2001 (ESA SP-475, January 2002)

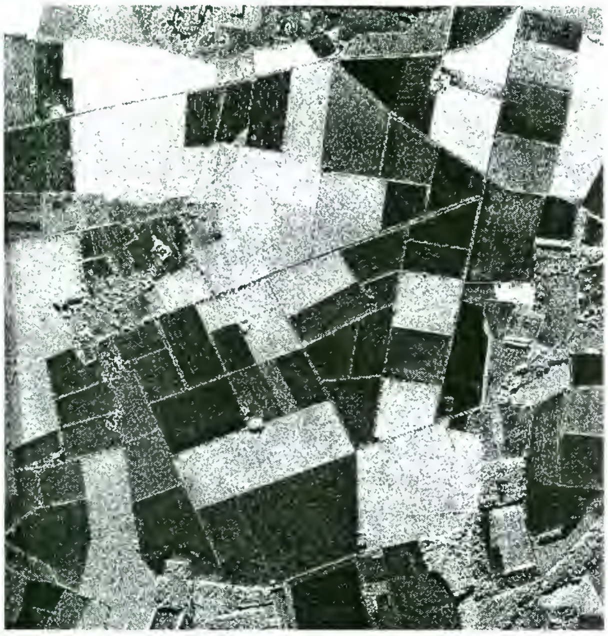

Figure 1: E-SAR

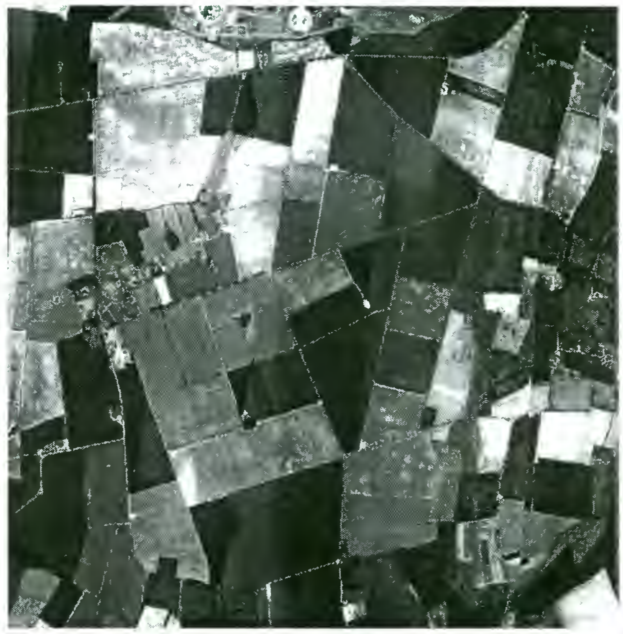

Figure 2: Hymap

the moisture status of the vegetation, soil and the leaf area index (LAI), as well as detailed measurements of the vegetation properties (such as crop height, stem and leaf size, and stem and leaf density, etc).

VEGETATION MODEL

A 'mean' geometric model of a wheat plant was generated within the Botanical Plant Modelling System (Lewis, 1999), based on field measurements of leaf length, leaf numbers and plant height. Additional information on leaf angles and internode distances was inferred from field photographs. Tiller number was inferred from stem density and measured plant densities. Statistics were generated on mean and standard deviation of the geometric parameters, and a set of five distinct plants generated by randomising over these distributions. Soil reflectance was simulated using the basis functions of Price (1990), with leaf reflectance and transmittance derived from the PROSPECT-REDUX model of Jaquemoud et al. (1996) using estimated chlorophyll content, leaf structure and water content parameters (40 ug/cm2, 2, and 0.035 cm, respectively). Stem reflectance was assumed equal to leaf reflectance. Head reflectrance was estimated using the same PROSPECT-REDUX model parameters as for the stem, but with a structural parameter of 10, representing an optically thick scattering medium.

Figure 3(a): Side view

Figure 3(b): Top view

Figure 3(c): Field photograph

MICROWAVE SCATTERING

Most approaches for modelling microwave signatures are based upon radiative transfer (Touré et al 1994, Cookmartin et al 2000, Saich and Borgeaud 2000, Macelloni et al 2001). Here we use a coherent scattering model called CASM which is similar to that described by Lin and Sarabandi (1999). The model adds up the complex scattering amplitudes of the elements within a simulation cell, weighting each by a term relating to the phase change for the propagation paths. For example, direct backscattering from the canopy, requires

$$\overline{F} = \sum_{p=1}^{p=N} \overline{T}^{(+p)} \overline{f}^{(p)} \overline{T}^{(-p)}, \qquad (1)$$

where f is the complex scattering amplitude (for either finite length cylinders or thin elliptical plane discs), T is the matrix of complex propagation terms, and the summation is over all N particles in the cell. To calculate backscattering coefficients, we average the intensity over a number of independent cells

$$\sigma_{\alpha\beta\gamma\delta} = \frac{4\pi}{A} < \overline{F}.\overline{F}^* > . \qquad (2)$$

where A is the area of the cell. The indices on the backscattering coefficient reflect the polarimetric nature of the total scattering matrix F in (1). As the model works with electric field rather than intensity, it also allows for prediction of interferometric signatures (though we do not show these here). As well as direct scattering from the vegetation canopy, the propagation paths in these simulations include double-bounce scattering events between vegetation and the ground. The underlying ground surface is treated as a smooth reflecting surface and direct backscattering is not included (in part because the datasets shown here always have incident angle greater than ~40°). The calculation of the phase change on each propagation path exploits the idea of an effective medium (and uses the Foldy approximation to calculate the propagation constant as a function of depth in the medium). As such, the model is based on horizontal layering of the vegetation canopy only insofar as the extinction is concerned. In the simulations shown here, the structure of the vegetation is degraded somewhat from the detailed model described above. The canopy is considered to consist of approximately vertical stems (to within 20°), each of which has a wheat head attached to the end of the stem, an associated flag leaf, and a set of thin elliptical discs representing other leaves. The leaves are assumed to have random orientations with the disc axis in the range 30°-90°; the flag leaves are principally vertical (normal axis in the range 60°-90°). We return to the importance of having degraded the detailed 3-d model in the discussion.

In Figures 4(a)-(c) we show the simulation results at L-, C- and X-bands, for the coherent solution generated by the model described above. The model input data re those that were measured for one of the wheat fields (and these are assumed representative of all of the fields). Each of the simulations assumes a 1m x 1m cell with appropriate numbers of stems and leaves to match the in-situ data. In the figures, we also show the field-averaged backscattering coefficients for wheat fields in the image data. The error bars on the predictions are one standard deviation, and represent uncertainties associated with variations in the model input parameters for the vegetation (derived from the in-situ measurements). It is worth pointing out that the error bars have been derived from the incoherent (radiative transfer) solutions - the coherent solution also has superimposed on it an additional variation (with a standard deviation in intensity ~ mean) originating from the coherent addition.

It is clear that whilst some cases match the experimental data, other model predictions are rather poor. Principal amongst these are (i) cross-polarisation overestimation at L-band, (ii) underestimation of both VV and cross-polarisation at C-band. Though we do not show the contributions to the signatures here, the VV powers in C- and X-bands are strongly dominated by the vegetation canopy (even more so than the cross-polarisation at C-band). The origin of this is not that the canopy is a strong scatterer for C-VV (because it underestimates the observed data) but rather that the vertically-oriented stems and heads are strong attenuators. Interestingly, the model predictions fit the observed data much more closely if we 'artificially lower' the extinction caused by the heads. This is shown in Figures 5(a)-(c). The latter two of these show that when the heads are excluded or when we reduce their size (both of which lower the extinction) the C- and X-VV powers are increased. Their extinction properties are the dominating effect and it is possible that these are being over-estimated. There is evidence from ground-based experiments (RADWHEAT 2001) that this also applies to the cylindrical stems from C-band measurements, though it is not clear from these datasets.

OPTICAL REFLECTANCE

Canopy spectral reflectance was simulated for the five plants described, for the viewing and illumination angles of the HYMAP wheat field samples. A field of plants was simulated at the required plant density and row spacing by 'cloning' (creating virtual copies) of the five different wheat plants. A random azimuthal rotation was applied to each cloned plant. The radiometric simulation was conducted using a modified

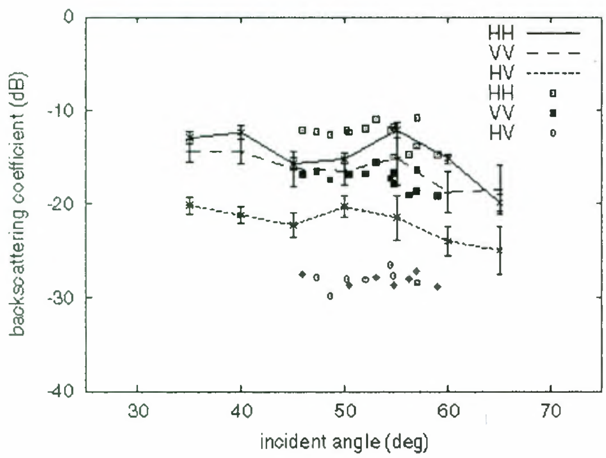

Figure 4(a): Simulation results compared with measured L-band (HH, VV and HV) data

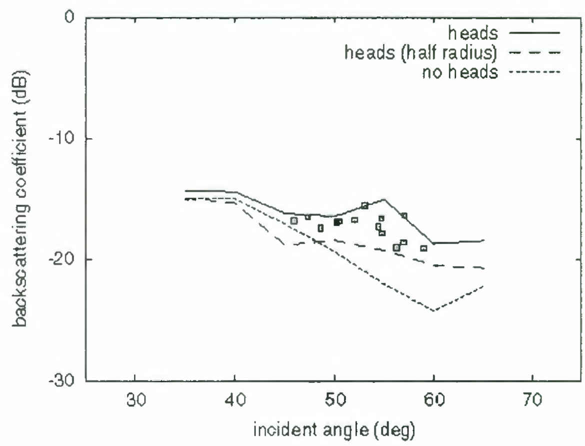

Figure 5(a): Simulation results for L-VV with different upper canopy structures

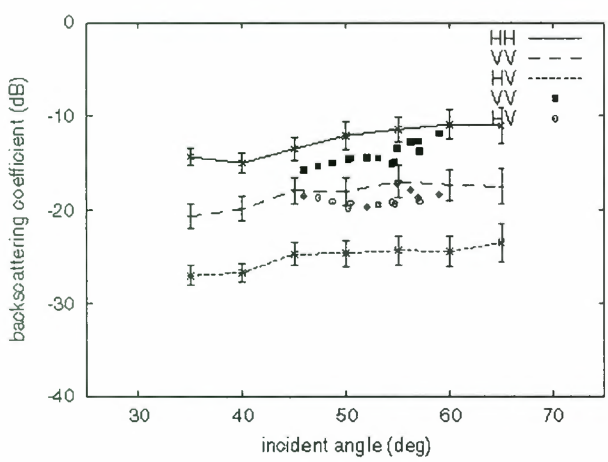

Figure 4(b): Simulation results compared with measured C-band (VV and HV) data

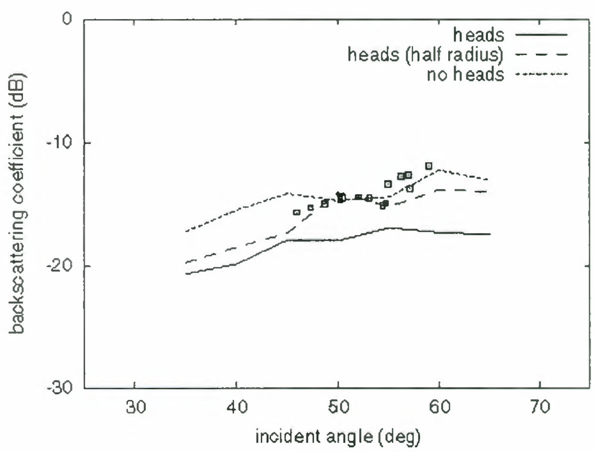

Figure 5(b): Simulation results for C-VV with different upper canopy structures

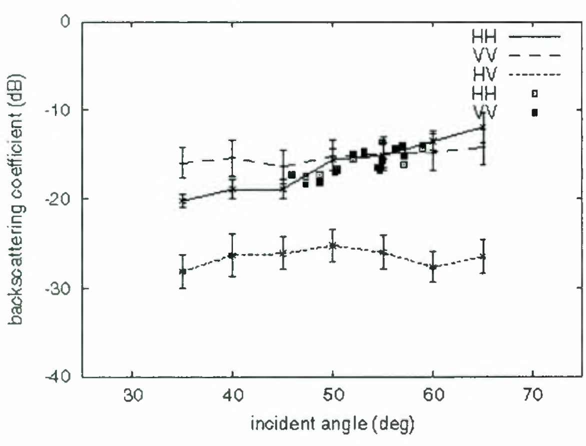

Figure 4(c): Simulation results compared with measured X-band (HH and VV) data

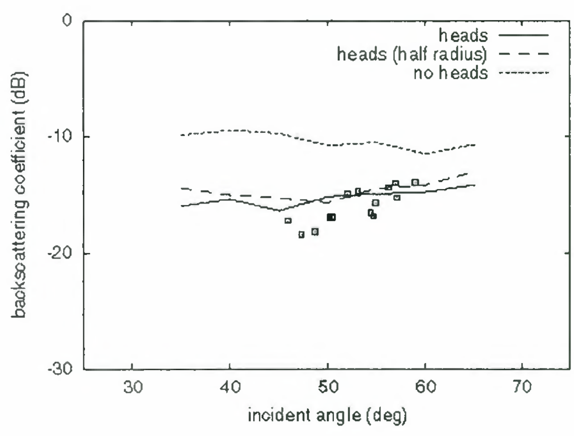

Figure 5(c): Simulation results for X-VV with different upper canopy structures modifications to ARARAT, which differentiate it from the original model described in Lewis (1999) is that only single 'ray paths' (Markov chains) are sampled for diffuse sampling for each primary ray of the simulation, allowing much more rapid calculation of multiple scattering. The original model used a branching sampling scheme for multiple diffuse scattering, sampling both reflectance and transmittance fields for each object intersected. The illumination field was simulated using the sky radiance model of Zibordi and Voss (1989) using standard mid-latidude atmospheric parameters.

Three versions of each canopy were simulated for each viewing/illumination angle scenario to investigate the role of scattering from the seed heads. These were: the 'full' canopy model described above; a representation with totally absorbing ('black') seed heads; and a geometric representation with the seed heads removed.

Figure 6 shows a typical example of the measured and simulated spectral reflectance data, for field 319. The overall shape of the reflectance spectrum is similar for all simulations and follows the main feaatures of the measured data. This is a reflection of the plant element scattering properties shown in figure 3. Spectral features in low reflectance regions such as at visible wavelengths and after 1400 nm match the plant element scattering features directly. Features in the higher scattering region of the near infrared become more exaggerated, due to multiple scattering effects. Whilst the spectral features of the simulation seem good, the magnitude of the 'full' simulation (with seed heads) is only around 60% of the measured spectrum.

Comparing Figures 3(b) and 3(c) suggests a possible reason for this lack of correspondence: even though the seed heads have a high reflectance assigned to them (figure 3(b)), they appear 'darker' than the leaves in figure 3(a), whereas figure 3(c) shows them to be brighter than the leaves, at least at visible wavelengths. The reason for this is the Lambertian shading of the geometric objects used to represent the seed heads (a cylinder capped by two spheres): a Lambertian cylinder viewed with an illumination angle at 90° to the viewing azimuth direction has a very low reflectance. In addition, around 50% of the viewed cylinder will be in cast shadow. For the simulations conducted here, around 8% of the area directly viewed by the sensor is 'sunlit' seed heads, with a similar or greater amount being shadowed seed head. A typical value for the leaves is 20-30% sunlit leaf, 40-50% shadowed leaf. The total projected proportions for the geometric model therefore seem reasonable, and the seed head reflectance is high, so the problem lies in the Lambertian assumption for scattering from the seed head cylinder.

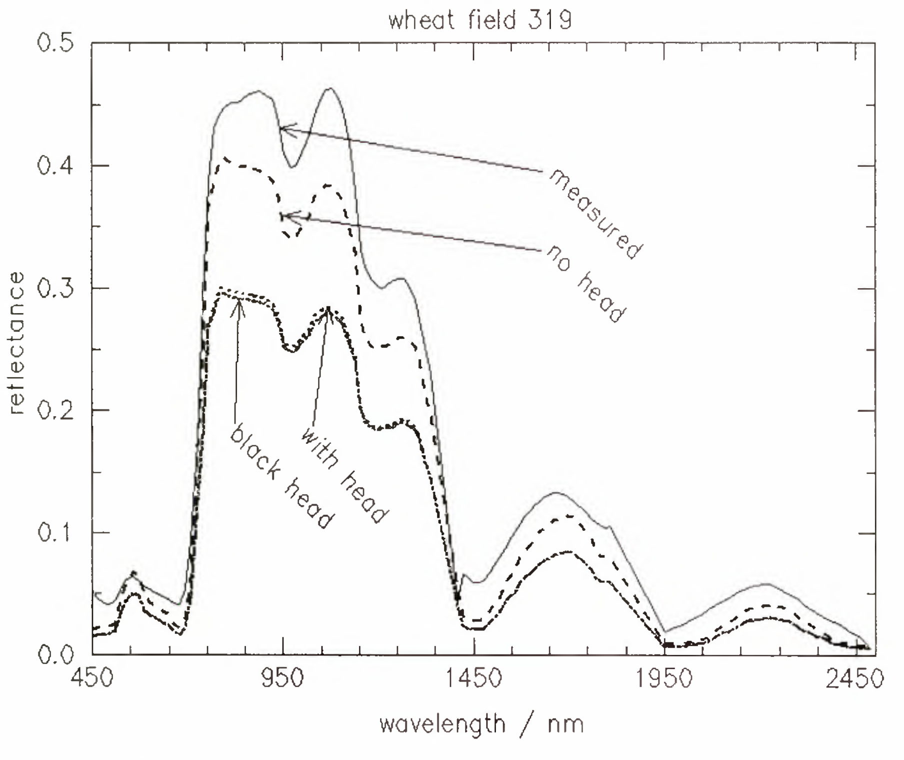

Figure 6: Simulated and measured reflectance data (WW field 319)

This is further demonstrated in figure 6, which shows the results of simulations using a canopy with no seed heads and one for which the seed heads are totally absorbing. The simulated reflectance for this latter case is only marginally lower than the case for a very bright seed head reflectance function, demonstrating the very low scattering phase function value for a Lambertian cylinder at this angular configuration.

DISCUSSION

We have shown that there can be a close relationship between the descriptions of vegetation canopies used by theoretical microwave and optical models, and seen explicitly that a detailed architectural model for wheat can easily be used to drive an optical reflectance model. Whilst the structural information from the vegetation model can be exploited, problems remain in the determination of appropriate phase functions (for example, for the cereal heads). In the microwave context, both aspects require further work. On the one hand it is important to improve the spatial description of the vegetation, in particular to use a correct representation of leaf curvature. Whilst such models exist (Stiles and Sarabandi 2000), they need to be validated in more general conditions (particularly under different incident angles, polarisations and wavelengths) and in view of the difficulty of gaining adequate air- and spaceborne datasets, such validation is likely to come through lab-based experiments. In addition, the possible overestimation of extinction properties of cylinders in these canopies, especially where they are in the near-field of one another and are oriented in similar directions, requires further investigation.

ACKNOWLEDGEMENTS

This work has been partly conducted under funding from the European Space Agency under contract 14940, and we would like to thank Dr. M. Borgeaud for his support. Some of the field data were collected by Paul Hobson and Jo Shaw (University of Wales Swansea) under NERC Grant GR3/11639. We would also like to thank the organisers of the SAR-Hyperspectral Airborne Campaign.

REFERENCES

Cookmartin, G., Saich, P., Quegan, S., Cordey, R. Burgess-Allen, P. and Sowter, A. (2000): Modeling Microwave Interactions with Crops and Comparison with ERS-2 SAR Observations, *IEEE Trans. Geoscience and Remote Sensing*, vol. 38, no. 2, pp 658-670.

Jacquemoud S, Ustin SL, Verdebout J, Schmuck G, Andreoli G, Hosgood B (1996): Estimating leaf biochemistry using the PROSPECT leaf optical properties model, *Remote Sensing of Environment*, vol. 56, no. 3, 194-202

Lewis, P. (1999): Three-dimensional plant modelling for remote sensing simulation studies using the Botanical Plant Modelling System. *Agronomie: Agriculture and Environment* Vol.19, No.3-4, pp.185-210

Lin, Y.C. and Sarabandi, K. (1999): A Monte Carlo Coherent Scattering Model for Forest Canopies using Fractal Generated Trees, *IEEE Trans. Geosci. & Remote Sensing*, vol. 37, 440-451.

Macelloni, G., Paloscia, S., Pampaloni, P., Marliani, F and Gai, M. (2001): The Relationship Between the Backscattering Coefficient and the Biomass of Narrow and Broad Leaf Crops, *IEEE Trans. Geosci. & Remote Sensing*, vol. 39, 873-884.

Price, J. (1990): On the information content of soil reflectance spectra, *Rem. Sens. Environ.*, vol. 33, 113-121.

RADWHEAT consortium (2001): *Advanced radar for measuring green area index (GAI), biomass and shoot numbers in wheat,* Final Report to BNSC LINK project R4/025.

Saich, P. and Borgeaud, M. (2000): Interpreting ERS SAR Signatures of Agricultural Crops in Flevoland, 1993-1996, *IEEE Trans. Geoscience & Remote Sensing*, vol. 38, no. 2, pp 651-657.

Stiles, J. and Sarabandi, K. (2000): Electromagnetic scattering from grassland - Part I: A fully phase-coherent scattering model, *IEEE Trans. Geoscience & Remote Sensing*, vol. 38, no. 1, 339-348.

Touré, A., Thomson, K.P.B., Edwards, G., Brown, R.J. and Brisco, B. (1994): Adaptation of the Mimics Backscattering Model to the Agricultural Context: Wheat and Canola Cases at L and C Bands, *IEEE Trans. Geosci. & Remote Sensing*, vol. 32, 47-61.

Zibordi, G. and Voss, K.J, (1989): Geometrical and Spectral Sky Radiance: Comparison between Simulations and Field Measurements, *Rem. Sens. Environ.*, vol. 27, 343-358

MERGING UNMIXED LANDSAT TM DATA IN A SEMI-EMPIRICAL SAR MODEL FOR THE ASSESSMENT OF HERBACEOUS VEGETATION BIOMASS IN A HETEROGENEOUS ENVIRONMENT

T. Svoray and M. Shoshany

Ben-Gurion University of the Negev, Department of Geography and Environmental Development, Department of Information Systems Engineering, Beer-Sheva 84105, Israel;
tsvoray@bgumail.bgu.ac.il
Bar-Ilan University, Geography Department, Ramat-Gan 52900, Israel;
m_shoshany@hotmail.com

ABSTRACT

In this paper we suggest a remote sensing methodology for herbaceous Areal Aboveground Biomass (AAB) estimations in the heterogeneous Mediterranean system. The methodology developed is based on a modification of the water-cloud model to the conditions of mixed environments including shrub, dwarf shrub and herb formations. The use of the Green leaf biomass Volumetric Density (GVD) as a canopy descriptor and the use of soil and vegetation fractions from Landsat TM data facilitated improvements in the application of the water-cloud model to the study area and enabled successful reproduction of the backscatter from the Mediterranean vegetation formations and the derivation of AAB values of herbaceous vegetation. The model was applied to the entire image domain and the AAB layers achieved prove capable of representing spatio-temporal patterns of changing AAB. Based on these results, the methodology provided in this paper lays a basis for the derivation of important and more advanced ecological and range management parameters, such as primary production, carrying capacity and dominance in the areal domain. The use of satellite images for quantitative mapping of these parameters may contribute significantly to our understanding of Mediterranean to semi-arid ecosystems and could provide an efficient tool for rangeland planners and decision makers.

INTRODUCTION

AAB of herbaceous vegetation represents one of the prime factors in determining functions of the ecosystem in semi-arid and Mediterranean regions. It constitutes a natural resource that influences substantially the sustainability of rural and nomadic societies of the desert fringe. Mapping of herbaceous vegetation AAB in heterogeneous environments has attracted considerable attention within the scientific community; but neither remote sensing methodology nor field techniques have succeeded in doing so fully. The aim of this paper is to suggest a remote sensing methodology for herbaceous AAB estimations in the heterogeneous Mediterranean environment.

STUDY AREA

The study area is a semi-arid phyto-geographical zone along a rainfall gradient with annual average between 450 mm and 250 mm, located in the central of Israel along the eastern coast of the Mediterranean basin. The dominant rock formation is mostly chalk with patches of Calcrete and the dominant soil is Brown Rendzina (Haploxerolls). Vegetation in this area varies from shrublands and garigue (dominated by *Quercus calliprinos* and *Phillyrea latifolia*), through dwarf shrubs (dominated by *Sarcopoterium spinosum*) to open areas with diverse grasslands vegetation (dominated by *Gramineae*). The spatial patterns represent wide range of transitional stages between areas of high homogeneity of mainly tall shrubs and grasslands with different compositions of the three vegetation formations. This diversity of patterns is a result of a long history (since the late bronze, approximately 5500 years ago) of human activity. Land use in this area is composed of agricultural crops in the wadi's and rangelands with controlled grazing pressures. The study area is characterized by wide range of "regeneration and degradation patterns" of patches representing various soil-vegetation relationships which will allow generalization of the methods to wider areas of transition between Mediterranean and arid regions.

METHODOLOGY

The methodology developed here is based on a modification of the well-known water-cloud backscattering model (Attema & Ulaby 1978) for its adaptation to the heterogeneous conditions of semi-arid and Mediterranean regions. A general form of the water-cloud model is expressed in equation 1:

$$\sigma^0 = A\cos\theta(1-\exp(-2BL/\cos\theta))+(C+D*VSM)\exp(-2BL/\cos\theta) \quad (1)$$

where θ represents radar radiation incidence angle; VSM is the volumetric soil moisture; L is some kind of

Proc. 3rd International Symposium, 'Retrieval of Bio- and Geophysical Parameters from SAR Data for Land Applications', Sheffield, UK. 11-14 September 2001 (ESA SP-475, January 2002)

a canopy descriptor; and A, B, C and D are empirically derived coefficients. Vegetation coefficients (A and B) were determined using non-linear regression code and the soil coefficients (C and D) were determined from the generalised empirical VSM-backscatter model presented in Shoshany *et al.* (2000). In order to utilise the power units system, the coefficients of the VSM-backscatter model were converted to power units using a first order approximation (as described in Xu *et al.* 1996). The adaptation of the generic form of the water-cloud model to our region is proposed through the use of relative cover fraction and a disintegration of σ^{o}_{veg} into the components that compose the vegetation layer: shrubs; dwarf shrubs and herbs.
Equation 2 represents this approach in details:

$$\sigma^{0} = A_s f_s \cos\theta(1-\exp(-2B_s GVD_s/\cos\theta)) + A_d f_d \cos\theta(1-\exp(-2B_d GVD_d/\cos\theta)) + A_h f_h \cos\theta(1-\exp(-B_h GVD_h/\cos\theta)) + f_h(C+ Dm_s)\exp(-2B_h GVD_h/\cos\theta) \tag{2}$$

where different A's and B's are the empirical coefficients of the vegetation formations; different f's are the relative cover fractions that were derived from the outcome of a phonological unmixing model based on the use of multi-temporal Landsat TM data (Shoshany and Svoray 2001). The canopy descriptor chosen – GVD – plays an important role in this application of the water-cloud model and it is further discussed in the next paragraphs.
Evidence of the low penetration depth of C-band SAR systems into forest canopies (Gabriel *et al.* 1999; Dobson *et al.* 1992) and the dominance of green leaf biomass in the upper part of woody Mediterranean canopies (Sternberg and Shoshany 2000) leads to an hypothesis that ERS-2 SAR backscatter of the woody formations is highly determined by the green leaf biomass, rather than the total AAB. Since this study is aimed at the estimation of herbaceous AAB in areas mixed with woody formations, another biophysical property than the AAB is suggested to correlate with the ERS-2 SAR backscatter. This biophysical property should be related to the green and wet leaves rather than the total biomass that includes the trunk, branches and dry leaves, which may not be participate in the backscatter of woody formations at C-band. In a previous study (Svoray *et al.* 2001) an index is suggested that represents the volumetric density of the green leaves within the canopy.
To begin with the study assumes that an initial approximation of the green leaf biomass density of the upper part of the canopy could be defined by equation 3:

$$GVD = \frac{Gb}{h} \tag{3}$$

where Gb is the green leaf biomass and h is the mean vegetation height. Such a formulation assumes that the leaves are uniformly distributed over the canopy. In this index, herbaceous vegetation, which consists primarily of green leaf biomass, may form an upper layer of high volumetric density despite its relatively low AAB. In contrast, the aboveground and green leaf biomass of trees are spread over much larger areas, and thereby form an upper layer of relatively low volumetric leaf density.
A similar correlation to that was found here between GVD and the ERS-2 SAR backscatter has been drawn by Prevot *et al.* (1993). This study proposed a canopy water content descriptor in which the water content within each cubic meter of the canopy was multiplied by the canopy height, yielding the areal water content in kg m^{-2}. However, Prevot *et al.* does not distinguish between the canopy components, mainly since they were studying agricultural crops. In the present study, the volumetric density of the green leaves is suggested as a common attribute that could determine the ERS-2 SAR backscatter from the different canopies.
An assessment of the relationship between GVD and backscatter for the same ERS-2 SAR image regions showed that GVD values of herbaceous vegetation increased from low values in February to high values in April, while their backscatter deceased between the two dates. All three woody formations exhibited relatively low GVD values with relatively high backscattering and limited seasonal variation. The following linear equation (4) describes the generalised relationship between GVD of all vegetation formations and their backscatter:

$$\sigma^{0} = -7.607*GVD - 8.5827 \tag{4}$$

A significant ($p<0.001$) coefficient of determination ($r^2=0.85$) was obtained for the relationships between backscatter and GVD. A parallel assessment of the relationship between LAI estimates derived from the literature available of the different vegetation formations and ERS-2 SAR backscattering for the image regions previously employed, indicated almost no correlation (r^2 of 0.14 with $p>0.05$) between the two data sets (Fig. 1).

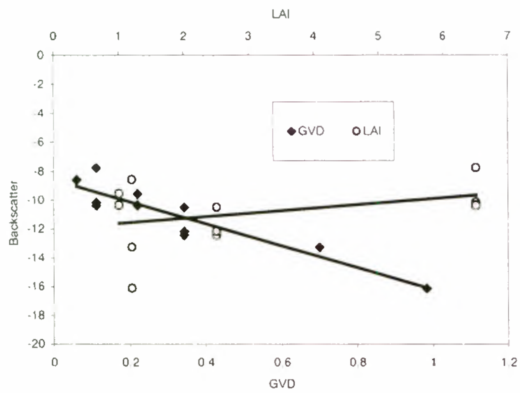

Fig. 1. Relationship between ERS-2 SAR backscatter and both GVD and LAI of Mediterranean vegetation formations

A careful look at the curve of the LAI–backscatter relationships proves also that an inversion exists between the LAI–backscatter relationship on the lower level of the range to that on the upper level of the range. This inversion clearly does not exist in the case of GVD. The main drawback of the GVD is the basic assumption that the leaves are uniformly distributed within the entire canopy volume. In order to avoid the approximation suggested by equation 3, the GVD of the upper part of the canopy was calculated, as a substitute to the GVD of the entire canopy.

This would make the assumption of uniformity more reliable. To determine the height of the upper part of the canopy, the part that is most responsive to the ERS-2 SAR backscatter within the vegetation canopies of the study area was determined based on the empirical study by Sternberg and Shoshany (2000), who have detailed the leaf distribution of several Mediterranean canopies in the current study area. This study was based on real measurements of the leaf biomass and water content of the vegetation formations, along branch segments of 20 centimeters from trunk to canopy surface. The results show that the first segment - from canopy surface to trunk (the upper 20 centimeters) - provides a particularly high foliage/wood biomass ratio. This implies that only in the first segment is the biomass of leaves considerably higher than the woody parts. It can be concluded here that this part of the canopy has the highest density of leaves and may prevent penetration (in C-band) of lower layers. Consequently, this layer may be considered most responsive to ERS-2 SAR backscatter.

Considering the results of Sternberg and Shoshany's study, a calculation of the GVD along the top 20 centimeters of the canopy is proposed here, thereby avoiding the perhaps groundless assumption of uniformly distributed leaves. This process may strengthen the relationship between ERS-2 SAR backscatter and green leaf volumetric density and provide a better representation of the total backscatter within the modified water cloud model. Thus, GVD values of the woody formations are averaged from the study of Sternberg and Shoshany (2000) (which was applied to representative woody formations of the study area), thus assuring appropriate values. The GVD of herbaceous vegetation was calculated for the entire canopy as its structure enables total penetration. Actual results were derived from field measurements.

Fig. 2 shows that the use of GVD from the top 20 centimeters only does not improve substantially the relationship between the GVD and the ERS-2 SAR backscatter. The coefficient of determination r^2 improved only slightly, from 0.85 to 0.86. Despite the small change in r^2 it is believed that this result better represents the physical rational of the relationship.

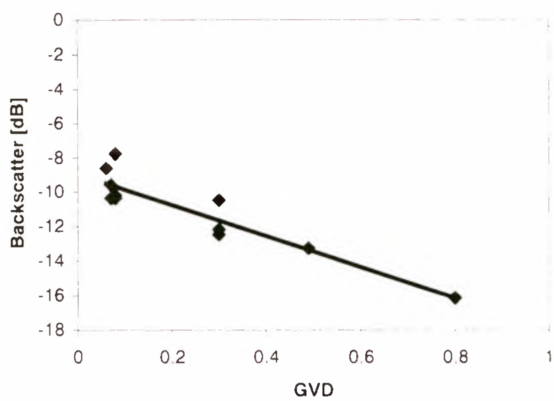

Fig. 2. The relationship between the ERS-2 SAR backscatter and GVD - calculated from part of the canopy (in the case of woody formations) and from the entire canopy (in the case of herbaceous formations).

The application of the models provided here to the entire image domain was utilized through the use of three ERS-2 SAR images that were radiometrically calibrated based on the Laur et al. 1997 method (equation 5):

$$\sigma^0_{ij} = \left[\frac{1}{N}\sum_{ij=1}^{ij=N} DN^2_{ij}\right]\frac{1}{k}C\left(\frac{\sin\theta i}{\sin\theta_{ref}}\right) \tag{5}$$

where N is the number of pixels within an area of interest; DN is the ERS-2 SAR image digital number and the average in the square parenthesis is calculated following the application of a 3x3 pixel window mean filter to reduce speckle effects; C accounts for updating the gain due to the elevation antenna pattern implemented in ERS SAR PRI data processing and θ_i, and θ_{ref} are the local and reference incidence angle respectively. The local incidences angle was calculated based on topographic consideration (Shoshany and Svoray this issue). For allowing mutual assessment of relationships between biomass estimated in the plots and the ERS-2 SAR backscatter from corresponding image pixels the three images were corrected geometrically with reference to topographic maps (1:50,000) and to DGPS readings taken during the field campaign.

RESULT AND DISCUSSION

The results achieved here show that the water-cloud model could successfully reproduce the backscatter from the Mediterranean vegetation formations (Fig. 3) and can be transformed to derive AAB values of herbaceous vegetation in mixed plots (Fig. 4).

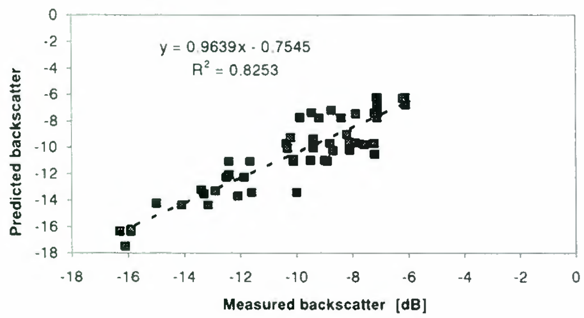

Fig. 3: Measured against reproduced backscatter in the study area.

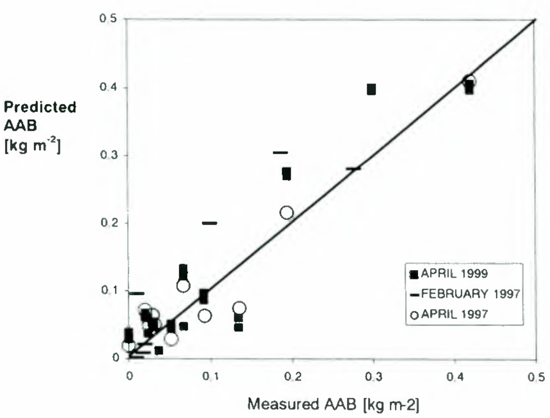

Fig. 4: Scatter plot of the relationship between measured and predicted AAB values from the modified mixed model

The developments required to achieve this were: (i) the inclusion of the vegetation fractions as a parameterisation for the surface heterogeneity (for the breakdown of the vegetation contribution σ^0_{veg} into the different contributors: $\sigma^0_{shrub;}$ $\sigma^0_{D.shrub;}$ σ^0_{Herb}); and (ii) the replacement of AAB with GVD as a canopy descriptor. Satisfactory results were found in testing as well as applying the model. However, it is important to note that the derivation of AAB from GVD requires the approximation of height data for the herbaceous canopies. This approximation could be further studied using data of larger wavelength, which will enlarge the penetration depth and thus may improve the estimations.

In the SAR configuration of the ERS-2 SAR (C_{vv} and 23^0 mean incidence angle), the vegetation canopy attenuates the radar backscatter of the under-surface soil. As a result, transformation of the direct relationship between SAR backscatter and AAB is possible but insufficient for the retrieval of AAB from the SAR backscatter. Consequently, the water-cloud model could fulfil this requirement. An examination of the AAB retrievals in comparison with field measurements of AAB revealed a high coefficient of determination in plots dominated by herbaceous vegetation (R^2=0.82) and in plots of mixed vegetation formations (R^2=0.8). The use of the new methodology developed here may allow the application of the water-cloud model to Mediterranean and semi-arid regions, where the soil effect is not only from beneath the vegetation layer but also between vegetation patches. This methodology may also improve attempts to apply the model to agricultural crops at the early stage of growth, when a large part of the soil is still exposed, or to non-irrigated agricultural crops in water-stressed areas.

Application of the water-cloud model to the entire image domain (Fig. 5) was attempted on the three dates and the results achieved captured a number of natural phenomena, such as: (i) an increase in AAB from mid-winter (February) to spring (April); (ii) large amounts of herbaceous vegetation AAB in heights versus relatively small amounts in mixed slopes; (iii) a dramatic decrease in herbaceous vegetation AAB toward the southern region of the study area, especially toward Lehavim.

These results may indicate the reliability of the model in the study area. Nevertheless, a number of restrictions were observed in the calculated images. The most questionable observation is the relatively high AAB values from May. Despite the fact that most of the image shows lower values of AAB in the natural vegetation zone, high values of AAB were still found in the wheat fields toward the south. Some of these fields were not yet harvested, but still the results appear relatively high considering the expected dryness of the region. Another questionable observation is the considerably low values of herbaceous vegetation AAB in the northern mixed areas. These errors are an opening to further studies that could improve the application of the water-cloud model to the conditions of the study area.

The methodology developed here could provide spatial AAB information for the assessment of the dynamics and status of the climatic gradient of central Israel. Moreover, by recalculating canopy constants the methodology could also assist in providing herbage AAB information in other hilly (but not mountainous) Mediterranean regions. The AAB information provided in this research could also be the basis for spatial data such as primary production, carrying capacity range conditions and dominance, which that are needed by range managers. The AAB layer provided here could also constitute the basis for GIS modeling of fire

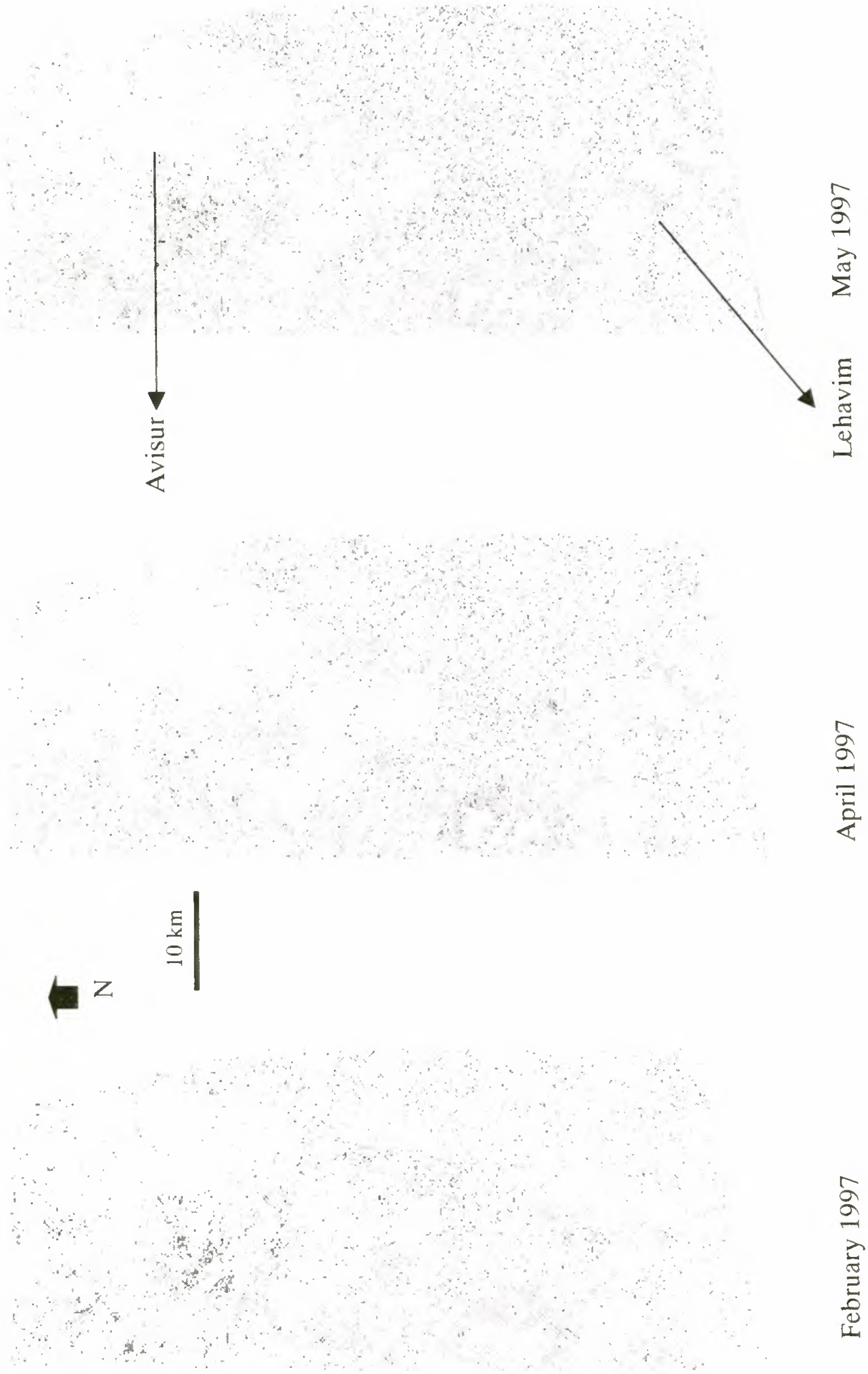

Fig. 5: AAB maps of herbaceous vegetation in the study area. Calculated by the transformed water cloud model for February (a), April (b) and May (c) 1997 ERS-2 SAR images. Shades of blue represent higher levels of AAB and shades of red refer to lower values.

hazards, to replace the existing, less informative NDVI layers.

ACKNOWLEDGMENT

This research consists a part of a Ph.D. research conducted by Tal Svoray at Bar-Ilan University under the supervision of Prof. Shoshany and Dr. Perevolotsky (Volcani Agricultural Rsesearch Institute). The Forest Authority (Keren Kaiemet Leisrael) and the Ministry of Agriculture of Israel are thanked for financing this project.

REFERENCES

Attema, E. P. W. and Ulaby, F. T. (1978): Vegetation Modeled as a Water Cloud. *Radio Science*, Vol. 13, pp. 357-364.

Dobson, M. C., Pierce, L. E., Sarabandi, K., Ulaby, F. T., and Sharik, T., 1992, Preliminary analysis of ERS-1 SAR for forest ecosystem studies. *IEEE Transactions on Geoscience. and Remote Sensing,* 30, 203-213.

Gabriel, J., Schmullius, C., Papathanassiou, K., Darizhapov, D., Tathkov, G., Tsybjitov, T., and Boerner, W., 1999, Tree height extraction using polarimetric SAR interferometry. In *Proceedings of IGARSS99 symposium,* Hamburg, Germany 28 june-2 July 1999 (Piscataway, NJ: IEEE) pp. 2131-2133.

Laur, H., Bally, P., Meadows, J., Sanchez, B., and Schaetter, E. (1997): *ERS SAR Calibration – Derivation of the Backscattering Coefficient Sigma-Nought. In* ESA ERS SAR PRI products. Document No: ES-TN-RS-PM-HL09, ESA web site http://uranus.esrin.esa.it/eeo/lft/ESC2.

Prevot, L., Dechambre, M., Taconet, O., Vidal-Madjar, D., Normand, M., and Galle, S. (1993): Estimating the characteristics of vegetation canopies with airborne radar measurements. *International Journal of Remote Sensing.* Vol. 14, pp. 2803-2818.

Shoshany, M., Svoray, T. (2001): Multi-date spectral unmixing and its application for the analysis of ecosystems transition along a climatic gradient. *Remote Sensing of Environment* (Accepted).

Shoshany, M., Svoray, T., Curran, P. J., Foody, G. M., Perevolotsky, A., (2000): Normalised ERS-2 SAR backscatter soil moisture index (NBMI): an empirical generalisation from a semi-arid transect. *International Journal of Remote Sensing*, 21, 2337-2343.

Sternberg, M., Shoshany, M., 2000, Aboveground biomass allocation and water content relationships in Mediterranean trees and shrubs at two climatological regions in Israel. *Plant Ecology,* (Accepted).

Svoray, T., Shoshany, M., Curran, P. J., Foody, G. M., and Perevolotsky, A., (2001): Relationship between green leaf biomass and ERS-2 SAR backscatter of four vegetation formations in the semi-arid zone of Israel. *International Journal of Remote Sensing*, Vol. 22, pp. 1601-1607.

Xu, H., Steven, M. D., Jaggard, (1996): Monitoring leaf area of sugar beet using ERS-1 SAR data. *International Journal of Remote Sensing*, Vol. 17, pp. 3401 - 3410.

OPERATIONAL CONTROL WITH REMOTE SENSING OF AREA-BASED SUBSIDIES IN THE FRAMEWORK OF THE COMMON AGRICULTURAL POLICY : WHAT ROLE FOR THE SAR SENSORS ?

X. Blaes[1], L. Vanhalle[2], G. Dautrebande[2] and P. Defourny[1]

[1] Department of Environmental Sciences – Geomatics, Université Catholique de Louvain
Croix du Sud 2/16, B-1348 Louvain-la-Neuve, Belgium, +32 10 47 26 13 (T), +32 10 47 88 98 (F)
blaes@biom.ucl.ac.be

[2] Ministry of Agriculture – Cellule de Techniques Spéciales en télédétection et systèmes d'information géographique
rue de Liroux 9, B-5030 Gembloux, Belgium, +32 81 62 65 89 (T), +32 81 62 65 98 (F)
laurent.vanhalle@cmlag.fgov.be

Abstract: In the framework of European Agricultural Guidance and Guarantee Fund (EAGGF) each EU member have to yearly control a proportion of the subsidized surface. Since 1995, the use of optical remote sensing for this control increases and becomes one of the major civilian operational applications of remote sensing. In Belgium the Cellule de Techniques Spéciales belonging to the Ministry of Agriculture run an automatic system based on the classification of minimum three high resolution images acquired during the growing season. The time constraint of this operation is very severe as this 39 crop discrimination must guide the in-situ observation of the cultivated fields. This SAR study focuses on two specific and critical issues related to this application :

- Can SAR images substitute the summer optical image which is the main current time constraint for the information delivery?
- Can SAR images increase the current accuracy obtained from the optical images?

Keywords: crop discrimination, parcel-based classification, SAR-optical combination, classification efficiency, waterfall strategy.

1. FRAMEWORK

With the acceptance of the so-called Plan Mac Sharry at the end of 1992, the European Union established a new Common Agricultural Policy (CAP). Since that time, European farmers can receive an area-based support for a number of crops: cereals, oil-seeds, proteaginous, grassland and fodder crops. This direct financial support intends to compensate the farmers' incomes reduction due to the important decline of the minimum guaranteed prices for these agricultural products.

To apply for financial support the farmers have to submit a dossier to the Ministry of Agriculture at the beginning of each year. This dossier includes a detailed plan showing the exact position and delineation of all the cultivated parcels based on 1/10,000 ortho-photos. For each parcel the dossier must mention the exact surface and the crop type.

As the CAP-support is area-based and variable according to the crop, a parcel declaration must be controlled at two different levels: first, the area can be biased due to errors in the delineation of the boundaries, and second the declared crop type might be wrong. In Belgium, CAP-support was asked for about 600,000 parcels. The EU prescribes a minimum sampling rate of 5%, i.e. 30,000 parcels in Belgium. In practice two strategies are followed: the random sampling and the image-based sampling. The first approach is applied throughout the country but it has a low efficiency. The image-based approach (Figure 1) needs at least three high resolution remote sensing data acquired either by the SPOT, Landsat or IRS-C satellites in March, June and July to detect the most suspicious parcels to be inspected on the field. As remote sensing serves as a filter to separate the correct and the suspicious declarations, the efficiency of the control is much higher than in the case of random sampling. This image-based sampling strategy is applied on three 'control zones', whose position is shifted from year to year.

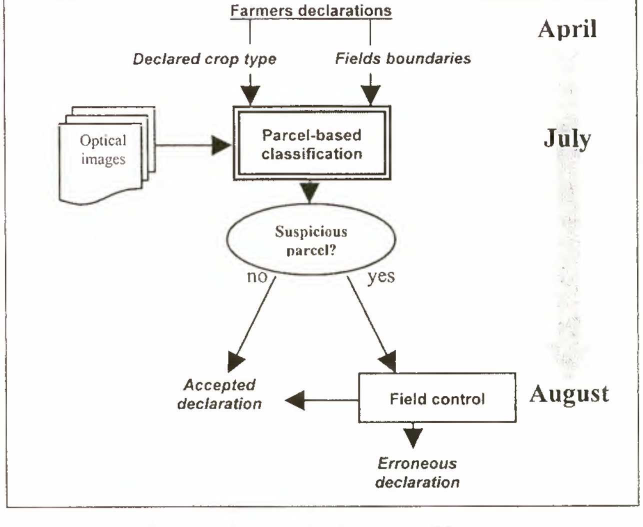

Figure 1: Belgian area-based subsidies control by remote sensing.

A supervised parcel-based classification using the maximum likelihood algorithm is applied to detect the erroneous declaration. In this system, the field boundaries and the corresponding crop type, provided by the farmers declarations, are used to define the training area.

The multispectral images acquired during the growing season allow to identify most of the crop types before

Proc. 3rd International Symposium, 'Retrieval of Bio- and Geophysical Parameters from SAR Data for Land Applications', Sheffield, UK, 11-14 September 2001 (ESA SP-475, January 2002)

their respective harvest with a relatively poor accuracy (cf. point 6.1). Moreover the time constraint of this operation is very severe as this identification must guide the in-situ observation of the standing crops. In the Northern part of Europe these three required images were not always acquired in time. The SAR images are systematically acquired as a backup solution. However, previous experiments have documented the limits of a SAR approach for the crop discrimination due to the spatial resolution [3], the C-band limitations [6], [1], [7], [10], [5], the single co-polarisation availability [6], [1], [7], and the data classification method [2], [11]. Synergism between SAR and optical sensors [4], [9], [8] and the SAR field-based classification [12], [8] were also studied.

2. Overall approach

This study focuses on two specific and critical issues related to this operational application :

- Can SAR images substitute the summer optical image which is the main current bottleneck for the information delivery ?
- Can SAR images increase the accuracy obtained from the optical images ?

3. Data set

The study area is located in the centre of the Belgium in the overlapping zone of all the SAR images (Figure 2). The data set includes 15 ERS-PRI, 3 RADARSAT-SGF and 3 optical images recorded during the 2000 growing season (Table 1). The declaration of crop affectation and the 6500 associated field boundaries were provided by the ministry. They correspond to 39 different crop types. Among these parcels, 900 were validated by field visits. Additional information consist in rainfall distribution and soil moisture measurements.

4. Images pre-processing

A digital elevation model was used to proceed to both, the geocoding and the radiometric correction of SAR images (according the method described by Ulander [13]). The per-field mean reflectance/backscattering coefficient is extracted from optical/SAR images. The border pixels are excluded using a 15-m buffer zone. These values averaged per field were used for all of the parcel-based classifications.

5. Methodology

Field boundaries and hourly meteorological data are used as a-priori knowledge for the different parcel-based classification schemes. The spectral signature of the 39 crops is defined using the 6500 parcels coming from the farmers declarations. Based on these signatures set each parcel is classified according to the maximum likelihood algorithm. The confusion matrix and the accuracy are assessed based on the subset of 900 ground-controlled parcels as the declared crop type does not always match the cultivated crop type. From a control point of view the main concern actually is the confusion between crops belonging to different subsidy levels. Therefore crops with the same subsidy level are clustered into groups which provide an aggregated version of the confusion matrices. Furthermore, two new concepts related to the control efficiency are also introduced to address the main objective of the whole system. Finally a detailed comparison between the current Belgian operational control system and the alternative SAR-optical system is carried out.

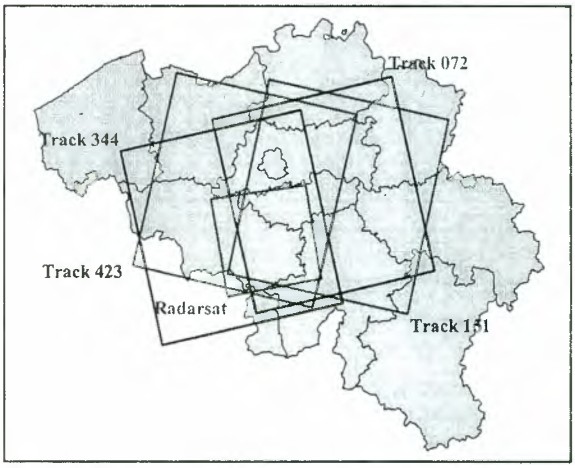

Figure 2: Radarsat, ERS and study area localization.

Dates	Image type	ERS-Track
4-2-2000	ERS-PRI	151
10-3-2000	ERS-PRI	151
21-3-2000	SPOT-XS	
28-3-2000	RADARSAT-SGF	
29-3-2000	ERS-PRI	423
8-4-2000	ERS-PRI	072
14-4-2000	ERS-PRI	151
27-4-2000	ERS-PRI	344
3-5-2000	ERS-PRI	423
15-5-2000	RADARSAT-SGF	
19-5-2000	ERS-PRI	151
7-6-2000	ERS-PRI	423
8-6-2000	RADARSAT-SGF	
8-6-2000	SPOT-XS	
17-6-2000	ERS-PRI	072
23-6-2000	ERS-PRI	151
6-7-2000	ERS-PRI	344
12-7-2000	ERS-PRI	423
28-7-2000	ERS-PRI	151
1-8-2000	LANDSAT-ETM	
16-8-2000	ERS-PRI	423

Table 1: SAR and optical images acquired in 2000.

6. Classifications result

Results presented in the first sections are expressed in term of overall accuracy referred below as OA. This values corresponds to the proportion of parcels for which the 'real' crop type match the 'detected' crop type. In the section 6.4, the classifications performances are expressed by the control efficiency referred later as Eff.

6.1. Optical images

When the three required optical images are available in due course, the overall classification accuracy reaches 75% (Table 2). The March image alone provides little information for crop discrimination (OA: 22%). On the contrary, June and August images have a good discrimination potential (OA: 58 and 64% respectively) and when one of these is missing, the accuracy sharply decreases. So, when the March and June images are taken into account, the accuracy only reaches 57%.

21/3	8/6	1/8	OA
X			22%
	X		58%
		X	64%
X	X		57%
X		X	67%
	X	X	71%
X	X	X	75%

Table 2: Overall accuracy for the crop discrimination obtained by classification of various combinations of optical images.

More specifically, when the last image is missing, most of the errors are due to the maize and fallow groups (Table 3).

		predicted								O.err (%)
		Ma	Ce	Ol	Pr	Gr	Fo	Fa	Ns	
actual	Ma	324				1		6	4	3
	Ce	1	271			4		2	4	4
	Ol			8				1		11
	Pr		3							100
	Gr	3	4			73		8	5	22
	Fo		1			6	5	1	10	78
	Fa	22	4	2		17	1	57	25	55
	Ns	1				1		1	20	13
C.err (%)		8	4	20		28	17	25	71	**85%**

		predicted								O.err (%)
		Ma	Ce	Ol	Pr	Gr	Fo	Fa	Ns	
actual	Ma	226				8		1	100	33
	Ce	2	252	1	1	15		3	8	11
	Ol		1	7				1		22
	Pr		1		1	1				67
	Gr	4	12			70		4	3	25
	Fo	6	2			5			10	100
	Fa	44	13	4		16	1	14	36	89
	Ns	1	2						20	13
C.err (%)		20	11	42	50	39	100	39	89	**66%**

Table 3: Confusion matrices at the group level for the classification of the 3 optical images (top table) and for the March and June optical images classification. The 39 crop types are aggregated by subsidy group: Ma = maize, Ce = cereals, Ol = oleaginous, Pr =proteaginous, Gr = grassland, Fo = fodder, Fa = fallow and Ns = non subsidized. The OA are given in the lower right cell of the tables. C. err. and O. err. are respectively the commission and omission errors.

6.2. SAR images

The choice of the a priori best SAR images for crop discrimination were based on ERS and Radarsat temporal profile averaged for the whole study area and the histogram distributions for the main crop types. ERS images acquired early in the year do not provide a good discrimination potential (Figure 3). They were not selected for the classification tests.

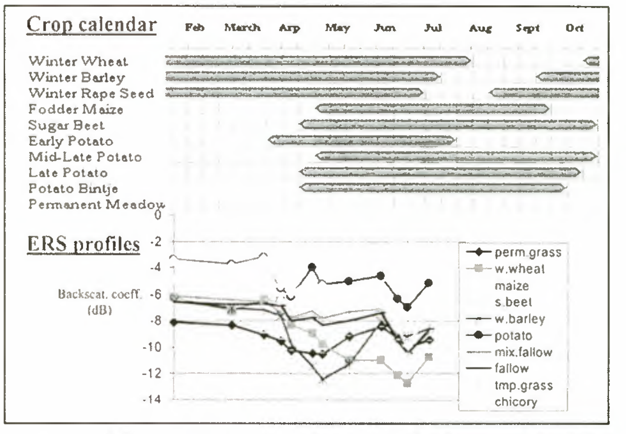

Figure 3: Relationship between the crop calendars and the ERS temporal profile of the main crops.

Classification tests were carried out using various SAR channels combination. The results (Table 4) show that bigger is the number of SAR images, higher the overal accuracy. Moreover, ERS and Radarsat provide the same results. However, the accuracy of 75% obtained using 3 optical images is never reached by ERS nor Radarsat images taken alone. So, SAR images can not replace the optical observations.

# E	# R	OA
2		37%
3		40%
5		49%
7		55%
9		61%
12		65%
	2	35%
	3	40%

Table 4: Overall accuracy for the crop discrimination obtained by classification of various combination of SAR images. #E and #R are respectively the number of ERS or Radarsat images considered for the tests.

6.3. SAR-optical combination

SAR images contribution improves the classification results obtained for the 2 first optical images (Table 5).

21/3	8/6	1/8	# E	#R	OA
X	X		3		62%
X	X		4		63%
X	X		5		66%
X	X		10		72%
X	X			2	63%
X	X			3	66%
X	X		3	2	66%
X	X		4	2	66%
X	X		5	1	68%
X	X	X	3		72%
X	X	X		3	77%
X	X	X	5		80%

Table 5: Overall accuracy obtained by classification of various combination of SAR images with 2 or 3 optical images.

This is the case both for ERS and Radarsat. The accuracy acquired using the 3 optical images is never reached by any combination of SAR dataand the 2 first SPOT images. On the other hand, the 3 optical images accuracy can be slightly improved when sufficient SAR data are available.

6.4. Efficiency maximisation

All the tests presented here above dealt with the classification overall accuracy. However the objective of the control system is only to detect at the best the erroneous declarations.

For a given parcel, the declaration can be correct or not, i.e. the declared crop does not correspond the cultivated crop. From a remote sensing point of view, a parcel can be accepted (declared crop matches the remotely sensed crop) or suspected (declared crop is different than the remotely sensed crop). These two points of view lead to the definition of the 4 possible cases (A to D).

	Remote sensing	
Declaration	Accepted	Suspected
Correct	A	B
Wrong	C	D

As the remote sensing aims to identify the parcels to be visited for ground control, the ***efficiency (Eff)*** of the field control can be expressed as the proportion of wrong declarations (D) in the set suspected by remote sensing (B+D). While the efficiency has to be maximised, the proportion of suspected parcels (D), with regard to the total number of wrong declarations (C+D), must simultaneously remain as high as possible. This will be expressed by the proportion of ***erroneous detected declarations (Edd)***. These concepts are defined by the following equations:

$$Eff = \frac{D}{B+D} \qquad Edd = \frac{D}{C+D}$$

The Figure 4 presents the classification tests results in a scatterogram based on the Efficiency and the proportion of Erroneous detected declaration. Optical classifications reach an efficiency of 17% with 3 images. When either June or August optical images is missing, 2% of efficiency are lost. When the August optical images is missing, the efficiency dramatically drops till 12%.

Among the 900 validated parcels 56 parcels have been erroneously declared in reality. So, a random selection of parcels to control by field visit would have an efficiency of 6%. By comparison the classification of a single March optical image hardly supports the control as the efficiency reaches only 7%. Using SAR images without any optical observation, the efficiency reaches 13% at the best. However, 2 optical images are always more efficient when they are combined with SAR. Such a combination can almost reach the same efficiency than 3 optical images without SAR. In the same way, 3 optical images are more efficient by combination with SAR. Up to 19% efficiency is obtained using 3 optical and 3 Radarsat or 5 ERS images.

A general remark for all sensor types is that higher is the number of images, better the efficiency.

6.5. Classification improvements

Large field selection

For all the completed tests, the full set of the 6500 available parcels were used as training area and all of them were classified.

Because of the speckle noise in the SAR images, the smaller fields have highly variable mean backscattering coefficients. For any given crop type, the small fields introduce more variability in the spectral signature.

Better spectral signature definition was expected using only the a priori most representative parcel means. In order to improve the classification accuracy, the spectral signatures were defined for each crop type using only the 75% of the larger fields. The 6500 parcels were then classified according to these new spectral signatures and the 900 validated parcels serve for the overall accuracy assessment at the crop level (Table 6).

# O	# E	# R	OA (all fields)	OA (largest fields)
	5		47%	48%
	12		65%	65%
2	3	2	66%	65%

Table 6: Comparison of the classification using spectral signatures based on all the 6500 declared parcel (all fields) and the classification using spectral signatures computed with 75% of the fields (larger fields only).

Curiously no improvement is observed by discarding 25% of the smaller fields for the signature computation. The Figure 5 shows that the selection does not improve much the spectral signatures. Indeed, the means remain at the same level and the variance is not strongly reduced. On the other hand, a more drastic selection (when only the largest 25% of the fields still remain) improves the spectral signatures. However, by selecting only the quarter of the largest parcels, the number of remaining fields becomes often too small to define spectral signatures for all of the 39 crop types.

Waterfall strategy

The overall approach assumes an unique temporal and spectral signature for a given crop. However, this is not necessarily relevant when, for a given crop, the seedling occurs at two different periods of the season. In order to bypass this problem, a waterfall strategy is proposed (Figure 6). This strategy relies to a first classification of all the fields and then to a second round of classification of only the suspected field. This second step is based on the spectral signature defined using only the fields remaining after the first step. At the end, the accepted parcels are those accepted at both turn. Of course the number of suspected parcels decreases with the second round. This approach clearly take into account the inter parcel heterogeneity for each crop.

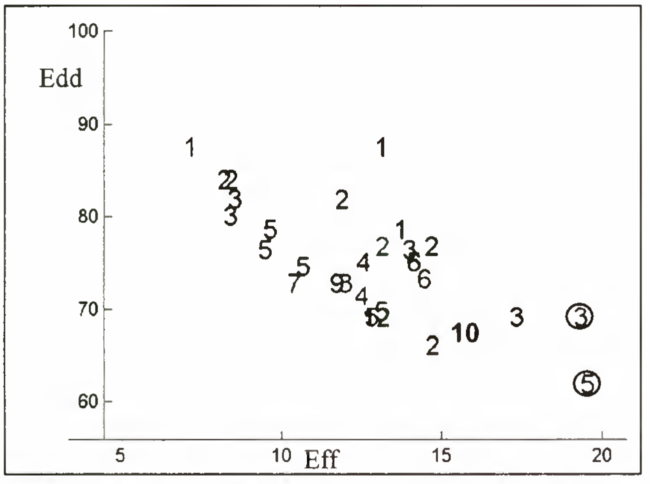

Figure 4: Efficiencies (Eff) and proportions of erroneous detected declarations (Edd) for all the classification tests. Each test is located in the Eff/Edd graph by the number of images used for. The black values correspond to the optical test (using 1 to 3 images). The blue values are tests using only SAR images. Red color is used to report tests using the 2 first optical images and various number of SAR images. The surrounded red values correspond to tests using 3 optical images with 3 or 5 SAR images.

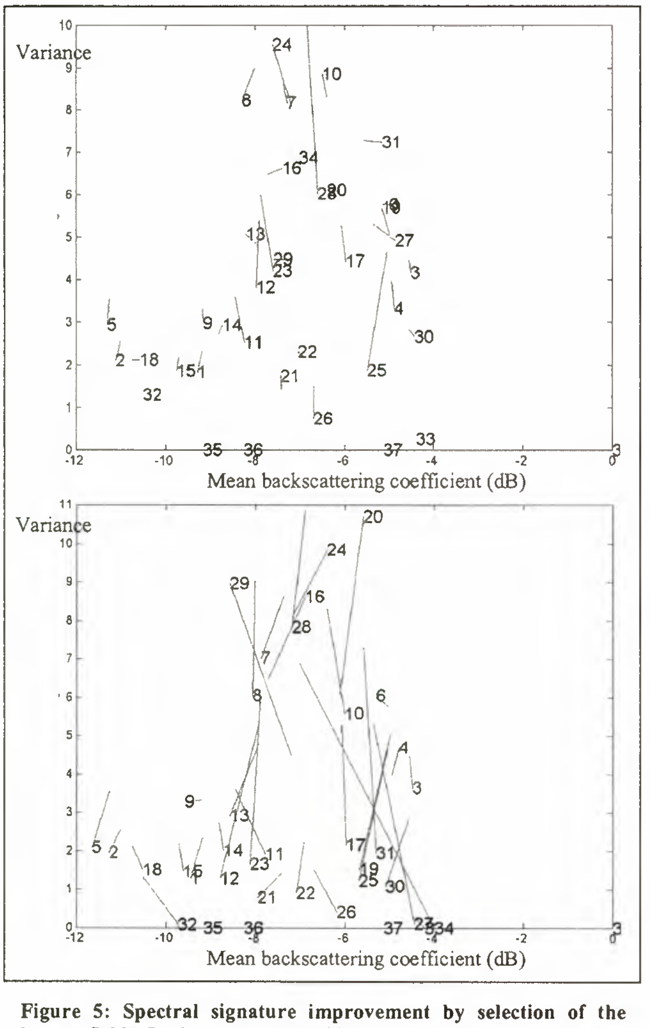

Figure 5: Spectral signature improvement by selection of the largest fields. In the top graph 75% of the parcels are selected and only 25% in the lower one. The beginning of the lines indicates the mean/variance computed for the 39 crop types using all fields mean values extracted from the 19th of May ERS image. The end of the lines (where the crop id is indicated) corresponds to the mean/variance values computed using the selection of the largest fields.

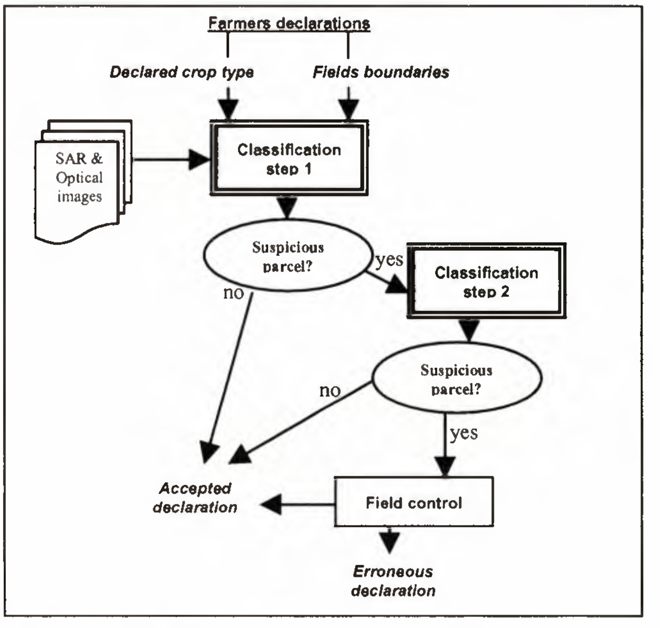

Figure 6: Waterfall strategy for the Belgian control.

The effectiveness of the waterfall scheme is determined by its capacity to accept, at the second round, only the fields wrongly suspected during the first step. This could be controlled by the observation of the efficiency and the proportion of erroneous detected declarations after the first and after the second step (Figure 7).

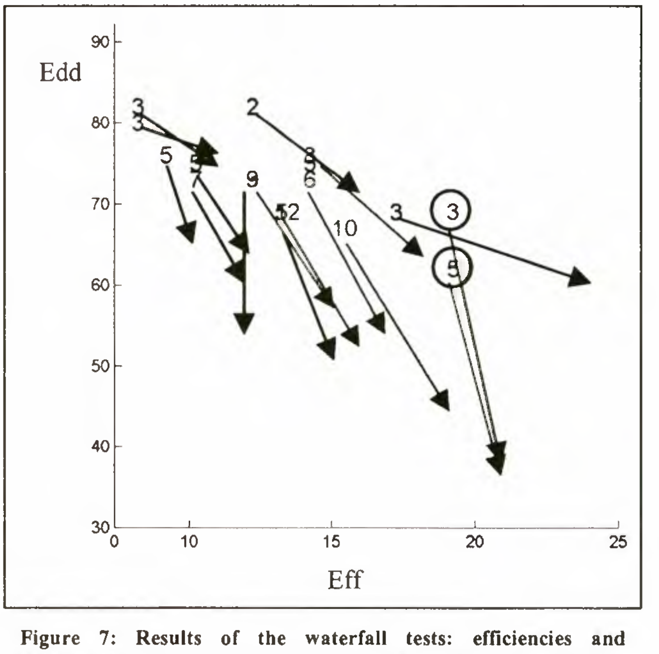

Figure 7: Results of the waterfall tests: efficiencies and proportions of erroneous detected declarations (Edd) after the first step (same legend than the Figure 4) and after the second step (indicated by the arrow).

Classifications dealing with 2 or 3 optical images are improved by the waterfall strategy: the efficiency increase (till 24% with 3 images) and the proportion of erroneous declaration detected remain relatively high.

The waterfall scheme applied to the SAR classifications gives better efficiency than the one-step approach but the proportion of erroneous detected declarations sharply decreases.

Better results (in efficiency and proportion of erroneous detected declarations) are also obtained for the SAR-optical combination after a second classification step.

7. Conclusions: what role for SAR sensors?

The currently available SAR data will never replace the optical images in the crop control system. However, a set of SAR images can partly substituted the last optical image and still provide a overall accuracy as high as 68% for 39 crops. In such a case the SAR contribution increase the overall accuracy of 11% and allow to reduce the information delivery time by one month. The SAR contribution has been found also quite positive when the 3 expected optical images are available. Indeed the SAR input still slightly increases the classification overall accuracy from 75% to 80%. More significantly the efficiency of the control system is improved by the SAR complementarity which contributes as much as the 3rd optical image.

While these results seem to clearly recommend the use of SAR in the current operational control system, no result allows to recommend specifically ERS or Radarsat for this application. On the other hand, the waterfall strategy was found as a very interesting concept to increase the efficiency of the field check. This is most efficient in the case of the full optical data set where the field visit efficiency may improved by 30%. These results are related to the operational Belgian system run since 1995 but will be probably also relevant to many other systems in EU due to their expected evolution.

8. References

[1] Anys, H., He, D. C., Wang, L., and Gwyn, Q. H. J., "Classification of multipolarized airborne radar data in agriculture," *International Journal of Remote Sensing*, vol. 15, no. 18, pp. 3831-3838, Dec.1994.

[2] Ban, Y., Treitz, P. M., Howarth, P. J., Brisco, B., and Brown, R. J., "Improving the accuracy of synthetic aperture radar analysis for agricultural crop classification," *Canadian Journal of Remote Sensing*, vol. 21, no. 1, pp. 158-164, 2000.

[3] Bouman, B. A. M. and Ulaby, F. T., "Crop classification possibilities with ERS-1 and JERS-1 configurations," *Remote Sensing of Environment*, vol. 40 pp. 1-13, 1992.

[4] Brisco, B. and Brown, R. J., "Multidate SAR/TM synergism for crop classification in western Canada," *Photogrammetric Engineering and Remote Sensing*, vol. 61, no. 8, pp. 1009-1014, Aug.1995.

[5] Ferrazzoli, P., Guerriero, L., and Schiavon, G., "Experimental and Model Investigation on Radar Classification Capability," *IEEE Transactions on Geoscience and Remote Sensing*, vol. 37, no. 2, pp. 960-968, 1999.

[6] Foody, G. M., Mac Culloch, M. B., and Yates, W. B., "Crop classification from C-band polarimetric radar data," *International Journal of Remote Sensing*, vol. 15, no. 14, pp. 2871-2885, Sept.1994.

[7] Freeman, A., Villasenor, J., Klein, J. D., Hoogeboom, P., and Groot, J., "On the use of multi-frequency and polarimetric radar backscatter features for classification of agricultural crops," *International Journal of Remote Sensing*, vol. 15, no. 9, pp. 1799-1812, Dec.1994.

[8] Lobo, A., Chic, O., and Casterad, A., "Classification of Mediterranean crops with multisensor data: per-pixel versus per-object statistics and image segmentation," *International Journal of Remote Sensing*, vol. 17, no. 12, pp. 2385-2400, 1996.

[9] Michelson, D. B., Liljeberg, B. M., and Pilesjo, P., "Comparison of algorithms for classifying Swedish landcover using Landsat TM and ERS-1 SAR data," *Remote Sensing of Environment*, vol. 71, no. 1, pp. 1-15, 2000.

[10] Schotten, C. G. J., VanRooy, W. W. L., and Janssen, L. L. F., "Assessment of the capabilities of multi-temporal ERS-1 SAR data to discriminate between agricultural crops," *International Journal of Remote Sensing*, vol. 16, no. 14, pp. 2619-2637, Sept.1995.

[11] Soares, J. V., Renno, C. D., Formaggio, A. R., Yanasse, C. D. F., and Frery, A. C., "An investigation of the selection of texture features for crop discrimination using SAR imagery," *Remote Sensing of Environment*, vol. 59, no. 2, pp. 234-247, Feb.1997.

[12] Tso, B. and Mather, P. M., "Crop discrimination using multi-temporal SAR imagery," *International Journal of Remote Sensing*, vol. 20, no. 12, pp. 2443-2460, Aug.1999.

[13] Ulander, L. M. H., "Radiometric slope correction of synthetic-aperture radar images," *IEEE Transactions on Geoscience and Remote Sensing*, vol. 34, no. 5, pp. 1115-1122, Sept.1996.

THE POTENTIAL OF SAR IN CROP CLASSIFICATION USING MULTI-CONFIGURATION DATA

F. DelFrate[1], G. Schiavon[1], D. Solimini[1]
M. Borgeaud[2], D. Hoekman[3], M. Vissers[3]

[1]Università Tor Vergata, Ingegneria, DISP, Viale Politecnico 1, I-00133 Roma, Italy
tel: +39 06 72597422, fax +39 06 72597460, e-mail: schiavon@disp.uniroma2.it

[2]European Space Agency, Electromagnetics Division TOS-EEP
Postbus 299, 2200 AG Noordwijk, The Netherlands
tel: +31 71 565 4830, fax: +31 71 565 4999, e-mail: maurice@xe.estec.esa.nl

[3]Department of Water Resources, Wageningen Agricultural University
Bode 82, Postbus 9101, 6700 HB Wageningen, The Netherlands
tel: +31 317 4 82894, fax: +31 317 4 84885, e-mail: dirk.hoekman@users.whh.wau.nl

ABSTRACT

This paper reports on a quantitative investigation which has been carried out, aimed at evaluating the performances of a neural network based crop classification technique. Backscattering coefficients measured in different SAR configurations (multipolarization/multitemporal) have been used as inputs of the algorithm. For this purpose, AirSAR and ERS data collected at the Flevoland site have been extracted from the ERA-ORA distributed library.

1. INTRODUCTION

The potential of SAR in classifying among different agricultural crop species has been demonstrated in several studies (Ulaby et al., 1986; Bouman and Hoekman, 1993; Ferrazzoli et al., 1999; Saich and Borgeaud, 2000). The performance of a classification exercise depends on the sensitivity of the measured backscattering coefficient to the differences in the bio-morphological structures of different species, which cause different interaction behaviour between the incident electromagnetic waves and the vegetation structures. It has been experienced that observations by SAR systems in a single configuration, which means one image taken at a certain time at one fixed frequency, polarization and incidence angle, are often inadequate to classify with the required accuracy, mainly when similar crops have to be separated. In those cases, the potential of a classification algorithm may be improved by operating in multifrequency and/or multipolarization and/or multiangle configuration. Additional benefits may be achieved by repeated overpasses (multitemporal techniques).

This paper reports on a quantitative investigation which has been carried out, aimed at evaluating the performances of a neural network based crop classification technique for different SAR configurations. A wide data set, consisting of AirSAR signatures collected at the Flevoland site in 1991 and of ERS backscattering coefficients collected at the same site through years 1993–95, has been used. The considered data set has been assembled within the ERA-ORA (European RAdar-Optical Research Assemblage) project, a concerted action supported by the European Commission within the RTD Programme on Environment and Climate (Fourth Framework Programme) in the field of space techniques applied to environmental monitoring and research. The essential objective of the Concerted Action is to improve the radar data analysis and utilization tools developed by European researchers for Earth observation from space.

AirSAR signatures span 3 frequencies, are fully polarimetric and partially multitemporal, since the site was overflown 4 times in summertime. Several combinations of SAR parameters have been considered, starting from a simple single configuration system, at C band, vv polarization, one date, through gradually increasing complexities, adding polarizations and number of overpasses, up to a C band system with hh, vv, hv polarizations, and multitemporal data. The percentage of misclassified fields, which in the first case is more than 40%, drops to very low values in the last cases (less than 4%), although only C band and linear polarizations (without phase information) have been considered. This is indeed a promising result in view of future exploitation of Envisat ASAR.

ERS data are single frequency and single polarization but are collected during the whole year. In this case the multitemporal character of the data has been fully exploited in the algorithm.

Proc. 3rd International Symposium, 'Retrieval of Bio- and Geophysical Parameters from SAR Data for Land Applications', Sheffield, UK, 11-14 September 2001 (ESA SP-475, January 2002)

Table 1. Data set characteristics.

	AirSAR		ERS (95 vs. 95)		ERS (93, 94 vs. 95)	
type	training	test	training	test	training	test
barley	10	4	5	3	18	8
corn	2	2	8	4	0	0
grass	11	8	21	9	68	30
potato	28	25	15	15	109	30
rape	4	3	1	1	0	0
s.beet	23	19	18	12	95	30
wheat	33	18	19	11	123	30
total	111	79	87	55	413	128

2. NEURAL NETWORK CLASSIFICATION ALGORITHM

The classification algorithm consists in a neural network with feedforward configuration. The neural network simulator (SNNS) developed at the University of Stuttgart (Germany) (Zell et al., 1995) has provided the basic software for the algorithm implementation. The net consists of a multilayer perceptron with two hidden layers. A typical architecture of the used nets is reported in Fig. 1. Training has been pursued by a scaled conjugate gradient (SCG) algorithm. This is a member of the class of conjugate gradient methods, general purpose second order techniques that help to minimize goal functions of several variables. Second order indicates that such methods use the second derivatives of the error function, while a first-order technique, like standard backpropagation, only uses the first derivatives. By using the SCG method the nets have generally been trained after a few hundreds of epochs, that is, the training phase was very short time consuming. For the purpose of classification, in the training phase the component of the output vector corresponding to the true class has been set to 1 while the others to 0. In the test phase a winner-and-take approach has been considered.

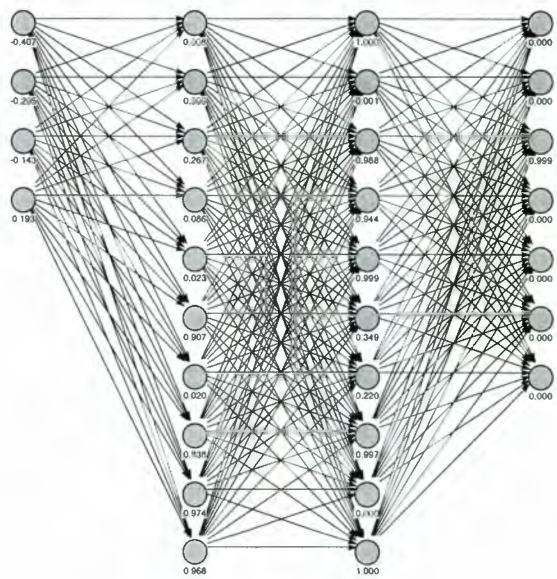

Figure 1. Neural network feedforward topology.

3. RESULTS

3.1. AirSAR data

The Flevoland '91 AirSAR signatures have been used to carry out a classification exercise intended to assess the improvement of accuracy brought in by progressively richer (in terms of polarizations and measurement dates) sets of data.

A training set of backscattering coefficients has been generated, by selecting the C-band 50° data relative to a number of fields, listed in column 2 of Table 1, of the crops listed in column 1, within the total number of fields imaged on the Flevoland '91 site. Multipolarization and/or multitemporal C-band σ^0's of the fields have trained the NN algorithm. Then, the trained network has been used to classify the fields of the test set, which included the remaining Flevoland '91 fields (column 3 of Table 1). The work has been repeated several times using different subsets of the available data. First of all, a very simple data set has been taken, i.e., σ^0 for C-band, vv polarization, one single flight. The data set complexity has gradually been increased, up to the most complete case, relative to C-band, hh, vv and hv polarizations, 4 flights (15 June, 3, 12, 28 July 1991). Poor classification performance has been obtained for the single polarization single flight case (overall accuracy (OA) = 55.7 %), while it improves when data acquired during all the four available flights in the same vv polarization are used (OA = 83.5 %). Still better performance is obtained when exploiting the other mentioned polarizations, achieving OA = 96.2 % in the most complete case. Table 2 reports the complete confusion matrix for the hh-vv-hv combination, one flight, while in Table 3 the same polarization combination, but for all the four dates, is considered. It is noticeable to observe that a quite high OA have been achieved in the last case, although only C-band and linear polarizations (without phase information) have been considered.

Tables 4 to 6 report the resulting confusion matrices for the hh-hv combination for increasing number of acquisition dates (1 to 3). Comparable results have been obtained for the vv-hv configuration. It can be observed that the addition of the crosspolar polarization produces an improvement of the OA even in the case of data acquired during one single flight (from 55.7 % to 88.6 %), but particularly when multitemporal data are used. This is a promising result in view of the future exploitation of the Envisat ASAR data, although before generalizing the results obtained in this exercise, the effects of the different incidence angles should be assessed. Note, however, that 50° is close to the maximum ASAR incidence angle.

3.2. ERS data

Fig. 2 compares multitemporal ERS trends collected over many different fields and in different sites and years. Three different codes are associated with different crop types. During vegetation development, i.e. from Day of Year ~150 to Day of Year ~200, σ^0's of wheat fields are clearly lower than σ^0's of potato and sugarbeet fields. In the other periods of the year, when soil scattering dominates, σ^0 variations are mainly due to soil conditions (moisture effects, essentially). As a consequence of this, small differences are observed among samples belonging to the same site and year, while site-to-site or year-to-year variations may be large. Fig. 2 indicates that a single-frequency, single-polarization radar, such as ERS SAR, may be useful for classification, provided multitemporal data are used, and that the most suitable data for this task are those acquired during the vegetation development period.

Therefore, a classification exercise has been performed, using ERS data collected over the Flevoland test site. At first all the available data collected during year 1995, which include acquisitions in 27 days from Day of Year 10 to 355, have been used. A training set of backscattering coefficients has been generated, with data relative to a number of fields of the same crops of the AirSAR case. Then, the trained network has been used to classify the remaining fields, which formed the test set (columns 4 and 5 of Table 1). The resulting confusion matrix is reported in Table 7, which shows a very good classification performance with only one field misclassified. Based on the considerations made commenting Fig. 2, the classification exercise has then been repeated selecting data acquired only on seven days during the vegetation development period. Results are reported in Table 8, not showing a substantial difference with the previous case, and therefore confirming what previously stated.

An inter-year classification exercise has then been performed, training a neural network algorithm using data acquired in years 1993 and 1994, and testing it on 1995 data. Data of the first two years didn't include all the crop types present in 1995, therefore results obtained in this case, and reported in Table 9, are not directly comparable with the others. Nevertheless, they can give some useful information. Dates of acquisition were not the same from year to year, therefore the dates of one year included in the datasets have been selected to be no more than one week apart from those of the other two years. The 1995 overpasse dates were the same seven days of the previous case. Despite, as expected, the OA is lower, the obtained results are encouraging, and substantial improvements might be envisaged when using the future Envisat ASAR data, with the addition of the crosspolar channel.

ACKNOWLEDGMENTS

This work has been partially supported by Agenzia Spaziale Italiana (ASI).

REFERENCES

Bouman B.A.M., D.H. Hoekman, 1993, "Multi-temporal multi-frequency radar measurements of agricultural crops during the Agriscatt-88 campaign in The Netherlands", Int. J. Remote Sensing, vol. 14, 1595–1614.

Ferrazzoli P., L. Guerriero, G. Schiavon, 1999, "Experimental and model investigation on radar classification capability", IEEE Trans. Geosci. Remote Sensing, vol. 37, pp. 960–968.

Saich P., M. Borgeaud, 2000, "Interpreting ERS SAR signatures of agricultural crops in Flevoland, 1993–1996", IEEE Trans. Geosci. Remote Sensing, vol. 38, pp. 651–657.

Ulaby F. T., Moore R. K, Fung A. K, 1986, Microwave Remote Sensing: Active and Passive - vol.III, Artech House, Dedham (MA, USA).

Zell A., G. Mamier, M. Vogt, et al., 1995, SNNS Stuttgart Neural Network Simulator User Manual, Report n. 6/95, University of Stuttgart, Institute for Parallel and Distributed High Performance Systems, Stuttgart, Germany.

Table 2. Confusion matrix describing the neural algorithm crop classification performance. Algorithm input characteristics: 3 polarizations (hh-vv-hv), 1 date, AirSAR measurements (Flevoland 1991).

classified	true class						
as	barley	corn	grass	potato	rape	s.beet	wheat
barley	3	0	3	0	0	0	0
corn	0	2	0	0	1	0	0
grass	1	0	5	0	0	0	0
potato	0	0	0	25	0	0	2
rape	0	0	0	0	2	0	0
s.beet	0	0	0	0	0	19	0
wheat	0	0	0	0	0	0	16

total number of samples = 79
correctly classified = 72
overall accuracy = 91.1 %

Table 3. Confusion matrix describing the neural algorithm crop classification performance. Algorithm input characteristics: 3 polarizations (hh-vv-hv), 4 dates, AirSAR measurements (Flevoland 1991).

classified	true class						
as	barley	corn	grass	potato	rape	s.beet	wheat
barley	4	0	0	0	0	0	0
corn	0	2	0	0	0	0	0
grass	0	0	7	0	0	0	0
potato	0	0	1	25	0	0	1
rape	0	0	0	0	3	0	0
s.beet	0	0	0	0	0	19	1
wheat	0	0	0	0	0	0	16

total number of samples = 79
correctly classified = 76
overall accuracy = 96.2 %

Table 4. Confusion matrix describing the neural algorithm crop classification performance. Algorithm input characteristics: 2 polarizations (hh-hv), 1 date, AirSAR measurements (Flevoland 1991).

classified	true class						
as	barley	corn	grass	potato	rape	s.beet	wheat
barley	3	0	2	0	0	0	0
corn	0	1	0	0	0	2	0
grass	0	0	6	0	0	0	3
potato	1	0	0	25	0	0	0
rape	0	0	0	0	3	0	0
s.beet	0	1	0	0	0	17	0
wheat	0	0	0	0	0	0	15

total number of samples = 79
correctly classified = 70
overall accuracy = 88.6 %

Table 5. Confusion matrix describing the neural algorithm crop classification performance. Algorithm input characteristics: 2 polarizations (hh-hv), 2 dates, AirSAR measurements (Flevoland 1991).

classified	true class						
as	barley	corn	grass	potato	rape	s.beet	wheat
barley	3	0	1	0	0	0	1
corn	0	1	0	0	0	0	0
grass	0	0	6	0	0	0	1
potato	0	0	1	25	0	0	0
rape	0	0	0	0	3	0	0
s.beet	0	0	0	0	0	18	0
wheat	1	1	0	0	0	1	16

total number of samples = 79
correctly classified = 72
overall accuracy = 91.1 %

Table 6. Confusion matrix describing the neural algorithm crop classification performance. Algorithm input characteristics: 3 polarizations (hh-hv), 3 dates, AirSAR measurements (Flevoland 1991).

classified	true class						
as	barley	corn	grass	potato	rape	s.beet	wheat
barley	3	0	1	0	0	0	0
corn	0	2	0	0	0	0	0
grass	0	0	7	0	0	1	0
potato	1	0	0	25	0	0	2
rape	0	0	0	0	3	0	0
s.beet	0	0	0	0	0	18	0
wheat	0	0	0	0	0	0	16

total number of samples = 79
correctly classified = 74
overall accuracy = 93.7 %

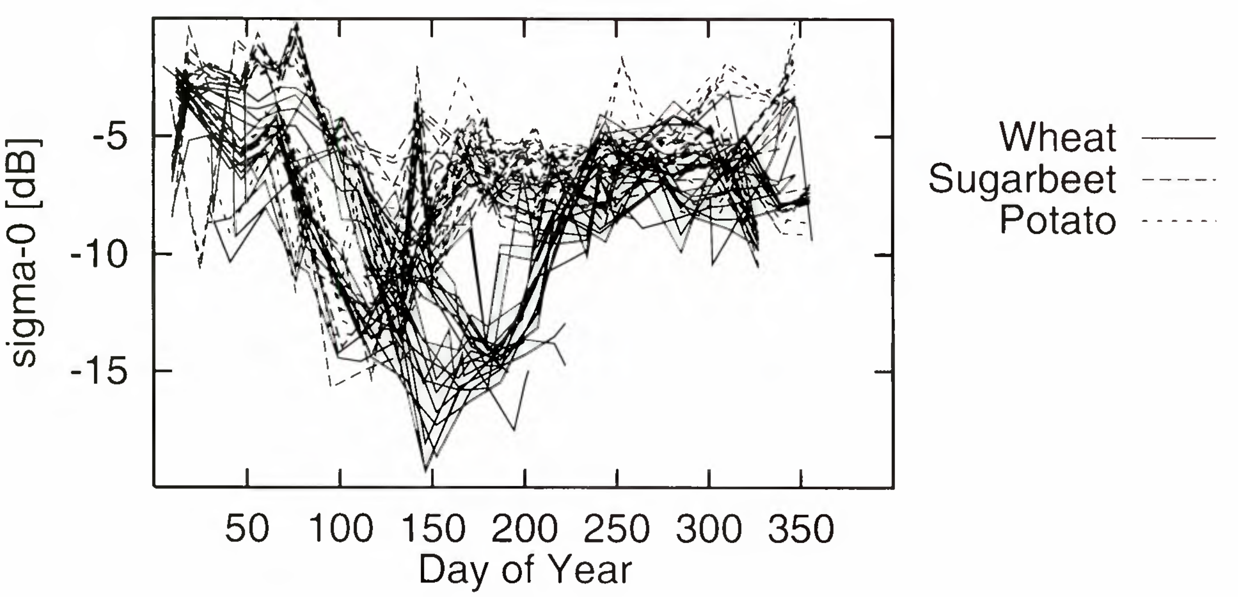

Figure 2. Different behaviours of σ^0's of different crops as resulting from ERS measurements taken over different sites and years.

Table 7. Confusion matrix describing the neural algorithm crop classification performance. Algorithm input characteristics: 1 polarization (vv), 27 dates, ERS measurements (Flevoland 1995).

classified	true class						
as	barley	corn	grass	potato	rape	s.beet	wheat
barley	3	0	0	0	0	0	0
corn	0	3	0	0	0	0	0
grass	0	0	9	0	0	0	0
potato	0	0	0	15	0	0	0
rape	0	0	0	0	1	0	0
s.beet	0	1	0	0	0	12	0
wheat	0	0	0	0	0	0	11

total number of samples = 55
correctly classified = 54
overall accuracy = 98.2 %

Table 8. Confusion matrix describing the neural algorithm crop classification performance. Algorithm input characteristics: 1 polarization (vv), 7 dates, ERS measurements (Flevoland 1995).

classified	true class						
as	barley	corn	grass	potato	rape	s.beet	wheat
barley	3	0	0	0	0	0	1
corn	0	4	0	0	0	0	0
grass	0	0	9	0	0	0	0
potato	0	0	0	15	0	1	0
rape	0	0	0	0	1	0	0
s.beet	0	0	0	0	0	11	0
wheat	0	0	0	0	0	0	10

total number of samples = 55
correctly classified = 53
overall accuracy = 96.4 %

Table 9. Confusion matrix describing the neural algorithm crop classification performance. Algorithm input characteristics: 1 polarization (vv), 7 dates, ERS measurements. Training set: Flevoland 1993/94, test set: Flevoland 1995.

classified	true class				
as	barley	grass	potato	s.beet	wheat
barley	8	0	0	0	5
grass	0	30	0	0	1
potato	0	0	30	2	0
s.beet	0	0	0	28	0
wheat	0	0	0	0	24

total number of samples = 128
correctly classified = 120
overall accuracy = 93.8 %

SYSTEMATIC INVESTIGATION ON THE EFFECT OF DEW AND INTERCEPTION ON MULTIFREQUENCY AND MULTIPOLARIMETRIC RADAR BACKSCATTER SIGNALS

T. Riedel[1], C. Pathe[1], C. Thiel[1], M. Herold[2] and C. Schmullius[1]

1:Remote Sensing Unit, Institute of Geography
Friedrich-Schiller-University, Loebdergraben 32, D-07743 Jena, Germany
tel.: +49-3641-948877 / fax: +49-3641-948852
e-mail: c.schmullius@geogr.uni-jena.de / c5tari@geogr.uni-jena.de

2: Remote Sensing Research Unit, Department of Geography,
University of California Santa Barbara, USA , Ellison Hall, Santa Barbara, CA 93106

ABSTRACT

This paper presents the first results of the TerraDew project. The investigation focus on the effect of dew and interception on the radar backscatter signal of agricultural vegetation. The impact differ with respect to frequency, polarization and crop type. The strongest influence on the radar signal is found at the cross-polarized L-band. No impact of free vegetation water was determined for L-VV-band. At C-band the back-scatter variations after a rain event strongly depends on the vegetation structure and the growth stage. The impact due to dew is independent from vegetation type. At X-band the backscatter varies after rain in contingent on the surface structure of the vegetation stand. No significant effect on the radar signal is found for dew at X-band. Furthermore the changes in scattering mechanism due to wet vegetation were investigated. The diurnal variations in polarimetric parameters extracted by the Cloude target decomposition theorem are low.

INTRODUCTION

Radar backscatter from land surfaces is primarily determined by structural and dielectric attributes of the target. Diurnal variations of the backscattering coefficient are the result of changes in soil moisture, plant water content or the amount of free water on the plant surface, resulting from dew, guttation or interception. Only few studies about the effect of dew and interception on the radar signal [1, 2, 3, 4] as well as the impact on the thematic interpretation of the SAR data have been published [5, 6, 7]. Most investigations referred to the crop type wheat [1, 8]. The examinations documented an increase of the radar backscatter signal due to water on the plant surface by 1 to 4 dB. The influence varies with frequency, polarization and vegetation structure. The underlying mechanisms causing the increased backscatter are still poorly understood [9, 10]. Altogether, it is impossible to draw a general conclusion of the effect of dew and interception on the radar backscatter with respect to different frequencies, polarizations and crop types.

The TerraDew project was initiated to contribute towards a better understanding of this problem. The project is funded by the German Ministry of Education and Research (BMBF). It focuses on the quantitative and systematic evaluation and modelling of the effects of free vegetation water on multifrequency and polarimetric radar data in special consideration of different crop types. In this paper the first results are presented and analysed.

EXPERIMENTAL DATA

The investigations were carried out on the airborne E-SAR system of the German Aerospace Center (DLR). The data were recorded on the 14th and 16th June 2000 at 6, 9 and 12 am. The data were acquired at X- (co-polarized), C- (VV and cross-polarized) and L-band (polarimetric). The absolute radiometric precision of the E-SAR data is about 2 dB.

The test site of this study covers a 3 km x 3 km area located around 25 km southwest of Munich, Germany. The region is intensively agriculturally used and is characterized by flat terrain. During the flight campaign extensive field data were obtained. Soil moisture measurements were taken along profiles applying gravimetric and Time Domain Reflectrometry (TDR) methods. Land use and different vegetation parameters such as vegetation height, row spacing, fractal cover and leaf area index were acquired. Furthermore microclimatologic data were collected to describe the amount of water on the plant surface and to retrieve the dew point.

METHODS

On the 14th June there was a heavy rainfall event of 24 mm at night. In the early morning of the second day of the campaign dew was deposited on the plant surfaces.

Proc. 3rd International Symposium, 'Retrieval of Bio- and Geophysical Parameters from SAR Data for Land Applications', Sheffield, UK, 11-14 September 2001 (ESA SP-475, January 2002)

For both events three radar measurements at 6, 9 and 12 am were available and included in the analysis. For each crop type the field mean values were calculated and the observed diurnal changes of σ^0 were interpreted. To describe the intra-field changes due to free vegetation water, ten windows with a size of 50 pixel, averaging the radar backscatter coefficient, were defined on representative pads and the daily trends in their mean-values were investigated.

The Cloude decomposition theorem was applied to the polarimetric L-band data to analyse the diurnal variations of the scattering mechanism. The decomposition algorithm is based on an eigenvector analysis of the coherence matrix and permits the extraction of information about independent scattering processes represented by the 3 decomposed matrices. These are weighted by their corresponding eigenvector. The eigenvalues (λ_{1-3}) of these matrices correspond to the contribution of the single scattering process to the radar signal. Based on the decomposed matrices the parameter alpha (α) as well as the physical features entropy (H) and anisotropy (A) are calculated. The alpha parameter with a range of $0° \leq \alpha \leq 90°$ represents the scattering mechanism. Thereby $\alpha = 0$ can be interpreted as surface scattering. As (α) increases, the surface becomes anisotropic. An α-value of 45° represents a dipole. If (α) reaches 90° the scattering process is characterised by double bounce. The parameter (H) is an indicator for the distribution of the scattering mechanism, whereby H = 0 correspond to deterministic scattering and H = 1 to totally random scattering. The anisotropy (A) yields no additional information about the relationship between λ_2 and λ_3 for medium values of (H). A high anisotropy signifies that besides the first scattering mechanism only the second contributes to the radar signal. If (A) is low, also the third process plays an important role [11, 12, 13].

DIURNAL VARIATIONS IN BACKSCATTER DUE TO DEW AND INTERCEPTION

The analyses indicate that the radar backscatter is influenced by intercepted precipitation and dew, whereby there are significant differences with respect to crop type, wavelength and polarization. Figure 1 shows the observed changes of the mean radar backscatter signals for different crops after a dew (16th June) and a rain (14th June) event.

At X-band no significant impact of dew on the σ^0-values was found. During the day most of the observed fields showed a slight decrease in backscatter about less than 1 dB. In contrast after the heavy rainfall on the 14th June significant changes of the σ^0-values could be observed for some crops, particularly for VV-polarization. The largest differences in the radar backscatter signal (up to 2.4 dB for the mean values of the different crop types and up to 4.0 dB for single fields) were found for crops with a regular surface structure like grassland and spiked grain (barley and wheat), whereby irregular crops like corn, potatoes and oat showed only a slight decrease.

The effect of intercepted precipitation on the radar backscatter at C-band depends on the vegetation structure and on the growth stadium of the crops. The trends for VV- and HV-polarization are similar, whereby the diurnal variations per field are greater for the cross-polarized backscatter. Narrow leaf crops with a height of less than 1 meter (most of the fields of grassland and summer barley) showed a strong decrease in sigma nought between 6 and 12 am. For example, after rain for one summer barley field (height 90 cm) σ^0 increases ~2.4 dB at VV-polarization. In contrast, fields either higher than 1 meter or after the beginning of the ripening process showed an opposed, but less obvious trend, in particular between 6 am and 9 am. For instance, the averaged backscatter of one summer barley field with a crop height of around 1 meter and after the beginning of the ripening process increase about 0.9 dB during the day for VV-polarization. The radar signal of winter barley fields in an advanced ripening stadium varies in a range of less than 1 dB during a day. For oat, a panicle grass with another vegetation structure than the other cereals, an increase in backscatter after rain of about 1.2 dB could be noticed at all fields. For the broad leaf crops (corn and potatoes) the backscatter variation over the day is low (less than 0.5 dB). In opposition to the impact of intercepted rainfall, the effect of dew on the radar signal is independent from vegetation type and structure, as shown in figure 2. It illustrates the difference in backscatter between 12 and 6 am for VV-polarization on Friday, i.e. for the dew event. An analysis of micro-climatologic data recorded with 28 temperature and air humidity sensors showed that at fields with an increasing backscatter during the day (pale), the dew point was reached for a few hours under the vegetation surface. In contrast, the radar signal decreases when the dew point was reached only for two hours or less within the vegetation stand. For HV-polarization the trend is similar, but the spatial variations are less noticeable. The reason for these differences can result from the higher absorption in VV-polarization due to moisture.

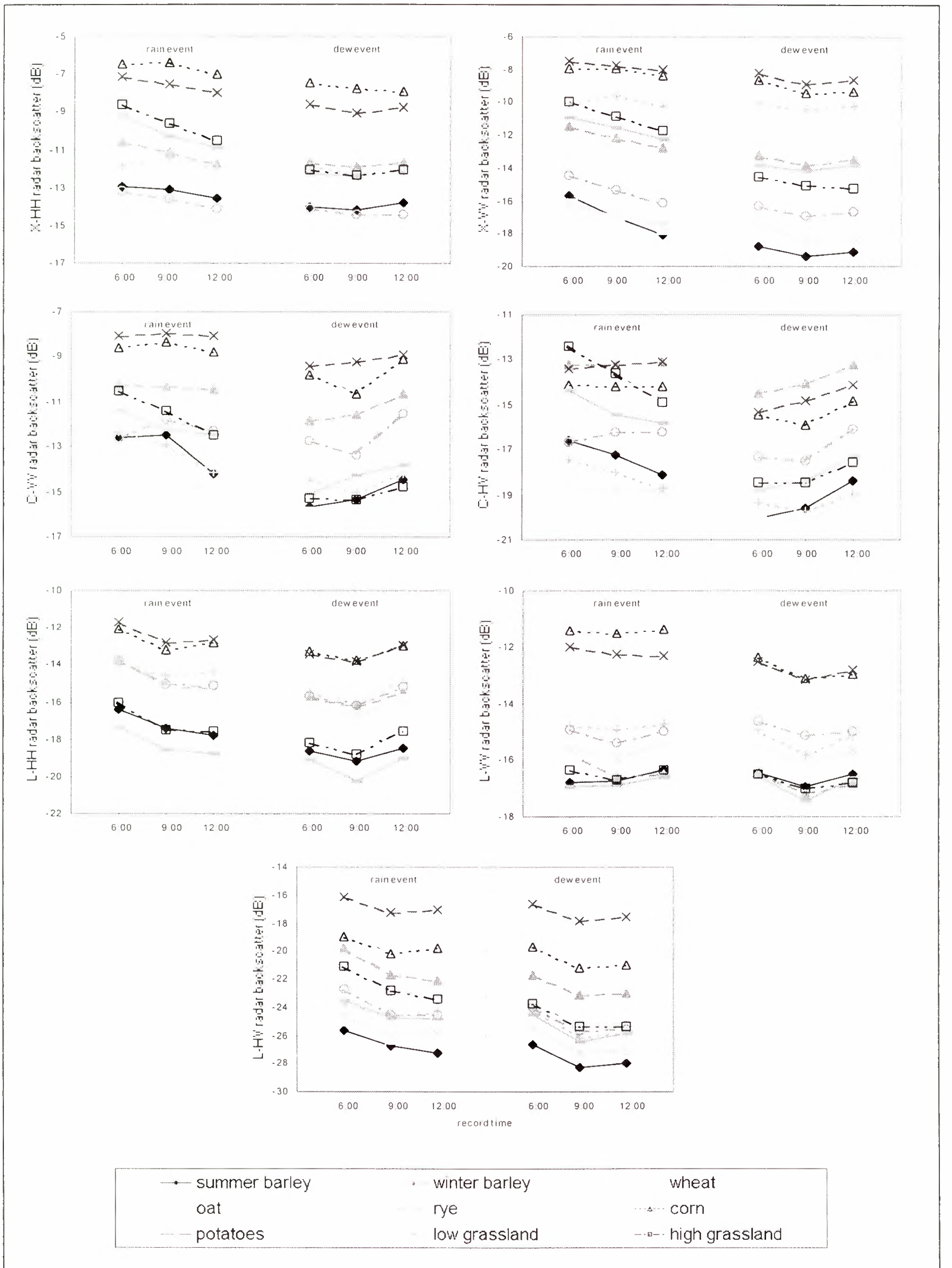

Figure 1: Diurnal changes of the mean radar backscatter for different crops after a dew and a rain event

Figure 2: Diurnal backscatter changes [dB] after a dew event at C-VV band, shown with field boundaries (pale: increase, dark: decrease)

At L-Band the influence of wet vegetation is less dependent of plant structure than at C-band. For HH-polarization all investigated crops show a slight decrease in radar backscatter signal after dew evaporation. The lowest σ^0-values were reached at 9 am. After rain an increase of σ^0 up to 1.5 dB could be noticed. With regard to all investigated frequencies and polarisations the strongest influence of dew and intercepted precipitation on the radar signal is found at the cross-polarized L-band. The diurnal decrease of σ^0 exceeded 1 dB for most agricultural crops at both days. The influence is lower for broad leaf crops in comparison to narrow leaf crops, e.g. the radar signal of single grassland fields increases up to 4 dB after rain, but only up to 1 dB for corn. For the broad leaf crops as well as for some cereals like oat and wheat a stronger effect on σ^0 could be noticed after the dew event. No effect of plant surface water on σ^0 was found for VV-polarization.

To sum up, at L-band the changes in backscatter for different fields of the same crop type are very similar. At X-band and especially at C-band no consistent trends for the different fields of one land use could be observed due to the dependence of the effect of dew and interception on the vegetation structure. Especially the magnitude in radar backscatter change significantly differs with crop type and field location.

Analyses of the intra-field variability showed that, within the pads, the trends observed for the whole fields are not detectable, even at L-band. The changes in backscatter differ due to field heterogeneities like different height, growth stage and winnowed cereals. For example, the radar backscatter of a summer barley field increases after rain at C-VV in one part of the field up to 4 dB (height: 60 – 70 cm), whereas in the same field (upper part), where the soil is saturated and the vegetation is lower (10 – 40 cm), the backscatter decreases (fig. 3).

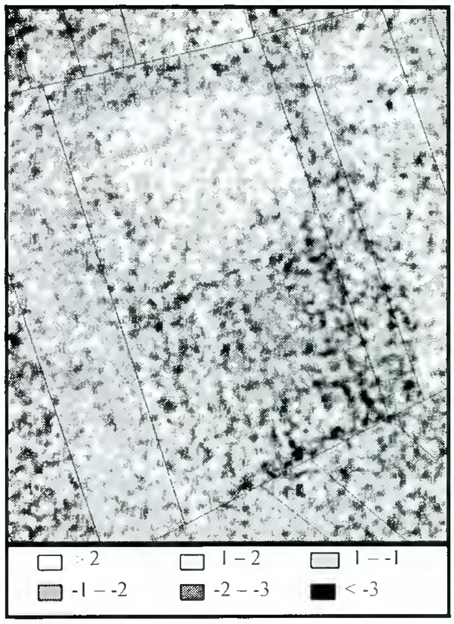

Figure 3: Diurnal backscatter changes [dB] after rain within a summer barley field at C-VV band (pale: increase, dark: decrease)

DIURNAL VARIATIONS IN SCATTERING MECHANISM DUE TO DEW AND INTERCEPTION

The mean diurnal changes in the parameters alpha, entropy and anisotropy extracted by Cloude decomposition are illustrated in figure 4 for different crops at L-band. In general, the changes in the Cloude polarimetric parameters are low. During the day α decreases, whereby the difference in backscatter mechanism is stronger after rain in comparison to dew. The strongest diurnal decrease in (α) of up to 4.5° is found for tall grassland, rye, winter and summer barley. The variations for single fields reached 7°. The entropy (H) of the crops is fairly high. For very high values ($H > 0.7$) the anisotropy (A) yields no additional information. This applies to broad leaf crops, winter barley and tall grassland. (H) increases on account of free vegetation water for all crops with the exception of tall grassland, winter barley and potatoes. The observed trends in anisotropy are opposed to the ones indicated in the entropy. That means, wet conditions decrease the contribution of the first scattering mechanism to the radar signal. Especially the importance of the third mechanism increases due to rain and interception as

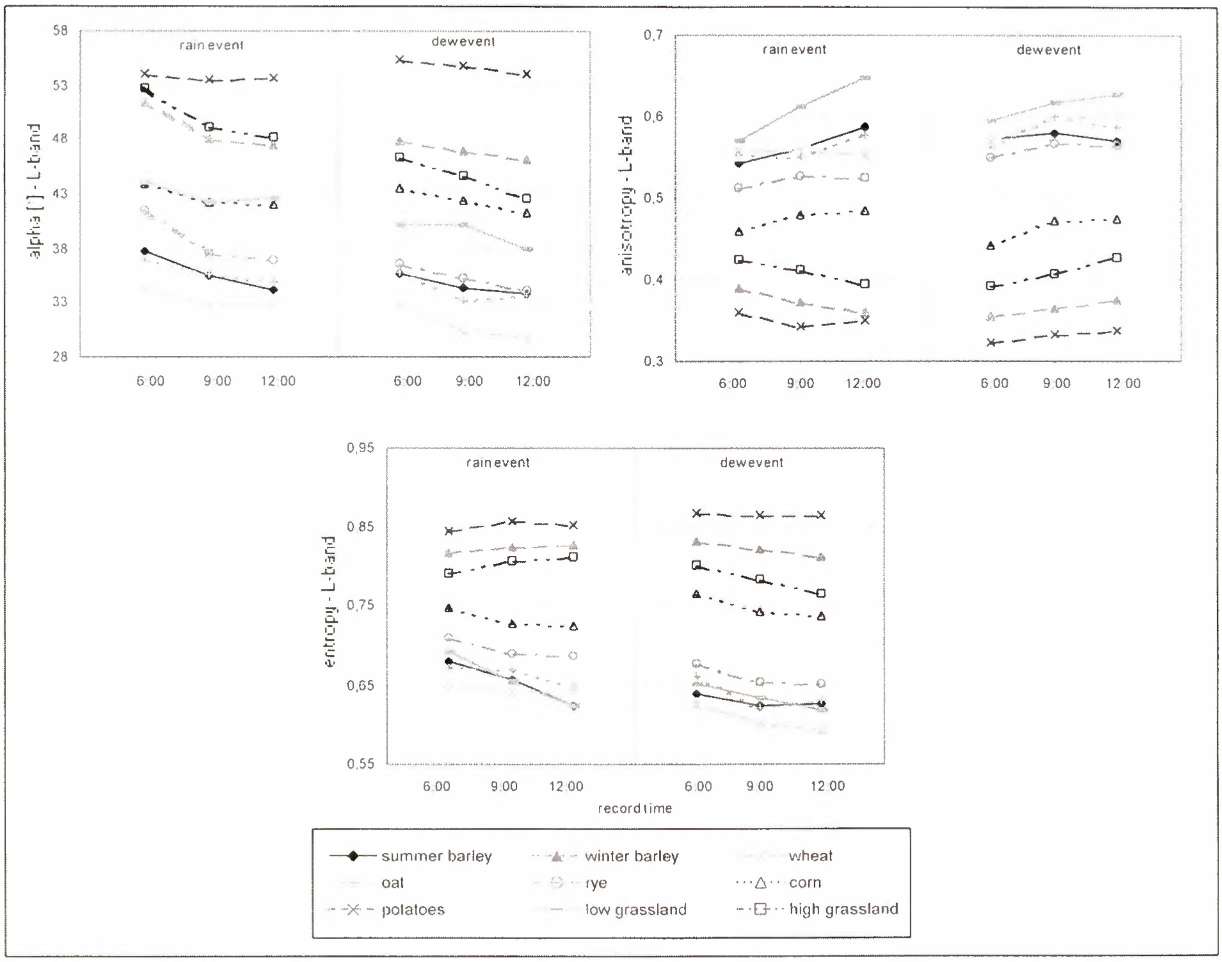

Figure 4: Diurnal changes of the parameter of the Cloude decomposition theorem for different crops at L-band

shown by the lower anisotropy at 6 am on both days of the campaign (with the exception of the crops characterised by a high entropy). In summary, first analysis of the Cloude decomposition showed that the scattering mechanisms changes slightly due to dew and intercepted rainfall. Hobbs [9] stated that for vegetation the increase in backscatter is much reduced because of the concur of different scattering mechanisms. This problem will be investigated in further data analysis.

DISCUSSION

As shown in figure 1 significant changes in L-band backscatter mainly occur between 9 am and 12 am, whereas the differences between 6 am and 9 am are fairly low. On the other hand, for shorter wavelengths a constant or even opposed trend is noticeable. The field observations showed that the free vegetation water on the top of the vegetation layer was already evaporated at the time of the second SAR observation (9 am). This fact probably caused the observed changes in backscatter between 6 am and 9 am at short wavelengths.

The investigations also show that the influence of intercepted rainfall and dew differs especially at C-band. Gillespie et al. [1] stated that after rain separated drops remain on the plant surface whereas dew deposits a more continuous film of smaller droplets. Perhaps this can result in the different effects in the backscatter signal.

Wheat showed only little changes in σ^0 in a range under 1 dB. This is in disagreement with other studies, which documented an increase in backscatter for wheat of up to 3 dB after rain or dew [1, 8]. Allan & Ulaby [3] stated, that the effects of irrigation on the radar backscatter is only ascertainable for about 1 hour. This fact might be of special importance as the rain event ended few hours before the data acquisition.

Furthermore, an analysis of the observed changes in backscattering and scattering mechanism should also focus on other factors that could affect the radar signal. For example, it is possible that the vegetation structure varies during the day due to the changes in leaf orientation with the sunset. Moreover, the loss (day) and regain (night) of water by the plants can cause different leaf orientation. Finally, dew and intercepted rainfall on the crop leaves can lead to a change in leaf orientation due to the added weight [2]. Additionally, during the field measurements it was observed that parts of the grassland were procumbent in the early morning hours as result of the heavy rainfall.

Furthermore, the absolute radiometric accuracy of the E-SAR data is approximately 2 dB. However, the SAR datasets used for this analysis were recorded and processed with the same sensor settings, equipment and processing procedure, so the relative processing error for comparative analysis of the different SAR data sets is assumed to be significantly lower than the absolute calibration error.

CONCLUSIONS

The investigations have shown that the effect of dew and intercepted rain on the backscatter signal differs with respect to frequency, polarization and crop type. For co-polarized X-band no significant effect of dew was ascertainable, whereas the backscatter increases after rain for crops with a regular surface vegetation structure like grassland and summer barley. At C-band the influence of intercepted rainfall for cereals depends on the plant height and the ripeness stage. For broad leaf crops the backscatter variation is low. The effect of dew on the radar signal is independent from vegetation type. The averaged σ^0-values decrease for all crops when dew was deposited on the plant surface. At L-band the effect of free vegetation water is independent from vegetation structure. Of all investigated frequencies and polarizations the strongest impact was determined for cross-polarization. The VV-polarized scene was the only one that was neither affected by intercepted rainfall nor by dew. The diurnal changes in the parameters of the Cloude target decomposition theorem are low.

ACKNOWLEDGEMENT

This study is funded through the German Ministry for Education and Science (BMBF), project-name TerraDew, project-ID 50EE0035.

REFERENCES

[1] GILLESPIE, T. J., B. BRISCO, R. J. BROWN & G. J. SOFKO (1990): Radar detection of a dew event in wheat .- Remote Sensing of Environment 1990, No. 33, p. 151 – 156.

[2] JACKSON, T. J. & L. MOY (1999): Dew effects on passive microwave observations of land surfaces .- Remote Sensing of Environment 1999, No. 70, p. 129 – 137.

[3] ALLEN, C. T. & F. T. ULABY (1984): Characterization of the microwave extinction properties of vegetation canopies .- Technical Report , University of Michigan, Radiation Laboratory, Mi, No. 1.

[4] SCHMULLIUS, C. & R. FURRER (1991): Frequency dependence of radar backscattering under different moisture conditions of vegetation-covered soil .- International Journal of Remote Sensing 1992, Vol. 13, No. 12, p. 2233 – 2245.

[5] PATHE, C., C. SCHMULLIUS, T. RIEDEL, M. HEROLD & C. THIEL (2001): On the influence of diurnal variations of surface wetness on classification of agricultural crops in multi-frequency and polarimetric SAR-data with regard to future TerraSAR-Applications .- same issue.

[6] BRISCO, B., R. J. BROWN & T. J. PULTZ (1992): The effects of free canopy water on SAR crop separability .- Proceedings IGARSS '89, Vancouver, BC, 10. – 14. July, p. 424 – 428.

[7] FISCHER, J. A., R. J. BROWN & B. BRISCO (1992): The effects of changes in soil moisture and rainfall on SAR data crop classification .- Proceedings 15th Canadian Symposium on Remote Sensing , Toronto, ON, p. 221 – 226.

[8] SOFKO, G., J. SLOBOSHAN, M. MC KIBBEN & J. KOEHLER (1989): Variation of microwave radar cross-section of wheat during the initial hours of a rainfall .- Proceedings 15th Canadian Symposium on Remote Sensing , Toronto, ON, p. 1191 - 1194.

[9] HOBBS, S. E., W. ANG & C. SEYNAT (1998): Wind and rain effects on SAR backscatter from crops .- Retrieval of Bio- and Geo-Physical Parameters from SAR Data for Land Application Workshop, ESTEC, 21. – 23. October 1998.

[10]SAICH, P. & M. BORGEAUD (1998): Interpreting agricultural crop signatures from Flevoland, 1993 – 1996 .- Retrieval of Bio- and Geo-Physical Parameters from SAR Data for Land Application Workshop, ESTEC, 21. – 23. October 1998.

[11]HELLMANN, M. & E. KRÄTZSCHMAR (1998): Interpretation of SAR-data using polarimetric techniques .- Retrieval of Bio- and Geo-Physical Parameters from SAR Data for Land Application Workshop, ESTEC, 21. – 23. October 1998.

[12]HELLMANN, M. (2000):Classification of fully polarimetric SAR-data for cartographic applications .- German Aerospace Center (DLR), research report 2000-19.

[13] CLOUDE, S. R. & E. POTTIER (1995) : A review of target decomposition theorems in radar polarimetry .- IEEE Transaction on Geosience and Remote Sensing 1996, Vol. 34 , No. 2, p. 498 – 518.

LAND-COVER MAP INFORMATION FROM POLARIMETRIC SAR USING KNOWLEDGE-BASED TECHNIQUES

Henning Skriver

Section for Electromagnetic Systems
Ørsted•DTU Department, Technical University of Denmark
Ørsteds Plads, Building 348, DK-2800 Lyngby, Denmark
tel.: +45 4525 3792, e-mail: hs@oersted.dtu.dk

ABSTRACT

The application of a knowledge-based classification approach has been studied for land-cover classification using polarimetric SAR acquired by the Danish L- and C-band polarimetric SAR (EMISAR). The advantage of knowledge-based and model-based techniques is that they are normally more robust than for instance supervised Bayes classification methods, because they are virtually independent of the specific SAR data used and the specific test site used. The classification scheme used is based on a scheme originally proposed by the University of Michigan, and it has been modified to cope with the different object classes in this case. The classification was evaluated using a large number of test areas, and for the broad classes forest, lake, spring crops, and winter crops very good results were obtained using acquisitions at both L- and C-band in April.

INTRODUCTION

Land-use classification by synthetic aperture radar (SAR) is a well-known remote sensing application. The main advantage of the SAR compared with optical and infrared sensors is the all-weather mapping capability of the SAR, which secure mapping at specific pre-determined acquisition times. The discrimination potential of SAR data is based on the sensitivity of the radar backscatter to the dielectric properties of the objects and to the object structure (i.e. the size, shape and orientation distribution of the scatterers) [1][2]. The possibility of identifying the individual classes is based on the fact that the dielectric properties and the structure of the relevant objects for land-use classification, such as the crop types, the forest types, the natural vegetations types, the different water areas, and urban areas, may be different. These properties may vary through the year, for instance for agricultural crops a distinct variation is seen through the growing season due to the development of crops [2]. The radar backscatter is also sensitive to e.g. the dielectric properties of the soil, the surface roughness, the terrain slope, the vegetation canopy structure (e.g. the row direction and spacing, and the cover fraction), and the specific directions of the objects (e.g. buildings) [1][3].

The polarimetric SAR measures the full polarimetric information for a target in the form of the scattering matrix [4]. Therefore, such data may be used to assess the full capabilities of SAR for land-use classification. Various methods have been used for such assessments, e.g. supervised Bayes classification [5], knowledge-based or model-based classification [6]-[9], and unsupervised classification based on polarimetric decomposition [10]-[12]. A very important aspect when evaluating and comparing the various classification approaches is the robustness of the algorithms, i.e. are they dependent on the specific data used or the specific test site used. The knowledge-based and model-based approaches have in this respect a very good potential, because they are based on model results and/or knowledge about scattering properties, and hence virtually independent of data and sites.

In this paper, a study of the potential of polarimetric SAR for land-use mapping using a knowledge-based method is presented. The analyses concentrate on the applicability of an advanced, high-resolution, airborne system, where polarimetric SAR data are available at two frequencies. Data from the Danish airborne SAR, EMISAR, are used. The EMISAR is the result of a research and development project initiated in 1986 at the former Electromagnetics Institute (EMI) of the Technical University of Denmark (now the Ørsted•DTU department), and it is a fully polarimetric and interferometric L- and C-band SAR [13][14]. The evaluation is based on a large number of test fields providing realistic classification results.

The paper is structured as follows. In the first section the SAR data and the test site will be described. The next section outlines the theoretical background for the parameters used. In the following section the knowledge-based classification methodology is described. Finally, results are presented, followed by the conclusions.

SAR DATA

The SAR data used in the study have been acquired by the fully polarimetric Danish airborne SAR system, EMISAR, which operates at two frequencies, C-band (5.3 GHz/5.7 cm wavelength) and L-band (1.25 GHz/24

Proc. 3rd International Symposium, 'Retrieval of Bio- and Geophysical Parameters from SAR Data for Land Applications', Sheffield, UK, 11-14 September 2001 (ESA SP-475, January 2002)

Fig . 1. Total power image of L-band EMISAR image from April

cm wavelength) [14]. The nominal one-look spatial resolution is 2 m by 2 m (one-look), the ground range swath is approximately 12 km and typical incidence angles range from 35° to 60°. The processed data from this system are fully calibrated by using an advanced internal calibration system [14]. In 1998 simultaneous L- and C-band data were acquired over a Danish agricultural test site on 21 March, 17 April, 20 May, 16 June, 15 July and 16 August.

Speckle reduction has been performed by first transforming the original one-look scattering matrix data into covariance matrix data, and hereafter these data have been averaged by a cosine-squared weighted 9 by 9 filter. The new pixel spacing in the images is 5 m by 5 m, and the effective spatial resolution is approximately 8 m by 8 m at mid-range. After the averaging the equivalent number of looks is estimated to 9-11 from homogenous areas in the images, which corresponds to a standard deviation for the backscatter coefficient of approximately 1.1 – 1.8 dB. This variation may not be sufficiently small to obtain appropriate classification accuracies, because the separation between the backscatter coefficients for some classes may be in the same range. Therefore, further speckle reduction may be necessary, but that has not been done in this paper.

The test site contains a large number of agricultural fields with different crops, as well as several lakes, forests, areas with natural vegetation, grasslands, and urban areas. A total power image of the L-band acquisition in April is shown in Fig. 1. The area is relatively flat, and corrections of the local incidence angle due to terrain slope are therefore as a first approximation not necessary. The crop types present in the area are for spring crops: beets, peas, potatoes, maize, spring barley, and oats, and for winter crops: rye, winter barley, winter wheat, winter rape, and grass. The forest areas consist primarily of two types of coniferous forest, i.e. Norway spruce and Caucasian fir, but also some coniferous forest areas are present. A land cover map was established for the test site including more than 350 test areas covering different incidence angles.

POLARIMETRIC SAR PARAMETERS

The covariance matrix is often used to represent polarimetric SAR data. One advantage is that the average properties of a group of resolution elements can be expressed using a single matrix. The average covariance matrix is defined as [4]

$$\langle \mathbf{C} \rangle = \begin{pmatrix} \langle S_{hh}S_{hh}^* \rangle & \langle S_{hh}S_{hv}^* \rangle & \langle S_{hh}S_{vv}^* \rangle \\ \langle S_{hv}S_{hh}^* \rangle & \langle S_{hv}S_{hv}^* \rangle & \langle S_{hv}S_{vv}^* \rangle \\ \langle S_{vv}S_{hh}^* \rangle & \langle S_{vv}S_{hv}^* \rangle & \langle S_{vv}S_{vv}^* \rangle \end{pmatrix}$$

where <> denotes ensemble averaging and * denotes complex conjugation, and S_{pq} is the complex scattering amplitude for receive polarization p and transmit polarization q (p and q are either v for vertical or h for horizontal). Reciprocity which normally applies to natural targets gives $S_{hv} = S_{vh}$ (backscattering alignment convention) [4], and results in the covariance matrix in (1) with rank 3.

The diagonal elements in the covariance matrix are related to the γ_{pq} backscattering coefficients by

$$\gamma^{o}_{pq} = \frac{4\pi}{A\cos\theta}\langle S_{pq}S_{pq}^* \rangle$$

where A is the illuminated area on the ground and θ is the local incidence angle. The advantage of the γ^{o} backscatter coefficient is that it has a slightly weaker dependence on the incidence angle than the σ^{o} backscatter coefficient. In discrimination applications the weaker dependence is an advantage, because the results will be less sensitive to the incidence angle.

The elements in the covariance matrix are sensitive to the dielectric properties of the vegetation and the soil, to the plant structure, to the surface roughness and to the canopy structure, as mentioned in the introduction. Factors such as the presence of double-bounce scattering, volume scattering and direct soil surface scattering also strongly influence the polarimetric parameters. The off-diagonal co-polarized element yields information about the correlation coefficient ρ_{hhvv} and the phase difference φ_{hhvv} between the HH and VV components. The correlation coefficient is close to 1 for surface scattering, and smaller for volume scattering, depending on the degree of polarization, and it is found to discriminate well between spring crops and winter crops early in the growing season [2]. The three primary sources for the phase difference are two-way propagation through the canopy, Fresnel reflection by the soil surface, and double-bounce surface-vegetation scattering [15]. Double-bounce scattering is also often seen in urban areas where for instance the streets and the buildings act like dihedral corner reflectors. The other off-diagonal elements are often not considered for applications, because they are zero for random distributed targets with azimuthally symmetry.

In addition to the covariance matrix parameters, texture information may be used in a classification scheme. Such information may provide important discrimination information for some object classes, where the polarimetric parameters are close, but where there are differences in the homogeneity of the classes. Due to the speckle noise, an appropriate texture measure must be normalized, like for instance the normalized variance. Ulaby et al. [16] define a texture measure where the measured normalized variance $M = (\sigma/\mu)^2$ is split into a normalized speckle variance S and a normalized texture variance T, where

$$T = \frac{M-S}{1+S}$$

The texture parameter T may be computed for each of the three elements in the diagonal of the covariance matrix.

KNOWLEDGE-BASED CLASSIFICATION METHOD

The knowledge-based classification scheme proposed by Pierce et al. [6] uses first the texture parameter T computed from L-HH, L-VV and C-HH and the phase difference between HH and VV at L-band to discriminate urban areas from the remaining areas. In Fig. 2 is shown a scatterplot of the T_{hh} for C-band in April and the φ_{hhvv} for L-band in April. In the scatterplot a single point represent the average value for an entire field. It is seen that the phase difference between HH and VV is not very large for the town class, where phase differences of about 180° and −180° degrees from the double-bounce interaction mentioned

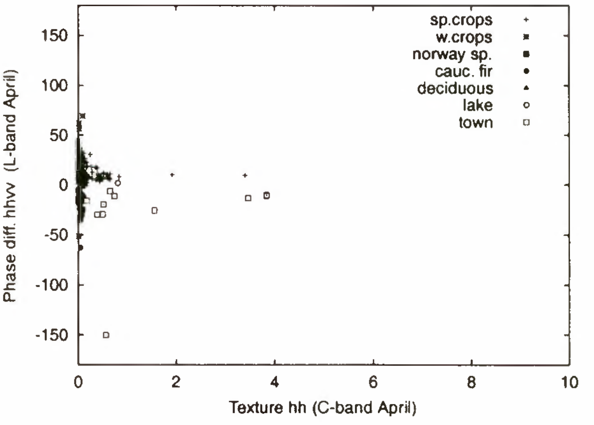

Fig. 2. Scatterplot of T_{hh}(C-April) and φ_{hhvv}(L-April)

above would have been expected, as seen in [6]. The reason is probably that the urban areas present in image are small villages, with a lot of trees and other vegetation types between the buildings, and the double-bounce scattering mechanism is therefore not very dominating. Also, in [3] was reported very large variability of the polarimetric parameters for these village areas. Due to these results no attempt was made in this case to discriminate between urban areas and the remaining areas.

The next decision rule used in [6] was to discriminate

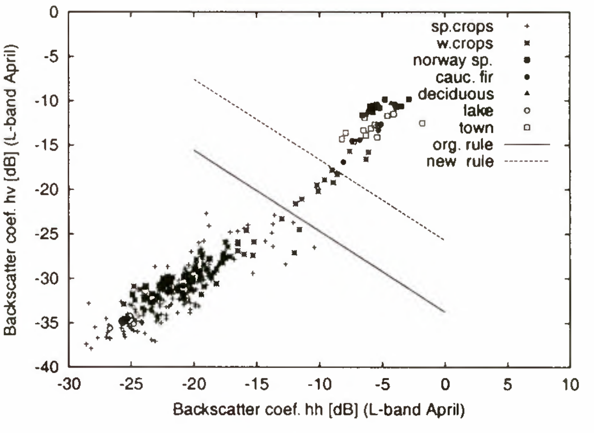

Fig. 3. Scatterplot of γ_{hv}(L-April) and γ_{hh} (L-April)

between tall vegetation and the remaining using the HH and HV backscatter coefficients at L-band. The rationale for this rule is the strong backscatter usually seen from forest areas, as can be seen in Fig. 1. In Fig. 3 is shown a scatterplot of the HH and HV backscatter coefficients at L-band in April. Also, in the scatterplot is plotted the original decision rule from [6] (transformed from the σ backscatter coefficient to the γ backscatter coefficient using $\gamma = \sigma + 2$ dB as an average transformation rule for the incidence angle interval for the images used, 35°-60°). It is seen that a number of winter crops will be classified as tall vegetation using the original decision rule. The winter crop exceeding the decision rule is winter rape, which has a very strong

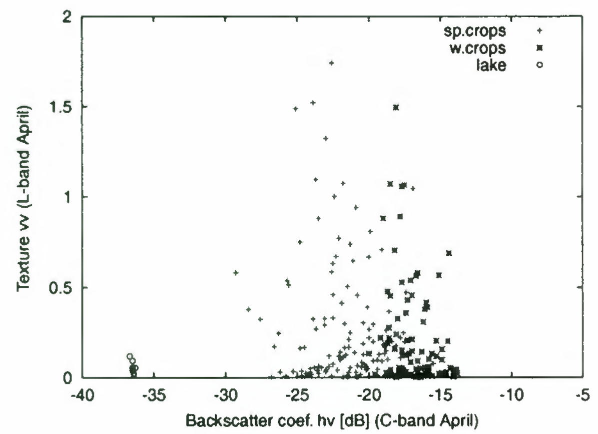

Fig. 4. Scatterplot of γ_{hv}(C-April) and T_{vv} (L-April)

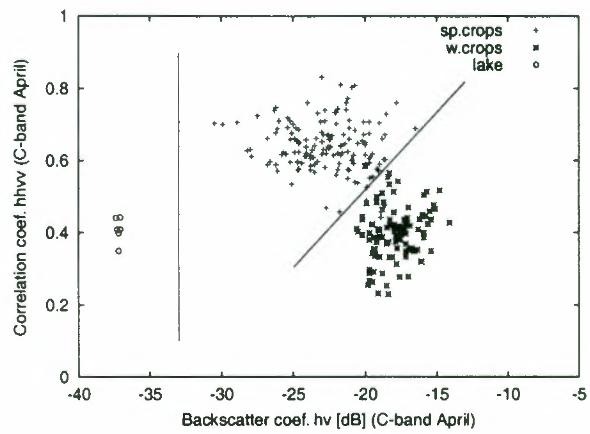

Fig. 5. Scatterplot of γ_{hv}(C-April) and ρ_{hhvv} (C-April)

backscatter [2]. Therefore, the decision rule was modified as shown in Fig. 3. A pixel is classified as tall vegetation, if the following condition is true

$$\gamma^{o}_{hv,L-April} = -0.91 \cdot (\gamma^{o}_{hh,L-April} + 3dB) - 23dB$$

Short vegetation and bare surfaces were separated as the next step in [6]. The bare surfaces were water surfaces and no bare soil surfaces were present. In our case, we have both water surfaces, i.e. the lakes, and bare surfaces in March and April, i.e. spring crops. In [6] the texture parameter T at L-VV and the HV backscatter coefficient at C-band were used to discriminate between the short vegetation and the bare surfaces (i.e. water). The scatterplot between these two parameters is shown in Fig. 4. In [6] the condition on the HV backscatter coefficient at C-band was that it should be larger than –27 dB (corresponding to about –25 dB for the γ backscatter coefficient in our case) for a pixel to be classified as short vegetation. It can be seen from Fig. 4 that this condition will discriminate between the lake and the winter crop (i.e. short vegetation) classes. The bare soil (i.e. spring crops) areas will, however, be mixed both with the lake class and the winter crops classes.

The original decision rule for discriminating between short vegetation and the remaining will therefore be modified to be able to discriminate between lake areas, bare soil areas (spring crops) and short vegetation areas (winter crops). In [2] it is shown that the correlation coefficient between HH and VV is a good discriminator between surface scattering and volume scattering especially at C-band. In Fig. 5 is shown a scatterplot for the HV backscatter coefficient at C-band in April and the correlation coefficient between HH and VV at C-band in April. Also, in the figure is shown the decision rules used to discriminate between the three above-mentioned classes. A pixel is classified as lake, if the following condition is true

$$\gamma^{o}_{hv,C-April} < -33dB$$

A pixel is classified as short vegetation (or winter crop) if the following condition is true

$$\rho_{hhvv,C-April} < 0.043 \cdot \gamma^{o}_{hv,C-April} + 1.38$$

If none of the last two conditions are true, the pixel is classified as bare soil (or spring crop). From Fig. 5 it is seen that some confusion exists between the spring crops and the winter crops. Hence, not a full separation can be expected between the bare soil and the short vegetation classes.

RESULTS

The decision rules described in the previous section were used to classify the EMISAR data acquired in April at both L- and C-band. The April acquisition was chosen because both short vegetation was present as winter crop fields as well as bare soil areas as spring crop fields. The images were classified into the classes: forest (or tall vegetation), winter crops (or short vegetation), spring crops (or bare soil) and lake (or water surfaces). The result of the classification is shown in Fig. 6, and it can be seen that the classification into the 4 broad land-cover classes has been performed fairly successfully.

As mentioned earlier, a large number of areas has been visited and classified on the ground and a land-cover map has been produced. Using this land-cover map a confusion matrix has been produced as shown in Table 1. Very high classification accuracy is seen for the forest and for the lake class. Some confusion is observed between the spring and winter crop areas, as expected from the overlaps seen in Fig. 5. If no attempt is made to discriminate between spring and winter crops extremely good classification accuracy is obtained. These results are comparable with the results reported in [6].

Fig . 6. Knowledge-based classification of L- and C-band EMISAR images from April. (Black areas: forest, dark grey: lake, light grey: spring crops and white: winter crops)

%	Forest	Lake	Spring crops	Winter crops
Forest	99.3	0.0	0.0	0.6
Lake	0.0	99.8	0.2	0.0
Spring cr.	0.5	0.3	77.9	21.3
Winter cr.	4.5	0.0	19.0	76.5

Table 1. Confusion matrix, i.e. percentage of correctly classified pixels for a large number of areas.

CONCLUSIONS

The knowledge-based classification scheme for polarimetric SAR images developed at University of Michigan for land-cover classification has been modified and applied to L- and C-band, polarimetric SAR data from the Danish EMISAR system acquired in April 1998. Two modifications were made. A decision rule was changed to not classify winter rape, which has a strong backscatter, as tall vegetation. In order to be able to discriminate between water surfaces, bare soil surfaces and short vegetation a new decision rule was suggested. This involved the use of the correlation coefficient between HH and VV at C-band mainly to discriminate between bare soil surfaces and areas with short vegetation.

The modified knowledge-based classification scheme was evaluated using a large number of test fields, and a very high classification accuracy was obtained (88%). If the spring crops and the winter crops were merged into a single crop class, an even better classification accuracy was obtained (98%).

ACKNOWLEDGMENT

Development of the EMISAR has been co-sponsored by the Thomas B. Thriges Foundation, the Danish Technical Research Council (STVF), the Royal Danish Air Force, the Technical University of Denmark, and the Joint Research Centre. The data acquisitions and data pre-processing have been sponsored by the Danish National Research Foundation. The Danish ESA Follow-on Research Programme has sponsored part of the work reported in the paper.

REFERENCES

[1] F. T. Ulaby, R. K. Moore, and A. K. Fung, Microwave Remote Sensing: Active and Passive, vol. III, Dedham, MA: Artech House, 1986.

[2] H. Skriver, M. T. Svendsen, and A. T. Thomsen, "Multitemporal C- and L-band Polarimetric Signatures of Crops", *IEEE Trans. Geosci. Remote Sens.*, vol. 37, no. 5, pp. 2413-2429, 1999.

[3] W. Dierking, and H. Skriver, "Change Detection for Topographic Mapping of Airborne Multi-Temporal Polarimetric SAR Imagery", accepted for *IEEE Trans. Geosci. Remote Sens.*, 2001.

[4] J. J. van Zyl, and F. T. Ulaby, "Scattering Matrix Representation for Simple Targets", in F. T. Ulaby and C. Elachi (editors), *Radar Polarimetry for Geoscience Applications*, Norwood, Artech House, Inc. 1990.

[5] J. S. Lee, and M. R. Grunes, "Classification of multi-look polarimetric SAR imagery based on complex Wishart distribution", *Int. J. Rem. Sens.*, vol. 15, pp. 2299-2311, 1994.

[6] L. E. Pierce, F. T. Ulaby, K. Sarabandi, and M. C.Dobson, "Knowledge-based classification of polarimetric SAR images", *IEEE Trans. Geosc. Rem. Sens.*, vol. 32, pp. 1081-1086, 1994.

[7] M. C. Dobson, F. T. Ulaby, and L. E. Pierce, "Land-cover classification and estimation of terrain attributes using synthetic aperture radar", *Remote Sens. Eviron.*, vol. 51, pp. 199-214, 1995.

[8] L. E. Pierce, K. M. Bergen, M. C. Dobson, and F. T. Ulaby, "Multitemporal land-cover classification using SIR-C/X-SAR imagery", *Remote Sens. Environ.*, vol. 64, pp. 20-33, 1998.

[9] P. Ferrazzoli, L. Guerriero, and G. Schiavon, "Experimental and model investigation on radar classification capability", *IEEE Trans. Geosc. Rem. Sens.*, vol. 37, pp. 960-968, 1999.

[10] J. J. van Zyl, "Unsupervised Classification of Scattering Behavior Using Radar Polarimetry Data", *IEEE Trans. Geosc. Rem. Sens.*, vol. GE-27, pp. 36-45, 1989.

[11] S. R. Cloude, and E. Pottier, "An entropy based classification scheme for land applications of polarimetric SAR", *IEEE Trans. Geosc. Rem. Sens.*, vol. 35, pp. 68-78, 1997.

[12] J. S. Lee, M. R. Grunes, T. L. Ainsworth, L. J. Du, D. L. Schuler, and S. R. Cloude, "Unsupervised classification using polarimetric decomposition and the complex Wishart classifier", *IEEE Trans. Geosc. Rem. Sens.*, vol. 37, pp. 2249-2258, 1999.

[13] S. N. Madsen, E. L. Christensen, N. Skou, and J. Dall, "The Danish SAR System: Design and Initial Tests", *IEEE Trans. Geosci. Remote Sens.*, vol. 29, pp. 417-476, 1991.

[14] E. L. Christensen, N. Skou, J. Dall, K. Woelders, A. Netterstrøm, J. H. Jørgensen, J. Granholm, and S. N. Madsen, "EMISAR: Polarimetric L- and C-band SAR", *IEEE Trans. Geosci. Remote Sens.*, vol. 36, pp. 1852-1865, 1998

[15] F. T. Ulaby, D. Held, M. C. Dobson, K. C. McDonald, and T. B. A. Senior, "Relating Polarization Phase Difference of SAR Signals to Scene Properties", *IEEE Trans. Geosci. Remote Sens.*, vol. 25, pp. 83-92, 1987.

[16] F. T. Ulaby, F. Kouyate, B. Brisco, and T. H. Lee Williams, "Textural information in SAR images", *IEEE Trans. Geosci. Remote Sens.*, vol. 24, pp. 235-245, 1986.

DETECTING ANTHROPOGENIC AND NATURAL DISTURBANCES IN WETLAND ECOSYSTEMS WITH MULTITEMPORAL ERS 2 DATA

J.M. Martinez[1], H. Karszenbaum[2], T. Le Toan[1], P. Kandus[3], J. Tiffenberg[2], P. Pratolongo[3], and G. Parmuchi[2]

[1] CESBIO, 18 Ave Edouard Belin, 31055 Toulouse, France
tel: +33 5 61 55 66 71 fax: +33 5 61 55 85 00 *E-mail*: jean-michel.martinez@cesbio.cnes.fr
[2]CONICET - Instituto de Astronomia y Fisica del Espacio (IAFE)
Pabellón IAFE, Ciudad Universitaria (1428), Buenos Aires, Argentina.
tel: +54-11-4783-2642 (Int. 225), fax: +54-11-4786-8114, *E-mail*: haydeek@iafe.uba.ar
[3]Laboratorio de Ecología Regional, Departamento de Biología - Facultad de Ciencias Exactas y Naturales, Universidad de Buenos Aires, Argentina, *E-mail*: pato@bg.fcen.uba.ar

ABSTRACT

Wetlands are areas where the frequent and prolonged presence of water at or near the soil surface drives the natural system. Next to Buenos Aires, the Lower Delta islands of the Paraná River constitute a fresh water wetland characterized by a complex mosaic of natural and man made ecosystems and an hydrologic regime defined by the Paraná and De la Plata rivers. Marshes cover up to 50% of the area, 20% of which are subjected to continues fire events. Monitoring broad-scale ecological responses to disturbance such as fire events can be facilitated by automated change-detection approaches using remotely sensed data. The objective of the work is to detect changes in this wetland using a time-series of ERS 2 data, and relate these changes to wetland characteristics and condition. The data set consisted of 14 ERS images (one of 1998 acquired during a El Niño episode, 6 of 1999 and 7 of 2000 using the 35-day repeat cycle) which were calibrated, co-registered, and temporally and spatially filtered. This presentation discusses temporal patterns of SAR response in the area, and presents a map of fire-disturbed areas.

INTRODUCTION

Wetlands are inherently dynamic systems. As such, monitoring efforts limited to single date of observation are typically insufficient to capture seasonal dynamics related to crucial hydrologic processes and other dynamic conditions. The potential value of SAR imagery has been addressed by several authors, (Richards et al. 1987, Pope et al. 1997, Hess et al., 1990, 1995, Kasischke et al., 1997, Townsend, 2001).

Imaging radars have three distinct characteristics which make them of significant value for monitoring and mapping wetland disturbances. First, the microwave energy transmitted to a large extent penetrates the vegetation canopy, and much of the backscattered energy detected by radars is a result of electromagnetic interactions at the ground layer. Second, the reflection of microwave energy from vegetated terrain is highly dependent on the dielectric constant of the vegetation and surface layers. The presence or absence of water in wetlands (which has a much higher dielectric constant than dry or wet soil) significantly alters the signature detected from these areas. A third important characteristic of imaging radars is their ability to operate independent of cloud cover and solar illumination, and therefore can monitor wetlands throughout periods where significant levels of precipitation are affecting water levels and vegetation growth patterns, as well as other dynamic processes such as fires. These are capabilities not always available with visible and near-infrared spectrum sensors.

Understanding the information content and learning how to exploit the multitemporal backscatter signatures of different types of scatterers in wetland ecosystems is our main goal. Two objectives were addressed: 1) to determine the temporal radar signature of woody and herbaceous ecosystems, 2) to identify and map disturbances through the analysis of temporal patterns of the backscattering coefficient.

Previous work in the area (Kandus et al., 1999, 2001, Parmuchi et al. 2001, and Karszenbaum et al., 2000) helped in establishing the overall framework for analyzing the ERS 2 multitemporal set.

STUDY SITE

The Lower Delta of the Paraná River covers approximately 2,700 km^2. This area is a deltaic plain located at the terminal portion of De La Plata River basin. The Lower Delta hydrology is determined mainly by the Paraná River and the De La Plata estuary. The former has its main flood peak in the period late-fall. The second one has a moon and wind tide regime. The combination of local topographic gradients and a regional flooding regime constitutes the primary factor that determines the emergent natural vegetation. Rushes and marshes cover the main portion of the region (Kandus et al., 1999, Karszenbaum et al., 2000). On the

Proc. 3rd International Symposium, 'Retrieval of Bio- and Geophysical Parameters from SAR Data for Land Applications', Sheffield, UK, 11-14 September 2001 (ESA SP-475, January 2002)

contrary, forests are restricted to levees and bars where soils are generally dry or flooded only during wind tides, and/or heavy fluvial floods. A large portion of the natural vegetation was replaced by *Salix* spp. and *Populus* spp. afforestation. Marshes cover up to 50% of the area, 20% of which are subjected to continues fire events. Fires are intentional for wildlife hunting activities or just to prevent fuel (dried biomass) accumulation. Dominant species of this type of marsh is *Schaenoplectus californicus*, a perennial equisetoid plant, up to 2.5 m tall growing in permanently flooded soils.

DATA DESCRIPTION

This work has been carried out within the framework of ESA AO3 232 project. A set of 14 descending ERS 2 scenes was available, one of 1998 acquired during a El Niño episode, 6 of 1999 and 7 of 2000 using the 35-day repeat cycle. Landsat 5 and 7 Thematic Mapper images, contributed by the Argentine National Agency for Space Activities (Comisión Nacional de Actividades Espaciales – CONAE), were also available, as well as panchromatic aerial photographs, field work, and a vegetation map generated from optical data (Kandus et al., 1999). Ancillary data include water level at Buenos Aires, and Baradero ports, and precipitation data. This information was used to evaluate the influence of climatic conditions on the backscattered radar signal for each land cover considered and for the images as a whole. Reports on fire events were obtained from the National Agricultural Technology Institute and from LANDSAT/TM NDVI time series of dates close to ERS 2 dates.

METHODOLOGY

Extraction of quantitative information from multi-temporal radar images involves several tasks. Figure 1 summarizes the overall methodology indicating input data (ERS 2 images and previous knowledge of the area, ancillary data), processes, and output products. When using multitemporal radar data, it is assumed that

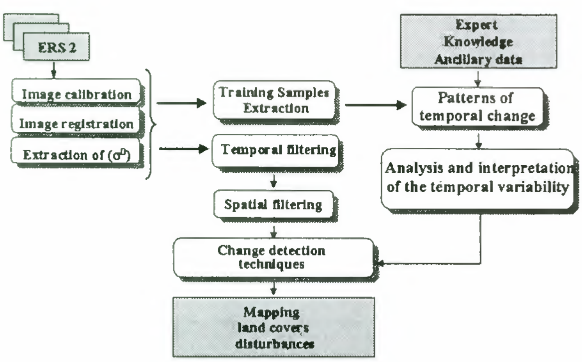

Figure 1: Methodology

information is contained in the multitemporal behavior of the coefficient of backscattering (σ^0). This requires an increase in the effective number of looks (ENL) of radar images and a reduction in the uncertainty of σ^0 values. An advantage of multitemporal data is that both temporal and spatial filtering can be used in order to achieve the required ENL (Quegan et al., 2000). Training samples were extracted from calibrated and co-registered images to obtain the radar response temporal patterns. Changes detection techniques were applied to previously filtered images. Thresholds were obtained from analysis of temporal signatures.

RESULTS AND DISCUSSION

Main land covers in this area are marshes, rushes and forest (natural and planted). Data analysis was made by selecting a wide range of well documented ground samples of each of the main land covers (forest, marshes, rushes, burnt rushes and marshes). To develop an understanding of the canopy characteristics backscatter within the marsh areas and relate these patterns to: coverage, phenology, canopy water content, soil water content, land use, main rivers influence, and proximity to micro-channels, we examined canopy behavior by sites. Figure 2 shows the temporal behavior

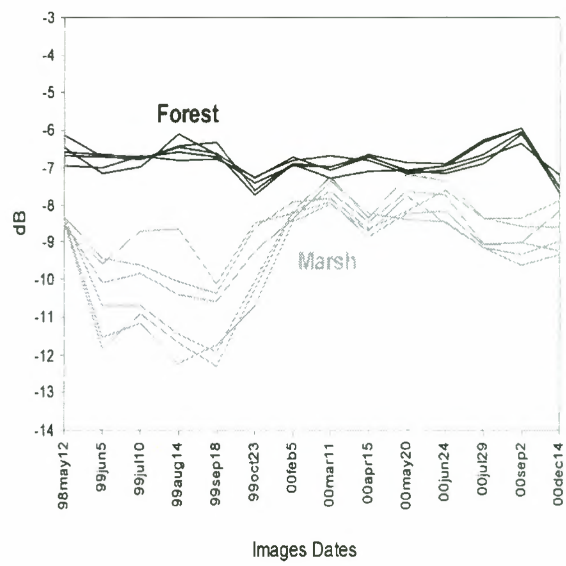

Figure 2: Forest and marshes radar temporal patterns

of the backscattering coeffcient of marshes (about ten different sites), and forest plantations. This graph clearly shows the differences in SAR response between years 1999 and 2000. Forest behavior is quite stable as it has already been reported by a good number of publications. Marshes temporal pattern on the other hand shows a dependence on environmental conditions. About 3 dB difference is observed among the marsh sites during 1999 (dry year). During the wet year (2000) this difference is considerably reduced. One of the hypothesis discussed was that on dry years, sites closer to micro-channels had a higher radar response from stronger vegetation-water interactions.. During the wet year, surface contribution and canopy moisture are probably similar among sites. Although no clear evidences were found to confirm these assumptions.

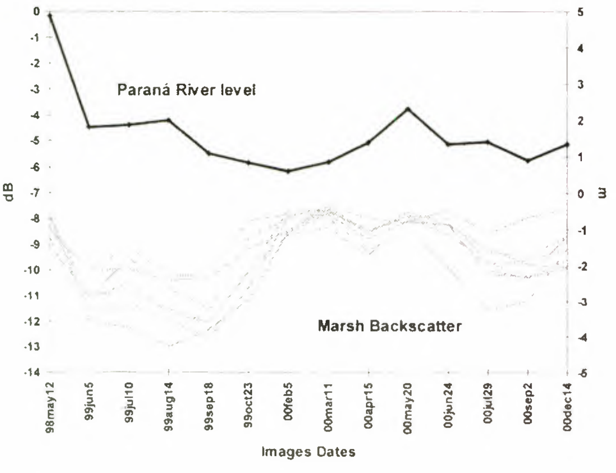

Figure 3: Water level influence on radar response

We next analyzed the relationship between Paraná's river water level and monthly precipitation with radar response of marshes. Figures 3 and 4 illustrate the

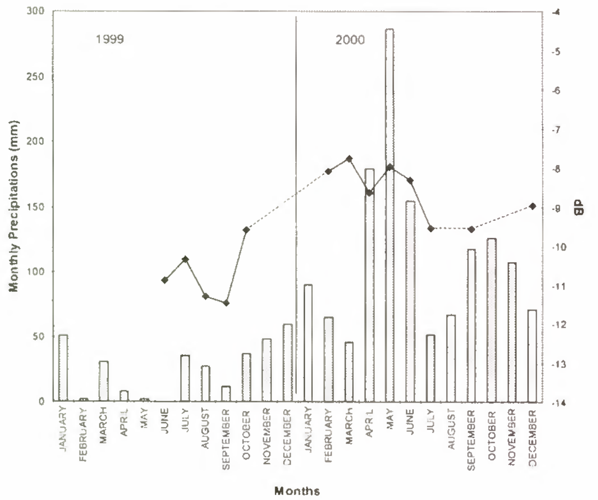

Figure 4: Influence of precipitation pattern on radar response of marshes

observed patterns. No clear influence of water level is observed except for the strong flood of 1998 (El Niño event). On the contrary Figure 4 shows a strong influence of the rain pattern on the radar response from marshes.

During winter time (June-August) marshes present dry and green above ground biomass, causing signal attenuation. This is clearly seen in the images as very dark areas. During the rainy year, vegetation moisture and possible additional surface water caused the increase in the overall radar response in marshes. Marshes are quite sensitive to environmental changes in C VV ERS 2 data, although this was not observed in CHH Radarsat data (Karszenbaum et al., 2000).

In addition, this overall pattern of strong inter-annual rain variability caused a sequence of continuous fires over approximately a six month period (spring and

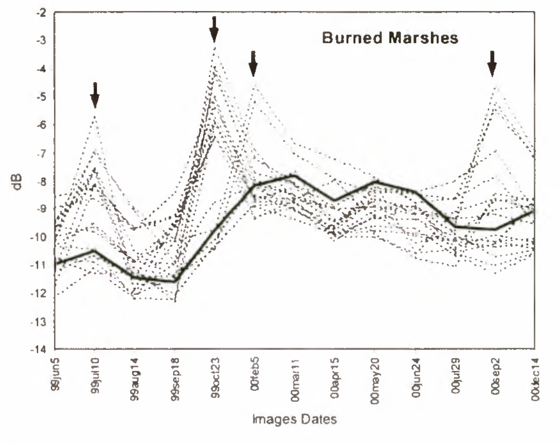

Figure 5: Patterns of burnt-regrowth in marshes. The dark line corresponds to an undisturbed site.

summer) to reduce the risk of unpredictable fires events due to marsh dryness. Fire-disturbed areas show a characteristic radar response in marshes and rushes. The next two figures show strong picks in radar backscatter (over 5 dB differences), indicating patterns of fire and regrowth observed with the 35 days image cycle.

Bourgeau-Chavez et al., 1999 have shown that burned forest typically exhibit enhanced backscatter with average backscatter values between 3 to 6 dB brighter than adjacent unburned forest. Accurate estimates of burn area may be obtained in this way. The enhanced brightness, which allows the fire scars to be easily detected and mapped is due to physical and ecological changes that result from fire. A similar behavior is observed in marshes, but with a temporally much shorter cycle. The effect of burnt vegetation and subsequent regrowth is easily seen in ERS 2 35-day repeat cycle as an enhanced brightness due to an increase in vegetation-water-signal interactions which may indicate a change in the dominant interaction mechanism from volume scattering to double bounce. This is followed by a decrease in SAR response once the marsh recovers its average density. This overall behavior was identified in the multitemporal ERS 2 set available, and fire-disturbed areas were mapped using a ratioing algorithm that combines three scenes, that is, before the pick, during the pick and after the pick. Next using a threshold procedure, the pixels were classified into two classes, burnt or unburned. In this way binary masks were generated from each three image combination. After adding them together, a map of the fire-regrowth patterns of the period was obtained. Figure 6 shows two small subsets of the area, one corresponds to an NDVI scene of April 24 (top image) and the other one to the ERS 2 scene of April 15. Patterns of burnt vegetation are seen in black in the NDVI image and in bright white in the ERS 2 scene. A good matching of patterns is observed. Nevertheless, date of fire, growing stage of vegetation and image acquisition time are critical elements for mapping these

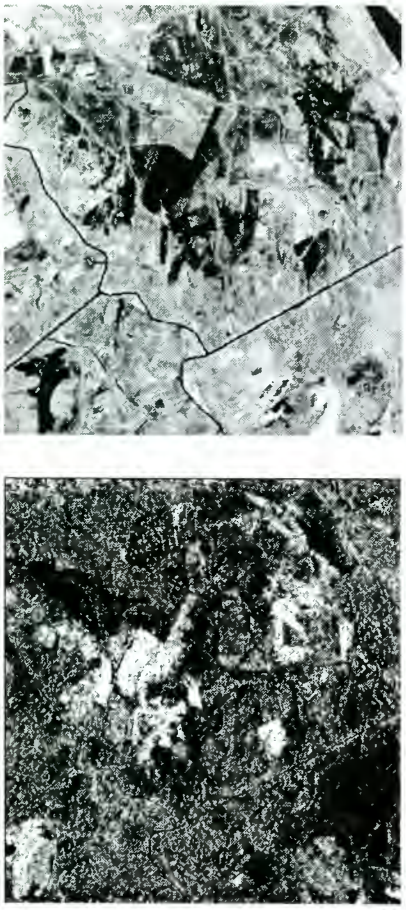

Figure 6: Top image: NDVI of April 24 2000, dark features correspond to burnt areas; botttom image, ERS 2 of April 15, bright features correspond to burnt vegetation.

events with radar data since the proposed mapping procedure is based on tracking areas where in three consecutive 35 days cycle image a pick value of the backscattering coefficient (about a 5 dB difference) is observed in between two lower values (see figure 5). In spite of all these constrains, a good summary of the frequency and extension of this disturbance was obtained. In addition, this is the first time that this fire-regrowth cycle was followed and mapped.

Figure 7 shows in white, polygons of burnt vegetation obtained from the change detection procedure implemented to map all abrupt changes (picks) found in

Figure 7: Polygons of burnt vegetation in white on top of ERS 2 scene of August 1999

the ERS 2 time series. These polygons are shown on top of the ERS 2 winter scene of August 1999 where no fires were detected. Figure 8 shows the complete thematic map obtained. Although this map shows all the

Figure 8: Map of burnt vegetation from ERS 2 SAR time series intensity data

burns in black, the classification procedure allows to map, identify (date) and determine the frequency of events for each fire-regrowth pattern observed.

The analysis of the complete time series reveal that over the period October 1999 - April 2000, 50% of the marshes were continuously burnt. Comparison with vegetation maps previously obtained (Kandus, 1999, Parmuchi, 2001) confirmed this number.

CONCLUSIONS

Although, owing to the characteristics of fire events, a validation map procedure based on test samples could not be developed, information was gathered from local managers of the largest forest plantations who had records of the situation. This informal way of validating the map confirmed its reliability. Procedures are being developed to use an existing LANDSAT/TM NDVI time series of close dates to the ERS 2 time series to validate the map obtained and quantify scope and limitations of the proposed procedure (tracking and mapping spots of abrupt intensity changes in successive images), and make a sensitivity analysis evaluation.

Nevertheless from the assumptions made and the basic concept of the algorithm (threshold scheme classification), it is clear that classification errors will occur in:

- areas that change from non disturbed conditions to disturbed ones, but where the radar backscatter change is less than 5dB.
- areas that were not burnt, but where the radar backscatter change was above 5dB because of other reasons, such as density, and surface water variations in marshes and rushes that may have caused the increase-decrease radar response.

From the results presented here, some general considerations may be drawn:

1. Combinations of images of successive dates (35 day cycle) may considerably improve information extraction from radar images. Although, in this study confusion exists when using single images, the combination of images of different dates faces these limitations suggesting that ERS 2 time series could be useful for monitoring fire events as well as vegetation conditions.
2. This study also illustrates the importance of data preparation (calibration, co-registration and filtering) when using threshold classification schemes for mapping disturbances at regional scale.

ACKNOWLEDGMENTS

This work has been carried out within the framework of ESA AO3 232 project. This research was funded by the Consejo Nacional de Investigaciones Científicas y Técnicas (CONICET) PID 0646/98, University of Buenos Aires and FonCyT/SECyT PICT Ns. 4503, 1417. The authors would like to thank the Comisión Nacional de Actividades Espaciales (CONAE) who provided LANDSAT/TM data, and ESA help desk (eohelp) for providing ERS 2 data and support.

REFERENCES

Bourgeau-Chavez L.L., Kasischke E. S and Rutherford M. D., (1999); Evaluation of ERS SAR Data for Prediction of Fire Danger in a Boreal Region. *International Journal of Wildland* Fire 9 (2): 183-194.

Hess L.L., Melack J. M., and Simonett D.S., (1990); Radar detection of flooding beneath the forest canopy: A review. *International Journal of Remote Sensing* 11 (7): 1313-1325.

Kandus P., Karszenbaum H. and Frulla L.A. (1999); "Land cover classification system for the Lower Delta of the Paraná River (Argentina): Its relationship with Landsat Thematic Mapper spectral classes". *Journal of Coastal Research* 15 (4): 909-926.

Kandus, P., Karszenbaum H., Pultz T., Parmuchi M. G., & Bava J., (2001); Influence of flood condition and vegetation status in the radar backscatter of wetland ecosystems. Analysis of multi-temporal/multi-angle RADARSAT SAR data. *Canadian Journal of Remote Sensing*. Accepted.

Karszenbaum, H., P. Kandus, M. Martinez, T. Le Toan, J. Tiffenberg, & M. G. Parmuchi, (2000); ERS-2, RADARSAT SAR backscattering characteristics of the Paraná River Delta Wetland, Argentina. *ESA publication SP-461*.

Kasischke, E., and Bourgeau-Chavez L. (1997); Monitoring South Florida Wetlands Unsing ERS-1 SAR Imagery. *Photogrammetric Engineering & Remote Sensing*. 63 (3): 281-291.

Quegan S., Le Toan T., Yu J.J, Ribbes F. and Floury N. (2000); Multitemporal ERS SAR Analysis Applied to Forest Mapping. *IEEE Transactions on Geoscience and Remote Sensing*. In press.

Parmuchi G., Karszenbaum, H., Kandus P.; Mapping Wetlands using multi-temporal RADARSAT data and a Decision based classifier. Submitted to the *Canadian Journal of Remote Sensing*.

Pope K. O., E Rejmankova, J. F. Paris, and R Woodruff; 1997. Detecting Seasonal Flooding Cycles in Marshes of the Yucatan Peninsula with SIR-C Polarimetric Radar Imagery. *Remote Sensing of Environment* 59: 157-166.

Richards, J. A., P. W. Woodgate, A. K. Skidmore; 1987. An explanation of enhanced backscattering from flooded forest. *International Journal of Remote Sensing*, 8, 1093-1100.

Townsend, P. A., 2001. Mapping Seasonal Flooding in Forested Wetlands Using Multitemporal Radarsat SAR. *Photogrammetric Engineering and Remote Sensing*, 67, 857-864.

ESA CO-ORDINATION FOR THE SCIENTIFIC EXPLOITATION OF ERS AND ENVISAT DATA

S. Rémondière*, Y.L. Desnos**, M. Borgeaud***, F. Palazzo*

* SERCO support to ESA ESRIN, Earth Observation Exploitation Development and Project Division
Tel: 39 06 941 80 686, Fax: 39 06 941 80 622, email: sylvie.remondiere@esa.int

** ESA ESRIN, Earth Observation Exploitation Development and Project Division

*** ESA ESTEC, Electromagnetics Division

Abstract

In 1998, the European Space Agency (ESA) has selected about 670 project proposals for the scientific exploitation of Envisat data, in addition to the on-going 270 ERS projects resulting from previous ESA Announcement of Opportunity. Within the new Data Policy for ERS and Envisat data distribution, scientists can submit a proposal at any time for category-1 use. The so-called Category-1 use is assigned to research and applications development projects in support of the mission objectives, including research on long term issues of Earth System science, research and development in preparation for future operational use.

All information submitted by the category 1 Project Leader to ESA is available to the Project Correspondent, an ESA expert appointed to follow closely a number of projects in a given discipline or geographic area. The correspondent is the ESA focal point with whom not only to raise technical matters, specific to individual projects, but also to discuss broader issues related to progress in research and development, science and application domains.

This paper will describe how ESA is monitoring the category-1 projects, including the AO projects. Example of actions in support to land applications using ERS and Envisat data will be presented.

1 Introduction

Over the last ten years ESA has released 6 Announcements of Opportunity to exploit ERS and now Envisat satellite data, with the goal to foster scientific knowledge and understanding of the Earth's environment. The primary objectives of all the AOs were to support scientific research, stimulate the development of algorithms and products and to support application demonstrations. Furthermore they allowed stimulating the transfer of scientific results into sustainable applications/services and to support the transfer of technology.

This paper is reporting on ESA's activity to support the scientific exploitation of ERS and Envisat satellite data. In a first part, the status of the on-going Announcement of Opportunity, namely the ERS AO3 and the Envisat AO are presented as well as ESA support to science and applications through the new data policy. In particular, Envisat AO projects for land applications are described. In a second part, we will describe how ESA is monitoring the projects proposed by scientific investigators distributed across the world.

2 About the scientific exploitation of ERS and Envisat data

2.1 Announcement of Opportunity

In October 1998, the results of the review of the 734 proposals submitted in response to the Envisat AO have been presented at the Earth Observation Programme Board (PB-EO), formalizing the final acceptance of 674 proposals. (A list of accepted proposals is available on the World Wide Web at http://esa-ao.org/accepted.pdf). The Envisat proposals are added to the on-going ERS projects resulting from previous AOs.

More than 40 different countries submitted proposals, subdivided in the three main categories defined from the Envisat AO objectives, namely:

- Scientific research
- Application development and demonstration
- Calibration and geophysical validation of Envisat data products

The repartition of the accepted proposals in these categories reveals that the large majority (64%) fails within the scientific domain, whilst 18% of the projects deals with calibration and validation of Envisat products and 18% with application development and demonstration.

Proc. 3rd International Symposium, 'Retrieval of Bio- and Geophysical Parameters from SAR Data for Land Applications', Sheffield, UK, 11-14 September 2001 (ESA SP-475, January 2002)

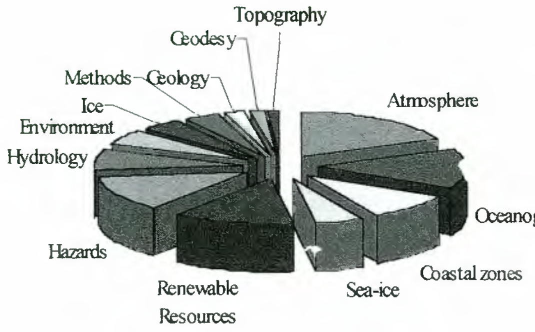

Figure 1: Thematic distribution of scientific projects

The interdisciplinary character of the Envisat mission is highlighted by the earth sciences disciplines identified in the AO proposals in figure 1. For example, Envisat data will be extensively used in studies dealing with oceanography, atmosphere, renewable resources and hazards.

2.2 The ERS and Envisat scientific projects related to Land

The large majority (66%) of the Envisat AOs for land applications deals with the study of renewable resources, hazards and hydrology, as shown in the figure 2.

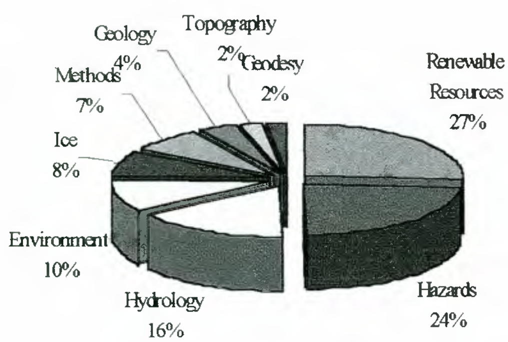

Figure 2: Thematic distribution of Envisat AO land projects

A detailed analysis of the scientific projects receiving ESA Earth observation data sets has been performed during the ESA Gothenburg Symposium, in October 2000. 175 project investigators gave their feedback on the ERS/Envisat data exploitation. Some results for the ERS/Envisat projects related to land applications are presented at the end of the paper.

The monitoring of changes in environmental processes is the main goal of the projects. It requires frequent observations from local to global scales. With its ten on board instruments the Envisat mission will provide new capabilities for Earth observation.

From a preliminary statistical analysis of data requirements of the accepted Envisat AO scientific projects for land applications it is clear that the synergistic use of sensors will be an important issue. The following figure is showing request for ASAR, MERIS and both ASAR and MERIS data for each application domain:

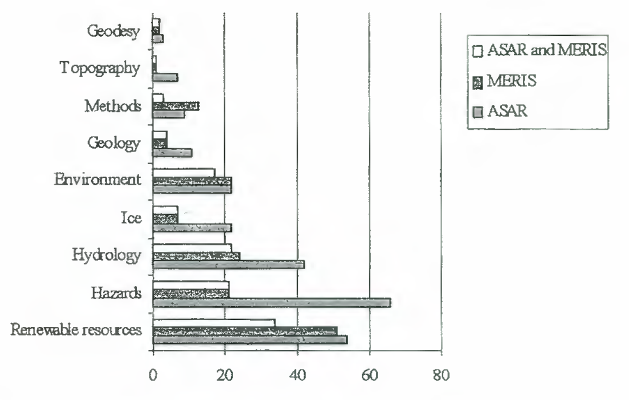

Figure 3: Envisat AOs: Number of projects per instrument and synergy

Continuity of observations from the ERS SAR to the Envisat ASAR is confirmed from the analysis of requested product types: ASAR image mode is the preferred product type for applications dealing with topography, ice, hazards and environment. The use of ASAR alternating polarisation is also a main issue: this mode is the first requested for renewable resources, hydrology and geology. The synergy with MERIS is tested on MERIS full resolution products.

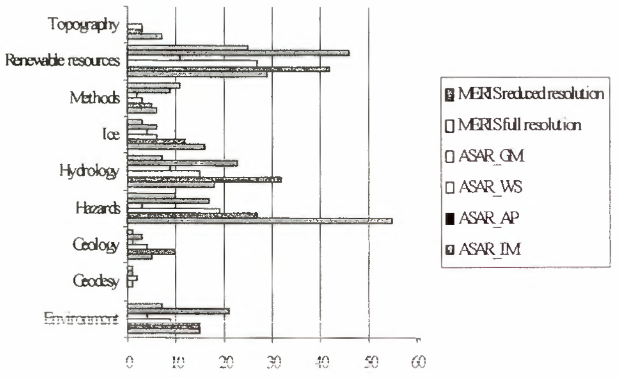

Figure 4: Envisat AOs: Number of project per product types

3 Since 2000, the category-1 use of data

The new Earth observation data policy

The possibility to conduct scientific researches using data provided from ESA continues beyond the Envisat AO. The new Data Policy, applicable for ERS and Envisat allows in fact submitting proposals at any time beyond the fixed dates imposed by an Announcement of Opportunity. The new Policy has been defined and approved by ESA Member States' Earth Observation Programme Board in 1998 and 1999 and aims to maximize the beneficial use of EO data from both ERS and Envisat satellites to stimulate a balanced development of Science, Public Utility and Commercial Applications.

According to the new Data Policy the conditions of data distribution for ESA EO data are directly related to category use. Two different categories have been defined:

- Category 1 use: research and applications development use in support of the mission objectives, including research on long term issues of Earth System science, research and development in preparation for future operational use, certification of receiving stations as part of the ESA functions, and ESA internal use.
- Category 2 use: all other users who do not fall into Category 1, including operational and commercial use.

ESA management of the Category 1 project proposals

A new Web site has been set up at http://projects.esa-ao.org for category-1 use. It enables the submission of proposals for category 1 use, the proposal evaluation and project reporting. The proposal submitted shall include the following items:

- Team composition, experience and innovation
- Executive summary and schedule
- Detailed description
- Data requirements: instruments and products, non ESA data, geographical area and date information.

After the receipt of the project proposal, a peer review is carried out by members of the Category 1 Advisory Group composed of EO experts appointed by ESA. The purpose of the review by the Category 1 Advisory Group is:

- To assess if the specific projects are in accordance with ESA data policy.
- To evaluate the scientific, application and technical merits of the proposed projects in relation to their technical feasibility.
- Within the overall context of the ESA Earth Observation mission objectives, the evaluation process is expected to identify opportunities to exploit the potential of the ESA Earth Observation mission.

In some cases the principal investigator is required to amend his proposal in order to meet the acceptance criteria and in accordance with the remarks expressed by the evaluators.

Final decisions concerning the acceptance of proposals for projects applying to the supply of free of charge data are made by the ESA Earth Observation Programme Board upon recommendation of Category 1 evaluators. Final decisions concerning the acceptance of proposals for projects applying to the supply of data at the reproduction price are made based on the recommendation of the Category-1 Advisory Group. These final decisions take into account the relevance to ESA Earth Observation mission of proposed projects, the overall balance between the different proposals and their requirements in terms of spacecraft resources.

Status of the Category 1 projects (August 2001)

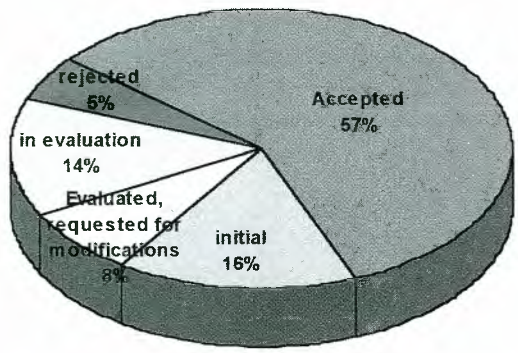

Figure 5: Category 1 project status

Since the opening of the ESA EO Projects Web Site dedicated to the submission/evaluation/monitoring of the new Category 1 projects some 98 proposals have been submitted: 16 are under Peer Review, 82 proposals have been evaluated. Out of the 82 evaluated proposals, 67 have been accepted, 6 have been rejected and 9 proposals are being updated according to the recommendation of the Category 1 Advisory Group. 18 proposals are still under preparation for submission by their Project leaders.

The maximum evaluation time for a proposal asking for data at reproduction costs generally does not exceed the 8 weeks.

4 The category-1 projects monitoring

The Agency has established a systematic process to monitor progress on projects. This has been developed for the ERS AO3 projects and has been active since November 1998.

Project correspondent

The key monitoring mechanism is a close and effective interaction with each project leader, throughout all phases of the projects. For this reason an ESA "Project Correspondent" is assigned for each Category 1 project, including the ERS or Envisat AOs.

All information submitted by the Project Leader to ESA is available to the Project Correspondent, an ESA expert appointed to follow closely a number of projects in a given discipline or geographic area. The correspondent is the ESA focal point with whom not only to raise technical matters, specific to individual projects, but also to discuss broader issues related to progress in research and development, science and application domains. This additional support to users complements the operational user services.

The Project Correspondent maintains regular contacts with project leaders on an individual basis. He analyses the reporting of the project investigators in order to report on project achievements, to highlight problems and issues, to contribute to ESA EO data promotion and to generate technical recommendations (e.g. for new products). He assesses content of the materials proposed from PIs for the public part of the Web site. He organises thematic sessions for ESA major conferences. In addition to these tasks, the Project Correspondent should facilitate exchanges between users, e.g. setting up groups of investigators with very similar interest or research goal to enable shared activities.

An example of ESA co-ordination to monitor scientific projects

A co-ordination method is proposed for the Envisat AO proposals related to the retrieval of soil moisture in the framework of the Envisat project correspondent scheme. The aim is to harmonise the collection of in-situ data with contemporaneous Envisat data acquisition, followed by a close monitoring and co-ordination of the research proposed by the project investigator in order to develop new applications and products.

Web site

The category-1 Web site (EO Projects Web-site at http://projects.esa-ao.org), active since September 2000, is used as a tool for projects monitoring.

It contains a Public site providing general information about ESA EO programmes and in particular about each project. It also contains a Private site, where all the produced reports, materials or publications can be stored and submitted on-line to ESA by the Project Leader. A correspondent site provides each correspondent a direct access to assigned projects, project proposals and all reports submitted on-line.

Reporting and publishing results

ESA is supporting quick publication/promotion of the interesting results of the ESA AO scientific projects. Each Project Leader can request to publish the achievements of his project as "Hot News" on the Public Site. In this way the public and ESA member states are informed about the latest findings from ESA

Theme	Main goal	Main parameter to retrieve	Main sensor characteristics used (SAR/ASAR)	1rst choice of improvement for SAR/ASAR	Main processing technique used with SAR/ASAR	Models used to extract information
Earth motion, earthquakes, geology, landslides, volcanoes	• Monitoring • Mapping	• Location of landscape • Landscape changes • Displacements • Soil moisture	Spatial resolution	Interferometric capability	Interferometry	Theoretical
Hydrology	• Mapping • Monitoring • Parameter retrieval		• Spatial resolution • Temporal resolution	Polarimetric multi-frequency	SAR multi-temporal analysis	Semi-empirical
Forestry, vegetation, agriculture	• Monitoring • Mapping		• Frequency • Spatial resolution	Polarimetric multi-frequency	SAR multi-temporal analysis	Semi-empirical
Land cover/Land use	Mapping		• Spatial resolution • Frequency	Revisit time	• SAR multi-temporal analysis • Interferometry • Texture analysis • SAR/optical combination	None

Table 1: Description of the ERS/Envisat land scientific projects

EO data use. Searching facilities such as browse by application, instrument, country, test site, Project Leader's name, institute, project title, objective and other keywords allow all the users to retrieve information about the EO projects.

Thematic workshops and conferences

In the exploitation phase of the Envisat mission the Agency with its Project Correspondents will organize a number of thematic workshops which will give the Project Leaders the opportunity to present results of their on-going AO research project activities and to discuss the state-of -the art in their respective earth sciences discipline. Position papers, progress reports on on-going projects and demos of running application prototypes will constitute the main form of communication in these workshops. One of the primary objectives is to foster the development of cross disciplinary and cross regional research activities and to encourage the development of innovative research ideas leading to new research projects or application developments. Good examples of more recent ESA-organised (& co-organised) are Fringe (November 99, Liege, ESA SP478), CEOS SAR subgroup (October 99, Toulouse, ESA SP450), ATSR workshop (June 99, ESRIN, ESA SP479). These workshops are complemented by ESA symposia like the ERS-Envisat symposium held in October 2000 in Gothenburg (ESA SP461), which has attracted a large audience and is presented in ESA Bulletin nr.105.

5 Conclusion

The work of the scientists within the framework of ESA category-1 data is the core process for scientific research and exploitation and foster the development of new applications in the field of Earth observation. The new Data Policy allowing to submit to ESA at any time new proposals will increase further flexibility to access Envisat data for scientific use.

The Agency's co-ordinated support to the Project Leaders with the correspondent scheme, the ESA EO Projects Web Site and the organisation of thematic workshops should further sustain the development of science, stimulate the development of algorithms and products and support application demonstrations.

Reference documents

Highlights of the ERS-Envisat Symposium 2000- The achievements of ESA's Earth Observation Programme. ESA Bulletin 105, February 2001.

Research Activities in response to the Announcement of Opportunity. . ESA Bulletin 106, June 2001.

User Feedback on ERS/Envisat Data Exploitation. Results of the Questionnaire Distributed at the ESA Gothenburg Symposium. March 2001, APP/AEU2001.004-D.

The Envisat AO soil moisture projects survey, Technical Note, 2001, TOS-EEP/2001.03/MB.

Hazards and DTM

Chairman: G. Wadge

SEISMIC FAULTS ANALYSIS IN CALIFORNIA BY MEANS OF THE PERMANENT SCATTERERS TECHNIQUE

Carlo Colesanti, Alessandro Ferretti, Claudio Prati and Fabio Rocca

Dipartimento di Elettronica e Informazione, Politecnico di Milano
Piazza Leonardo da Vinci, 32 -20133 Milano, Italy
Tel: ++390223993573 Fax: ++390223993413 E-mail: rocca@elet.polimi.it

ABSTRACT

Spaceborne differential radar interferometry (1-4) has already proven its potential for mapping ground deformation phenomena in application to, among others, volcano dynamics (5), co-seismic (6-7) and post-seismic (8-10) displacements of faults and slope instability (11). However, atmospheric disturbances (12-16) as well as phase decorrelation (17) have prevented hitherto this technique from achieving full operational capability. These drawbacks are overcome by carrying out measurements on a subset of image pixels corresponding to natural or artificial stable reflectors (Permanent Scatterers, PS) and exploiting temporal series of interferometric data (18-19). Results obtained by processing 55 Synthetic Aperture Radar acquisitions of ERS satellites (European Space Agency) over Southern California, show that this approach allows one to push measurement accuracy very close to its theoretical limit of one millimetre. Though a full 3D displacement field cannot be recovered, the spatial density of measurements (up to 300 PS/km^2), their accuracy and economic competitiveness, are far higher than corresponding values achievable with static GPS (20). PS time series analysis is therefore a powerful tool for risk assessment and is going to contribute significantly to improve our understanding of fault dynamics, stress accumulation and strain accommodation, evolution of soils, as well as systematic stability check of individual buildings and infrastructures.

INTRODUCTION

The interferometric technique involves phase comparison of Synthetic Aperture Radar (SAR) images, gathered at different times with slightly different looking angles (1-4). It has the potential to detect millimetric target displacements along the sensor-target (Line-of-Sight, LOS) direction. Apart from cycle ambiguity problems, limitations are due to temporal and geometrical decorrelation (17), and to atmospheric artefacts (12-16).

Temporal decorrelation makes interferometric measurements unfeasible where the electromagnetic profiles and/or the positions of the scatterers change with time within the resolution cell. The use of short revisiting times in not a solution, since slow terrain motion (e.g. creeping) cannot be detected. Reflectivity variations as a function of the incidence angle (i.e. geometrical decorrelation) further limit the number of image pairs suitable for interferometric applications, unless this phenomenon is reduced due to the point-wise character of the target (e.g. a corner reflector). In areas affected by either kind of decorrelation, reflectivity phase contributions are no longer compensated by generating the interferogram (17), and possible phase variations due to target motion cannot be highlighted (2). Finally, atmospheric heterogeneity superimposes on each SAR image an atmospheric phase screen (APS) that can seriously compromise accurate deformation monitoring (2, 12). Indeed, even considering areas slightly affected by decorrelation, it may be extremely difficult to discriminate displacement phase contributions from the atmospheric signature, at least using individual interferograms (2, 12, 21).

THE PERMANENT SCATTERERS TECHNIQUE

Atmospheric artefacts show a strong spatial correlation within every single SAR acquisition (13-15), but are uncorrelated in time. Conversely, target motion is usually strongly correlated in time and can exhibit different degrees of spatial correlation depending on the phenomenon at hand (19) (e.g. subsidence due to water pumping, deformation along seismic faults, localised sliding areas, collapsing buildings, etc.). Atmospheric effects can then be estimated and removed by combining data from long time series of SAR images (18, 19), as those in the ESA-ERS archive, gathering data since late 1991. In order to exploit all the available images, and improve the accuracy of APS estimation, only scatterers slightly affected by both temporal and geometrical decorrelation should be selected (18, 19).

Phase stable point-wise targets, hereafter called Permanent Scatterers (PS), can be detected on the basis of a statistical analysis on the amplitudes of their electromagnetic returns (18).

All available images are focused and co-registered on the sampling grid of a unique master acquisition, which should be selected keeping as low as possible the dispersion of the normal baseline values. In order to make comparable the amplitude returns relative to different acquisitions, radiometric correction is carried

Proc. 3rd International Symposium, 'Retrieval of Bio- and Geophysical Parameters from SAR Data for Land Applications', Sheffield, UK, 11-14 September 2001 (ESA SP-475, January 2002)

out through power normalisation. Then, amplitude data are analysed on a pixel-by-pixel basis (without spatial averaging) computing the so-called amplitude stability index (18, 19), i. e. the ratio between the average amplitude return relative to each individual pixel and its standard deviation. The amplitude stability index lets infer precious information about the expected phase stability of the scattering barycentre of each sampling cell (18). Simple thresholding (e.g. with a value of 2.5-3) on the amplitude stability index allows the identification of a sparse grid of Permanent Scatterers Candidates (PSC), points that are expected having a PS behaviour. (PSC are actually a small subset of the PS as a whole, since the phase stability of many PS cannot be inferred directly form the amplitude stability index).

Exploiting the Tandem pairs, a conventional InSAR Digital Elevation Model can be reconstructed (1, 22). In alternative an already available DEM can be re-sampled on the master image grid.

Given N+1 ERS-SAR data, N differential interferogram can be generated with respect to the common master acquisition. As already mentioned, since Permanent Scatterers are not affected by decorrelation, all interferograms, regardless of their normal and temporal baseline can be involved in the PS processing.

The phase of interferogram i is:

$$\phi_i = \frac{4\pi}{\lambda} r_{Ti} + \alpha_i + n_i + \phi_{topo-res} \tag{1}$$

where λ = 5.66 cm, r_{Ti} is the possible target motion (with respect to its position at the time of the master acquisition), α_i is the atmospheric phase contribution, n_i is the decorrelation noise $\phi_{topo-res}$ is the residual topographic phase contribution due to inaccuracy in the reference DEM.

Goal of the PS approach is the separation of these phase terms. The basic idea is to work on the PSC grid computing in each interferogram i the phase difference $\Delta\phi_i$ relative to pairs of PSC within a certain maximum distance (e.g. 2 km).

In fact, since APS is strongly correlated in space, the differential atmospheric phase contributions relative to close PSC will be extremely low (for points less than 1 km apart $\sigma_{\Delta\alpha}^2$ is usually lower than 0.1 rad^2 (14)).

The phase difference relative to close PSC is, therefore, only slightly affected by APS.

Moreover, if both PSC, effectively exhibit PS behaviour (i.e. are not affected by decorrelation), n_i and, consequently, Δn_i will show a very low variance as well.

Assuming the target motion is uniform in time (i. e. constant rate deformation), the first term in (1) can be written as $(4\pi/\lambda)vT_i$, where v is the average deformation rate along the ERS Line of Sight (LOS) and T_i is the temporal baseline with respect to the master acquisition.

For a couple of PSC (1,2), respectively in positions (n_1,m_1) and (n_2,m_2), the phase difference in each interferogram i is:

$$\Delta\phi_{1,2,i} = \frac{4\pi}{\lambda}\Delta v_{1,2}T_i + K_\varepsilon \Delta\varepsilon_{1,2}B_{n,i} + w_{1,2,i} \tag{2}$$

where $\Delta v_{1,2}$ and $\Delta\varepsilon_{1,2}$ are the differential LOS velocity and the differential DEM inaccuracy relative to the PS couple at hand. $B_{n,i}$ is the normal baseline relative to interferogram i and $w_{1,2,i}$ is the residual phase term, gathering decorrelation noise, differential APS and possible time non-uniform deformation.

Since N differential interferograms are available, for each couple of PSC we are facing N equations in the unknowns $\Delta v_{1,2}$ and $\Delta\varepsilon_{1,2}$. Unfortunately the phase values $\Delta\phi_{1,2,i}$ are wrapped, and, therefore, the system is non-linear. In fact, even if no deformation is occurring, the differential residual topographic phase will often exceed one phase cycle in large baseline interferograms (e. g. for a 1200 m baseline interferogram the ambiguity height is around 7.5 m).

The unknowns can be estimated in a ML sense as the position ($\Delta v_{1,2}$,$\Delta\varepsilon_{1,2}$) of the peak in the periodogram of the complex signal $e^{j\Delta\phi(1,2,i)}$ (which is actually available on an irregular sampling grid in both dimensions temporal and normal baseline, T_i and $B_{n,i}$).

Of course this is feasible only as long as $w_{1,2,i}$ is low enough.

As soon as $\Delta v_{1,2}$ and $\Delta\varepsilon_{1,2}$ are available, the phase differences $\Delta\phi_i$ can be unwrapped correctly (of course assuming $|w_{1,2,i}|<\pi$). Integrating the unwrapped phase differences relative to every couple of PSC, each interferogram can be unwrapped in correspondence of the sparse PSC grid.

Moreover $\Delta v_{1,2}$ and $\Delta\varepsilon_{1,2}$ can be integrated as well (assuming $v = v_0$ and $\varepsilon = \varepsilon_0$ for a reference point), obtaining v and ε.

The unwrapped atmospheric phase contribution relative to each PSC can be obtained as the difference:

$$[\alpha_i]_{uw} = [\phi_i]_{uw} - \frac{4\pi}{\lambda}vT_i - K_\varepsilon \varepsilon B_{n,i} \tag{3}$$

Of course, eventual time non-uniform deformation phenomena with a spatial low-pass character analogous to the one of APS are, so far, wrongly interpreted as atmospheric artefacts. The two phase contributions exhibit, however, a different behaviour in time: APS is uncorrelated whereas non-linear motion (NLM) is usually strongly correlated.

Assuming a time decaying exponential correlation for NLM, corrected with a 1 year periodic term (for possible NLM seasonal effects), APS and time non-uniform deformation can be separated at PSC, through Wiener filtering along time dimension (taking account of the irregular sampling in time, induced by missing ERS acquisitions).

Due to the high spatial correlation of APS, even a sparse grid of PSC enables to retrieve the atmospheric components on the whole of the imaged area, provided that the PS density is larger than 3-4 PS/km^2 (14). Kringing interpolation (23) allows optimum filtering and re-sampling of APS on the regular SAR grid of ERS differential interferograms.

Even though precise state vectors are available for ERS satellites (24), the impact of orbit indeterminations on the interferograms cannot be neglected (19). Estimated

APS is actually the sum of two contributions: atmospheric effects and orbital fringes due to baseline errors (19). However, the latter correspond to low-order phase polynomials and do not change the low-wavenumber character of the signal to be estimated on the sparse PS grid.
Differential interferograms are compensated for the retrieved APS (actually APS + orbit indetermination phase term), and the same v, ε estimation step, previously carried out only at PSC and on phase differences, can now be performed working on APS corrected interferograms on a pixel-by-pixel basis, identifying all Permanent Scatterers.
Of course, a sufficient number of images should be available (usually at least 25-30), in order to properly identify PSC and correctly estimate $\Delta v_{1,2}$ and $\Delta \varepsilon_{1,2}$.
At the PS, sub-metre elevation accuracy (due to the wide dispersion of the incidence angles available, usually ± 70 millidegrees with respect to the reference orbit) and millimetric terrain motion detection (due to the high phase coherence of PS) can be achieved, once APSs are estimated and removed (18, 19). In particular, the relative target LOS velocity can be estimated with unprecedented accuracy (sometimes even better than 0.1 mm/yr., exploiting the long time span on very stable PS). The higher the accuracy of measurements, the more reliable the differentiation between models of the deformation process under study (20), a key issue for risk assessment.
Final results of the multi-interferogram Permanent Scatterers approach are (18, 19):

- Map of the PS identified in the image and their co-ordinates: latitude, longitude and precise elevation (accuracy on elevation better than 1m);
- Average LOS deformation rate of every PS (accuracy between 1 and 0.1 mm/yr., depending on the number of available interferograms and on the phase stability of each single PS);
- Displacement time series showing the relative (i.e. with respect to a selected unique reference image) LOS position of PS in correspondence of each SAR acquisition. Time series identify therefore the LOS motion component of PS as a function of time (accuracy on single measurements usually ranging from 1 to 3 mm).

As in all differential interferometry applications, results are computed with respect to a reference point of known elevation and motion.

RESULTS

In Fig. 1 is displayed a perspective view of the LOS velocity field estimated exploiting 55 ERS acquisitions from 1992 to 1999 over Southern California. More than 500,000 PS were identified, with an average density of as many as 150 PS/km^2. The reference point, supposed motionless, was chosen at Downey (in the centre of the test site, 20 km SE of downtown Los Angeles), referring to the data of a permanent GPS station of the Southern California Integrated GPS Network (SCIGN) (25).
Apart from subsidence phenomena due to oil and gas extraction (26) and water pumping (19), clearly visible in the picture, local maxima of the velocity field gradient are strongly correlated to the map of known active faults in the area (27). The position of hanging walls can be inferred very precisely whenever a high density of accurate measurements is available (Fig. 2). In particular, the velocity field shows local abrupt variations that correlate well with blind thrust faults (28, 29), that is, shallow-dipping reverse faults that (i) terminate before reaching the surface, (ii) exhibit millimetric yearly slip rates and (iii) are difficult to locate and map before occurrence of co-seismic displacements along them. Identification and monitoring of blind thrusts faults is therefore a crucial challenge for reliable seismic risk assessment. The velocity field mapped in Fig. 1 shows a local gradient near central Los Angeles in very good agreement with the estimated location and slip-rate of the so-called Elysian Park blind thrust fault (28). Further velocity field discontinuities have been identified in the area where recently was claimed the identification of the Puente Hills blind thrust (29).
The comparison with displacement time series relative to eleven GPS stations of the SCIGN (25, 30) (Table 1 and Fig. 3), gathering data since at least 1996 (for a reliable estimation of target velocity), highlights good agreement and allows to appreciate the main differences: the PS technique shows about one order of magnitude better accuracy than static GPS, and allows for much higher spatial sampling (hundreds of benchmarks per square kilometre, revisited every 35 days). However, SAR displacement data are not 3D, and the temporal resolution of GPS and spaceborne SAR are not comparable: this calls for a synergistic use of SAR data (world-wide, with monthly frequency) and GPS data (where and when available). It is worth noting that combination of SAR data relative to both ascending and descending satellite overpasses improves significantly the results nearly doubling the PS density, reducing the time interval between two passes, and allowing the retrieval of 2D displacement along both vertical and east-west direction (with different accuracy values).
The sensitivity of SAR and GPS are complementary each other to some extent. Indeed, SAR data are very sensitive to the vertical motion of the target, whereas GPS performs more poorly (20); on the other hand, ca. north-south displacements (nearly orthogonal to the range direction) can hardly be detected by means of SAR data only. Moreover, SAR data accuracy, in particular the low-wavenumber components of the velocity field, decreases with the distance from the reference point. Considering the Kolmogorov turbulence model for atmospheric artefacts (13-15, 23+) (with power 0.2 rad^2 1 km apart from the GCP: heavy turbulence conditions), the accuracy of target velocity estimate (with respect to the reference point) is theoretically better than 1 mm/yr. within ca. 16 km from the GCP, even assuming strongly unfavourable weather conditions on every acquisition day. Therefore, if the PS

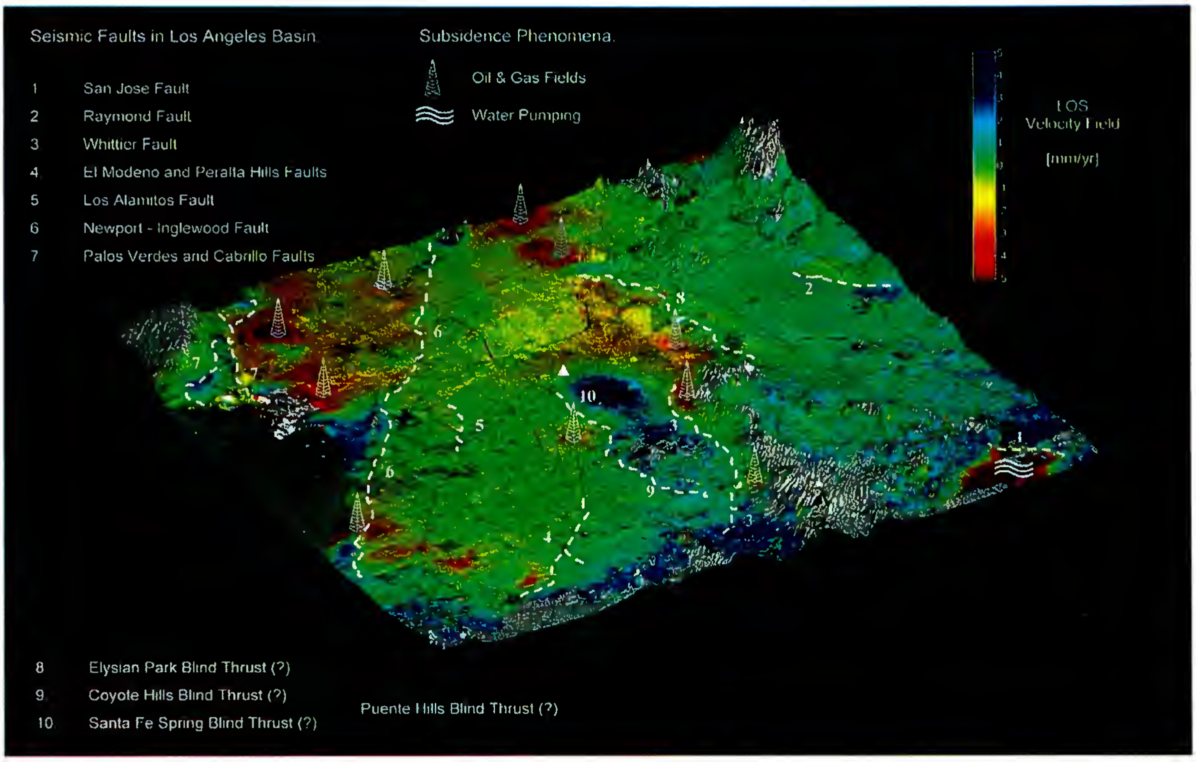

Figure 1. Perspective view of the estimated velocity field in the direction of the ERS satellites Line-of-Sight, on an area ca. 60 x 60 km^2 in the Los Angeles basin. The system sensitivity to target displacements is expressed by the unitary vector (10): e=0.41, n=-0.09; u=0.91 (east, north, up) relative to Downey, (25) approximately in the centre of the test site. Thus interferometric sensitivity is maximum for vertical displacements. The reference digital elevation model was estimated directly from SAR data (22) and no a-priori information was used with exception of the co-ordinates of one Ground Control Point. Vertical scale has been exaggerated for visualisation. The velocity field is superimposed on the incoherent average of all the images, and values were saturated at ± 5 mm/yr. for visualisation purposes only. The reference point, marked in white and supposed motionless, was chosen at Downey, where a permanent GPS station (DYHS) is run since June 1998 by SCIGN (25). Areas with low PS density are left uncoloured as well as areas affected by strongly time non-uniform motion (e.g. the harbour of Long Beach (26)), since in this case the average deformation rate is not a very significant index. Dashed lines denote known faults and suggested locations of blind thrust faults (27-29). Areas affected by subsidence due to water pumping (Pomona (19)) and oil or gas withdrawal (26) can be identified immediately.

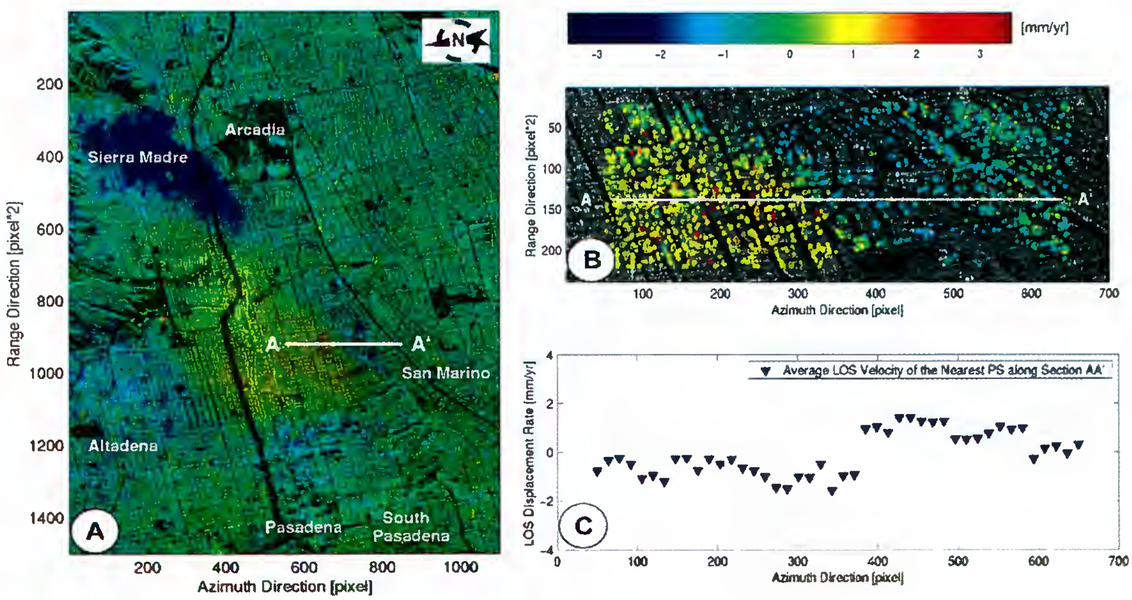

Figure 2. (A) Estimated LOS velocity field across the Raymond fault. In order to minimise interpolation artefacts, data are reported in SAR co-ordinates (range, azimuth) rather than in geographical co-ordinates. The sampling step is about 4 meters both in slant range and azimuth (ERS images have been interpolated by a factor of two in range direction). PS density is very high (over 200 PS/km^2), so that the estimated LOS velocity field looks continuous. As in Fig. 1, velocity values are computed with respect to the reference point in Downey (25) supposed motionless.

(B) Close-up on cross section AA'. Location and velocity of the PS have been highlighted and their density can be better appreciated. The relative dispersion of the velocity values in the two areas separated by the fault is lower than 0 4 mm/yr.

(C) LOS displacement rates relative to the PS along section AA'. The stepwise discontinuity of about 2 mm/yr. in the average deformation rate can be identified easily and the hanging wall of the fault can be located with an accuracy of a few tens of meters.

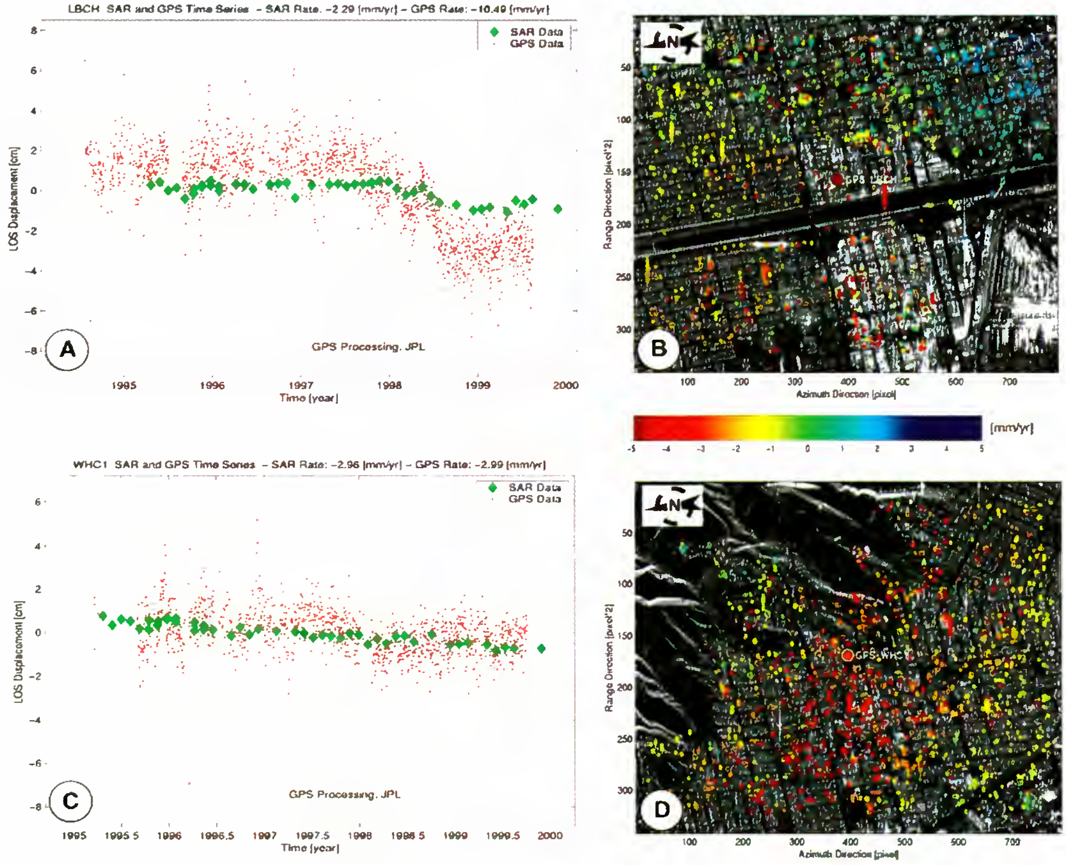

Figure 3. (A) Comparison between JPL GPS time series (30), relative to the SCIGN station LBCH at Long Beach (25), and the estimated displacement of the PS nearest to the GPS receiver. On this station, poor agreement between the LOS velocity values estimated by the two systems was found (see Table 1 for details). However, both time series trend similarly, showing centimetric subsidence in 1998. The different signal-to-noise ratios are mainly due to the operating frequencies of the two systems: L-band for GPS and C-band for SAR.
(B) Close-up on the area hosting the permanent GPS receiver LBCH and the 800 closest PS. The colour of each PS benchmark indicates its average LOS velocity (values are saturated to ±5 mm/yr. for visualisation purposes only).
(C) Same as in (A) for the SCIGN permanent GPS station WHC1 (25, 30), located at Whittier College. The agreement SAR-GPS is extremely good.
(D) Same as in (B) for the area surrounding the GPS station WHC1 (1000 PS available). Sharp subsidence phenomena in this area are due to oil extraction at the Whittier oil field (26).

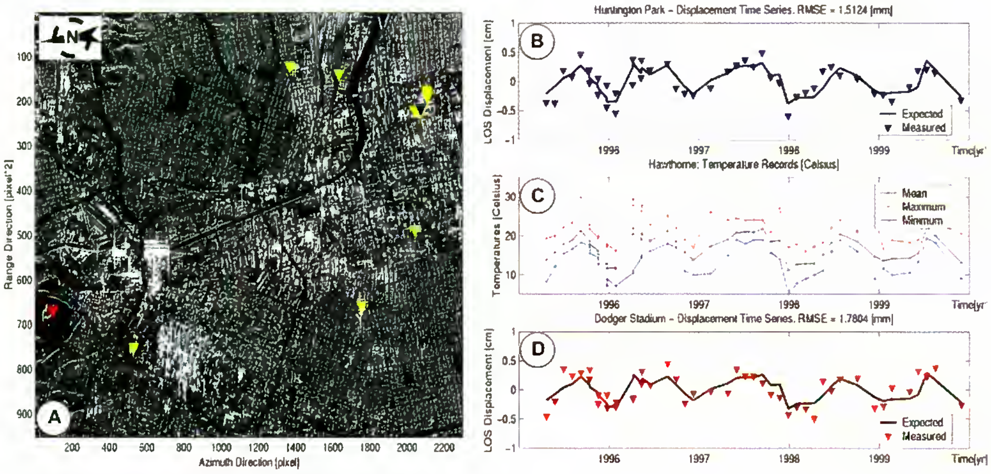

Figure 4. (A) Location map of PS showing high correlation coefficients (>0.7) between LOS displacement time series and air temperature records synchronous to ERS acquisitions (31). Data are reported in SAR co-ordinates. All targets correspond to high reflectivity pixels.
(B) Comparison between the time series of the PS identified by the blue triangle in (A) and the temperature records properly scaled to fit the data (least square error fitting adopting a simple linear model for thermal dilatation). The amplitude of the oscillation is about 1 cm, while the root mean square error between expected and measured deformation is 1.5 mm. The maximum-mean temperature difference is ca. 10°C.
(C) Temperature records. Only minimum, mean and maximum temperatures detected at Hawthorne (Los Angeles) on ERS acquisition days, (starting from 1995) were available (31). The best match was found using mean values. All ERS images were acquired at 18:30 UTC (10:30 local time).
(D) Same as in (B) for a Permanent Scatterer at the Dodger Stadium in Los Angeles.

Table 1. Comparison between GPS and PS SAR average deformation rates along the ERS Line-of-Sight

Station ID	Location	GPS * [mm/yr.]	SAR-b † [mm/yr.]	Δ [mm/yr.]	SAR-μ ‡ [mm/yr.]	SAR-σ ‡ [mm/yr.]	N §
AZU1	Azusa	-0.21	0.38	0.59	1.46	0.89	14
BRAN	Burbank	-4.19 #	0.39	4.58 #	0.45	0.1	2
CIT1	Pasadena	2.12	2.01	-0.11	1.44	0.38	48
CLAR	Claremont	6.27	4.91	-1.36	3.52	0.77	41
HOLP	Hollydale	-3.12	-2.53	0.59	-1.54	0.71	7
JPLM	Pasadena	1.49	0.6	-0.89	0.65	0.66	49
LBCH	Long Beach	-10.48 #	-2.29	8.19 #	-3.29	0.65	7
LEEP	Hollywood	-0.37	0.25	0.62	-0.09	0.50	33
LONG	Irwindale	4.58 #	1.32	-3.26 #	0.31	0.51	18
USC1	Los Angeles	-4.41	-4.42	-0.01	-3.57	0.55	26
WHC1	Whittier	-2.99	-2.96	0.03	-3.08	0.41	9

* SCIGN GPS data processed at JPL (25, 30). The LOS projection of the common-mode regional term (-19.3 mm/yr., estimated exploiting JPL GPS solutions, provided in May 2000 (30)) has been removed from GPS rates.

† Best match among the N PS nearest to the estimated position of the GPS station. For CLAR, JPLM, LBCH and LEEP stations (25), just the nearest PS has been considered.

‡ Mean and standard deviation of the velocity values of the N nearest PS. The dispersion value should not be confused with the accuracy of the technique, since it strongly depends on the gradient of the velocity field, influenced by local deformation phenomena like motion along active faults and subsidence in correspondence of oil fields.

§ Number of PS identified in a 100 m ray circle around the estimated position of the GPS receiver. Due to a lower PS density, for CLAR and JPLM stations a 500 m ray circle was used, while for LEEP a 1500 m ray was needed.

JPL GPS solutions are not consistent with GPS rates (available on the web) estimated at these stations by Scripps Orbit and Permanent Array Center (SOPAC) (25, 32). Compensating for the LOS common mode term (-17.9 mm/yr, estimated exploiting SOPAC deformation trends, May 2000), SOPAC rates along LOS direction are:
BRAN: -0.45 mm/yr.
LBCH: -2.60 mm/yr.
LONG: -0.36 mm/yr.
in much better agreement with PS SAR results.

density is high, and the target motion strongly correlated in time, APS estimation and removal allow detecting relative LOS displacements with accuracy up to 1 mm on single acquisitions (equivalent to a phase shift of only 13° at the operating frequency of the ERS-1/2 radar sensors).
Such accuracy is compatible with target displacements never measured hitherto by means of spaceborne radar interferometry as, for instance, thermal dilation of metallic-like targets. As a proof, Fig. 4 displays PS time series in central Los Angeles versus air temperature records synchronous to ERS acquisitions (31). Several high-reflectivity targets have been detected, showing sharp seasonal behaviour (Fig. 4) and providing a first example of millimetric motion detection of individual natural targets (not corner reflectors) in full-resolution SAR interferograms, with no spatial smoothing.
Having demonstrated the sensitivity of the method, we expect PS analysis to play a major role whenever accurate geodetic measurements are needed (20), especially in urban areas, where the building density (related to the PS density) is widely sufficient for a precise identification of the motion phase component. This opens new possibilities for reliable risk assessment and for monitoring hazardous areas, including time/space monitoring of strain accommodation on faults, subsiding areas and slope instability, as well as precision stability check of single buildings and infrastructures.

ACKNOWLEDGEMENTS

ERS-1 and ERS-2 SAR data were provided by ESA-ESRIN under contract no. 13557/99/I-DC. The continuous support of ESA and namely of L. Marelli, M. Doherty, B. Rosich, and F. M. Seifert is gratefully acknowledged. We are grateful to the Southern California Integrated GPS Network (in particular M. Heflin of JPL) and its sponsors, the W. M. Keck Foundation, NASA, NSF, USGS, SCEC, for providing data used in this study.
Finally we would like to thank Ing. R. Locatelli, Ing. F. Novali and Ing. M. Basilico who developed most of PS processing software we used.

REFERENCES

1. A. K. Gabriel, R. M. Goldstein, H. A. Zebker, J. Geophys. Res. 94, 9183 (1989).
2. D. Massonnet, K. L. Feigl, Rev. Geophys. 36, 441 (1998).
3. P. A. Rosen, et al., Proc. IEEE 88, 333 (2000).
4. R. Bamler, P. Hartl, Inverse Problems 14, R1 (1998).
5. D. Massonnet, P. Briole, A. Arnaud, Nature 375, 557 (1995).
6. D. Massonnet et al., Nature 364, 138 (1993).
7. G. Peltzer, F. Crampe, G. King, Science 286, 272 (1999).
8. G. Peltzer, P. A. Rosen, F. Roges, K. Hudnut, Science 273, 1202 (1996).
9. D. Massonnet, K. L. Feigl, M. Rossi, F. Adragna, Nature 369, 227 (1994).
10. D. Massonnet, W. Thatcher, H. Vadon, Nature 382, 612 (1996).
11. B. Fruneau, J. Achache, C. Delacourt, Tectonophysics 265, 181 (1995).
12. D. Massonnet, K. L. Feigl, Geophys. Res. Lett. 22, 1537 (1995).
13. R. F. Hanssen, Tech. Rep. No. 98.1 (Delft University Press, Delft, 1998).
14. S. Williams, Y. Bock, P. Pang, J. Geophys. Res. 103, 27051 (1998).
15. R. Goldstein, Geophys. Res. Lett. 22, 2517 (1995).
16. H. A. Zebker, P. A. Rosen, S. Hensley, J. Geophys. Res. 102, 7547 (1997).
17. H. A. Zebker, J. Villasenor, IEEE Trans. Geosci. Rem. Sensing 30, 950 (1992).
18. A. Ferretti, C. Prati, F. Rocca, IEEE Trans. Geosci. Rem. Sensing 39, 8 (2001)
19. A. Ferretti, C. Prati, F. Rocca, IEEE Trans. Geosci. Rem. Sensing 38, 2202 (2000).
20. T. A. Herring, Proc. IEEE 87, 92 (1999).
21. D. T. Sandwell, E. J. Price, J. Geophys. Res. 103, 30.183 (1998).
22. A. Ferretti, C. Prati, F. Rocca, IEEE Trans. Geosci. Rem. Sensing 37, 705 (1999).
23. H. Wackernagel, Multivariate Geostatistics - 2nd Edition (Springer-Verlag, Berlin, 1998).
24. R. Scharroo, P. Visser, G. J. Mets, J. Geophys. Res. 103, 8113 (1998).
25. Southern California Integrated GPS Network (SCIGN) – Web Site, http://www.scign.org/
26. Department of Oil Properties, City of Long Beach – Web Site, http://www.ci.longbeach.ca.us/oil/dop/brochure.html
27. California Division Mines and Geology Fault Activity Map of California and Adjacent Areas (Calif. Dept. of Conservation, Sacramento, 1994).
28. M. Oskin, et al., Bull. Geol. Soc. Am. 112, 693 (2000).
29. J. H. Shaw, P. M. Shearer, Science 283, 1516 (1999).
30. M. Heflin, et al., http://sideshow.jpl.nasa.gov/mbh/series.html
31. U.S. National Weather Service Temperature Data available on the web: http://www.wunderground.com
32. Scripps Orbit and Permanent Array Center (SOPAC) – Web Site, http://www.lox.edu

HAZARD MAPPING WITH MULTI-TEMPORAL SAR AND INSAR

Andreas Wiesmann[1], Urs Wegmüller[1], Marc Honikel[2], Tazio Strozzi[1], Charles L. Werner[1]
[1]Gamma Remote Sensing, Thunstrasse 130, 3074 Muri BE, Switzerland
Tel: +41 31 9517005, Fax: +41 31 9517008, e-mail: wiesmann@gamma-rs.ch, http://www.gamma-rs.ch
[2]Institute of Geodesy and Photogrammetry, Swiss Federal Institute of Technology Zurich, Switzerland, mhonikel@geod.baug.ethz.ch

ABSTRACT

In our hazard mapping methodology multi-temporal SAR backscattering and multi-temporal coherence data are considered. Process models are used to characterize the targets before, during and/or after the hazard event. Forward models describe the effect on the backscatter and coherence data, allowing development of a strategy and to specify the classification algorithm used.
Results presented for these different types of hazard events are forest storm damage, flood, and avalanche mapping. The temporal behavior of the backscattering coefficient and the temporal behavior of the coherence (determined from ERS tandem data) permitted detecting the change, leading to a damage map. For the investigated events, the presented methodology proved to be robust and reliable. Careful radiometric calibration, coregistration, geolocalisation, and estimation schemes were found to be important for the quality of the results.

INTRODUCTION

Hazard mapping has become urgent due to increased rate of natural disasters affecting human lives and infrastructure, and the higher usage of risk areas by human populations.
In hazard mapping the interest is mainly in the area of damage assessment, both the extent and level of damage. In many cases the level of the damage only includes damaged versus intact areas. The assessment of the damage is important for the evaluation of the event and serves also as input for the characterization of risk and planning of protection measures. Spaceborne SAR data are well suited for this application due to their "all weather", and day/night capability.
In recent years an increasing number of hazard events occurred. In Switzerland, for example, immense damage caused by a series of avalanches in February 1999, was followed by flooding in spring and heavy storms in late December. The assessment of the damage is not only important for the evaluation of the event but serves also as input to the characterization of the risk and for the planning of protection measures. Satellite-based remote-sensing data have a high potential for the assessment of damages after such catastrophes. Data acquisitions during or after the event combined with archived data (representing the condition before the event) allow in many cases to map the change, which occurred. SAR and InSAR data are particular useful for this purpose because of the very high potential for change detection, the large area coverage, the "all-weather" capability, and the day/night access of the radar sensors.
In hazard mapping the interest is mainly pointed to the assessment of the spatial extent and the level of the damage (although in many cases the level of the damage only includes damaged versus intact areas).
In a first step we define process models to describe changes of the target due to the hazard. In a second step a forward model is defined describing the effect on the information layers. Finally, classification results are presented and discussed.

CHANGE DETECTION

Typical SAR parameters appropriate for change detection are multi-temporal backscattering-coefficients and coherence estimates. These parameters estimated from SAR images acquired during or after the event are compared to reference data without damage. Appropriate estimation schemes are essential for the successful application of the methodology and include good relative and absolute calibration, accurate coregistration of the information layers, filtering and classification. Precise geocoding is necessary for multi-sensor data fusion and also for an adequate presentation of the data particularly to non-specialist users. The processing chain was set up using GAMMA Software [1].

PROCESS MODEL

In order to identify SAR and InSAR parameters well suited for the hazard mapping, it is first necessary to assess the effect of the hazard event. Table 1 describes the state before and after the selected events forest storm damage, flooding and avalanche. For the damage mapping it is also important to consider the time frame of the event. Forest storm damage and avalanches happen in a short time but leave traces that can be detected for a longer time. Flooding is a dynamic event and leaves not necessarily traces that can be observed by EO. Therefore the data availability during the event is crucial.

Proc. 3rd International Symposium, 'Retrieval of Bio- and Geophysical Parameters from SAR Data for Land Applications', Sheffield, UK, 11-14 September 2001 (ESA SP-475, January 2002)

Table 1:

Before hazard	During/After hazard
Forest storm damage (Figure 1)	
1) intact forest	partially broken trees partially uprooted trees decreased canopy height exposed lying trunks ground visibility changed
Flood (Figure 2)	
2) forest 3) farmland 4) urban area	trees in water shallow water surface buildings, obstacles in water
Avalanche (Figure 3)	
5) snow covered area	piles of compressed snow with rocks, trees and soil

Figure 1: Damaged forest near Treiten after storm "Lothar" in January 1999.

Figure 2: The area of Bern Airport seen from the west. Picture copyright by M. Imhof, Zimmerwald.

Figure 3: Avalanche cone. The handle of the Swiss Army Knife is about 10cm long.

FORWARD MODEL

For the definition of the forward models, the effect of the change (Table 1) on the information layers backscattering coefficient σ^0 and coherence γ must be investigated. This can be done using (simple) models or reference datasets using a similar approach as [2] used for land use classification (Table 3). For the investigated cases even simple signature based rules were sufficient (Table 2, Figure s 4-6). Table 2 shows the general rules determined from the processes in Table 1.

Table 2

	Change
Forest storm damage	
1) intact forest	γ increase, σ^0 uncertain
Flood	
2) forest 3) farmland 4) urban area	σ^0 increase σ^0 decrease, γ decrease σ^0 increase
Avalanche cone	
5) snow covered area	σ^0 increase

Forest can be discriminated from non-forest by its low coherence [2]. Storm damaged forest has more stable scatterers and less volume scattering, therefore the coherence is higher than for the intact forest [3].

Figure 5 shows that σ^0 for open water is significantly lower than for any other land type. However, rough water has a much higher σ^0. The classification depends therefore on the meteorological conditions. Multi temporal data can help to improve the classification and give additionally insight in the flood dynamics. The coherence for water is generally low.

Figure 6 shows σ^0 for various snow types. It is shown that σ^0 depends on the wetness but also strongly on the surface roughness. The backscattering coefficient of rough wet snow is significantly larger (>5dB) than for smooth wet snow. Figure 7 shows the σ^0 values obtained from an ERS SAR scene for different areas. It shows the same significant high backscattering for the avalanche cone. The "snow free" signatures can not be compared because in Figure 7 it's the signature of a meadow while in Figure 6 it's the signature of stone and rock.

Table 3: Classification scheme as proposed by [2].

landuse class	γ	$<\sigma^o>$ [dB]	$\Delta\sigma^o$ [dB]	texture
urban	> 0.4	> -7.0	> 0.0	> 1.0
layover	< 0.2	> -2.0	< 2.0	
water	< 0.2	< -15.0	> 2.0	
geom. change	< 0.3		> 2.0	
diel. change	> 0.3		> 2.0	
sparse vegetation	> 0.6		< 2.0	
med. vegetation	0.35-0.6		< 2.0	
forest	< 0.35	< -2.0	< 2.0	

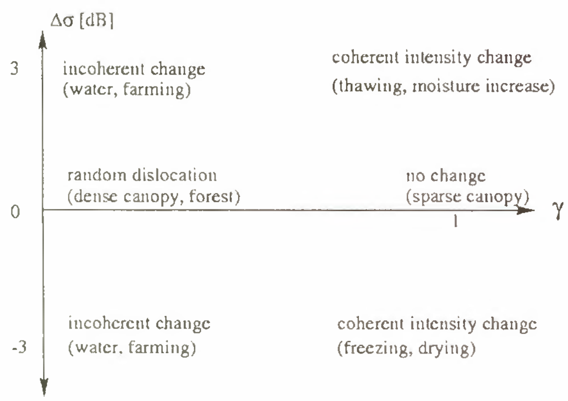

Figure 4: Degree of coherence and backscatter intensity change for different types of temporal change.

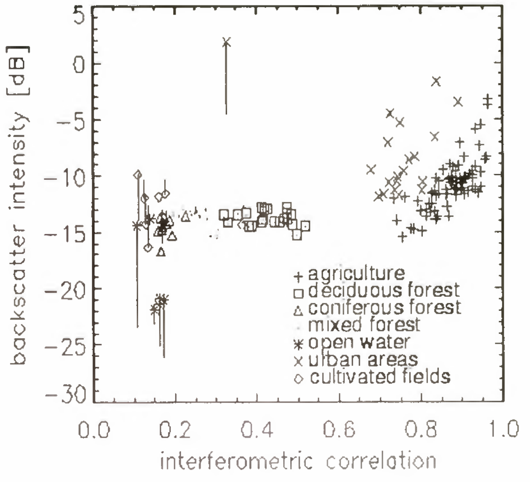

Figure 5: Backscatter intensity versus degree of coherence for a variety of surface classes for ERS data [4]. If the backscatter change between the first and second data acquisition exceeds 0.5 dB the change is indicated by a vertical line.

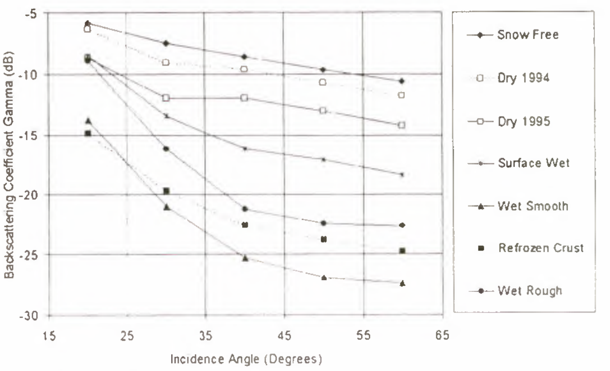

Figure 6: 5 GHz v-pol. Scatterometer data from Strozzi et al. [5].

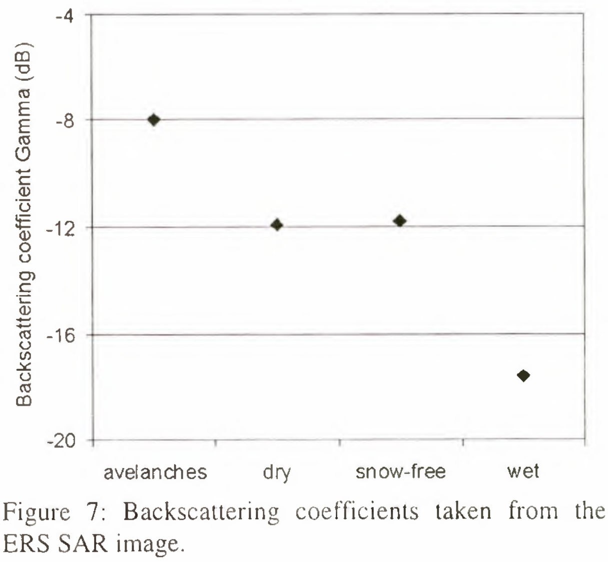

Figure 7: Backscattering coefficients taken from the ERS SAR image.

RESULTS

Forest storm damage

For the test site Treiten, Switzerland, ERS tandem data of 26/27 Nov 1995 (before the storm) and 9/10 Jan 2000 (after) were used. Figure 8 shows a Dynamic Coherence Product, increasing coherence is shown in the red channel, the averaged backscattering coefficient before the storm in green, and the coherence before the storm in blue. In this representation intact forests appear in green, agricultural fields in blue, and forest damage in orange. Some orange spots can also be found in non-forested areas. But this is not a problem as usually it is known from an available conventional forest map or a remote sensing based landuse map where the forest stands are.

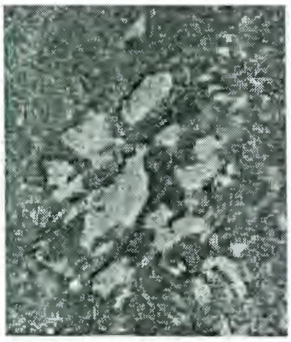


Figure 8 (left) 9 (right). Dynamic coherence Product (left) and air photo (right) of storm damaged forest in Treiten.

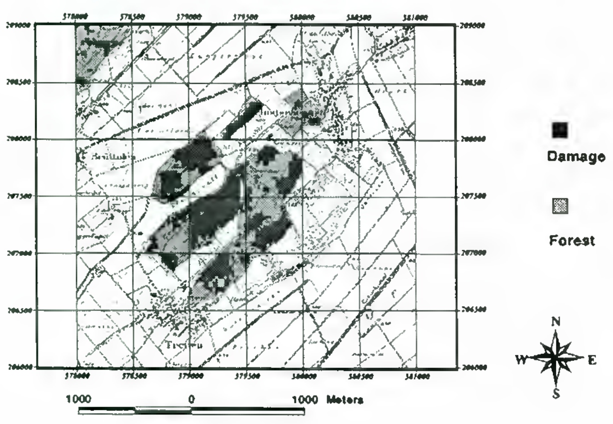

Figure 10. ERS interferometry based forest damage map of Treiten.

The Dynamic Coherence Product clearly shows the heavy damage of the forest, which is confirmed by the air photo of the forest after the storm (Figure 9). Figure 10 shows the ERS interferometry based forest damage map of Treiten. The damage classification is solely based on the coherence increase. A quality assessment of different remote sensing methods investigating the Lothar damages was done in France. The dynamic coherence method turned out to be the most accurate classification approach. The accuracy for areas with more than 50% damage was 89% [6].

Flooding

Bern Airport Switzerland is situated between the river Aare and the river Gürbe. In spring 1999 heavy rains combined with increased snowmelt runoff due to the century-high snowfalls in winter 1998/1999 lead to heavy floods in several parts of Switzerland. On May 15 the airport Bern-Belpmoos had to be closed. It remained closed until May 25. In Figure 11 a SAR RGB composite (red: 21 Apr 1999, green: 26 Mai 1999, blue: 26 Mai 1999) is shown.


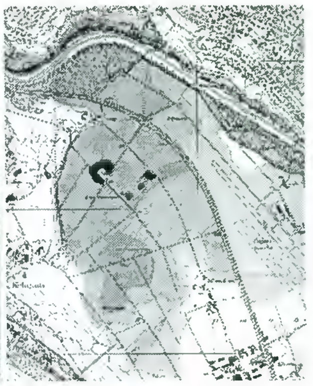

Figure 11 (left) 12 (right). RGB composite (left) and flood map (right) of the airport of Bern. The flood map is provided by the Tiefbauamt of the Canton of Bern, Switzerland.

Figure 13: Flood layer (blue) obtained from ERS data combined with the geographic map of the area. Grid size is 1 km.

The red channel represents the situation before the flood, while the blue and green channel shows the situation at the end of the flood. Figure 12 shows the flood map of the authorities. The colors indicate the maximum water depth (yellow < 20cm, blue 20-50 cm, orange 50-100 cm, brown 100-200 cm, black > 200 cm). The red areas in the RGB correspond well to areas that were flooded. It is shown that the areas close to the airport are not flooded anymore. The flooded area in the knee of the river is not indicated in the RGB. This area is forested. Figure 13 shows the flood map of Mai 25. The classification is based on multi-temporal σ^0. The result is in good agreement with the official flood map and the topography. Again, the flooded forest is not classified as flooded area.

Avalanches

In February 1999 a high number of avalanches occurred in Switzerland due to the large amount of new snow. Figure 14 shows a RGB composite (red: 22 Jan 1999, green: 26 Feb 1999, blue: 24 Sep 1999) of the backscattering coefficient of the Ulrichen area, Switzerland. From the forward model we expect high backscattering of the avalanches. In the RGB they should show up in green. Indeed, several avalanche cones can well be identified in the RGB. Figure 15 shows an air photo of the encircled avalanche in Figure 14. Even the fine structures of the cone are visible in the RGB. At the Swiss Federal Institute for Snow and Avalanche Research (SLF) the avalanche cones were mapped. Figure 16 shows the map of this avalanche debris.

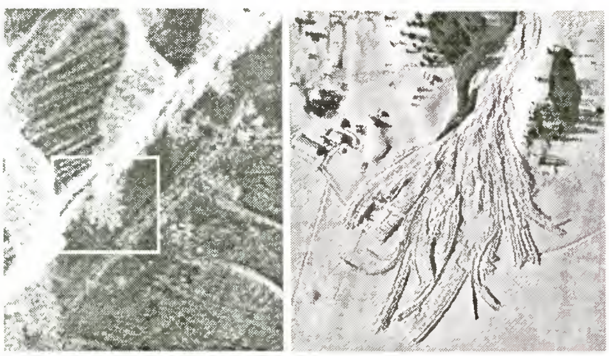

Figure 14 (left) 15 (right). RGB composite of Ulrichen (left) and air photo of the Ulrichen Avalanche (right). The air photo is property of the SLF.

CONCLUSIONS

In this paper we have shown that SAR and InSAR are powerful tools to map risk and hazard damages. The temporal behavior of the backscattering coefficient and the coherence turned out to be valuable information layers.

For the investigated events, the methodology proved to be robust and reliable. It is our expectation that it is also applicable for other risk and hazard types.

The quality of the product depends on the quality of the calibration, the coregistration of the information channels and the geolocalisation.

Hazard mapping depends heavily on data availability and reliability. Future systems with beam steering possibilities will allow a more timely coverage, leading to a much better data availability and lower reaction time. However, in the near future there will be no tandem mission, and therefore no 1-day coherence. This is a serious drawback, especially for forest applications.

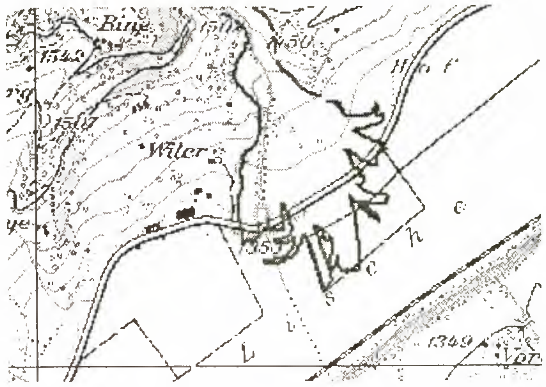

Figure 16. Avalanche map of the Ulrichen Avalanche. Copyright SLF, Davos.

ACKNOWLEDGMENTS

Ground information used in the Flooding Section was provided by the Tiefbauamt of the Canton of Bern, Switzerland. Ground information in the Avalanches Section was provided by the Swiss Federal Institute for Snow and Avalanche Research (SLF), Davos, Switzerland.

This work was supported by the KTI project CIRSTEN, and ESA contracts 14568/00/NL/OA. ESA is acknowledged for the ERS data provided under ERS AO3-175 and CAT-1 (C1P.1006). ERS SAR data copyright ESA, processing by GAMMA Remote Sensing using Gamma Software.

REFERENCES

[1] Werner L. C., U. Wegmüller, T. Strozzi, and A. Wiesmann, Gamma SAR and Interferometric Processing Software, Proceedings of ERS-ENVISAT Symposium, Gothenburg, Sweden, 2000.

[2] Strozzi T., P. B. G. Dammert, U. Wegmüller, J-M. Martinez, A. Beaudoin, J. Askne, and M. Hallikainen, Landuse mapping with ERS SAR interferometry, IEEE Trans. Geosci. Remote Sensing, Vol. 38, No. 2, pp. 766-775, 2000.

[3] Wiesmann A., L. Demargne, F. Ribbes, M. Honikel, H. Yesou, U. Wegmüller, Forest storm damage assessment with ERS Tandem data, Proceedings of ERS-ENVISAT Symposium, Gothenburg, Sweden, 2000.

[4] Wegmüller U., Land applications of SAR interferometry, in Microwave Physics and Technique, Groll and Nedkov (ed.), Kluwer academic publisher, Dordrecht, The Netherlands, (ISBN 0-7923-4582-7), pp. 235-250, 1997.

[5] Strozzi T., A. Wiesmann, C. Mätzler, Active Microwave Signatures of Snowcovers at 5.3 and 35 GHz. Radio Science, 32, 479-495, 1997.

[6] Wiesmann A., F. Ribbes, M. Honikel, H. Yésou, D. Rigal, M.-C. Delucq, L. Demargne, U. Wegmüller, Forest storm damage assessment with ERS Tandem data, submitted to Rem. Sens. Env. 2001.

ON THE USE OF RADARSAT-1 FOR MONITORING MALARIA RISK IN KENYA

S.G.Ross[1], M.C.Thomson[2], T.Pultz[1], C.M.Mbogo[3], J.L.Regens[4], C.Swalm[5], J.Githure[6], G. Yan[7], W.Gu[8], and J.C.Beier[8]

[1] Natural Resources Canada, Canada Centre for Remote Sensing, 588 Booth Street, Ottawa, ON. K1A 0Y7 CANADA
Tel: (613) 947-1271 Fax: (613) 947-1385 shannon.ross@ccrs.nrcan.gc.ca
[2] MALSAT Research Group, University of Liverpool School of Tropical Medicine, Liverpool L3 5QA UK
[3] Kenya Medical Research Institute, Center for Geographic Medicine Research, Coast, P.O. Box 428 Kilifi, KENYA
[4] University of Oklahoma, Institute for Science and Public Policy, SEC 510, Norman, OK 73019-1006 USA
[5] Tulane University, Entergy Spatial Analysis Research Laboratory, 1430 Tulane Avenue, New Orleans, LA 70112 USA
[6] International Centre of Insect Physiology and Ecology (ICIPE), Kasarani, P.O. Box 30772, Nairobi, KENYA
[7] State University of New York at Buffalo Cook 109, Department of Biological Sciences, Buffalo, NY 14260 USA
[8] Tulane University, Department of Tropical Medicine, 1430 Tulane Avenue, New Orleans, LA 70112 USA

ABSTRACT

The incidence and spread of vector-borne infectious diseases are increasing concerns in many parts of the world. Earth observation techniques provide a recognised means for monitoring and mapping disease risk as well as correlating environmental indicators with various disease vectors. Because the areas most impacted by vector-borne disease are remote and not easily monitored using traditional, labour intensive survey techniques, high spatial and temporal coverage provided by spaceborne sensors allows for the investigation of large areas in a timely manner. However, since the majority of infectious diseases occur in tropical areas, one of the main barriers to earth observation techniques is persistent cloud-cover.

Synthetic Aperture Radar (SAR) technology offers a solution to this problem by providing all-weather, day and night imaging capability. Based on SAR's sensitivity to target moisture conditions, sensors such as RADARSAT-1 can be readily used to map wetland and swampy areas that are conducive to functioning as aquatic larval habitats. Irrigation patterns, deforestation practises and the effects of local flooding can be monitored using SAR imagery, and related to potential disease vector abundance and proximity to populated areas.

This paper discusses the contribution of C-band radar remote sensing technology to monitoring and mapping malaria. Preliminary results using RADARSAT-1 for identifying areas of high mosquito (*Anopheles gambiae* s.l.) abundance along the Kenya coast will be discussed. The authors consider the potential of RADARSAT-1 data based on SAR sensor characteristics and the preliminary results obtained. Further potential of spaceborne SAR data for monitoring vector-borne disease is discussed with respect to future advanced SAR sensors such as RADARSAT-2.

INTRODUCTION

Remote sensing is widely used in natural resource applications such as agriculture, forestry, geology, hydrology and ice/oceans. However, significantly less research has been done using satellite remote sensing in the social sciences or public health. In recent years, several scientists have considered the applicability of remote sensing in conjunction with Geographic Information Systems (GIS) for monitoring human health, with varying levels of success. For the most part, it has been found that space-borne remotely sensed data can provide the spatial resolution and coverage needed to assess disease risk (specifically malaria) in a given area, and that GIS provides a useful tool for image analysis (Bryceson, 1989; Wood *et al*, 1991, 1994; Pope *et al*, 1992; Conner *et al*, 1997; Thomson *et al*, 1997, 2000; Hay *et al*, 1997, 1998, 2000; Beck *et al*, 2000).

Several issues need to be addressed, however, including the need for a multi-disciplinary approach, and the need for an effective tool with characteristics suitable for disease habitat identification. The need for a multi-disciplinary approach when considering the use of geomatics technology to human health applications is clear (Wood *et al*, 1993; Mayer, 1983). A combined effort from remote sensing scientists, geographers, and epidemiologists is required in order to make efficient use of satellite imagery for medical purposes. This study combines the expertise of researchers in all these fields, in order to assess the applicability of SAR remote sensing for monitoring malaria in coastal Kenya.

Proc. 3rd International Symposium, 'Retrieval of Bio- and Geophysical Parameters from SAR Data for Land Applications', Sheffield, UK, 11-14 September 2001 (ESA SP-475, January 2002)

A further limitation noted in much of the past research done using remote sensing for disease monitoring is the problem of cloud cover. Since most of the vector-borne diseases in question are prevalent in tropical areas, there is a high incidence of cloud cover, which results in limited imaging opportunities with optical sensors such as Landsat TM. The obvious solution to this problem is the use of radar data. However, there has been little research done on the use of SAR remote sensing technology for monitoring and mapping disease risk, likely due to the complexity associated with SAR image interpretation and usability. This paper ~~will~~ addresses this concern and considers the needs of the user community in order to facilitate the use of SAR remote sensing, specifically RADARSAT-1, for monitoring vector-borne disease risk.

RADARSAT-1

Launched in November 1995, RADARSAT-1 is a Canadian initiative involving the Canadian Space Agency (CSA) and private industry. The RADARSAT-1 spacecraft carries a C-band Synthetic Aperture Radar (SAR) sensor that transmits and receives horizontally polarised (HH) microwave signals to image the earth both day and night. The chosen frequency of RADARSAT-1 (5.3 GHz) can penetrate clouds and haze, increasing the temporal coverage significantly over optical sensors. RADARSAT-1 technology has been proven useful for monitoring many of the Earth's natural resources and environmental changes, including land applications related to hydrology, agriculture, and land use mapping.

RADARSAT-1 has the unique ability to steer its variable mode radar beam over a wide area. The flexible swath width (50-500 km), spatial resolution (8-100 m), and incidence angle (10-60 degrees) provides users with many data options which can be suited to a variety of applications (see Table 1 for RADARSAT-1 operating beam mode specifications). When selecting remotely sensed data, users must consider the trade-off between spatial coverage and spatial resolution. RADARSAT's wide area swaths provide excellent regional coverage (up to 500 km) with a coarse spatial resolution, while detailed studies may be carried out using fine resolution data with a swath coverage of 50 km.

RADARSAT-1 operates in a sun-synchronous polar orbit at an altitude of approximately 798 km, providing complete global coverage on a regular and timely basis. The ground track of the satellite is repeated every 24 days, however the steerable beam capability and wide swath coverage allows for most regions on the Earth to be imaged more frequently. High latitudes (north of 70°) may be imaged on a daily basis, as is done in the Canadian Arctic regions, while areas closer to the equator can achieve repeat coverage every 3-6 days.

Mode	Approximate Incidence Angle [degrees]	Approximate Swath Width [km]	Approximate Resolution: [1] Rg x Az [m]	Approximate Looks [2] [Rg x Az]
Standard	20-49	100	25 x 28	1 x 4
Wide	20-39	150	25 x 28	1 x 4
Extended Low	10-23	170	40 x 28	1 x 4
Extended High	50-60	75	20 x 28	1 x 4
Fine	37-48	50	10 x 9	1 x 1
ScanSAR Wide	20-49	500	100 x 100	4 x 2
ScanSAR Narrow	20-40	300	50 x 50	2 x 2

[1] Ground resolution varies in range, [2] Range and processor dependent

Table 1: Characteristics of RADARSAT-1 operating beam modes

SAR and VECTOR-BORNE DISEASE MONITORING

As mentioned, there have been few published results on the applicability of SAR imagery specifically for disease monitoring, particularly using recent spaceborne SAR sensors. Pope (1992) considered the use of a high-resolution airborne three-band polarimetric radar system (ERIM / NADC P-3 SAR) for the identification of central Kenyan Rift Valley Fever vector habitats. This work concluded that airborne SAR imagery is useful for detecting flooded areas that can be related to active vector habitat sites of the Kenyan Rift Valley Fever virus. In particular, Pope notes the advantage SAR's 'all-weather capability' and sensitivity to moisture as major advantages.

There have been several published concerns that may account for the limited use of SAR imagery for health applications. In particular, the complexity of SAR imagery is associated with difficult image interpretation and information extraction (Hay *et al*, 2000). With this, a steep learning curve is often required in order to understand what is seen in a SAR image, as opposed to the more inherent interpretation of optical images. In addition, in the past, there has been a lack of well-calibrated SAR data, which limits confidence in results obtained from SAR data. RADARSAT-1, however provides fully calibrated data in all operating beam modes so that the user is not faced with this challenge. A final noted challenge relates to topography problems unique to SAR images, as well as inherent image speckle. These are valid concerns based on historical use of SAR data, which has for the most part been airborne. However, current commercial image processing software packages are available to deal with unique SAR characteristics, such as speckle interference and topographic effects. Although many of these packages require significantly more effort to facilitate accurate analysis, increasingly user-friendly packages are being developed as the availability and use of commercial SAR data increases with sensors such as RADARSAT, ERS, JERS and ENVISAT. Some of the advantages of spaceborne SAR imaging for disease monitoring are the capability for long-term monitoring, regional coverage, and near-real time data access capabilities. Additionally, interpretability of areas of flooded vegetation is likely easier with SAR, as opposed to optical remote sensing.

PROPOSED METHODOLOGY

The methodology of using SAR data for disease monitoring is similar to that used with optical remote sensing in recent years. With well-calibrated, multi-temporal RADARSAT-1 imagery, a geo-referenced, co-registered dataset may be used for image classification. Advanced intelligence-based classification routines such as object-oriented algorithms are most suitable for SAR data, since an assumption of normal data distribution can pose a problem with common routines such as parameterised supervised classifications. The availability and usability of advanced classification algorithms is increasing with the development of advanced classification software packages, which are designed to contend with some of the inherent challenges of SAR data. For this research, *eCognition* software was used to apply an object-oriented segmentation routine to the SAR data.

Based on SAR's sensitivity to vegetation structure and surface moisture conditions, ecological variables relating to vector breeding grounds may be readily identified with a classified SAR image. The land cover parcels associated with the disease vector under investigation may then be correlated with ground data of vector abundance. With this, areas of high vector abundance are tagged as high to low risk, depending on proximity to areas populated by the vectors host (e.g. human hosts for malaria carrying mosquito vectors). The use of GIS for cluster analysis and buffer zone generation around host areas can serve as a tool to produce disease risk maps, and will be investigated by the authors in future research.

CASE STUDY: COASTAL KENYA

Preliminary research was conducted over a 30-site area on the coast of Kenya. The area covers three main districts: Kwale, Kilifi and Malindi. The full study site is home to two-thirds of the rural population of coastal Kenya, where malaria is a severe health concern. The environment consists of forest, savanna, mangrove swamps and wetland vegetation. Agriculture plantations (mainly coconut, sisal and cashews) are also found along the coast. The ground elevation ranges from sea level to approximately 400 metres above sea-level (ASL) and there are several small rivers that flow from the highlands to the Indian Ocean. The water bodies in the area fluctuate in size depending on the seasonal rainfall, with rainy seasons typically occurring in May/June and October/November.

Figure 1 provides a map of the study area, with ground truth sites identified. During December 1997, *Anopheles gambiae* mosquito abundance data was collected for these 30 sites in the study area. This information was correlated with the land cover classification obtained from the RADARSAT imagery in order to assess the usefulness of SAR for identifying areas of potentially high mosquito abundance.

RADARSAT-1 Standard mode beam 7 data was collected over the study area in March 1999 and March 2001. These data have an approximate spatial resolution of 25 metres, swath width of 100 kilometres, and incident angle range of 45°-49°. These data were collected from the RADARSAT data archive and were the only data collected over the area in the past five years. Future data acquisitions will be carried out during the rainy season in the area, and compared with more timely ground truth collection. For the purposes of this study, the 1999 and 2001 data were used as input to the image classification. Figure 2 shows the original RADARSAT-1 (1999 and 2001) images analysed in this research.

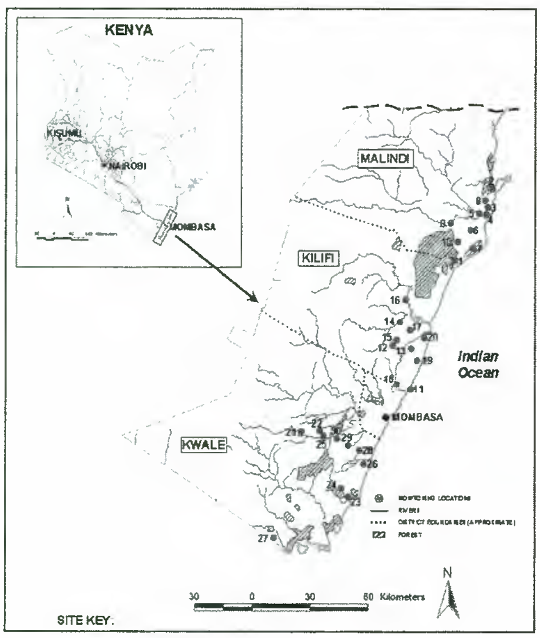

Figure 1: Coastal Kenya Study Area

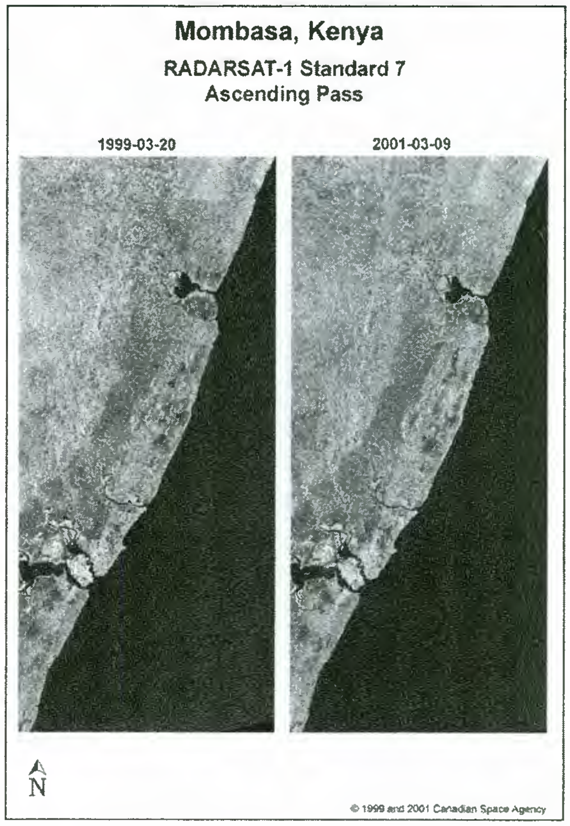

Figure 2: RADARSAT-1 Standard 7 images of the study area along Kenya coast.

A new tool, *eCognition* software, was used to perform the image classification. Using a segmentation routine to extract homogenous areas in the image, the classification algorithm then classified segments based on user input ground training sites. The following general land cover classes were identified: Forest (type 1 and 2), grassland, agriculture, wetland, populated and water, using a minimum of 12 training sites per class. Input image layers for the classification included original images for each date, mean filtered (7 by 7) and homogeneity texture images (7 by 7). These input layers were found to provide the best classification results.

The resulting classifications clearly identified wetland areas around the town of Mombasa, and the many streams that drain into the Indian Ocean. Coconut plantations are identified in Kilifi and Kwale districts, as well as the Shimba hills (forest type 1: indigenous species). Mangrove forests (forest type 2) near the coast are also identified. Throughout the center of the study area, the Kaya-Bombo forest was classified correctly as forest type 2. Also, sisal plantations are classified as agriculture in the center of the area, along the coast. The Arabuko forest is identified in the north and mainly consists of indigenous tree species. Small wetland patches are identified throughout the scene.

Mosquito collections done six times in each of the 30 sites during the first year (1997-1998) revealed significant temporal variation, with most of the mosquitoes being collected in one 2-month period. By overlaying the mosquito abundance data, it was found that areas of high Anopheles mosquito abundance closely corresponded to wetland classified areas, as well as grassland and forest type 2, for both 1999 and 2001. Moderately high abundance areas were found to correspond with grassland and forest type 1 areas. Areas of low mosquito abundance mainly corresponded with agriculture areas. Wetland classes around water bodies were clearly identified, and are likely to correspond to areas of high mosquito abundance.

Quantitative accuracy assessment was difficult to conduct due to lack of ground truth information for test sites. Qualitative assessment shows obvious classification confusion found between wetland and urban areas, due to the high degree of corner reflection occurring with both targets. Forest type 2 and agriculture areas were also confused in some areas, due to similar backscatter properties. Differences in moisture levels between 1999 and 2001 were seen, with clearly wetter conditions occurring in 2001.

The preliminary research described here will be further developed using more extensive, time series data sets. Current bi-weekly ground data collection is being carried out (including mosquito larvae abundance, habitat size, pH, vegetation cover, nutrient levels, rainfall, etc.) and concurrent RADARSAT-1 data will be collected for late 2001, during the rainy season. In order to perform useful accuracy assessments of the resulting classifications, increased number of training and test sites will be identified.

Continued research will analyse classifications obtained from RADARSAT-1 data using a GIS in order to associate areas of potentially high mosquito abundance with proximity to populated areas. With this, areas of high malaria risk may be readily identified. The potential is significant for the application of SAR data to become automated and perhaps a web-based tool. Health officials, decision-makers and policy analysts all over the world could use timely and accurate disease risk map information in order to organize and implement effective disease control and mitigation strategies.

DISCUSSION

The successes of RADARSAT-1 will be further developed with the launch of RADARSAT-2 in 2003. RADARSAT-2 will provide all imaging modes of RADARSAT-1, as well as some new modes that incorporate significant innovations and improvements. Hence, the satellite will offer data continuity to RADARSAT-1 users and new data that will support development of improved and new applications. The new capabilities associated with RADARSAT-2 will allow for high-resolution imaging (up to 3 metres), right and left-looking geometry and fully polarimetric remote sensing. The selective look direction option will increase imaging revisit time and allow for increased temporal resolution to better provide near-real time imagery for disease outbreak monitoring. High spatial resolution (3m.) data will allow for local analysis of small area larval habitats that persist through long dry seasons. Polarimetric data will provide increased information content useful for improved land cover classifications with single-date imagery.

One of the main advancements with RADARSAT-2 will be its capability for multiple and fully polarimetric imaging. Although the scientific community has not had much opportunity to explore the possibilities of space-borne polarimetry, several studies using airborne multi-polarized SAR have concluded that classification accuracy is higher as compared to single linearly polarized data (Foody *et al.*, 1994; Lee *et al.*, 1994; Schmullius *et al.*, 1997). Although C-band, HH polarization is optimal for monitoring environments where vector breeding is likely to occur (e.g. wetlands), increased information content with multi and fully polarimetric data will facilitate accurate land cover mapping (Ambrosia *et al.*, 1989; Pultz *et al.*, 1991).

REFERENCES

Ambrosia, V.G., K.G. Linthicum, C.L. Bailey, and P.D. Sebesta., 1989, Modelling Rift Valley Fever (RVF) disease vector habitats using active and passive remote sensing systems, Proceedings of the International Geoscience and Remote

Sensing Symposium (IGARSS '89), 12th Canadian Symposium on Remote Sensing, Vancouver, B.C., Canada.

Beck, L.R., B.M. Lobitz, and B.L. Wood., 2000, Remote sensing and human health: new sensors and new opportunities, Emerging Infectious Diseases, 6.

Connor, S.J., S.P. Flasse, A.H. Perryman, and M.C. Thomson., 1997, The contribution of satellite derived information to malaria stratification, monitoring and early warning. World Health Organization, WHO/MAL/97.1079, 32.

Foody, G.M., M.B. McCulloch, and W.B. Yates., 1994, Crop Classification from C-band Polarimetric Radar Data, International Journal of Remote Sensing, 15(14):2871-2885.

Hay, S.I., R.W. Snow, and D.J. Rogers., 1998a, From predicting mosquito habitat to malaria seasons using remotely sensed data: Practice, problems and perspectives, Parasitology Today, 14(8):306-313.

Hay, S.I., R.W. Snow, and D.J. Rogers., 1998b, Predicting malaria seasons in Kenya using multitemporal meteorological satellite sensor data, Transactions of the Royal Society of Tropical Medicine and Hygiene, 92:12-20.

Hay, S.I., 1997, Remote sensing and disease control: Past, present and future, Transactions of the Royal Society of Tropical Medicine and Hygiene, 91:105-106.

Hay, S.I., 2000, An overview of remote sensing and geodesy for epidemiology and public health applications, Advances in Parasitology: Remote Sensing and Geographical Information Systems in Epidemiology (Donald P. Albert, Wibert M. Gesler and Barbara Levergood, editors), Ann Arbor Press, Chelsea, Michigan, pp. 2-27.

Lee, J.-S., M.R. Grunes, R. Kwok., 1994, Classification of multi-look polarimetric SAR imagery based on complex Wishart distribution, International Journal of Remote Sensing, 15(11):2299-2311.

Lewis, A.J, and F.M.Henderson., 1998, Radar Fundamentals: The Geoscience Perspective, Principles and Applications of Imaging Radar, Manual of Remote Sensing, Vol. 2 (Floyd M. Henderson and Anthony J. Lewis, editors), John Wiley and Sons, Inc. New Your, NY, pp. 131-181.

Mayer, J.D. 1983. The role of spatial analysis and geographic data in the detection of disease causation. Soc. Sci. and Med. 17:1213-1221.

Pope, K.O., E.J. Sheffner, K.J. Linthicum, C.L. Bailey, T.M. Logan, E.S. Kasischke, K. Birney, A.R. Njogu, and C.R. Roberts., 1992, Identification of central Kenyan Rift Valley Fever virus vector habitats with Landsat TM and evaluation of their flooding status with airborne imaging radar, Remote Sensing of Environment, 40 :185-196.

Pultz, T., R. Leconte, L. St.Laurent, L. Peters., 1991, Flood mapping with airborne SAR imagery, Canadian Water Resources Journal, 16(2):173-189.

Schmullius, C. C. and D.L. Evans., 1997, Synthetic aperture radar (SAR) frequency and polarization requirements for applications in ecology, geology, hydrology, and oceanography: a tabular status quo after SIR-C/X-SAR, International Journal of Remote Sensing, 18(13):2713-2722.

Thomson, M.C., S.J. Connor, P.J.M. Milligan, and S.P. Flasse., 1997, Mapping malaria risk in Africa: What can satellite data contribute?, Parasitology Today, 13(8):313-318.

Thomson, M.C. and S.J. Connor., 2000, Environmental information systems for the control of arthropod vectors of diseases, Medical and Veterinary Entomology, 14:227-244.

Thomson, M.C., V. Obsomer, M. Dunne, S.J. Connor, and D.H. Molyneux., 2000, Satellite mapping of Loa loa prevalence in relation to Ivermectin use in West and Central Africa, The Lancet, 356:1077-78.

Wood, B.L., L.R. Beck, S.W. Dister, and M.A. Spanner., 1994, The global monitoring and disease prediction program, Sistema Terra, year III:38-39.

Wood, B.L., R.K. Washino, S.M. Palchick, L.R. Beck, and P.D. Sebesta., 1991, Spectral and spatial characterization of rice field mosquito habitat, International Journal of Remote Sensing, 12 :621-626.

JERS SAR INTERFEROMETRY FOR LAND SUBSIDENCE MONITORING

Tazio Strozzi, Urs Wegmüller, Charles Werner, Andreas Wiesmann

Gamma Remote Sensing, Thunstrasse 130, 3074 Muri BE, Switzerland
tel: +41 31 9517005 / fax: +41 31 9517008

e-mail: strozzi@gamma-rs.ch / wegmuller@gamma-rs.ch / cw@gamma-rs.ch / wiesmann@gamma-rs.ch

ABSTRACT

In this paper the potential of L-Band repeat-pass differential SAR interferometry for land subsidence monitoring is evaluated using JERS SAR data. Bologna, Mexico City and the Ruhrgebiet were selected as application sites representing slow to fast deformation velocities. The investigation includes feasibility aspects as the data availability, the temporal decorrelation over different landcover classes and the range of useful spatial baselines, an analysis of the achieved deformation accuracy and considerations on the complementarity to ERS SAR interferometry and levelling surveys.

In spite of the rather limited data availability, land subsidence maps could be generated for the three selected application sites. Unlike with ERS C-Band SAR data, JERS L-Band interferometry permitted to retrieve subsidence values also over vegetated areas and forest when using interferograms of less than one year acquisition time interval and short baseline. In addition, the longer L-Band wavelength was found to be superior in the case of large deformation gradients that lead to phase unwrapping problems in C-Band interferometry.

I. INTRODUCTION

Land subsidence monitoring with differential SAR interferometry using data of the European Remote Sensing Satellites ERS-1 and ERS-2 has reached operational readiness. Land subsidence maps were generated in numerous cases for different surface deformation velocities and extents [1]. In several cases, the subsidence maps were validated with levelling surveys indicating a very high accuracy. This does not mean that all subsidence mapping problems are solved with SAR interferometry, though, but rather that the technique has a very good potential, that it reached some robustness, and that our understanding is sufficient to more easily evaluate its potential for new cases, i.e. to decide on the strategy to use, to assess the feasibility, to assess the expected processing effort and data costs, and to indicate an accuracy. In spite of this, it is important to keep in mind the limitations of the technique. In most cases it was not possible, for example, to generate a subsidence map with complete coverage due to temporal decorrelation for certain surface types. In addition, a quantitative interpretation of the interferometric phase was not possible in the case of high fringe rates resulting from large displacement gradients, due to phase unwrapping problems.

These limitations are closely related to the C-Band frequency (5.3 GHz, 5.7 cm wavelength) of the ERS SAR. Especially lower frequencies are very promising to avoid some of these problems. The use of L-Band SAR (1.3 GHz, 23.5 cm wavelength) is attractive for land subsidence mapping because of the expected lower temporal decorrelation over vegetated areas and of the larger wavelength permitting to better analyze large deformations. Therefore, it allows to achieve a more complete spatial coverage with displacement information.

In this paper the potential of L-Band repeat-pass differential SAR interferometry for land subsidence monitoring is evaluated using SAR data of the Japanese Earth Resources Satellite JERS-1. The selected application sites of Mexico City, Bologna and the Ruhrgebiet are characterized by different displacement velocities, extents of the subsiding area and landuse covers. In addition, for these sites subsidence maps derived from ERS SAR data and levelling surveys are available for comparison and validation.

II. MEXICO CITY (MEXICO)

Mexico City (Fig. 1) is built on highly compressible clays and by reason of strong groundwater extraction a total subsidence of more than nine meters has been observed over the last century. Two independent ERS SAR differential interferograms in ascending and descending modes, both with an acquisition time interval of 139 days, were used to derive a subsidence map for the time period December 1995 to May 1996 in [2]. Consistent results were found with the two interferograms and their results averaged (Fig. 2). The observed maximum subsidence velocity was larger than 40 cm/year. The coverage with subsidence information derived from ERS SAR interferometry is limited to the urban area with missing information near the Texcoco Lake and to the South in the Chalco Plain.

JERS SAR data suitable to map land subsidence in Mexico City were also found in the archive, but SAR processing with far-range extension [3] had to be performed in order to enlarge the coverage to the west of the city. A SAR image acquired on 17 March 1994 and five other images acquired every 44 days between 3

Proc. 3rd International Symposium, 'Retrieval of Bio- and Geophysical Parameters from SAR Data for Land Applications', Sheffield, UK, 11-14 September 2001 (ESA SP-475, January 2002)

April 1996 and 26 September 1996 permitted to compute a series of interferograms with acquisition time intervals between 44 and 924 days and perpendicular baselines between 222 and 3689 m. For baselines larger than around 2000 m we found complete decorrelation. For baselines between around 1000 and 2000 m the phase signal is visible but noisy. For baselines smaller than around 1000 m high coherence is observed.

Two interferograms acquired between March 1994 and September 1996 and three interferograms between April 1996 and September 1996, all with baselines shorter than 1026 m, were selected for further analysis. The topographic phase component was estimated based on a DEM derived from an ERS-1/2 Tandem pair. For the geometric referencing between the JERS and ERS data, terrain corrected geocoding with a global DEM and a fine registration using an intensity cross-correlation method [4] were used. The terrain flattened interferograms were unwrapped and stacking of the two interferograms acquired between March 1994 and September 1996 and of the three interferograms acquired between April 1996 and September 1996 was applied to combine the individual results into single maps with reduced errors.

The coverage with subsidence information derived from the interferograms with 2 years acquisition time interval (Fig. 3) is restricted to the urban area and is similar to that obtained with ERS SAR data. L-Band SAR interferometry for acquisition time intervals of less than 176 days (Fig. 4), on the other hand, permitted to extend the coverage with subsidence information to vegetated areas. The spatial coverage with subsidence information of Fig. 4 is mainly limited by the area where the ERS Tandem pair used to derive the DEM could be unwrapped. The L-Band interferograms of less than 176 days acquisition time interval could be unwrapped without any particular difficulty, whereas for the ERS SAR interferograms with acquisition time intervals of 139 days and the JERS SAR interferograms with 2 years time interval the fringe rate was in some areas very high and hard to be resolved. The mosaic of combined ERS and JERS results (Fig. 5) gives an impressive overview of the subsidence in Mexico City in 1996, with settlements of more than 50 cm/year in some areas. This result is also in general agreement with two levelling surveys performed in 1994 and 1996 (Fig. 6). However, with SAR interferometry a larger area could be monitored at low cost.

III. BOLOGNA (ITALY)

At Bologna, Italy, (Fig. 7) land subsidence is caused by ground-water exploitation for industrial, domestic and agricultural uses [5]. Maximum subsidence velocities of 6 to 8 cm/year were observed with precision levelling surveys during the time period 1987-1991 (Fig. 10). Using the interferogram stacking technique we produced a subsidence map for the time period 1992-1993 (Fig. 8) based on six ERS SAR scenes [6]. The subsidence information derived from ERS SAR interferograms of around one year acquisition time interval is restricted to built-up areas. A phase unwrapping algorithm for sparse data [7] was used to retrieve subsidence values also for the suburbs of Bologna and the neighboring small towns. However, in comparison to levelling surveys, the spatial coverage with subsidence data outside Bologna is incomplete.

Limited data availability strongly restricted the selection of JERS SAR data to map subsidence at Bologna. Only four scenes were acquired by JERS over Bologna, between 24 July 1993 and 14 April 1994, and only two interferograms with perpendicular baselines of less than 2000 m showed coherence. The two interferograms have acquisition time intervals of 88 and 264 days. Considering that subsidence in Bologna does not exceed 8 cm/year, we expect large errors from the analysis of these data. However, these data were further processed in order to investigate the coherence over non-urban areas. An external DEM with a pixel size of around 200 m x 200 m was used for terrain corrected geocoding and removal of the topographic phase component.

The results of the JERS SAR differential interferometric analysis (Fig. 9) confirm the higher correlation of L-Band interferometry in comparison to C-Band one. The subsidence signal in Fig. 9 is affected by large-scale errors due to the estimation of the baseline and atmospheric artifacts. Nevertheless, a general similarity to the results of the levelling surveys performed in 1987 and 1991 (Fig. 10) is still visible. A more complete validation with levelling data was not performed, because of the unsatisfactory JERS SAR data availability. More pairs with longer acquisition time intervals and short baselines would be required for an improved analysis at this site with relatively low deformation rates of a few cm/year.

IV. RUHRGEBIET (GERMANY)

Coal mining in the German Ruhrgebiet causes significant surface movement [8]. Due to legal requirements the mining company Deutsche Steinkohle AG (DSK) is obliged to assess the environmental impact of the excavations. Surface movement caused by mining is a very dynamic process with high spatial and temporal variability. For mining areas with high subsidence velocities, ERS interferometric pairs with acquisition time intervals of only one or a few 35 day repeat cycles are most appropriate [9].

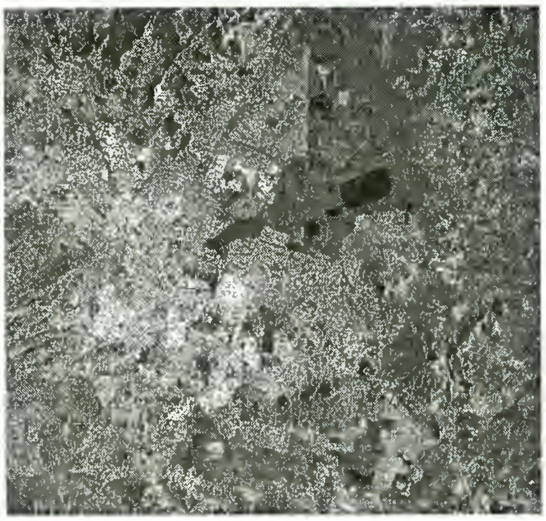

Fig. 1. Mexico City: ERS SAR backscattering coefficient. The image width is about 20 km.

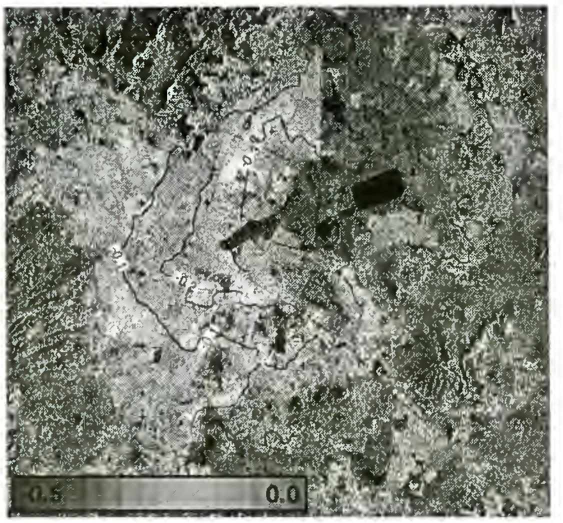

Fig. 2. Mexico City: Subsidence rates in m/year derived from 2 ERS pairs between December 1995 and May 1996.

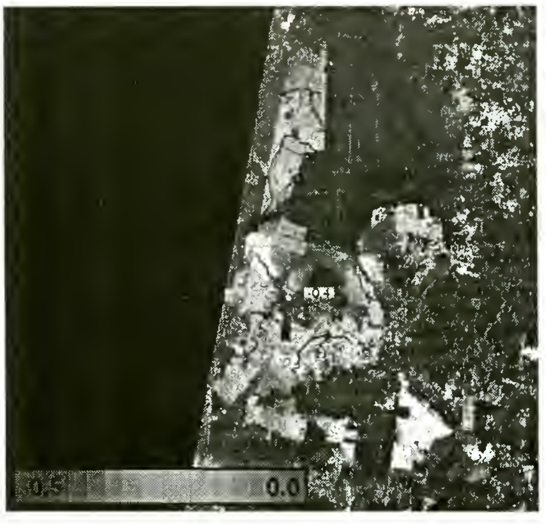

Fig. 3. Mexico City: Subsidence rates in m/year derived from 2 JERS pairs between March 1994 and September 1996.

Fig. 4. Mexico City: Subsidence rates in m/year derived from 3 JERS pairs between April 1996 and September 1996.

Fig. 5. Mexico City: Combined ERS and JERS subsidence rates in m/year for 1996.

Fig. 6. Mexico City: Subsidence rates in cm/year derived from leveling surveys in 1994 and 1996 (courtesy Dr. Vega).

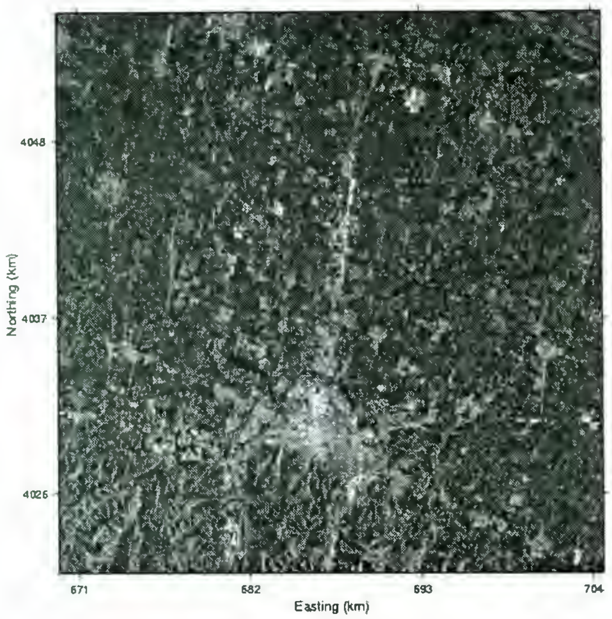

Fig. 7. Bologna: JERS SAR backscattering coefficient.

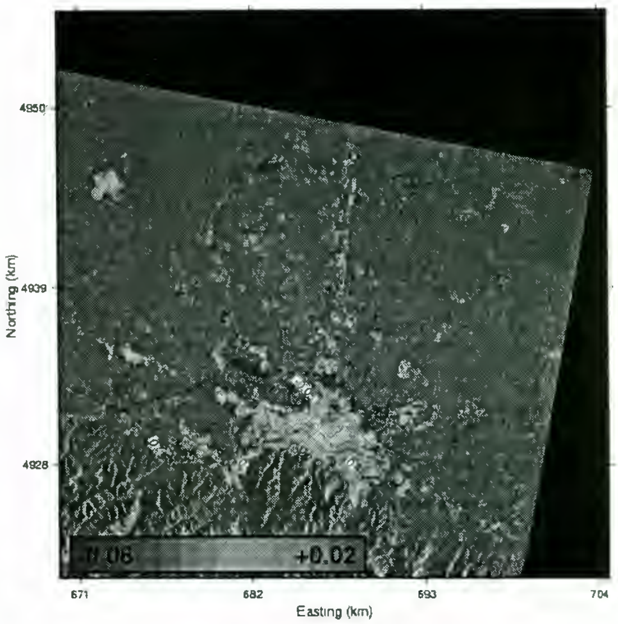

Fig. 8. Bologna: Subsidence rates in m/year derived from 6 ERS pairs between May 1992 and July 1993.

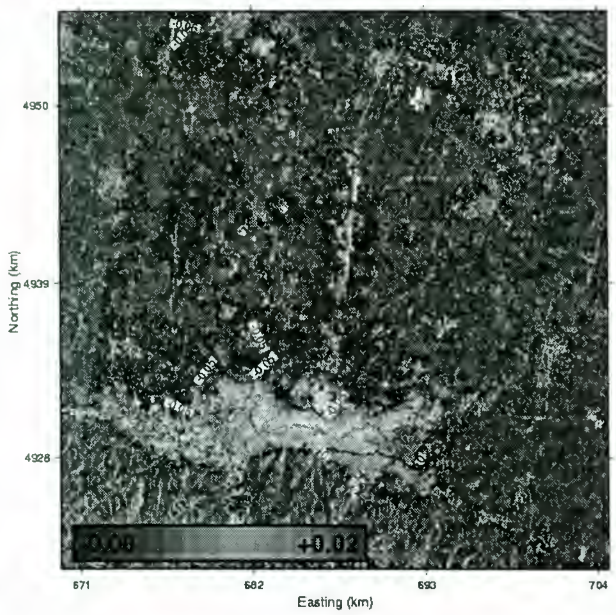

Fig. 9. Bologna: Subsidence rates in m/year derived from 2 JERS pairs between July 1993 and April 1994.

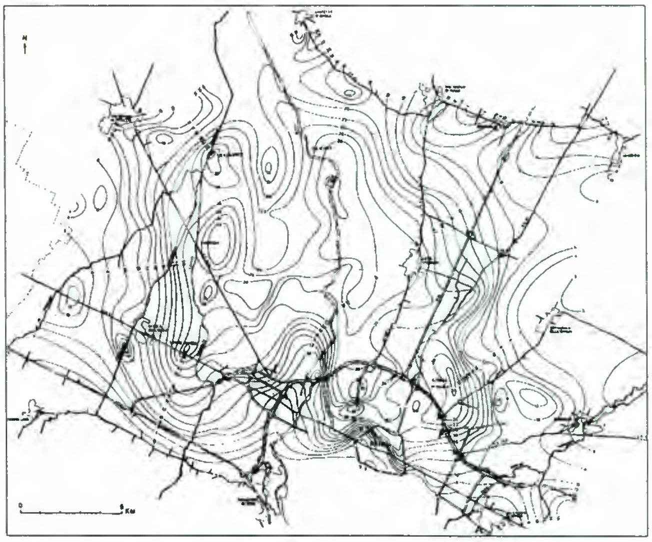

Fig. 10. Map of the vertical ground movements (in cm) from two levelling surveys in 1983 and 1987 in Bologna [5].

An example for a 70 days interferogram is shown in Fig 12. For non-urbanized areas (see Fig. 11), the ERS phase signal is noisy, but a clear subsidence signal can be identified in the urban area in the Southwest corner. Also shown are mining informations, with yellow boxes indicating the mining activity up to the first acquisition date and cyan boxes the mining works up to the second acquisition date. A major difficulty in the quantitative interpretation of the ERS interferograms was the phase unwrapping of the high fringe rates over ongoing excavation. Up to displacements of about 6 to 8 cm in the observation period reliable estimations were obtained. Higher deformation rates were not accurately caught resulting in a significant underestimation for settlements between 10 and 30 cm [8].

Also for the Ruhrgebiet JERS SAR data selection was strongly restricted by the few acquisitions found in the archive. Only 7 scenes, permitting to compute 5 interferograms with baselines shorter than 2000 m and acquisition time intervals of less than 132 days, are available. The JERS SAR data analysis for the

Ruhrgebiet is still ongoing and here we report only on interferograms with topographic and displacement phase terms not yet separated from each other. Far-range extension was applied to enlarge the study area and improve the coverage of active mining areas.

In the interferogram shown in Fig. 13, with a perpendicular baseline of 502 m and an acquisition time interval of 88 days, the coherence is high even for forests, resulting in a significantly increased spatial coverage with subsidence information in comparison to ERS SAR interferometry. For agricultural areas more decorrelation is observed. Three clear subsidence signals appear in the interferogram at positions where mining was ongoing. In all three cases the displacement causes only a phase difference of one fringe or less because of the reduced sensitivity of the long L-band wavelength, which permits to easily unwrap the phase. The analysis of the other interferograms showed, that (i) the coherence over urban areas is high for baselines up to 1500 m, (ii) the coherence over forest diminishes in particular with increasing baseline, but for interferograms of up to 1350 m it is still useful, (iii) the coherence over agricultural fields diminishes with increasing time interval from 44 days to 176 days. The available data were not sufficient to study seasonal effects. Future work will include the derivation of deformation maps and a quantitative validation with ground truth (mining information, subsidence data).

Fig. 12. Ruhrgebiet: ERS interferogram for the time period 7 July 1996 – 15 September 1996 (-161 m, 70 days, ascending mode) with superimposed mining information. Mining information courtesy DSK.

Fig. 11. Ruhrgebiet: Color composite of ERS Tandem coherence (red), backscattering coefficient (green) and temporal variability of the backscattering coefficient (blue). The image width is about 10 km.

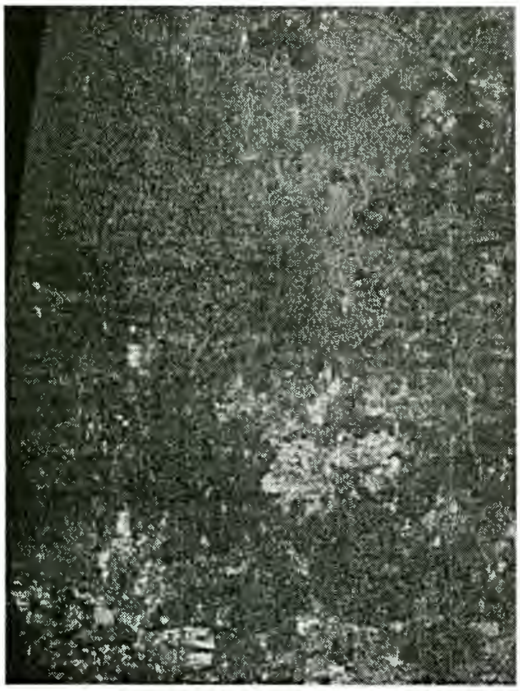

Fig. 13. JERS interferogram for 24 June 1996 – 20 September 1996 (502 m, 88 days, descending mode).

V. DISCUSSION

JERS SAR interferometry for land subsidence monitoring was applied to Mexico City, Bologna and the Ruhrgebiet. In spite of the limited data availability, land subsidence maps for the three application sites could be generated and validated with subsidence maps derived from ERS SAR interferometry and levelling surveys. Range extended SAR processing was applied in some of the examples to cover areas of interest of up to a few kilometers outside the normal swath.

It was demonstrated that L-Band interferograms of less than one-year acquisition time interval allowed the retrieval of subsidence values also for vegetated areas and forest. It was also found that high deformation gradients, which could not be resolved with ERS, can be resolved with L-Band interferometry because of the reduced sensitivity at the longer wavelength. Such high gradients are, for example, often observed above active mining. Based on this we conclude that L-Band differential SAR interferometry is particularly well suited for the measurement of large displacements (> 10 cm) and displacements in forested areas. This is complementary to ERS differential SAR interferometry, which is better suited for the measurement of slow displacements in urban areas.

Future work will concentrate on the quantitative validation of the displacements in the Ruhrgebiet with ground truth and on the analysis of slow displacements of few cm/year with the stacking of multiple interferograms. In expectation of the L-Band PALSAR system onboard the Japanese ALOS satellite scheduled for a launch in 2003, we conclude that L-Band differential SAR interferometry has a very high potential for subsidence monitoring provided that data are regularly acquired in a single interferometric mode with small enough baselines.

ACKNOWLEDGMENT

We acknowledge Dr. Ing. G.E. Figueroa Vega, Comisión de Aguas del Valle de México, and Prof. G. Bitelli, University of Bologna, for the leveling data of Mexico City and Bologna, respectively, and Dipl.-Ing. V. Spreckels, University of Hannover c/o Deutsche Steinkohle AG (DSK), for the mining data of the Ruhrgebiet. The Italian National Geologic Survey is acknowledged for the DEM of Bologna. Mining information courtesy DSK. ERS data copyright ESA. JERS data copyright NASDA. ERS SAR data analysis supported by the ESA Data User Programme. JERS SAR data courtesy of J-2RI-001 and ALOS-RA-94. ERS SAR data of Mexico City courtesy of A03-178.

REFERENCES

[1] T. Strozzi, U. Wegmüller, L. Tosi, G. Bitelli and V. Spreckels, "Land Subsidence Monitoring with Differential SAR Interferometry", PE&RS, in press.

[2] T. Strozzi and U. Wegmüller, "Land Subsidence in Mexico City Mapped by ERS Differential SAR Interferometry", Proceedings of IGARSS'99, Hamburg, Germany, 28 June - 2 July 1999.

[3] C. Werner, U. Wegmüller, T. Strozzi and A. Wiesmann, "Gamma SAR and Interferometric Processing Software," Proceedings of the ERS-ENVISAT Symposium, Gothenburg, Sweden, 16-20 October 2000.

[4] U. Wegmüller, C. Werner, T. Strozzi and A. Wiesmann, "Automated and precise image registration procedures", Proceedings of the MultiTemp 2001 Conference, Trento, Italy, 13-14 September 2001.

[5] M. Barbarella, L. Pieri and P. Russo, "Studio dell'abbassamento del suolo nel territorio bolognese mediante livallazioni ripetute: analisi dei movimenti e considerazioni statistiche", INARCOS, 506, 1-19, 1990.

[6] T. Strozzi, U. Wegmüller and G. Bitelli, "Differential SAR Interferometry for Land Subsidence Mapping in Bologna", Land Subsidence – Vol. II, Proceedings of the Sixth International Symposium of Land Subsidence, Ravenna, Italy, 24-29 September 2000.

[7] M. Costantini and P. Rosen, "A generalized phase unwrapping approach for sparse data", Proceedings of IGARSS'99, Hamburg, Germany, 28 June - 2 July 1999.

[8] V. Spreckels, U. Wegmüller, T. Strozzi. J. Musiedlak, and H.C. Wichlacz, "Nutzung von InSAR-Daten zur großflächigen Erfassung von topographischen Veränderungen über Abbaubereichen der Deutsche Steinkohle AG (DSK)", Tagung des Deutschen Markscheider Vereins (DMV), Trier, Germany, 26-28 September 2001.

[9] U. Wegmüller, T. Strozzi, C. Werner, A. Wiesmann, N. Benecke and V. Spreckels, "Monitoring of mining-induced surface deformation in the Ruhrgebiet (Germany) with SAR interferometry", Proceedings of IGARSS 2000, Honolulu, Hawaii, 24-28 July 2000.

EXTRACTION OF SURFACE TOPOGRAPHY FROM SAR STEREO PAIRS USING AN AIRBORNE X-BAND SENSOR: PRELIMINARY RESULTS

A. Schubert[1], D. Small[1], F. Holecz[2], E. Meier[1], D. Nüesch[1]

[1] Remote Sensing Laboratories, University of Zürich; Winterthurerstrasse 190; CH-8057 Zürich; Switzerland
Tel: +41 1 635 6523 FAX: +41 1 635 6842, Email: {schubert,daves,meier,nuesch}@geo.unizh.ch
[2] sarmap s.a.; Cascine di Barico; CH - 6989 Purasca; Switzerland
Tel: +41 91 600 9366 FAX: +41 91 600 9369, Email: francesco.holecz@sarmap.ch

ABSTRACT

The two most reliable methods for extracting surface topography from SAR image pairs are interferometry and stereogrammetry. Although the high-resolution results obtained by interferometry have been the main focus for research into digital surface model (DSM) generation in recent years, it has been shown that the use of a lower-resolution DSM, obtained in this study by processing a SAR stereo pair, can aid in the generation of an interferometric DSM. In addition, height information for areas where the interferometric technique fails is often available in a stereogrammetrically-derived DSM. Because of the increasing availability of stereoscopic and interferometric coverage generated by air- and spaceborne sensors in the near future, the combination of radargrammetric stereo SAR with interferometry is becoming more feasible.

This paper describes the extraction of high-resolution topographical information from SAR imagery, using stereogrammetry based on multiresolution wavelet-matching. The data were obtained by a single airborne sensor over a test site in Switzerland. The resulting stereogrammetric DSMs are compared to an existing interferometric DSM. The limits of the stereoscopic technique are further investigated through simulation of the radar backscatter using a reference digital elevation model (DEM) and nominal backscatter values mapped from the DEM into radar geometry. Sources of possible geometric errors in the stereo DSMs are studied.

It is concluded that using a multiresolution stereo matching approach combined with good sensor positioning information makes automatic generation of a high-quality DSM possible. The latter can subsequently be used to improve the accuracy of a high-resolution InSAR-derived height map.

INTRODUCTION

Extracting surface height information from SAR-amplitude stereo pairs dates back to work done in the 1960s, pioneered by La Prade [1], and is described in detail by Leberl [2]. Computing technology has only more recently made it possible to automate the process digitally. Satellites such as ENVISAT-1 and RADARSAT-1 are quickly increasing the availability of near-simultaneous stereo SAR and InSAR data. This has caused a recent surge of interest in height-extraction techniques based on the fusion of stereo and InSAR (for examples, see [3] and [4]).

The motivation for pursuing the integration of stereo within an InSAR framework is to overcome the weaknesses inherent in the latter method, namely:

- Ground control points (GCPs) are required for interferometric **phase calibration**; the stereo matching algorithm used here is fully automatic.
- InSAR topography estimation requires a delicate **phase-unwrapping** step, which can be greatly aided by an existing low-frequency DSM such as may be provided by stereogrammetry.
- Areas of **low coherence** in interferograms, especially due to temporal decorrelation during multi-pass InSAR or vegetation presence, are topographically unresolvable or provide unsatisfactory height estimates at best. This is not a problem inherent to stereo SAR.

Stereogrammetry relies on image matching, which does not always provide accurate parallax estimation in areas with few features. However, with a coarse-to-fine matching implementation using wavelets, which are by their nature sensitive to phenomena at multiple scales, even homogeneous image regions can be properly matched as long as they are bounded by recognisable features or textures, and do not dominate the image. The SNR of the disparity field over these regions can be improved by an adaptive smoothing process during coarse-to-fine matching, at the cost of poorer resolution in the final product.

Therefore, although a stereo DSM will not provide nearly the height resolution of an InSAR DSM, InSAR processing can benefit from the availability of stereo.

The scope of this paper does not extend beyond stereo processing. The Remote Sensing Laboratories at the University of Zurich has many years of experience in InSAR processing and topography estimation, and the necessary software and know-how is available. However, the implementation of a stereo processing chain is a recent addition, and its fine-tuning is still under way. Its

Proc. 3rd International Symposium, 'Retrieval of Bio- and Geophysical Parameters from SAR Data for Land Applications', Sheffield, UK, 11-14 September 2001 (ESA SP-475, January 2002)

subsequent merging with the existing InSAR processor is expected to be a relatively smooth process.

STEREO SAR PROCESSING

The processing chain consists of the following steps:

- SAR focusing with motion compensation
- Choice of image pair suitable for stereogrammetry
- Speckle reduction
- Coarse mapping of slave into master geometry
- Coarse radiometric adjustment of slave with respect to the master radiometry
- Disparity field (parallax) estimation
- Height map generation and geocoding

Fundamental requirements for achieving the theoretical resolution of the system are the availability of high precision DGPS and high frequency attitude data of the platform, the precise measurement of the antenna positions with respect to the GPS system, knowledge of exact time synchronization and range delay, and the consideration of all related geodetic and cartographic transforms.

Based on the post-processed real platform positions collected by the navigation system, an ideal flight path is generated. Motion displacements in range and azimuth direction as well as velocity variations with respect to these ideal flight paths are then calculated. Successively, the motion instabilities of the platform are corrected, before the SAR focusing step.

The stereogrammetric processing consists of the disparity estimation, or matching, and its subsequent conversion to heights in a map geometry through one of two paths: simplified analytic calculation of a slant-range height map and its conversion to map geometry, or direct estimation of map heights by numerically solving the range-Doppler equations for the stereo geometry.

DISPARITY FIELD ESTIMATION

The image matching problem has been studied actively for the last 20 years by researchers in fields such as computer vision, medicine, biology, and remote sensing because of the need to correlate images that vary slightly from one to the next, either spatially or temporally. The matching algorithms described in the literature can be roughly classified as being area- or gray-level-based, feature-based [5], or hybrids. Their implementation within multiresolution, or coarse-to-fine frameworks has led to hybrid algorithms that now make stereo matching all the more feasible.

The matching approach used during this work was first outlined by H-P. Pan in 1996 [6], which he called *uniform full-information image matching.* It depends on a wavelet multiresolution decomposition of the image. A complex discrete wavelet transform using Magarey-Kingsburys wavelets [7] is calculated for the pair, which produces lossless representations of the images on multiple resolution levels. At each level a new quarter-resolution approximation image is generated, as well as three detail images of the same size, permitting lossless reconstruction of the image from the previous level. By minimising the *similarity distance* for all homologous points at all levels of resolution beginning with the coarsest level, we incrementally fine-tune the estimated disparities at each finer level, eventually generating a disparity field for the image pair at one quarter the original resolution. At each level of matching, the disparity field is regularised to provide a global compromise between feature similarity and disparity field continuity. This regularisation, described for example in [8], was an improvement on the original algorithm and reduced the signal-to-noise ratio of the subsequent height reconstructions. This improved version of the algorithm was found to be quite well adapted to radar amplitude image pairs, as long as the slave image was first transformed into the slant-range reference frame of the master image before matching. This transformation is necessary in order to remove the first-order geometric differences between the two images arising from their different look angles. The resulting disparity field describes the range differences between the two sensor positions and the pixel ground locations.

HEIGHT MAP GENERATION

For a given homologous pixel pair, the horizontal, or range, component of the disparity field generated by the matching process is a direct measurement of the difference in range from that point to each of the sensors. Given these range differences for all points, and given accurate flight position and velocity information, the following four equations must be satisfied for each pair of homologous points:

$$|\vec{P}-\vec{S}_1| - |\vec{r}_1| = 0 \tag{1}$$

$$\frac{-2}{\lambda}\cdot\frac{(\vec{P}-\vec{S}_1)(\vec{v}_{S_1})}{|\vec{P}-\vec{S}_1|} + f_{d_1} = 0 \tag{2}$$

$$|\vec{P}-\vec{S}_2| - |\vec{r}_1| - \delta_r = 0 \tag{3}$$

$$\frac{-2}{\lambda}\cdot\frac{(\vec{P}-\vec{S}_2)(\vec{v}_{S_2})}{|\vec{P}-\vec{S}_2|} + f_{d_2} = 0 \tag{4}$$

where:

$\vec{P}$	=	ground point positions
1, 2	=	master (1) and slave (2) antenna
$\vec{S}$	=	antenna positions
$\vec{r}$	=	slant ranges $\vec{P}$ to $\vec{S}$
$\vec{v}$	=	sensor velocities relative to $\vec{P}$
f_d	=	Doppler frequencies
δ_r	=	range differences (disparities)
λ	=	radar wavelength

These equations are over-determined, but may be solved numerically, taking into account the non-zero squint for each sensor. The solution of the four equations for the case of a non-zero squint geometry yields a height for each homologous pair in an Earth-centred global cartesian reference system [9]. This geo-referenced height field is then transformed into a Swiss map geometry to allow comparison with other available height models.

SAR SYSTEM AND DATA

This airborne InSAR system was designed and manufactured at Aero-Sensing Radarsysteme GmbH. The characteristics of the AeS-1 SAR system during acquisition of the data used in this study are shown in Table 1.

Frequency [GHz]	9.6
Polarisation	HH
Bandwidth [MHz]	400
Swath width [km]	2.2
Incidence angle [deg]	45
PRF [Hz]	10320
Radiometric resolution [dB]	1.8-1.0
Positioning	DGPS and IMU

Table 1: SAR system parameters

In particular the following features of this InSAR system have to be considered:

- The maximum selectable system bandwidth allows a ground range resolution of better than 0.5 meters.
- The platform is equipped with integrated real time Differential Global Positioning System (DGPS) and an Inertial Motion Unit (IMU). This provides extremely accurate positioning information of the platform.

The AeS-1 InSAR data of the site 'Küttigkofen', in northwestern Switzerland (47.2^{o}N, 7.5^{o}E), were acquired on April 24th, 1999 using a range bandwidth of 400 MHz and 2.2 km swath width. The site is located between the cities of Solothurn and Berne and covers an area of about 6 km^2. The area was chosen according to the following criteria:

- Terrain ranging from flat to hilly with height differences of up to 150 meters and several different terrain features and ground cover types.
- Digital land registry data of 1:5000 scale (grid size 1m) available.
- Digital surface model (DSM) data, collected on July 1st 1999, having a grid size of 1m and height resolution of 0.1m available.

RESULTS AND DISCUSSION

The height model used to validate the results was obtained using the DoSAR airborne InSAR system from Dornier (for a description of this system and DSM generation using it, refer to [10]). Figure 1 shows the DoSAR height model for the Küttigkofen test site.

Fig. 1. The DoSAR digital surface model [m]

The high quality of the DoSAR model was established by comparing it at various locations to ground control points (GCPs) with precisely-known positions. Table 1 summarises the statistics for 169 GCPs distributed across the entire DoSAR scene.

Number of points used	169
Total area covered [km^2]	210
Mean height difference [m]	-0.040
Mean absolute height difference [m]	0.795
Standard deviation [m]	1.044

Table 2: Validation of the DoSAR DSM using GCPs distributed over the entire scene

It was found that the multiresolution matching approach, implemented in MATLAB, was well-adapted to the SAR image pair used during this study. Even without speckle reduction (using a 5x5 Frost filter), the matches found by the algorithm resulted in accuracies of one pixel or better over most of the image. This was verified by using the estimated disparity field to resample the slave image and comparing the result to the master image. It was possible to compare the pixel positions of bright corner reflectors in both scenes manually, and in all cases an accuracy of one pixel or less was noted. Figure 2 shows the master, resampled slave, and the difference between them for a part of the Küttigkofen scene. The almost perfect absence of bright pixels in the difference indicates a good correspondence was found between the master and slave images. It is important to note that because of radiometric differences between the two input images arising from the different view geometries and speckle, even a perfect match - which is defined purely geometrically as a vector field - does not result in a resampled slave that exactly matches the master *radiometrically*. In this sense it is more convincing to manually compare image positions of individual homologous pixel pairs.

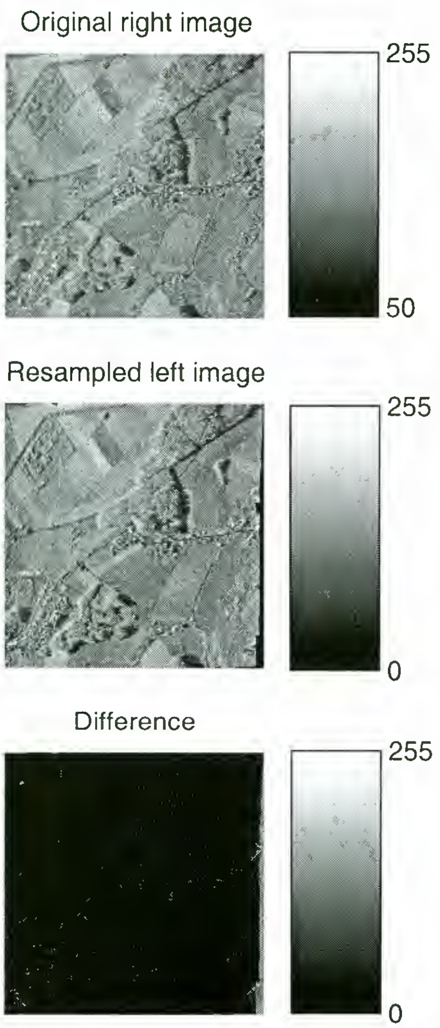

Fig. 2. Master image, resampled slave, and their difference (8-bit grayscale levels)

In order to evaluate the performance of the height reconstruction process given a disparity field under controlled conditions, a radiometric SAR image simulator, described in [11], was used to create a stereo pair with geometric properties identical to those of the real pair. The DoSAR DSM was used to generate the simulations. As can be seen in Figure 3, the most obvious difference between a real and simulated image is the lack of information in areas where the backscatter depends on the surface characteristics. This is to be expected, since the DoSAR DSM contains no information about the landcover. In spite of this, the matching algorithm was observed to work nearly perfectly even in image areas with few features or textural variations.

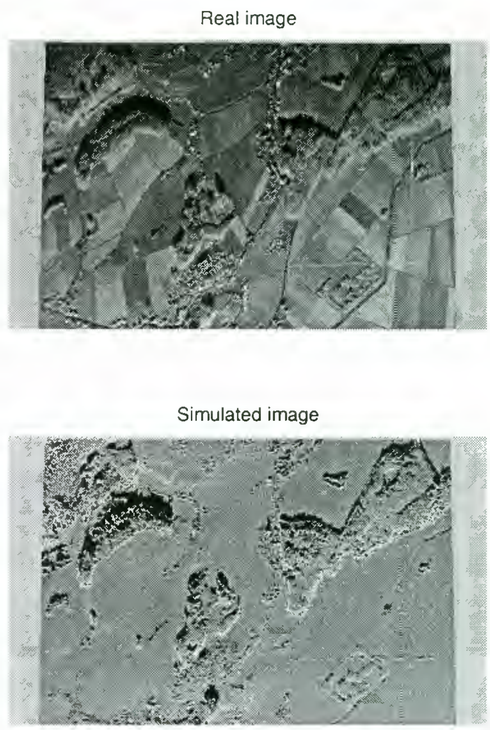

Fig. 3. Real image and simulation of the same scene

The resulting disparity field for the simulated pair was then used to geocode the scene into Swiss map geometry, by solving Equations (1) through (4) as described earlier. Figure 4 shows the resulting height map. The differences between it and the DoSAR reference are shown in Figure 5; the error statistics are summarised in Table 3.

The equivalent results for the DSM obtained using the real image pair are shown in Figure 6, Figure 7, and Table 4.

The most striking features of both Figures 5 and 7 is that the heights of the three forest stands visible in the images are consistently underestimated, and the radar shadow regions are overestimated.

The radar shadows above the northern edges of these regions are assigned heights much greater than the ground level over which they lie. This is to be expected, since the shadows 'appear' to stem directly from the northern edges of the forest stands, resulting in a parallax between the shadow regions equal to the parallax between the stand northern tree edges themselves. In this sense, the heights erroneously assigned to the shadows will approximate the stand heights along their northern edges.

Fig. 4. DSM obtained using the *simulated* pair [m]

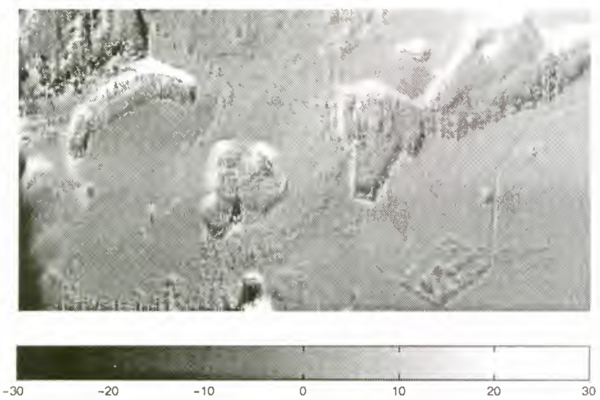

Fig. 5. Height error for the *simulated* pair (m)

Mean height error [m]	-2.7
Standard deviation [m]	18.3
Points with < 5m error [%]	56.1
Points with <20m error [%]	86.1
Points with <50m error [%]	94.0

Table 3: Error statistics for DSM obtained from the simulated pair

More surprising is the consistent height underestimation of the forest stands and relatively large amount of noise, even in the simulation reconstruction. It can only be concluded that a geometric error is present in the current geocoding process. This is supported by the following facts:

- The matching has been shown to be accurate to one pixel or less.
- The same flight path and motion information used to simulate the stereo pair was used during geocoding.
- The motion and Doppler centroid data corresponding to the motion-compensated amplitude pair have been verified as being correct to within one pixel.

Fig. 6. DSM obtained using the *real* pair [m]

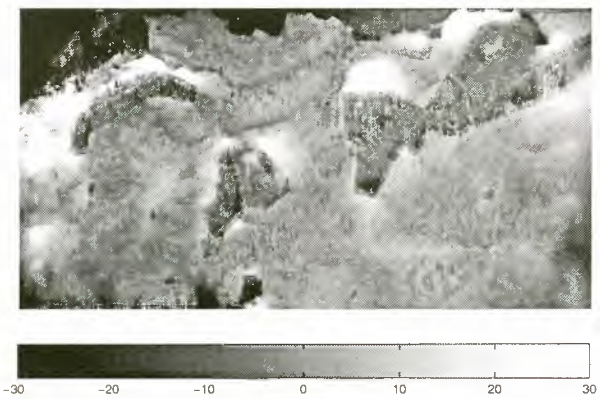

Fig. 7. Height error for the *real* pair [m]

Mean height error [m]	-6.9
Standard deviation	23.1
Points with < 5m error [%]	45.6
Points with <20m error [%]	86.4
Points with <50m error [%]	95.2

Table 4: Error statistics for the DSM obtained from the real pair

Based on this information, and in light of the results, it is clear that the DSMs obtained are not yet of the quality that should be obtainable with the available data.

This conclusion is reinforced by Figure 8. The general trend of height underestimation in proportion to true height is clearly visible, and is indicated by a linear least-squares fit. The vertical arm-like structures springing from the central region are due to random noise about fixed height levels such as the ground, shadow effects, and random height estimation errors near the image edges.

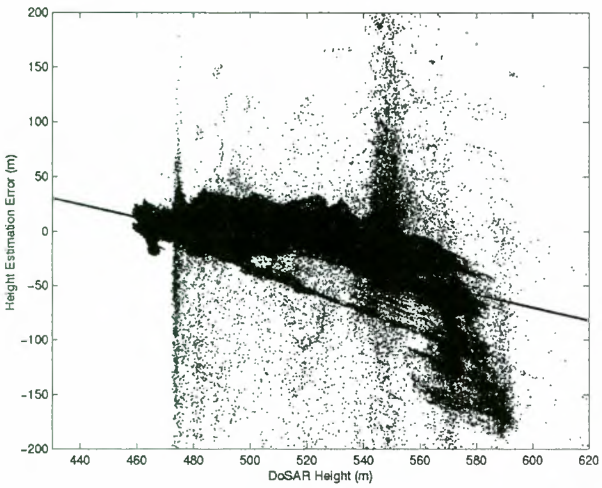

Fig. 8. Height error versus DoSAR height for the DSM obtained from the real pair, with least-squares-fit line

CONCLUSIONS AND OUTLOOK

The central requirements for obtaining a DSM of a resolution near the theoretical limits of the system using stereogrammetry have been met. Given a pair of SAR amplitude images suitable for stereogrammetry, these are:

- the ability to find the correspondence between the two images that brings one into alignment with the other (stereo matching)
- the availability of accurate positioning information for the sensor over both scenes

These conditions are the most difficult to satisfy in the context of stereo SAR processing in general. Therefore, it can be stated that the stereo processing problem has effectively been solved. The matching and geocoding are possible without GCPs, and provide height estimates for all image locations. It is expected that the geometric error observed in the results so far will quickly be rectified, and subsequent work will focus on the integration of the stereo processing chain into the already-existing InSAR framework.

The radiometric simulations will be made more realistic by implementing a landcover-dependent backscatter mechanism. This will fill in the homogeneous regions visible in the current simulated images with radiometric variations closely linked to the type of landcover (soil, crops, etc.), based on backscatter statistics for the landcover types encountered.

By adjusting the stereo baseline in the simulations, it will be possible to determine to what extent the acquisition geometry plays a role in the quality of the resulting stereogrammetric height map.

REFERENCES

[1] La Prade G., 1963. An analytical and experimental study of stereo for radar. Photogrammetric Engineering and Remote Sensing 29(2), pp. 294-300.

[2] Leberl F.W., 1990. Radargrammetric image processing. Artech House, Los Angeles, USA, Chapters 12-13.

[3] Gelautz M., Paillou Ph., and Chen C., 1999. Topographic Surface reconstruction using interferometric and stereo techniques. Proc. IGARSS'99.

[4] Elizavetin I.V., 1999. Merging of stereo and interferometric processing for improved DEM generation. Proc. IGARSS'99, pp. 2099-2107.

[5] Toutin T., Gray L., 2000. State-of-the-art of elevation extraction from satellite SAR data. ISPRS Journal of Photogrammetry and Remote Sensing 55(2000), pp. 13-33.

[6] Pan H-P., 1996. General stereo image matching using symmetric complex wavelets. Wavelet applications in signal and image processing IV, Proc. SPIE 2825, 1996.

[7] Magarey J., Kingsbury N., 1996. Motion estimation using a complex-valued wavelet transform. Wavelet applications in signal and image processing IV, Proc. SPIE 2825, 1996.

[8] Magarey J., Dick A., 1998. Multiresolution stereo image matching using complex wavelets. International Conference on Pattern Recognition no. 14, 1998.

[9] Holecz F., Pasquali P., Moreira J., Meier E., Nüesch D., 1998. Automatic generation and quality assessment of digital surface models generated from AeS-1 InSAR data. Proc. EUSAR'98, pp. 57-60.

[10] Goblirsch W. et al, 1995. Accuracy of interferometric elevation models generated from DoSAR airborne data. Proc. IGARSS'95, pp. 770-774.

[11] Small D., 1998. Absolute radiometric correction in rugged terrain: a plea for *integrated* radar brightness. Proc. IGARSS'98, pp. 330-332.

Soils and Hydrology

Chairman: M. Davidson

SURFACE PARAMETER ESTIMATION USING FULLY POLARIMETRIC L- AND P-BAND RADAR DATA

I. Hajnsek[1], K. P. Papathanassiou[1] & S. R. Cloude[2]

1: German Aerospace Center, Institute of Radio Frequency Technology and Radar Systems, Department: SAR Technology, P.O. BOX 1116, D-82234 Wessling, e-mail: irena.hajnsek@dlr.de, kostas.papathanassiou@dlr.de

2: AEL Consultants, 26 Westfield Avenue, Cupar, KY15 5AA, Fife, Scotland, Tel/Fax : (44) 1334 653958 e-mail: scloude@aelc.demon.co.uk

ABSTRACT -- This work presents a first qualitative and quantitative comparison of fully polarimetric SAR data at L- and P-band with respect to surface parameter estimation. The potential combination of these two frequencies to obtain more robust estimates and/or to extend the validity range of the inversion algorithms is investigated using experimental data acquired by DLR's airborne SAR system and simultaneously collected ground measurements used for the validation of the inversion results. The main problems of using lower frequencies are critical discussed and suggestions are made in order to resolve them.

1 INTRODUCTION

Investigations concerning surface parameter estimation from SAR data have been addressed firstly for single frequency and single polarisation data mainly due to the restricted operation mode of the early SAR systems. However, the technical development of SAR sensors enabled the operation at dual or multiple frequencies and/or polarisations making such data available to the remote sensing community. This triggered the development of more robust surface parameter inversion algorithms with a broader validity range. The proposed approaches concerning either single frequency (X- , C- or L-band) fully polarimetric data [1], [2], [3] or dual/multiple frequency [4], [5] dual polarisation configurations. From these investigations, the combination of C- and L-band [6] for the retrieval of surface parameters from bare surfaces, especially for the estimation of the surface RMS height, correlation length and fractal dimension, appears to be a promising one. Other investigations proposes the combination of L- and P-band data to measure subcanopy soil moisture.

In this work, the potential of estimating surface parameters, as volumetric soil moisture and surface roughness, over bare agricultural fields using L- and P-band fully polarimetric data is investigated. Due to the fact that roughness affects the scattering process in terms of k_s ($k = 2\pi/\lambda$ and s is the surface RMS height) i.e. scaled by the wavelength, the combination of two or more frequencies promises the coverage of a wider class of natural surfaces and more robust estimates. However, changing the wavelength may imply also a change of the physical properties of the scattering process. This can affect the applicability of the inversion algorithms.

Thus, this study is trying to answer the following questions:

- Are lower frequencies, as P-band suitable for surface parameters estimation ?
- Does the change of frequency influences the observed scattering mechanisms ?
- Is the combination of L- and P-band a promising one, with regards to surface parameters estimation ?

In the following the suitability of combining L- and P-band with respect to surface parameters estimation is discussed based on first qualitative and quantitative experimental results.

2 EXPERIMENTAL DATA

The test site Alling is located in Southern Germany and is predominantly covered with agricultural fields. In the frame of the *S*urface *PA*rameter *R*etrieval *C*ollaboration (*SPARC*) project, DLR's experimental airborne E-SAR system acquired, in March and July 2000, fully polarimetric data of the test site at L-band (1.3 GHz) and P-band (450 MHz), see Figure 1. Simultaneously ground measurements of volumetric moisture content and surface roughness were collected over different bare and vegetated agricultural fields. The volumetric moisture content measurements were performed using stick cylinders and TDR. Surface roughness s and surface correlation lengths l was measured using scaled boards and a laser profilometer [7] in two directions: perpendicular (PPF) and parallel to the flight direction (PAF). The measurements are summarised in Fig. 2. The results presented in the following are obtained from the data collected in March 2000.

Proc. 3rd International Symposium, 'Retrieval of Bio- and Geophysical Parameters from SAR Data for Land Applications', Sheffield, UK. 11-14 September 2001 (ESA SP-475, January 2002)

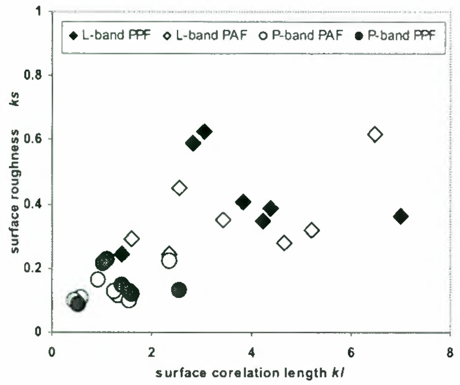

Figure 2. Ground measured plot: surface roughness *ks* - surface correlation length *kl*, using scaled board method.

3 INVERSION MODEL CONDITIONS

As concluded in previous studies [3], L-band with a wavelength of about 23 cm is an eligible frequency for the estimation of surface parameters. The much longer P-band wavelength of about 63 cm leads to a significantly different backscattering behaviour - compared with L-band - with important implications on the applicability range of surface parameter inversion algorithms. Concerning surface parameters inversion the most effective range lies for the surface roughness between $0.3 << ks << 1$. It corresponds to a surface RMS height variation about $1 << s$ [cm] $<< 4$ at L-band, while the corresponding range at P-band is about $3 << s$ [cm] $<< 11$. The combination of these two frequencies covers a significant wider range of natural bare surface conditions.

In order to answer the posed questions, in the first step the performance of P-band is investigated. Therefore, two sets of applicability conditions used to identify "pure" surface scattering regions have been employed. The first one is used mainly from empirical and/or semi empirical inversion algorithms based on polarimetric scattering amplitudes ratios [1], [2]

$$|HH|/|VV| < 1 \text{ and} \quad (1)$$
$$|HV|/|VV| < 0.079$$

The first condition accounts for a Bragg-like scattering behaviour while the second one ensures the exclusion of mainly vegetation covered areas. The results of the combined conditions, shown in Fig. 3, for the L-band data and in Fig. 5 P-band data. The disappointing small amount of valid areas obtained at P-band results mainly due to application of the second validity condition.

The second one relies on second order polarimetric scattering entropy and alpha-angle which are obtained from the eigenvector decomposition of the polarimetric coherency matrix [T] [3].

$$\text{Scattering Entropy} \qquad 0 > H > 0.5 \qquad (2)$$

$$\text{Mean a-Angle} \qquad 0 > \alpha > 43°$$

Also here the same tendency with a very small amount of valid areas at P-band is observed. In contrary, L-band indicates the highest amount of valid areas which are clearly distinguished by the field borders. A visual comparison makes clear that the validity restrictions in terms of the statistical polarimetric scattering parameters are much more severe than the ones for the scattering amplitude ratios, leading to a significant smaller amount of valuable areas. However, the comparison with the collected ground-information verifies the correctness of these criteria in terms of determining pure surface scatterers.

Two possible reasons can be accounted for: the first is the influence of the system noise and the second is the change of surface scattering characteristics due to the high penetration capability into the ground, with changing wavelength from L- to P-band. Both critical points are investigated in the following.

4 REMOVAL OF ADDITIVE NOISE

The backscattering from bare fields is much weaker in P-band than in L-band (due to the about three times lower *ks* values) and reaches even for rough surfaces very fast values about -30 [dB]. Such values are close to the system noise floor, and consequently affected by noise. Additive noise leads on the one hand side to biased estimates for the amplitude ratios of Eq. 1. On the other hand, it leads to an overestimation of the eigenvalues of [T] and consequently to an overestimation of the scattering entropy and an underestimation of the scattering anisotropy. Conventional polarimetric speckle filtering - which accounts mainly for multiplicative noise - is not sufficient enough in order to remove this additive noise level from the data. Therefore, a novel noise filtering approach, based on the variation of the <HVVH*> correlation has been developed and applied on the data [8].

The proposed method for the removal of additive noise - as thermal or system noise - is based on the correlation between the two acquired cross-polarised channels. The measured scattering matrix – after calibration – consists of the underlying scattering matrix [*S*] affected by an additive noise matrix [*N*]

$$[S]=\begin{bmatrix} S_{HH} & S_{HV} \\ S_{VH} & S_{VV} \end{bmatrix} \text{ and } [N]=\begin{bmatrix} n_{HH} & n_{HV} \\ n_{VH} & n_{VV} \end{bmatrix} \quad (3)$$

The additive noise term is modelled as a zero-mean Gaussian white noise process with noise power N [9]

$$\langle n_{ij} n^*_{ij} \rangle = \langle n_{mn} n^*_{mn} \rangle = N \quad \text{and} \quad \langle n_{ij} n^*_{mn} \rangle = 0 \quad (4)$$

For monostatic SAR systems and reciprocal scatterers $S_{HV} = S_{VH}$ and thus - in the absence of noise - S_{HV} and S_{VH} are completely correlated. As the two cross channels are measured independently by the SAR system they are affected by different realisations of the noise process which reduces their correlation. With decreasing SNR, the correlation between the S_{HV} and S_{VH} channels decreases allowing an assessment of the noise level.

Consequently, the presence of additive noise makes the tree dimensional scattering backscattering problem a four dimensional one. Addressing the four-dimensional Pauli-scattering vector $\vec{k}_4^{'}$

$$[\vec{k}_4^{'}] = \frac{1}{\sqrt{2}} \begin{bmatrix} S_{HH} + S_{VV} + (n_{HH} + n_{VV}) \\ S_{HH} - S_{VV} + (n_{HH} - n_{VV}) \\ S_{HV} + S_{VH} + (n_{HV} + n_{VH}) \\ i(S_{HV} - S_{VH} + (n_{HV} + n_{VH})) \end{bmatrix} \quad (5)$$

the 4x4 coherency matrix [T] is formed and is by definition hermitian PSD

$$[T] = \left\langle \vec{k}_4^{'} \cdot \vec{k}_4^{'+} \right\rangle \quad (6)$$

The diagonalisation of $[T_4]$ according to

$$[\Lambda_4] = [U_4][T_4][U_4]^{-1} \quad (7)$$

leads to the 4-dimensional diagonal form

$$[\Lambda_4] = \frac{1}{\sqrt{2}} \begin{bmatrix} \lambda_1 + N & 0 & 0 & 0 \\ 0 & \lambda_2 + N & 0 & 0 \\ 0 & 0 & \lambda_3 + N & 0 \\ 0 & 0 & 0 & N \end{bmatrix} \quad (8)$$

In the absence of noise, $[T_4]$ is in general (for distributed scatterers) of rank 3, and has only three non-zero eigenvalues. However, the presence of noise makes $[T_4]$ to be of rank 4 with four non-zero eigenvalues where the fourth (minimum) eigenvalue coresponds to the noise power of the noise subspace of $[T_4]$, i.e. $\lambda_4 = N$. In this sense, the noise filtering is performed by subtracting N from the first three eigenvalues of $[\Lambda_4]$. The obtained eigenvalues can be either directly used for the estimation of the polarimetric entropy, anisotropy and alpha angle, or be transformed back into the a "filtered" cohererency matrix $[T_4]$ - according to Eq. (7).

Figs. 4 and 6 show the valid regions obtained after applying the additive noise filtering for the L- and P-band data sets. The significant improvement in terms of applicability of the scattering models makes clear the strong influence of additive noise. As expected, the effect of noise is especially critical at P-band, but, even with a weaker impact, noise effects are present also at L-band. However, for the P-band data the valid regions are even after filtering disappointing small.

Our two interpretations for this are a remaining noise level which cannot be sufficiently removed or, what seems much more evident, the change of frequency implies the change of scattering mechanisms.

5 SURFACE ROUGHNESS ESTIMATION

The inversion algorithms used in this study, are based on the second order statistics of surface scatterers and considering only the estimation of one surface parameters the surface roughness. The correlation coefficient between different polarisations has been observed to correlate with dielectric constant and/or rms height measurements.

One of the first investigations has been made by [5] using the circular polarisation coefficient $|\gamma_{LLRR}|$, relating it to the ground measured RMS height and obtaining a high correlation. Since this parameter depends only on the surface roughness and is insensitive to the azimuth topographic tilt, it is robust to perform quantitative surface roughness estimates [11],[12]. The circular polarisation coefficient is defined as:

$$\gamma_{LLRR} := \frac{|< S_{LL}\, S_{RR}^{*} >|}{\sqrt{< S_{LL}\, S_{LL}^{*} > < S_{RR}\, S_{RR}^{*} >}} \quad (12)$$

More recently the polarimetric scattering anisotropy obtained from the eigen-decomposition of the coherency matrix indicated to have a sensitive estimate for the surface roughness. The anisotropy can be interpreted as a generalised rotation invariant expression for $|\gamma_{LLRR}|$, in case where the coherency matrix is diagonal. The anisotropy, A, is defined as the relation between the second and third eigenvalue:

$$A := \frac{\lambda_2 - \lambda_3}{\lambda_2 + \lambda_3} \quad (13)$$

Both parameters, $|\gamma_{LLRR}|$ and A, are by definition normalised between 0 and 1 and indicating a nearly linear relationship to the surface roughness

$$1 - |\gamma_{LLRR}| = ks = 1 - A \quad (14)$$

The anisotropy is by definition characterised by low values and is therefore a very 'noisy' parameter [10][12]. The amplitudes of the secondary scattering mechanisms, expressed by the second and third eigenvalues may be in comparison very small, down to –25 [dB] or even less. As this is close to the system noise floor, A is strongly affected by noise effects. After

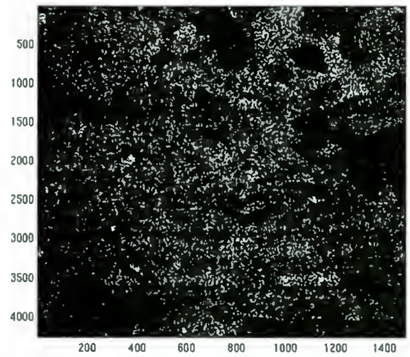

March 2000 Alling test site L-Band
Figure 3: Condition HH/VV < 1 and HV/VV < 0.079

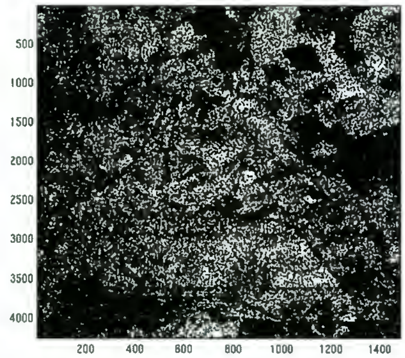

March 2000 Alling test site L-Band **Noise Filtered**
Figure 4: Condition HH/VV < 1 and HV/VV < 0.079

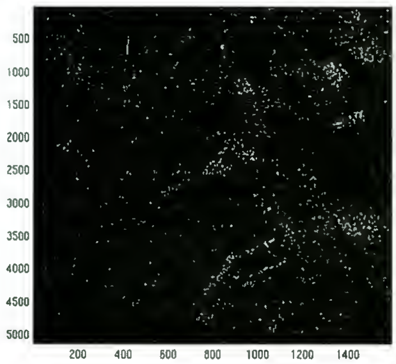

March 2000 Alling test site P-Band
Figure 5: Condition HH/VV < 1 and HV/VV < 0.079

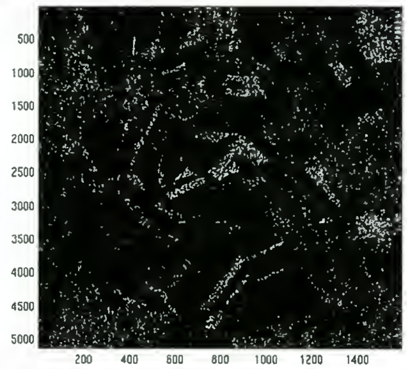

March 2000 Alling test site P-Band **Noise Filtered**
Figure 6: Condition HH/VV < 1 and HV/VV < 0.079

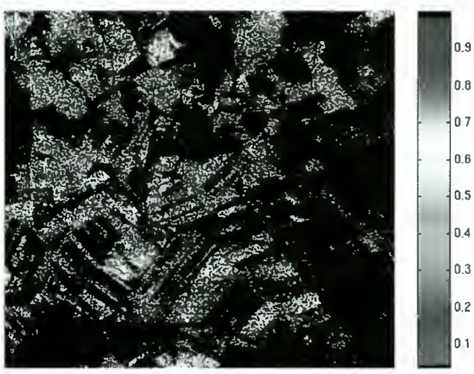

March 2000 Alling test site L-Band **Noise Filtered**
Figure 7: *ks* from A

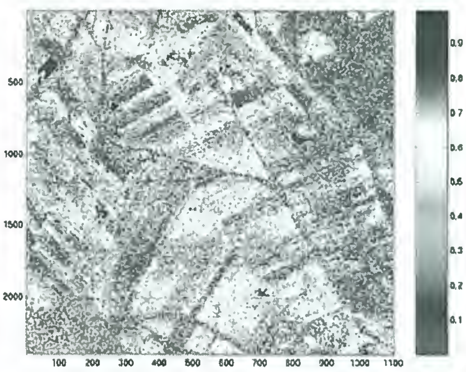

March 2000 Alling test site L-Band **Noise Filtered**
Figure 8: *ks* from LLRR circular coherence

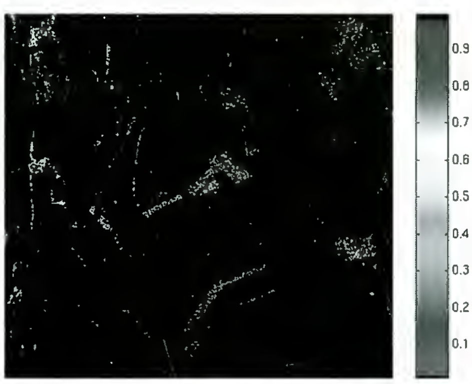

March 2000 Alling test site P-Band **Noise Filtered**
Figure 9: *ks* from A

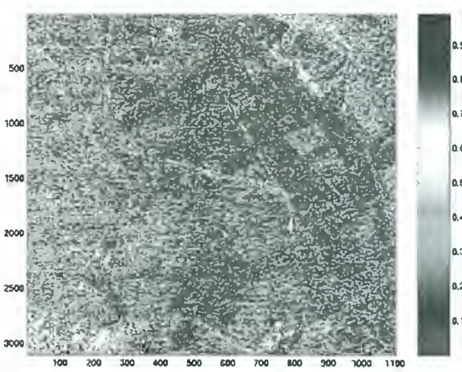

March 2000 Alling test site P-Band **Noise Filtered**
Figure 10: *ks* from LLRR circular coherence

applying the additive filtering and performing A the influence is reduced.

In Figs. 7 - 10 the surface roughness maps estimated from the anisotropy and from the LLRR circular coherence for L- and P-band are presented. For both approaches it can be assert that fields which appear rough at L-band appear smooth at P-band. It is encouraging that at least on the valid fields the two frequencies lead to equivalent results.

The quantitative comparison between the ground measured and estimated surface roughness values is presented in Figs 10 - 12. The results obtained from the L-band by using the anisotropy values are plotted in Fig. 11. The obtained estimates from both methods are in general overestimated, where the LLRR circular coherence leads to a smaller RMS error of about 0.18 while the surface roughness values obtained by using the anisotropy show a RMS error of 0.46.

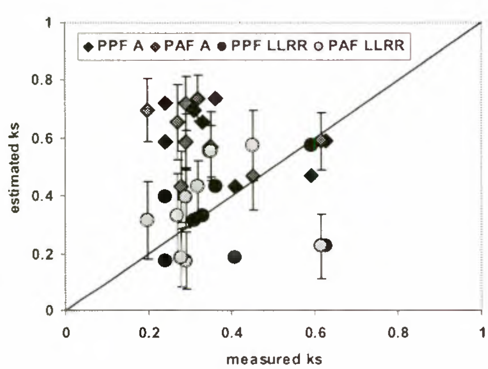

Figure 11: Measured (perpendicular PPF, and parallel PAF to the flight direction) versus estimated surface *ks* values obtained at L-band from anisotropy, and LLRR circular coherence.

The estimates obtained from P-band are also overestimated but with a significant smaller rms error - compared to the L-band estimates – of about 0.19 for the anisotropy and about 0.11 for the LLRR circular coherence (Fig. 12).

Considering now the estimation of surface roughness without taking the frequency into account than the estimates made with L-band indicates a better performance with smaller RMS errors than the estimates made with P-band (Fig. 13).

Eventually, the comparison of the inverted surface roughness values at L- and P-band over commonly valid areas lead to a wider range of surface roughness estimates indicating the potential of combining these two frequencies in order to obtain better parameter estimates. Additionally, the valid regions at P-band include also vegetated areas, which are not covered by the validity regions at L-band indicating the potential of P-band for extracting surface parameters even at the presence of vegetation.

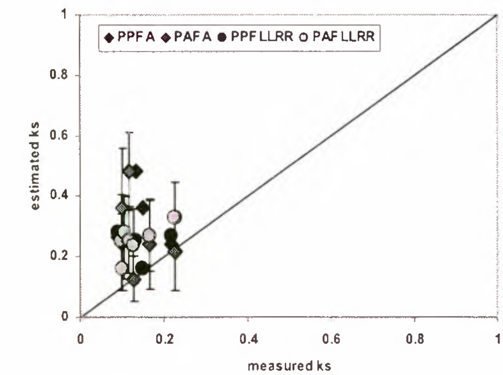

Figure 12: Measured (perpendicular PPF, and parallel PAF to the flight direction) versus estimated surface *ks* values obtained at L-band from anisotropy, and LLRR circular coherence.

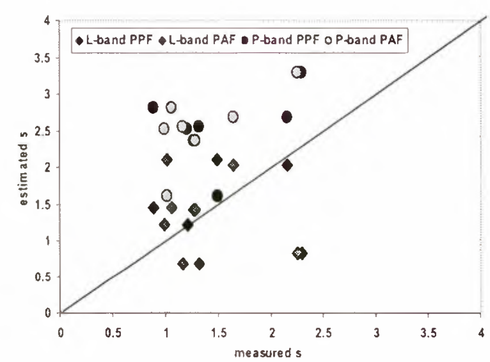

Figure 13: Measured versus estimated surface roughness *s* obtained form the LLRR circular coherence for perpendicular, PPF, and parallel, PAF, estimates to the flight direction.

6 CONCLUSIONS AND DISCUSSION

The presented early results of using two frequency fully polarimetric data for surface parameter estimation makes the effect of low backscattering from agricultural areas at lower frequencies clear.

Especially at P-band, two effects leading to inaccurate estimates. The first one is the influence of system noise and the second is the change of scattering mechanisms. For the reduction of system noise effects an effective additive filtering method has been proposed. The removal of noise effects increases significantly the amount of valid areas for surface parameter estimation. Even at L-band noise effects are present albeit with a weaker impact. The second effect appears much more severe, as the change of scattering mechanism requires a new concept which accounts for volume scattering over bare fields, which is in particular needed for the soil moisture estimation. Volume scattering, caused by the penetration into the soil can be accounted for a vertical soil moisture retrieval.

The promising results are the conformity of the inverted roughness values obtained individually from the two frequencies as well as the indication that P-band may allow the estimation of surface roughness at the presence of low vegetation. Based on this, we can state that P-band, with regards to the remaining fields, is suitable for surface parameter estimation.

Concerning the estimation of surface roughness two methods has been chosen which presented different estimation accuracy. The LLRR circular coherence seems to be more robust as the Anisotropy. The reasons is that A has by definition low values which makes it more sensitive to additive noise and is limited by a smaller dynamic range as the LLRR circular coherence. Therefore is the RMS error for *ks* obtained form the LLRR circular coherence smaller than obtained from the Anisotropy.

Even if taking the higher RMS error for surface roughness estimation with P-band into account, it can be stated, that for the remaining fields a combination of this two frequencies covers a wider range of natural rough surface conditions appearing on different cultivated agricultural fields.

7 ACKNOWLEDGMENTS

The authors would like to thank Ralf Horn, Thanassis Potsis, and, Rolf Scheiber, for their effort to obtain valuable P-band data.

8 REFERENCES

[1] Y. Oh, K. Sarabandi & F. T. Ulaby,' An Empirical Model and an Inversion Technique for Radar Scattering from Bare Soil Surfaces', *IEEE Transactions of Geoscience and Remote Sensing*, vol. 30, no. 2, 1992, pp.370 – 381.

[2] P. C. Dubois & J. J. van Zyl,' An Empirical Soil Moisture Estimation Algorithm Using Imaging Radar', *IEEE Transaction of Geoscience and Remote Sensing*, vol. 33, no.4, 1995, pp. 915 – 926.

[3] S. R. Cloude, I. Hajnsek, & K. P. Papathanassiou, 'An Eigenvector Method for the Extraction of Surface Parameters in Polarimetric SAR', *Proceedings of the CEOS SAR Workshop*, Toulouse 1999, ESA SP-450, pp. 693 – 698, 1999.

[4] M. Borgeaud & J. Noll, 'Analysis of theoretical surface scattering models for polarimetric microwave remote sensing of bare soils' *International Journal of Remote Sensing*, vol. 15, no. 14, pp. 2931-2942, 1994.

[5] F. Mattia, T. Le Toan, J.-C. Souyris, G. De Carolis, N. Floury, F. Posa & G. Pasquariello, 'The Effect of Surface Roughness on Multifrequency Polarimetric SAR Data', *IEEE Transactions on Geoscience and Remote Sensing*, vol. 35, no. 4, pp. 954-966,1997.

[6] M. Zribi, V. Ciarellti, D. Vidal-Madjar, 'An Inversion Model of Soil Roughness Based on Two Radar Frequency Measurements', *Proceedings IGARSS'99*, Hamburg 1999, vol. II, pp. 2528 – 2530, 1999.

[7] M.W.J. Davidson, T. Le Toan, F. Mattia, G. Satalino, T. Mannier, & M. Borgeaud, 'On the characterisation of agricultural soil roughness for radar remote sensing studies', *IEEE Transactions on Geoscience and Remote Sensing*, vol. 38, no. 2, pp. 630-640, 2000.

[8] I. Hajnsek, K. P. Papathanassiou & S. R. Cloude, 'Additive Noise Filtering for Polarimetric Eigenvalue Processing', *Proceedings of IGARSS'01*, Sydney 2001.

[9] D. Just & R. Bamler, 'Phase Statistics of Interferograms with Applications to Synthetic Aperture Radar', *Applied Optics*, vol. 33, pp. 4361-4368, 1994.

[10] I. Hajnsek, S.R. Cloude, J.S. Lee & E. Pottier, 'Inversion of Surface Parameters from Polarimetric SAR', *Proceedings of IGARSS'00*, vol. III, pp. 1095-1097, Hawaii 2000.

[11] D. L. Schuler, J.S. Lee, D. Kasilingham & G. Nesti, 'Remote Sensing of Surface Roughness using Polarimetric SAR Data' *Proceedings of IGARSS'01*, Sydney 2001, in print.

[12] I. Hajnsek, K. P. Papathnassiou, S.R. Cloude,' L-band versus P-band for Surface Parameter Estimation' *Proceedings of IGARSS'01*, Sydney 2001, in print.

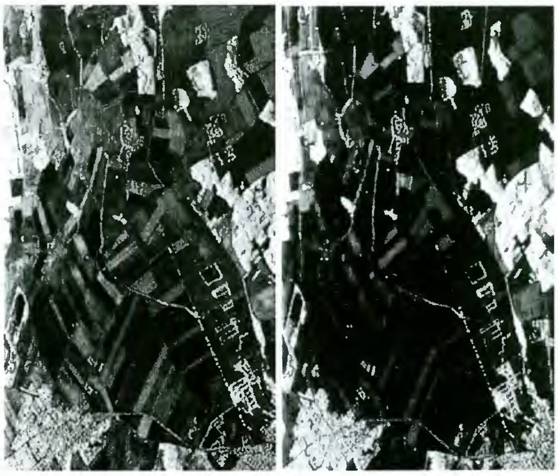

Figure 1: Alling Test site, March 2000, L- (left) and P- (right) band images presented as RGB with the Pauli components.

REMOTE MEASUREMENT OF THE EVAPORATION OF GROUNDWATER FROM ARID PLAYAS

G.Wadge[1] and D.J.Archer[2]

1. Environmental Systems Science Centre,
University of Reading, Reading, UK
Tel: 44 1899 318742
Fax: 44 1899 316413
Email: gw@mail.nerc-essc.ac.uk

2. Natural Resources Institute
University of Greenwich, Chatham, UK
Tel: 44 1622 734317
Email: d.j.archer@ukgateway.net

ABSTRACT

We propose that in the restricted circumstances of an arid playa it should be possible to infer the rates of evaporation of groundwater using radar backscatter measurements. To test this we use an empirically derived relationship between backscatter and surface roughness and a model of how surface roughness changes with a continuous process of halite crystal efflorescence. From these we calculate the volume of groundwater that must have evaporated to produce that roughening effect. The method is illustrated with data from the ERS-1 SAR sensor that imaged the Chott el Djerid playa in southern Tunisia during 1992-93. The playa surface is flat and lacks vegetation. The backscatter generally rises over the playa during the summer months and is reduced abruptly by the onset of winter rains as the halite crust formed by evaporation dissolves. The method appears to be valid for the summer months (March-October) on this playa. Independent meteorological station measurements of pan evaporation give evaporation rates lower than the radar-derived rates by factors of 2-3. Shallow-level recycling of sodium and chloride ions during dissolution of the halite crusts by winter rains may account for this disparity.

EVAPORATION ON PLAYAS

Playas are intracontinental basins with a negative annual water balance (Rosen, 1994). Some playas have lakes within them, often temporary (e.g. Bryant, 1999). Some playas are supplied mainly by groundwater, and it is the evaporation of this regionally discharging groundwater that is the subject of our study. Groundwater beneath playas rises a short distance (10s cm) to the surface by some mechanism, usually ascribed to capillary pressure. At the water/air boundary water vapour molecules escape upwards if there is sufficient energy available. Diffusional processes affect the movement and concentration of water vapour in the air at and above the surface (Shuttleworth, 1991). Wind aids the removal of water vapour, reduces the vapour pressure gradient and helps the evaporation process. On arid playas this process is simplified by the absence of vegetation. The main source of energy producing water vapour molecules is solar irradiation. Hence evaporation is at a peak during the summer daytime hours. The groundwater supplying playas contains salts. These are largely dissolved during passage of the water through salt-bearing strata of the aquifer. For large playas connected to major regional aquifers the solute content of the groundwater may be constant, reflecting the buffering action of the aquifer to temporal variations of water throughput. During evaporation these salts are deposited. In arid zone playas (< 200mm annual rainfall) with high temperatures and rates of evaporation, the salts deposited are dominated by gypsum ($CaSO_4.2H_2O$) and halite (NaCl). It is the appearance specifically of halite crystals at the surface of playas during evaporation that gives us the signal that we can measure remotely. It is the assumption, discussed later, that the base supply of solute concentration from the aquifer is constant that allows us to use the measurements to infer evaporation rates.

RADAR BACKSCATTER FROM THE SURFACE OF THE CHOTT EL DJERID

A series of fourteen ERS-1 SAR scenes were acquired in 1992-93 over the large arid playa of the Chott el Djerid in southern Tunisia (Wadge, 1993, Wadge et al., 1994).

Proc. 3rd International Symposium, 'Retrieval of Bio- and Geophysical Parameters from SAR Data for Land Applications', Sheffield, UK, 11-14 September 2001 (ESA SP-475, January 2002)

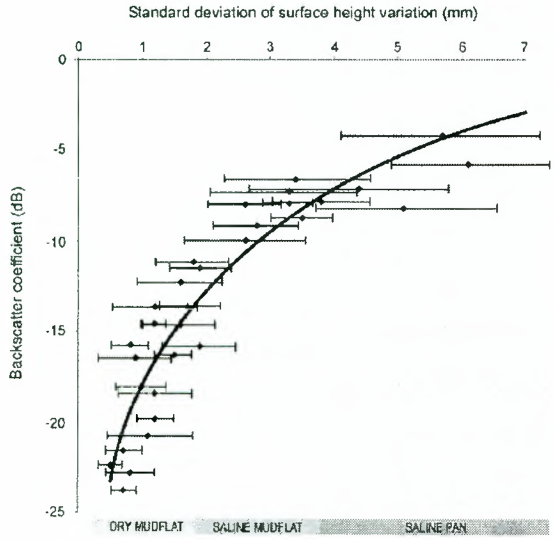

Fig.1. ERS-1 SAR backscatter coefficients versus field measurements of the standard deviation of surface height variation. Mean values and standard deviations are shown. The curve is a logarithmic fit with an r^2 =0.87 (from Archer and Wadge, 2001).

On five occasions (September, 1992, January 1993, March 1993, June1993 and October 1993) whilst ERS-1 was imaging the playa, field measurements were made at 13 sites along a road that crosses the northern part of the Chott el Djerid (Archer, 1995). These measurements included gravimetric moisture content (the main determinant of the dielectric behaviour), and surface roughness with a pin profilometer. Surface roughness was calculated as the root mean square of the height change measured by the profilometer averaged over several metres of measurement and normalised to a horizontal datum. Because the Chott el Djerid is essentially flat we know that the main factors controlling backscatter must be limited to surface roughness and dielectric properties.

From the field measurements Archer (1995) was able to show that the remotely sensed backscatter from ERS-1 is almost entirely controlled by the surface roughness properties of the Chott el Djerid.

Figure 1 shows the logarithmic relationship between surface roughness and backscatter derived from the field measurement data and the fit to these data has the form:

$$\text{Backscatter} = 7.82 \log_n(\text{Roughness}) - 18.33 \, . \qquad (1)$$

Archer and Wadge (2001) presented results from theoretical models of the backscatter that would be expected from the surface of the Chott el Djerid. These models use a linear dielectric mixture model, based on the proportions of halite, gypsum, silicates, water and air typically observed in the surface deposits of the playa. These dielectric values, together with surface correlation length values are used within the Integral Equation Model (IEM) to simulate the backscatter of C-band radar from the surface. The results show a good fit to the empirical relationship between roughness and backscatter (equation 1) and give us confidence in our use of that relationship here.

The spatial and temporal variance of backscatter from the Chott el Djerid is high and reflects the dynamic character of the playa (Wadge, 1993). Part of this is an annual cycle of change in backscatter across the Chott el Djerid as a whole, which we infer to be a process of surface roughening during summer and smoothing during winter. Generally from April to October the surface becomes rougher as more brine-rich groundwater evaporates at the surface depositing halite efflorescence. This abruptly ends with the onset of the winter rains and the partial dissolution of the halite. If we can understand the process that controls roughening due to halite growth during these summer months we have a way to convert the backscatter time series into rates of halite growth.

MODELS OF HALITE EFFLORESCENCE

Whilst isomorphic forms of halite may develop during the relatively rare periods when a lake has formed on the surface of the playa and evaporated, the dominant form of halite growth during the summer months is evaporation from capillary-fed films of solution to produce granular forms. These growths are focused at specific sites (individual capillaries) often several centimetres apart. The areal density of sites increases and average height increases with time to form continuous crusts. During our field measurement programme we sampled the surface roughness every 5 mm (though the vertical precision was < 1mm). This was insufficient to characterise the microtopography of the individual granular forms of halite crust as they evolved. Hence we need a model of their growth and values of roughness derived from it. One such is the focused granular model created by fitting a series of 1 mm cubic crystal facets to a Gaussian distribution and replicating this every 40 mm. The upward growth occurs by adding a fixed number of new facets at each step. Field observations suggest a variant to this in which the more distal limits of growth are truncated to give a pedestal form. The height (y) of such a granular pedestal form with distance away from the source (x) is given by:

$$y = e^{-(x-\mu)^2/2\sigma^2} / \sigma\sqrt{2\pi} \quad \text{for } -1 < x > +1 \quad , \ (2)$$

where μ is the mean and σ is the standard deviation. Here we have chosen the distance of the pedestal edge

(10 mm) to be one quarter the capillary spacing (40 mm). This is arbitrary but seems reasonable from field observations. Fig. 2 shows the roughnesses created by these model surfaces as the maximum surface height increases. The two granular models give similar, linear relationships for these two variables. For

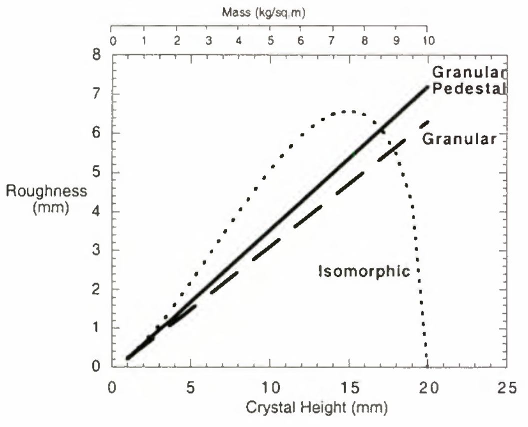

Fig.2 Roughness values for three halite efflorescent crystal growth models in terms of the maximum crystal heights and the masses involved.

reference, the behaviour of a comparably rising isomorphic model, such as might be produced by lake evaporation, with initial 40 mm growth spacing shows strongly non-linear behaviour. Our crystal growth–roughness model could be refined with more precise field measurements, but we feel that the focused pedestal granular model is a reasonable approximation to what we find on the Chott el Djerid surface. When we extend the model multiplicatively into three dimensions we can calculate the increase in the mass of halite (specific gravity = 2175 kgm^{-3}) over an area per roughness increment at 1.418 kg m^{-2}/mm of roughness increase (Fig.2).

EVAPORATION RATES AND PATTERNS

The halite only grows continuously from about March to the onset of the winter rains, and this restricts us to about 7-9 months of the year. Within any one measurement interval (35 days) we will assume that the net roughness change is proportional to the net increase of halite mass derived from the efflorescence model. Applying the empirical relationship between backscatter and roughness we can produce a roughness map for each ERS-1 image. For an interval between image acquisitions we can calculate a roughness change image and by calibration with the focused granular pedestal model derive an incremental increase in halite mass for that interval.

Next we must assume a value for the solute content of the groundwater that flows into the Chott el Djerid from the underlying aquifer. As the groundwater rises beneath the playa it comes into contact with increasingly saline host rocks. The groundwater equilibrates with these rocks and there is a strong positive solute gradient over two to three orders of magnitude towards the halite-rich centre of the playa and upwards towards the surface (Roberts and Mitchell, 1987). Our initial assumption here is that this gradient is preserved during this process. Other than adding Na^+ and Cl^- to the surface each year there is no other net change to the sodium chloride budget. Multiple measurements of the ionic concentrations in these waters show that the base-level salinity of groundwater from the Chott el Djerid aquifer is about 2-3 g/l (Mamou, 1976, Roberts and Mitchell, 1987). About half the molality of the groundwater is accounted for by the sodium and chloride ions that go to form the halite. Thus we can estimate that about 1.25 g of sodium chloride will be deposited for the evaporation of each litre of groundwater.

Dividing the mass of halite measured by the radar by 1.25 gm/l over each 35 day interval of time gives the aggregate volume of water evaporated. Repeating this for each of the 4 available intervals in 1992 and 1993 gives us two, albeit short, time series of images of evaporation for the southern Chott el Djerid (Fig.3). These sets of images display overall somewhat similar patterns in both years with maximum evaporation around July. The southeast corner of the area also shows distinct NE-trending features in both years. However, there are some striking differences between the two years. The WNW-trending ovoid feature in the 1992 sequence shows low evaporation early on, increasing later in the year. The large NE-trending linear feature in the 1993 sequence displays a similar evolution through the year, but neither are seen across both years.

PAN EVAPORATION MEASUREMENTS

There is a meteorological station at the town of Tozeur immediately west of the Chott el Djerid , and about 60 m higher, whose records of daily pan evaporation we have used to compare with the radar evaporation. Figure 4 shows the 35-day net evaporation values derived from radar with equivalent pan-measured values. All values are of the same order of magnitude but the radar-derived values are 2-3 times those of the pan values, except for the May-June 1992 and March-May 1993 periods. This may mean that the radar method is measuring significantly higher levels of evaporation from the playa during the summer months than occur in the neighbouring town. Alternatively, it may mean the radar method is incorrectly calibrated. It does appear that the evaporation from the Chott el Djerid is not limited by the rate of water supply through the capillary zone. Were this to be the case, we would expect evaporation values lower than those for the free-water surface case of pan evaporation.

DISCUSSION

One possible cause of incorrect calibration would be if our assumption of a value of 2.5 g/l salinity of the playa groundwater was too low. This would cause overestimates of the amount of water to be evaporated. For this figure to be, say, twice as great as this, we would have to invoke either more saline groundwaters or some additional recycling of Na^+ and Cl^-. It is conceivable that the salinity in 1992 was higher than that measured in previous decades (Mamou, 1976; Roberts and Mitchell, 1987), but we have no supporting evidence. We know that the smoothing of the playa surface by the heavy winter rains involves dissolution of halite crystals. The dissolved Na^+ and Cl^- ions must move downward into the capillary zone during the winter and may move back to the surface in the next summer's cycle of halite growth. Such

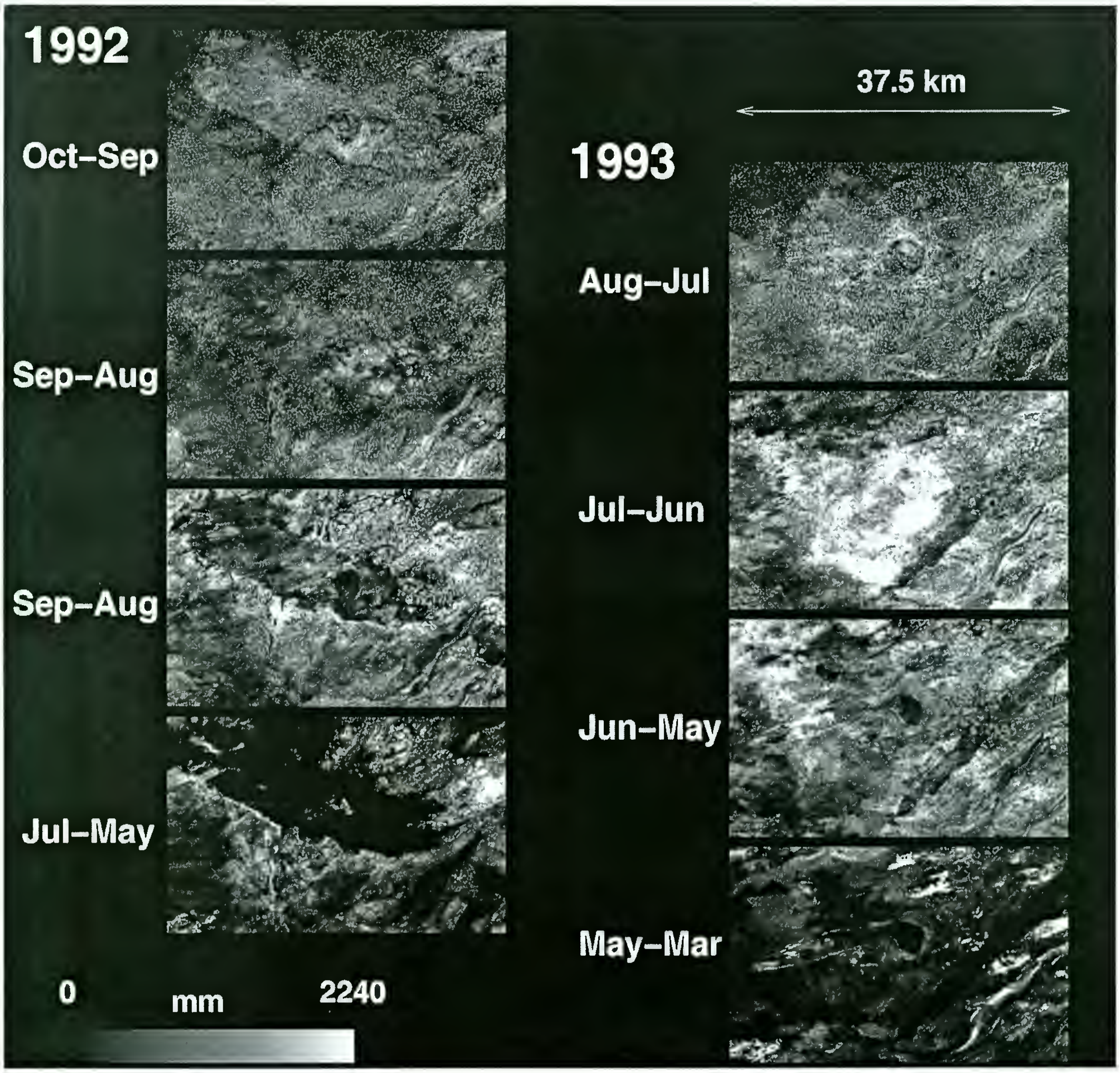

Fig.3 Images of the evaporation measured by ERS-1 SAR for each 35 (70) day interval for the summer months of 1992-93. The area is 37.5 x 25 km in the south central part of the Chott el Djerid . Note that zero or negative values of evaporation are shown in black.

summer-winter recycling of Na^+ and Cl^-, therefore, provides a mechanism for higher apparent rates of summer evaporation without negating the assumption of long-term conservation of the existing evaporite sediments.

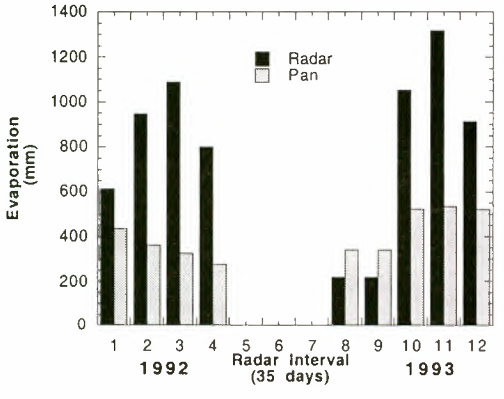

Fig.4 Evaporation totals for 35 day intervals over the area of southern Chott el Djerid shown in fig.3 compared to equivalent totals measured at an evaporation pan in Tozeur.

To better understand the validity of this approach further study is required to:

- Validate the halite efflorescence roughness models
- Measure the *in situ* capillary fluxes
- Determine the annual cycle of the near-surface solute budget

ACKNOWLEDGEMENTS

This work was supported by the Natural Environment Research Council grants GR9/630 to GW and a research studentship NSS/91/PES/1 to DJA. ERS-1 SAR data was supplied by ESA to GW as part of the ERS-1 AO-1 programme.

REFERENCES

Archer, D.J. (1995) Monitoring geological processes on the Chott el Djerid playa using ERS-1 SAR. PhD thesis, University of Reading.

Archer, D.J. and Wadge, G. (2001) Modelling the backscatter response due to salt crust development. *IEEE Trans. Geoscience and Remote Sensing,* (in press).

Bryant, R.G. (1999) Application of AVHRR to monitoring a climatically sensitive playa, case study: Chott el Djerid, Southern Tunisia. *Earth Surface Processes and Landforms*, 24, 283-302.

Mamou, A.,(1976) Contribution a l'etude hydrogeologique (de la Presqu'ile de Kibili). PhD thesis, University Pierre et Marie Curie, Paris, 171 pp.

Roberts, C.R. and Mitchell, C.W. (1987) Spring mounds in southern Tunisia. In, L. Frostick and I. Reid (eds.) *Desert sediments: ancient and modern.* Geological Society Special Publication 35, 321-334.

Rosen, M.R. (1994) The importance of groundwater in playas: a review of playa classifications and the sedimentology and hydrology of playas. In, Rosen, W.R. (ed.) *Paleoclimate and basin evolution of playa systems.* Geological Society of America Special Paper 289, 1-18.

Shuttleworth, W.J. (1991) Evaporation models in hydrology. In, T.J.Schmugge and J-C. Andre (eds.) *Land surface evaporation.* Springer, New York, 93-120.

Wadge, G. (1993) Multitemporal SAR image of the Chott el Djerid, Tunisia. *Earth Observation Quarterly*, 42, 8-10.

Wadge, G., Archer, D.J. and Millington, A.C. (1994) Monitoring playa sedimentation using sequential radar images. *Terra Nova*, 6, 391-396.

THE PYLA DUNE EXPERIMENT: SUB-SURFACE MOISTURE DETECTION BY COMBINING GPR AND AIRBORNE SAR

Ph. Paillou, Th. August-Bernex

Observatoire Astronomique de Bordeaux, BP 89, 33270 Floirac, France
tel: +33 557-77-61-26 fax: +33 557-77-61-10 e-mail: paillou@observ.u-bordeaux.fr

G. Grandjean

BRGM, 45060 Orléans, France

Ph. Dreuillet

ONERA, 91761 Palaiseau, France

J. Achache

CNES, 75039 Paris, France

ABSTRACT

We study the penetration capabilities of low frequency SAR, particularly L and P-bands, for the mapping of sub-surface moisture in arid areas. Our experiment site is the Pyla dune, a bare sandy area allowing high signal penetration and presenting large sub-surface wet structures at varying depths. The SAR penetration depth is estimated by inverting a scattering model for which the sub-surface structure geometric and dielectric properties are determined by the GPR data analysis. We observed a specific phase difference between HH and VV channels, due to a wet layer covered by dry sand. A flight of the new RAMSES P-band facility was performed recently: such a low frequency SAR should be able to detect sub-surface moisture down to at least ten meters.

INTRODUCTION

Over arid areas, low frequency SAR (i.e. L and P-bands) allows us to investigate the sub-surface down to several meters [Elachi *et al.*, 1984; Schaber *et al.*, 1997]. So far, few studies were conducted in that field, despite the fact that low frequency radar can be used for the retrieval of sub-surface parameters such as moisture and geological interfaces. The aim of the presented study is to quantify the penetration capabilities of microwaves, particularly for L and P-bands, for the mapping of sub-surface heterogeneities due to moisture and/or sedimentary structures. Our approach consists in combining airborne SAR data and GPR (ground penetrating radar) profiles in order to model the scattering mechanisms, GPR being used as a source for reliable ground truth measurements.

The Pyla dune in France was chosen as a suitable test site for fieldwork experiment, as it presents a large sandy area of variable thickness for which airborne SAR data sets are available [Grandjean *et al.*, 1999]. This area is particularly interesting for radar sounding, since sand allows a high signal penetration and large sub-surface structures (paleosoils, corresponding to moisture tanks) can be observed. A polarimetric analysis of L-band (1.6 GHz) SAR images, provided by the French airborne facility RAMSES, have shown that sub-surface scattering occurs at several places in the Pyla dune. This was confirmed by GPR sounding experiments. We used GPR imaging to characterize the 3D geometry and dielectric properties of the sub-surface structures, and then constrain a two-layers scattering model (IEM) which allowed to derive the SAR penetration depth. Results obtained with RAMSES L-band data show a 4 meters penetration depth, suggesting that lower frequency ranges, such as P-band, should allow the detection of sub-surface moisture down to at least 10 meters in arid areas [Grandjean *et al.*, 2001]. We also observed a specific signature (phase difference between HH and VV channels) of wet layers covered by dry sand. An explanation for this phenomena, which allows to increase the investigation depth of radar, is proposed here.

Four RAMSES flights were performed in April and May 2001 over the Pyla region, to operate the new P-band (435 MHz) capacity of this airborne SAR. This experiment will allow to explore potentials of the low frequency domain for sub-surface moisture detection, and should lead to innovative Earth observation systems for hydrogeology in arid regions.

THE PYLA DUNE

The Pyla dune in France is shown in figure 1. It was chosen as a suitable laboratory site for fieldwork validation, as it presents a large sandy area (2.5 by 0.5 km) of variable thickness (5 to 110 m), for which several radar data sets are available. This area is particularly interesting for radar sounding since sand allows a high signal penetration. The Pyla dune contains large sub-surface

Proc. 3rd International Symposium, 'Retrieval of Bio- and Geophysical Parameters from SAR Data for Land Applications', Sheffield, UK, 11-14 September 2001 (ESA SP-475, January 2002)

structures constituted by paleosoils (old vegetation). These buried paleosoils, which correspond in fact to moisture tanks, and others small irregularities in the dune represent structural and textural objects detectable with radars, since they present a high permittivity value due to their water content.

Figure 1: Aerial view of the Pyla sand dune.

GPR EXPERIMENT

GPR profiles were realized 500 and 900 MHz frequencies (P and L-band) along a line of 150 m long, running from the beach to the top of the dune. Figure 2 shows the 500 MHz profile with buried paleosoils. It indicates a very good penetration of the signal, which can be estimated to 30 m. Paleosoils appear clearly as high reflective layers, roughly horizontal, with some sedimentary patterns visible between them.

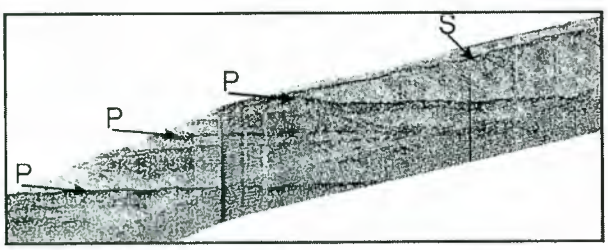

Figure 2: 500 MHz GPR profile of the Pyla dune. P indicates the main reflectors (paleosoils); and S indicates sedimentary patterns inside the upper sand layer.

In order to understand microwave interactions observed for GPR data, radar wave propagation in complex geological structures was simulated. The modeling method used here was conceived to simulate GPR experiments in 3D heterogeneous and dispersive media, without increasing significantly computation times [Bitri and Grandjean, 1998]. The GPR modeling procedure was used to estimate the dielectric model providing the best fit to the observed profiles. This was performed by a trial and error approach. A multi-layer dielectric model of the dune was validated by comparing the observed backscattered power at the surface to the simulated one [Grandjean *et al.*, 2001]. Dry sand appeared to have a permittivity around 5, while wet paleosoils present a high permittivity of 24.

In addition, surface roughness measurements were conducted using a laser profiler. Two 20 m long roughness profiles were collected, parallel and perpendicular to the coast line direction, in order to derive the standard deviation of surface height and correlation length [Baghdadi *et al.*, 2000].

AIRBORNE SAR

A. The RAMSES Airborne Facility

RAMSES is an airborne SAR developed by ONERA since several years [Boutry, 1996]. It disposes of a wide range of frequencies available (W to P band), and the P-band is operational since the end of 2000. RAMSES is flying onboard a Transall C160 aircraft which proposes high accuracy GPS for trajectory monitoring (cf. figure 3).

Figure 3: The RAMSES SAR flying onboard a Transall C160.

The P-band operates at 435 MHz using a 1.3 x 0.8 m patch antenna, and is full polarimetric with an incidence angle ranging from 40 to 80 degrees. A high bandwidth of 70 MHz allows a range resolution of 3.5 m, and the emitted power is more than 500 W. Several operation modes are available (direct chirp, deramping chirp, step frequency) and onboard calibration is performed. The P-band capability can be combined to another frequency band such as S, C, or X-band.

B. Modeling of Radar Penetration for L-band

A RAMSES L-band (1.6 GHz) SAR image of the Pyla dune is shown in figure 4. It was acquired in June 1998, with a mean incidence angle of 55°, a heading of 20°N, and is calibrated. The resolution is 0.7 m in range and 0.9 m in azimuth, allowing clear observation of some sub-surface structures in the Southern part of the dune (bottom of figure 4c).

A polarimetric analysis was performed to characterize the electromagnetic interaction and to detect regions where sub-surface scattering occurs. The dune area presents a non-uniform behavior: smooth and thick sand layers correspond to very weak backscatter areas (i.e. the sum of a weak surface scattering and a weak volume scattering process in the upper sand layer, with a depolarization ratio around 1/3), while paleosoils appearing as linear structures show depolarization ratio VH/VV with intermediate values between surface and volume scattering (indicating that non pure surface scattering occurs here). These areas correspond in fact to subsurface scattering zones, as confirmed by GPR measurements.

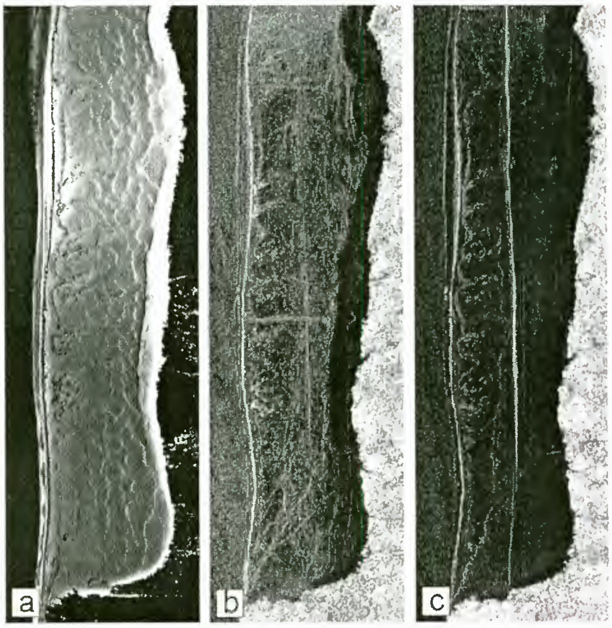

Figure 4: Aerial photography of the Pyla dune (a, source IGN), and RAMSES L-band image of the dune for HH polarization (b) and HV polarization (c).

A two-layers scattering model, combining both surface and volume components and based on the Integral Equation Model [Fung, 1994], was constrained using the GPR modeling results and the roughness measurements. Considering the first order radiative transfer solution, the total backscattered power can be written as the sum of the surface scattering term from the top layer, the volume scattering term in the first layer, and the non-coherent scattering from the bottom layer attenuated by the first layer:

$$\sigma^0(\theta) = \sigma^0_{S1}(\theta) + \sigma^0_{V1}(\theta) + \sigma^0_{S2}(\theta). \quad (1)$$

We studied the ratio R between the backscattered power σ_A of a two-layers zone (where sub-surface scattering on a paleosoil covered by dry sand occurs) and the backscattered power σ_B of a single layer zone (where the first sand layer thickness is too large to let the paleosoil appear), for both HH and VV polarizations. Figure 5 compares the theoretical value of R to experimental values derived from RAMSES data. It shows that L-band (1.6 GHz) allows a 4 m penetration depth, suggesting that lower frequency ranges such as P-band (435 MHz) should allow the detection of subsurface moisture down to at least 14 m in the Pyla dune [Grandjean *et al.*, 2001].

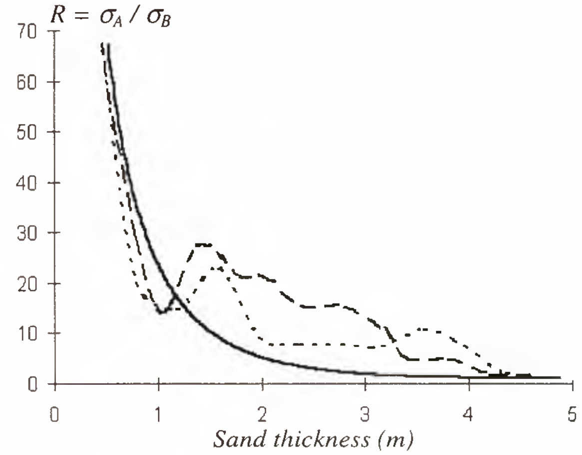

Figure 5: Theoretical R ratio (plain line) compared to the experimental one (dot lines), as a function of the thickness of the sand layer which covers the wet paleosoil (HH polarization).

C. The HH-VV Phase Difference

We observed a specific phase difference between HH and VV channels for regions where sub-surface scattering occurs (i.e. a wet layer covered by dry sand), as presented in figure 6. The phase difference starts close to zero for the ocean surface and then shows a strong increase, up to 25°, for the first ten meters after the point where a paleosoil outcrops, while the correlation between HH and VV signals remains high (the location of the outcrop corresponds to a peak in the HH and HV images). It should be noticed that $\phi_{HH\text{-}VV}$ traces the buried paleosoil far after the HH and HV amplitude signals have disappeared, allowing to "see" down to 6.5 m deep (that is 2.5 m deeper than in figure 5).

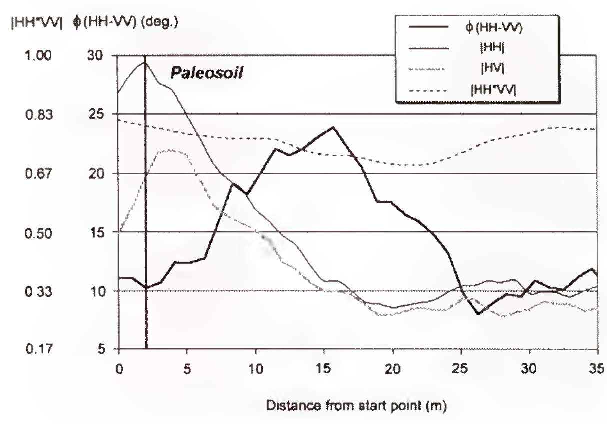

Figure 6: $\phi_{HH\text{-}VV}$ profile across a buried paleosoil.

The reason for the phase difference observed in figure 6 could be an anisotropic medium, since the sand covering paleosoils is stratified and presents various structures due to water run-off. Such sand stratums could lead to different behavior for H and V polarizations, the effect being only observed for the wave backscattered by a buried paleosoil which travels through the covering sand layer. A reflection on a permittivity gradient might also explain the observed phase difference, since a single reflection on a permittivity gradient changes the phase of the incident wave, the reflection coefficient being different for H and V polarizations (WBK model [Elmore and Heald, 1985]). Paleosoils can be seen as large wet stratums filled with water coming from the upper and lower sand. As the sand-paleosoil interface is not sharply defined, one should observe a moisture gradient and then a high permittivity gradient at this interface.

Numerical simulation of the $\phi_{HH\text{-}VV}$ behavior is being carried out using a FDTD code, in order to derive some specific polarimetric signature of sub-surface moisture [Paillou *et al.*, 2001].

THE "PYLA 2001" EXPERIMENT

Four RAMSES P-band flights were performed over the Pyla region during April and May 2001, under good meteorological conditions, corresponding to more than 50 acquisition paths. This experiment was performed within the "low frequency radar working group" set up by CNES and will explore potentials of the low frequency domain for sub-surface moisture detection (Pyla sand dune), biomass evaluation (Nezer forest), mapping of the ocean bathymetry and salinity (basin of Arcachon, estuary of the Gironde), and archaeology (S[t] Germain d'Esteuil, Dignac, Moulin du Fâ) [Paillou *et al.*, 2001b]. A dedicated calibration site was set up in the Nezer forest, with specific reflectors developed for the P-band (cf. figure 7).

Figure 7: A P-band reflector developed by ONERA.

We present here preliminary results of the "Pyla 2001" experiment, since a huge amount of data still has to be processed and calibrated. Final results of the airborne campaign are expected for the middle of 2002.

Figure 8 shows a P-band quick-look (20 MHz bandwidth) of the Pyla sand dune (the dark structure in the middle of the image). Patterns of the ocean surface are visible on the left part of the image, while the Landes forest is on the right part of the scene, showing topographic structures due to the underlying coastal dunes. The quality of the RAMSES data appears to be excellent, with a signal dynamic range of more than 70 dB and very rich polarimetric information.

Figure 8: RAMSES P-band quick-look of the Pyla dune, the ocean is on the left and the Landes forest is on the right.

FUTURE WORK

Although main results are still to come, the "Pyla 2001" experiment already proved that the P-band capacity of RAMSES is operational. High resolution, full polarimetric and multi-incidence data can be acquired at 435 MHz, and the French scientific community disposes now of a competitive sensor. Extending our results obtained for the Pyla dune to a P-band (435 MHz) SAR, we expect penetration capabilities of at least 14 m with HH or VV amplitude signal, and up to 24 m when considering the $\phi_{HH\text{-}VV}$ signal.

As a lot of technical challenges are still to solve for an orbital P-band radar (frequency allocation, ionospheric effects, antenna technology), we believe that an airborne P-band facility will be of first importance for the radar community in the next years. The "Pyla 2001" experiment was a validation campaign for the RAMSES sensor, and we foresee now to fly the Transall over arid areas in Egypt . Preliminary fieldwork and orbital L-band data studies were performed in order to prepare a P-band RAMSES flight over Egypt during 2003 [Grandjean *et al.*, 2001b]. Several test sites will be selected for various low frequency radar applications: mapping of sub-surface moisture and geology in the Southern Egyptian desert, mapping of vegetation along the Nile, salinity and bathymetry mapping near the Nile estuary, and archeological vestiges detection in the Alexandria and Louxor regions.

REFERENCES

C. Elachi, L. E. Roth, G. G. Schaber (1984): Spaceborne radar subsurface imaging in hyperarid regions. *IEEE Transactions on Geoscience and Remote Sensing*, vol. GE-22, no 4, pp. 383-388, 1984.

G.G. Schaber, J.F. McCauley, C.S. Breed (1997): The use of multifrequency and polarimetric SIR-C/X-SAR data in geologic studies of Bir Safsaf, Egypt. *Remote Sensing of the Environment*, vol. 59, pp. 337-363, 1997.

G. Grandjean, Ph. Paillou, Ph. Dreuillet, P. Dubois, J.-C. Souyris, N. Baghdadi, J. Achache (1999): Radar penetration in soils: Towards a new system for Earth subsurface observation. *CEOS SAR Worshop*, Toulouse, France, October 1999.

G. Grandjean, Ph. Paillou, P. Dubois, T. August-Bernex, N. Baghdadi, J. Achache (2001): Subsurface structures detection by combining L-band polarimetric SAR and GPR data: Example of the Pyla Dune (France). *IEEE Transactions on Geoscience and Remote Sensing*, vol. 39, no 6, pp. 1245-1258, 2001.

A. Bitri, G. Grandjean (1998): Frequency–wavenumber modeling and migration of 2D GPR data in moderately heterogeneous dispersive media. *Geophysical Prospecting*, vol. 46, pp. 287-301, 1998.

N. Baghdadi, Ph. Paillou, G. Grandjean, P. Dubois, M. Davidson (2000): Relationship between profile length and roughness parameters for natural surfaces. *International Journal of Remote Sensing*, vol. 21, no 17, pp. 3375-3381, 2000.

J.-M. Boutry (1996): ONERA airborne SAR facilities. *2nd International Airborne Remote Sensing Conference*, San Francisco, USA, June 1996.

A. K. Fung (1994): *Microwave Scattering and Emission Models and their Applications*. Norwood, MA: Artech House, 1994.

W. Elmore, M. Heald (1985): *Physics of Waves*. New York: Dover, 1985.

P. Paillou, T. August-Bernex, G. Grandjean, P. Dreuillet, J. Achache (2001): Sub-surface imaging by combining airborne SAR and GPR: Application to water detection in arid zones. *IGARSS'01*, Sydney, Australia, July 2001.

P. Paillou, T. August-Bernex, E. Heggy, P. Dreuillet, D. Le Coz, O. Duplessis, C. Coulombeix, P. Borderies, J.-M. Boutry, G. Grandjean, N. Baghdadi, H. Dupuis, V. Lafon, R. Garello, J.-M. Le Caillec, I. Champion, M. Dechambre, R. Chapoulie, M. Martinaud, G. Ruffié, A. Podaire, J. Achache (2001b): The Pyla 2001 experiment: Flying the new RAMSES P-band SAR facility. *CORISTA-EARSeL Remote Sensing by Low-Frequency Radars*, Naples, Italy, September 2001.

G. Grandjean, Ph. Paillou, N. Baghdadi, E. Heggy, Th. August-Bernex (2001b): Sub-surface imaging with low frequency SAR. Field validation in Egypt using a ground-penetrating radar. *3rd Int. Symp. on Retrieval of Bio- and Geophysical Parameters from SAR Data for Land Applications*, Sheffield, UK, September 2001.

THE INFLUENCE OF A PRIORI INFORMATION ON SOIL MOISTURE RETRIEVAL FROM SAR DATA

Giuseppe Satalino (1), Guido Pasquariello (1), Francesco Mattia (2),
Malcolm Davidson (3), Thuy Le Toan (3), Maurice Borgeaud (4)

(1) IESI-CNR, via Amendola 166/5, 70126 Bari (Italy)
pho.: 080 5481612; email: Satalino@iesi.ba.cnr.it
(2) ITIS-CNR, c/o CGS-ASI, Loc. Terlecchia, 75100 Matera (Italy)
pho.: 0835 377282; email: Mattia@itis.mt.cnr.it
(3) CESBIO, 18 av. Edouard Belin bpi 2801, 31401 Toulouse Cedex 4, (France)
pho.: 05 61558501; email: Thuy.Letoan@cesbio.cnes.fr
(4) European Space Agency (ESA), ESTEC (The Netherlands)
pho.: 71-565-4830; email: Maurice.Borgeaud@esa.int

ABSTRACT

In this paper, a study on the influence of a priori information on the retrieval of soil moisture from SAR data is carried out. A priori information on the surface state has been exploited in two different soil moisture retrieval algorithms and subsequently their performances are compared. The first algorithm is based on a Neural Network trained by the Integral Equation Method (IEM) model. The second algorithm is an ITerative Method, based on the direct IEM model, which estimates soil moisture by an iterative search.
The paper investigates the difference between the algorithms performances as a function of the accuracy of the a priori information. In addition, the algorithms robustness versus measurement errors is evaluated. Finally, the two approaches are applied to experimental data acquired during the 1st SIR-C/X-SAR mission and results are discussed.

INTRODUCTION

Soil moisture content represents a key parameter in numerous applications which would benefit from frequent and spatially comprehensive measurements of soil moisture. The retrieval of soil moisture (*Mv*) from SAR data may be achieved by exploiting either experimental relationships between σ_0 measurements and *Mv* or model-based methods. The latter consist of inverting theoretical models predicting σ_0 as a function of relevant surface parameters. Model-based methods are expected to be more robust because they can cope with very different surface conditions whereas experimental σ_0-*Mv* relationships are usually site dependent. The performances of model-based retrieval algorithms mainly depend on: 1) the accuracy of the direct models to predict backscatter from soil surfaces; 2) the intrinsic ambiguity of the inverse problem which is due to the multiplicity of surface parameters which can be associated to the same radar measure; 3) the level of measurement errors. In addition, the attainable accuracy for the retrieved parameter may significantly depend on the specific method selected to perform the inversion task. In general, the accuracy of each method can be improved by injecting a priori information on the surface state such as guess values for surface roughness and for soil moisture content. A priori information on roughness could be extracted, for instance, from the site agricultural calendar (i.e. agricultural tillage states may be related to surface roughness parameters [Jackscon *et al.*, 1997]) or from SAR data themselves by using a SAR roughness discriminator [Mattia *et al.*, 1997]. A priori information on soil moisture could be obtained from meteorological data.
In this paper, the influence of a priori information on the performances of two model-based methods for soil moisture retrieval are quantitatively assessed. In addition, the impact of realistic SAR measurement errors on the accuracy of retrieved soil moisture is investigated. The backscattering model adopted in the retrieval algorithms is the Integral Equation Method (IEM) model [Fung, 1994]. The two model-based methods are: a Neural Network (NN) algorithm trained by the IEM model and an ITerative model-based Method (ITM) which exploits an iterative search starting from an initial guess value.
In the next section, the two methods are described. Then, the role of the a priori information is discussed. Consequently, the two algorithms are applied to both simulated and experimental data set. The latter consists of SIR-C/X-SAR data acquired during the first mission over the Oberpfaffenhofen site. Finally, the results are discussed and some conclusions are given.

NEURAL NETWORK APPROACH

As a notation, let $\mathbf{f}_M$ be a vector function of the non-linear direct physical model M (i.e. IEM), $\mathbf{p}$ and $\mathbf{m}$, the input and output parameter vectors, respectively, so that $\mathbf{f}_M(\mathbf{p}) = \mathbf{m}$. The parameter retrieval problem consists of finding the parameter vector $\mathbf{p}$ associated to the measurement $\mathbf{m}$. However, in soil moisture applications

Proc. 3rd International Symposium, 'Retrieval of Bio- and Geophysical Parameters from SAR Data for Land Applications', Sheffield, UK, 11-14 September 2001 (ESA SP-475, January 2002)

the problem is usually *ill posed,* mainly because it may occur that different set of parameters $\mathbf{p}_1, \ldots, \mathbf{p}_l$ can correspond to the same measurement $\mathbf{m}$, i.e. $\mathbf{f}_M(\mathbf{p}_i) = \mathbf{m}$, $i=1, \ldots, l$. This means that the relationship between parameters $\mathbf{p}$ and measurements $\mathbf{m}$, does not satisfy the uniqueness condition.

The inversion algorithm based on the Neural Network approach (NN) finds an explicit model *pseudo-inverse* function $\mathbf{f}_M^{-1}$ so that given a measurement vector $\mathbf{m}$, the corresponding parameter vector $\mathbf{p}$ is the mean between all possible parameters $\mathbf{p}_1, \ldots, \mathbf{p}_l$, i.e. $\mathbf{p}=\mathbf{f}_M^{-1}(\mathbf{m})$. More precisely, the NN algorithm represents a function $\mathbf{f}_{M(w)}^{-1}$ which approximates the pseudo-inverse function $\mathbf{f}_M^{-1}$.

In the following, this property of the $\mathbf{f}_{M(w)}^{-1}$ function is briefly demonstrated. To do so, it may be worth reminding that the general expression of an approximating function represented by a NN is a combination of non-linear function g (such as sigmoidal, radial or polynomial function) of its input, weighted by some coefficients w, i.e.:

$$\mathrm{f}_{M(w)k}^{-1}(\mathbf{m}) = \sum_i w^{(2)}{}_{k,i}\, g\ \Big(\sum_j w_{i,j}{}^{(1)} m_j\Big) \tag{1}$$

The approximated *pseudo-inverse* function $\mathbf{f}_{M(w)}^{-1}$ is defined when the proper coefficients w permit to fit the underlying relationship between the measurements and the parameters. The searching of the proper coefficients w is performed by means of a NN training session by using a training data set. This is composed by samples of measurements and parameters ($\mathbf{m}$, $\mathbf{p}$) as simulated by the direct model. The NN training session ends when the Mean Square Error (MSE) objective function:

$$MSE_p = 1/(2N)\sum_{t,k} (\mathrm{f}_{M(w)k}^{-1}(\mathbf{m}^t) - \mathrm{p}_k{}^t)^2 \tag{2}$$

is minimized, where MSE_p is computed on N samples of the parameter space, $\mathbf{f}_{M(w)k}^{-1}(\mathbf{m}^t)$ is the kth component of the tth estimated parameter and $\mathbf{p}_k^t$ is the expected one. Under the hypothesis that the parameters correspondent to a measurement $\mathbf{m}$ spread out with continuity around a mean value, a NN trained by minimizing the MSE criteria, finds a function which approximates the conditional expected value $E[\mathbf{p}|\mathbf{m}]$:

$$\mathrm{f}_{M(w)}^{-1}(\mathbf{m}) \cong E[\mathbf{p} \mid \mathbf{m}] = \int \mathbf{p} P(\mathbf{p} \mid \mathbf{m}) d\mathbf{p} \tag{3}$$

As a consequence, the expected error of the estimated parameter p_k can be expressed as:

$$MSE_{p,k} = \iint (\mathrm{f}_{M(w)_k}^{-1}(\mathbf{m}) - \mathrm{p}_k)^2 P(\mathrm{p}_k, \mathbf{m}) d\mathrm{p}_k d\mathbf{m} = \quad (4)$$

$$= \iint (\mathrm{f}_{M(w)_k}^{-1}(\mathbf{m}) - \mathrm{p}_k)^2 P(\mathrm{p}_k \mid \mathbf{m}) P(\mathbf{m}) d\mathrm{p}_k d\mathbf{m} =$$

$$= \int (E[\mathrm{p}_k{}^2 \mid \mathbf{m}] - E^2[\mathrm{p}_k \mid \mathbf{m}]) P(\mathbf{m}) d\mathrm{m} = \int \sigma_{\mathrm{p},k}^2(\mathbf{m}) P(\mathbf{m}) d\mathrm{m}$$

In synthesis, if the extremes of the accepted solution for a measurement $\mathbf{m}$ is $[\mathbf{a}, \mathbf{b}]$, then the solution $\mathbf{p}$ found by a NN, trained with the MSE objective function, approximates the mean of $[\mathbf{a}, \mathbf{b}]$. In addition, its local intrinsic expected error is σ^2_p [Bishop, 1995], as shown in Fig. 1.

A second property which can be requested to the retrieval algorithm is to be robust versus possible corruption of input data (i.e. measurement errors; model errors, etc.). To achieve this, a regularization technique has been adopted. It consists of training the NN with data corrupted by noise [Satalino *et al.*, 2000]. This has been simulated by adding random Gaussian values, having 0.5 and 1.0 dB of standard deviation, to the IEM simulated values. It may be worth mentioning that the adopted levels of errors are consistent with the measurement errors expected for radar sensors such as on ERS2 and ENVISAT platforms.

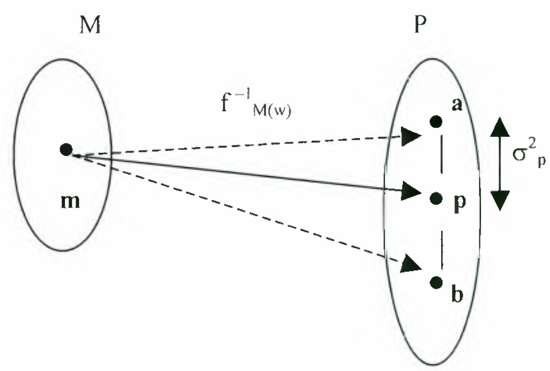

***Figure 1**. Parameter retrieval by NN. The expected error is σ_p^2*

THE ITERATIVE METHOD APPROACH

The Iterative Method (ITM) for the parameter retrieval finds the parameter $\mathbf{p}$ correspondent to a measurement $\mathbf{m}$ by means of an iterative scheme based on a gradient descending algorithm. The method is based on the direct model function $\mathbf{f}_M$, and updates a guess initial value $\mathbf{p}^0$ until reaching a final value $\mathbf{p}_F$ by following the rule:

$$\mathbf{p}^{t+1} = \mathbf{p}^t - \eta\, \partial SE^t_m / \partial \mathbf{p} \tag{5}$$

The objective is to minimize the Square Error (SE):

$$SE^t{}_m = \left\| \mathrm{f}_M(\mathbf{p}^t) - \mathbf{m} \right\|^2 \tag{6}$$

where SE^t_m is obtained on the measurement space at iteration t, $\mathbf{f}_M(\mathbf{p}^t)$ is the estimated measurement and $\mathbf{m}$ is the expected one. For ill posed problems, $SE_m = 0$ or smaller than a given tolerance does not imply that the final parameter $\mathbf{p}_F$ is equal to the true value $\mathbf{p}_T$. In fact, more solutions are associated to the same measurement and all are feasible. As a consequence, given a measurement $\mathbf{m}$, and under the hypothesis that for each component k of the vector parameter $\mathbf{p}$: a) the solution p_{Fk} is uniformly distributed in a range $[a_k, b_k]$; b) the true value p_{Tk} is uniformly distributed around solution

$p_{Fk;}$ c) p_{Fk} and p_{Tk} span the same range $[a_k, b_k]$ and are independent; then the local *MSE* on the parameter space P is:

$$MSE_{p,k} = \iint (p_{Fk} - p_{Tk})^2 P(p_{Fk})P(p_{Tk})dp_{Fk}dp_{Tk}$$

$$= \int p_{Fk}{}^2 P(p_{Fk})dp_{Fk} - 2E[p_{Fk}]E[p_{Tk}] + \int p_{Tk}{}^2 P(p_{Tk})dp_{Tk}$$

$$= 2E[p_k{}^2] - 2E^2[p_k] = 2\sigma^2{}_{p,k} \qquad (7)$$

In synthesis, if the range of the accepted solution for a measurement **m** is **[a, b]**, then the solution $\mathbf{p}_F$ found by an iterative scheme lies inside the range, and has a local intrinsic expected error of $2\,\sigma^2_p$ [Davis *et al.*, 1993], as depicted in Fig. 2. In the algorithm implementation, the iterations stop when the SE'_m value of (6) reaches a given tolerance. Moreover, the derivative of SE in (5) has been estimated by using a MLP trained to fit the direct model. In fact, a trained MLP has an expression that is derivable respect to the parameter, as requested in the updating rule.

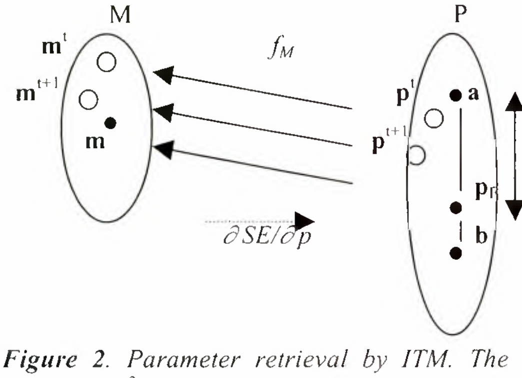

***Figure** 2. Parameter retrieval by ITM. The expected error is* $2\sigma_p^2$

THE INFLUENCE OF THE A PRIORI INFORMATION

The errors affecting the above described retrieval algorithms may be reduced adding a priori information on the range of variability of surface parameters. For instance, for the NN algorithm, a priori information on surface state could be used to delimit the variability range of the profile height RMS (s). As a consequence, a reduction of the solution ambiguity is expected and then a NN trained on a sub-set of data should retrieve soil moisture with higher accuracy.
Analogously, ITM can give better results if the searching of the solution starts from proper guess values (i.e. for roughness and/or for soil moisture content) as well as if the solution is constrained within a sub-range of variability.
In the following, these improvements are firstly quantitatively assessed on simulated data. Then, the retrieval algorithms are applied to experimental data.

DATA SET AND RESULTS

SIMULATED DATA

Simulated data were generated by using the IEM model in the following configuration: frequency $\lambda = 1.25$ *GHz (L band)*, polarization $p = HH$ and VV, incidence angle $\theta = 23°$ *and* $45°$. This configuration will be referred to as 2p:L. The exploited ranges of surface parameters are: Δs = [*0.6 cm, 6.0 cm*], ACF *exponential* with $\Delta\, l$=[*6 cm, 24 cm*], $\Delta\varepsilon'$ (Rel. Diel. Const.) = [*3+j0.1, 20 +j5*], which corresponds to a soil moisture range of $\Delta Mv \cong$ [*3%, 40%*].
Tables 1 and 2 show the Root Mean Square (RMS) errors for the retrieved soil moisture values using the NN-based algorithm applied to IEM L-band data. The 1st and 2nd rows of both tables report the results obtained without and with using a priori information on the surface roughness state, respectively. The exploited a priori information consisted of training the NNs with simulated IEM data corresponding to a reduced range of roughness parameters. In particular, only relatively smooth surfaces were considered (i.e. s ranged between 0.6 and 1.6cm).
Table 1 has been obtained using the not regularised NN-based algorithm. The results quantify the inversion error, which represents the intrinsic ambiguity of data (i.e. a measure of the set of soil moisture values corresponding to the same σ_0 measurements). Conversely, Table 2 has been obtained using the regularised NN-based algorithm.

***Table** 1. Inversion errors by using the not regularised NN algorithm. The 1st and 2nd rows show the RMS errors without and with a priori information on surface roughness, respectively*

RMS error on *Mv*%	**Test data**	
Data Configuration	**IEM data**	
	θ = 23°	**θ = 45°**
[2p:L], i.e. 0.6cm<s<6cm	5.26	3.33
[2p:L] + a priori, i.e. 0.6cm<s<1.6cm	2.68	2.15

***Table** 2. Measurement errors by using the regularised NN algorithm. The 1st and 2nd rows show the RMS errors without and with a priori information on surface roughness, respectively*

RMS error on *Mv*%	**Test data**	
Data Configuration	**IEM data**	
	θ = 23°	**θ = 45°**
	0.5/1.0 dB	**0.5/1.0 dB**
[2p:L], i.e. 0.6cm<s<6cm	6.92/7.45	4.63/6.05
[2p:L] + a priori, i.e. 0.6cm<s<1.6cm	7.05/7.40	5.19/6.74

This means that both the training and testing data sets have been perturbed by adding a zero mean random Gaussian noise with standard deviation 0.5 and 1.0 dB. In this respect, the results shown in Table 2 include not only the inversion errors but also the unavoidable measurement errors

In Table 1, the inversion errors significantly reduce when adding a priori information. On the contrary, in Table 2, the errors computed with and without a priori information are slightly different. This result implies that measurement errors almost destroy the a priori information when using NN-based retrieval algorithm.

Table 3 summarizes the results obtained using the ITM algorithm. The RMS errors on soil moisture estimates have been reported as a function of different initializations of the guess values. They have been obtained using the expected parameters randomly perturbed with increasing errors. The perturbation on the true values $\mathbf{p}^0=(s, l, \varepsilon')$, ranged from 10% to 50% of their total range Δs, Δl, $\Delta\varepsilon'$, respectively. In addition, the errors on the solution have been estimated as a function of the tolerance adopted to stop the iterative scheme. It can be observed that RMS error increases both with the tolerance on σ^0 and with the level of perturbation of the guess values $\mathbf{p}^0$. The ITM method shows a performance in terms of RMS error that is similar to the performance of the NN based method, when the perturbation of the guess value is within the 40% of the initial range. For example for data at 23°, the RMS error obtained by the ITM method (with 0.5dB tolerance) is 7.12, whereas the RMS error obtained by the regularized NN is 6.92.

In summary, the ITM method can outperform the performance of the NN method if the guess values (i.e. s^g, l^g, ε^g) fall around the true solution within an interval of 40% of their variability ranges (i.e. Δs, Δl, $\Delta\varepsilon$).

Furthermore, to better evaluate the performance of the ITM algorithm in the retrieval, the a priori information was firstly restricted to two parameters, and then to one parameter only. Table 4 shows the results obtained by ITM using a priori information on s and Mv, i.e. constraining two parameters out of three.

***Table 3**. Inversion error by using ITM. Guess values for s, l and Mv are the expected parameters randomly perturbed by an increasing noise*

RMS error on Mv%	IEM data					
Conf. [2p:L]	$\theta = 23°$			$\theta = 45°$		
Perturb. on p	**Toler. on σ_0 (dB)**			**Toler. on σ_0 (dB)**		
	0.10	**0.25**	**0.50**	**0.10**	**0.25**	**0.50**
10 %	1.69	1.75	1.86	1.25	1.63	1.82
20 %	3.23	3.44	3.55	1.98	2.68	3.26
30 %	4.64	5.20	5.34	2.66	3.40	4.40
40 %	5.88	6.79	7.12	3.33	4.02	5.23
50 %	6.93	8.06	8.72	4.06	4.68	5.93

The parameter l is left free after starting with a guess value equal to its mean value (i.e. l^g=15 cm). The results are similar to values shown in Table 3. This means that the a priori knowledge on the correlation length is not determinant on the retrieval accuracy of Mv.

Table 5 and 6 show the results obtained constraining only one parameter (i.e. Mv and s, respectively).

***Table 4**. Inversion error by using ITM. Guess values for s and Mv are the expected parameters randomly perturbed by an increasing noise, whereas for l is its mean*

RMS error on Mv%	IEM data					
Conf. [2p:L]	$\theta = 23°$			$\theta = 45°$		
Perturb. on p	**Toler. on σ_0 (dB)**			**Toler. on σ_0 (dB)**		
	0.10	**0.25**	**0.50**	**0.10**	**0.25**	**0.50**
10 %	2.14	2.22	2.24	2.21	2.09	2.01
20 %	3.52	3.73	3.89	3.03	3.08	3.29
30 %	4.82	5.37	5.61	3.43	3.74	4.40
40 %	5.92	6.88	7.32	3.67	4.17	5.21
50 %	6.94	8.13	8.90	3.88	4.51	5.81

***Table 5**. Inversion error by using ITM. A guess value for Mv is the expected parameter randomly perturbed by an increasing noise, whereas for s and l are the corresponding mean*

RMS error on Mv%	IEM data					
Conf. [2p:L]	$\theta = 23°$			$\theta = 45°$		
Perturb. on *p*	**Toler. on σ_0 (dB)**			**Toler. on σ_0 (dB)**		
	0.10	**0.25**	**0.50**	**0.10**	**0.25**	**0.50**
10 %	3.18	3.35	3.37	2.40	2.44	2.53
20 %	5.19	5.95	6.10	3.09	3.19	3.60
30 %	6.27	7.65	8.12	3.44	3.74	4.51
40 %	6.83	8.45	9.47	3.67	4.16	5.24
50 %	7.20	8.94	10.40	3.85	4.48	5.80

***Table 6**. Inversion error by using ITM. A guess value for s is the expected parameter randomly perturbed by an increasing noise, whereas for l and Mv are the corresponding mean*

RMS error on Mv%	IEM data					
Conf. [2p:L]	$\theta = 23°$			$\theta = 45°$		
Perturb. on *p*	**Toler. on σ_0 (dB)**			**Toler. on σ_0 (dB)**		
	0.10	**0.25**	**0.50**	**0.10**	**0.25**	**0.50**
10 %	5.59	6.83	7.53	3.80	4.58	5.90
20 %	6.10	7.31	7.98	3.86	4.61	5.96
30 %	6.48	7.75	8.36	3.86	4.60	6.00
40 %	6.87	8.23	8.87	3.88	4.62	6.05
50 %	7.28	8.59	9.36	3.91	4.65	6.11

Table 5 shows that the performance of ITM on estimating soil moisture are similar to those obtained by the regularized NN approach when the a priori information on *Mv* approximates the true values within a range between 20% and 30% of its variability. On the contrary, Table 6 shows that performances similar to NN can be obtained using guess values only for *s* with an error not exceeding 10%.
These results obtained on simulated data give a trend of soil moisture retrieval errors as a function of the a priori information accuracy. In summary, soil moisture retrieval improvement may be achieved using ITM rather than the NN approach if relatively good (i.e. errors within 30%) guess values on *Mv* and *s* are available.

EXPERIMENTAL DATA

The developed retrieval algorithms have been applied to experimental SAR data acquired over the Oberpfaffenhofen site in Germany during April 1994. The exploited data set consists of fully polarimetric L-band data acquired at 27° incidence. Qualitative ground data on the site are available for more than 100 agricultural fields. They have been classified according to their agricultural stage. For instance, bare fields have been separated into *sown* (i.e. smooth) and *ploughed* (i.e. rough) surfaces. Vegetated fields were classified according to the crop type and the phenological state.
Although soil moisture content was not measured during the ground campaign, soils were saturated due to rainfall on the area. Consequently volumetric soil moisture content can be estimated to be Mv=0.35 +/- 0.1 gr/cm^3 corresponding to a relative dielectric constant approximately ranging between 12 and 25.
Additional roughness information are available in the frame of a ground campaign conducted over several bare fields on the same site, in March 2000. Quantitative measurements were carried out using the CESBIO-ESA laser profiler. The analysis of this data set can provide reference values for the surface roughness parameter characteristic of the area. For instance, the *s* parameter measured over seedbed and ploughed surfaces was found equal to 0.9±0.4 cm and 2.0±0.6 cm, respectively. In this analysis, only data referring to 38 fields classified as bare fields (i.e. either seedbed or ploughed) have been exploited.
In order to obtain guess values for the surface roughness state (i.e. the *s* parameter) the absolute value of correlation coefficient between circularly co-polarized components (i.e. $|\rho_{RRLL}|$) has been exploited. Past studies (see for instance [Mattia *et al.*, 1997]) have shown that this coefficient is extremely sensitive to surface roughness and almost insensitive to soil moisture content. On the contrary, the correlation coefficient between linearly polarised components (i.e. $|\rho_{HHVV}|$) was found little sensitive to roughness and quite sensitive to the presence of vegetation on the surfaces (i.e. a vegetation layer can quickly de-correlate HH and VV channels). For the data set under study, Figure 3 displays $|\rho_{HHVV}|$ versus $|\rho_{RRLL}|$. Fields are labelled as sown (i.e. smooth) and ploughed (i.e. rough). As can be seen, in most cases the $|\rho_{RRLL}|$ coefficient correctly discriminates between rough and smooth surfaces. On the contrary, $|\rho_{HHVV}|$ is generally high for ploughed fields and some sown surfaces. However, in the case of several sown fields it presents unusually low values. This behaviour probably indicates that on these surfaces there was a not negligible layer of grass.
To run the ITM retrieval algorithm, the guess values for the *s* coefficient has been obtained exploiting a simple thresholding approach relating $|\rho_{RRLL}|$ to *s* values. For the *Mv* parameter, a guess value of 35% has been adopted. Both for the NN and ITM algorithms, a tolerance of 0.5 dB has been used and the results are shown in Figure 4.

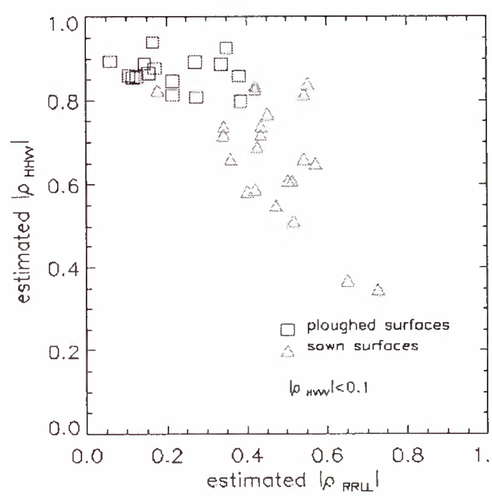

Figure 3. *$|\rho_{HHVV}|$ vs $|\rho_{RRLL}|$ (Oberpfaffenhofen site, SIR-C L band data at 27° incidence, April 1994)*

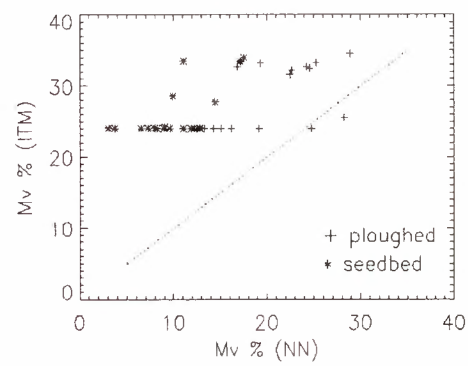

Figure 4. *Soil moisture estimations from experimental measurements: ITM vs NN estimations (tol.: 0.5dB)*

It can be noted that NN generally under-estimates the soil moisture content. In addition, results not shown here demonstrate that the NN tends to over-estimate the soil roughness values. On the contrary, the ITM algorithm correctly predicts the expected soil moisture values (*Mv%* around 35) both for seedbed and ploughed fields. In addition, ITM returns realistic values also for the surface roughness parameters.
However, Figure 4 shows that some ITM predictions are stuck around Mv%=25. For those cases, the ITM algorithm did not converge to feasible solutions. Most of these data concern with sown surfaces. By increasing the ITM tolerance to 1.0 dB, all the data concerning ploughed surfaces converge to the expected values, whereas several data concerning sown fields do no yet converge. This behavior may be explained noticing that these not converging data coincide with the fields having low value for the $|\rho_{HHVV}|$ coefficient (see Fig. 3). This means that for these fields, the vegetation layer present on their surfaces has significantly modified their scattering signatures, which cannot anymore successfully described by IEM.

CONCLUSIONS

Two model-based methods for soil moisture retrieval from L-band SAR data have been illustrated and the influence of the a priori information on the accuracy of the retrieved soil moisture content has been investigated.
Systematic results on a data set simulated by means of the IEM model and consisting of HH and VV L-band data at two incidence angles (i.e. 23° and 45°) have been illustrated. The study demonstrates that, the first retrieval algorithm, i.e. the Neural Network based method, estimates *the mean* of all possible solutions, whereas the second one, i.e. the ITerative model based Method, estimates *one* of all possible solutions. As a consequence, in absence of other information, the soil moisture retrieval error obtained by the NN method is smaller compared to the error obtained by using the IT Method. On the contrary, using *a priori* information on the variability range of surface parameters, the IT Method may retrieve soil moisture content with a smaller error than the NN method. More precisely, according to our analysis, IT Method retrieves soil moisture with better accuracy than NN method for guess values falling in a range of 30%-40% from the true values.
Finally, the developed retrieval algorithms have been applied to SIR-C data acquired over the Oberpfaffenhofen site (Germany) in April 1994. Results show that NN generally under estimates soil moisture values, whereas ITM algorithm correctly estimates soil moisture content provided that accurate a priori information about soil state is fed to the algorithm.

ACKNOWLEDGMENT

This work has been supported by ASI I/R/167/00 and ESA-ESTEC under contract n.13677/99.

REFERENCES

- Bishop, C. M. (1995): *Neural Networks for Pattern Recognition*, Clarendon Press – Oxford.
- Davis D. T., Z. Chen, L. Tsang, J. N. Hwang, A. T. C. Chang (1993): Retrieval of snow parameters by iterative inversion of a neural network, *IEEE Trans. Geosc. Remote Sensing*, Vol. 31, No 4, July 1993.
- Fung A. K. (1994): *Microwave Scattering and Emission Models and their Applications*, Norwood, MA:Artech House.
- Jackson, T. J., H. McNairn, et al. (1997): First order surface roughness correction of active microwave observations for estimating soil moisture, *IEEE Trans. Geosc. Remote Sensing,* **35**(4): 1065-1069.
- Mattia F., T. Le Toan, J. C. Souyris, G. De Carolis, N. Floury, F. Posa and G. Pasquariello (1997): The effect of Surface Roughness on Multifrequency Polarimetric SAR data, *IEEE Trans. Geosc. Remote Sensing*, Vol. 35, No. 4, July 1997, pp. 954-966.
- Satalino G., F. Mattia, T. Le Toan, M. Davidson, G. De Carolis, G. Pasquariello, M. Borgeaud (2000): On the impact of C-band SAR calibration errors on soil moisture retrieval, *Proceedings of Committee on Earth Observation Satellites*, CEOS SAR Workshop '99, R. A. Harris, L. Ouwehand, Editors, ESA Publication Division, ESA SP-450, pp. 467-472 .

Snow and Ice

Chairman: H. Rott

PROGRESS AND CHALLENGES IN RADAR REMOTE SENSING OF SNOW

Martti Hallikainen, Jouni Pulliainen, Jaan Praks, and Ali Arslan*

Laboratory of Space Technology, Helsinki University of Technology
P. O. Box 3000, FIN-02015 HUT, Finland
tel: +358 9-4512371 / fax: +358 9 4512898, email: martti.hallikainen@hut.fi
**Nokia Corporation, Helsinki, Finland*

ABSTRACT

The article is a review of radar remote sensing of snow, including the basics, recent progress, present challenges, and emerging technologies and methods in the field.

SYMBOL LIST

The main parameters in radar remote sensing of snow along with the corresponding symbols and abbreviations are listed in Table 1 and they are used throughout this presentation.

Table 1: Symbols and abbreviations of parameters in radar remote sensing of snow.

Parameter	Symbol or Abbreviation
Snow-covered area	SCA
Snow water equivalent	SWE
Snow wetness	SW
Permittivity	$\varepsilon = \varepsilon' - j\varepsilon''$
Backscattering coefficient	σ^0
Incidence angle	θ

Snow wetness is defined by volume and incidence angle is counted from vertical ($\theta = 0^\circ$ for nadir).

NEED FOR SNOW INFORMATION AND PRESENT DATA COLLECTION METHODS

Most of the snow cover is located in the northern hemisphere, where the mean snow-cover extent varies from 46.5 million km^2 in January to 3.8 million km^2 in August (Robinson et al., 1993). Changes in the annual distribution of snow related to the climate change have been observed during the last decades (Serreze et al., 1999). In addition to playing a significant role in the global climate, the cryosphere is a sensitive indicator of changes in the climate system. Better understanding of the interactions and feedback mechanism of the land/cryosphere system and their adequate parameterisation in climate and hydrological models is needed) (Allison et al., 2000), (Guyenne, 1995).

The amount and timing of snowmelt runoff from snow and glaciers is valuable information for management of water resources, including flood and avalanche prediction and hydropower operation in many countries. One of the main problem with hydrological models is lack of information on the spatial distribution of model variables and parameters (Guneriussen et al., 2001a). Information on snow is needed on various temporal and spatial scales, ranging roughly from one to ten days (temporal resolution) and from 0.1 km to 100 km (spatial resolution).

Present approaches to collect information on snow range from traditional ground-based methods to airborne gamma-ray measurement and to the use of optical satellite imagery and microwave (radiometer and radar) imagery. The level of these methods varies from those purely in research phase to those used operationally.

Ground-based methods are applied operationally in many countries. In Finland the number of snow courses (a few km long paths with typical land-cover type distribution, along which snow depth and water equivalent data are collected) used operationally is about 160, scattered all over the country. The results are reliable, but derivation of regional values from these temporally and spatially sparse data is problematic.

Operational airborne snow cover mapping using gamma-ray techniques has been performed in North America since the 1980's (Carroll et al., 1989). This method provides SWE and SCA along the flight path under both dry and wet snow conditions, but calibration and use over some land-cover types is problematic.

Canada has actively developed spaceborne microwave radiometry for snow mapping since the 1980's (Goodison, 1989).

Optical satellite measurements are easy to interpret (excluding the problem with clouds) for snow-covered area, but no data are available under dark and cloudy conditions. The U.S. National Weather Service has been mapping SCA with GOES satellite data since 1983 (Allen and Mosher, 1986).

Proc. 3rd International Symposium, 'Retrieval of Bio- and Geophysical Parameters from SAR Data for Land Applications', Sheffield, UK, 11-14 September 2001 (ESA SP-475, January 2002)

Microwave radiometry can provide snow water equivalent of dry snow cover with adequate accuracy, assuming that regionally tuned interpretation algorithms are used, e.g. (Hallikainen and Jolma, 1992). Additionally, discrimination of wet snow from dry snow works well, when time series of data are used. The main problems are the effects of snow grain size and vegetation (forest canopies), and poor spatial resolution.

U.S. National Oceanic and Atmospheric Administration (NOAA) has measured snow cover on a weekly basis in the northern hemisphere since 1986 using a variety of sensors, including the Scanning Radiometer (SR) and the Very High Resolution Radiometer (AVHRR) (Matson, 1991). The current NOAA product is a daily snow-cover product (Ramsay and Robinson, 2000).

With the launch of the Terra satellite on 18 December 1999 new snow mapping possibilities became available. The Moderate Resolution Imaging Spectroradiometer (MODIS) has recently started providing various products for snow-covered area (SCA), Table 2.

Table 2. MODIS snow-covered area products from the U.S. National Snow and Ice Data Center (NSIDC) (http://nsidc.org/NASA/MODIS/snow_products.html).

Data Type	Coverage (km)	Spatial Resolution	Temporal Resolution
MOD10_L2	1354 by 2000	500 m	Swath (scene)
MOD10L2G	1200	500 m	Day of multiple coincident swaths
MOD10A1	1200	500 m	Day
MOD10A2	1200	500 m	8 days
MOD10C1	Global	0.25°	Day
MOD10C2	Global	0.25°	8 days

These products are considered provisional at the time. Product quality may not be optimal, and incremental product improvements are still occurring.

Development of radar methods to collect information on snow has been slower in spite of early ground-based experiments on the effect of dry and wet snow to the backscattering coefficient of terrain (Stiles and Ulaby, 1980). The main advantages of radar-based methods over microwave radiometry and optical methods are better insensitivity to atmospheric effects (due to lower frequencies for radar) and much better spatial resolution (on the order of meters instead of kilometers), and measurement capability at night and through clouds, respectively. For example, the average cloudiness in Finland (latitude 60° to 70° N) is in winter about 70 % and, additionally, days are very short. About 70 % of the land area in Finland is covered by boreal forests, further complicating the use of optical satellite data.

In spite of the higher degree of complications for interpreting radar data, the SCA products in Table 2 are presently the reference, against which new methods should be compared. Due to the limitations of optical methods at high latitudes, an operational snow mapping method there should include the use of radar data.

MICROWAVE DIELECTRIC PROPERTIES OF SNOW AND SOILS

Water controls the dielectric properties of snow and soils. The basic investigations in this field include a study by Hallikainen et al. (1986) for wet snow, a study by Mätzler et al. (1996) for dry snow, and those by Dobson et al. (1985) and Hallikainen et al. (1985) for soils. Experimental data and theoretical models for the dielectric properties of soils at temperatures below 0°C are scarce (Hallikainen et al., 1985). Other investigations include a study by Tiuri et al. (1984) for wet snow. Recently, a new model for the microwave complex permittivity of wet snow was presented (Hallikainen and Vänskä, 2001), extending the validity range down to the MHz range.

With the possible introduction of higher frequencies for radar remote sensing of snow (Rott, 2001), studies concerning the extinction (absorption and scattering) properties of dry snow in the 10 to 30 GHz range are needed. Presently available information covers a frequency range of 18 to 90 GHz (Hallikainen et al., 1987) but the accuracy of results below 35 GHz is limited due to the measurement method.

BACKSCATTER MODELING

The backscattering coefficient of snow-covered terrain includes contributions from the snow-air interface, the snow layer (volume scattering), and the underlying ground surface. The observed backscattering coefficient is affected by several snow and soil parameters, including the following (Ulaby et al., 1986): Snow layer thickness, snow volumetric water content, snow wetness, snow temperature, snow density, surface roughness (snow-air and snow-soil interfaces), and snow layering. Depending on geographical area, the effects of boreal forest (Koskinen et al., 1997) and those of relief, aspect angle, layover, and radar shadowing (Nagler and Rott, 2000) may be important.

Based on studies by Kendra et al. (1998) and by Koskinen et al. (2000), the discrete particle model for snow volume scattering agrees with experimental data at C-band only if the snow particle size is assumed to be substantially larger than the visually observed value.

Shi and Dozier (2000b) eveloped a physically-based first-order backscatter model for dry snow. The cross-polarisation signal is only generated from the snow-ground interaction terms and it can be used to investigate co-polarisation signals. As discussed later, this model has been used to infer snow depth and particle size from SIR-C/X-SAR measurements. Previously, they developed a C-band polarimetric backscatter model for wet snow (1995), accounting for surface and volume scattering and including a total of five various coherent/incoherent scattering terms, out of which three terms represent surface-volume interaction terms. Mätzler and Wiesmann (1999) recently extended their previously developed emission and backscattering model to handle coarse-grained snow.

Ulaby et al. (1996) developed a semiempirical backscatter model for 35 and 95 GHz. The model expressions are given for each linear polarisation combination in terms of incidence angle and four snow parameters: depth, density, particle diameter, and wetness. The model accuracy was reported to be on the order of 1 to 3 dB. Other millimeter-wave backscatter models for snow include those of Mead et al. (1993) and Tjuatja et al. (1996). A review on modelling for millimeter-wave remote sensing of snow has been presented by O'Neill (1994).

Basic problems in backscatter modelling include characterisation of snow medium and vegetation (forest). The stickiness parameter is emerging to account for the effect of snow particle lumping (Ding et al., 1994). The transmissivity of boreal forest canopies has been estimated from microwave radiometer measurements at frequencies above 6.8 GHz, suggesting that the values are above 0.9 at L-band (Kruopis et al., 1999). Further studies are needed.

SNOW-COVERED AREA AND SNOW MELT

Determination of snow-covered area from radar data is a complex problem, because snow may be either wet or dry and soil may be either frozen or thawed. Moreover, the volumetric wetness of snow can have values between 0 and 5 % and that of thawed soil can have values between 5 and 30 %, changing the value of the backscattering coefficient correspondingly. Vegetation may partially mask snow and underlying ground. In practice, water authorities are mostly interested in snow melt runoff, changing the problem to that of discriminating wet snow from thawed snow-free ground within a basin.

An operational snow melt monitoring system was adopted for use in Finland recently (Metsämäki et al., 2001), (Koskinen et al., 1999). It employs AVHRR images, weather permitting, and ERS-2 SAR images, when available. The system supports run off prediction. The SAR method is based on pixel-wise comparison of present image with reference image(s) for wet snow-free ground, e.g. from the previous snow season (Koskinen et al., 1997). The change in the value of the backscattering coefficient from that for wet snow to that for snow-free ground (about 3 dB at C-band, depending on land-use category) is assumed to depend linearly on the fraction of snow-covered ground within a pixel. The effect of boreal forest canopies is compensated using the method presented in (Pulliainen et al., 2001). Using their modelling approach, verified by comparisons of computed results with ERS SAR data and airborne HUTSCAT scatterometer data, Koskinen et al. concluded that the SCA algorithm relying on reference images for snow-free ground works better than that employing reference images for dry snow (2000).

Similar SAR-based methods for have been developed for other geographical areas. The method relying on ERS-2 SAR and RADARSAT data was demonstrated in Austria (Nagler and Rott, 2000). In Canada Baghdadi et al. demonstrated the use of C-band SAR data for mapping of wet snow, employing ERS-1 SAR data (1997) and airborne polarimetric data (1998) and, additionally, they investigated the potential and limitations of RADARSAT data for wet snow monitoring (2000). Experiments on snow melt monitoring with RADARSAT SAR images were conducted also by Li, S. et al. (2000). Bernier et al. (1998) studied the use of ERS SAR time series to monitor dry and shallow snow cover. The use of a high incidence angle was observed to help in the discrimination of wet snow from snow-free ground; the same was confirmed by Guneriussen et al. (2001b).

The use of airborne L- and C-band polarimetric data was tested in Norway for discrimination of wet snow from bare snow-free ground and vegetated snow-free ground (Holden et al, 1998). The best classification accuracy for discriminating wet snow from bare snow-free ground was obtained with the C-band span (87 %), followed by C-band VV and HH polarisations. In the case of vegetated snow-free ground C-band HV and VH polarisations gave the best accuracy (95 %), closely followed by corresponding L-band channels.

The results from airborne C-band polarimetric radar experiment in the Alps under summer melt and rainstorm conditions showed that the best separabilities between wet snow, glacier ice and other surfaces (rock, moraine, grassland) are obtained with three polarimetric parameters (Shi et al., 1994). They are the degree of polarisation, depolarisation factor ($\sigma^0_{hv}/\sigma^0_{vv}$), and total power in VV polarisation. For discrimination of wet snow-covered areas from snow-free areas the separabilities (difference between class mean values divided by sum of standard deviations) ranged from 1.4 to 2.1.

One of the present challenges is to examine the use of SAR systems operating above X-band to further improve determination of snow-covered area.

CLASSIFICATION OF WET SNOW, DRY SNOW, AND SNOW-FREE GROUND

Hallikainen et al. (1995) used data sets from ERS-1 SAR, airborne HUTSCAT scatterometer (C- and X-band, 4 linear polarisations), and airborne microwave radiometer data at 24, 35, 48 and 94 GHz to discriminate dry snow, wet snow, frozen snow-free ground and wet snow-free ground. A specific combination of radar and radiometer data for discriminating each parameter in the case of several land-use categories and forest types was determined.

Stiles and Ulaby (1980) demonstrated that the capability of radar to discriminate wet snow from dry snow by radar improves with increasing frequency. Since the highest frequency of a satellite-borne SAR system so far is 5.3 GHz, Nghiem et al. (2001) used data from the Ku-band SeaWinds scatterometer onboard the QuikSCAT satellite to investigate snow signatures. They carried out a ground-based Ku-band scatterometer campaign in Alaska and applied its results to the satellite data. The final outcome was daily global snow cover maps with four separate categories: Snow, melting snow, refrozen snow, and snow-free ground. They also showed the evolution of seasonal snow cover over the northern hemisphere in 1999-2001 with time-series SeaWinds imagery.

Methods based on airborne radar polarimetry were suggested for studying changes in L- and C-band polarimetric descriptors (entropy, alpha angle, and anisotropy) due to seasonal changes in snow-covered areas in the Alps (Ferro-Famil et al., 1999).

The use of (a) Ku-band and even higher frequencies, (b) SAR polarimetry, and (c) combined radar and microwave radiometer measurements for large-scale applications are some of the present challenges.

SNOW WATER EQUIVALENT

Opposing results on the dependence of the backscattering coefficient vs. snow water equivalent have been presented over a period of 20 years. Ulaby and Stiles (1980) showed that the correlation between σ^0 and SWE is positive at 8.2 and 17 GHz. Based on their experimental results they developed a semiempirical model to characterise the relationship. They considered the direct volume backscattering component from the snow volume and the surface backscattering component from the snow-ground interface. Kendra et al. (1998) also found a positive correlation between the two quantities from their data over a smooth subsurface. However, this positive correlation only existed over a frozen subsurface, whereas there was no correlation over the thawed subsurface (Bernier and Fortin, 1998). On the other hand, Strozzi (1996) observed a negative correlation between σ^0 and SWE at 5.3 GHz. Rott and Mätzler (1987) observed no particular difference between dry snow-covered and snow-free areas at 10.4 GHz.

This dispute was explained by Shi and Dozier (2000b); they concluded from their theoretical studies that the correlation between σ^0 and SWE for a given incidence angle and polarisation may vary from positive to negative, depending on snow and soil characteristics.

Shi and Dozier (2000a, 2000b) estimated snow water equivalent for a test site (snow depths up to 5 m) using SIR-C/X-SAR data at L-band, C-band, and X-band. They first inferred snow density with L-band VV and HH data and then determined snow depth and particle size with C-band and X-band data. This algorithm is based on a polarimetric dry snow backscatter model and consequent characterisations and parameterisations of various terms and relationships in order to decrease the number of unknown components in backscatter contributions. The algorithm performs well for incidence angles higher than 30°. The density of snow for a test site in China was determined with L-band polarimetric data using a similar approach (Li, Z. et al., 2000).

Arslan et al. (2001) investigated retrieval of SWE of dry snow form airborne SAR C-band data during the ESA EMAC'95 Snow and Ice Campaign in northern Finland. They used an empirical model and data for non-forested areas. This approach provided good results only after massive spatial averaging of radar data. This is likely to be caused by the large variability in soil type (agricultural land, clear cut, and bogs) and, consequently, in surface roughness.

The use of polarimetric descriptors for retrieval of snow information from airborne L- and C-band data in the boreal forest zone was tested by Praks et al. (1998). Their study showed that entropy of natural targets is high and the amount of polarimetric information in backscatter is low. The alpha angle (related to the backscatter mechanism) increases with increasing snow depth, but has considerable scatter and is also affected by forest stem volume.

Obviously, polarimetric multifrequency SAR data will not be available from satellites in the near future. Another new technique, SAR interferometry, already proven in space, was recently applied to snow studies. Guneriussen et al. (2001c) determined a relationship between the InSAR phase and SWE. The results imply that small changes in snow characteristics between InSAR image acquisitions may introduce an increase in the DEM height error. Li and Sturm (2001) had a similar approach. They constructed an interferogram from a pair of SAR images spanning a snow precipitation event, and another SAR interferogram from a pair of SAR images acquired a week earlier. The second pair was used to remove the topographic component, revealing the spatial distribution of the snow precipitation event, obviously with reasonable accuracy.

Koskinen (2001) investigated the feasibility of using interferometric L- and C-band SAR imagery for determining the extent and depth of wet snow cover. He was able to determine the snow extent using SAR intensity and Landsat imagery; however, the accuracy of the digital elevation model (DEM) available for interferometric height calibration was not adequate. A reference interferometric height measurement would be needed for the purpose.

The use of SAR interferometry for SWE mapping is no doubt one of the major challenges in this area.

SNOW WETNESS

Investigations have shown both negative and positive correlations between the backscattering coefficient and snow wetness (Stiles and Ulaby, 1980), (Shi and Dozier, 1992), possibly due to different surface roughness values. On the other hand, European SAR algorithms for retrieval of snow-covered area employ observed negative correlation between σ^0 and wetness for reasonable snow wetness and depth values (Koskinen et al., 1997), (Nagler and Rott, 2000), (Guneriussen et al., 2001b).

Shi and Dozier (1995) applied their backscatter model for wet snow in a test site with an average annual SWE of 800 mm, showing that the relationship between σ^0 and SW is controlled by the relative contribution of volume and surface scattering mechanisms. Their results indicate that rough surface tends to cause positive correlation and smooth surface negative correlation depending, additionally, on snow characteristics and incidence angle.

Based on their modelling approach, Koskinen et al. (2000) concluded that, for snow and land-use conditions typical of the boreal forest zone, the difference in the C-band VV-polarisation (ERS SAR) backscattering coefficient between dry and wet snow increases with increasing wetness. It finally saturates to a value of about 7 dB at SW = 4 %; typical scatter due to varying snow and land-use conditions is of the order of 5 dB. The corresponding difference between snow-free ground and wet snow was determined to be practically the same, with substantially smaller scatter.

Ulaby et al. (1996) investigated the use of 35 and 95 GHz for retrieval of snow characteristics. Although the role of snow particle size is substantial even at 35 GHz (as in microwave radiometry), the backscattering coefficient is highly sensitive to snow wetness, exhibiting a dynamic range of about 20 dB for the wetness range of 0 to 6 % for HV polarisation, incidence angle 40 degrees.

The use of higher frequencies for SW mapping is a challenge for near-future research.

MILLIMETERWAVE RADAR STUDIES OF SNOW

Millimeter-wave backscatter from snow has been discussed to some degree in previous sections. Additional work includes measurements at 35, 95, and 225 GHz (Chang et al., 1994) and analysis of 215 GHz measurements and a geometrical optics model development (Narayanan and McIntosh, 1990).

EMERGING METHODS AND SENSORS

New methods for radar sensing of snow include SAR polarimetry, SAR interferometry, and high-frequency SAR. Although various decomposition techniques have been introduced (Cloude and Potier, 1996), the covariance matrix eigenvalue-based decomposition theory proposed by Cloude (1992), has been generally adopted for use in remote sensing. Few studies have been conducted so far to thoroughly test the feasibility of SAR polarimetry and interferometry for retrieval of snow characteristics. The proposal for a space-borne high-frequency SAR (Rott, 2001) is an interesting initiative that, if successful, will lead to a dedicated SAR mission for global snow mapping.

REFERENCES

Allen, M. W. and Mosher, F. R. (1986): Monitoring snow pack conditions with an interactive geostationary satellite system. *Proc. 54th Annual Western Snow Conference*, pp. 51-60, Phoenix, AZ, USA, 15-17 April 1986.

Allison, I., Barry, R. G., and Goodison, B. E. (2000): World Climate Research Programme Climate and Cryosphere (CLIC) Project – Initial Sequence and Coordination Plan (*http://www.np.no/clic*).

Arslan, A.N., Praks, J., Koskinen, J., and Hallikainen, M. (2001): An empirical model for retrieving snow water equivalent from C-band polarimetric SAR data. *Report 45, Laboratory of Space Technology, Helsinki University of Technology*, 35 pp., 2001.

Baghdadi, N., Gauthier, Y., and Bernier, M. (1997): Capability of multitemporal ERS-1 SAR data for wet snow mapping. *Remote Sens. Environ.*, vol. 60, pp. 174-186, 1997.

Baghdadi, N., Livingstone, C. E., and Bernier, M. (1998): Airborne C-band SAR measurements of wet snow areas. *IEEE Trans. Geosci. Remote Sensing*, vol. 36, pp. 1977-1981, Nov. 1998.

Baghdadi, N., Gauthier, Y., Bernier, M., and Fortier, J.-P. (2000): Potential and limitations of RADARSAT SAR data for wet snow monitoring. *IEEE Trans. Geosci. Remote Sensing*, vol. 38, pp. 316-320, Jan. 2000.

Bernier, M. and Fortin, J-P. (1998): The potential of times series of C-band SAR data to monitor dry and shallow snow cover. *IEEE Trans. Geosci. Remote Sensing*, vol. 36, no. 1, pp. 226-243, Jan. 1998.

Carroll, T. R., Baglio, J. V., Verdin, J. P., and Holroyd, E. W. III (1989): Operational mapping of snow cover in the United States and Canada using airborne and satellite data. *Proc. 15th Canadian Symposium on Remote Sensing and IGARSS'89*, pp. 1257-1259, Vancouver, B.C., Canada, 10-14 July 1989.

Chang, P., Mead, J., McIntosh, R., Davis, R., and Boyne, H. (1994): A detailed study of the backscatter characteristics of snowcover measured at 35, 95 and 225 GHz. *Proc. IEEE 1994 Int. Geoscience and Remote Sensing Symposium (IGARSS'94)*, pp. 1932-1934, Pasadena, CA, USA, 8-12 Aug. 1994.

Cloude, S. R. (1992): Uniqueness of target decomposition theorems in radar polarimetry. In: *"Direct and Inverse Methods in Radar Polarimetry,"* Editors: Boerner, W. M. et al., Kluwer Academic Publishers, pp. 773-791, 1992.

Cloude, S. R., Potier, E., (1996) A review of target decomposition theorems in radar polarimetry. *IEEE Trans. Geosci. Remote Sensing*, vol. 34, pp. 498-518, March 1996.

Ding, K., Zurk, L., and Tsang, L. (1994): Pair distribution functions and attenuation rates for sticky particles in dense media. *J. Electromagn. Waves Applicat.*, vol. 8, 1585-1604, 1994.

Dobson, M.C., Ulaby, F.T., Hallikainen, M., and El-Rayes, M.(1985): Microwave dielectric behavior of wet soil - Part II: Dielectric mixing models. *IEEE Trans. Geosci. Remote Sensing*, vol. GE-23, pp. 35-46, Jan. 1985.

Ferro-Famil, L., Pottier, E., Saillard, J., Dedieu, J., Bernier, M., and Fortin, J. (2000): The potential of full polarimetric SAR data to classify dry snowcover. *Proc. IEEE 1999 Int. Geoscience and Remote Sensing Symposium (IGARSS'99)*, pp. 1792-1794, Hamburg, Germany, 28 June - 2 July 1999.

Goodison, B. (1989): Determination of areal snow water equivalent on the Canadian prairies using passive microwave satellite data. *Proc. Joint 15th Canadian Symposium on Remote Sensing and IGARSS'89*, pp. 1243-1246, Vancouver, Canada, 10-14 July 1989.

Guneriussen, T. et al. (2001a): Description of Work; Development of Generic Earth Observation Based Snow Parameter Retrieval Algorithms. *Project Proposal to European Union*, EESD Programme, 2001.

Guneriussen, T., Johnsen, H., and Lauknes, I. (2001b): Snow cover mapping capabilities using RADARSAT standard mode data. *Canadian J. Remote Sensing*, vol. 27, pp. 109-117, April 2001.

Guneriussen, T., Hogda, K. A., Johnsen, H., and Lauknes, I. (2001c): InSAR for estimation of changes in snow water equivalent of dry snow. *IEEE Trans. Geosci. Remote Sensing*, in press, to appear in Oct. 2001.

Guyenne, T. (editor) (1995): Scientific Achievements of ERS-1. *ESA SP-1176/1*, ESA-ESTEC, 162 pp., Noordwijk, The Netherlands, 1995.

Hallikainen, M., Ulaby, F.T., Dobson, M.C., and El-Rayes, M. (1985): Microwave dielectric behavior of wet soil - Part I: Empirical models and experimental observations. *IEEE Trans. Geosci. Remote Sensing*, vol. GE-23, pp. 25-34, Jan. 1985.

Hallikainen, M., Ulaby, F.T., and Abdelrazik, M. (1986): Dielectric properties of snow in the 3 to 37 GHz range. *IEEE Trans. Ant. Propagat.*, vol. AP-34, pp. 1329-1340, Nov. 1986.

Hallikainen, M., Ulaby, F.T., and Van Deventer, T.E. (1987): Extinction behavior of dry snow in the 18 to 90 GHz range. *IEEE Trans. Geosci. Remote Sensing*, vol. GE-25, pp. 737-745, Nov. 1987.

Hallikainen, M. and Jolma, A. (1992): Comparison of algorithms for retrieval of snow water equivalent from Nimbus-7 SMMR data in Finland. *IEEE Trans. Geosci. Remote Sensing*, vol. 30, no. 1, pp. 124-131, 1992.

Hallikainen, M., Kurvonen, L., Koskinen, J., Jääskeläinen, V., and Mäkynen, M. (1995): Combined use of radar and microwave radiometer in retrieval of snow characteristics. *Proc. IEEE 1995 Int. Geoscience and Remote Sensing Symposium (IGARSS'95)*, pp. 1511-1514, Florence, Italy, 10-14 July 1995.

Hallikainen, M. and Vänskä, T. (2001): A new model for the microwave dielectric properties of wet snow. *Unpublished.*

Holden M., Schistad, A., and Solberg, R. (1998): Wet snow-cover mapping by L-and C-band polarimetric SAR. *Proc. IEEE 1998 Int. Geoscience and Remote Sensing Symposium (IGARSS'99)*, pp. 1533-1537, Seattle, WA, USA, 6-10 July 1998.

Kendra, J. R., Sarabandi, K., and Ulaby, F. T. (1998): Radar measurements of snow: Experiment and analysis. *IEEE Trans. Geosci. Remote Sensing*, vol. 36, pp. 864-879, May 1998.

Koskinen, J., Pulliainen, J., and Hallikainen, M. (1997): The use of ERS-1 SAR data in snow melt monitoring. *IEEE Trans. Geosci. Remote Sensing*, vol. GE-35, pp. 601-610, May 1997.

Koskinen, J., Metsämäki, S., Grandell, J., Jänne, S., Matikainen, L., and Hallikainen, M. (1999): Snow monitoring using radar and optical satellite data. *Remote Sens. Environ.*, vol. 69, pp. 16-29, 1999.

Koskinen, J., Pulliainen, J., and Hallikainen, M. (2000): Effect of snow wetness to C-band backscatter – a modeling approach. *Report 41, Laboratory of Space Technology, Helsinki University of Technology*, 20 pp., 2000.

Koskinen, J. (2001): Snow monitoring using interferometric TOPSAR data. *Proc. IEEE 2001 Int. Geoscience and Remote Sensing Symposium (IGARSS'01)*, 3 pp., Sydney, Australia, 9-13 July 2001.

Kruopis, N., Praks, J., Arslan, A.N., Alasalmi, H., Koskinen, J., and Hallikainen, M., (1999): Passive microwave measurements of snow-covered forest areas in EMAC'95. *IEEE Trans. Geosci. Remote Sensing*, vol. 37, pp. 2699-2705, 1999.

Li, S., Sturm, M., Kyriazis, S., and Logan, T. (2000): Mapping snowmelt sequence at Ivotuk, Alaska, using RADARSAT SAR images acquired with different standard beams. *Proc. IEEE 2000 Int. Geoscience and Remote Sensing Symposium (IGARSS'2000)*, pp. 481-483, Honolulu, Hawaii, USA, 24-28 July 2000

Li, S. and Sturm, M. (2001): Derivation of spatial distribution of snow precipitation using interferometric SAR technique. *Proc. IEEE 2001 Int. Geoscience and Remote Sensing Symposium (IGARSS'01)*, 3 pp., Sydney, Australia, 9-13 July 2001.

Li, Z., Guo, H., and Shi, J. (2000): Estimation of snow density with L-band polarimetric SAR data. *Proc. IEEE 2000 Int. Geoscience and Remote Sensing Symposium (IGARSS'2000)*, pp. 1757-1759, Honolulu, Hawaii, USA, 24-28 July 2000.

Matson, M. (1991) NOAA satellite snow cover data. *Paleogeography and Paleoecology*, vol. 90, pp. 213-280, 1991.

Mead, J. B., Chang, P. S., Lohmeier, S. P., Langlois, P. M., and McIntosh, R. (1993): Polarimetric observations and theory of millimeter-wave backscatter from snow cover. *IEEE Trans. Geosci. Remote Sensing*, vol. 31, pp. 38-46, Jan. 1993.

Metsämäki, S., Vepsäläinen, J., Pulliainen, J., Koskinen, J., Huttunen, M., and Hallikainen, M. (2001): The applicability of C-band SAR and optical data for snow monitoring in Boreal forest. *Proc. Third Int. Workshop on Retrieval of Bio- & Geo-physical Parameters from SAR Data for Land Applications*, 6 pp., Sheffield, UK, 11-14 Sept. 2001.

Mätzler, C. (1996): Microwave permittivity of dry snow, *IEEE Trans. Geosci. Remote Sensing*, vol. 34, pp. 573-581, March 1996.

Mätzler, C. and Wiesmann, A. (1999): Extension of the microwave emission model of layered snowpacks to coarse-grained snow. *Remote Sens. Environ.*, vol. 70, pp. 317-325, 1999.

Nagler, T. and Rott, H. (2000): Retrieval of wet snow by means of multitemporal SAR data. *IEEE Trans. Geosci. Remote Sensing*, vol. 38, pp. 754-765, March 2000.

Narayanan, R. M. and McIntosh, R. E. (1990): Millimeter-wave backscatter characteristics of multilayered snow surfaces. *IEEE Trans. Geosci. Remote Sensing*, vol. 28, pp. 693-703, May 1990.

Nghiem, S. V., Tsai, W.-Y., Neumann, G., Sturm, M., Taras, B., Perovich, D. K., and Elder, B. (20001): Remote sensing of snow with SeaWinds scatterometer. *Proc. IEEE 2001 Int. Geoscience and Remote Sensing Symposium (IGARSS'01)*, 3 pp., Sydney, Australia, 9-13 July 2001.

O'Neill, K. (1994): A review of modeling for millimeter wave remote sensing of snow. *Proc. IEEE 1994 Int. Geoscience and Remote Sensing Symposium (IGARSS'94)*, pp. 1925-1928, Pasadena, CA, USA, 8-12 Aug. 1994.

Praks, J., Koskinen, J., Arslan, A., Kruopis, N., Alasalmi, H, and Hallikainen, M. (1998): Cloude's target decomposition theorems applied to EMISAR data acquired during EMAC'95 snow campaign. *IEEE 1998 Int. Geoscience and Remote Sensing Symposium (IGARSS'98)*, pp. 1538-1540, Seattle, WA, USA, 6-10 July 1998.

Pulliainen, J., Koskinen, J., and Hallikainen, M. (2001): Compensation of forest canopy effects in the estimation of snow covered area from SAR data. *Proc. IEEE 2001 Int. Geoscience and Remote Sensing Symposium (IGARSS'01)*, 3 pp., Sydney, Australia, 9-13 July 2001.

Ramsay, B. H. and Robinson, D. (2000): Prospects for the Interactive Multisensor Snow and Ice Mapping System. *Proc. 57th Eastern Snow Conference*, Syracuse, N.Y., USA, 17-19 May 2000.

Rott, H. (2001): Requirements for a high frequency spaceborne SAR mission to measure the extent and properties of the seasonal snow cover. *Proc. Third Int. Workshop on Retrieval of Bio- & Geo-physical Parameters from SAR Data for Land Applications*, 6 pp., Sheffield, UK, 11-14 Sept. 2001.

Rott, H. and Mätzler, C. (1987): Possibilities and limits of synthetic aperture radar for snow and glacier surveying. *Ann. Glaciol.*, vol. 9, pp. 195-199, 1987.

Shi, J. and Dozier, J. (1992): Radar response to snow wetness. *Proc. IEEE 1992 Int. Geoscience and Remote Sensing Symposium (IGARSS'92)*, pp. 927-929, Houston, TX, USA, 26-29 May 1992.

Shi, J., Dozier, J., and Rott, H. (1994): Snow mapping in Alpine regions with synthetic aperture radar. *IEEE Trans. Geosci. Remote Sensing*, vol. 32, pp. 152-158, Jan. 1994.

Shi, J. and Dozier, J. (1995): Inferring snow wetness using C-band data from SIR-C's polarimetric synthetic aperture radar. *IEEE Trans. Geosci. Remote Sensing*, vol. 33, pp. 905-914, July 1994.

Shi, J. and Dozier, J. (2000a): Estimation of snow water equivalence using SIR-C/X-SAR, part I: Inferring snow density and subsurface properties. *IEEE Trans. Geosci. Remote Sensing*, vol. 38, pp. 2465-2474, Nov. 2000.

Shi, J. and Dozier, J. (2000b): Estimation of snow water equivalence using SIR-C/X-SAR, part II: Inferring snow depth and particle size. IEEE *Trans. Geosci. Remote Sensing*, vol. 38, pp. 2475-2488, Nov. 2000.

Stiles, W. H. and Ulaby, F. T. (1980): The active and passive microwave response to snow parameters. 1. Wetness. *J. Geophys. Res.* Vol. 85, no. C2, pp. 1037-1044, 1980.

Strozzi, T. (1996): Backscattering measurements of snow covers at 5.3 and 35 GHz. *Ph.D. dissertation*, Inst. Applied Physics, Univ. Bern, Bern, Switzerland, 1996.

Tiuri, M., A. Sihvola, E. Nyfors, and M. Hallikainen, (1984): The complex dielectric constant of snow at microwave frequencies. *IEEE J. Oceanic Engin.*, vol. OE-9, pp. 377-382, 1984.

Tjuatja, S., Fung, A. K., Comiso, J. C. (1996): Scattering and emission from dry snow in the range 35-140 GHz. *Proc. IEEE 1996 Int. Geoscience and Remote Sensing Symposium (IGARSS'96)*, pp. 2008-2010, Lincoln, USA, 27-31 May 1996.

Ulaby, F. T. and Stiles, W. H. (1980): The active and passive microwave response to snow parameters. 2. Water equivalent of dry snow. *J. Geophys. Res.* Vol. 85, no. C2, pp. 1045-1049, 1980.

Ulaby, F. T., Moore, R. K., and Fung, A. K. (1986): *Microwave Remote Sensing – Active and Passive, vol. III: From Theory to Applications*. Artech House, 1100 pp., 1986.

Ulaby, F., Siqueira, P., Nashashibi, A., and Sarabandi, K. (1996): Semi-empirical model for radar backscatter from snow at 35 and 95 GHz. *IEEE Trans. Geosci. Remote Sensing*, vol. 34, no. 5, pp. 1059-1065, Sept. 1996.

Process Modelling

Chairman: A. Rosenqvist

REMOTE SENSING DATA ASSIMILATION IN LAND SURFACE PROCESS MODELLING

BACH Heike [1], MAUSER Wolfram [2]

(1) Vista Geowissenschaftliche Fernerkundung GmbH
Luisenstr. 45, D-80333 München, Germany
Tel. +49-89-52389802, Fax +49-89-52389804
Email: bach@vista-geo.de

(2) Institute for Geography, University of Munich
Luisenstr. 37, D-80333 Munich, Germany
Tel. +49 89 2180 6674 , Fax +49 89 2180 6675
Email: w.mauser@iggf.geo.uni-muenchen.de

ABSTRACT

Land surface process models describe the energy-, water-, carbon- and nutrient-fluxes at the land surface on a regional scale by combining a given set of environmental parameters and variables (e.g. water balance model, plant physiology model, atmospheric boundary layer model, erosion model). They need spatially distributed input parameters, which can be delivered from remote sensing analyses using both optical and microwave sensors. Thus, land surface process models are the main drivers for four dimensional data assimilation (4DDA) which is based on the synergistic data utilization of remote sensing and ancillary data both in space and time.

To ensure the constant flow of the necessary input parameters and variables, the development of adequate data-assimilation and data-fusion techniques is mandatory. Parameter models operate at the centre of this data fusion process to convert remote sensing measurements into a set of model input parameters and variables. Different strategies to use remote sensing derived parameters in models are demonstrated. They span from the simple delivery of static input-parameters, over the provision of dynamic model parameters, model forcing and recalibration of internal model variables, to inversion and validation of land surface process models.

Examples will illustrate these different data assimilation strategies using SAR and optical data sources. The integration of land surface parameters derived from remote sensing (e.g. land use, digital terrain model, surface soil moisture) in flood forecast is a rather straight forward task. For water balance modelling, soil moisture and snow cover assessment will be illustrated. This task is already more complex, since a continuous process must be simulated and the data assimilation must avoid inconsistencies in model performance. The application of remote sensing data assimilation methods for crop growth and agricultural production models further requires complex feedback mechanisms. Examples will be presented from the ESA-study *GeoBIRD* (Bach et al. 2001).

INTRODUCTION

Progress has been made in the bio-geophysical modelling of land surface processes on different scales. Complex land surface process models of local validity were developed in plant ecology and boundary layer meteorology to understand the feedback between soil and atmosphere as well as to understand plant growth and carbon assimilation of single plants and plant canopies. Their development was based on a wealth of experimental data gathered on experimental sites over a broad range of land surface types. These models need a large to very large number (sometimes more than 100) of input parameters to accurately reproduce observations. Simplified models were derived from these complex models as early as in the late 80's driven by the need of meteorologist for a somewhat better representation of the land surface in global and mesoscale circulation models. Both developments, on the complex, small, verifiable scale as well as on the abstract, simplified and global scale created a gap in the description of land surface processes on the regional scale of landscapes. Nevertheless, this scale is most relevant for applications since most environmental management decisions in terms of land-use, land management and environmental protection are made on this scale.

Today, with the need to better understand fluxes of carbon, water and nutrients on the scale of landscapes it has become clear, that modelling of the spatial interactions of hydrological and biological processes on the landscape level is a scientific task by itself. It has become a tool of major importance to check the depth of our understanding of environmental processes and interactions. Regional landscape models have now developed to a stage of maturity to serve as a valuable tools

Proc. 3rd International Symposium, 'Retrieval of Bio- and Geophysical Parameters from SAR Data for Land Applications', Sheffield, UK, 11-14 September 2001 (ESA SP-475, January 2002)

for decision-making within a practical framework. Land surface process models and their predictive abilities will eventually form the basis to intelligently balance the conflicts between nature and man in a future world, which is marked by the need of sustainable landscape management within the boundary conditions of growth in human population and prosperity.

Models need data at several stages of their execution cycle. Data is necessary as parameters describing the state of the described system, as dynamic state variables expressing changes within the system and for the validation of the model results. Since landscape models describe a process, which takes place in time *and* space they have to be spatially distributed by their very nature. Spatially distributed process models need spatially distributed data on all levels. This is where remote sensing as the science of the interaction between natural objects and electromagnetic waves enters the stage. Remote sensing provides the necessary data to be able to shift from point measurements to spatial measurements. However, scale, resolution and temporal availability of remote sensing observations need to be matched with the studied phenomena. Hence data assimilation and data fusion techniques are required. 4DDA (four dimensional data assimilation) is the keyword in the upcoming future.

The actual scientific status of data assimilation in land surface process models is still in an early stage. The level of processing of remote sensing data often rarely exceeds simple land use classifications. One main reason for this lies in the fact, that the presently available Earth observation (EO) instruments to study the land surface do not have a very suitable set of system parameters to adequately study dynamic land surface processes. To fully utilise the potential of the EO instruments to quantitatively deliver spatial fields of model parameters the full synergy between the whole range of available sensors (optical and microwave) and their ability to interact with models has to be exploited.

It is evident that remote sensing is the most efficient and in many aspects also the only way to quantitatively assess spatial distributions of input parameters for land surface process models. However there are currently limitations and open questions in the determination of land surface parameters both with optical and microwave data. Even with a perfect set of advanced sensors these problems can only be solved with improvements in processing algorithms and assimilation procedures. The main causes for limitations in accuracy are:

- The land surface parameters cannot directly be measured by remote sensing. Instead the interaction of the Earth's surface with electromagnetic waves is quantified. These scattering- and absorption-properties of the surface (reflectance, transmission, absorption, or scattering) must be converted into meaningful land surface variables such as leaf area or soil moisture using *parameter models*. Often parameter models consist of inversion procedures of radiative transfer models, which model the remote sensing (RS) process. Of course this indirect approach may introduce errors in the retrieval of land surface properties.
- Undesired influences are contained in the measured remote sensing signal, which have to be eliminated. In the optical spectral range the atmosphere influences the measured signal through absorption and scattering processes in the atmosphere. Advanced atmospheric correction schemes have to be applied before any further analysis. The synthetic aperture microwave signal is strongly influenced and disturbed by the speckle noise.
- The spectral information is often ambiguous. This is again true both for optical and microwave data. With one observation of a sensor with a given geometry and spectral configuration two different land use types (e.g. forest and corn) may provide the same spectral signature. However their biophysical properties (leaf area, height, biomass, carbon-fixation) might differ strongly. The radar backscatter of the land surface is influenced by at least two factors, the dielectric constant and surface roughness. With one observation alone and using existing spaceborne SAR systems these two factors can hardly be discriminated.
- Information might be hidden because parameters that are necessary for modelling processes on the land surface may not be identical with the parameters that can be derived from remote sensing. For instance with C-band SAR the soil moisture of the soil surface (top 2-5 cm) can be measured. However the soil moisture of the whole root zone (which may be 15 – 250 cm thick) is required for water balance calculations.

These difficulties and discrepancies are some of the underlying causes why remote sensing still does not play a central role in modelling of land surface processes on the regional scale. They will not be overcome simply by using new generation sensors alone. In addition the assimilation of remote sensing data in process models must be accepted as a central task of research for the next years. Remote sensing activities, which are solely driven by remote sensing science or technology will sooner or later loose not only financial support but also attraction. If however Earth observation sources are routinely used in land surface process models, which are of relevance for practical applications, e.g. for watershed or agricultural production management, remote sensing will remain a most relevant and fascinating field of research.

DATA ASSIMILATION STRATEGIES

There are several possible options to use remote sensing data within a land surface process model. The main difference between the different approaches lies in the goal and the degree of abstraction.

Option 1: Determination of fields of static model input parameters using remote sensing data and substitution of classically derived parameter values through remote sensing derived parameter values in the model.

Examples are land use and terrain elevation information. The values of the parameters change very slowly with time and are therefore used to initialise land surface process models. Therefore remote sensing data with limited temporal resolution is sufficient for this purpose.

Option 2: Dynamic model parameters update through remote sensing measurements.

In this case remote sensing measurements are converted into values of dynamically changing physical parameters of the land surface. Their values are introduced from outside the model instead of deriving them inside the model based on some reasonable physical assumption like conservation laws for mass and energy. The model is therefore forced into a realistic representation of the physical behaviour of the system instead of accumulating errors in an uncontrolled way. Examples are leaf area index (LAI) and albedo.

The assimilation of land surface parameters derived from remote sensing by externally feeding the parameter values into the model, which are then temporally interpolated, is illustrated in *Fig. 1*.

Option 3: Parameter determination through model recalibration or model inversion.

Recalibration is used whenever the model misbehaves. To recalibrate internal model parameters, the process model is run again for the antecedent time steps, which led to the present state, with the values of a set of internal model parameters being optimised until the model reproduces the measured parameter value. This procedure produces a new set of values for the model initialisation parameters, which are then used for the determination of the further development of the system. This procedure is illustrated in *Fig. 2* for the case of surface soil moisture.

The challenge of this option is the selection of internal parameters to be optimised. For this purpose, sensitivity studies are required. In this example soil hydraulic properties can be adjusted until simulation and observations correspond.

For model inversion the procedure described above is inverted. For this purpose the original process model is extended to be able to also simulate remote sensing observations (e.g. at sensor radiances, backscatter values) from parameter values calculated by the model.

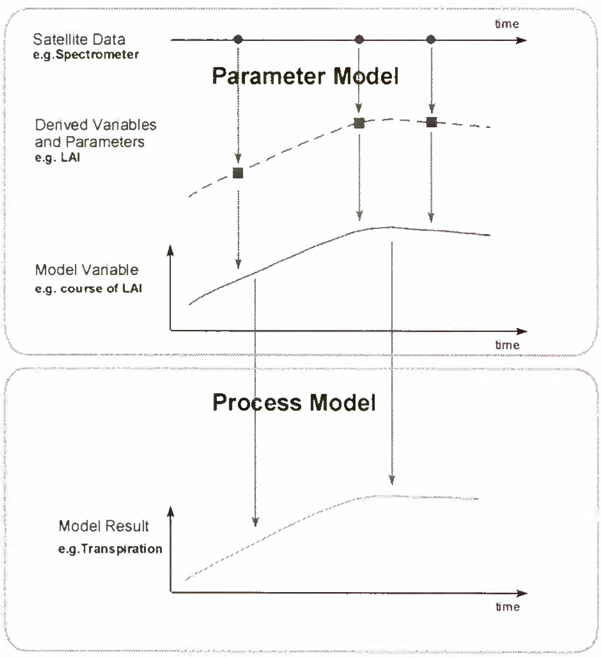

Figure 1: Forcing of model behaviour through externally providing measured LAI values

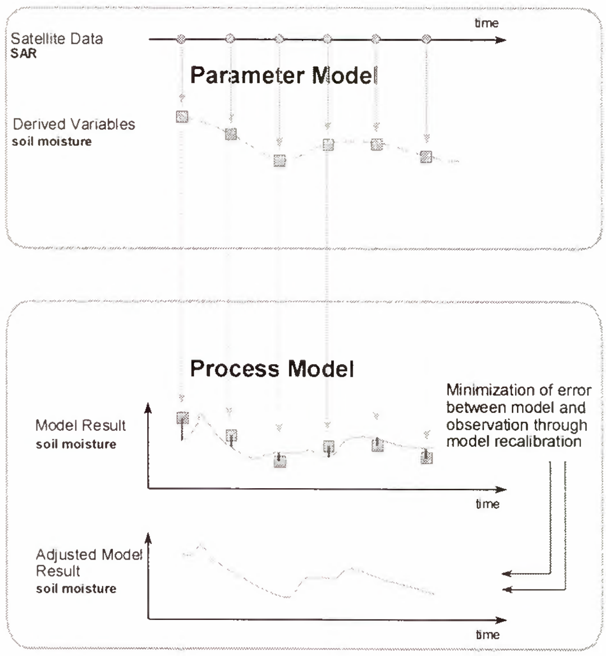

Figure 2: Recalibration through estimation of an optimal set of parameters to represent remote sensing measurements

Instead of forcing a model into a certain direction through measurements the model is fed with a virtual set of parameter values. The outputs of the process model (e.g. LAI , biomass or plant height) then in turn can be converted into simulated radiances or backscatter intensities. These values are then compared with the radiances or backscatters values measured with remote sensing instruments. The model parameters are varied systematically until model results and remote sensing measurements coincide. One then concludes, that the chosen virtual parameter set of the inverse model correctly represents the natural situation.

While this procedure can universally be applied, the conclusion is only true when a unique solution exists for the inversion problem. This is hard to prove and hardly the case for complex models and arbitrarily chosen sets of parameters. One approach, which relaxes the problem is to only change one parameter when inverting. This can be done to derive e.g. static soil hydraulic properties from a comparison of time series of microwave measurements and the results of an inversion of a soil hydraulic model combined with an inverse radar backscatter model.

Option 4: Direct comparison of model results and remote sensing measurements.

Some land surface model parameters can be directly compared with remote sensing measurements. This is possible whenever the physical model parameter is related to a radiation flux or a surface property directly resulting from radiative transfer. Examples are surface temperature, albedo, surface soil moisture, snow covered area, inundated area, etc. Remote sensing measurements of these properties can be used for spatial verification / validation as long as the measured values (not the parameters themselves) are not used within the model.

Examples for these 4 options of data assimilation will follow.

STATIC MODEL INPUT PARAMETERS FROM REMOTE SENSING

The flood model IFFS serves as example for the first two options. IFFS is a hydrological model used for the translation of rainfall into runoff. The most important results of IFFS are the peak discharge of a flood, which is responsible for the extent of flooding and the discharge volume, which is necessary to manage reservoirs for flood retention purposes. IFFS consists of two parts (Bach et al., 2000 b). The first part of the system describes the watershed properties and is assumed to be temporally static (see *Fig. 3*).

An interferometrically derived elevation model is used as prime remote sensed data source for IFFS to determine topographic information on the watershed. The phase information of a tandem pair of ERS SAR data served as basis. The relative vertical accuracy of the DEM of 10 m is sufficient for the extraction of flow patterns in hilly and mountainous regions to generate the hydrological structure of the runoff model. Additionally, optical satellite data are classified to deliver the land cover distribution. Together with a soil map, the watershed is then classified into hydrologic relevant classes of water storage capacity, which is expressed in dimensionless CN-values. In addition to remote sensing data, only information on the reservoirs (storage volume, discharge curve) is required for this static set-up of the hydrological model.

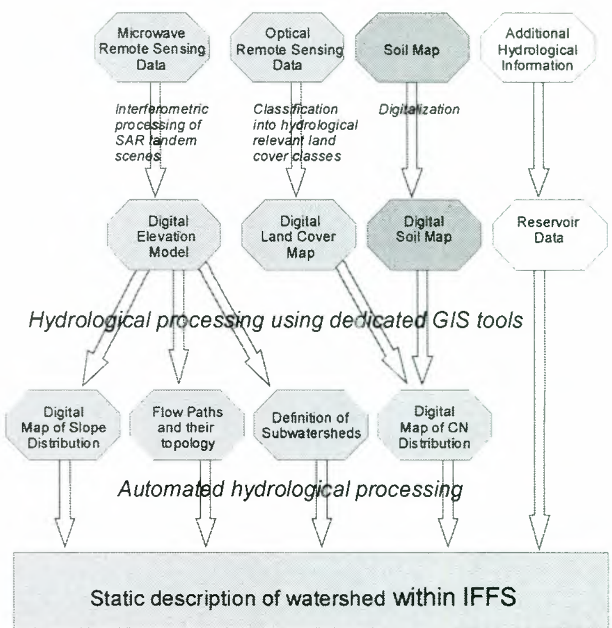

Figure 3: Static model input parameters from remote sensing as used in the flood model IFFS

UPDATING OF DYNAMIC MODEL PARAMETERS

The second part of IFFS consists of the modelling of the reaction of discharge on a rainfall input (see *Fig. 4*). For this dynamic part of the system, rainfall information is required as the driving variable. Different options are possible to generate this information. Meteorological station data can be interpolated, but also remote sensing data can be used (METEOSAT, weather radar). Numerical Weather Prediction (NWP) models further allow to forecast the rainfall.

Within the dynamic part of IFFS (*Fig. 4*), also soil moisture information is of crucial relevance for runoff modelling because it determines the extent of saturation of the watershed and thereby the partitioning of rainfall into surface runoff and infiltration. The same amount of rainfall, which normally does not lead to a significant increase in water level, can cause a severe flood, if the soil has already been filled with water and the storage capacity is close to zero. Because information on the actual soil moisture distribution is normally missing, it is estimated in hydrological models by utilising an antecedent precipitation index, that is derived from rainfall measurements of the preceding days, or a moisture index, that is derived from actual discharge values. However, this parameter can not reflect adequately the full temporal and spatial variability of soil moisture. Large errors in flood and inundated area forecast may occur as a result. Therefore SAR data are used to derive soil moisture distributions, which have the potential to improve the antecedent moisture characterisation of the watershed. With this information, the actual water storage capacity of the soil is determined as input into the rainfall-runoff model (see *Fig. 5*).

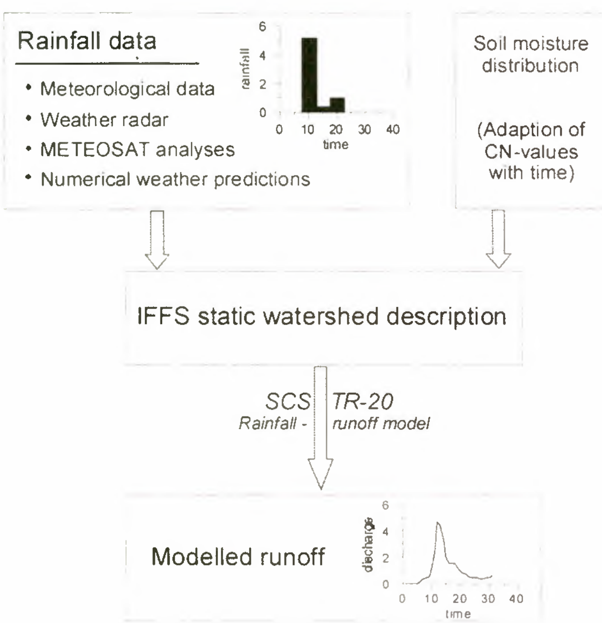

Figure 4: Updating of dynamic model parameters in IFFS through the provision of soil moisture maps

The inversion procedure to derive soil moisture from ERS-SAR images will be described below. It is restricted to non-forested areas, since C-band microwaves can not penetrate forest. For the hydrological application gaps of information are however not allowed. Therefore the soil moisture derived on the forest-free parts of the subwatersheds is assigned to the whole subwatersheds in an appropriate way as illustrated in *Fig. 5*.

See colour plate

Figure 5: Provision of ERS derived soil moisture distribution for the flood model IFFS

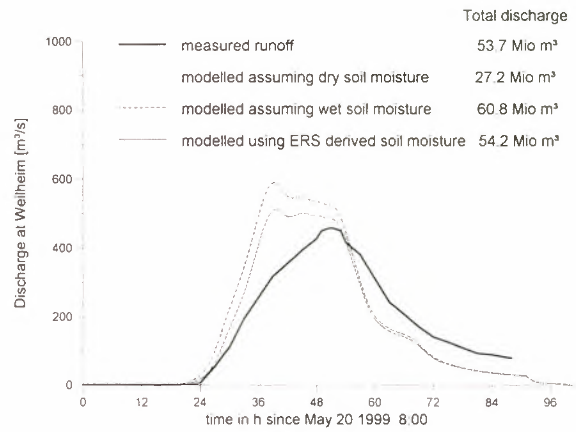

Figure 6: Sensitivity of modelled runoff for 2 extreme soil moisture situations (wet, dry) and comparison of model result using ERS-derived soil moisture to update model performance

Fig. 6 shows results of flood calculations for a 200 years flood in the 800 km² Ammer catchment in the Bavarian part of the Alps, which caused exceptional damage. In the graph the measured discharge is compared with modelled discharge produced with different soil moisture information. The dotted curve shows the model result under the assumption of a dry watershed, which means several dry days before the rainfall. As can be seen, the simulated discharge values are much too small and not even enough to produce a flood alert. The total amount of discharge produced under this assumption is only about half of the observed discharged water volume (27 vs. 53 Mio m³). The broken curve shows the result of the model calculation using a wet watershed, which means rainfall directly before the flood. In this case the model overestimates the peak discharge as well as discharge volume. When using soil-moisture information derived from ERS-data taken the day before the flood the solid grey line shows the closest correspondence between measured and modelled peak discharge and discharge volume. This clearly demonstrates the potential for improved flood simulation, which lies in the use of remote sensing derived model parameters in integrated modelling environments like IFFS.

INVERSION OF SOIL MOISTURE FROM ERS-SAR MEASUREMENTS

The moisture content of the top soil-layer, which was used in IFFS, was retrieved from ERS SAR data by using a semi-empirical approach. Its principles are shown in *Fig. 7*. A first prerequisite is to physically correct the influence of *topography* on backscatter and resolution of the SAR-image and thereby to convert backscatter into σ^0-values of flat terrain (Riegler & Mauser, 1998). The approach then empirically corrects influences on σ^0-values from *vegetation type* and *bio-*

mass to convert σ^0 values into dielectric constant of soil-water mixture of an equivalent bare field with an RMS-roughness of 2.4 cm acc. to Ulaby (1994) (Rombach & Mauser, 1997). Finally the dielectric constant is converted into soil-moisture using *soil physical properties*.

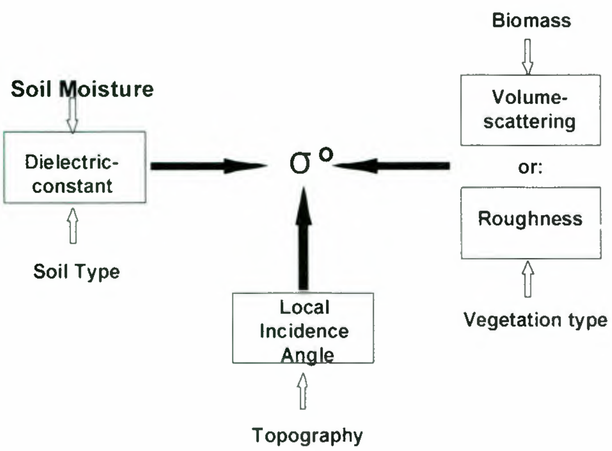

Figure 7: Soil moisture retrieval from ERS data using the IGGF approach

The necessary information on land cover can be gathered through the classification of optical remote sensing data, the soil physical properties come from a soil map. This model works well for annual vegetation if all the ancillary data is available with the appropriate accuracy. Although it is a semi-empirical model based on measurements in Southern Germany it could be successfully applied in the Flevoland test-site without further adaptations (*see Fig. 8*). The comparison of field-measured and modelled soil moisture values for different land covers in Flevoland is shown in *Fig. 8*.

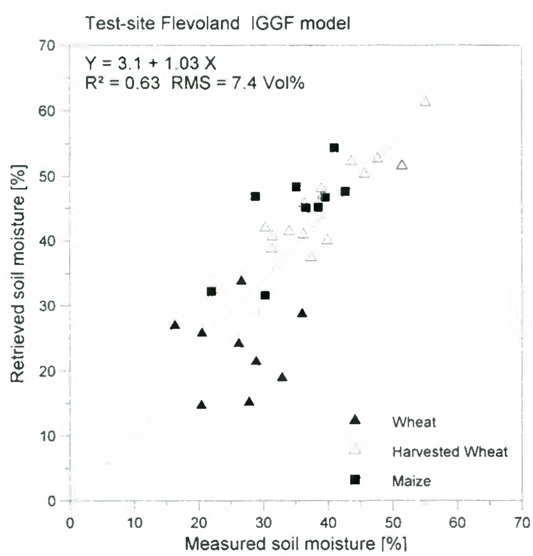

Figure 8: Comparison of the measured and ERS-derived soil moisture for a dutch test–site Flevoland (Mauser, 2000)

PARAMETER DETERMINATION THROUGH MODEL INVERSION

Model inversion is a common technique to derive a desired physical quantity. Whenever the model result is already known (e.g. through measurements) one can work his/her way backwards through the model to arrive at the unknown physical quantity of interest, which produces the measured result. This approach is valid if the model produces unique solutions.

Radiative transfer models (like GeoSAIL (Bach et al. 2000a)) can be inverted to determine surface parameters from remotely sensed surface reflectances. An extended methodology of model inversion consists in combining GeoSAIL and the growth model PROMET-V (Schneider & Mauser 2000, Mauser & Schädlich 1998). Its purpose is to optimise the performance of a vegetation growth model and is illustrated in *Fig. 9*.

The approach is based on two feedback-loops, which are established to ensure that a stable, most probable and spatially variable output of the growth model (namely biomass, yield, plant height) is assured through the use of remote sensing data. *Fig .9* contains two branches, a remote sensing based retrieval of plant parameters through radiative transfer modelling to the left and a land surface process model based retrieval of plant parameters from meteo-data and geo-biophysical maps to the right. As an example the case of leaf area index (LAI) is demonstrated in *Fig. 9*.

Optical remote sensing data are first atmospherically corrected using the atmosphere correction procedure PULREF (Bach & Mauser, 1994). The observed reflectance spectra are then compared with modelled spectra calculated with the optical RS model GeoSAIL (Bach et al. 2000 a, Verhoef, 1984). Total leaf area, fraction of brown leaves and surface soil moisture are retrieved using an inversion loop. The golden section method is applied to minimise the spectral matching error between remotely sensed and modelled spectra.

The standard concept of model inversion is extended by using the growth model as additional information source (first feedback to GeoBIRD-INV1) to determine the valid range of the surface parameter from the land surface process model. The valid range produced by the growth model takes into account influences like the course of the weather during the considered year of observation, the quality of the soil and management practices. The free model parameter is adjusted within the given range of validity until a best match between remotely sensed and modelled reflectance spectra is reached.

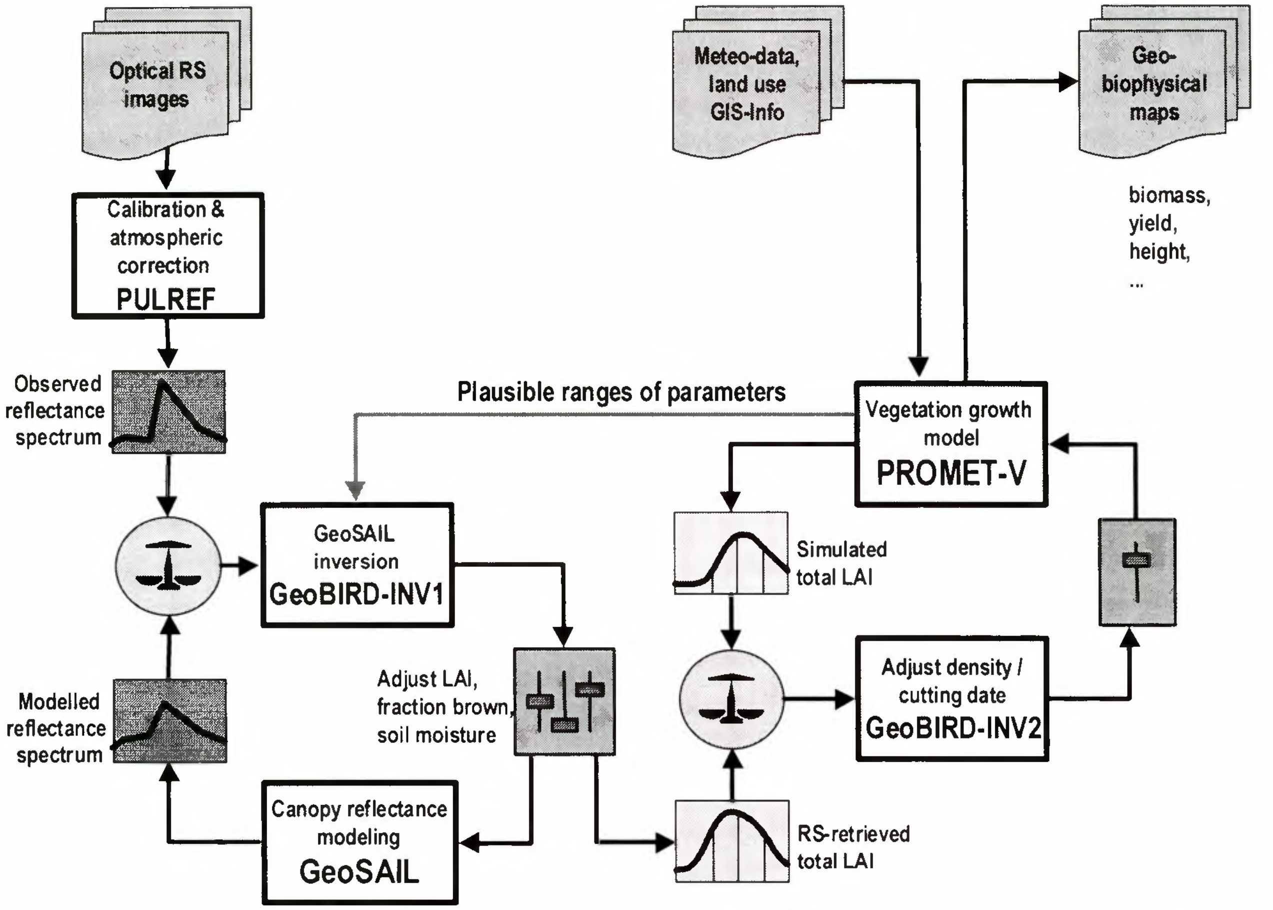

Figure 9: Methodology for the combination of a growth model (PROMET-V, right) and an optical remote sensing model (GeoSAIL, left) for enhanced retrieval of bio-geophysical land surface parameters. In the left feedback loop land surface parameters (LAI, fraction of brown leaves and surface soil moisture) are derived from optical remote sensing data. In the right feedback loop the growth model is adjusted to allow the improved simulation of biomass, canopy height and yield.

A second feedback loop is applied to recalibrate and re-initialise the land surface process model PROMET-V based on the outputs from the remote sensing model. GeoBIRD-INV2 uses the LAI obtained from the GeoSAIL inversion as input. Internal model parameters of PROMET-V are now adjusted until the modelled LAI of the growth model and the LAI retrieved from RS observation fit best. From sensitivity analyses, it was found that plant density is the most sensitive land surface parameter for crops. In case of meadows, the days of cutting proved to be the most crucial and at the same time the least known parameter. Both parameters are also spatially highly variable. To take care of the high degree of spatial variability in the natural processes, PROMET-V is re-initialised on a pixel-by-pixel basis using those values of plant density or cutting date which provide a modelled LAI that best matches the LAI derived from the remote sensing observations. This feedback between optical observation and growth model considerably improves both the representation of the natural spatial variability and the overall accuracy of the results of bio-physical maps produced by the growth model PROMET-V, as can be seen in *Fig. 10*.

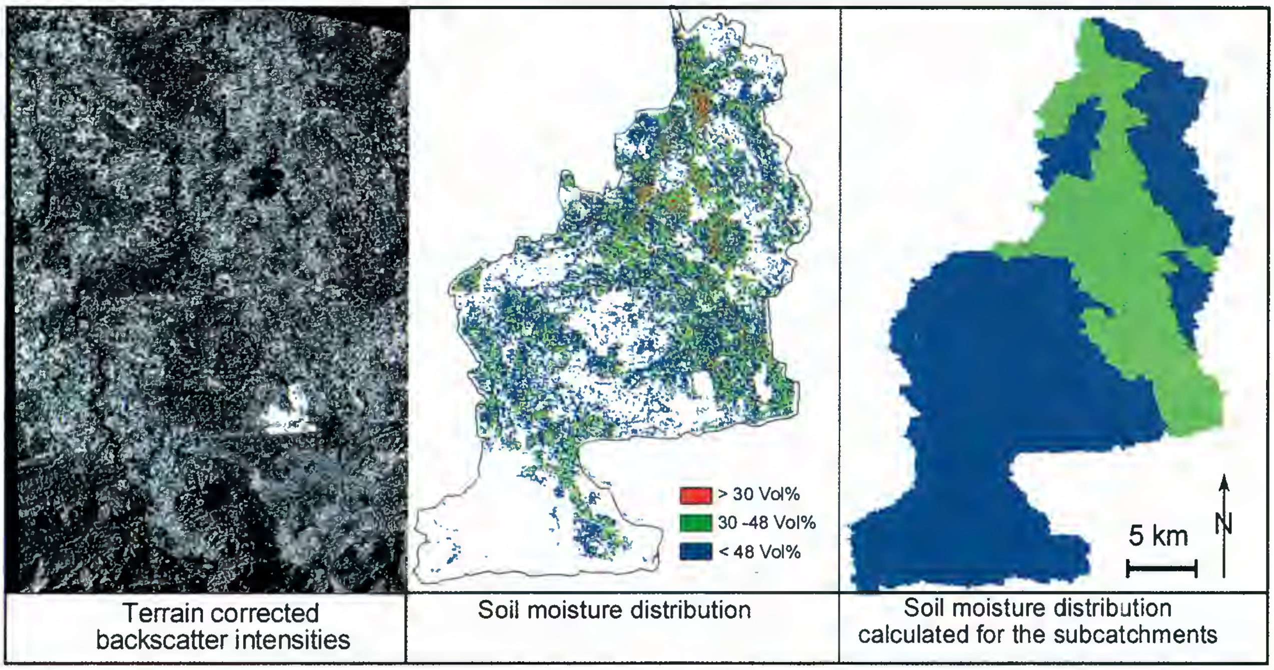

Figure 5: Provision of ERS derived soil moisture distribution as dynamic input to the flood model IFFS

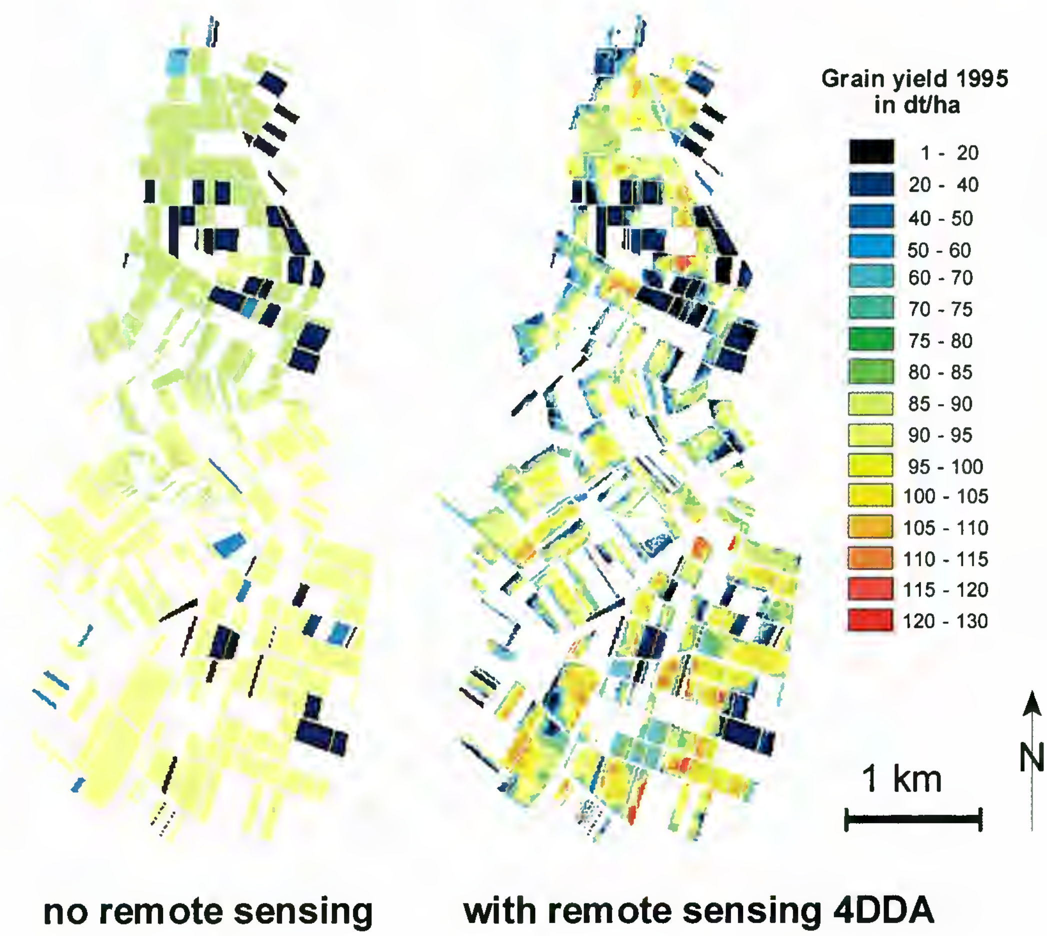

Figure 10: Comparison of model results on plant production using standard GIS map layers as input (left side) and applying the 4DDA technique as described in Fig. 9 (right side). The spatial heterogeneity is much better represented using the remote sensing data as input. Compared to yield measurements the RMS-error of yield retrieval amounts only 8.8 dt/ha (8 %) using 4DDA (1 dt = 0.1 t).

2.4 DIRECT COMPARISON OF MODEL RESULTS AND REMOTE SENSING MEASUREMENTS

Remotely sensed land surface parameters can also be used to validate the results of regional, spatially distributed land surface models and thereby check the spatial performance of models. This strategy of using remote sensing data can be applied to a large range of modelled variables. It covers the comparison of modelled and measured patterns of emitted long wave radiation from the land surface (Mauser and Schädlich, 1998), which checks the performance of land surface energy balance models, the comparisons of modelled and measured spatial patterns of backscatter values, which may check the spatial performance of plant architectural models and the comparison of the modelled and measured spatial extents of snow cover, which allows to check the spatial performance of snow accumulation and snowmelt models.

An example of such a comparison is given in *Fig. 11*. In the left image the snow cover pattern of the State of Baden-Württemberg has been derived from a NOAA/AVHRR image. The centre image shows the results of the spatial snow cover model SNOW-D, which is run by the German Weather Service (DWD). The right image shows the spatial comparison of the snow covered areas derived by the two methods. The different grey levels show areas, where snow cover is indicated by the NOAA/AVHRR without modelled snow cover, where observations and model coincide and areas, where no snow is indicated by the AVHRR-image and where the model shows snow cover. On average the model calculations result in a snow cover, which is 12% larger than the snow cover, which is derived from satellite data. A closer analysis of the patterns shows that snow cover only partly coincides with elevation and that additional factors like land use and rainfall patterns have to be taken into account to improve the spatial performance of the model.

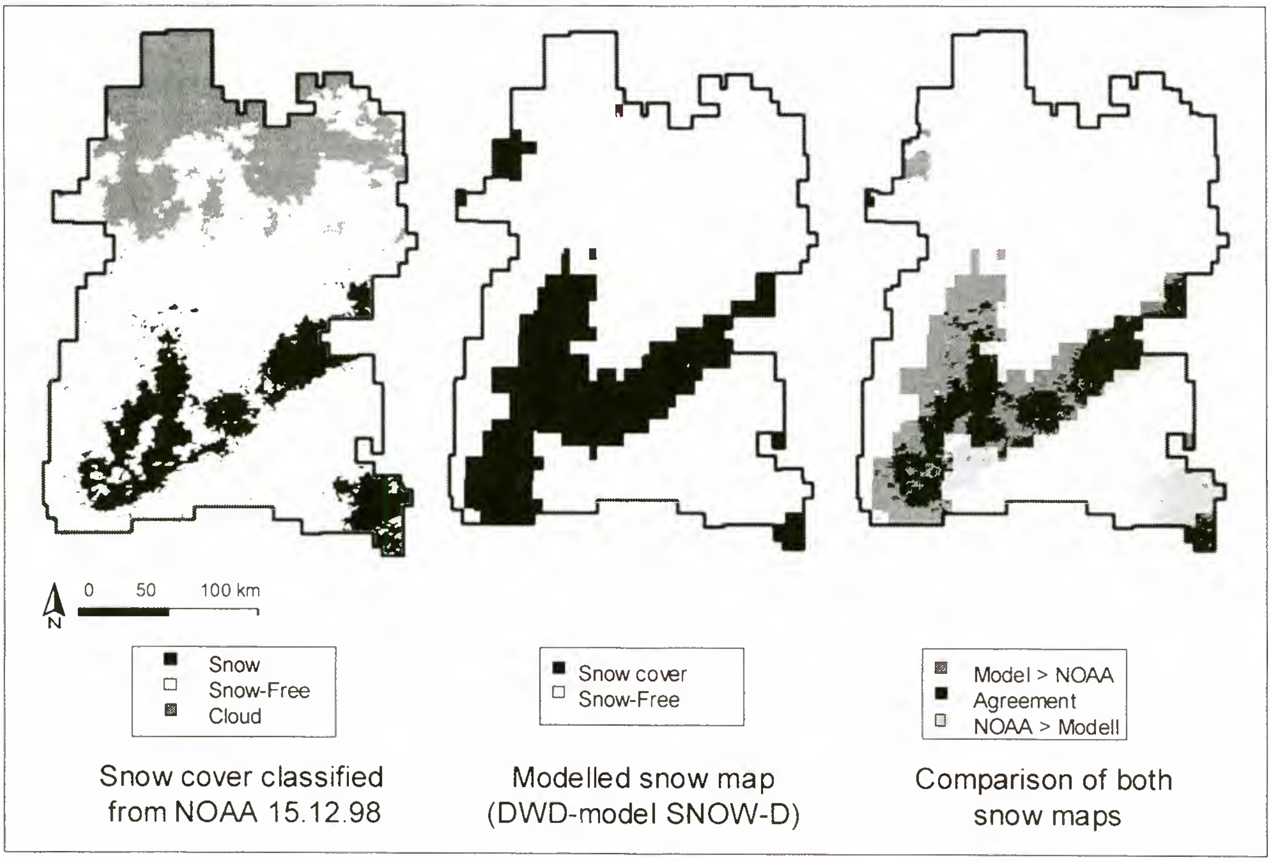

Figure 11: Verification of snow cover results of the SNOW-D model of the German Wheather Service and snow cover classifications with NOAA-AVHRR

CONCLUSIONS

The preceding examples showed, that several procedures have already been established to assimilate remote sensing data into complex regional land surface process models. In each case the potential of improvement of model performance towards a more realistic and accurate description of land surface heterogeneity was demonstrated. The proper treatment of spatial heterogeneity of the land surface is the key for the extended application of land surface process models in planning and decision making.

Measurements of the spatial heterogeneity of the land surface is the domain of remote sensing. 4DDA of remote sensing data into land surface process models will therefore strongly improve land surface process modelling and should become a central future research task in remote sensing.

Information from the land surface process model can further be used to improve the understanding and interpretation of remote sensing measurements. Land surface models can constrain the retrieval of land surface properties from remote sensing measurements to meaningful values.

To fully exploit the potential of remote sensing the whole range of available sensors has to be activated and the complete information content, which accumulates over consecutive observations, has to be extracted and utilized within integrated model/observation environments. Data assimilation techniques using optical remote sensing data currently are more sophisticated than SAR based methods. The maturity of the techniques should be balanced through research into combined applications and modified model structures, which can handle both data sources.

The weather independency of SAR-systems makes them a prime candidate for dynamic land surface process models. This is also where the demand for remote sensing data is largest. Ironically, no sensor with high temporal availability (1-3 days) is yet available to exploit this advantage of SAR. It would strongly enhance the acceptance of microwave remote sensing data among the land surface modelling community.

ACKNOWLEDGEMENTS

The results presented here were funded in the ESA Contract GeoBIRD Ref.: 12950/98/NL/GD and in the project InFerno funded by DLR (Kz: 50EE0053). Thanks to Florian Appel for his efforts in image processing. ERS-SAR data were kindly provided by ESA in its PI-programme.

REFERENCES

Bach, H., Schneider, K., Verhoef, W., Stolz, Mauser, W., R., Van Leeuwen, H., Schouten, L., Borgeaud, M., 2001, "Retrieval of geo- and biophysical information from remote sensing through advanced combination of a land surface process model with inversion techniques in the optical and microwave spectral range", Proc. of the 8th Intern. Symp. "*Physical measurements and signature in remote sensing*", Aussois, CNES, pp. 639-647

Bach, H., Verhoef, W., Schneider, K., 2000 a, "Coupling remote sensing observation models and a growth model for improved retrieval of (geo)biophysical information from optical remote sensing data", *Remote Sensing for Agriculture, Ecosystems and Hydrology*, SPIE Vol. 4171, pp. 1-11

Bach, H., Lampart, G., Ludwig, R., Mauser, W., Strasser, G., Taschner, S., 2000 b, Application of SAR-data for flood modelling in Southern Germany, Proc. of ERS-ENVISAT-Symposium Gothenburg 2000, *Looking down to Earth in the New Millennium*, ESA SP-461, p.123

Bach, H., Mauser, W. (1994): Atmospheric correction of hyperspectral data in terms of the determination of plant parameters, *Recent Advances in Remote Sensing and Hyperspectral Remote Sensing*, EUROPTO Series, SPIE 2318, pp.52-62.

Mauser W., 2000, "Comparison of ERS SAR data derived soil moisture distributions with SVAT model results", Proceedings of ERS-ENVISAT-Symposium Gothenburg 2000, *Looking down to Earth in the New Millennium*, ESA SP-461

Mauser, W., Schädlich S., 1998, "Modelling the Spatial Distribution of Evapotranspiration On Different Scales Using Remote Sensing Data", *Journal of Hydrology*, 212-213, pp. 250-267

Riegler G., Mauser W. (1998): Geometric and radiometric terrain correction of ERS SAR data for applications in hydrologic modelling, *Proc. IGARSS'98*, Seattle, pp. 2603-2605

Rombach, M., Mauser, W., 1997, "Multi-annual analysis of ERS surface soil moisture measurements of different land uses", Proc. 3.ERS Symposium, "*Space at the service of the environment*", ESA SP-414

Schneider K. and Mauser W., 2000, "Using Remote Sensing Data to Model Water, Carbon and Nitrogen Fluxes with PROMET-V", *Remote Sensing for Agriculture, Ecosystems and Hydrology*, SPIE Vol. 4171, pp.12-23

Verhoef, W., 1984, "Light scattering by leaf layers with application to canopy reflectance modeling: the SAIL model", *Remote Sens. Environ.*, Vol. 16, pp. 125-141

WHAT CAN RADAR REMOTE SENSING DO FOR IMPROVING OUR KNOWLEDGE OF THE GLOBAL CARBON CYCLE?

Wolfgang Wagner

Institute of Photogrammetry and Remote Sensing
Vienna University of Technology
Gusshausstrasse 27-29,
1040 Vienna, Austria
Tel: +43-1-58801-12225, Fax: +43-1-58801-12299
E-mail: ww@ipf.tuwien.ac.at, http://www.ipf.tuwien.ac.at/

ABSTRACT

Stirred by raising concerns about potentially harmful impacts of global change and by the long political struggle around the Kyoto-Protocol, scientists have started to explore the mechanisms of the global carbon cycle in more depth. Often the magnitude of carbon fluxes and carbon pools is not sufficiently well known due to the lack of environmental data. Therefore new methods to collect relevant biogeophysical parameters are urgently needed. Such data will be useful for monitoring land-use, land-use change and forestry (LULUCF) activities specified in the Kyoto-Protocol and for improving our understanding of the global carbon cycle and its feedback mechanisms with changing climate patterns in general. This article discusses relevant aspects of the Kyoto-Protocol and monitoring requirements. For clarity, it is suggested to distinguish two sets of requirements: 1) requirements arising from the "Kyoto" reporting guidelines, and 2) requirements arising from the scientific need to better quantify the global carbon balance. These provide the framework for discussing the potential use of radar remote sensing. This article further elaborates the arguments first presented in Wagner (2001).

INTRODUCTION

Since the dawn of the Industrial Era major chances have occurred in the global carbon cycle. Mostly due to fossil fuel combustion and the clear-cutting of forests the atmospheric carbon dioxide (CO_2) concentration has risen by about 28 %, affecting the Earth's radiation budget. Among the long-lived and globally mixed greenhouse gases CO_2 contributes most (60 %) to the warming-up of the lower atmosphere and surface (IPCC, 2001). To prevent an further uncontrolled increase of CO_2 and the other greenhouse gases (CH_4, N_2O, halocarbons) the international community adopted in December 1997 at the third Conference of the Parties (COP3) in Kyoto the so-called Kyoto-Protocol, which contains for the first time legally-binding commitments to limit or reduce greenhouse gas emissions. Ensuing political arguments could – after the withdrawal of the United States – be resolved in July 2001 at the sixth session of the Conference of the Parties (COP6) in Bonn. It is to be expected that 55 states will ratify the Kyoto-Protocol until 2002 which will then enter into force.

BIOLOGICAL SINKS AND SOURCES

Besides reductions in fossil-fuel emissions the Kyoto-Protocol allows that "biological sinks" are included in the calculations of the amounts of emissions assigned to each country in the commitment period 2008-2012. A "sink" is defined as a process, activity or mechanism which removes a greenhouse gas from the atmosphere. An ecosystem represents a sink for CO_2 if its assimilation of carbon through photosynthesis exceeds its loss through respiration and extraction (harvest) (WBGU, 1998). Correspondingly, a "source" is a process, activity or mechanism that releases CO_2 to the atmosphere. Article 3 Paragraph 3 of the Kyoto-Protocol limits the biological sources and sinks to "afforestation, reforestation, and deforestation (ARD)" defined on the basis of a change in land use as decided at COP6. Article 3 Paragraph 4 of the Kyoto-Protocol further provides for the possibility of using additional "land-use change and forestry" activities such as "forest management", "cropland management", "grazing land management" and "revegetation" (COP6) to meet reduction commitments. Together these activities are denoted as "land-use, land-use change and forestry" (LULUCF) activities.

The inclusion of LULUCF activities has been a controversial issue in the debate around the Kyoto-Protocol. One criticism has been that LULUCF activities are but a distraction from the real task of reducing fossil fuel use. In fact, in the short term the saving potential of LULUCF activities is larger than the proposed emission reductions while in the long term it must be considered that the carbon storage capacity of the biosphere has a natural limit. The biosphere can thus be regarded as being only a temporary buffer of industrial emissions. In light of these concerns it was agreed at COP6 to limit the total of additions and subtractions resulting from LULUCF activities in the commitment period 2008-2012 to a maximum of 1 % of the base year (1990) emissions of a country, times five.

Proc. 3rd International Symposium, 'Retrieval of Bio- and Geophysical Parameters from SAR Data for Land Applications', Sheffield, UK, 11-14 September 2001 (ESA SP-475, January 2002)

Another reason for concern has been the lack of objective, comparable and cost-efficient methods for monitoring LULUCF activities. A complete inventory of all agricultural and forested land is exceedingly expansive. But, as many scientists have pointed out, only a complete account of all sinks and sources applied over long time and large space scales (full carbon accounting) is the appropriate basis for any accounting system for terrestrial carbon (Steffen et al., 1998). The more pragmatic position taken on by IPCC is to use a partial carbon accounting approach to the discontinuous commitment periods. It was agreed at COP6 "That the treatment of these [LULUCF] activities be based on sound science" and that "Consistent methodologies be used over time for the estimation and reporting of these activities".

MONITORING REQUIREMENTS

When discussing monitoring requirements arising from LULUCF activities it is suggested to distinguish two areas:

1. Requirements arising from agreed reporting instructions based on the "Revised 1996 IPCC Guidelines for National Greenhouse Gas Inventories" (which were approved at COP3 in Kyoto) and complementary documents (*"Reporting Requirements"*);

2. Requirements arising from the need to better understand and quantify the full carbon balance over large areas and long time periods to meet the guiding principles of "sound science" and "consistent methodologies" (*"Scientific Requirements"*).

REPORTING REQUIREMENTS

To demonstrate the compliance with the Kyoto-Protocol each country must report sinks and sources during the commitment period 2008-2012 based on the Revised 1996 IPCC Guidelines and supplementary documentation. As the Kyoto-Protocol considers only anthropogenic activities, only human-induced sinks and sources are relevant. For transparency and reconstruction worksheets are used to cover the various LULUCF activities. As one example, Table-1 shows the necessary input parameters and steps to complete Worksheet 5-1 which is used to report "Changes in Forest and Other Woody Biomass Stocks" for different forest ecosystems and tree species.

Variable	Name	Unit	Input or Formula
A	Area of forest/biomass stocks	kha	Input
B	Annual growth rate	kt dm/ha	Input
C	Annual biomass increment	kt dm	C=A×B
D	Carbon fraction of dry matter		Input
E	Total carbon uptake increment	kt C	E=C×D
F	Commercial harvest (if applicable)	1000 m^3 roundwood	Input
G	Biomass conversion/expansion rate (if applicable)	t dm/m^3	Input
H	Total biomass removed in commercial harvest	kt dm	H=F×G
I	Total traditional fuelwood consumed	kt dm	FAO data
J	Total other wood used	kt dm	Input
K	Total biomass consumption	kt dm	K=H+I+J
L	Wood removed from forest clearing	kt dm	from Worksheet 5-2
M	Total biomass consumption from stocks	kt dm	M=K-L
N	Carbon fraction		Input
O	Annual carbon release	kt C	O=M×N
P	Net annual carbon uptake (+) or release (-)	kt C	P=E-O
Q	Conversion to CO_2 annual emission (-) or removal (+)	Gg CO_2	Q=P×44/12

Table 1: Steps for filling in Worksheet 5-1, Module "Land use change and forestry", Submodule "Change in forest and other woody biomass stocks" according to the Revised 1996 IPCC Guidelines (IPCC, 1996).

SCIENTIFIC REQUIREMENTS

The terrestrial carbon cycle is closely coupled with the global energy and water cycles and progress in modelling carbon fluxes has advanced in accordance with improvements of global climate models.

While significant progress has already been made in modelling the land surface and land-atmosphere fluxes, problems remain to be solved in the areas of moisture processes, runoff prediction, land-use change, the treatment of snow, sub-grid scale heterogeneity, and freeze/thawing processes at high latitudes (IPCC, 2001; Cramer et al., 1999; Kicklighter et al., 1999). In general, it can be said that the lack of homogeneous, thoroughly validated global datasets derived from in-situ and remotely sensed observations continues to hamper efforts to verify and improve models.

Recognising the policy imperative for a global carbon observing system the key observation requirements have been reviewed by various working groups and panels. The Terrestrial Carbon Theme Team established by the Integrated Global Observing Strategy Partnership (IGOS-P) has identified the following key themes of a future operational network of satellite and ground observations: land cover and land use, biomass, seasonal growth cycle, fires and other disturbances, solar radiation, surface-atmosphere fluxes, methane related products, soil moisture, canopy biochemistry (IGOS-P, 2001). A more complete list of parameters useful for model-input or verification/validation can be found in Cihlar et al. (2000).

RADAR REMOTE SENSING

It is outside the scope of this paper to provide a comprehensive list of carbon-relevant biogeophysical products that can be retrieved from radar measurements of current or planned missions. Rather the potential use of radar remote sensing is discussed in more general terms in the light of the requirements laid out above.

FULFILLING REPORTING REQUIREMENTS

A major point to note is that the Kyoto-Protocol considers only human-induced sinks and sources. As LULUCF activities must be allowed to be carried out on land units of vastly different size, Synthetic Aperture Radars (SARs) with a resolution of a few meters are needed to map also small land units (< 1ha). Even if the spatial resolution of current and soon to be launched SAR sensors is only in the order of 10-30 m they are deemed useful to map initial areas of different land types. SAR systems which will be available in the commitment period 2008-2012 will have a spatial resolution in the order of one or a few meters and will therefore be better able to determine the extent and rate of changes as a result of LULUCF activities. The retrieval of additional parameters such as the annual growth rate or carbon fraction of dry matter (Table 1) is either not physically possible or appears too difficult. According to IPCC (2000) "The utility of data from satellites raises the question of whether such data will be used as a primary source of data by countries reporting sources and sinks of carbon or whether they will be used for verification."

Experiences made with the use of remote sensing for *agricultural monitoring* (area assessment and yield monitoring) and for *agricultural control* (combat fraud) in Europe point into the direction that it may be the better choice to use remote sensing only for verifying LULUCF activities. In this case remote sensing only has to answer the question "How likely is it that the reported LULUCF activities correspond to reality?" which is more easily done than providing accurate numbers when used as a primary tool for reporting. Also, it should be considered that the strengths of remote sensing – objectivity and consistency – make it an ideal technique for verification and control activities.

FULFILLING SCIENCE REQUIREMENTS

While the reporting requirements put rather stringent bounds on the use of radar remote sensing (high spatial resolution, only area mapping), the many open issues surrounding the science of the terrestrial carbon balance leave much room for innovative radar remote sensing products at a large range of time and space scales. Biomass, soil moisture, wetland dynamics, freeze/thawing, rice field mapping etc. are all of interest to the study of the terrestrial carbon balance. These parameters can either be used for verification and validation, or as driving variable if they are available at every carbon model grid point. If the parameter describes a dynamic process (e.g. soil moisture) it must also be available at regular time intervals. In the following section two radar products of relevance for full carbon accounting are presented as demonstration cases.

EXAMPLES

SOIL MOISTURE FROM SCATTEROMETER DATA

Plants loose water for carbon dioxide at an exchange rate as high as 400 molecules of water per CO_2 molecule fixed (Donovan and Sperry, 2000). The water stored in the soil within reach of the plants is therefore of central importance for determining gross primary productivity (GPP) and net primary productivity (NPP). In most global carbon models moisture availability is simulated on the basis of monthly long-term means of climatic variables, with large differences observed depending on the modelling strategy for the effect of water stress on NPP (Cramer et al., 1999). A comparison of model outputs of different NPP models gives useful insight, but substantial progress in better modelling the water balance and its effect on NPP can only be expected if *in-situ* or remotely sensed soil moisture data become available.

At microwave frequencies radiation emitted from (passive techniques) and reflected by (active techniques) the earth's surface are strongly dependent on the moisture content of the soil due to the pronounced increase of the soil dielectric constant with increasing water content. Both passive and active techniques must account for the confounding effects of vegetation and surface roughness on the measured signal. In fact, accounting for these effects has proven to be a major scientific challenge. Currently it is hold that using passive techniques the effect of soil moisture dominates over that of surface roughness, while the converse is true for radars (Jackson et al., 1999; Kerr et al., 2000). Therefore a passive microwave concept has been chosen for the Soil Moisture and Ocean Salinity Mission (SMOS) which will provide global soil moisture data at a resolution in the order from 30-50 km and with a high repetition rate of 3-5 days. SMOS has been selected as ESA's second Earth Explorer Opportunity Mission and is foreseen to be launched around 1995.

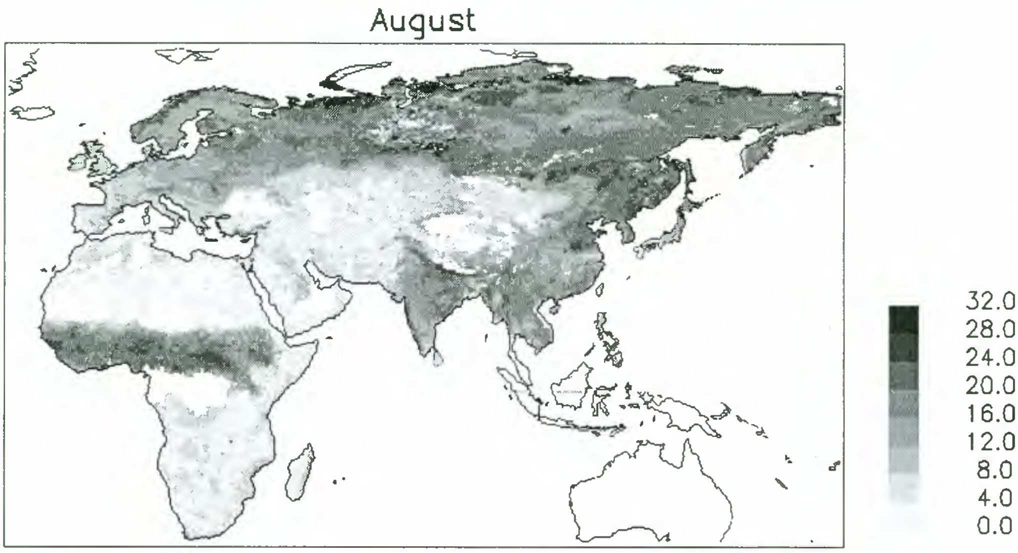

Figure 1: Average plant available water content in upper meter of the soil in millimetres for the month August for Africa, Europe and Asia estimated from a global hydrologic soil map and ERS Scatterometer data acquired in the years 1992-2000. White areas represent missing data either due to lack of data (Australia), strong azimuthal effects which are currently not considered in the algorithm (desert areas), closed forest cover (Central Africa) or snow surfaces (Himalayan).

Given the higher spatial resolution of SARs and the predominant role of radiometers in large scale soil moisture studies, spaceborne scatterometers like the one on ERS-1/2 have initially not appeared to be attractive sensors for soil moisture monitoring. Nevertheless, significant progress with both semi-empirical models and change-detection approaches has been made in recent years. An evaluation of operational land applications of scatterometers conducted on behalf of EUMETSAT concluded that the change detection approach developed by Wagner et al. (1999a/b) is the most mature method (Wismann and Woodhouse, 2001).

A validation of the accuracy of scatterometer derived soil moisture data with an extensive set of gravimetric in-situ measurements in the Ukraine and Russia showed that the water content in the first meter of the soil can be estimated with an accuracy of about 0.06 m^3m^{-3}. This allows to distinguish about five soil moisture levels. Due to the wide swath width of scatterometers soil moisture products can be provided at a global scale and regular time intervals (daily, weekly, decade). For a part of the land surface area no soil moisture information can be given, either because of dense forest cover, azimuthal effects over desert areas (sand dunes) or because open water surfaces cover a significant portion of the scatterometer pixel (wetlands, inundation, rice cultivating areas). Figure 1 shows a soil moisture map of Africa, Europe and Asia depicting the mean condition for August (based on the years 1992-2000). More examples can be found at the website of the Institute of Photogrammetry and Remote Sensing, Vienna University of Technology: http://www.ipf.tuwien.ac.at/ww/home.htm.

BURNT AREA MAPPING WITH SAR TANDEM DATA

Forest fires are amongst nature's primary carbon cycling mechanisms. Their net effect on the global carbon balance depends on the balance between disturbance and forest regeneration. An increased occurrence of fires in a forest ecosystem – e.g. caused by increased human ignitions or dryer soil conditions – may have the effect that the ecosystem becomes a carbon source, while in years with relatively few fires it acts as a carbon sink. Information on the spatial and temporal variability of forest fire activity is therefore of prime importance for a better understanding of the global carbon balance. But over remote areas such information is often not available. Conard and Ivanova (1997) point out that perhaps the largest source of error in estimates of carbon release through forest fires in Russia is inaccurate knowledge of burnt areas, but also fire type (crown or surface fires) is important. Optical sensors achieving daily coverage like the Advanced Very High Resolution Radiometer (AVHRR) have demonstrated their utility for operational fire monitoring and burnt area assessment (e.g. http://ckm.iszf.irk.ru/index_e.htm). Nevertheless, to obtain more accurate estimates of the area burnt and to be better able to determine fire type higher-resolution sensors should be used as a complementary data source.

One radar technique which has proven to be particularly useful for forest mapping is repeat-pass interferometry. Between 1995 and 1998 the two satellites ERS-1 and ERS-2 were operated in a tandem modus. Thereby it was possible to acquire SAR images from the same spot of the earth with a time difference of one day.

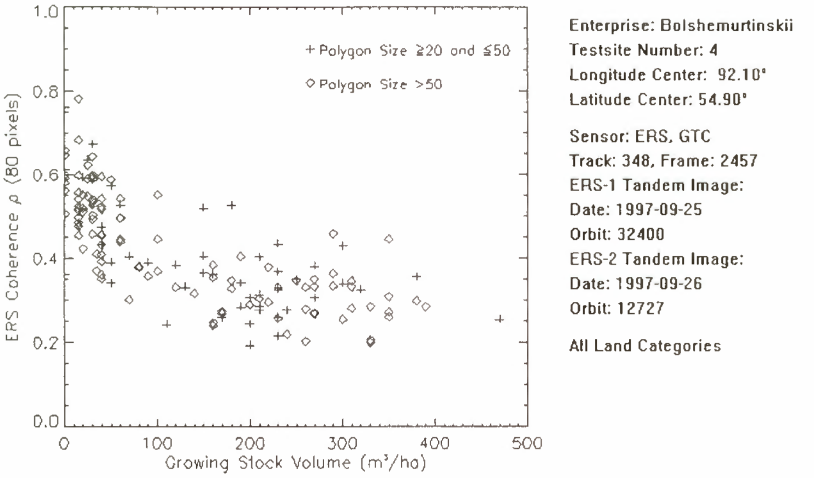

Figure 2: Tandem coherence versus growing stock volume for a testsite located in the Bolshemurtinskii enterprise. The data were collected and processed within the framework of the SIBERIA project (Schmullius et al., 2001).

The degree of correlation between the two SAR images is called the coherence. It is high if the relative geometry of the sensors and scatterers remains nearly unchanged between the acquisitions. But when the baseline and/or the target characteristics change due to rain or other environmental effects then the coherence is low. Over forested terrain, wind, that moves the scatterers (needles, branches) near the tree-tops from one acquisition to the next, causes a decorrelation of the signal.

The relationship between the coherence and forest parameters like stem volume or height varies significantly from image to image, but a monotonous decrease with increasing biomass is generally observed, particularly at low biomass levels (Fig. 2). At higher biomass the coherence approaches a limiting value. Therefore the tandem coherence is particularly suited to map burnt forest areas as they have a low standing biomass. In the SIBERIA project (Schmullius et al., 2001) a 1 million km^2 large forest maps was produced using ERS tandem coherence data and SAR images from the Japanese Earth Resources Satellite JERS-1. The classification separated three low biomass classes (0-20, 20-50 and 50-80 m^3/ha growing stock volume) from one large forest class containing all forests with a growing stock volume greater than 80 m^3/ha. The final forest map and much more technical details can be found at the SIBERIA website: http://pipeline.swan.ac.uk/siberia/.

CONCLUDING COMMENTS

"Kyoto" presents a real chance to demonstrate the usefulness of remote sensing for convention and environmental monitoring. But "overselling" has to be avoided by all means. In the past much has been promised and too often potential users have been disappointed. Therefore one should be very clear when discussing the potential use of remote sensing for "Kyoto". In this article it is suggested to distinguish reporting from scientific requirements. This allows to draw a clear line between the various remote sensing initiatives in this field. For meeting reporting requirements, high-resolution imagers are needed because it is not possible nor meaningful to restrict LULUCF activities to areas exceeding a certain size. Having in mind the experiences made in the agricultural sector it is further suggested that remote sensing should primarily be used for verification and control rather than as a primary data source.

On the other hand, a wide range of optical, thermal and microwave sensors will provide useful information to tackle some of the unsolved scientific questions surrounding the global carbon cycle. Two techniques from the radar world are presented as demonstration cases in this article: the use of scatterometers for retrieving soil moisture and SAR interferometry to map burnt areas. A scatterometer comparable in design to the ERS Scatterometer will be available in the future: The Advanced Scatterometer (ASCAT) on board of the METOP satellites. This instrument will make it possible to monitor soil moisture over a long time period at short time intervals. Thus it will contribute to better model the global carbon balance and to better interpret yearly fluctuations of the atmospheric CO_2 content. Unfortunately, the future of SAR interferometry is less secure. (Presently, the employment of a RADARSAT-2/3 tandem mission is discussed, but with a different orbit configuration than ERS-1/2.) Nevertheless, for scientific studies the data acquired during the ERS-1/2 tandem mission in 1995-1998 represent a valuable, global data source on forests. Even a simple forest/non-forest map could be of high value for the study of the carbon cycle, if available at a global scale.

ACRONYMS

ARD	Afforestation, Reforestation and Deforestation
ASCAT	Advanced Scatterometer
AVHRR	Advanced Very High Resolution Radiometer
COP	Conference of the Parties to UNFCCC
ERS	European Remote Sensing Satellite
ESA	European Space Agency
EUMETSAT	European Organisation for the Exploitation of Meteorological Satellites
FAO	Food and Agriculture Organisation of the United Nations
IGOS-P	Integrated Global Observing Strategy Partnership
IPCC	Intergovernmental Panel on Climate Change
JERS	Japanese Earth Resources Satellite
LULUCF	Land-Use, Land-Use Change and Forestry
METOP	Meteorological Operational polar satellites of EUMETSAT
RADARSAT	Radar Satellite (Canada)
SAR	Synthetic Aperture Radar
SIBERIA	SAR Imaging for Boreal Ecology and Radar Interferometry Applications
SMOS	Soil Moisture and Ocean Salinity Mission
UNFCCC	United Nations Framework Convention on Climate Change
WBGU	German Advisory Council on Global Change

REFERENCES

Cihlar,J., A. S. Denning, J. Gosz. (Eds.) (2000) Global Terrestrial Carbon Observation: Requirements, present status, and next steps, Report of a Synthesis Workshop, 8-11 February 2000, Ottawa, Canada, http://www.ccrs.nrcan.gc.ca/ccrs/eduref/biblioe.html.

Conard, S. G., G. A. Ivanova (1997) Wildfire in Russian boreal forest – Potential impacts of fire regime characteristics on emissions and global carbon balance estimates, Environmental Pollution, 98(3):305-313.

Cramer, W., D. W. Kicklighter, A. Bondeau, B. Moore III, G. Churkina, B. Nemry, A. Ruimy, A Schloss and the participants of the Potsdam NPP Model Intercomparison (1999) Comparing global models of terrestrial net primary productivity (NPP): overview and key results, Global Change Biology, 5(suppl. 1):1-15.

Donovan, L. A. and J. Sperry (2000) Scaling the soil-plant-atmosphere continuum: from physics to ecosystems, Trends in Plant Science, 5(12):510-512.

IGOS-P (2001) Carbon Cycle Observation Theme: Terrestrial and Atmospheric Components, GTOS-25, Revised version, February 2001, http://www.fao.org/GTOS/pubs.html.

IPCC (1996) Revised 1996 IPCC Guidelines for National Greenhouse Gas Inventories, http://www.ipcc.ch/pub/guide.htm.

IPCC (2000) Land Use, Land-Use Change, and Forestry, Cambridge University Press, Cambridge, United Kingdom, also at http://www.ipcc.ch.

IPCC (2001) IPCC Third Assessment Report - Climate Change 2001: The Scientific Basis, http://www.ipcc.ch.

Jackson, T., R. Bras, A. England, E. T. Engman, D. Entekhabi et al. (1999) Soil Moisture Research Mission, NASA Post-2002 Land Surface Hydrology Mission, http://lshp.gsfc.nasa. gov/Post2002/smm3.html.

Kerr, Y. H., J. Font, P. Waldteufel and M. Berger (2000) The Soil Moisture and Ocean Salinity Mission – SMOS, Earth Observation Quarterly, 66:18-26.

Kicklighter, D. W., A. Bondeau, A. L. Schloss, J. Kaduk, A. D. McGuire and the participants of the Potsdam NPP Model Intercomparison (1999) Comparing global models of terrestrial net primary productivity (NPP): global pattern and differentiation by major biomes, Global Change Biology, 5(suppl. 1):16-24.

Schmullius, C. and the SIBERIA Team (2001) SAR Imaging for Boreal Ecology and Radar Interferometry Appications (SIBERIA), Centre of Earth Observation, 4th Framework Programme of the European Community, Final Report Co. No. ENV4-CT97-0743-SIBERIA.

Steffen, W. and the members of the IGBP Terrestrial Carbon Working Group (1998) The Terrestrial Carbon Cycle: Implications for the Kyoto-Protocol, Science, 280: 1393-1394.

Wagner, W. (2001) Beiträge der Radarfernerkundung zur Erfassung des globalen CO_2-Kreislaufs, Österreichische Zeitschrift für Vermessung & Geoinformation, 2/2001, pp. 64-71.

Wagner, W., G. Lemoine, H. Rott (1999a) A Method for Estimating Soil Moisture from ERS Scatterometer and Soil Data, Remote Sens. Environ., 70:191-207.

Wagner, W., G. Lemoine, M. Borgeaud, H. Rott (1999b) A Study of Vegetation Cover Effects on ERS Scatterometer Data, IEEE Trans. Geosci. Remote Sensing, 37(2):938-948.

WBGU (1998) The Accounting of Biological Sinks and Sources under the Kyoto-Protocol – A Step Forwards or Backwards for Global Environment Protection? http://www.awi-bremerhaven.de/WBGU.

Wismann V., I. Woodhouse (2001) Evaluation of Operational Land Applications of Scatterometers, Final Presentation held at EUMETSAT, Darmstadt, June 8, 2001.

SYSTEMATIC DATA ACQUISITIONS – A PRE-REQUISITE FOR MEANINGFUL BIOPHYSICAL PARAMETER RETRIEVAL?

Å. Rosenqvist
National Space Development Agency of Japan, NASDA
Earth Observation Research Center, EORC
Triton Square, X-Tower 22F, 1-8-10 Harumi, Chuo-ku, 104-6023 Tokyo, Japan
Tel/Fax: +81-3-6221 9074 /-9192, Email: ake.rosenqvist@nasda.go.jp

ABSTRACT

Retrieval of bio- and geophysical parameters from remote sensing data is an important field of research, and the prospect of extracting such information in an operational manner with a high degree of accuracy is somewhat of a holy grail and a strong driver of current scientific work.

Meaningful parameter retrieval however requires not only the availability of appropriate sensors and inversion algorithms, but also that the data that are to be utilized are acquired in a planned and systematic manner. Regional extrapolation of locally developed retrieval algorithms is imperative if the applications are to be more than of mere academic interest, and spatially consistent data over large areas thus become a requirement. The terrestrial parameters that we are attempting to characterize and quantify are furthermore in a state of constant change as a result of both human-induced and natural events, and unless we take the temporal dynamics of these phenomena into account, we will lack the temporal context and our measurements will merely constitute snap-shots in time.

Providing systematic, repetitive observations over large areas is *potentially* one of the strengths of remote sensing technology, and one where it could provide substantial support to both scientific and commercial applications. However, high resolution remote sensing data are generally not acquired systematically, neither in time nor in space, and this is considered a serious impediment extensive use of the technology, and for the development of operational applications.

In this paper, various aspects of requirements for systematic data acquisitions are discussed, with emphasis on the needs for regional scale parameter retrieval, relevant in the context of climate change research and terrestrial carbon cycle science.

INTRODUCTION

Model development - an example

Development of algorithms for retrieval of specific parameters on the ground from satellite remote sensing data, be it above-ground biomass or soil moisture contents, may typically evolve as follows: Beginning with theoretical modelling to assure good understanding of the interaction between the ground target and the signal, the next step generally entails real data observations over a small field site with well measured ground parameters, which in turn may lead to an improved theoretical model and subsequently to repeated satellite observations over the site. The model may then be modified to cope with slightly different target characteristics and additional data observations may be performed to investigate the influence of e.g. environmental changes or variations in sensor characteristics. Ultimately, a sufficiently robust algorithm may have been developed, which allows parameter retrieval also outside the immediate study area, and it may now be of interest to apply the algorithm at a scene level, or preferably, at a regional scale to any environment that fulfils the criteria to which the algorithm has been designed to work.

Up to this point, it has been the skill of the researcher and the information contents of the data sets utilized that have governed the ultimate quality and usefulness of the algorithm developed. Applications at regional scales however, or even locally in areas different from that of the study site, require the availability of remote sensing data with the specific type of characteristics as to which the algorithm has been developed. And to be sure, such data rarely exist.

More often than not, it is the inadequacy of existing (high resolution) satellite data archives, rather than the models per se, that is the limiting factor for extended and operational retrieval of bio- and geophysical parameters.

The inadequacy of current data archives

High resolution satellite data are typically not collected homogeneously over large areas, but instead in a fragmented manner over several local sites that have been specifically requested by commercial or scientific users. The AO programmes of most satellite missions are good examples of this, aimed at satisfying the diverse and local interests of the scientific investigators. This results in that some passes may be acquired systematically over long times, while the data coverage over neighbouring passes may be totally neglected.

Proc. 3rd International Symposium, 'Retrieval of Bio- and Geophysical Parameters from SAR Data for Land Applications', Sheffield, UK, 11-14 September 2001 (ESA SP-475, January 2002)

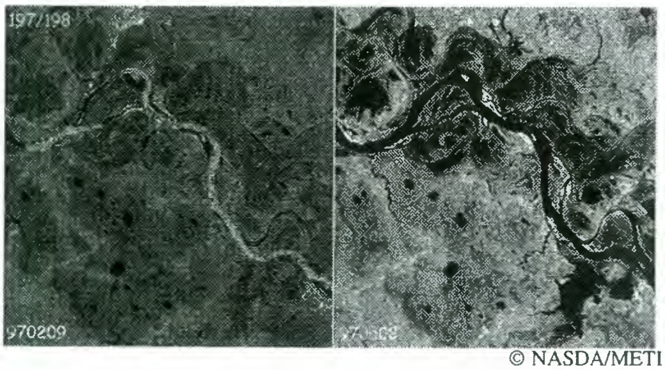

Figure 1. Yenisey river, Russia. JERS-1 L-band SAR data acquired during frozen (left) and thawed (right) conditions.

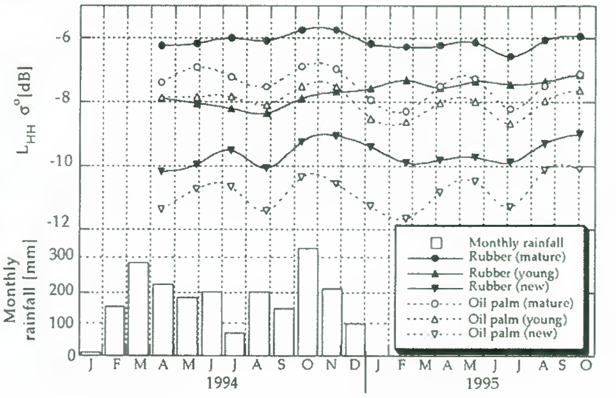

Figure 2. Seasonal backscatter variations for rubber and oil palm.

Commercial satellite operations result in a similar situation; data are principally acquired over sites requested by paying customers.

Most satellite missions generally also entail some kind of background mission objective, typically a "global coverage" goal, aimed at obtaining at least one acquisition over each node on the Earth. The actual usefulness of such global archives should however be seriously questioned. The misleading notion that SAR data are "weather independent" seems to prevail, and the data are generally acquired without any respect to seasonal effects (figures 1 and 2).

Coarse resolution data archives

Fragmented data archives is typically a problem for high resolution sensors and the usefulness of systematic and consistent data observations can be demonstrated by coarse resolution satellites such as e.g. MODIS and NOAA AVHRR. Despite the low 1-km spatial resolution, AVHRR data are utilized extensively by scientists all over the world. The success of NOAA AVHRR data with respect to wide usage, can be attributed to a few main factors:

- Global coverage (sensor always on);
- Repetitive temporal coverage (any year, any season)
- Long-term consistency (since early 1980's)
- Low prices (affordable to anyone anywhere).

The popularity of AVHRR data can be probably be attributed at least as much to its tremendous data archive, as to the sensor itself.

Applying the AVHRR acquisition strategy directly to high resolution sensors is however not feasible due to various technical constraints (power, data volumes, on-board storage etc.) and we will in the following discuss acquisition strategies from the aspect of high resolution data, and in particular Synthetic Aperture Radar.

SYSTEMATIC ACQUISITIONS - WHAT IS IT?

Spatial and temporal consistency

For regional scale applications, such as biomass retrieval over extensive ecological regions, it is an absolute requirement that data acquisitions are performed in both a spatially and temporally consistent manner. Spatial consistency here in principle means large regional coverage without acquisition gaps. Temporal consistency refers to limiting the time period of the regional data capture in order to minimize backscatter variations caused by seasonal differences between passes. Gaps that inevitably do occur occasionally should be covered during the next cycle for minimal impact. Daily acquisitions within the target area should in principle yield a full regional coverage within one satellite repeat cycle (~ 30-45 days).

The existing data archives are however not altogether fragmented and inadequate for regional studies. Most satellites have during several occasions during their lifetime been subject to dedicated acquisition campaigns with regional emphasis. Within the Global Rain Forest and Boreal Forest Mapping (GRFM/GBFM) projects (Rosenqvist *et al.* 2000), JERS-1 SAR data were acquired systematically over the entire rain forest and boreal forest zones on the Earth. And similarly, within the SIBERIA project (Schmullius *et al.* 2000), ERS-1, ERS-2 and JERS-1 data were collected over central Siberia for a regional forest assessment. Several more such examples exist, also with RADARSAT.

However, despite the significantly improved utility for regional scale applications that such intensive acquisition campaigns bring about, it should be noted that they still are far from perfect. For one thing, the spatial coverage is only limited to the campaign area and for any study outside this, only the standard archive is available. Within the campaign area however, the spatial component is adequately fulfilled

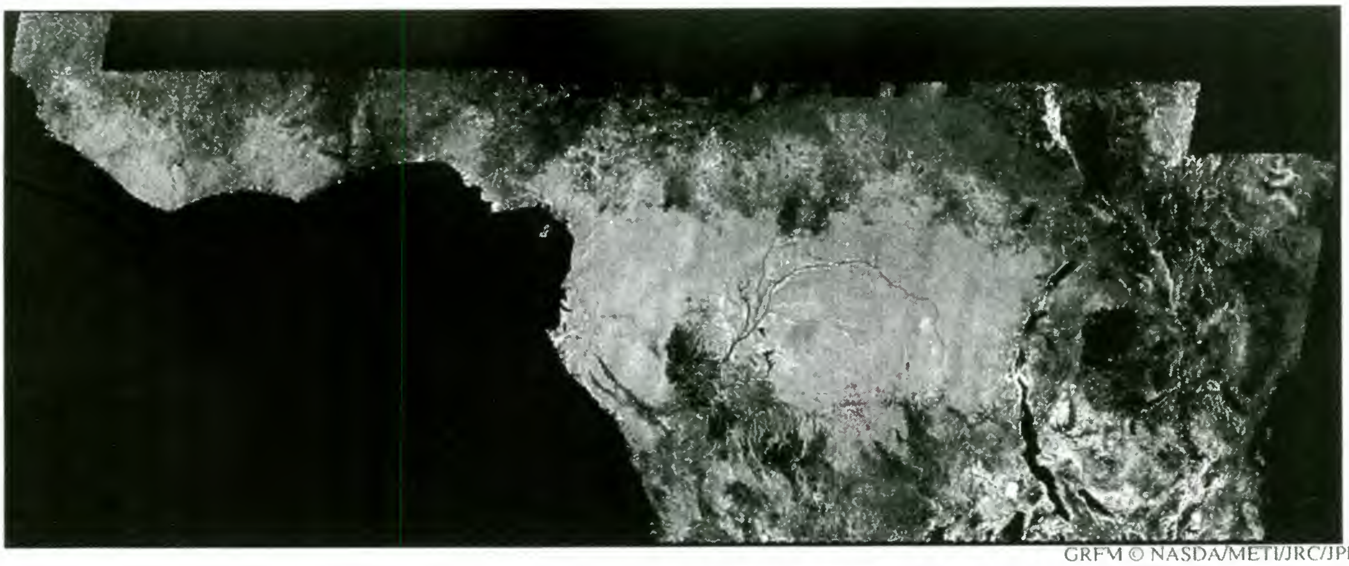

Figure 3. Regional JERS-1 coverage over Equatorial Africa (106 passes) acquired Jan.7-March.7, 1996, within the Global Rain Forest Mapping project.

and the data can be analyzed at any scale from local to regional or sub-continental. The requirement for temporal homogeneity is largely also fulfilled (with the exception of occasional missed acquisitions that have been replaced with passes with deviating dates) and if mosaicked, the composite can in principle be treated as one image. What is lacking is the temporal repetition component.

Adequate repetition frequency

Most of the terrestrial parameters that we want to characterize and quantify are in a state of constant change and in many cases, it is these changes that we are interested in. Carbon cycle science and Kyoto Protocol support are predominantly focused around this change component, and hence, unless we take the temporal dynamics of the terrestrial parameters into account, we will lack the temporal context and our measurements will merely constitute snap-shots in time.

Adequate temporal repetition should thus be added to an optimal data acquisition strategy, on top of the requirements for spatial and temporal homogeneity. But what is actually "adequate" repetition? - It naturally depends on the ground parameter of interest. Agricultural crops, for instance, generally have life cycles spanning over a few months, and in order to sample the different growth stages properly, every-cycle acquisitions (3-6 weeks with current hi-res satellites) during the cultivation period are required. The same high frequency is required for studies of seasonal inundation phenomena in major river basins, which are characterized by rapid variations.

Forest and forest biomass, on the other hand, are subject to longer growth cycles of several decades, although deforestation events may happen anytime. For monitoring of changes in forest cover, annual or bi-annual repetition frequency would probably be more adequate, depending on the intensity of land cover changes. Monitoring of desertification and forest degradation in semi-arid zones is yet another application area. These processes are often even more long-term and 3-5 year repetition may perhaps be sufficient in such areas.

So, consequently, the temporal repetition frequency of the acquisitions have to be adapted with respect to the land use, and a land use based stratification of the Earth may thus be required in a global data acquisition plan.

Timing

Timing is also an important component of repetitive observations, as seasonality may introduce bias in time series of data. Annual acquisitions of e.g. forest cover should therefore preferably be planned during the same season every year, favourably during seasons with stable dielectric conditions. Spring acquisitions should be avoided in the boreal and temperate zones as thaw and snowmelt may obscure actual changes. In the tropical zone, dry season is preferred due to lower and more stable dielectrics and larger radiometric dynamic range between base soils and vegetation cover.

Long term continuity

Assuring long-term continuity of acquisitions with intercomparable sensors is well known requirement. It is imperative for any kind of climate change related research, as well as for operational support to the Kyoto Protocol, which, it should be noted, is open-ended.

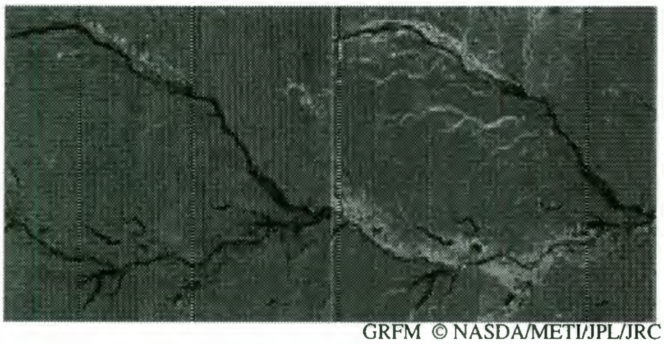

Figure 4. Central Amazon river basin, Brazil. Spatially and temporally homogeneous L-band SAR data coverages during low water (left) and high water (right) seasons.

Leaving the temporal and spatial aspects of data acquisition planning, sensor configuration and consistency is also an issue to consider.

Sensor consistency

It is well known that radar frequency, polarization and incidence angle have strong effect on the backscatter and for good and bad, the JERS-1 and ERS-1/2 satellites featured instruments with fixed sensor parameters. On one hand, this assured inter-comparability between scenes acquired over the same area at different times, but on the other hand, extraction of additional information by use of e.g. multiple incidence angles, was not possible. Variable incidence angles are available with RADARSAT-1, and with the launch of ENVISAT, ALOS and RADARSAT-2, both incidence angles and polarization have to be specifically selected.

This introduces a conflict of interests as different applications have different requirements. There is also a conflict of interests between basic research, e.g. investigations of the effects of variable incidence angles and polarizations, and more operational applications, among those e.g. regional scale extraction of biophysical parameters.

In order to avoid, or at least to minimize, fragmented acquisitions with a multitude of different sensor combinations, this issue should be addressed by the science community and a "best trade-off" set of sensor parameters should sought. Because, more than optimal sensor configuration, the availability of spatially and temporally consistent, and inter-comparable, data at regional scales, is likely to govern the extent of remote sensing data used in an operational manner in the future.

CONCLUSIONS

The title of this paper, *Systematic data acquisitions - a prerequisite for meaningful biophysical parameter retrieval?*, is posed as a question, and as a brief summary of what has been discussed above, the reply should be "yes". It may be argued that "meaningful" biophysical parameters can be extracted even from a single scene, but without the spatial or temporal context, such activities will probably be more of academic interest than anything else.

Parameter inversion is an important area of research *because* of its potential impact on regional and global scale issues of public concern. Climate change is real and the UNFCCC Kyoto Protocol is an evidence that the general public all over the world want to see a change. The general public is also tax-payers who have the right to demand that the resources spent on Earth Observation satellites are utilized in favour of the public and the environment.

Going for a comprehensive and long-term data acquisition strategy is a win-win scenario for the public, the science community as well as for the space agencies. It is obvious that the establishment of comprehensive and consistent data archives in line with what has been discussed above, would stimulate both scientific and commercial utilization of satellite data. The inability for remote sensing technology to take off to become operational can to a large extent be attributed to the ignorance of the importance of systematic observations. It is time for a change and this is the way to go. Hallelujah.

REFERENCES

Å. Rosenqvist, M. Shimada, B. Chapman, A. Freeman, G.F. De Grandi , S. Saatchi and Y. Rauste, 2000. *The Global Rain Forest Mapping Project - a review.* International Journal of Remote Sensing, 2000, Vol. 21, No. 6&7, pp 1375-1387.

C. Schmullius, H. Balzter, M. Davidson, D. Geveau, M. Gluck, A. Luckman, S. Nilsson, A. Öskog, S. Quegan, Y. Rauste, A. Roth, A. Svidenko, K. Tansey, T. Le Toan, J. Vietmeier, W. Wagner, U. Wegmüller, A Wiesmann, Y. Y. Yu, *SAR Imaging for Boreal Ecology and Radar Interferometry Appications (SIBERIA)*, C. Schmullius (Ed.), 3nd Progress Report, 4th Framework Programme of the European Commission, Co. No. ENV4-CT97-0743-SIBERIA, Deutsches Zentrum für Luft- und Raumfahrt (DLR), Oberpfaffenhofen, Germany, February 2000.

EMBEDDING REMOTE SENSING DATA IN MODELS FOR FOREST CARBON DYNAMICS

S. Quegan[1], T. Le Toan[2]

[1]*Sheffield Centre for Earth Observation Science*
University of Sheffield, Hicks Bldg, Hounsfield Rd, Sheffield S3 7RH UK
tel: +44 114 222 3778/fax: +44 114 222 3809/email: s.quegan@sheffield.ac.uk
[2]*Centre d'Etudes Spatiales de la Biosphère,*
18 Avenue Edouard Belin, Toulouse cedex31401 France
tel: +33 561 556671/fax: ++33 561 558500/email: thuy.letoan@cesbio.cnes.fr

ABSTRACT

The conceptual framework within which Earth Observation (EO) data can be absorbed into dynamic biophysical models of forests is described. The specific quantities relevant to this problem that can be derived from EO data are identified, together with the types of sensors necessary and available. Radar has unique capabilities in detecting freeze-thaw events over large areas, but its most telling contribution to quantitative estimates of carbon fluxes is through measurements of biomass. This is best demonstrated in a form suitable for interfacing to models by the large-scale biomass maps of central Siberia produced in the SIBERIA project. However, their production required Tandem coherence measurements, which are no longer available. Of the current and upcoming radar satellites, only ALOS-PALSAR seems capable of providing estimates of biomass on the routine basis needed for carbon modelling. This will require systematic, large-scale data acquisition and reliable biomass product recovery to be demonstrated. If such a general framework can be established, it also provides a context for absorbing data from non-satellite sources, such as VHF airborne systems.

1. INTRODUCTION

The largest single source of uncertainty in the global carbon budget, amounting to 1.3 Gt C y^{-1}, is due to terrestrial ecosystems (IPCC, 2000). There are major uncertainties in the spatial distribution of carbon stocks and carbon exchange, in the response of terrestrial ecosystems to CO_2/N fertilization and climatic variation, and in the estimates of carbon emissions due to human induced or natural disturbances. In addition, current estimates of emissions from land use change and disturbance are primarily based on tropical regions, and ignore significant extra-tropical fluxes

Forests cover 28% of the land surface but contain 46% of the terrestrial carbon, stored as biomass and soil organic carbon. In addition, changes in forest extent, such as deforestation or the northward spread of the boreal forest in a warming climate, exert major feedbacks on climate (Betts et al., 1997). Forest ecosystems therefore play a dominant role in the terrestrial carbon budget. However, there is deep uncertainty and disagreement among the scientific community about whether forests act as a source or a sink of carbon, and how this depends on forest type, age and history, and site and climatic conditions. Such uncertainty, combined with the lack of reliable methods to monitor and verify national carbon sequestration projects, creates major problems in international treaty negotiations.

The extent of this uncertainty is well illustrated by two recent authoritative reports on carbon fluxes, from which Figs. 1(a) and (b) are taken (with some minor modifications). It can be seen that, while both reports are in rough agreement about the sources of atmospheric carbon and its net increase, they differ significantly in the estimated strengths of the ocean and biospheric sinks. For the period 1989-1998, IPCC (2000) gives an inferred value for the net terrestrial uptake of carbon (the net biome production [NBP]) as 0.7 Gt C y^{-1}. In contrast, the corresponding value in the Royal Society report (2001) is 1.5 Gt C y^{-1}. In the face of such uncertainty, it is not surprising that the Kyoto protocol negotiations were difficult.

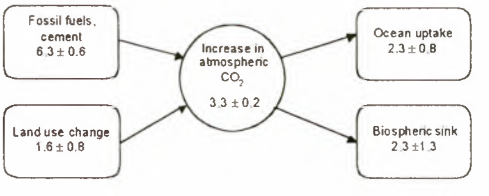

Figure 1(a) Estimated carbon sources and sinks 1989-98 (Gt C y^{-1}) (IPCC, 2000).

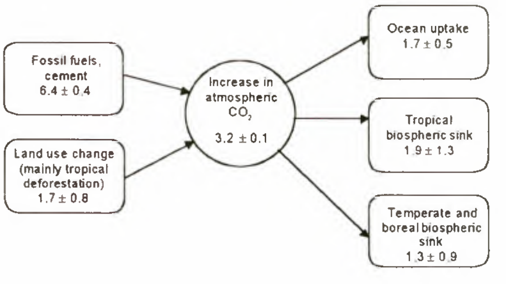

Fig. 1(b) Estimated carbon sources and sinks in the 1990's (Gt C y^{-1}) (Royal Society, 2001).

Proc. 3rd International Symposium, 'Retrieval of Bio- and Geophysical Parameters from SAR Data for Land Applications', Sheffield, UK, 11-14 September 2001 (ESA SP-475, January 2002)

Methods for measuring and monitoring carbon stocks produce estimates of unknown reliability. At a regional scale, methods are based upon measurements at a small number of field sites, which may not represent the spatial variability of the region. At the global scale, estimates are based on global inventories and surveys which are incomplete and inconsistent as regards factors needed to calculate carbon stocks (IPCC, 2000; FAO, 1995). In addition, annual increases in forest carbon (the net ecosystem production [NEP]) cannot be recovered from this approach, despite it being known that NEP shows significant annual and inter-annual variation. NEP is, however, readily simulated and extended both spatially and temporally by process models, but such models suffer from inadequate representation of state variables (for example, human impacts may be ignored) and are only weakly tied to data which can constrain their calculations.

The need to take a more integrated approach to quantifying terrestrial carbon stocks and fluxes, which combines data sources and models, is well recognised (IGOS-P, 2000; GOFC, 1999). Earth Observation (EO) data have a key role to play in this process, by producing consistent, regular and large-scale measurements of forest function and structure and associated factors, such as land cover.

2. THE TERRESTRIAL CARBON BALANCE

Two equations form the quantitative basis for discussing the terrestrial carbon balance, namely the mass balance equation:

$$\Delta C = \Delta B_A + \Delta B_B + \Delta L + \Delta S \qquad (1)$$

and the process (source-sink) equation:

$$\Delta C = P - R_P - R_H - D, \qquad (2)$$

where the symbols are defined as follows:

- ΔC carbon sequestration by vegetation and soil,
- B biomass (A: above and B: below ground),
- L litter,
- S soil carbon,
- P photosynthesis,
- R respiration (P: plant and H: heterotrophic),
- D carbon loss by disturbance.

Eq. (1) can also be regarded as an allocation equation, giving the destination of the carbon produced or lost by the processes described in (2). This allocation significantly affects the processes, so the equations are strongly coupled.

3. CARBON CYCLE-EARTH OBSERVATION INTERFACES

The relation of these two equations to EO data is shown schematically in Fig. 2, adapted from IPCC (2000). The leftmost of the central two columns corresponds roughly to (1) and is expressed in forestry terms. The right central column corresponds precisely to (2) and uses ecological terms. To left and right are the interfaces to EO data. It can be seen that remote sensing is capable of providing direct measurements relevant to ΔB_A (above ground biomass can be measured by optical and radar sensors, up to a saturation level), P (fAPAR and possibly other determinants of biochemical activity) and D (land cover change and fire extent), and can supply information helpful in estimating some of the other terms (such as soil moisture and temperature, which affect soil carbon processes expressed through ΔS).

In fact, the relation between EO data and (1) and (2) has further aspects, since these flux equations obey various constraints and boundary conditions. A more complete picture is given by Fig. 3, in which the upper part shows a time-dependent vegetation model (essentially a solver of (1) and (2)) fed with input data on atmospheric conditions and soil type (this is representative of the current generation of such models (Cramer et al., 2001)). The lower part of the figure shows the range of ways in which EO data can interact with this overall structure.

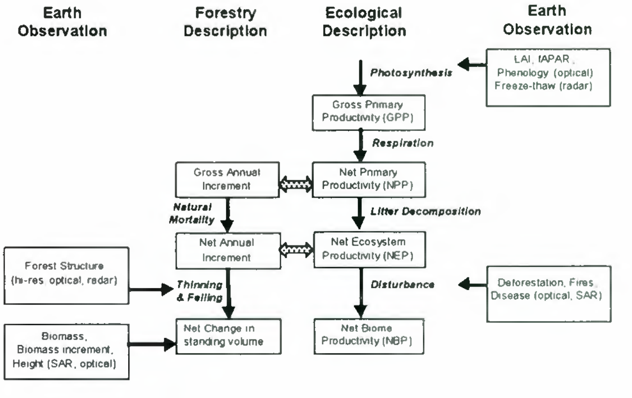

Fig. 2 Earth Observation-Forestry-Ecology Interfaces

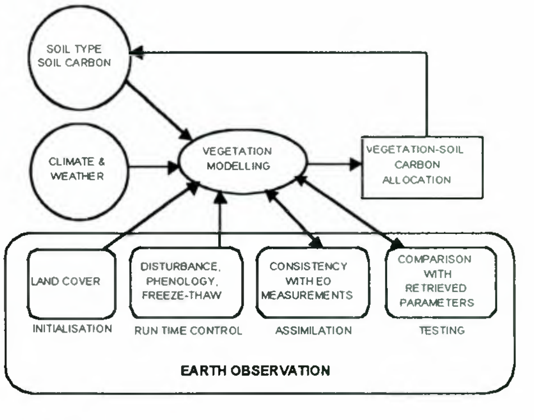

Fig. 3 Carbon Cycle – Earth Observation Interfaces

Initialisation of the calculation can be constrained by current land cover. Run-time changes due to disturbances (land cover changes, fire) can also be provided by EO, together with the timing of important biophysical switches (freeze-thaw, snow cover) and plant development indicators (greening up and senescence). Assimilation of data into the models is possible through terms in the process equation (2), particularly though use of coupled vegetation-radiation models connecting vegetation functional variables (especially fAPAR and albedo) to quantities observed by a satellite. Finally, we have quantities more closely related to the mass balance equation (1) (for example, biomass and forest height). These can be used for testing model predictions, but provide no direct insight into where the model is failing if there are discrepancies between observed and calculated values.

The conceptual structure shown in Fig. 3 does not have an intrinsic scale, but the dynamic vegetation models (DVMs) currently capable of running within this structure are designed to operate at continental to global scale. At the opposite extreme are models used for local scale calculations (individual stands). Such models, whether designed for the needs of science or forestry, tend to be data rich and site specific, and have little need for EO data. However, an important issue is whether these two extreme scales can be brought together through models which operate at a regional scale (for example, at catchment to country scale), because of the need for national carbon monitoring and reporting. This will require significant methodological developments, driving from both large and small scale, as illustrated by Fig. 4. Key issues in getting to the regional scale are:

- the substantially more comprehensive range of processes which must be absorbed by current DVMs, which will involve rethinking their basic assumptions;
- significantly improved assimilation of data, from EO and other sources;
- the extent to which local models can be generalised, using methods from the DVMs;
- the extent to which data loss in the local models as we coarsen the scale can be mitigated by other data sources, especially EO.

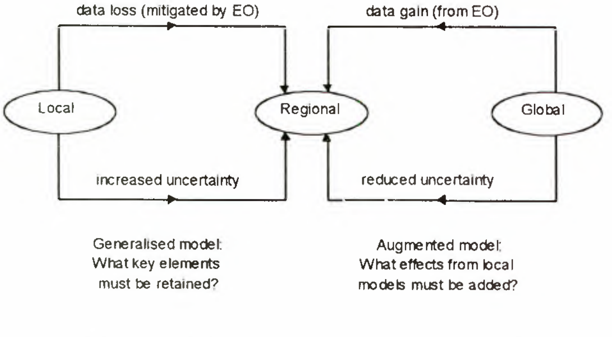

Fig. 4 Using models and data for translation between scales.

4. RECOVERING MODEL VARIABLES USING EO DATA

The carbon assessment methods and models make use of different sources of data, with requirements at time scales ranging from invariant data (DEMs, soil maps) to daily meteorological data, and remote sensing data. Table 1 summarises the relevant land surface variables and the main EO data sources that can provide these variables at different spatial and temporal scales. This non-exhaustive list indicates systems under study by (*).

The operational status of the quantities derived from EO data is very varied. In the optical domain, AVHRR data has a well-developed data reduction and supply chain, and can be built into operational information systems (for example, mapping vegetation status using NDVI, or snow cover), as long as data gaps due to cloud cover can be accommodated. The ground segment of the Terra mission is working towards routine supply of a range of products, including fAPAR, albedo and LAI. For these data sources, the ability to interpret the satellite data in terms of geophysical properties (although requiring more caution than is generally exercised) has encouraged data exploitation. In the radar domain, the situation is quite different. Data supply (at least for the ERS and Radarsat satellites) has not been a major problem, other than cost, but there are few examples of readily available, robust derived products for land applications. This is discussed further in the next section.

Land surface variables	**Earth Observation data**		
	High spatial resolution <100 m	***Medium sp. resolution 100 m< res<1 km***	***Low spatial resolution >1 km***
Land use & land cover Disturbances (clearcut, fires..)	**Landsat TM, SPOT Envisat ASAR, Alos PALSAR, Radarsat**	**Envisat MERIS, Terra MODIS**	**NOAA / AVHRR, SPOT/ VGT**
LAI, fAPAR, albedo		**Envisat MERIS, Terra MODIS, Terra MISR, POLDER**	**NOAA / AVHRR, SPOT/ VGT**
Vegetation phenology		**Envisat MERIS, Terra MODIS**	**NOAA / AVHRR, SPOT /VGT**
Canopy height			**VCL* (Lidar)**
Biomass	**Envisat InSAR, Alos PALSAR, TerraSAR***	**P-band SAR***	
Land surface temperature			**ERS ATSR2, Envisat AATSR MODIS, AVHRR**
Soil moisture	**Envisat ASAR**		**SMOS***
Snow water equivalent			**SSM/I**
Freeze/thaw			**ERS Scat, QuickSCAT Seawind**

Table 1: Information relevant to forest carbon modelling which can be recovered from EO data, and the systems potentially capable of providing this information.

5. THE ROLE OF RADAR REMOTE SENSING

Table 1 and Fig. 2 indicate where radar and SAR can contribute to quantifying carbon dynamics. Information on land cover dynamics is usually most easily acquired from optical data, with radar playing a complementary role when cloud cover is a problem. Large scale freeze-thaw maps derived from scatterometers have been produced (e.g., Boehnke and Wismann, 1997). These are uniquely radar products, relying on strong dielectric changes in plant materials at or around the freezing point. Similar products could be produced from a low resolution SAR, such as the Envisat ASAR in global mode. Methods to recover soil moisture from SAR data are still the subject of much debate (see, for example, Borgeaud [2001] in these proceedings), and are only just beginning to have an impact on process modelling (see Bach and Mauser [2001] in these proceedings).

In terms of quantities which can be directly applied in models for forest carbon dynamics, radar is the key technology for measuring above ground biomass (see (1) and Sect. 2). This is clear from Table 1, while in Table 2 we summarise the contribution made by different types of radar system.

The sensitivity of the radar backscatter to biomass results from the relationship between the signal and the biomass of the vegetation elements involved in the interaction. In the microwave region, the nature of the dominant scatterers (and to a lesser extent, the attenuators) in a forest canopy changes with the wavelength. If the scatterers are too small compared to the wavelength, their backscatter contribution is not significant. In general, the main scatterers at X band (3 cm wavelength) are leaves or needles, at C band (6 cm), leaves, twigs and small branches, at L band (25 cm), primary and secondary branches, and at P band (70 cm), the trunk and larger branches. As a consequence, since the signal saturates when the number of scatterers becomes important, saturation occurs at levels of biomass which increase from X to P band.

Biomass range	*Remote sensing data*
Up to 50 tons/ha	**L-band SAR** (ALOS-PALSAR*, TerraSAR*) **C-band InSAR**
Up to 150 tons/ha	**P-band SAR***
Up to 500 tons/ha	**VHF SAR** (airborne)

Table 2: The approximate ranges of biomass sensitivity for different SAR sensors. (*) denotes future sensors.

Experimental studies with AIRSAR and E-SAR over different types of forests (temperate, boreal and tropical) (Le Toan et al., 1992, Dobson et al., 1992, Beaudoin et al., 1994, Hsu et al, 1994, Rignot et al., 1995, Hoekman and Quinones, 2000, Mougin et al., 1998) indicate that the backscatter intensity saturates at 30, 50 and 150-200 tons/ha respectively at C, L and P bands. Note that the saturation values quoted here and in Table 2 are indicative of a range and depend on the experimental conditions (e.g. radar incidence angle, polarisation) and forest characteristics.

At C band, the sensitivity of the backscatter intensity to forest biomass variation at very early stages of growth depends strongly on the ground conditions, including soil moisture, soil frost, snow cover and vegetation status. In addition, the low dynamic range of the backscatter between 0 and 30 tons/ha has prevented the development of robust inversion algorithms using ERS (or RADARSAT) intensity data.

C band interferometric coherence acquired at short time intervals, as in the Tandem ERS missions, shows a decline with increasing biomass, caused by an increased contribution by the temporally unstable scatterers in the vegetation canopy as biomass increases. In the SIBERIA project, ERS Tandem data were used, together with JERS data, to map forest biomass up to 80 m^3/ha (or 50 tons/ha) in central Siberia (Schmullius et al., 2001). The importance of this project was to show that geophysical parameters highly relevant to quantifying the carbon dynamics of boreal forests could be recovered at continental scale (750,000 km^2) from SAR data, given the appropriate data, methods and scale of effort. An unfortunate aspect of this achievement is, however, that the data types needed to produce this type of map are no longer available, and in the case of Tandem data, will not be available for the foreseeable future.

The saturation in Tandem coherence at a biomass level of 80 m^3/ha observed in the SIBERIA project may be considerably increased under very low temperature conditions (Askne et al., 2001, in these proceedings). This could be due to deep freezing of the vegetation, causing severe reduction in the dielectric constant of the leaves and twigs. The dominant scattering elements then change from these more usual plant components to larger elements.

At L band, the backscatter results from a more complex interaction, where the main scatterers are the primary or secondary branches. Since the soil backscatter at L band is often lower than that of the canopy, the signal increases with increasing biomass until saturation. This increasing trend has been observed in a majority of cases with JERS-1 (L band, HH polarisation and 35° incidence angle) until saturation at approximately 50 tons/ha. However, the sensitivity to biomass is small, of the order 2-3 dB for the biomass range up to 50 tons/ha, and depends on the ground conditions. During the lifetime of JERS (1992-1998), several works have been published on the use of JERS data for forest mapping, but few provided biomass maps. The forthcoming L-band polarimetric ALOS-PALSAR is expected to provide data with the same saturation level but with higher sensitivity to biomass and a reduction in disturbing conditions, particularly at cross polarisation. The dynamic range of L-HV as observed by airborne SARs exceeds 5 dB (Melon et al. (2001), in these proceedings). With the continuous provision of ALOS-PALSAR data, biomass maps similar to those provided in the SIBERIA project could be a valuable contribution to validating the biomass increments in regenerating forests predicted by carbon dynamics models.

A P-band SAR, with saturation level up to 150 to 200 tons/ha, is capable of covering the biomass range of most forests, except mature tropical forests. The dynamic range of the backscatter, which is the contrast between the forest backscatter at saturation level and at low biomass level, has been found to exceed 12 dB at P band, HV polarisation and 40° incidence angle. The large dynamic range is particularly fitted to robust algorithms inverting the backscatter signal into biomass classes, e.g. of intervals of 10-15 tons/ha. Until recently, P-band spaceborne SARs could not be envisaged, mainly because no frequency was allocated for remote sensing at P band. At present, the official request for frequency allocation appears to have a good chance of success in the next World Radio Conference. With this condition, it is probable that a P band SAR payload will be defined and launched in the future.

In recent works, even longer wavelengths have been studied. The CARABAS-II system, developed by the FOI (Swedish Defence Research Establishment), is an airborne ultra-wideband and widebeam SAR operating in the lower VHF band (20-90 MHz). Experiments and physical modelling indicate that VHF SAR backscatter is sensitive to biomass up to 500 tons/ha. Such a system, although not envisaged as a spaceborne payload, could provide complementary airborne coverage over large areas of high biomass range. The right way to assess the role of such sensors is in the context of the whole information system needed to follow forest dynamics.

6. CONCLUSIONS

Understanding the role of forests in the terrestrial carbon cycle is a scientific goal of the highest scientific, political and economic interest. Tackling this problem requires the combined resources of ecologists, modellers, statisticians and remote sensing scientists. SAR and other microwave sensors can make specific, well-defined contributions to this problem. In particular, radar is uniquely fitted, amongst all EO technologies, to provide estimates of biomass. However, there is a long way to go from turning this potential into a product which is meaningful in terms of forest carbon models. Even with the right sensor (and ALOS-PALSAR is certainly a step in this direction), experience in the SIBERIA and other large-scale projects has shown the need for systematic data acquisition and quality controlled product generation from that data. Failure to rise to this challenge will lead to SAR being marginalised in one of the major environmental issues of the age. Conversely, a serious attempt to get SAR retrieved information into a modelling context will yield significant scientific gains, providing a framework to both assess and use radar data.

REFERENCES

Askne J., M. Santoro, G. Smith and J.E.S. Fransson, 'Large area boreal forest investigations using ERS InSAR' Proc. of the 3rd International Symposium on Retrieval of Bio- and Geophysical Parameters from SAR data for Land Applications, Sheffield, 11-14 September 2001

Bach, H. and Mauser, W., 'Remote sensing data assimilation in land surface process modelling', Proc. 3rd International Workshop on Retrieval of Bio- and Geophysical Parameters from SAR Data for Land Applications, Sheffield, 11-14 September 2001.

IPCC Special Report, Land Use, Land-Use Change, and Forestry, (Watson et al.). Cambridge University Press (2000).

Beaudoin, A., T. Le Toan, S. Goze, E. Nezry, A. Lopes, E. Mougin, C. C. Hsu, H. C. Han, J. A. Kong and R. T. Shin, 'Retrieval of forest biomass from SAR data', *Int. J. Remote Sensing*, **15**, 2777-2796, (1994).

Betts, R.A., Cox, P.M., Lee, S.E. & Woodward, F.I. 'Contrasting physiological and structural vegetation feedbacks in climate change simulations'. *Nature*, 387, 796-799 (1997).

Boehnke K. and Wismann V.R., 'Thawing processes during Siberian spring observed by ERS scatterometer and SAR', *Proc. IGARSS'97*, Singapore, pp. 1826-1828 (1997).

Borgeaud, M., 'On the usefulness of SAR data to retrieve surface soil parameters', Proc. 3rd International Workshop on Retrieval of Bio- and Geophysical Parameters from SAR Data for Land Applications, Sheffield, 11-14 September 2001.

Cramer, W., Bondeau, A., Woodward, F. I., Prentice, I. C., Betts, R. A., Brovkin, V., Cox, P. M., Fisher, V., Foley, J. A., Friend, A. D., Kucharik, C., Lomas, M. R., Ramankutty, N., Sitch, S., Smith, B., White, A., Young-Molling, C., 'Global response of terrestrial ecosystem structure and function to CO_2 and climate change: results from six dynamic global vegetation models', *Global Change Biology*, vol 7., 357-373 (2001).

Dobson M. C., F. T. Ulaby, T. Le Toan, A. Beaudoin, E. Kasischke and N. L. Christensen, 'Dependence of radar backscatter on coniferous forest biomass', *IEEE Trans. Geosci. Remote Sensing*, **30**, no. 2, pp. 412-415, 1992.

FAO Forest resources assessment 1990: Global Synthesis, FAO Forestry Paper 124 (1995).

GOFC Design Team, A Strategy for Global Observation of Forest Cover (1999).

Hoekman, D.H. and Quinones, M.J., 'Land cover type and biomass classification using AirSAR data for evaluation of monitoring scenarios in the Colombian Amazon', *IEEE Trans. Geosci. Remote Sensing*, **38**, no. 2, 685-696, 2000.

Hsu, C. C.,C. Han, R. T. Shin, J. A. Kong, A. Beaudoin and T. Le Toan, 'Radiative Transfer theory for polarimetric remote sensing of pine forest at P band', *Int. J. Remote Sensing*, **15**, 2943-2954, 1994.

Le Toan T., A. Beaudoin, J. Riom and D. Guyon, 'Relating forest biomass to SAR data', *IEEE Trans. Geosci. Remote Sensing*, **30**, 403-411, 1992.

Melon P, T. Le Toan, G. Picard, N. Delbart and M. Davidson 'On the information content of L band polarimetric SAR data over forested areas' Proc. of the 3rd International Symposium on Retrieval of Bio-and Geophysical Parameters from SAR data for Land Applications, Sheffield, 11-14 September 2001.

Mougin E, Proisy C. et al., 1998, 'Radar Remote Sensing of a mixed deciduous forest during EMAC 94', Proc. EMAC final meeting, ESTEC, pp 105-109, April 1997, ESTEC.

Rignot, E.J.M., Zimmermann, R. and van Zyl, J.J., 'Spaceborne applications of P band imaging radars for measuring forest biomass', *IEEE Trans. Geosci. Remote Sensing*, **33**, pp. 1162-1169. 1995

Roy. Soc. Policy Doct. 10/01, *The role of land carbon sinks in mitigating global climate change,* The Royal Society (2001).

Schmullius, C., J. Baker, H. Balzter, M. Davidson, D. Gaveau, M. Gluck, A. Holz, T. Le Toan, A. Luckman, U. Marschalk, S. Nilsson, S. Quegan, Y. Rauste, A. Roth, V. Rozhkov, V. Sokolov, A. Shvidenko, V. Skuding, T. Strozzi, K. Tansey, J. Vietmeier, L. Voloshuk, W. Wagner, U. Wegmüller, A. Wiesmann and J.J.Yu, 'SIBERIA – SAR Imaging for Boreal Ecology and Radar Interferometry Applications', European Commission 4th Framework Project ENV4-CT98-0743 (DG12-EHKN), Final Report, September 2001.

Terrestrial Carbon Theme Team, IGOS-P Carbon Cycle Observation Theme Report: Terrestrial and Atmospheric Components (draft), October, 2000.

Posters

Agriculture, Land Cover and Hazards

ASSESSING LAND FEATURES IN SEMI-ARID REGIONS FROM MULTI-TEMPORAL SAR DATA.

M. Bianchini, G. Macelloni, S. Paloscia, P. Pampaloni, and E. Santi
Istituto di Ricerca sulle Onde Elettromagnetiche – CNR – Firenze, Italy
Tel.: +39 055 4235 220 / fax: +39 055 4235 290 / e-mail: paloscia@iroe.fi.cnr.it

N. Aqid, D. Ouazar
Ecole Mohammedia d'Ingenieurs – Rabat, Morocco

M. Zribi
Centre d'Etude des Environments Terrestre et Planetaires - Velizy, France

ABSTRACT

In this paper an experiment aimed at evaluating the potential of SAR systems in monitoring hydrological parameters in a large watershed of a semi-desert area was described. Remote sensing and ground truth measurements were carried out in Morocco, within the framework of the EC project FLAUBERT (FLood in Arid Units By Earth Remote Techniques). ERS/C-band SAR and JERS/L-band SAR images collected from October 97 to June 99 were analyzed. In spite of the very low changes in space and time, the spatial and temporal analysis of L- and C-band backscattering showed the capability of SAR to point out yearly variations due to vegetation cycle and rain events and to map semi-arid vegetation. By using interferometric coherence a separation of several soil and vegetation classes in the same image was obtained.

INTRODUCTION

The utility of remote sensing for monitoring land surface characteristics in arid and semi-arid regions, where conventional methods are very expensive and time consuming, is well recognized in recent literature (Deroin et al. 1997, Tansey et al. 1998). However, the operational capabilities of relatively new sensors such as the Synthetic Aperture Radar (SAR) are not yet fully exploited.

The main parameters controlling surface water cycle in arid and semi-arid regions are the relative distribution of bare rock areas, the spatial and temporal distribution of wild and agricultural vegetation, soil moisture and surface roughness. The potential of Synthetic Aperture Radar (SAR) in monitoring these quantities has been the subject of several studies carried out mostly in vegetated regions. In desert areas, backscattering variations are mainly caused by surface slope and surface roughness, since in general soil moisture is very small and has no significant effect on the backscattering (Deroin et al. 1997, Evans et al. 1992).

THE EXPERIMENT

Remote sensing and ground truth measurements were carried in 1999/2000 on a flat, arid region located in Morocco. The test area fitted exactly with the Foum Tillicht catchment. This basin of 1259 km^2 is the left upstream branch of the Ziz watercourse in South-East Morocco. It belongs to an arid zone, where the average yearly precipitation is 160 mm, with a short humid season alternated with a long dry one. On this site, several preliminary activities were carried out by the Ecole Mohammedia d'Ingenieurs – Rabat. The basin was divided in five hydrologic sub-basins. For each sub-basin, a classifier which identified nine classes (different types of soil and vegetation cover) was developed from optical data and validated in several field campaigns.

The analysis of SAR data was focused on a flat region which included bare and uniformly vegetated areas zones. Each area was classified on the basis of soil porosity (high and medium) and vegetation type. A sparse cover of vegetation grew on the muddy and schistous surfaces with a variable stone cover. The main species growing on limestone, muddy soil and schistous soil were Mugwort (Artemesia Herb alba) and Alfa (Stipa tenacissima), the latter with various densities. Systematic measurements of soil moisture and plant water content were not worked out, but, according to meteorological data available from ground stations, soil and vegetation could be considered very dry. In some areas, statistical and fractal parameters of soils were extracted from roughness measurements carried out by means of a pin profilometer.

The backscattering coefficient of ten selected areas was extracted from five ERS/C-band and four JERS/L-band SAR images. In addition, coherence maps obtained from repeat pass interferometry, at time intervals

Proc. 3rd International Symposium, 'Retrieval of Bio- and Geophysical Parameters from SAR Data for Land Applications', Sheffield, UK, 11-14 September 2001 (ESA SP-475, January 2002)

between two and ten months, were combined to obtain a composite image with a significant information content on land characteristics. Both types of information were compared with ground data. Due to the high stability of the area, we assumed that soil surface characteristics, vegetation cover, and vegetation density did not change significantly during the season

SAR DATA ANAYSIS

- *Sensitivity to vegetation cover*

The temporal evolution of backscattering coefficient ($\sigma°$) was analyzed for each site by using a series of C-band ERS-1/2 and L-band JERS-1 images collected between June 1998 and October 1999 and between October 1996 and June 1998, respectively. The analysis showed that the spatial variation of the backscattering coefficient at the same date was comparable to the temporal variation observed in each area and remained below 3 dB. This result is similar to those obtained by other authors on arid lands (Deroin et al. 1997). However, the annual variations of L-band $\sigma°$ (Fig. 1) show for all sites a maximum in winter '98, which could reasonably correspond to a rainy season and therefore to higher values of soil moisture.

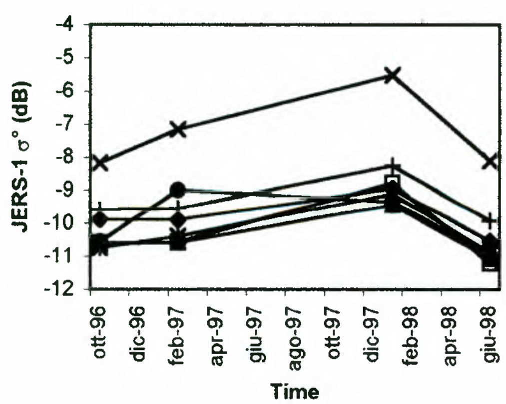

Fig. 1 – Temporal variations of JERS-1/L-band σ^0 measured in some of the test areas.

The sensitivity to vegetation cover (VC) of the two main types of vegetation existing in the area (Alfa and Mugwort) was tested at both bands. At L-band, as the VC increased, backscattering decreased for Alfa and, to a lesser extent, for Mugwort. Instead, at C-band the decrease was very clear only for Alfa (Fig. 2) (Paloscia et al. 2001). These diagrams suggest the possibility of operationally retrieving the vegetation cover from SAR data.

In arid regions NDVI can give reasonable information on vegetation canopy, although the presence of rocks can affect the reflectance of the images. In this case SAR data can add some information, as it can be noted in the diagram of Fig. 3, where a direct comparison of

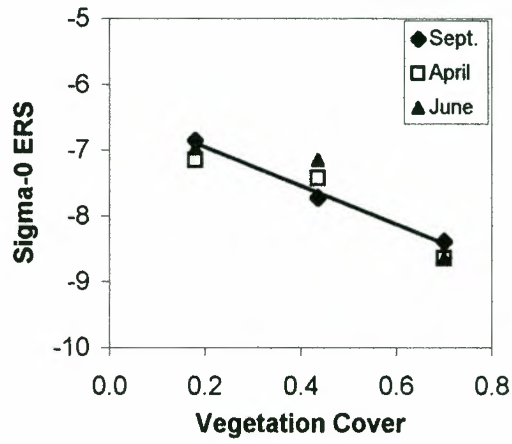

Fig. 2 – ERS/C-band σ^0 as a function of Vegetation Cover measured on Alfa canopies.

optical and radar data is shown. We can observe that NDVI (Normalized Difference Vegetation Index) is able to better separate Alfa and Mugwort than the ERS backscattering. However, the spread of data in $\sigma°$ is related to the vegetation cover, the latter changing from 0.2 to 0.7 from the right to the left of the clusters (Paloscia et al 2001).

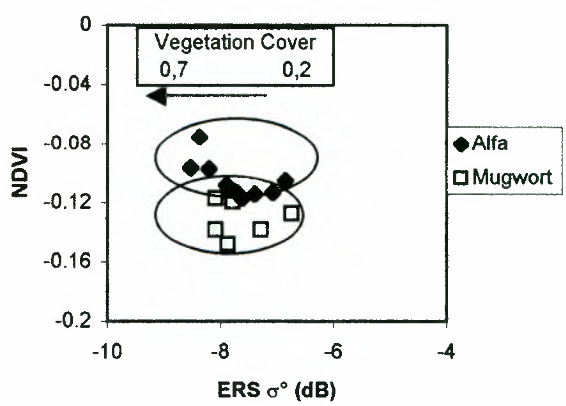

Fig. 3 – NDVI vs. σ^0 at C-band for Alfa and Mugwort

- *Sensitivity to soil surface characteristics*

Due to the nature of the soils present in the area, a quantitative description of their surface including stone cover, stone shape, stone dimensions, etc, appeared very difficult to obtain. Thus, soil surface was characterized qualitatively by assuming four classes of stone cover, from 1 for little stones to 4 for stones with a dimension larger than 30 cm.

At L-band σ^0 was not related to the surface characteristics, whereas, at C-band, a general increasing trend as a function of stone dimensions could be noted

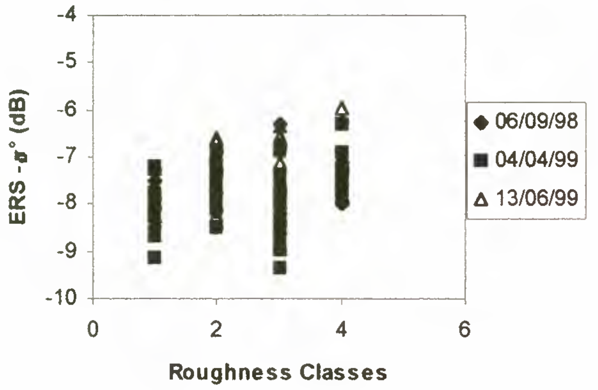

Fig. 4 – JERS-1/L-band σ^0 as a function of the stony classes.

in spite of a rather high dispersion of points, especially for class 3 (Fig. 4).

Although the description of surface characteristics is no directly related to geometrical quantities, these results are in agreement with hose obtained by Deroin et al. (1997). In their study the authors found that C-band σ^0 of arid land increased ass a function of the maximum height of the rocks (h_{max}, in cm) and proposed the following empirical relationship between these two quantities:

$$h_{max}=23\ e^{0.2\sigma^0}$$

By applying this relationship to our data, we found that the maximum height of rocks ranged from 3.5 to 6.8 cm and was in reasonable agreement with ground observations (Paloscia et al., 2001).

- *Interferometric analysis*

The identification of some land features in the area was carried out by using coherence maps obtained from repeat pass interferometry (Wegmuller et al. 1997). The interferometric analysis of Morocco area, including the five test-sites, was carried out using six ERS-SAR-SLCI images (CEOS format) collected from ESA-ESRIN within the framework of this project and of the ESA ERS project AO3. The images were acquired in the following dates: 14/04/1997, 01/09/1997, 10/10/1999, 08/05/2000, 17/07/2000 and 25/09/2000.

By coupling these 6 SLCI images two by two, 15 different coherent images were produced. In particular, two couples were used for obtaining two maps which showed the highest resolution and the minimum noise respect to the others. Couple 1: 14/04/1997– 01/09/1997 and couple 2 : 17/07/2000 – 25/09/2000. After the co-registration, interferogram and coherence maps were realized. From the coherence maps (Fig. 5 a and b) we note that, in general, for the couple 1 the coherence is in general low (black =low coherence and white = high coherence) whilst for the couple 2 the coherence is rather high.

Fig. 5 - coherence maps: couple 1 (a): 14/04/1997– 01/09/1997 and couple 2 (b): 17/07/2000– 25/09/ 2000. (black = low coherence and white = high coherence) (Area dimensions: 28 x 32 Km^2)

The high mean value of coherence for the couple 2 is due to the fact that both images were acquired during the summer period where, due to the absence of rain events, vegetation and soil remains practically in the same condition. Vice versa, for the couple 1, the images were collected in two different periods: the first in April where vegetation and soil were in the most wet period of the year and the second in September where soil and vegetation were in very dry condition. In addition we can assume that the major effects is due to vegetation and not to the soil moisture, since in the image is possible to distinguish some area (corresponding to bare soil) where the coherence is high whilst if we had an high mean value of soil moisture for the first image (for example due to a rain event) a low level of the coherence was expected in the whole image.

To better investigate these aspects a color composite image (RGB) was obtained by combining the coherence of the 2 couples of ERS images and the difference between the two coherence images. This approach made it possible mapping semi-arid vegetation and separating five land classes: mountains or rocky areas, deserts, areas covered by spontaneous semi-arid vegetation, humid areas with agricultural vegetation, and rivers or ridges (Paloscia et al. 2001). To validate this INSAR classifier, a comparison with an optical classifier, which was developed and tested by EMI team, was carried out.

A visual inspection of the images demonstrated that the two classifiers were in good agreement to each other.

CONCLUSIONS

The capability of L- and C-band SAR data in assessing land features has been confirmed, also in semi-arid lands. The analysis of backscattering coefficient of JERS-1 and ERS satellites showed a rather good agreement with the vegetation cover of at least one type of natural vegetation (Alfa). The interferometric analysis pointed out that using two coherence images a classification map showing five different cover classes can be obtained.

REFERENCES

Deroin J.P., A. Company, and A .Simonin, "An empirical model or interpreting the relationship between backscattering and arid land surface roughness as seen with SAR", *IEEE Trans. on Geosci. and Remote Sensing,* vol.35, pp. 86-92, 1997

Evans D.L., T.G.Farr, J.J.van Zyl, "Estimates of surface roughness derived from synthetic aperture radar (SAR) data", *IEEE Trans. on Geosci. and Remote Sensing,* vol.30, pp. 382-338, 1992

Paloscia S., M.Bianchini, G.Macelloni, P.Pampaloni, E.Santi, N.Aquid, D.Ouazar, M.Zribi, "Estimating vegetation cover and soil roughness in semi-arid regions from multi-temporal dual-frequency SAR data" *Proc. of Geoscience. and Remote Sensing Symposium (IGARSS 2001).*

Tansey K.J., and A.C.Millington, "Remote sensing of desert surface processes and properties using multi-temporal radar imagery", *Proc. of Geoscience. and Remote Sensing Symposium (IGARSS'98),* vol. 3, pp. 1348-1350, 1998.

Wegmüller U., T.Strozzi, T.Farr, and C.Werner, "Arid land surface characterization with repeat pass SAR interferometry", *IEEE Trans. on Geosci. and Remote Sensing,* vol.35, pp. 86-92, 1997

POTENTIAL CONTRIBUTION OF ENVISAT ASAR ALTERNATING POLARISATION AND WIDE-SWATH MODES IMAGES FOR CROP DISCRIMINATION AT THE REGIONAL SCALE

X. Blaes[1], F. Holeck[2] and P. Defourny[1]

[1] Department of Environmental Sciences – Geomatics, Université Catholique de Louvain
Croix du Sud 2/16, B-1348 Louvain-la-Neuve, Belgium, +32 10 47 26 13 (T), +32 10 47 88 98 (F)
blaes@biom.ucl.ac.be, defourny@biom.ucl.ac.be

[2] Sarmap s.a.
Cascine di Barico, CH - 6989 Purasca, +41 91 600 9366 (T), +41 91 600 9369 (F)
francesco.holecz@sarmap.ch

Abstract: This experimental study was carried out in the framework of the DUP project "Dedicated Remote Sensing Product Generation for the Agro-Industry: Cereal Case" leaded by Synoptics b.v. (NL). The main objective is to investigate the potential contribution of the ENVISAT images for the discrimination of the main crops at a regional scale. ASAR Alternating Polarisation (AP) and Wide Swath (WS) modes have been simulated from 15 ERS images over Belgium. A quantitative approach was completed using 791 parcels corresponding to the following crops: winter wheat, winter barley, spring wheat, spring barley, grasses, sugar beet, maize and potato. The impact of the spatial resolution of the ASAR sensor is assessed through the comparison of the results obtained for the AP (30m) and WS (150m) modes with regards to the field size. Both pixel-based and parcel-based unsupervised classification approaches have been applied. Dedicated interpretation schemes were developed for specific crop discrimination. The promising results obtained from the 150-m ASAR signal are expected to be further enhanced by the very high acquisition rate of the WS mode, i.e. an acquisition every 3 to 5 days.

Keywords: crop discrimination, ENVISAT, Wide Swath-ASAR, coarse spatial resolution.

1. INTRODUCTION

The SAR sensors capabilities for agriculture monitoring have been largely documented in the literature but the temporal resolution and the spatial extension of the acquisition was often found as a major constraint for any operational use. The potential contribution of coarser SAR sensor, such as the Wide Swath (WS) mode of the ASAR sensor, has not been investigated yet. In the framework of the project "Dedicated Remote Sensing Product Generation for the Agro-Industry: Cereal Case" leaded by Synoptics b.v. (NL) [2] and sponsored by the Data User Programme (ESA-ESRIN), two main questions have been addressed with regards to the ASAR use for crop inventory with regards to agro-business needs :

(i) what is the ASAR WS signal content for the crop discrimination?

(ii) would it be possible to process the ASAR WS signal without any a priori information?

The first question deals with the impact of the 150-m spatial resolution of the ASAR sensor. This resolution is coarser than the current SAR sensors in orbit but the signal speckle is expected to be slightly reduced because of the larger number of look (ENL > 11.5). This scaling issue is based on the comparison of the results obtained for the respective AP and WS modes time series simulated from the same ERS data set. In this first step temporal profiles and parcel-based classifications are computed using a priori field boundaries knowledge in order to put the emphasis on the 150-m signal content analysis. In this perspective the contribution of the higher temporal resolution of the ASAR WS mode, i. e. an acquisition every 3 to 5 days, is discussed.

The second step investigates the accuracy of the pixel by pixel classification and documents the impact of the a priori knowledge of the field boundaries for the ASAR WS data interpretation.

2. AVAILABLE DATA

The study relies on a data set including 15 ASAR WS and AP simulations (from ERS SLC) acquired from early January 95 to late October 95 (Figure 1). The field data set consists of about 800 parcels covering 8 crops and the hourly rainfall distribution for 5 meteorological stations. The first four images were acquired during the ERS F phase from four different orbits while the following were recorded during the G phase from only 2 adjacent tracks (151 and 423). The study area located in the Région limoneuse (Belgium) was selected to include environmental variability including various topographic and field size conditions.

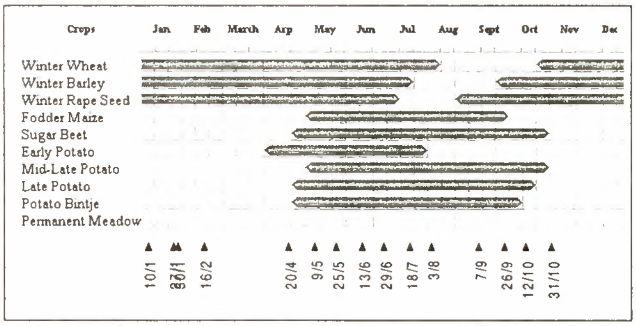

Figure 1: Crop calendars as observed for the study area in 1995. The distribution of the 15 ERS acquisition dates are also shown at the bottom.

Proc. 3rd International Symposium, 'Retrieval of Bio- and Geophysical Parameters from SAR Data for Land Applications', Sheffield, UK, 11-14 September 2001 (ESA SP-475, January 2002)

The image and vector data set has been integrated in an image processing system to extract the signal mean per object, i.e. per field. For the AP simulations, a buffer zone of 1 pixel around the field boundaries was used to discard the mixel located at the field edges. On the other hand, no buffer zone could be used for the WS simulation because of the critical field size with regards to the 150-m resolution.

For the inter-calibration simulation each simulated image has to be adjusted using a coefficient computed to match the track averaged value of a forest zone to the temporal signal mean calculated by track. The temporal signal average of the 151 AP mode track serves as reference.

The data management system used for the research allows to address the various issues using respectively image processing system, regular tables processor or advanced statistical packages, such as the SAS software, according to the analytical requirements.

3. ASAR SIMULATION METHODOLOGY

3.1. Alternating Polarization Mode

The acquisition scheme of ASAR AP raw data is shown in the Figure 2a. The system acquires echoes in a first polarisation for a time interval TB (burst), then switches in a second polarisation for a time interval of same length (burst), then back to the first polarisation and so on. The unfocussed response of three point targets at different azimuth positions is drawn as a solid line: different parts of the Doppler history are acquired at different polarizations, corresponding to different bursts. The theoretical instantaneous azimuth spectrum of the AP data is illustrated in the Figure 2b for a case when the burst time TB is exactly equal to half of the aperture time TA.

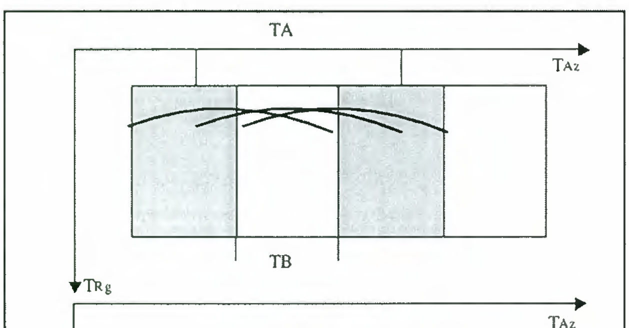

Figure 2: ASAR Alternating Polarization data: temporal distribution of the ASAR AP data (a) and spectral distribution of the ASAR AP data (b).

The polarization separation filter, shown in Figure 3, can be constructed easily by referring Figure 2b. The basic filter is composed of a summation of NS/2 ideal band pass filters of bandwith BWB, spaced in the frequency domain by a distance 2BWB. Its frequency response may be written as:

$$H(f) = \sum_{k=-Ns/4}^{Ns/4} rect(\frac{f - 2kB_{wb}}{B_{wb}})$$

where: NS = TA / TB
= f PRF / fM TB
= f PRF / BWB

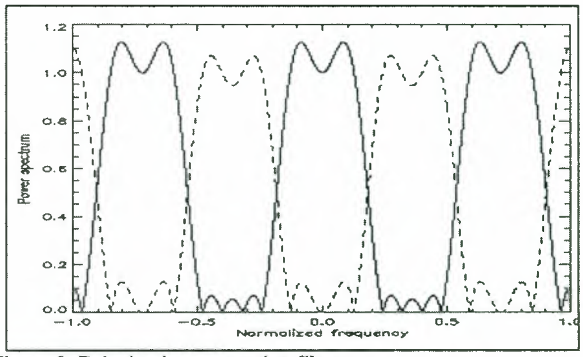

Figure 3: Polarization separation filter.

Summarizing, the AP simulation chain can be described as follows:

i. Single Look Complex (SLC) azimuth filtering according to AP burst pattern.

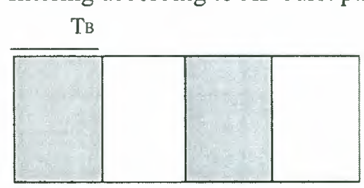

ii. Detection.
iii. Multilooking

3.2. Wide Swath Mode

The WS mode simulation can be straightforward derived from the AP mode. Therefore, the simulation chain can be summarised as follows:

i. SLC azimuth filtering according to WS SAR burst pattern.

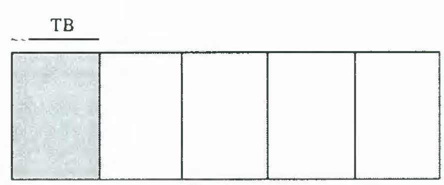

ii. SLC range filtering to reduce the bandwidth.
iii. Detection.
iv. Multi-looking.

A detailed description of the algorithms is given in Pasquali et al., 1999 [1].

4. Object-based approach

4.1. WS signal sensitivity to crop types

The WS signal content was first assessed using the mean profiles of the largest fields, i.e. bigger than 6 WS pixels, located in the study area. The differences between the temporal profiles of the main crops (Figure 4a) clearly demonstrate a differentiation of the ASAR WS temporal profiles according to the crop type.

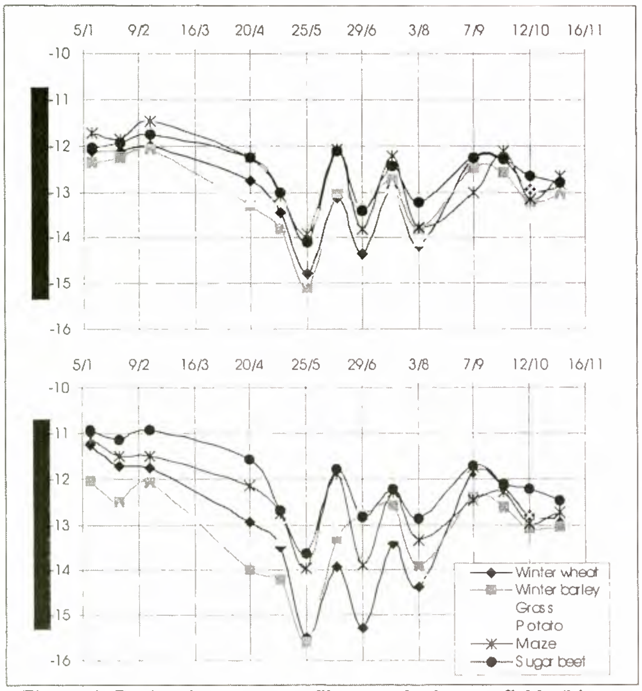

Figure 4: Regional average profile over the largest fields (bigger than 6 pixels) for the ASAR WS mode (top graph) and ASAR AP mode (bottom graph). The curves are computed using 95 winter wheat, 27 winter barley, 70 grasses, 20 potato, 5 maize and 88 sugar beet fields.

This information content was compared to the ASAR AP mode time series for the same set of fields (Figure 4b). For a given date, the range between the signal of the various crop types was almost two times larger for the AP mode than for the WS mode. The variation over time for the different crops were more independent in the AP mode than in the WS mode. The WS signal range between crops is smaller and the profile shape of barley or grasses tends to be more similar to the overall trend. This is of course related to the smoothing effect associated to the mixed pixel (border pixel) which is much stronger for the WS mode.

However, the WS regional profiles are quite consistent to the AP profiles, despite the small number of pixels included in each field. It must be noticed that the spring wheat and spring barley profiles were not plotted because the number of large fields for these crops was too small.

4.2. Scaling issues

Field size impact according to each crop

The variability of the profiles due to field size must be studied using subset including the same number of fields for each size class. This was only possible for winter wheat and sugar beet, thanks to their field size diversity. Figure 5 indicates an impact of field size of maximum 0.5 dB on the mean for winter wheat crop. The impact on the mean is stronger for the drier days of the period with contrasted crop stages in the fields (29 June and 3 August). However, the evolution of the standard deviation of the means according to the size class shows a strong influence of the field size; the bigger variations over time are observed for the smaller fields. The sugar beet case leads to similar conclusions but is not presented here.

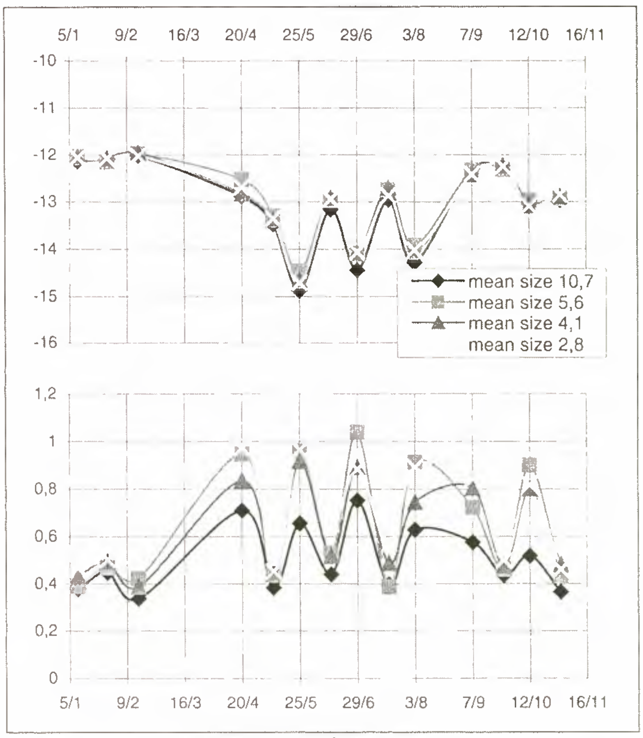

Figure 5: Field size impact on WS winter wheat regional profiles computed from the same number of fields (n = 63 for each subset). The top graph presents the evolution of the means and the bottom one shows the standard deviation of the means. The mean fields size is expressed in WS pixels.

Field size impact on crop discrimination

For this purpose the fields were clustered into 4 subsets defined by field size intervals. However, the number of fields belonging to each size class varied much.

The differences between the profiles of the 6 studied crops decreased with the size of the fields included in the regional average. The discrimination power is lost for the small fields in the WS mode. While the smaller fields introduced some noise in the profile, the overall crop profiles including all the fields still allowed some crop discrimination. This impact is clearly illustrated by the Figure 6 for the wheat – barley discrimination possible in early April and late June. On the opposite no field size effect was observed for the AP mode (the smaller fields still include 26 AP pixels).

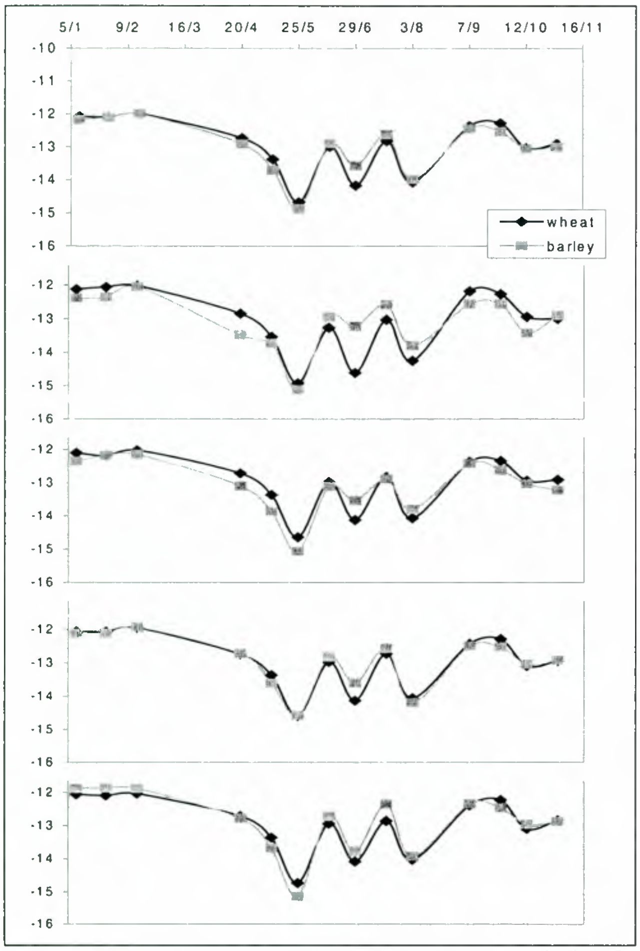

Figure 6: Wheat and barley profiles for all the fields (graph a) and for subsets with decreasing fields sizes: equal or bigger than 10 pixels (b), from 6 to 9 pixels (c), equal 4 or 5 pixels (d) and equal 2 or 3 pixels (e). The field size is expressed in WS pixels.

4.3. Temporal issues

The coarse pixel size is expected to be balanced by the very high temporal resolution of the ASAR WS mode. Of course it is not obvious to document the effect of a 3 to 5-day temporal resolution using a 16 or 19-day temporal resolution data set. However, the latter demonstrated the strong interaction between rainfall and crop types, and its specific variation during the season. Such an approach could foreseen only if a very high temporal resolution is available.

The regional profiles obtained for the different crops shown in the Figure 4 are strongly affected by the rainfall distribution. The two peaks observed in June and in July can be directly related to the rainfall distribution. The cumulated rainfall corresponding to the 24-h period before the acquisition reaches 14 mm on the 13 June and 2 mm on the 18 July and on the 7 September. There is virtually no rainfall recorded for the 24-h period before the other acquisitions.

The most interesting point is the evolution of the relative sensitivity of the crop signal to the soil moisture. This evolution varies according to the crop type and could be used to discriminate them. For instance, the mid-June moisture affects much more the sugar beet signal than the winter wheat (difference between the 25 May and 13 June signals is much higher for sugar beet). On the opposite, the mid-July soil moisture influences much more the winter wheat profile than the sugar beet one (difference between the 18 July and the 3 August signals is much higher for winter wheat). Various indices have been tested to discriminate the crop type using this contrasting behaviours with regards to the soil moisture. A simple threshold of the ratio of these two temporal differences reaches a classification accuracy of 70 % between leafy and cereals crops, if the grasses are not considered. These results are clearly promising and are expected to be enhanced if the time interval between consecutive acquisitions is reduced. The probability to get the appropriate data set for such an interpretation approach is quite high using the ASAR WS mode (Figure 7).

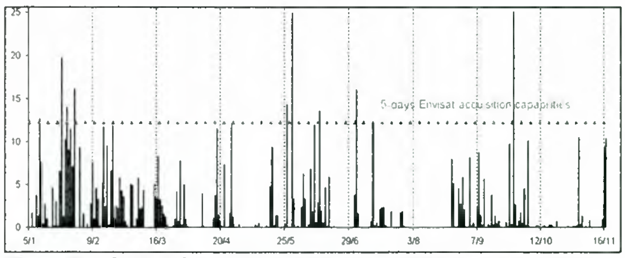

Figure 7: ASAR WS mode acquisition capabilities with regards to the 24-h cumulated rainfall for the year 1995.

On the opposite the high temporal resolution should allow to discard all the acquisitions affected by recent rainfalls without any consequence on the temporal profile. This would be a critical step forward for a more automatic classification.

4.4. Parcel-based classification

The results described above call for the investigation of crop discrimination using parcel-based algorithms. Because the bigger parcels contributed for most of the crop production, only 306 parcels were considered for the classification (59% of the surface covered by the 791 parcels). These bigger parcels showed also more consistencies in their time profiles.

Various interpretation schemes have been applied. From Figure 4 several combinations of dates have been tested using unsupervised classifications. The best results were obtained using April, May and June images and provided an overall accuracy of 67%. This would have the main advantage of delivering the results before the end of June. Just better accuracy (68%) was achieved using time series indices in addition to this combination. Table 1 fully describes the results of the various combinations. The first index, called range index, corresponds to the difference between the maximum backscattering value of the time series and the minimum value. The second index is the ratio between two values: the difference between the backscattering of the 13 June and 25 May and, on the other hand, the difference between the 18 July and the 3 August. As it was explained in the previous section, this ratio index takes into account the differential rainfall effect on the different crop types.

Used channels	Accuracy	Delivery time
1) 20/4, 25/5, 13/6 & 29/6	67%	End of June
2) Range & ratio index	59%	September
3) 20/4, 25/5, 13/6, 29/6, range & ratio index	68%	September
4) 9/5,·25/5, 29/6, 3/8 (dry days)	63%	August
5) 13/6, 18/7, 7/9 (wet days)	63%	September
6) 3-step strategy :	83%	
step 1 : grass discrimination 10/1, 28/1, 7/9	85%	
step 2 : cereals discrimination 13/6, 18/7, ratio index	85%	
step 3 : wheat/barley discrimination 20/4, 25/5, 29/6	82%	September

Table 1: Performances of parcel-based unsupervised classification applied to different data combinations.

The relevant information for a specific discrimination provides some noise for an other discrimination. Therefore a 3-step strategy was proposed for the cereals identification. First January and September images were used to distinguish the grasses from the other crops with an accuracy of 85%. Then the cereals/no cereals classification based on the June, July and the differences ratio reached an accuracy of 85% as well. Finally the winter wheat and the winter barley were distinguished the best with an accuracy of 82% using the April, May and June images. The June date alone contributes for 79% of this discrimination. This 3-step strategy classifies correctly 83% of fields between the winter wheat, the winter barley and the other crops.

5. Pixel-based classification approach

5.1. Classification

The per-pixel classification is the most simple way to extract the information and it does not required any ancillary data. An unsupervised classification has been applied to cluster the pixels of the agricultural zone (mask of the agricultural region covering 2 NUTS) into 69 classes based on the following dates : 20 April, 25 May, 13 June and 29 June. The 69 clusters have been grouped and labelled based on the field information belonging to one NUTS zone. The other NUTS zone was used to validate the classification and the labelling into crop types. Only 3 different labels were attributed : winter wheat, grasses, and sugar beet. The overall accuracy of this classification reaches only 47% of the pixels (Table 2).

This result can be carefully compared with the 67% accuracy obtained by the parcel-based 1-step classification using the same dates combination. However this was 67% of parcels and concerns only the bigger parcels, while the 47% result includes all the agricultural pixels without any field size consideration. Furthermore, the parcel-based classification accuracy could not be assessed using an independent validation set.

Real classes	Attributed classes: WW	WB	G	P	M	SB	OM
WW	243		88			68	39,1
WB	64		51			54	100
G	82		136			60	51,1
P	6		0			16	100
M	14		8			20	100
SB	113		33			219	40
COM	53,4	0	57	0	0	49,9	

General accuracy: 46,9%

Table 2: Confusion matrix of the per-pixel classification approach. The omission and commission errors (respectively OM and COM) are expressed in percentage of pixels; other values are the number of pixels. The class symbols are WW= Winter wheat, WB= Winter barley, G= Grasses, P= Potato, M= Maize and SB= Sugar beet.

5.2. Colour composites

Based on the temporal profile presented in the Figure 4, some colour composites have been made using different combinations of channels. The most simple way is to assign an image channel to each of the 3 colours (red, green and blue). Figure 9 presents such a combination of 3 dates : the 20 April, the 29 June and the 7 September. On this composite, cities appear in white or green. The temporal profile of the 6 main crops show a higher backscattering coefficient on the first and/or the last date than in the second one (Figure 4). Therefore, the majority of the agricultural areas is coloured in red, blue and magenta (additive colour mixing of the red and blue). This composite was compared with a map indicating the main crop types in the region. The cereal fields appear principally in blue (higher value at the third date than the two first), the sugar beet and potato fields appear mainly in magenta (low value at the second date) and the grass parcels are coloured in green (due to a more stable profile than the other crops).

The composite presented in Figure 10 was built using only neo-channels : the difference of the intensity of the 13 June and the 25 May, the intensity difference of the 18 July and the 3 August and the ratio of the first difference by the second. The first important thing to note is the high level of noise. However, most of the cereal fields appear in green and most of the leafy crops are in magenta. This composite represents the differential rainfall effect on the different crop types.

Not all crops are discussed here. So, in all of the colour composites, even if the majority of the fields of one considered crop type appear in the same colour, not all fields of this colour do probably correspond to this crop type. Moreover, the observed colour composites were made using Wide Swath simulation, i.e. with pixels of 100 meters resolution. This critical pixel size is represented in the Figure 8, with regards to the fields size. So, the WS pixels have to be considered as mixels.

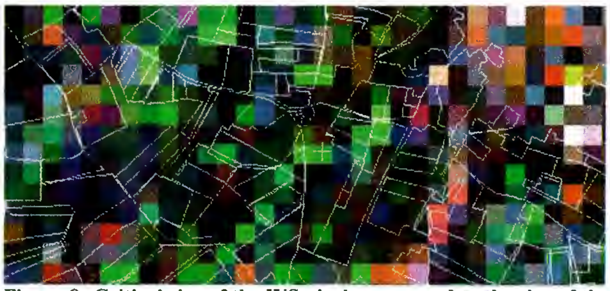

Figure 8: Critical size of the WS pixels compared to the size of the fields (drawn in white).

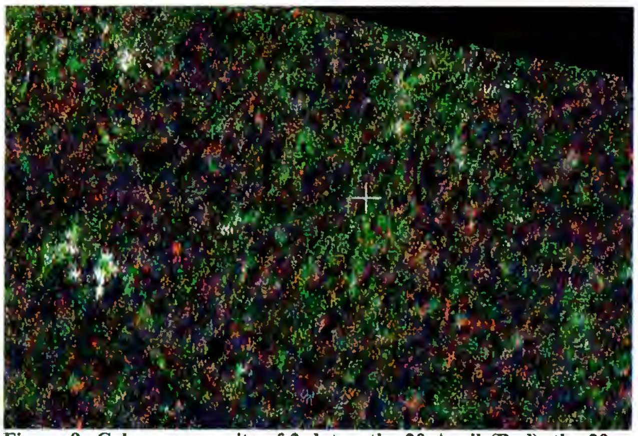

Figure 9: Colour composite of 3 dates: the 20 April (Red), the 29 June (Green) and the 7 September (Blue).

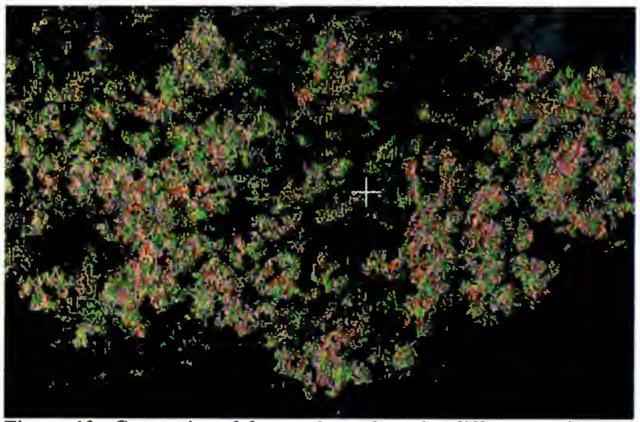

Figure 10: Composite of 3 neo-channels : the difference of the intensity of the 13 June and the 25 May (R), the difference of the intensity of the 18 July and the August (G) and the ratio of the first difference by the second (B). Non-agricultural area are masked.

6. PRACTICAL AND POTENTIAL OPERATIONAL USE OF RESULTS

This study used a set of ASAR WS simulated images to figure out what kind of crop information could be extracted and when this could be delivered in an operational context.

The results clearly demonstrate the following:

- Field boundaries are a prerequisite for crop identification.
- It is feasible for large fields (> 6 ha) to distinguish between winter wheat and winter barley with an accuracy higher than 80% (thanks to field boundaries a priori information). This result can be delivered by the end of June because most of the discrimination is due to the shift of the ripening phase between both crops. Very similar performances are obtained for the leafy crops or specifically for the sugar beet at the same conditions.
- Grasses are easily detected with an accuracy of 85%.
- The WS mode is useful for crop area estimation but sensitive to the field size distribution. The larger is the fields, the better the discrimination. The crop area made up by small fields can not be considered.
- High temporal resolution will have a great impact on crop identification results if detailed rainfall distribution figures are also available.

It is important to keep in mind that the results presented here were obtained from a time series of 15 images while the ASAR WS mode will provide 60 images for the same period. The experiment clearly demonstrated the usefulness of rainfall data as ancillary information. The same classification performances were achieved from the dry dates as from the wet dates, as long as they are processed separately. Furthermore, new indices based on good knowledge of the crop stages and their respective interaction with soil moisture for the signal backscattering, are expected to further enhance the current results.

The study has been carried out in a region with rather medium to small field sizes compared to the important European regions for agriculture production. It is therefore difficult to be sure that field boundaries will remain a prerequisite.

These conclusions of course assume that the simulations used in this experiment correspond to the quality of the ASAR WS images provided by the sensor once it will be in orbit.

7. REFERENCES

[1] Pasquali P., D. Small., F. Holecz, A. Schubert, E. Meier, and D. Nuesch: ENVISAT ASAR ESL Alternating Polarization Mode Product Study and Simulation, Final Report, Remote Sensing Laboratories, University of Zurich, 1999.

[2] van der Werf N., DUP Dedicated Remote Sensing Product Generation for the Agro-Industry: cereal Case, Final report, Synoptics, Wageningen, The Netherlands, 30 June 2000.

FARM CROP AND AGRI-ENVIRONMENT END-USER REQUIREMENTS FOR REMOTE SENSING

P.M.R. Dampney*, J.A. Slater and M. Silgram

*Corresponding author: ADAS Boxworth, Cambridge CB3 8NN, UK
Tel: +44 (0)1954 268213; Fax: +44 (0)1954 267659
email: peter.dampney@adas.co.uk; jacqueline.slater@adas.co.uk; martyn.silgram@adas.co.uk

ABSTRACT

This paper outlines the range of requirements that farmers and those concerned with protecting the environment may have for remote sensing-derived information. Remote sensing researchers and system developers must have a clear understanding of these requirements so that research can be effectively focused. Key issues include:- the relevance of derived information, measurement accuracy, spatial resolution, timeliness, reliability of information supply, robustness of interpretation, data handling, cost and end-user confidence.

INTRODUCTION

Unless research is carried out for purely academic reasons, it is important for research scientists to have a good understanding of the potential end-uses of their research. Without this understanding, the strategy and priorities of a research programme can be miss-directed. This can lead to wasted effort, missed opportunities, unanswered questions and proposed solutions which are either impossible or difficult to implement on a commercial operational basis.

The science of remote sensing/Earth Observation (EO) is very different to those of agronomy and environmental management. It should be no surprise therefore that there is often a weak understanding of each others science, aims and objectives, and practical constraints. Although the situation is improving, it is suggested that there is still plenty of scope for a much closer working relationship between the EO science and information provider communities and the agri-environment end-user community. Without a close working relationship between these communities, the full potential of EO may not be realised.

This paper is directed to research scientists and system developers working in the field of remote sensing and EO who are carrying out research to develop practical uses for EO based information for crop management by farmers and for measuring and monitoring the natural land and water environments. The aim of this paper is to identify the information requirements of these end-user communities. The use of EO for classifying agricultural crop types is not considered.

ARABLE CROP MANAGEMENT

As in most businesses, farmers need information in order to take decisions. The information must be understandable, at an appropriate level of accuracy, and supplied in a form that can be easily applied in practice. It must also be provided reliably and at a time when it is relevant. Of most importance, the end-user must have confidence in the information, and consider it to be more cost-effective than alternative sources of information that may meet the same requirement.

Over many years, agronomic scientific research has identified numeric criteria/thresholds which should be used in practice as the basis for field-level decisions such as the selection of agro-chemical products and fertilisers, or their application rates. For example, the ADAS/University of Nottingham Centre for Agronomy has demonstrated the potential advantages of managing winter wheat according to crop physiological or 'Canopy Management' guidelines. In essence, this approach is geared to achieving an optimum crop canopy structure in terms of defined wheat plant and shoot populations, and the green area index (GAI) that will intercept most incoming radiation. Excessive shoot populations or amounts of green tissue are usually non-productive and are well known to aggravate disease and lodging problems. Agronomic research has shown that crop input decisions (e.g. use of nitrogen fertilisers, growth regulators, fungicides, herbicides) are likely to be most accurate where the crop condition in individual fields and field areas is measured quantitatively and then the use of inputs related to defined target benchmarks. The Wheat Growth Guide (HGCA, 1997) represents an important output of wheat physiological research. The Guide provides benchmark values for a typical wheat crop, providing farmers with a framework against which the management of their own crop can be measured, and input decisions made. Parameters found to be important include plant population (plants/m^2), shoot number (shoots/m^2), green area index (GAI) and nitrogen uptake (kg N per ha).

Proc. 3rd International Symposium, 'Retrieval of Bio- and Geophysical Parameters from SAR Data for Land Applications', Sheffield, UK, 11-14 September 2001 (ESA SP-475, January 2002)

However, there are currently no practical or cost-effective methods for gathering quantitative crop information. Thus, current methods of day to day decision-making are largely based on either subjective assessments from manual crop walking, or from representative crop or soil sampling which produces an average piece of information for a field or part of a field. Such sampling will not measure any crop or soil variation within the field which can be practically significant in many farming landscapes. Current methods used in practice also tend to be laborious, time-consuming and thus expensive.

The shortage of cost-effective crop measurement methods is a major limitation that is restricting the practical adoption of agronomic research knowledge by farmers. It is thus restricting the ability of farm businesses to move forward profitably and in an environmentally friendly way. As highlighted by Sylvester Bradley et al. (1995), Dampney et al. (1998) and King and Dampney (1999), remote sensing techniques seem to offer a potential solution to this problem. The development of reliable, robust and cost-effective sensing techniques to aid farm and field level crop management decisions is a recognised research requirement of the agricultural industry.

Remote sensing may also be able to provide information to aid whole farm management. Farmers (especially UK farmers) are managing increasingly large land areas and manual crop inspection is time-consuming and expensive. EO information could provide a means for rapid 'office-based' identification of crop or soil variations within individual fields across the whole farm allowing targeting of crop inspections, early warning of the location of pest or disease attacks, and comparison of crop development between fields to assist in the timing and prioritisation of crop management operations. Until robust quantitative interpretation models are developed for optical/radar data, this type of application identifying *relative* differences between cropped areas, but still requiring ground inspections, may have most potential for commercial development.

The development of non-destructive remote sensing techniques seems to offer a potentially cost-effective approach for gathering quantitative information rapidly over large areas and with good spatial structure. However, there are different remote sensing technologies (e.g. radar, reflectance) that may be more or less applicable to meet certain end-user requirements. There are different sensing platforms (e.g. satellites, aircraft, tractors, hand-held) and associated information delivery systems which will have different advantages and disadvantages, and there are different competitor methods to remote sensing that will be considered before the farmer or his adviser decides what to use or purchase. Finding the best solution for meeting a particular requirement will require an integrated approach taking account of all of these factors, and probably others as well. It is not within the scope of this paper to consider the merits of different sensor technologies.

In order to be practically useful and valued, it is important that a sensor based information service meets a range of customer needs. Significant weaknesses in any one aspect could seriously influence the potential value of the information.

Information relevance
The information must relate to an end-user requirement so that it can be used to help a decision process. A system that can measure something with a high degree of accuracy, but which has no relevance to a decision-making process, will be of no practical value. Table 1 summarises the range of decisions taken in a typical winter wheat cropping year, and the soil and crop growth information needed to take those decisions. In most cases, decisions also take account of field history, crop variety, experience and target markets. Most decisions are taken in the autumn and spring when crops are young or very rapidly growing. A similar basis for decision making is used for other arable crops though the details and timing may be different. For irrigated crops, irrigation decision-making is an additional requirement, currently based on calculated soil moisture deficits and/or fixed point measurements of this deficit.

Measurement accuracy and spatial resolution
In agricultural systems, perfect accuracy is rarely achievable. An acceptable degree of accuracy might be considered as something that equals or improves on a current standard, or which has a better cost-effectiveness. Information at an appropriate spatial resolution is important. Very high resolution is not likely to be cost-effective or indeed needed as the farmer will not usually be able to differentially manage very small crop areas. It is unlikely that farmers will wish to manage cropped areas smaller than 0.1 ha.

Timeliness
Information must be provided at a calendar time when it is needed (see Table 1). It must also be provided within an acceptable time lapse between acquisition and delivery to the end-user. Information provided *after* a decision has been taken will usually be of little use and will be regarded as a waste of money. In reality, information delivery within 7 days of acquisition is needed for most practical purposes.

Table 1: Information requirements for a typical winter wheat farmer

Farm decision	Timing	Soil or crop growth information needed	Commonly used current methods
Soil cultivations	Aug-Oct	Soil type and structural condition	Manual soil inspection
Seedrate	Sept-Oct	Soil type, seedbed tilth	Manual seedbed inspection
Nitrogen fertiliser use	Feb-May	Soil nitrogen supply, crop green area index (GAI)	Manual crop inspections (canopy and colour), soil chemical analysis
Weed control (herbicides)	Nov-Mar	Weed identification and population at young vegetative stage or when in head	Manual inspection
Pest control (pesticides)		Pest type and level	Manual inspections
Disease control (fungicides)	Apr-June	Disease type, disease level, early identification of disease foci	Manual crop inspections, regional diseases forecasts
Lodging control (plant growth regulators)	Mar-Apr	Shoot population, soil type	Manual inspection of crop and soil

Reliability of information supply

Farmers need to decide on their core information sources well ahead. For example, many farmers employ a consultant to walk crops throughout the season and provide crop management advice. Although remote sensing may have the potential to replace some current information sources, farmers must be convinced that any new method will be useful, cost-effective and supplied in a reliable way. Otherwise they may be left with no information on which to base decisions. The poor reliability of EO-based optical information due to UK cloud cover and short day-lengths particularly in the winter/spring months is well known, but is not a problem suffered by radar/SAR based systems. Sensors mounted on farm machinery may be an alternative way of implementing sensor technologies on farms, though would not achieve the near-instantaneous cover of large areas that is possible using airborne or space-borne sensors.

Robust interpretation of information

To be of practical use, a user must be able to interpret and apply information in a practical way. Currently, in spite of much research, there are no clearly proven methods (inversion algorithms) for reliably and robustly interpreting remotely sensed information into quantitative crop or soil measurements. Robustness of interpretation is crucially important and interpretation must be accurate under a range of environmental and crop conditions – e.g. the effects of different light levels (optical); soil conditions, crop surface moisture and wind, crop row direction, land slope (radar); crop variety characteristics.

Data handling

Raw data must be processed, interpreted and transmitted in a practically useable and user-friendly form, recognising that many farmers and advisers have weak skills in electronic data management, and limited time on a day to day basis for handling and making use of information. The compatibility of data from different sources is of increasing importance and it is essential that data is provided in a form that can be integrated with the electronic data handling systems used on farms.

Cost

The information must be cost-effective. Costs must include those associated with training and the on-farm equipment purchases needed for a new approach (e.g. computers for data handling, precision farming equipment).

End-user confidence

End-users (i.e. farmers and their advisers) will not adopt new technologies unless they are confident that the investment of cost and time is warranted. The agricultural industry is currently in decline and in the last few years has become increasingly sceptical of new 'precision farming' technologies where there has been strong publicity of new approaches to crop management but often with little convincing hard evidence from research or demonstration farm activities to show a good chance of positive cost-benefit. An aggravating problem is there has been insufficient encouragement for farmers to use the new technologies and approaches in a simple way before attempting more sophisticated and complex uses.

AGRI-ENVIRONMENT

Rural Policy & Environmental concerns
Rural development measures are experiencing a major expansion in support, with the UK Government switching from food production aids to support for the environment and the broader rural economy (Coates, 1999). The England Rural Development Programme provides a range of measures to encourage more environmentally beneficial farming and to facilitate the movement of farming, forestry and other rural businesses and communities towards changing markets. This approach benefits wildlife, the landscape and historic interest of the countryside, whilst helping farmers to modernise and restructure the farming industry. The principal agri-environment (AE) schemes, run by DEFRA (Department for Environment, Food and Rural Affairs) are the Countryside Stewardship Scheme (CSS) and Environmentally Sensitive Areas (ESAs). These two schemes alone already account for about 20,000 management agreements with farmers and landowners (JRC, 2001).

Coupled with this, there is a need to balance profitable agriculture with the maintenance of water quality within the standards laid down by national and international legislation, including the EU Habitats Directive and Nitrates Directive. The latter in particular has been the driver for several successful initiatives aimed at reducing losses from land with the objective of maintaining concentrations in water bodies below 50 mg/l (e.g. Lord & Archer, 1999). Concerns are now focusing on the planned implementation of the Water Framework Directive, which came into force in December 2000. Environmental concerns include losses of nitrogen, phosphorus, sediment and pesticides from fields into water courses. Nitrogen and phosphorus can contribute to the risk of eutrophication of water bodies with associated ecological impacts, while erosion and sediment loss can cause the siltation of river beds, inhibiting fish spawning.

End-users and their information needs
In contrast to profit-driven crop management applications, where farmers and their advisers are the primary end-users of EO information, agri-environment (AE) applications are typically driven by the needs of policy makers and their technical advisors at local, regional, national and international levels (Table 2).

In common with farmers and their advisers, policy makers and their technical advisors share the need for EO derived information that is cost-effective compared with alternative sources, of an appropriate level of accuracy, supplied in an interpreted form that is relevant to their needs, can be readily understood and is time.

Table 2. Example end-users of remotely sensed imagery to support the implementation of agri-environment policy

Spatial scale	Example end-user(s)	Example policy "drivers"
Field or farm	Farm managers; local EA* advisers, AE scheme Project Officers (DEFRA)	Local Environment Action Plans (LEAP)
River catchment or aquifer, designated area (e.g. ESA)	EA* regions, DEFRA policy makers & advisors	Water Framework Directive, England Rural Development Programme
National	DEFRA policy makers & advisors; EA*; NAW**; SEERAD***	Nitrate Vulnerable Zones (NVZ), Nitrates Directive, Habitats Directive, England Rural Development Programme
International	EU policy makers; Trans-boundary river commissions	OSPAR**** reporting

* Environment Agency
** National Assembly for Wales
*** Scottish Executive Environment and Rural Affairs Department
**** Oslo-Paris Convention for the Protection of the Marine Environment of the North East Atlantic

From the technical advisors perspective, remote sensing techniques have the advantages that the information derived could be available relatively quickly, is both spatially and temporally precise and is potentially available for relatively large areas at an affordable cost. These factors contrast with alternative sources of contextual data, such as agricultural census sources, which are retrospective (often over 2 years old), often spatially aggregated to parish or parish group level, and do not provide the same level of contextual information on the *management* of agricultural land, which is of such importance in limiting the risk of pollution loss from individual fields and in managing and monitoring agri-environment schemes.

Information gathering by technical advisors is often associated with specific government-led initiatives such as ESAs, Nitrate Sensitive Areas (NSAs) or NVZs.

Many of the agri-environment initiatives have a common requirement for a substantial GIS and image processing component to develop, implement and monitor the effects of more environmentally benign forms of land management. EO data are already being used at the various defined stages of the AE scheme chain (Figure 1) and have further potential to provide policy makers with the information they need. This potential is being encouraged by a number of research initiatives, such as the new NERC-funded LOCAR (LOwland CAtchment Research) thematic programme.

Figure 1. Stages of the AE chain

Analysis of end-user needs at each stage in the AE chain is necessary to ensure the development of relevant applications of EO data. For example, with compliance monitoring and other regulatory control, remote sensing may be considered as an alternative to site control and has been fully recognised as an "on-the-spot check" in the control of arable aids. A recent study (JRC, 2001) identified the following criteria as important for determining which AE measures might lend themselves to compliance monitoring using EO data.

- The measure is **widespread** and of **economic** importance.
- The measure is currently **costly** to control e.g. by site visits to measures operating in remote and inaccessible parts of the country.
- The measure is currently **difficult to control** directly by on-the-spot field visits particularly where management actions associated with the measure have to be implemented on many farms over a short period.
- The measure has the potential to be **fully controlled** by remote sensing.
- Remote sensing has the potential to be a cost-effective way of **supporting** or **targeting** traditional checks.

Applying the end-users criteria above, identified that EO data from current satellite based sensors, including IKONOS, SPOT, ERS and Landsat, have a potential role to play in the compliance monitoring of a range of field scale management practices (such as the cutting of hay meadows, heather burning and retention of winter stubbles) and in identifying the presence of small scale features of the landscape (such as hedges, walls, grass margins and beetle banks). The end-user requirements need to be kept under review by the research community. The movement restrictions imposed as a consequence of the current foot and mouth outbreak in the UK, resulted in the suspension of site visits for agri-environment management. The outbreak has heightened awareness of EO data as a visualisation tool, particularly in the absence of site visits, allowing simple presence / absence and measurement tasks to be performed for the management of agri-environment schemes.

Satellite imagery, including RADAR and optical imagery is well established as an operational and cost-effective means of detecting land-use change when monitoring the environmental impact of ESAs (Slater & Brown, 2000). However, from the end-users point of view, the application of remote sensing techniques needs to extend well beyond the identification of individual land use types. Research has demonstrated that site-specific factors of relevance to the agri-environment sector can be measured using satellite optical and radar data. Factors such as surface roughness (a function of cultivation method and timing, soil type and antecedent rainfall), effective slope length, and fractional ground cover (limiting the erosive power of incident precipitation), all affect erosion risk potential, surface runoff and the associated loss of sediment, phosphorus and surface-applied slurries from fields to watercourses. A BNSC LINK-funded consortium involving ADAS, Reading University and Infoterra (formerly NRSC) has demonstrated how such remotely sensed information may be used to constrain uncertainty in model predictions of nutrient pollution at both field and catchment scale (Hutchins *et al.*, 2000, Silgram *et al.*, 2001). Such applications of remote sensing can strengthen our understanding of the relationship between land use management and nutrient loss processes by identifying areas at high risk of loss both within and between fields. Methodologies and algorithms for processing remotely sensed imagery are of particular relevance to the developing implementation strategy for the new Water Framework Directive, which adopts the catchment as a *de facto* unit for environmental management.

Policy makers and agri-environment advisors require interpreted results from the analysis of remotely sensed data. They often have neither the time nor photo-interpretation skills to deal directly with EO data. As desktop GIS software packages such as ArcView become simpler for non-technical staff to use, Windows based applications are increasingly being developed as an effective means of distributing analysed EO data in the form of maps and reports. RDS is currently exploring ways of making remotely sensed data (orthophotography) directly accessible to agri-environment advisors.

ACKNOWLEDGEMENTS

The authors would like to thank those EO research scientists and system developers who have worked with them for their willing co-operation and keen interest to share and develop knowledge, with the common aim of developing improved and cost-effective information sources for farmers and others concerned with managing the environment.

REFERENCES

Coates D., (1999). The implementation of agri-environment policies. Proceedings of the ADAS Agriculture and the Environment Conference. 14-16 April 1999. University of Warwick. pp 26-30.

Dampney P.M.R, Bryson, R, Clark, W and Strang, M (1998). The use of sensor technologies in agricultural cropping systems – a scientific review and recommendations for cost-effective developments. Review report to MAFF, 125pp.

EA (2001). Water resources for the future: A strategy for England and Wales. Environment Agency, Bristol. 97pp.

HGCA (1997). The Wheat Growth Guide. Home-Grown Cereals Authority, Caledonia House, 223 Pentonville Road, London N1 9HY, 31pp, priced £5.

Hutchins, M., Silgram, M., Davenport, I., Settle, J., Robinson, S., Simmonds, L. & Veck, N. (2000). The role of earth observation techniques in improving field-scale predictions of runoff, erosion and pollutant fluxes *Aspects of Applied Biology* **60**, 219-224.

Joint Research Centre (2001). UK Pilot. Control of agri-environment measures using remote sensing & GIS. EC Contract 15467-1999-11 F1ED ISP GB. Unpublished ADAS/RDS report to the JRC.

King, J and Dampney, P.M.R. (1999). The potential of remote sensing technologies for measuring soil parameters. Review report to MAFF, 81pp.

Silgram H., Hutchins M, Settle J, Simmonds L.P and Veck, N (2001). Using earth observation techniques for constraining uncertainty in sediment loss predictions. Remote Sensing and Hydrology 2000 (Proceedings of symposium in Santa Fe, New Mexico, USA; April 2000), IAHS Publication **267**, 501-503.

MONITORING CROP CYCLES BY SAR USING A NEURAL NETWORK TRAINED BY A MODEL

F. Del Frate[1], P. Ferrazzoli[1], L. Guerriero[1]
T. Strozzi[2], U. Wegmüller[2], G. Cookmartin[3], S. Quegan[3]

[1]Università Tor Vergata, Ingegneria, DISP, Via di Tor Vergata 110, I-00133 Rome, Italy
Tel. +39 06 72597420, Fax +39 06 72597460, E-mail ferrazzoli@disp.uniroma2.it

[2]Gamma Remote Sensing, Thunstrasse 130, CH-3074 Muri BE, Switzerland
Tel. +41 31 951 70 05, Fax +41 31 951 7008, E-mail strozzi@gamma-rs.ch

[3]Sheffield Centre for Earth Observation Science, Hicks Building
University of Sheffield, Sheffield S3 7RH, UK
Tel. +44 114 22 3803, Fax +44 114 222 3809, E-mail s.quegan@sheffield.ac.uk

ABSTRACT

An algorithm, based on an electromagnetic model and a neural network, aimed at monitoring the multitemporal evolution of wheat fields, is described. Three different sites are used to validate the model, provide reference ground data, and test the algorithm.

1. INTRODUCTION

In the last decades, important advances have been achieved in the agricultural applications of SAR. Since the 70's, several ground based experiments proved a significant radar sensitivity to crop parameters, and results were summarized in important books (Ulaby et al., 1986). Further experimental studies were were carried out by means of airborne SAR campaigns. Finally, the launches of ERS, RADARSAT and JERS made it possible to monitor crop cycles continuously by means of spaceborne SAR's.

In parallel, crop scattering models are being refined. Vegetation elements such as leaf, stem and ear have been represented as discrete elements and their scattering and absorption cross-sections computed by theories developed for canonical shapes, that is discs and cylinders. Further developments are in progress, leading to include multiple scattering, leaf curvature and coherent interactions.

From the application point of view, the objective is the solution of the retrieval problem. It means that the evolution of important vegetation variables such as Leaf Area Index (LAI, m^2/m^2) and Biomass (kg/m^2) has to be estimated by means of SAR acquisitions. This problem is considered in the present paper, with specific reference to wheat fields. Three main steps may be identified: i) to adopt a convenient radar configuration, ii) to establish a reliable relationship between the backscatter coefficient σ° and the vegetation variables, and iii) to solve the inverse problem. As far as the first step is concerned, several studies indicate that the ERS configuration (i.e. C band, VV polarization, 23°), in spite of its limitations, may lead to interesting results for some crops, such as wheat and rice (Cookmartin et al., 2000; Le Toan et al., 1997). The second step is still in progress. Important advances have been achieved, but some studies indicate that present models are not yet sufficiently accurate (Cookmartin et al., 2000; Stiles et al., 2000). Finally, the third problem is very complex, since σ° depends on several soil and vegetation variables. Therefore, inversion based on a single radar observation is not feasible. Multiple observations are needed, and the problem shows difficult aspects in any case.

The idea suggested in this work is to use an electromagnetic model and a known multitemporal set of detailed ground data, collected in a reference site, to generate a multitemporal set of simulated σ°'s which, on its turn, is used to train a neural network. Then, a test site is considered. The network, using as input a multitemporal set of experimental σ°'s collected over the test site, estimates the differences between the crop cycle of the reference site and the crop cycle of the test site and, hence, the time evolution of its vegetation variables. Of course, the so obtained algorithm is based on some approximations, which will be critically discussed in the paper. However,

Proc. 3[rd] International Symposium, 'Retrieval of Bio- and Geophysical Parameters from SAR Data for Land Applications', Sheffield, UK, 11-14 September 2001 (ESA SP-475, January 2002)

it shows the advantage of fully exploiting the potential of multitemporal data and training the network with model outputs which consider the evolution of all vegetation variables.

Section 2 describes the experimental data, collected by the ERS-2 SAR over wheat fields of the Driffield (UK) site and by the RASAM scatterometer over wheat fields of the Central Plain (CH) site. The experimental data have been made available in the framework of an EEC Concerted Action, named ERA-ORA. Also some information about the reference site is given. Section 3 describes the electromagnetic model used to train the retrieval algorithm. The latter is described in Section 4. Section 5 shows and discusses the obtained results. Finally, indications about further studies, required to improve the accuracy of the algorithm, are given.

2. THE EXPERIMENTS

Three data sets are considered in this work. ERS-2 signatures collected at the Driffield site in 1997, as well as detailed ground truth, are used to critically estimate the accuracy of the electromagnetic model. RASAM signatures collected at the Central Plain site in 1988, with some fundamental ground data, are used to test the retrieval procedure. Finally, in order to train the neural network, the model is run using as input a detailed ground data set, collected at the French Avignon site with a sampling time of 3 days.

2.1. Model validation site (Driffield)

In 1997, several fields were monitored at the Driffield site by ERS-2 SAR. During the campaign, the important soil and vegetation variables were measured. In particular, multitemporal signatures of 3 wheat fields (numbered by 2, 3 and 5) are available. Radar data are accompanied by detailed information about soil moisture and soil roughness, as well as dimensions and moisture of leaf, stem and ear. The experiment is described and discussed by Cookmartin et al. (2000), where details are available. Some aspects, which are important to our objective, are summarized below.

Figure 1 shows the temporal evolution of volumetric Soil Moisture Content (SMC), crop biomass and backscatter coefficient measured by ERS-2. It is evident that simultaneous effects of soil drying and crop growing occur in springtime. Both effects contribute to lower the backscatter coefficient. Therefore, inversion of a single parameter by means of empirical methods is not reliable, but physical models are required to single out the different effects. For all the three fields a clear σ° minimum is observed at Day of Year (DoY) $\sim$ 150, followed by a slight σ° increase. The biomass, on its turn, shows the highest values in a subsequent time interval, i.e. between DoY 150 and DoY 200.

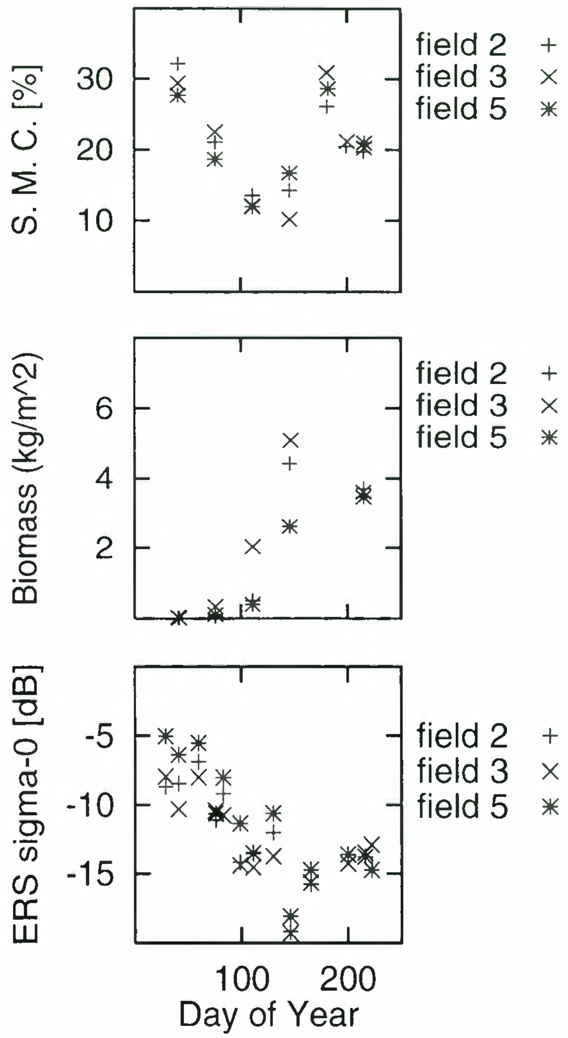

Figure 1. Temporal evolution of Soil Moisture Content, biomass, and σ° (measured by ERS) in the 3 fields of Driffield site

Figure 2 compares, in the three fields, the trends of geometrical variables, such as leaf width, stem diameter and ear diameter. Although with some differences, the time evolutions follow similar rules among the three fields. Therefore, developing retrieval algorithms based on a reference field, as it is done in this paper, appears to be reasonable. Of course, the accuracy of the algorithm will be improved if the reference field is taken in the same climatic zone and is of the same species and variety.

2.2. Test site (Central Plain)

RASAM is a microwave radiometer/scatterometer system. It operated over several fields in Switzerland between 1984 and 1991. Signatures were collected at the frequencies of 2.5, 3.1, 4.6, 7.2, 10.2 and 11.0 GHz, at several angles between 10° and 70°, and at VV, HH, HV and VH polarizations (Wegmüller, 1993). Ground data covered some significant parameters such as soil moisture, soil roughness, crop height, crop biomass, etc. In this paper, the retrieval

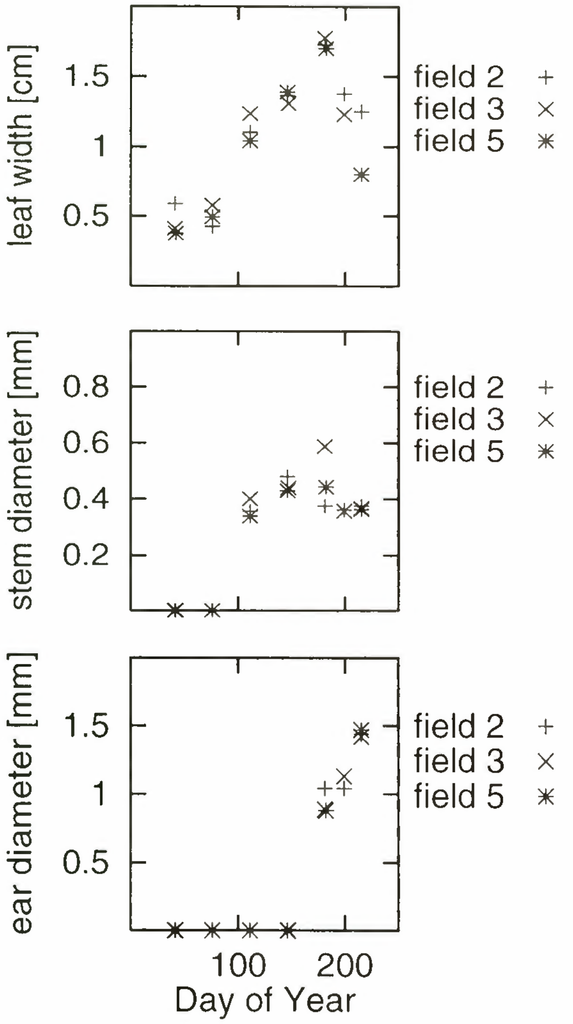

Figure 2. Temporal evolution of leaf width, stem diameter and ear diameter in the 3 fields of Driffield site

procedure is tested using multitemporal signatures collected over a wheat field in 1988 at the Central Plain site.

Figure 3 shows the time evolution of Soil Moisture Content, biomass and σ°. Two frequency bands, i.e 3.1 GHz (S) and 10.2 GHz (X), two polarizations, i. e. VV and HH, and an angle of 30° are taken. The SMC remains relatively high (i.e. $> 25\%$) during the whole cycle, with some limited and rapid variations. SMC effects on σ° are appreciable at S band, HH polarization, while are not evident at X band and/or at VV polarization. As far as general σ° trends are considered, a minimum similar to the one observed in Fig. 1 for ERS is noted at S band (particularly at VV polarization), while at X band the trend is monotonic decreasing.

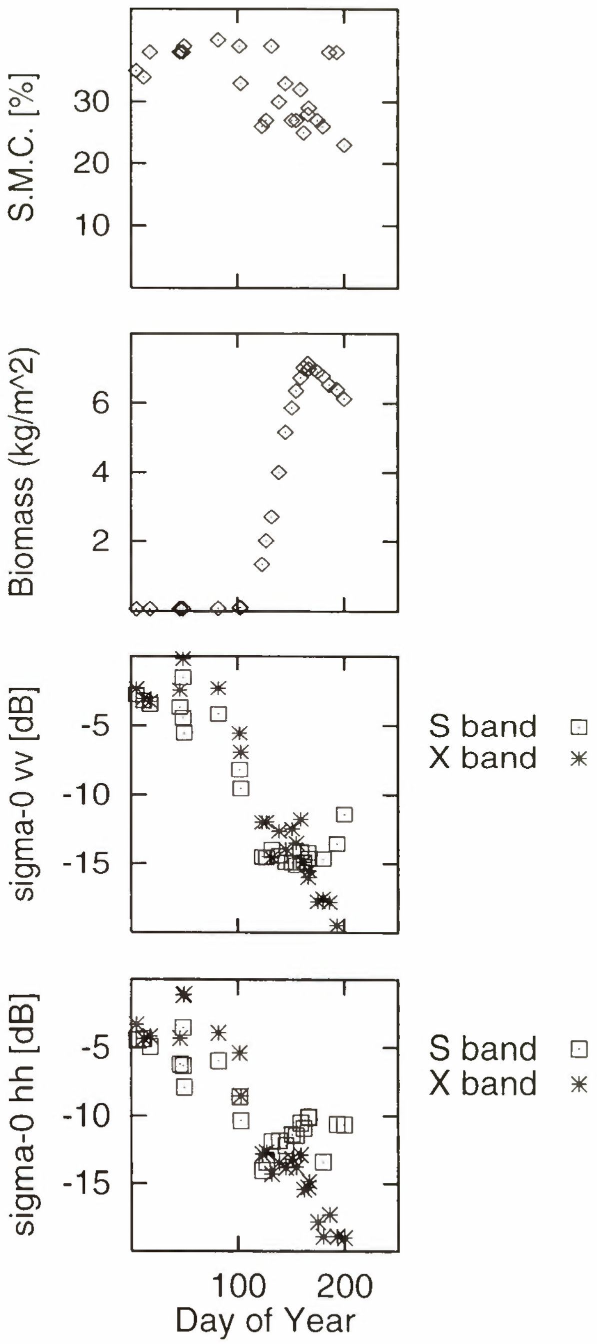

Figure 3. Temporal evolution of Soil Moisture Content, biomass, and σ° in the field of Central Plain site

2.3. Reference site (Avignon)

As it will be shown in the next Section, the neural network has been trained using a multitemporal set of simulated signatures with short sampling time. Of course, the same short sampling time was required for the ground data used as model inputs. Measurements carried out over a wheat field in 1993 at the French Avignon site have been used. Data covered all the important biophysical and geometrical vegetation variables, with a sampling time of 3 days. Details about the site and the measurements are given by Ferrazzoli et al. (2000).

3. THE MODEL

The model assumes the vegetation medium to be a homogeneous half-space with rough interface, representing the soil, overlaid by an ensemble of discrete lossy scatterers, representing the plant constituents.

The electromagnetic properties of the soil are described by its bistatic scattering coefficient. The latter is computed by the Integral Equation method with an exponential correlation function. The electromagnetic properties of the scatterers, which represent the plant constituents, are described by their bistatic scattering cross sections. Dielectric elements of simple shape, such as discs and cylinders, are used. For discs, representing leaves, the Physical Optics approximation is adopted. Cylinders represent stems and ears. For these kinds of scatterers computations are carried out assuming the internal field to be the same as that of an infinite length cylinder.

Once the bistatic scattering cross sections of the scatterers have been computed for a discrete set of incidence and scattering directions, the electromagnetic behaviour of the ensemble of scatterers is obtained. To this end, the matrix doubling algorithm is used, under the assumption of azimuthal symmetry. The same algorithm is used to combine the vegetation layer scattering contribution with that due to the soil. The backscatter coefficient of the whole medium is finally computed.

Details about the model are given in Bracaglia et al. (1995). In order to simulate the particular geometry of a wheat crop, we consider a lower layer filled with thin vertical cylinders, representing stems, and an upper layer filled with vertical cylinders, representing ears, respectively (Ferrazzoli et al., 2000). Discs, representing leaves, are distributed along the vertical direction. A uniform lower half-space with rough interface represents the soil.

The model is tested against Driffield data, since ground truth in this site are sufficiently detailed to be used as inputs. Figure 4 shows the results for the three wheat fields. A general agreement is observed during the growing phase, up to ~ DoY 150. Both the model and the experimental data show a decreasing σ° trend, which is due to both the soil drying and the vegetation attenuation increase. After this decreasing period, both simulated and experimental data sets show a minimum, followed by a slight increase in the late part of the cycle. A disagreement

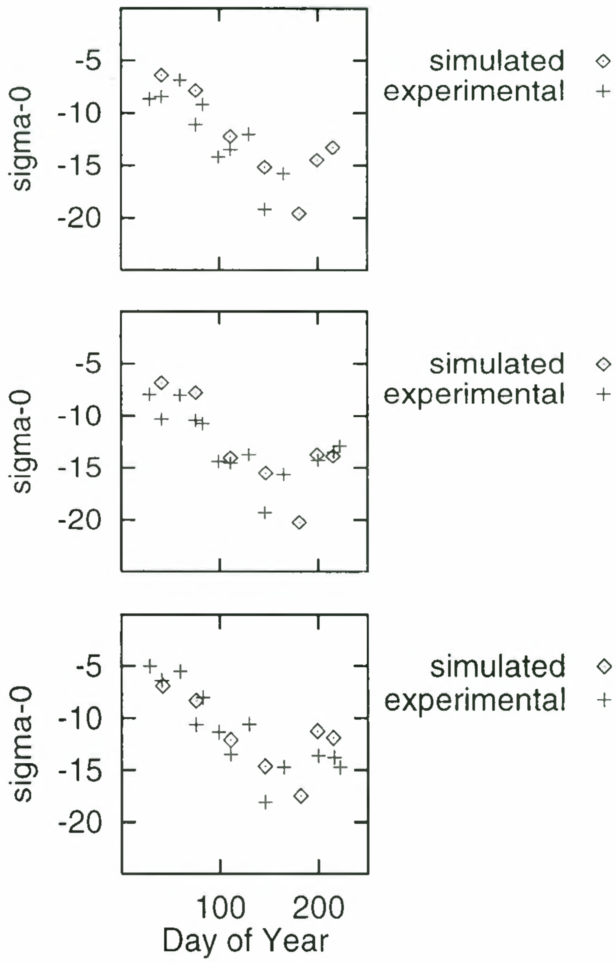

Figure 4. Comparison between experimental (ERS) and simulated σ°'s in the 3 fields of Driffield site

is observed in the location of the minimum. In the experimental data, it occurs at ~ DoY 150, i.e in the early earing, while in the simulations is located in the mature phase. Apparently, the model overestimates ear attenuation. This problem, which has been observed in other works and leads to an inaccuracy in the retrieval, needs further investigations.

4. THE RETRIEVAL ALGORITHM

A retrieval algorithm has been developed and tested over the Central Plain site. Neural simulations are based on the Stuttgart University neural network simulator (SNNS). The topology is formed by a multi-layer perceptron with two hidden layers, while a sigmoid function is applied as activation function of the network units. The retrieval process is subdivided into two phases: training and test.

4.1. Training

A reference site, for which a multitemporal set of detailed ground truth is available, is selected. For each Day of Year of the reference site $[DoY]_{REF}$ the model is run to simulate $\sigma°$'s at the required frequencies, polarization and angles. Vegetation inputs are given by the ground data measured at the reference site. As far as soil variables are concerned (i.e. soil moisture, height std. and correlation length), a parametric approach is adopted: computations are carried out for several values of soil variables. It is also introduced a "density factor" F_d in the computations. This means that $\sigma°$'s are simulated for a field with a number of plants per m^2 (N) which may be different from the value measured at the reference site (N_{REF}). The $F_d = N/N_{REF}$ ratio is varied up to a maximum value of 2. In this way a set of simulated $\sigma°$'s is generated, covering several $[DoY]_{REF}$'s, several situations of soil variables and F_d's, and the selected frequencies, polarizations and angles. Model outputs are used to train the neural network. As a result of the training phase, multitemporal sets of backscatter coefficients are associated to crop cycles which may differ from the reference cycle in crop density, and also in temporal location and temporal duration, as it will be better clarified in the next Section.

4.2. Test

A test site is considered. A multitemporal set of $\sigma°$'s measured at the same frequencies, polarizations and angles as those of the training phase, is taken. Soil parameters are assumed to be known, and taken from ground data of the test site. As far as vegetation parameters are considered the network, using experimental $\sigma°$'s as input, estimates the differences between the multitemporal ground data of test field and the ones of reference field. These differences may concern the density factor, the temporal location and the temporal duration. The outputs provided by the network are the F_d factor and a couple of parameters, named a and b, containing information about the temporal evolution of the cycle, as indicated below.

Let Y_R be the retrieved value of a vegetation variable for a given Day of Year in the test site, $[DoY]_{TEST}$, and Y_M be the measured value of the same variable for a given Day of Year in the reference site $[DoY]_{REF}$. Some variables, such as biomass and LAI, are dependent on density. In this case we have:

$$Y_R([DoY]_{TEST}) = F_d \cdot Y_M([DoY]_{REF}) \qquad (1)$$

with:

$$[DoY]_{REF} = [DoY]_{REF0} + a \cdot ([DoY]_{TEST} - [DoY]_{REF0} + b) \qquad (2)$$

where $[DoY]_{REF0}$ is the starting day of the reference cycle.

Other variables, such as dimensions and moistures of leaf, stem and ear are not dependent on the density. For these variables, formula (1) is modified into:

$$Y_R([DoY]_{TEST}) = Y_M([DoY]_{REF}) \qquad (3)$$

while formula (2) is unmodified. In this way all vegetation variables may be estimated for the whole test cycle.

The proposed method adopts some simplifying assumptions which could be restrictive. In the reality, the test field may differ from the reference field in other properties besides density, temporal location and temporal duration. However, this restriction could be overcome in the future by some refinements such as: i) introduction of other parameters, besides a, b and F_d, ensuring a higher degree of flexibility to the algorithm; ii) availability of reference ground data taken in the same environment as that of the test field.

In spite of its limits, the proposed algorithm may be a step towards the solution of the retrieval problem. It must be considered that, in the model adopted by us, the backscatter coefficient is influenced by: soil moisture, surface height std. and correlation length, number of plants per m^2, dimensions and moistures of leaf, stem and ear, leaf orientation distribution, for a total of 14 variables. The number is even higher in models adopting multi-scale surface representations and/or coherent approaches. Therefore, a direct mathematical inversion of such a large system of relationships is extremely difficult. On the other hand, methods based on simple relationships between $\sigma°$ and a single variable are much less general, in that are heavily influenced by the specific properties of the adopted data sets.

5. RESULTS

The procedure described in Section 4 has been applied using a wheat field of Avignon site as reference and another wheat field of Central Plain site as test. Among the several frequencies, polarizations and angles of RASAM, the following ones have been selected: 3.1 GHz, 4.6 GHz, 10.2 GHz frequencies; HH and VV polarizations, 30° angle.

This selection ensures the use of diversified information sources, but it avoids to introduce too many nodes in the network. On the basis of available ground data of Avignon site, $[DoY]_{REF0}$ has been set equal to 110.

The procedure leads to the following results:
$a = 0.71$, $b = 26$, $F_d = 2$
By using formulas (1) and (3), respectively, the multitemporal trends of crop biomass and crop height may be retrieved. Figure 5 compares the retrieved data sets with the directly measured ones. As far as biomass is concerned, the algorithm correctly predicts the Central Plain field to be denser than the

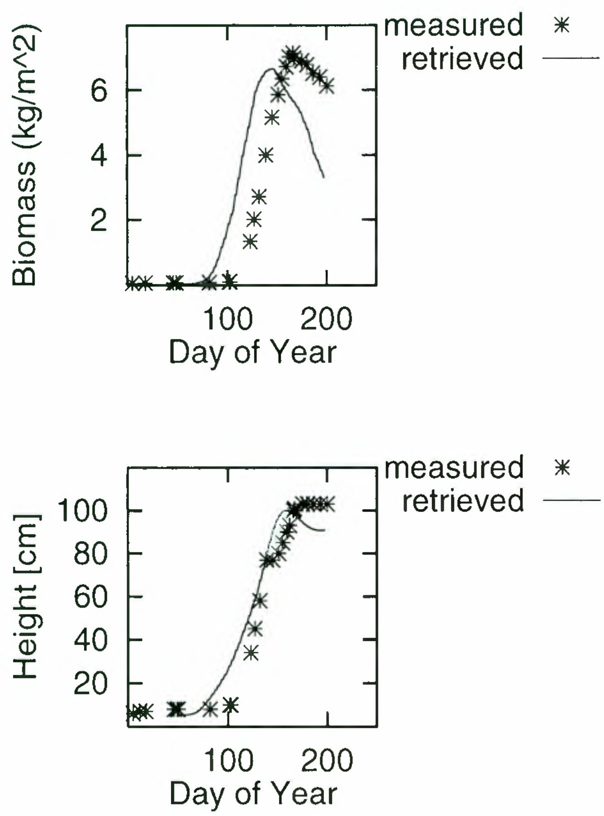

Figure 5. Comparison between experimental and retrieved vegetation parameters at Central Plain site

Avignon field, with $F_d = 2$. On the contrary, there is an evident error in the time evolution, since the cycle predicted by the algorithm is earlier than the measured one. This inaccuracy, which is less evident in crop height trends, is related to the modeling problems already identified in Figure 4 for the Driffield site. The algorithm tends to predict an earlier cycle to compensate for the delay in σ° introduced by the model. The latter, on its turn, is due to an overestimation of ear attenuation in the late part of the cycle. Therefore, refinements in the electromagnetic model are required. In particular, geometric and dielectric properties of stem and ear need to be better represented.

A good fitting of biomass trend at test site would have been obtained with:
$a = 0.6$, $b = 10$, $F_d = 2$

The height trend is better reproduced than the biomass trend. This result could be due to some agronomic differences between the Avignon field and the Central plain field, not sufficiently considered by three simple parameters such as a, b and F_d. Algorithms with a higher degree of flexibility could lead to better results, in the future.

6. CONCLUSIONS

An algorithm has been proposed to retrieve the multitemporal evolution of wheat fields using a reference site, a model and a neural network. The accuracy of the results needs to be improved. Further studies, aimed at refining the electromagnetic model and introducing a higher degree of flexibility in the algorithm, are required.

ACKNOWLEDGMENTS

The data of Avignon test site have been kindly made available by J.-P. Wigneron, from INRA. The data of Driffield and Central Plain sites have been made available in the framework of the ERA-ORA Project, founded by ECC.

REFERENCES

Bracaglia M., Ferrazzoli P., Guerriero L., 1995, "A fully polarimetric multiple scattering model for crops", Remote Sensing of Environment, vol. 54, 170-179.

Cookmartin G., Saich P., Quegan S., et al., 2000, "Modeling microwave interactions with crops and comparison with ERS-2 SAR observations", IEEE Trans. Geosci. Remote Sensing, vol. 38, 658-670.

Ferrazzoli P., Wigneron J.-P., Guerriero L., Chanzy A., 2000, "Multifrequency emission of wheat: modeling and applications", IEEE Trans. Geoscience and Remote Sensing, vol. 38, 2598-2607.

Le Toan T., Ribbes F., Li-Fang W., et al., 1997, "Rice crop mapping and monitoring using ERS-1 data based on experiment and modeling results", IEEE Trans. Geosci. Remote Sensing, vol. 35, 41-56.

Stiles J. M., Sarabandi K., Ulaby F. T., 2000, "Electromagnetic scattering from grassland - part II: measurement and modeling results", IEEE Trans. Geosci. Remote Sensing, vol. 38, 349-356.

Ulaby F. T., Moore R. K, Fung A. K, 1986, Microwave Remote Sensing: Active and Passive - vol.III, Artech House, Dedham (MA, USA).

Wegmüller U., 1993, "Signature research for crop classification by active and passive microwaves", Int. J. Remote Sensing, vol. 14, 871-883.

MULTITEMPORAL INSAR IN LAND-COVER CLASSIFICATION

Marcus E. Engdahl[*a], Juha Hyyppä[b]

[a] Laboratory of Space Technology, Helsinki University of Technology
[b] Finnish Geodetic Institute

*email: mengdahl@avasun.hut.fi, tel: +358 9 451 2170, fax: +358 9 451 2898, Laboratory of Space Technology, Helsinki University of Technology, P.O.Box 3000, FIN-02015 HUT, Finland

ABSTRACT

In this study the potential of ERS-1/2 Tandem INSAR data in land-cover classification was investigated at a 2500km2 study area around the Helsinki metropolitan area in southern Finland. A time-series of 14 ERS-1/2 Tandem image pairs was processed into 28 5-look intensity images, 14 Tandem coherence images and two coherence images with a longer temporal baseline (35 and 245 days). All image data was co-registered and orthorectified into map coordinates using an INSAR DEM. The dimension of the input dataset was reduced with Principal Components Transformation (PCT) prior to classification with an unsupervised ISODATA classifier. Classification accuracy was assessed with aerial orthophotos, digital base maps and the Finnish National Forest Inventory (NFI). The overall producer's accuracy for six classes (agricultural fields, dense forest, sparse forest, mixed urban, dense urban, water) was found to be 88%.

1.INTRODUCTION

Land-cover classification is one of the most important applications of remote sensing. The usability of optical satellite data in land-cover classification is severely limited by cloud cover in many parts of the world. Synthetic Aperture Radar (SAR) can penetrate cloud cover, but the potential of C-band single polarization intensity images in land-cover classification is limited. Interferometric SAR (INSAR) can provide complementary information to the backscatterd intensity in the form of interferometric coherence. The use of multitemporal INSAR datasets can increase the number of reliably distinguishable land-cover classes. In this study the potential of multitemporal C-band INSAR in land-cover classification was investigated.

2. SAR INTERFEROMETRY

Synthetic Aperture Radar (SAR) has inherent advantages over optical sensors due to its ability to penetrate cloud cover and image the ground in all weather and lighting conditions. SAR interferometry, which is based on coherent combination of two or more SAR images, can be used to retrieve information of the target area that is complementary to the information contained in individual SAR intensity images. SAR interferometry was first introduced by Graham, originally for topographic mapping [1]. A SAR interferometer is formed by relating the signals from two spatially separated radar antennas. In repeat-pass satellite interferometry the SAR interferometer is formed by relating two complex SAR images of the target area acquired at separate times from a nearly exactly repeating orbit. The physical separation of the antennas at the times of the image acquisitions is called the *interferometric baseline* and the temporal separation of the two acquisitions is called the *temporal baseline*.

2.1 INTERFEROMETRIC COHERENCE

Interferometric coherence, or the complex correlation between the images in an interferometric pair carries information that is complementary to the information in SAR intensity images. The coherence is a quantitative measure that is directly related to the amount of phase noise present in the SAR interferogram. The value of coherence varies between 0 (incoherence) and 1 (perfect coherence), and it is reduced by volume scattering effects and random dislocations of the scatterers. Since volume scattering effects and scatterer movement generally happen in vegetation canopies, they can be distinguished from bare surfaces by their low coherence. The additional information contained in the interferometric coherence significantly improves the potential of SAR data for land-cover classification and the retrieval of geo- and biophysical parameters [2].

3. STUDY AREA

The Helsinki metropolitan area in southern Finland (near 60°N, 25°E) was chosen as the test area for the land-cover classification study. About a million people live inside the 2500km2 study area, which has diverse land-cover from lakes and boreal forests in the Nuuksio National park to dense urban settlement in the Helsinki city center. The study area is predominantly quite flat, with some gentle hills.

Proc. 3rd International Symposium, 'Retrieval of Bio- and Geophysical Parameters from SAR Data for Land Applications', Sheffield, UK, 11-14 September 2001 (ESA SP-475, January 2002)

4. DATA

4.1 SAR DATA

The SAR data used in the study consists of 14 ERS-1/2 Tandem image pairs (28 images total) acquired with the C-band SARs on-board the European Space Agency's (ESA) ERS-1 and ERS-2 satellites. The imagery was acquired during the ERS-1/2 Tandem mission in 1995-1996, when the satellites were flown in the same orbital plane so that ERS-2 imaged the same area on the ground 24 hours after ERS-1. Due to the relatively short temporal baseline of 24 hours and the short interferometric baselines, the data collected during the Tandem mission is useful in studies of natural targets, which decorrelate quite rapidly in C-band. The data span a whole year from the summer of 1995 to the summer of 1996.

4.2 REFERENCE DATA

Aerial orthophotos and oblique aerial images of the town of Vantaa ($238km^2$) in 1 meter resolution were used for gathering reference points for the agricultural and urban classes. Reference points for the two forest classes were gathered from the operationally National Forest Inventory (NFI) [3]. National base maps were used in addition to the aerial images in gathering reference point for the water- and dense urban - classes. The reference classes are:

1. Water Bodies
2. Agricultural fields
3. Dense forest (stem volume > $100m^3$/ha)
4. Sparse forest (stem volume 50-$100m^3$/ha)
5. Low residential area (single- and double family housing)
6. High residential area (residential flats, 3-7 stories high)
7. Industrial buildings (halls and warehouses)
8. Dense urban (city center, multistory buildings, 5-8 stories high)

At least 100 reference points were gathered for each reference class.

5. DATA PROCESSING

5.1 INTERFEROMETRIC PROCESSING

SAR data were interferometrically processed and geocoded using a commercial software package by Gamma Remote Sensing Research and Consulting AG [4]. In order to reduce the demands on disk space and processing power the 100x100km full ERS SAR-scenes were cut to 50x50km size for interferometric processing. Common band filtering (also called spectral-shift filtering) was applied before interferogram generation in order to minimize the effects of the baseline geometry on coherence estimation [5]. At this stage multi-looking (5 azimuth looks) was performed in order to improve on the estimates of the interferometric phase and coherence. After multi-looking the pixel size of the image data is approximately 20 metres in both azimuth and slant range at the ERS nominal look angle of 23°. The resulting 5-look interferograms were flattened using high-quality orbit information distributed by the DLR. The interferometric coherence was estimated with a square 5x5 pixel window using Gaussian weighing of the samples. In addition to the Tandem coherence images with a temporal baseline of 24 hours, two coherence images with longer temporal baselines were computed (35 and 245 days). These longtime coherence images are used to detect man-made features with high backscatter, which can remain interferometrically stable for years [6]. Also, 5-look intensity images were generated and radiometrically calibrated for range spreading loss, antenna gain, normalized reference area and the calibration constant [7].

5.2 GEOCODING

The Tandem data used in this study was acquired from two separate satellite tracks. In order to create a unified dataset all image data had to be orthorectified into map coordinates. This was accomplished by creating a simulated SAR image from an INSAR DEM, using the simulated SAR image for co-registration of the two image sets and orthorectifying the co-registered set with the INSAR DEM. Judging visually, the image data from different tracks coincide perfectly, which implies that sub-pixel accuracy was achieved.

5.3 TEMPORAL FILTERING

Reliable estimates of the backscattered intensity σ^0 from a distributed target require that the estimated number of looks (ENL) is sufficiently large. Spatial filtering, for example speckle filtering, is usually used to increase the ENL, which causes loss of spatial resolution. In properly co-registered multitemporal datasets it is possible to employ temporal filtering, which in principle increases radiometric resolution without degrading spatial resolution. The theory of temporal filtering is discussed in [8], here we use a simple temporal filter, which is described in [9]. The simplified filter is defined as:

$$J_k(x,y) = \frac{\langle I_k \rangle}{N} \sum_{i=1}^{N} \frac{I_i(x,y)}{\langle I_i \rangle} \qquad (1)$$

Where *(x,y)* are the spatial coordinates in an image, *J* is the set of temporally filtered images, *I* the set of unfiltered images and <*I*> is a spatial estimate for *I*. Since a spatial estimate for *I* is needed in equation (1), some loss of spatial resolution is unavoidable. We temporally filtered both our 28 intensity images, and our 14 Tandem coherence images.

Judging visually, the temporally filtered images display markedly diminished speckle with little or no reduction in spatial resolution. In fact, narrow linear structures are more clearly visible in the filtered images, than in the unfiltered ones.

7. PRINCIPAL COMPONENTS TRANSFORMATION

Due to the large number of SAR intensity and coherence images, it was necessary to reduce the dimensions of the image datasets prior to classification. Principal Components Transformation (PCT) transforms a set of correlated images into a new set of uncorrelated images. It transforms the input dataset along orthogonal axes, whose directions are defined by the variability in the input dataset. The first Principal Component (PC) is along the axis of maximum variance in the input dataset, the second PC is along the axis of maximum variation orthogonal to the first PC, and so forth.

7.1 SUBTRACTING THE TEMPORAL AVERAGE

Since the direction of the first PC affects the directions of all the other PCs due to the orthogonality constraint, the data mean ought to be subtracted from the input data before applying the PCT. If the subtraction is not done, the first PC will point towards the data mean and the PCT cannot work optimally. The so-called temporal average images were subtracted from the Tandem coherence and Tandem mean image datasets before applying PCT. Temporal averaging refers to the simple procedure of computing the average of the co-registered time-series of images. It produces images that have high resolution and low noise [10,11,12], which are therefore well suited for visual inspection or simple initial classification. Figures 1 and 2 demonstrate the effect of temporal averaging of SAR Tandem coherence images.

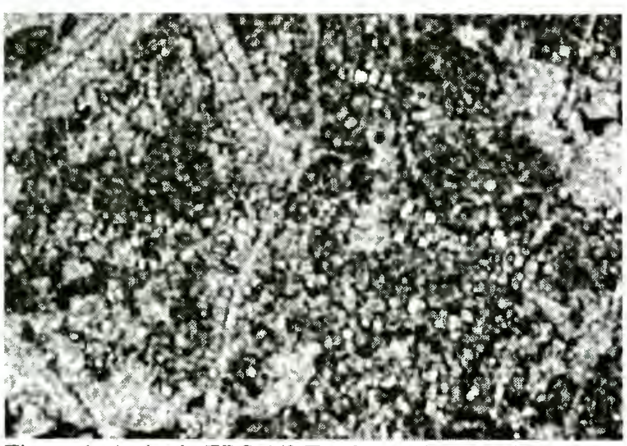

Figure 1: A single ERS-1/2 Tandem coherence image

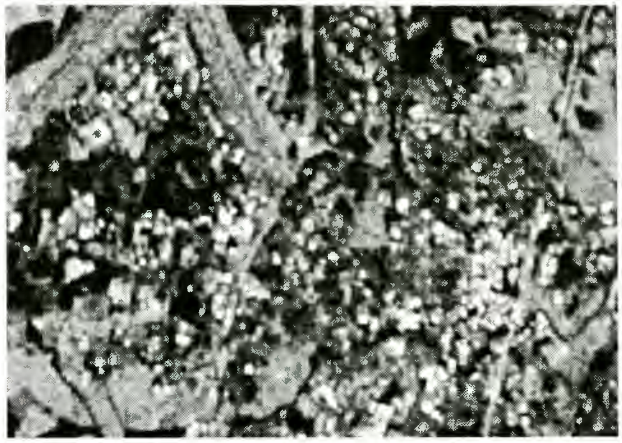

Figure 2: A temporal average of 14 coherence images

7.2 WATER-MASKING

If water-areas are included in the intensity and coherence datasets, the first PC will highlight the water-bodies. This happens on intensity image time-series because differing wind conditions make large differences in backscatter from water, and on coherence image time-series because free water has extremely low coherence during summer and ice has often quite a high coherence. Since we were not interested in water, but land-cover, the water-areas were excluded by using a water-mask that was created by thresholding backscatter intensity ratio images.

9. ISODATA CLASSIFICATION

The images chosen as input images for the classifier were:

1. Temporal average of the backscattered intensity images
2. Temporal average of the Tandem coherence images
3. Average of the two coherence images with long temporal baselines (35 and 245 days)
4. 1st principal component of Tandem coherence
5. 2nd principal component of Tandem coherence
6. 1st principal component of backscattered intensity

The 2nd principal component of the intensity time-series was omitted because it appeared to contain mostly noise. The input images were stretched to span values 0-255 and converted into 8bit format.

The ISODATA (also called c-means) algorithm is an unsupervised technique that looks for 'natural' clusters in the data. It requires the number of clusters as an input, which is somewhat problematic since the optimal number of clusters is not known. Therefore, we varied the number of clusters systematically, and choose the number that produced the best differentiation between the reference classes. 14 classes were found to be a good number of clusters for our dataset. The output of the ISODATA classifier was filtered with a 3x3 pixel majority filter.

9. RESULTS AND DISCUSSION

The result of the unsupervised classification was compared with the known land cover types (ground truth) at the reference points. As expected, INSAR classification could not properly differentiate between the high residential, low residential and industrial building classes as defined in the reference data. These classes were combined to a 'mixed urban' class, which covers both residential and industrial areas. When similar classifier output classes were combined, the number of classes in the classified image reduced from 14+1 (ISODATA classes + water class from water mask) to 5+1. These classes were: Agricultural Fields, Forest, Vegetation, Mixed Urban, Dense Urban and Water.

Table 1 shows how the reference points were distributed in the classified image. The values are in percentage points, the sum of each column is 100, and producer's accuracies are displayed in bold. The overall producer's accuracy is **88%**.

Figure 3 illustrates the distribution of pixel values in the combined classes. Field-class has a higher average Tandem coherence that the forest-classes, as expected. It is a combined class from two classes found by ISODATA, which shows in the large standard deviation in the intensity PC1. These two kinds of fields exhibit different behavior over the time-series, probably due to differing farming practices, but our ground truth data do not allow us to tell what the difference between these field types is.

Dense forest – class has lower coherence than the sparse forest – class, which is to be expected. They also differ in the coherence PC1 and PC2 due to their different behavior over the time-series.

Urban classes are problematic in SAR-based classification. The visibility of man-made structures in SAR intensity images depends on their orientation with respect to the satellite line-of-sight. Urban classes are characterized by high backscatter from man-made targets but due to the orientation problem even large structures may stay undetected. This problem could be mitigated by viewing the urban area from different angles, i.e. using images from both ascending and descending orbits. Dense urban – class has high level of backscatter due to reflections from man.made structures, and it also stays coherent for long periods of time, as shown by the longtime coherence. The mixed urban – class is a combination of 9 ISODATA classes, which shows in the quite large standard deviation in the pixel values. It is also a diverse class in the ground, since it encompasses industrial warehouses, multistory residential buildings and low-density residential areas, with trees and small parks. In the mixed urban class both backscattered intensity and longtime coherence are also in average higher than for the non-urban classes, but the standard deviation is large.

Due to the interferometric processing and geocoding process some parts of the classified image have no data – practically all of these areas were on water where movement of the sea-ice had caused steep hills to appear in the DEM.

The classification accuracy in this study was found to be significantly better than in the previous studies [12,13]. This is probably due to the use of high quality reference data and a large number of Tandem pairs.

ACKNOWLEDGEMENTS

The authors wish to thank the European Space Agency for the SAR data and the town of Vantaa for the aerial orthophotos.

		Reference Class					
		Agricultural Fields	Dense Forest	Sparse Forest	Mixed Urban	Dense Urban	Water
Assigned Class	Agricultural fields (25%)	**97**	2	8	1	0	0
	Dense Forest (21%)	0	**88**	1	4	0	0
	Sparse Forest (18%)	1	11	**86**	4	0	0
	Mixed Urban (20%)	2	0	5	**80**	9	0
	Dense Urban (1%)	0	0	0	12	**91**	0
	Water (14%)	0	0	0	0	0	**90**
	No Data	0	0	0	0	0	10

Table 1. Distributions of the reference points in the classified image. Producer's Accuracies displayed in bold. The overall producer's accuracy is **88%**.

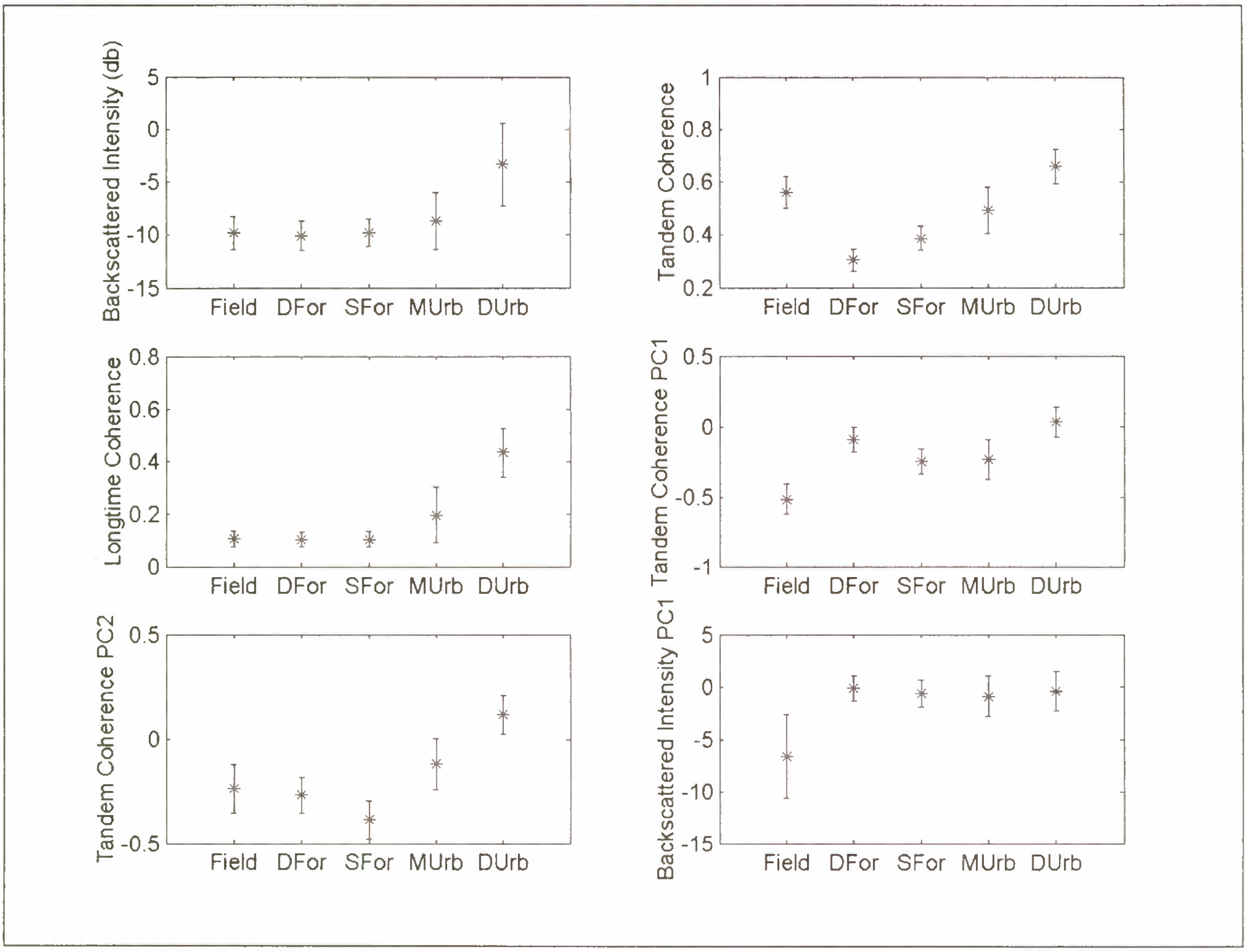

Figure 3: Pixel values of the classes in the classified dataset. ±1 standard deviation indicated with an error bar.

REFERENCES

1. L.C. Graham, "Synthetic Interferometer Radar for Topographic Mapping", Proceedings of the IEEE, vol.62, no.6, pp.763-768, June 1974
2. U. Wegmüller, and C. Werner, "Retrieval of Vegetation Parameters with SAR Interferometry", IEEE Transactions on Geoscience and Remote Sensing, vol.35, no.1, pp.18-24, January 1997
3. M.Katila, E.Tomppo, "Selecting estimation parameters for the Finnish multisource National Forest Inventory", Remote Sensing of the Environment, 76 (2001), pp. 16-32
4. U.Wegmuller, C. Werner and T. Strozzi, "SAR Interferometric and Differential Interferometric Processing Chain", Proceedings of IGARSS'98, Seattle, USA, 6-10 July 1998, vol.2, pp.1106-1108
5. F. Gatelli, A. Monti Guarnieri, F. Parizzi, P. Pasquali, C. Prati and F. Rocca, "The Wavenumber Shift in SAR Interferometry", IEEE Transactions on Geoscience and Remote Sensing, vol.32, no.4, July 1994
6. S. Usai, R. Klees, "SAR Interferometry on a Very Long Time Scale: A Study of the Interferometric Characteristics of Man-Made Features", IEEE Transactions on Geoscience and Remote Sensing, vol.37, no.4, July 1999, pp. 2118-2123
7. H. Laur, P. Bally, P. Meadows, J.I. Sanchez, B. Schaettler and E. Lopinto, "Derivation of the Backscattering Coefficient σ^0 in ESA ERS SAR PRI Products", ESA-ESRIN, ES-TN-RS-PM-HL09, Issue 2, Rev.4, May 1997
8. A. Lopes, E. Nezry, R. Touzi and H. Laur, "Structure detection and statistical adaptive filtering in SAR images", International Journal of Remote Sensing, vol.14, no.9, 1993, pp.1735-1758
9. S. Quegan, T. Le Toan, Jiong Jiong Yu, F. Ribbes and N. Floury, "Multitemporal ERS SAR Analysis

Applied to Forest Mapping", IEEE Transactions on Geoscience and Remote Sensing, vol.38, no.2, March 2000, pp. 741-753

10. P.J. Meadows and H. Laur, "Exploitation of ERS SAR Imagery for Land Applications", Proceedings of the Second International Workshop on the Retrieval of Bio- and Geo- Physical Parameters from SAR Data for Land Applications, Noordwijk, The Netherlands, 21-23 October, 1998, pp.43-50
11. M.E. Engdahl and J. Hyyppä, "Temporal Averaging of Multitemporal ERS-1/2 Tandem INSAR Data", Proceedings of IGARSS'2000, International Geoscience and Remote Sensing Symposium, Hawaii, USA, July 20-24, 2000, 3 pages
12. T. Strozzi, P.B.G Dammert, U Wegmüller, J-M Martinez, J.I.H. Askne, "Landuse Mapping with ERS SAR Interferometry", IEEE Transactions on Geoscience and Remote Sensing, vol.38, no.2, March 2000, pp. 766-775
13. P.B.G. Dammert, J.I.H. Askne and S. Kühlmann, "Unsupervised Segmentation of Multitemporal Interferometric SAR Images", IEEE Transactions on Geoscience and Remote Sensing, vol.37, no.5, September 1999, pp. 2259-2271

UPSCALING WATER CYCLE PARAMETERS USING GEOMORPHOMETRIC TERRAIN PARAMETERS AND TOPOGRAPHIC INDICES DERIVED FROM INTERFEROMETRIC DEM

N. Etzrodt[(1)], R. Zimmermann [(2)], O. Conrad [(1)]

[(1)]Institute for Geography, University Göttingen
D-37073 Göttingen, GERMANY, Phone: (49)-551-398015, Email: netzrod1@gwdg.de
[(2)] Max-Planck-Institute for Biogeochemistry, Jena,
D-07701 Jena, GERMANY, FAX: (49)-3641-643710, Email: reiner.zimmermann@bgc-jena.mpg.de

ABSTRACT

For assessing a regional water balance in boreal landscapes the extend to which evapo-transpiration is subject to spatial variations needs to be known. Water cycle parameters such as transpiration rates of vegetation are depending on both the vegetation type and hydro-pedologic stand conditions since poor soil drainage respective seasonal soil drought affect water consumption by vegetation.

The spatial distribution of the pristine boreal vegetation types can be obtained by SAR or optical remote sensing sensors on a regional scale. Many works have been dealing with this subject in the past and it is widely known how remote sensing can contribute to vegetation mapping.

To assess hydro-pedologic stand conditions on a regional scale an alternative method is required. Our approach to resolve this problem is based on the fact that soil water status is essentially a function of topographic properties. For that reason morphometric terrain parameters derived from a Digital Elevation Model (DEM) has been used to indicate regions with homogeneous hydro-pedologic stand conditions, so called 'hydropedotopes'.

To delineate the required hydropedotopes two indicators pertaining to soilwater status and pedo-hydrology were derived from InSAR DEM: (1) The wetness-index and (2) the vertical distance to streams and bottom lines.

In a further step the resulting map of hydropedotopes is intersected with a remote sensing derived map of the actual spatial distribution of the boreal vegetation types. This step results in a map which marks out landscape units of homogeneous properties in terms of vegetation type and hydro-pedologic conditions which is the basis for upscaling canopy transpiration measurements.

From our approach which uses in addition to conventional remote sensing data the results of an automated digital terrain analysis we expect a substantially enhanced knowledge of the spatial variability of water flux rates conditional on canopy transpiration. Fig. 1 illustrates the process of our approach at a glance.

INTRODUCTION

Classification and mapping of general vegetation cover types is a common application of coherence and backscatter images derived from SAR Interferometry (InSAR). However, the specific advantages and possibilities of InSAR derived Digital Elevation Models (InSAR DEM) for an advanced landscape analysis and a mapping of functional site quality properties are yet widely unexplored. One aspect of our work is to close this gap by utilization the spatial relationship between variability of hydro-pedologic vegetation habitat conditions and terrain properties.

In case of the remote and inaccessible ecosystems of the Siberian boreal zone the high spatial resolution capability and large coverage of InSAR DEM is studied by a quantitative analysis of geomorphometric terrain properties. This approach of terrain analysis shows its potential to determine the spatial extent of edaphic-hydrologic properties such as poor soil drainage, seasonal soil drought, water availability to plants and proximity to groundwater. The need to assess such edaphic-hydrologic habitat conditions arises since most boreal forests regenerate after fire which results in a mosaic of successional stages overlaying varying edaphic preconditions.

In view of the fact that functional site quality properties in terms of hydro-pedologic vegetation habitat conditions can be assessed by InSAR DEM analysis the estimation of regional water balances in boreal landscapes can be further refined and improved.

Proc. 3rd International Symposium, 'Retrieval of Bio- and Geophysical Parameters from SAR Data for Land Applications', Sheffield, UK, 11-14 September 2001 (ESA SP-475, January 2002)

THE CENTRAL SIBERIAN STUDY AREA

The area around the Russian settlement of Zotino (60° 50' N and 89° 40' E), located at the west bank of the Yenissey river was selected for analysis. The Yenissey river separates in a fairly abrupt transition the western Siberian lowlands with pleistocene sand deposits and moderate topography from the central Siberian mountains with dissected peneplains of mesozoic sediment rock. West of the Yenissey a mosaic of peat bogs, dense riparian forests on mesotrophic fluvial plains and sandy hills with poor podzols and Scots Pine (*Pinus sylvestris*) forests of varying density prevail. East of the Yenissey mesotrophic podzolised brown soils carry dense and productive mixed coniferous forests which interchange with fire induced successional stages of deciduous stands.

DEM QUALITY ASSESSMENT AND PREPROCESSING

For the central Siberian test site an interferometrically derived DEM is available. The InSAR DEM was acquired in October 1997 during an ERS-1/ERS-2 tandem acquisition phase. Interferometric processing was performed by DFD-DLR (Oberpfaffenhofen, Germany).

Previous to the actual digital terrain analysis a quality check of the InSAR-DEM was performed. By a visual evaluation it could be identified that the terrain height values are overlaid by a random noise in the height-dimension of few meters. To smooth the InSAR DEM surface a mean filter algorithm was applied.

In the range of the floodplain of Yenissey river a number of pixels show an unreasonable height value. Presumably for these pixels interferometric height measuring was not possible due to low coherence as a result of flooded land surface. Consequently it was supposed that the affected pixels are situated in the same terrain height as the Yenissey river. As an adjustment the height value of the river was assigned to the affected pixels.

After the aforementioned improvements the quality of the resulting DEM has turned out fairly satisfactory and subsequently a quantitative accuracy assessment was performed by the aid of another digital elevation model derived from a topographic map which was considered as the most reliable reference elevation data source. As the most relevant result of the accuracy assessment it can be stated that the divergence between InSAR DEM and topographic map are dependent on the actual terrain elevation which is leading to substantial inaccuracies within the hilly terrain eastward of Yenissey river. Regions which show unacceptable inaccuracies as large self contained valleys without any outward flowpath have been masked out before further processing of the InSAR DEM.

For all that the InSAR DEM being considered still contains artefacts as so called pits (or sinks) and artificial planes. The occurrence of pits and artificial planes is not specific to interferometric DEM. They occur within virtually every digital elevation model, regardless of their origin and they are negligible for most applications of a DEM but not for a hydrologic terrain analysis.

Pits are defined as closed depressions without any flowpaths directing outward. The horizontal extent of pits is mostly in the dimension of a few pixels and the vertical extent rarely exceeds a fraction of a meter. Artificial planes are clusters of pixels with identical elevation values which are mostly generated due to truncation of decimal places. In terms of a hydrology-orientated analysis these artefacts cause difficulties on operation of automated algorithms. Thus the position of pits and artificial planes have been located within the InSAR DEM and the artefacts were removed. By the application of a proper algorithm pits were filled up until a flowpath finds a way out of the sink. Likewise artificial planes were removed by an iterative averaging of the borders of the artificial planes.

The preprocessing of the InSAR DEM results in a digital elevation model which is 'completely drained'. This means that each pixel of the DEM has at least one direct neighbour with lower altitude where the drainage flowpath is directed to. In later steps the preprocessed DEM is taken as a firm basis for a hydrology-orientated digital terrain analysis.

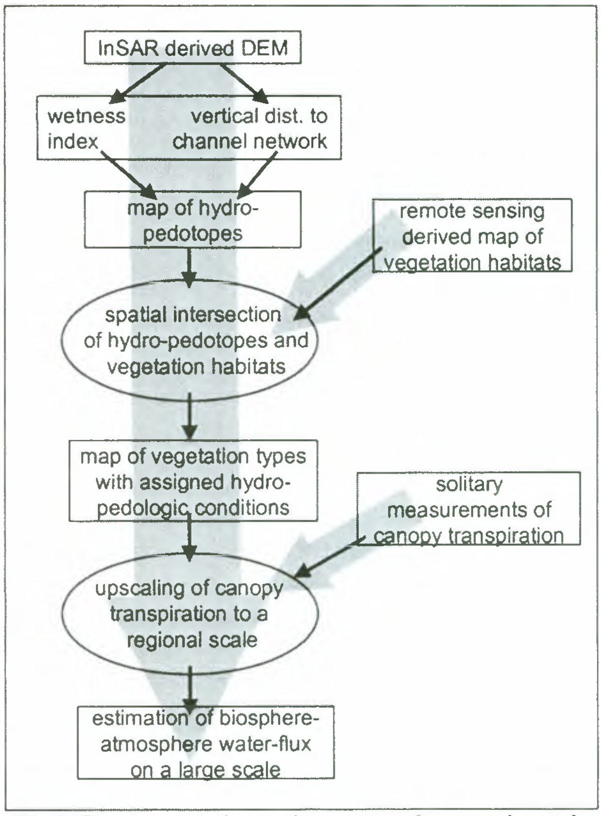

Fig. 1: The approach of upscaling water cycle properties on the basis of conventional remote sensing data as well as hydro-pedologic information derived from InSAR DEM.

DIGITAL TERRAIN ANALYSIS BASED ON INSAR DEM

Objective of the InSAR DEM-Analysis is to delineate hydropedotopes which are defined as zones with homogeneous soil water status and hydro-pedologic conditions. For that reason two indicators pertaining soil hydrology were derived from InSAR DEM: (1) The wetness-index and (2) the vertical distance to streams and bottomlines.

The wetness-index *TCI* of each pixel is calculated from the local catchment area a and the local slope angle β after equation (1):

$$TCI = \ln \frac{a}{\tan \beta} \qquad (1)$$

In this context the local catchment area is defined as the area of all pixels contributing their runoff to the pixel in question. The calculation of the local catchment area is based on the perception of *multiple flow*. Compared to the *steepest descent* model the first mentioned presumes for each pixel more than one runoff flow direction whilst the *steepest descent* model only takes one runoff flow direction per pixel into account.

The equation (1) points up that the wetness-index indicates areas of convergent respective divergent runoff. This means that a large wetness-index specifies regions of poor soil drainage and high water availability whereas regions of low TCI are susceptible to temporary soil drought.

Fig. 2 proves the correlation between wetness-index and soil-moisture content by means of a set empirical observed soil-moisture data. The data have been measured under different geologic and land-use conditions. In case of the homogeneous geologic situation within the west Siberian part of the testsite even a better correlation can be expected.

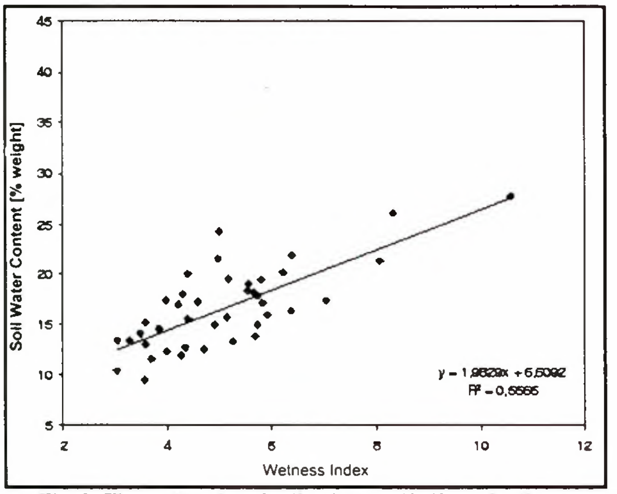

Fig. 2: The scatterplot of soilmoisture (40-60 cm depth) vs. wetness-index shows the significance of TCI as an indicator for soilmoisture content in consideration of numerous land-use types and geologic conditions.

As mentioned before the vertical distance to streams and bottomlines is used as an additional estimate to indicate hydro-pedologic habitat conditions. This method is based on the fact that in case of the west Siberian vegetation pattern which subsists on pleistocene sandy sediments a rather good correlation between soil water status and the distance to groundwater table can be expected. The groundwater table again can be approximated on a regional scale by an imaginary surface which is interpolated from the altitude of existent watercourses and bottom lines. Occasionally this surface is called 'potential groundwater table'. Hence the term 'distance to potential groundwater table' is used synonymous for the vertical distance to streams and bottom lines.

Before calculation of the distance to potential groundwater table the channel network has to be defined. For our purposes a rather detailed network was needed which marks out both large rivers and small streams which can not be detected by remote sensing only. For that reason the channel network has been derived directly from the InSAR DEM by utilisation of values of the local catchment area. Each pixel with a local catchment area of at least $35 \cdot 10^6$ m^2 was considered as an element of the channel network.

Based on the DEM derived channel network and the InSAR DEM itself the vertical distance to channel network was calculated by an enhanced algorithm, developed at the Institute for Geography in Göttingen (Germany). The resulting product gives a picture of the vertical distance to potential groundwater table as an spatially continuous attribute of the central Siberian landscape without any atypical interruptions.

Subsequent to the digital terrain analysis the two outcoming products have been classified into discrete categories of landscape units which form the desired hydropedotopes characterized by their homogeneous hydro-pedologic properties.

The whole procedure of digital terrain analysis was performed with the aid of the software 'DiGeM'. DiGeM is a windows-based tool for digital terrain analysis comprising all worksteps from DEM-preprocessing up to dynamic runoff simulations. This software was developed at the Institute for Geography in Göttingen (Germany) and is at present still subject to further upgradings.

APPLICATION OF INSAR DEM-DERIVED PRODUCTS FOR UPSCALING WATER CYCLE PARAMETERS

It is known that the spatial variation of canopy water loss is determined by stand density, species composition and accordingly sapwood area. We hypothesize, that in the variegated landscapes of western and central Siberia spatial variations of water cycle parameters such as transpiration rates are additionally determined by hydropedologic stand conditions. In consequence significant errors may introduced in the upscaling process of canopy transpiration rates if variances of the soilwater status are ignored and simply a remote sensing derived vegetation map is used for an estimation of quantitative water cycle characteristics on a large scale. Starting from this assumption we are going to do a scaling up of *in situ* tree transpiration measurements from small scale single plots to a regional scale by using two sources of spatial information: (1) distribution of vegetation types derived from remote sensing and (2) knowledge of soil water status, signified by the above mentioned map of hydropedotopes deduced from InSAR DEM.

An *in situ* assessment of tree transpiration rates have been carried out at individual trees of major central Siberian species as *Pinus sylvestris*, *Betula sp.*, *Pinus sibirica*, *Abies sibirica*, *Picea obovata*, *Populus tremula* and *Sorbus sp.* Sap flux density in the hydroactive xylem was derived from continuous measurements of heat dissipation after GRANIER. The temperature differences between the stem tissue and the heated probe were monitored every 30 s and a 10 minute mean value was stored on a data-logger for each sensor. Whole tree transpiration was calculated form sap flux density and the cross section area of hydroactive tree xylem where the thickness of hydroactive xylem was determined on tree discs and drilling cores.

As a first step of the upscaling process five forest types have been specified. The forest types have been defined by their separability by means of a remote sensing data classification. In order to extrapolate the stand sap flux density [$g_{water} \cdot s^{-1} \cdot ha^{-1}{}_{forest\text{-}area}$] from individually measured sap fluxes [$g_{water} \cdot s^{-1} \cdot m^{-2}{}_{sapwood\text{-}area}$] groundtruth data of the hydroactive xylem cross section area of each species and each forest type have been used. As a result a specific stand sap flux density value is available for each of the forest types in question.

By combination of stand sap flux density values of each forest type with the remote sensing derived information concerning their spatial distribution a preliminary assessment of an area wide estimation of canopy transpiration rates will be obtained. At this point no InSAR DEM derived information concerning soil water status have been taken into account.

To compensate this deficiency in future steps the information of hydropedotopes will be implemented into the upscaling process of xylem flux values. On the evidence of their hydro-pedological landscape characteristics to each hydropedotope attributes concerning their evapo-transpiration rate will be assigned. As a last step of the upscaling procedure a spatial intersection of this information with the preliminary estimation of canopy transpiration rates is proposed. From this workstep we expect an substantially refined assessment of canopy transpiration rates on a regional scale.

REFERENCES

Beven, K. J. & Kirkby, M. J.: (1979): A physically based variable contributing area model of basin hydrology. Hydrological Sciences, Bd. 24(1), 43-68

Freeman, T. G.: (1991): Calculating Catchment Area with divergent Flow based on a regular Grid. Computers & Geosciences, Bd. 17(3), 413-422.

Kelliher F. M. et al (1998): Evaporation from a central Siberian pine forest. Journal of Hydrology, 205, 279-296.

Zimmermann, Reiner, E.D. Schulze, Chr. Wirth et al (2000): Canopy transpiration in a chronosequence of Central Siberian pine forests. (Global Change Biology 6, S. 25-37).

Zimmermann Reiner, T. Mette, N. Etzrodt et al: Tree transpiration and water flux control of successional forests in Central Siberia (in preparation).

CHANGE DETECTION IN MULTISENSOR REMOTE-SENSING DATA FOR DESERTIFICATION MONITORING

Diego Fernàndez Prieto

Earth Observation Applications Department, European Space Agency, ESA-ESRIN,
Via Galileo Galilei, 00044 Frascati (Rome), Italy
diego.fernandez@esa.int

Abstract - The objective of this paper is twofold: methodological and operational. From a methodological viewpoint, it aims at exploring various approaches to merge the information provided by different type of sensors in unsupervised change-detection problems. From an operational perspective, this work aims at providing an insight into the complementary capabilities of optical and SAR images to identify land-cover transitions within the context of desertification monitoring. The experimental analysis was carried out by using Landsat-5 TM and SAR images acquired at different dates in a wetland area of Tuscany, Italy, affected by desertification processes. Experiments demonstrate the effectiveness of merging both types of data and confirm remote sensing as a powerful technology to monitor desertification processes in a regular basis.

I. INTRODUCTION

In the last years, some international treaties of primary importance, such as the Kyoto protocol, the UN Convention to Combat Desertification (UNCCD), and the Ramsar Convention on Wetlands, have been signed as a result of the growing concern of the international community about the dramatic environmental problems that affect our planet. Monitoring land degradation, preventing drought, and avoiding wetland destruction, are some of the key program actions planned in the context of these fundamental treaties. To accomplish such challenging objectives, as stated in the Kyoto protocol, "... *promote the maintenance and the development of systematic observation systems...* " [1] is a mandatory issue. However, some methodological and practical limitations exist that render the development of operational systematic observation systems a complex and still unresolved problem. EO technology may play a key role in overcoming such drawbacks, and the present paper aims at providing a small contribution to demonstrate it.

Among the most interesting methodologies to monitor the land surface at its variations from space is worth mentioning the change-detection techniques [2]-[4]. The increasing number of papers dealing with change detection in multitemporal remote-sensing images published in the past few years [2]-[4] confirms this topic as one of the most interesting in the area of remote-sensing image analysis. This interest arises from the wide range of applications in which change-detection methods can be employed, ranging from environmental monitoring, agricultural surveys, and urban studies, to natural hazard management, and forest monitoring [2]-[4].

Usually, change detection involves the analysis of two registered multispectral remote-sensing images acquired in the same geographical area at two different times. Such an analysis aims at identifying land-cover changes that have occurred in the study area between the two times considered. In the remote-sensing literature, two main approaches to the change-detection problem have been proposed: the supervised approach and the unsupervised one [3], [4]. The former is based on supervised classification methods, which require the availability of a multitemporal ground truth in order to derive a suitable training set for the learning process of the classifiers. The latter performs change detection by making a direct comparison of the two multispectral images considered, without relying on any additional information. Although the supervised approach exhibits some advantages over the unsupervised one [4], the generation of an appropriate multitemporal ground truth is usually a difficult and expensive task. Consequently, the use of effective unsupervised change-detection methods is fundamental in many applications in which a ground truth is not available. (For a detailed survey of both supervised and unsupervised change-detection methods, we refer the reader to [2], [4]).

This paper deals with the widely used type of unsupervised techniques that perform change detection through a direct comparison of the original raw images acquired in the same area at two different times [3]. This type of approaches are usually applied in a single sensor basis, without exploiting the potential synergies that may arise from the combinations of different information sources in the change-detection process. In this context, the objective of this paper is twofold: methodological and operational. From a methodological viewpoint, it aims at exploring various approaches to merge the information provided by different type of

Proc. 3rd International Symposium, 'Retrieval of Bio- and Geophysical Parameters from SAR Data for Land Applications', Sheffield, UK, 11-14 September 2001 (ESA SP-475, January 2002)

sensors in unsupervised change-detection problems. From an operational perspective, this work aims at providing an insight into the complementary capabilities of optical and SAR images to identify land-cover transitions within the context of desertification monitoring.

The experimental analysis was carried out by using Landsat-5 TM and ERS-2 SAR images acquired at different dates in a wetland area of Tuscany, Italy, affected by desertification processes. On the one hand, Optical images were used to identify changes in the vegetation cover. On the other hand, SAR images were exploited to evidence variations in the land surface structure. Experiments demonstrate the effectiveness of merging both types of data and confirm remote sensing as a powerful technology to monitor desertification processes in a regular basis.

The paper is organised as follows. The next section provides an overview of classical unsupervised change-detection techniques. Section III provides a description of the proposed methodology. The experimental analysis is reported in Section IV. Finally, conclusions are drawn in Section V.

II. UNSUPERVISED CHANGE DETECTION

The change-detection process performed by classical unsupervised techniques is usually divided into three main sequential steps: 1) pre-processing, 2) image comparison and 3) analysis of the difference image. These steps are detailed in the following.

Preprocessing - Unsupervised change-detection algorithms usually take two digitised images as input and return the locations where differences between the two images can be identified. To accomplish such a task, a preprocessing step is necessary aimed at rendering the two images comparable in both the spatial and spectral domains.

Concerning the spatial domain, the two images should be co-registered so that pixels with the same coordinates in the images may be associated with the same area on the ground. This is a very critical step, which, if inaccurately performed, may render change-detection results unreliable [5]. With regard to the spectral domain, changes in illumination and atmospheric conditions between the two acquisition times may be a potential source of errors and should be taken into account in order to obtain accurate results. This problem can be mitigated by performing a radiometric calibration of the images. To this end, two different approaches can be taken: absolute calibration and relative calibration. The reader is referred to [6] for a detailed description of these techniques.

Image comparison - The two registered and corrected images (or a linear or non-linear combination of the spectral bands of such images [2]) are compared, pixel by pixel, in order to generate a further image ("difference image"). The difference image is computed is such a way that pixels associated with land-cover changes present gray-level values significantly different from those of pixels associated with unchanged areas [2]. For example, the univariate image *differencing* (UID) technique generates the difference image by subtracting, on a pixel basis, a single spectral band for each of the two multispectral images under analysis. The choice of the spectral band to be subtracted depends on the specific type of change to be detected. An analogous concept is followed by the widely used change vector analysis (CVA) technique. In this case, several spectral channels are considered at each date (i.e. each pixel of the image considered is represented by a vector whose components are the gray-level values associated with that pixel in the different spectral channels selected). Then, for each pair of corresponding pixels, the so-called "spectral change vector" is computed as the difference in the feature vectors at the two times. At this point, the pixels in the difference image are associated with the modules of the spectral change vectors; it follows that unchanged pixels present small gray-level values, whereas changed pixels present rather large values.

Analysis of the difference image - Land-cover changes can be detected by applying a decision threshold to the histogram of the difference image. For instance, when the CVA technique is used (i.e. each pixel in the difference image is associated with the module of the difference between the corresponding feature vectors in the original images), changed pixels can be identified on the right side of the histogram as they are associated with large gray-level values. The selection of the decision threshold is of major importance as the accuracy of the final change-detection map strongly depends on this choice. Although in the image processing literature some automatic techniques for choosing a suitable decision threshold for change-detection problems have been proposed [3], in remote-sensing applications such a choice has generally been made by using non-automatic heuristic strategies based on trial-and-error approaches [2].

In spite of their relative simplicity, the information derived from this type of techniques is usually limited to a simple binary map pointing out pixels associated to either changed or not-changed areas, without providing valuable additional information about the nature and the degree of change of the land-cover transitions identified. Such a limited information is a direct result of the lack of ground-truth data, as we are dealing with unsupervised methods. In addition, the single-sensor approach classically used in this type of techniques limits the nature of the changes identified depending on the specific characteristics of the sensor used. For instance, optical data allows changes in the spectral response of land-cover to be detected, whereas SAR images allows variations in the structure and the dielectric characteristics of the land surface to be identified. In this context, the efficient exploitation of the complementary information provided by different type of sensors in the change-detection process may improve the results derived by classical techniques and provide the end-user with a more complete view of the variations affecting the area of interest. In the following, different alternatives to perform data fusion in unsupervised change detection techniques are explored.

III. METHODOLOGY

Let $\mathbf{X}_D^1,\ldots,\mathbf{X}_D^S$ be S co-registered difference images, each one associated to a different sensor s. Each difference image $\mathbf{X}_D^s$ was derived from the application of one the above-mentioned techniques to two co-registered remote-sensing images, $\mathbf{X}_1^s$ and $\mathbf{X}_2^s$, acquired by the sensor s in the same geographical area at two different times, t_1 and t_2.

Data fusion approach have been widely studied and successfully applied in remote sensing, specially in the context of classification techniques [7], [8]. However, not much work was carried out aimed at extend data-fusion approaches to other methodological domains, such as unsupervised change detection techniques.

The main idea of the proposed methodology consists in extending the classical data-fusion theory, typically used in supervised classification, to the unsupervised change-detection problem. In this context, we will distinguish among three main levels of fusion: feature, decision and output-level based fusion. In the following, these three main fusion levels are analysed.

A. Feature level

In the feature-based fusion, the sensor measurements are merge on a pixel by pixel basis. In the unsupervised change detection this involves the concatenation of the data from different sensors as if they were measurements from one single sensor, and use the resulting staked vectors at both dates to compute the difference image. For example, if $X(i,j)_1^{TM}=\left(x_1^1,\ldots,x_k^1\right)$ and $X(i,j)_2^{TM}=\left(x_1^2,\ldots,x_k^2\right)$ are the feature vectors of the pixel of coordinates (i, j) from the Landsat TM at the times t_1 and t_2, respectively, and $Y(i,j)_1^{SAR}=\left(y_1^1,\ldots,y_l^1\right)$ and $Y(i,j)_2^{SAR}=\left(y_1^2,\ldots,y_l^2\right)$ are the corresponding feature vectors from the ERS-2 SAR, then the resulting staked vectors are $\left(x_1^1,\ldots,x_k^1,y_1^1,\ldots,y_l^1\right)$ and $\left(x_1^2,\ldots,x_k^2,y_1^2,\ldots,y_l^2\right)$. At this point, the difference image can be computed by using classical approaches, such as the CVA technique. Then, as in single-sensor approaches, changes can be identified by thresholding the difference image.

At this fusion level, other classical unsupervised change-detection approaches, such as the Principal Component Analysis [2] can be also used to evidence changes occurred in the area of interest between both dates under consideration. In this approach, the above *(k+l)*-dimensional vector of the same area acquired at two different dates, are concatenated and treated as a single *2(k+l)*-dimensional data set. The first principal components of this data set point out the unchanged areas and the major differences associated with overall radiation and atmospheric changes present in the images; the last components usually isolate changes in land-covers [2].

B. Decision level

At this fusion level, the information extracted from sensors is represented as measures of belief in a given event. This degrees of belief take generally their values in a real closed interval (e.g., [0,1], [-1,1], etc.) and are modelled in different ways, depending on the specific mathematical framework selected: e.g., probabilities in classification approaches based on the Bayesian theory, mass, belief or plausibility functions in Dempster-Shafer evidence theory, and membership degrees to a fussy set in fuzzy set theory [9].

In our case, the unsupervised nature of the problem faced hinders probabilistic approaches to be used. This suggests the fuzzy theory as the most suitable framework to perform unsupervised change-detection at this fusion level.

In our case, the application of the fuzzy theory requires the information provided by each sensor s to be represented by two membership functions, $f_c^s(i,j)$ and $f_u^s(i,j)$, associated with changed and unchanged areas, respectively. To carry out this task, we will exploit the particular nature of the image difference: i.e., pixels belonging to changed areas are likely to present grey-level values different from those of pixels associated with unchanged regions. For instance, in the case of the CVA, low grey-level values are likely associated with unchanged areas, whereas high grey-level values are likely associated with changed ones. In this context, a simple yet effective way to model the membership functions is proposed. In particular, for each sensor s, the membership degree to the fuzzy set "changed area" can be defined in a range [0,1] as:

$$f_c(i,j)^s=\left(\frac{1}{\max\left(\mathbf{X}_d^s\right)-\min\left(\mathbf{X}_d^s\right)}\right)\left(X_d^s(i,j)-\min\left(\mathbf{X}_d^s\right)\right).$$

Analogously,

$$f_u(i,j)^s=\left(\frac{1}{\min\left(\mathbf{X}_d^s\right)-\max\left(\mathbf{X}_d^s\right)}\right)\left(X_d^s(i,j)-\max\left(\mathbf{X}_d^s\right)\right).$$

Other alternatives can be found and other models can be applied depending on the particular technique used to derive the difference image (e.g., *image rationing*, *univariate image differencing*).

At this point, a fusion operator $F_c\left(f_c^1,\ldots,f_c^S\right)$ can be used to merge the information provided by the different sensors under consideration. The selection of the fusion operator is a key issue, as the final result depends on this choice. Several fusion operator have been proposed [9], which present different behaviours in terms of severity or indulgence when conflictual situations occur and of their decisiveness. In [9], a detailed analysis of most common operators proposed in the literature is provided. Among the different kinds of operators investigated in such a work (e.g., context independent constant behaviour, context independent variable behaviour, and context dependent operators), the context dependent behaviour operators seems to provide the most suitable framework to merge data from different sensor in unsupervised change detection. For instance, when combining membership degrees from two sensors 1 and 2, such an operator can take the form

$$\mu_c(i,j) = F\left[f_c^1(i,j), f_c^2(i,j), r(1,c), r(2.c), gr(1), gr(2)\right],$$

where $r(s,c)$ is the reliability of the sensor s given the class change, and $gr(s)$ is the global reliability of sensor s. This allows to assign a numerical degree of reliability to each source. Other interesting operators are those, which behaviour depends on a measure of conflict. This type of operator permits to combine the information related to each class (changed and unchanged areas) in a way, which is adapted to the conflict between the sources concerning each class.

More simplistic yet effective operators exists, which can be selected depending on their behaviour (severe, indulgent or cautious) and the specific practical problem faced.

C. Output level

At this fusion level, the change-detection maps derived from different sensors are merged by using different voting principles [10]. To further explain this kind of fusion strategy it is necessary to introduce some notation. Let $\mathbf{M}_s = \{M_s(i,j), 1 \le i \le I, 1 \le j \le J\}$ be the change-detection map associated to the sensor s derived by using a classical technique. Each pixel $M_s(i,j)$ can take to opposite values (e.g., 0, 1) associated with unchanged and changed areas respectively. In this context, the most conservative voting rule id the following

$$E(i,j) = \begin{cases} j & if\ M_s(i,j) = j\ \forall s \\ Unknown & Otherwise \end{cases}.$$

A slight modification of the above expression could lead to a less conservative fusion model, which assign the winner class for each pixel by voting by majority. For example, if 3 out of 5 sources vote for the same class, then this label is taken as the final result.

It is worth noting that in this fusion scheme, reliability factors can be also taken into account. In particular, the vote of each sensor can be weighted depending on the reliability of the sensor with respect to the selected class. Then, the final result is derived by the following decision rule

$$\sum_{s=1}^{S} \delta_u(M_s(i,j))\alpha_u^s \underset{unchanged}{\overset{changed}{\lesseqgtr}} \sum_{s=1}^{S} \delta_c(M_s(i,j))\alpha_c^s$$

where α_k^s, with $0 \le \alpha_k^s \le 1$, is the reliability factor for the sensor s with respect to the class k and

$$\delta_k(M_s(i,j)) = \begin{cases} 1 & if\ M_s(i,j) = k \\ 0 & otherwise \end{cases}.$$

Other approaches can be used depending on the particular problem at hand. The reader is referred to [10] for a detailed analysis of this kind of fusion techniques.

IV. EXPERIMENTAL ANALYSIS

The experimental analysis was carried out on a wetland area in a semi-arid region affected by land-degradation processes. It is worth noting that, in this paper, we consider the wider definition of desertification provided by the UNCCD (REF). In particular the data set used is composed of a multitemporal set of images acquired by the Landsat-5 and the ERS-2 SAR sensors in the Daccia Botrona wetland in Tuscany, Italy. The area is affected by a serious problem of salinisation, which is modifying the vegetation typologies and their distribution in the area. Images were acquired in July 1997 and August 1998, so that a couple of TM and SAR images may be available for each date (see Fig. 1). Images were co-registered by using the SAR 1997 image as a reference.

In this preliminary phase of the project, experimental analysis is limited to a qualitative comparison of the results provided by the different fusion strategies above explained. In particular, three main experiments were carried out, one fore each of the fusion levels specified in Section III: feature, intermediate and output fusion levels.

The three results will be compared with the results derived by the single sensor approach. The change-detection map for the TM sensor was derived by using the CVA technique with the bands 4 and 5, whereas the *image rationing* technique was used to identify changes in the SAR images [REF]. Results of the single sensor approach are shown in Fig. 1(c) and (f). As one can see the changes identified are significantly different.

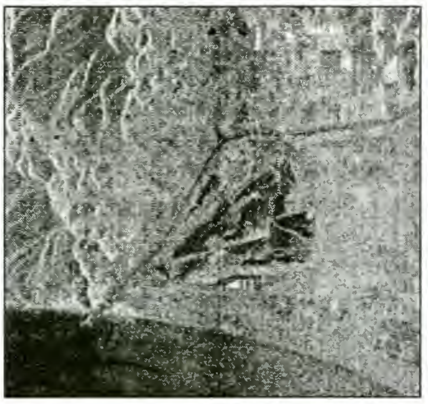

Fig.1(a) 1997 ERS-2 SAR image

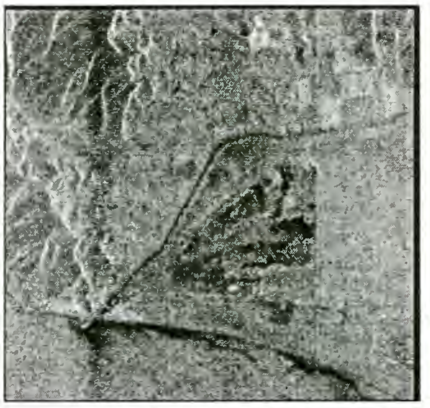

Fig.1(b) 1998 ERS-2 SAR image

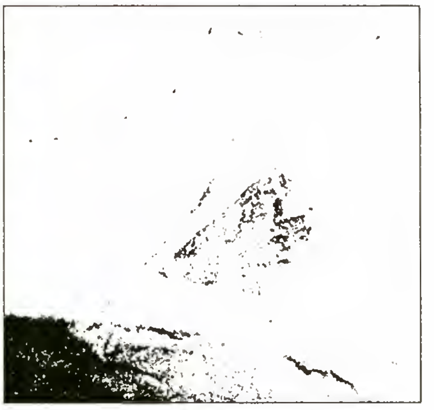

Fig.1(c) Result from SAR data

Fig.1(d) 1997 TM-band4 image

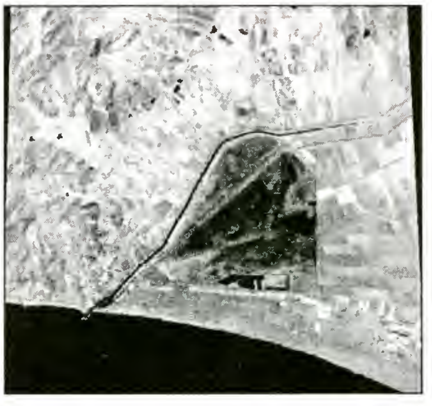

Fig.1(e) 1998 TM-band4 image

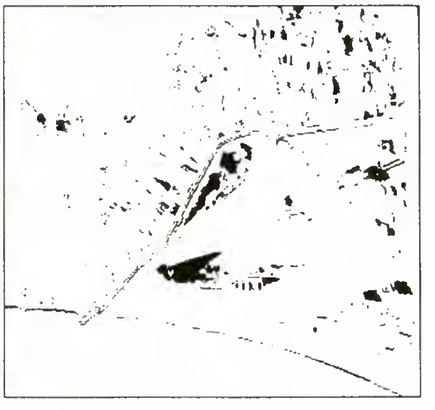

Fig.1(f) Result from TM data

Concerning the first fusion level (i.e., feature), the change detection map was derived by using the staked vector approach and the CVA technique (see Fig. 2). As one can see the result incorporates the main changes pointed out by both types of sensors.

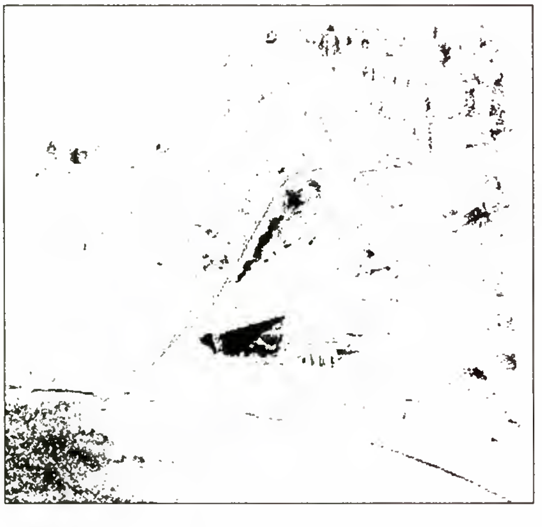

Fig. 2. Change detection result at feature fusion level.

The intermediate fusion level was implemented by using a simple yet effective fusion operator

$$\mu_c(i,j) = \frac{f_c^{TM}(i,j)r(TM,c) + f_c^{SAR}(i,j)r(SAR,c)}{r(TM,c) + r(SAR,c)},$$

were $r(TM,c)$=0.8 and $r(SAR,c)$=0.6. Such a selection depends on the degree of noise of both types of images. At this point, such a fuzzy information can be either displayed in a likelihood of change map (see Fig. 3(a)) or it may be defuzzied and displayed in a classical change-detection map (see Fig. 3(b)). In the first case, the fuzzy map provides the end-user with a significant level of information concerning the degree of change occurred in the are under analysis: i.e., high membership values (e.g., close to 1) are associated with high degrees of change, whereas low membership values are associated with low degrees of change. Once the fuzzy map is defuzzied (e.g., by considering membership values over 0.75), the information is reduced to a binary map, as those provided by classical approaches.

Finally, concerning the output fusion level, the combination of the single-sensor change-detection maps was carried out by using the most conservative voting rule (see Fig. 4). As one can see, the result provides a significant low level of information due to the cautious strategy used. Less conservative strategies may increase the level of information provided by the fusion of the single sensor approaches.

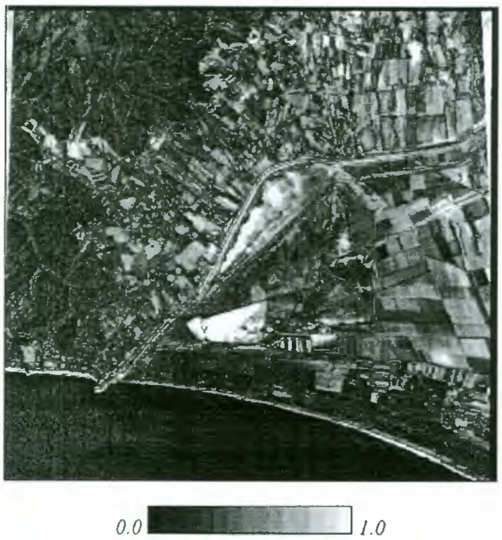

Fig. 3(a). Fuzzy information. Intermediate fusion level

Fig. 3(a). Defuzzied map. Intermediate fusion level

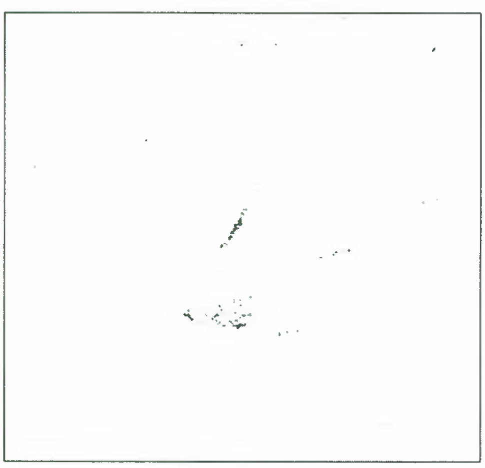

Fig. 4. Change detection result at the output fusion level

V. CONCLUSIONS

In this paper, various approaches to merge the information provided by different type of sensors in unsupervised change-detection problems were investigated. In particular, three main fusion levels were considered: feature, intermediate, output. Different fusion strategies were proposed for each of these three fusion levels. An experimental analysis was carried out by using Landsat-5 TM and SAR images acquired at different dates in a wetland area of Tuscany, Italy, affected by desertification processes. Experiments show that different fusion strategies provide rather different levels of information. The intermediate revealed as the fusion level that allows end-user to acquire a higher level of information, specially, as the degree of change is concerned. Further experiments will be carried out in order to perform an accurate quantitative analysis of the different fusion strategies proposed in this paper.

ACKNOWLEDGEMENT

This research was supported by the European Space Agency (ESA-ESRIN).

REFERENCES

[1] Kyoto Protocol to the UN Framework Convention on Climatic Change – Kyoto, 1997.

[2] A. Singh, “Digital change detection techniques using remotely sensed data,” *Int. Journal of Remote Sensing*, vol. 10, no. 6, pp. 989-1003, 1989.

[3] L. Bruzzone and D. Fernàndez Prieto, “Automatic analysis of the difference image for unsupervised change detection,” *IEEE Trans. on Geoscience and Remote Sensing*, vol. 38, no. 3, pp. 1171-1182, 2000.

[4] L. Bruzzone and S. B. Serpico, “An iterative technique for the detection of land-cover transitions in multitemporal remote-sensing images,” *IEEE Trans. on Geoscience and Remote Sensing*, vol. 35, no. 4, pp. 858-867, 1997.

[5] X. Dai and S. Khorram, “The effects of image misregistration on the accuracy of remotely sensed change detection,” *IEEE Transactions on Geoscience and Remote Sensing*, vol. 36, no. 5, pp. 1566-1577, 1998.

[6] P. S. Chavez, Jr. and D. J. MacKinnon, “Automatic detection of vegetation changes in the southwestern united states using remotely sensed images,” *Photogrammetric Engineering & Remote Sensing*, vol. 60, no. 5, pp. 1285-1294, 1994.

[7] J. A., Beneditksson, P. H. Swain, “Consensus theoretic classification methods,” *IEEE Trans. Syst., Man, Cybern.*, vol.22, pp.688-704, 1992.

[8] A.H. S. Solberg, A.K. Jain, and T. Taxt, "Multisource Classification of Remotely Sensed Data: Fusion of landsat TM and SAR Images," *IEEE Transactions on Geoscience and Remote Sensing*, vol. 32, no. 4, pp. 768-777, 1994.

[9] I. Bloch, "Information Combination Operators for data Fusion: A Comparative review with Classifiaction," *IEEE Trans. Syst., Man, Cybern.*, vol.25, no. 1, pp.52-67, 1996.

[10] L. Xu, A. Krzyzak, and C.Y. Suen, "Methods of Combining Multiple Classifiers and Their Applications to handwriting Recognition," *IEEE Trans. Syst., Man, Cybern.*, vol.22, no. 3, pp.419-435, 1992.

USING VERY HIGH RESOLUTION DATA TO ASSESS THE LIMITATIONS OF POLARIMETRIC INTERFEROMETRY FOR HEIGHT MEASUREMENT

J L Gómez Dans, S Quegan and J C Bennett

Sheffield Centre for Earth Observation Science, University of Sheffield
Hicks Building Hounsfield Rd Sheffield S3 7RH United Kingdom
e-mail: j.l.gomez-dans@sheffield.ac.uk

ABSTRACT

Very high resolution polarimetric measurements of man-made and natural targets within the University of Sheffield GB-SAR indoor Ground-based Microwave Facility allow us to investigate the basic processes in polarimetric interferometry. The target comprised two layers of nails, one with the nails predominantly vertical and the other predominantly horizontal, which were embedded in expanded polystyrene. These two layers were then placed one above the other with a vertical separation of 15 cm, and were imaged by the GB-SAR system at X band. Very successful interferometric height measurements of the separation of the two layers were possible using *a priori* knowledge about the scattering properties of the two layers. Using coherence optimisation techniques, the height recovery showed bi-modality, with peaks separated by the inter-layer height difference. Simulations indicated instabilities in the coherence optimisation technique for targets comprised purely of orthogonal scattering mechanisms.

1. INTRODUCTION

In the last decade, advances in SAR technology have resulted in a wealth of new products being available, utilising multi-frequency, polarimetric and interferometric data. However, these products have been mostly examined on their own. The challenge is to blend all these products to gain a better understanding of the phenomena being observed.

This is particularly true with polarimetric interferometry. In this area, both polarisation and interferometric information are closely coupled to architectural features of the scene, and a joint interpretation of both fields is highly desirable. One such approach was proposed by (Cloude & Papathanassiou, 1998). In this work, we investigate their proposed algorithm in the light of some experiments performed with artificial targets.

The structure of this paper is as follows: first, a brief review of coherence optimisation is presented, followed by the description of an experiment performed in the University of Sheffield GB-SAR facility to assess the procedure for measuring the height separation of different layers, followed by an analysis of the experimental set-up and numerical simulations. Finally, the results and simulations are discussed.

2. THEORETICAL BACKGROUND

Polarimetric SAR data are usually recorded in the V/H basis and stored as a three-dimensional vector

$$\underline{v} = [S_{VV}, S_{HH}, S_{VH}]^T . \quad (1)$$

The data can be converted to any other basis by projecting the data vectors onto unit vectors $\underline{p}$ that make up the new basis.

In an interferometric scenario, two vectors $\underline{v}$ and $\underline{v}'$, are needed to deal with each antenna position[1]. The Cloude *et al.* algorithm selects the pair of vectors $\underline{p}$ and $\underline{p}'$ so that the interferometric coherence of the projection is maximal. This is equivalent to maximising

$$|\rho| = \left| \frac{\langle \underline{p}^{*T} \mathcal{Q} \underline{\mathbf{p}}' \rangle}{\sqrt{\langle \underline{p}^{*T} \mathcal{T} \underline{p} \rangle \langle \underline{p}'^{*T} \mathcal{P} \underline{p}' \rangle}} \right| \quad (2)$$

over $\underline{p}$ and $\underline{p}'$, where ^{*T} denotes conjugate transpose and $\langle\cdot\rangle$ is the expected value. In Eq. 2, we use the covariance matrices of each image, plus the cross-covariance matrix of the image pair:

$$\mathcal{T} = \langle \underline{v} \cdot \underline{v}^{*T} \rangle; \ \mathcal{P} = \langle \underline{v}' \cdot \underline{v}'^{*T} \rangle; \ \mathcal{Q} = \langle \underline{v} \cdot \underline{v}'^{*T} \rangle, \quad (3)$$

[1] In this paper, a symbol without an apostrophe relates to the first antenna, and a symbol with an apostrophe, to the second.

Proc. 3rd International Symposium, 'Retrieval of Bio- and Geophysical Parameters from SAR Data for Land Applications', Sheffield, UK, 11-14 September 2001 (ESA SP-475, January 2002)

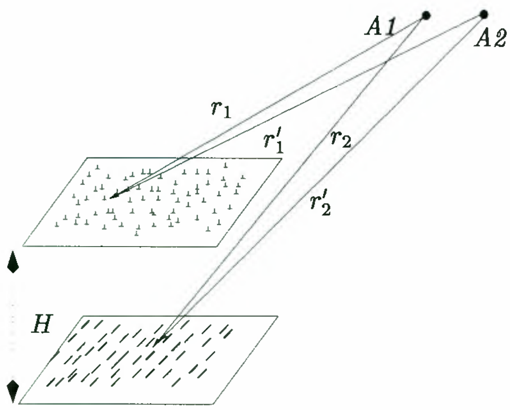

Figure 1. Geometry for two layered structure.

This optimisation problem leads to a pair of coupled eigenvalue-eigenvector problems:

$$\mathcal{M}_1 = \left[\mathcal{T}^{-1}\mathcal{Q}\right]\left[\mathcal{P}^{-1}\mathcal{Q}^{*T}\right]\; ; \; \mathcal{M}_1\underline{p} = \lambda\underline{p} \qquad (4)$$

$$\mathcal{M}_2 = \left[\mathcal{P}^{-1}\mathcal{Q}^{*T}\right]\left[\mathcal{T}^{-1}\mathcal{Q}\right]\; ; \; \mathcal{M}_2\underline{p}' = \lambda\underline{p}' \qquad (5)$$

The eigenvalues λ_i in Eqns. 4-5 are common, and correspond to the squares of the coherence values associated with each pair of eigenvectors, *i.e.*, $|\rho^{(i)}| = \sqrt{\lambda^{(i)}}$, $1 \leq i \leq 3$. The maximum coherence is attained with the vectors that relate to the highest eigenvalue. It is noted that the matrices are usually of full rank, but in the event of them being of rank < 3, the algorithm can be converted to a problem of lower dimension.

For Gaussian data, maximising the coherence is equivalent to minimising the uncertainty in the phase measurement, and hence making the height measurement from interferometry as accurate as possible. However, a deeper possible interpretation of the eigenvalue decomposition is that the eigenvectors, if orthogonal, correspond to different scattering processes. Hence the phase differences between the interferometric heights from the three eigenvector pairs correspond to scattering from different layers in the medium. As a highly idealised example, consider a forest, where one of the eigenvector pairs may relate to the scattering from the upper part of the canopy and another to a soil return. The difference between the interferometric heights of the corresponding eigenvector pairs would then represent the forest height.

3. EXPERIMENTAL RESULTS

In order to explore the performance of the algorithm, an artificial target was imaged in the University of Sheffield's GB-SAR facility (Morrison et al., 2001), (McDonald et al., 1998). The target was constructed by embedding steel nails in expanded polystyrene tiles to form two layers separated by a height H (see Fig. 1). In this experiment, H was set to 0.15 m. The top and bottom layers were populated with vertically and horizontally oriented nails respectively. With this set-up, it was expected that the scattering matrices for each layer would be approximately of the form

$$\mathcal{S}_1 = \begin{bmatrix} 1 & 0 \\ 0 & 0 \end{bmatrix} \; \mathcal{S}_2 = \begin{bmatrix} 0 & 0 \\ 0 & 1 \end{bmatrix}, \qquad (6)$$

up to scaling constants. Imaging was at X-band, with a bandwidth of 4 GHz centred at 10 GHz, providing a resolution of 0.06 m in range and azimuth at the centre of the target (resolution varied slightly due to changes of range and look angle over the target region). On average, there were around 6 nails per resolution cell.

Two scans were made, with a horizontal baseline of 0.06 m. The interferometric heights derived using the VV, HH and VH basis are shown in Fig. 2(a). The distributions are uni-modal, with VV maximising at around 0.15 m and HH at 0 m, corresponding to the vertical and horizontal nail layers, respectively[2]. The VH channel shows bi-modality, slightly biased towards the vertical layers. This bi-modality means that the VH channel is retrieving information from both layers.

The interferometric heights resulting from coherence optimisation are shown in Fig. 2(b). In this case, the distributions are bi-modal modes at 0 and 0.15 m.

In this work, we explore the reasons for this behaviour by means of simple analysis and numerical simulations.

4. THEORETICAL ANALYSIS

For the scenario presented in Sec. 3, the VH channel contribution is negligible, and will be ignored. This reduces the problem from 3 to 2 dimensions.

The algorithm proposed in (Cloude & Papathanassiou, 1998) uses a Pauli-basis vectorisation of the data. In the set-up presented in Sec. 3, the use of the VV-HH basis greatly simplifies analysis, and will be used in this discussion.

For single scattering from discrete scatterers of the form given in Eq. 6, the data recorded at the two antenna positions can be written as

$$\begin{aligned} \underline{v} &= \begin{bmatrix} \alpha\sum_{p=1}^{N_1}\exp(-jk2r_{1p}) \\ \sum_{q=1}^{N_2}\exp(-jk2r_{2q}) \end{bmatrix} \\ \underline{v}' &= \begin{bmatrix} \alpha\sum_{p=1}^{N_1}\exp(-jk2r'_{1p}) \\ \sum_{q=1}^{N_2}\exp(-jk2r'_{2q}) \end{bmatrix}. \end{aligned} \qquad (7)$$

In the above expression, the effect of range attenuation has been neglected, N_1 and N_2 are the number

[2]The reference height is arbitrary. In this work, it has been fixed as that of the bottom layer.

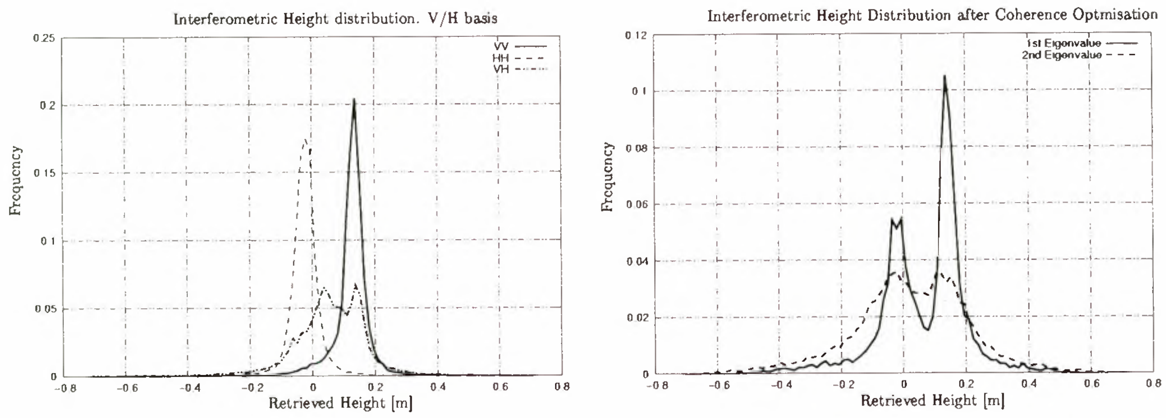

(a) V/H Basis

(b) Coherence Optimisation

Figure 2. Retrieved height histograms for experimental data in the V/H basis and after coherence optimisation.

of scatterers in each layer (these two numbers are held constant), r_{ip} (r'_{ip}) is the distance from the first (second) antenna to scatterer p in the i-th layer, and k is the wavenumber. α accounts for changes in the relative RCS between the two layers. The covariance matrices are given by

$$\mathcal{T} = \mathcal{P} = \begin{bmatrix} \alpha^2 N_1 & 0 \\ 0 & N_2 \end{bmatrix} \quad (8)$$

$$\mathcal{Q} = \begin{bmatrix} \alpha^2 N_1 \exp(j\phi_1) & 0 \\ 0 & N_2 \exp(j\phi_2) \end{bmatrix} \quad (9)$$

where ϕ_i is the interferometric phase for each layer.

In Eqns. 8-9 we assume that the propagation phases are uniformly distributed in $[-\pi, \pi]$ for each scatterer, and that the different scatterers are independent. This being the case, $\mathcal{M}_1$ and $\mathcal{M}_2$ in Eqns. 4 and 5 are identity matrices, with a degenerate eigenvalue spectrum $\{1, 1\}$ and eigenvectors $\{[1,0]^T, [0,1]^T\}$, which are the scattering mechanisms for VV and HH in the V/H basis. This result is independent of α.

In reality, the covariance has to be estimated, leading to perturbations on the ideal forms in Eqns. 4-5. The effects on the eigenvalues are small but there can be significant effects on the eigenvectors, as we now show.

Consider the case where there is an RCS difference between the two layers. The estimation of $\mathcal{M}_1$ and $\mathcal{M}_2$ will result in each of them having a form similar to

$$\begin{bmatrix} \sigma_1 & \gamma_1 \\ \gamma_2 & \sigma_2 \end{bmatrix}, \quad (10)$$

where the main diagonal elements have a magnitude close to unity, and $|\gamma_i| \ll |\sigma_i|$, for $i = 1, 2$. The eigenvalues of this matrix are very close to unity, and are given by

$$\lambda_{1,2} = \frac{\sigma_1 + \sigma_2 \pm \sqrt{(\sigma_1 - \sigma_2)^2 + 4\gamma_1\gamma_2}}{2} \quad (11)$$

$$\approx 1 \pm \sqrt{\gamma_1 \gamma_2}, \quad (12)$$

where the λ_1 is the positive solution and λ_2 the negative solution. The associated eigenvectors can be written as $\underline{e_i} = [e_{i1}, e_{i2}]^T$, for $i = 1, 2$ indicating the i-th pair of eigenvectors, with

$$e_{11} = \sqrt{\frac{\gamma_1}{\gamma_2}} e_{12} \quad (13)$$

$$e_{12} = -\sqrt{\frac{\gamma_1}{\gamma_2}} e_{22}. \quad (14)$$

The perturbations of the off-diagonal elements in Eq. 10 will be responsible for instabilities in the eigenvectors.

Because of the different RCS of the layers, the non-zero value of the off-diagonal elements has a dependence on α. In this case, $|\gamma_1/\gamma_2| \propto \alpha^{-4}$. For large values of α, the first component of the eigenvector will be much smaller than the second, which corresponds to a scattering mechanism similar to $[0,1]^T$ (HH). Similarly, if the value of α is small, the eigenvector will be similar to $[1,0]^T$, indicating a VV scattering mechanism.

In other words, the eigenvectors for both first and second eigenvalues will tend to be aligned with the scattering mechanism of the weaker layer. Hence the two eigenvectors will give little or no height discrimination.

A more detailed analysis of the perturbations can be performed as follows. Consider a matrix $\mathcal{A}$, equal to either $\mathcal{M}_1$ or $\mathcal{M}_2$ in Eqns. 4,5. The perturbed matrix will be denoted by

$$\mathcal{A}_\epsilon = \mathcal{A} + \mathcal{E}\epsilon, \quad (15)$$

where $\mathcal{E}$ is a perturbation of $\mathcal{A}$. $\mathcal{E}$ is unitary 2x2 complex matrix, and ϵ is the scaling of the perturbation. $\mathcal{A}_\epsilon$ will have eigenvectors denoted by

$\underline{p_n}(\epsilon)$, $1 \leq n \leq 2$. It can be shown (see, for example Quarteroni et al. (2000), Property 5.5, p. 190) that

$$||\underline{p_n} - \underline{p_n}(\epsilon)||_2 \leq \frac{1}{\min_{n \neq m} |\lambda_n - \lambda_m|} ||\mathcal{E}||_2 + \mathcal{O}(\epsilon^2), \tag{16}$$

for all n. where $||\mathcal{E}||_2$ is equal to the largest eigenvalue of $\mathcal{E}$.

Eq. 16 states that the Euclidean norm of the difference of the eigenvectors is inversely proportional to the spacing of the eigenvalues. So if two of the eigenvalues are very close, then minor variations in the matrices will provoke major variations in the eigenvectors.

The previous analysis can be extended to a more general situation. If the layers can be represented by orthogonal scattering mechanisms other than VV or HH, the data vectors for this case, $\underline{v_0}$ and $\underline{v_0}'$, can be written as a transformation of $\underline{v}$ and $\underline{v'}$ using an orthogonal transformation matrix $\mathcal{R}$. In this case, the covariance matrices $\mathcal{T}'$, $\mathcal{P}'$ and $\mathcal{Q}'$ can be written as

$$\mathcal{T}' = \mathcal{R}\mathcal{T}\mathcal{R}^{*T}; \; \mathcal{P}' = \mathcal{R}\mathcal{P}\mathcal{R}^{*T}; \; \mathcal{Q}' = \mathcal{R}\mathcal{Q}\mathcal{R}^{*T}, \tag{17}$$

leading on to a modified version of Eqns.4-5:

$$\begin{aligned} \mathcal{M}'_1 &= \mathcal{R}[\mathcal{M}_1]\mathcal{R}^{*T} && (18)\\ \mathcal{M}'_1\underline{p_0} &= \lambda\underline{p_0} && (19)\\ \mathcal{M}'_2 &= \mathcal{R}[\mathcal{M}_2]\mathcal{R}^{*T} && (20)\\ \mathcal{M}'_2\underline{p'_0} &= \lambda\underline{p'_0} && (21)\\ & && (22) \end{aligned}$$

The eigenvectors for the new target are given by $\underline{p_0}$ and $\underline{p'_0}$, and are related to the eigenvectors in Eqns.4-5 by the transformation matrix $\mathcal{R}$. The eigenvalues are the same as those in Eq.4(5). The implication of this is that if a target comprises two layers in which the scatterers are identical, but for which the the scattering mechanisms in the two layers are orthogonal, then the algorithm will not be able to discriminate the two layers.

5. NUMERICAL SIMULATIONS

In this section, simple simulations of the theory outlined in Secs. 3 and 4 are presented. The simulation parameters are described in Table 1.

We consider first the case when the two layers have identical RCS, shown in Fig. 3. The retrieved height for the VV and HH channels is shown at the expected levels, whereas the results from the optimisation are uniformly distributed between the two expected levels. For both VV and HH, the mean and standard deviation are 0.66 and 0.01.

The above analysis shows that coherence optimisation does not yield meaningful heights if the eigenvalues are similar. In order to assess how critical this

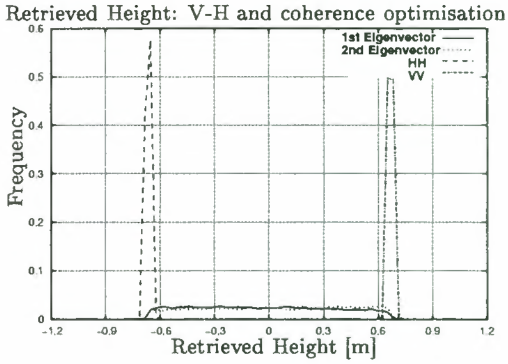

Figure 3. Retrieved height distribution.

Table 1. Simulation Parameters.

Parameter	Value
Angle of incidence, θ	45°
Height layer I, H_1	-0.65 m
Height layer II, H_2	+0.65 m
Baseline, B	1 m
Range to target, R_0	141 m
No. of scatterers in footprint, N_s	40
No. of looks, N_L	20
Frequency	5 GHz
Footprint size	0.2x0.2x0.01m
Unambiguous Height	8.4 m

condition is, we now consider what happens when the scatterers in the two layers have different RCS.

A way to study the effect of the relative RCS between the layers on the retrieved eigenvectors is to examine the angle between the eigenvector and a pure VV or HH scattering mechanism[3]. Simulations can be used to examine the angle, and were carried out with the parameters previously shown in Table 1 and various values of α (see Eq.7). In the simulations, α was varied between -20 and 20 dB, and the mean angle between the first eigenvector and a pure VV scattering mechanism is shown in Fig. 4. This mean angle is the average of 40000 experiments. Also shown in Fig. 4 is the standard deviation of the angle.

When the RCS is identical for the two layers, the eigenvector's angle with VV is 45°, with a large standard deviation of around 20°. This large deviation is due to the eigenvalues being very close, showing the effects of minor perturbations, as in Eq. 16. When the vertical layer has a much larger RCS than the horizontal layer, it is the latter that is retrieved as the first (and second) eigenvector. Similarly, when the horizontal layer has a larger RCS, vertical scattering mechanisms are retrieved. Fig. 5 shows this behaviour in terms of retrieved height for two values of α, -10 and 10 dB. The distributions are unimodal, with a mode at approximately the height of the upper or lower layer. The mean values and standard deviations of the two distributions are respectively

[3]The angle between two unitary vectors $\underline{x_1}$ and $\underline{x_2}$ is defined as $\arccos(|\underline{x_1} \cdot \underline{x_2}^{*T}|)$.

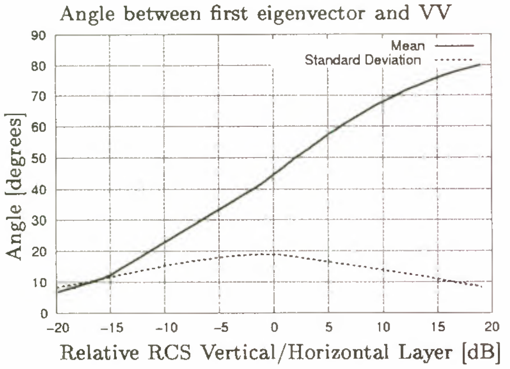

Figure 4. Effect of relative RCS between layers.

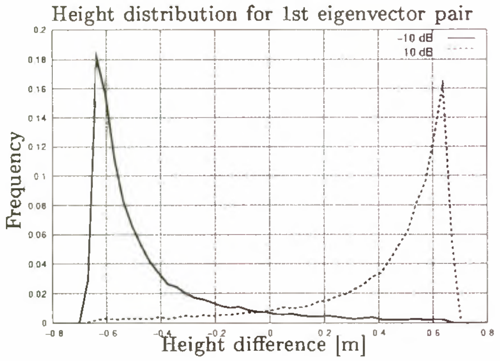

Figure 5. Retrieved height for two different layer RCS ratios, 10 dB and -10 dB. The mean and standard deviation for the -10 dB case are, respectively, -0.45 and 0.25. For the 10 dB case, 0.43 and 0.27.

-0.45 and 0.25 for the 10 dB case, and 0.43 and 0.27 for α =-10 dB.

The difference in height between the first and second pairs of eigenvectors is shown in Fig. 6. The descriptive statistics of these distributions are shown in Table. 2. The first and second eigenvector are clearly similar when the RCS of the layers are different. Simulations for the case of equal RCS between the two layers show a uniform distribution between the VV-HH and HH-VV heights, -1.2 m and 1.2 m.

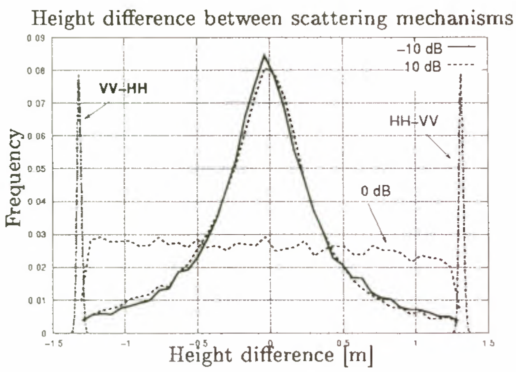

Figure 6. Height difference between the heights retrieved by the first and second eigenvectors for different layer RCS ratios.

Table 2. Mean and standard deviation (SD) of distributions shown in Fig. 6.

Distribution	Mean	S.D.
$\alpha = -10dB$	-0.021	0.46
$\alpha = 10dB$	-0.043	0.46
$\alpha = 0dB$	-0.048	0.75
Difference VV and HH	-1.33	0.01

6. DISCUSSION

When the RCS for the two layers is identical, the retrieved heights are uniformly distributed. The estimation of $\mathcal{M}_{1,2}$ in Eqns. 4-5 yields matrices with similar eigenvalues. Minor changes in the matrices will result in large variations of the eigenvectors, as in Eq. 16. The estimations of height using these vectors result in uniform height distributions.

When RCS of the layers is different, there is a clear biasing of the eigenvectors towards either a VV or an HH-type scattering mechanism. The eigenvector will be similar to VV if the HH layer has a larger RCS than the VV layer, and vice-versa. This behaviour arises from the relative value of γ_1 and γ_2 in Eq. 10. The ratio $|\gamma_1/\gamma_2|$ is plotted in Fig. 7. On the left hand side of Fig. 7, $|\gamma_1/\gamma_2| > 1$, and the associated eigenvectors will be similar to $[1,0]^T$, and hence close to a VV scattering mechanism. On the right hand side of the figure, the situation reverses, and when the vertical layer has a larger RCS than the horizontal layer, the eigenvectors are similar to $[0,1]^T$ (an HH scattering mechanism). The spread of the retrieved heights is shown in Fig. 5. Fhe large mean angles and standard deviations at the edges of Fig. 4 are due to the effect of perturbations in the estimated covariance matrices, which translate into unstable eigenvectors.

The height difference distributions shown in Fig. 6 show that for different RCS values for each layer, the first and second eigenvectors represent the same scattering mechanism (VV or HH). The spread of the distributions is again due to the instability of the eigenvectors. When the layers have equal RCS, the eigenvectors will show an even larger variability as minor perturbations in the covariance matrices have a major effect on the retrieved eigenvectors.

The above simulations do not, however, explain the bi-modality found with the experimental data presented in Sec. 3. A main difference between measured and simulated data is the number of scatterers per footprint. Whereas for the simulations this was constant and large (50 per resolution cell), there were on average only 6 nails per resolution cell in the measured data. This number might fluctuate from one cell to another due to the random positioning of the nails and the variation of resolution cell size with look angle. The effect of this is that the estimation of the covariance matrices departs from matrices that resemble identity matrices, as the main diagonal ele-

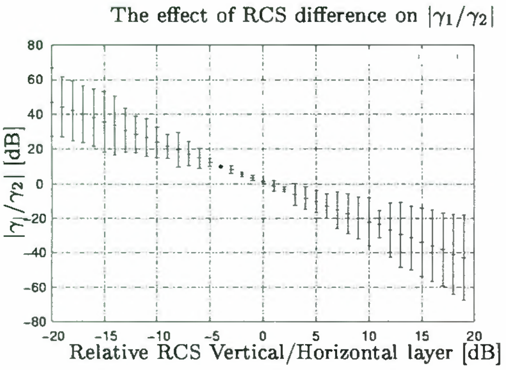

Figure 7. Effect of α in the estimation of the off-diagonal elements in Eqns.4-5 (error bars show standard deviation).

ments vary. The elements of Eq. 10 can be written as $\sigma_1 \neq \sigma_2$ and $\sigma_i \gg \gamma_i$ $i = 1, 2$. The relative weighting of the main diagonal terms will vary from one region of the image to another, and hence, in some areas the eigenvector associated with the highest eigenvalue will be similar to VV, and to HH elsewhere.

From this work, it appears that coherence optimisation in polarimetric interferometry will yield erroneous answers in the case of targets that can be represented in terms of layers exhibiting orthogonal scattering mechanisms. Such targets yield an unstable estimation of optimal scattering mechanisms due to the eigenvalues being very close.

REFERENCES

S R Cloude, K Papathanassiou, "Polarimetric SAR Interferometry", IEEE Trans. Geosci. and Remote Sensing, vol. 36, pp. 1551-1565, Sept 1998.

A Quarteroni, R Sacco & F Saleri, "Numerical Mathematics", Springer-Verlag, New York, 2000

K Morrison, J C Bennett, G Cookmartin, A McDonald, A Race & S Quegan, "Three-dimensional X-band SAR imaging of a small conifer tree", Int. J. of Remote Sensing, vol 22, 4, pp. 705-710, 2001

A McDonald, J C Bennett, G Cookmartin, K Morrison & S Quegan, "The NERC GB-SAR facility", Proc. 24th Annual Conf of the Remote Sensing Society, Univ of Greenwich, pp. 309-315, 1998

ACQUISITION AND EVALUATION OF FIELD MEASUREMENTS FROM THE ALLING-SAR 2000 CAMPAIGNS

M. Herold[2], H. Zwenzner [1], I. Hajnsek[3], M. Davidson[4] & C. C. Schmullius[1]

1: Remote Sensing Unit, Department of Geography, Friedrich Schiller University, Germany
Loebdergraben 32, D-07743 Jena, Tel. ++49-3641-948877, e-mail: c.schmullius@geogr.uni-jena.de

2: Remote Sensing Research Unit, Department of Geography, University of California Santa Barbara
Ellison Hall, Santa Barbara, CA 93106, Tel. ++1-805-8934196, e-mail: martin@geog.ucsb.edu

3: Institute of Radio Frequency Technology and Radar Systems, German Aerospace Center (DLR), Department: SAR Technology, P.O. Box 1116, 82230 Wessling, Oberpfaffenhofen, Germany,Tel. ++49/8153-28-2363,
e-mail: irena.hajnsek@dlr.de

4: CESBIO – UMR 5639 CNES-CNRS-UPS, 18 Avenue Edouard Belin, 31401 Toulouse Cedex 4, France,
e-mail: davidson@cesbio.cnes.fr

Abstract -- The paper presents and investigates the field data acquired over the test site Alling, located in South Germany, in conjunction with the SAR measurement campaigns using the airborne E-SAR system. An overview of the campaigns will be presented, as well as an introduction to the test area and an evaluation of the methods and sampling schemes applied. The collected land surface parameters are soil moisture, surface roughness, land use/cover and leaf area index. These measurements are integrated into a digital database. The investigations indicate that accuracy and problems related to different data and methods are important considerations in use of these types of coordinated field measurements in thematic remote sensing data analysis for land surface parameter retrieval from multi-parameter SAR data.

1. Introduction

A series of SAR-measurement campaigns in the Alling test site (Germany) were conducted in the year 2000 using the Experimental SAR-system (E-SAR) of the German Aerospace Center, Institute of Radio Frequency Technology and Radar Systems. Simultaneously to the flight campaign intensive field measurements has been done in order to allow for quantitative evaluation and validation of developed land surface parameter retrieval algorithms for a multi-parameter SAR systems. The campaigns were organized and sponsored by the British Defense Evaluation and Research Agency (DERA) and the German Aerospace Center (DLR). The field measurements were coordinated and organized by the Department of Geography, University of Jena in cooperation with Institute of Radio Frequency Technology and Radar Systems, DLR Oberpfaffenhofen and the Centre D'Etudes Spatiales de la Biosphere (CESBIO), Toulouse. The various SAR/field datasets are and will be investigated in the "Surface Parameter Retrieval Consortium" (SPARC) an international science cooperation.

This paper will give an overview of the recorded field data and will critically review the occurred problems during the measurement campaign with respect to the applied measurement methods. The surface parameters discussed in this paper are field measurements of soil moisture, surface roughness, land use/cover and leaf area index. At the beginning an introduction to the physio-geographic characteristics of the study area will be given.

2. Overview of Measurement Campaigns

The SAR-data were acquired using the Experimental airborne SAR-system (E-SAR) of the German Aerospace Center (DLR, Horn 1996). The SAR-measurements were recorded in two major campaigns in $28/29^{th}$ of March and 26^{th} of July 2000. They included multi-frequency (X-, L- and P-band) and polarimetric SAR-data as well as single-pass (X-band) and repeat pass (L-band) interferometry.

According to the season of the field measurements the campaign in March was focused on soil moisture and surface roughness estimation. The weather during the March campaign was dominated by cloudy and foggy conditions with temperatures between 5° C and 10° C. A significant amount of rain fell before the March campaign. The soils in the area were characterized by wet conditions due to melting snow water and rain prior to the campaign. The July campaign had, besides the soil moisture measurements, a stronger focus on the acquisition of vegetation parameters. Only a few areas were free of vegetation and suitable for surface roughness measurements. The weather conditions in July can be characterized as partly cloudy and sunny with temperatures between 15° and 20° C, hence the soil moisture measurement were generally lower than those collected during the March campaign.

3. Study Area

The data were acquired in a study site near the village Alling, 25 km south east of Munich, in Germany, close to the German Aerospace Center (DLR) at Oberpfaffenhofen. The study area is located in the transition zone between the foothills of the German Alps and the plains of the Isar-Inn which are composed of glacial and post-glacial sediments (Grottenthaler 1980). The topography is characterized by variations of sedimentary plains, hilly terraces and moraine formations with a maximum

Proc. 3rd International Symposium, 'Retrieval of Bio- and Geophysical Parameters from SAR Data for Land Applications', Sheffield, UK, 11-14 September 2001 (ESA SP-475, January 2002)

elevation of 604 m above sea level at the Altmoräne von Germannsberg. The lowest elevation can be found in the wetland Oberes Moos near Alling, where the elevation is 543 m above sea level (Bayer 1995).

Figure 1 shows a color air photo of the study area that was acquired in March 2000, one week before the SAR data take. It shows the typical characteristics of the landscape with the villages Gilching in the bottom right and Alling in the upper right. The study area is located between these villages and can be divided into three major landscape units.

Figure 1: Color air photo of the study area with discriminated landscape units demarked.

Unit I represents a sedimentary plain with typical small-scale agricultural land use patterns, mainly crop cultivation. The soils classes in this unit are characterized by sand-gravel sediments, mainly cambisols and lessives. These soils show typical agricultural use characteristics like low soil profile depth and low organic matter content. Landscape unit II shows the wetland area "Oberes Moos" that is partly drained for agricultural use and includes some small lakes for fish farming. The land is mainly cultivated with pasture and meadow. The soils in this wetland area show typical wet conditions (gleyic soils) and high organic matter contents. Landscape unit III shows an old moraine formation which is characterized by significant topography. These areas are used for agriculture and forestry. The soils are cambisols and lessives modified by former and recent land cultivation.

4. Field Measurements and Mapping

The field observations should acquire the most important land surface parameter relevant for radar backscatter and the retrieval of thematic information from the SAR-signal. The field data were recorded parallel to the SAR data takes in working groups of 2-3 people with 5-6 groups for each campaign. The majority of the field data were post-processed and integrated into a digital database at the University of Jena, Germany.

4.1. Soil Moisture

Soil moisture is defined as the amount of water in soil that can be evaporated out of the soil matrix at 105 degrees Celsius (Scheffer & Schachtschabel 1998). Soil moisture can be described in volume percent (vol% - volumetric moisture) or in mass percent (mass% - gravimetric moisture). Because actual soil moisture conditions can be influenced by a variety of factors (e.g. precipitation, evapotranspiration, runoff, physical soil properties) it can be highly spatially and temporally variable (Western et al. 2001).

The methods and equipment used in this study provided direct measures of gravimetric moisture using cylinders (Scheffer & Schachtschabel 1998) and volumetric moisture using Time Domain Reflectrometry (TDR, Brisco et al. 1992, Dalton & van Genuchten 1986). The TDR units "TRIME FM2", manufactured by the German company IMKO, measure the moisture content based on the time delay of electromagnetic waves which respond to the dielectric properties of the soil in frequencies between 600 Mhz and 1 Ghz. The length of the sensor probes is 16 cm. The probes were injected into the soil at an approximate 45 degree angle to the surface. The measurements of soil moisture acquired were the mean of the top 5 - 7 cm of the soil profile. The imaginary part of the dielectric constant (ε", energy loss term) was neglected during the measurements. The volumetric moisture values (in vol.%) that are provided by the TRIME TDR instruments can be converted into the real part of the dielectric constant ε' using the following equation. This equation was provided by the manufacturer. VM is the measured volumetric moisture in parts of one:

$$\varepsilon' = 2.95316 + 0.41*(VM) + 156.036*(VM)^2 - 116.943*(VM)^3$$

The gravimetric technique for measuring soil moisture uses soil samples taken with a 5 cm high cylinder. The samples are weighted under moist conditions and weighted again after drying to a constant dry-weight at 105 degrees Celsius at the Laboratory of Geo-ecology at the University of Jena. The difference of the weight of wet versus dry samples determines the gravimetric moisture (in mass %). The TDR and gravimetric samples are generally point measures. A specific strategy in the spatial arrangement of the measurement points was applied in order to capture the spatial patterns of soil moisture. This pattern also allowed for measurements to cover different types of land cover categories with a sufficient density of measurement points. This is important with regards to the variations in the SAR image, i.e. in near and far range and in topographically varying terrain. With consideration of the test area size and the spatial resolution of the sensor, the measurement points were located along profiles that were identified in the field with a point distance of 20 – 50 m. Every point was sampled with 2-5 (usually 3) TDR measurements in a circle of 1-2 m. Gravimetric samples were taken at some points to get a secondary verification measurement of the soil water content.

TDR1	TDR2	TDR3	TDR4	Mean	Variance
30.0	28.5	29.9	-	29.5	0.7
24.7	28.7	28.2	-	27.2	4.7
31.5	33.1	32.5	-	32.4	0.7
27.3	33.2	30.4	-	30.3	8.7
26.9	33.1	28.7	-	29.6	10.2
30.1	30.9	31.2	-	30.7	0.3
32.8	26.5	30.7	-	30.0	10.3
31.0	32.6	29.8	-	31.1	2.0
34.1	30.4	-	-	32.3	6.8
31.2	33.2	-	-	32.2	2.0
38.9	36.5	-	-	37.7	2.9
34.7	31.4	28.0	-	31.4	11.2
34.0	29.1	33.1	-	32.1	6.8
36.2	40.7	31.8	33.5	35.5	15.1
38.8	41.2	39.7	-	39.9	1.5
37.2	39.2	-	-	38.2	2.0
27.5	30.0	29.1	-	28.9	1.6
22.8	26.8	26.0	-	25.2	4.5
32.1	32.2	-	-	32.2	0.0
37.3	34.5	30.8	-	34.2	10.6
35.2	31.7	31.8	-	32.9	4.0
31.7	35.4	31.9	-	33.0	4.3
34.7	37.2	32.9	-	34.9	4.7
40.2	34.1	40.7	-	38.3	13.5
34.0	31.3	31.1	-	32.1	2.6
41.7	33.8	30.5	-	35.3	33.1

Table 1: TDR measurements acquired at 26 points on the field 513 at 28th of March 2000.

Table 1 shows examples of TDR measurements on the field 513. The soil moisture measures on every point show a fair amount of variance between the single measures, at least for some specific locations. They mainly result from inaccuracies in the TDR measurements due to the method itself and from small-scale soil heterogeneities of texture and agricultural cultivation. The overall variance of all measures at this field (mean 6.3 [vol. %], median 4.4 [vol. %]) is a good error indicator for single TDR measurements. Hence, the mean soil moisture value of 2-4 measurements for every point is a more accurate soil moisture representation for a specific location that will be discussed in the following evaluations.

The TDR measurement units were calibrated for "general agricultural soils" that usually have a low organic matter content. The important influences of the soil dielectric constant are the water content and the physical properties. If soil texture is assumed to be homogenous, the organic matter content (OM) becomes an important variable for describing changes in dielectric properties induced by the soil physics (Adams 1973, O'Neill & Jackson 1990). Because the organic matter properties are highly variable, 45 soil samples from the upper 5 cm of the soil were taken and analyzed. The organic matter content analysis used soil material smaller than 2 mm and derived the mass loss at 600 degree Celsius (burning of org. matter-dry ashing) for 5 g of sample material. This method usually works well for higher organic matter content. The lowest derived values (~ 5 %) can be considered to be erroneous. Usual values for agricultural soils in this area have organic matter content values of ~ 1 %. A geostatistical approach (ordinary kriging) was used to derive a spatial distribution of organic matter for the area and to assign an organic matter content value to each measurement point (see Fig. 4)

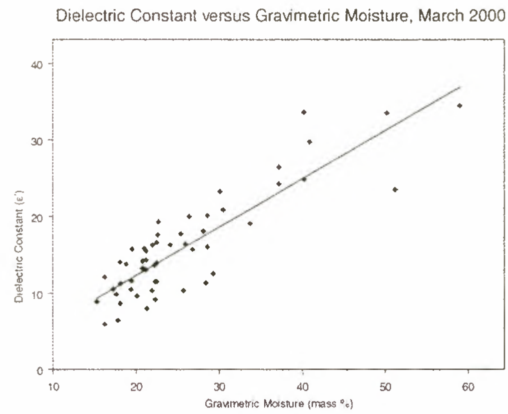

Figure 2: Relationship between gravimetric moisture and the dielectric constant (TDR) for the measurement points.

The evaluation of the TDR measurements (mean point values) as an important source of spatial information about the distribution of soil moisture in these field campaigns will be based on the independent measurements of gravimetric moisture and organic matter content. To provide a wider statistical base for the analysis the evaluation will be done for the field measurement campaigns in March and June. The campaign in June was conducted for another research project in the same area using the same methods and equipment. In general, the measurements in June covered a wider range of organic matter content values and will be used for accordant investigations.

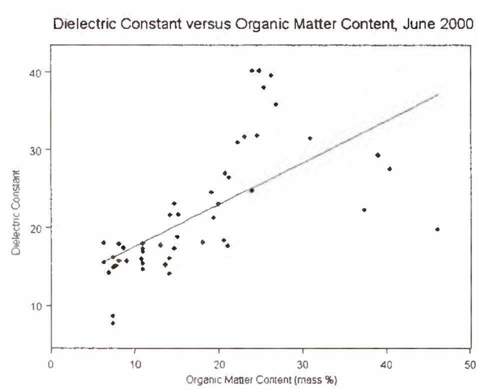

Figure 3: Relationship between organic matter content and dielectric constant for the measurement points.

A plot of gravimetric moisture and dielectric constant derived from TDR measurements, see Figure 2, shows (76% described variance for March, 85% for June) a good overall accuracy for the TDR measurements. For higher soil moisture values there seems to be a higher scatter around the regression line indicating a trend of unequal variance. This results from inaccurate measurements for moister soil conditions.

A positive relationship is shown for organic matter content (OM) versus dielectric constant (DC, Figure 3). This relationship between organic matter content and soil water content can be accounted for three reasons:
1) the presence of organic matter can increase the water holding capacity of the soil,
2) an accumulation of organic matter in the soil generally results from moister conditions, such as in wetlands, fens or swamps and
3) the organic matter content can influence the dielectric properties of the soil.

There is a significantly higher scattering especially for OM values higher than 30 %, this indicates relatively dry conditions in the DC measurements. This trend contradicts the general understanding and the field observations. These points should have higher moisture conditions or should be similar to areas with lower OM conditions. In areas with more than 30 % organic matter the soil moisture estimation error increases significantly.

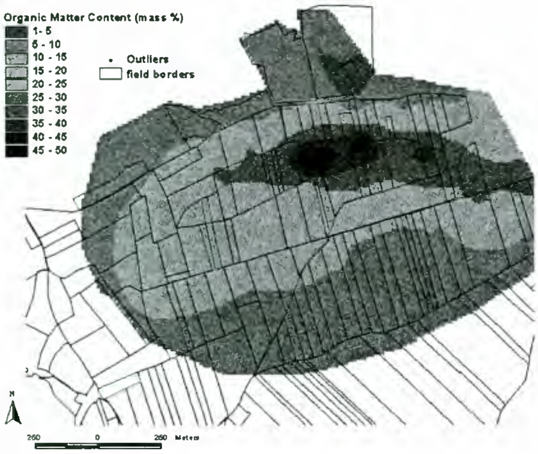

Figure 4: Spatial distribution of the organic matter content. The red dots indicating critical areas where soil moisture has been measured.

The map in Figure 4 shows the problematic points are close to each other in the lens of high organic matter content located in the center of the wetland. This central area in the wetlands should probably be excluded from the remote sensing data analysis due to the obvious errors with the soil moisture measurements in this area.

A non-linear trend can be noticed in the scatter plots of DC versus OM (Figure 3). This trend indicates a different regression slope for values lower and higher than ~18-20 % OM. If the problematic measurements with an OM more than 30 % are omitted from the dataset (at total of 4 points for the June campaign), a multiple regression model of organic matter and gravimetric moisture predicting dielectric constant shows a very strong correlation (R^2= 0.90). Approximately 85 % of the variance in the DC measures are described by the gravimetric moisture; an additional 5 % is represented by the organic matter content, mainly the exponential increase of DC values for areas with more than 18-20 % OM. This indicates a significant contribution of the OM values to the DC measurements.

4.2. Surface Roughness

The micro-scale surface roughness variations in most parts of the test site are determined by the agricultural cultivation. The surface roughness was measured with two methods during the March campaign (scaled boards and Laser Profiler). Only one method (scaled boards) was used in the July campaign. Generally, the selection of the sample fields depends on the method, the sample areas of the other field measurements (e.g. soil moisture test sites), and the field roughness conditions in terms of representing all of the land cultivation/tillage conditions in the test area. In March, the roughness sampling covered all important field roughness categories (seedbed, old ploughed, fresh ploughed).

Figure 5: Illustration of the two methods for measuring surface roughness: scaled board and laser profiler from CESBIO-ESA (Davidson et al. 2000).

The measurements were carried out within one day of the flight campaign and one day after. A relatively fast and efficient approach is to use of thin rectangular metal boards with a standardized raster on it (Ulaby & Batlivala 1976). The boards used for this campaign were of 1 m length and scaled with a 5 cm raster (Figure 5). They are placed on the ground so that the soil surface is clearly visible in front of the board. A picture is taken of the soil surface with the scaled board in the background. The boards are placed side by side to record roughness structures with a distance larger than 1 m. If the field is not located on a slope, the boards were leveled with a spirit level. Several measurements (2–17 samples) were carried out for every sampled agricultural field in parallel as well as perpendicular to the flight direction. At most of the roughness measurement points soil moisture samples were taken as well.

For further data processing the pictures taken of the board profiles were imported into a Geographic Information System (GIS). A digital vector profile was digitised with one-centimeter sampling density. Problems occurred when the surface was covered with organic material, e.g. vegetation, litter or mulch. Therefore, some profiles had to be excluded from further processing. An IDL script was applied to calculate the roughness parameters RMS height (s) and correlation length (l) from the vectorized profile.

Another method of measuring surface roughness was applied during the March campaign. The laser profiler system supported by CESBIO-ESA in Toulouse scans the surface with a profile length of 5 meters and a horizontal sampling density of 5 mm (see Figure 6) (Davidson et al. 2000). The instrument consists of two special supports, supporting a 5 m beam on which a motor-driven chariot with the laser distance meter rides along. Using a theodolite the beam can be displaced in exactly the same direction in order to record profiles up to 25 m. The data were recorded to an attached laptop PC. Profiles of 20-25 m were measured on five fields with different cultivation conditions, also parallel and perpendicular to the row direction. Table 2 shows examples of the roughness measurements during the March campaign.

Field Number	Roughness Category	Number of Board Profiles	Board Profiles		TDR-field mean soil moisture in vol%
			s in cm	l in cm	
263, 264	ploughed	17	1,729	13.35	23.3
255	harrowed	12	0.973	5.50	-
256	seedbed	17	1,077	13.82	24.9
682, 683	fresh ploughed	17	2,997	13.18	35.0
772	ploughed	12	1,909	10.00	32.3
752	ploughed	2	2,165	16.00	24.5
703/2-705/2	ploughed	2	1,534	10.00	46.8
644	harrowed	6	1,254	15.50	(49.1)
648/1	seedbed	2	1,246	25.50	(36.4)
651/1	ploughed	6	1,907	9.83	24.7
652	seedbed	4	1,278	14.00	31.0
513	seedbed	6	1,243	22.33	32.6
797-799	ploughed	6	1,788	8.33	-
773	ploughed	4	2,631	14.50	(18.6)

Table 2: Examples of roughness measures (field mean values) for 14 sampled fields in March 2000, field mean soil moisture measurements in prentices are based on just one or two measurements.

The advantage of the board measurements is their simple application and fast handling on the fields. The afterwards, scanning, digitising and computing of the board profile pictures into the RMS height and surface correlation length is an extensive and time-consuming procedure. On the other hand side the longer profile length measured by the laser profiler, 5 m to 25 m, and the finer resolution makes the laser profiler measurements statistical robust, especially for rougher surfaces and small-scale roughness variations (Davidson et al. 2000). The data handling of the laser profiles is more comfortable due to the direct obtained digital values.

4.3. Land Use/Cover

The land cover/use was mapped for most part of the study area. The field mapping was based on large scale general parcel maps (scale 1:5000, Vermessungsamt Fürstenfeldbruck; Starnberg, map/nr.: SW 1-9, SW 1-10 und N.W.I.10). Mapping equipment used in these field campaigns include, a compass, tape measure, photo camera and special mapping forms. The information acquired for every field included: land use and cultivation, vegetation type, vegetation height, row direction and other relevant descriptions that were observed. All of the relevant geospatial information was included in a GIS database that was georeferenced to the digital field map that was derived from the SAR data and the 1:5000 parcel maps.

4.4. Leaf Area Index

The leaf area index (LAI) is a dimensionless index that is used to quantify the ratio of overall leaf area to covered land surface area. It is an important parameter in description and modeling of vegetation structures and density, as well as for hydrologic properties respectively (Chen & Chilar 1996). Different methods have been developed and evaluated to derive the LAI with different types of field measurements (Gower et al. 1999, Whitford et al. 1995). The measurements during the July campaign were accomplished with a CI-100 Digital Canopy Imager (CID, 1997). It uses an indirect measurement of the plant structure by digital analysis of a photographic image taken through a "fish lens" (150° lens opening) usually oriented from the ground vertically upwards as shown in figure 6.

Figure 6: Example of corn using fish eye lens picture taken with the DCI Plant Canopy Analy

Vegetation	Field number	Measure-ments	Veghöhe (cm)	LAI Field M ean	LAI Standard Deviation
Grassland	692/3	10 (7)	30 - 100	1,68	0,16
Sugar pea	797-799	13 (7)	75 - 100	1,88	0,62
Oat	652	14 (5)	90 - 100	1,05	0,17
Corn	772/1	13 (10)	210 - 268	1,71	0,26
Wheat	647	15 (2)	110	2,16	0,22
Summer barley	649	11 (6)	60	1,76	0,27
Grassland	705	16 (13)	90	2,07	0,55
Grassland	706	26 (17)	40 - 65	1,89	0,30
Tritikale	654/3	12 (4)	130	1,98	0,41
Clover	772	27 (12	20 - 30	2,19	0,46
Potatoes	651/1	15 (14)	50 - 80	2,56	0,92

Table 3: Features of the LAI measurements acquired during the July campaign, the measurement number represents the total samples taken for every field and in

pretences number measurements finally used for field mean LAI estimation.

Compared to direct LAI acquisition methods, this method tends to have errors due to the method itself, changing lightning conditions and the plant heterogeneities, usually cause on overestimation of the LAI (Helmschrot 1999). In order to acquire a representative LAI value for fields of short vegetation in the test area a specific sampling scheme was applied to lower the amount of error. Every measured crop/field was sampled with 10 to 27 measurements (Table 3). The measurements were taken diagonally in the row direction. All sample pictures were evaluated and some of them excluded due to inappropriate lightning conditions (e.g. outshining) and other obvious errors. The pictures were digitally processed and the mean value was derived as representative value for the LAI (Table 3).

5. Final Remarks

In these study the quantitative and qualitative method to measure surface and vegetation parameters has been presented acquired on the test site Alling in March and July 2000. The main scope for the ground measurements campaigns was the use of the data for the validation of inversion algorithms (Davidson et al. 2000, Hajnsek et al. 2001, Herold et al. 2001). All collected field data are included into a substantial digital database that contain several important measurements of land surface parameters relevant to the sensitivity of the radar backscatter. Different methods, specific sampling schemes and data evaluation methods have been used to allow accurate and sophisticated description and acquisition of these parameters.

From the SAR modeling point of view ground measured data are considered to correspond to the correct estimates of surface parameters. Even if this is correct we should point out that ground measured data containing error as well. These errors are provoked due to the sampling methods used and allow only an approximation of the real surface parameters. Uncertainties often occurring during the measurement processes or during the post-processing (e.g. digitizing, laboratory analysis) of the collected data. Accordingly, all field information data need to be applied and analyzed with care and the knowledge of the problems and errors, partially discussed in this paper, should be addressed in any research involving these data.

6. References

Adams, W. A. (1973): The effect of organic matter on the bulk and true densities of some uncultivated podzolic soils, Journal of Soil Science, 24, pp. 10-17.

Bayer, T. (1995): Untersuchung des Informationsgehaltes und rechnergestützte Klassifikation multifrequenter und multipolarisierter DC-8 SAR-Daten des Untersuchungsgebietes Gilching /Oberpfaffenhofen. Dissertation, DLR Forschungsbericht 95-14. DLR, Oberpfaffenhofen.

Brisco, B., Pultz, T. J., Brown, R. J., Topp, G. C., Hares, M. A. & Zebchuk, W. D. (1992): Soil moisture measurements using portable dielectric probes and time domain reflectometry. Water Resources Research, 23, 1339 – 1346.

Dalton, F.N. & van Genuchten, M.Th. (1986): The TDR method for measuring soil water content and salinity.- Geoderma, 38, pp. 237-250.

Chen J. M. & Cihlar, J. (1996): Retrieving leaf area index of boreal conifer forests using Landsat TM images. In: Remote Sensing Environment, 55, 153-162.

CID, Inc. (1997): Digital Plant Canopy Imager CI-100. Instruction Manual. Vancouver.

Davidson, M. W. J., Le Toan, T., Mattia, F., Satalino, G., Manninen, T. & Borgeaud, M. (2000): On the characterization of agricultural soil roughness for radar remote sensing studies, IEEE Transactions on Geoscience and Remote Sensing, 38, 2, 630-640.

Gower, S. T., Kucharik, C. J. & Norman, J. M. (1999): Direct and indirect estimation of leaf area index, f_{APAR} and net primary production of terrestrial ecosystems, Remote Sensing Environment, 70, 29-51.

Grottenthaler, W. (1980): Geologische Karte von Bayern 1:25000 Erläuterungen, Blatt 7833 Fürstenfeldbruck. Bay. GLA, München.

I. Hajnsek, K. P. Papathnassiou, S.R. Cloude, 'L-band versus P-band for Surface Parameter Estimation' *Proceedings of IGARSS'01*, Sydney 2001, in print.

Helmschrot, J. (1999): Integration von Fernerkundung, GIS und empirischer Geländeaufnahme zur Parameterisierung physiographischer Faktoren für die distributive hydrologische Modellierung. Eine Fallstudie im semiariden Flußeinzugsgebiet des Umzimvubu, Ostkap Provinz, Südafrika.- Diplomarbeit, Institut für Geographie der Friedrich-Schiller-UniversitätJena (unveröffentlicht), 144 S.

Herold, M., Shi, J.C. & Schmullius C. (2001): Multi-parameter airborne SAR remote sensing of soil moisture in agricultural areas, *Proceedings of IGARSS'01*, Sydney 2001, in print.

Horn, R. (1996): The DLR Airborne SAR Project E-SAR, http://www.dlr.de/NE-HF/projects/ESAR/igars96_scheiber.html, Version September 1999.

O'Neill, P. & Jackson, T. J. (1990): Observed effects of organic matter content on the microwave emissivity of soils, Remote Sensing of Environment, 31, pp. 175-182.

Scheffer. F. & Schachtschabel P. (1998): Lehrbuch der Bodenkunde, Stuttgart.

Ulaby, F. T. & P. P. Batlivala (1976) "Optimum Radar Parameters for Mapping Soil Moisture," IEEE Trans. Geosci. Remote Sensing, vol. GE-14, no. 2, April 1976.

Western, A. W., Grayson, R. B. & Bloeschl, G. (2001): Scaling of soil moisture: a hydrologic perspective, Journal of Hydrology, in press.

Whitford, K. R., Colqhoun, I.J., Lang, A.R.G. & Harper, B.M. (1995): Measuring leaf area index in a sparse eucalypt forest: a comparison of estimates from direct measurement, hemispherical photography, sunlight transmittance and allometric regression, Agricultural and Forest Meterology, 74, S. 237-249.

A PRIORI ACCURACY ASSESSMENT OF THE DEM DERIVED BY INSAR

Cozmin Lucau, Benoît Moreau, Eric Le Boulengé, Pierre Defourny

Department of Environmental Sciences – Geomatics, Université Catholique de Louvain
Croix du Sud 2/16, B-1348 Louvain-la-Neuve, Belgium, +32 10 47 26 13 (T), +32 10 47 88 98 (F)
lucau-danila@biom.ucl.ac.be, defourny@biom.ucl.ac.be

Abstract: The main objective is to assess statistically the InSAR DEM accuracy with regards to dGPS elevation. The spatial analysis of the systematic error demonstrated the need for correction of local trends by plan equation locally computed. The analysis of the random error leads to propose a model to predict a priori the Z error as a function of the relief roughness and the phase coherence. This serves as an a priori estimation of the error which can be expected from a given pair of SAR images in a given region.

Keywords: DEM accuracy, SAR interferometry, ERS, GPS.

1. INTRODUCTION

SAR interferometric Digital Elevation Model (DEM) becomes a remote sensing product available off the shelf. However the absolute accuracy to be expected for such product remains a main critical issue for the potential user. Previous experiences [4] have demonstrated the influence of the slant range and incident angle accuracies, the baseline and the crossing angle between the two selected orbits, the topographic features type, and the InSAR techniques. However, the quality of the interferometric phase also varies with the land cover type, the atmospheric conditions (wind, rainfall event, etc), and some other surface parameters (moisture, etc).

Indeed the accuracy assessment of a DEM requires the estimate of the errors in planimetry (X,Y) and in altimetry (Z). Of course these are interrelated but must be analysed separately based on a representative set of samples. Three specific issues must be taken into account for InSAR DEM assessment. (i) The X,Y,Z errors depend on the relief type due to the SAR signal nature. (ii) The Z error estimation requires the correction of the X,Y planimetric errors. (iii) The X,Y error estimation is only feasible for clearly visible features. Such a dedicated sampling and statistical analysis strategies have been developed for the DEM quality control. This research also aims to propose a method to provide a priori accuracy information about the DEM to be derived by InSAR techniques from a given image pairs. The study was completed with the support of the Région Wallonne for the Centre Spatial de Liège and with their close collaboration.

2. DATA SET

An unique reference data set has been collected and compiled to achieve the experiment. The study area covers the Ardennes region characterised by a hilly relief in the South-Esat of Belgium. Typical InSAR DEM's were produced by the Centre Spatial de Liège from the ascending images acquired on the 14th and 15th April 1996 during the ERS-1/2 Tandem phase (quadrant 999, orbit 24838 (E1) and orbit 5208 (E2)). The altitude ambiguity is 170 m. Phase coherence and PRI images were also made available for the study. In this region the planimetric reference is a 1-m digital orthophoto mosaic acquired in 1995 for the whole study area.

Three sources of information are combined for the Z error estimation. A 1:50,000 contour-derived DEM covers the whole country with the following technical specification : a confidence interval varying between 3.8 to 10.2 meters for a 90% probability [10]. A grid-derived DEM produced by automatic photogrammetric restitution provides the top surface elevation every 40 m along a systematic grid sampling. This elevation corresponds to the top of the land cover, i.e. the top of the forest canopy, the building roof, etc. The two latter sources were delivered by the National Geographic Institute of Belgium. The third one consists of a dedicated set of 320 points distributed over the study area and which can be precisely located on the orthophoto mosaic and on the coherence or the PRI images. The X,Y,Z coordinates of these points were measured by dGPS using a TRIMBLE ProXR receiver and a dedicated TRIMBLE base station. The differential correction is applied in post-processing to reduce the impact of the differential age of the correction factor and insures an error inferior to 1 m all over the study area.

Proc. 3rd International Symposium, 'Retrieval of Bio- and Geophysical Parameters from SAR Data for Land Applications', Sheffield, UK, 11-14 September 2001 (ESA SP-475, January 2002)

3. METHODOLOGY

The overall approach relies on two main factors influencing the DEM accuracy : the relief type and the coherence level. These variables have been selected because they can be a priori known before the DEM generation. The sampling strategy of the reference points was therefore stratified according to both criteria. The selected topographic variable is the local roughness measured by the local standard deviation of the elevation computed within a moving window of 1 km². The phase coherence image is directly derived from the SAR images pair.

Four zones characterized by contrasted conditions with regards to the topographic roughness and the coherence level have been selected. Each zone corresponding to 4 1:25,000 map sheets covers 320 km² (figure 1). A set of 80 reference points were measured by dGPS in each zone. These points fulfilled the following conditions : (i) these are landmarks clearly identified on the coherence or PRI images, (ii) their spatial distribution is as uniform as possible, (iii) they lie 40 m away from any forest or building, (iv) the dGPS coordinates are averaged from 90 measurements using the C/A code received from at least 5 satellites with a Position Dilution of Precision (PDOP) inferior to 4.

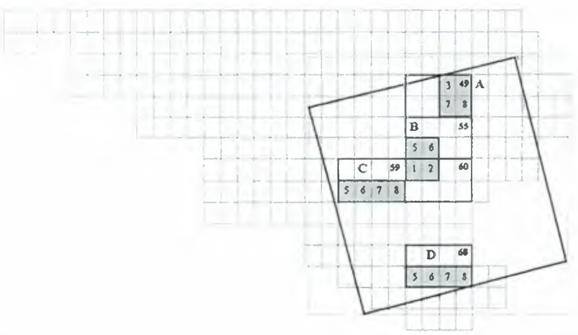

Figure 1 : Selection of the four zones A (high roughness - low coherence), B (high roughness - high coherence), C (low roughness - low coherence) and D (low roughness - high coherence) within the SAR scene.

Once the dGPS reference points campaign is validated, the statistical analysis address successively three objectives : the planimetric accuracy assessment, the elevation accuracy assessment and the prediction model development. The systematic and random components of the elevation error are separately investigated. The statistical approach is based on the residues distribution analysis with regards to the proposed stratification criteria and on multivariate methods.

4. RESULTS

4.1. Validation of the dGPS campaign

The comparison between the best available DEM derived from digital photogrammetry and the dGPS points (figure 2) allows to carefully validate the reference data set of this experiment. Regression analysis between the NGI elevation and the dGPS elevation for each zone shown no significant influence of the zone to the dGPS elevation accuracy. While all the coefficient of determination are above 0,99, the NGI DEM seems to slightly overestimate the elevation (Root Mean Squared Error (RMSE) between 1.6 to 2.4 m). These values match the technical specifications announced by the NGI.

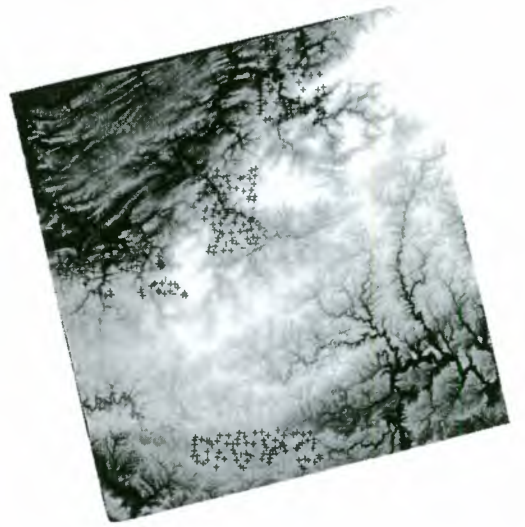

Figure 2 : NGI 1:50,000 DEM and spatial distribution of the dGPS reference points located throughout the 4 zones.

4.2. Planimetric accuracy assessment

The first DEM produced with 40-m grid cells could not be geometrically rectified because of the lack of accurate control point to select. Module images have then been generated at 16 m resolution to make a color composite combining both images and the average of both. Finally 5 control points have been simultaneously identified on the SAR color composite and on the 1-m orthophoto mosaic. A first order polynomial function was computed and applied with a RMSE of 0.93 pixel, i.e. 14.88 m. Such a planimetric accuracy is quite compatible with the precaution taken for the dGPS reference points selection, i.e. area as flat as possible 40 m away from any object.

4.3. Elevation accuracy assessment

The elevation Z_{InSAR} estimated by interferometry is the sum of the real elevation Z_{real} and two different error component, namely the bias b and the random error E :

$$Z_{InSAR}(x,y) = z_{real}(x,y) + b(x,y) + \mathrm{E}(x,y)$$

Analysis of the systematic error in InSAR DEM

The comparison between the 1:50,000 DEM and the InSAR DEM highlights a bias which could be expressed as plan equation :

$$b(x,y) = a_0 + a_x x + a_y y$$

The next step is to estimate the parameters of this systematic error plan based on the reference set of dGPS points. Assuming Z_{dGPS} equal to Z_{real} the difference between the Z_{InSAR} and Z_{dGPS} has been computed for the 320 points and the plan parameters estimated by the least squared method. The Z_{InSAR} elevation is then corrected for its systematic error b thanks to this plan equation. Once the error component removed and three outliers eliminated the Z_{InSAR} RMSE reaches 15.5 m.

The remaining difference observed between the adjusted Z_{InSAR} and the Z_{dGPS} is systematically investigated for each zone. The analysis of the distribution of these residues highlights different bias according to the zone and the altitude. As shown in the figure 3 there is a negative bias for the high altitude in zone A while zone C shows similar bias for the low altitude and zone B a positive bias.

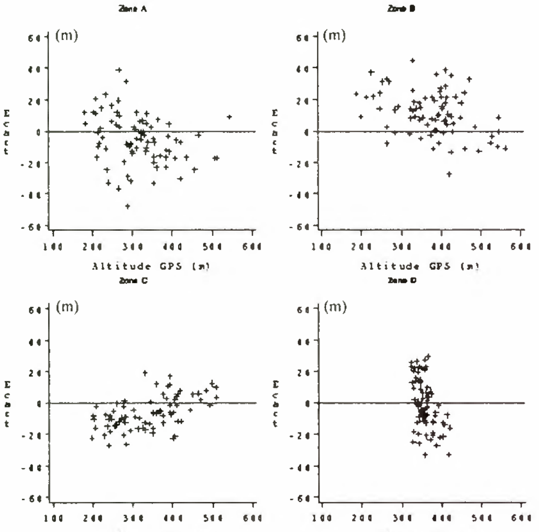

Figure 3 : Residues between the Z_{InSAR} corrected by a single plan and the Z_{dGPS} plotted per zone and per altitude.

These trends appear to be spatially distributed on the figure 4. A regression analysis of the residues as a function of the longitude and the latitude for each zone demonstrates the existence and the need of four different error plans instead of a single one for the whole scene. Further examination would probably allow to relate these error plans to the phase unwrapping procedure and more specifically to the way this manages the fringe discontinuities.

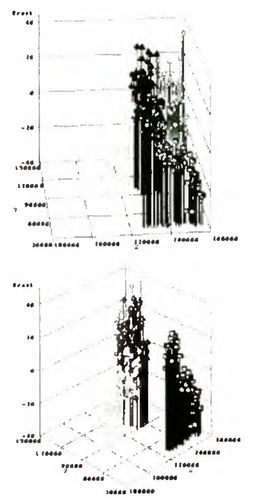

Figure 4 : Four different 3-D views of the same spatial distribution of the residues between the Z_{InSAR} corrected by a single plan and the Z_{dGPS} .

As explained previously for a single plan the plan parameters have been recomputed per zone from the dGPS reference points and applied to adjust the Z_{InSAR} . This adjusted Z_{InSAR} does no longer show any bias as clearly illustrated in the figure 5. However the dispersion of the residues appears to be different from one zone to an other. However no additional systematic trend was found neither by visual examination neither by statistical exploration. From these results it can be concluded that the size of these zones allow to fit a local plan to remove the systematic error unlike the level of the whole scene.

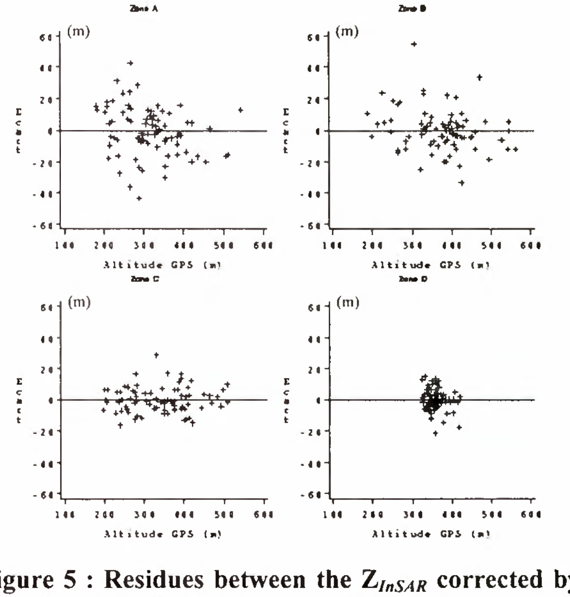

Figure 5 : Residues between the Z_{InSAR} corrected by four different plans (one different for each zone) and the Z_{dGPS} plotted per zone and per altitude.

Analysis of the random error in InSAR DEM

The causes of the random error distributions may be investigated thanks to the stratification of the reference sampling. As plotted in the figure 5 the dispersion of the difference between the adjusted Z_{InSAR} and the Z_{dGPS} is twice larger for the zone A and B compared to D. The respective RMSE are reported in the table 1. The confidence interval for the standard deviation of the error on Z is estimated for each zone by the square root of the confidence interval for the variance of random gaussian variable. Figure 6 shows the decrease of this confidence interval from the zone A to zone D. The constrated results obtained for the difference zones call for further investigation of the role of the stratification variables to the random error distribution.

Zone	Coherence	Roughness	Estimation of the error standard deviation (m)
A	Low	High	15.5
B	High	High	12.0
C	Low	Low	8.1
D	High	Low	6.8

Table 1 : Estimation of the error standard deviation for each zone.

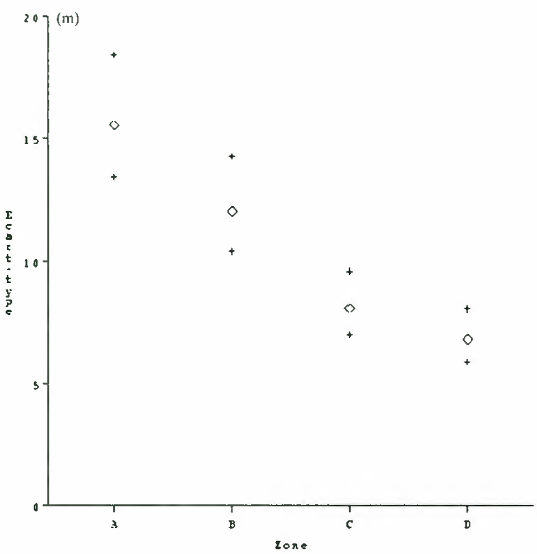

Figure 6 : Confidence interval of the error standard deviation of Z for each zone.

4.4. Prediction model

The InSAR coherence and the topographic roughness variables have been respectively recoded in four intervals. While the previous analysis proceed by zone the investigation at this stage focuses at the pixel level. As these variables are in a raster format a coherence interval and a roughness interval have been affected to each dGPS reference point based on its geographic position and independently to the zone it belongs to. The different combination of the coherence and the roughness intervals made 16 different classes. The frequency of points corresponding to each class remains relatively high as reported at the table 2. The standard-deviation of the difference between the adjusted Z_{InSAR} and the Z_{dGPS} is computed for each class. As show in the figure 7 the coherence and the topographic roughness respectively influence the elevation accuracy. The two variables appear independent but linearly cumulative.

Points		Roughness 1 (0-10)	Roughness 2 (10-20)	Roughness 3 (20-30)	Roughness 4 (>30)
Coherence	1 (<0.65)	18	31	16	9
	2 (0.65- 0.70)	11	12	16	7
	3 (0.70-0.75)	24	33	20	9
	4 (>0.75)	40	42	15	13

Table 2 : Number of dGPS reference points belonging to each class based on the coherence and roughness combination. The interval values for these two variables are indicated between brackets.

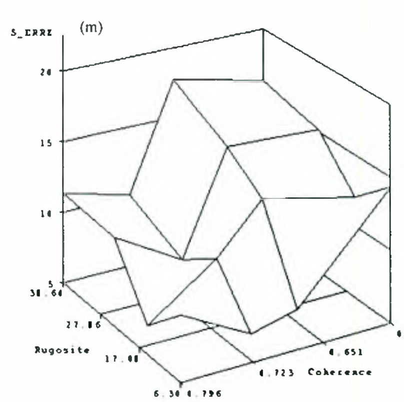

Figure 7 : Errors computed per class from the dGPS data set and plotted as a function of the coherence and the roughness.

These results can be smoothed by a multivariate regression in order to propose a prediction model of the adjusted Z_{InSAR} error as a function of the roughness and the coherence observed for a given location. The predicted standard deviation S_{pred} of the Z_{InSAR} error can then be a priori estimated for each grid cell by :

$$S_{pred} = 25.34 - 23.6 * Coh + 0.12 * Rough$$

These results indicate that the standard deviation of the error may be inferior to 5 m in favourable conditions, i.e. coherence higher than 0.75 and roughness below 10. At the opposite the error may have a standard deviation higher than 15 m in bad situations, i.e. coherence lower than 0.65 and roughness higher than 30 (figure 8).

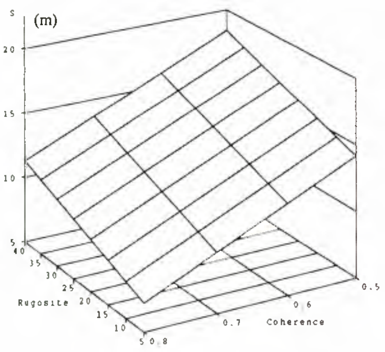

Figure 8 : Errors predicted by the regression model based on the coherence and the roughness.

Based on this model a map of the predicted error is produced (figure 9). The RMSE average value for the whole scene is 11.44 (mean error equal to 11.24 m). This average includes the very noisy lines where the error is abnormally high. Of course this accuracy can be reached thanks to the computation of local plan for the systematic error correction.

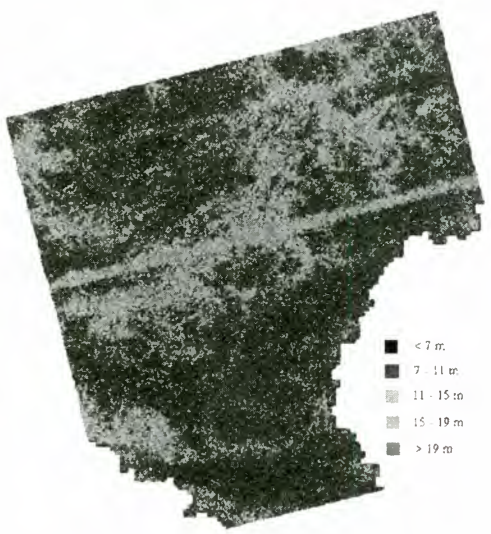

Figure 9 : Map of the predicted error by the roughness – coherence model for the whole study area.

5. Conclusions

This statistical investigation of the InSAR DEM planimetric and altimetric accuracies leads to some useful conclusions. While 40-m grid cell is a suitable resolution for a DEM, such a resolution did not allow to rectify or georeference it precisely. Higher spatial resolution of SAR composite is required to select a good set of GCP's and obtain a planimetric accuracy lower than 1 pixel. It must also be noticed that the spatial resolution increase is associated with a non-linear increase of the noise for the Z estimation. The calibration of the elevation values through a single plan to remove the systematic error appears to be a very coarse solution. Indeed local trends observed at the zone level, i.e. 320 km, can easily be taken into account to increase the RMSE values from 15.5 m to 11 m. Further investigations are required to identify the technical reasons of these local trends and to adjust the zone size for local modelling accordingly. Least but not last, the analysis of the random error component demonstrates their strong relationships with the roughness of the topography and the InSAR phase coherence both at the zone and at the pixel levels. Therefore the concept of a priori prediction model of the standard deviation error has been proposed based on these two variables available before the DEM generation. This model has been successfully computed for the study area and allows to predict the elevation error for any given pixel of the scene. Such promising results call for additional experiment to repeat the approach in other environments. This would allow to confirm the feasibility of the a priori prediction of the error expected for a DEM to be generated from a given images pairs in a given area. Such a priori information is of great interest for any potential InSAR DEM users.

Acknowledgments

The authors are grateful to Dr. Dominique Derauw for his fruitfully collaboration.

6. References

[1] Deraw D., 1999, *Phasimétrie par Radar à Synthèse d'Ouverture ; théorie et applications*, Thèse présentée à l'Université de Liege, 126 p. ;

[2] Council's GIS Standards Committee, 1999, *Positional Accuracy Handbook*, Land Management Information Center, p.9.

[3] P.C. Kyriakidis, A.M. Shortridge, M.F. Goodchild, *Geostatistics for conflation and accuracy assessment of digital elevation models*, Int.J.Geogr.Inf.Sc. vol 13, no. 7, pp. 677-707, oct. 1999.

[4] Xiaoqing W., Karl-Heinz T., Wehr A., 1997,*The Effects of different Land Covers on the Accuracy of Interferometric DEM*, Proceedings Fringe 96 Workshop, Zurich, Switzerland, vol. 2, p.33 – 41. Available: http://www.geo.unizh.ch/rsl/fringe96/papers/thiel-wu-2/

[5] C.S. Nielsen, R. Forsberg, S. Ekholm, 1997, *Merging of Elevations from SAR Interferometry, Satellite Altimetry, GPS and Laser Altimetry in Greeland,* Proceedings Third ERS Symposium, Florence, Italy, vol 1, p. 415-420.

[6] M. Crosetto, F.P.Aragues, 1999, *Radargrammetry and SAR interferometry for DEM generation : validation and data fusion*, Proceedings SAR Workshop, Toulouse, France, pp367-372.

[7] L. Kenyi, H. Raggam, 1997, *Accuracy assesment of interferometrically derived DTMs*, Proceedings Fringe 96 Workshop, Zurich, Switzerland, p.51 – 56.

[8] J.P. Muller, A. Mandanayake, K. Murray, D. Holland, 1997, *Assesement of intereferometric SAR DEM for UK National mapping*, Proceedings Fringe 96 Workshop, Zurich, Switzerland, p.71 – 80.

[9] D. Small, D. Nüesch, 1997, *Validation of Height Models from ERS Intreferometry*, Proceedings Fringe 96 Workshop, Zurich, Switzerland, vol. 2, p.43-53.

[10] Institute Géographique de Belgique Données numériques, Modele Numérique de Terrain http://www.ngi.be/FR/FR1-5-6.asp

[11] U.S. Departement of the Interior,1998, *Standards for Digital Elevation Models*, U.S. Geological Survey, National Mapping Division.

[12] Bolstad P. V., Stowe T., 1994, *An evaluation of DEM accuracy : elevation, slope and aspect*, Photogrammetric Engineering & Remote Sensing, Vol 60 (11), p 1327-1332.

[13] Defourny P., Hecquet G., Philippart T., 1999, *Digital Terrain Modeling: Accuracy Assessement and Hydrological Simulation Sensitivity.* In Spatial Accuracy Assessement: Land Information Uncertainty in Natural Resources, pp. 61 – 70.

[14] Li Z.,1994, *A comparative study of the accuracy of digital terrain models (DTMs) based on various data models*, ISPRS Journal of Photogrammetry & Remote Sensing, Vol 49 n° 1, pp.2 - 11.

RADAR AND GROUND MEASUREMENTS ON WHEAT FIELDS OVER THE MATERA SITE: AN EXPERIMENTAL STUDY

Francesco Mattia (1), Anna Maria Gatti (1), Franco Posa (2), Angelo D'alessio (2), Claudia Notarnicola (2), Enzo Sabatelli (3), Michele Rinaldi (4),
Giuseppe Satalino (5), GuidoPasquariello (5), Thuy Le Toan (6), Ghislain Picard (6), Malcolm Davidson (6)

(1) *Istituto di Tecnologia Informatica Spaziale (ITIS)-CNR, Matera,* Italy,
email: Mattia@itis.mt.cnr.it
(2) *INFM e Dipartimento Interateneo di Fisica, Bari, Italy*
(3) *ENEA-C.R. Trisaia - Rotondella, Matera, Italy*
(4) *Istituto Sperimentale Agronomico, Bari, Italy*
(5) *Istituto Elaborazione Segnali ed Immagini (IESI)-CNR, Bari, Italy*
(6) *Centre d'Etudes Spatiales de la BIOsphere (CESBIO), Toulouse, France*

ABSTRACT

This paper describes ground and radar measurements collected on wheat fields over the Matera site in Italy during the 2001 growing season. The objective of the paper is twofold. Firstly to investigate the relationship between the C-band backscatter with wheat biomass and with the underlying soil moisture content. Secondly to provide well documented data in order to validate electromagnetic scattering models for cereal crops.
From March to June 2001 six ERS-2 overpasses of the site have been acquired. In addition, eight C-band ground-based scatterometer acquisitions, at HH and VV polarisation, with incidence angles ranging between 23° and 60° have been achieved. Coinciding with ERS-2 and scatterometer acquisitions ground data in terms of soil moisture, wheat biomass and canopy structure have been collected. This paper describes the experiments and presents the first data analysis.

INTRODUCTION

Electromagnetic (em.) scattering from wheat fields has attracted remarkable interest in the microwave remote sensing community since many years [Le Toan et al. 1984; Ulaby et al., 1985; Ferrazzoli et al., 1994]. This is an important topic both from a scientific and an application point of view. The scientific interest arises from the complex nature of the interaction between em. waves and wheat canopy. At the same time, the possibility of retrieving wheat biomass and soil moisture content from radar data is of considerable importance for agronomic applications.
However, in spite of recent progress in modelling scattering from wheat or grass-like canopies [Stiles and Sarabandi, 2000a; Picard et al., 2001] theoretical predictions are far from being fully validated and open questions still remain. In addition, in order to assess the use of simple empirical approaches to retrieve wheat biomass, radar and ground data acquired over the complete range of growing conditions are necessary.

In this context, the objectives of this paper are to:

- experimentally investigate the relationship between both sub canopy soil moisture content and wheat biomass and C-band radar backscatter at HH or VV polarisation and at different incidence angles;
- provide well documented radar and ground data for validation of theoretical direct models.

To achieve these objectives an experiment has been carried out at the Matera test site in Italy from March to June 2001. Radar and ground data have been acquired over 4 different wheat fields during the growing season. Radar data consist of both ERS-2 data and C-band scatterometer measurements at different incidence angles and polarisations. Ground data include fresh biomass and canopy structure measurements as well as sub canopy soil moisture content and surface roughness. In the next section, the overall experiment is briefly described. Then the ground data as well as the methodology used are summarised. Subsequently the sensitivity of scatterometer and ERS-2 data to relevant ground parameters is illustrated. Finally some conclusions are given.

MEASUREMENT CAMPAIGN

The selected site is an area close to Matera (Italy) (Fig.1). This is a predominantly agricultural area mainly devoted to wheat cultivation. The topography of the

Fig. 1 Matera in the Basilicata region

Proc. 3rd International Symposium, 'Retrieval of Bio- and Geophysical Parameters from SAR Data for Land Applications', Sheffield, UK, 11-14 September 2001 (ESA SP-475, January 2002)

area is characterised by undulating hills alternating with relatively flat stretches of land lying within the valleys. Four wheat fields, identified as field 1, 2, 3 and 4, have been selected over a flat area called Rondinelle. Fields 1, 2 and 3 range between three and ten hectares, field 4 is smaller than one hectare. According to the local crop management scheduling, durum wheat (i.e. Triticum durum Desf.) is usually sown at the end of December. In fact, a temporal shift of approximately twenty days occurred between the sowing period of field 2 with respect to fields 1, 3 and 4. Normally wheat reaches its full growth at mid May and is harvested approximately at mid June depending on weather conditions. From March to June 2001 eight ground and scatterometer measurements have been carried out over field 4. In addition, ground measurements over fields 1, 2 and 3 have been conducted during six ERS-2 overpasses. Table 1 summarises the dates for which ground and radar data (i.e. scatterometer and/or ERS-2) have been acquired.

Date	Sensor	ERS-2 orbit	ERS-2 track	Ground measur. (fields)
08/03	Scatt.			4
16/03	ERS-2 & Scatt.	30866	451	1 & 2 & 3 & 4
04/04	ERS-2 & Scatt.	31138	222	1 & 2 & 3 & 4
20/04	ERS-2 & Scatt.	31367	451	1 & 2 & 3 & 4
04/05	Scatt.			4
09/05	ERS-2 & Scatt.	31639	222	1 & 2 & 3 & 4
24/05	Scatt.			4
25/05	ERS-2	31868	451	1 & 2 & 3
13/06	ERS-2 & Scatt.	32140	222	1 & 2 & 3 & 4

Table 1 Dates for which radar and ground data are available

GROUND DATA

The collected data include: wheat phenological stage, wheat biomass (i.e. fresh weight of wheat/m^2 separated into weight of stems, leaves and ears); canopy structure (i.e. geometric description of canopy) and soil measurements (i.e soil roughness and soil moisture content as well as soil texture). Table 2 lists the achieved ground data. Soil roughness profiles have been acquired only once during the first ground campaign (i.e. on March 8) when wheat was at a very early stage. A 4m long needle-like profiler was exploited to measure soil roughness along directions parallel, perpendicular and at 45° with respect to the row directions. Soil moisture content for each field has been measured using the gravimetric method. Over the area, the typical volumetric soil moisture content is between 25 and 15% in March-April, whereas in May-June it may range between 15 and 5%. However, due to a few days of continuous raining, the maximum soil moisture value (i.e. 27-30%) was reached on May 9. Consequently, between May 4 and 9 there was a difference of approximately 15-20% in the volumetric soil moisture content of the area.

The majority of ground measurements have been carried out on site within three hours from ERS-2 overpasses and during the scatterometer acquisitions. Typically, for each field, ground data have been collected at three different locations.

Canopy structure measurements
Plant density (plant/m ^{2})
Row spacing
Stems/plant
Leaves/stem
Stem diameter
Stem length
Ligule position
Leave shape
Leave thickness
Flag leaf geometry:
Shape/inclination/curvature
h/width/thickness
Ears:
length/width/thickness
Agronomic measurements
wet/dry weight of stems/m ^{2}
wet/dry weight of leaves/m ^{2}
wet/dry weight of ears/m ^{2}
Soil measurements
4m long roughness profile
soil moisture content at 0.05m depth

Table 2 Ground data acquired during the experiment

For each location, a whole set of ground data has been acquired. 30 measurements of plant geometry (i.e. stem height and orientation; flag leaf length, width and inclination; ear length, width and thickness, etc.) have been carried out on site. In addition, either 1 or 0.5m (depending on the wheat growing stage) of plants along the row direction has been collected, separated into stems, leaves and ears, and then weighted, within 1-2h, to obtain the fresh wheat biomass. The stems density (i.e. number of shoots/m^2) was estimated too. Its mean value was approximately 400 shoots/m^2 with a maximum spread of ±200 shoots/m^2. Besides, a second set of plants (i.e. typically 15) has been collected in order to characterise the finer geometrical details (i.e. stems radius at different heights, leaves thickness, etc.) in laboratory. The components of these plants have been scanned to permit an accurate characterisation of shapes of stems, leaves and ears. Wheat water content has been separately measured for stems, leaves and ears by drying the collected samples in an oven at 72° for 24h.

As an example, Figures 2 and 3 show the stems height and the total fresh wheat biomass measured during the campaign, respectively. As can be seen, there is a significant variability in the wheat variables collected over different fields, i.e. plant height in March-April and wheat biomass in April and May.

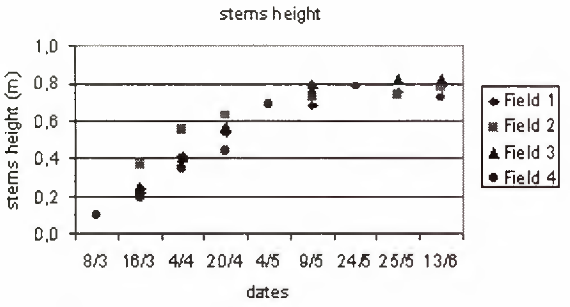

Fig.2 Measured stems height

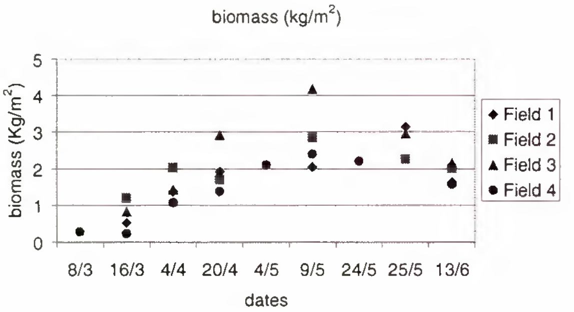

Fig.3 Measured fresh wheat biomass

This is partly due to soil variability and partly to differences in crop management of fields. For instance, field 2 has been fertilised with nitrogen and weed-controlled whereas fields 1, 3 and 4 have not been treated. These differences produce a significant variability between the canopy parameters of different wheat fields.

SCATTEROMETER DATA

The scatterometer sensor employed in this experiment has been realised and run by the team of the University of Bari [Sabatelli et al., 1999]. The sensor is a C-band FM-CW radar which can measure backscattering coefficient between +10dB and –40dB, for target distances between 10 and 60m and for incidence angles ranging between 10° and 60°. A dedicated software allows the sensor control, data processing and displaying. Table 3 summarises the main sensor specifications.

During the experiment, the sensor has been mounted on a truck platform at 15m from ground (Fig.4). Measurements at HH and VV polarisation for an incidence angle ranging between 23° and 60° have been carried out.

For each incidence angle, 36 independent samples were acquired by azimuthally rotating the platform.

Parameter	Value
Center frequency	5.3 GHz
Instrument model	Linear FM-CW radar
Modulation band	300 MHz
Modulation signal	Triangular (60 Hz)
Antenna type	Horn antenna
Antenna beamwidth	6.4°
Antenna gain	15 dB
Polarisation modes	VV, VH, HV, HH
Range resolution	0.65m
Calibration	Internal (delay line) External (corner reflector)
Measurement error	± 1dB

Table 3 Scatterometer specifications

External calibration using a trihedral corner reflector has been performed for each incidence angle at the beginning and at the end of the acquisition.

Due to the acquisition geometry, the angle between range and wheat row direction is not constant during each acquisition (it approximately ranges between 20° and 160°). However, a recent study [Stiles et al., 2000b] has shown that at C-band the effect of wheat row direction on backscattering coefficient is not very important.

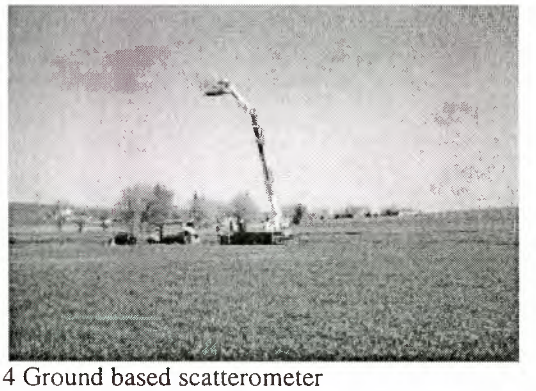

Fig.4 Ground based scatterometer

Subsequently the independent samples have been calibrated and then averaged in order to estimate the backscattering coefficient.

Figure 5 shows the backscattering coefficient as a function of the incidence angle for two different acquisition dates (i.e. April 4 and May 24) at VV polarisation. During the first acquisition wheat was at the booting stage, whereas during the second acquisition, wheat was at the ripening stage. Trends similar to those shown in Figure 5 have already been observed and interpreted [Stiles et al., 2000b; Quegan et al., 2001]. In this respect, it is worth mentioning that the main scattering mechanisms for wheat fields consist of direct scattering from soil, direct scattering from canopy and double bounce canopy-soil [Picard, 2001]. In addition, VV polarised incidence waves interact much more with the canopy than HH polarised waves. This is due to the canopy symmetry, which is determined by vertical stems. At C-band, the relative importance of these mechanisms depends on the wheat stage and on the incidence angle/polarisation. When wheat is at an early stage (i.e. on April 4), the main backscatter contribution comes from soil regardless of incidence angle. Consequently the backscatter monotonically decreases as a function of incidence angle. On the contrary, for fully developed wheat the predominant scattering mechanism depends on the incidence angle. At small incidence, the soil (i.e. direct and double bounce) is still the predominant mechanism. At higher incidence angles, the soil contribution is considerably attenuated (i.e. the wave travels through a thicker canopy layer). Consequently, the scattering from the canopy becomes dominant. This happens around 40° incidence then, from there the backscatter increases.

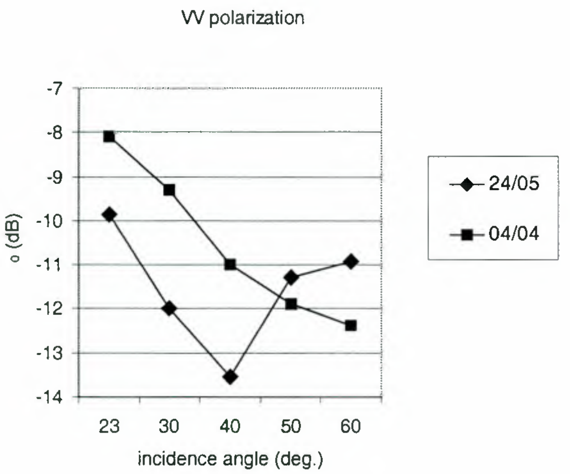

Fig. 5 Backscattering coefficient, at VV polarisation, as a function of the incidence angle for two different dates.

An interesting question under discussion is the sensitivity of radar backscatter to soil moisture content as a function of incidence angle, polarisation, wheat growth stage and soil moisture. In our experiment, ground and radar measurements were carried out during two close dates, namely May 5 and 9. Between these two campaigns there was a heavy rain. Consequently a difference in soil moisture content around 15-20% was measured on field 4. Since all the other parameters were considered to have small change at field 4 between these two close dates, the sensitivity of radar backscatter to soil moisture content in medium-wet conditions can be studied. Fig. 6 displays the HH and VV backscatter for both dates.

As can be seen, at small incidence angles, where the soil contribution is expected to be dominant, there is a significant difference between the backscatter of the two dates. This difference is higher at HH than at VV polarisation. At higher incidence (i.e. 40° for HH and 40°-50° for VV), this difference tends to decrease and it is again quite significant at 60°.

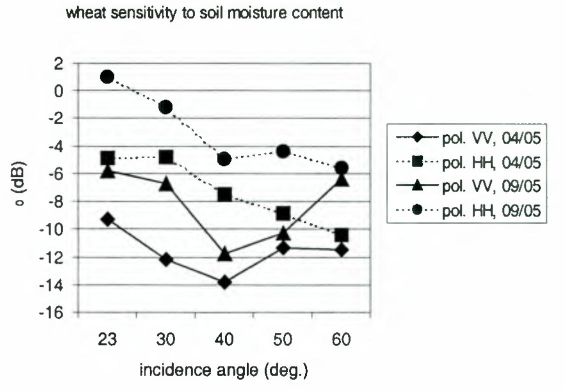

Fig.6 Backscattering coefficient, at VV and HH polarisations, as a function of incidence angle for two different dates

While the trends between 20° and 50° are similar to other results obtained by indoor measurements [Quegan et al., 2001], the behaviour at 60° incidence has not yet been observed and modelling is required to assess its origin. To further assess the backscatter sensitivity to soil moisture content, Figure 7 shows the backscatter at HH and VV polarisation versus the soil moisture content for all the acquisitions and at 23° incidence. The figure indicates that:

- at HH polarisation, there is a good correlation between the radar backscatter and the soil moisture, meaning that the backscatter results mainly from the soil contribution and is moderately affected by vegetation through the whole growing season;
- at VV polarisation, although the soil contribution is still dominant, the effect of vegetation is to significantly modulate the backscatter level as a function of wheat growing stage. Consequently, the radar sensitivity to soil parameters is masked by changes in the canopy parameters.

According to these results, a C-band radar configuration at HH polarisation and small incidence angles, may have a good potential to monitor soil moisture changes in presence of wheat canopy. However, it should be emphasised that these multi-temporal data concern backscatter from a single field. To assess the potential of such a configuration for monitoring soil moisture over larger areas, the backscatter sensitivity to soil moisture content should be studied under different field conditions (i.e. differences in plant density, species, soil roughness).

Finally, Figures 8 and 9 illustrate the HH and VV backscatter sensitivity to total above ground wheat biomass for 23° and 40° incidence, respectively. At 23° incidence, the HH backscatter is dominated by soil moisture changes rather than by biomass changes. On the contrary, VV polarisation shows quite a clear decreasing trend as a function of increasing wheat biomass.

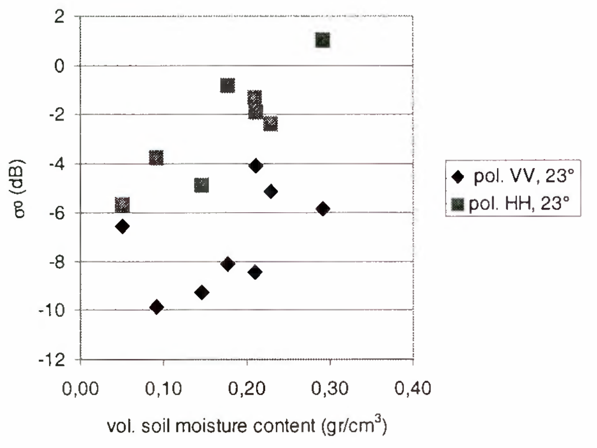

Fig.7 Backscattering coefficient, at VV and HH polarisation and 23° of incidence, as a function of soil moisture content

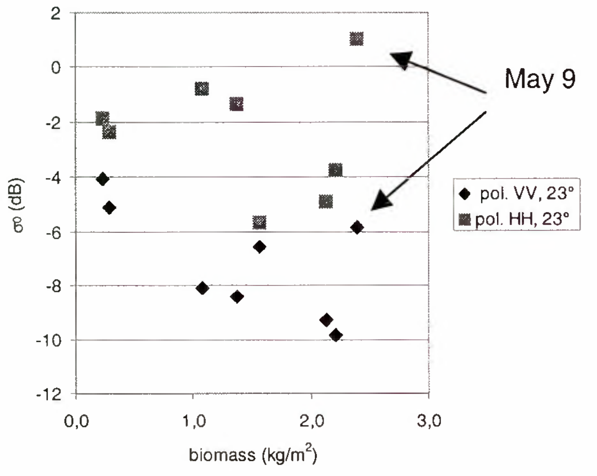

Fig.8 Backscattering coefficient, at VV and HH polarisation and 23° of incidence, as a function of total fresh biomass

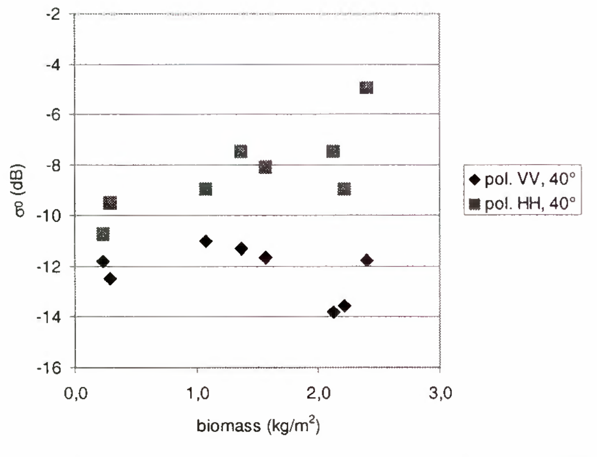

Fig.9 Backscattering coefficient, at VV and HH polarisation and 40° of incidence, as a function of total fresh biomass

However, abrupt changes in soil moisture content can significantly disturb this trend as it is the case for data collected on May 9 (i.e. the wettest day).

At 40° incidence, while the VV backscatter has a small dynamic range (then losing sensitivity both to biomass and soil moisture content), the HH backscatter shows a certain sensitivity to biomass. Again, in this case the robustness of the trend should be assessed versus different soil roughness conditions.

ERS-2 SAR DATA

The ERS-2 SAR images exploited in the study consist of six standard ESA PRI products. All the images were acquired for descending orbits and along two adjacent tracks. In effect, the selected area is at the intersection between two ERS-2 swaths (i.e. the wheat fields were imaged under two slightly different local incidence angles) and for this reason an interval of approximately 20 days between two consecutive acquisitions has been obtained. Data were calibrated and co-registered using the ESA TOOLBOX software package. For each field the number of pixels averaged to calculate the σ_0 ranged between 100 and 400.

Figure 10 shows the σ_0 ERS-2 SAR data versus the acquisition dates. This is a typical trend for wheat scattering at C-band, VV polarisation and 23° incidence [Cookmartin et el., 2001]. The decreasing of σ_0 level as a function of wheat growing stage is due to the fact that the prevalent effect of canopy is to absorb rather than scatter the em. radiation [Picard, 2001]. However, just before harvesting (i.e. on June 13) the canopy becomes almost "transparent" to the impinging em. waves and consequently the backscatter response is not any more attenuated by the canopy layer. It is worth mentioning that this general trend is significantly affected by soil moisture changes (see the difference between May 9 and 25).

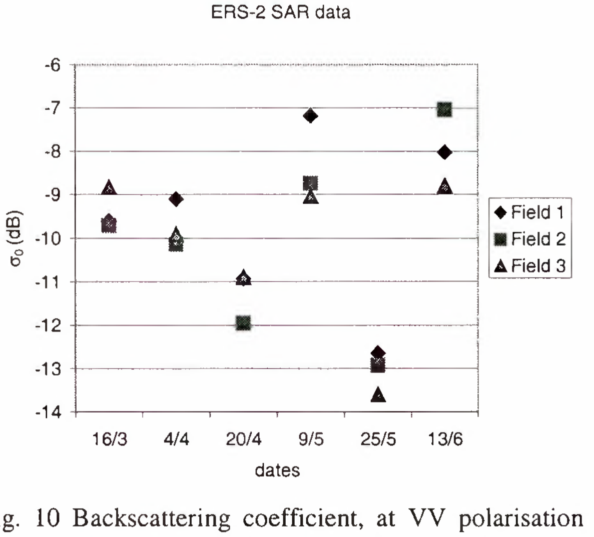

Fig. 10 Backscattering coefficient, at VV polarisation and 23° of incidence, as a function of ERS-2 acquisition dates

In Figure 11, the VV backscatter at 23° incidence versus wheat biomass is shown. Both scatterometer and ERS-2 SAR data are included in the graph. As can be seen, there is an overall decreasing of backscatter as a function of biomass increasing. However, a large spread for the same biomass values is also present. This is due to differences in the canopy development and in the soil surface conditions between fields. This large spread makes extremely difficult any empirical algorithm of wheat biomass retrieval.

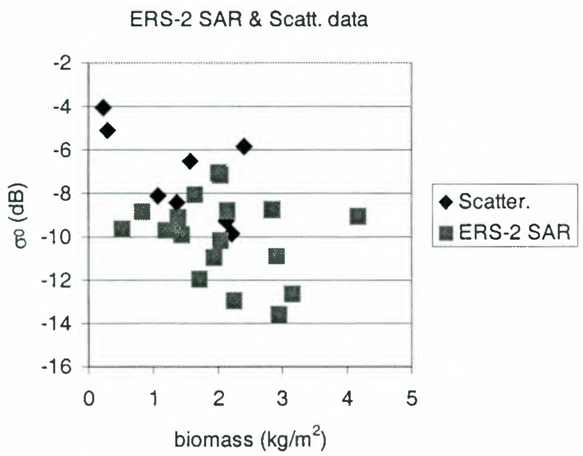

Fig. 11 Backscattering coefficient, at VV polarisation and 23° of incidence, as a function of total fresh biomass

CONCLUSIONS

The paper describes radar and ground measurements carried out on 4 wheat fields over the Matera test site during the 2001 growing season. The data set includes multi-temporal scatterometer measurements at different incidence angles and at VV and HH polarisations over the same wheat field. In addition, ERS-2 SAR data from March to June 2001 over 3 different fields have been acquired. The sensitivity of radar backscatter to sub canopy soil moisture and to fresh wheat biomass has been experimentally investigated as a function of the incidence angle and polarisation. Our findings show a good sensitivity of HH backscatter to soil moisture conditions beneath the canopy for small incidence angles. Conversely, backscatter at VV polarisation has been found most sensitive to wheat biomass for small incidence angles. However, it is worth mentioning that ERS-2 SAR data have demonstrated that the σ_0 values for the same wheat biomass suffer from a large spread due to the variability of canopy biomass and structure as well as of surface conditions.

Future work will be dedicated to investigate the possibility of quantitatively retrieve sub canopy soil moisture from SAR data.

ACKNOWLEDGEMENTS

This work has been supported by the Italian Space Agency (ASI) under contract I/R/167/00. The authors wish to acknowledge Mino Marzo from ASI for providing useful information about the ERS-2 SAR data quality.

REFERENCES

Cookmartin, G., Saich, P., Quegan S., Cordey R., Burgess-Allen P., Sowter A.,"Modelling Microwave Interactions with Crops and Comparison with ERS-2 SAR Observations", IEEE Trans. on GEosc. and Rem. Sensing, vol. 38, n.2, March 2000;

Ferrazoli, P., L. Guerriero,"Interpretation and Model Analysis of Maestro 1 Flevoland Data" Intern. Journal of Rem. Sensing, vol.15, n.14, 1994;

Le Toan T., Lopes A., Huet M.,"On the relationships between radar backscattering coefficient and vegetation canopy charachetistics", Proceedings IGARSS'84 Symp., Strasbourg, France, Aug. 1984;

Picard G., Le Toan T., et al., "A backscatter model for wheat canopies. Comparison with C-band multiparameter scatterometer measurements", Proceedings 3rt International Symposium on Retrieval of Bio- and Geophysical Parameters from SAR Data for Land Applications, Sheffield (UK), 11th-14th September 2001;

Quegan S., et al.,"High resolution measurements of scatteringin wheat canopies – implications for crop canopy retrieval", Proceedings 3rt International Symposium on Retrieval of Bio- and Geophysical Parameters from SAR Data for Land Applications, Sheffield (UK), 11th-14th September 2001;

Sabatelli, V., Casarano D., Buono G., Paparella F., Posa F.,"An FM-CW Scatterometer radar: Design, Implementation and Use on Natural Surfaces", Alta Frequenza, vol. 11, n.3, July-Sept. 1999;

Stiles, J., Sarabandi K.,"Electromagnetic Scattering from Grassland-Part I: a Fully Phase Coherent Scattering Model", IEEE TRans. on GEosc. and Rem. Sensing, vol. 38, n.1, January 2000a;

Stiles, J., Sarabandi K., Ulaby F.,"Electromagnetic Scattering from Grassland-Part II: Measurement and Modeling Results", IEEE TRans. on GEosc. and Rem. Sensing, vol. 38, n.1, January 2000b;

Ulaby F., Moore R., Fung A.K., Microwave Remote Sensing: Active and Passive, Artech Hause, 1985, vol. III

INFLUENCE OF DIURNAL VARIATIONS OF SURFACE WETNESS ON CLASSIFICATION OF AGRICULTURAL CROPS USING MULTI-PARAMETRIC E-SAR DATA WITH RESPECT TO FUTURE TERRASAR APPLICATIONS

C. Pathe[1], C. C. Schmullius[1], T. Riedel[1], M. Herold[2], A. Müller[1], C. Thiel[1]

1: Remote Sensing Unit, Department of Geography, Friedrich Schiller University,Germany, Loebdergraben 32, D-07743 Jena, Tel. ++49-3641-948877, e-mail: c.schmulius@geogr.uni-jena.de
2: Remote Sensing Research Unit, Department of Geography, University of California Santa Barbara,USA , Ellison Hall, Santa Barbara, CA 93106, Tel. 001-805-8934196, e-mail: martin@geog.ucsb.edu

Abstract: **This paper presents the first results of a study investigating the impact of plant surface wetness on thematic SAR data analysis. The investigations are based on SAR data recorded on two days at different times and extensive field measurements of plant parameters and microclimatological data acquired during the data take. The results show an influence of surface wetness on classification accuracy depending on the amount of water on the plants and the used radar bands and geometrical resolutions. Generally, the classification accuracy increases with decreased amount of free plant surface water. Further investigations within the TerraDew-Project will investigate the influence of plant water content and soil moisture as well with polarimetric SAR data analysis of scattering mechanisms in the canopy.**

INTRODUCTION

Radar backscatter signals from land surfaces are influenced by geometric and dielectric properties of the observed objects on the ground. Diurnal variations of surface wetness, that is plant surface wetness caused by dew, guttation or interception as well as plant water content and soil moisture, can result in different radar backscatter signals from the same area.

A number of studies describe an increase in radar backscattering while water is present on plant surfaces. A varying influence with frequency, polarization and plant structure is reported with a maximum backscatter difference of 2-4 dB for X- and C-band [1, 2, 3]. Weather effects on interferometric SAR data have a negative effect because of decreasing the coherence [4]. Impacts on thematic SAR data analysis caused by surface wetness on plant surfaces are also found in some studies [5, 6, 7, 8]. But altogether until today there are only a few studies published on these phenomena and "... it is impossible to reach a general conclusion on the effects of dew on sigma naught. [9]"

This study presents the first results of an investigation on the impact of plant surface wetness on thematic SAR data analysis. It is part of the TerraDew-Project, funded by the German Ministry of Research and Education (BMBF Project-ID 50EE0035), which investigates the influence of surface wetness on radar backscatter with respect to frequency, polarization and land cover type. A quantification of dew amount and a model to describe these effects will be acquired. The results of the Terra Dew Project will contribute to an increased understanding of phenomena in SAR image data affected by plant and surface wetness and are of great importance to future space borne missions, especially for parameterization of the planned TerraSAR satellite.

STUDY AREA

The study area "Alling" covers an area of about 3x3 km and is located 30 km southwest of Munich (Fig.1). It is a roughly flat terrain on a fluvial terrace with a moraine in the northern part. South of the moraine there is an area with a high ground water level which is mainly used as grassland.

Fig. 1: Study area

Proc. 3rd International Symposium, 'Retrieval of Bio- and Geophysical Parameters from SAR Data for Land Applications', Sheffield, UK, 11-14 September 2001 (ESA SP-475, January 2002)

The study area represents a rural landscape with primarily agricultural land use. The main crop types, cultivated on relatively small fields, are grain (barley, wheat, rye, oat), maize, potatoes, rapeseed and sugar peas.

FIELD DATA

The investigations are based on a field campaign carried out on Wednesday, the 14th and on Friday, the 16th June 2000. SAR image data were obtained with the E-SAR system operated by the German Aerospace Center (DLR) in Oberpfaffenhofen. Images were taken on both days at 6 a.m., 9 a.m. and 12 a.m. Altogether 6 datasets comprising of 3 radar bands at different polarizations were recorded. Table 1 shows the features of the SAR images acquired. The SAR data were pre-processed at the German Aerospace Center, which included motion compensation, processing of raw data, radiometric calibration, generation of ground range images, multilook processing and geometric correction. The E-SAR images then were resampled to a pixel size of 1 m. To examine possible impacts of surface wetness on SAR image data, as they will be received from the future TerraSAR satellite with an expected pixel size of 4 m, E-SAR data were used as input for a simulation algorithm.

Table 1: SAR image data specifications

	X	C	L
Polarizations	hh, vv	vh, vv	hh, hv, vv
Frequency / Wavelength	9.6 GHz 3.1 cm	5.3 GHz 5.7 cm	1.3 GHz 23.08 cm
Looks	4	4	4
TerraSAR Simulations are available only at X- and L-band			

After the calculation of the radar brightness β^0 and the radar backscattering coefficient σ^0 a first view on the data showed, that the speckle noise in the images had to be reduced. For that purpose a GammaMAP filter with a filter kernel of 5 by 5 pixels was applied.
During the flight campaign extensive field data were obtained. Records of land use, vegetation type, vegetation height and density, biomass (wet and dry), LAI, fractal cover, soil moisture (TDR measurements and samples), micro-climatologic data (air temperature, dew point, precipitation, humidity, incoming and reflected radiation, wind speed and direction) and visual dew descriptions are available.
Based on the land use mapping a digital map with all the information gathered during the field campaign was generated and served as a basis for further classification.

DATA ANALYSIS

The classification scheme as showed in Fig. 2 was developed and applied on all record times. For a first analysis of the information content, SAR image data were processed with an unsupervised classification using isodata clustering. The separation of the classes "settlement/forest" and "shadow/water" was done only once using all 7 possible bands/polarizations. Only pixels assigned to the class "agricultural fields" were topic of further examination.

Fig. 2: Classification scheme

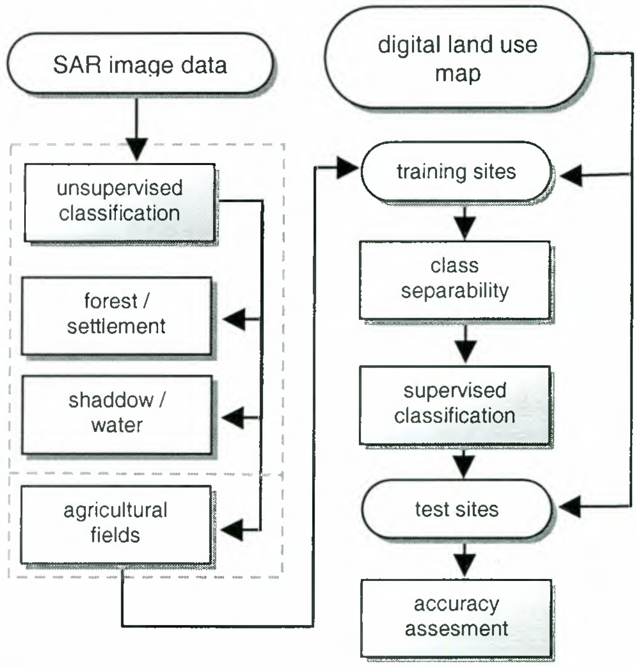

Using the digital land use map test sites for all land use categories found in the study area were selected. For investigation of the impact of surface wetness on thematic radar analysis, possible radar bands of the coming TerraSAR satellite proposed with X- and L-band, were used for classification. After comparing backscattering characteristics and evaluating the separability of different classes types, 5 classes were formed as input for X-band classification and 6 classes for X + L-band classification (Tab.2).

Tab.2: Classes used for supervised classification

	X + L band	X band
Class 1	clover	oats
Class 2	rye (ripe), winter barley, grassland	rye, summer barley, wheat
Class 3	rye, summer barley, wheat	rye (ripe), winter barley, grassland
Class 4	oats	sugar pea, clover
Class 5	sugar peas	maize, potatoes, rapeseed
Class 6	maize, potatoes, rapeseed	
Due to different levels of ripeness rye was split into two classes		

All fields not used as test sites were selected as training sites. They were taken to form a classification error matrix to compute the producers and users accuracy. At the end the weighted overall accuracy was calculated which incorporates the number of pixels in each class.

RESULTS

The field observations and the climatological data show varying amounts of water on plant surfaces present at different times. On Wednesday at 6 a.m. the vegetation reached the full interception holding capacity due to a heavy rainfall of 24 mm/m² in the night before. This intercepted water evaporated during the following hours so there was fewer water on the plants at 9 a.m. and no noticeably water present at 12 a.m., the time of the last data take. A similar trend in surface wetness was also observable on Friday. Measurements of air temperature and dew point showed a period of dew formation in the early morning hours of that day. This little dew layer evaporated before noon and during the last flight at 12 a.m. the vegetation surfaces were dry. In general it can be said, that there was a greater amount of water present during the observation time on the Wednesday than on the Friday.

The main purpose of this work is not to gain for the best possible classification result but to use a fixed set of test sites for every classification procedure. An overview of the classification results are presented in Figures 3 for X-band classification and 4 for X+L-band classification. Both graphs show a similar trend. Those classifications derived from SAR data recorded in the morning at 6 a.m. show a less accurate classification than those recordings at 12 a.m. This effect is observable for X-band as well as for X+L-band classification. Only TerraSAR X-band classification and E-SAR X+L-band classification of Friday 12 a.m. are an exception from this general trend. The biggest difference in overall accuracy between 6 a.m. and 12 a.m. is found for X-band classification on Wednesday with 10.7 % for E-SAR data and 10.4 % for TerraSAR Simulation. Comparing classification results of X-band classification and X+L-band classification it can be said that overall accuracies achieved using two radar bands are much better than using only X-band. Tables 3 to 6 show the producers and users accuracies for each class. It is obvious that classifications using E-SAR resolution agree better with ground truth data than those using TerraSAR resolution. The change of moisture content within the canopy has different effects on accuracy of several classes. The recognition of some classes is improved by plant surface wetness and in some cases it is degraded. A good representation is achieved for cereals at X+L-band classifications and broad leaved plants like potatoes and maize. Earlier investigations within the TerraDew-Project by [10] show an increased radar backscatter when vegetation surfaces are wet after precipitation or a dew event and decreasing radar backscatter with evaporation during the morning hours.
It is assumed, that all land surface properties like vegetation height, plant structure and roughness are equally the same on both days. The only condition that has changed during the morning hours is the surface wetness of plants and plant water content with a larger amount of water on the plants on Wednesday. It can be concluded, that the presence of water on plant surfaces has a negative effect on thematic SAR data analysis by decreasing the classification accuracy.

A closer look at the influence of soil moisture and plant water content as well as the scattering mechanisms related to these observed phenomena will be the topic of further research within the TerraDew-Project, which will also include polarimetric analysis of L-band data.

Fig. 3: Comparison of overall accuracies for X-band classification

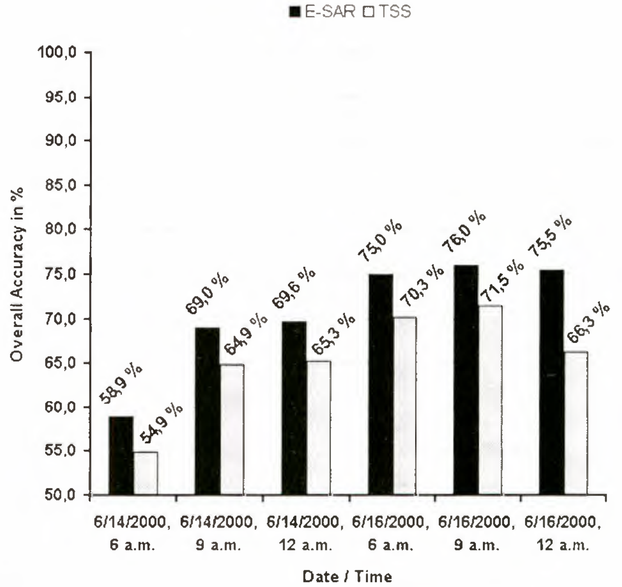

Fig. 4: Comparison of overall accuracies for X+L-band classification

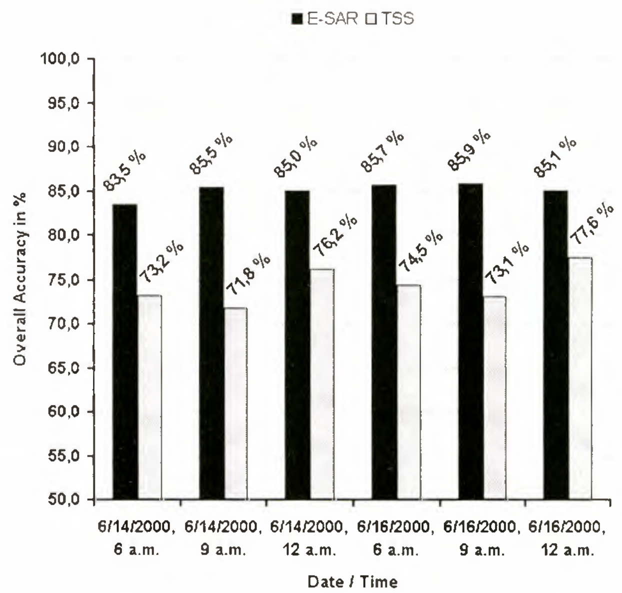

Tab. 3: ESAR X-band classification: Comparison of Producers / Users Accuracy

Date / Time	Class 1	Class 2	Class 3	Class 4	Class 5
6/14/2000, 6 a.m.	90.7 / 17.7	94.5 / 92.8	19.9 / 81.3	59.2 / 11.7	86.1 / 74.4
6/14/2000, 9 a.m.	83.6 / 18.1	95.1 / 92.8	41.8 / 90.6	60.5 / 18.3	89.1 / 76.3
6/14/2000, 12 a.m.	85.8 / 17.1	94.3 / 92.8	44.0 / 90.1	49.0 / 17.2	91.3 / 76.6
6/16/2000, 6 a.m.	84.2 / 34.0	91.5 / 84.1	57.7 / 88.5	54.9 / 20.0	91.3 / 88.6
6/16/2000, 9 a.m.	89.0 / 34.6	91.6 / 88.1	60.6 / 89.4	54.3 / 18.9	90.0 / 89.4
6/16/2000, 12 a.m.	82.4 / 31.7	92.8 / 85.8	60.9 / 90.6	49.5 / 18.4	86.2 / 87.0

Tab. 4: TerraSAR-Simulation X-band classification: Comparison of Producers / Users Accuracy

Date / Time	Class 1	Class 2	Class 3	Class 4	Class 5
6/14/2000, 6 a.m.	80.0 / 11.6	93.1 / 90.8	17.0 / 79.0	43.3 / 9.7	79.3 / 67.9
6/14/2000, 9 a.m.	66.1 / 11.5	93.9 / 91.0	39.1 / 86.3	39.6 / 13.7	82.8 / 72.0
6/14/2000, 12 a.m.	69.0 / 12.0	93.0 / 90.7	39.5 / 86.5	35.7 / 13.1	86.1 / 72.0
6/16/2000, 6 a.m.	71.6 / 18.3	90.1 / 80.9	53.6 / 85.6	33.4 / 14.8	85.2 / 84.8
6/16/2000, 9 a.m.	76.6 / 19.7	89.5 / 85.4	57.0 / 86.1	36.6 / 15.1	83.5 / 84.0
6/16/2000, 12 a.m.	69.0 / 18.0	90.5 / 82.6	45.4 / 86.2	38.0 / 11.3	81.7 / 82.6

Tab. 5: ESAR X+L-band classification: Comparison of Producers / Users Accuracy

Date / Time	Class 1	Class 2	Class 3	Class 4	Class 5	Class 6
6/14/2000, 6 a.m.	51.2 / 25.3	74.1 / 89.2	93.9 / 95.1	88.7 / 48.8	69.2 / 51.9	93.8 / 84.4
6/14/2000, 9 a.m.	54.6 / 28.5	77.6 / 91.3	94.2 / 95.1	81.8 / 55.6	78.5 / 61.5	95.3 / 84.7
6/14/2000, 12 a.m.	49.4 / 24.4	77.5 / 90.2	92.7 / 94.8	87.3 / 50.4	70.0 62.5	96.6 / 88.4
6/16/2000, 6 a.m.	52.6 / 33.2	79.2 / 91.1	92.7 / 90.3	83.3 / 67.6	58.6 / 37.4	97.1 / 89.9
6/16/2000, 9 a.m.	51.0 / 27.5	80.4 / 90.2	91.8 / 91.8	84.5 / 77.2	69.1 / 44.4	96.1 / 91.9
6/16/2000, 12 a.m.	49.3 / 31.8	77.9 / 91.8	93.9 / 88.1	81.8 / 70.0	62.5 / 34.0	95.8 / 91

Tab. 6: TerraSAR X+L-band classification: Comparison of Producers / Users Accuracy

Date / Time	Class 1	Class 2	Class 3	Class 4	Class 5	Class 6
6/14/2000, 6 a.m.	46.7 / 17.9	54.9 / 86.2	91.9 / 93.1	69.2 / 20.0	47.4 / 19.0	91.6 / 79.3
6/14/2000, 9 a.m.	44.0 / 18.1	52.7 / 87.7	94.1 / 92.2	53.3 / 15.8	61.4 / 14.3	86.9 / 82.7
6/14/2000, 12 a.m.	43.5 / 19.2	60.8 / 88.2	92.0 / 92.1	67.3 / 24.0	54.9 / 19.4	94.0 / 84.1
6/16/2000, 6 a.m.	54.4 / 27.1	59.9 / 84.4	86.7 / 81.9	61.5 / 35.6	56.7 / 15.6	94.5 / 88.2
6/16/2000, 9 a.m.	43.6 / 12.4	55.9 / 88.3	92.8 / 81.9	66.0 / 40.1	41.2 / 19.4	89.2 / 86.3
6/16/2000, 12 a.m.	37.4 / 20.8	66.3 / 87.3	91.0 / 85.8	58.2 / 36.3	39.1 / 14.1	93.8 / 86.5

COMPARISON OF PIXEL-BASED AND OBJECT-ORIENTED CLASSIFCATIONS

Besides the investigation of possible effects of surface wetness on thematic SAR image analysis the full E-SAR dataset, as presented in Table 1 was used to compare a conventional pixel based maximum likelihood classification and an object-oriented classification approach. This new object-oriented approach is implemented in the software eCognition (Definiens Imaging GmbH), which will be presented in brief below.

As a first step image objects are extracted by a knowledge-free automatic segmentation of the imagery. The patented segmentation technique of eCognition creates a hierarchical network of image objects in different scales, which represents the image information in different spatial resolutions simultaneously. The resulting objects are attributed not only with spectral statistics but also with shape information, relations to neighbouring objects and texture, which is derived from the distribution of sub-objects in the hierarchical network. With this information a fuzzy classification of the image objects can be performed.

Three different levels of image objects have been created representing different scales. In level 1 very small image objects represent buildings or trees. They are used for subsequent feature extraction. Large objects on level 3 are classified as settlements if their sub-objects on level 1 have a high contrast. This feature is a powerful texture measure provided by the multiscale approach of eCognition, which makes it possible to examine texture based on sub-objects. Level 2 is the main classification level. First, in level 3 classified settlement objects are transferred to level 2. Secondly, a fuzzy rule base, using spectral- and shape-information and class related features, classifies the remaining objects. In the available high dimensional feature space grassland and crop types were easier classified using samples and the Nearest Neighbour classifier than by describing them with user-defined membership functions. However, they are used to model local knowledge for classification refinement. For example

the following assumption: Areas completely or nearly completely surrounded by a special crop type belong to this crop type.
Classification accuracies were computed for the results of both classifiers. The overall accuracy achieved with the object-oriented classifier is 86,2 % compared to 79,8 % calculated for the pixel-based classifier. It must be stated, that the object-oriented classification additional contained the classes forest and settlement. They were not classified in the pixel-based classification, but could reliable be distinguished in the object-oriented approach.
The comparison of accuracies of single classes indicates similar values for both classifications. Class separability problems are comparable for both classifications, e.g. confusion between clover and grassland.
The variability of the backscatter in areas of interest is very high due to the high resolution and the speckle noise in the SAR data. This results in a typical "salt and pepper" classification with the pixel-based approach. The object-oriented approach shows visually more homogenous fields, which makes it easier to use the result in a Geographic Information System (GIS), which is important for the use of thematical information, e.g. in maps.

REFERENCES

[1] **Gillespie, T. J., Brisco, B., Brown, R. J. & Sofko, G. J.** 1990, Radar detection of a dew event in wheat, Remote Sensing of Environment, 33, 151-156.

[2] **Sofko, G., J. Sloboshan, M. Mc Kribben, J. Koehler & B. Brisco** 1989, Variation of microwave radar cross-section of wheat during the initial hours of a rainfall, IGARSS'89, Vancouver, BC July 10-14, 1191-1194.

[3] **Allen, C.T., B. Brisco & F.T. Ulaby** 1984, Modeling the temporal behavior of the microwave backscattering coefficient of agricultural crops. RSL Tech. Rep. 360-21, Remote Sensing Laboratory, Univ. Kansas Center for Research Inc, Lawrence, KS, USA.

[4] **Hobbs, S.E., Ang, W., Seynat, C**. 1998, Wind and Rain Effects on SAR Backscatter from Crops, Proc. ESTEC-Workshop 21-23 Oct.

[5] **Fischer, J.A., R.J. Brown & B. Brisco** 1992, The effect of changes in soil moisture and rainfall on SAR data crop classification. Proc. 15th Canad. Symp. Rem. Sen., Toronto, ON, 221-226.

[6] **Brisco, B., R.J. Brown & T.J., Koehler, J. A., Sofko, G. J. & Mc Kibben, M. J.** 1990, The dinurnal pattern of microwave backscattering by wheat, Remote Sensing of Environment, 34, 37-47.

[7] **Brisco, B., R.J. Brown & T.J. Pultz** 1989, The effects of free canopy water on crop seperability. Proc. IGARSS'89, Vancouver, BC, July 10-14, 424-428.

[8] **Brisco, B. & R.J. Brown** 1998, Agricultural applications with radar. In: F.M. Henderson & A.J. Lewis, Principles and application of imaging radar, Manual of remote sensing, 3rd edition, Vol. 2, p. 393 ff.

[9] **Jackson, T.J., Moy, L.** 1999, Dew Effects on Passive Microwave Observations of Land Surfaces - Active and Passive, in: Remote Sensing of Environment, 70: pp. 129-137.

[10] **Herold, M., Pathe, C., Schmullius C**. 2001, The effect of free vegetation water on the multi-frequency and polarimetric radar backscatter – first results from TerraDew 2000 campaign, Proceedings of International Remote Sensing and Geoscience Symposium (IGARSS), Sydney, July2001, on CD Rom.

A BACKSCATTER MODEL FOR WHEAT CANOPIES. COMPARISON WITH C-BAND MULTIPARAMETER SCATTEROMETER MEASUREMENTS.

Ghislain Picard*, Thuy Le Toan*,
Francesco Mattia**; Anna-Maria Gatti**,
Franco Posa ***, Angelo D'alessio***, Claudia Notarnicola***, Enzo Sabatelli****

*Centre d'Etudes Spatiales de la BIOsphere (CESBIO), Toulouse, France
**Istituto di Tecnologia Informatica Spaziale (ITIS)-CNR, Matera, Italy
***Dipartimento di Fisica del Politecnico di Bari, Bari, Italy
****ENEA-C.R. Trisaia-Rotondella, Matera, Italy

ABSTRACT

This paper describes a theoretical study on radar backscatter from a wheat canopy, based on experimental data. The objective is to interpret C-band SAR data provided by ERS, RADARSAT, and the forthcoming ENVISAT.

In a first step, ERS data and scatterometer data over the growth season at two test sites are compared with results of a first order coherent modelling. For fully-developed wheat canopies, however, this type of modelling fails to correctly estimate the attenuation of the incident wave within the canopy, resulting in a predicted backscattering coefficient one order of magnitude lower than that observed by the SAR system. The main reason for these observed discrepancies between theory and observation is identified to be the sparse medium assumption in the original model, an assumption which does not apply to fully-grown wheat canopies. Accordingly, we propose higher order modelling based on numerical solution of multiple scattering Foldy-Lax equation. The new modelling improves the backscatter estimate for the both test site.

INTRODUCTION

Since the launch of ERS-1 in 1991, followed by RADARSAT and ERS-2, several studies have been conducted to investigate the temporal variation of the radar backscatter from key crop types, with the aim of deriving methods and algorithms for crop monitoring, using the widely available C-band SAR data. While the temporal behaviour of ERS and RADARSAT backscatter of crops such as rice[1], or soybean[2] has been analysed and interpreted by theoretical modelling, attempts to interpret C-band backscatter temporal variation of wheat have been only partially successful [3][4]. Using a second order Radiative Transfer (RT2) model, the authors found large differences between the model predictions and measurements, during the fully-grown stage of wheat. The same problem occurs with the first order coherent modelling developed at CESBIO. In general the problem has been attributed to the overestimation of the attenuation through the canopy by these models. The attenuation is not only a critical issue for modelling but also for developing robust inversion algorithm. It determines the contribution of the ground and consecutively the variability of the total backscatter due to soil moisture, the most rapidly varying parameter. The interest in evaluating correctly attenuation and backscattering coefficient leads us to consider higher order modelling. The aim in developing more accurate but complex modelling is to determine the validity domain of simpler (e.g. first order) modelling. In this paper the modelling work focuses on the VV polarisation at C-band since it is known to cause problems due to strong interactions between the wave and the vertical stems. The HH polarisation as well as lower frequencies should be more accurately modelled by first order modelling, but has been shown to be less sensitive to wheat parameters.

The experimental data were provided by two measurement campaigns: one in France with ERS data, and one in Italy with scatterometer data.

In the first part of this paper, we attempt to determine the cause of the large attenuation predicted by the models. After revisiting the assumptions underlying first order modelling, we present the coherent model developed at CESBIO. Then, the two measurement campaigns used for testing modelling are detailed. In the third part, the first order modelling result are compared with radar data, and discussions about the interaction mechanisms and the attenuation estimate are given. A new approach for higher order modelling is presented in the fourth part and compared with data. In the last part, concluding remarks and further work are presented.

FIRST ORDER MODELLING

ASSUMPTIONS

First order modelling is based on two main approximations:

- single scattering is the most significant interaction mechanism, the others mechanisms are neglected.
- the attenuation is calculated as if scatterers do not interact with one another.

Proc. 3rd International Symposium, 'Retrieval of Bio- and Geophysical Parameters from SAR Data for Land Applications', Sheffield, UK, 11-14 September 2001 (ESA SP-475, January 2002)

These conditions apply to sparse medium with small albedo. Both radiative transfer modelling and coherent modelling have been used. However the coherent modelling is more adapted to agricultural crops since the clusters of scatterers may cause important coherent effects.

Multiple scattering radiative transfer modelling has been developed to relax the first approximation, but the attenuation is still computed as in first order modelling.

COHERENT MODELLING

An advanced first order model has been proposed [5]. This fully phase-coherent model includes the curvature of leaves, and takes into account the vertical variability of the attenuation.

A similar model has been developed at CESBIO in order to interpret C-band ERS data. The backscattered electric field is computed using the distorted Born approximation and the effective field in the medium is estimated using the Foldy-Lax approximation.

Since the scatterers in the canopy are not uniformly distributed, the attenuation is calculated locally. The medium is splitted into thin horizontal layers. In each layer, the local attenuation is computed using the optical theorem, implying that the attenuation depends on the height in the canopy.

Furthermore, because the stems extend themselves from the bottom to the top of the canopy, the scatterers are splitted into small elementary scatterers. Then, the backscattered fields from elementary scatterers are summed up taking into account the local effective field. This leads to a more realistic scattering diagram for the stems compared with the previous modelling which tend to overestimate the backscattering coefficient.

The leaves are modelled by curved elliptic cross section cylinders [6] using the Rayleigh-Gans approximation. However, the width of the leaves is not small enough at C-band ($\varepsilon^{1/2}k_0 l \approx 2$) where ε is the dielectric constant of stems, k_0 is the wave number and l is the half width of the leaves. Since the leaves contribution is weak, the error should be acceptable.

The attenuation of leaves can not be derived from the optical theorem because the forward scattering under the Rayleigh-Gans approximation is not accurate enough. The scattering loss has to be included according to [7; p. 138].

The underlying ground backscattering is computed with the IEM model [8].

MEASUREMENTS CAMPAIGNS

The ground measurements providing input parameters for the models have been collected at two sites, chosen to take into account the effects of the wheat species, the meteorological conditions and the agricultural practices. The first campaign was conducted during spring 2000, in the south-western France, in a valley mainly seeded with winter wheat. One 4.5 ha field was selected and in-situ measurements were collected during four ERS overpasses from March to June. The second campaign was in south Italy in 2001 and consists in both intensive ground measurements and scatterometer [9] acquisitions over one field. Nine measurements from March to June provide multi-incidence (from 23 to 60 degrees) and multi-polarisation (HH,VV and HV) data. This data set is used to validate models both as a function of incidence and wheat growth stage. Details on the experiment and the data analysis are given in [10].

The vegetation data collected consisted of measurements of canopy structure as well as agronomic data, such as fresh biomass and shoot number. The structural data were used to determine input parameters for the modelling and included measurements of the dimensions and orientations of the individual components, e.g. ears, leaves and stems, canopy height and the number of leaves per shoot. Dielectric data consisted of vegetation gravimetric moisture contents and soil moisture.

The two sites differ mainly in the stem density (500 stems/m2 in Italy and 1200 stems/m2 in France) and the ground conditions (dry and rough in Italy, and wet and smooth in France).

FIRST ORDER MODELLING RESULTS AND DISCUSSION

The modelling result is compared with the ERS backscattering coefficient for the French test site in figure 1, and with scatterometer data for the Italian site at VV polarisation and 40 degrees of incidence in figure 2.

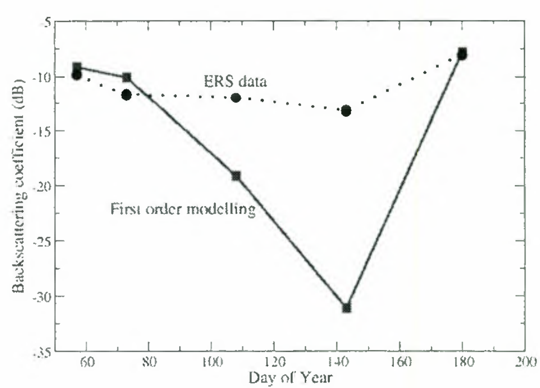

Figure 1. ERS data and first order modelling results at the French test site

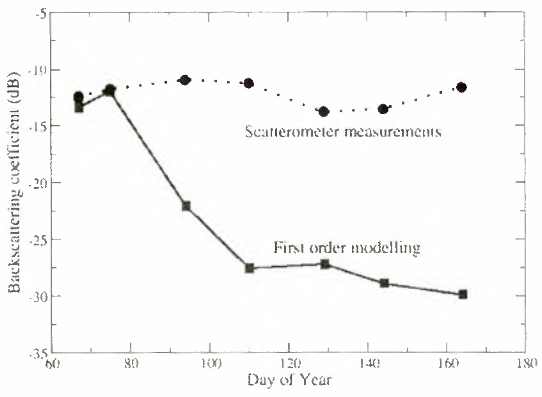

Figure 2. Scatterometer data at 40 degrees incidence angle and first order modelling

Both plots show that the backscattering coefficient is under-estimated by the model when the wheat canopies are fully-developed. Similar results have been obtained using the second-order RT2 modelling at SCEOS [3]. The observed disagreement is due to the under-estimation of the ground backscattering and the double bounce backscattering.

By decomposing the scattering mechanisms, we observe that the direct backscattering from the canopy is normally weak (figure 3):

- the leaves backscattering is weak because of their weak volume (figure 4).
- the stems interact weakly with the incident wave because the incidence angles up to about 45 degrees are grazing with respect to the vertical stems.

Attenuation measurements and analysis of 3D backscatter images at SCEOS using GBSAR [4][11] point out the problem of the attenuation estimates. The total two ways attenuation estimated by the modelling is too high, about 60dB (3[rd] ERS flight over the French test site) and 50dB (6[th] scatterometer measurement at 40 degrees on the Italian site).

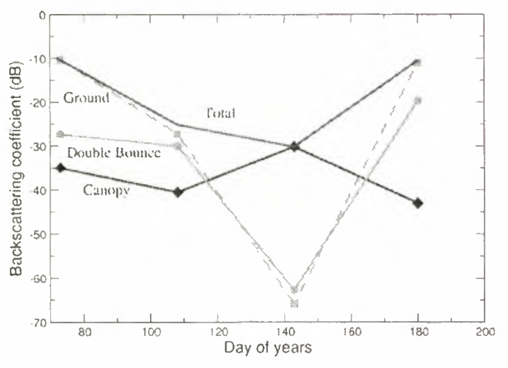

Figure 3. Decomposition in interaction mechanism at C-band 23 degrees incidence angle.

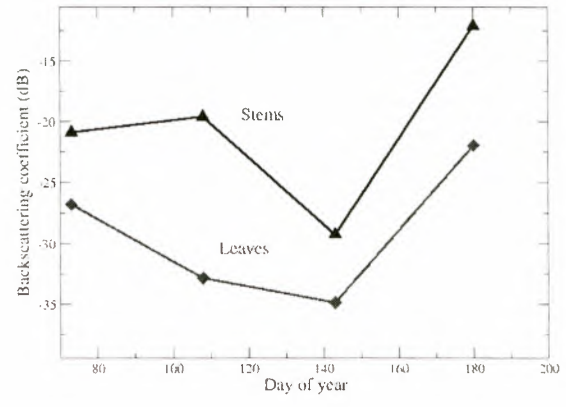

Figure 4. Contribution of leaves and stems at 23 degrees at the French test site.

HIGHER ORDER MODELLING

Higher order interactions needed to be taken into account in order to solve two problems:

- The Foldy-Lax approximation used to compute the attenuation is only valid for sparse medium where scatterers are assumed not to interact with one another. It is likely that, in the case of wheat canopies at fully-grown stage, one can no longer consider the medium as a sparse (with the upper limit around 0.1% in volume). In this condition, the higher order interactions need to be considered to correctly estimate the attenuation in the canopy. In fact, the illuminated stems screen the stems behind them, particularly along the rows. The shadowed stems do not contribute neither to the attenuation nor to scattering. We expect then a lower attenuation than in the case of non interacting stems.
- In first order modelling, the Born series is truncated at the first term assuming the scatterer albedo is small, i.e. the wave is much more absorbed than scattered. This is not the case for the wheat stems for which the scattering loss is about twice the absorption. Then, the scattered wave, especially in the forward direction, can interact with other stems or with the ground and can give significant multiple scattering.

Using multiple scattering radiative transfer modelling could solve partially the second problem, but not the first one. Furthermore, as mentioned previously, coherent effects in crop canopies can not be neglected.
However, calculating multiple scattering interaction increases the complexity of the electromagnetic problem to be solved. Several studies have been carried out for spherical, or spheroidal scatterers [7 pp. 432-562] but are not suitable for wheat canopy modelling. In [12], multiple scattering of cylindrical scatterers is addressed

using a method similar to the T-matrix. Our approach was to simplify the description of the medium in order to use this method . The wheat canopy is considered as a layer of vertical stems over a flat ground. The leaves and ears are neglected in a first step as suggested by the first order modelling results.

MULTIPLE SCATTERING EQUATION

The new modelling presented here is based on the multiple scattering Foldy-Lax equation.
This equation is written in the case of vertical cylinders over a flat ground [12]. The equation (set) is solved for a scene, i.e. for given positions of cylinders. The solutions for different Monte Carlo realisations are averaged to compute the backscattering coefficient.

NUMERICAL SOLUTION

The major problem is to solve the equation set. In [12], the equation is solved using an iterative method up to the second order. The first order term is analytically equivalent to the first term in the Born series. The second order term takes into account all interaction mechanisms including two interactions with the canopy and up to three reflections on the ground.
As a first step, the method has been extended to compute higher order. The interest of this method is to provide the contribution of physical interaction mechanisms. However, the resulting series was not convergent at high stems density. For fully developed stems, this iterative method fails for density above 200 cylinders per square meter. An other approach is required to attain up to 1000 cylinders per square meter.

The equations set have been discretised. This procedure leads to a system of linear equations with a huge number of unknowns, typically hundreds thousand. A GMRES iterative solver has been used and a fast convergence is obtained. Then, the scattered field is computed in the direction of interest.
In order to take into account the direct backscatter of the ground, the attenuation through the wheat canopy is derived from the forward scattered field using the optical theorem. The attenuated backscatter of the ground is added incoherently to the canopy backscatter as in first order modelling.

HIGHER ORDER MODELLING RESULTS AND DISCUSSION

Firstly, we present the comparison between attenuation estimated by first and higher order modelling. In the second part, the estimated backscattering coefficient is compared with backscatter variations as a function of time and incidence.

ATTENUATION

Figures 5 and 6 show the attenuation through a fully developed wheat canopy as a function of the stems density for 23 and 40 degrees of incidence angle.

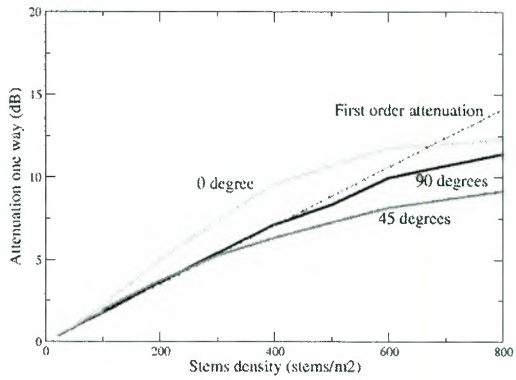

Figure 5. Attenuation for different azimuth angles at 23 degrees incidence angle. Comparison with first order attenuation.

The first order attenuation, i.e. attenuation for non interacting cylinders, in dash line, is linear with the stem density. The three plain curves show attenuation estimated by higher order modelling for different azimuth angles: 0 degree (the incident wave is parallel to the rows), 45 degrees and 90 degrees.

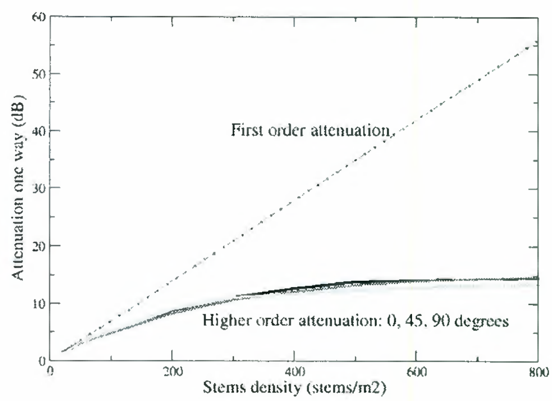

Figure 6. Attenuation for different azimuth angles at 40 degrees incidence angle. Comparison with first order attenuation

The attenuation variations depend on the incidence angles: at 40 degrees, the attenuation is much lower than the first order attenuation. At 23 degrees, the attenuation is very sensitive to the orientation of the radar wave direction with respect to row direction.
The higher order effect becomes significant for density higher than about 300 cylinders per square meter, or

approximately 0.3% in fractional volume. This fractional volume is quite low if compared with higher order result in slab of spherical scatterers [7 pp. 546-548], but is explained by the vertical structure of the medium which interacts strongly with the vertically polarised wave.
Using first order attenuation causes under-estimation of the ground contributions (direct and double bounce) of about 40 dB in the case of low stems density at 40 degrees (on the Italian test site) or about 50 dB in the case of high stems density at 23 degrees (French test site).

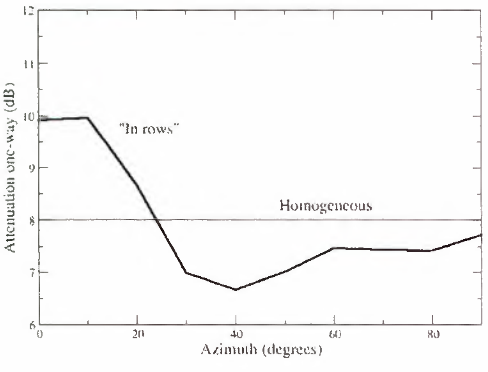

Figure 7. Attenuation at 23 degrees incidence angle as a function of azimuth angle for two distributions of stems: homogeneous, and in rows (450 cylinders/m^2).

The second significant effect is the sensitivity of the attenuation to the orientation of the radar look direction with respect to the rows. Even for non-interacting scatterers, the screening of near neighbours in the rows has a strong impact on the total attenuation. Figure 7 show attenuation as a function of azimuth angle, for a random distribution of stems (450 cylinders per square meter), and for stems seeded in rows. It appears that when the incident wave is parallel to the rows, the screening and/or coherent effects play a major role. It is to be noted that the azimuth effects could be less important if leaves were included in modelling.

BACKSCATTERING COEFFICIENT

The estimated backscattering coefficient is compared with data for both test sites in figures 8, 9 and 10. All the results show as expected improvements with the higher order modelling, but full agreement between the data and the modelling results depends on the site and the incidence angle.
On the French site, modelling results are in agreement with data over all the season. For the Italian test site, the level of the backscatter is correctly estimated for both 23 and 40 degrees incidence angle, but the temporal variations at 23 degrees disagree with the data. One possible explanation is the high sensitivity to the ground parameters, i.e. surface roughness and soil moisture.

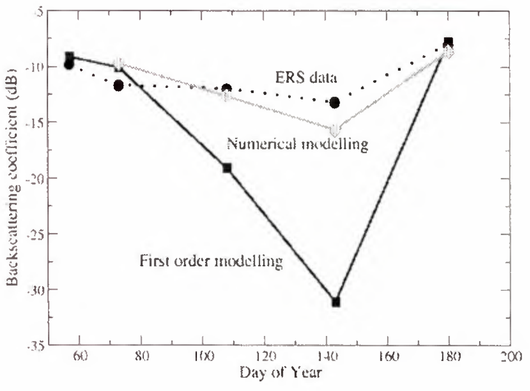

Figure 8. First and higher order modelling compared with ERS data.

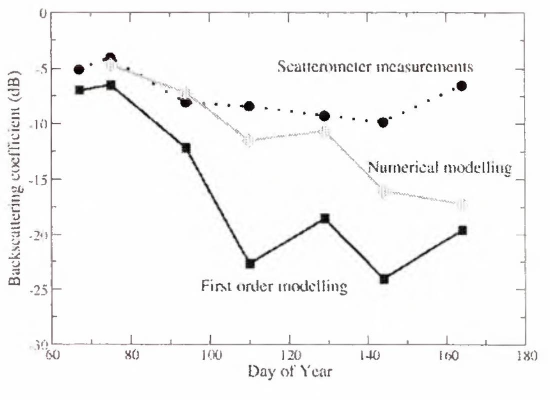

Figure 9. First and higher order modelling compared with scatterometer data at 23 degrees incidence angle

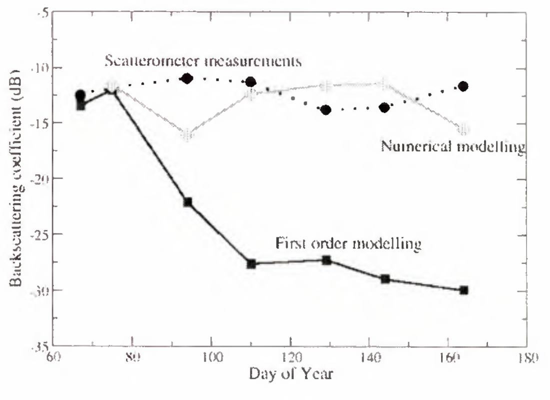

Figure 10. First and higher order modelling compared with scatterometer data at 40 degrees incidence angle

In fact, the double bounce is the main mechanism and then results are sensitive to the ground reflection coefficient. If included in the modelling, the complete scattering diagram of rough surfaces should reduce this sensitivity.

The variation of backscattering coefficient as a function of the incidence angle in figure 11 leads to the same conclusion. The ground contribution has to be improved especially for low incidence angle.

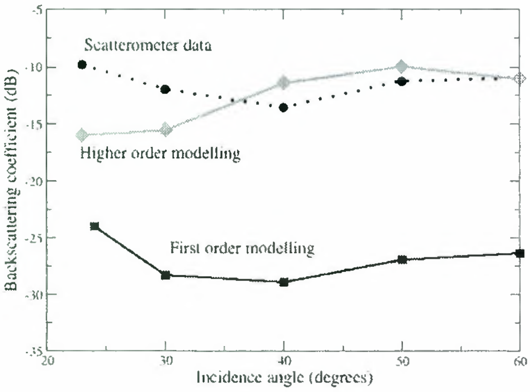

Figure 11. Backscattering coefficient versus incidence angle at day of year 144 at the Italian test site.

CONCLUSION

In this paper, we have exposed the difficulty to model correctly the attenuation and the backscattering coefficient of wheat canopies. Since the fully developed wheat canopies are not sparse, the assumptions for first order modelling are not valid, and higher order modelling is required. The modelling work, although relying on a simple description of the wheat canopies (e.g. no leaves and ears) permit to study multiple interactions in dense vegetated media, to define validity domain for first order modelling, and to test future approximated multiple scattering modelling.

ACKNOWLEDGEMENTS

This work was supported by ESA-ESTEC under contract 12008/96/NL/NB.

REFERENCES

[1] Le Toan T. , Ribbes F., Floury N., Wang L., Kong J.A., Kurosu T. and Fujita M. "Rice Crop Mapping and Monitroing Using ERS-1 Data Based on Experiment and Modeling Results". *IEEE Transaction on Geosciences and Remote Sensing*, Vol 35, N°1, pp 41-56, Jan 1997

[2] S.V. Nghiem, Le Toan T, Kong J.A., Han H.C. and Borgeaud M. "Layer Model with Random Speroidal Scatterers for Remote Sensing of Vegetation Canopy". *Journal of electromagnetic waves and applications*, Vol 7, N°1, pp 49-76, 1993

[3] G. Cookmartin, P. Saich, S. Quegan, R. Cordey, P. Burgess-Allen and A. Sowter, "Modeling Microwave Interactions with Crops and Comparison with ERS-2 SAR Observations"., *IEEE Trans. Geosci. Remote Sensing,* vol. 38, No 2, pp. 658-670, March 2000.

[4] S.C.M. Brown, G. Cookmartin, K. Morrison, A.J. McDonald, S. Quegan, C. Anderson, R. Cordey and P.M.R. Dampney, "Wheat Scattering Mechanisms Observed in Near-Field Radar Imagery Compared with Results from a Radiative Transfer Model". *International Geoscience and Remote Sensing Symposium*, Honolulu, HA, USA, July 2000, pp. 2933-2935.

[5] J. M. Stiles, K. Sarabandi, "Electromagnetic Scattering fron Grassland-Part I: A Fully Phase-Coherent Scattering Model". ", *IEEE Trans. Geosci. Remote Sensing,* vol. 38, No 1, pp. 339-348, January 2000.

[6] K. Sarabandi, T. B. A. Senior, "Low-Frequency Scattering From Cylindrical Structures at Oblique Incidence", *IEEE Trans. On Antennas and Propagation,* Vol 28, no 5, pp. 879-885, September 1990

[7] L. Tsang, J. A. Kong, R. T.Shin, "Theory of Microwave Remote Sensing", *Wiley series in remote sensing,* 1985

[8] A. K. Fung, "Microwave Scattering and Emission Models and their Applications", *Artech House*, pp 163-218, 1994

[9] V. Sabatelli, D. Casarano, G. Buono, F. Paparella, F. Posa, "An FM-CW scatterometric radar: design, implementation and use on natural surfaces", *Alta Frequenza*, vol.11, n.3, 1999

[10] F. Mattia, A.M. Gatti, F. Posa, A. D'alessio, C. Notarnicola, E. Sabatelli, M. Rinaldi, G. Satalino, G. Pasquariello, T. Le Toan, G. Picard, M. Davidson, "Radar and Ground measurements on wheat fields over the Matera site: an experimental study", *Proceeding Retrieval of Bio- & Geo-physical Parameters from SAR Data for Land Applications*, Sheffield, September 2001

[11] S. Quegan, "High resolution measurements of scattering in wheat canopies - implications for crop canopy retrieval", *Proceeding Retrieval of Bio- and Geophysical Parameters from SAR Data for Land Applications*, Sheffield 2001

[12] L. Tsang, K. H. Ding, G. Zhang, C. C. Hsu, J. A. Kong, "Backscattering Enhancement and Clustering Effects of Randomly Distributed Dielectric Cylinders Overlying a Dielectric Half Space Based on Monte-Carlo Simulations", *IEEE Trans. On Antennas and Propagation*, Vol 43, no 5, pp. 488-499, May 1995

SCENE UNDERSTANDING FOR SETTLEMENTS FROM METRIC RESOLUTION SAR

Marco Quartulli and Mihai Datcu
DLR IMF-BW, Oberpfaffenhofen, Wessling, Germany

ABSTRACT

Satellite and airborne remote sensing has reached a new level of sophistication, but available interpretation methodologies cannot cope with the huge amounts of acquired data. At the same time, new generations of high resolution SAR sensors have opened the perspective on novel applications related to the understanding of complex observations.

At meter resolution, mainly for man-made scenes, the complexity of the scene structures and of imaging phenomenology can be very high. This is reflected in the complexity of the observed images. New methods are needed for their interpretation, both for 2- and 3- dimensional analysis. The present work proposes methods of 2–dimensional information extraction from SAR and InSAR metric resolution observations.

Key words: Model based, information extraction, settlement reconstruction.

1. INTRODUCTION

New image understanding methods are needed to address the large amount of complex scenes that is going to be produced in the forecoming years by next generation high resolution synthetic aperture radar (SAR) sensors. These methods must be able to deal with the uncertainty that is present in the problem in form of missing or ambiguous data. It is thus a direct necessity that they have a probabilistic foundation.

Several assumptions can be used to give a basis to such scene understanding algorithms:

- the most compact encoding of the data is by the probabilistic model that describes it best
- a large number of sources of information coexist within the same observation data set
- the understanding of a scene requires complementary or multisensor observations.

On one hand, the multiplicity of the sources of information available in a single interferometric or polarimetric observation suggests using the methods of data and information fusion. On the other hand, the complexity of the data and of the acquisition mechanisms suggests using hierarchical models. A hierarchic Bayesian modeling and learning paradigm can be used for both data and information fusion and for interactive exploration of the scene identity.

This work presents the image formation phenomenology relevant for metric resolution observations, a concept for quasi-complete image content characterization, and methods for supervised learning for scene classification by information fusion with examples using X–band very high resolution imagery.

2. HIGH–RESOLUTION SAR: A QUASI–COMPLETE DESCRIPTION OF DATA

Image information extraction from very high resolution radar data has until now been typically approached in specific application–dependent frameworks such as military target recognition [5], [4]. This has the advantage that very detailed and strong prior models are available to characterize the data.

Some very important civilian applications can benefit from this direct target–oriented approach, as is the case of road extraction from satellite imagery [1]. They cannot be a general solution, though: the main difference between such specialized problems and the broader domain of image information extraction for data navigation and exploitation is that in this latter case the application area — that is, the exact nature of the information that is needed for data exploitation — is not a–priori well defined.

This requires the definition of an acceptably general description of the data to be later used in deriving more precise information that is pertinent to the application domain [3].

In the case of traditional low resolution data, many approaches consider that a quasi–complete description of the data is obtained by extracting information

Proc. 3rd International Symposium, 'Retrieval of Bio- and Geophysical Parameters from SAR Data for Land Applications', Sheffield, UK, 11-14 September 2001 (ESA SP-475, January 2002)

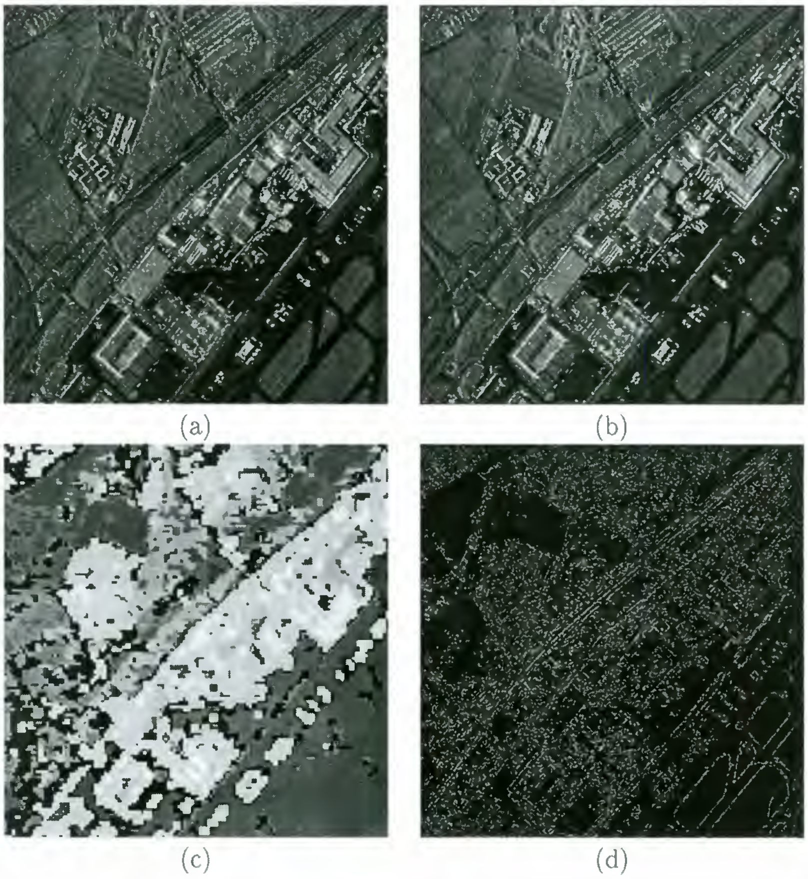

Figure 1. A quasi–complete description of a low–resolution radar scene by means of information extraction: (a) original image (b) extracted backscatter (c) texture classes (d) extracted edges. FGAN airborne SAR data.

about the texture and the geometry of the scatterers on the scene (see figure 1).

Although is performs remarkably well in the traditional case of low resolution imagery, the defined approach to quasi–complete image description tends to be limitative when either additional information sources are considered (as is the case of radar polarimetry and interferometry) or when the system resolution grows to a level where 3–d information becomes an distinctive element in the data (see for instance figure 2).

In this case, even if additional complications such as the modified image statistics or the changing appearance of speckle noise are not considered, new considerations are needed.

We investigate the problem of the definition of a general framework that implies a quasi–complete description of image information in the case of high resolution SAR and InSAR data. We make explicit reference to the problem of settlement understanding as a particular case of complex and varied environment scene.

The main deficiency of traditional methods is their lack of capability to relate the extracted information to a three dimensional space. This can be obtained by specifying a model that is hierarchic: high–level and application–dependent scene features already belonging to the semantic level — houses, gardens, roofs — are identified relying upon lower level object features —horizontal and vertical planes —, that are in turn built upon two dimensional signal level classes. A graphical description of such a hierarchical model is given in picture 4. The coupling between the different model levels is accomplished using Bayesian inference, that further defines parameter estimation algorithms.

The communication between the different model levels is a central point of the approach: it must be implemented in a way that is able to resolve any inconsistencies between the different descriptions. The uncertainties of the the acquisition and of the acquired scene cannot be efficiently solved in the first stage only of the hierarchical model: each level must be able to handle missing information in a probabilistic way. In this sense, a hierarchical prior model is more complex than one exactly specifying the target structure to be retrieved in the data. On the other hand, it allows a generic description of the image content, if the last level of inference, the "semantic" one, is left out of the processing chain and iteratively built by the user at run time, as in [3].

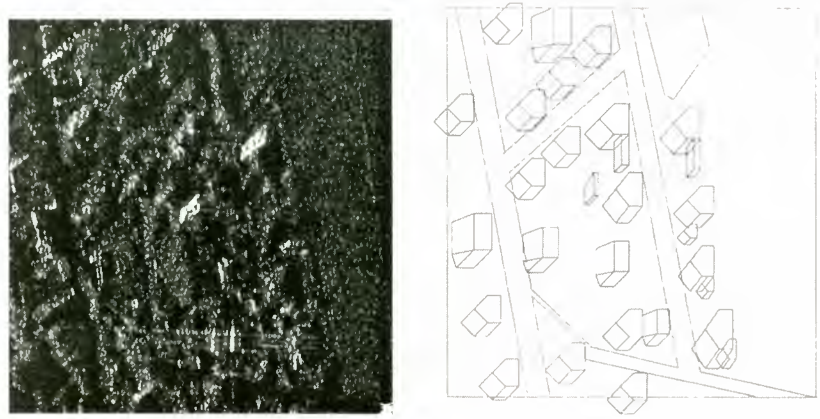

(a) high resolution image intensity (b) ground truth map

Figure 2. High resolution SAR data: 3–d information emerges as foundamental information content

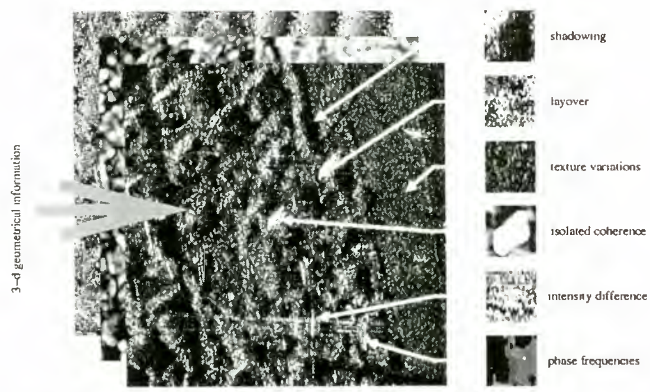

Figure 3. High resolution InSAR phenomenology: basic signal features extracted from intensity, coherence and interferometric phase

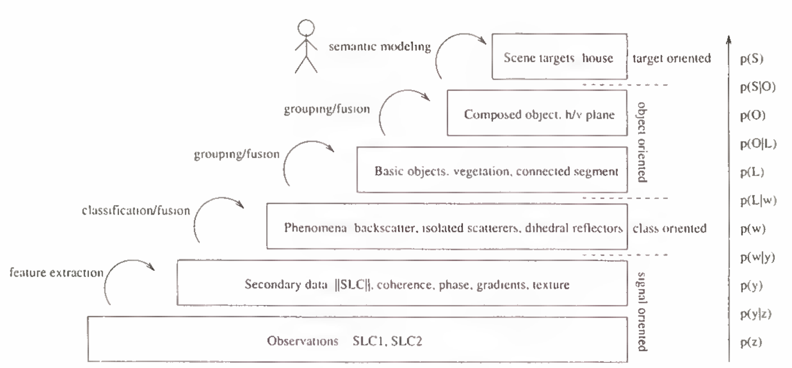

Figure 4. Hierarchical system model: higher–level features are built upon lower level ones

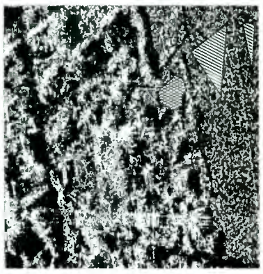

(a) master intensity with training regions

(b) built-up area classification/fusion

(c) 2–d building clustering

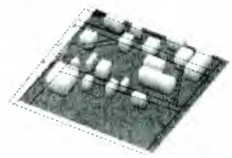

(d) 3–d view with mean absolute phase as height

Figure 5. High resolution data: (a) intensity image. Training areas identify built–up and bare soil areas. (b) classification/fusion results: built–up areas are reported in black (c) rectangles fitted to extracted housing areas (d) three dimensional view using mean absolute phase as building height

3. AN APPLICATION EXAMPLE

A partial implementation of the described hierarchical system is used for building extraction in a very high resolution X-band scene. The signal features generated from an interferometric couple — intensities, coherence, phase — are first subject to noise–reduction filtering and secondary signal feature generation. The clean backscatter, texture parameters and phase gradients thus obtained are separately subject to unsupervised clustering, and then interactively fused according to a given "house" example as in [2] and in [3]. The classified map is used to generate a first simple object map by clustering it assuming rectangular–shaped objects. The resulting rectangular–shaped objects are used with the unwrapped interferometric phase to build the 3–d view in figure 5(d).

4. CONCLUSIONS AND FUTURE WORK

A hierarchical modeling approach has been presented that points towards a quasi complete description of high resolution interferometric SAR data using a hierarchical modeling approach with Bayesian inference as the central parameter estimation mechanism. The concept has been demonstrated by means of a simple prototype used for building extraction.

5. ACKNOWLEDGEMENTS

The authors wish to thank AeroSensing RadarSysteme GmbH and FGAN eV for providing the data used.

REFERENCES

F.Tupin, H.Maitre, J.-F.Mangin, J.M.Nicolas, and E.Pechersky. Detection of linear features in SAR images: Application to road network extraction. *IEEE Trans. Geosci. and RS.*, 36(2):434–453, 1998.

M.Datcu and K.Seidel. Bayesian methods: applications in information aggregation and data mining. *International Archives of Photogrammetry and Remote Sensing, Part 7-4-3 W6*, 32:68–73, 1999.

M.Schröder, H.Rehrauer, K.Seidel, and M.Datcu. Interactive learning and probabilistic retrieval in remote sensing image archives. *IEEE Trans. on Geoscience and Remote Sensing*, 38:2288–2298, 2000.

R.Chellappa, Q.Zheng, S.Kuttikkad, C.Shekhar, and P.Burlina. Site model construction for the exploitation of E-O and SAR images. *To appear in a book on Progress in IU, ed: O. Firschein and T. Strat, Morgan Kauffman Ltd.*

R.Kothari and D.Ensley. On the use of model order for detecting potential target locations in SAR images. *Proc. SPIE on Algorithms for Synthetic Aperture Radar Imagery V*, 3370:351–357, 1998.

MULTI-BASELINE AIRBORNE POL-INSAR MEASUREMENTS FOR THE ANALYSIS AND INVERSION OF SCATTERING PROCESSES WITHIN VEGETATION MEDIA

O. Stebler, E. Meier, D. Nuesch

Remote Sensing Laboratories (RSL), University of Zurich-Irchel, Winterthurerstrasse 190, CH-8057 Zurich, Switzerland
T: +41 1 635 51 03, F: +41 1 635 68 42, E: stebler@geo.unizh.ch

Abstract –**The interferometric decomposition identifies arbitrary scattering mechanisms in two interferometric SAR images and optimises the interferometric coherence. Polarimetric SAR interferometry (Pol-InSAR) is sensitive to the distribution of oriented objects in vegetation layers. It has been demonstrated in various studies that the estimated scattering mechanisms have different vertical loci that can be related to certain vegetation structures.**

Additionally, theoretical scattering models allow for the reconstruction of the quasi-three-dimensional spatial distribution of such interferometric scattering mechanisms within multi-layer morphologies and the derivation of vegetation-related physical parameters. This paper deals with a sensitivity analysis of the behaviour of the amplitude of the complex interferometric coherence as a function of the aforementioned geo- and biophysical model parameters as well as various acquisition characteristics. Therein, the polarisation-dependent sensitivity of the coherence to these parameters is analysed. The role of the complex interferometric coherence statistics, which are polarisation-dependent, will be shown for the particular case of the estimation of surface topography beneath a vegetation cover by means of Pol-InSAR.

These investigations are based on a coherent Pol-InSAR scattering model consisting of a random volume over a multi-polarising ground. The measurements and the theoretical simulations are based on the configuration of a real airborne experiment. This data set provides multi-baseline L-band scattering matrices acquired by the SIR-C system for the lake Baikal test site as well as by the DLR experimental SAR sensor (E-SAR) for a pre-alpine Swiss test site.

I. INTRODUCTION

The introduction of polarimetric SAR (Pol-SAR) into interferometric SAR (InSAR) has basically resulted in the optimisation of the interferometric coherence and has led to a general formulation of vectorial interferometry [1]. The interferometric SAR images are expressed in an arbitrary polarisation basis (i.e. optimal polarisations or singular polarisations), or arbitrary scattering mechanism in each image, that maximises the interferometric coherence and minimises volumetric decorrelation effects. Tab. 1 shows the amplitude of the complex interferometric coherence as a function of the wavelength, the baseline, and the polarisation basis for a SIR-C data set.

Nevertheless, the singular vector estimation remains baseline-dependent [6] (Tab. 1). Therefore, the differential interferometric phase between different singular polarisations contains a considerable amount of noise, although the vertical loci of the scattering mechanisms in the interferograms are apparent [1], [6]. In order to derive geo- and biophysical parameters from polarimetric InSAR (Pol-InSAR) data a coherent scattering model has been proposed [9], [5].

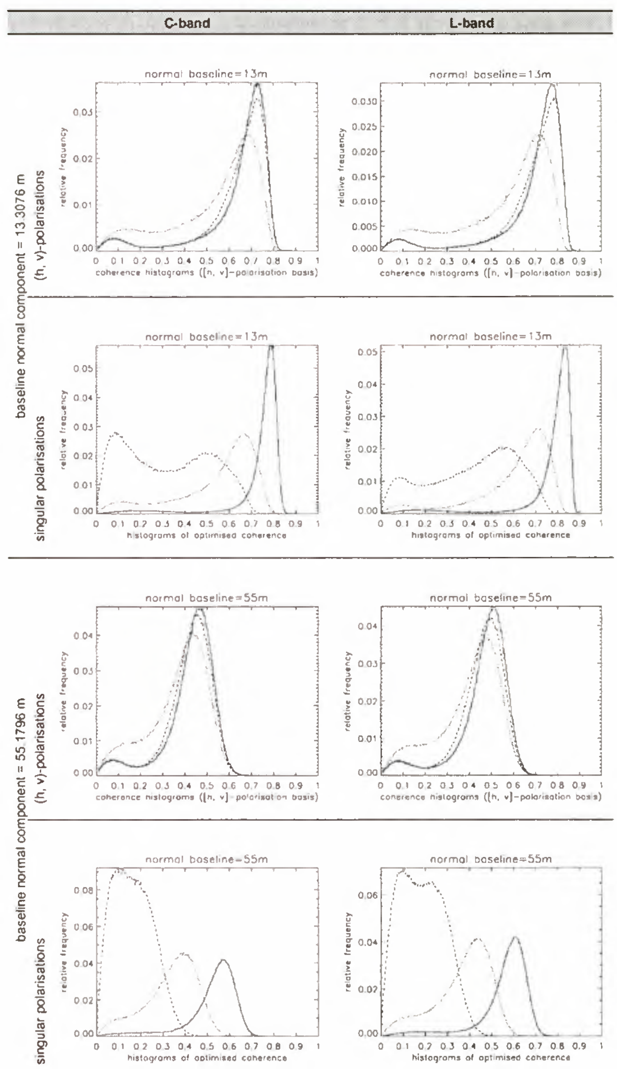

Tab. 1. Histograms of $|\gamma|(\lambda, B, \text{polarisation})$ (__: hh-hh, v_1 ; ....: hv-hv, v_2 ; ---: vv-vv, v_3). (SIR-C, SRL-2).

Proc. 3rd International Symposium, 'Retrieval of Bio- and Geophysical Parameters from SAR Data for Land Applications', Sheffield, UK, 11-14 September 2001 (ESA SP-475, January 2002)

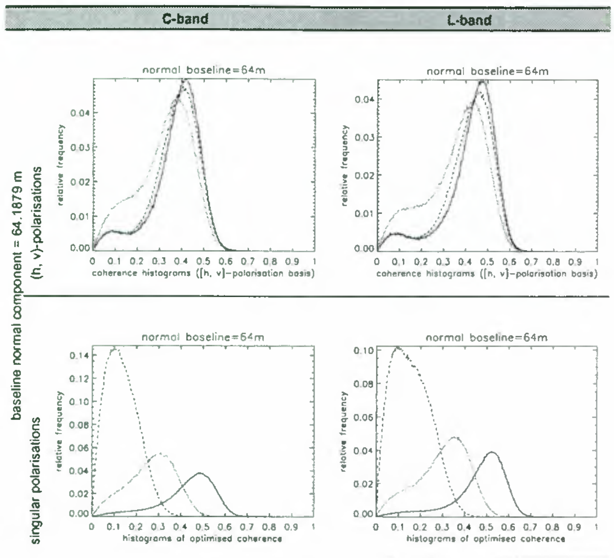

Tab. 1. Histograms of $|\gamma|(\lambda, B, \text{polarisation})$ (__: hh-hh, ν_1 ; ....: hv-hv, ν_2 ; ---: vv-vv, ν_3). (SIR-C, SRL-2).

II. Method

The well known coherent model consisting of a random volume over a multi-polarising ground used for the simulations in this paper addresses the complex interferometric coherence γ according to [9] in the form

$$\gamma(m(\underline{w})) = e^{i\phi_{topo}} \cdot \frac{\gamma_{vol}|\gamma_{temp}| + m(\underline{w})}{1 + m(\underline{w})}, \text{ where} \quad (1)$$

- ϕ_{topo} = the argument of the interferometric coherence of the topography,
- γ_{vol} = the interferometric coherence of the volume (I, I_0 = volume integrals; h_v = height of the volume [m]; σ = extinction coefficient of the volume [Npm^{-1}]; h' = height above ground [m]; θ_0 = mean incidence angle [rad] at slant range R [m]; $\Delta\theta$ = incidence angle difference [rad]; $\Delta\kappa_z$ = effective vertical interferometric wavenumber [m^{-1}]; κ = wavenumber [m^{-1}]; B = baseline [m]):

$$\gamma_{vol} = \frac{I}{I_0} \qquad \begin{cases} I = \displaystyle\int_0^{h_v} e^{\frac{2\sigma h'}{\cos\theta_0}} \cdot e^{i\Delta\kappa_z h'} dh' \\ I_0 = \displaystyle\int_0^{h_v} e^{\frac{2\sigma h'}{\cos\theta_0}} dh' \end{cases} \quad \text{with} \quad (2)$$

$$\Delta\kappa_z = \frac{\kappa B \cos\theta_0}{R \sin\theta_0}, \quad (3)$$

- $|\gamma_{temp}|$ = the amplitude of the temporal interferometric coherence (for the simulations $|\gamma_{temp}| = 1$ assumed), and
- $m(\underline{w})$ = the (polarisation-dependent) effective ground-to-volume amplitude ratio:

$$m(\underline{w}) = \frac{m_{ground}}{m_{volume}} \cdot \int_0^{h_v} e^{\frac{2\sigma h'}{\cos\theta_0}} dh'. \quad (4)$$

It has been shown in the literature that the singular polarisations provide the largest dynamic range of $m(\underline{w})$ values and therefore lead to an optimal conditioning of the inversion problem. Equations (1) - (4) describe the coherent scattering scenario using at least six parameters ($|\gamma_{temp}| = 1$). Therefore, six observables are required (the complex interferometric coherence for all the three [optimal] polarisation states) to make the inversion of the data solvable.

III. Simulations

The following simulations provide a complete overview of the performance of the Pol-InSAR scattering model – introduced in the previous section – as a function of several system parameters. Generally, the simulations are based on a real airborne multi-baseline L-band Pol-InSAR campaign carried out with the DLR experimental SAR system (E-SAR) in 2000 for a Swiss test site. Nonetheless, the system parameters are specified where necessary and indicated for each simulation (Fig. 1 - Fig. 6).

Fig. 1 shows the amplitude of the interferometric coherence $|\gamma|$ as a function of the extinction coefficient σ and the height of the volume h_v for the smallest and the largest baseline of our multi-baseline E-SAR experiment.

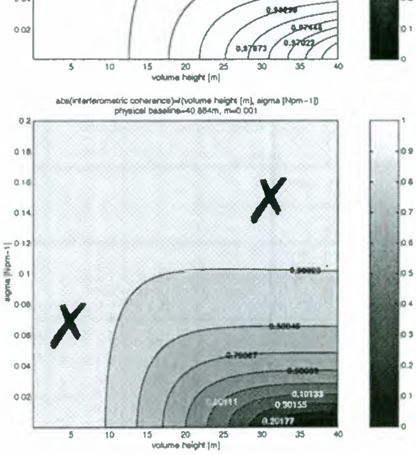

Fig. 1. $|\gamma|_{m=-30\text{dB}}(h_v, \sigma)$ as a function of the baseline ($\theta_0 = 53.4°$, $R = 5018.5$m, $\lambda = 0.23$m) [8].

These simulations demonstrate the extinction-height ambiguity (χ in Fig. 1), which is an interferometric property also described in the literature for different system parameters and/or surface characteristics. Normally, volume and ground scattering are coupled but for high or low values of the two vegetation parameters height and density, the scattering contributions become approximately decoupled.

The influence of h_v is especially critical for low and medium vegetation densities ($\sigma \approx 0.02\,\mathrm{Npm}^{-1}$). Larger baselines amplify this effect, leading to an increased volume decorrelation.

Fig. 2 shows $|\gamma|$ as a function of the effective ground-to-volume amplitude ratio $m(\underline{w})$, which represents the role of polarisation in this model. Generally, the considerable high noise of the interferometric phase of a volume scatterer indicates scattering contributions from targets with differing elevations in a particular resolution cell. On the other hand, the high amplitude of the interferometric coherence of the topography strongly indicates a localised interferometric phase centre.

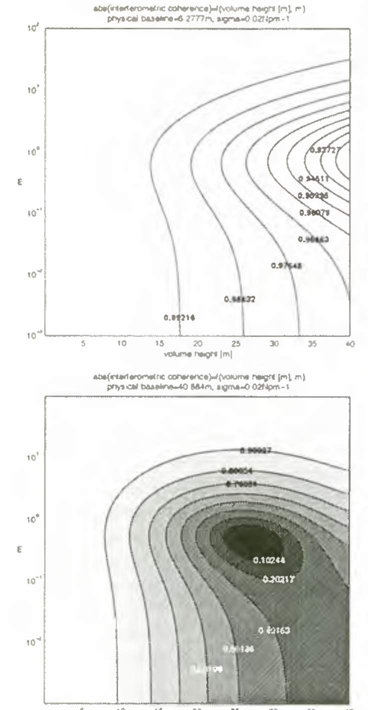

Fig. 2. $|\gamma|_{\sigma = 0.02\,\mathrm{Npm}^{-1}}(h_v, m)$ as a function of the baseline (for acquisition parameters see Fig. 1) [8].

For this reason, the amplitude of the interferometric coherence of the ground has a stronger influence on $|\gamma|$ than $|\gamma_{vol}|$. Fig. 2 and Fig. 3 both express $|\gamma|$ as a function of the same parameters, assuming (frequency-dependent) constant extinction coefficients. Additionally, Fig. 3 takes different system centre frequencies into account (C- vs. P-band). In Fig. 4, $|\gamma|$ is modelled using the variables $m(\underline{w})$ and σ.

Starting from low $m(\underline{w})$ values, $|\gamma|$ *decreases* with *increasing* ground contribution, since for $0 < m(\underline{w}) < 10^0$ the effective vertical distribution of the scattering elements increases (ground *and* volume scattering contributions) despite the existence of a localised scattering centre on the ground. At $m(\underline{w}) = 10^0$ the ground contribution reaches the order of the volume contribution, minimising the vertical distribution of the scattering elements and therefore leading to higher $|\gamma|$ values. The simulations in Fig. 2 - Fig. 4 indicate that for later inversion of the data, the estimation of $m(\underline{w})$ is primarily critical in the range of $10^{-1} < m(\underline{w}) < 10^0$ (especially for frequencies and/or polarisations with low $m(\underline{w})$ values or narrow $m(\underline{w})$ spectra). Additionally, special attention must be paid to the asymmetric relation between $m(\underline{w})$ and $|\gamma|$ which is additionally enforced by the frequency (Fig. 3) and/or baseline (Fig. 2, Fig. 4).

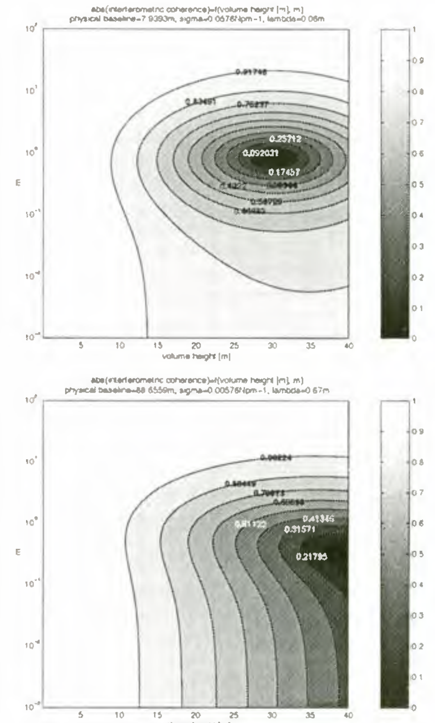

Fig. 3. $|\gamma|(h_v, m, \sigma)$ as a function of the system centre frequency, keeping B/λ constant (for acquisition parameters see Fig. 1) [8].

To emphasize this point, the sensitivity of $|\gamma|$ on system parameters and/or geo- and biophysical surface properties such as vegetation height and density has been estimated and analysed as a function of $f(m(\underline{w}), h_v)$ (Fig. 5, top), $f(m(\underline{w}), \sigma)$ (Fig. 5, bottom), $f(m(\underline{w}), B)$ (Fig. 6, top), and $f(m(\underline{w}), \Delta\theta)$ (Fig. 6, bottom).

The sensitivity of $|\gamma|$ regarding h_v or σ is directly related to the difference between two $m(\underline{w})$ values (or to the width of the $m(\underline{w})$ spectrum). $|\gamma|$ sensitivity as a function of $m(\underline{w})$ is more pronounced for high than for low h_v or σ values. Therefore, polarisations with a large dynamic range in their $m(\underline{w})$ values lead to a better conditioning of the inverse problem.

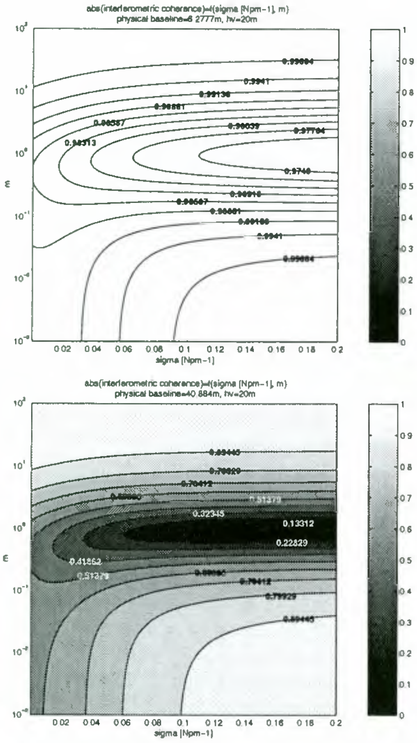

Fig. 4. $|\gamma|_{h_v=20\mathrm{m}}(\sigma, m)$ as a function of the baseline (acquisition parameters see Fig. 1) [8].

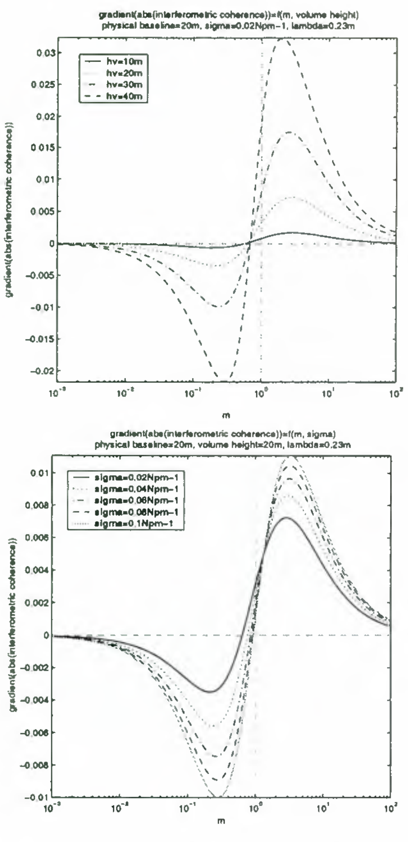

Fig. 5. Gradient of $|\gamma|$: $\delta|\gamma|/\delta h_{v_{\sigma=0.02\mathrm{Npm}^{-1}}}(h_v, m(\underline{w}))$ (top), $\delta|\gamma|/\delta\sigma_{h_v=20\mathrm{m}}(\sigma, m(\underline{w}))$ (bottom) [8].

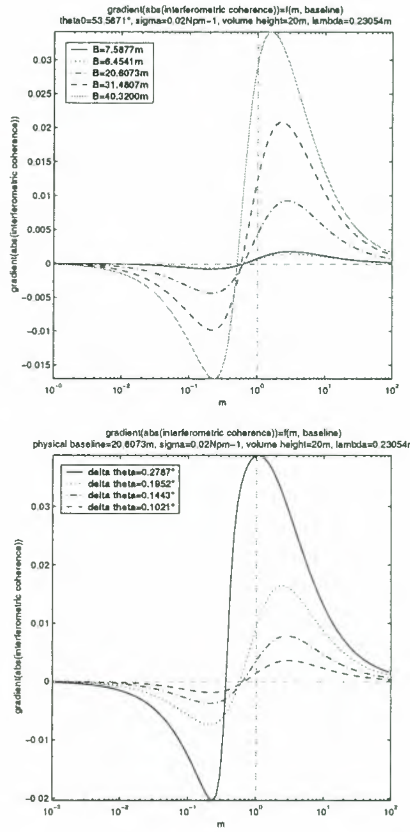

Fig. 6. Gradient of $|\gamma|$: $\delta|\gamma|/\delta B(B, m(\underline{w}))$ (top), $\delta|\gamma|/\delta\Delta\theta(\Delta\theta, m(\underline{w}))$ (bottom).

For small baselines the model predicts a low dependency of $|\gamma|$ on the polarisation states. With increasing baseline volume contributions gain weight (Fig. 6, top) leading to an enhanced sensitivity to distributed vertical scattering contributions causing an enlarged spectrum of coherence amplitude values. For the later inversion of the geo- and biophysical parameters the consequences are that small baselines with high interferometric coherence amplitudes do not *a priori* lead to a well-conditioned inversion problem. On the other hand, large baselines with high second moments of the interferometric phase cause a system to be ill-conditioned. Depending on the system frequency intermediate baselines are optimal. Such baselines still ensure well-preserved coherence amplitude values. In this case, the second moment function of the interferometric phase does not affect the separability of different vertical phase scattering centers.

Additionally, the strong dependency of the coherence amplitude of different polarisation states on the baseline requires the consideration of the actual flight track geometries.

The performance of coherence amplitude values is also biased by the incidence angle, which is a function of slant range as well as a function of the topography. For large incidence angle differences between two antennas (i. e. near range situation for horizontal parallel tracks) volume decorrelation is maximal. In this case, the coherence amplitudes are again strongly dependent on the polarisation states. For proper inversions, the incidence angle variation must therefore be accounted for.

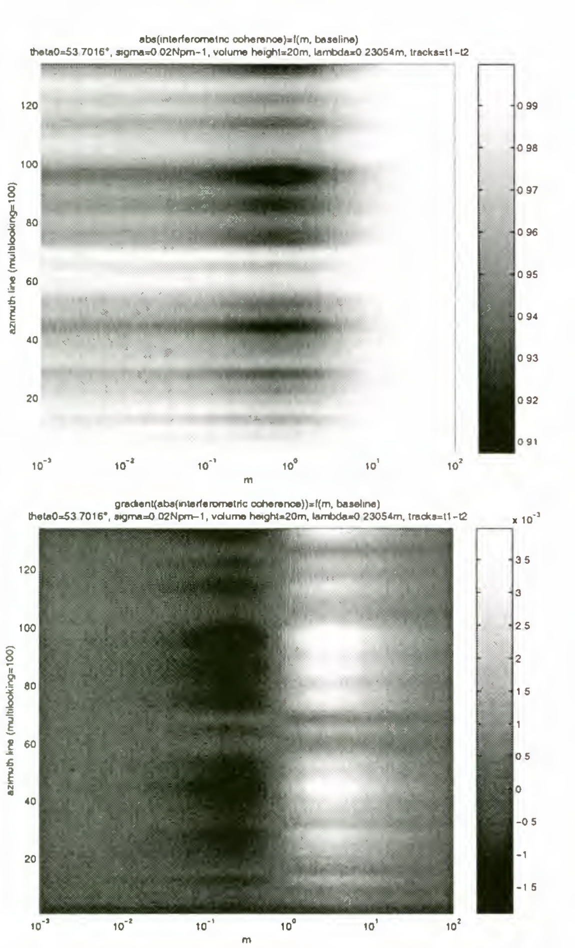

Fig. 7. $|\gamma|(B, m(\underline{w}))$ (top), gradient of $|\gamma|$: $\delta|\gamma|/\delta B(B, m(\underline{w}))$ (bottom). B(azimuth) and $\bar{B} = 7.588\text{m}$. E-SAR, L-band.

As already mentioned, the consideration of actual baseline geometries is required for an appropriate estimation of (3). Fig. 7 and Fig. 8 show the variation of the coherence amplitude (top) as well as its gradient (bottom) as a function of the baseline variation over azimuth and as a function of the (polarisation-dependent) effective ground-to-volume amplitude ratio (note the case-specific scaling of the dependent variables). The figures represent two extreme cases: the average baseline for two interferometric E-SAR tracks in Fig. 7 is $\bar{B} = 7.588\text{m}$ while for Fig. 8 it is $\bar{B} = 40.320\text{m}$. For both cases, an intermediate incidence angle of $\theta_0 \approx 53°$ and a volume height of $h_v = 20\text{m}$ were selected. The variation of the baseline vector along the flight track forces the conditioning of the inversion problem to be azimuth *and* range variant. This implies that these directional effects have to be compensated for during the modeling of Pol-InSAR observables (forward modeling) as well as during geo- and biophysical parameter extraction (inversion modeling). Forthcoming studies have to evaluate the robustness of the parameter inversion under different acquisition scenarios.

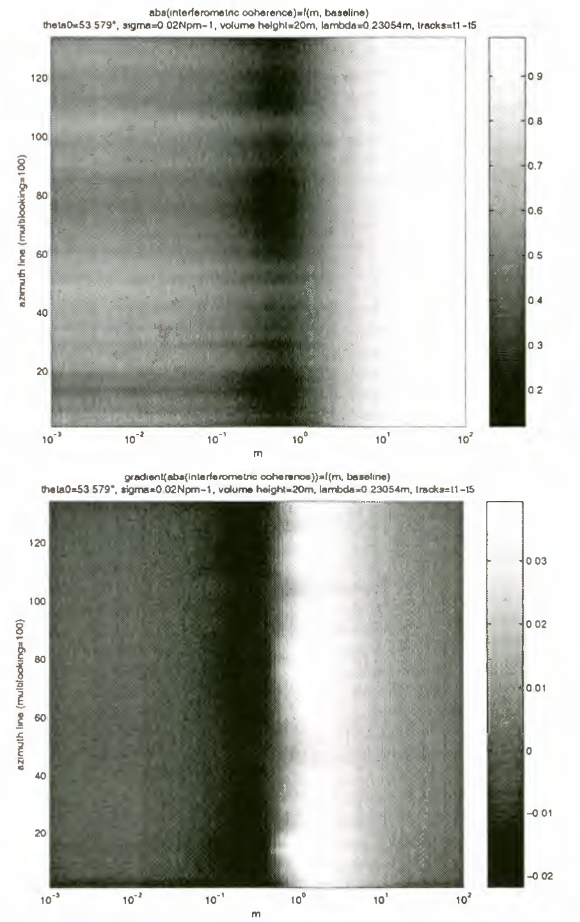

Fig. 8. $|\gamma|(B, m(\underline{w}))$ (top), gradient of $|\gamma|$: $\delta|\gamma|/\delta B(B, m(\underline{w}))$ (bottom). B(azimuth) and $\bar{B} = 40.320\text{m}$. E-SAR, L-band.

IV. Pol-InSAR Coherence Statistics

Since the amplitude of the interferometric coherence is polarisation-dependent, the statistics of the amplitude and phase of the interferometric coherence is also a function of the polarisation state.

The estimation of topography using a complex scattering model consisting of a random volume over a multipolarising ground is generally proposed as the intersection point of a regression line through the coherence values with the complex unitary circle [2]. Here we propose an enhanced method of topography estimation considering the polarisation-dependent statistics of the individual complex coherence values.

Fig. 9 shows the standard deviation of the amplitude of the interferometric coherence as a function of different degrees of freedom df analytically described by the well-known generalised hypergeometric function. After estimating the degrees of freedom (i.e. effective number of looks, ENL or number of statistically independent samples), this function is used to estimate the intersection point (with its argument ϕ_{topo}) using a weighted least-squares (WLS) fit (Fig. 10).

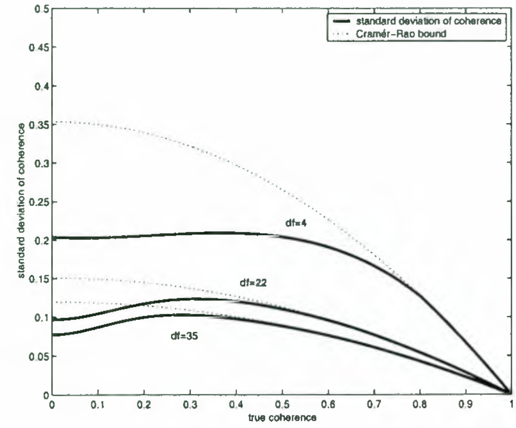

Fig. 9. Standard deviation of the $|\gamma|$ estimate for different degrees of freedom df.

Fig. 10 shows the correct representation of the coherence samples and their statistics in the complex unitary circle. The radial 90%-confidence interval has been calculated using the Goodman *a posteriori* density function [4], [3], [7]. The angular standard deviation was estimated through the signal-to-noise ratio Ξ_{int} of the interferogram. The position and the size of the individual probability segments in the complex unitary circle are directly related to the radial distance of the complex coherence samples. The low df was intentionally selected to demonstrate the considerable angular variation of the individual coherence estimates.

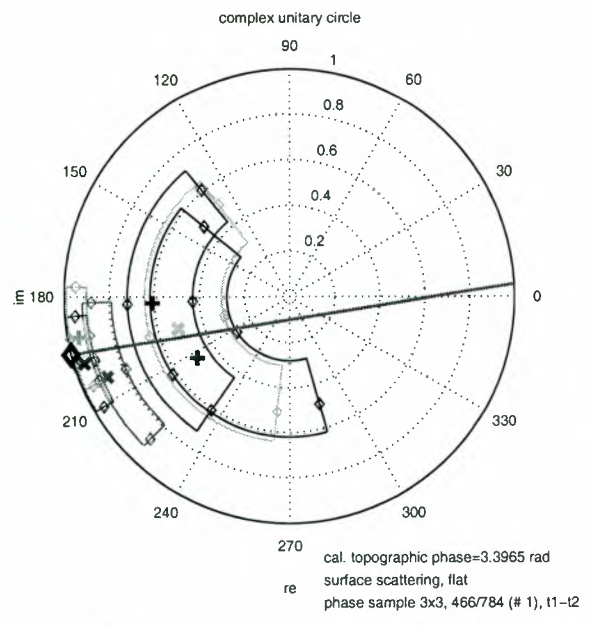

Fig. 10. Simultaneous confidence statements for $\gamma(m(\underline{w}))$ in the complex unitary circle for a low df ('+' singular polarisations; 'x' (h, v)-polarisations; ♦ projection of the coherence samples onto the boundaries of the probability segments, and intersection point). ϕ_{topo} estimation using WLS fit. E-SAR, L-band.

V. Summary

In this paper we simulated the behaviour of the amplitude of the interferometric coherence as a function of geo- and biophysical model parameters as well as various acquisition characteristics. The simulation results allow for the evaluation of the performance of a scattering model consisting of a random volume over a multi-polarising ground. The present results reveal the strong sensitivity of the amplitude of the interferometric coherence to the polarisation and to various acquisition parameters. Inversion algorithms should pay special attention to this polarisation-dependent sensitivity and to the polarisation-dependent complex coherence statistics.

References

[1] Cloude S. R., Papathanassiou K. P., "Polarimetric SAR interferometry", *IEEE Transactions on Geoscience and Remote Sensing*, vol. 36(5):1551-1565, September 1998.

[2] Cloude S. R., Papathanassiou K. P., Boerner W. M., "A fast method for vegetation correction in topographic mapping using polarimetric radar interferometry", *Proc. of EUSAR 2000*, pp. 261-264, Munich, Germany, 23-25 May 2000.

[3] Foster M. R., Guinzy N. J., "The coefficient of coherence: its estimation and use in geophysical data processing", *Geophysics*, 32(4):602-616, 1967.

[4] Goodman N. R., "Statistical analysis based on a certain multivariate complex Gaussian distribution (an introduction)", *Annals of Mathematical Statistics*, 34(1):152-177, 1963.

[5] Papathanassiou K. P., Reigber A., Cloude S. R., "Vegetation and ground parameter estimation using polarimetric interferometry", *Proc. of the CEOS SAR Workshop*, pp. 347-358, Toulouse, France, 26 - 29 October 1999.

[6] Stebler O., Pasquali P., Nuesch D., "Investigation of multi-baseline singular value estimation within POL-InSAR measurements", *Proc. of EUSAR 2000*, pp. 257-260, Munich, Germany, 23-25 May 2000.

[7] Stebler O., Pasquali P., Small D., Holecz F., Nüesch D., "Analysis of ERS-SAR Tandem time-series using coherence and backscattering coefficient", *Proc. of the Fringe '96 workshop on ERS SAR interferometry*, ESA SP-406, pp. 71-81, Zurich, Switzerland, 30 September-2 October 1996.

[8] Stebler O., Meier E., Nüesch D., "Multi-baseline airborne Pol-InSAR measurements for the estimation of scattering processes within vegetation media", *Proc. of the IEEE IGARSS*, Sydney, Australia, 9-13 July 2001,

[9] Treuhaft R. N., Siqueira P. R., "Vertical structure of vegetated land surfaces from interferometric and polarimetric radar", *Radio Science*, vol. 35(1):141-177, January-February 2000.

POTENTIAL ROLES FOR SPACE-BORNE SAR IN DISASTER MANAGEMENT AND HUMANITARIAN RELIEF

Urs Wegmüller[1], Andreas Wiesmann[1], Marc Honikel[2], Tazio Strozzi[1], Charles L. Werner[1]

[1]Gamma Remote Sensing, Thunstrasse 130, 3074 Muri BE, Switzerland

Tel: +41 31 9517005, Fax: +41 31 9517008, e-mail: wegmuller@gamma-rs.ch

[2]Institute of Geodesy and Photogrammetry, Swiss Federal Institute of Technology Zurich, Switzerland, mhonikel@geod.baug.ethz.ch

ABSTRACT

This contribution is an assessment of possible roles of space-borne SAR in disaster management and humanitarian relief projects. Time constraints, data selection, and the selected approach depend strongly on the specific task requested. Different categories of tasks were identified, including rapid mapping (i.e. making cartographic information available for a poorly mapped area in a short period of time), hazard mapping (i.e. mapping the spatial extent and the degree of damage which occurred in a hazard event), thematic mapping for reconstruction planning, and risk assessment. The results of an evaluation of the methodology, potential, and limitations of SAR for rapid mapping and hazard mapping based on specific examples are presented.

1. EO INFORMATION REQUIREMENTS OF DISASTER MANAGEMENT AND HUMANITARIAN RELIEF PROJECTS

A wide range of geo-spatial information requirements arise from disaster management and humanitarian relief projects, which can be roughly divided into the three main categories:

- rapid mapping (i.e. making cartographic information available for a poorly mapped area in a short period of time)
- hazard mapping (i.e. mapping the spatial extent and the degree of damage which occurred in a hazard event)
- thematic mapping for reconstruction planning, and risk assessment

Main differences between the three categories are in the time and data availability constraints. The rapid in "rapid mapping" expresses that map-type information is required in a very short time, for example to organize international support immediately after a natural disaster or political conflict. The data used in the rapid mapping does not necessarily need to be real-time acquisitions. Archived data may also serve the same purpose and has of course the advantage of a better availability. One major element in "rapid mapping" is the unavailability of adequate geo-spatial information from other sources. A clear distinction between availability and existence has to be made. Detailed maps may exist for the area of interest but may not become available because of logistics problems, security or commercial interests. Considering the timeliness and importance of the demand the requirements concerning the information content should be as low as necessary. Of course, high-resolution, easy-to-understand, geometrically correct products are preferred. But more basic products such as geocoded EO data (optical or SAR imagery) may serve for many purposes already, if timely enough available. To many users SAR imagery is not familiar, therefore an adequate presentation of the information is essential.

For the hazard mapping EO data during or shortly after the hazard event are required. Space-borne remote sensing data have a good potential for the assessment of damages after natural disasters and similar catastrophes. Data acquisitions after the hazard event combined with archived data representing the state before the event allow in many cases to map the change which occurred. One major advantage of SAR as compared to optical imagery is its "all-weather" capability. In spite of this advantage the delay time to the next acquisition can be quite long. In the case of ERS the repeat-cycle is, for example, 35 days. Nevertheless, SAR sensors with beam-steering, such as Radarsat, and the planned ENVISAT ASAR and ALOS PALSAR, are much preferred, in this context, as they allow to acquire data within a few days of the hazard event, at most. In addition multi-temporal SAR data and SAR interferometry have very good potentials for change detection. The timeliness of the availability of the EO based information is sometimes very important, requiring very short delay times for the availability of archived and newly acquired data. Raw data as well as the final products may be transferred over the internet.

Thematic mapping for reconstruction planning, and risk assessment is a very wide topic which may more or less cover all applications possible. The main information requirements are for general mapping tasks as part of the building up of geo-information data bases. In particular, digital elevation models are a high priority requirement. Furthermore, general landuse mapping tasks and EO based products as input for risk assessment (flooding, erosion, etc.). In this context the information quality and

Proc. 3rd International Symposium, 'Retrieval of Bio- and Geophysical Parameters from SAR Data for Land Applications', Sheffield, UK, 11-14 September 2001 (ESA SP-475, January 2002)

cost are more important than time constraints. Sustainability, technology transfer and education are other aspects which are usually important in such projects.

2. POTENTIAL ROLES FOR SPACE-BORNE SAR

2.1 Rapid mapping

As already stated above SAR based products are usually not the first choice in rapid mapping. Provided data availability and budget constraints permit this high resolution (~1meter, for example IKONOS) or multi-spectral (~20meter, for example Landsat TM or SPOT) optical imagery is preferred. As alternative where necessary but also because of its complimentary information content SAR data have the potential to play an important role. Many potential users are not very familiar, though, with SAR data processing and interpretation – and under the extreme pressure typically present when rapid mapping is required it is not adequate to evaluate a "new" technique. To avoid the above described "contact problem" interested users should get familiar with SAR imagery without "rush" situation in preparation of the later timely use of this technique.

Examples for satellite SAR based rapid mapping products are:

- Backscatter maps
- Coherence products
- Digital elevation models (DEMs)

Typically, these products should not be in the range-Doppler SAR imaging geometry, but in the transformed (geocoded) map geometry. Accurate, so-called terrain corrected, SAR geocoding requires knowledge of the actual terrain height. Terrain height errors, as present in inaccurate or low resolution DEMs or when assuming a constant terrain height for an entire scene, as done in the so-called ellipsoid-corrected SAR geocoding, result in positioning errors. In the case of ERS, for example, height errors translate into about 2 (far range) to 3 (near range) times larger positioning errors. Therefore, the geometric accuracy depends strongly on the quality of the digital elevation model. The use of a global DEM is clearly preferred over the use of ellipsoid corrected geocoding. In some cases an adequate alternative is to generate a DEM with SAR interferometry. The limitations of this technique in areas of low coherence (in the case of ERS this is over water, forest and other dense vegetation) and for rugged terrain (layover causing information gaps and phase unwrapping problems) have to be carefully considered though.

The information content of the SAR based rapid mapping products depends of course also on the sensor used and the exact processing applied. In SAR backscatter maps much of the geo-spatial information is identified based on the features geometries. In high resolution airborne SAR images even untrained observers easily identify many scene features. This is, unfortunately, somewhat more difficult, with the lower resolution space-borne SAR imagery, where untrained users may find an interpretation very difficult because of the high signal noise. With multi-temporal SAR data information on temporal variability and change becomes available. In addition, multi-temporal and spatial filtering can be used to significantly reduce the signal noise.

Interferometric SAR data have an even better potential for landuse mapping. For more densely vegetated landscapes C-band ERS-1/2 Tandem pairs with just one day acquisition interval are best suited and allow to discriminate classes as open water, forest, urban area, and low vegetation (grassland, agricultural fields etc.) as discussed in more detail in Wegmüller and Werner, 1995, 1997, Strozzi et al., 2000. Mapping of urban areas (Strozzi and Wegmüller, 1998), and land cover mapping in semi-arid and arid zones (Wegmüller et al., 2000) can also be done with the longer 35 day acquisition intervals which will also be available from ENVISAT ASAR. L-band interferometry also has a comparable potential for landuse mapping even with relatively long 44 and 46 day repeat cycles of JERS and the planned ALOS PALSAR (Wegmüller et al., 1997, Luckman et al., 1998, 2000, Wiesmann et al., 2000).

The potential of SAR interferometry to derive a DEM of an area of interest in a short time at a reasonable price is of course very attractive for rapid mapping. There are important limitations which have to be kept in mind. The feasibility and DEM quality depend strongly on relief type and land cover. In many cases the generated DEM may have gaps with no information (or just interpolated information) because of layover and very low coherence over water and forest. To predict the expected quality is very difficult and the expected quality is not easy to describe to less experienced users.

2.1.1 Sample products

Timeliness of the product availability and user-awareness of the potential of the SAR based products were found to be very important issues in the rapid mapping application. Products were generated for a test case to address these issues with the following objectives:

- define rapid mapping products
- set up efficient and robust processing chain for a timely production of these products
- generate sample products
- show sample products to potential users

For the test case an area at the Rumanian-Ukrainian border was selected. Eight ERS SAR scenes were available for the investigation, including one ascending orbit Tandem pair with one additional scene of the same track / frame, one descending orbit Tandem pair with two additional scenes of the same track / frame, and one scene of a different descending track. These data are well suited for multi-temporal and interferometric analysis.

The main rapid mapping sample products generated include:

- SAR backscattering maps
- ERS-1/2 Tandem coherence products
- Interferometric DEMs

Figure 1 shows a SAR backscatter map based on ERS data of the three different frames available. The SAR data of the different scenes were individually processed, calibrated, and terrain corrected geocoded using the Gtopo30 global DEM, and then combined into a single mosaic space-map. For the map UTM Zone 34, WGS84, and a pixel spacing of 20 m were used. Easting and northing coordinates are indicated as image labels and geographic coordinates as small black crosses within the image. The digital version of the map can be transferred over the internet and can easily be displayed or printed.

Figure 2 shows a 40km x 40km section of the interferometric DEM which was generated from the descending ERS Tandem pair. The heights are indicated using a color scale and with contour lines. No validation could be performed, but the height accuracy of this INSAR DEM is expected to be only around 20 m because of quite obvious atmospheric distortions in the flatter areas and because of relatively high signal noise over low coherence areas as the forests. The same map geometry as in Figure 1 was selected.

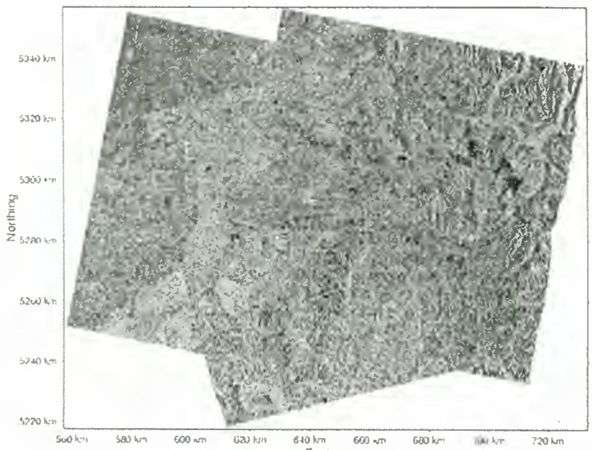

Figure 1. SAR backscatter map for Rumania-Ukraine border area (UTM Zone 34, WGS-84, 20m pixel spacing), generated by mosaicing 1 ascending and 2 descending ERS frames. The white squares indicate the locations of the map sections of Figures 2/3 and 4.

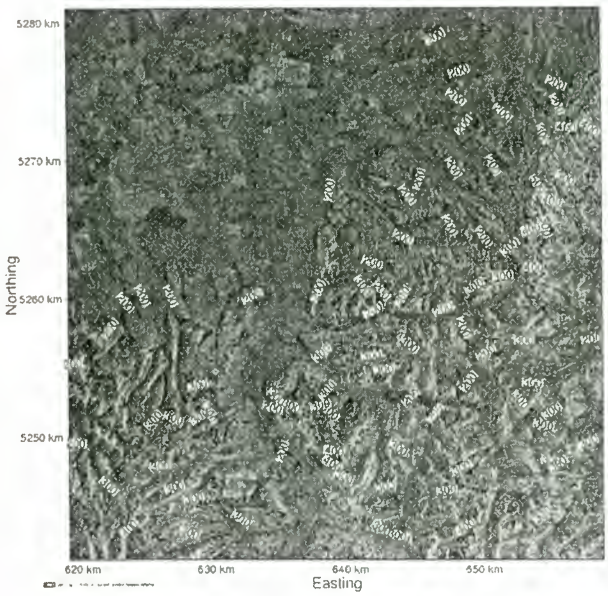

Figure 2. Digital Elevation Model (DEM) generated with ERS-1/2 Tandem interferometry (color scale and contour lines were used to indicate the terrain heights; the SAR backscattering is used as image brightness, UTM Zone 34, WGS-84, 20m pixel spacing).

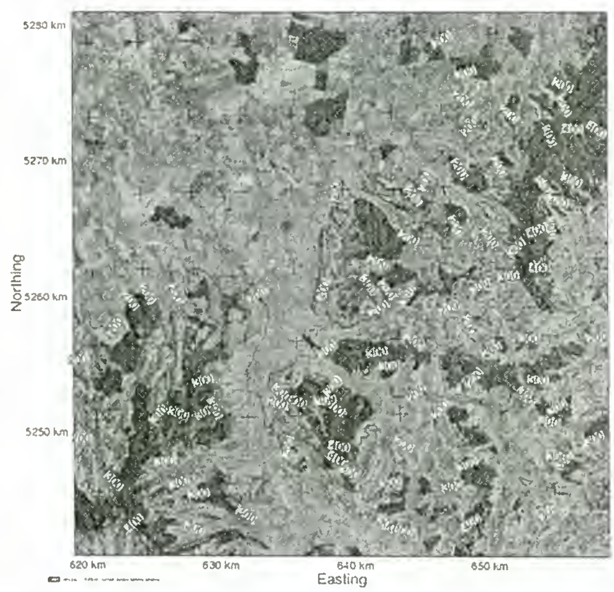

Figure 3. ERS-1/2 Tandem coherence product "ortho" (red: coherence, green: average backscattering, blue: backscatter ratio, UTM Zone 34, WGS-84, 20m pixel spacing). The Tandem coherence allows to better identify image features and to better distinguish different land cover types. On top of the coherence product topographic information derived from the INSAR DEM has been added.

Figure 3 shows a 40km x 40km section of the coherence product "ortho". This space-map is higher in content and easier to interpret than the backscatter map of Figure 1. The color coding is red: Tandem coherence, green: backscattering coefficient (average of Tandem acquisitions), and blue: backscatter change (defined as absolute value of ratio of Tandem acquisitions expressed in dB). Green color indicates forest (low coherence, intermediate backscattering, low backscatter change), yellow color urban areas (high coherence, high backscattering, low backscatter change), blue to turquoise colors open water (low coherence, low to high backscattering, high backscatter ratio), and red to orange colors open landscapes (intermediate to high coherence, low to high backscattering, low backscatter change). Furthermore, moisture change and freeze/thaw changes are indicated by high blue components. The INSAR derived contour lines of Figure 2 were added to complete this space-map. The same map geometry as in Figure 1 was selected.

2.2 Hazard mapping

Hazard mapping is usually based on change detection techniques. Multi-temporal and interferometric SAR is well suited for change detection (Wiesmann et al., 2001). Data during or shortly after the hazard event and reference data before the event are required. As stated before, despite the all-weather day-and-night capability of SAR significant data availability constraints exist also for SAR because of the relatively long orbit repeat cycles (ERS: 35 days, ENVISAT: 35 days, JERS: 44 days, ALOS: 46 days). This important constraint is much reduced for SAR instruments with beam-steering (Radarsat, ENVISAT, ALOS), which typically allow short reaction times of just a few days. The probability that adequate reference data are available is high thanks to the large SAR data archives.

A typical processing sequence for multi-temporal SAR change detection includes radiometric calibration, co-registration of the images to a common geometry, multi-temporal and spatial filtering, rationing, and change classification, for example by simple thresholding, geocoding, and visualization of the result. Coherence, as an indicator of random displacements of scatterers within the SAR resolution cell, and the interferometric phase, indicating coherent displacement of the combined scattering phase center can also be used in the context of change detection.

The missing experience of users in the interpretation of SAR and INSAR based products can be overcome in the hazard mapping by providing products at information level, such as for example a flood map which is a raster or vector data set simply indicating if an area is flood or not on a certain date. The generation of such products requires adequate SAR data processing which requires a specialist understanding.

2.2.1 Sample products

For the selected area at the Rumanian-Ukrainian border the time period of interest for the mapping of a flood event was 5. – 20. Nov. 1998. Unfortunately no ERS acquisitions could be found for this time period. The nearest acquisition dates were 14-Oct-1998 before the flood and 7-Dec-1998 and 11-Jan-1999 after the flood. These data were ordered as it was not clear how long the flood could still be observed. Unfortunately, the November flood could not be identified in the December data. This clearly demonstrates the data availability constraint mentioned above. In the January 1999 scene we detected a small area flooding, though, whose existence was not known to us before the data analysis.

A flood map was generated with a multi-temporal SAR analysis. The four scenes of the same ERS track / frame were registered to the same reference geometry (in range-Doppler coordinates), and temporally and spatially filtered. Then the ratio between the January 1999 and December 1998 image was used to classify the extent of the flood. Finally the result was geocoded and visualized. Figure 4 shows the flooded area in red. The information is also available as a vector data set.

For further examples of hazard maps it is referred to Wiesmann et al., 2001.

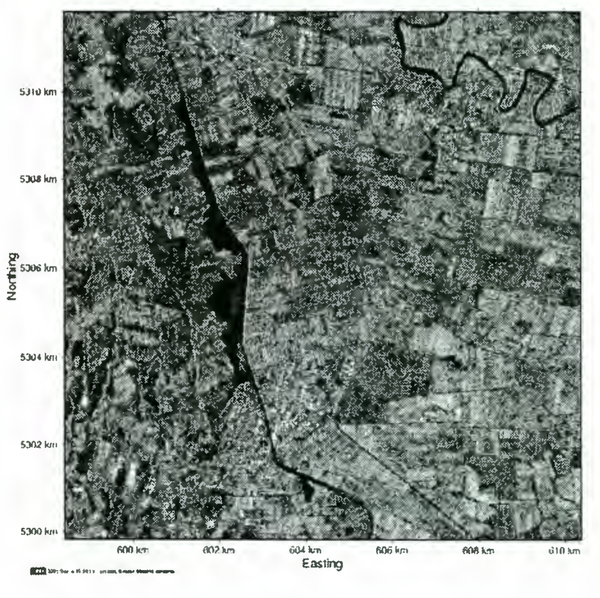

Figure 4. Multi-temporal SAR and change detection methods were used to map the flood extend on 11-Jan-1999. The information is available in map form (UTM Zone 34, WGS-84, 20m pixel spacing), with red indicating the flooded area) and as vector data.

2.3 Thematic mapping for reconstruction planning and risk assessment

The use of EO based information for thematic mapping for reconstruction planning and risk assessment is a very wide field. Most SAR based applications are of interest in this context. Main products used are space-maps as described in the rapid mapping section and especially digital elevation models.

Differential interferometric deformation maps are of high interest in the context of seismic, volcanic, and landslide deformation mapping. The potential to measure geophysical displacements in the cm to m range from space and the available archive with historic information make this technique a quite unique source of information.

In the thematic mapping for reconstruction planning and risk assessment not so much the timeliness of the information but its quality and price are important.

3. CONCLUSIONS AND OUTLOOK

Space-borne SAR has a good potential to support disaster management and humanitarian relief projects but so far, this potential has been strongly under-utilized because decision makers were not enough aware of this potential and time constraints did not allow for an evaluation of a new techniques. It has to be understood that the interpretation of a SAR backscatter image is difficult for an untrained user due to the special SAR imaging geometry and image content. Steps to improve the awareness and acceptance of SAR based information are to present the products in a better accessible form and to train the users in the interpretation of the specific products as well as in the general understanding of the potential and limitations of this technique.

4. ACKNOWLEDGEMENTS

This work was supported by the KTI project CIRSTEN. ERS data copyright ESA, courtesy of ERS AO3-175.

5. REFERENCES

Wegmüller U. and C. L. Werner, SAR interferometric signatures of forest, IEEE Trans. Geosci. Remote Sensing, Vol. 33, No. 5, pp. 1153-1161, 1995.

Wegmüller U. and C. L. Werner, Retrieval of vegetation parameters with SAR interferometry, IEEE Trans. Geosci. Remote Sensing, Vol. 35, No. 1, pp. 18-24, 1997.

Wegmüller U., T. Strozzi, and C. Werner, Forest applications of ERS, JERS, and SIR-C interferometry, Proceedings of IGARSS'97, 4-8 August, Singapore, pp. 790-792, 1997.

Luckman A., J. Baker, and .U. Wegmüller, Repeat-pass interferometric coherence measurements of tropical forest from JERS and ERS satellites, Proceedings of IGARSS'98, 6-10 July, Seattle, WA, USA, 1998

Strozzi T. and U. Wegmüller, Delimitation of Urban Areas with SAR Interferometry, Proceedings of IGARSS'98, 6-10 July, Seattle, WA, USA, 1998.

Luckman A., J. Baker, and U. Wegmüller, Repeat-pass interferometric coherence measurements of disturbed tropical forest from JERS and ERS satellites, Remote Sens. Environ. Vol. 73, pp. 350-360, 2000.

Strozzi T., P. B. G. Dammert, U. Wegmüller, J-M. Martinez, A. Beaudoin, J. Askne, and M. Hallikainen, Landuse mapping with ERS SAR interferometry, IEEE Trans. Geosci. Remote Sensing, Vol. 38, No. 2, pp. 766-775, 2000.

Wegmüller U., T. Strozzi, T. Farr, and C. Werner, Arid land surface characterization with repeat-pass SAR interferometry, IEEE Trans. Geosci. Remote Sensing, Vol. 38, No. 2, pp. 776-781, 2000.

Wiesmann A., U. Wegmüller, T. Strozzi, and C. Werner, "JERS INSAR coherence over Siberian boreal forest", Proceedings of ERS-ENVISAT Symposium, Gothenburg, Sweden, 16-20 Oct. 2000.

Wiesmann A., Wegmüller U., Honikel M., T. Strozzi, and C. Werner, "Potential and methodology of satellite based SAR for hazard mapping", Proceedings of IGARSS 2001, Seattle, Australia, 9-13 July 2001.

Posters

Forestry, Soils and Snow & Ice

RETRIEVING SURFACE ROUGHNESS AND SOIL MOISTURE FROM SAR DATA USING NEURAL NETWORKS

N. Baghdadi, S. Gaultier and Ch. King
BRGM, ARN/MSO, 3 avenue C. Guillemin, BP 6009, 45060 Orléans, France
Phone: +33 238 64 32 02 Fax: +33 238 64 33 61 e-mail: n.baghdadi@brgm.fr

ABSTRACT

An inversion technique based on neural networks has been implemented to estimate surface roughness and soil moisture over bare fields using ERS and RADARSAT data. The neural networks were trained with a simulated data set generated from the Integral Equation Model. Later the networks were applied to an experimental data set spanning a wide range of surface roughness and soil moisture, with backscattering coefficients for three radar configurations (VV-23°, HH-39°, HH-47°). Approaches based on two and three radar image configurations were examined and tested. Although the three-image configuration produces slightly more accurate results, a two-image configuration gives results of comparable accuracy when a favourable combination of incidence angles is adopted. Soil moisture and surface roughness were estimated respectively at about 7.6% and 0.47 cm using the root mean square error.

INTRODUCTION

In many parts of the world, excessive runoff and soil erosion are amongst the major sources of damage. Monitoring tools at catchment scale are necessary for improving flood prediction and water-resource management. Surface runoff occurs when rainfall intensity exceeds soil infiltration capacity [Boiffin *et al.*, 1988; Le Bissonnais, 1990]. In agricultural areas, roughness plays a role of trapping water, which increases infiltration and in turn reduces downstream runoff. More specifically, it has been proved in loamy contexts that smooth soils are commonly crusted and have a poor infiltration capacity compared to rough soils [Le Bissonnais *et al.*, 1998]. Therefore, the mapping of soil roughness states could offer a reliable key for assessing those surfaces that could potentially contribute to runoff in agricultural contexts.

The backscattering signal is closely correlated to soil surface roughness and is also a function of moisture content [*Ulaby et al.*, 1986]. Experimental results and studies using simulation models have shown that high-incidence backscattering is more sensitive to surface roughness than low-incidence backscattering. In addition, the C-band at low-incidence angles is optimal for soil moisture estimation [Ulaby *et al.*, 1978; Autret *et al.*, 1989]. In this study, we discuss the application of neural networks to retrieving the parameters of surface roughness (rms) and soil moisture (mv).

DATA SETS

Two data sets were used. The first is a simulated data set generated from the Integral Equation Model (IEM) and served to train the neural networks [Fung, 1994]. The second is an experimental data set used to validate the inversion results.

The IEM model is one of the most widely used models. Its success is partly due to its applicability to a wide range of surface roughness and soil moisture. However, much work has revealed a poor agreement between IEM simulations and measured data [Baghdadi *et al.*, 2001; Zribi *et al.*, 1997; Rakotoarivony *et al.*, 1996]. Baghdadi *et al.* (2001) propose a semi-empirical calibration of the IEM to improve its performance, with consideration of only three radar configurations (VV-23°, HH-39°, HH-47°). The discrepancy between the measured and simulated backscattering coefficients is assumed to be directly related to the poor accuracy of the correlation length measurements, considering that the other IEM input parameters (rms height, soil moisture and incidence angle) are relatively accurate. Baghdadi *et al.* (2001) thus propose an "optimal" correlation length (L_{opt}), which is a empirical calibration parameter. The parameter L_{opt}, which integrates the true correlation length as well as the imperfections of the IEM, depends on rms surface height and radar configuration (frequency, polarization and incidence angle).

A realistic data set combining a wide range of soil variables (rms and mv) and corresponding backscattering coefficients was generated from the calibrated IEM. We considered a total of 5376 elements corresponding to 56 surface roughness values (rms between 0.25 and 3 cm with a step of 0.05 cm), 24 soil moisture values (mv between 4% and 50% with a step of 2%), and three radar configurations (VV-23°, HH-39°, HH-47°). The data set was contaminated by a zero mean Gaussian random noise to assimilate it to a measured data set. A noise level of 1 dB, corresponding to the calibration errors of satellite images, was selected for the backscattering coefficient.

The experimental data set was collected within the framework of the European FLOODGEN campaign of 1998 [Baghdadi *et al.*, 2001] in the Pays de Caux region

Proc. 3rd International Symposium, 'Retrieval of Bio- and Geophysical Parameters from SAR Data for Land Applications', Sheffield, UK, 11-14 September 2001 (ESA SP-475, January 2002)

of northern France (long. 0°50' W and lat. 49°47' N). The site consists mainly of agricultural fields on low-relief plateaux with homogeneous soil composed of about 67% loam, 13% clay and 17% sand.

One ERS image (VV-23°) and two RADARSAT images (HH-39° and HH-47°) were acquired respectively on 8, 9 and 23 February 1998. Absolute calibration of the ERS and RADARSAT images was carried out, which enabled the derivation of backscattering coefficients (σ^0).

In conjunction with the satellite overpasses, a field survey was conducted on crop-sowing fields (wheat, sunflower and corn) with a low vegetation density (<20%) and on ploughed fields in order to measure the soil characteristics. The data set contains 28 measurements of surface roughness and soil moisture. The rms values fluctuate between 3 mm and 3 cm. The soil moisture contents range from 30 to 40%.

THE INVERSION TECHNIQUE

A technique based on neural networks was developed to estimate surface roughness and soil moisture from SAR data [Kohonen, 1988; Atkinson and Tatnall, 1997]. Retrieval of soil moisture and surface roughness parameters needs at least two SAR channels. The neural network most commonly encountered in remote sensing is of the feed-forward back-propagation multi-layer perceptron (MLP) type. The MLP neural network consists of one input layer, one output layer, and one or more hidden layers in between. The input vector contains the measurements ($\sigma°$-values), and the output vector contains the quantity to be retrieved from these (rms surface height and soil moisture).

The simulated data set was divided randomly into a training set (2688 elements) and a validation set (2688 elements). The training phase is carried out with the training set and the optimum network is defined, which minimises the error (SSE: Sum Square Error) in the validation set between the measured backscattering values and those predicted by the network. Later, the performance of the neural network was evaluated using the experimental data set.

Two cases are considered in this study:

- Input to the network is a set of two or three $\sigma°$-values: (VV-23°; HH-39°), (VV-23°; HH-47°), (HH-39°; HH-47°), and (VV-23°; HH-39°; HH-47°). Output is rms surface height and soil moisture.

- In order to reduce ambiguity in the retrieval problem, a constraint on the soil moisture conditions is introduced: slightly moist soil or very moist soil. The two moisture classes could be: mv <20% for dry to slightly moist soils and mv ≥20% for wet soils. parameters.

RESULTS AND DISCUSSION

A MLP neural network with one hidden layer of twenty nodes was found to best model the relationship between the soil parameters (rms surface height and soil moisture) and the backscattering coefficients. These characteristics are the result of a compromise between accuracy and computation time.

The results obtained using backscattering coefficients contaminated by a Gaussian noise with a standard deviation of 1 dB show that beyond a certain rms threshold, which depends on the images used and ranges from 1.5 cm to 2 cm, the neural network has great difficulty in retrieving the parameter rms (Figure 1a). For data beneath this threshold, rms estimation is good despite a slight bias, whereas for data above this threshold, estimation is poor with a considerable bias for all configurations (two or three radar images). For all points with an rms between 1.5 cm and 3 cm, the network yields an rms of approximately 1.75 cm. This is because the radar in C-band is not highly sensitive to changes in rms at high rms ranges (threshold dependent on the angle of incidence). For mv values between 4% and 35%, we note an overestimation of about 5%, and for mv values above 35%, the network underestimates soil moisture (Figure 1b). Table 1 shows the inversion results for the simulated data set. When no constraint on mv is introduced, the use of the two-image configuration HH-47° and VV-23° seems to give optimal results for rms and mv estimation. An accuracy comparable to that obtained with this optimal configuration (HH-47° and VV-23°) is also noted for rms estimation using the HH-47° and HH-39° configuration (RMSE about 0.6 cm), and for mv estimation using the HH-39° and VV-23° configuration (RMSE about 9.4%). The results also show a slight improvement in retrieval of both surface roughness and soil moisture (by 0.6 mm for rms and 0.4% for mv) when three radar images are used rather than two radar images.

The RMSE on mv is reduced by a third when a constraint on mv is introduced. In the case of a network based on three radar images, the RMSE drops from 8.9% without the constraint on mv to 6.1% with the constraint on mv (average for the entire data set). The introduction of a constraint on mv only slightly improves the rms results (cf. Table 1).

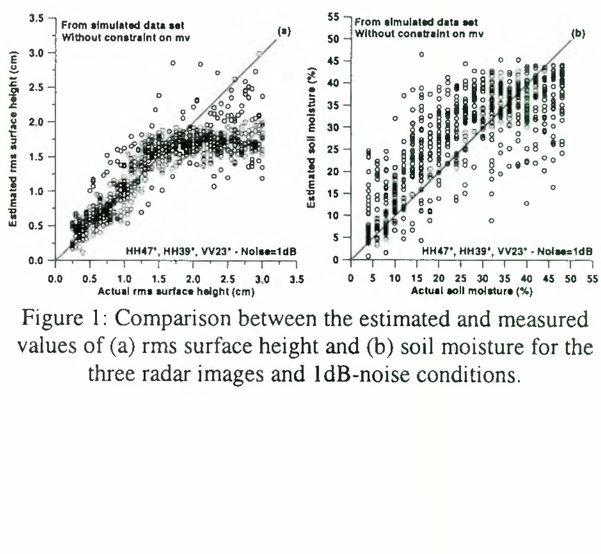

Figure 1: Comparison between the estimated and measured values of (a) rms surface height and (b) soil moisture for the three radar images and 1dB-noise conditions.

Noise on σ_0=1 dB	Surface height (rms)			Soil moisture (mv)		
Without constraint on mv	MAE (cm)	RMSE (cm)	d	MAE (%)	RMSE (%)	d
HH 47° and HH 39°	0.45	0.60	0.79	9.31	11.45	0.74
HH 47° and VV 23°	0.42	0.58	0.81	7.36	9.34	0.85
HH 39° and VV 23°	0.53	0.68	0.71	7.57	9.46	0.83
HH 47°, HH 39° and VV 23°	0.39	0.52	0.84	6.97	8.92	0.86
With constraint on mv ***Dry to slightly moist soils (mv≤20%)***	MAE (cm)	RMSE (cm)	d	MAE (%)	RMSE (%)	d
HH 47° and HH 39°	0.39	0.51	0.85	3.34	4.15	0.70
HH 47° and VV 23°	0.48	0.55	0.73	2.76	3.76	0.76
HH 39° and VV 23°	0.57	0.73	0.62	2.86	3.59	0.77
HH 47°, HH 39° and VV 23°	0.41	0.56	0.83	2.74	3.51	0.81
With constraint on mv ***Wet soils (mv>20%)***	MAE (cm)	RMSE (cm)	d	MAE (%)	RMSE (%)	d
HH 47° and HH 39°	0.39	0.54	0.83	7.65	9.21	0.47
HH 47° and VV 23°	0.37	0.52	0.84	7.53	9.36	0.62
HH 39° and VV 23°	0.47	0.61	0.77	7.15	8.86	0.64
HH 47°, HH 39° and VV 23°	0.36	0.49	0.86	7.07	8.68	0.61

Table 1: Statistics for the estimation of surface height and soil moisture for 1-dB noise conditions.

The retrieval capacity of neural networks trained by theoretical backscattering coefficients generated by the IEM model was then tested using the experimental data set. The networks used are those obtained using data contaminated with a Gaussian noise with a standard deviation of 1 dB (simulated data). The resulting networks, one without constraint on mv and the other with, were then analysed. Considering that the elements of the field data set have a moisture corresponding to what we call 'wet soils' (mv >20%), we applied the neural networks developed using the simulated data set with the constraint on mv. Table 2 gives the statistical results obtained for the estimation of rms and mv according to the two- and three-image configurations considered. The estimations of surface roughness (rms) and soil moisture (mv) are illustrated in Figures 2 and 3.

Experimental data	Surface height (rms)				Soil moisture (mv)			
Without constraint on mv	Bias (cm)	MAE (cm)	RMSE (cm)	d	Bias (%)	MAE (%)	RMSE (%)	d
HH 47° and HH 39°	-0.06	0.41	0.51	0.73	6.40	8.93	11.17	0.33
HH 47° and VV 23°	-0.006	0.48	0.57	0.58	7.71	8.46	11.95	0.44
HH 39° and VV 23°	0.20	0.53	0.62	0.56	5.97	7.35	9.64	0.48
HH 47°, HH 39° and VV 23°	-0.13	0.43	0.54	0.74	8.38	9.38	12.44	0.47
With constraint on mv ***Wet soils (mv>20%)***	Bias (cm)	MAE (cm)	RMSE (cm)	d	Bias (%)	MAE (%)	RMSE (%)	d
HH 47° and HH 39°	0.13	0.37	0.47	0.79	-2.50	4.26	5.63	0.41
HH 47° and VV 23°	0.06	0.38	0.48	0.77	1.47	6.65	8.64	0.29
HH 39° and VV 23°	0.22	0.47	0.59	0.70	3.21	6.81	7.81	0.41
HH 47°, HH 39° and VV 23°	0.02	0.37	0.47	0.80	-0.23	6.01	7.60	0.35

Table 2: Statistics for the estimation of surface height (rms) and soil moisture (mv) using the experimental data set.

The introduction of a constraint on mv provides a good agreement between the estimated and measured soil moisture, with a significant decrease of the bias and the RMSE on the estimation of mv. This decrease varies according to the images used, with an average improvement of some 5% for the bias and 4% for the RMSE. The results obtained for rms estimation are practically the same with or without the constraint on mv. The best rms and mv estimation results were obtained with a combination of three radar configurations. Nevertheless, the use of two images, one high incidence (47°) and the other low incidence (23°), provides results of comparable accuracy because VV-23° yields less errors in the mv estimation while HH-47° yields less errors in the rms estimation. The network based on the HH-47°, HH39° and VV-23° configuration for input gives an RMSE of 0.47 cm for rms and 7.6% for mv, whereas the network based on the HH-47° and VV-23° configuration gives an RMSE of 0.48 cm for rms and 8.6% for mv. With the introduction of a constraint on mv, the residual bias is less than 0.1 cm for rms estimation and less than 1.5% for mv estimation if we adopt optimal image configurations. We also note an overestimation of rms surface height in low roughness regions (rms ≤1.5 cm) and an underestimation in high roughness regions (rms >1.5 cm).

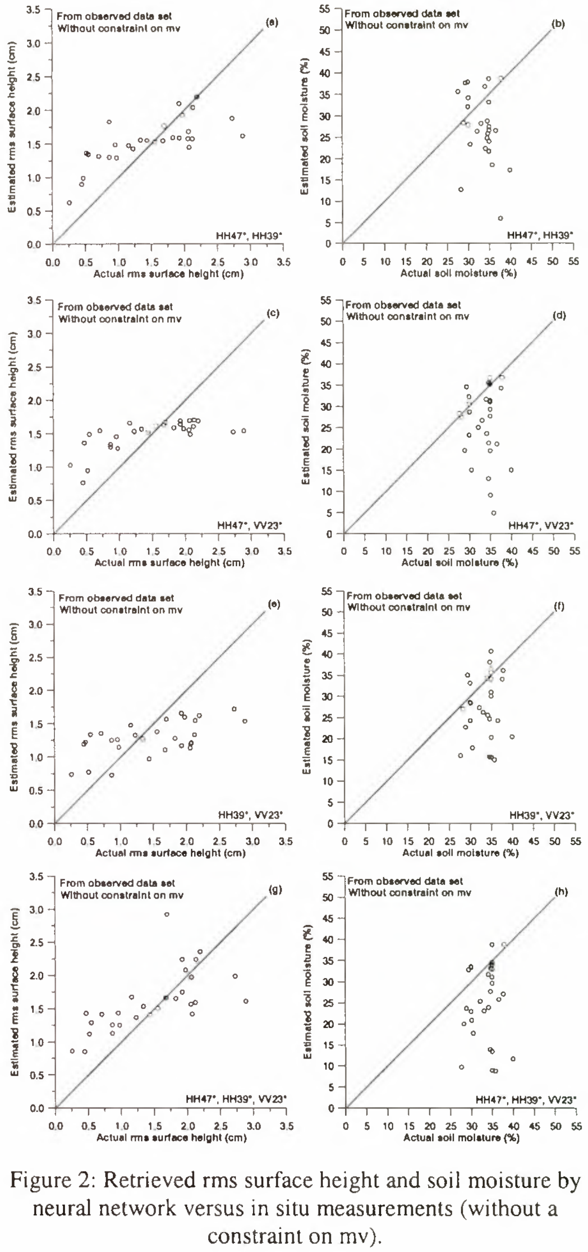

Figure 2: Retrieved rms surface height and soil moisture by neural network versus in situ measurements (without a constraint on mv).

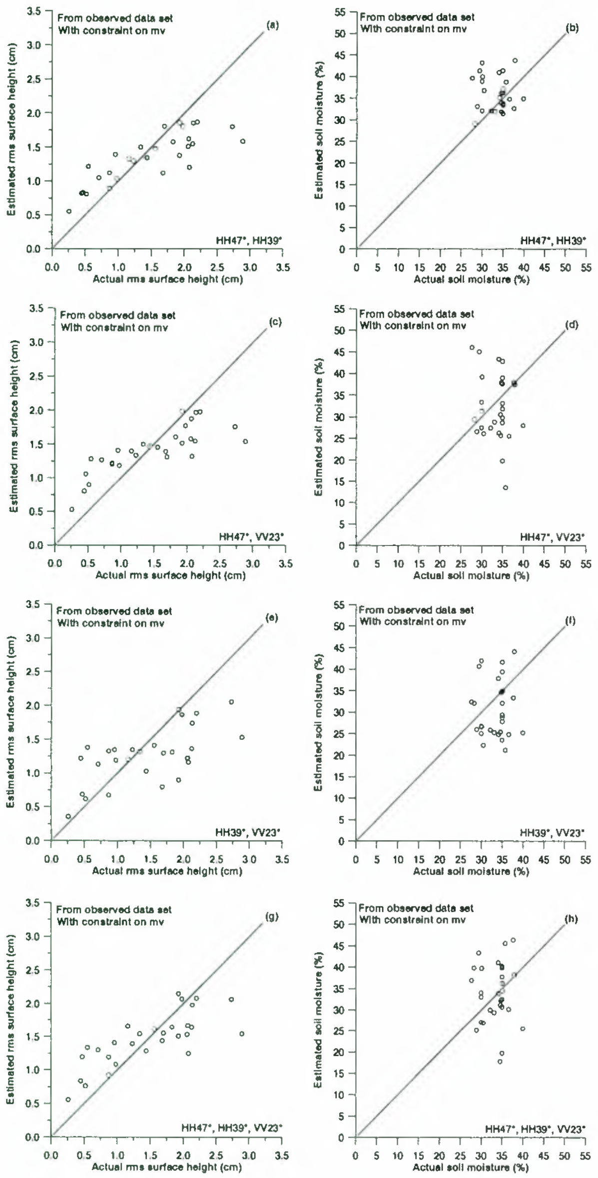

Figure 3: Retrieved rms surface height and soil moisture by neural network versus in situ measurements (with a constraint of wet soils on mv).

CONCLUSIONS

The objective of this study was to assess the capacity of estimating surface roughness and soil moisture over bare fields using SAR data. An inversion technique based on neural networks was implemented. A calibrated IEM model was used to generate a data set for training of the neural networks. These networks were later applied to ERS and RADARSAT measurements (VV-23°, HH-39° and HH-47°) to estimate surface roughness and soil moisture. The results of this study indicate that neural networks trained with data generated by the electromagnetic model IEM are able to retrieve the parameters of surface roughness and soil moisture with acceptable accuracy. Nevertheless, we note that the introduction of a constraint of pre-information on soil moisture improves mv estimation. The relationship between the inversion results and the radar configurations adopted has also been explored. The inversion errors obtained with the three-image configurations were slightly less than with the two-image configuration. The retrieval errors on the experimental data set were 0.47 cm for rms and 7.6% for mv. The best estimation of soil moisture occurred when the multi-configuration measurements of backscattering coefficients included an image with a low incidence angle (23°). Inversion of the surface roughness parameter gives a more accurate result with a high incidence angle (47°). Inversion of surface roughness, however, revealed that the technique is limited to values greater than approximately 1.75 cm.

Future studies should have more in situ samples and radar configurations for the validation of this technique.

ACKNOWLEDGEMENTS

This work has been financed by the European project FLOODGEN (ENV4-CT96-0368) and the BRGM research programme PRD316. The authors would like to thank Marie Weiss and Thierry Fourty for their support concerning neural networks.

REFERENCES

Autret M, Bernard R., and Vidal-Madjar D., 1989. Theoretical study of the sensitivity of the microwave backscattering to the soil surface parameters. *International Journal of Remote Sensing*, vol. 10, no. 1, pp. 171-179.

Atkinson P.M., and Tatnall A.R.L., 1997. Neural networks in remote sensing: Introduction. *International Journal for Remote Sensing*, vol. 18, no. 4, pp.699-709.

Baghdadi N., King C., Chanzy A., and Wigneron J.P., 2001. An empirical calibration of the integral equation model based on SAR data, soil moisture, and surface roughness measurement over bare soils. *International Journal of Remote Sensing: in press.*

Boiffin J., Papy F., and Eimberck M., 1988. Influence des systèmes de culture sur les risques d'érosion par ruissellement concentré: I. Analyse des conditions de déclenchement de l'érosion. *Agronomie*, vol. 8, pp. 663-673.

Fung A. K., 1994. Microwave Scattering and Emission Models and their Applications. Artech House, Inc., Boston, London, 573 pages.

Kohonen T., 1988. An introduction to neural computing. *Neural Networks*, vol. 1, pp. 3-16.

Le Bissonnais Y., 1990. Experimental study and modelling of soil surface crusting processes. In Bryan R.B. (Ed.), *Soil erosion – experiments and models*, Catena, Suppl., 17, pp. 13-28.

Le Bissonnais Y., Benkhadra H., Chaplot V., Fox D., King D., and Daroussin J., 1998. Crusting, runoff and sheet erosion on silty loamy soils at various scales and upscaling from m² to small catchments. *Soil & Tillage Research*, vol. 46, no. 1-2, pp. 69-80.

Rakotoarivony L., Taconet O., Vidal-Madjar D., Bellemain P., and Benallègue M., 1996. Radar backscattering over agricultural bare soils. *Journal of Electromagnetic Waves and Applications*, vol. 10, no. 2, pp. 187-209.

Ulaby F. T., Batlivala P. B., and Dobson M. C., 1978. Microwave backscatter dependence on surface roughness, soil moisture and soil texture: Part I - Bare soil. *I.E.E.E. Transactions on Geoscience and Remote Sensing*, vol. 16, pp. 286-295.

Ulaby F. T., Moore R. K., and Fung A. K., 1986. Microwave Remote Sensing: Active and Passive. *Volume Scattering and Emission Theory-Advanced Systems and Applications*. Artech House, Inc., Dedham, Massachusetts, vol. 3, 1100 pages.

Zribi M., Taconet O., Le Hegarat-Mascle S., Vidar-Madjar D., Emblanch C., Loumagne C., and Normand M., 1997. Backscattering behavior and simulation: Comparison over bare soils using SIR-C/X-SAR and ERASME 1994 data over Orgeval. *Remote Sensing of Environment*, vol. 59, pp. 256-266.

FOREST STAND STRUCTURE FROM AIRBORNE POLARIMETRIC INSAR

H. Balzter[1], P. Saich[2], A.J. Luckman[3], L. Skinner[3], and J. Grant[4]

[1] *Centre for Ecology and Hydrology, Monks Wood, Abbots Ripton, Huntingdon, Cambs, PE28 2LS, UK*
tel. +44-(0)1487 772400 / fax: +44-(0)1487 773467, email: heiko.balzter@ceh.ac.uk
[2] *Department of Geography, University College London, 26 Bedford Way, London WC1 0AP, UK*
[3] *Department of Geography, University of Wales Swansea, Singleton Park, Swansea SA2 8PP, UK*
[4] *Faculty of Biology, Vrije Universiteit van Amsterdam, de Boelelaan 1087, 1081 HV, Amsterdam, The Netherlands*

ABSTRACT

Interferometric SAR at short wavelengths can be used to retrieve stand height of forests. We evaluate the precision of tree height estimation from airborne single-pass interferometric E-SAR data at X-band VV polarisation and repeat-pass L-band polarimetric data. General yield class curves were used to estimate tree height from planting year, tree species and yield class data provided by the Forest Enterprise. The data were compared to tree height estimates from X-VV single-pass InSAR and repeat-pass polarimetric InSAR at L-band acquired by DLR's E-SAR during the SHAC campaign 2000. The effect of gap structure and incidence angle on retrieval precision of tree height from interferometric SAR is analysed. Appropriate correction methods to improve tree height retrieval are proposed. The coherent microwave model CASM is used with a Lindenmayer system tree model to simulate the observed underestimation of stand height in the presence of gaps.

INTRODUCTION

Increasingly throughout Europe Forest Enterprises are using remote sensing to provide spatial information on the condition of forests that would not otherwise be available. In the UK, the Forestry Commission maintains a very comprehensive GIS database with data on tree species, planting year, soil type, and other ecological factors for all managed forest stands. However, because of the cost of forest mensuration, only stands mature enough for harvesting are being surveyed thoroughly. Young stands are inspected visually after 5 years to replant trees to fill gaps in areas of high tree mortality if required. The UK Forestry Commission manages large mainly coniferous plantations at Thetford, East Anglia. To improve timber production forecasts, monitoring the proportion of surviving trees following the planting is important. A sufficient stand density ensures timber quality and biomass allocation to the stem rather than to branches. The gap structure is very difficult to survey from the ground in dense forest stands, and interpretation of airphotos is labour intensive. Gap structure is also vital to rare ground-nesting bird species (night jar and wood lark) and plays a crucial role in conservation management. Besides gap fraction, mean top height of a stand is useful to improve the accuracy of long-term timber production forecasts. Top height together with basal area and a species-specific "form height" factor is used to estimate standing timber volume. Top height can be estimated from the GIS using a simple yield class model and data on stand age, species and yield class. The yield class estimates the expected incremental growth of a stand given the particular ecological conditions, mainly soil type, nutrient content, pH, slope and aspect.

SAR polarimetry and interferometry can potentially provide the required biophysical variables (Balzter 2001, Cloude and Papathanassiou 1998, Saich et al. 2001). We use airborne E-SAR data acquired during the SAR and Hyperspectral Airborne Campaign (SHAC) 2000, which was funded by the Natural Environment Research Council and the British National Space Centre, to evaluate the precision of tree height retrieval from X-band single-pass InSAR and L-band polarimetric repeat-pass interferometric data.

E-SAR POLARIMETRIC INTERFEROMETRY

During the SHAC 2000 campaign polarimetric and interferometric L-band imagery and interferometric X-band images were acquired by the German DLR aircraft. The E-SAR acquisition characteristics are given by Table 1.

Table 1: E-SAR acquisitions over Thetford forest during the SHAC campaign 2000.

Date	Band	Polarisation	InSAR Mode	Baseline
	X	VV	Single-pass	1.5 m
	L	quad-pol	Repeat-pass	~10 m

The X-band InSAR processing was carried out by DLR including the DEM product. The L-band data were delivered as coregistered single-look complex images with a motion compensation algorithm applied. Interferometric processing was done at CEH using the Gamma Interferometric SAR Processor. The SLC images were filtered in range and azimuth direction by common spectral band filtering. Then SLC1 was multiplied by the conjugate complex of SLC2, and normalised. The interferogram was multi-looked in range (2 looks) and azimuth (6 looks). Coherence estimation was carried out using an adaptive window size. The phase difference was flattened, filtered by an adaptive filter (6 pixel window) and unwrapped by a region growing algorithm. After a refined baseline estimation topographic height was derived using a least-squares method and 12 ground control points. The height images were transformed from slant to ground range and reprojected to the British National Grid. This processing chain was repeated for L-band HH, HV and VV polarisations.

TREE HEIGHT ESTIMATION

Tree height was estimated by subtracting a ground DEM from a surface DEM. As gound DEM an Ordnance Survey (OS) DEM derived from digitised contour lines (10 m pixel spacing) was used initially. An alternative, which may be more accurate, would be to interpolate a ground DEM from the imagery itself using unvegetated areas as control points. Surface DEMs were the X-VV, L-HH, L-HV and L-VV InSAR DEMs. Figure 1 shows a 3D representation of tree height estimated from the X-VV and OS DEMs. Boundaries between even-aged stands and a line of trees along a bridleway are clearly visible.

The precision of the estimated tree height was assessed using tree height values derived from stand age and yield class given by the Forestry Commission GIS database and published general yield class curves (Figure 2). The yield class is a rough indicator of expected incremental growth based on stand conditions, and its relation to maximum stand height h can be approximated by

$$h = \frac{1.1 \cdot a^4 - 199 \cdot a^3 + 9032 \cdot a^2 + (28032 \cdot yc - 41001) \cdot a}{10^{-6}}$$

where a is the stand age in years. Stand height estimated by the above equation is strongly correlated to stand height measured in the field using a SUUNTO clinometer with r^2=0.97.

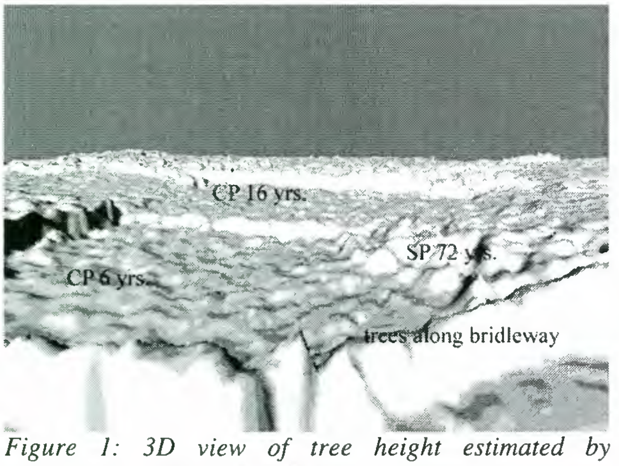

Figure 1: 3D view of tree height estimated by subtraction of X-VV InSAR DEM and OS DEM. CP = Corsican Pine, SP = Scots Pine. Stand age in years is indicated.

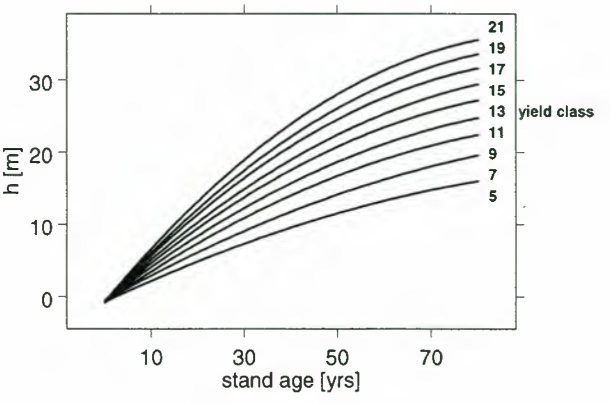

Figure 2: General yield class curves for Corsican Pine used by the Forestry Commission for production forecasts. h = maximum stand height.

Figure 3 shows the results of subtracting the OS ground DEM from the X-VV InSAR DEM compared to stand height estimates from the yield class model. The SAR method systematically underestimates height due to a partial penetration into the crown layer. For tall stands the underestimation increases nonlinearly, because of gaps in the stand increasing the soil contribution to the received signal. The InSAR height is a spatially averaged height, and not the maximum top height. Similar results were observed using the L-band DEMs and a LIDAR DEM.

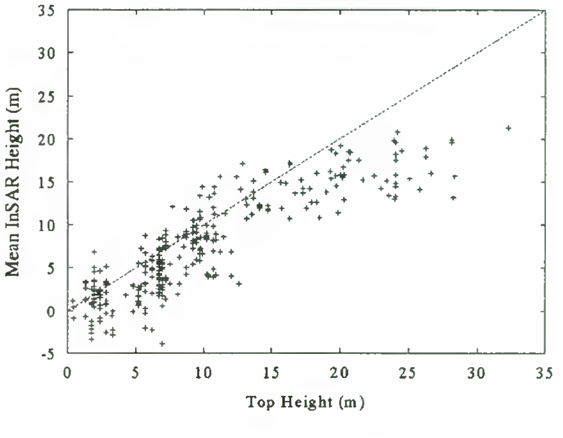

Figure 3: Mean stand height estimated from X-VV InSAR DEM and OS DEM compared to top height from the yield class model. For tall stands the InSAR DEM underestimates stand height.

Similar results are found at L-band, but with a much greater variation of InSAR height values and a greater number of points with high top height values that have been underestimated by the InSAR method. The scatterer geometry at L-band is very different from that at X-band. Different height variations within forest stands has been observed (Figure 4). This phenomenon remains to be explored in more detail.

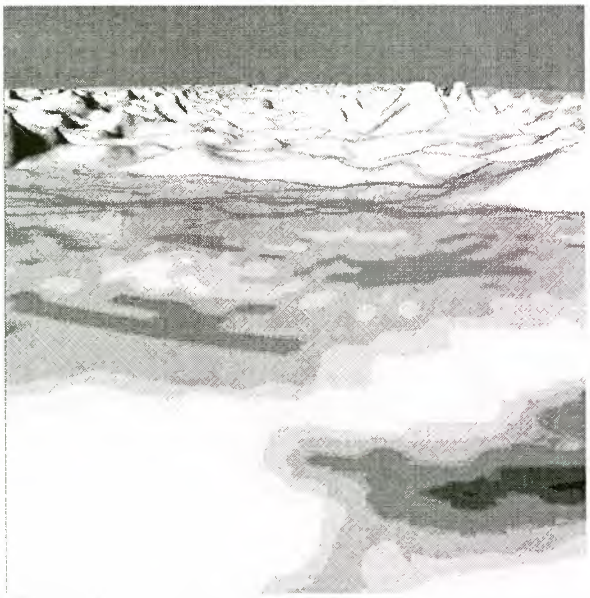

Figure 4: 3D view of L-HV InSAR DEM showing the6 year old CP stand from Figure 1 in the front and the 16 year old at the back. The height variation is much stronger than at X-band.

GAP EFFECTS

The observed underestimation of height by the InSAR DEMs can be explained by the decreasing fractional cover of older stands (Figure 5).

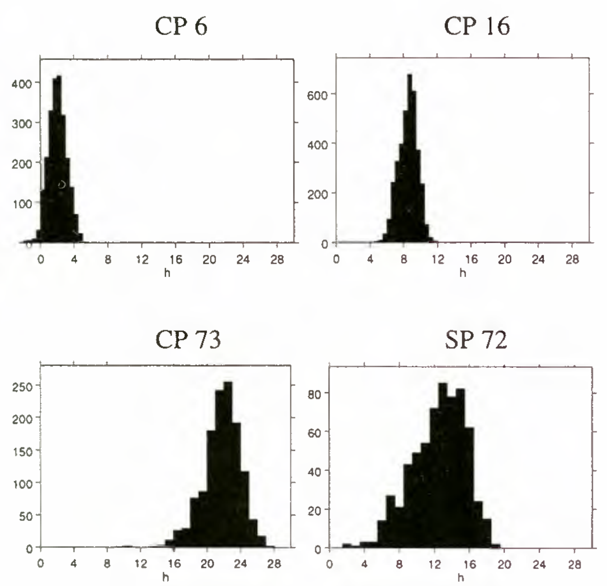

Figure 5: Histograms of tree height estimated by subtracting X-VV InSAR DEM and OS DEM for the stands shown in Figure 1 and an additional 73 year old CP stand. Gap fraction increases with stand age.

To improve the height estimation, a simple gap fraction model was developed using the ground data from the SHAC 2000 field campaign (Figure 6).

$$G = 1 - N \cdot A \cdot 10^{-4}$$

with G = gap fraction at nadir, N = number of trees [ha^{-1}], and A = mean area coverage of an individual tree crown [m^2].

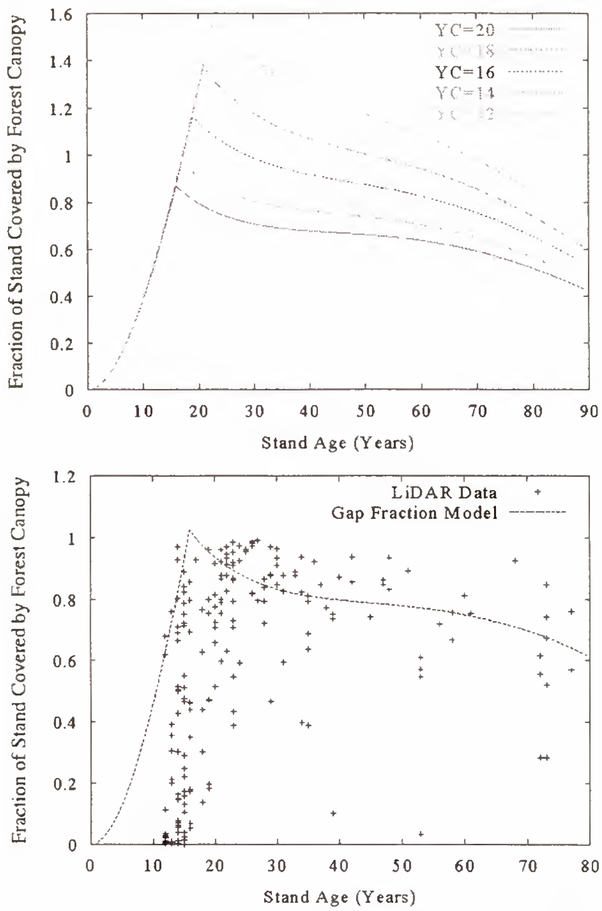

Figure 6: Gap fraction model for increasing stand age and different yield classes (top). Model fit compared to gap estimates from LIDAR image acquired by the Environment Agency (bottom). © Laine Skinner, Swansea.

For higher yield classes, the thinning regime is more rigorous, leading to a larger gap fraction despite thicker stems for old stands. The crowns do not seem to form a closed canopy anymore.

INCIDENCE ANGLE EFFECTS

Older stands with a larger gap fraction are more prone to incidence angle effects. In the near range a larger proportion of the radar signal penetrates the forest canopy through gaps right to the soil. This effect results in an increased underestimation of stand height in the near range for older stands (Figure 7). In the far range this effect is much weaker, as larger gaps are required for the radiation to pass through to the ground.

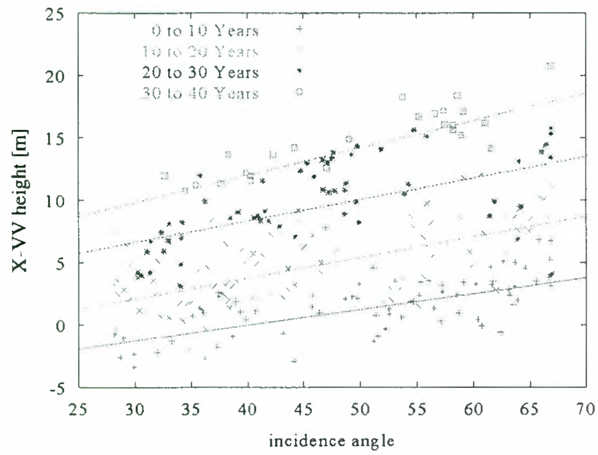

Figure 7: Dependence of estimated tree height on E-SAR incidence angle and stand age.

Using the mean slope from Figure 7 the following correction model was derived:

$$h_{i,corr} = h_i - 0.171 \cdot \theta_i$$

where $h_{i,corr}$ is the corrected mean stand height of stand i, h_i is the mean stand height of stand i before incidence angle correction, and θ_i is the incidence angle at the centre of stand i.

IMPROVEMENTS IN PRECISION

Mean stand height was calculated from the X-VV InSAR DEM applying the gap fraction and incidence angle corrections described in the previous sections. The results of the correction methods are shown in Figure 8. Both the gap model (Figure 8a) and the incidence angle correction (Figure 8b) reduce the bias of stand height estimation for older stands. A combination of both methods (Figure 8c) gives the best results.

Table 2: Root mean square error [m] and r^2 between top height estimated from X-VV InSAR DEM and OS DEM and from the yield class model. The gap fraction model was applied to all stands taller than 15 m.

Correction method	rmse	r^2
none	4.1	0.77
gap fraction	3.1	0.75
incidence angle	3.2	0.84
gap+angle	4.0	0.89
gap+angle+bias	2.9	0.89

Table 2 shows improvements in precision achieved by combinations of the correction methods. The rmse is improved by both correction methods, but a bias of 2.7 m is introduced. The rmse contains the bias as well as the random error σ_e,

$$rmse = \sqrt{bias^2 + \sigma_e^2}$$

so that removal of the bias reduces the rmse further (Table 2 last row).

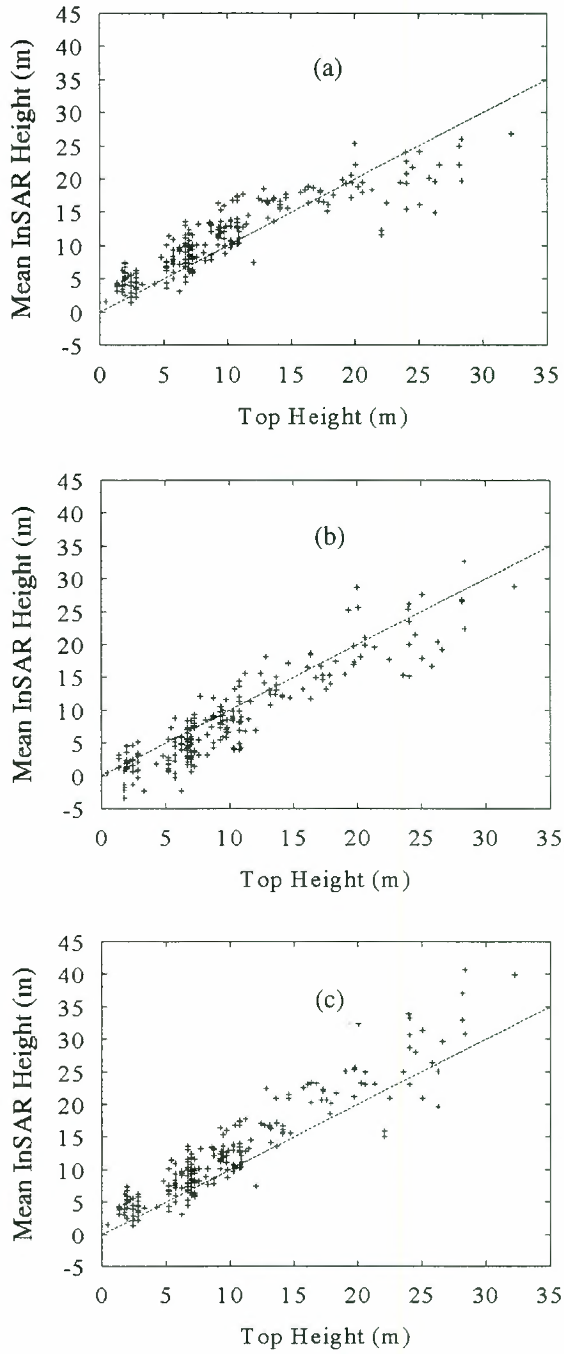

Figure 8: Mean stand height from X-VV InSAR DEM and OS DEM compared to top height from yield class model. Results of gap model (a), incidence angle correction (b) and both corrections (c).

COHERENT MODELLING

The microwave scattering model is described elsewhere (Saich et al. 2001). It is based on the coherent addition of single scattering from vegetation elements, along with double-bounce scattering between the vegetation and ground. The scattering amplitudes (weighted by a term incorporating the phase change due to the propagation path) for all the elements in a simulation cell are summed and the intensity is calculated.. Backscattering and interferometric signatures are obtained by averaging over a large number of independently generated simulation cells. As such, the model allows for prediction of both the backscattering coefficient and complex interferometric coherence.

Our model for the trees is based on a Lindenmayer system (Prusinkiewicz and Lindenmayer 1990) and is shown in Figure 9. We have not yet attempted to tune these L-system trees to match those at Thetford forest, and therefore our simulation results will be indicative of the effects we expect to see, rather than a quantitative match.

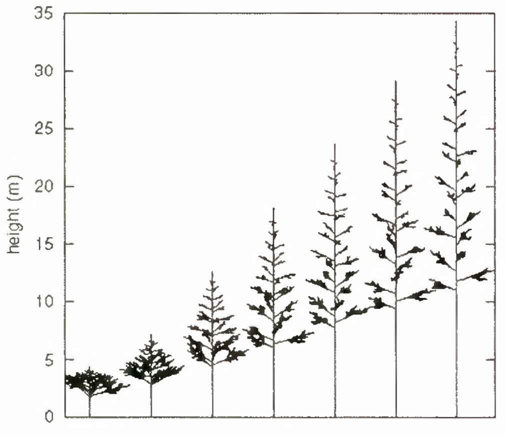

Figure 9: Simplified Lindenmayer system model of pine trees used by the coherent microwave model CASM.

Figure 10 shows the modelled effective height at X-VV for a range of tree densities. As expected the tree height is underestimated by the InSAR height for increasing tree height (see also observed response in Figure 3). This effect is stronger for stands with lower tree density, i.e. larger gap fraction because of the ground contribution to the phase signal.

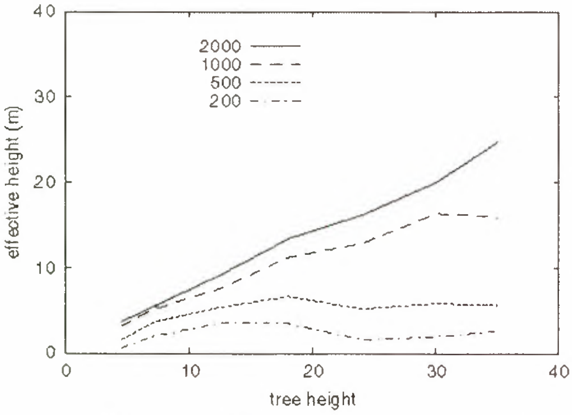

Figure 10: Effective interferometric height at X-band VV polarisation modelled by the coherent microwave model CASM for tree densities between 200 and 2000 ha^{-1}. 45 ° incidence angle.

Compared to the interferometric heights at L-band (Figure 11), the X-band height is more representative of the overall tree height. For L-HH, the retrieved InSAR height is usually very small as these signatures are dominated by ground scattering effects. Figure 11 also shows the effect of polarisation on the interferometric height. This information could potentially be useful to retrieve forest structural parameters other than top height.

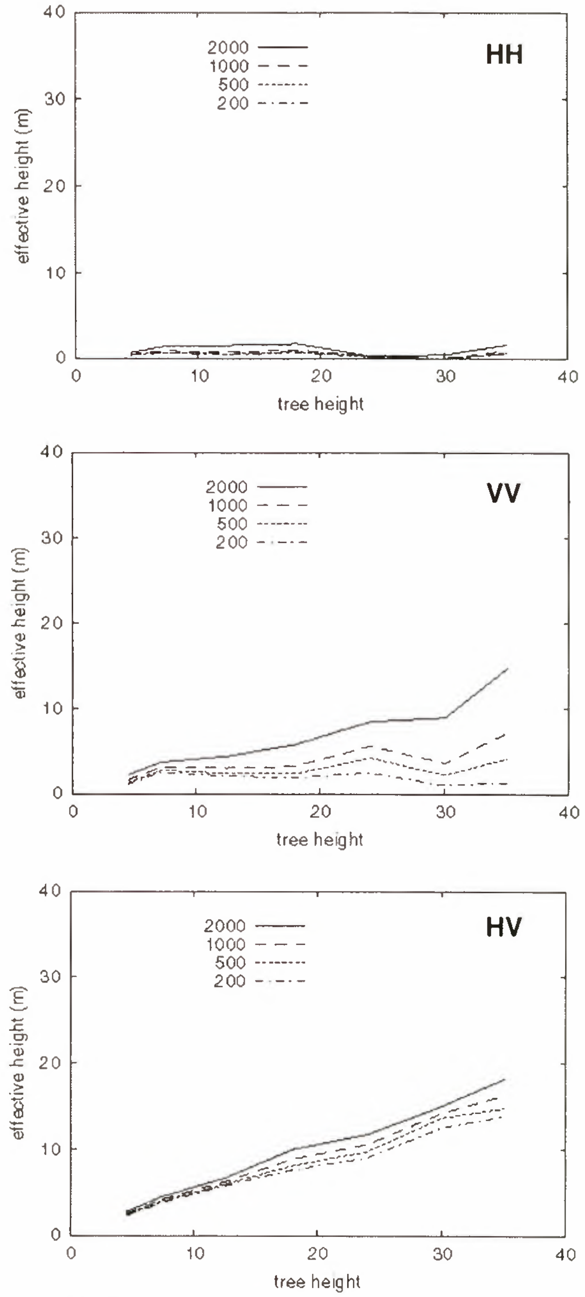

Figure 11: Effective interferometric height at all L-band polarisations modelled by the coherent microwave model CASM for tree densities from 200 to 2000 ha^{-1}. 45 ° incidence angle.

In Figure 12 we show the uncertainties in scattering height derived from the ensemble of simulations. These show that uncertainties can be quite large (even where the coherence is close to 1 as is the case for the L-HH simulations).

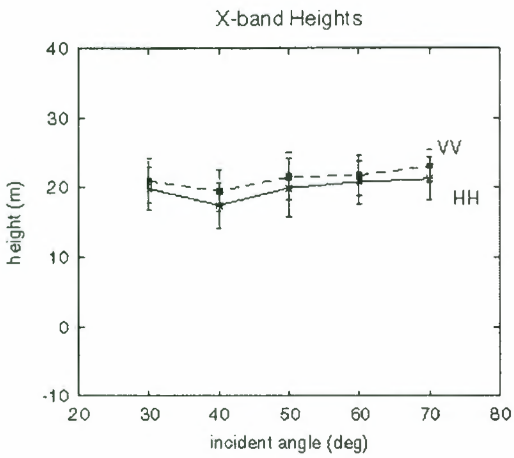

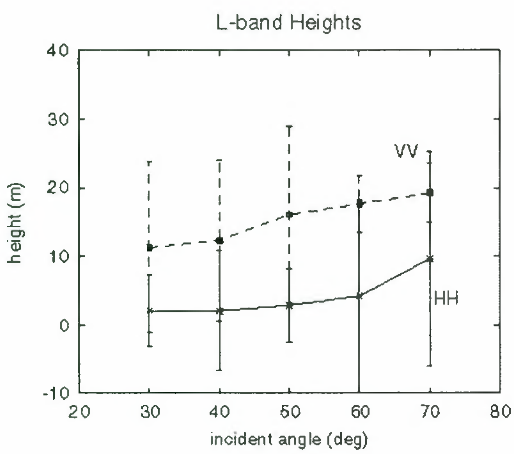

Figure 12: Mean and standard deviation of the effective interferometric height at X- and L-band modelled by CASM as a function of incidence angle. Assumed 100% ground cover.

FUTURE RESEARCH

The results of the microwave modelling suggest that effective interferometric height can be strongly affected by the tree density. This is likely to be the result of increased penetration into the forest canopy and through gaps to the forest floor. The effect is particularly marked at X-band.

We have demonstrated that simple gap and incidence angle corrections can improve tree height estimation, particularly for mature stands. This has great practical importance for forest managers who are mainly interested in retrieving tree height to determine the optimal time for harvest.

Better knowledge of gap fraction and the spatial distribution of gaps in a stand is required to be fed into a geometric model to jointly correct for ground contribution and incidence angle effect.

The coherent microwave model CASM has shown strong potential to underpin the observed radar reponse by theoretical model results. Particularly its ability to model the radar response to very complex vegetation structures (Figure 9) distinguish it from the past generation of models.

The challenge for the future will be to better model

- spatial distribution of trees,
- more 'natural' shape of Lindenmayer system trees,
- introduce natural variability into L-system stand models;
- and to understand and utilise the polarimetric interferometric response at L-band.

ACKNOWLEDGEMENTS

This work is funded by the UK Natural Environment Research Council (NERC) under the New Observing Techniques Programme, NER/Z/S/2000/01282, and CASE studentship grant held by Laine Skinner. Jennifer Grant (VUA) received funding from the British Council. © E-SAR data by British National Space Centre and NERC.

REFERENCES

Balzter, H. (2001). "Forest mapping and monitoring with interferometric Synthetic Aperture Radar (InSAR)." Progress in Physical Geography 25: 159-177.

Cloude, S. R. and K. P. Papathanassiou (1998). "Polarimetric SAR interferometry." IEEE Transactions on Geoscience and Remote Sensing 36: 1551-1565.

Prusinkiewicz, P. and A. Lindenmayer, A. (1990). The algorithmic beauty of plants, New York: Springer.

Saich, P., Balzter, H., Luckman, A. and L. Skinner (2001): Deriving forest characteristics using polarimetric InSAR measurements and models. Proceedings of the International Geoscience and Remote Sensing Symposium, IGARSS 2001, Sydney, 9-13 July 2001, CDROM.

MONITORING OF SOIL MOISTURE AND RAIN PRECIPITATION'S WITH IN-SITU MEASUREMENTS AND ERS C-BAND RADAR BACKSCATTERING DATA

Maurice Borgeaud [(1)], Nicolas Floury [(1)], Betlem Rosich Tell [(2)]

[(1)] European Space Agency, Electromagnetics Division
TOS-EEP, ESTEC, Postbus 299, 2200 AG Noordwijk, The Netherlands
Tel: +31-71-565-4830, Fax: +31-71-565-4999, maurice@xe.estec.esa.nl

[(2)] European Space Agency, Data handling Division
APP-AD, ESRIN, Via Galileo Galilei, CP 64, 00044 Frascati, Italy
Tel: +39-6-9418-0616, Fax: +39-6-9418-0280

ABSTRACT

In order to improve a better quantitative understanding of the effect of soil moisture of bare soils on C-band SAR data, five dedicated "weather" stations with soil moisture probes, rain gauges, and temperature thermometers have been installed through the Flevoland test site since April 2000. Soil moisture is collected every ten minutes at two different depths (5 and 10cm) while rain precipitation is gathered at the same sampling time interval by rain gauges. Since the spring of 2001, soil temperature measurements are also acquired at these two different depths. In addition to the in-situ data, spaceborne SAR data at C-band measured by ERS-2 are also collected (3 images every 70 days), taking advantage that the test site is close-by the locations of the ESA transponders used for calibration of the SAR data. Both in-situ data as well as the radar measurements are incorporated in a database and a detailed analysis can be performed. In this paper, the variations of the backscattering coefficient due to soil moisture changes are shown as well as the effect of rain on the soil moisture at different depths. In addition, the effect due to the variations of the soil temperature on the soil moisture is also illustrated.

INTRODUCTION

In the recent years, SAR data have become more and more available due to the increasing number of spaceborne SAR instruments flying, or which flew, around the Earth (e.g. ERS-1/2, JERS-1, RADARSAT-1) and soon ENVISAT and RADARSAT-2. In order to go beyond the simple step of image interpretation and to retrieve quantitatively geo- or bio-physical information, it is necessary to check the proposed models and inversion algorithms. Very often however, the lack of good-quality in-situ data makes the validation of these models difficult.

To help solving this problem, the agricultural Flevoland test site (35 km East of Amsterdam in the Netherlands) has been intensively monitored since early 2000 by collecting detailed in-situ data on the ground and archiving the SAR images acquired when ERS-2 was flying over the site.

IN-SITU DATA

One of the requirements for in-situ data is to have good-quality, reliable, and as often as possible measurements. In the case of soil moisture, it was decided to install five stations spread out through the 10x10 Km agricultural site. Each station, as shown on Fig. 1 is made out of a rain gauge, a data logger, and two "Theta" soil moisture probes. Measurements are automatically performed every 10 minutes and the content of the memory of the data logger is downloaded every month on a laptop. The rain gauge is based on the flipping bucket method (1 pulse per 0.2 mm of rain) and the body of the rain gauge has an aerodynamic design with a special profile to reduce drag and turbulence.

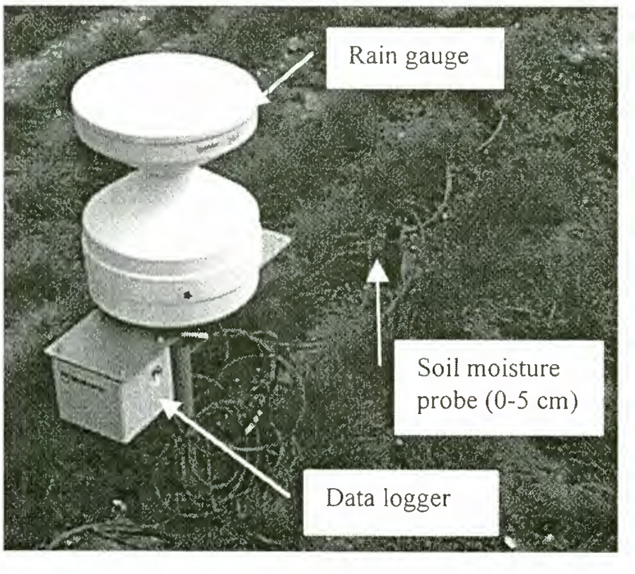

Fig. 1: Automatic collection of in-situ data: Rain gauge, soil moisture probe, and data logger

Proc. 3rd International Symposium, 'Retrieval of Bio- and Geophysical Parameters from SAR Data for Land Applications', Sheffield, UK, 11-14 September 2001 (ESA SP-475, January 2002)

Fig. 2: Installation of the "Theta" probe at a depth of 10 cm

The "Theta" probes measure the soil moisture by applying a 100 MHz signal via a specifically designed transmission line whose impedance is changed as the impedance of the soil varies. Two of these probes are connected to the data logger, one acquiring the soil moisture on a 0-5 cm depth while the other one is buried at a depth of 10 cm (Fig. 2). Since April 2001, soil temperature probes at a depth of 5 and 10cm have been also added to the stations.

The exact locations of the probes (green crosshair) are shown on Fig. 3 using an ERS-2 image background acquired on 23 June 2000. The corresponding fields, for which the backscattering coefficient values are extracted, are also displayed (red rectangles). The stations are kept at the same location during the whole year but for a few changes allowing farmers to work in their fields. Since the stations are located in agricultural areas, vegetation grows around them and Fig. 4 illustrates for instance the change of environment around the Koekoek station during the first part of 2000.

RADAR DATA

One of the reason to select the Flevoland area is due to the fact that the quality of the ERS-2 SAR data is regularly monitored by using three ESA transponders deployed close to the agricultural region of interest. During the calibration procedure, a small imagette of 25x25 km is extracted from the main image in PRI format.

The checkout occurs once per orbit on a descending path (acquisition at 12h34 local summer time) and once every other orbit on an ascending path (acquisition at 23h40 local summer time) which corresponds to approximately three imagettes every 70 days. Table 1 summarizes the acquisition performed in 2000.

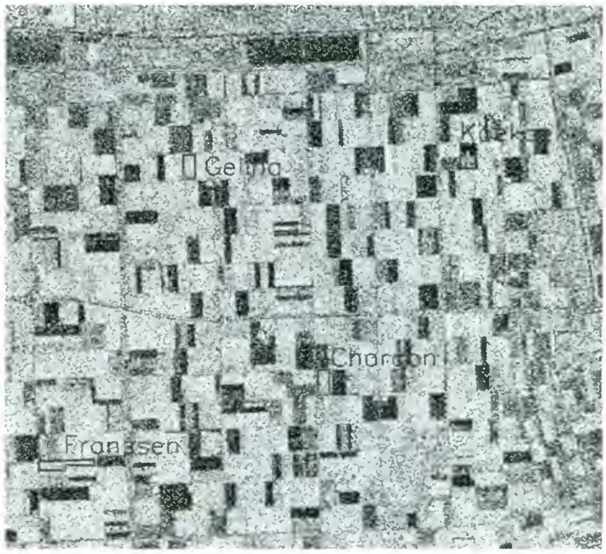

Fig. 3: ERS-2 image of 23 June 2000 with locations of the probes (green crosshair) and corresponding fields (red rectangles) for which the ERS-2 backscattering coefficient values are extracted.

Fig. 4: Change of vegetation around the Koekoek station. Top left: 5 April, top right: 27 June, bottom left: 28 July, bottom right: 30 August 2000

ANALYSIS OF IN-SITU DATA

In Fig. 5, the different measurements acquired from 5 April to 29 September 2000 over the area near Koekoek are shown. The horizontal axis indicates the dates of the measurements while the left vertical axis shows the volumetric soil moisture acquired and the right vertical axis provides information about the rain. The variations of the soil moisture at 0-5 cm and 10 cm depth are shown respectively in red and green. As expected, smoother variations of the soil moisture at 10 cm depth can be observed compared the very peaky signal of the soil moisture at 0-5 cm depth.

Date	Orbit	Acquisition times (local)
14 April 2000	Descending	12h34
10 May 2000	Ascending	23h40
19 May 2000	Descending	12h34
23 June 2000	Descending	12h34
19 July 2000	Ascending	23h40
28 July 2000	Descending	12h34
1 Sept. 2000	Descending	12h35
27 Sept. 2000	Ascending	23h41
6 Oct. 2000	Descending	12h34
10 Nov. 2000	Descending	11h34
6 Dec. 2000	Ascending	22h40
15 Dec. 2000	Descending	11h34

Table 1: ERS-2 acquisitions over the Flevoland test site in 2000

At the end of June, the station was moved to a different location on the same field but with less vegetation present, which explains the abrupt transition of the soil moisture at 10 cm depth. In addition, the amount of rain accumulated per period of 10 minutes (in mm) is shown in blue on Fig. 5. Since measurements are performed every 10 minutes, each curve is made out of more than 25000 points!

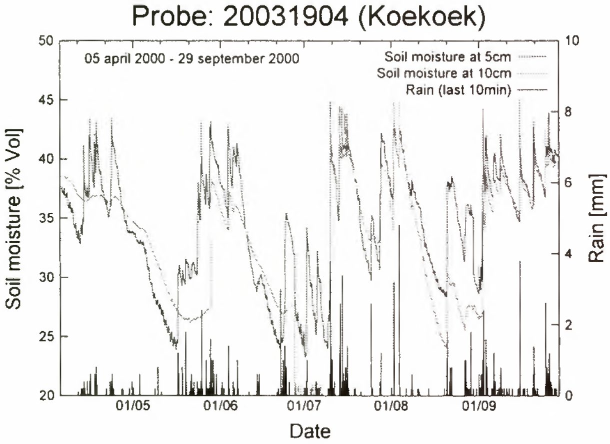

Fig. 5: In-situ data acquired over the Koekoek location from 5 April to 29 September 2000. Volumetric soil moisture is shown in red (0-5 cm depth) and green (10 cm depth) while the rain measurements are indicated in blue (amount of rain accumulated in 10 minute sample periods)

In order to investigate the daily variation of the soil moisture, Fig. 6a shows a detailed view of Fig. 5 during 15 days at the end of the May – early June 2000 period. It can be seen that the soil moisture variations at 0-5 cm depth are very sensitive to rain events. As soon as it rains, the soil moisture at 0-5 cm depth drastically increases. On the other hand, changes of the soil moisture at 10 cm depth are due mainly to large amount of accumulated rain. In Fig. 6b, the variations of the soil moisture are shown at the Chardon location during the first days of June 2000. Worth noticing are the oscillation forms (almost 2% vol. peak to peak) of the soil moisture curves during drying periods, with a minimum of the soil moisture taken place daily around 6-7h and a maximum occurring around 16-17h local time.

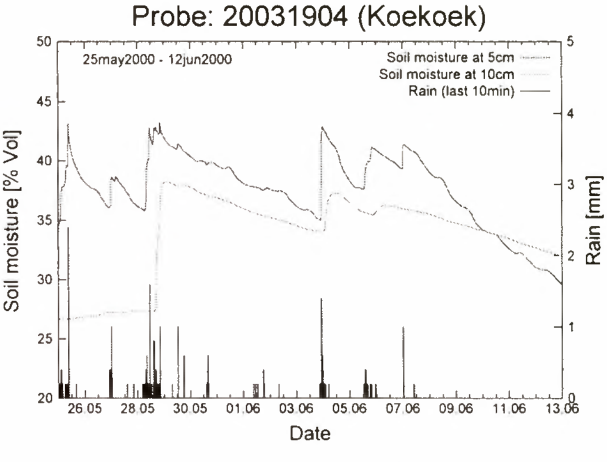

Fig. 6a: Variations of the soil moisture for the Koekoek location from 25 May to 12 June 2000

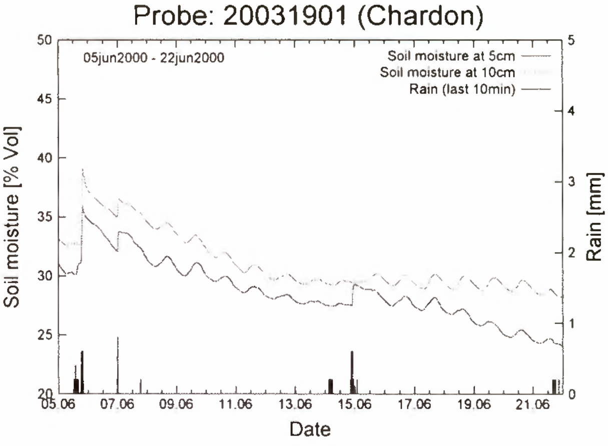

Fig. 6b: Variations of the soil moisture for the Chardon location from 5 June to 22 June 2000

These oscillations may be explained by the additional in-situ measurements acquired in the summer of 2001. Two temperature probes were installed at a depth of 5cm and 10 cm. The variations of the soil moisture at a depth of 5cm at three different locations in a same agricultural field (Geling location) are shown on Fig. 6c during the last 10 days of June 2001. It can be observed that the oscillations in the soil moisture measurements are related to the variations of the soil temperatures.

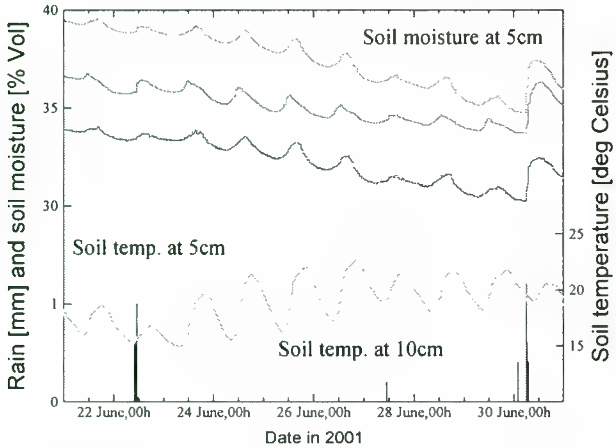

Fig. 6c: Rain, soil moisture at a depth of 5cm, and temperaturs at a depth of 5 and 10cm during the last 10 days of June 2001at the station Geling.

Just before and during the ERS-2 acquisition of 19 May 2000 at 12h34, localized rain events took place as indicated in Fig. 7a. It can be observed that rain was registered on three out of the four probes around 12h30 local time. At location Franssen, 1 mm of rain fell between 12h20 and 12h30 and 3 mm during the following 10 minutes. However, no rain fell at Koekoek (yellow) before the ERS-2 acquisition and very little rain was recorded at location Chardon (0.2 mm between 12h30 and 12h40). Fig 7b shows the ERS-2 image with the location of the fields using the same color code as in Fig. 7a. The areas with wetter soils are bright (locations Franssen in green, Geling in blue) whereas the darker values of backscattering coefficient values indicate soil with much smaller amount of soil moisture (at Chardon and Koekoek).

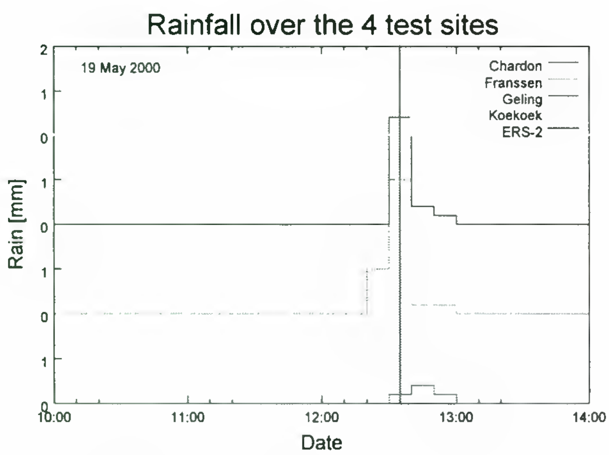

Fig 7a: Rainfall over the 4 stations on 19 May 2000 (Chardon in red, Franssen in green, Geling in blue, Koekoek in yellow). The vertical line indicates the time of the ERS-2 acquistion

Fig. 7b: ERS-2 image over Flevoland site acquired on 19 May 2000 at 12h34 local time with locations of the stations

ANALYIS OF ERS-2 SAR DATA VS IN-SITU DATA

The variations of the ERS-2 backscattering coefficient are shown on Fig. 8. The fields selected to extract the σ_0 values are illustrated in Fig. 3 corresponding to at least 500 pixels of ERS-2 PRI images per field.

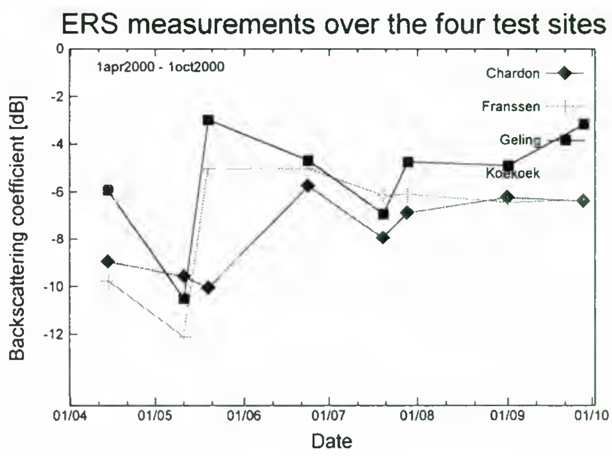

Fig. 8: ERS-2 σ_0 values as a function of time for the four stations spread out through the Flevoland test site

Grass is grown at the Koekoek location and was cut early July, which explains the jagged form of the backscattering coefficient. Sugar beets are grown on the three other sites and the σ_0 temporal curves are typical for that crop (decrease of the signal in April-May due to growing vegetation and then increase of the backscattering coefficient during the end of spring and early summer period).

Because of the effect of vegetation, it is difficult to relate the value of the backscattering coefficient to the soil moisture. However, due to the fact that the grass in location Koekoek was cut in early July, this field could be used to correlate the σ_0 values with the soil moisture measurements as shown in Fig. 9. Most of the points (in red) are closely located to the regression curve that can be computed as shown by the green line in Fig. 9. The two out-lying points correspond to values when the grass was very tall just before being cut. Therefore, one may assume that C-band electromagnetic waves are not penetrating this thick and wet vegetation layer since no correlation between soil moisture at 0-5 cm and σ_0 values are observed for these two points. Based on the regression line (R^2=0.8) between the backscattering coefficient [σ_0] and the soil moisture [sm] at 0-5 cm depth for the six valid points of Fig. 9, one may derive the following simple approximation to predict the soil moisture at 0-5 cm depth:

$$\boxed{sm \approx 1.66 \cdot \sigma_0 + 50} \quad [\sigma_0 \text{ in dB, sm in \% vol.}]$$

Note this formula applies only for the grass fields that were identified on the Flevoland site in 2000, as long as the vegetation layer is not too thick.

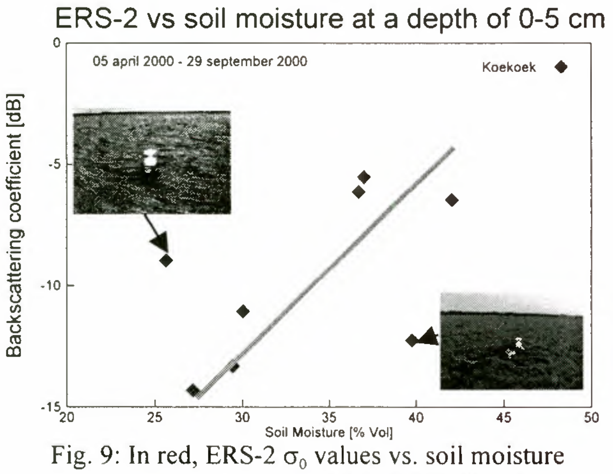

Fig. 9: In red, ERS-2 σ_0 values vs. soil moisture measurements at 0-5 cm depth for the Koekoek location. In green, regression line for the 6 valid points. The two imagettes showing thick grass layers explain the reason why the two corresponding points were not considered.

For the soil moisture at 10 cm depth, no clear correlation could be found between the backscattering coefficient and the soil moisture which confirms the fact that electromagnetic waves at C-band do not penetrate that deep in the soil.

CONCLUSIONS

In order to improve a better quantitative understanding of the effect of soil moisture of bare soils on SAR data, five dedicated "weather" stations with soil moisture probes and rain gauges have been installed through the Flevoland test site since early 2000. Because of calibration requirements, this site is also regularly imaged by ERS-2, and soon ENVISAT Using the detailed soil moisture and rainfall measurements, it has been shown that the top soil moisture (0-5 cm depth) is highly sensitive to rain while, at a 10 cm depth, the moisture is more dependant on the accumulated amount of rain fall. Diurnal variations of the soil moisture have been observed during drying periods and soil temperature measurements allow a precise monitoring of this effect as well as explaining the possible cause related to a significant soil vapour flow. Furthermore, a good correlation has been observed between backscattering coefficient values and soil moistures at 0-5 cm depth for fields covered by grass, as long as the vegetation layer is not too thick. Based on the very good quality of the data acquired so far, it is planned to keep collecting these detailed local measurements after the launch of ENVISAT. Owing to the fact that the site will be imaged very regularly by this new satellite for calibration purposes and the new multi-polarisation capabilities of ASAR (HH , HV, VV combinations of polarisation's, though not simultaneous), a very useful database of in-situ data and spaceborne SAR data will be generated..

ACKNOWLEGMENTS

The authors would like to acknowledge the help of Martin Vissers, who installed and downloaded the in-situ measurements from the data logger.

THE GLEN AFFRIC PROJECT : FOREST MAPPING USING DUAL BASELINE POLARIMETRIC RADAR INTERFEROMETRY

S. R. Cloude[(1)], I.H. Woodhouse[(2)], J. Hope[(3)], J.C. Suarez Minguez[(3)], P. Osborne[(4)], G.[1] Wright[(5)]
[(1)]AEL Consultants, Cupar, Fife, KY15 5AA, Scotland, e-mail : scloude@aelc.demon.co.uk
[(2)]The University of Edinburgh, Dept. of Geography, Drummond St., Edinburgh, EH8 9XP, Scotland
[(3)]Forest Research, Midlothian, EH25 9SY, Scotland
[(4)]The University of Stirling, Dept. of Environmental Sciences, Stirling, FK9 41A, Scotland
[(5)]Macaulay Land use Research Institute, Craigiebuckler, Aberdeen, AB15 8QH, Scotland

Abstract— In this paper we introduce the Glen Affric radar project, a multi-disciplinary program addressing the potential of polarimetric radar interferometry to provide quantitative vegetation structural information of importance in forest mapping and ecology studies. We present for the first time a comparison of results from L-band repeat pass SAR imagery with detailed in-situ measurements of forest height for the test site.

I. INTRODUCTION

The conservation and management of remaining natural and semi-natural habitats of the countryside is now of greater importance than ever before, due to continuing pollution, physical destruction and fragmentation, which may lead to increasing rates of species extinction, loss of diversity and general deterioration in habitat quality [1]. A fundamental requirement for management is widespread and frequent monitoring, which can only be done effectively using some form of remote sensing.

The key approach taken in this project is to investigate the use of fully coherent polarimetric SAR data in this important role. SAR is sensitive to structural parameters of vegetation and, in particular, L-band polarimetric SAR is especially suited to vegetation mapping because it is sufficiently sensitive to both canopy and sub-canopy parameters. By utilising the capability of repeat pass interferometry we have the potential to produce a true ground DEM of the test site (without vegetation bias), estimate forest height and canopy extinction [2,3]. The use of repeat pass fully polarimetric interferometry is fundamental for the following reasons:

- The influence of surface topography can be accounted for in the polarimetric analysis without the requirement for external reference DEMs
- Tree canopy height and density can be directly inferred from the data
- The Polarimetric response from the canopy can then be considered separately of the signal from the forest floor, leading to improved estimates of surface conditions such as roughness and moisture content.

These results are expected to allow both general species discrimination and determination of structural biophysical parameters, giving a more complete description of the vegetation than is possible using current remote sensing approaches.

II. THE GLEN AFFRIC TEST SITE

In Scotland, the natural regeneration of the Caledonian forest (consisting principally of Scots pine, *Pinus sylvestris*) over wide areas is seen as a major objective for Scottish conservation managers. Native pinewoods are specified in the EU Directive on the Conservation of Natural and Semi-natural Habitats and of Wild Fauna and Flora (92/43/EEC) (generally referred to as the "EU Habitats Directive") and are a key habitat specified in the UK Biodiversity Action Plan [4]. Effective monitoring is required if the impact of specific active strategies, as well as other environmental change factors, is to be measured and understood. Furthermore, European legislation now requires national conservation agencies, such as Scottish Natural Heritage, to monitor change and report on the status of nationally and internationally important conservation areas.

The routine application of optical remote sensing to conservation management of semi-natural vegetation areas in the UK has been limited due in part to the inability of available data to provide meaningful quantitative information needed for ecological interpretation as a result of coarse spectral and spatial resolutions. The problem of spectral inseparability may be addressed by analysing data of high spectral resolution and such data are becoming recognised as a tool in ecological investigations [5,6]. However, work is required to determine the appropriate scale of observation for particular ecological applications so that new technologies can be successfully applied to ecological studies.

Proc. 3rd International Symposium, 'Retrieval of Bio- and Geophysical Parameters from SAR Data for Land Applications', Sheffield, UK, 11-14 September 2001 (ESA SP-475, January 2002)

In order to address these issues, a BNSC-NERC sponsored radar measurement campaign was held in the UK in May/June 2000. Glen Affric was one of the selected sites and 6 radar passes were gathered with offset baselines of 10 and 20m enabling single and dual baseline interferometric analyses. In this paper we summarise the objectives and show results from the data analysis and comparison with ground truth.

Test Site Location and Topography

The test area is located in the North West Highlands of Scotland as shown in figure 1. The area is mountainous and combines several important challenges for radar remote sensing, including heterogeneous forest cover, sloped terrain and a broad distribution of tree heights.

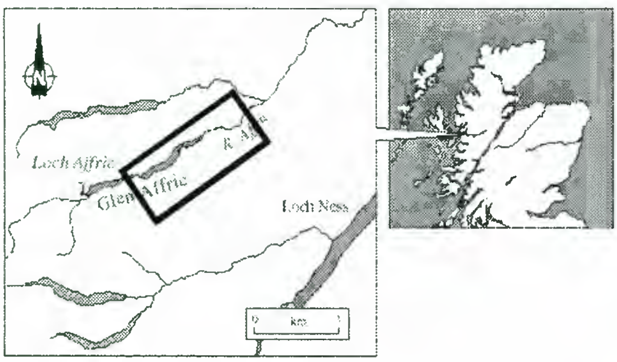

Figure 1 : Location of Glen Affric Test Site

Despite its relative isolation, the site has been extensively studied using conventional aerial photography combined with comprehensive ground surveys and hence provides a good site for quantitative validation studies [8,9,10].

To illustrate the nature of the terrain slopes in the region we show in figure 2 a radar-derived unwrapped phase image of a portion of the south side of the loch. This phase image was obtained from the 10m baseline data using the coherence maximiser [2] to reduce as far as possible the phase noise. The main forested test regions lie along the loch side and we can clearly see the varied topography of the site.

Figure 3 shows a photograph of our forest test stand in the scene. We note the mixed species and heterogeneity of the tree cover. Tree heights vary from a few meters up to 30m or more for the large Scots Pines.

III. FOREST SCATTERING MODEL

To interpret the coherence information for the test site we need to employ a multi-layer coherent model of forest scattering.

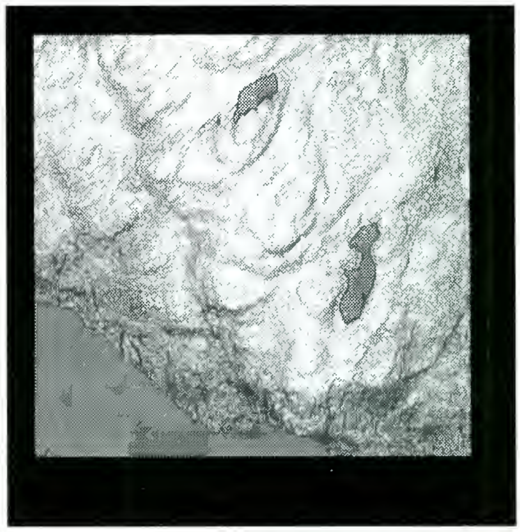

Figure 2 : Relative Height Map Obtained From 10m Baseline Repeat Pass Radar Interferometry

Figure 3 : Forest Test Stand in Glen Affric

According to the 2-layer model derived in [2,3,11], the complex interferometric coherence for a random volume over a ground can be written as a function of polarisation scattering mechanism $\underline{w}$ as

$$\tilde{\gamma}(\underline{w}) = e^{i\varphi} \frac{I_2 + m(\underline{w})}{I_1 + m(\underline{w})} \qquad -1)$$

where only m is a function of polarisation and I_1 and I_2 are volume integrals as shown in equation 2.

$$\begin{aligned} I_1 &= \frac{1}{p_1}(e^{p_1 h_v} - 1) \\ I_2 &= \frac{1}{p_2}(e^{p_2 h_v} - 1) \end{aligned} \qquad -2)$$

The complex propagation constants p_1 and p_2 are defined as

$$p_1 = \frac{2\sigma}{\cos\theta_o}$$
$$p_2 = \frac{2\sigma}{\cos\theta_o} + i\frac{4\pi B_n}{\lambda R \sin\theta_o} \qquad -3)$$

where B_n is the normal component of the baseline of the interferometer. We see that we have 4 unknown parameters, namely

m – the ground to volume scattering amplitude
σ – the mean volume extinction
h_v – the height of the forest
ϕ - the ground topographic phase

However we have only two measurements (the amplitude and phase of the coherence). Hence a single channel interferometer is not able to provide unambiguous structural information. We see that by adding a second polarimetric channel we will add two new measurements while adding only one new unknown (m) and hence obtain a deficit through 4 measurements to 5 unknowns. Similarly, by adding a third channel we obtain 6 measurements for 6 unknowns. Hence by employing full polarimetric interferometry we can invert equation 1 to obtain quantitative parameter estimates.

The inversion is implemented in 3 stages:

Stage 1 : Least Squares Line Fit

The first stage is to find the best-fit straight line inside the unit circle of interferometric coherence. To do this we vary two phase variable ϕ_1 and ϕ_2 as shown in figure 4. Each pair defines a line and we choose the pair that minimises the MSE between the line and set of coherence points. We use 9 points for each line fit, obtained from interferograms in the following polarisation channels

opt1,opt2,opt3,HH-VV,HH+VV,HH,VV,HV,LL

where 'opt' are the optimum coherence states obtained using the algorithm in [2]. The state LL is left circular polarisation at either end of the baseline.

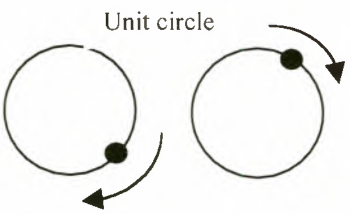

Figure 4 : Phase based least square line fit

Stage 2 : Vegetation Bias Removal

In the second stage we must choose one of the pair ϕ_1,ϕ_2 as the underlying ground topographic phase. This we do by selecting the point with the highest count of polarisation channels lying between the candidate ground point and the HV phase. This provides a quick method for selecting the ground point ϕ.

Stage 3 : Height and Extinction estimation

To estimate the two remaining parameters we use the line and estimate of ϕ together with equation 2 to find the intersection point between the line and the curve corresponding to equation 2.

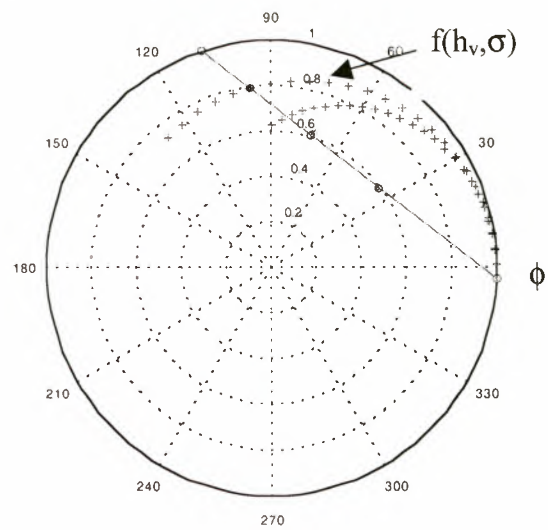

Figure 5 : Height and Extinction estimates, non-physical solution (lower curve), correct solution (upper curve)

Figure 5 shows two such intersections, one of which crosses the line to bisect coherence values. This cannot be a physical solution, as it generates negative ground contributions. We take as the true solution the parameters which cause the curve to intersect the line at the coherence value furthest from ϕ (upper curve in figure 5). This ensures non-negative ground scattering components and makes the weak assumption that in at least one of the 9 polarisation channels we observe a very small ground-to-volume scattering ratio. This can be reasonably assumed in the HV channel as well as in at least one of the optimum coherence channels.

Note that the model assumes a uniform density of scatterers from ground to crown. However, on inspection of figure 3, we can see that this is not typical of the Scots pine tree structure. Previous validations of this algorithm have been carried out, but only on dense pine trees with more uniform vertical density profiles [11] Hence this site represents an interesting new test for the technique. Analysis of the model indicates that the effect of such high canopies will be to overestimate the extinction and the tree height. Dual baseline techniques are expected to resolve this canopy structure problem but here we are interested in the errors caused in single baseline inversions by such structural features.

In anticipation of this problem, we have modified the model of equation 1 as follows

- We assume that σ is known from a prior modelling or other means. Here we set it to a value of 0.1 dB/m for L-band, although for shallow canopies the value chosen does not strongly influence the results.
- We introduce a new free parameter into the integral I_2, namely the phase elevation of the canopy as shown in equation 4.

$$I_2 = \frac{1}{p_2}(e^{p_2 h_v} - 1)e^{i\phi_{can}} \qquad -4)$$

We can now estimate the canopy depth, ground topography and tree height using the inversion scheme.

IV. RADAR DATA ANALYSIS

To demonstrate the basic quality of the radar data, we show in figure 6 composite images of the three optimum channels (opt1,opt2 and opt3) for the 10m (lower) and 20m (upper) baselines.

The forested regions are clearly shown as dark areas with low coherence. Note how the longer baseline is more sensitive to the smaller vegetation cover. Here we concentrate only on the shorter 10m baseline.

This coherence data was combined with the other 6 channels and used as input into our model based parameter estimation technique to estimate the local forest height. Figure 7 shows a map of vegetation height obtained from this algorithm.

V : TREE HEIGHT VALIDATION STUDIES

The next stage of our studies was to validate the heights obtained in the map shown in figure 7. To do this concentrated effort on a mixed stand close to the southern shore of the Loch.

Ground Truth Measurements

Since the test site was heterogeneous and rather sparse, with ground variations of 20m, simple stand averaging of tree heights was inappropriate. Detailed survey transects were therefore taken over two test sites, taking measurements of x, y and z of the tree base (and occasional spot heights), species, diameter at breast height (dbh) and tree height.

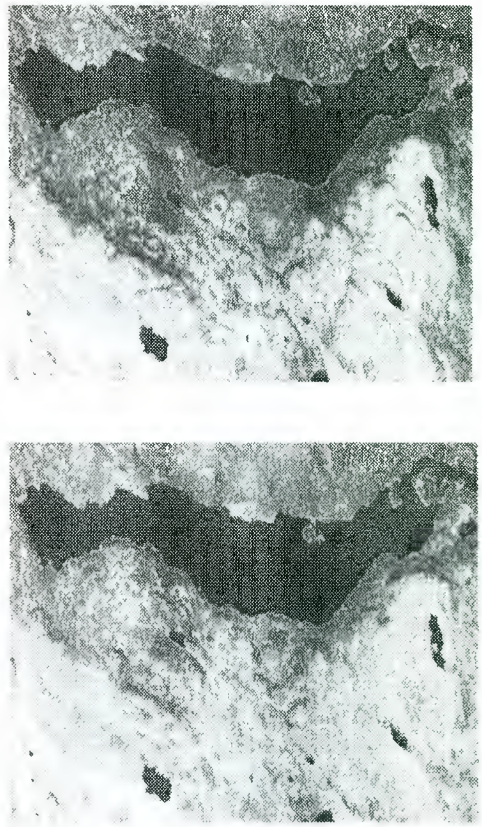

Figure 6: RGB Optimum Interferometric Coherence Images for 10m (lower) and 20m (upper) baselines

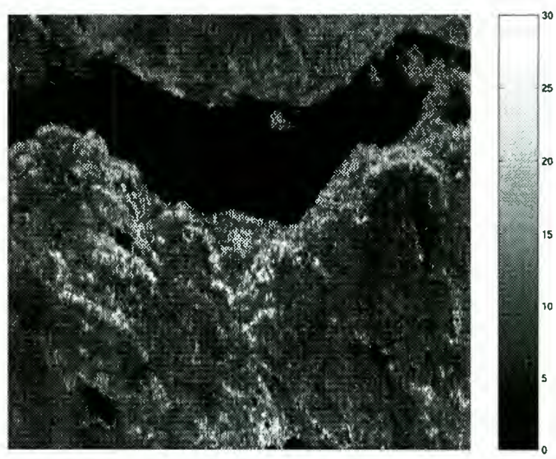

Figure 7 : Vegetation Height Map Obtained from 10m Baseline Data

When possible the height of start of crown and crown width were also measured. The height to crown was measured to the lowest live first-order branch. All measurements were related to a single "reference point" that was located using a GPS. Two main transects were made – one in approximately the SAR range direction, the other perpendicular to this.

The relative accuracy of the tree measurements are less than 1m (x, y, z) for the ground locations and approximately +/- 2m for height for the largest trees. As can be seen from figure 3, a major source of error is simply deciding what constitutes the top of the tree. In addition, the fact that not all the larger trees were vertical meant that the x,y locational uncertainty for the crown is also a further +/- 2m.

The absolute location errors are dependent upon (a) the 3-D accuracy of the GPS location of the reference point, and (b) the orientation of the "reference direction". The second of these is the most problematic, as with no visible landmarks a simple compass bearing was used as an indication of orientation. To compensate for this, 3-D measurements were also made along the centre of an access track to allow final adjustments to the absolute locations. The tree locations and spot heights (points) are shown in figure 8, as well as the expected crown locations.

The E-SAR flight geometry was used to determine the range and azimuth locations of the tree bases and spot heights, as well as the tree crowns. Two corner reflectors located at either end of the complete data take were used to help correlate the image co-ordinates to map co-ordinates. All calculations were carried out in the UK Ordnance Survey projection with altitudes above mean sea level. We estimate final locational uncertainties (for ground points) between field data and SAR data to be in the region of +/- 3m in azimuth and +/- 5m in range (approx. 4 pixels). Crown locations are more uncertain and are considered below.

Representation of Ground Data

The detailed test site consisted primarily of Scots Pine, with a few birch (<5% of total number and all less than 10m tall). For visualising the data, pines with a dbh less that 30cm are given as conical crowns, otherwise they are represented by a hemi-spheroidal shape model using information on crown height and width. It should be noted that this crown shape represents the outermost elements of the branch structure, rather than an actual well-defined crown (which as can be seen from Figure 3 is never well defined for the taller pines).

For about 20% of the trees the crown width or height were not measurable but for visual purposes the following relationships are used: crown width = one third of the tree height, and height to crown = one half of the tree height.

Comparison Between Retrieved and Measured Tree Heights

Figure 9 shows the range and azimuth transects respectively and clearly demonstrate that the retrieved height pattern is well correlated with the measured trees.

Underlying topography is not shown in these images. Trees that lie within 5m off the transect line are included in the comparison and are located in the figure by their true horizontal distance along the transect. The starred points and connecting line represent the retrieved height value for the crown **slant range** location in the retrieved data (i.e. spot heights will be unchanged, but trees of a given height are compared against the retrieved values corresponding to their slant range ("lay-over") location). In order to help account for locational errors, the retrieved height shown is actually a 3x3 pixel average centred on the slant range location.

This way of comparing the data is required to account for the expected response from individual trees. In such cases the retrieved height will be located not at the base of the tree, but rather at the slant range location of the crown. This approach to the retrieval procedure introduces another locational uncertainty since the height of the scattering centre (and hence slant range) will not be the same as the measured tree height. Such uncertainties may help explain the results of the range transect in Figure 9 whereby some of the taller trees do not always seem to be well correlated in range location to the higher retrieved values. Despite this, the correlation between measured and retrieved heights in the range transect give a linear Pearson's correlation co-oefficient R=0.88. For the azimuth transect the results also appear well correlated with R=0.90.

Discussion of Results

Despite the reasonable correlation, there are three noticeable discrepancies between the radar results and ground truth. The first is that the retrieval process generally appears to underestimate the tree heights. This is fully expected, as the L band response is sensitive to combined ground and canopy features in all polarisation channels.

The second is that where the field measurements imply no trees, the retrieval can indicate positive tree heights of about 5m and up to as much as 10m. This is caused by SNR coherence problems in non-vegetated areas yielding spurious phase shifts in the data. Masking based on the HH/VV polarimetric coherence should help identify such areas.

A third problem is that in some instances the retrieval *significantly* underestimates the tree height. For example, in the range transect, at around 20m, there is a sharp change between small pines and taller ones behind. The retrieval process does not identify the taller trees until nearer 25m. It is quite possible that what is happening here is that the slant range distances for the shorter canopy at 15m coincide with the slant range to the taller crowns at 20-25m. With canopy scattering from two distinct locations and no clear ground response, it is possible that in this case the current method fails to determine a realistic tree height. It is problems of this nature will be the focus of future studies, which include a forthcoming NERC funded research project.

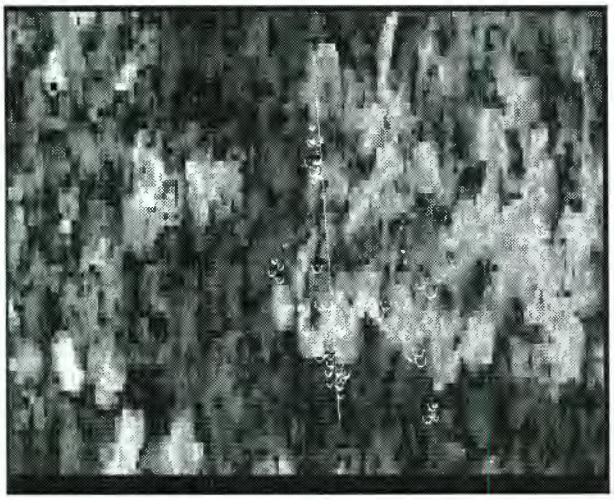

Figure 8: Location of Ground Truth Measurement Points superimposed on Radar Derived Tree Height Map

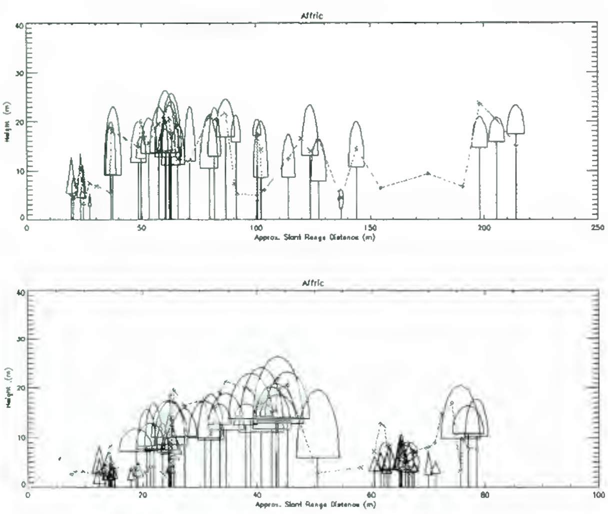

Figure 9 : Tree height Estimates vs. ground truth for the two transects: azimuth (upper) and range (lower)

V1. CONCLUSIONS

In this paper we have introduced the Glen Affric radar project and described the test site and its importance as a validation site for an assessment of polarimetric radar interferometry. We have shown, through ground truth validation that the radar data is capable of providing important quantitative structural forest information. Future studies will concentrate on further comparisons of the radar observations with ground truth, especially for underlying ground topography and canopy structure.

VII ACKNOWLEDGMENTS

The data provided for the Glen Affric project was collected under the UK NERC/BNSC sponsored SHAC campaign.

REFERENCES

[1] Tipping, R., et al. (1999). Woodland biodiversity, palaeo-human ecology and some implications for conservation management. *Journal of Biogeography* 26, 33-43.

[2] Cloude, S.R., Papathanassiou, K.P. (1998). Polarimetric SAR Interferometry. *IEEE Trans. Geosci. & R S.*, 36:1551-1565.

[3] Papathanassiou K P, S R Cloude, A Reigber, "Single and Multi-Baseline Polarimetric SAR Interferometry over Forested Terrain", Proceedings of 3rd European SAR Conference EUSAR 2000, Munich, Germany, May 2000, pp 123-126

[4] Anon. (1994). Biodiversity: the UK Action Plan. HMSO:London.

[5] Ustin, S. L., Wessman, C. A., Curtiss, B., Kasischke, E., Way, J., Vanderbilt, V. C. (1991). Opportunities for using the EOS imaging spectrometers and synthetic aperture radar in ecological models. *Ecology*, 72:1934-1945.

[6] Shaw, D.T., Malthus, T.J., Kupiec, J.A. (1998). High spectral resolution data for monitoring Scots pine (*Pinus sylvestris* L.) regeneration. *Int. Jour. R. S.*, 19:2601-2608.

[7] Treuhaft R N, P. Siqueria, 2000 "Vertical Structure of Vegetated Land Surfaces from Interferometric and Polarimetric Radar", Radio Science, Vol. 35(1), pp 141-177, January

[8] Gauld, J.H. et al, (1991). The measurement and analysis of land cover changes in the Cairngorms. MLURI Technical Report for the Scottish Office Environment Department and the Scottish Office Agriculture and Fisheries Department.

[9] Pyatt, D.G. (1995). *An Ecological Site Classification for Forestry in Great Britain*. Edinburgh: Forestry Commission Research Information No. 260.

[10] Pyatt, G.G. (1997). A site classification for Scottish native woodlands. *Botanical Journal of Scotland* 49, 455-467.

[11] Papathanassiou K P, Cloude S R "Single Baseline Polarimetric SAR Interferometry", *IEEE Trans. Geosci. & R S.*, IGARSS 2000 Special Issue, to be published, 2001.

EXTRACTION OF SURFACE PARAMETERS FROM SAR DATA USING POLARIMETRIC DESCRIPTORS

L. Ferro-Famil, S. Allain, E. Pottier

A. R. T. Laboratory , The University of Rennes
FRE CNRS 2272, Radar Polarimetry Division
Campus de Beaulieu - Bat 11.D, 263 Avenue General Leclerc
CS 74205, 35042 Rennes Cedex, France
Ph/Fax : (+33) 2 99 28 67 14 / (+33) 2 99 28 69 63
E-mail : laurent.ferro-famil@univ-rennes1.fr

Abstract - In this paper is introduced a method to extract surface geophysical parameters from polarimetric SAR data descriptors. A natural soil is modeled under the form of a two-scale process : a large-scale stochastic surface depicts terrain topography which modulates the local orientation of the SAR resolution cells. The SPM model is used to determine the average polarimetric properties of the complete scene. It is shown that the discrimination of different soil dielectric properties values from a representation onto planes defined by pertinent polarimetric indicators necessitates to know a priori the small-scale roughness conditions. A solution to this problem is proposed by means of a representation into a three-dimensional space defined by the H-A-$\underline{\alpha}$ parameters. A soil parameter inversion method based on Artificial Neural Networks is introduced and is applied to the case of soil moisture retrieval

I. INTRODUCTION

Many studies have shown the usefulness of SAR data analysis for surface parameters extraction. Soil physical parameters such as roughness or volumetric moisture content may be inverted by observing the backscattered signal amplitude variations with respect to the incidence angle, frequency or polarization. Some empirical models were developed to directly invert these physical quantities using non-linear functions of the scattering coefficients.

More recently, natural surface characterization studies have been led using relevant parameters provided by incoherent polarimetric decomposition theorems [1-3]. Three polarimetric indicators, H, A and $\underline{\alpha}$ [4][5]were shown to be highly related to the soil dielectric constant and RMS height. The retrieval of a soil dielectric constant was based on the use of scattering coefficients derived from the Small Perturbation Model (SPM). A perturbation technique was applied, by the way of azimuthal rotations, on coherency matrices modeled for a range of dielectric constants. The entropy, H, and $\underline{\alpha}$ parameters resulting from the polarimetric decomposition of the perturbed coherency matrices were plotted in the (H-$\underline{\alpha}$) plane and were shown to describe distinct curves for different dielectric constants. The inversion algorithm consisted then in a look-up table procedure.

Full polarimetric measurements of rough surfaces showed that the RMS height was almost linearly related to the anisotropy, A, independently of the dielectric constant value.

This paper aims to define in an accurate way the dependence between rough surface geophysical properties and some polarimetric indicators using a surface simulated as a stochastic process.

In order to model in a realistic way the response of a soil observed by a SAR sensor, the soil surface is considered to be a two-scale process, the order of magnitude of the small and large scales being fixed by the SAR spatial resolution.

The surface is mathematically defined by its correlation function and correlation length, its height probability density function and standard deviation. The pixels constituting this large-scale surface are considered to represent SAR resolution cells with given range and azimuth dimensions.

Each cell is associated to a coherency matrix calculated from the SPM model using the local information given by the large-scale surface.

Similarly to what is done during SAR data analysis, the global polarimetric response of the scene is obtained by an incoherent averaging of the different pixel responses modulated by the large-scale characteristics.

The result of this process consists in a distributed matrix which is analyzed with a polarimetric decomposition theorem delivering three main parameters, the entropy H, the anisotropy A and $\underline{\alpha}$, the indicator of the nature of the scattering mechanism.

It is then shown that two-dimensional plots of the simulated results in the (H- $\underline{\alpha}$), (H-A) and (A- $\underline{\alpha}$) planes

Proc. 3rd International Symposium, 'Retrieval of Bio- and Geophysical Parameters from SAR Data for Land Applications', Sheffield, UK, 11-14 September 2001 (ESA SP-475, January 2002)

are not suitable for a reliable inversion of the surface geophysical parameters when the small-scale correlation length varies. The representation of the polarimetric information in a three-dimensional space defined by the H, A and $\underline{\alpha}$ axis permits to obtain separate curves for different surface configurations and can lead to a reliable inversion for any large-scale and cell-scale configuration.

The inversion algorithm is based on the use of Artificial Neural Networks (ANN). A Multi-Layer Perceptron is trained on a wide variety of surface conditions and allows a fast inversion of a surface dielectric constant and RMS slope from its H-A-$\underline{\alpha}$ parameters.

The inversion technique is applied to polarimetric SAR data acquired at L band by the DLR (German Aerospace Center) E-SAR airborne sensor over the Weiherbachtal site (Germany).

II. POLARIMETRIC SCATTERING MODEL

II.1. Large-scale surface generation

As mentioned previously, a stochastic surface is defined by its correlation function, $\varphi_{xx}(\tau)$ and correlation length, L_c, its height probability density function and standard deviation, σ_h. One realization of this stochastic variable may be obtained by processing a Gaussian white noise through a correlating filter so that the output signal follows a zero mean Gaussian probability density function with a standard deviation equal to σ_h and with a correlation length equal to L_c.

This processing may be summarized by the following equation :

$$\mathbf{S}(x,y) = FT^{-1}(\sqrt{\mathbf{S}_0(f_1,f_2)}) * \mathbf{B}(x,y) \qquad (1)$$

where FT stands for Fourier Transform and * for the convolution operator. The variables **B**, **S** and $\mathbf{S_0}$ are two-dimensional arrays associated to the Gaussian white noise, the correlated surface and the Fourier Transform of the correlation function respectively. A fast way to implement the surface generator consists in replacing the convolution by a simple product by using the Fourier Transform of the noise array.

It is important to note that in practice the width of the correlation function is limited around the origin. This precaution permits to generate wide stochastic surfaces within a reasonable amount of time.

In Fig.1 is depicted a realization of a stochastic surface.

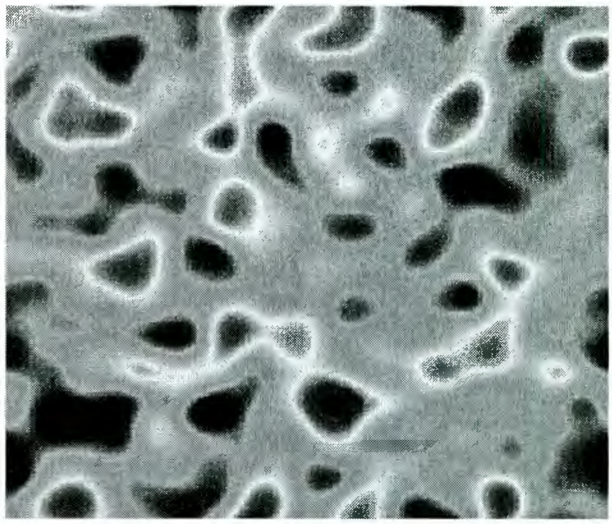

Fig. 1 : Realization of a stochastic surface

II.2. Application of a local scattering model

The soil surface is considered to be a two-scale process. The large scale characteristics, consisting in slopes in range and azimuth directions, are used as inputs to a SPM scattering model for each pixel. The SPM model response represents the scattering from the small-scale rough surface modulated by the large-scale shape as indicated in Fig. 2.

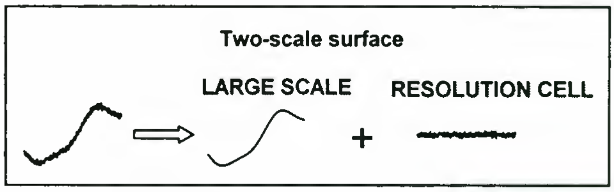

Fig. 2 : Surface decomposition into a two-scale model

A. Orientation angle extraction

In order to be used as inputs of a scattering model, the large-scale slope terms have to be transformed into incidence angle and azimuthal orientation, in the radar basis, for each pixel of the image. The range incidence angle, θ_r, and the azimuth angle, ϕ_r, are given by the following expressions [6]:

$$\begin{aligned}\theta_r &= a\cos\left(\frac{Z_x \sin\theta_0 + \cos\theta_0}{1+Z_x^2+Z_y^2}\right)\\ \phi_r &= \frac{1}{2} a\tan\left(\frac{2Z_y(Z_x\cos\theta_0 - \sin\theta_0)}{(Z_x\cos\theta_0-\sin\theta_0)^2 - Z_y^2}\right)\end{aligned} \qquad (2)$$

where θ_0 stands for the radar look angle with respect to the nadir, Z_x and Z_y represent the large scale surface slopes in range and azimuth respectively.

B. Scattering model in the radar basis

The Small Perturbation Model permits to calculate scattering coefficients for slightly rough surfaces as functions of the incidence angle in the radar basis, θ_r, the soil dielectric constant, ε, the small-scale surface spectrum, W and its correlation length and height standard deviation, L_{c_s} and σ_{h_s} respectively. The first order model polarimetric scattering coefficients are expressed as :

$$S_{pq}S^*_{rs} = 8k^4\sigma^2_{h\_s}\cos(\theta_r)^4\alpha_{pq}\alpha^*_{rs}W(2k\sin\theta_r) \quad (3)$$

with, in the Gaussian case,

$$W(2k\sin\theta,0) = \frac{L^2_{c\_s}}{2}\exp\left[(kL_{c\_s}\sin\theta)^2\right] \quad (4)$$

where α_{pq} represents the modified Fresnel scattering coefficient in polarization pq. The first order cross-polar scattering term, α_{pq}, is equal to 0.

The different scattering coefficients are gathered into a single matrix representation under the form of a coherency matrix, $\mathbf{T}(\theta)$, defined as :

$$\mathbf{T}(\theta) = \mathbf{k}\mathbf{k}^\dagger \quad (5)$$

$$\text{with } \mathbf{k} = \frac{1}{\sqrt{2}}[S_{HH}+S_{VV}, S_{HH}-S_{VV}, 2S_{HV}]^T \quad (6)$$

In order to take into account the orientation of the resolution cell around the radar line of sight , the coherency matrix $\mathbf{T}(\theta)$ has to be transformed by the way of a special unitary rotation matrix as indicated in the following expression :

$$\mathbf{T}(\theta,\phi) = \mathbf{U}(\phi)\,\mathbf{T}(\theta)\,\mathbf{U}(\phi)^{-1} \quad (7)$$

In Fig. 3 is represented the image of the span or total polarimetric power calculated from $\mathbf{T}(\theta,\phi)$.

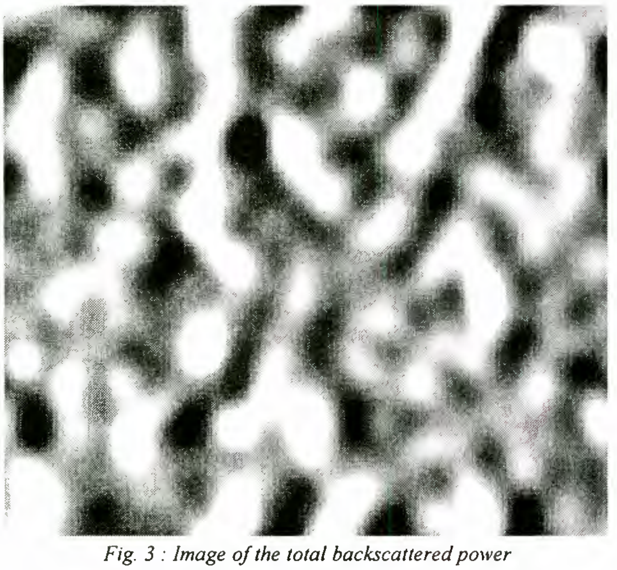

Fig. 3 : Image of the total backscattered power

An average coherency matrix, $\langle\mathbf{T}\rangle = E[\mathbf{T}(\theta,\phi)]$, is obtained by an incoherent summation over the large-scale surface. This matrix is in general distributed since the different coherency matrices $\mathbf{T}(\theta,\phi)$ are not collinear. The polarimetric information contained in $\langle\mathbf{T}\rangle$ is a function of the large- and small-scale roughness parameters, L_c, σ_h, L_{c_s}, σ_{h_s} and of the dielectric constant ε.

II. MODEL RESULTS POLARIMETRIC ANALYSIS

Many polarimetric indicators have been developed for remotely sensed data inversion in terms of target physical properties. Recently, the use of incoherent de composition theorems led to an interpretation of an average incoherent fully polarimetric representation in terms of average scattering mechanism and random aspect of the global scattering [4][5].

II.1.Eigenvector/value based decomposition theorem.

A distributed matrix, $\langle\mathbf{T}\rangle$, has its rank superior to one and cannot be related to a single scattering matrix and has to be decomposed in order to identify the global mean scattering phenomenon.

An eigenvector/eigenvalue based decomposition theorem presented in [4][5] permits to split a distributed matrix, $\langle\mathbf{T}\rangle$, into a weighted sum of three orthogonal unitary matrices representing each a pure scattering mechanism :

$$\langle\mathbf{T}\rangle = \mathbf{V}\boldsymbol{\Sigma}\mathbf{V}^\dagger = \sum_{i=1}^{3}\lambda_i\mathbf{v}_i\mathbf{v}_i^\dagger = \sum_{i=1}^{3}\lambda_i\mathbf{T}_i \quad (8)$$

where $\mathbf{V}$ and Σ represent the distributed target eigenvector and eigenvalue matrices respectively. The unitary eigenvectors are parameterized using four angular variables.

$$\mathbf{v}_i = [\cos\alpha_i, \sin\alpha_i\cos\beta_i e^{j\gamma_i}, \sin\alpha_i\sin\beta_i e^{j\delta_i}]^T \quad (9)$$

A statistical analysis of the decomposition is used in order to extract the mean scattering phenomenon. Each scattering mechanism is weighted by its pseudo-probability p_i corresponding to its relative power with respect to the total power.

The mean decomposition parameters are calculated according to (9).

$$(\bar{\alpha},\bar{\beta},\bar{\delta},\bar{\gamma}) = \sum_{i=1}^{3}p_i(\alpha_i,\beta_i,\delta_i,\gamma_i) \quad (10)$$

The three main parameters of this decomposition are :

- $\bar{\alpha}$, the indicator of the mean scattering mechanism. A value close to 0 corresponds to the scattering on a surface, for a dipole $\bar{\alpha}$ equals $\pi/4$ and reaches $\pi/2$ when the target consists in a metallic dihedral scatterer
- The entropy, H, which indicates the random behavior of the global scattering.
- The anisotropy, A, which represents the relative importance of the secondary mechanisms.

These three parameters are roll-invariant and have been widely used in natural target properties inversion [1-3] as well as polarimetric classification procedures [7][8].

II.2. Two-dimensional projections

The polarimetric indicators provided by the decomposition theorem are generally used to define projection planes [1-3]. The polarimetric properties of media presenting different geophysical parameters are expected to result into distinct characteristics after projection onto one of these planes. In this way, the concerned polarimetric variables could directly act as inputs of an inversion algorithm.

Fig. 4 shows the projection of the polarimetric characteristics of stochastic dielectric surfaces onto the (H-$\underline{\alpha}$), (H-A) and (A-$\underline{\alpha}$) planes.

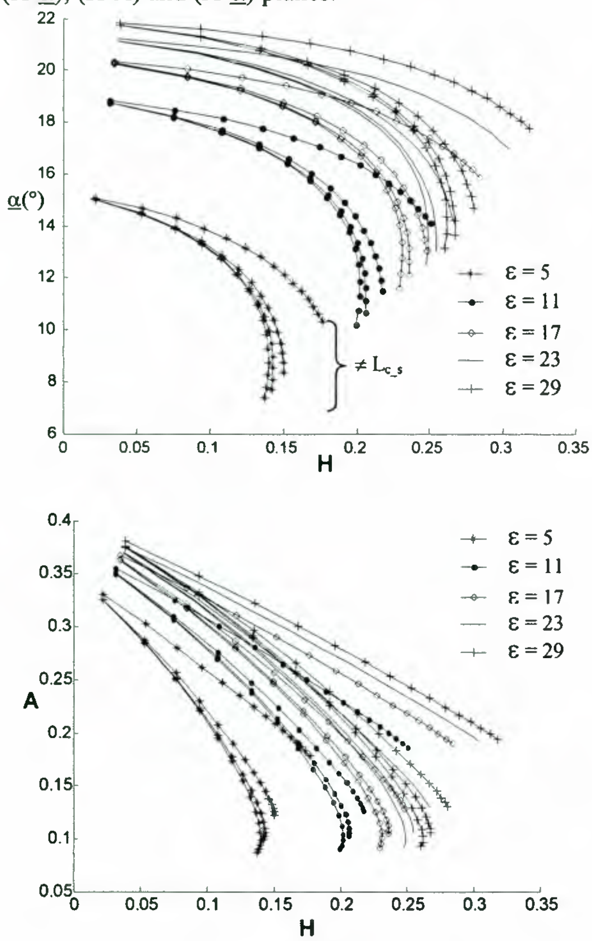

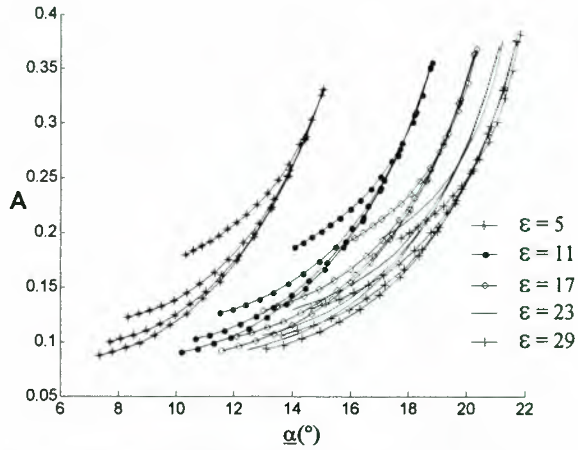

Fig. 4 : Projection of the polarimetric characteristics of stochastic dielectric surfaces onto the (H-$\underline{\alpha}$), (H-A) and (A-$\underline{\alpha}$) planes

It can be seen in Fig.4 that for a given dielectric constant, the location of the polarimetric parameters follow continuous curves as the large-scale roughness varies. Curves corresponding to a dielectric constant may have different shapes according to the small scale correlation length. In fact, depending on the small-scale roughness, the characteristics of different dielectric constants may have one or more common points. For this reason we can conclude that a two-dimensional polarimetric representation is not well suited for the inversion of a natural surface characteristics if the surface small-scale roughness is not a priori known.

II.3. Three-dimensional projections

The polarimetric characteristics of the stochastic dielectric surfaces are projected into the three-dimensional (H-A-$\underline{\alpha}$) space. The results of this projection are shown in Fig. 5.

It can be seen that the projection of the polarimetric data into the (H-A-$\underline{\alpha}$) space permits to discriminate the different groups of curves corresponding to distinct dielectric constants. The simultaneous variation of the three polarimetric parameters as the small-scale roughness changes permits to avoid any common points between the characteristics.

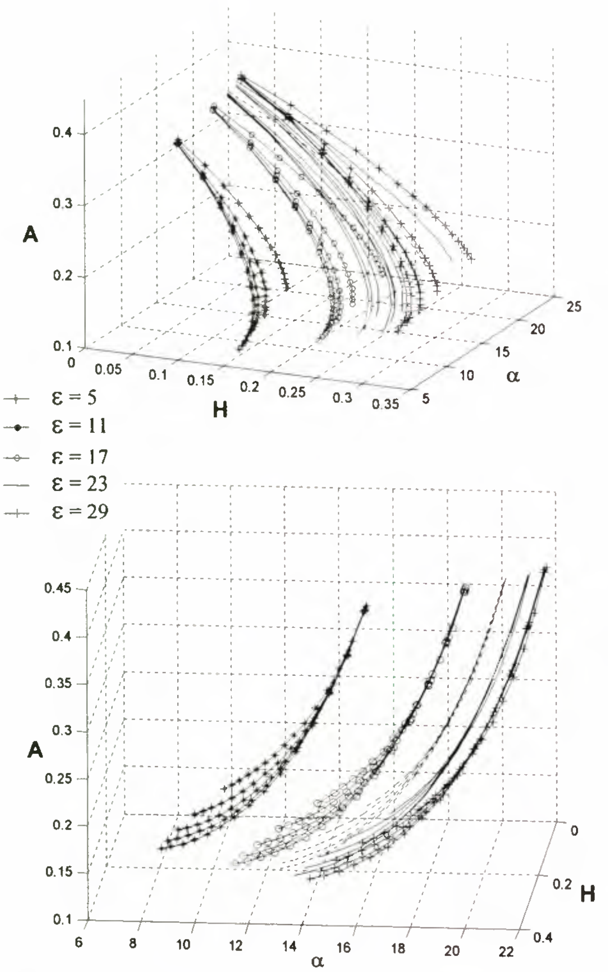

Fig. 5 : Projection of the polarimetric characteristics of stochastic dielectric surfaces into the (H-A-α) space.

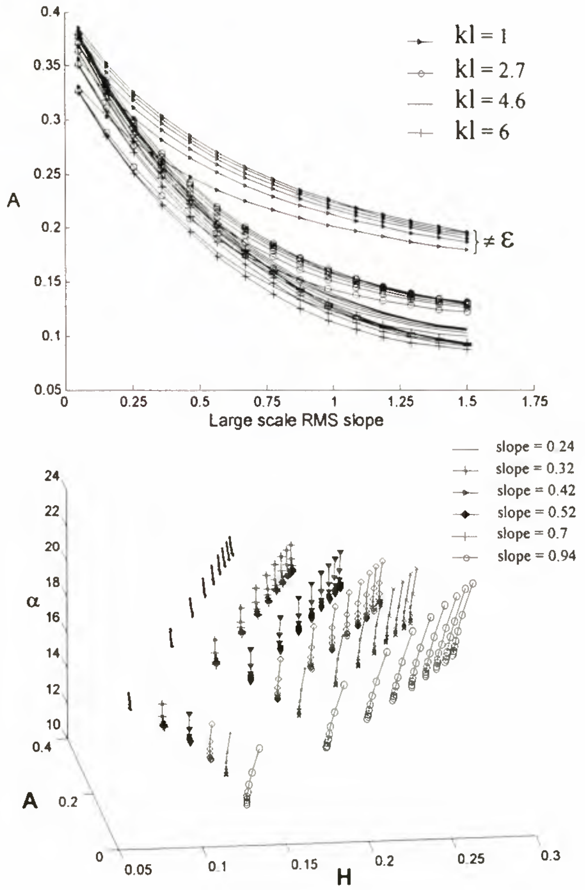

Fig. 6 : Projection of the polarimetric characteristics of stochastic dielectric surfaces into the (H-A-α) space.

As mentioned previously, the polarimetric parameters are sensitive to the large-scale roughness. In Fig. 6. are shown the variations of the anisotropy, A, versus the small-scale RMS slope. These characteristics are quasi-independent of the value of the dielectric constant. For large RMS slopes, small-scale roughness variations may cause some changes in the anisotropy value. Similarly to the dielectric constant, the large-scale is shown to follow distinct curves after projection of the characteristics in the (H-A-α) plane as can be seen in Fig. 6.

The three-dimensional representation of the polarimetric properties of a stochastic rough surface using the (H-A-α) space permits to separate dielectric characteristics as the surface geometrical properties vary. This representation is also well suited for the determination of the large-scale roughness conditions.

III. SURFACE PARAMETER RETRIEVAL

III.1. Surface Model Inversion

As mentioned previously, the polarimetric data projection into the (H-A-α) space permits to separate different dielectric constants and different large scale RMS slopes. The characteristics described by these parameters in the three dimensional space are non-linear and may not be easily inverted by a look-up table procedure.

We propose then to use an Artificial Neural Network (ANN) based inversion method.

A Multi-Layer Perceptron (MLP) is trained on (H-A-α) sets simulated for a wide variety of surface geometrical and dielectric conditions. The training stage ends when the MLP error function reaches a sufficiently low minimum. The inversion procedure consists then in applying a set of (H-A-α) parameters at the network input and simply calculating the output value as a function of the different layers weights.

III.2. Volumetric moisture content retrieval

The DLR airborne E-SAR sensor, at L band, acquired a fully polarimetric data set over the site of Weiherbachtal (Germany). Simultaneously, ground-truth measurements were done on several agricultural fields. A detailed description of the ground-truth information can be found in [1-3].

Among the six test zones, only three, 2, 4 and 5, were found to be valid from a polarimetric point of view, the remaining fields presenting highly heterogeneous polarimetric characteristics. Volumetric moisture content were measured at different depths, 0-4 cm and 4-8 cm.

Average (H-A-$\underline{\alpha}$) sets are extracted from the polarimetric SAR data corresponding to the valid inversion zones and are processed through the trained MLP. The dielectric constants at the ANN output are converted to volumetric moisture content using Topp algorithm [1-3].

The retrieval results are presented in Fig. 7.

The retrieved moisture content is plotted versus both measured ones. For a correct inversion the measured m_v are located on both sides of the unity slope line drawn in Fig.7. In this case, the estimated m_v is contained within the range defined by the measured ones.

The inversion approach works correctly for the fields 4 and 5, but fails for zone 2, the estimated m_v being slightly lower than the ones measured at a depth of 4 cm.

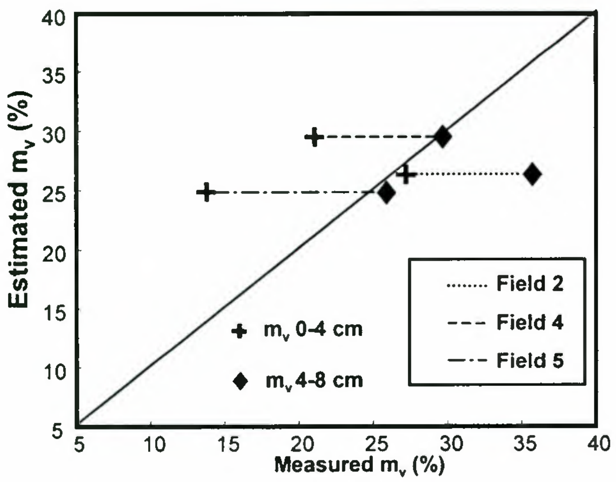

Fig.7 : Estimated versus measured volumetric moisture content over the Weiherbachtal site (Germany).

III. CONCLUSION

This paper introduces a method to extract surface geophysical parameters from polarimetric SAR data descriptors. A modeling of a natural soil under the form of a two-scale process provides a more realistic approximation of real measurement conditions. The SPM model is used to determine the average polarimetric properties of a large-scale surface. It is shown, from the analysis of polarimetric descriptors, that the discrimination of the soil dielectric properties from a two-dimensional representation necessitates to know a priori the small-scale roughness conditions.

A solution to this problem is proposed by means of a three-dimensional representation into the (H-A-$\underline{\alpha}$) space. A soil parameter inversion method based on Artificial Neural Networks is introduced and is applied to the case of soil moisture retrieval.

III. REFERENCES

[1] S. R. Cloude, I. Hajnsek, K.P. Papthanassiou, " An eigenvector method for the extraction of surface parameters in polarimetric SAR", Proc. CEOS, Toulouse, France, October 1999.

[2] I. Hajnsek, E. Pottier, S. R. Cloude, " Slope correction for soil moisture and surface roughness retrieval", Proc. EUSAR, May 2000, Hamburg, Germany.

[3] I. Hajnsek, S.R. Cloude, J.S. Lee, E. Pottier, " Inversion of Surface Parameters from Polarimetric SAR data", IGARSS 2000, HAWAI, USA.

[4] S. R. Cloude, E. Pottier " A Review of Target Decomposition Theorems in Radar Polarimetry ", *IEEE Trans. on Geoscience and Remote Sensing*, vol. 34, n°2, pp 498-518, September 1995.

[5] S. R. Cloude, E. Pottier " An Entropy Based Classification Scheme for Land Applications of Polarimetric SAR ", *IEEE Trans. Geosc. Rem Sen.*, vol. 35, 1, pp 68-78, 1997.

[6] E. Pottier, "Unsupervized classification scheme and topography derivation of POLSAR data based on the H-A-alpha polarimetric decomposition theorem", 4th Int. Workshop on Radar Polarimetry, Nantes, France, July 1998

[7] L. Ferro-Famil, E.Pottier, "Dual frequency polarimetric SAR data classification and analysis" Progr. In Electromag. Research, PIER 14, pp.251-276,2001.

[8] J.S. Lee, M.R. Grunes, T.L. Ainsworth, L. Du, D.L. Schuler and S.R. Cloude "Unsupervised Classification of Polarimetric SAR Images by Applying Target Decomposition and Complex Wishart Distribution ", *IEEE Trans. on Geosc. and Rem. Sens.*, vol. 37, 5, pp 2249-2258, 1999.

A COMPARISON BETWEEN LASER, NEEDLE-LIKE AND MESHBOARD TECHNIQUES FOR SOIL ROUGHNESS MEASUREMENTS

AnnaMaria Gatti (1), Francesco Mattia (1), Christophe D'Haese (2), Niko E.C. Verhoest (2), Malcolm Davidson (3), Thuy Le Toan (3), Maurice Borgeaud (4)

(1) *Istituto di Tecnologia Informatica Spaziale (ITIS)-CNR, Matera, Italy,* e-mail:francesco.mattia@itis.mt.cnr.it
(2) *Laboratory of Hydrology and Water Management (LHWM), Ghent, Belgium*
(3) *Centre d'Etudes Spatiales de la BIO-sphere (CESBIO), Toulouse, France*
(4) *European Space Agency (ESA), ESTEC, TOS-EEP, Noordwijk, the Netherlands*

ABSTRACT

The objective of this work is to compare soil roughness measurements obtained using three different profilers: the first one is a sophisticated laser jointly developed by ESA and CESBIO; the second and third ones are a needle-like mechanical device and a meshboard profiler developed at ITIS and LHWM, respectively. The analysed data sets consist of roughness measurements acquired over the Matera site (Italy) and the Marestain site (France) in 1998 and 2000, respectively. Over the Matera site, laser and needle-like roughness profiles have been measured for one smooth and one rough field. Over the Marestain site, roughness profiles using the laser and the meshboard techniques have been collected over one medium rough soil. The paper compares the estimates of roughness parameters, i.e. the rms-height (s) and correlation length (l), obtained with the different methods, as a function of the number of profiles recorded (N) and of their length (L).

INTRODUCTION

The study of radar backscatter from bare surfaces is an important problem in SAR remote sensing because of its implications in retrieving physical parameters such as soil moisture content and surface roughness. Modelling of electromagnetic scattering from random surfaces has been object of theoretical and experimental studies since many years; nevertheless, the topic still attracts scientific interest, for instance, as far as concerns the characterisation of soil surfaces. In fact, most of theoretical models describing surface scattering assume ideal soil statistics seldom found in real conditions. In this respect, collecting accurate ground data is necessary in order to assess realistic soil surface statistics and consequently improve model predictions. To characterise soil surfaces, the main parameters commonly measured are the soil moisture content, the soil texture and the surface roughness. The latter probably being the most difficult to be accurately measured. In the past different methods for soil roughness acquisition were used.

In this context, two ground campaigns over the Matera site (Italy) and over the Marestaing site, near Toulouse, (France) have been carried out in autumn 1998 and in winter 2000, respectively. A large number of long roughness profiles were acquired over agricultural surfaces in coincidence with several ERS acquisitions. The roughness profiles were measured by means of a novel very accurate laser profiler jointly developed by CESBIO and ESA which is able to measure profiles up to 25m [Le Toan et al., 2000]. The analysis of these long profiles, along with similar measurements conducted in other European sites, has been very useful to better understand the statistical properties of surface roughness with an emphasis on the multi-scale properties of agricultural surfaces [Davidson et al., 2000].

However, the CESBIO-ESA laser profiler is a unique, sophisticated and expensive device, which cannot substitute simpler and cheaper methods of measuring surface roughness. In the past, several scientific teams have used mechanical methods to characterise surface roughness over spatial scales usually ranging between 1 and 4m.

In addition, these methods will probably be still used during near future ground campaigns (for instance in coincidence with the forthcoming ENVISAT acquisitions). In this respect, it is necessary to assess the performances of simple mechanical profilers versus more sophisticated laser profilers.

To investigate this aspect, part of the roughness measurements conducted over the Matera and Marestaing sites were carried out using both the CESBIO-ESA laser profiler and mechanical profilers (i.e. either a 4m long needle-like profiler or a 4m long meshboard profiler). The objective of this study is to assess under which conditions the laser measurements are in good agreement with mechanical measurements. More generally, the aim of this study is to ascertain limits and potential of mechanical roughness measurements versus laser measurements.

In the next sections, the three measuring techniques are briefly described and the experimental data set is illustrated. Then, the analysis is reported and results are discussed. Finally, some conclusions are given.

Proc. 3rd International Symposium, 'Retrieval of Bio- and Geophysical Parameters from SAR Data for Land Applications', Sheffield, UK, 11-14 September 2001 (ESA SP-475, January 2002)

THE PROFILERS

While the CESBIO-ESA laser profiler (Figure 1a) is able to record roughness profiles up to 25m the needle-like (Figure 1b) and the meshboard (Figure 2) profilers can measure soil roughness profiles up to 4m.
The laser profiler records the surface profile using a laser distance meter lodged within a motor-driven carriage travelling along an aluminium I-shaped rod [Le Toan et al., 2000]. This apparatus records the distance between the beam and soil surface every 0.005m with a vertical precision of ± 0.0015m. The system is operated by a laptop which also stores the digital profiles.

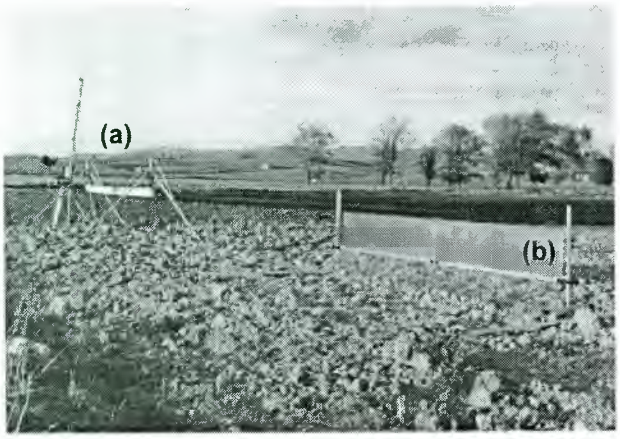

Figure 1: CESBIO-ESA laser profiles (a); ITIS-CNR needle-like profiler (b)

The needle-like profiler simply consists of an aluminium plate 4m long and 0.43m high, with an aluminium rod welded at its basis. Upon this rod there are 320 holes 0.0125m apart through where the needles slide. Two T-shaped poles are used to sustain the plate. When the mechanical profiler is mounted the needles fall on the ground and they delineate the profile of the soil situated below the plate. Then a photo of the profile is taken. The meshboard profiler [D'Haese, 2000] basically consists of a 4m long plate which is inserted in the soil and subsequently photographed. In both cases, once the photos of soil profiles have been taken, a digitisation process is required in order to transform the profile into x, y coordinates. Finally, in order to obtain a standard horizontal spacing of 0.005m (i.e. the resolution of laser measurements), the digitised profiles are interpolated.
Mechanical measurements are affected by several source of errors including coarse resolution, destructive nature of measure, parallax errors, etc. In particular in [D'Haese et al., 2000], errors related to the digitisation process have been deeply investigated when using the mesh-board device.

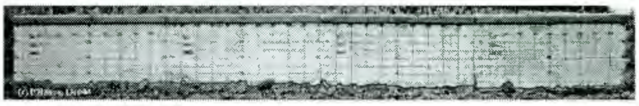

Figure 2: LHWM meshboard profiler

THE DATA SET

During November 1998 and February 2000, two dedicated experiments aimed at comparing the performances of a needle-like and a meshboard profiler with those of the CESBIO-ESA laser profiler were

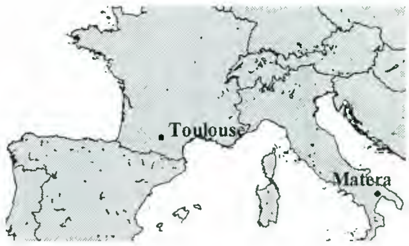

Figure 3: Matera and Marestaing sites

carried out over the Matera site (I) and the Marestaing site (F), respectively (Figure 3). Over a flat area called Rondinelle, located close to Matera , two bare fields (one smooth, named field A, and one rough, named field B) were selected. Whereas, over the Marestaing site only one, fairly rough, flat field was selected (field C). The Field A was ploughed in July and harrowed in August. Since then, it has not been worked . The Field B has been ploughed but not harrowed and showed no evidence of erosion due to rainfall. On the contrary, the field C had been ploughed before winter and, by February the field was significantly eroded by rainfall. All the profiles have been acquired long the plough direction. For each field, the roughness profiles were acquired using both the laser and the mechanical device (i.e. either the needle-like or the meshboard profiler). Special care was taken to measure, as far as possible, the same profiles with both instruments. Firstly, the laser was used to record the long roughness profile. Then, by shifting several times the 4m long mechanical device the same profile was recorded with the mechanical technique. Table 1 summarises the whole data set.

Table 1: Profiles measured over Matera and Marestaing

	laser	needle - like	meshboard
Field A	2 (L =20 m)	10 (L = 4 m)	
Field B	1 (L =20 m)	5 (L =4 m)	
Field C	11 (L = 25 m)		21 (L = 4 m)

ANALYSIS OF ROUGHNESS PROFILES

In the context of microwave remote sensing applications, in order to characterise roughness properties of soil surfaces, statistical parameters such as the profile height rms (s), the profile autocorrelation function (ACF) as well as the associated correlation length (l) have been usually exploited. These parameters completely represent the surface statistics under the assumption that surface roughness may be considered a stationary Gaussian single scale process. From an experimental point of view, previous studies [Borgeaud, 1996] have often found a strong spread of these parameters (particularly of the correlation length) even within apparently homogeneous fields. In general, such a kind of variability can be partly attributed to the intrinsic variability of surface roughness, which often cannot be represented as a Gaussian single scale process [Davidson et al., 2000], and partly to inaccuracies or limitations in the measurement technique.

In this paper the focus is on quantifying the measurement errors associated to mechanical profilers. For this reason, the analysis will be limited to 4m long profiles measured both by laser and mechanical profilers.

As a mathematical framework for the study, a simple model for the effect of error measurements on roughness parameters will be assumed. This model is represented by the following equation:

$$\eta_m = \eta_r + \varepsilon_e \qquad (1)$$

where η represents the estimate of either s or l parameter. More precisely: η_m is the value extracted from one profile of given length L obtained with a certain profiler; η_r is the value which would have been obtained, over the same length L, if measurement errors were negligible (i.e. $\varepsilon_e \approx 0$). It is worth mentioning that η_r depends on the place where it is estimated due to the intrinsic variability of surface roughness. In other words η_r can be modelled as:

$$\eta_r = \eta_t + \varepsilon_r \qquad (2)$$

where η_t now represents the parameter true value and ε_r is its random component due to the intrinsic roughness variability. It is reasonably to assume that both measurement errors (i.e. ε_e) and the intrinsic variability of surface roughness within an homogeneous field (i.e. ε_r) are uncorrelated and have zero mean. It should be emphasised that all previous quantities contain a dependence on L (i.e. the profile length over which are estimated).

In this paper, two aspects are specifically investigated:

- the minimum profile length (L) which should be recorded in order to have a good agreement between roughness parameters extracted from laser and mechanical measurements;
- the minimum number (N) of independent s and l estimates which should be averaged in order to limit their variability within a given range.

To do so, the laser measurements are considered to have negligible measurement errors and used as benchmark for needle-like and meshboard measurements.

To give an overview of the data set, Table 2 reports the average, standard deviation (std) and coefficient of variation (CV%) for the s and l parameters estimated over 4m long profiles. As can be seen, the agreement between s and l parameters extracted from laser and mechanical measurements on fields A, B and C is very good.

Table 2: Roughness parameters estimated over 4m long profiles

Field A		l (cm)	s (cm)
needle-like	average	10.85	1.94
	std	9.63	0.58
	CV%	88.8	29.66
laser	average	10.60	1.63
	std	8.00	0.54
	CV%	75.4	33.10
Field B		**l (cm)**	**s (cm)**
needle-like	average	6.60	3.13
	std	3.96	0.70
	CV%	60.0	22.28
laser	average	6.80	3.29
	std	3.65	0.60
	CV%	53.7	18.28
Field C		**l (cm)**	**s (cm)**
meshboard	average	28.00	2.82
	std	8.30	0.72
	CV%	29.7	25.48
laser	average	26.50	3.67
	std	10.60	0.70
	CV%	40.1	19.10

It should be noted that CV for l is always significantly higher than for s.

In the next subparagraph the correlation between roughness parameters extracted from laser and mechanical measurements as a function of profile length (L) will be investigated. Subsequently the effect of averaging roughness parameters (i.e. s and l) estimated over N independent profiles will be described.

VARIABILITY OF S AND L AS A FUNCTION OF L

In this part of the study, the specific objective is to assess the minimum profile length to be recorded in order to have a good agreement between roughness parameters (i.e. s and l) extracted from laser and mechanical measurements. This study has been restricted to measurements carried out over field A and B with laser and needle-like profilers. To attain this, each 4m long profile, commonly measured by the laser and mechanical profiler, has been divided into sub-profiles of 1, 2, 3 and 4m. Subsequently, for each sub-profile the ACF, the s and l parameters have been estimated. The number of sub-profiles with different length and for each field is given in Table 3.

Table 3: Number of sub-profiles for fields A and B

length profiles L	N° subprofiles = N	
	Field A	Field B
1 m	40	20
2 m	20	10
3 m	10	5
4 m	10	5

Figures 4, 5 and 6 show the correlation between l parameters extracted from laser and needle-like measurements over 1, 2 and 4m long profiles, respectively. In the figures the values of the squared correlation coefficient for both field A and B are reported. As can be seen, for 1 and 2m long profiles the correlation between laser and needle-like measurements is very low. This means that, for these profiles, needle-like measurements are affected by large measurement errors. On the contrary, for profiles 4m long an overall good correlation is observed (significantly better over field B than field A). This result indicates that, for longer profiles, measurement errors play a minor role. A similar trend holds for the s values not displayed here.

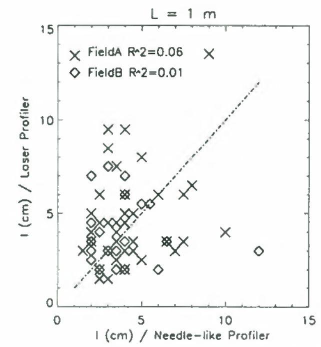

Figure 4: Correlation between l values estimated from laser and needle-like measurement referring to 1m long profiles

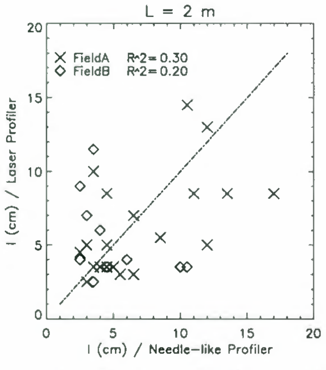

Figure 5: Correlation between l values estimated from laser and needle-like measurement referring to 2m long profiles

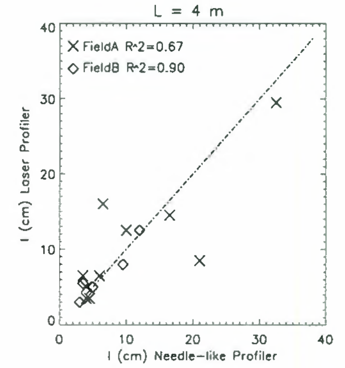

Figure 6: Correlation between l values estimated from laser and needle-like measurement referring to 4m long profiles

While measurement errors on l estimates become less important as the profile length increases (i.e. $\varepsilon_e \rightarrow 0$), the intrinsic roughness variability shows an opposite trend at least in the case of field A. In other words, the spread of l estimates increases as the profile length increases. Such an effect usually indicates that probably field A may be better described by multi-scale than single-scale statistics.

VARIABILITY OF S AND L AVERAGES AS A FUNCTION OF N

In order to reduce the variability in the s and l estimates, an average over N independent measurements can be performed. In Figure 7, for field A and B, the average of l estimated from laser versus needle-like measurements is displayed as a function of increasing profile length.

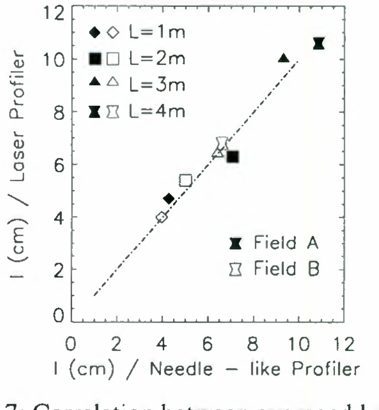

Figure 7: Correlation between averaged l values estimated from laser and needle-like measurements

As can be seen, the agreement is quite good whatever the profile length (an analogous result holds for the s parameter). This is because averaging a large number of profiles (see Table 3) both reduces roughness intrinsic variability (i.e. ε_r) and error measurements (i.e. ε_m). However, estimates over shorter profiles are affected by systematic errors. This can be easily demonstrated by noting that in Figure 7 the average correlation length of field A, estimated over 4m long profiles, is significantly higher than the average correlation length of field B, estimated over the same distance. However, this difference tends to reduce when the estimates are performed over shorter profiles. For instance, for 1m long profiles the average correlation length of field A and B are almost the same. This systematic error is due to the fact that any profiler behaves as a band pass filter with a lower and higher frequency related to the profiler length and the profiler resolution, respectively. Even assuming that the soil roughness under study is a stationary Gaussian single scale process, in order to obtain a reliable estimate of l, the profiler length L must be much larger than l [Oh and Kay, 1998]. For 1m long profiles this condition is usually not fulfilled. Consequently the estimates of l over short profiles suffer from important systematic errors. For this reason in the following we concentrate on 3-4m long roughness profiles.

A second aspect, which has been investigated, is the variability of s and l values as a function of the number of independent estimates averaged. To do so, the following averages have been computed, both for the laser and mechanical measurements:

$$\overline{\eta}_L(N) = \frac{1}{N}\sum_{i=1}^{N}\eta_m(i) \qquad (3)$$

$$C\% = \frac{\left|\overline{\eta}_L(N) - \overline{\eta}_L(k)\right|}{\overline{\eta}_L(N)} * 100 \qquad (4)$$

$$k = 1 \ldots N-1$$

where η stays for s or l and N as a function of L is reported in Table 3.

The C% coefficient is the relative error expressed as percentage between the estimate of the η parameter obtained averaging k samples and η estimated averaging all the samples. In Figure 8 and 9 the comparison between C% for laser and needle-like measurements referring to l and s estimates is reported, respectively. The parameters have been estimated over 4m long profiles, in Figure 8 the C% refers to estimates of l over field A whereas in Figure 9 it refers to estimates of s over field B. Analogous trends hold for the other cases.

As can be seen, the C% values both for laser and needle-like measurements overall decrease as a function of the number of averaged samples (k). Since the estimates of roughness parameters are performed over 4m long profiles, the effect of measurement errors is less important than the intrinsic variability of surface roughness.

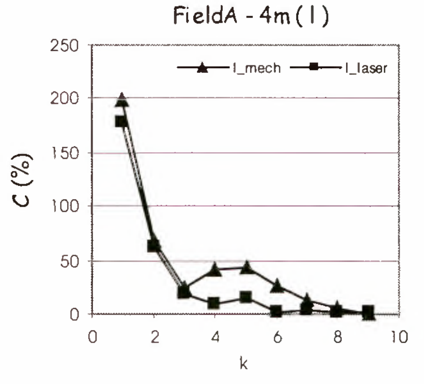

Figure 8: Comparison between the relative error of the l parameter, estimated from laser and needle-like measurements over 4m long profiles on field A, as a function of the samples averaged (k)

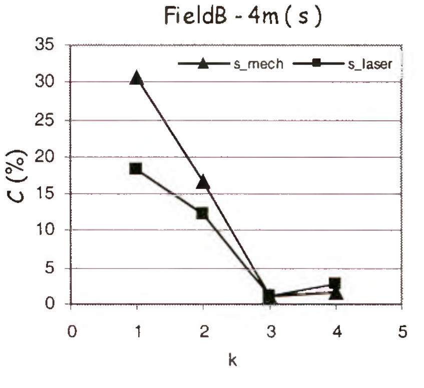

Figure 9: Comparison between the relative error of the s parameter, estimated from laser and needle-like measurements over 4m long profiles on field B, as a function of the samples averaged (k)

In this respect, the difference between C% for laser and needle-like measurements is not very large. However, it should be noted that C% for laser measurements is always smaller than for needle-like measurements. This means that laser measurements are more stable than needle-like measurements. For the case of needle-like measurements, in Table 4 the values of coefficient C% are reported as a function of the number of profiles (k) used to calculate (4). Those values hold both for s and l parameters. It is worth mentioning that the smooth field (Field A) requires a larger number of independent measurements than the rough field (Field B) to achieve the same level of variability.

Table 4: Relative error affecting s and l parameters extracted from needle-like measurements of 3-4m long profiles.

	C%	Field A	Field B
L = 3 and 4 m	40%	6	3
	30%	7	4
	20%	8	5

are informally known as Nubian sandstones, and by low sporadic outcrops of granite and granitic gneiss of the Precambrien African shield. Vegetation is almost entirely absent except at the minor oases or wells, known as *birs* The desert floor is mostly covered by yellowish to slightly reddish windblown sand in extensive, thin, flat to undulating sheet deposits.

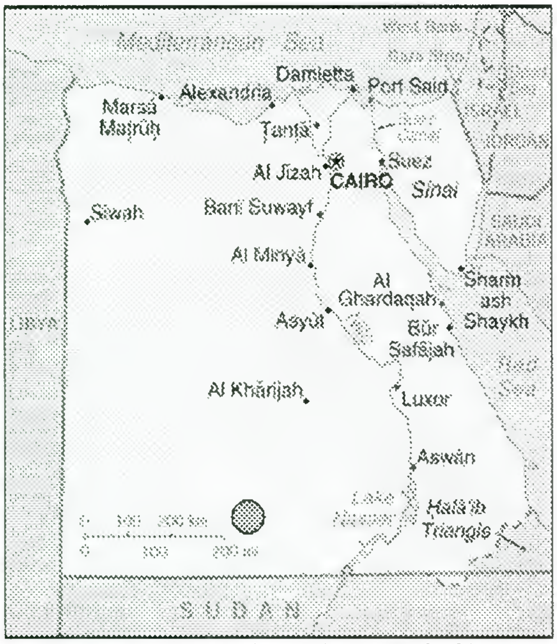

Figure 1: The dot shows the Bir Safsaf location

The studied sites were identified on the SIR-C radar scenes by comparison with LANDSAT 7 ETM+ data (Figure 2). This led us to locate three specific zones for which visible images indicate quite homogeneous sand cover whereas SIR-C data show various linear subsurface structures (corresponding to sharp transition in the total backscattered power σ_0). A GPR field experiment was then planned to validate the fact that σ_0 variations are related to subsurface structures.

EXPERIMENT AND PRELIMINARY RESULTS

The field work took place from 13th to 18th February 2001, and was conducted in cooperation with the Egyptian authorities. The work consisted to perform series of GPR profiles, surface roughness measurements, and geological material sampling in the three selected sites of the Bir Safsaf area. We operated the GPR of BRGM (a GSSI-SIR-10) with 500 and 900 MHz antennas. Roughness measurements were acquired using a needle profiler. A specific task consisted to position the GPR profiles and roughness measurements with a precision of few tens of meters with respect to the structures selected in the SAR images. This was performed by coupling in real time a GPS facility and geocoded SAR images.

Roughness measurements were first performed. For each sites (Figure 3), they confirmed the LANDSAT observations, i.e., surface topography is flat and rather smooth (2 mm < H_{RMS} < 10 mm).

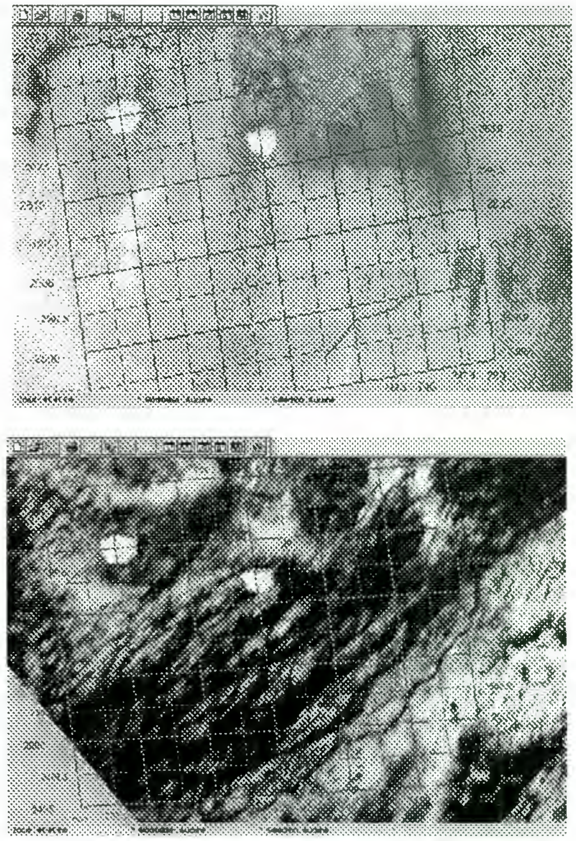

a)

b)

Figure 2: comparison between LANDSAT 7 (a) and SIR-C (b) scene of the same area

GPR profiles were afterwards carried out. Their length varied from 2 to 3 km in order to have a long enough section to be compared to SIR-C data. For each of the 500 and 900 MHz frequency profiles, common data processing (spatial resampling, frequency and dip filtering, etc) was performed to enhance the signal to noise ratio.

In order to compare the SIR-C backscattered power with GPR data, we computed along the GPR profile the integrated power *P,* taken as the instantaneous amplitude integrated in time:

$$P = \int \sqrt{S^2(t) + Q^2(t)}\, dt$$

S(t) being the GPR amplitude signal in time, and Q(t) being the quadrature signal of S.

This quantity can be somehow compared to the σ_0, extracted from the SIR-C pixels located along the GPR profiles. Figure 4 shows, for the third site, the backscattered power at L and C bands, the GPR power curves and sections at 500 and 900 MHz, respectively after and before the integration in time.

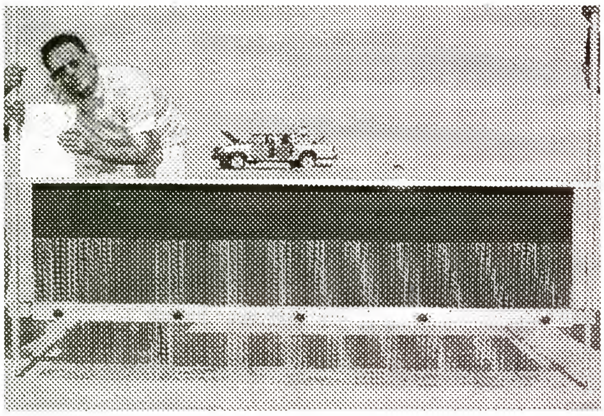

Figure 3: roughness measurements

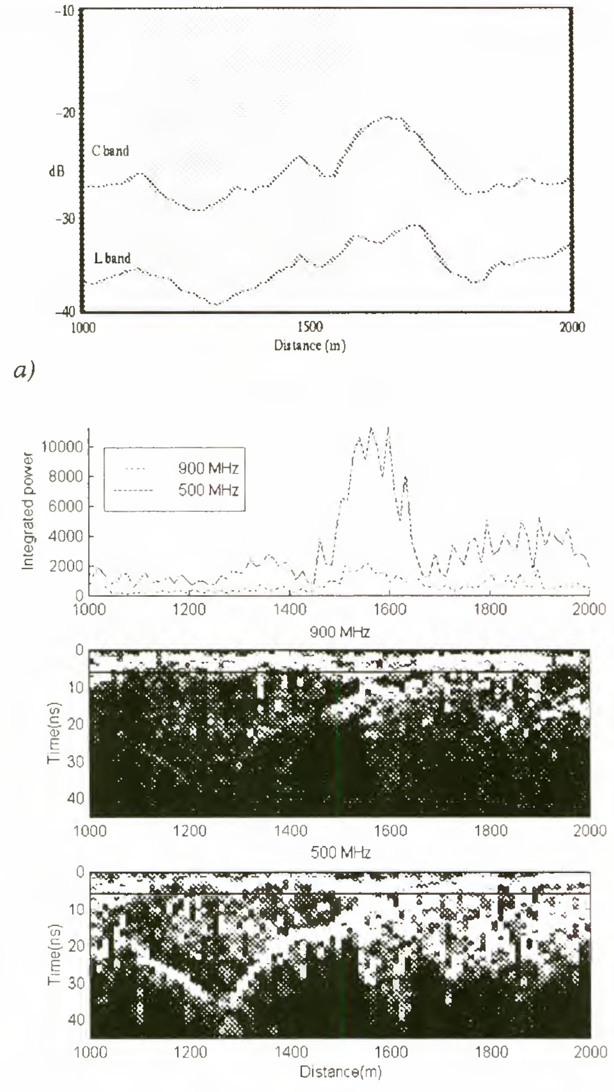

Figure 4: 0 for C and L bands (a), GPR power curves (in dB) and related sections for 500 and 900 MHz frequencies versus the profile distance (b)

These preliminary results shows that important differences exist between the 500 and 900 MHz GPR sections, but also between GPR power and SIR-C σ_0 curves. We can comment on several points:

- A higher penetration depth is observed for GPR-500 MHz compared to GPR-900 MHz. The top and the bottom of a subsurface layer, which is about 2 m deep, observed between 1000 and 1600 m, are clearly identified in the GPR-500 MHz section, but are hardly identified in the 900 MHz one. This shows the frequency effects on the penetration when considering buried structures: the lower the frequency, the deeper we can detect. This also explain why the L-band (1.2 Ghz) data from SIR-C do not show this deeper subsurface structure.
- The high power anomaly located between 1500 and 1600 m in figure 4b seems to be related to reflective stones (the carbonate nodules observed by [Schaber *et al.*, 1986]) located just below the surface and probably forming the bottom of the first layer. The discrepancy between the two sections indicates that GPR-500 MHz is more sensitive to them compared to GPR-900 MHz. In consequence, the penetration at 900 MHz reach few tens of centimeters, while it is much more at 500 MHz.
- The difference between SIR-C C and L band backscattered power in SIR-C data is only a shift in amplitude, indicating a moderate but identical penetration for the two bands, mainly controlled by the first centimeters of the subsurface.
- The correlation between GPR and SIR-C data is not straightforward. The probable causes are: (i) the difference in horizontal resolution related to the two methods (25 m pixels in SAR images, 10 cm in GPR profiles), (ii) the spatial integration of the SAR sensing technique compared to the GPR which measures the reflected power at one point, (iii) the difference in SIR-C and GPR acquisition systems, side-looking with narrow bandwidth and down-looking with large bandwidth respectively. This last point make SAR more sensitive to the diffuse component whereas GPR is more sensitive to the specular component of the backscattered signal.

CONCLUSION

We confirmed here that low frequency radar (L-band) can retrieve subsurface information where other classical sensors (optical, IR) cannot. If these information is not related to the surface properties, i.e. roughness, subsurface structures are the remaining candidates to explain the backscattered signal.

GPR/SIR-C comparison does not give a clear information concerning the penetration of L-band in the Southern Egyptian Desert, but some correlation between the two signals could be observed, when taking into account the diffusive nodules in the near subsurface.

and the number of scattering processes (entropy H). Both parameters were plotted in the entropy-alpha-feature space (Fig. 2) to distinguish different land cover classes.

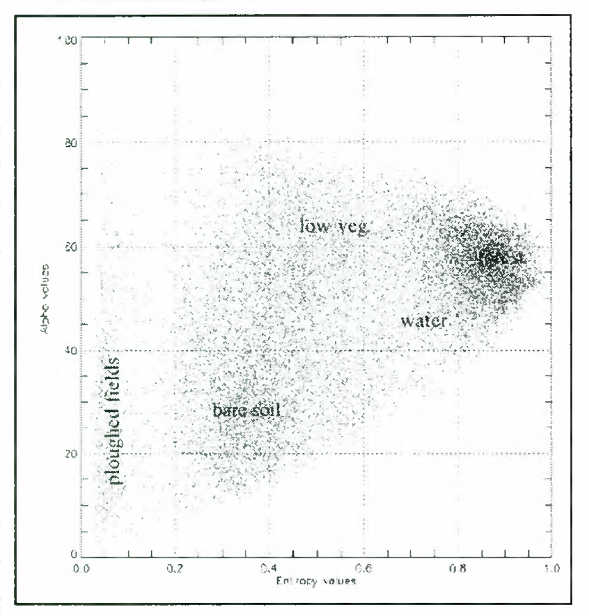

Figure 2: Entropy-alpha-feature space.

LAND COVER CLASSIFICATION

The land cover classification has been carried out on two levels according to Dobson et al. 1995 and Herold et al. 2000. In the first level the classes settlement/forest, water/ shadow and short/no vegetation had been distinguished on the base of an unsupervised isodata-clustering of the L-HH, L-VV, L-HV, X-HH and X-VV intensities.

In the second level the mixed classes settlement/forest and short/no vegetation had been distinguished in separate steps. In both cases a supervised maximum likelihood classification was applied. The class short/no vegetation has been separated using the intensities and polarisation parameters into the sub-classes rape, grassland, winter cereals, ploughed and seedbed (Fig. 3). Each sub-class was separated using the best suitable SAR parameter. In the case of the class "ploughed" the α-angle, $\alpha 1$ and L-HV have been used according to their differences to other classes. The signature of the class short/no vegetation is not influenced by the sparse vegetation in March, which is penetrated more or less completely, the backscatter of the L-Band is rather dominated by the surface roughness.

For the distinction of settlements and forest, texture information had to be incorporated since a separation based only on spectral information was not possible. The calculation of the euklidean distance as suitable texture parameter was carried out on the L-Band intensities with a 5 x 5 window. Meanwhile forest areas show primarily volume scattering, double bounce scattering is characteristic for settlements. Using all polarisation parameters and the intensity it was also possible to distinguish two forest classes, yound and mature forests. The classification accuracy was over 80 %.

SOIL MOISTURE DETERMINATION

For the Zeulenroda testsite the relationship between the radar (Intensity, Principle Components, Polarimetry) and the land surface parameters soil moisture and moist biomass have been investigated using empirical regression models. The soil moisture is mostly correlated with the Principal Components 1 (PC1) and 3 (PC3), the intensities L-VV and L-HV as well as the first Eigenvalue (λ_1). Figure 4 shows the soil moisture distribution derived from the radar backscatter (right), in comparison to the soil moisture distribution based on interpolated TDR-measurements (left). The coincidence is very good, the dry areas on the upper slope as well as the moist places on the lower slope are shown in the right dimension. The correlation coefficient is $r = 0.85$. Displayed is the mean value of the 5 polarimetric parameters, which also reduces the Speckle effect.

For validation purposes the results have been compared to the Multiple Flow Topographical Index (Fig. 5) and to the storage capacity (Fig. 6). The Topographical Index shows runoff lines due to the high resolution interferometric E-SAR DHM (5 m grid, < 1 m vertical resolution). It detects the local watershed, but it traces the soil moisture conditions only limited.
This is different with the storage capacity. It has been generated through the overlay of the porosity (derived from the soil grain size) and the root depth (derived from land use). Here the local topography is traced with the southern moist lower slope and the northern, potentially dryer upper slope. This soil moisture distribution is confirmed by the radar acquisition of 30.03.99 (Fig. 4, right).

This unique comparison of 4 different measurement methods confirms the possibility of L-Band SAR data to determine soil moisture. The radar data derived distribution seems to be more realistic than the ones derived from geostatistical methods.

Another significant correlation ($r = 0.92$) could be recognised between the SAR data and the moist biomass. Fig. 7 shows the distribution for the agricultural fields in the Zeulenroda testsite. The highest values are maize, the lowest recently ploughed fields. The moist biomass is strongly correlated with the plant water content, providing important information on the amount of water taken out of the system through harvesting.

Figure 3: Land cover classification.

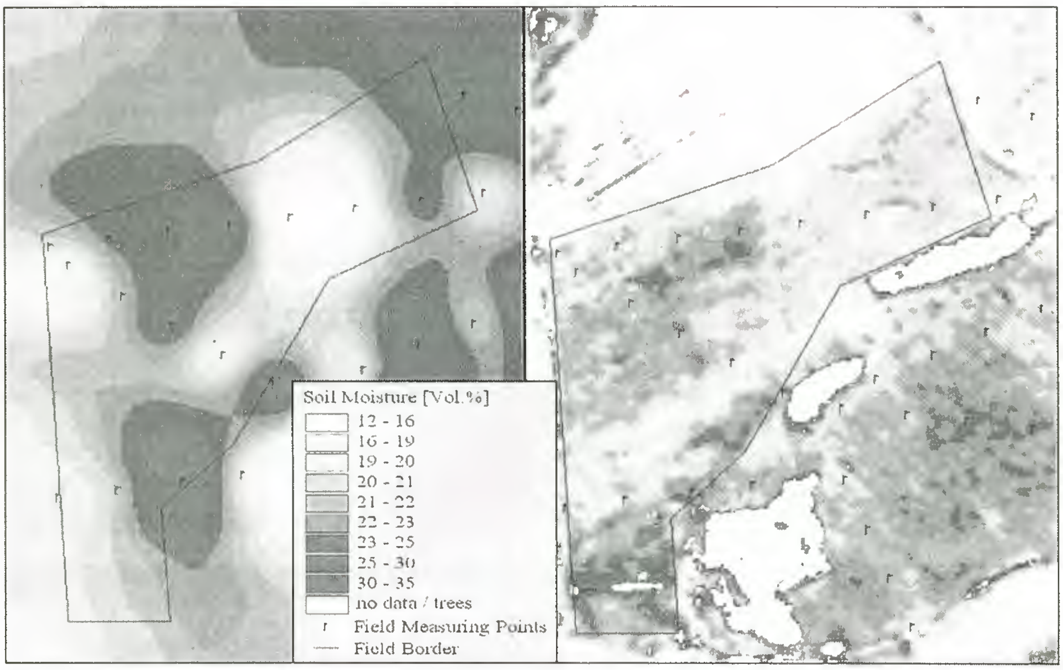

Figure 4: Soil moisture distribution based on interpolated TDR-measurements (left) and on polarimetric radar back-scatter (PC1, PC3, L-VV, L-HH, λ_1) (right).

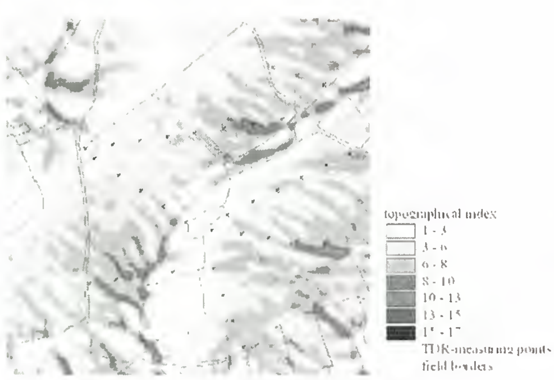

Figure 5: Multiple Flow Topographical Index.

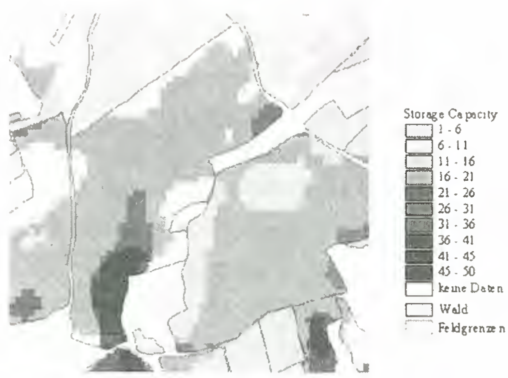

Figure 6: Storage Capacity (based on porosity and root depth).

Figure 7: Moist biomass distribution on agricultural fields in Zeulenroda testsite. The dark areas are crops i.e. maize, the bright areas are recently ploughed fields.

CONCLUSION

This study has shown, that the eigen vector decomposition is an approach for the extraction of hydrologically relevant parameters (land cover, biomass, soil moisture) from multipolarimetric SAR data. The land surface parameters are represented through different SAR paramenters. The land cover classification using polarimetric parameters seems to be an extension to the intensity based classification, not an alternative. For agricultural applications the information on moist biomass and soil moisture is reliable, providing more realistic spatial patterns, but a higher timely resolution is required.

The results could be seen as basic research on L-Band polarimetry and backscatter signature information for fututre spaceborne missions like ALOS.

ACKNOWLEDGEMENTS

This study is founded by the German Research Association (DFG) under contract HO 1840/5-1.

REFERENCES

Cloude, S.R. and Pottier, E. (1996): A Review of Target Decomposition Theorems in Polarimetry. *IEEE Trans. on Geoscience and Remote Sensing,* Vol. 34, No. 2, p. 498-518, 1996.

Dobson, M.C., Ulaby, F.U. and Pierce, L.E. (1995): Land cover classification and estimation of terrain attributes using synthetic aperture radar. *Remote Sensing of Environment*, 51, pp. 199-214, 1995.

Engman, E.T. and Chauhan, N. (1995): Status of microwave soil moisture measurements with remote sensing. *Remote Sensing of Environment*, 51, pp. 189-198, 1995.

Hellmann, M., Jaeger, G., Kraetzschmar, E. and Habermayer, M. (1999): Classification of full polarimetric SAR data using artificial neural networks and fuzzy algorithms. *Proceedings IGARSS, Hamburg, 1999*, vol. V, pp. 1995-1997, 1999.

Herold, M., Hochschild, V. and Schmullius, C. (2000): Multifrequente und multipolarimetrische Radarfernerkundung hydrologisch relevanter Parameter der Landoberfläche. *Photogrammetrie, Fernerkundung, Geoinformation*, 5, pp. 355-360, 2000.

LAI-ESTIMATION OF BOREAL FORESTS USING C-BAND VV AND HH POLARIZATION RADAR IMAGES

Manninen, T.[1], Stenberg, P.[2], Voipio, P.[3], Smolander, H.[3] and Häme, T.[1]

[1]*VTT Automation, Remote Sensing*
P.O. Box, 1304, FIN-02044 VTT, Finland
Tel. +358-9-4566285, Fax +358-9-4566475
Email: Terhikki.Manninen@vtt.fi, Tuomas.Hame@vtt.fi
[2]*University of Helsinki, Department of Forest Ecology,*
P.O.Box 27, FIN-00014 University of Helsinki, Finland
Pauline.Stenberg@helsinki.fi,
Tel. +358-9-191 58105, Fax +358-9-191 58100
[3]*Finnish Forest Research Institute, Research Station of Suonenjoki,*
Juntintie 40, FIN-77600 Suonenjoki, Finland
Pekka.Voipio@metla.fi, Heikki.Smolander@metla.fi
Tel. +358-17-513811, Fax +358-17-513068

ABSTRACT

The leaf area index (LAI) is directly related to the growth potential of a forest. Therefore it is an important parameter both from economical and environmental point of view. LAI determination using optical images is problematic in boreal forests, but ENVISAT ASAR should have potential in LAI estimation, as its wavelength is close to the needle size of boreal forests. While waiting for ENVISAT data the LAI estimation using VV and HH polarisation has been studied using ERS and Radarsat images. The first results of Scots pine are promising. This research is carried out in the ENVISAT AO-project "ENVISAT in boreal forest mapping and LAI estimation" (=ENBOR FORMAL).

INTRODUCTION

The leaf area index (LAI) is a key structural characteristic of forest stands because of the role of green leaves in controlling many biological and physical processes driving the exchange of matter and energy flow. LAI correlates strongly with the fraction of absorbed photosynthetically active radiation, which determines the energy available for growth. The amount of leaf area responds rapidly to different stress factors and (changes in) climatic conditions. The subsequent decrease or increase in LAI is directly reflected in future biomass production. It is widely recognised that the LAI could serve as a key indicator to characterise the condition and growth potential of the forest ecosystem. Unfortunately, the lack of reliable methods for assessing the LAI at larger geographical scales has so far limited this application.

Remote sensing is the only reasonable alternative for LAI estimation at regional scales. However, it has turned out that the normalised difference vegetation index (NDVI) obtained from optical images and used globally for LAI determination is not succesful in boreal forests (Häme et al. 1997, Nilson et al. 1999). Therefore a method is sought for retrieving LAI for boreal forests using microwaves. Backscattering modelling has indicated that the LAI has a large effect on simulated C-band backscatter, if the leaf size is comparable to the wavelength. In boreal forests the leaf (or needle) size is of the order of a few cm, so that LAI retrieval from C-band data could be expected (Wang et al. 1995). The alternating polarisation capability of ENVISAT has extra possibilities in trying to find out a relationship between the backscattering properties of a forest and the LAI values.

LAI MEASUREMENTS

The test site was in Tuusula (60.3° N, 24.5 ° E), Southern Finland, comprising an area of 443 ha. About half of the area is forested with Norway spruce *(Picea abies* L.) or Scots pine (*Pinus sylvestris* L.) dominated stands of different age. Many of the Scots pine stands were situated in a relatively large marsh area. Stand level ground measurements of the standard forest parameters were available from a previous investigation (Hallikainen et al. 1997). The year of measurement was 1997, i.e., two years prior to this investigation. A high resolution optical mosaic image covering the test site was also available (Holm and Rautakorpi 1997, Holm 1998).

Measurements of leaf area index (LAI) were made using the LAI-2000 Plant Canopy Analyzer (Li-Cor Inc., Nebraska, USA) between the 24th of May and 2nd of June, 1999 (Welles et al. 1996). The estimate of LAI provided by the LAI-2000 is obtained by inversion from measured canopy transmittance (gap fraction), and is based on the assumption that leaves are randomly (Poisson) distributed in the canopy space (Stenberg 1996). The optical sensor of the LAI-2000 consists of five detectors arranged in concentric rings, which measure radiation < 490 nm (where scattering from

Proc. 3rd International Symposium, 'Retrieval of Bio- and Geophysical Parameters from SAR Data for Land Applications', Sheffield, UK, 11-14 September 2001 (ESA SP-475, January 2002)

leaves is minimal) from different sections of the sky. LAI is computed from the ratio of below- and above-canopy readings in the five zenith angle bands of the detectors.

The selection of stands for measurement of LAI was based on the criteria that stand size (area) should be larger than 1 ha, and that the sample should include as large as possible variation in forest stand variables (age, stem volume, basal area, and tree height). A fairly wide range in these variables was obtained for the whole sample, however, within each of the two species the range was considerably smaller. All the Norway spruce stands had high values of stand volume and basal area, whereas the Scots pine stands were less dense (Stenberg et al. 2001).

LAI-2000 measurements were made in regular grids in a homogeneous part of each stand. The measurement design varied with size and shape of the stand. The number of measurement points was between 12 and 36, and the points were situated 3 to 20 m apart. Most commonly, a 30 x 30 m square grid with 16 measurement points situated at 10 m intervals was used. Two LAI-2000 units were used to obtain simultaneous readings below and above the canopy. "Above-canopy" readings were collected automatically every 15 s in an open field within the experimental area. A view cap occluding 90^{o} of the sensor's azimuthal field of view (FOV) was used to prevent direct sunlight from reaching the sensors, and at same time occlude the operator from the FOV. During measurements the sensors were oriented so, that the FOV was always the same for the above- and below-canopy readings.

The computation of LAI was performed separately for each measurement point, and these "pointwise" estimates of LAI were averaged over the gridpoints to give plot LAI. Grid averaged estimates of LAI by the LAI-2000 ranged between 2.4 and 3.8 in the spruce stands, and between 0.26 and 2.5 in the pine stands. Grids were measured twice to check the stableness of the LAI-estimates, which was found good (difference in estimated LAI from the two measurements was typically in the order of 1- 2 %). The Scots pine stand having the LAI value 0.26 was later on dropped from the microwave analysis, because it consisted of only seed trees in a clear cutting, so that a large part of the backscattering came from the ground.

Landsat TM images revealed that the stands were so inhomogeneous, that the mean LAI values corresponding to grids located in the stands could not be taken to represent the whole stand. This is supported also by the modest correlation between the standwise mean basal area and the gridwise mean LAI value (*Figure 1*).

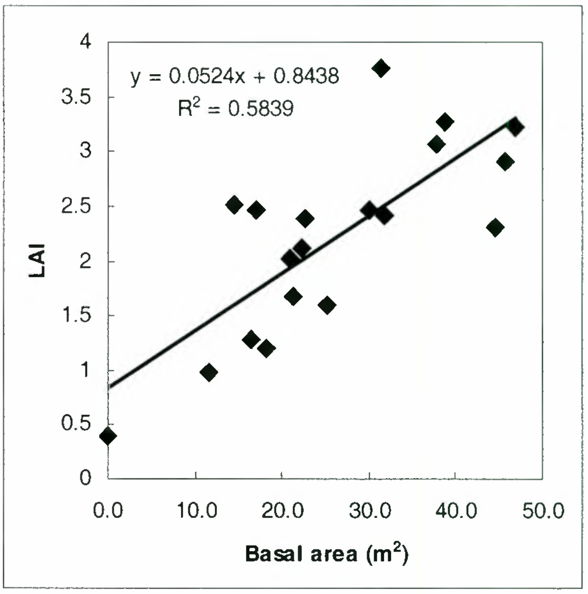

Figure 1: The relationship between the grid averaged estimates of LAI (1999) and the standwise mean values of the basal area (1997) in Tuusula.

REMOTE SENSING DATA

Since no ENVISAT ASAR data is so far available, one ERS-2 SLC image (resolution 7.9 m x 4 m) and one Radarsat Standard 1 image (resolution 25 m, pixels size 30 m) were acquired to get a first impression of using dual polarization in LAI estimation. The closest possible image pair corresponding to the time of the LAI measurements was May 25 (Radarsat) and May 29 (ERS). Due to the differences in resolution and imaging date, this radar image pair can be used only in testing the chances of ENVISAT ASAR in LAI estimation, not in producing real estimation algorithms.

When comparing the backscattered intensity and the LAI values, one has to know, how large area actually is represented by one LAI-2000 measurement. This area can be determined from the tree height and the co-ordinates of the LAI measurements. Namely the radius of the area seen by the LAI instrument is about 3.5 times the dominant tree height (LI-COR 1992).

Because most of the stands were inhomogeneous, the radar intensities to be compared with the LAI values were calculated only from the area represented by the LAI measurements (*Figure 2*). In many cases it was evident, that the LAI measurement points of the grid were so close, that the measurements were partly overlapping. Therefore a weighted mean radar intensity value was determined by using as the weight the number of the LAI points the pixel in question affected (*Figure 3*). In some cases the ERS SLC intensities contained very strong peaks or gaps often related to topographical features. Therefore the ERS weighted

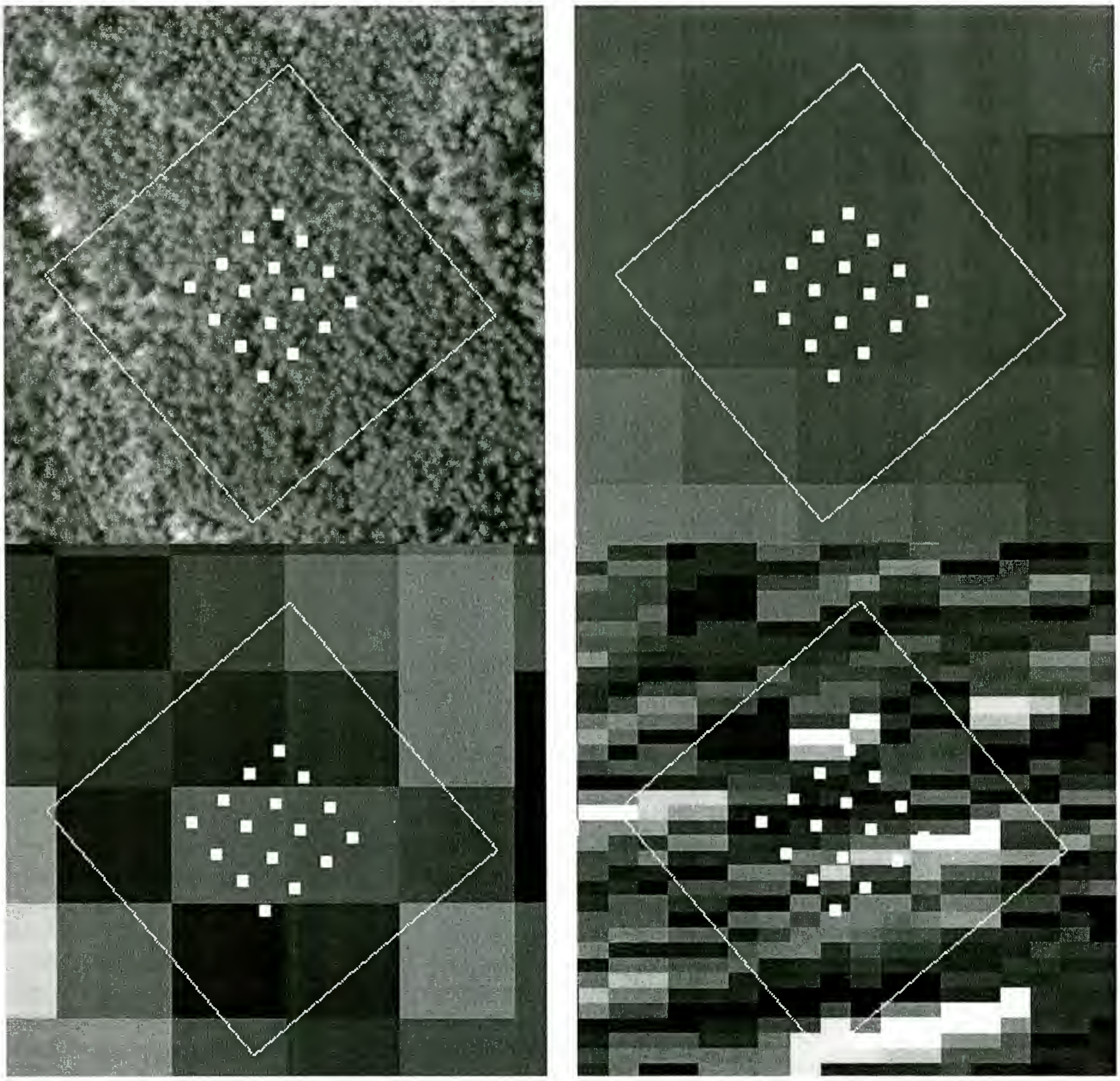

Figure 2: The LAI measurement grid and the rectangle covering the area affecting the LAI measurements of one stand. The background shows the optical mosaic (top left) Landsat TM RGB composition of channels 5, 4 and 3 (top right), intensity of Radarsat (bottom left) and intensity of ERS (bottom right).

means were calculated by dropping away 1 % of the highest and lowest values.

RESULTS AND DISCUSSION

Both SAR images used correspond to wet conditions typical of spring. This comes also evident from the weak negative relationship between the backscattered intensity and biomass (Figure 4). As expected, the weighted means produced better results than normal means. The relationship between the radar intensity and the LAI mean values is shown for Scots pine and Norway spruce in Figure 5. No strong correlation can be detected. A corresponding image for the median intensity had slightly less scatter, but the correlation remained poor. To reduce the effect of the actual intensity level, which is sensitive to the moisture content, the ratio of the weighted radar intensities was studied as well. The ratio of the weighted mean intensities of ERS and Radarsat (i.e. VV/HH) turned out to have a strong linear correlation with the LAI values of Scots pine (Figure 6). For Norway spruce no obvious relationship was found, but the difficulty was that there were only 7 Norway spruce stands, all having LAI values in the range 2.4 ... 3.8. The LAI values for Scots pine were in the range 0.4 ... 2.5. Also the stem volume values of the Norway spruce stands were all large, 282 ... 535 m^3/ha. The Scots pine stands included also young canopies and the stem volume range was 7 ... 437 m^3/ha. Considering the scarcity of the spruce data no definite conclusions about its LAI estimation using this radar intensity ratio can be drawn. Also the fact, that there

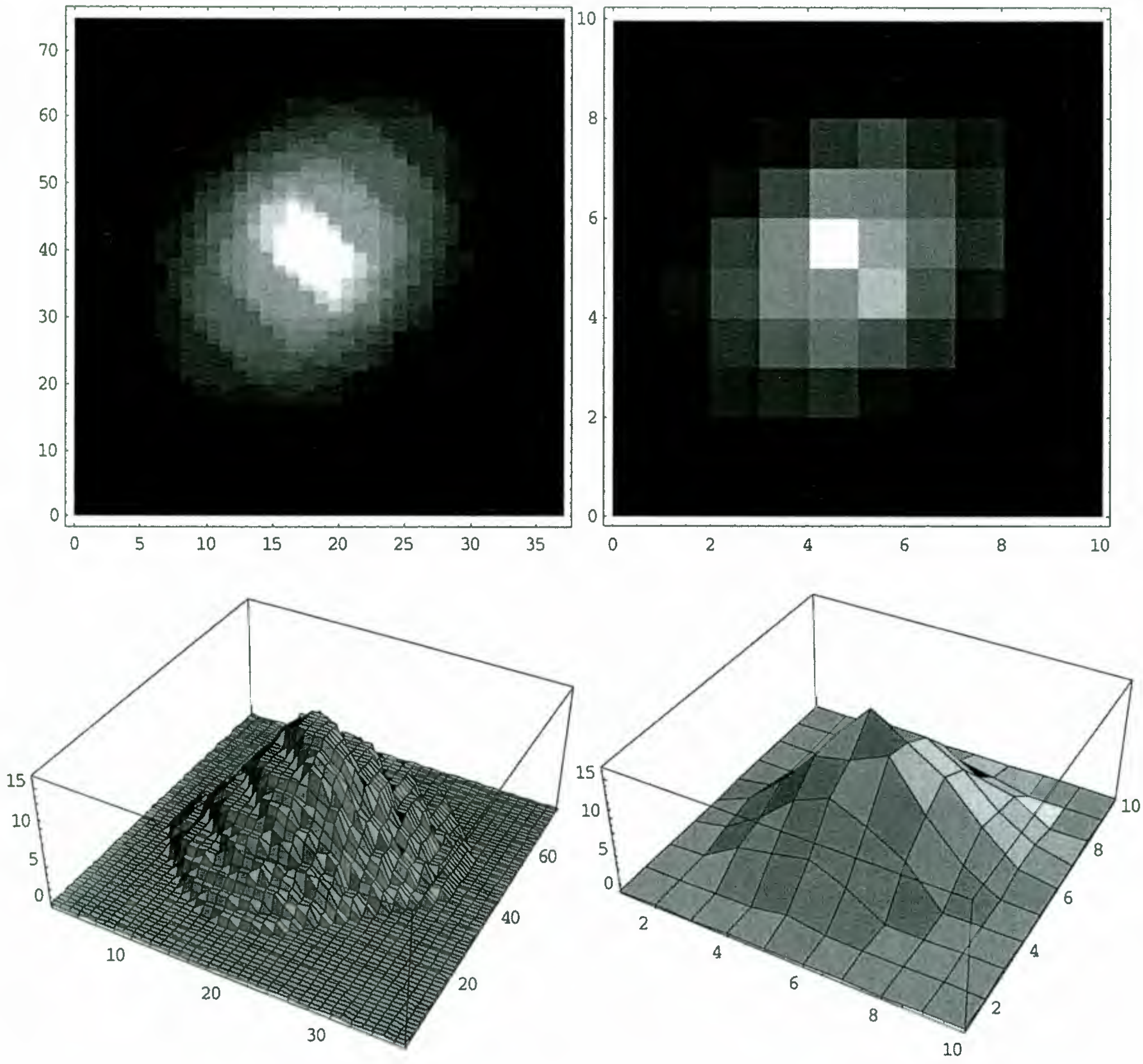

Figure 3: Example of the weights used for ERS (left) and Radarsat (right) within one rectangle covering the area affecting an LAI measurement grid.

was almost no overlap in the LAI values of the stands dominated by spruce or pine, prevents conclusions concerning the effect of species. No strong correlation with the standwise mean stem volume for either species was detected for the radar intensity ratio (Figure 7).

The observed behaviour of the ratio of the VV and HH polarisation vs. LAI is quite good for Scots pine, when one takes into account that the radar images had different resolution, different number of looks and they observed the target on different days. Moreover, the geolocation relative to each other of the two radar images certainly introduced some error, which will not appear in the use of ENVISAT ASAR data. In addition, the incidence angle used here is 23° and the difference of backscattering caused by polarisation should increase with increasing incidence angle, when more of the backscattering comes from the canopy and less from the canopy gaps. Thus the alternating polarisation possibility of ENVISAT ASAR up to the incidence angle of 45° should improve the results. With the existing data it was not possible to test the use of cross polarisation, which should be even more sensitive to the shape of the target. Whether one should prefer the cross polarisation to a like polarisation remains to be seen, when ENVISAT ASAR data will be available.

Since the LAI values represent subareas of stands and stem volumes are defined for the whole stand area, it is not possible to compare directly, which of the two parameters really has stronger correlation with the mean intensity ratio. However, the coefficient of determination for correlation of the standwise mean intensity ratio and the stem volume was negligible despite of the fact, that only single storey canopy stands were included here to reduce the scatter (Figure 7), whereas the LAI results contain also canopies of several storeys (Figure 6). Certainly the backscattering is not

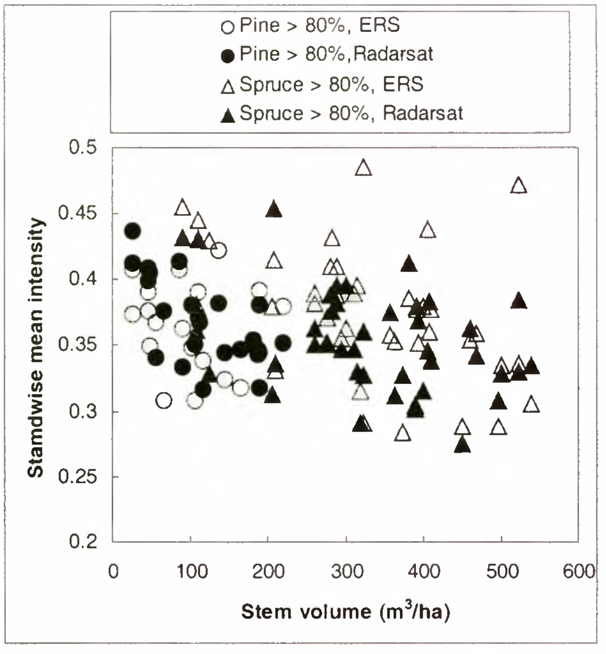

Figure 4: The standwise mean intensity of ERS (1999) and Radarsat (1999) vs. the standwise mean stem volume (1997). Although the radar images are taken almost two years after the ground truth measurements, only one growth season is between them.

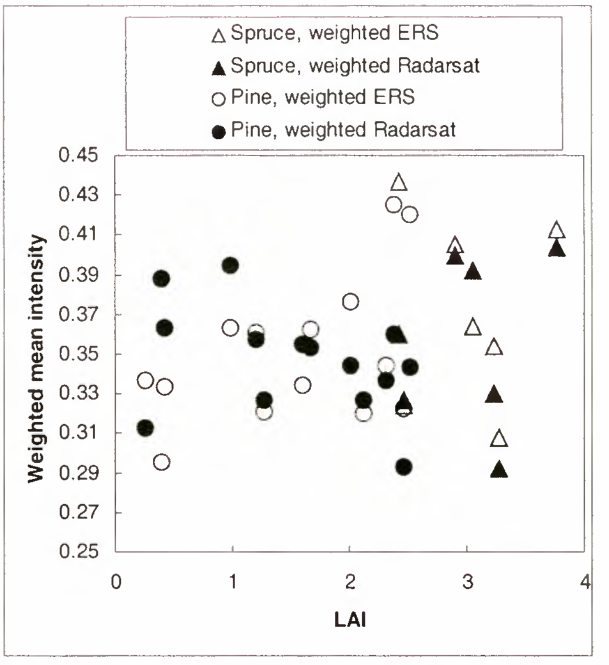

Figure 5: The weighted mean intensity of ERS and Radarsat vs. the gridwise mean LAI.

only caused by LAI, but is sensitive to many structural forest parameters of which LAI is just one. In normal conditions there is a strong correlation between LAI and other structural parameters, but in cases of diseased and dead standing trees, this correlation eventually breaks down. On the other hand, especially in the abnormal cases the LAI gives important additional information. Therefore it would be really useful to study both theoretically and experimentally the effect of reducing the LAI value without changing other forest parameters.

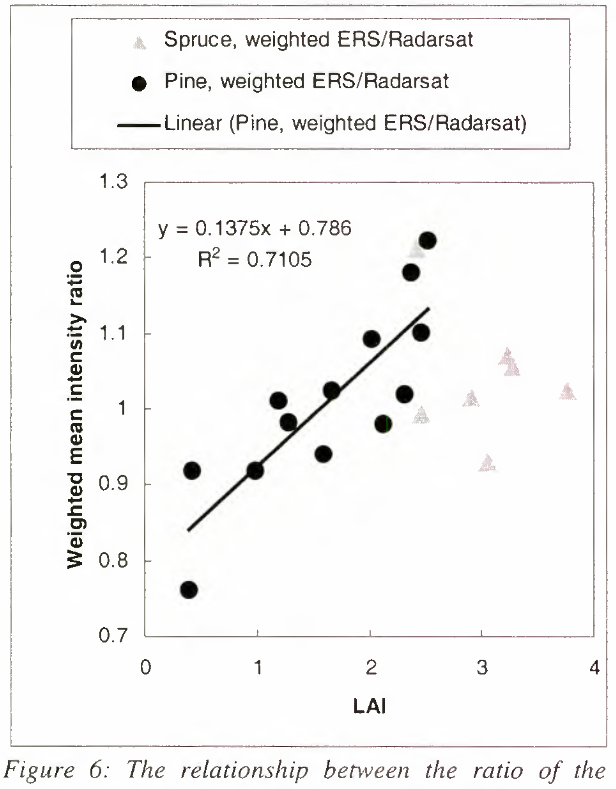

Figure 6: The relationship between the ratio of the weighted mean intensities of ERS and Radarsat and the leaf area index for Scots pine and Norway spruce.

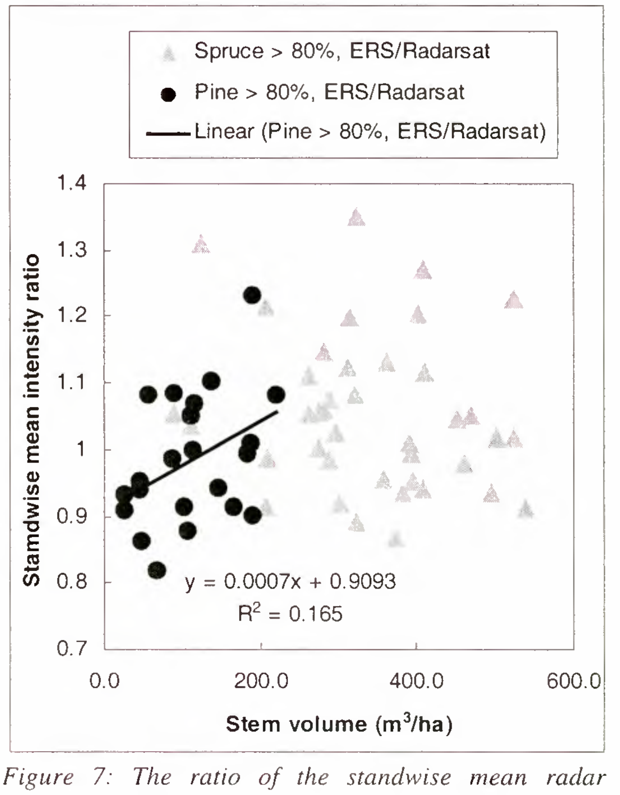

Figure 7: The ratio of the standwise mean radar intensity vs. the stem volume.

For the reciprocal backscattering case : $S_{HV} = S_{VH}$.. For extended targets such as forest stands, it is necessary to average measurements over a sufficient number of independent samples, in order to have reliable estimations. To preserve the correlation between channels during the averaging process, the polarimetric measurements have to be expressed in a way to preserve the second order moments. Polarimetric information is expressed on linear combinations arising from the Pauli matrices, allowing to define a complex vector

$$k = \frac{1}{\sqrt{2}}[S_{HH} + S_{VV} \quad S_{HH} - S_{VV} \quad 2S_{HV}]^T,$$

and then derive the coherence matrix defined as

$$T = kk^{*T}.$$

The polarimetric covariance matrix is defined as :

$$\rho_{HHVV} = \frac{\langle S_{HH} . S_{VV}^{*} \rangle}{\sqrt{\langle |S_{HH}|^2 \rangle \langle |S_{VV}|^2 \rangle}}$$

The Entropy and the mean alpha angle is derived from the eigenvalue decomposition of the averaged coherence matrix, $<T>$ [CLO 96]. The $<T>$ matrix is decomposed into :

$$\langle T \rangle = \lambda_1 e_1 e_1^{*T} + \lambda_2 e_2 e_2^{*T} + \lambda_3 e_3 e_3^{*T},$$

where λ_i and e_i are the eigenvalues and eigenvectors, which are expressed as :

$$e_i = e^{i\Phi_i} \begin{bmatrix} \cos\alpha_i \\ \sin\alpha_i . \cos\beta_i . e^{i\delta_i} \\ \sin\alpha_i . \sin\beta_i . e^{i\gamma_i} \end{bmatrix}$$

The entropy is then defined by using the eigenvalues :

$$H = \sum_{i=1}^{3} -P_i \log_3 P_i \qquad \text{with } Pi = \frac{\lambda_i}{\sum_j \lambda_j}.$$

H varies from 0 for isotropic scattering to 1 for a totally random scattering, it can be considered as an indicator of the randomness of the medium.

The average alpha angle is defined by using the eigenvalues and the eigenvectors :

$$\bar{\alpha} = P_1\alpha_1 + P_2\alpha_2 + P_3\alpha_3.$$

This mean alpha angle is an indicator of the averaged scattering mechanisms, ranging from 0° (surface scattering) to 90° (double bounce scattering), with value of 45° corresponding to dipole scattering.

IV. ESTIMATION OF THE POLARIMETRIC PARAMETERS UNDER STUDY

One of the issues encountered when measuring physical quantities is the reliability of the estimators used, especially on SAR data due to speckle. Generally the precision depends on the number of independent samples used for the estimation, then on the Equivalent Number of Look (ENL). To preserve statistical properties of the data. polarimetric quantities can be estimated in the slant geometry, and results are projected in the ground geometry. For a given stand, distribution of estimator is obtained, and the statistical properties depend on the window size (here 5*5 and 11*11) used to estimate the polarimetric measurements.

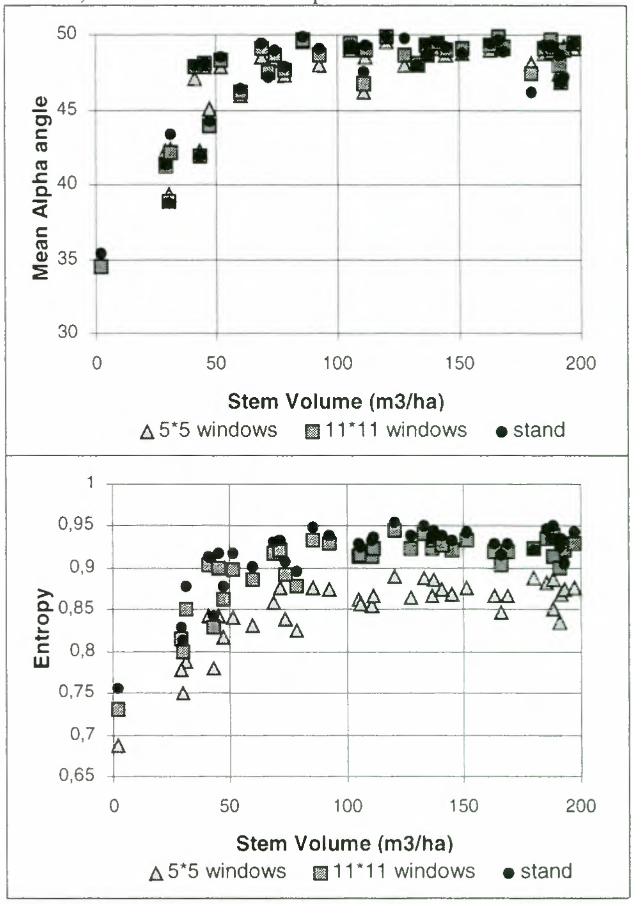

*Figure 1 : mean alpha angle and entropy as a function of forest stem volume (m^3/ha), estimated with sliding windows of 5*5 and 11*11, and on the equivalent coherence matrix of the whole stand.*

Figure 1 presents measurements obtained on the Ruokolahti site with sliding windows of 5*5, 11*11, and the value estimated on the stand average coherence matrix, for alpha angle and entropy. The variation of alpha angle as a function of ENL, similar to the backscattering coefficient estimation : increasing the number of looks does not affect the convergence to the true value, only uncertainty and the errors decrease. The estimated value of the entropy increases with the number of independent samples used to define the equivalent coherence matrix, similarly to the polarimetric coherence estimation : the estimator is biased, and the bias and uncertainty are reduced with the increase of number of looks.

Entropy and coherence biases have been assessed by applying estimators on simulated images, the statistical properties of which are chosen according to measurements obtained on the Landes SAR images.

Coherence matrix has been extracted from homogeneous stands at several growth stages by spatial averaging (maximum likelihood estimates of the covariance matrix for gaussian distributed data, [QUE95]).

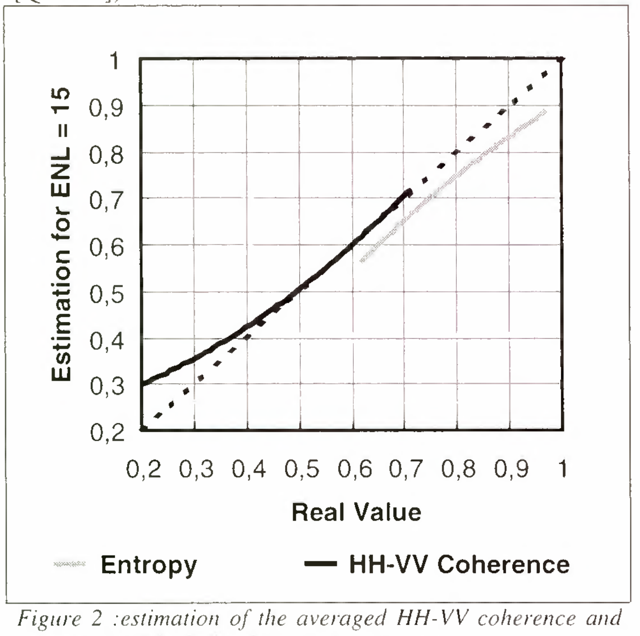

Figure 2 :estimation of the averaged HH-VV coherence and entropy for15 look simulated SAR data versus real values.

Figure 2 presents the estimation of the entropy and the HH-VV coherence on 15-look simulated SAR data versus the true value. The dynamic range of both parameters correspond to the one measured on real images over forest (i.e. 0.3-0.7 for coherence and 0.6-0.9 for entropy). Bias for HH-VV coherence appears only for values under 0.4 (over the saturation point), whereas a bias of at least 0.5 is constant in the entropy estimation in the dynamic range of interest. In the range of sensitivity of the coherence to forest biomass, the bias is negligible, which is not the case for the entropy estimation. These bias decrease with increasing ENL.

The number of look should then be increased to minimize the error, but also to ensure a negligible bias. The results shows that this constraints are satisfied with a sliding windows of 11 by 11 pixels, corresponding to an ENL around 70.

V. EXPERIMENTAL RESULTS ON THE LANDES SITE : RAMSES SAR DATA.

Sensitivity of polarimetric parameters to forest biomass is assessed using estimation based on stand boundaries. As shown in figure 1 the number of look should be high enough to avoid variation of the precision depending on the stand size. For this, only stands having a ENL larger than 100 have been considered in the analysis. Figure 3 presents the relationships between HV backscattering coefficient, HH-VV coherence, entropy, mean alpha angle and the stem volume on the Landes site.

σ°_{HV} is sensitive to volume stand up to 70-80 m^3/ha, with values increasing from around –25 dB for soil stands to –13 dB for forested stands at the saturation level. A dynamic larger than 10 dB is observed, but some dispersion occurs, especially after the saturation level.

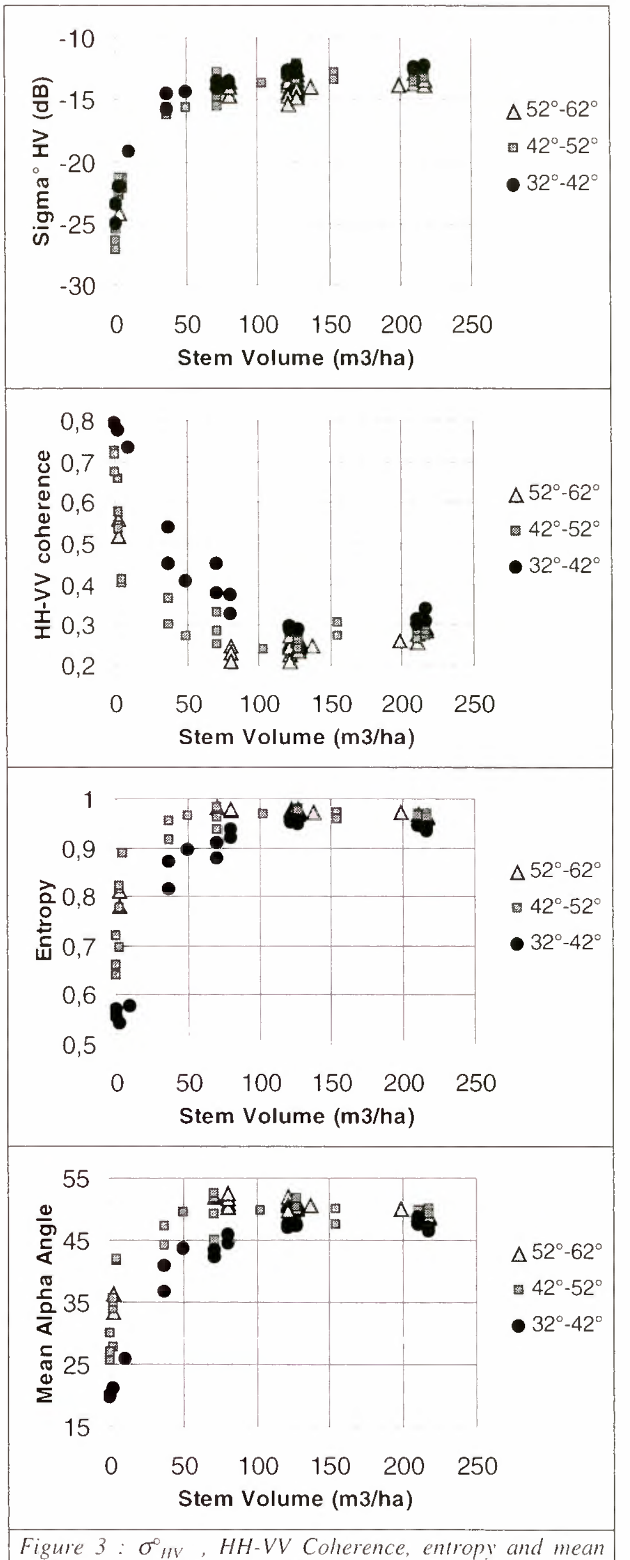

Figure 3 : σ°_{HV} , HH-VV Coherence, entropy and mean alpha angle as a function of forest stem volume (m^3/ha)

However for analysis purposes, GIS has been back-projected in the slant geometry : average coherence matrix can then be estimated for each stand, and the true value of discriminator is obtained.
The sensitivity is observed for the same range of stem volume for the polarimetric measurements in figs.4, (around 70-80 m^3/ha). The dynamic is slightly larger for coherence (decrease from 0.8 to 0.2 with stem volume) than for entropy (increase from 0.55 to 0.95). The alpha angle is ranging from 20° to 53° for increasing stem volume. However, a strong dispersion appears for all polarimetric parameters, which degrades the relationship with volume. This could be explained by natural variability of the stands, but over the Landes forest, it is mainly caused by variation in incidence angle. Figure 4 presents the variation of HH-VV coherence with incidence angle for bare stands (vegetation volume < 5 m^3/ha), and forest stands of 35, 80 and 125 m^3/ha. With increasing stem volume, the coherence as well as its sensitivity to incidence angle decreases. The loss of sensitivity is however hindered by the loss of coherence caused by the depolarization induced by the longer path in the canopy. For biomass retrieval using polarimetric measurements, the dependency in incidence angle should be considered, and low incidence angle should be preferred. The same sensitivity to incidence angle and loss of dynamic have been observed for entropy and alpha angle. Polarimetric measurements appear more adapted for forest parameter retrieval at low incidence angle.

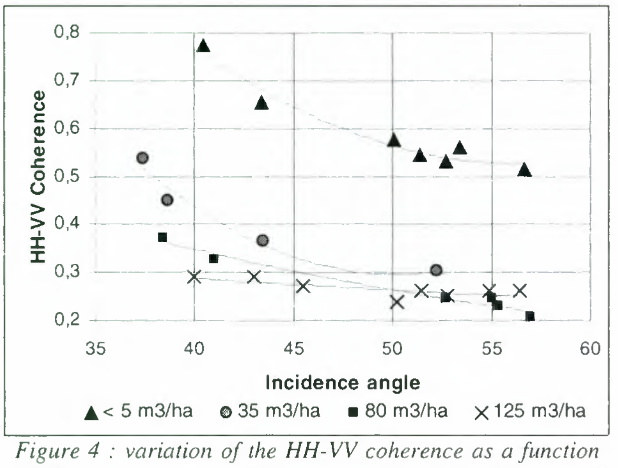

Figure 4 : variation of the HH-VV coherence as a function of the incidence angle, for soil stands and forest stands of 35, 80 and 125 m^3/ha

Finally, strong correlations between the polarimetric parameters are shown in figure 5, presenting the HH-VV coherence and entropy versus the mean alpha angle. All parameters appear strongly correlated (R^2 over 0.98). Most of the information contained in the covariance matrix lie in the diagonal terms (i.e. backscattered intensities) and in the correlation between copolarized waves : like and cross polarized responses is uncorrelated.

This analysis shows the common sensitivity range of all parameters, and the higher dynamic range provided by $\sigma°_{HV}$. Fully polarimetric data does not appear to provide important additional information content, but may be robust to some disturbances present in natural forest.
We propose in the following to compare the sensitivity observed on a plantation with the case of a natural forest

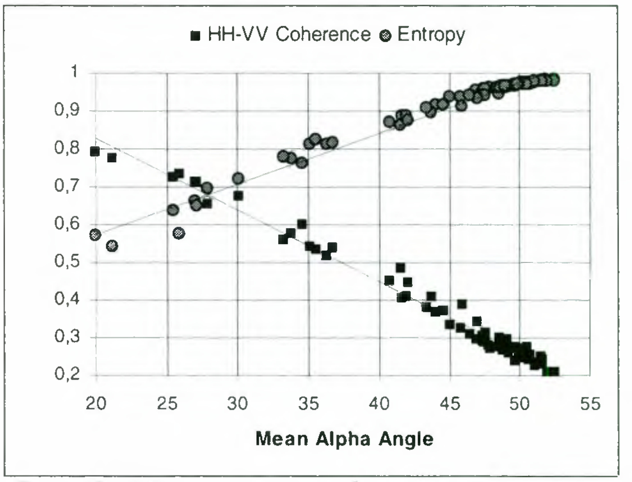

Figure 5 : HH-VV coherence and entropy as a function of mean alpha angle for the Landes site dataset

VI. COMPARISON BETWEEN PLANTATION AND NATURAL FOREST.

The figure 6 shows the comparison of $\sigma°_{HV}$, HH-VV coherence, entropy and mean alpha angle versus stem volume for the Landes plantation and the natural Ruokolahti forest. The first observation is the sensitivity of all measurements to volume is observed up to around 60 m^3/ha. Secondly there are more dispersion in the data points in the natural forest. Finally a reduced dynamic range is observed for every parameters concerning the ESAR data over the Ruokolahti site compared to RAMSES data over the Landes site. This can be caused by differences between the SAR systems, such as noise level or calibration errors, by uncertainties in ground data for the two test sites, but also by disturbances induced by natural variability occurring in the Ruokolahti site. This impact of disturbances appears when analyzing the dependency on the incidence angle, for which a high dispersion appear, caused by natural variation.
For instance concerning low volume stands, bare stands are generally covered by low vegetation layers in Ruokolahti, creating depolarization and volume scattering, inducing increase of cross-polarization and loss of coherence for low forest volume classes.
In the following, stands of Scots pine are analysed as regard the main perturbing effects.

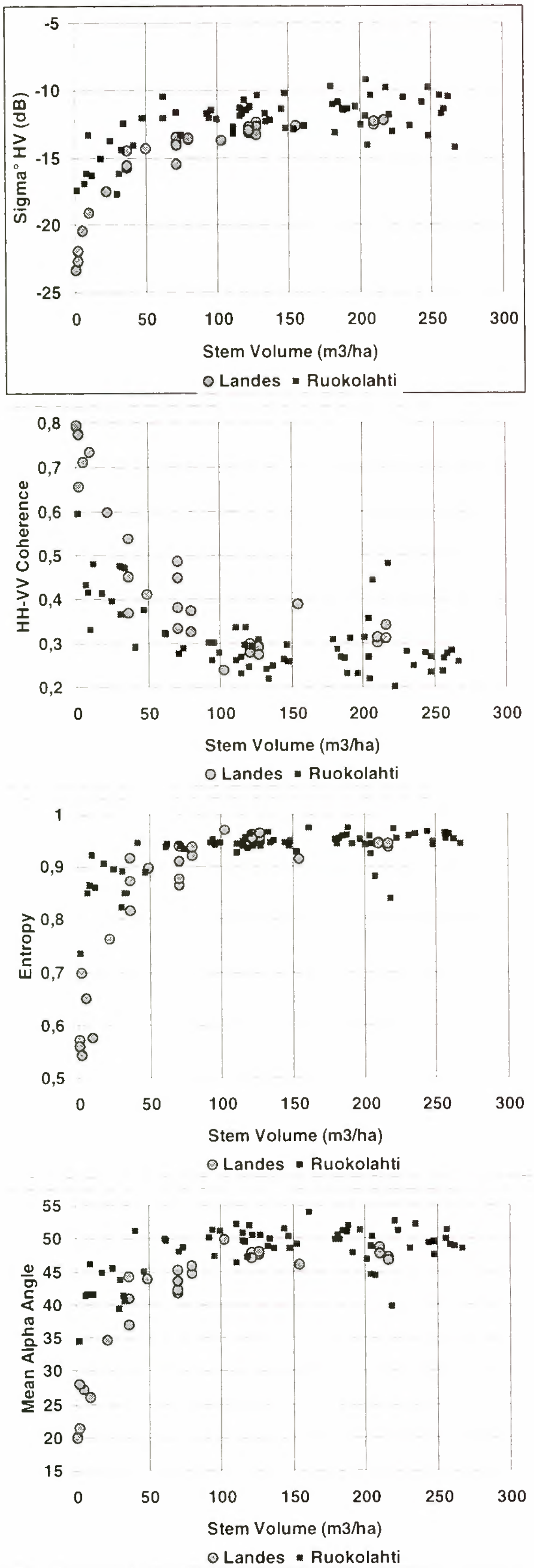

Figure 6 : comparison between the Landes forest and the Ruokolahti site of $\sigma°_{HV}$, HH-VV coherence, entropy and mean alpha angle as a function of forest stem volume (m^3/ha

a) Effect of Soil type

Stands with peat soil and common soil are compared. Despite the small number of peat soil stands at low biomass, the analysis shows a reduced sensitivity to biomass for all polarimetric measurements. The loss of sensitivity (fig. 7) is caused by the volume scattering which occurs over the peat soil. From the polarimetric point of view, there are small differences between mature forest and young forest on peatland.

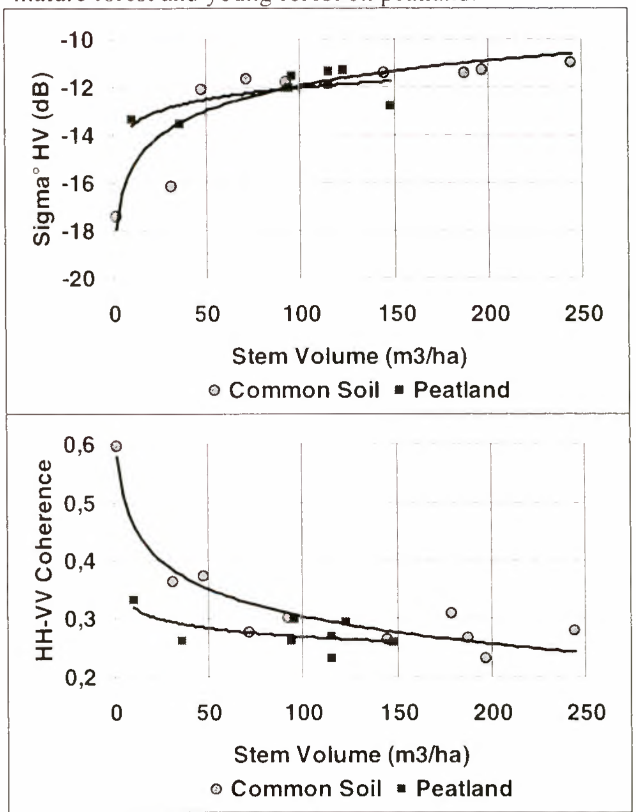

Figure 7 : comparison of measurements forest stands on common soil and on peatland.

Analysis of the co-polarized backscattering coefficient showed that $\sigma°_{HH}$ and $\sigma°_{VV}$ were less affected, and thus have to be considered for forest parameter retrieval purposes in case of peat soil.

a) Effect of Slope

Figure 8 presents the comparison of stands with slope under and over 8°. The slope seems to affect all polarimetric parameters under study, mainly by decreasing their sensitivity and by reducing their dynamic range (especially for entropy and mean alpha angle). $\sigma°_{HV}$ and the HH-VV coherence seem less affected, but dispersion of the data is high.

The changes of surface orientation and tilting induce changes in physical interaction mechanisms [LEE 00]. However volume scattering caused by the canopy does not drastically change for the slope range considered, which explains the reduced impact on $\sigma°_{HV}$. The polarimetric coherence is more affected through variation of ground coherence than by change in vegetation contribution. e.g. for entropy and alpha angle, which are dependent of all terms of the scattering matrix. On the other hand, the comparison with results obtained for $\sigma°_{HH}$ and $\sigma°_{VV}$ showed that polarimetric coherence is less affected by slope than $\sigma°_{HV}$.

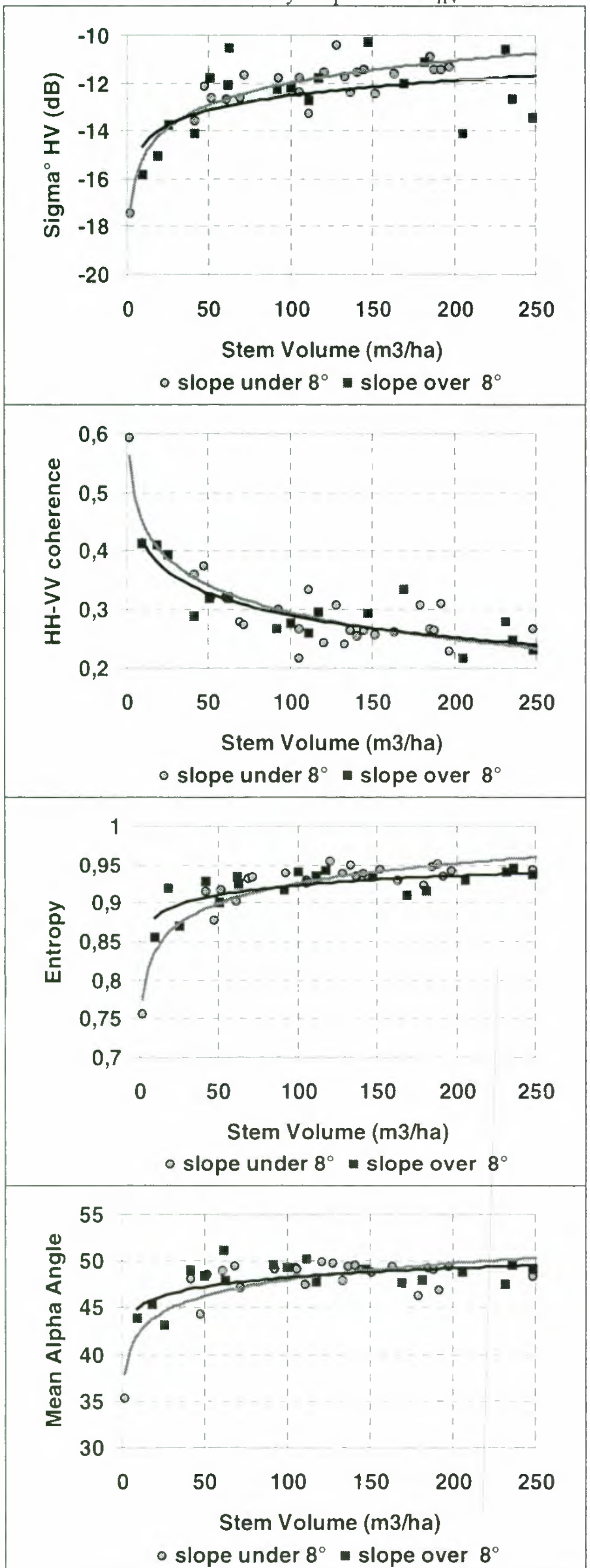

Figure 8 : comparison of measurements between flat stands (slope under 8°) and sloped stands.

VII. CONCLUDING REMARKS.

The analysis of L-band polarimetric data over one plantation and one natural forest pointed out the following. The results obtained on the plantation forest showed that all polarimetric discriminators have similar sensitivity range to forest volume, as compared to backscattering coefficients. The dependency of the relationships to the incidence angle must be integrated in retrieval algorithm using airborne data . For spaceborne SARs, low incidence angle provides higher dynamic range of the polarimetric measurements.

For classification purposes, numerous studies have shown the advantages of integrating all information derived from polarimetric decomposition. However for forest parameter retrieval, polarimetric estimators appears highly correlated, and are affected by every type of disturbances. From the analysis, combinations of backscattering coefficients and HH-VV polarimetric coherence appear to provide several schemes of robust parameter retrieval algorithms, depending on the disturbing effect affecting the measurements.

BIBLIOGRAPHY

[TOA 92] Le Toan T., Beaudoin A.,Riom J., Guyon D. "Relating Forest Biomass to SAR data", *IEEE Transactions on Geoscience and Remote Sensing*, Vol. 30, No 2, pp 403-411, 1992

[DOB 92] Dobson M. C., Ulaby F. T., Le Toan T., Beaudoin A., Kasischke E. S., Christensen N. L., "Dependence of radar backscatter on coniferous forest biomass", *IEEE Transactions on Geoscience and Remote Sensing*, Vol. 30, No 2, pp 412-415, 1992

[SOU 96] J.C. Souyris, T. Le Toan, N. Floury, C. Hsu, L. Wang, J.A. Kong Microwave Remote Sensing of Natural Targets: Theory and Experiment, AGARD SPP Symposium on « Remote Sensing : A valuable Source of Information », 1996.

[CLO 96] Cloude S.R., Pottier E., "A reviews of target decomposition theorems in radar polarimetry", *IEEE Transactions on Geoscience and Remote Sensing*, Vol 34, No 2, pp 498-518, March 1996.

[QUE 95] Quegan S., Rhodes I. "Statistical models for polarimetric data : consequences, testing and validity", *International Journal of Remote Sensing*, Vol. 16, pp 1183-1210, 1995.

[LEE 00] J. Lee, D.L. Schuler, T.L. Ainsworth, Polarimetric SAR Data Compensation for Terrain Azimuth Slope Variation, IEEE Transactions on Geoscience and Remote Sensing, vol. 5, pp. 2153-2163, sept. 2000.

THE APPLICABILITY OF C-BAND SAR AND OPTICAL DATA FOR SNOW MONITORING IN BOREAL FOREST

S. Metsämäki, J. Vepsäläinen, J. Pulliainen*, J. Koskinen, M. Huttunen, M. Hallikainen*
Finnish Environment Institute
P.O. Box 140, FIN-00251 Helsinki, FINLAND
Tel: +358-9-40300646 Fax : +358-9-40300691 Email : sari.metsamaki@vyh.fi
*Helsinki University of Technology, Laboratory of Space Technology

ABSTRACT- Optical remotely sensed data is used operationally to map snow extent in several countries. Also space-borne SARs have shown their usefulness in estimation of Snow Covered Area (SCA) under wet snow conditions, i.e. in the spring melt period. However, in boreal forest zone, forest cover deteriorates the accuracy of present empirical algorithms. These algorithms are typically based on pixel-wise or region-wise linear interpolation between reference images representing total (wet) snow cover and totally melt-off conditions.

This paper presents two approaches to estimate regional SCA in forested areas 1) linear interpolation method for SAR data using backscattering model to compensate the influence of forest canopy and 2) inversion of empirical reflectance model for optical data (first implemented for NOAA/AVHRR). The SCA estimates are calculated for third class sub-drainage areas used by an operative hydrological model (The Watershed Simulation and Forecasting System, WSFS). The average size of sub-areas is 60 km^2. For SAR-data, the SCA estimation algorithm, as well as the validity of the employed model, is tested for the River Kemijoki drainage area in Northern Finland. For AVHRR-data, the estimates are performed and validated for all drainage basins of Finland. The SCA estimates from both methods are compared with ground observations. In addition, AVHRR-estimates are compared to predictions produced by the WSFS.

For SAR-method, the preliminary results show that, in contrast to commonly used linear interpolation algorithms, the developed algorithm typically yields higher values of SCA for forested areas than for open areas, which is in agreement with natural snow melt process. Moreover, comparison of SAR-derived and AVHRR-derived SCA estimates shows the potential of synergetic use of both data.

I. INTRODUCTION

Estimation of Snow Covered Area (SCA) during the spring melt period is important for various hydrological and meteorological forecasting applications, including such operative end-use tasks as flood prevention and optimization of hydropower production. Regional SCA is an essential state variable in hydrological models used for forecasting the run-off in a sub-catchment scale. Hydrological models have difficulties in the estimation of rapid changes in SCA and, therefore, the estimation of run-off can be highly erroneous.

Space-borne SARs have shown their usefulness in SCA estimation under the spring melt period [1]-[3]. Even single-channel systems, such as the C-band ERS-2 SAR, have found to be useful. However, in the boreal forest zone, the forest cover deteriorates the accuracy of present empirical algorithms as the level of backscatter and the transmission through the forest canopy significantly change with time depending on weather conditions. As well, the accuracies of algorithms are affected by the temporal changes of snow wetness and snow grain size/surface roughness of (wet) snowpack. The empirical SCA-estimation algorithms are typically based on pixel-wise or region-wise linear interpolation between reference images representing 100% (wet) snow cover and snow-free conditions. This paper introduces an adaptive inversion algorithm to estimate regional SCA in forested areas. The developed algorithm estimates, for the given radar observation, the magnitude of backscatter and attenuation caused by forest canopy and then calculates the backscattering from ground layer. SCA is estimated from this backscattering coefficient using linear interpolation techniques [2].

The general behavior of visible and near-infrared reflectance of snow is rather well known [4]-[6]. The highest values are observed from pure dry snow at visible wavelengths. The reflectance decreases as snow ages, mainly due to the impurities and growing grain size, related to snow wetness. At near-infrared region, reflectance is almost as high, but the decrease caused by the growing grain size is more distinct. Other natural objects, on the other hand, have clearly lower reflectance at both visible and near-infrared regions. With remote sensing data, several ground objects contribute to observed reflectance within a pixel: snow, bare ground, vegetation etc. Therefore, the observed reflectances change according to regional proportions of these. With full snow cover, highest reflectances are observed, but they gradually decrease as snow disappears. By monitoring this decrease, the regional

Proc. 3rd International Symposium, 'Retrieval of Bio- and Geophysical Parameters from SAR Data for Land Applications', Sheffield, UK, 11-14 September 2001 (ESA SP-475, January 2002)

fraction of Snow Covered Area (SCA) can be estimated. However, forest canopy reduces the signal from the ground and snow underneath. Therefore, we estimate here the SCA by applying an empirical reflectance model that includes different contributors to reflectance, including the forest transmissivity as an important factor.

II. TEST SITE AND MATERIAL

For SAR-method, the performance of the SCA estimation algorithm, as well as the validity of the employed forest transmissivity and backscattering model, is tested for the River Kemijoki drainage basin, Northern Finland (see Fig. 1). Time series of ERS-2 SAR-images together with ground truth data for eight weather stations representing the winter/spring periods of years -97 and 2000 are employed in the validation. The available reference data includes the weather station observed temperature information, snow depth information, precipitation information, and SCA information. Additionally, the backscattering model uses digital land cover and forest classification data with a 25 m spatial resolution.

For optical data, the method development and the validation of SCA-estimates was performed for a comprehensive network of weather stations (53) and snow courses (165) over the area of Finland.

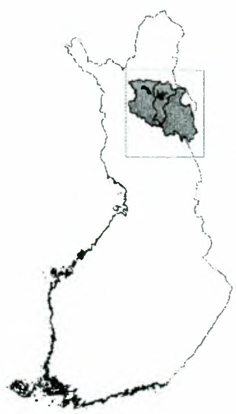

Fig. 1. The location of River Kemijoki drainage basin.

III. METHODOLOGY

A. ERS-2 SAR

The forest backscattering model-aided method to estimate SCA during spring-melt period was first introduced in [7]. It is based on the use of the semi-empirical HUT model that describes the C-band ERS-2 SAR observations ($\sigma°$) of conifer-dominated boreal forests as a function of total stem volume [8]:

$$\sigma°(V,\chi) = \sigma°_{surf} \cdot \exp\left(\frac{-2\kappa_e(A(\chi))\cdot V}{\cos\theta}\right) + \frac{\sigma_V(B(\chi))\cos\theta}{2\kappa_e(A(\chi))}\left[1-\exp\left(\frac{-2\kappa_e(A(\chi))\cdot V}{\cos\theta}\right)\right]$$

$$\equiv \sigma°_{surf} \cdot t(V,\chi)^2 + \sigma°_{can}(V,\chi) \qquad (1)$$

where V is the forest stem volume [m^3/ha] and χ is a scalar variable that defines, through the empirical relations A and B, the levels of (a) the canopy extinction coefficient κ_e [1/m^3/ha] and (b) the forest canopy volume backscattering coefficient σ_V [1/m^3/ha]. $\sigma°_{surf}$ is the backscattering coefficient of snow covered or snow-free terrain and θ is the angle of incidence. The first term of (1) defines the backscattering contribution of the ground and/or snow surface layer $\sigma°_{surf}$, and additionally, the two-way transmissivity through the forest canopy t^2. The second term $\sigma°_{can}$ defines the forest canopy backscattering contribution.

The value of χ in (1) is dependent on the water content and frost status of forest canopy. Applying cloud model for volume scattering and experimental data from [5], the following expressions for describing κ_e and σ_V under varying conditions are obtained:

$$\kappa_e(A(\chi)) = a_0 \cdot \chi \qquad (2)$$

$$\sigma_V(B(\chi)) = b_0 \cdot \chi^2 \qquad (3)$$

where constant coefficients $a_0 = 2.78 \cdot 10^{-3}$ ha/m^3 and $b_0 = 9.99 \cdot 10^{-4}$ ha/m^3. The values of κ_e and σ_V correspond to dry summer conditions as $\chi = 1$ (values originally determined from HUTSCAT airborne ranging scatterometer data [9]).

For partially snow covered ground, the average backscattering coefficient of forests, representing a certain stem volume class V_i inside the region under investigation, can be given as a function of SCA fraction:

$$\sigma°(V_i,\chi,SCA) = \sigma°_{surf}(SCA)\cdot t(V_i,\chi)^2 + \sigma°_{can}(V_i,\chi)$$

$$= \left[SCA\cdot\sigma°_{snow} + (1-SCA)\cdot\sigma°_{ground}\right]\cdot t(V_i,\chi)^2 + \sigma°_{can}(V_i,\chi) \qquad (4)$$

where $\sigma°_{snow}$ is the backscattering coefficient of snow covered ground, and is $\sigma°_{ground}$ is that of the snow-free ground surface, respectively.

The developed SCA estimation algorithm is based on non-linear fitting of the backscattering model given by (1) – (4) to single-temporal SAR observations, with $\sigma°_{surf}$(SCA) and the scalar variable χ as two parameters to be optimized. The fitting of the model to SAR observations requires that average backscattering coefficients for various stem volume classes have to be calculated for each individual region under investigation. The algorithm also requires the use of two reference images representing 100% wet snow cover and totally snow-free conditions. The algorithm can be stated as a two step process:

(a) Estimation of χ and the level of backscatter from snow/ground surface layer σ°_{surf} by a non-linear minimization procedure for each region (drainage basin sub-are) of a single image.

As the backscattering coefficient modeled by (1) - (4) is denoted by σ° we can write the minimization problem as:

$$\min_{\chi,\sigma^{\circ}_{surf}} \sum_{i=1}^{N} w_i \cdot \left(\langle \sigma^{\circ}_{OBSERVED,i} \rangle - \sigma^{\circ}(V_i, \chi, \sigma^{\circ}_{surf}) \right)^2 \tag{5}$$

where N is the number of forest stem volume classes and $\langle \sigma^{\circ}_{OBSERVED,i} \rangle$ is the observed mean backscattering coefficient for the stem volume class V_i in the region under investigation. Additionally, if the areal coverage of different stem volume classes varies considerably within the region, an areal weighing factor w_i has to be included in (5).

(b) Determination of SCA separately for each region based on the estimated level of σ°_{surf}.

Applying the estimate of snow/ground backscatter $\bar{\sigma}^{\circ}_{surf}$ obtained by (5), it is a straight forward problem to calculate the estimate for SCA (as two reference images are available, the other representing 100% wet snow cover and the other snow-free (melt-off) conditions). Based on (4), the average SCA for stem volume classes $V_1 \ldots V_N$ is

$$SCA = \frac{\bar{\sigma}^{\circ}_{surf} - \sigma^{\circ}_{groundref}}{\sigma^{\circ}_{snowref} - \sigma^{\circ}_{groundref}} \tag{6}$$

where $\sigma^{\circ}_{ground,ref}$ is the reference value for the backscatter from snow free ground surface layer and $\sigma^{\circ}_{snow,ref}$ is the reference value for the wet snow covered surface, respectively. They are both determined by applying the minimization procedure (5) to the reference images.

B. NOAA AVHRR

For optical data, the estimation of SCA is accomplished by applying an empirical reflectance model where SCA is included to describe the relative proportion of the radiative contributors underneath the forest canopy. In the model, the reflectance from the target is expressed as a function of forest canopy transmissivity and generally applicable reflectance values for wet snow, snow-free ground and forest canopy, as follows [10]:

$$\rho(SCA) = (1-t^2) * \rho_{forest} + t^2 \left[SCA * \rho_{snow} + (1-SCA) * \rho_{ground} \right] \tag{7}$$

where ρ_{snow}, ρ_{ground} and ρ_{forest} are the reflectances for wet snow, snow-free ground and forest canopy, respectively. $\rho(SCA)$ stands for observed reflectance at specific snow conditions, that is, for a specific value of SCA. The value for forest transmissivity t is characteristic for each calculation area, i.e. drainage basin in this case. It describes how much of the upwelling radiance is originated underneath the forest canopy. With full snow cover (SCA=100%), a simple expression for t^2 is obtained from (7):

$$t^2 = \frac{\rho(SCA = 100\%) - \rho_{forest}}{\rho_{snow} - \rho_{forest}} \tag{8}$$

For each drainage basin i, the forest canopy transmissivity was estimated by an apparent regional transmissivity $\hat{t}^2_i$. $\hat{t}^2_i$ was obtained from AVHRR mosaic, which is produced from images at the full cover dry snow period (SCA=100%) from the years 1999 and 2000. An average reflectance for each drainage basin, $\rho_{mean,i}$, was calculated from the mosaic, with water areas excluded. In non-vegetated or scrub land areas, found only in Northern Finland, this average is close to the value of plain snow, ρ_{snow}, while in the other parts of Finland, lower reflectances are observed due to the contribution of forest canopy. Assuming the consistent reflectance of dry snow throughout the study area, the proportion of forest canopy can be estimated using the observed reflectances. During melting season, this proportion remains, while the relative fractions of the other radiative contributors, snow and ground, are changing. The apparent transmissivity $\hat{t}^2_i$ is obtained from (8):

$$\hat{t}^2_i = \frac{\rho_{mean,i} - \rho_{forest}}{\rho_{snow} - \rho_{forest}} \tag{9}$$

Formula (9) yields a low transmissivity for areas with dense forests and high transmissivity for totally open areas.

After determining the apparent transmissivity $\hat{t}^2_i$ for each drainage basin, the value of SCA during the melting season is calculated by inverting (7), as follows:

$$SCA_i = \frac{\frac{1}{\hat{t}^2_i} * \rho(SCA) + (1 - \frac{1}{\hat{t}^2_i}) * \rho_{forest} - \rho_{ground}}{\rho_{snow} - \rho_{ground}} \tag{10}$$

In this study, valid values for ρ_{snow}, ρ_{ground} and ρ_{forest} were derived from AVHRR dataset by selecting the representative areas, using The National Land Use and Forest Map of Finland [11] as a reference. Note that in (10), ρ_{snow} refers to wet snow, explicitly. For wet snow and bare ground, the representativeness of AVHRR data is validated with *in situ* snow data from weather stations and snow courses. The values are listed in Table I.

Table I. Reflectance values (%) for snow, snow-free ground and forest canopy.

	$\rho_{snow\ dry(wet)}$	ρ_{ground}	ρ_{forest}
VIS	92 (87)	4.5	2.0
NIR	87 (73)	13.0	11.8

At the very end of the melting season, the appearance of seasonal vegetation increases the observed reflectance, easily leading to overestimations of SCA. This is considered by employing a particular threshold rule for normalized difference vegetation index (NDVI), calculated from the AVHRR observations. With this rule, areas with high NDVI are automatically classified as snow-free.

IV. SAR RESULTS

A. Behavior of Backscatter and Model Performance

The C-band backscattering coefficient observed by a space-borne SAR is highly sensitive to changes in snow conditions. A typical example is depicted in Fig. 2, which shows the evolution of $\sigma°$ for the region around the Savukoski weather station in the spring of 1997. The level of $\sigma°$ is high during dry snow and snow-free conditions, but low during wet snow or partially melt-off conditions. The correlation of $\sigma°$ to stem volume changes from positive to negative depending on conditions.

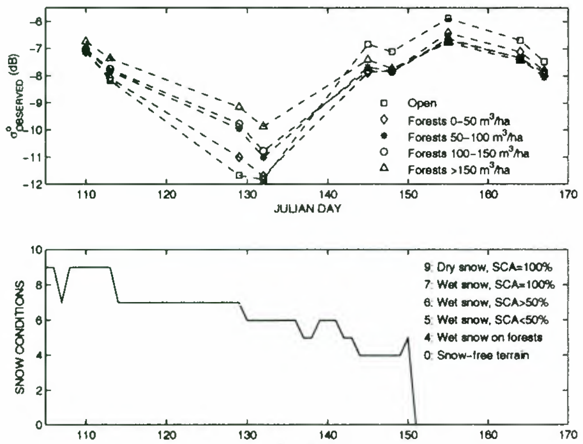

Fig.2. Behavior of ERS-2 SAR-derived $\sigma°$ at the vicinity of the Savukoski weather station for the spring -97. The diurnal weather station observed snow conditions information is shown for comparison.

Fig. 3 shows the modeled backscattering coefficient $\sigma°$ as a function of forest stem volume, together with the observed mean $\sigma°$-values of different stem volume classes. The depicted case is the 1997 Savukoski observations, i.e. the same observations as those shown in Fig. 2. The model-based $\sigma°$-curves are obtained by fitting the backscattering model (1) – (3) into SAR-data according to the non-linear procedure (5) with two variables χ and $\sigma°_{surf}$ as parameters to be optimized. The fitting procedure is carried out using observations from four stem volume classes, excluding observations from unforested areas (N = 4).

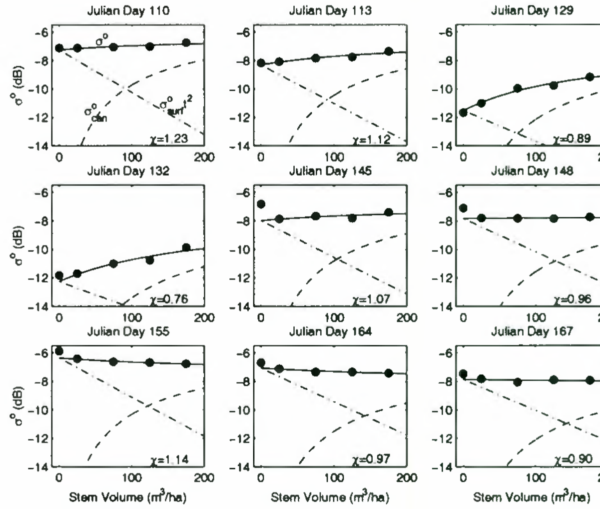

Fig.3. Fitting of the backscattering model (1) – (3) into stem volume class-wise averaged $\sigma°$-values for the Savukoski weather station (corresponding to Fig. 2). The fitting is performed by (5) for four stem volume classes with V > 0 m^3/ha. ($\sigma°$-values for open areas are also depicted but they were not included in model fitting). Dotted lines show the estimated behavior of different backscattering contributions.

B. SCA Estimation Results

The algorithm testing is carried out by determining separate estimates of SCA for forested and non-forested areas. Both estimates are determined according to (6). Fig. 4 shows an example of SCA estimation results for the Savukoski site. The improvement obtained by using the adaptive forest canopy correction (5) is directly indicated, as the estimates according to linear interpolation algorithm (without forest canopy correction) are also shown. Fig. 4 also present the evolution of weather station-observed SCA for comparison. Fig. 4 demonstrates that the employment of adaptive forest canopy correction produces higher estimated values of SCA for forested areas than the linear interpolation algorithm (the same applies for all investigated cases from the years 1997 and 2000). The SCA estimates obtained by linear interpolation for forested areas are evidently incorrect as they show lower values than those obtained by linear interpolation for open areas (the snow always melts-off first from open areas, and therefore, SCA should be higher for forests than for open areas). Thus, it can be concluded that the correction obtained by using the adaptive algorithm improves the quality of SCA estimates.

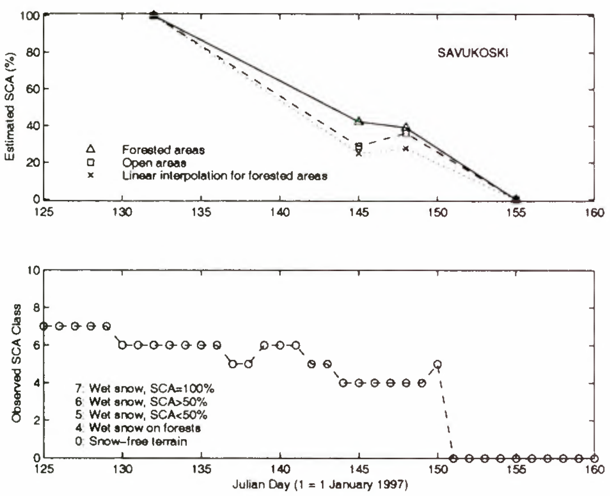

Fig. 4. SCA estimation results of the Savukoski weather station for the snow melt period of 1997 including comparison with weather station-observed snow conditions.

V. NOAA AVHRR RESULTS

The SCA estimates are compared to observations provided by 4 km-long snow courses and weather stations. In addition, the estimates were compared with calculations of the operative hydrological model (WSFS).

Image data with only a limited set of viewing geometries has been employed in method testing. Data with view zenith angle $2_v < 30^{\circ}$ for both forward and backward scattering directions have been accepted (NOAA-14 and NOAA-15).

Generally, SCA estimates accord well with the ground observations. The results are presented in Table II. The best results are achieved for full snow cover and for completely snow-free situations. At partial snow cover conditions, the shortage of field data hampers the validation. However, only the results with snow category 'partial snow cover, SCA<50%' contains considerable number of underestimations.

Table II. Comparison between daily observations at weather stations and snow courses and the SCA-estimates from AVHRR-data (SCA_{AVHRR}). Agreement is presented for categories of SCA_{AVHRR}.

Snow data from weather station	Mean of SCA_{AVHRR}	Agreement (%)	N (492)
Snow-free (SCA=0%)	1.2%	92.5	202
Full snow cover (SCA=100%)	100%	96.3	216
Partial snow cover (SCA>50%)	74.5%	75.7	37
Partial snow cover (SCA<50%)	18%	37.8	37

In addition to the data from weather stations, SCA estimates were compared to the values of SCA produced by the hydrological model (WSFS). In Fig. 5, time series for SCA from AVHRR as well as WSFS for a drainage basin is presented. According to the Figure 5, WSFS gives higher values throughout the melting season. Figure 6, on the other hand, indicates that for another basin, WSFS gives too low values when compared with both AVHRR-derived SCA and weather station data. In general, the hydrological model calculations and SCA estimates agree well with each other, which is a promising result regarding the usability of remote sensing data-based estimates as input to hydrological models.

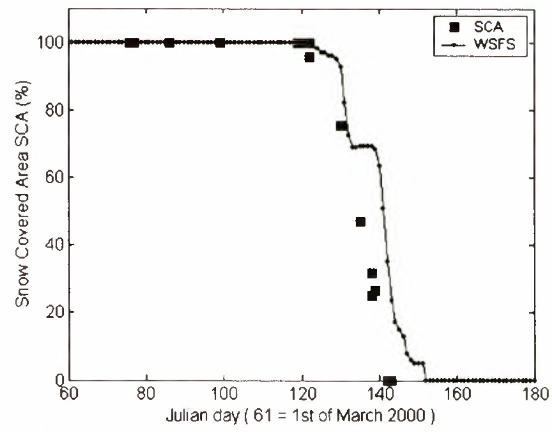

Fig. 5. Estimates of SCA from hydrological model (WSFS) and AVHRR for a drainage basin.

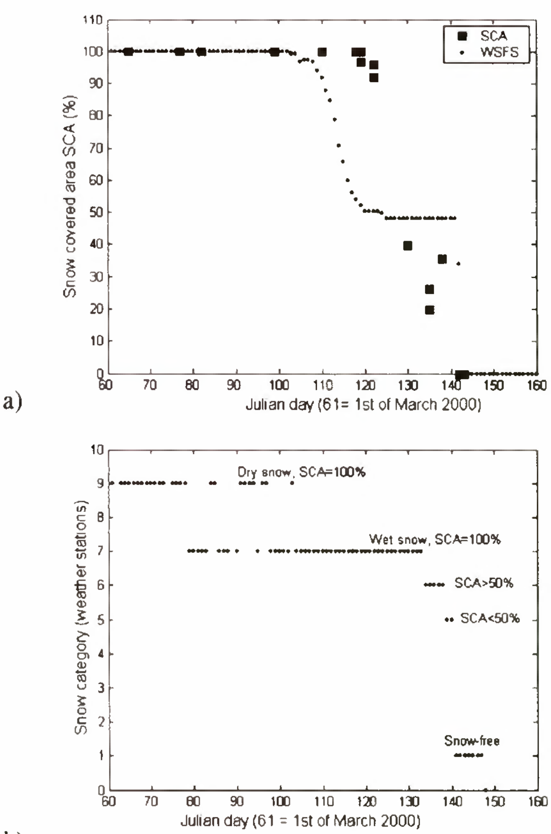

Fig. 6. a) Estimates of SCA from hydrological model (WSFS) and AVHRR for a drainage basin b) information on snow cover from the weather station

VI. COMPARISON OF RESULTS FROM SAR AND OPTICAL DATA

The preliminary comparison between AVHRR-derived SCA-estimate and ERS-2 SAR derived SCA estimate is performed for a single day May 14, 2000. Although SAR data were originally processed to 100 m × 100 m resolution, the results are averaged for each sub-drainage basin, to be comparable with AVHRR estimates. Both SCA estimates included the novel processing methods explained in Chapter III. The comparison in Fig. 7 shows a considerable correspondence between AVHRR and SAR estimates.

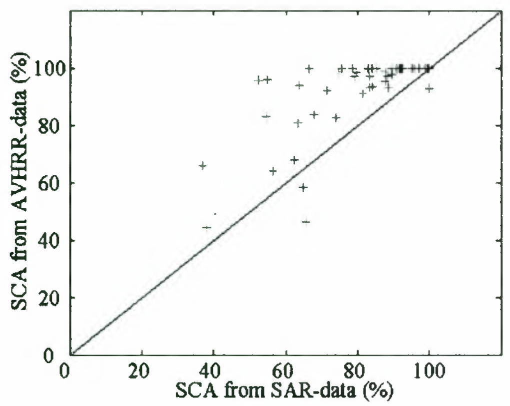

Fig 7. Estimates for SCA derived from AVHRR-data and SAR-data, on the 14th May, 2000.

VII. CONCLUSIONS

In this paper, a method for estimating regional values for Snow Covered Area (SCA) from (1) optical remote sensing data and (2) microwave SAR data are presented. In the method development and testing, ERS-2 SAR data over the area of Northern Finland are used. The estimation method for optical data is in operative use for all drainage basins of Finland. The novel forest canopy compensation methods are developed both for optical and SAR data. The methods have been validated with ground data and compared with operationally used hydrological model. Our results indicate that

1. The average (large scale) C-band backscattering properties of conifer-dominated boreal forests of Northern Finland can be well described by a simple semi-empirical model.
2. The semi-empirical backscattering model-based method to compensate for forest canopy effects improves the SCA estimation accuracy when compared with the performance of standard linear interpolation algorithms.
3. The inversion of empirical optical reflectance model is likely to give estimates for SCA with good accuracy. The advantages of the model is that no auxiliary terrain information is needed. Moreover, the method is applicable for other calculation units and optical data as well.
4. The potential of synergetic use of SAR and optical data is evident. It would benefit the operative snow monitoring particularly in the areas with long cloudy periods.

VIII. REFERENCES

[1]. N. Baghdadi, Y. Gauthier, and M. Bernier, M., "Capability of multitemporal ERS-1 SAR data for wet snow mapping," *Remote Sens. Environ.*, vol. 60, pp. 174-186, 1997.

[2]. J. Koskinen, J. Pulliainen, and M. Hallikainen, "The use of ERS-1 SAR data in snow melt monitoring," *IEEE Trans. Geosci. Remote Sensing,* vol. 35, pp. 601-610, 1997.

[3]. J. Shi, and J. Dozier, "Mapping seasonal snow with SIR-C/X-SAR in mountainous areas," *Remote Sens. Environ.*, vol 59, pp. 294-307, 1997.

[4]. D. Hall, and J. Martinec, Remote Sensing of Ice and Snow, Chapman and Hall, New York, 1995.

[5]. J. Dozier, S.R. Schneider, and D.F. McGinnis, JR, Effect of grain size and snowpack water equivalence on visible and near-infrared satellite observations of snow. *Water Resources Research*, 17, pp.1213-1221, 1981.

[6]. E.T. Engman and R.J., Gurney, Remote sensing in hydrology, Chapman and Hall, London, 1991.

[7]. J. Pulliainen, J. Koskinen, and M. Hallikainen, "Compensation of forest canopy effects in the estimation of snow covered area from SAR data," *Proc. IEEE 2001 Int. Geosci. Rem. Sensing Symp. (IGARSS 2001)*, 3 pp., Sydney, Australia, 9-13 July 2001.

[8]. J. Pulliainen, L. Kurvonen, and M. Hallikainen, "Multi-temporal behavior of L- and C-band SAR observations of boreal forests," *IEEE Trans. Geosci. Remote Sensing*, vol. 37, pp. 927-937, 1999.

[9]. J. Pulliainen, K. Heiska, J. Hyyppä, and M. Hallikainen, "Backscattering properties of boreal forests at the C- and X-band," *IEEE Trans. Geosci. Remote Sensing*, vol. 32, pp. 1041-1050, 1994.

[10]. J. Vepsäläinen, S. Metsämäki, J. Koskinen, M. Huttunen, J. Pulliainen, "*Estimation of Snow Covered Area by Applying Apparent Regional Transmissivity*" *Proc. IEEE 2001 Int. Geosci. Rem. Sensing Symp. (IGARSS 2001)*, 3 pp., Sydney, Australia, 9-13 July 2001.

[11]. A. Vuorela, Satellite Image Based Land Cover and Forest Classification of Finland. *Proceedings of the Finnish-Russian Seminar on Remote Sensing in Helsinki 29 August – 1 September 1994*. Reports of the Finnish Geodetic Institute 97:2, pp. 42-52, 1997.

FEASIBILTY OF DINSAR FOR MAPPING COMPLEX MOTION FIELDS OF ALPINE ICE- AND ROCK-GLACIERS

Thomas Nagler, Christoph Mayer, and Helmut Rott

Institute for Meteorology and Geophysics
University of Innsbruck, Innrain 52, A-6020 Innsbruck, Austria
Tel: 0043 512 507 5495 Fax: 0043 512 507 2924
Email: thomas.nagler@uibk.ac.at

ABSTRACT

Possibilities and methods of differential SAR interferometry (DINSAR) for mapping the motion of alpine ice and rock glaciers of small spatial extent were investigated. Test sites for these studies were the glacier Hintereisferner (covering 8 km^2 in area) and several of its small side glaciers, and the rock glaciers Inner and Outer Hochebenkar, located in the Ötztaler mountains, Austria. For mapping the motion of the ice glaciers only one-day repeat pass SAR images from the ERS Tandem Mission, acquired during winter, were useful. 35-day repeat pass interferometric images did not show sufficient coherence. On the rock glaciers the coherence is preserved over longer periods. 35-day ERS SAR repeat pass interferograms from summer were used for motion analysis. The topographic phase was derived by differential methods using several one-day tandem pairs and applying the multi-baseline technique. The surface-parallel flow assumption was used for estimating the velocity vectors. The accuracy of the interferometric motion is assessed by comparison with field measurements and aerial photogrammetric analysis. The detail of the interferometric motion does not match the photogrammetric maps, but spaceborne DINSAR is a very cost-effective tool for comprehensive regional surveys and monitoring of ice and rock glaciers with good accuracy.

INTRODUCTION

Differential SAR interferometry (DINSAR) has been widely applied for mapping ice motion in polar areas and of mountain glaciers of medium to large spatial extent (Rosen at al., 2000). In this paper we investigate the potential of this technique to map the motion field of small alpine ice and rock glaciers and compare the satellite data with field measurements and air photo analysis. Information on the dynamics of glaciers is of interest for climate research and hydrology, but only very few glaciers are surveyed by means of field measurements. The Austrian glacier inventory, for example, lists 925 glaciers covering a total area of about 500 km^2, pointing out that the majority of glaciers is smaller than 1 km^2, which is also the case for most rockglaciers.

It is obvious that in situ measurements of motion can be performed only on few glaciers, though information on a larger number of glaciers would be needed to obtain a comprehensive picture of the climatic response. Remote sensing offers an economic tool for glacier surveys over extended regions. In particular, ERS-1 and ERS 2 SAR data represent a very valuable archive for studying the motion of ice and rock glaciers.

TEST AREAS

Ice and rock glaciers in the Ötztal Alps, Tyrol, Austria were selected for case studies. The Landsat-7 ETM+ image from 13 September 1999 shows the locations of the test sites (Fig. 1).

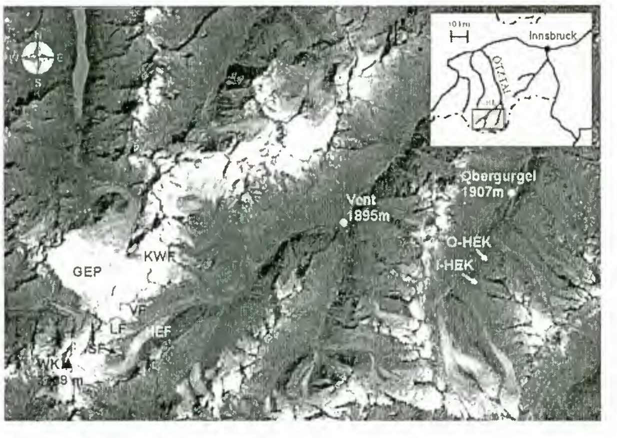

Figure 1: Landsat-7 ETM+ image (panchromatic band) of the test area Ötztal, Austria, from 13 September 1999. Glaciers: HEF – Hintereisferner, KWF – Kesselwandferner, GEP - Gepatschferner, SF - Stationsferner, LF – Langtauferer Joch Ferner, VF – Vernaglwandferner. Rock-glaciers: O-HEK – Outer Hochebenkar; I-HEK - Inner Hochebenkar.

The study on the use of DINSAR for ice motion analysis was carried out on the glacier Hintereisferner (HEF) and several of its small side glaciers. HEF covers an area of 8.1 km^2 and extends in elevation from 2500 m above sea level (a.s.l.) to the peak Weisskugel at 3739 m. The glacier is about 7 km long, the width of the terminus in the ablation area decreases from 1 km at the equilibrium line to about 300 m near the front. Two side-glaciers, Stationsferner (SF) and

Proc. 3rd International Symposium, 'Retrieval of Bio- and Geophysical Parameters from SAR Data for Land Applications', Sheffield, UK, 11-14 September 2001 (ESA SP-475, January 2002)

Langtauferer-Joch-Ferner (LF), are loosely connected with the main glacier. In addition, the motion of Vernaglwandferner (VF) was analysed, which covers a total area of 0.8 km^2 and can be separated in two parts according to the ice flow. Measurements of mass balance and dynamics of Hintereisferner have been carried out at an annual basis since 1952 (Kuhn *et al.*, 1999). Due to strongly negative balance during the last twenty years the motion slowed down considerably since 1980. In the 1970s and 1980s annual ice motion measurements were made at an extended network of stakes, but for recent years motion data are available only for a few points.

Rock glaciers are ice-rock mixtures subject to creep. The surface layer usually consists of boulders and rocks of various size with very little vegetation. In the Alps rock glaciers can be found at elevations above about 2300 m and are usually considered to be of permafrost origin. Investigations of rock glaciers are of interest for studies of climate change, hydrogeology and hazards related to mass movements. Active Alpine rock glaciers typically show motions between centimeters up to several meter per year, depending on the size, topography, and internal composition. Inactive rock glaciers, which do not move, are usually relicts from previous colder climatic conditions.

The Hochebenkar rock glaciers near Obergurgl (Fig. 1) were selected for the study, because motion data from field surveys (Schneider, 1999) and from aerial photogrammetry (Kaufmann and Ladstädter, 2000) are available for comparison with the DINSAR analysis. The rock glacier Outer Hochebenkar extends from 2800 down to 2350 m a.s.l. and is about 1200 m long. The active layer, which is up to 50 m thick, is made up of ice mixed with sand, silt and rock fragments. On top are several meters of coarse rock debris. The upper section of the rock glacier, which is slowly moving, is about 500 m wide, whereas the main part of the terminus, which shows faster motion, is about 300 m wide. During the most active period in the 1960s up to 5 m per year were measured near the front (Vietoris, 1972). The rock glacier Inner Hochebenkar is 1300 m long and extends from 2650 m to 2950 m in elevation. Its main part is inactive. There are two active regions on the southern and northern sections of the tongue which are separated by an inactive zone. These two active zones were first identified by means of ERS DINSAR analysis (Rott and Siegel, 1998) and later on confirmed by means of photogrammetric motion analysis (Kaufmann and Ladstädter, 2000).

DINSAR ANALYSIS

The motion fields of the investigated targets are characterised by comparatively small spatial extent and significant spatial variability. On Hintereisferner the velocity ranges from 0 to about 30 m/a. The side glaciers are considered to be slower, but no field measurements are available. The velocity of the rock glaciers shows significant temporal variability. Maximum velocities of about 2 m/a were measured on the lower terminus of Outer Hochebenkar rock glacier in the period 1997 to 1999 (Schneider, 1999), whereas the upper, wider part is characterised by velocities between 0.1 and 0.5 m/a.

The selection of the time span for the DINSAR analysis depends on the coherence of the target and on the magnitude of velocity. For the glaciers in the Ötztal Alps we found that phase coherence is completely lost for 35 day repeat pass data even in winter when snow and ice do not melt (Rott and Siegel, 1997). Over one day time spans the coherence can decrease significantly in case of snow fall or wind erosion and deposition of snow. In summer, when the surfaces melt, the coherence is usually very low even for one day repeat pass pairs. Therefore only one-day repeat pass data from the ERS Tandem Mission from winter were used for the DINSAR analysis.

Because of the lack of vegetation, rock glacier surfaces are in principle well suited for interferometric analysis over long time spans. However, in particular in zones of strong shear the signal may decorrelate within comparatively short time if individual rocks within a SAR resolution element follow different trajectories. Another reason for decorrelation is winter snow which usually results in complete decorrelation within the time scale of a few weeks. Considering that the velocities of the main area of the Hochebenkar rock glaciers are below one meter per year and taking into account the loss of coherence in winter due to differences in propagation through the snow pack, we selected 35 day repeat pass data from summer for the motion analysis.

The interferometric data base is specified in Table 1. For Hintereisferner images from the ascending pass of ERS were selected because in these images the glacier is located on a back slope and the main flow direction is across track. The images from the descending pass are of little use because of extensive foreshortening and layover. Four Tandem Pairs over one-day repeat pass periods from winter were available. The coherence in the image pairs Nr. 2, 3 and 4 is good (degree of coherence above 0.5) and the DINSAR analysis was carried out with these pairs. Pair Nr. 1 (6/7 December 1995) was not used because the coherence was low on parts of the glacier surfaces.

The motion analysis on the Hochebenkar rock glaciers is based on the five week repeat data from the descending passes of July and August 1995 (image pairs Nr. 8 and 9). Both pairs have short perpendicular baselines (22 m and 2 m, respectively) which is a good basis for accurate elimination of the topographic phase. For determining the topographic phase, the three tandem pairs with one-day time span (Nr. 5, Nr. 6 and Nr.7) were used. The coherence is slightly lower in the image data from 6/7 December 1995 (Nr. 7) than in the other two pairs, but it is still useful for interferometric analysis. Because reduced coherence is observed in the image pairs from both the descending (Nr. 7) and ascending orbit (Nr. 1), it can be concluded that a meteorological event is responsible for the partial decorrelation. According to weather data foehn winds causing snow drift were blowing on the mountains.

Table 1. ERS-1/2 Interferograms used in the study.

Nr.	*Dates*	B_{perp} *[m]*
Track 444, Frame 927, Ascending orbit (Hintereisferner)		
1	6/7 December 1995	209
2	10/11 January 1996	160
3	14/15 February 1996	135
4	20/21 March 1996	293
Track 437, Frame 2655, Descending orbit (Hochebenkar)		
5	19/20 July 1995	-20
6	23/24 August 1995	-81
7	6/7 December 1995	-100
8	19 July/23 August 1995	-22
9	20 July/23 August 1995	-2

For separating the displacement- and topography-dependent phase components, we applied the differential technique based on several SAR images (Joughin et al., 1998). Another option would be the use of synthetic interferograms calculated from accurate digital elevation data (DEM). However, the available DEMs are based on aerial surveys from more than 20 years ago, and the topography of the investigated ice and rock glaciers changed significantly during that period. In order to reduce possible disturbing effects resulting from different atmospheric propagation conditions in the various images and to minimise phase unwrapping errors, the topographic phase was derived by combined processing of multiple interferometric image pairs with different baselines (multi-baseline interferometry; Ferretti *et al.*, 1999).

Each differential interferogram used for calculating the topographic phase was based on two one- day repeat pass tandem pairs (4 images). It was assumed that the motion is the same in the various tandem pairs. This is a valid approach for comparatively slowly moving Alpine glaciers in winter. On Alpine glaciers temporal changes of motion are usually related to changes of water pressure in summer. The tandem pairs used for the interferometric motion analysis of Hintereisferner are separated only by 5 and 10 weeks in time (between 10 January and 21 March 1996). The three differential interferograms used for multi-baseline processing of topography reveal perpendicular baselines (B_{perp}) of 25 m (derived from image pairs Nr. 2 and Nr. 3), 133 m (Nr. 2 and Nr. 4), and 163 m (Nr. 3 and Nr. 4). For calculating the topography of the rock glaciers and the surrounding areas, two differential interferograms with baselines of 60 m (Nr. 5 and Nr. 6) and 80 m (Nr. 5 and Nr. 7) were used. On the main parts of the rock glaciers the displacement-dependent phase in the one-day repeat pass data is very small, so that possible temporal changes of velocity should have very little impact for differential processing of the topographic phase.

For quantitative studies of the dynamics and mass fluxes of ice and rock glaciers the velocity vector is needed. We assumed surface *[S(x,y)]* parallel flow (Joughin et al., 1998) for which the three-component velocity vector, **v**, can be written as

$$\mathbf{v} = \mathbf{v}_h + \left[\nabla_{xy} S(x,y)\right]^T \mathbf{v}_h \hat{z}$$

where $\mathbf{v_h}$ is the horizontal velocity vector, and $\hat{z}$ is the unit vector in the vertical direction. The second term on the right hand side is the vertical velocity. In the two test sites, Hintereisferner and Hochebenkar, we solved for the velocity vector by using only single pass data and estimating the flow direction from the direction of the downhill slope. This is suitable in these cases because the main flow direction of the ice and rock glaciers is close to the across track direction.

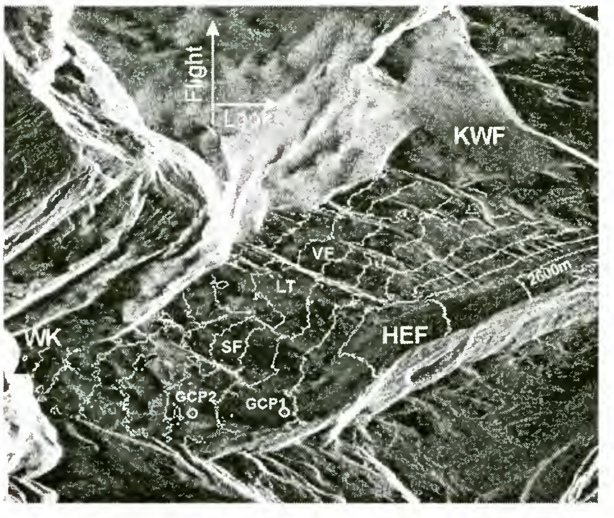

Figure 2: Section of multitemporal average ERS SAR amplitude image of the Hintereisferner area. . White lines are 100 m elevation contours from the DINSAR analysis.

MOTION OF HINTEREISFERNER

Several products of the interferometric processing chain are shown in Figures 2 to 5. The amplitude image (Fig. 2) is a multitemporal composite from the 8 images of the interferometric pairs Nr. 1 to 4 listed in Table 1. The bright layover zones of the steep slopes facing the radar are dominating features in the image. Due to strong volume scattering in the frozen firn below the winter snow, the firn areas of the glaciers, in particular the large plateau of Kesselwand- and Gepatschferner, show higher reflectivity than the ice areas. Topographic contour lines in 100 m altitude intervals, derived from the interferometric data, are superimposed to the amplitude image. The topography of the main part of the Hintereis terminus is comparatively flat (about 5° inclination), whereas the side glaciers are steeper (about 15°to 20°).

Figure 3: Image of motion-dependent relative phase on Hintereisferner and side glaciers, derived from the ERS tandem pair Nr. 4 (20/21 March 1996). On cycle of the grey scale corresponds to a phase shift of 2 π.

Fig. 3 shows the image of the motion-dependent relative phase derived from the ERS tandem pair of 20/21 March 1996. The analyses of the tandem pairs of January and February 1996 result in the same velocities. Because the phase differences are sensitive to the velocity component in range only, changes of ice flow direction cause phase differences. This is evident on the tongue of Hintereisferner, where a secondary minimum of the motion phase is apparent at the elevation of about 2800 m due to a deviation of the flow direction by about 40° from across-track.

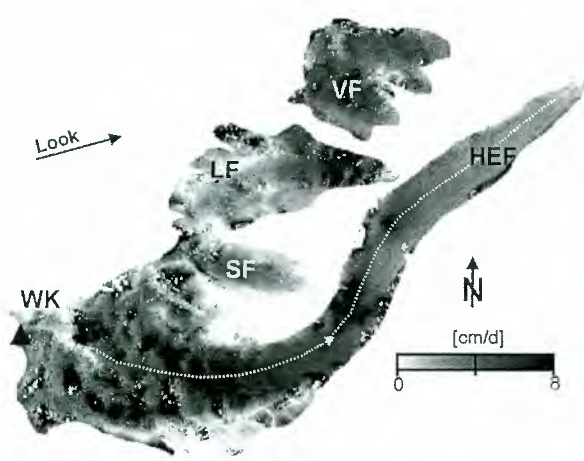

Figure 4: Map of the magnitude of the velocity vector, derived from ERS tandem pair Nr. 4 (20/21 March 1996) under the surface-parallel flow assumption. The dotted white line indicates the central flow line.

In order to facilitate the interpretation of the interferometric analysis, the ice velocity was calculated with the surface-parallel flow assumption and geocoded (Fig. 4.). This assumption is exactly valid only if the surface is strictly steady state during the time interval spanned by the interferometric pair. Also for glaciers which are in steady state in terms of mass over annual intervals, the flow is not strictly surface-parallel. In the ablation zone the ice velocity vector is inclined slightly upward and in the accumulation zone slightly downward. Taking into account the measured accumulation and ablation rates and annual field measurements of motion, it can be concluded that the deviations from the surface-parallel assumption on Hintereisferner are small. In winter, when there is no ablation, the upward movement of the surface in the ablation area is estimated to range from about 0 mm/day near the equilibrium line to about 3 mm/day at 2600 m elevation. Related errors should have very little effect on the horizontal velocity and on the magnitude of the velocity vector retrieved by DINSAR.

More critical errors for deriving the flow direction result from the topographic phase. In particular in areas where the glacier is flat, small phase disturbances may result in significant errors of the flow direction. Joughin *et al.* (1998) suggest to average over 10 to 20 ice thicknesses for estimating the flow direction from the downhill slope. On Hintereisferner (with average ice thickness of about 130 m) this would require averaging over more than 1 km, which is unfeasible because locally the flow direction changes significantly over smaller distances and because the width of the terminus is less than 1 km. For the velocity map in Fig. 4 the surface slope was averaged over 300 m distances. Therefore this motion map is noisier than the image of the motion component in range (Fig. 3).

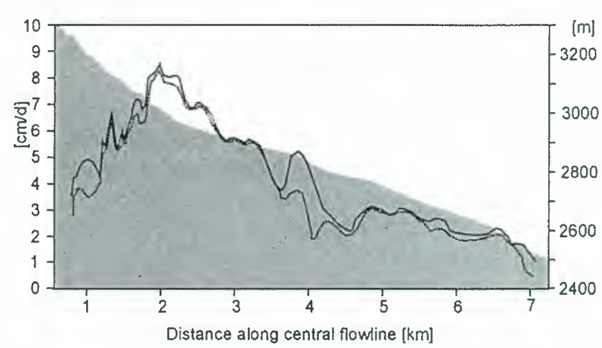

Figure 5: Ice velocity along the central flow line of Hintereisferner. Velocity component in range in cm/day projected to the surface (dashed line) and magnitude of the velocity vector assuming surface-parallel flow (full line). The boundary between the grey and white area corresponds to the elevation profile along the flowline.

Recent field data of motion for comparison are only available at a profile on the Hintereisferner terminus at 2600 m elevation. The interferometric motion in the center of this profile is 2.3 cm/d (corresponding to 8.4 m/year under the assumption of constant motion) which agrees within 20% with the mean annual motion measured in the field. The longitudinal profile along the central flowline (Fig. 5) shows the velocity maximum of 8 cm/d at an elevation of about 3000 m, which corresponds approximately to the boundary between the firn and ice area. Significant differences between the velocity in range and the velocity under the surface-parallel assumption are apparent at km 1 and km 4 downstream along the central flow line (Fig. 5). At km 1 is a steep crevasse zone, at km 4 the surface is quite flat and the flow deviates strongly from the across track direction. In nearly flat areas the estimation of the flow direction from the local slope is problematic and often noisy due to inaccuracies in the DEM. In this case the deviation between the flow and SAR look direction has been limited to 45°.

Among the tributary glaciers, Langtauferer-Joch-Ferner shows the highest velocity, with a pronounced maximum of 8 cm/d where the glacier becomes narrow about 200 m in elevation above the confluence with the Hintereisferner tongue. The side glaciers Vernaglwandferner and Stationsferner reach velocities up to 5 cm/d in their central parts.

MOTION ANALYSIS OF ROCK GLACIERS

In the multi-temporal SAR amplitude image (Fig. 6) the rock glaciers stand out from the surroundings due to the higher reflectivity of the very rough surfaces. For the motion analysis the two five-week interferograms from summer 1995 (Nr. 7 and 8 in Table 1) were used. Fig. 7 shows magnitude of the surface parallel displacement in slant range geometry from the image pair 20 July 1995 to 23 August 1995. This figure is less noisy than the previous interferometric analysis of the rock glaciers (Rott and Siegel, 1999) which did not apply the multi-baseline technique.

Figure 6: Section of multitemporal average ERS SAR amplitude image of Hochebenkar. White lines correspond to 100 m elevation contours from DINSAR analysis. The Inner and Outer Hochebenkar rock glaciers are outlined.

The interferometric analysis of the 35-day repeat pass data is suitable to derive the velocities of the moving parts of Inner Hochebenkar rock glacier (I-HEK) and of the upper part of Outer Hochebenkar (O-HEK) rock glacier. On the lower, narrow part of the terminus of O-HEK, however, the motion is too fast and the shear is too high to be resolved with 35-day interferograms. The complex structure of the velocity field is evident in Fig. 8, based on aerial photogrammetric analysis and field measurements (Kaufmann and Ladstädter, 2000; Schneider, 1999). The largest displacement on O-HEK derived by interferometry amounts to 5 cm in 35 days (corresponding to 52 cm/a) if surface parallel flow is assumed and is located at an elevation of 2670 m . At this position Fig. 8 shows velocities between 20 and 60 cm/a for the 7-years period. This confirms that the interferometric analysis provides useful data, though spatially detailed information on the motion field cannot be obtained. On the lower part of O-HEK the 35 day image pairs are not coherent.

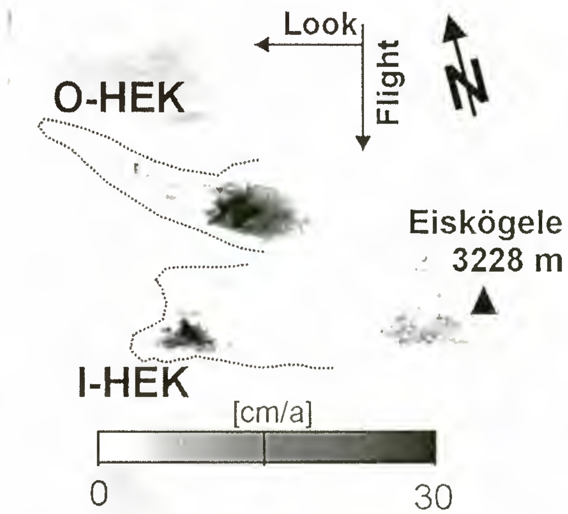

Figure 7: Surface displacement across track of the Hochebenkar rock glaciers (slant range geometry) derived by means of DINSAR from the ERS image pair Nr 9 (20 July 1995 – 23 August 1995).

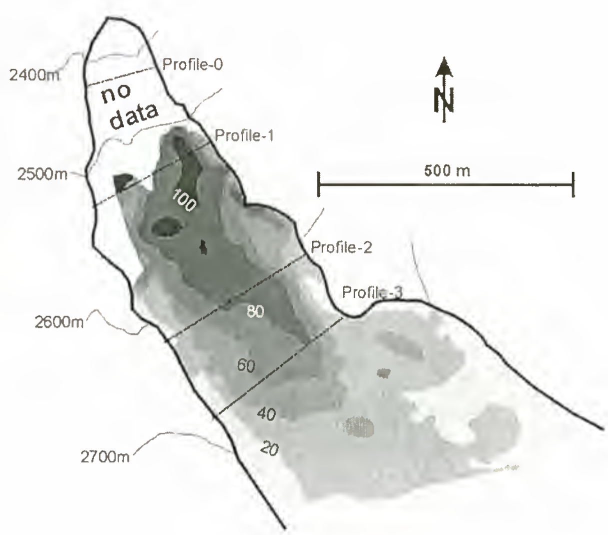

Figure 8: Sketch map of Outer Hochebenkar rock glacier with mean annual horizontal flow velocity of the period 1990-1997 (after Kaufmann and Ladstädter, 2000).

The interferometric analysis of I-HEK shows that two sections of the lower terminus, on the orographically left and right parts of the rock glacier, are in motion, and the main parts of the glacier are stagnant. This agrees with the photogrammetric velocity map of the period 1981-1997 of Kaufmann and Ladstädter (2000) which shows a moving section, about 400 m x 250 m in extent, on the left to central part of the terminus immediately above the front, with mean velocities between 2.5 cm/a and 40 cm/a. The moving section on the right (northern) side is only about 100 m wide and 500 m long, and only a small part of this section shows velocities above 20 cm/a (up to 30 cm/a). In the interferogram the moving section on the left side is clearly pronounced and shows velocities of up to 4 cm in 35 days (corresponding to 42 cm/a). This is in reasonable agreement with the airphoto analysis, in particular taking into account that the motion of the rock glaciers may change over the years. The section on the right side of I-HEK is not well resolved in the interferogram, because it is very narrow, but the interferogram provides at least a qualitative hint that this part is also moving.

CONCLUSIONS

The investigation confirm that interferometric ERS SAR images are very useful for mapping the motion of Alpine ice and rock glaciers. Though it is not possible to derive the spatial details of the small scale velocity fields, DINSAR is able to provide spatially averaged quantitative information on motion not only for large glaciers, but down to glaciers covering less than 1 km^2 in area. Of particular interest is the synoptic coverage by spaceborne SAR, which enables surveys and monitoring of many glaciers at low costs because a single scene covers a very large area compared to aerial surveys.

The multi-baseline technique (Ferretti *et al.*, 1999), using several one-day repeat pass interferograms, was applied for deriving the topographic phase in the differential analysis. For mapping the motion of the Alpine ice glaciers only one-day repeat pass SAR images from the ERS Tandem Mission, acquired during winter, were found to be useful. The 35-day repeat pass interferometric images were not coherent even in winter, due to temporal change of propagation in the snowpack. On rock glaciers the coherence is preserved over longer periods. Taking into account that 0.1 m/a to 1m /a is the typical range of velocities on the investigated rock glaciers, 35-day repeat pass interferograms from ERS SAR data from summer were used for motion analysis. The surface-parallel assumption was used for estimating the velocity vectors from single pass interferograms. This assumption provides accurate results from comparatively smooth motion fields only if accurate topographic data from INSAR or other sources are available. The comparison with field measurements and aerial photogrammetric analysis shows good accuracy of the interferometric velocity if areas with strong shear are avoided.

ACKNOWLEDGEMENTS

These investigations were supported by the IDNDR programme of the Austrian Academy of Sciences and by the European Commission, DG Research, Project EVG1-CT-1999-00008 (MUSCL). We would like to thank V. Kaufmann for providing data of the photogrammetric analysis of the Hochebenkar rock glaciers. The ERS SAR data were kindly made available by ESA for the project AO3-239.

REFERENCES

Ferretti A., C. Prati and F. Rocca (1999): Multibaseline InSAR DEM reconstruction: The wavelet approach. *IEEE Trans. Geosc. Rem. Sens.,* Vol. 37, 705-715.

Joughin I., R. Kwok, and M.A. Fahnestock (1998): Interferometric estimation of three-dimensional ice-flow using ascending and descending passes. *IEEE Trans. Geosc. Remote Sensing*, Vol. 36, 25-37.

Kaufmann V. and R. Ladstädter (2000): Spatio-temporal analysis of the dynamic of the Hochebenkar rock glaciers (Ötztal Alps, Austria) by means of digital photogrammetric methods. *Proc. of 6th Int. Symposium on High Mountain Remote Sensing Cartography.*

Kuhn M., E. Dreiseitl, S. Hofinger, G. Markl N. Span, and G. Kaser (1999): Measurements and models of the mass balance of Hintereisferner. *Geografiska Annaler*, Vol. 81 A (4), pp 659 - 670.

Rosen P.A., S. Hensley,I. R. Joughin, F. K. Li, S. N. Madsen, E. Rodriguez, and R. M. Goldstein (2000): Synthetic Aperture Radar Interferometry. *Proceedings of the IEEE,* Vol. 88, No. 3, 333-385.

Rott H. and A. Siegel (1997): Glaciological studies in the Alps and in Antarctica using ERS Interferometric SAR. *Proc. of ESA Fringe 96 Workshop, Zürich. ESA SP 406, Vol. II,* 149-159.

Rott H. and A. Siegel (1998): Interferometric Analysis of Surfaces in Non-Steady Motion. *ESA SP-441*, 571-577.

Schneider B. (1999): Die Bewegungsmessungen am Blockgletscher im Äußeren Hochebenkar (Ötztaler Alpen, Tirol) seit 1938. Diploma Thesis, University of Innsbruck, 137 pp.

Vietoris L. (1972): Über den Blockgletscher des Äußeren Hochebenkars. *Z. für Gletscherkunde und Glazialgeologie,* Vol 8, 1972.

ASSESSMENT OF INSAR TREE MAPPING ACCURACY IN TROPICAL RAIN FORESTS

Kemal Unggul Prakoso

Wageningen University, Department of Environmental Sciences, Sub-department of Water Resources
Nieuwe Kanaal 11, 6709 PA Wageningen, The Netherlands
Tel: +31 (0) 317 483576, Fax: +31 (0) 317 484885
E-mail: Kemal.Unggulprakoso@users.whh.wau.nl

ABSTRACT

Well-characterised reference sites are of major importance for accuracy assessment and validation of tree mapping algorithm, which is derived from single track InSAR C-, X-band Dornier system acquired during the ESA-MOF INDREX-96. A challenging study area was chosen in a 7.2 ha FIEPLP (Forest Inventory & End Product Linking Program) plot area in East-Kalimantan Indonesia. All trees of this site are described by position, geometrical dimensions and species name.

Since no ground control points such as corner reflectors were used for this research, the validation of the results is realised by using visual reference points. As a first step the crown projections terrestrially measured, then the InSAR crown projection map was derived to verify their planimetric accuracy and to make a first evaluation of the vegetation cover as observed by InSAR. To match trees identified by the InSAR with trees measured terrestrially, an algorithm was designed to evaluate the 3D positions and crown dimensions of all trees measured in the field with InSAR derived tree 3D positions and crown dimensions. The resulting table for candidate matches contains the distance data that can give the information for assessing the positional accuracy and tree crown size projection.

This study report how is modelling can be implemented for forestry in Indonesia and shows possible ways for the improvement of tree parameter estimation.

1. INTRODUCTION

Indonesia's tropical forests are among the world's richest. Some 75% of the country is covered by forests (143 million hectares), half of it "production forest". Processed wood products generate up to 18% of the national income from exports. Unfortunately many parts of the production forest (20 million Ha) have never been covered with any reasonably good or usable image, especially the hilly and mountainous parts, which are difficult to access and have a highly complex nature [1]. Accurate information is scarcely available and difficult to obtain because of cloud cover. Aerial photography, which is currently applied on a routine basis to collect information up to the tree level largely fails to provide this information in time because of cloud cover.

X- and C-band high-resolution Interferometry Synthetic Aperture Radar (InSAR) images acquired during the INDREX'96 airborne campaign [2] will be used for 3D tree mapping of tropical rain forest trees. The forest parameters such as: tree position, number of trees, crown dimension and vegetation height will be the output of the product. It could be important indicator information to reach an operational status and to evaluate the potential of usefulness InSAR data for automatic tree mapping as a tool to observe forest parameters. However, at present there is little experience with the use of InSAR data for this field of application, and the main factor that motivates the choice of InSAR data for this application.

2. STUDY SITE AND DATA SETS

To assess of the InSAR tree mapping accuracy, a 7.2 Ha (300 by 240 m) secondary forest has been chosen as study area. Located in East-Kalimantan, Indonesia and overlaps with two high resolution 1.5 m, X- and C–band airborne InSAR from DoSAR, it is situated on the footslopes of the Mt. Meratus, with minor slopes around 10%. The vegetation in most parts consists of tropical lowland and montane evergreen rain forest and is dominated by species belonging to the family of the Dipterocarpaceae which in trade better known as 'meranti' [3]. Field observations have been made around May 1999 and local technicians have been continuing these observations ever since.

Proc. 3rd International Symposium, 'Retrieval of Bio- and Geophysical Parameters from SAR Data for Land Applications', Sheffield, UK, 11-14 September 2001 (ESA SP-475, January 2002)

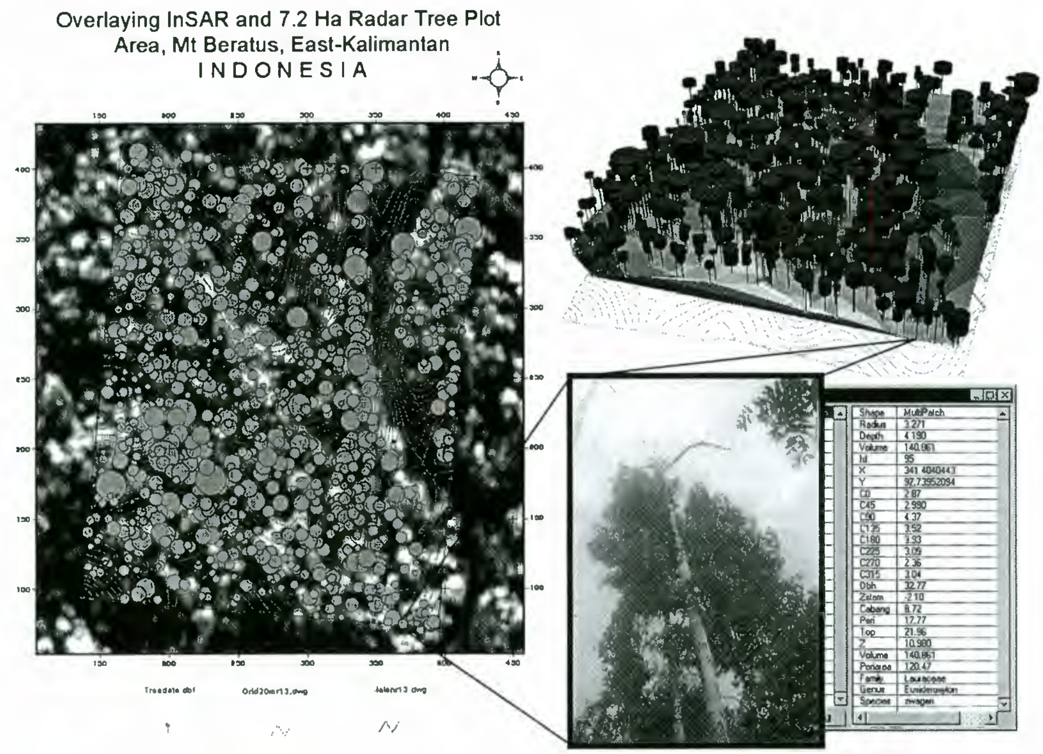

Figure 1: InSAR overlaying with ground data derived from FIEPLP methodology and 3D perspective view consist database of individual tree and several photographs for uncommon trees canopy.

2.1 Ground Data

In total, 1064 individual trees were selected and measured using a FIEPLP methodology. From 7.2 Ha (300 by 240m) area, for every tree with a diameter breast height (DBH) bigger than 20 cm, the following data was collected: tree stem co-ordinates, extreme co-ordinates from tree crown in eight directions, height of the tree top, height of the periphery, height of the bottom of the crown, DBH and species.

For accurate measurements of tree stem co-ordinates, one point (set to 0,0,0) which very clear on the image was pointed as reference. A grid was made by placing wooden pole 20 meters apart for making corrections in case of elevations. Terrain height of these grid points were measured relative to one of the grid points with accuracy +/- 0.5 m.

Tree stem position was measured using tape, Compass, Clinometer and calculate with basic triangular method. The azimuth angle of a tree was measured from two reference points within the chosen strip line from grid. Tree stem height derived with interpolation height from the pole in the grid.

The tree crown co-ordinates were determined by measuring the distances from the stem to the eight extreme distances of the crown. Electronic distance measurements were made in eight directions to determine tree crown projection.

Tree heights were measured relative to the stem base using a Clinometer. Object related errors could occur in dense stands, where the top or the stem base is not clearly visible. Height measurements of hardwoods can yield to overestimation because branches can be mistaken for the tree top. Another error occurs when the tree is leaning either towards or away from the observer, bad vision, faulty instrument operation and incorrect techniques when taking readings.

The diameters of the trees were measured at 1.3-meter height (DBH), using diameter tape. In these case errors can occur when the tape is not placed exactly around the measurement plane, perpendicular to the stem. This causes an overestimation of the DBH, which is in order of 0.5% for a tilting angle of 5%. Other error occur when cross sections are not circular, resulting in an overestimation of the basal area.

The result calculation of ground data in figure 1 shows irregularities of height distribution of main canopy (between 25-35 m) and emergent trees (between 40-60 m) and various crown projection. This assumed to be correct and used for references and validation.

2.2 InSAR Data

For investigation of the InSAR tree mapping accuracy, the high-resolution 1.5 m, X- and C–band InSAR from DoSAR will be used. Data acquired has been collected from the INDREX'96 campaign over test sites in Indonesia [2].

3. PROCESSING

The processing steps, algorithm aspects and first result for this experiment have been explained [4], [5]. To summarise, the InSAR tree mapping process and field data will describe in figure 2.

First step of the interferometric processing was a precise co-registration of the image pairs of the individual looks to a sub-pixel level. Then a phase difference and coherence image is computed. After phase-coherent look summation, the multi look phase difference image has been unwrapped using the coherence image to mask the shadow areas. For height generation the unwrapped phases are converted to height using geometry given by the reference track, which was used during the InSAR processing.

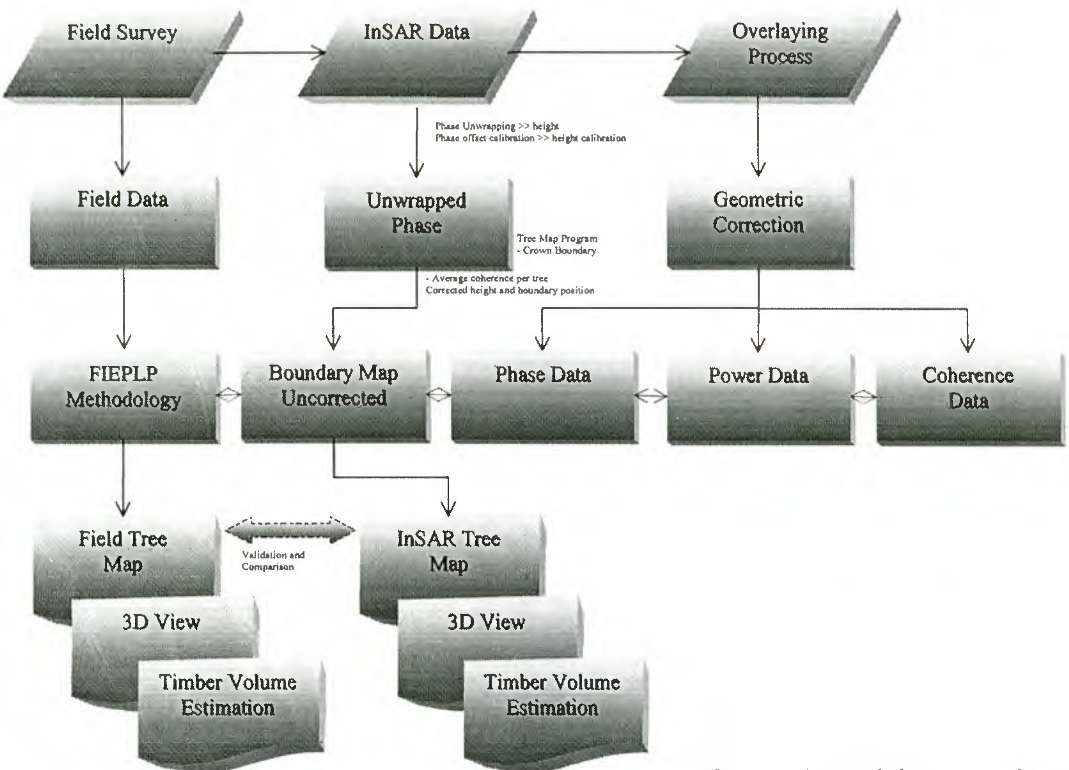

After having an unwrapped phase data, the next step is fine tuning crown boundary of the trees by means of objective function [7], which both edge and regions information are used in a model based segmentation. Limiting the number of circular mask = 3 seems appropriate for representing a tree crown boundary. To increase the number of finding trees, the value of the initial circular mask number can be increased (figure 3a circular mask =5, figure 4a circular mask=3). The lower circular mask number will produce more trees than the bigger one, but it will also decrease accuracy.

While optimal boundaries have been found in range coordinate r and azimuth coordinate x, the corrected height and boundary position still needed because of the height variation of scatters within a resolution cell. The displacements can be corrected by application of Van Cittert-Zernike theorem [6].

The result from InSAR tree map look very dense because polygon crown boundary delineation into raster area (Figure 4). For comparison purpose, a co-ordinate transformation (rotation and translation) was applied to vector format. That was applied to the local co-ordinate to bring both sources into the same co-ordinate and projection and to overlay one to each other to make easiest analysis.

Figure 2: Validation and processing chain flow diagram of InSAR tree map and field data derived from FIEPLP methodology

In the next step, the data (roads, contour and crown boundary) are then transfer to ArcView using a linear translation and rotation to make all of them overlay one to each other. With overlaying process it will be convenient for qualitative assessment and for checking interest feature (Figure 4b).

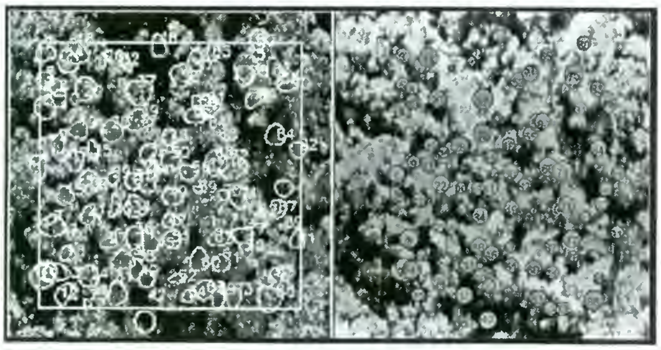

(a) (b)

Figure 3. (a) InSAR tree map with circular mask=5, (b) Transformation into vector format.

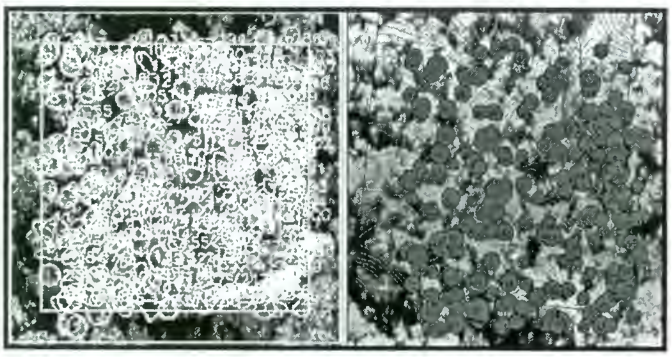

(a) (b)

Figure 4: (a) InSAR tree map with circular mask=3. For comparison purpose, a reference source was created in local co-ordinate reference source with contour line and logging road to check the planimetric position. (b) A co-ordinate transformation was applied to the local co-ordinate.

By overlaying maps of InSAR and field data of the same scale and system projection, two possibilities can be distinguished: positional and interpretations errors. Position error refers to error in which it is certain that the delineated object is intended to be the same but a small differences occur due e.g. to the limited ground resolution of the applied image data and limited registration accuracy. An interpretation error refers to a situation in which terrain object that belong to a different class is not distinguished (i.e tree in the logging road). Verification and validation of the results, can be done perfectly by overlaying fieldwork data on the InSAR tree map, which requires several reference control points, transformation and rotation.

The output of InSAR tree mapping will appear as tree map boundary on the orthographic projection in a bitmap or postscript file and show co-ordinate in ground range and azimuth direction with the same orientation as the radar image. A 3D perspective of the canopy visualisation of crown of the trees could also show up on the screen in 180 degrees and from radar point of view with a 55^{o} incidence angle for better qualitative assessment. This will give a much better perception and very useful when one wants to know which trees should be visible on the radar image.

4. ACCURACY ASSESSMENT

4.1 Assessment of tree position with nearest features

Tree map position accuracy refers to how precisely it is on the map relative to their true location on the field. For each tree data feature, a first qualitative comparison was made between the field data and InSAR tree mapping data to look at the commission and omission errors. There was no commission error, and the omission error, less than 1 per cent (tree in logging road) and this feature will not be used for the future evaluations.

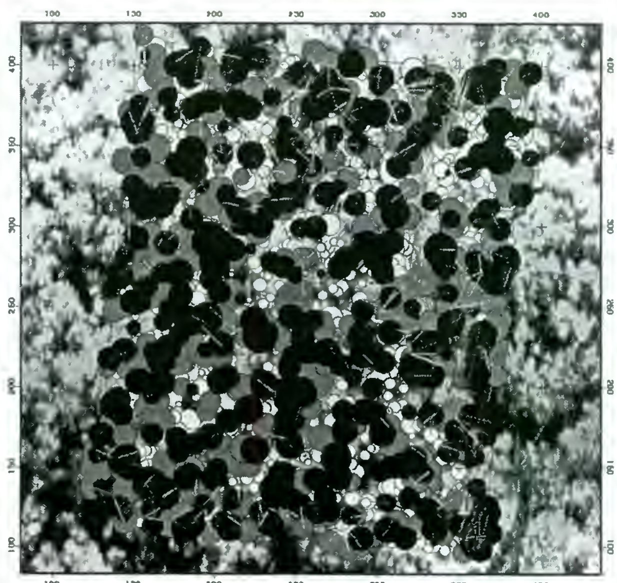

Figure 5: The nearest distance between the centre of the closest data is showed with lines. InSAR C-band (mid grey) and InSAR X-band (dark grey) with connecting line to the field data (light grey).

The algorithm then steps through each tree field data and then compared to tree mapping data. The result then creates a result table containing the distance and height information. The positional accuracy can be defined trough measures of the difference between the apparent location of the tree map data as recorded in the database, and the true location. The algorithm calculates the distance between the centred of the closest data. If the data intersect or if one lies within the other, the distances will be set to zero, to calculate the closest distances to the centred features enclosed by other features. Line graphics have been drawn connecting the centred of the closest features (figure 5).

The percentage of a 1.5-m (1-pixel) classes distance computed for each tree data. Table 1 gives the results for the tree positions. It shows 3-m rms accuracy (65%) for C-band and (62%) for X-band. The percentage decreases proportionally to the size of 25-m rms. The origins of most of these errors were due to misinterpretation related to fluctuations of low coherence data (lay-over regions), or effect specific to radar (number of looks, incidence angle) and centre position of the tree caused of irregularity of crown dimension.

Table 1. General results of comparison for tree position between InSAR C-, X-band and field data.

Accuracy (m)	# of Tree C-band	%	Cumu-lative	# of Tree X-band	%	Cumu-lative
< 1.5	313	58.95	58.95	239	55.97	55.97
3	36	6.78	65.73	29	6.79	62.76
4.5	25	4.71	70.43	37	8.67	71.43
6	38	7.16	77.59	31	7.26	78.69
7.5	44	8.29	85.88	20	4.68	83.37
9	22	4.14	90.02	16	3.75	87.12
10.5	23	4.33	94.35	17	3.98	91.10
12	11	2.07	96.42	5	1.17	92.27
13.5	4	0.75	97.18	7	1.64	93.91
15	5	0.94	98.12	3	0.70	94.61
16.5	3	0.56	98.68	6	1.41	96.02
18	2	0.38	99.06	4	0.94	96.96
19.5	2	0.38	99.44	4	0.94	97.89
21	1	0.19	99.62	3	0.70	98.59
22.5	1	0.19	99.81	2	0.47	99.06
24	0	0.00	99.81	0	0.00	99.06
25.5	1	0.19	100.00	3	0.70	99.77
27				1	0.23	100.00
Total	531	100	100	427	100	100

Unfortunately, abundant difficulties exist in identifying the true location of a data because of problems with evident in estimation of crown cover, which cannot be precisely measured from InSAR cause by complexity of vegetation itself. In addition, field observation of tree cover is problematic, as estimation of crown from the ground (i.e., below tree canopies) is fundamentally different from estimation made from above the canopy. Estimation from below may include vegetative cover from small tree that cannot be seen from above by X and C-band data. InSAR X-band could detect 427 number of the tree and C-band detect 531 trees, this bias of number of trees and position might be caused by a different baseline length between X- and C-band [8] which affect the height variation of scatters. The result from InSAR clearly shows that only the emergent tree and main canopy layer can be well detected; while the second and third lowest layer of the canopy could not be detected as a tree. Individual tree crowns, especially the ones that dominate the canopy, can be delineated well on the height image, this is often the case with crowns in the upper part of main canopy. In the future to be fair for comparison, the second and third layer below main canopy should be ignore to avoid confusion in validation and the terrain slope should also put into account.

4.2 Tree crown projection assessment

Figure 6 shows subset crown dimension in ortho-projection onto the xy-plane. The dimensions of each emergent tree crown look alike and reasonably agree with field data as long as the InSAR data can detect and distinguish very clear a single tree.

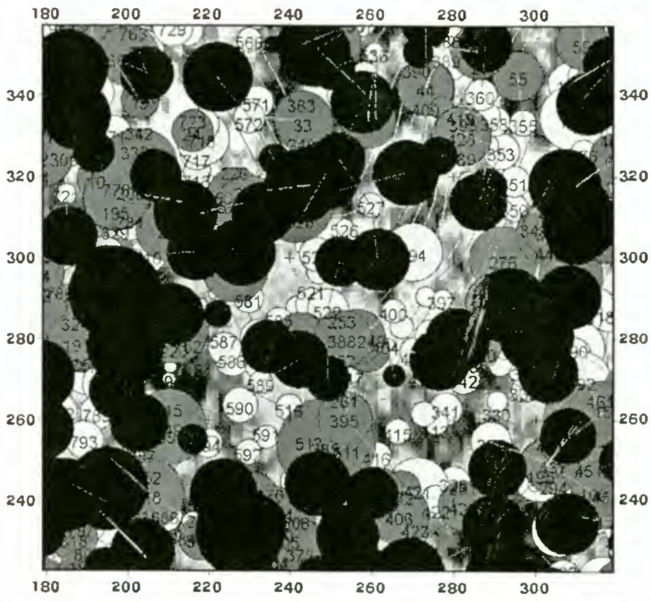

Figure 6: Subset (140 by 140 m) ortho-projection of crown boundary represents in average circle of InSAR C-band (mid grey), X-band (dark grey) to the field data (light grey).

For instance, for a single tree location between co-ordinate x 240 – 250 and y co-ordinate 290 – 300, although the crown dimension looks similar, differences still occurs in some cases. In case of a group of trees with the same height, it will detect one crown boundary; but if the heights are different, the InSAR will detect only the emergent. In most cases when several tree crowns have same height of the canopy (mostly in the main canopy layer), InSAR will detect group of the trees and causing the over estimation of crown dimension. In cases obscured by other emergent tree crowns (shadow), they are not imaged and the InSAR cannot detect them.

The crowns are also not imaged when they are in the second or third layer below from main canopy. When tree crowns are in the upper part of the canopy, but are merged together, it is very difficult to separate them on the image. This is often the case with crowns in the second highest layer of the canopy, because of competition between trees to reach the highest layer. When a gap appears, they take advantage of the available light and grow trough to the canopy and beyond. It could be the effect of fieldwork taken 3 years later after InSAR data acquisition and several trees had died in this period and new pioneer trees have grown significantly. Due to time differences, interpretation or comparison result could be affected.

5. CONCLUSIONS

A simple method has been presented accuracy evaluation of tree parameter extraction from InSAR data. The procedure compares InSAR tree mapping by computing the percentage of the position lying within given nearest distance of the reference source.

In tree position, the general accuracy of InSAR tree mapping used C-band about 3-m rms and can detect more of the tree than X-band data. This difference comes mainly from the physical characteristics, which cannot be precisely measured from InSAR cause of complexity of vegetation itself, also variation of height distribution between upper part, main canopy and second layer below.

For tree crown projection, a dimension of crown size in general is over estimated, this phenomena is well known cause as can be seen from visual interpretation does not reveal any individual crown and useless to compare with field data as a consequence crown size represent group of the trees. When the InSAR data can detect and distinguish very clear a single tree, the crown size looks alike and reasonably agrees with field data.

These assessments imply for tropical rain forests, InSAR tree mapping should to be used in combination FIEPLP measurements for operational use cause of complexity of vegetation. As a tool for collecting information of tree parameters seems to have the potential to facilitate the planning and management of the forests.

Acknowledgement. I acknowledge MoFEC, Tropenbos and Gibbon foundation for realisation of this research and MOF-Tropenbos Kalimantan project for assistance and logistic support. I also thank to radar group in water resources department WU for assistance and ideas.

6. REFERENCES

[1] Hidayat, H. 1993. Forest inventory and monitoring over production forest areas in Indonesia, GIS World Symposium, Vancouver, British Columbia, Canada.

[2] Attema, E., M.G. Wooding and J-C. Morin. 1996. INDREX-96 Experimenters Handbook, Unpublished.

[3] Soerianegara, I., Lemmens, R.H.M.J. 1993. Timber trees: major commercial timbers. PROSEA, Plant Resources of South-East Asia. No. (5). Wageningen: Pudoc. 610p.

[4] Prakoso, K.U, B. Suryokusumo and D. H. Hoekman. 1999. Radar tree mapping and Fieplp methodology to support sustainable forest management. In proceeding of Final results workshop Indonesian radar experiment, ESTEC, The Netherlands.

[5] Prakoso, K.U, B. Suryokusumo. 2000. Interferometric SAR tree mapping: potentials and limitations in support of sustainable forest management in Indonesia, M.Sc thesis Wageningen University and research Centre, Wageningen, The Netherlands.

[6] Hoekman, D.H. and C. Varekamp. 2000. Observation of Tropical Rain Forest Trees by Airborne High-Resolution Interferometric Radar. IEEE transactions on geoscience and remote sensing, vol 39 no 3, March 2001.

[7] Varekamp, C. and D.H. Hoekman. 2001. Segmentation of high-resolution InSAR data of a tropical forest using Fourier parameterized deformable models. International Journal Remote Sensing, 2001, vol. 22, no. 12, 2339-2350.

[8] Varekamp, C. 2000. Canopy reconstruction from interferometric SAR, Ph.D thesis, Wageningen University, The Netherlands. 88 pp.

REMOTE SENSING OF BOREAL FOREST WITH POLARIMETRIC L- AND C-BAND SAR

Jaan Praks and Martti Hallikainen

Helsinki University of Technology, Laboratory of Space Technology
P.O. Box 3000, FIN-02015 HUT, Finland
Tel: (+358) 9 451 4779, Fax (+358) 9 451 2898,
e-mail: Jaan.Praks@hut.fi

ABSTRACT

The aim of this study is to find the most suitable polarimetric analysis techniques for boreal forest remote sensing under variable weather conditions with L- and C-band SAR. Extensive ground truth data is combined with polarimetric SAR images for analysis. By using fully polarimetric SAR images from two imaging dates the temporal stability and relation to forest properties of different polarimetric descriptors is studied.
Results show, that best parameter for forest biomass mapping is L-band HV backscattering coefficient. Application of complicated polarimetric analysis techniques did not gave additional benefit.

INTRODUCTION

L- and C– and SAR instruments are proved to be useful in forest remote sensing as they are sensitive to forest biomass. Green (1998) shows relationships between spruce forest biomass and polarimetric SAR backscatter. Proisy et al. (2000) show how polarimetric SAR can be used in mangrove forest remote sensing.
However SAR measurements are also sensitive to weather related scene properties. One of the major temporal cahnge in boreal forest zone for SAR imaging is snowmelt season. How polarimetric SAR analysis techniques can improve biomass retrieval possibilities under variable conditions is not yet fully investigated.
In this study we use multitemporal SAR images to find out, what kind of polarimetric features of L- and C-band SAR images are most suitable for boreal forest remote sensing under changing imaging conditions. As the forest timber volume and related characteristics are changing over time very slowly we can draw a conclusion, that remotely sensed parameters describing same properties should also correlate between two close measurement dates. In this study we have calculated polarimetric SAR covariance matrix for 821 pine forest stands from images before snowmelt and during the snow melt from L- and C-band polarimetric images. From covariance matrix different polarimetric parameters are calculated and compared between two dates and with forest stand parameters.

MATERIAL

The forest test site of this study is located in northern Finland near the city of Oulu at the coordinates $25^0 40'$ $64^0 50'$. One set of L- and C-band images were measured under almost dry snow conditions on 22-23 March and another set during the snowmelt (wet snow) period on 2-3 May 1995. The images were acquired with similar imaging geometry. Forest test site was in the incidence angle range 48^0-57^0. Images were acquired during EMAC-95 campaign with EMISAR, see (Dall et al 1997) and (Hallikainen et al. 1997) for details. The forest between two imaging dates was untouched. However, weather conditions were considerably different as described in table 1.

Table 1. Weather conditions during image acquisition.

	22-23 March	2-3 May
Air temperature (C^0)	−11.9 −2.2 5.7 (min, mean, max)	−5.3 1.5 5.5 (min, mean, max)
Snow temperature (C^0)	−6.1 −2.1 0.0 (min, mean, max)	–
Snow depth (cm)	55	21
Snow wetness (% vol)	0.31	1.08

In the imaged area forest stand information is available for 923 forest stands with a total area of 754 ha. Most of the stands (821) are Scots pine-dominated forest on mineral ground or pine mires. Forest assessment has been carried out during the years 1995 and 1996. For each forest stand following parameters are measured: stand area, habitat and soil type, mean age, development class, basal area, number of stems per hectare, mean diameter, mean height, dominant species, stem volume and some silviculture parameters.
For this study only Scots pine-dominated stands were selected and used. The average size of the pine stands in the area is 0.8 ha. Overview of stand parameters is given in table 2.

Proc. 3rd International Symposium, 'Retrieval of Bio- and Geophysical Parameters from SAR Data for Land Applications', Sheffield, UK, 11-14 September 2001 (ESA SP-475, January 2002)

Table 2. Scots pine forest properties at the test site.

	Min	Median	Max
Stem volume (m^3/ha)	0.5	31	196
Age (years)	1	40	120
Height (m)	1	8	18
Diameter (cm)	2	11	25
Number of stems (1/ha)	1	13	160

METHODS

The EMISAR covariance matrix image product is used for the analysis. The images were provided in σ^0 calibration and in ground range projection, calculated by using the flat Earth approximation. As the test site is located in flat area this assumption is well valid. We rectified images to the Finnish coordinate system by using ground control points. The complex number images were treated as two layer real number images. Finally, the images were resampled to 5 m resolution.

The rectified images were combined with the forest stand vector map and an average covariance matrix was calculated for each forest stand. From average covariance matrix we calculated also coherency and normalized coherency matrices (proposed by Praks and Hallikainen (2000)) and coherency matrix eigenvalue decomposition parameters such as target entropy, average alpha angle and anisotropy, proposed by Cloude (1996).

Here are some definitions used in this work. Covariance matrix C is defined as

$$[C]=\left\langle \bar{k}_C \bar{k}_C^{*}\right\rangle = \begin{pmatrix} C_1 & C_2 & C_3 \\ C_2^{*} & C_5 & C_6 \\ C_3^{*} & C_6^{*} & C_9 \end{pmatrix}, \tag{1}$$

where target vector k_C is defined by the means of scattering matrix elements S_{xx} as follows;

$$\bar{k}_C = \left[S_{hh}, \sqrt{2}S_{hv}, S_{vv}\right]^T. \tag{2}$$

Coherency matrix T is defined in a similar way; however, target vector k_T is defined as

$$\bar{k}_T = \frac{1}{\sqrt{2}}\left[S_{hh}+S_{vv}, S_{hh}-S_{vv}, S_{hv}+S_{vh}\right]^T. \tag{3}$$

Superscript T refers to matrix transpose and superscript * refers to complex conjugate matrix transpose.

The main diagonal elements of the covariance matrix C are directly backscattering coefficients for HH, HV and VV polarization, off diagonal elements are covariance between all amplitudes and phases. The main diagonal of the coherency matrix can be interpreted as backscattered power for odd bounce scattering (surface), even bounce scattering (dihedral) and cross polarized scattering.

The normalized coherency matrix N is defined as follows,

$$[N]=\left\langle \bar{k}^{*}\bar{k}\right\rangle^{-1}\left\langle \bar{k}\bar{k}^{*}\right\rangle, \tag{4}$$

where $\langle ... \rangle$ denotes ensemble average and * denotes complex conjugate transpose. Since the trace of the covariance matrix (also known as *span*) can be interpreted as the total backscattered power, we say that the matrix is normalized by the means of total power. The normalized coherency matrix is a Hermitian matrix which is linearly related to the covariance matrix and coherency matrix. The matrices have the same eigenvectors and proportional eigenvalues. Indexing notation for all elements of these matrices is as in (1).

TEMPORAL STABILITY

Parameters describing temporally stable forest descriptors should have high temporal correlation. We compared polarimetric parameters calculated for same forest stands from March and May SAR images. The polarimetric parameters are covariance, coherency and normalized coherency matrix elements (for complex elements both magnitude and phase angle), total power, decomposition parameters; average alpha angle, entropy, anisotropy and normalized coherency matrix invariants. Correlation was calculated between each May-March parameter pair list. As mentioned earlier, the list has 821 stands. Some of the correlation coefficients are given in table 3.

As expected for forests, L- band parameters are generally more stable under temporal changes than C-band parameters. In table 3 all corresponding correlation are higher for L-band. Highest correlation for both bands is for cross polarized backscattering σ_{VH} (equivalent to T_9 and C_5). This indicates that trees cause crosspol backscattering, and amount of crosspolarized response is least dependent on weather conditions. However, the general backscattering level varies from image to image and is dependent on moisture conditions. Also high correlation is for third, the smallest eigenvalue. This is caused by the fact that smallest eigenvectors direction is close to HV polarization because cross polarized response is always smaller that lienar polarization response. Correlation between HV polarisation and smallest eigenvalue for forested areas is very close to one for all our images.

Very high correlation is also between L-band Alpha angles and first element of normalized coherency matrix. These parameters are also highly correlated as shown by

Table 3. Correlation coefficients (R) between the polarimetric stand parameters in March and May. Correlation calculated using 821 data points.

	L-band	C-band
Target decomposition parameters		
Entropy	0.77	0.62
Alpha	0.90	0.28
Anisotropy	0.43	0.29
Total power (span)	0.86	0.70
1st eigenvalue	0.76	0.58
2nd eigenvalue	0.83	0.78
3d eigenvalue	0.93	0.85
Coherency matrix elements		
T_1	0.76	0.58
T_2	0.75	0.22
T_3	0.18	0.15
T_5	0.84	0.49
T_6	0.35	0.20
T_9 (~HV)	0.93	0.85
Covariance matrix elements		
C_1 (~HH)	0.81	0.48
C_2	0.18	0.16
C_3	0.43	0.26
C_5 (~HV)	0.93	0.85
C_6	0.33	0.20
C_9 (~VV)	0.79	0.74
Normalized coherency matrix (NCM) elements		
N_1	0.90	0.23
N_2	0.68	0.3
N_3	0	0
N_5	0.75	-0.1
N_6	0.17	0.11
N_9	0.74	0.64

Praks in (2000). Both parameters describe scattering mechanism. L-band scattering mechanism is dominated by branch and trunk reflections and this seems to be temporally stabile. Same parameters for C-band have low correlation. This indicates, that scattering mechanism for C-band radar is less dependent on forest biomass.

As on figure 1 can be seen, alpha angle in the May image was systematically higher than that in March. Also backscattering level between March and May cross polarized backscattering are different as seen from figure 2.

Correlation for normalized coherency matrix (NCM) elements is systematically lower than correlation for corresponding coherency matrix elements (table 3). This can be explained by the fact that most of the total backscatter power information is removed from NCM by normalizing. However, the first element of NCM and the sum of squared elements of NCM gave very similar results to corresponding alpha and entropy parameters

We did not find significant correlation between any of the phase variables we used.

Table 4. Correlation coefficients (R) between polarimetric SAR parameters and forest parameters.

	22-23 March		2-3 May	
	L-band	C-band	L-band	C-band
Correlation (R) with stem volume				
Cross pol	0.71	0.50	0.68	0.39
Total power	0.70	0.39	0.68	0.34
Alpha	0.64	-0.1	0.59	0.28
Entropy	0.35	0.3	0.45	0.29
N_1	-0.66	0	-0.64	-0.28
Correlation (R) with mean tree height				
Cross pol	0.61	0.46	0.59	0.38
Total power	0.6	0.4	0.58	0.35
Alpha	0.65	0	0.62	0.23
Entropy	0.25	0.2	0.42	0.26
N_1	-0.65	0	-0.65	0.24
Correlation (R) with stand age				
Cross pol	0.45	0.4	0.43	0.3
Total power	0.52	0.46	0.42	0.21
Alpha	0.52	0.1	0.51	0.28
Entropy	0.18	0.1	0.39	0.31
N_1	-0.51	0.1	-0.53	0.28

RELATION TO GROUND TRUTH

Calculated polarimetric parameters for each stand were compared with ground truth. Target entropy, anisotropy, alpha angle and covariance, normalized covariance and coherency matrix elements were compared against forest age, stem volume, number of stems per hectare, forest type, soil type and other parameters.

One has to keep in mind that most of the forest parameters correlate with each other. For example, age and basal area are connected to stem volume, the number of stems per hectare is dependent on site fertility, etc. For this reason it is difficult to find the forest parameters which are most closely related to backscattering properties.

Out of all parameters available to us, stem volume gives highest correlation with backscattering properties. Thus we conclude that stem volume describes best the physical properties of forest causing the backscattering in polarimetric L-and C-band images. As expected, we found that crosspolarized backscattering, total power and alpha angle gave the highest correlation with stem volume. An overview of obtained correlation coefficients is presented in table 4. The best results were achieved for L-band images. Alpha angle has exponential relationship with stem volume as shown on figure 3 and cross polarization has more linear relationship with stem volume as shown on figure 4. Also the total backscattered power has good correlation with stem volume, figure 5.

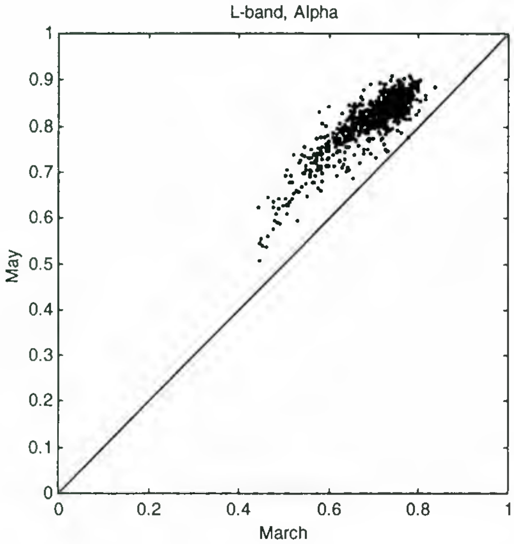

Figure 1. Scatterplot between L-band alpha angle in March and May.

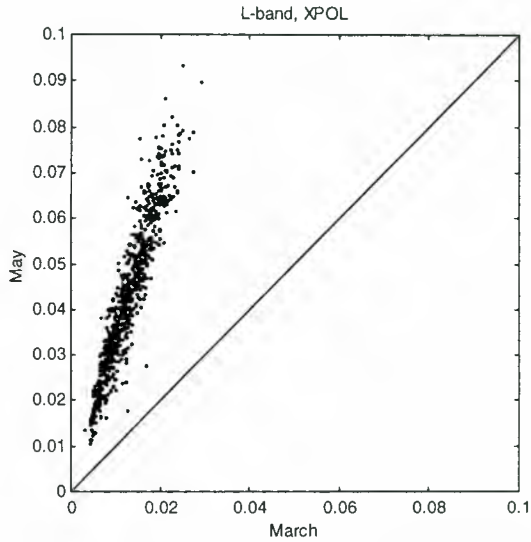

Figure 2. Scatterplot between L-band cross polarized backscattering (linear scale) in March and May.

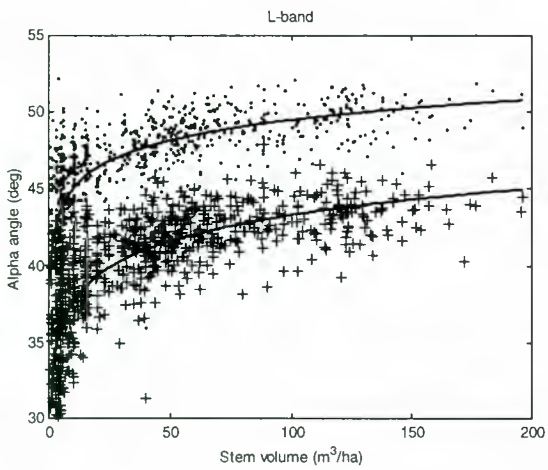

Figure 3. L-band alpha angle relation to stem volume. Marker + denotes March and dot denotes May.

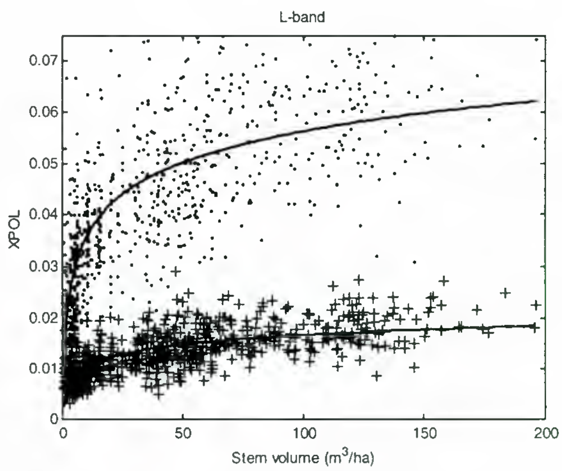

Figure 4. L-band cross polarized backscattering relation to stem volume. Marker + denotes March and dot denotes May.

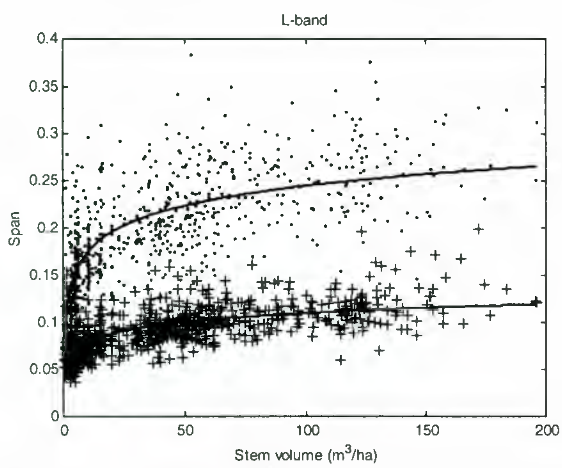

Figure 5. L-band total backscattered power relation to stem volume.

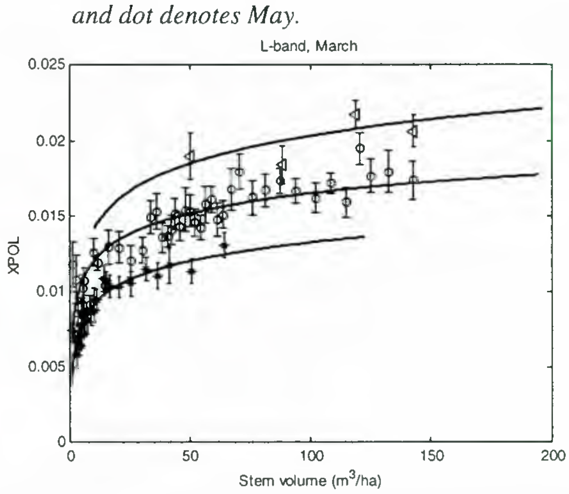

*Figure 6. L-band cross polarized backscattering relation to stem volume for different soil fertility classes. <- Moist mineral soil, o-dryish mineral soil and * dry mineral soil.*

The influence of incidence angle in this narrow range (between 48°-57°) was very small compared to other effects. Incidence angle effects are studied in more detail by Alasami et al. (1998).

Positive correlation between the forest stem volume and scattering mechanism (alpha angle) shows that fraction of double reflection in L-band increases with stem volume. The general level of alpha angle is higher for moist conditions, indicating that wet snow/ground causes more double reflection.

As it can be seen on figure 6, also parameters describing soil fertility have influence to backscattering. Soil fertility can determine the shape and size of crown and branches.

CONCLUSION

In this study extensive forest ground truth dataset is combined with multitemporal SAR images. Polarimetric parameters are calculated and compared with ground truth for 821 Scots pine stands. In agreement with previous studyes we can conclude that, for boreal forest biomass remote sensing L-band SAR is more suitable than C-band SAR. Simple HV polaristion backscattering correlates best with stem volume under changing weather conditions. Well suitable parameters for forest biomass remote sensing are also total backscattered power, alpha angle and first element of normalized coherency matrix. However, complicated polarimetric parameters seems to have no benefit over simple cross polarized backscattering.

Forest stem volume seems to describe best those forest physical properties causing cross polarized backscattering. However, the general backscattering level differences between images can complicate significantly stem volume retrieval.

The anisotropy and entropy of the target in L- and C-band correlate with stem volume weakly. Lack of temporal correlation between phase variables indicates complex multiple scattering.

REFERENCES

Alasalmi, H., Praks, J., Arslan, A., Koskinen, J. and Hallikainen, M., (1998): Investigation of snow and forest properties by using airborne SAR data: Second International Workshop on Retrieval of Bio- and Geo-physical Parameters from SAR Data for Land Applications, ESA-ESTEC, Nordwijk, Netherlands, 1998, pp. 495-502.

Cloude, S. R., E. Potier, (1996): A review of target decomposition theorems in radar polarimetry: IEEE Transactions on Geoscience and Remote Sensing, Vol. 34, No. 2, March 1996, pp. 498-518.

Dall, J., Woelders, K., Kristensen, S. S., Grinder-Pedersen, J., Skriver, H., Madsen, S. N., Christensen, E. L., (1997): EMISAR Deployment in the EMAC Campaigns: EMAC-94/95 Final Results Meeting, ESA, Nordwijk, Holland, 14-16 April 1997, pp.19-25, (ISSN 1022-6656 September 1997).

Green, R. M., (1998): Relationships between polarimetric SAR backscattering and forest canopy and sub-canopy biophysical properties: International Journal of Remote Sensing, 1998, vol. 19, No 12, pp. 2395-2412.

Hallikainen, M., Koskinen, J., Praks, J., Arslan, A., Alasalmi, H. and Makkonen, P., (1997): Mapping of snow with airborne sensors in EMAC'95: ESA EMAC 94/95 Final Results Workshop, Noordwijk, Netherlands, 1997, pp, 143-153.

Praks, J., Alasami, H., Hallikainen, M., (2001): Polarimetric properties of boreal forest in L- and C-band SAR images: Proceedings of IGARSS'2001, Sydney, Australia

Praks, J., Hallikainen, M., (2000): A novel approach in polarimetric covariance matrix eigendecomposition: Proceedings of IGARSS'2000, Honolulu, USA, vol. 3, pp. 1119 -1121.

Proisy, C., E. Mougin, F. Fromard, M. A. Karam, (2000): Interpretation of polarimetric radar signatures of mangrove forests: Remote Sensing of Environment, 2000, vol. 71, pp. 56-66.

EMPIRICAL ASSESSMENT AND MODELING OF TOPOGRAPHIC INDUCED VARIATIONS IN THE RADAR BACKSCATTERING FROM DIFFERENT VEGETATION FORMATIONS IN MEDITERRANEAN ENVIRONMENT

M. Shoshany and T. Svoray

Bar-Ilan University, Environmental Information Laboratory, Geography Department, Ramat-Gan 52900, Israel; m_shoshany@hotmail.com

Ben-Gurion University of the Negev, Department of Geography and Environmental Development, Dept. of Information Systems Engineering, Beer-Sheva 84105, Israel; tsvoray@bgumail.bgu.ac.il

ABSTRACT

Retrieval of biophysical parameterizations of arid and semi-arid vegetation is important for wide range of applications, from desertification assessments through net primary production for grazing management, to assessment of fire hazards. However, as substantial part of the Earth terrain is hilly and mountainous there is a need to understand the effect of topography on the radar backscattering. For shrubs, herbaceous vegetation and soil such backscatter was found to decrease non-linearly with angle of incidence. Furthermore , it was found that the effect of green leave biomass at the top of the canopy is most pronounced at angles larger than 35 degrees.

INTRODUCTION

Remote sensing studies of vegetation cover, biomass and productivity must then consider the topographic effect on the reflected radiance in the different wavelength bands. For that purpose there had been conducted numerous empirical and theoretical assessments of the Bidirectional Reflectance Distribution Function (BRDF) of different vegetation and soil (e.g., Shoshany, 1992) types, for the visible and near-IR spectral regions. However, relatively little attention was given to the understanding of the angular variations in the radar backscattering from vegetation canopies in undulating terrain. Existing studies (See for example : Teillet et. al., (1985), Imhoff, 1995; van Zyl (1993), Beaudoin et. al. (1994), Pairman et. al., (1997) and Luckman (1997)) divide the topographic effect on the radar backscattering into four components : incident flux density, volume scatter, surface scatter and double-bounce scatter.

In essence, topography is changing both the illuminating and viewing geometries , thus varying the penetration and attenuation of the radar signal by the vegetation boundary layer. These effects belong to the general problem of the radiative transfer of microwave energy within the structures formed by vegetation (e.g. : Saich and Lewis, 2001; Brown et al., 2001; Ferrazzoli, 2001; Macelloni et al., Le Toan, 2001; and Quegan, 2001). However, In natural terrain there are two geometries formed (Figure 1) : one related to the normal to the surface and the other related to the trees / shrubs trunk vertical position.

This study aims at assessing empirically the topographically induced backscatter variations from shrubs (garrigue), dwarf shrubs (Bata), herbaceous growth and soil in Mediterranean environments. There are two justifications for such study : firstly, to allow differentiation between vegetation types according to their angular variations ; and secondly, to improve retrievals of biophysical parametereizations on the basis of angular backscattering variations. Three ascending ERS-2 SAR images of a hilly terain in central Israel were acquired for the purpose of such assessment. Using Digital Elevation Model (DEM) the local incidence and backscattering angles could be calculated.

STUDY AREA

The study area is a semi-arid phyto-geographical zone along a rainfall gradient with annual average between 450 mm and 250 mm, located in the central of Israel along the eastern coast of the Mediterranean basin. The dominant rock formation is mostly chalk with patches of Calcrete and the dominant soil is Brown Rendzina (Haploxerolls). Vegetation in this area varies from shrublands and garigue (dominated by *Quercus calliprinos* and *Phillyrea latifolia*), through dwarf shrubs (dominated by *Sarcopoterium spinosum*) to open areas with diverse grasslands vegetation (dominated by *Gramineae*). The spatial patterns represent wide range of transitional stages between areas of high homogeneity of mainly tall shrubs and grasslands with different compositions of the three vegetation formations. This diversity of patterns is a result of a long history (since the late bronze, approximately 5500

Proc. 3rd International Symposium, 'Retrieval of Bio- and Geophysical Parameters from SAR Data for Land Applications', Sheffield, UK, 11-14 September 2001 (ESA SP-475, January 2002)

years ago) of human activity. Land use in this area is composed of agricultural crops in the wadi's and rangelands with controlled grazing pressures. The study area is characterized by wide range of "regeneration and degradation patterns" of patches representing various soil-vegetation relationships which will allow generalization of the methods to wider areas of transition between Mediterranean and arid regions.

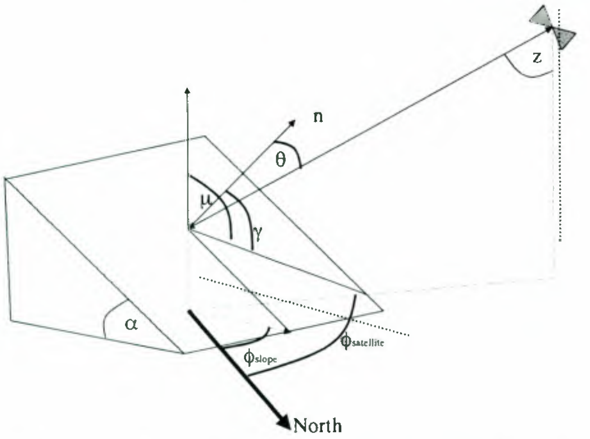

Figure 1 : Viewing and illuminating geometries on the tilted slope unit (note angles formed with the vertical vector representing trunk position)

DATA

Three ERS2 images were acquired for this study from the dates : 29th of February, 10th of April and 17th of May 1997. These dates represent the main phases of the seasonal vegetation phytophenology of this region (Shoshany et. al., 1995). The images were radiometrically calibrated using Laur et. al., (1997) method, excluding computations regarding illumination geometry :

$$\sigma^0{}_{ij} = \left[\frac{1}{N}\sum_{ij=1}^{ij=N} DN_{ij}^2\right]\frac{1}{k}C\left(\frac{\sin\theta i}{\sin\theta_{ref}}\right)$$

where N is the number of pixels within an area of interest; DN is the ERS-2 SAR image digital number and the average in the square parenthesis is calculated following the application of a 3x3 pixel window mean filter to reduce speckle effects; C accounts for updating the gain due to the elevation antenna pattern implemented in ERS SAR PRI data processing and θ_i, and θ_{ref} are the local and reference incidence angle respectively (not included in the calibration).

For allowing derivation of illumination / viewing geometries for image regions of characteristic vegetation and soil cover, the three ERS-2 SAR images were corrected geometrically with reference to topographic maps (1:50,000) and to DGPS readings taken during the field campaign.

These characteristic sites were selected according to our field knowledge , and the specific delination of homogenous surface cover sites was done by incorporation information from air photographs.

Illumination and viewining geometries for each site area were derived using the DTM produced by Hall (Hall, 1994). The following equations were used (Figure 1):

Incidence Angle :

$$\theta = \arccos(\cos\alpha\cos z + \sin\alpha\sin z\cos(Daz))$$

Pairmans' Angle

$$\varphi = \arccos(\cos\alpha\sin z + \sin\alpha\cos z\cos(Daz))$$

Trunk - Illumination Grazing Angle

$$\gamma = (\pi/2 + \alpha * \cos(Daz)) - z$$

RESULTS AND DISCUSSION

Shrub sites for this study were delineated mainy on north and south facing slopes thus forming incidence angles larger than 24 degrees. From figure 2 it is clear that there is a non linear relationship between the backscatter and the incidence angle. Such non linearity is increasing in dates representing the time before the regrowth of young green leaves. May backscattering decreases relatively slower with increasing incidence angle, forming a significant difference from the previous records at angles larger than 53 degrees. This finding is most important since it indicate that the radar may poick the net primary production of each year. Utilization of illumination and viewing geometries at this high range of incidence angles might be achieved by using ascending and descending images for steep and moderately steep slopes.

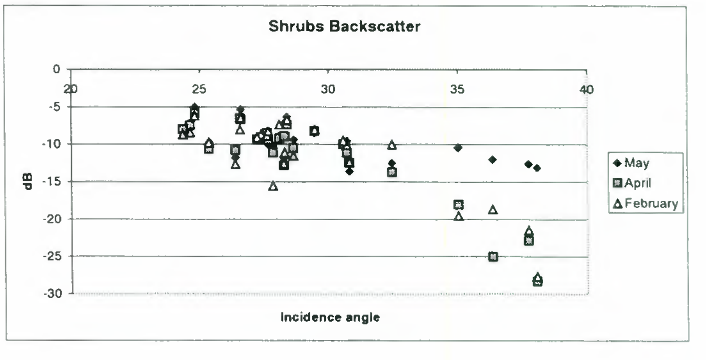

Figure 2 : The change in ERS2 backscatter with angle of incidence

Herbaceous growth had been monitored at its maximum biomass during April. As was observed with shrubs, the backscattering pattern is non-linear and its' decreasing rate is increasing with incidence angle. As Herbaceous growth sites were sampled also in areas of lower incidence angles than those observed for shrubs, and as found in an earlier work by Svoray et. al., (2001) that green leaf biomass at the top of the canopy and that of Herbaceous growth are of the same magnitude , it is of value to integrate the two data sets. Thus the May data for shrubs and the herbaceous data for April were combined (Figure 3). A clear continuation is apparent in the data as well as similarity in backscatter in sites of similar incidence angles.

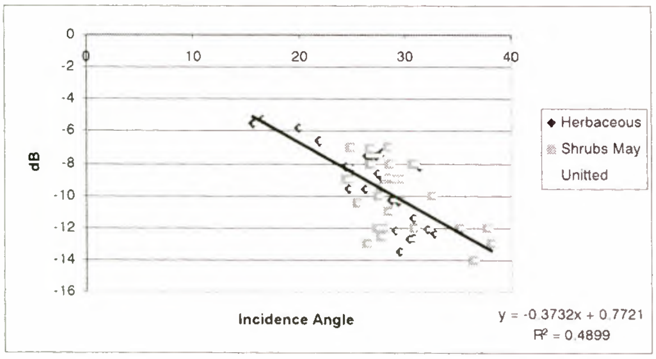

Figure 3 : Backscattering from shrubs and Herbaceous growth.

Bare soil is a dominant surface component in arid and semi arid regions and it has an important effect on the surface backscatter in low and medium density vegetation cover (Svoray et al., 2001). Its backscatter pattern shows inverse nonlinear relationships with the incidence angle (Figure 4), with increased rate of change in angles larger than 35 degrees. However, it is interesting to note that the "soil backscattering line" is also diverging from the "vegetation backscattering line" with increasing incidence angle. The distance formed between the two data sets could facilitated quantification of the relative biomass.

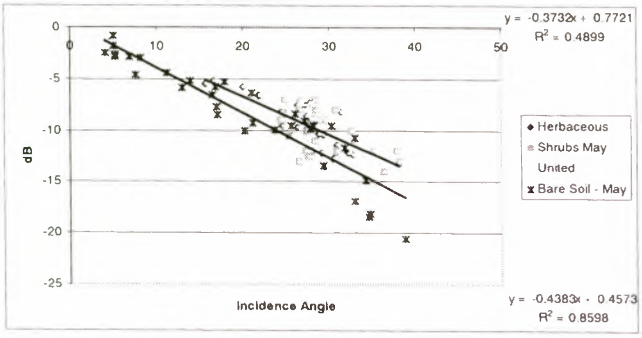

Figure 4 : Backscattering differences between the soil and vegetation.

CONCLUSIONS

This inquiry had indicated clearly that varying the incidence angle may provide important data for discriminating between soil and vegetation, and for quantifying green biomass at the top of the canopy. Implementation of this strategy for mapping surface and vegetation boundary layer properties in large areas require integrating radar data from ERS2 ascending and descending scan directions or by synergy of different instruments, e.g. E-SAR, XSAR and RADARSAT.
However, there is a substantial research yet to be conducted with existing data sets like those utilized here for assessing and modeling other geometrical parameterizations such as trunk-illumination geometries.

ACKNOWLEDGMENT

The Forest Authority (Keren Kaiemet Leisrael) and the Ministry of Agriculture of Israel are thanked for financing this project.

REFERENCES

Beaudoin, A., Le Toan, T., Gwyn, Q. H. J., 1990, SAR observations and modeling of the C-band backscatter variability due to multiscale geometry and soil moisture. *IEEE Transactions on Geoscience and Remote Sensing,* 28, 886-895.

Brown, S.C.M., Quegan, S., and Bennet, J.C., 2001, High resolution measurements of scattering in wheat canopies – implications for crop canopy retrieval. (In this volume).

Ferrazzoli, P., 2001, SAR for agriculture : advances, problems and prospects. (In this volume).

Imhoff, M. L., 1995a, A theoretical analysis of the effect of forest structure on synthetic aperture radar backscatter and the remote sensing of biomass. *IEEE Transactions on Geoscience. and Remote Sensing,* 35, 1-18.

Imhoff, M. L., 1995b, Radar backscatter and biomass saturation: ramifications for global biomass inventory. *IEEE Transactions on Geoscience. and Remote Sensing,* 33, 511-518.

Laur, H., Bally, P., Meadows, J., Sanchez, B., and Schaetter, E. (1997): *ERS SAR Calibration – Derivation of the Backscattering Coefficient Sigma-Nought. In* ESA ERS SAR PRI products. Document No: ES-TN-RS-PM-HL09, ESA web site http://uranus.esrin.esa.it/eeo/lft/ESC2.

Le Toan, T., 2001, Retrieval of forest information from SAR data. (In this volume).

Luckman, A., The effect of topography on mechanisms of radar backscatter from coniferous forest and upland pasture. *IEEE Transactions on Geoscience and Remote Sensing,* 36, 1830-1834.

Macelloni, G., Paloscia, S., Pampaloni, P., Bruscaglioni, P., and Poggi, P., 2001, Simulating backscattering from forests: A comparison of coherent and incoherent approaches with experimental data. (In this volume).

Pairman, D., Belliss, S. E., McNeill, S. J., 1997, Terrain influences on SAR backscatter around Taranaki, New Zealand. *IEEE Transactions on Geoscience and Remote Sensing*, 35, 924-932.

Saich, P., and Lewis, P., 2001, Comparison of HYMAP ? E-SAR data with models for optical reflectance and microwave scattering from vegetation canopies. (In this volume)

Shoshany, M., 1992, A Simulation of bidirectional reflectance distributions for various surface microstructures. *Int. J. of Remote Sensing,* 13(12), 2355-2361.

Shoshany, M., Kutiel, P. and Lavee, H., 1995, Seasonal vegetation cover changes as indicators of soil types along a climatological gradient: a mutual study of environmental patterns and controls uremote sensing. *International Journal of Remote Sensing* 16: 2137 - 2151.

Shoshany, M., Svoray, T., Curran, P., Foody, G., and Perevolotsky, A., 2000, The relationships between ERS-2 SAR backscatter and soil moisture : generalization from a humid to semi-arid transect. *International Journal of Remote sensing, 21(11), 2337-2343.*

Svoray, T., Shoshany, M., Curran, P. J., Foody, G. M., and Perevolotsky, A. (2001): Relationship between green leaf biomass and ERS-2 SAR backscatter of four vegetation formations in the semi-arid zone of Israel. *International Journal of Remote Sensing*, Vol. 22, pp. 1601-1607.

Teillet, P. M., Guindon, B., Meunier, J. F., Goodenough, D. G., 1985, Slope-aspect effect in synthetic aperture radar imagery. *Canadian Journal of Remote Sensing,* 11, 39-49.

van Zyl, J. J., Chapman, B. D., Dubois, P., Shi, J., 1993, The effect of topography on SAR calibration. *IEEE Transactions on Geoscience and Remote Sensing,* 31, 1036-1043.

van Zyl, J. J., 1993, The effect of topography on radar scattering from vegetated areas. *IEEE Transactions on Geoscience and Remote Sensing,* 31, 153-160.

SAR MONITORING FOR TROPICAL FOREST IN INDONESIA

Ruandha A. Sugardiman

Department of Environmental Sciences, Sub-department of Water Resources
Wageningen University, The Netherlands
Tel: + 31 317 483576/ Fax: +31 317 484885
E-mail: ruandha.sugardiman@users.whh.wau.nl

ABSTRACT

A large number of ERS-1/2 SAR scenes of a tropical rain forest test site in East-Kalimantan, Indonesia, of the October 1993 - February 2000 (21 images) period have been studied. Extensive fieldcheck was also conducted to collect field information about landcover, landuse, fire damage and when the fire was happening.
The objective is to study its potential for land cover change monitoring.

Also an attempt is made to simulate the use of Envisat-ASAR as replacement of the current ERS-SAR data for future monitoring system. AirSAR-PACRIM 2 campaign data of September 2000 are used for this purpose.

This on-going study is examining the use of SAR data for land cover type mapping at large scale and to assess accuracy.

Key words: SAR; ASAR; tropical forest; monitoring.

1. INTRODUCTION

The availability of data from orbital SAR systems allowed the observation of land cover regardless of the sometimes-limiting weather conditions.
ERS-SAR data have been used in many landcover changes monitoring studies before, also at the Guaviare *Tropenbos* site in Colombia and in Indonesia. In the thesis of Bijker (1997) a monitoring system for Guaviare is described linking land cover change models and multi-temporal ERS-SAR observations. Mapping accuracy in the order of 60-70% was obtained for forest, secondary vegetation, pastures and natural grasslands.

AirSAR data have been studied also for biophysical forest type characterisation in Colombian Amazon. The following results may indicate the high level of accuracy obtained: 15 classes can be differentiated, the average radar map agreement ranges from 68-94% (depending on the type of map and approach) and for only a few classes the agreement is less than 70%. (Hoekman, 2001).
In September 2000, NASA's AirSAR during PACRIM-2 campaign (Pacific Rim) collected fully polarimetric C-, L- and P-band data in Sungai Wain, East Kalimantan area.

In November 2001, the European Space Agency will launch Envisat, an advanced polar-orbiting Earth observation satellite that will ensure the continuity of the data measurements of the ESA ERS satellites.
One of the Envisat instruments is ASAR, an **A**dvanced **S**ynthetic **A**perture **R**adar, operating at C-band, ASAR ensures continuity with the image mode (SAR) and the wave mode of the ERS-1/2 AMI (active microwave instrument).

For this purpose to simulate Envisat-ASAR data, Sungai Wain AirSAR data are used.

As an illustration tables 1, 2, 3 and 4 list some of the major characteristics of the systems which use is discussed in this paper.

Table 1. ERS-SAR sensor and image parameters

Characteristics	ERS
Centre frequency	5.3 GHz
Bandwidth	15.5 MHz
Polarisation	VV
Incidence angle at mid-swath	23 degrees
Swath width	100 km
Number of looks	3
Operating altitude	782 km
Range resolution	<33 m
Azimuth resolution	<30 m
Ground range pixel spacing	12.5 m
Azimuth pixel spacing	12.5 m

Table 2. Some relevant AirSAR image specifications*)

Mode	PolSAR	XTI2
Full polarimetry	C, L & **P-band**	P-band
Interferometry		C, L - band
Height resolution for low-relief terrain (m)		1-3
Height resolution for high-relief terrain (m)		3-5
Approx. DEM resolution (m)		10 x 10
Bandwidth	40 MHz	
Approx. SR pixel size (m)	**4 x 3**	
Approx. SR resolution (m)	**5 x 5 m**	
Independent looks per pixel	**8 (?)**	
Noise Eq. Sigma0	**-45 dB (C, L&P)**	
Absolute calibration	**< 3dB**	
Relative calibration between channels	< 1.5 dB	
Relative polarisation calibration within	< 0.5 dB	

*) http://airsar.jpl.nasa.gov/engineering/specs/char_table.html

Proc. 3rd International Symposium, 'Retrieval of Bio- and Geophysical Parameters from SAR Data for Land Applications', Sheffield, UK. 11-14 September 2001 (ESA SP-475, January 2002)

Table 3. ASAR high resolution product quality**)

ASAR HIGH RESOLUTION PRODUCTS	Image Mode (IM)	Alternating Polarisation (AP)
Precision Image	Pixel = 12.5 m Res. < 30 m ENL > 3	Pixel = 12.5 m Res. < 30 m ENL > 1.8

**) http://envisat.esa.int/

Table 4. ASAR image swath geometry for IM and AP**)

ASAR Swathes	Swath Width [km]	Near Range Incidence Angle	Far Range Incidence Angle
IS1	108.4 - 109.0	14.1 - 14.4	22.2 - 22.3
IS2	107.1 - 107.7	18.4 - 18.7	26.1 - 26.2
IS3	83.9 - 84.3	25.6 - 25.9	31.1 - 31.3
IS4	90.1 - 90.6	30.6 - 30.9	36.1 - 36.2
IS5	65.7 - 66.0	35.5 - 35.8	39.2 - 39.4
IS6	72.3 - 72.7	38.8 - 39.1	42.6 - 42.8
IS7	57.8 - 58.0	42.2 - 42.6	45.1 - 45.3

**) http://envisat.esa.int/

2. LAND COVER CHANGE AND FIRE DAMAGE MONITORING

The study at the East-Kalimantan *Tropenbos* test site relates to land cover change and fire damage monitoring with main emphasis on early detection. The terrain is very hilly and typical for the rugged topography encountered in most Indonesian forest areas. The modulating effects of slope angle and slope aspect on the backscatter intensity complicate processing of data of hilly terrain. New multi-temporal segmentation techniques (Oliver and Quegan, 1998) in combination with backscatter change classification techniques have been applied to deal with this problem.

The result show that fire affected areas can be delineated well, but that it is sometimes hard to estimate the intensity of the fire damage accurately. Combining ERS-SAR observations during the fire period with land cover class information obtained by ERS-SAR in the pre-fire period and observations of 'hot spots' (i.e. fires) by NOAA-AVHRR, together with knowledge of the types of fire occurring in this area, can be shown to yield very reliable results. The classification result of an independent validation through fieldwork campaigns showed high accuracy for almost all land cover types, before as well as after the fire period. For agricultural areas the result may seem poor. However, these areas comprise a mixture of gardens, rice fields, (fruit) tree plantations and forest remnants. Since agricultural areas are confused with plantations and forests, which also occur *within* the agricultural areas, the result may be much better when interpreted accordingly. Another result is that burnt forests are not always detected (85.2%). This is believed to be the result of ground fires, leaving the upper canopy largely intact during several months after the ground fire, thus disabling the C-band SAR to detect such a condition. It was also found that susceptibility to fire might be well assessable by using the stability of the radar backscatter level in the pre-fire period as an indicator.

ERS-SAR multi-temporal segmentation gave an overall accuracy of around 82,4%.

Fire damage map was the final result of this study, which visualises the distribution of burnt areas and their extents/ areas (figure 1).

Figure 1. Fire damage map

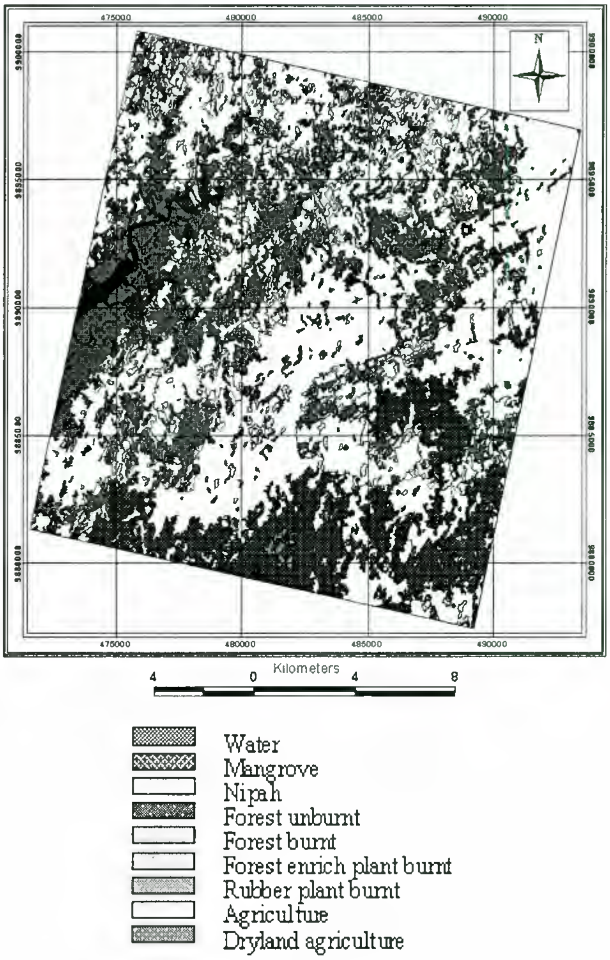

3. SIMULATION ASAR FROM AIRSAR

It is of interest to simulate IM and AP ASAR images. How can we do this from AirSAR data? Creating a larger pixel size (by resampling, block averaging, etc) and a lower resolution (by low-pass filtering) is not very difficult. To get a low number of ENL (3 and 1.8, resp.) is less straightforward. Moreover, what do we know about the correlation of slant and ground range of ASAR pixels? Can we assume the same as for ERS-1/2?

Another problem is the incidence angle. It is not possible to simulate other incidence angles than those measured by AirSAR. Consequently the range will be roughly between 25-65 degrees, within a 10 km strip. This coincides with ASAR swaths IS3 until IS7.

4. CONCLUSION AND RECOMMENDATION

The ERS SAR is an operational system and, in principle, data can be obtained routinely and frequently. The resolution of the ERS SAR is sufficiently high, for example, to verify the spatial extent of plantations and reforestation obligations. Alternatively, the future ASAR may be utilised.
In the future more advanced spaceborne SAR systems may become available, which can achieve a much higher mapping accuracy and may be utilised for monitoring a wide variety of land cover dynamics at scales of 1:100,000 and smaller.

Further research is needed to improve the methodology to obtain more accurate results as a practical and applicable methodology for fire damage monitoring

5. ACKNOWLEDGEMENT

Special thanks are given to colleagues, i.e. Dirk Hoekman, Martin Vissers, Muljanto Nugroho, Kemal Unggul Prakoso, Bambang Suryokusumo and Wisnu Wardhana for their valuable comments and materials. We would like to extent our gratitude to the Ministry of Forestry, Tropenbos International, and Gibbon Foundation for their assistance, i.e. materials and financial supports.

6. REFERENCE

Bijker, W. (1997): Radar for rain forest: A monitoring system for land covers change in the Colombian Amazon, *Doctoral Thesis, ITC, Enschede*, the Netherlands, 189 p.

European Space Agency. (1999): INDREX (INDonesia Radar EXperiment). *Final Results Workshop Proceeding. ESA SP-489. ESTEC*, 9 November 1999 - Jakarta, 30 November 1999.

Grim, R.J.A, F.M. Seifert, D.H. Hoekman, C. Varekamp, Y.A. Hussin, M.A. Sharifi, M. Weir, K.U. Prakoso, R.A. Sugardiman, M. Nugroho, B. Suryokusumo. (August 2000): SIRAMHUTAN Sistem Informasi untuk Manajemen HUTAN, A demonstration projects for forestry in Indonesia, *BCRS Publication* NRSP-2 report 00-07.

Hoekman, D.H., and M.J. Quiñones (2001): Biophysical Forest Type Characterisation in the Colombian Amazon by Airborne Polarimetric SAR. *Submitted to IEEE Transactions on Geoscience and Remote Sensing, 26 April 2001.*

Kuplich, T.M. (2000): The study of ERS-1 SAR and Landsat TM synergism for land use classification, *International Journal of Remote Sensing*, Vol. 21, No. 10, pp.2101-2111.

Le Toan, T. (1995): Assessment of ERS-1 SAR data for forest studies in Southeast Asia, *ESA Earth Observation Quarterly (EOQ)* No. 48, June 1995, ESA-ESRIN.

Oliver, C and S. Quegan. (1998): Understanding Synthetic Aperture Radar Images, *Artech House.*

Pohl, C. (1996): Geometric Aspects of Multisensor Image Fusion for Topographic Map Updating in the Humid Tropics. *PhD Thesis. ITC, Enschede*, The Netherlands, 159 p.

Sugardiman, R.A. (2000): Fire damage assessment using remote sensing (A case study using Radar and NOAA~AVHRR data in East Kalimantan). *M.Sc. Thesis Wageningen University, Wageningen*, The Netherlands, 86 p.

ESTIMATING SOIL MOISTURE IN RAINFED PADDY FIELDS USING ERS-2 C-BAND SAR DATA

Donald M. Ugsang*, Kiyoshi Honda, Apisit Eiumnoh, and Mitsuharu Tokunaga
Space Technology Applications and Research Program
School of Advanced Technologies, Asian Institute of Technology,
P.O. Box 4 Klong Luang, Pathumthani 12120, Thailand
Tel: +66-2 524-6148, Fax: +66-2 524-6147, *E-mail: donald@ait.ac.th

ABSTRACT

This study evaluates the potential and limitations of using ERS-2 C-band SAR data for estimating soil moisture in rainfed paddy fields. Results of the study show that ERS-2 C-band SAR data can be used to measure soil moisture at the top 5-cm layer of the soil profile in rainfed paddy fields. An empirical function was established to estimate the soil moisture content from the backscattering coefficient of the ERS-2 C-band SAR data, with an accuracy of $R^2 \sim 0.91$. The function was established under two conditions. First, when the rainfed paddy fields were bare until they are covered with rice crop at the early vegetative growth stage – 38 cm in height or 425 and 102 g/sq.m. in wet and dry biomass, respectively. Second, when the change in surface roughness throughout the growing period is small.

Keywords: ERS-2 SAR, Backscattering Coefficient, Soil Moisture, Surface Roughness, Vegetation Height and Biomass

1 INTRODUCTION

Soil moisture is one of the dynamic parameters in energy and hydrological processes. While remote sensing of soil moisture can be achieved to some extent by all regions in the electromagnetic spectrum, only the microwave region offers the potential for quantitatively measuring soil moisture from space (Engman and Gurney, 1991). For the past two decades several studies were directed on the retrieval of soil moisture from Synthetic Aperture Radar (SAR) data. Experiments conducted using SAR data showed strong linear correlation between soil moisture of the first few cm layer of the soil profile and the radar backscatter coefficient (Wooding et al. 1992, Ferrazzoli et al. 1992, Dobson and Ulaby 1986) or the value of the digital number (Mohan et al. 1992, Demircan et al. 1993 as cited by Le Toan 1994)

Within the scientific goals of the GEWEX Asian Monsoon Experiment-Tropics (GAME-T), a microwave remote sensing campaign was undertaken to evaluate the potential of ERS-2 C-Band SAR data for quantitative estimation of soil moisture at different growth stages of rice crop in rainfed paddy fields. From July 1997 to December 1998, a series of field measurements were conducted on soil moisture, surface roughness, and plant parameters concurrent to each ERS-2 C-band SAR image acquisition.

2 SITE DESCRIPTION

The study area is a large, non-irrigated, paddy field located in the western part of Sukhothai Province in Thailand. The general topography is flat, with average mean sea level variations from 52 to 56 meters. It has a tropical monsoon climate with clearly defined wet and dry seasons (Table 1). The wet season lasts from late May to October, with maximum precipitation occurring in September (264.4 mm average). The dry season lasts from November to April. Land use consists mainly of rice crop. Cultivation is highly seasonal and starts at the onset of the rainy season. During the campaign period, land preparation was done about two to three weeks before the 18 July 1998 observation. Following final land leveling, the seeds were broadcasted at a rate of about 125kg/ha. Harvesting was done before 5 December 1998. The paddy fields were kept fallow until the next cropping season.

Table 1. Mean (1974-1994) monthly climatic parameters from Si Samrong Agromet Station.

Month	Rainfall (mm)	Pan Evaporation (mm)
January	5.2	116
February	5.6	138
March	20.0	202
April	49.1	226
May	160.6	201
June	138.9	174
July	128.7	171
August	189.1	164
September	264.4	141
October	154.2	127
November	22.4	114
December	9.1	112

Proc. 3rd International Symposium, 'Retrieval of Bio- and Geophysical Parameters from SAR Data for Land Applications', Sheffield, UK, 11-14 September 2001 (ESA SP-475, January 2002)

3 INVESTIGATED PARAMETERS

3.1 Soil Moisture

Ground parameters were measured concurrent to every ERS-2 C-band SAR image acquisition. Intensive soil moisture measurements were conducted every 25 meters in about 10 hectares of paddy fields. Soil samples collected from the upper 5 cm layer of the soil profile were oven dried for 24 hours at 105 ^{0}C. Gravimetric (SM_{Gra}) and volumetric (SM_{Vol}) moisture content of the soil samples (Figure 1) were calculated from

$$SM_{Gra} = (Mw - Md)/ Md \quad (1)$$

$$SM_{Vol} = SM_{Gra} * (\rho_b/\rho) \quad (2)$$

where Mw = weight of the wet sample, Md = weight of the dry sample, ρ_b = bulk density of the sample, and ρ = the density of water.

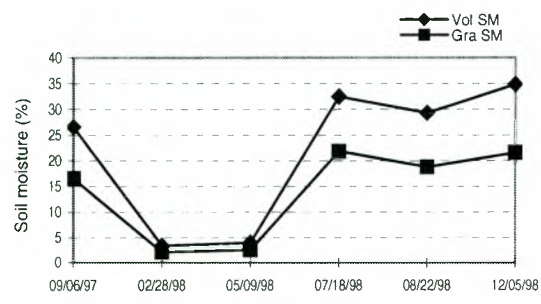

Figure 1. Averaged gravimetric and volumetric soil moisture content of soil samples measured concurrent to ERS-2 C-Band SAR image acquisitions.

3.2 Surface Roughness

Surface roughness affects the backscatter response from the target. However, studies by Engman and Wang (1987) and Tansey et al. (1997) indicated a weak relationship between backscatter and root mean square (RMS) height of the surface. Generally, a rough surface will increase radar signal return (Dallemand et al., 1993) decreasing the sensitivity of radar backscatter to soil moisture. Controlling this factor is a key to operational application of SAR remote sensing in soil moisture studies (Birkett, 1997). For a wide range of surfaces, monitoring temporal variations of soil moisture is possible if roughness conditions are assumed constant (Tansey et al., 1997) or having small changes due to weathering (Le Toan et al., 1994).

Surface roughness was not measured frequently as that of soil moisture. Measurement of the parameter, expressed as root mean square (RMS) height variation of the soil surface, was made using a roughness board of 130 x 45 cm size with a horizontal resolution of 1 cm and a vertical resolution of 0.1 cm. The first measurement was done during the fallow period (averaged RMS height = 1.10cm) when the paddy field is assumed to have the smallest root mean square height variation. The second measurement was taken during the start of land preparation (averaged RMS height = 2.21cm) when the paddy field will have its maximum height deviation from the mean (Figure 2). Land preparation is concluded by land leveling, where big soil clods are broken into smaller pieces. Throughout the growing season, from planting to harvesting, it is assumed that no significant changes in surface roughness occurred.

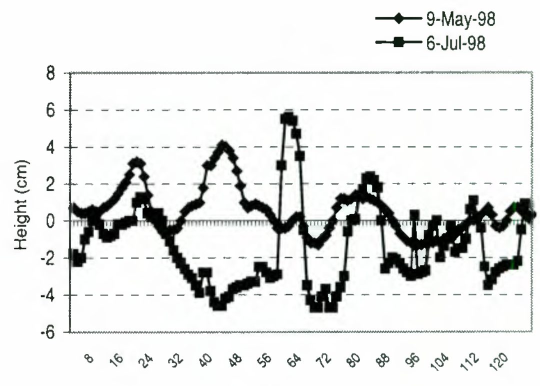

Figure 2. Typical surface profiles of the study area; a) surface roughness (averaged RMS height from 2 measurements = 1.10 cm) on 9 May 1998 dry season, where the field is kept fallow; b) surface roughness during land preparation on July 6, 1998 (averaged RMS height from 2 measurements = 2.21 cm).

3.3 Vegetation

The presence of vegetative cover affects radar measurement of soil moisture (Schmugge et al., 1979). While the effect of vegetation may be negligible on the early stages of crop growth, it becomes significant at the later growth stages when vegetation becomes dense (Le Toan et al., 1997). Studies of Aschbacher et al. (1995) and Kurosu et al. (1994) demonstrated that plant height is a good parameter for characterizing rice crop growth and yield. While Le Toan (1996) reported that biomass is more difficult to obtain with accuracy than the height, Jackson and Schmugge (1989) proposed that an estimate of the latter could provide a good representation of the vegetation effects.

Measurements of plant height (Figure 3) and biomass (Figure 4) were done concurrent to image acquisitions. The plant biomass referred to in this study includes only the plant parts above the soil surface.

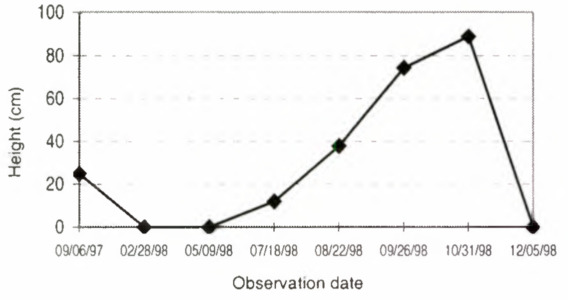

Figure 3. Height of rice crop at different growth stages. The 28 February and 9 May 1998 imaging dates represent the fallow period. The crop was just a few days old on 18 July 1998. Plant height is zero after harvesting, although some dry straws covered the soil surface during the 5 December 1998 observation.

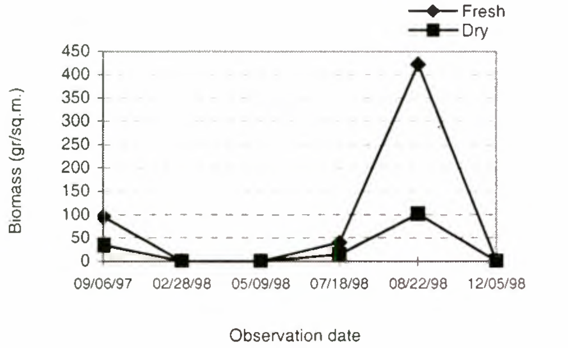

Figure 4. Fresh and dry biomass at different growth stages. The measurements on 26 September and 31 October 1998 were not reflected. The field was flooded during the 26 September 1998 observation date. There was no SAR data available for the 31 October acquisition date.

4 ERS2 C-BAND SAR DATA

While 10 field measurements were conducted concurrent to ERS-2 C-band SAR image acquisitions, only 7 SAR data sets (Table 2) are available for analysis. The data sets represent the different growing stages of the rice crop, from fallow and land preparation to harvest. The SAR data, processed by EECF Italy, are three-look precision images (PRI) with 12.5 x 12.5 pixel size. The backscattering coefficients were derived using Laur's Method (Laur, 1992).

Table 2. ERS-2 C-band SAR data

Observation Date	Orbit	Track/Frame
06/09/97	12440	061/3267
28/02/98	14945	061/3267
09/05/98	15947	061/3267
18/07/98	16949	061/3267
22/08/98	17450	061/3267
26/09/98	17951	061/3267
05/12/98	18953	061/3267

The original images were projected to UTM coordinates using ground control points identifiable both on the imagery and on the ground. Nearest neighbor resampling was used with an RMS transformation error of approximately half pixel at maximum. The backscatter coefficient was derived from an average of 544 pixels (about 8.5 hectares), more than the minimum 5-ha field size recommended for speckle-limited accuracy in ERS image (Wooding et al., 1995). Speckle filters were applied to the original images to further reduce the effect of speckle.

5 RESULTS AND DISCUSSION

The radar backscattering coefficients σ^0 from the field vary over the growing season from fallow period and early crop establishment to maturity and harvest. The reason for this variation is directly related to the changes in soil moisture as shown in Table 3 and Figure 5. During the fallow period (February and May) the dry bare fields provide very low backscatter (-11 to -13 dB). A sharp increase of the σ^0 (-5.22 dB) could be observed on the 18 July 1998 observation date, corresponding to the increase in soil moisture content (32.49% by volume). A gradual decrease in the σ^0 is observed on the 22 August 1998 image on which a small drop in the soil moisture content (29.27% by volume) was also recorded. During the 26 September 1998 experiment, the field was covered with water varying between 3-15 cm in depth. The observed radar backscatter (-8.64 dB) on this imaging date results mainly from the multiple interaction between the vegetation and the standing water. After the harvest, the σ^0 slightly increases (-6.56 dB) with the field covered by dry straws but not flooded.

Table 3 . Radar backscattering coefficients and corresponding volumetric soil moisture and vegetative state during each ERS-2 acquisition.

Observation Date	Radar Backscatter	SM_{Vol} (%)	Vegetative State
06/09/97	-6.55	26.54	rice: 24.9 cm
28/02/98	-11.26	3.39	bare (fallow)
09/05/98	-12.92	3.96	bare (follow)
18/07/98	-5.22	32.49	rice: 12.0 cm
22/08/98	-7.37	29.27	rice: 37.8 cm
26/09/98	-8.64	Flooded	rice: 74.3 cm
05/12/98	-6.56	34.80	rice harvested

5.1 Radar Backscatter and Soil Moisture

The relationship between radar backscatter coefficient and volumetric soil moisture, observed from the top 5-cm of the soil profile, is established in the function:

$$SM_{vol} = 5\sigma^0 + 63.75$$

Results of the analysis indicate a good agreement between the observed backscatter coefficient and percent volumetric soil moisture (R^2=0.91). The analysis excludes the data sets of 26 September 1998, as the paddy fields were flooded during this observation date. The volumetric moisture content of saturated soils in the paddy fields is ~ 40%. The correlation coefficient between the backscatter coefficients and the observed soil moisture shows a very slight improvement (0.913) in speckle-filtered images, e.g., Lee 5x5 and Gamma 3x3.

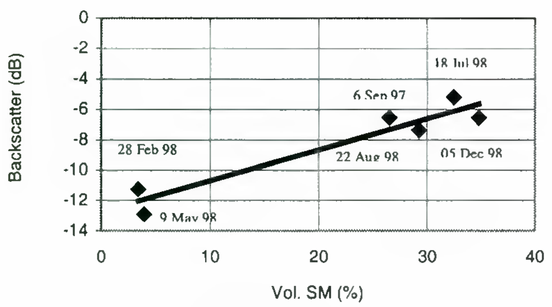

Figure 5. Observed radar backscatter values from the original image plotted against the volumetric soil moisture (R^2 = 0.91).

Figure 6 shows the ERS-2 C-band SAR sub-scenes acquired at different dates. The 9 May 1998 sub-scene, acquired during the fallow period (where soil moisture is low), shows a darker tone compared to 18 July 1998 sub-scene acquired during the early crop establishment, where the soil moisture is high.

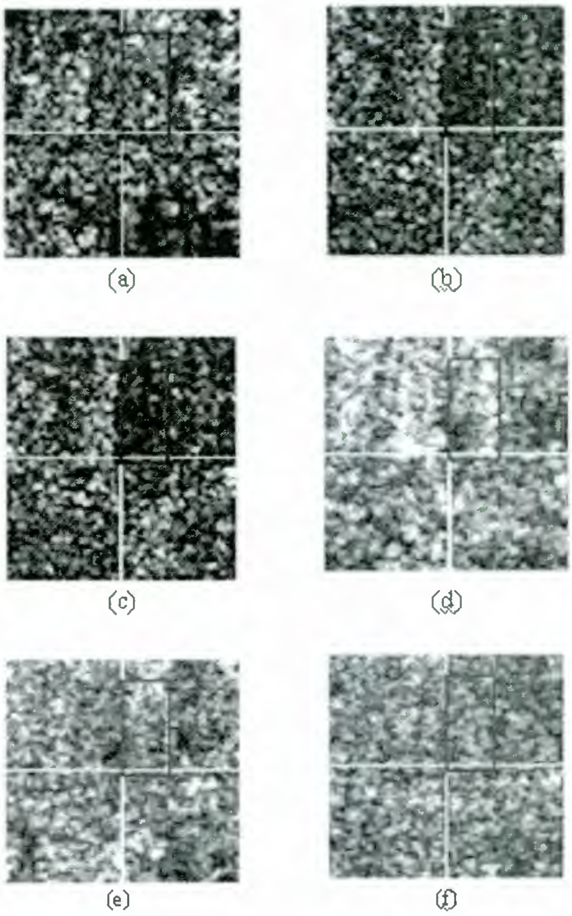

Figure 6. ERS-2 C-band SAR sub-scenes acquired during (a) 6 September 1997, (b) 28 February 1998, (c) 9 May 1998, (d) 18 July 1998, (e) 22 August 1998, and (f) 26 September 1998.

5.2 Radar Backscatter and Surface Roughness

Small changes in surface roughness do not have significant contribution to anomalies in estimating soil moisture using ERS-2 C-band SAR data. In the case of rainfed paddy fields, the range in surface roughness is from 1.10 cm to 2.21 cm. It should be noted that the surface roughness of 2.21 cm was measured during land preparation. Land preparation is finalized by land leveling, thus, during planting/sowing, surface roughness of the paddy fields would be less than 2.21 cm.

In assessing soil moisture in rainfed paddy fields using ERS-2 C-band SAR data, the effect of surface roughness to the total radar backscatter is small and insignificant, thus negligible compared to the influence of soil moisture variation. This finding is consistent with the recommendations of ESA (1997) and Le Toan (1994) in using SAR remote sensing for soil moisture studies.

5.3 Radar Backscatter and Vegetation Parameters

While vegetation attenuates radar backscatter from the soil, results of the analysis showed that its effect is not significant on the early stages of vegetative growth (from seed broadcasting until it reaches 38 cm in height or 425 g/m^2 in wet biomass based on 22 August 1998 data). At the early growth stages, the contribution of vegetation to the total radar backscatter from the paddy fields is minimal compared to that of the moisture content of the soil.

Comparison between the observed backscatter coefficient and plant height showed a very poor agreement with R^2 equals to 0.23 (Figure 7). Similar findings were observed when expressed as a function of plant biomass with R^2 of 0.07 and 0.11 for wet and dry biomass, respectively.

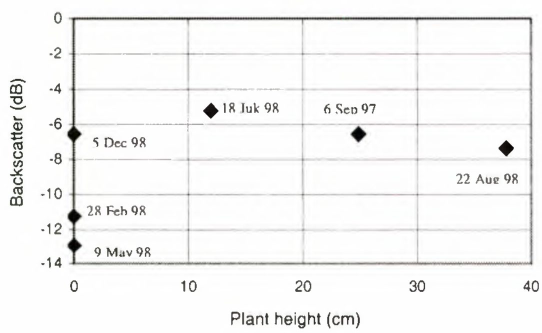

Figure 7. Observed backscatter values from the original image plotted against plant height (R^2= 0.23).

6 Conclusion and Recommendation

The results of the study have shown that ERS-2 C-band SAR data can be used to quantitatively estimate soil moisture during fallow period and at various growth stages of rice crop in rainfed paddy fields. The following specific conclusions are made from the results of the study:

An empirical model to estimate soil moisture (SM_{vol}) of the top 5-cm layer of the soil profile from radar backscattering coefficient (σ^0) was established under two important conditions: (a) First, when the rainfed paddy fields were bare and until the rice crop was at the early vegetative growth stages- 38 cm in height or 425 and 102 g/m^2 in wet and dry biomass, respectively; and (b) second, when the range at which surface roughness changes throughout the growing period is small, allowing the effect of surface roughness parameter to the total backscatter from the field to be considered negligible. The range of surface roughness from 1.10 during fallow to 2.21 cm during land preparation is typical in the study area.

The attenuating effect of vegetation on the radar backscatter from the soil is not significant at the early vegetative growth stages of rice, allowing the inference of the moisture content of the soil underneath. Beyond these early vegetative growth stages i.e., when rice plants exceed 38 cm in height or 425 g/m^2 in wet biomass, the radar backscatter from the vegetation and its effect on the soil moisture-radar backscatter coefficient relationship needs to be studied. Therefore, additional measurements are recommended to understand the radar backscatter and soil moisture relationship, and the effect of vegetation at the later stages of vegetative growth, including reproductive and ripening phases of rice.

Other SAR systems with different configurations may provide potential for SAR remote sensing of soil moisture. It would be interesting to examine the use of RADARSAT and ENVISAT SAR data for soil moisture measurement. The standard modes of the C-band SAR system in RADARSAT allows imaging of areas at varying incidence angles between 20° and 49° with a variety of swath width and resolution (Ahmed et. al., 1990). Likewise, the new features of ASAR on board ENVISAT facilitate image acquisitions at multiple incidence angles and with dual polarization (ESA, 1998). Data acquired from both systems are expected to open up new possibilities for quantitative soil moisture retrieval under variable soil conditions (i.e. differences in moisture content and surface roughness) and vegetative cover (i.e. growth stages of the plants and planting density).

VII Acknowledgement

The ERS-2 SAR.PRI imageries were provided by the European Space Agency under ESA AO3-380 Project. The authors would like to thank the Japan Sub-committee for GAME-Tropics and Mr. Panya Polsan of the Hydrological Center 2, Royal Thai Irrigation Department for support in the conduct of field measurements.

VIII References

Ahmed, S., Warren H.R., Symonds, M.D., and Cox, R.P., 1990. The Radarsat System. *IEEE Transactions on Geoscience and Remote Sensing*, 38, 4: 598-602

Aschbacher, J., Pongsrihadulchai, A., Karnchanasutham, S., Rodprom, C., Paudyal, D.R., and Le Toan, T., 1995.

Assessment of ERS-1 SAR Data for Rice Crop Mapping and Monitoring. *Proceedings IGARSS 1995,* Florence, Italy, 10-14 August.

Birkett, C., Blyth, K., Fellah, K., Van Halsema, E., Kerr, Y., Mauser, W., Nagler, T., Ragab, R., Rombach, M., Rott, H., and Larry, S., 1997. *Satellite Data in Hydrology: Experience with ERS*, SP 1207. ESA Publications Division, ESTEC, Noordwijk, The Netherlands.

Dallemand, J.F., Lichtenegger, J., Raney, R.K., and Schumann, R., 1993. *Radar Imagery: Theory and Interpretation Lecture Notes*, RSC Series Number 67. FAO Publications Division, Viale delle Terme di Caracalla, Rome, Italy.

Demircan, A., Romback, M., and Mauser, W., 1993. Extraction of Soil Moisture from Multi-temporal ERS-1 data of the Freiburg Test-site. *Proceedings IGARSS 1993*, 1794-1796.

Dobson, M.C., and Ulaby, F.T., 1986. Active Microwave Soil Moisture Research. *IEEE Transactions on Geoscience and Remote Sensing*, 24, 1: 23-26.

Engman, E.T., and Gurney, R.J., 1991. *Remote Sensing in Hydrology*. Chapman and Hall, New York, USA.

Engman, E.T., and Wang, J.R., 1987. Evaluating Roughness Models of Radar Backscatter. *IEEE Transactions on Geoscience and Remote Sensing*, GE25, 6:709-713.

ESA, 1998. Envisat - Europe's Earth-Observation Mission for the New Millennium. *Earth Observation Quarterly*, No. 60, 43pp

Ferrazzoli, P., Palosei, S., Pampolini, P., Schiavon, G., Solimini, D., and Coppo, P., 1992. Sensitivity of Microwave Measurement to Vegetation Biomass and Soil Moisture Content: A Case Study. *IEEE Transactions on Geoscience and Remote Sensing*, 30, 4: 750-756.

Jackson, T.J., and Schmugge, T.J., 1989. Passive Microwave Remote Sensing for Soil Moisture: Some Supporting Research. *IEEE Transactions on Geoscience and Remote Sensing*, 27, 2:225-236.

Kuroso, T., Suitz, T., Fujita, M., Chiba, K., and Moriya, T., 1994. Rice Crop Monitoring with ERS-1/SAR: A First Year Result. *Proceedings Second ERS-1 Symposium*, Hamburg, Germany, ESA SP-361, 1: 97-102.

Laur, H., 1992. *Lecture Note on ERS-1 SAR Calibration: Derivation of Backscattering Coefficient in ERS-1.SAR.PRI Products*, Issue 1, Revision 0.

Le Toan, T., Ribbes, F., Wang, L.F., Floury, N., Ding, K.H., Kong, J.A., Fujita, M., and Kuroso, T., 1997. Rice Crop Monitoring Using ERS-1 Data Based on Experiment and Modeling Results. *IEEE Transaction on Geoscience and Remote Sensing*, 35, 1:41-56.

Le Toan, T., 1996. Satellite Assessment for Rice in Indonesia (SARI) - Phase 1: Demonstration Case Study. *EWSE*, Centre for Earth Observation, Directorate General JRC, European Commission, September 1998. URL: http://ewse.ceo.org/anonymous/construct/build.pl/663855.

Le Toan, T., Smacchia, P., Souyris, J.C., Beaudoin, A., Merdas, M., Wooding, M., and Lichteneger, J., 1994. On the Retrieval of Soil Moisture from ERS-1 SAR Data. *Proceedings Second ERS-1 Symposium - Space at the Service of Our Environment*, Hamburg, Germany, ESA SP 361, 883-888.

Mohan, S., Metha, N.S., Metha, R.L., and Al, 1992. Assessment of ERS-1 SAR Data for Soil Moisture Estimation. *Proceedings First ERS-1 Symposium*, Cannes, November 1992, 635-639.

Schmugge, T.J., Jackson, T.J., and McKim, H.L., 1979. Survey of In-situ and Remote Sensing Methods for Soil Moisture Determination. *Proceedings of the Fifth Annual William T. Pecora Memorial Symposium on Remote Sensing*, Sioux Falls, South Dakota. American Water Resources Association, Mineapolis, Minnesota, 333-352.

Tansey, K., White, K., Millington, A., and Battikhi, A., 1997. "Comparison of Modelled Backscatter Response and ERS-1 SAR Data for Desert Surfaces, The Eastern Badia of Jordan", *Earthnet Online*, ESA, September 1998. URL:http://florence97.ers-symposium.org/program-details/data/tansey/index.html.

Wooding, M.G., Griftiths, G.H., Evans, R., Bird, P., Kenward, D., and Keyte, G.E., 1992. Temporal Monitoring of Soil Moisture Using ERS-1 SAR Data. *Proceedings First ERS-1 Symposium,* Cannes, November 1991, 641-648.

Wooding, M.G., Attema, E., Aschbacher, J., Borgeaud, M., Cordey, R.A., De Groof, H., Harms, J., Lichtenegger, J., Nieuwenhuis, G., Schmullius, C., and Zmuda, A.D., 1995. *Satellite Radar in Agriculture: Experience with ERS-1*, SP-1185, ESA Publications Division, ESTEC Noordwijk, The Netherlands.

Conclusions

CONCLUSIONS

S. Quegan – Symposium Chairman

Sheffield Centre for Earth Observation Science, University of Sheffield,
Hicks Building, Hounsfield Rd, Sheffield S3 7RH, UK.
Tel: +44 114 222 3778 Fax: +44 114 222 3809 Email: S.Quegan@sheffield.ac.uk

These conclusions are a distillation of inputs from session chairmen: Henning Skriver (Technical University of Denmark, Lyngby), Paolo Pampaloni (IROE-CNR, Florence), Jan Askne (University of Chalmers), Dirk Hoekman (University of Wageningen), Malcolm Davidson (ESA-ESTEC), Geoff Wadge (Earth System Science Centre, Reading), Helmut Rott (University of Innsbruck) and Ake Rosenqvist (NASDA).

Agriculture and land cover.
The papers under this topic concentrated on three main issues: selection of optimum radar configurations, the use of modelling for interpretation of polarimetric backscatter and methods for parameter retrieval.

Multitemporal acquisitions are essential for land cover and crop classification even when full polarimetric SAR data are available at L- and C-band. In this regard, despite it being obvious to the radar community, it is still important to stress the all-weather capabilities of radar systems compared to optical systems like SPOT and Ikonos. Polarimetric information is observed to be very important at L-band, but at C-band the situation is more complicated. Airborne SAR results show that the additional information in the full polarimetric data is limited, but full polarimetry may be needed to understand the scattering observed in very high resolution measurements with ground-based C-band SAR. A very important issue is the study and understanding of the temporal and spatial variability of backscatter signatures for different vegetation classes.

The C-band Envisat ASAR and the L-band ALOS-PALSAR are expected to contribute significantly to agricultural applications. It is important that European users are ensured access to the latter data. Appropriate software packages also need to be made available for users, especially for the future polarimetric satellite SARs, together with demonstration projects showing users the potential of SAR polarimetry.

Results indicate that the interferometric coherence may add valuable information for land cover classification. A large archived data set is available from the ERS Tandem mission that could be used for a worldwide forest/non-forest map, but it has not yet been exploited. Also relevant for land cover mapping is SRTM data, and users are recommended to obtain access to these data, if possible.

More basic research is needed on understanding the interaction of microwaves and vegetation, including collaboration with the optical community to develop models with a common physical basis. For some crops (notably wheat), models including multiple scattering and coherent effects seem essential in order to match theory with observations. Further investigation of permittivity models also seems advisable. It was emphasized that high quality *in situ* data, gathered according to a standard scheme, are needed to support the modelling.

Forestry
Improved electromagnetic modelling has been essential in giving better insight into wave-forest interaction mechanisms. Probably the most important developments have been in the formulation of 3-D coherent and radiative transfer models which exploit geometric descriptions of tree growth and the forest canopy. There has been significant progress in understanding canopy penetration (using HUTSCAT data and models) and the importance of the ground contribution under differing environmental conditions. We have also learned a lot about which canopy elements dominate the scattering and attenuation at different frequencies, polarisations and incidence angles, and hence about what causes the saturation in the backscattering coefficient as biomass increases. However, relationships between radar measurements and forest biophysical parameters depend on forest type and conditions, tree species, etc. Further experiments are therefore needed under various forest conditions to derive robust relationships for inversion purposes.

Most papers in the workshop set out to relate radar measurements to biomass (or stem volume) and/or tree height, although recovery of extinction coefficients was also considered. The majority of papers dealt with airborne systems (Hutscat, ESAR, DoSAR, GeoSAR, ESAR) for methodology research, often using more advanced techniques (e.g. polarimetric interferometry). Exploitation of satellite SAR was reported in only a few papers, but very important was the demonstration of continental scale biomass mapping in Siberia by combining ERS tandem coherence and JERS backscatter. Archived data will allow this approach to be extended to the rest of the boreal zone, but no current

Proc. 3rd International Symposium, 'Retrieval of Bio- and Geophysical Parameters from SAR Data for Land Applications', Sheffield, UK, 11-14 September 2001 (ESA SP-475, January 2002)

sensors can provide new data for this type of survey. ERS Tandem InSAR seems capable of mapping an enhanced range of biomass under low temperature conditions, and methodology for the use repeat pass JERS is being developed. Several papers dealt with polarimetric L-band data (looking towards ALOS-PALSAR and TerraSAR) for biomass retrieval; these tended to confirm previous reports about biomass saturation, with the best single channel being L-HV. There was similar confirmation of the sensitivity of VHF to a large biomass range. Height and structure recovery was mainly based on high resolution airborne data. Polarimetric interferometry seems promising, but there is still limited validation or assessment of the effects of forest structure and ground conditions. Similar remarks apply to single pass interferometry; thorough testing of its ability to recover forest parameters seems essential (for example, to assess the value of a satellite Cartwheel configuration for forest and biomass applications). Reported steps in this direction included first results on height recovery with combined P and X band InSAR. As a general principle, it was noted that comparison of new sensors and techniques on well-documented common sites would be valuable.

Soils and Hydrology

The soils and hydrology session was very varied, ranging from a review of the physical relationship between the soil surface parameters and electromagnetic scattering, to an interesting application in which SAR-based surface roughness maps are used as an indirect way of estimating ground water evaporation in arid areas. Along the way sensors with frequencies ranging from C to VHF bands and a variety of retrieval techniques were considered. Some overall unifying elements and problems to be solved could be identified. Prior knowledge on roughness statistics helps considerably in constraining soil moisture recovery, and can be included in a Bayesian approach. Such knowledge may be gained using polarimetry; this is important in view of forthcoming SAR missions. Multiple frequencies also help to reduce the uncertainty in soil moisture retrieval. The importance of well-validated scattering models in the development of robust site-independent soil parameter retrieval algorithms was underlined in several presentations. Further efforts in this area are required, for instance in developing scattering models capable of predicting cross-polar radar backscatter and in documenting the accuracy of existing co-polar scattering models using high quality *in situ* measurement databases. We need a clearer picture about what depth in the soil is being sensed, for a given sensor configuration, as this significantly affects the interpretation and value of the measurement. The gap between research into soil parameter retrieval and applications also needs to be closed. A step in this direction could be the benchmarking of existing retrieval algorithms based on criteria such as accuracy, robustness, computational complexity and the inclusion of prior information. This would provide guidance to the user community in moving beyond the current use primarily of empirical regression to recover soil moisture. The extension of locally-developed retrieval algorithms to the regional scale and a tighter integration of soil moisture retrieval techniques with land-surface process models through assimilation constitute important research areas, especially since the demand for operational soil moisture estimates at these scales is very strong.

Hazards and DEMs

This session showed how SAR can contribute to hazard management in three ways: preparedness, monitoring/forecasting and post-event relief. Interferometry has proved to be a critically important technology for this purpose. Initial concerns about the degradation of interferograms by atmospheric perturbations have largely been swept away in urban areas by the development of the permanent scatterer technique. This is effectively operational as a means of detecting subsidence, and allows tectonic strain rates to be mapped when the associated motion is not vertical. Extending the technique to non-urban areas is highly desirable. L band seems to offer this possibility: positive results on surface motion in vegetated/forest areas were displayed.

Disasters often occur in cloudy conditions, making SAR a preferred technology. This capability has been exploited successfully to detect forest storm damage, avalanche and flood by applying proper problem analysis: the detection methods must be matched to the physics. However, success varies from case to case. For floods, much can be gained by assimilating the data into a process model. Timing is very important in many disaster scenarios, as regards the satellite observing the event at all (the revisit time) and seeing it under the necessary conditions (e.g, flood is hard to detect in strong winds). SAR can also be useful in improving general knowledge about land cover and conditions, and susceptibility to hazards.

Interferometry is also, of course, a critical technology in producing DEMs, and methods to quantify the accuracy in InSAR DEM are well advanced. There are also significant advantages in considering InSAR in conjunction with radargrammetry.

Snow and ice

SAR is an attractive technology for remote sensing of snow and ice because of its all-weather operation, independent of solar illumination (particularly important at high latitudes) and its sensitivity to physical properties of these targets. Current satellite SARs show little sensitivity to dry snow, but methods to detect snow-covered area (using the wet/dry change in backscatter) have been developed and applied operationally, taking account of topography and vegetation cover, in the latter case by making use of forest scattering models. Looking more to the future, experimental methods to infer snow water equivalent (SWE), snow-covered area and snow liquid water content have been developed using fully polarimetric and multi-frequency SAR data. Interferometric coherence over one day intervals allows clear discrimination of wet snow from bare ground, and preliminary studies with airborne InSAR indicate possibilities also for dry snow mapping. A particularly interesting prospect is the development of a spaceborne 17 GHz polarimetric SAR for measuring SWE in dry snow, and to assess the effects of layering in the snowpack, although validated inversion methods have not yet been demonstrated. An important development has been the assimilation of SAR data (along with optical remote sensing data) into process models for the hydrology of basins dominated by meltwater and for glacier mass balance. Interferometric SAR has also become a powerful tool in mapping glacier dynamics, both in remote areas where there is little supporting data, and as an adjunct to more detailed field measurements for more accessible glaciers. Full exploitation of the potential of this tool requires major efforts in data handling and analysis, but large scale maps of glacier topography and ice surface velocity have been produced.

Process modelling. This important session brought together many strands implicit in the more specific themes of the conference and expressed a general philosophy about the direction in which SAR applications research should be heading. The keynote paper outlined the very significant recent advances in the use of SAR data to support hydrological modelling. The models provide a framework within which SAR can be assimilated, along with other forms of data. They also point the way forward: soil moisture was identified as the most important quantity needed by the models, and one where further effort is unquestionably needed. The other presented papers were more conceptual, and all essentially concerned with the part SAR and remote sensing can play in carbon cycle monitoring and the Kyoto process. The major conclusions were that SAR has clear contributions to make to this problem, but we are at present far away from having the methods and unified data structures needed before these contributions can be realised. Now is, however, a special time, when political will is on the side of science in wanting answers to important, interesting and difficult questions. It is therefore a golden opportunity for the field, and one we ignore to our cost.

Participants List

Sophie Allain
University of Rennes I
Lab. ART, Radar and Polarimetry Group
F.R.W. CNRS 2272
Universite de Rennes 1 - UFR S.P.M.
Campus de Beaulieu
Bat. 11.C, Bureau 106
263 Avenue General Leclerc
CS 74205 Rennes Cedex 35042
France

Tel: +33 299 286 712
Fax: +33 299 286963
Email: sophie.allain@univ-rennes1.fr

Craig Anderson
BAE Systems ATC
Space Systems Group
Advanced Technology Centres
West Hanningfield Road
Chelmsford CM2 8HN
UK

Tel: +44 (0)1245 242 662
Fax: +44 (0)1245 475 244
Email: craig.anderson@baesystems.com

Jan Askne
Chalmers University of Technology
Department of Radio and Space Science
Rannvagen 6
Gothenburg S-412 96
Sweden

Tel: +46 (0)31 772 1843
Fax: +46 (0)31 772 1884
Email: askne@rss.chalmers.se

Heike Bach
VISTA Geowissenschaftliche Fernerkundung GmbH
Luisenstr. 45
Munich D-80333
Germany

Tel: +49 89 523 89 802
Fax: +49 89 523 89 804
Email: bach@vista-geo.de

Nicolas Baghdadi
Bureau de Recherche en Géologie Minière (BRGM)
Land Use Planning
Service Amenagement et Risques Naturels (ARN)
3 Avenue C. Guillemin
B.P. 6009
Orléans Cedex 2 45060
France

Tel: +33 2 38 64 32 02
Fax: +33 2 38 64 33 99
Email: n.baghdadi@brgm.fr

Heiko Balzter
Centre for Ecology and Hydrology
Section for Earth Observation
Monks Wood
Abbots Ripton
Huntingdon PE28 2LS
UK

Tel: +44 (0)1487 772 471
Fax: +44 (0)1487 773 467
Email: heiko.balzter@ceh.ac.uk

Ursula Benz
Definiens A.G.
Rindermarkt 7
Munich D-80331
Germany

Tel: +49 89231180 46
Fax: +49 89231180-90
Email: ubenz@definiens.com

Xavier Blaes
Université Catholique de Louvain
Department of Environmental Sciences - Geomatics
Place Croix du Sud (BTE 16)
B-1348 Louvain-la-Neuve
Belgium

Tel: +32 10 47 26 13
Fax: +32 10 47 88 98
Email: blaes@biom.ucl.ac.be

Maurice Borgeaud
European Space Agency
Electromagnetics Division
TOS-EEP, ESTEC
PO Box 299
Noordwijk 2200 AG
The Netherlands

Tel: +31 71 565 4830
Fax: +31 71 565 4999
Email: maurice.borgeaud@esa.int

Rob Bryant
University of Sheffield
Dept. of Geography
Geography Building
Winter Street
Sheffield S10 2TN
UK

Tel: +44 114 222 7966
Fax: +44 114 279 7912
Email: r.g.bryant@sheffield.ac.uk

Elaine Chapin
Jet Propulsion Laboratory
Radar Science and Engineering Section
California Institute of Technology
4800 Oak Grove Drive M/S 300-235
Pasadena
CA 91109-8099
USA

Tel: +1 818 354 0497
Fax: +1 818 393 3077
Email: elaine.chapin@jpl.nasa.gov

Shane Cloude
AEL Consultants
26 Westfield Avenue, Cupar
Fife KY15 5AA
Scotland, UK

Tel: +44 1334 653 958
Fax: +44 1334 653 958
Email: scloude@aelc.demon.co.uk

Ralph Cordey
BAE SYSTEMS Advanced Technology Centre
Great Baddow
Chelmsford CM2 8HN
UK

Tel: +44 1245 242651
Fax: +44 1245242103
Email: ralph.cordey@baesystems.com

Peter Dampney
ADAS Boxworth
Research Division
Adas Boxworth Research Centre
Battlegate Road
Boxworth
Cambridge CB3 8NN
UK

Tel: +44 1954 268 213
Fax: +44 1954 267 659
Email: peter.dampney@adas.co.uk

Malcolm Davidson
Centre d'Etudes Spatiales de la BIO-sphere (CESBIO)
18 Ave. Edouard Belin
F-31401 Toulouse
France

Tel: +33 561 55 85 84
Fax: +33 561 55 85 00
Email: davidson@cesbio.cnes.fr

Pierre Defourny
Catholic University of Louvain
Department of Environmental Sciences
Place Croix du Sud 2 (BTE 16)
B-1348 Louvain-la-Neuve
Belgium

Tel: +32 10 47 23 74
Fax: +32 10 47 99 98
Email: defourny@mila.ucl.ac.be

Fabio Del Frate
Tor Vergata University
Dipartimento Informatica Sistemi e Produzione (DISP)
Via Tor Vergata 110
I-00133 Rome
Italy

Tel: +39 06 725 97421
Fax: +39 06 725 97460
Email: delfrate@disp.uniroma2.it

Marcus Engdahl
Helsinki University of Technology
Laboratory of Space Technology
P.O. Box 3000
FIN-02015 Helsinki
Finland

Tel: +358 9 4512 170
Fax: +358 9 4512 898
Email: mengdahl@avasun.hut.fi

Leif Eriksson
Friedrich Schiller University
Institut fur Geographie
Löbdergraben 32
D-07743 Jena
Germany

Tel: +49 3641 948 878
Fax: +49 3641 948 852
Email: leif.eriksson@geogr.uni-jena.de

Norbert Etzrodt
Georg-August University Goettingen
Institute for Geography
Goldschmidtstr. 5
D-37977 Goettingen
Germany

Tel: +49 551 398 015
Fax: +49 551 391 2139
Email: netzrod1@gwdg.de

Diego Fernández-Prieto
European Space Agency (ESA-ESRIN)
Earth Observation Applications Department
Via Galileo Galilei, PO Box 64
I-00044 Frascati (Rome)
Italy

Tel: +39 06 941 806 76
Fax: +39 06 941 805 52
Email: diego.fernandez@esa.int

Paolo Ferrazzoli
Tor Vergata University
Facolta di Ingegneria, Dipartimento di Informatica
Sistemi e Produzione
Via di Tor Vergata 110
I-00133 Rome
Italy

Tel: +39 06 725 97420
Fax: +39 06 725 974 60
Email: ferrazzoli@disp.uniroma2.it

Laurent Ferro-Famil
University of Rennes I
Laboratoire Antennes Radar Telecom
F.R.E. CNRS 2272
Universite de Rennes 1 - UFR S.P.M.
Campus de Beaulieu
Bat. 11.D, Bureau 118
263 Avenue General Leclerc
CVS 74205
Rennes Cedex 35042
France

Tel: +33 2 99 28 67 12
Fax: +33 2 99 28 69 63
Email: laurent.ferro-famil@univ-rennes1.fr

Annamaria Gatti
Consiglio Nazionale delle Ricerche
Istituto de Tecnologia Informatica Spaziale (ITIS)
c/o CGS-ASI
Localita Terlecchia
I-75100 Matera
Italy
Tel: +39 0835 377 225
Fax: +39 0835 339 027
Email: annamaria.gatti@itis.mt.cnr.it

Jose Gomez-Dans
University of Sheffield
Sheffield Centre for Earth Observation Science
(SCEOS)/Dept. of Electronic & Electrical Engineering
Sir Frederick Mappin Building
Mappin Street
Sheffield S1 3JD
UK

Tel: +44 114 222 5582
Fax: +44 114 272 2097
Email: J.L.Gomez-Dans@sheffield.ac.uk

Mª Del Carmen Gonzalez-Sampedro
University of Valencia
Faculty of Physics, Department of Thermodynamics
Dr Moliner 50
Burjassot
E-46100 Valencia
Spain

Tel: +34 96 398 31 13
Fax: + 34 96 398 33 85
Email: mcgonzal@uv.es

Gilles Grandjean
BRGM
Geophysics Dept.
ARN
BP 6009
F-45060 Orléans
France

Tel: +33 2 38 64 34 75
Fax: +33 2 38 64 33 61
Email: g.grandjean@brgm.fr

Stéphane Guillaso
University of Rennes I UFR S.P.M.
Lab. ART, Radar and Polarimetry Group
F.R.W. CNRS 2272
Campus de Beaulieu
Bat. 11.C,
263 Avenue General Leclerc
CS 74205
Rennes Cedex 35042
France

Tel: +33 299 28 67 12
Fax: +33 299 286 963
Email: stephane.guillaso@univ-rennes1.fr

Irena Hajnsek
German Aerospace Centre (DLR)
Institute of Radio Frequency Technology
and Radar Systems
PO Box 1116
D-382230 Wessling
Germany

Tel: +49 8153 28 2363
Fax: +49 8153 28 1449
Email: irena.hajnsek@dlr.de

Martti Hallikainen
Helsinki University of Technology
Laboratory of Space Technology
PO Box 3000
FIN-02015 HUT
Finland

Tel: +358 9 451 2371
Fax: +358 9 451 2898
Email: martti.hallikainen@hut.fi

Volker Hochschild
Friedrich-Schiller-Universitaet Jena
Institut fuer Geographie
Loebdergraben 32
D-07743 Jena
Germany

Tel: +49 3641 948 855
Fax: +49 3641 948 852
Email: c5voho@geogr.uni-jena.de

Dirk Hoekman
Wageningen University
Dept. of Environmental Sciences
Nieuwe Kanaal 11
6709 PA Wageningen
The Netherlands

Tel: +31 317 482894
Fax: +31 317 484885
Email: dirk.hoekman@users.whh.wau.nl

Haydee Karszenbaum
Institute of Astronomy and Space Physics (IAFE)
Dept. of Remote Sensing
Pabellon IAFE
Ciudad Universitaria
C.C. 67 Suc. 28
Buenos Aires 1428
Argentina

Tel: +54 11 4783 2642 (int. 225)
Fax: +54 11 4786 8114
Email: haydeek@iafe.uba.ar

Gordon Keyte
Qinetiq
Bldg A8 room 1056
Cody Technology Park
Ively Road
Farnborough
Hants GU14 OLX
UK

Tel: +44 1252 393 026
Fax: +44 1252 396 336
Email: gkeyte@qinetiq.com

Thuy Le Toan
Centre d'Etudes Spatiales de la Biosphere (CESBIO)
18 Avenue Edouard Belin
Toulouse cedex 4 31401
France

Tel: +33 561 556671
Fax: +33 561 558500
Email: Thuy.Letoan@cesbio.cnes.fr

Richard Lucas
University of Wales, Aberystwyth
Institute of Geography and Earth Sciences
Aberystwyth, Ceredigion SY23 3DB
UK

Tel: +44 1970 622 612
Fax: +44 1970 622659
Email: rml@aber.ac.uk

Cozmin Lucau
Université Catholique de Louvain
Department of Environmental Sciences-Geomatics
Place Croix du Sud (BTE 16)
B-1348 Louvain-la-Neuve
Belgium

Tel: +32 10 47 26 13
Fax: +32 10 47 88 98
Email: lucau-danila@biom.ucl.ac.be

Adrian Luckman
University of Wales, Swansea
Department of Geography
Singleton Park
Swansea SA2 8PP
UK

Tel: +44 1792 295 524
Fax: +44 1792 295 955
Email: a.luckman@swansea.ac.uk

Giovanni Macelloni
IROE- CNR
Remote Sensing Department
via panciatchi 64
I-50127 Firenze
Italy

Tel: +39 055 423 5213
Fax: +39 055 410 893
Email: giovanni@iroe.fi.cnr.it

Terhikki Manninen
Technical Research Center of Finland
Dept of Automation, Measurement Technology
Otakaari 7
PO Box 1304
Espoo FIN-02044 VTT
Finland

Tel: +358 9 456 6285
Fax: +358 9 456 7029
Email: terhikki.manninen@vtt.fi

Jean-Michel Martinez
CESBIO
18 Avenue Edouard Belin
F-31055 Toulouse
France

Tel: +33 561 55 66 71
Fax: +33 561 55 85 00
Email: martinez@cesbio.cnes.fr

Francesco Mattia
Consiglio Nazionale delle Ricerche
Istituto di Tecnologia Informatica Spaziale (ITIS)
c/o CGS-ASI, Loc. Terlecchia
I-75100 Matera
Italy

Tel: +39 835 377 282
Fax: +39 835 33 90 27
Email: mattia@itis.mt.cnr.it

Heather McNairn
Canada Centre for Remote Sensing
Natural Resources Canada
588 Booth Street
Ottawa, Ontario K1A 0Y7
Canada

Tel: 613 947 1815
Fax: 613 947 1385
Email: Heather.McNairn@CCRS.nrcan.gc.ca

Pierre Melon
Centre d'Etudes Spatiales de la BIO-sphere (CESBIO)
18 Ave. Edouard Belin
F-31401 Toulouse
France

Tel: +33 561 55 85 12
Fax: +33 561 55 85 00
Email: pierre.melon@cesbio.cnes.fr

Tony Milne
University of New South Wales
Dept. of Geography
School of Geography
Sydney 2052
Australia

Tel: +61 2 9385 2731
Fax: +61 2 9451 4628
Email: t.milne@unsw.edu.au

Keith Morrison
Qinetiq, Radar
St Andrew's Road
Malvern, Worcs. WR14 3PS
UK

Tel: +44 1684 897 107
Fax: +44 1684 894 185
Email: kmorrison@qinetiq.com

Maxim Moskalevsky
Institute of Geography, Russian Academy of Sciences
Dept. of Glaciology
Staromonetny Pereulok 29
Moscow 109017
Russia

Tel: +7 095 959 0032
Fax: +7 095 959 0033
Email: moskal@online.ru

Eoin O Clerigh
Wiesenpfad 3
D-644055 Fischbachtal
Germany

Tel: +49 170 904 2336
Fax: +49 6166 920 115
Email: oclerigh@eumetsat.de

Simonetta Paloscia
CNR-IROE
Remote Sensing
via Pamciatichi 64
I-50127 Firenze
Italy

Tel: +39 055 423 5220
Fax: +39 055 423 5290
Email: paloscia@iroe.fi.cnr.it

Paolo Pampaloni
CNR-IROE
Remote Sensing
via Panciatichi 64
I-50127 Florence
Italy

Tel: +39 055 423 5205
Fax: +39 055 423 5290
Email: pampa@iroe.fi.cnr.it

Tim Pearson
Remote Sensing Applications Consultants Ltd.
2 Prospect Place, Mill Lane
Alton
Hants GU34 2SX
UK

Tel: +44 1420 88777
Fax: +44 1420 87111
Email: tim@rsacl.co.uk

Marcela Quinones
Wageningen Agricultural University
Dept. of Environmental Sciences
Nieuwe Kanaal 11
6709 PA Wageningen
The Netherlands

Tel: +31 317 482 765
Fax: +31 317 484 885
Email: marcela.quinones@users.whh.wau.nl

Ghislain Picard
Centre d'Etudes Spatiales de la Biosphere (CESBIO)
18 Ave. Edouard Belin
F-31401 Toulouse
France

Fax: +33 561 55 85 00
Email: ghislain.picard@cesbio.cnes.fr

Wolfgang Rack
Alfred-Wegener-Institute for Polar & Marine Research
PO Box 120161
D-27515 Bremerhaven
Germany

Tel: +49 471 4831 1642
Fax: +49 471 4831 1149
Email: wrack@awi-bremerhaven.de

Corinna Priezsch
Infoterra GmbH, EO Application Department
An der B31
D-88039 Friedrichshafen
Germany

Tel: +49 7545 83197
Fax: +49 7545 85650
Email: Corinna.Prietzsch@astrium-space.com

Sylvie Remondiere
ESRIN/ESA
Earth Exploitation Development and Project Division
Via Galileo Galilei, PO Box 64
I-00044 Frascati (Rome)
Italy

Tel: +39 06 941 80 686
Fax: +39 06 941 80 622
Email: Sylvie.Remondiere@esa.int

Marco Quartulli
DLR, IMF-BW
Oberpfaffenhofen
D-82234 Wessling
Germany

Tel: +49 8153 28 2451
Fax: +49 8153 28 1444
Email: marco.quartulli@dlr.de

Tanja Riedel
Friedrich-Schiller-University
Department of Geography
Lobdergraben
D-07740 Jena
Germany

Tel: +49 3641 948875
Email: c5tari@geogr.uni-jena.de

Shaun Quegan
University of Sheffield
Sheffield Centre for Earth Observation Science
(SCEOS)
Hicks Building, Hounsfield Road
Sheffield S3 7RH
UK

Tel: +44 114 222 3778
Fax: +44 114 222 3809
Email: s.quegan@sheffield.ac.uk

Fabio Rocca
Politecnico di Milano
Dipartimento di Elettronica ed Informazione
Piazza Leonardo da Vinci 32
I-20133 Milano
Italy

Tel: +39 02 2399 3573
Fax: +39 02 2399 3413
Email: rocca@elet.polimi.it

Ake Rosenqvist
NASDA Earth Observation Center, EORC
Triton Square X-Tower 22F
1-8-10 Harumi, Chuo-ku
Tokyo 104-6023
Japan

Tel: 00 813 6221 9074
Fax: 00 813 6221 9192
Email: ake.rosenqvist@nasda.go.jp

Helmut Rott
University of Innsbruck
Institut für Meteorologie und Geophysik
Innrain 52
A-6020 Innsbruck
Austria

Tel: +43 512 507 5455 (5499)
Fax: +43 512 507 2924
Email: helmut.rott@uibk.ac.at

Michel Rouzé
CNES
DPI/EOT
18 Avenue Edouard Belin
Toulouse Cedex 4 31401
France

Tel: +33 5 61 28 25 61
Fax: +33 5 61 27 40 13
Email: michel.rouze@cnes.fr

Paul Saich
University College London
Department of Geography
26 Bedford Way
London WC1H 0AP
UK

Tel: +44 20 7679 4282
Fax: +44 20 7679 4293
Email: psaich@geog.ucl.ac.uk

Aurélie Sand
CNES
Earth Science and Applications
DPI/EOT
18 Avenue Edouard Belin
Toulouse 31401 Cedex 4
France

Tel: +33 561 27 43 89
Fax: +33 561 28 28 99
Email: aurelie.sand@cnes.fr

Giuseppe Satalino
CNR-IESI
via Amendola 166/5
I-70126 Bari
Italy

Tel: +39 080 548 1612
Fax: +39 080 548 4311
Email: satalino@iesi.ba.cnr.it

Christiane Schmullius
Friedrich-Schiller-University (FSU)
Geoinformatics and Remote Sensing
Loebdergraben 32
D-07743 Jena
Germany

Tel: +49 3641 948877
Fax: +49 3641 948852
Email: c.schmullius@geogr.uni-jena.de

Adrian Schubert
University of Zürich
Remote Sensing Laboratories, Dept. of Geography
Winterthurerstr. 190
CH-8057 Zürich
Switzerland

Tel: +41 1 635 6523
Fax: +41 1 635 6842
Email: schubert@geo.unizh.ch

Jiancheng Shi
University of California, Santa Barbara
Inst. for Computational Earth System Science (ICESS)
Santa Barbara
CA 93016
USA

Tel: +1 805 893 2309
Fax: +1 805 893 2578
Email: shi@icess.ucsb.edu

Maxim Shoshany
Bar-Ilan University
Geography Department
52900 Ramat-Gan
Israel

Tel: +972 3 531 8340
Fax: +972 3 534 4430
Email: m_shoshany@hotmail.com

Henning Skriver
Technical University of Denmark
Oersted-DTU
Oersteds Plads
Building 348
DK-2800 Lyngby
Denmark

Tel: +4545 253792
Fax: +4545 931634
Email: hs@oersted.dtu.dk

Gary Smith
Chalmers University of Technology
Department of Radio and Space Science
SE-412 96 Göteborg
Sweden

Tel: +46 31 772 1844
Fax: +46 31 772 1884
Email: smith@rss.chalmers.se

Krystyna Stankiewicz
Institute of Geodesy and Cartography
Remote Sensing Department
ul. Jasna 2/4
00-950 Warsaw
Poland

Tel: +48 22 827 76 13
Fax: +48 22 827 03 28
Email: krystyna.stankiewicz@igik.edu.pl

Tazio Strozzi
Gamma Remote Sensing
Thunstrasse 130
Muri BE 3074
Switzerland

Tel: +41 31 951 70 05
Fax: +41 31 951 70 08
Email: strozzi@gamma-rs.ch

Juan C. Suárez Mínguez
Forestry Commission, Silviculture
Northern Research Station
Roslin, Midlothian EH25 9SY
Scotland, UK

Tel: +44 131 445 2176
Fax: +44 131 445 5124
Email: juan.suarez@forestry.gsi.gov.uk

Ruandha Agung Sugardiman
Wageningen University
Department of Environmental Sciences
Water Resources Nieuwe Kanaal 11
6709 PA Wageningen
The Netherlands

Tel: +31 317 483 576
Fax: +31 317 484 885
Email: ruandha.sugardiman@users.whh.wau.nl

Tal Svoray
Ben-Gurion University of the Negev
Dept. of Geography & Environmental Development
Dept. of Information Systems Engineering
PO Box 653
84105 Beer-Sheva
Israel

Tel: +972 8 647 2002
Fax: +972 8 6472 821
Email: tsvoray@bgumail.bgu.ac.il

Christian Thiel
Friedrich-Schiller University
Institute of Geography, Geoinformatics & Remote Sensing
Loebdergraben 32
D-07743 Jena
Germany

Tel: +49 3641 948875
Fax: +49 3641 800 1972
Email: c5thch@geogr.uni-jena.de

Donald Ugsang
Asian Institute of Technology
Asian Centre for Research on Remote Sensing (ACRoRS)
Klong Luang
PO Box 4
Pathumthani 12120
Thailand

Tel: +66 2 524 6148
Fax: 66 2 524 6147
Email: donald@ait.ac.th

Kemal Unggul Prakoso
Wageningen University
Department of Environmental Sciences,
Sub-department of Water Resources
Nieuwe Kanaal 11
6709 PA Wageningen
The Netherlands

Tel: +31 317 483576
Fax: +31 317 484885
Email: Kemal.Unggulprakoso@users.whh.wau.nl

Laurent Vanhalle
Belgian Ministry of Agriculture
CTS
Rue de Liroux 9
B-5030 Bembloux
Belgium

Tel: +32 81 626 587
Fax: +32 81 626 598
Email: laurent.vanhalle@cmlag.fgov.be

Geoff Wadge
University of Reading
Environmental Systems Science Centre (ESSC)
Harry Pitt Building
Reading RG6 6AB
UK

Tel: +44 1189 318 741
Fax: +44 1189 316 413
Email: gw@mail.nerc-essc.ac.uk

Wolfgang Wagner
Vienna University of Technology
Institute for Photogrammetry and Remote Sensing
Gusshausstrasse 27-29
A-1040 Vienna
Austria

Tel: +43 1 58801 12201
Fax: +43 1 58801 12299
Email: ww@ipf.tuwien.ac.at

Andreas Wiesmann
Gamma Remote Sensing
Risk and Hazard Dept.
Thunstrasse 130
Muri BE 3074
Switzerland

Tel: +41 31 951 7005
Fax: +41 31 951 7008
Email: wiesmann@gamma-rs.ch

Mark Williams
DSTL
R016 St Andrews Road
Great Malvern
Worcs WR14 3PS
UK

Tel: +44 1684 771398
Fax: +44 1684 894 481
Email: mlwilliams2@dstl.gov.uk

Trish Wright
BAE Systems ATC
Space Systems Group
Advanced Technology Centres
West Hanningfield Road
Chelmsford CM2 8HN
UK

Tel: +44 1245 242 668
Fax: +44 1245 475 244
Email: patricia.wright@baesystems.com

Gary Wright
Macaulay Institute
Land Use Systems
Craigiebuckler
Aberdeen AB15 8QH
Scotland, UK

Tel: +44 1224 318 611 ext 2231
Fax: +44 1224 311 556
Email: g.wright@mluri.sari.ac.uk

Late additions:

Steffen Gruenler
Friedrich-Schiller-University (FSU)
Geoinformatics and Remote Sensing
Loebdergraben 32
D-07743 Jena
Germany

Tel: +49 3641 948883
Fax: +49 3641 948852
Email: c8grst@geogr.uni-jena.de

Carsten Pathe
Friedrich-Schiller-University (FSU)
Geoinformatics and Remote Sensing
Loebdergraben 32
D-07743 Jena
Germany

Tel: +49 3641 948883
Fax: +49 3641 948852
Email: c5paca@geogr.uni-jena.de

Hendrik Zwenzner
Friedrich-Schiller-University (FSU)
Geoinformatics and Remote Sensing
Loebdergraben 32
D-07743 Jena
Germany

Tel: +49 3641 948883
Fax: +49 3641 948852
Email: c7zwhe@geogr.uni-jena

European Space Agency
Agence spatiale européenne

Contact: ESA Publications Division
c/o ESTEC, PO Box 299, 2200 AG Noordwijk, The Netherlands
Tel (31) 71 565 3400 - Fax (31) 71 565 5433